

Extraction of Single and Double Differential Cross-Sections on Argon for CC1 μ 2p0 π Event Topologies in the SBND

Emilio Peláez Cisneros

August 15, 2024

Abstract

The precise measurement of cross-sections for a variety of interactions is critical to the success of upcoming flagship neutrino experiments. Of special interest are neutrino interactions that leave the nucleus in a 2-particle 2-hole state (2p2h). This note will present cross-section measurements for the production of 2p2h states on Argon. Using SBND data collected from the **period** of operation, we select events corresponding to a charged-current ν_μ interaction that left the Argon nucleus in a 2p2h state. These interactions produce a topology with one muon and two protons in the final state (CC1 μ 2p0 π). This analysis targets both single differential and double differential cross-section measurements for CC1 μ 2p0 π event topologies in a variety of kinematic variables. Comparisons are made to a set of theoretical models that explore different cross-section modeling configurations. Code for this analysis is available on [GitHub](#).

Contents

1	Introduction and motivation	3
2	Generator analysis	3
2.1	Signal definition	3
2.2	Generators	3
2.3	Variables definition	4
2.4	Pre-FSI events	17
2.5	Double differential plots	20
2.6	Pure MEC events	31
3	SBND analysis	34
3.1	Fiducial volume	34
3.2	Signal definition	34
3.3	Variable plots	37
3.4	Interaction and topology breakdown	40
3.5	Signal efficiency	45
3.6	Migration and response matrices	48
3.7	Systematics	55
3.8	Wiener-SVD unfolding	59
3.9	Closure test	62
3.10	Event rate uncertainties	65
4	Cross-section results	68
4.1	Cross-section uncertainties	68
5	Fake data studies	71
5.1	MEC 2x weight	71
5.2	QE 2x weight	71

6 Appendices	76
6.1 Cross section systematics	76
6.2 Flux systematics	343
6.3 Statistical systematics	435
6.4 POT	439
6.5 Number of targets	443
6.6 Detector	447
6.7 Reinteraction	451
7 References	455

1 Introduction and motivation

2 Since many current and next generation neutrino oscillation experiments will utilize dense nuclear targets,
3 such as liquid argon (LAr), it is critical to characterize the impact of nuclear effects on neutrino cross-sections.
4 One area of interest are neutrino events that eject 2 nucleons from the nucleus, leaving it with 2 holes: known
5 as 2-particle 2-hole states (2p2h). The general picture is that the neutrino has a charged-current interaction
6 with a neutron in the nucleus, producing a proton with significant momentum; this proton interacts with
7 another proton, producing the 2p2h state. While the majority of 2p2h states are caused by Meson Exchange
8 Currents (MEC) [15], some nuclear effects, such as Short-Range Nucleon-Nucleon correlations (SRC) [10],
9 can also produce these states. In an accelerator-based liquid argon time projection chamber (LArTPC)
10 experiment, such as SBND, a charged-current (CC) muon neutrino (ν_μ) interaction that results in a 2p2h
11 state would have a final state topology of 1 muon, 2 protons, and no charged or neutral pions. While
12 there are existing measurements of CC1 μ 2p0 π events on argon, the analyses were statistically limited and
13 no cross-sections were extracted [1, 19]. There was a previous report with single differential cross-section
14 measurements from the MicroBooNE detector [20], but this document presents the first double differential
15 cross-section measurements of CC1 μ 2p0 π topologies on argon, using data collected from the period of SBND
16 operations.

17 2 Generator analysis

18 2.1 Signal definition

19 We choose charged-current muon neutrino interactions that result in one muon, two protons, no charged pions
20 with $P_\pi > 70$ MeV/c, no neutral pions or heavier mesons, and any number of neutrons. These interactions
21 are denoted as CC1 μ 2p0 π . We require the momentum of the muon and protons to be in the following ranges
22 (in MeV/c):

$$100 < P_P < 1200 \quad 300 < P_\mu < 1000 \quad (1)$$

23 2.2 Generators

24 The following generators are used to create events, which are then discriminated using the signal definition
25 above: NuWro, GiBUU, NEUT, GENIE G18, GENIE AR23. Information about these generators is
26 summarized in Table 1.

Name	Generator/Configuration
G18	GENIE v3.0.6 G18_10a_02_11a
AR23	G18 with SuSAv2 MEC model
NuWro	NuWro 19.02.1
NEUT	NEUT v5.4.0
GiBUU	GiBUU 2021

Table 1: Generator and configuration data.

27 The GENIE configurations we used are:

- 28 (i) GENIE G18 [2, 3]: This modern model configuration uses the local Fermi gas (LFG) model [9],
29 the Nieves CCQE scattering prescription [23], which includes Coulomb corrections for the outgoing
30 muon [11], and random phase approximation (RPA) corrections [22]. Additionally, it uses the
31 Nieves MEC model [25], the KuzminLyubushkin-Naumov Berger-Sehgal RES [6, 28, 16], Berger-Sehgal
32 COH [7] and Bodek-Yang DIS [29] scattering models with the PYTHIA [26] hadronization part, and
33 the hA2018 FSI model [4].
- 34 (ii) GENIE AR23: Same as the G18 model configuration but using the SuSAv2 MEC model.

35 The alternative event generators are:

- 36 (i) NuWro [12]: Includes the LFG model [9], the Llewellyn Smith model for QE events [18], the Nieves
37 model for MEC events [24], the AdlerRarita-Schwinger formalism to calculate the Δ resonance explicitly [13],
38 the Berger-Sehgal (BS) COH [7] scattering model, an intranuclear cascade model for FSI [24],
39 and a coupling to PYTHIA [26] for hadronization.
- 40 (ii) NEUT [14]: Corresponds to the combination of the LFG model [8, 9], the Nieves CCQE scattering
41 prescription [23], the Nieves MEC model using a lookup table [25], the Berger Sehgal RES [6, 13, 5]
42 and BS COH [7] scattering models, FSI with medium corrections for pions [2, 3], and PYTHIA [26]
43 purposes.
- 44 (iii) GiBUU [21]: Uses similar models to GENIE, but they are implemented in a coherent way by solving
45 the Boltzmann-Uehling-Uhlenbeck transport equation [21]. The modeling includes the LFG model [9],
46 a standard CCQE expression [17], an empirical MEC model, and a dedicated spin dependent resonance
47 amplitude calculation following the MAID analysis [21]. The DIS model is from PYTHIA [26]. GiBUU's
48 FSI treatment propagates the hadrons through the residual nucleus in a nuclear potential consistent
49 with the initial state.

50 2.3 Variables definition

51 Given the momentum vectors for the leading proton \vec{p}_L , recoil proton \vec{p}_R , and muon \vec{p}_μ , we define several
52 variables. First, we define the momenta and opening angle of each variable, denoted as $|\vec{p}|$ and $\cos(\theta_{\vec{p}})$, with
53 the appropriate index for each momentum vector. These variables are plotted in Figure 1.

54 We also define variables relating the multiple momentum vectors. First, the opening angle between the
55 protons in the lab frame, given by

$$\cos(\theta_{\vec{p}_L, \vec{p}_R}) = \frac{\vec{p}_L \cdot \vec{p}_R}{|\vec{p}_L| |\vec{p}_R|}. \quad (2)$$

56 Then, the opening angle between the total proton momentum ($\vec{p}_{\text{sum}} = \vec{p}_L + \vec{p}_R$) and the muon, given by

$$\cos(\theta_{\vec{p}_\mu, \vec{p}_{\text{sum}}}) = \frac{\vec{p}_\mu \cdot \vec{p}_{\text{sum}}}{|\vec{p}_\mu| |\vec{p}_{\text{sum}}|}. \quad (3)$$

57 The momentum transverse to the direction of the neutrino beam, which we denote $\delta\vec{P}_T$ and is given by

$$\delta\vec{P}_T = \vec{p}_T^\mu + \vec{p}_T^L + \vec{p}_T^R. \quad (4)$$

58 For the transverse momentum, we will be interested in its magnitude $|\delta\vec{P}_T|$. Finally, the angular orientation
59 of the transverse momentum with respect to the transverse muon is defined as

$$\delta\alpha_T = \cos^{-1} \left(\frac{-\vec{p}_T^\mu \cdot \delta\vec{P}_T}{|\vec{p}_T^\mu| |\delta\vec{P}_T|} \right). \quad (5)$$

60 We plot the differential cross sections of these variables for the given generators in Figure 2. We can also
61 see the cross section by event type for all variables and all generators in Figures 3 to 12.

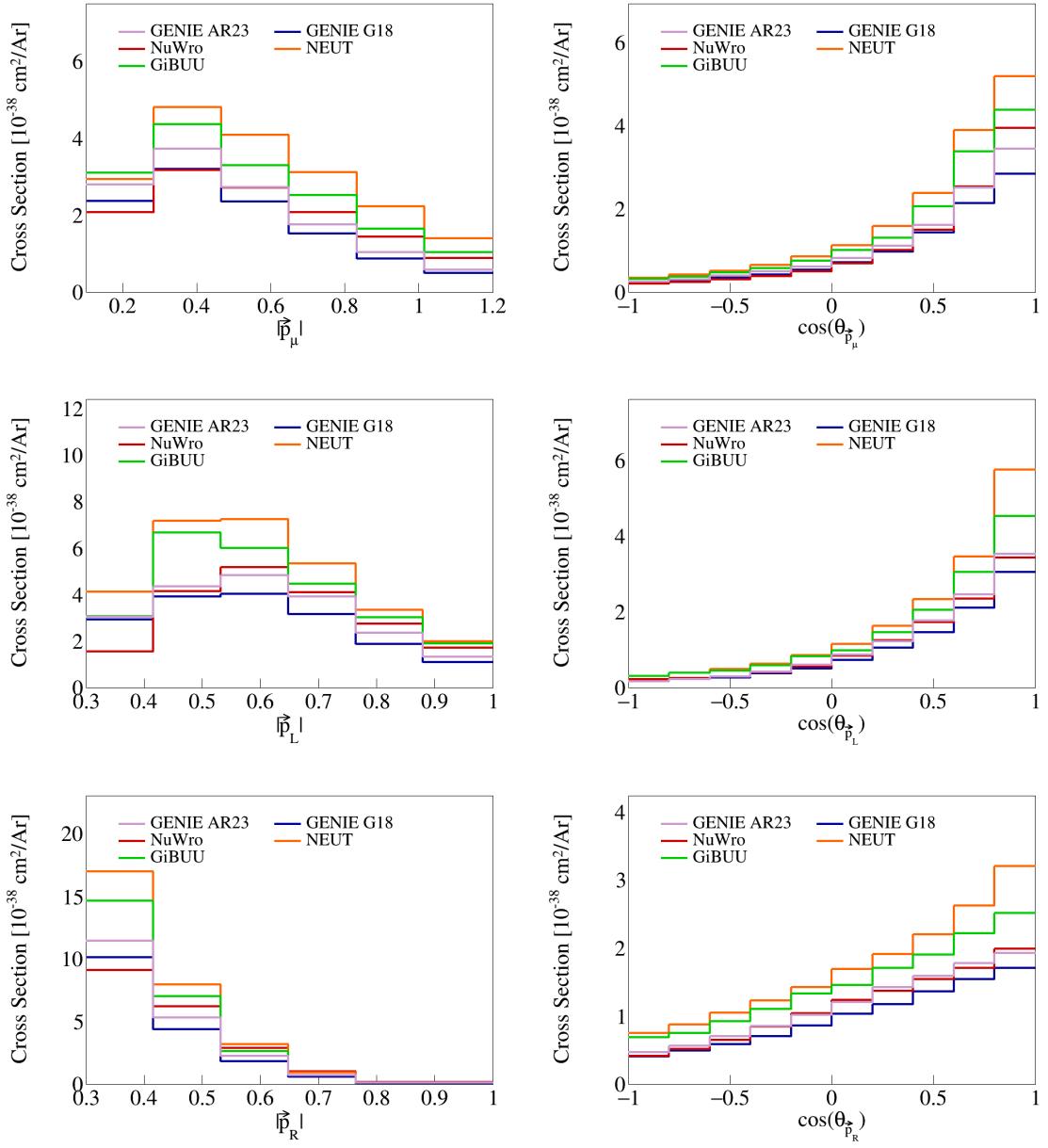


Figure 1: Cross sections for momentum and opening angles of individual particles.

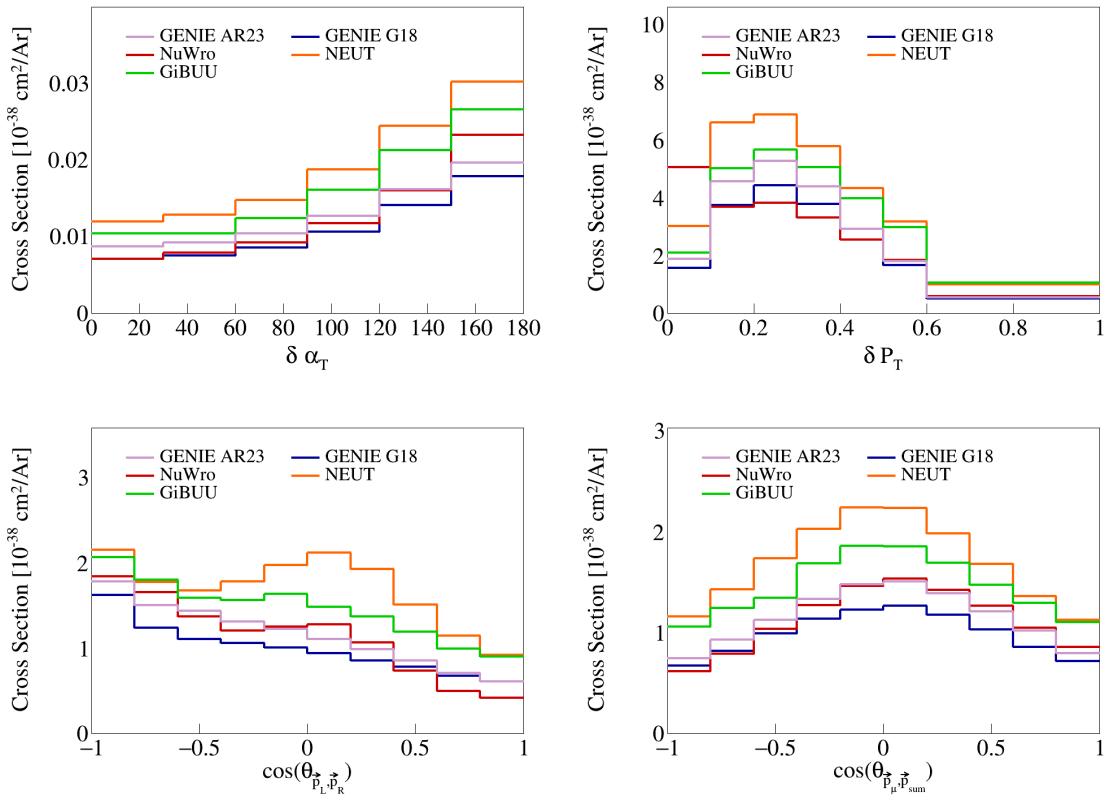


Figure 2: Cross sections for opening angles and transverse momentum.

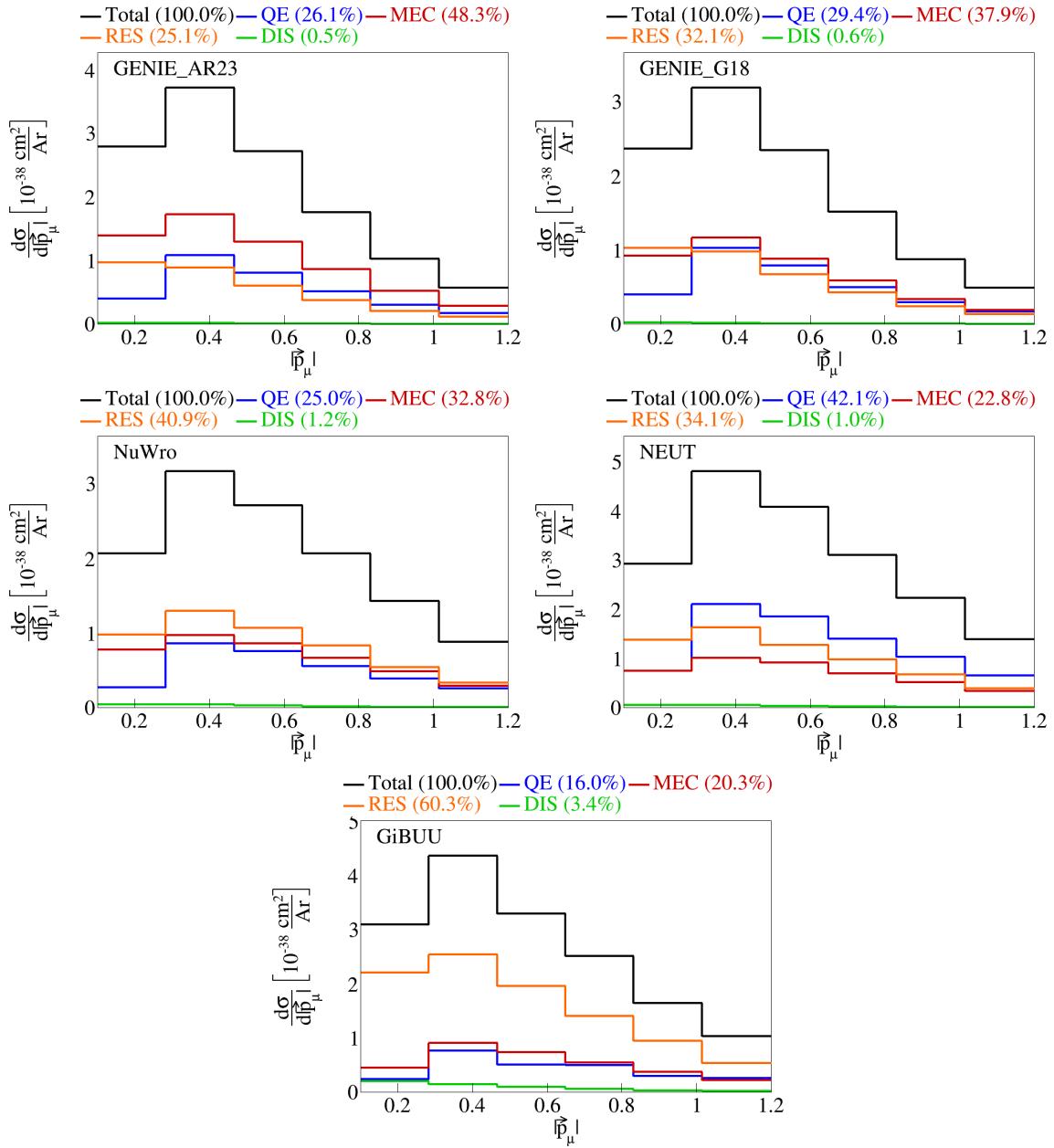


Figure 3: Event interaction breakdown for $|\vec{p}_\mu|$.

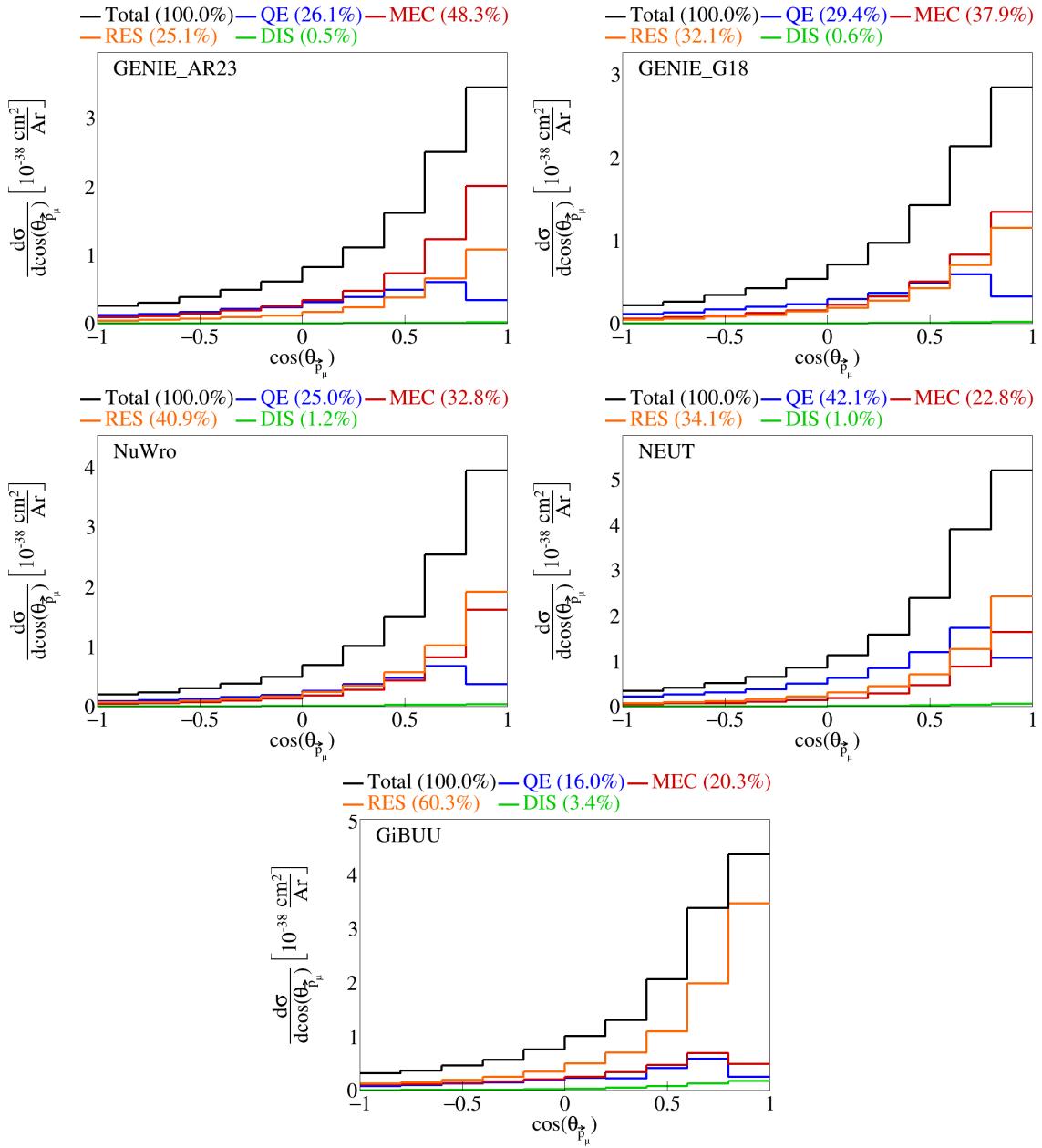


Figure 4: Event interaction breakdown for $\cos(\theta_{\vec{p}_\mu})$.

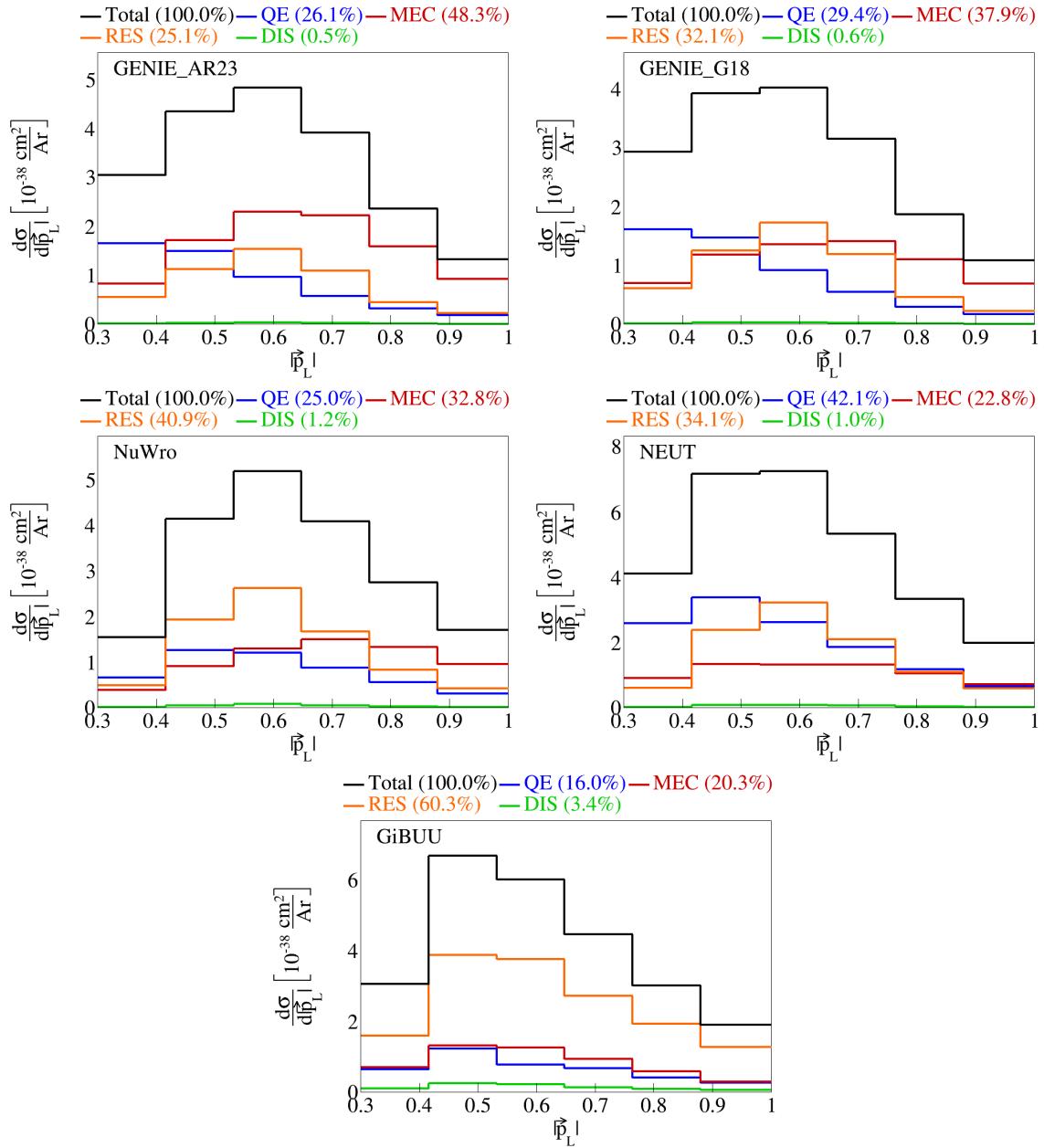


Figure 5: Event interaction breakdown for $|\vec{p}_L|$.

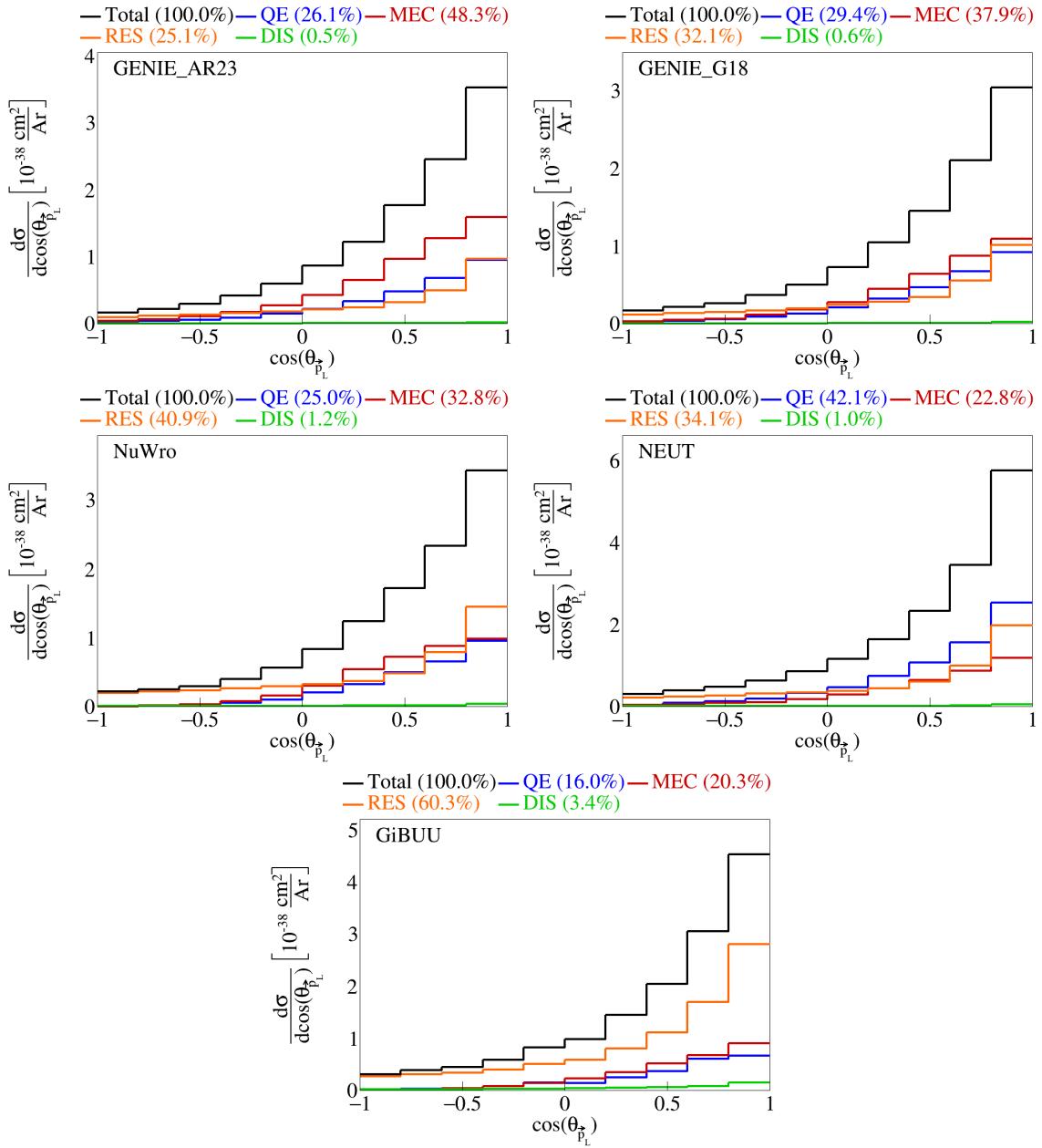


Figure 6: Event interaction breakdown for $\cos(\theta_{\vec{p}_L})$.

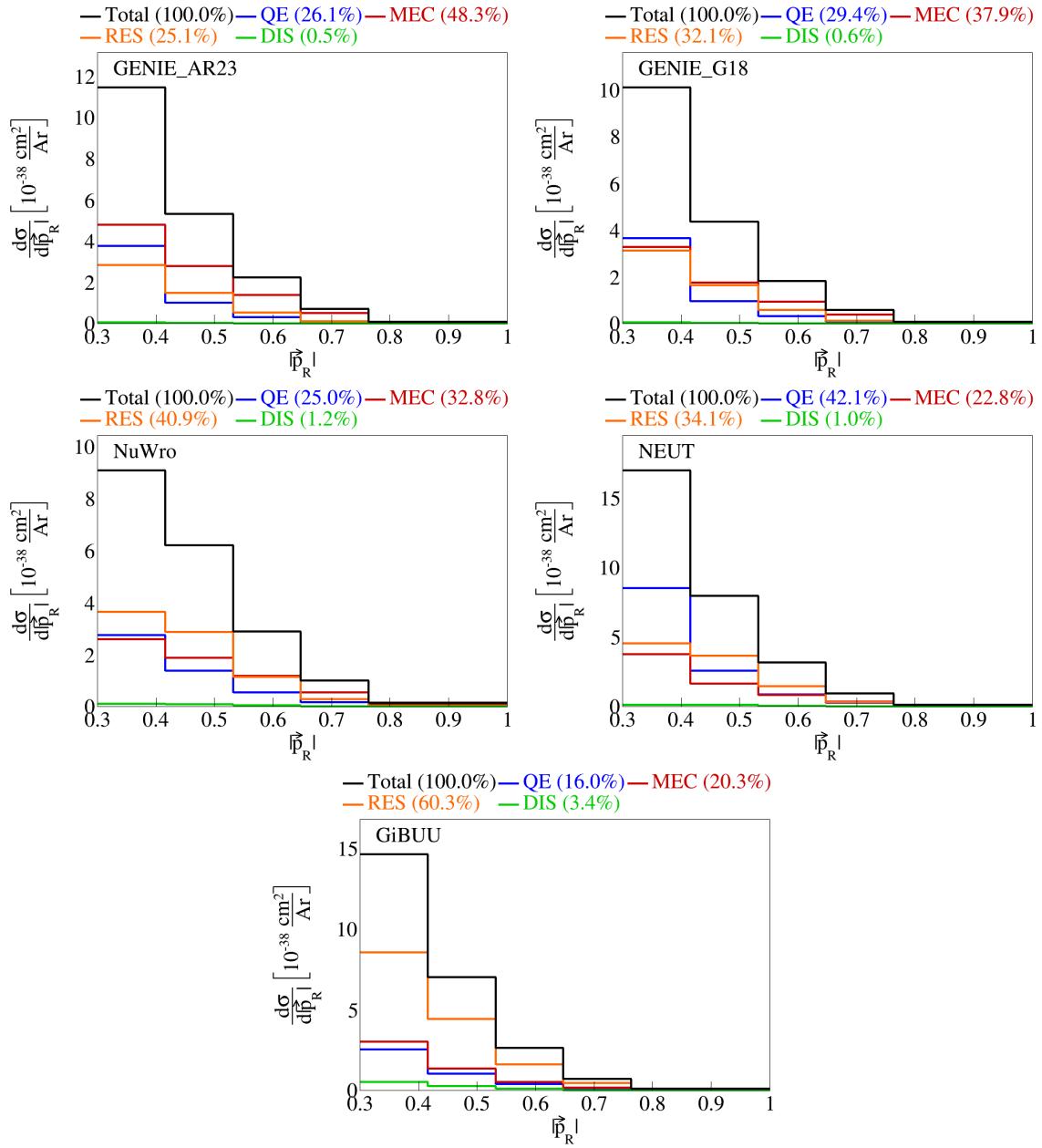


Figure 7: Event interaction breakdown for $|\vec{p}_R|$.

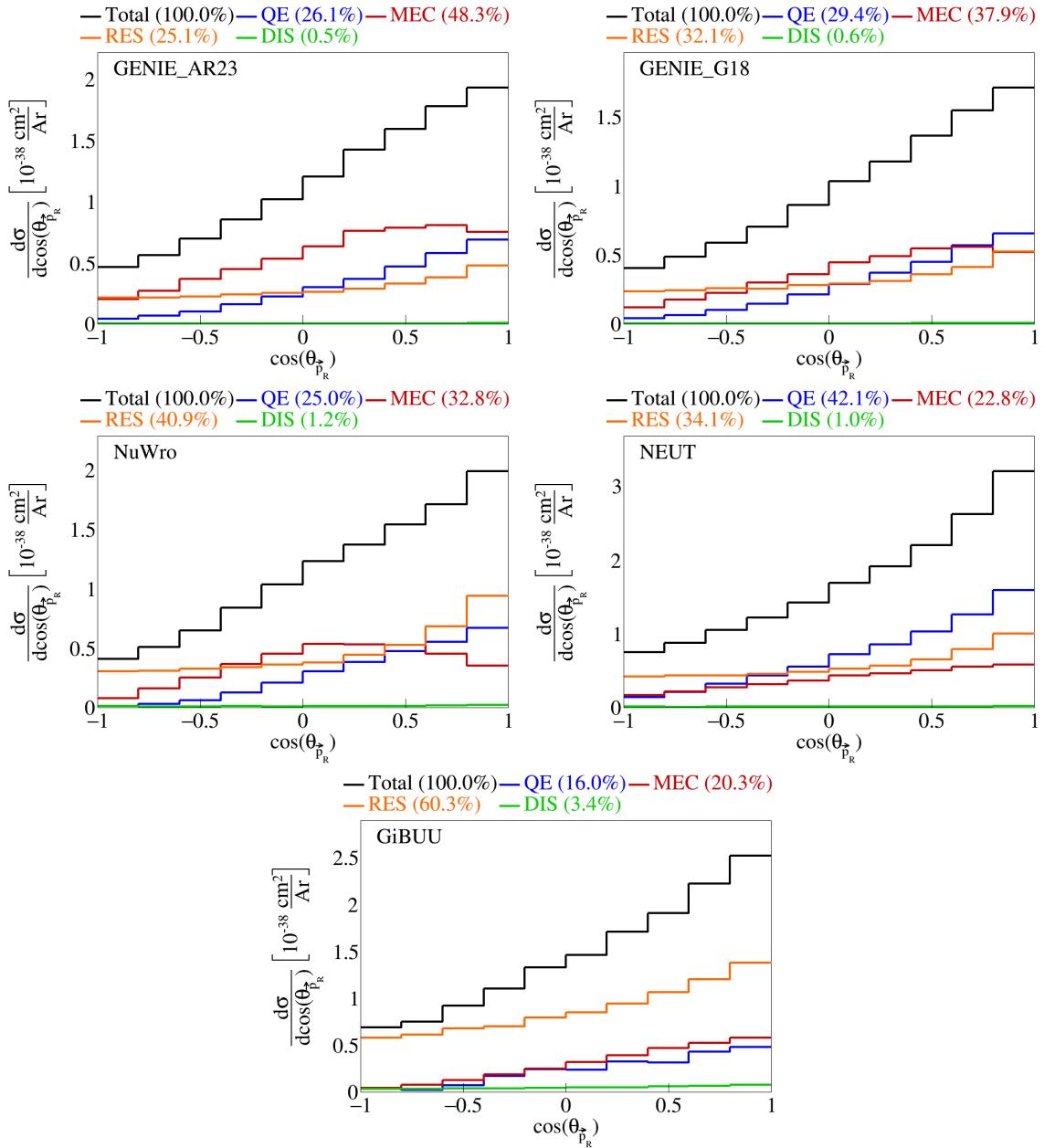


Figure 8: Event interaction breakdown for $\cos(\theta_{\vec{p}_R})$.

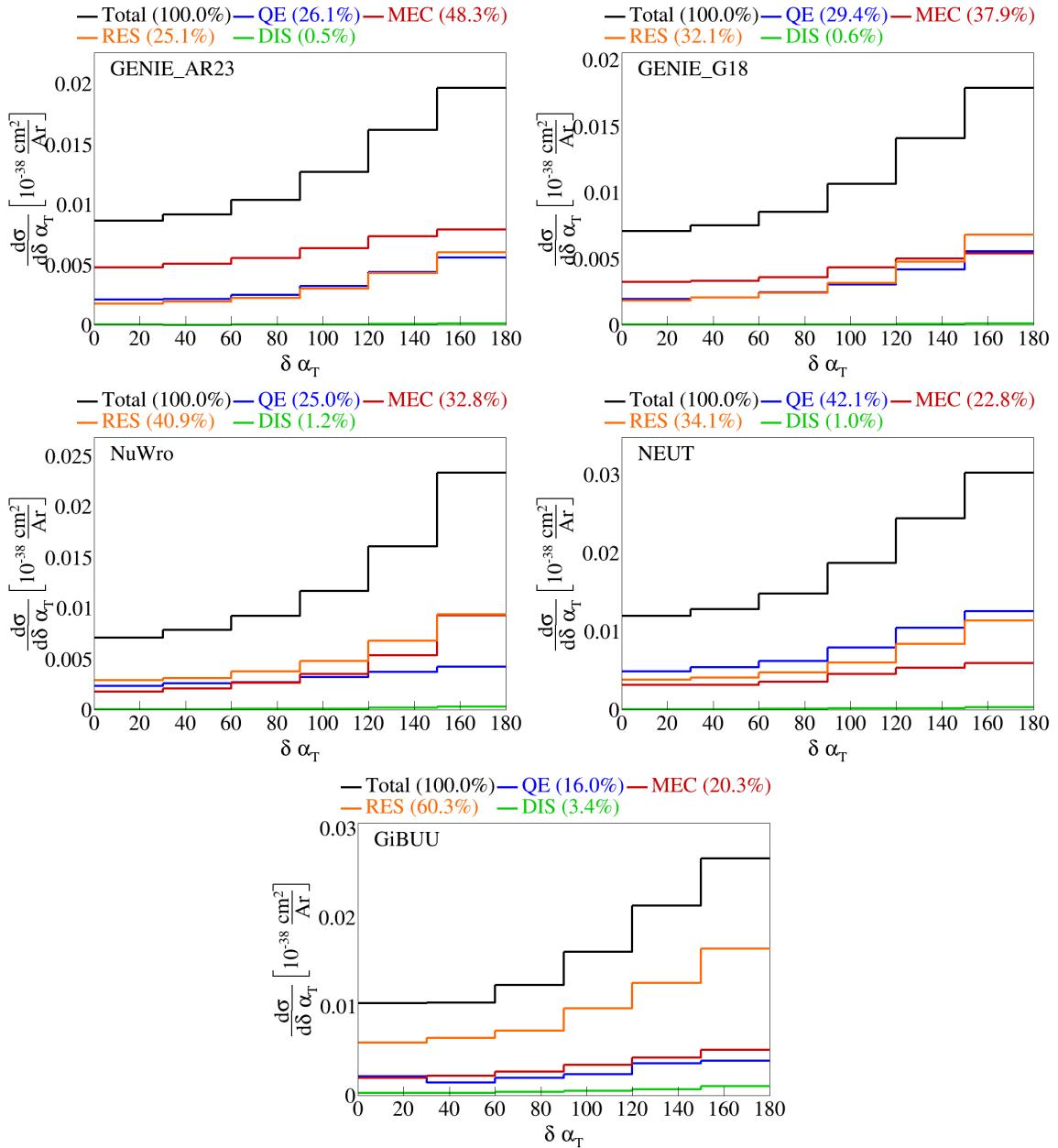


Figure 9: Event interaction breakdown for $\delta \alpha_T$.

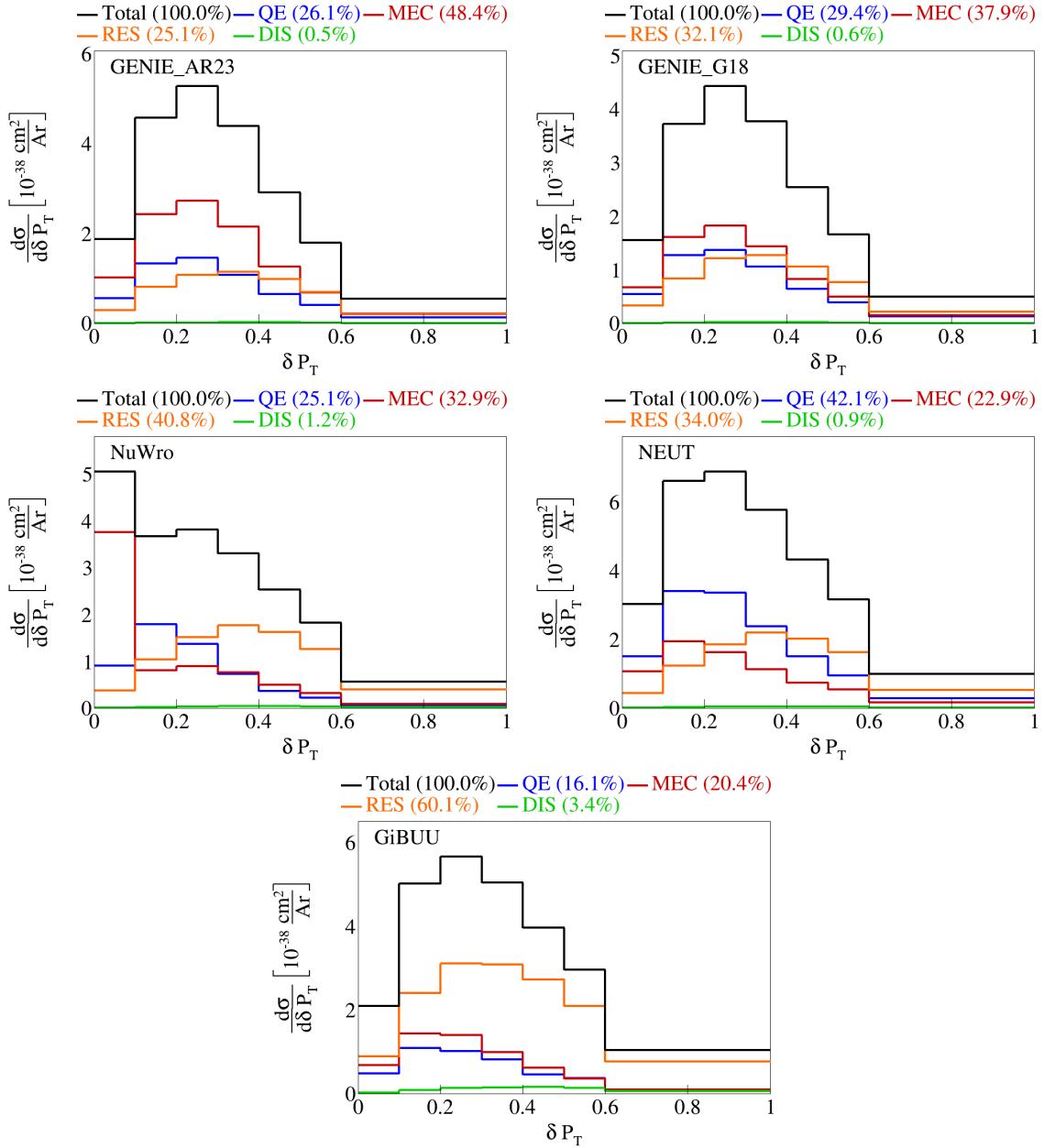


Figure 10: Event interaction breakdown for $|\delta \vec{P}_T|$.

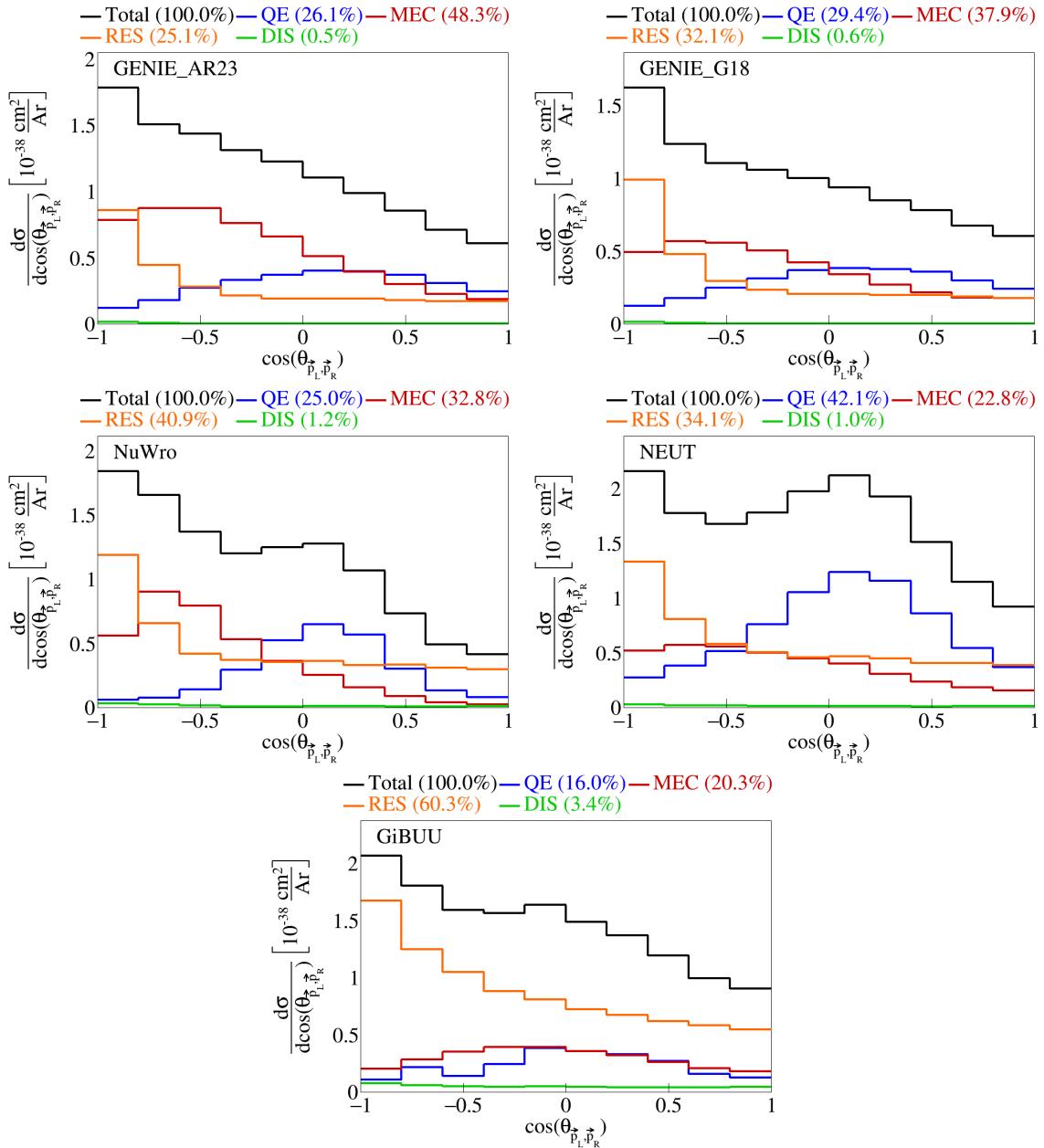


Figure 11: Event interaction breakdown for $\cos(\theta_{\vec{p}_L, \vec{p}_R})$.

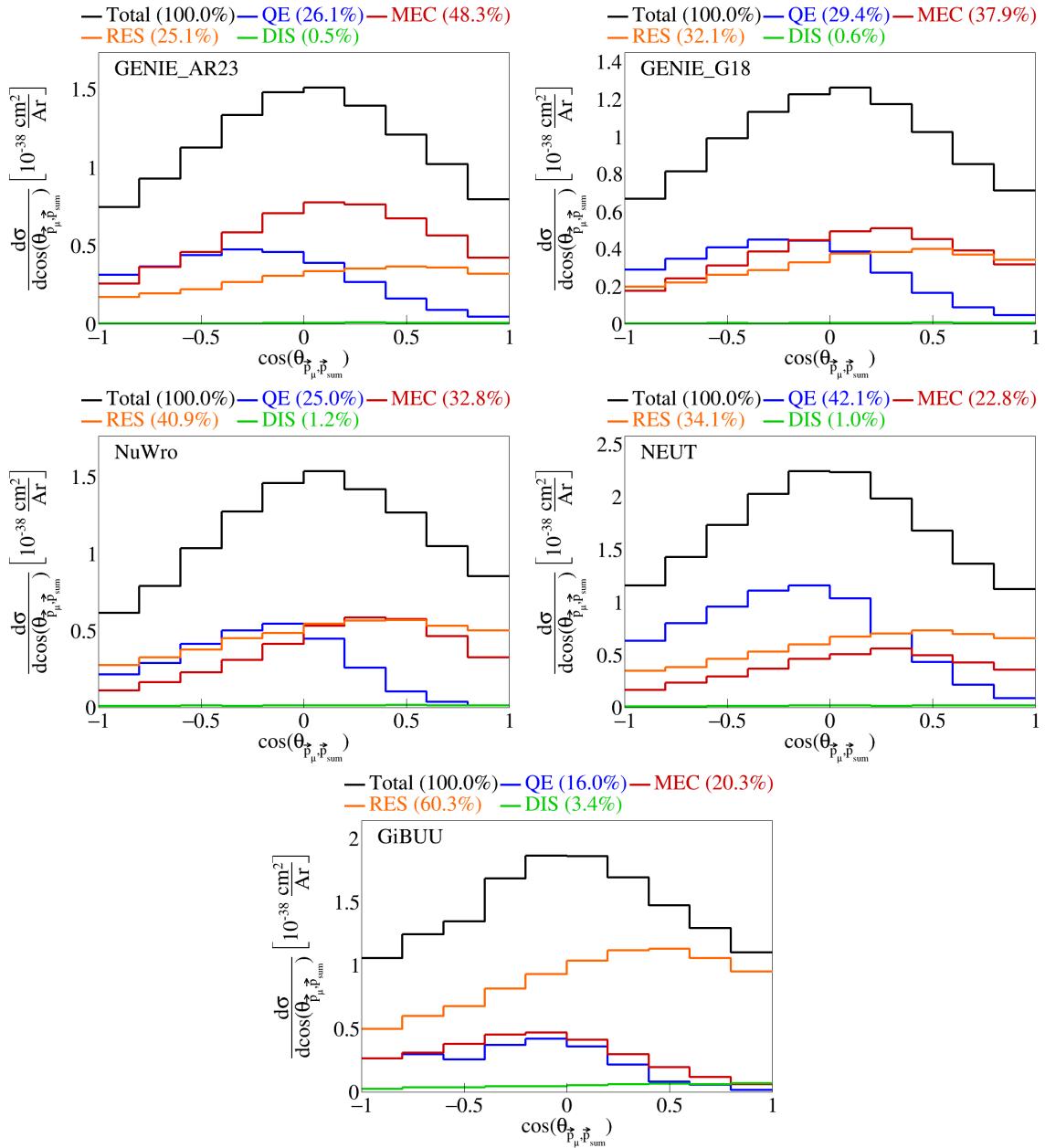


Figure 12: Event interaction breakdown for $\cos(\theta_{\vec{p}_\mu, \vec{p}_{\text{sum}}})$.

62 **2.4 Pre-FSI events**

63 To investigate why the percentage of MEC events for some generators is low, we performed event selection
64 before any final state interactions took place and plotted the interaction breakdown. For both GENIE tunes,
65 NEUT, and NuWro, we got 100% MEC events pre-FSI. For GiBUU, only 4.1% MEC versus 76.2% RES and
66 16% DIS events pre-FSI. The interaction breakdown for $|\vec{p}_\mu|$ for all the generators are shown in Figure 13.
67 Since GiBUU is the outlier, we checked the specific interaction mode for the resonance events. We got that
68 10 has 39.3%, 11 has 34.7%, 12 has 0.0136%, 13 has 26 %, and 27, 22, and 23 all have zero percent of the
69 resonance events. We also checked the event interaction breakdown for GiBUU samples generated without
70 final state interactions, in which we found that 100% of the events are MEC, shown in Figure 14.

71 Note that the difference between these two GiBUU samples is that in the former, the samples were
72 generated with final state interactions, and then we look at the state before the final state interactions
73 reportedly took place, and in the latter the event generation was done without any final state interactions.

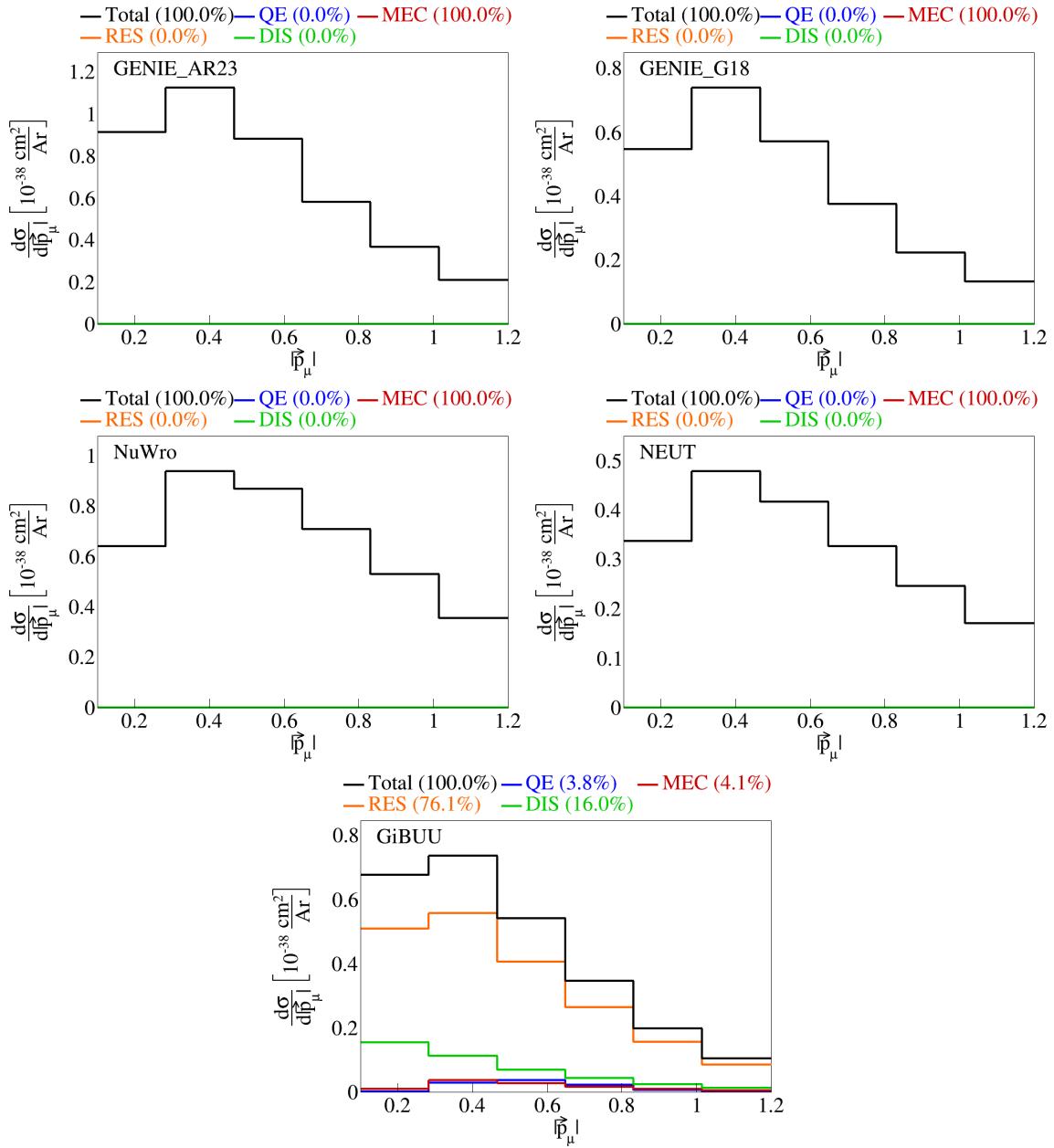


Figure 13: Event interaction breakdown of $|\vec{p}_\mu|$ before final state interactions.

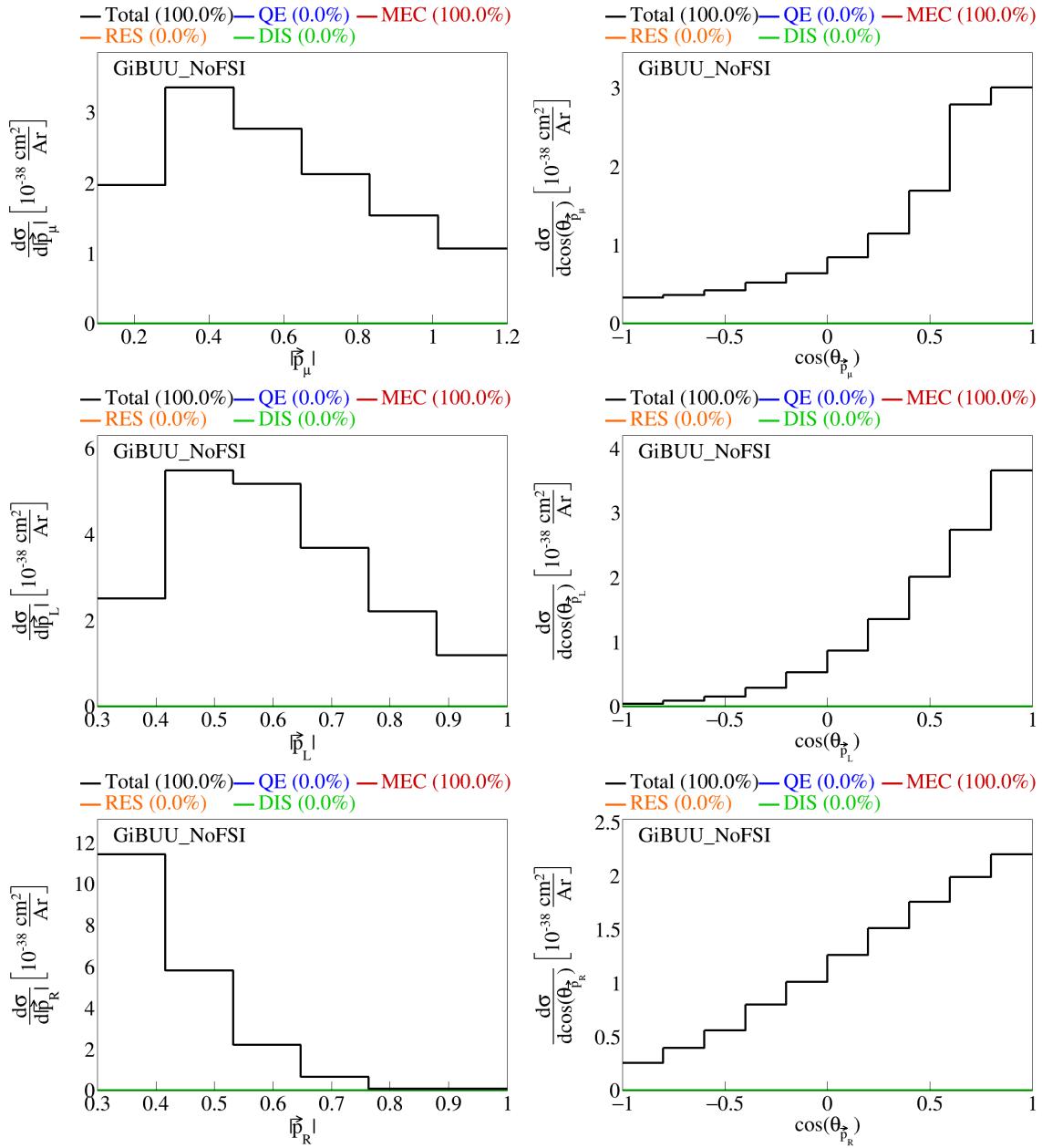


Figure 14: Event interaction breakdown for final events from GiBUU events with no FSI.

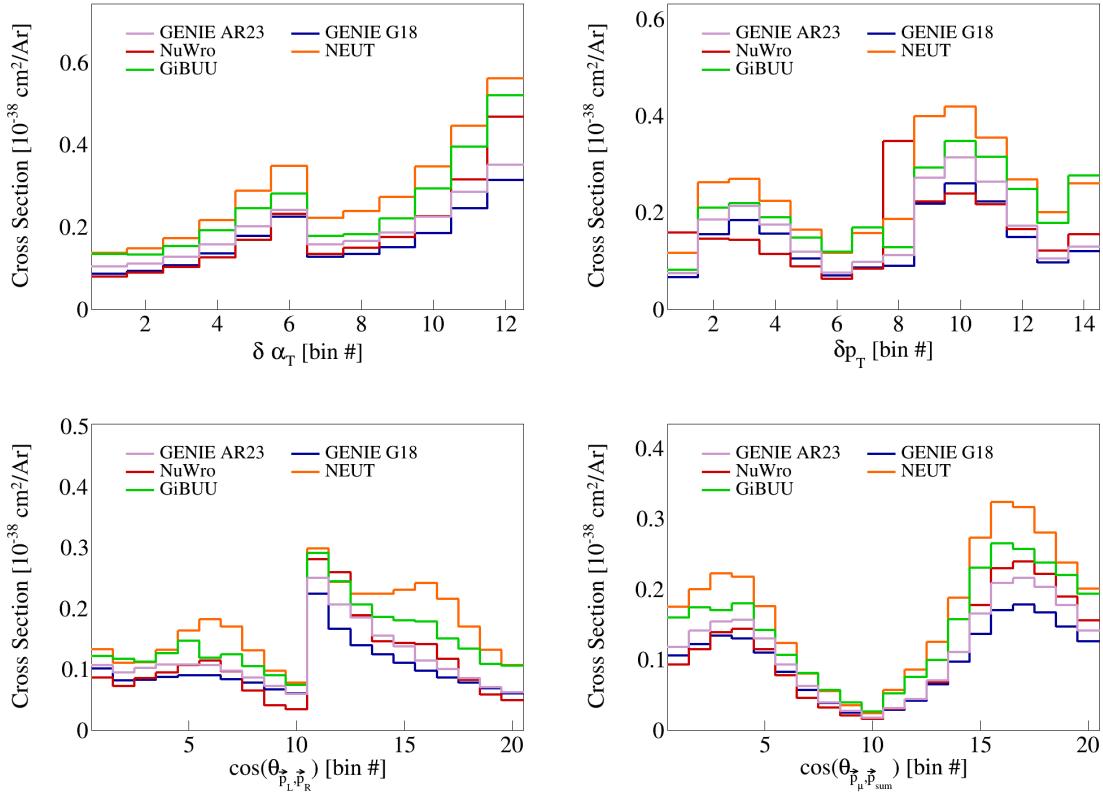


Figure 15: Double differential serial plots, all in $\cos(\theta_{\vec{p}_\mu})$.

74 2.5 Double differential plots

75 For our double differential variables, we look at δP_T , $\delta \alpha_T$, $\cos(\theta_{\vec{p}_L, \vec{p}_R})$, and $\cos(\theta_{\vec{p}_\mu, \vec{p}_{\text{sum}}})$ in $\cos(\theta_{\vec{p}_\mu})$. We
 76 have two bins for $\cos(\theta_{\vec{p}_\mu})$, the first one going from -1 to 0.5 and the second from 0.5 to 1 . Therefore, these
 77 are irregular bins, with the first holding a larger range than the first. These plots are shown in Figure 15.
 78 Note that, in these plots, the horizontal axis is defined by bin number of the double differential measurement,
 79 not the value of the variable. This is because we are representing two variables in a single axis, but we can
 80 slice the plots to get our usual horizontal axis.

81 We slice the double differential plots into two plots each, so that we have the variable of interest in the
 82 horizontal axis instead of bin numbers, and each slice corresponds to one bin of $\cos(\theta_{\vec{p}_\mu})$. These plots are
 83 shown in Figure 16, and the plots broke down by interaction are in Figures 17 to 20. In these plots, the
 84 bins contents have been reweighted appropriately, by dividing the content of each bin by the width of the
 85 bin for the variable in the axis multiplied by the width of the $\cos(\theta_{\vec{p}_\mu})$ slice. Note that the plots for the
 86 $0.5 < \cos(\theta_{\vec{p}_\mu}) < 1$ slice have more events in general, although they span a smaller phase space of $\cos(\theta_{\vec{p}_\mu})$,
 87 as it can be seen by the scale of the vertical axis. We performed the same double differential analysis for
 88 the events before final state interactions. These are shown in Figure 21, and the corresponding interaction
 89 breakdown plots are in Figures 22 to 25.

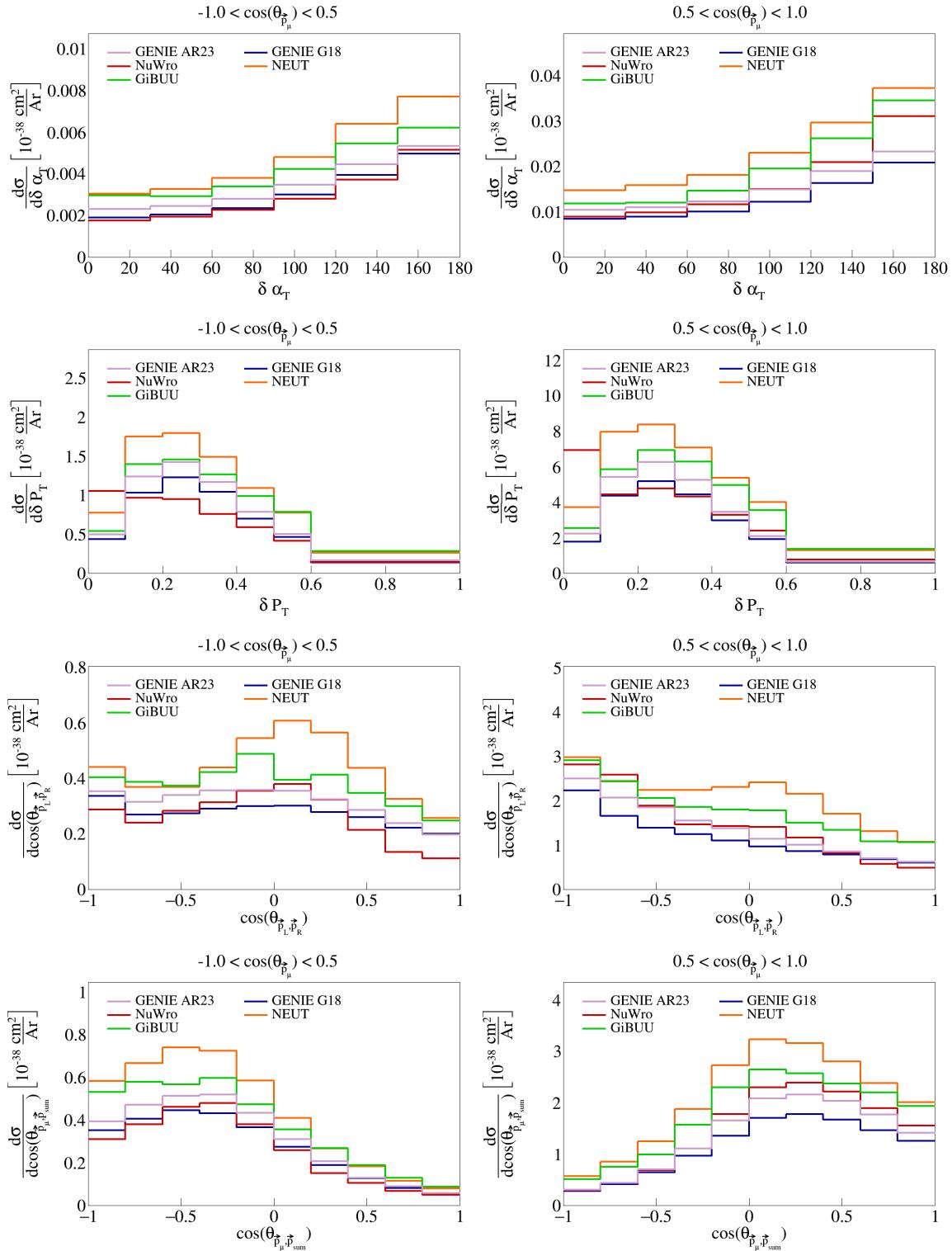


Figure 16: Sliced double differential plots.

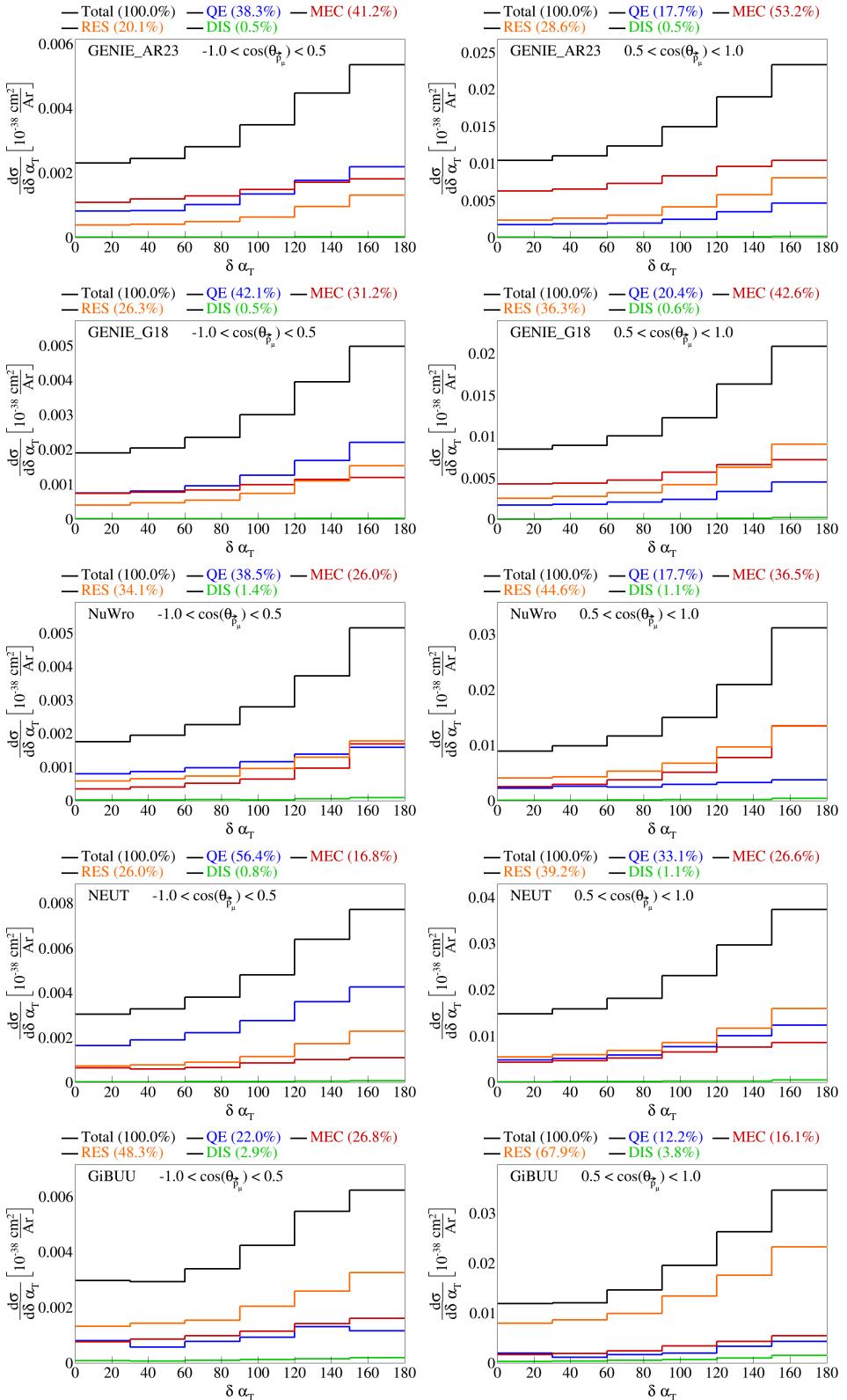


Figure 17: Interaction breakdown for sliced double differential plots for $\delta\alpha_T$ in $\cos(\theta_{\vec{p}_\mu})$.

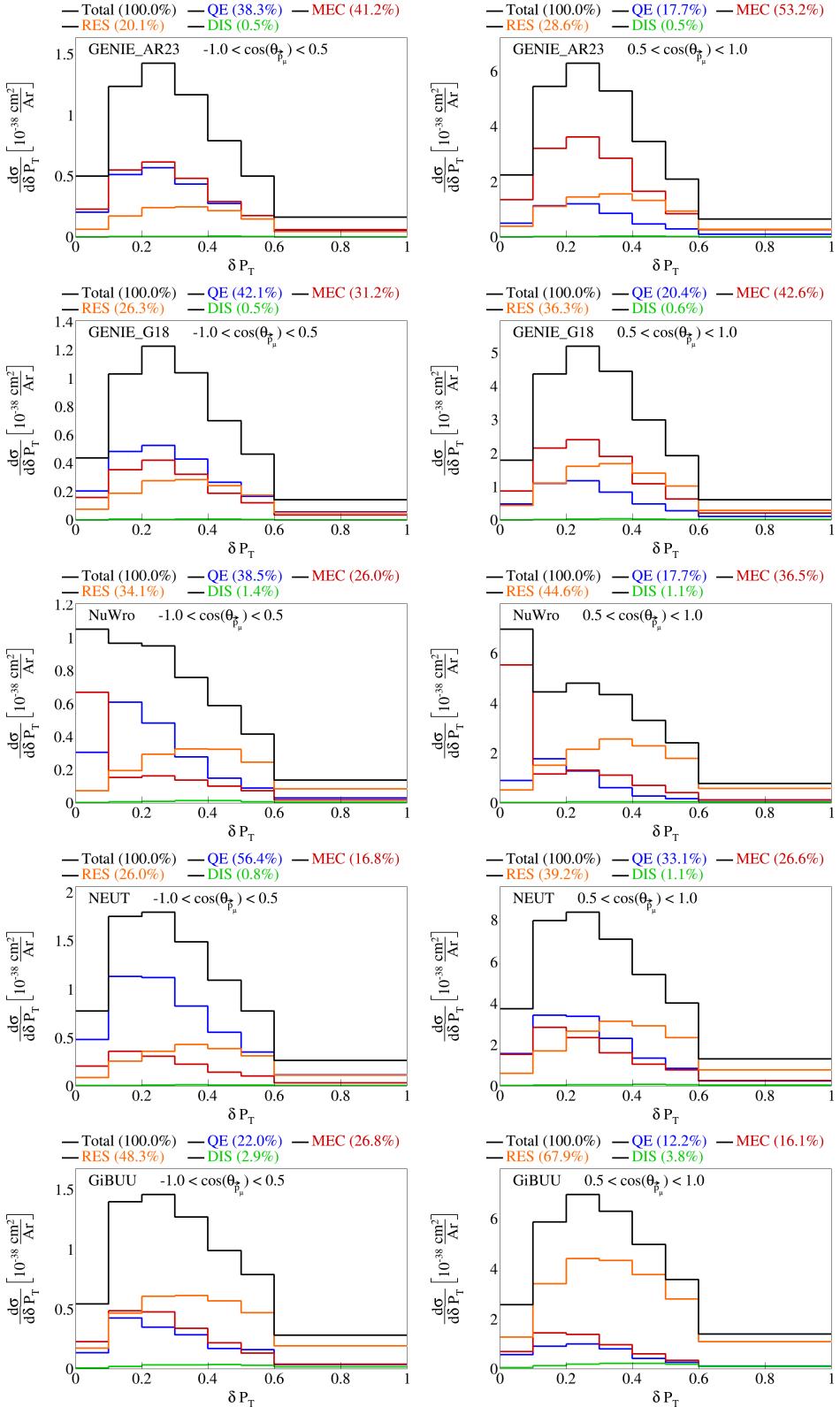


Figure 18: Interaction breakdown for sliced double differential plots for $|\delta \vec{P}_T|$ in $\cos(\theta_{\vec{p}_\mu})$.

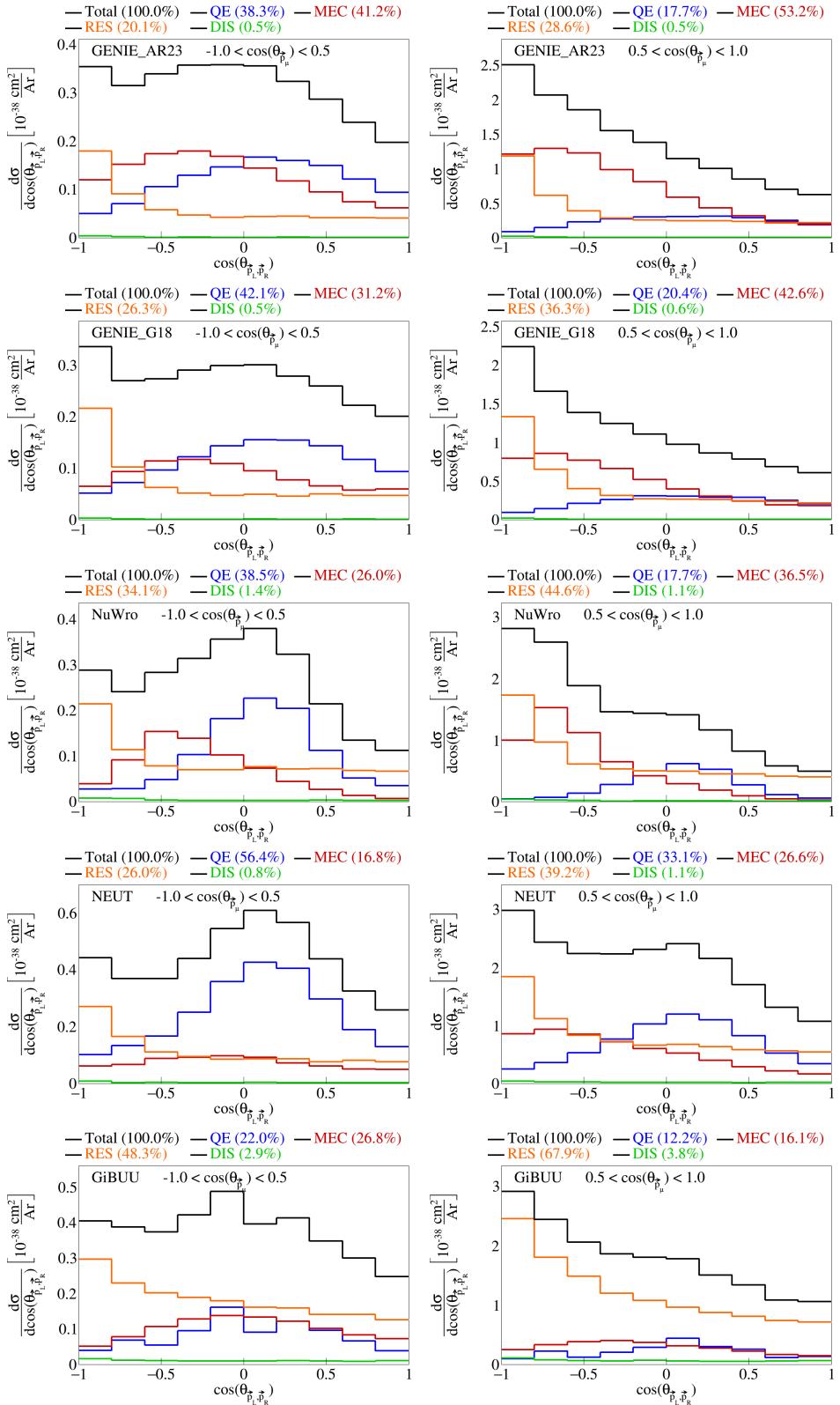


Figure 19: Interaction breakdown for sliced double differential plots for $\cos(\theta_{\vec{p}_L, \vec{p}_R})$ in $\cos(\theta_{\vec{p}_\mu})$.

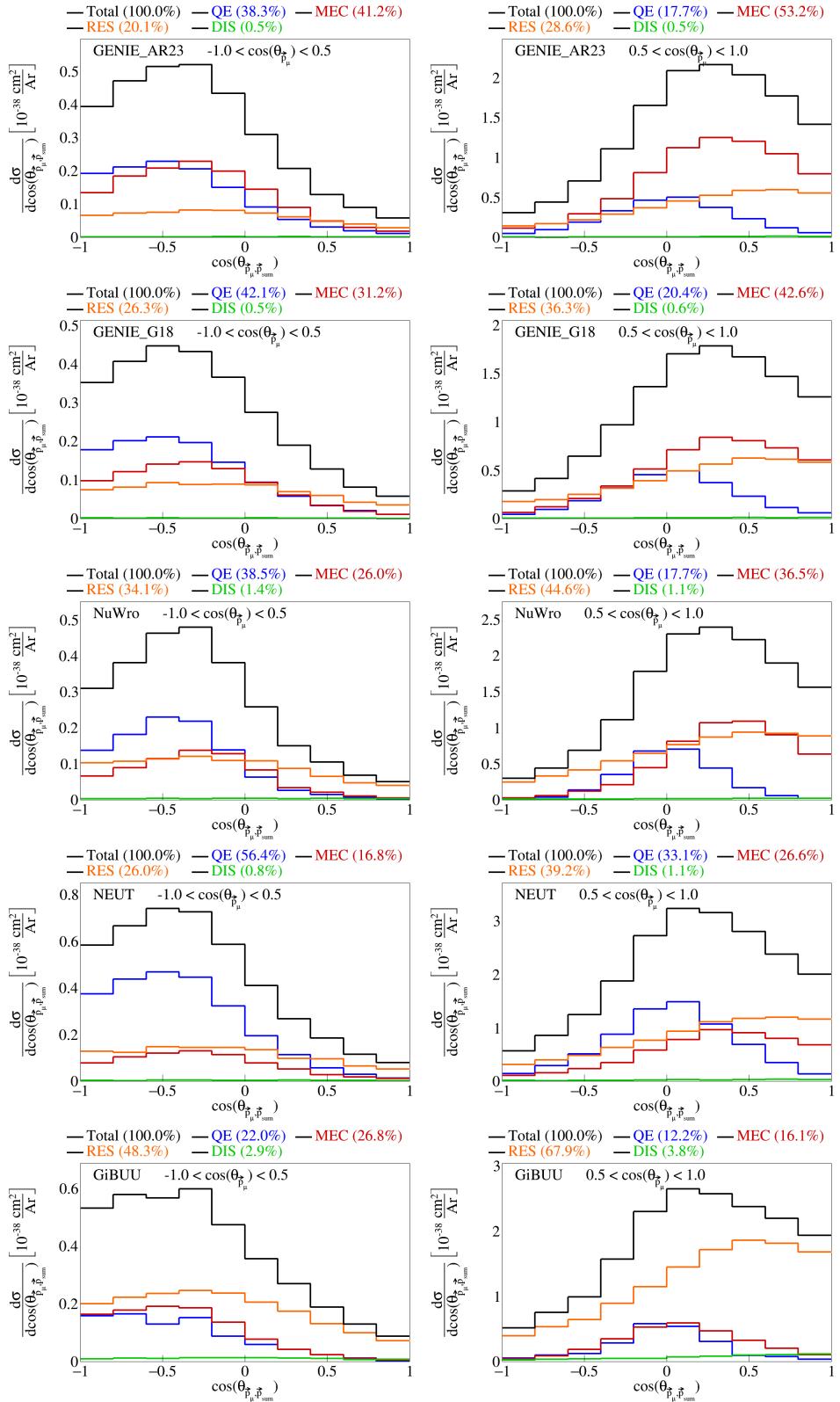


Figure 20: Interaction breakdown for sliced double differential plots for $\cos(\theta_{\vec{p}_\mu, \vec{p}_{\text{sum}}})$ in $\cos(\theta_{\vec{p}_\mu})$.

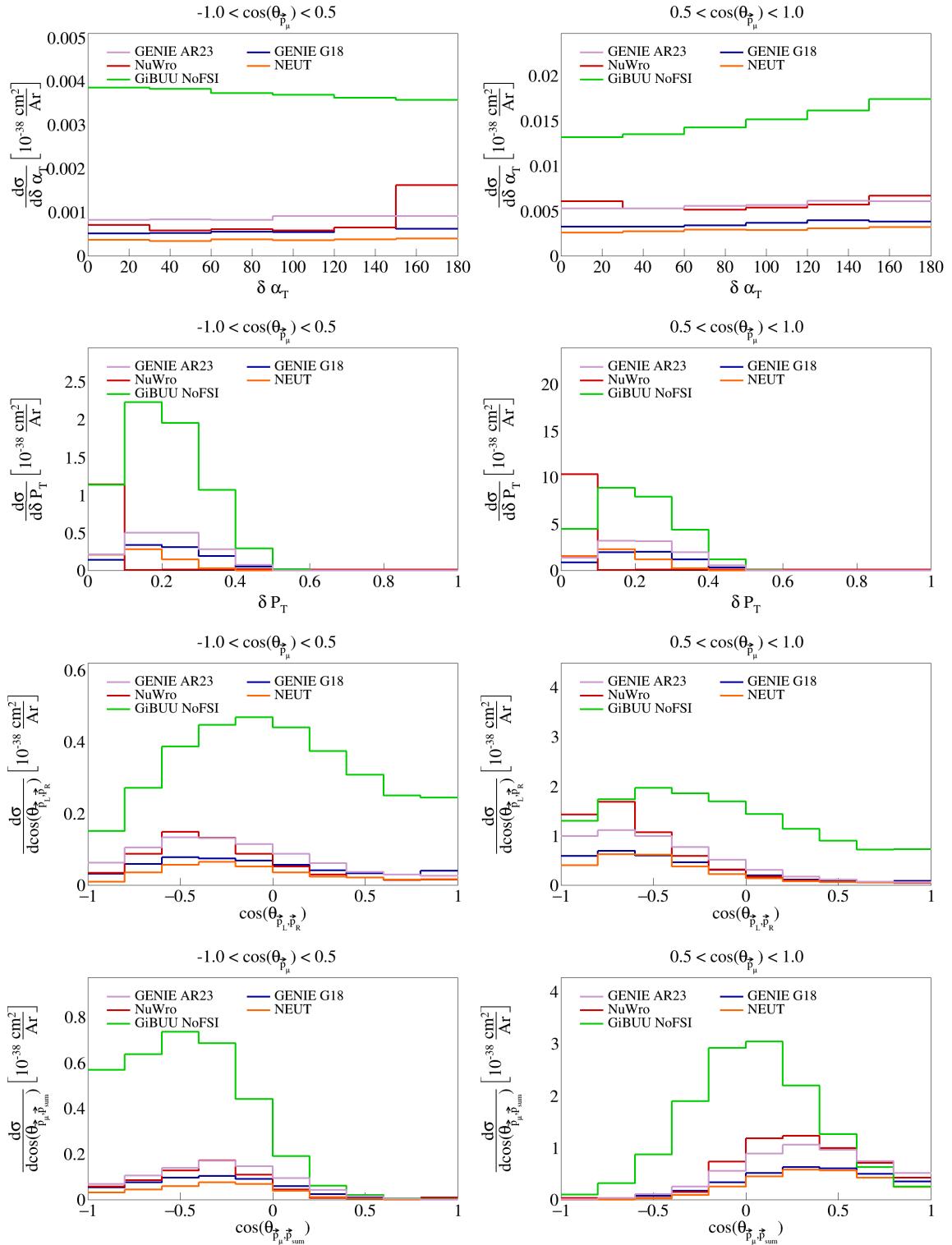


Figure 21: Sliced double differential plots for pre-FSI events.

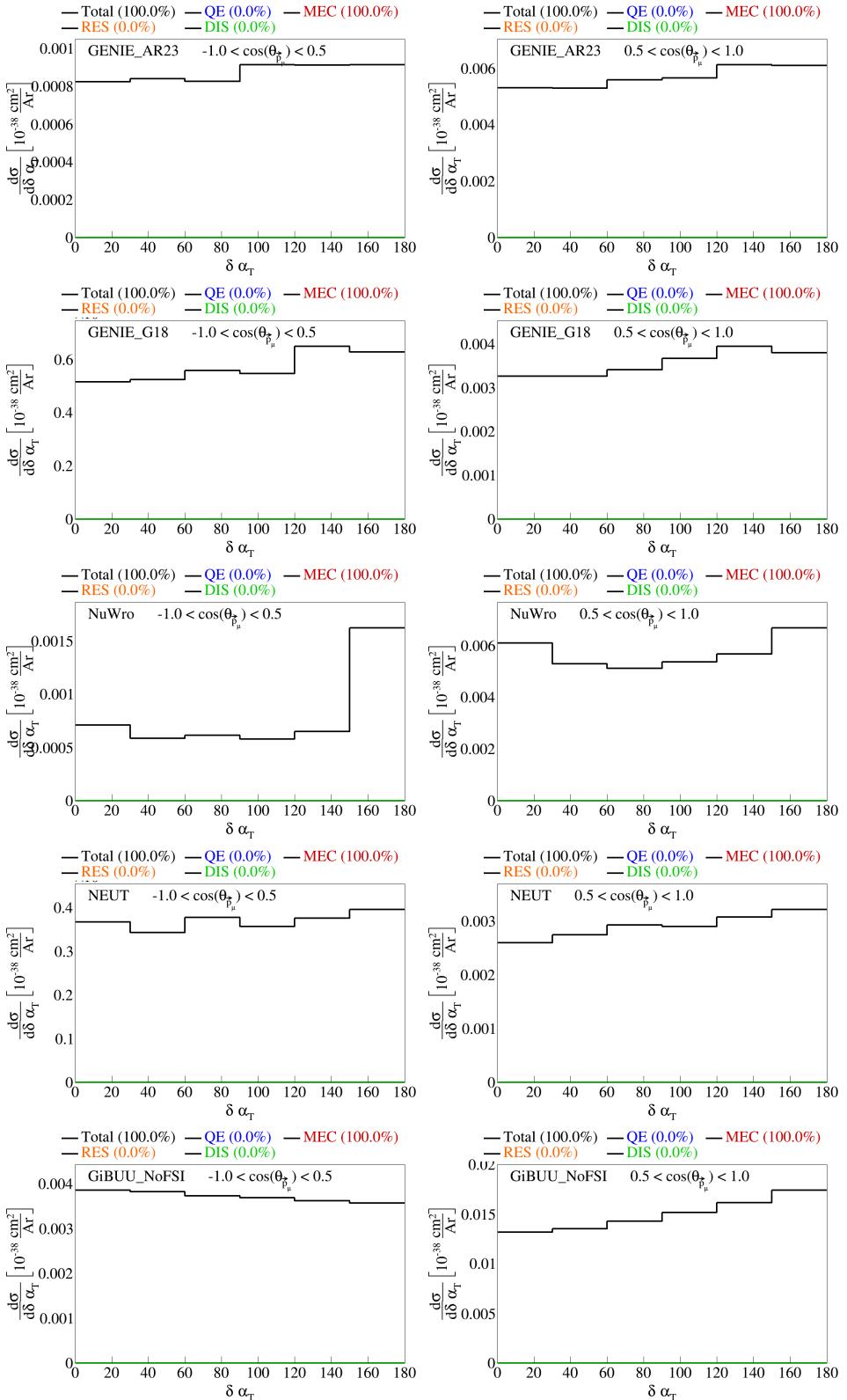


Figure 22: Interaction breakdown for sliced double differential plots for pre-FSI $\delta\alpha_T$ in $\cos(\theta_{\bar{p}_\mu})$.

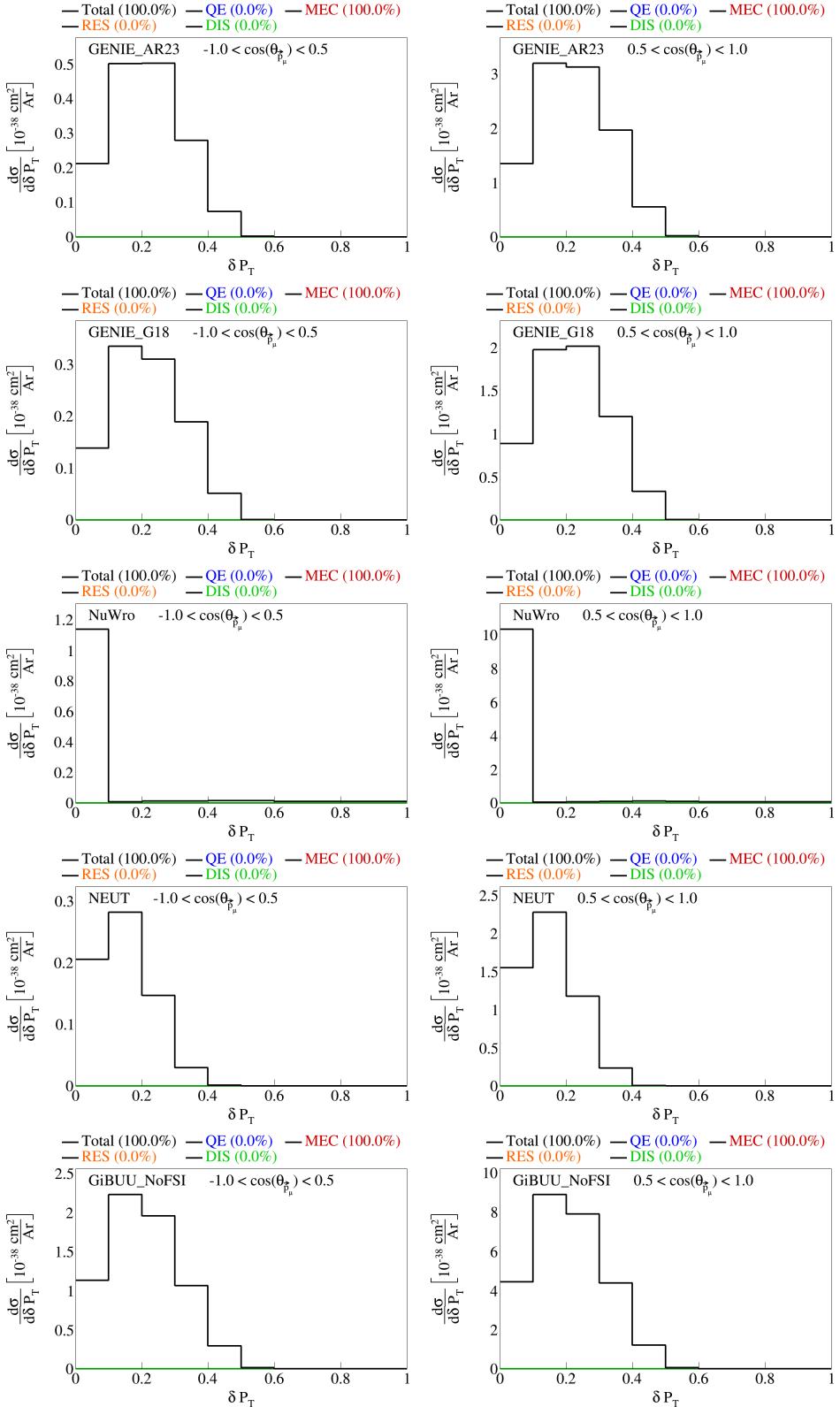


Figure 23: Interaction breakdown for sliced double differential plots for pre-FSI $|\delta \vec{P}_T|$ in $\cos(\theta_{\bar{p}_\mu})$.

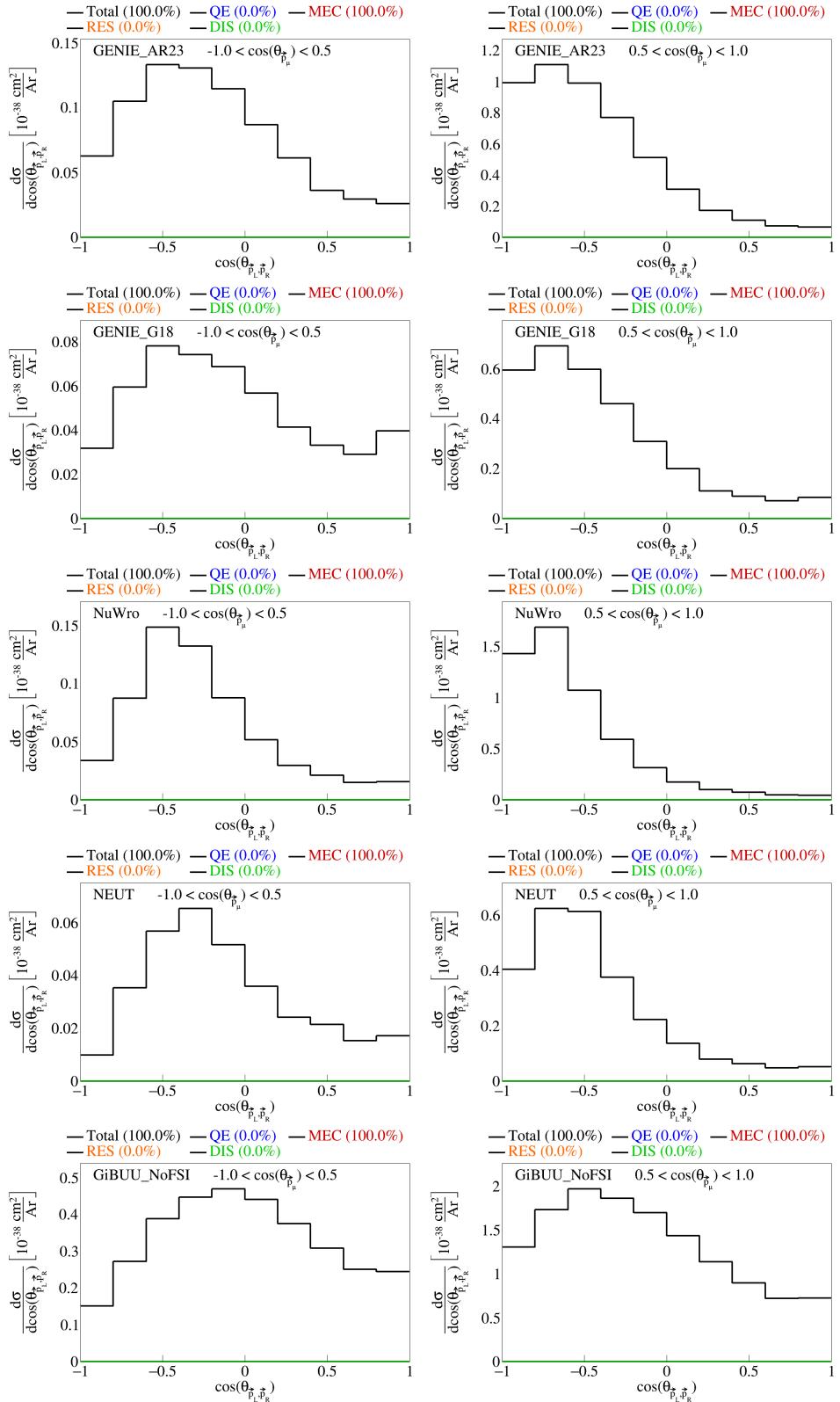


Figure 24: Interaction breakdown for sliced double differential plots for pre-FSI $\cos(\theta_{\vec{p}_L, \vec{p}_R})$ in $\cos(\theta_{\vec{p}_\mu})$.

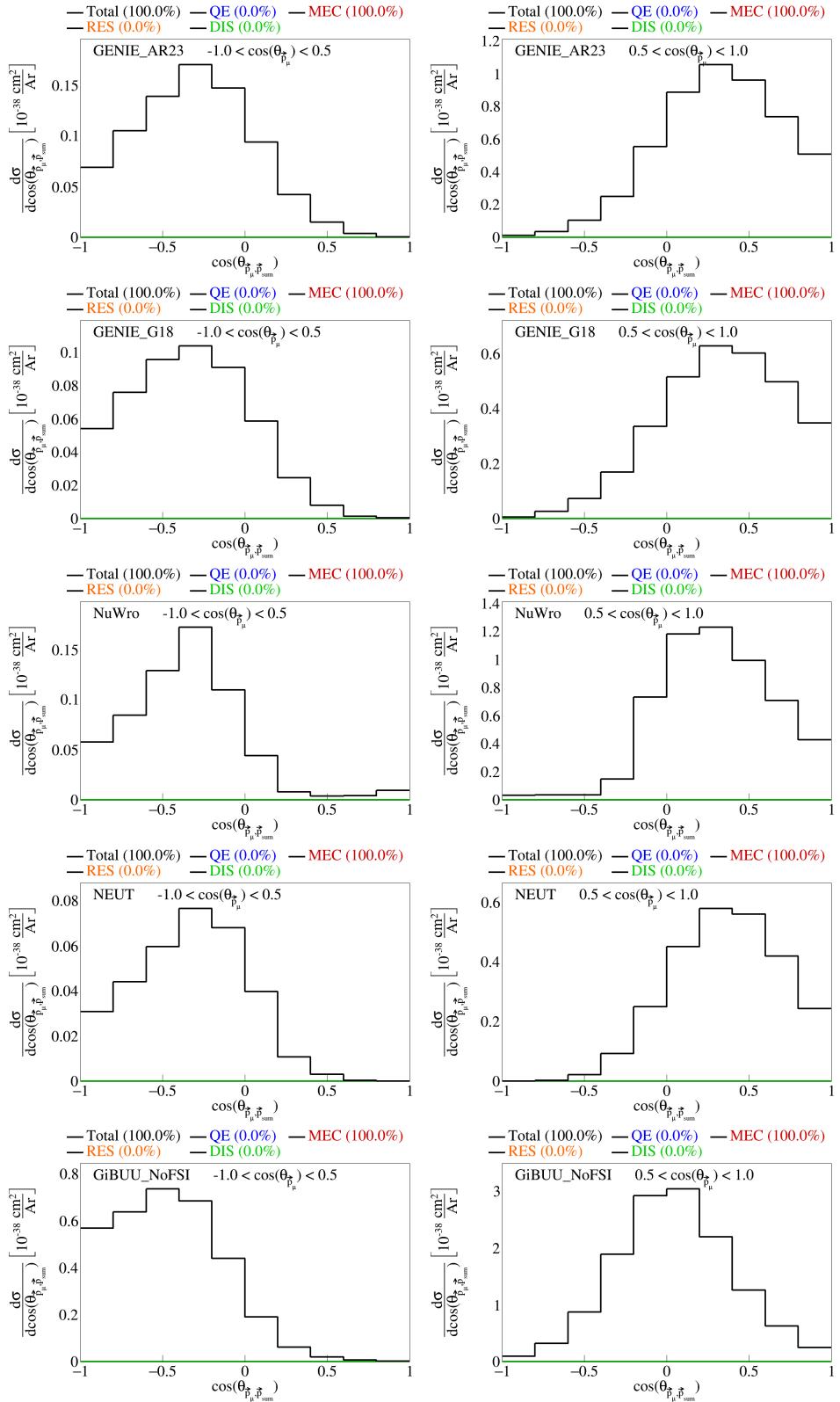


Figure 25: Interaction breakdown for sliced double differential plots for pre-FSI $\cos(\theta_{\vec{p}_\mu, \vec{p}_{sum}})$ in $\cos(\theta_{\vec{p}_\mu})$.

⁹⁰ **2.6 Pure MEC events**

⁹¹ We also generated pure meson exchange current events using different configurations to get the MEC splines.
⁹² These were all generated using different tunes of GENIE: AR23, G18 with Empirical MEC model, and G18
⁹³ with Nieves MEC model. The plots for the transverse kinematic variables are shown in Figure 26. The sliced
⁹⁴ double differential plots are shown in Figure 27.

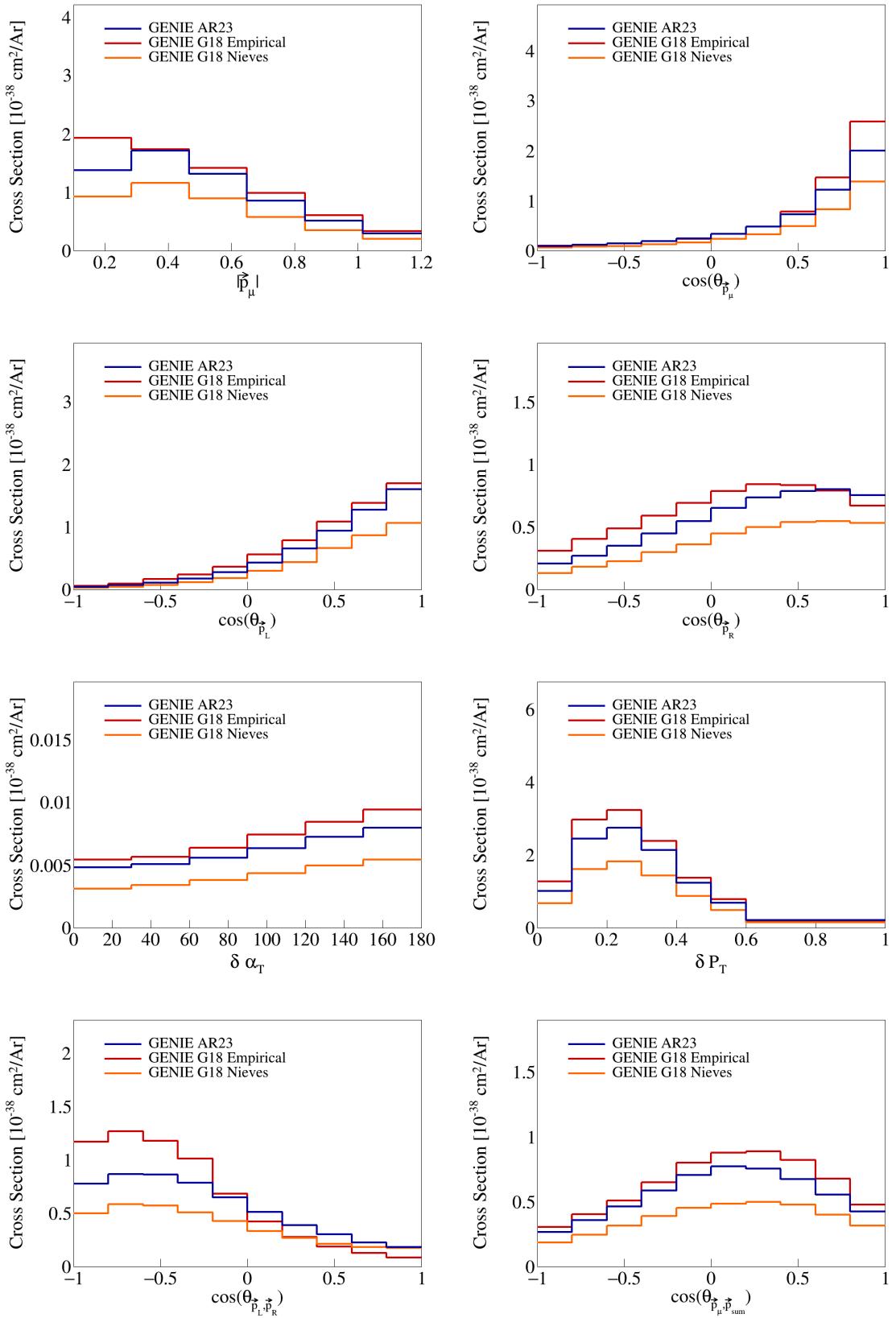


Figure 26: Variable plots for pure MEC events.

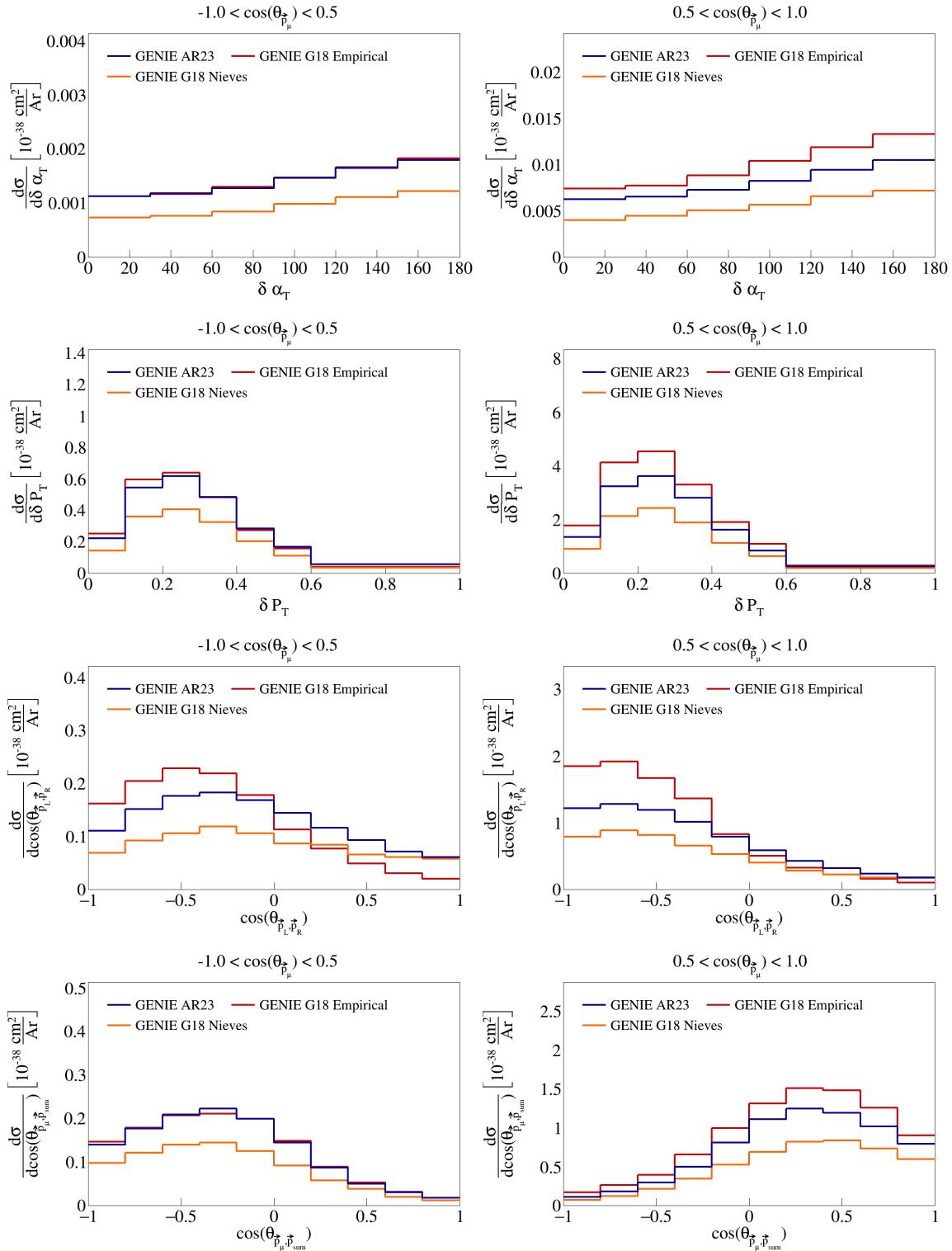


Figure 27: Sliced double differential plots for pure MEC events.

95 3 SBND analysis

96 The CAF files used for this analysis are available in the Fermilab gpvms at the path

97 `/pnfs/sbnd/persistent/users/twester/sbnd/v09_78_04/cv/*.flat.caf.root`

98 where the asterisk means that all the files in the directory with the extension `.flat.caf.root` will be used.

99 3.1 Fiducial volume

100 To perform the analysis of SBND data, we have to define the fiducial volume of the detector, which represents
101 a central part of the detector in which we will accept signals. The fiducial volume is given by the following
102 ranges:

$$5 < |x| < 180 \quad |y| < 180 \quad 10 < z < 450 \quad (6)$$

103 where x , y , and z are the coordinates in the detector frame, all in centimeters.

104 3.2 Signal definition

105 To perform analysis on experiment data, we will be using the CAFAna framework. This allows us to perform
106 cuts based on the reconstructed and Monte Carlo data (if available, i.e., only in the case of dealing with
107 simulated events), to discriminate events. To discriminate events based on their Monte Carlo data, we
108 perform a simple `TruthCut` that checks the following:

- 109 (i) That the neutrino interaction takes place in the fiducial volume.
- 110 (ii) That the neutrino is a muon neutrino.
- 111 (iii) That the interaction is a charged current interaction.
- 112 (iv) That there is only one muon in our allowed momentum range.
- 113 (v) That there are only two protons in our allowed momentum range.
- 114 (vi) That there are no charged/neutral pions in our defined momenta ranges.

115 Using the reconstructed event data, the cut we have to use is not as simple as in the Monte Carlo data
116 case. We now have to use a `Cut` that looks at different variables of the reconstructed event to determine if
117 it is a signal event. We perform the following cuts:

- 118 (i) Cosmic: that the event is not a cosmic event by Pandora's criteria, i.e., requiring `nu_score > 0.4` to
119 check how neutrino-like the event is, and `fmatch.score < 7` with $0 < fmatch.time < 1.8$ to check the
120 event comes from the beam.
- 121 (ii) Vertex in FV: that the reconstructed vertex for the neutrino interaction takes place in the fiducial
122 volume defined above.
- 123 (iii) One muon: that there is one muon track with $L_{\text{track}} > 50$ cm, starting point in the fiducial volume,
124 $\chi^2_\mu < 30$, $\chi^2_p > 60$, with momentum in our allowed range; if there are multiple candidate tracks, the
125 one with the longest track length is chosen.
- 126 (iv) Two protons: that there are two proton tracks with $\chi^2_p < 100$, full track in the fiducial volume, and
127 that these have momentum in our allowed range.
- 128 (v) No charged pions: that there are no other reconstructed tracks with momentum in the allowed range
129 for charged pions inside the fiducial volume.
- 130 (vi) No neutral pions: that there are no reconstructed particles with a positive `trackScore` less than 0.5
131 indicating a shower, so we don't allow any neutral pions.

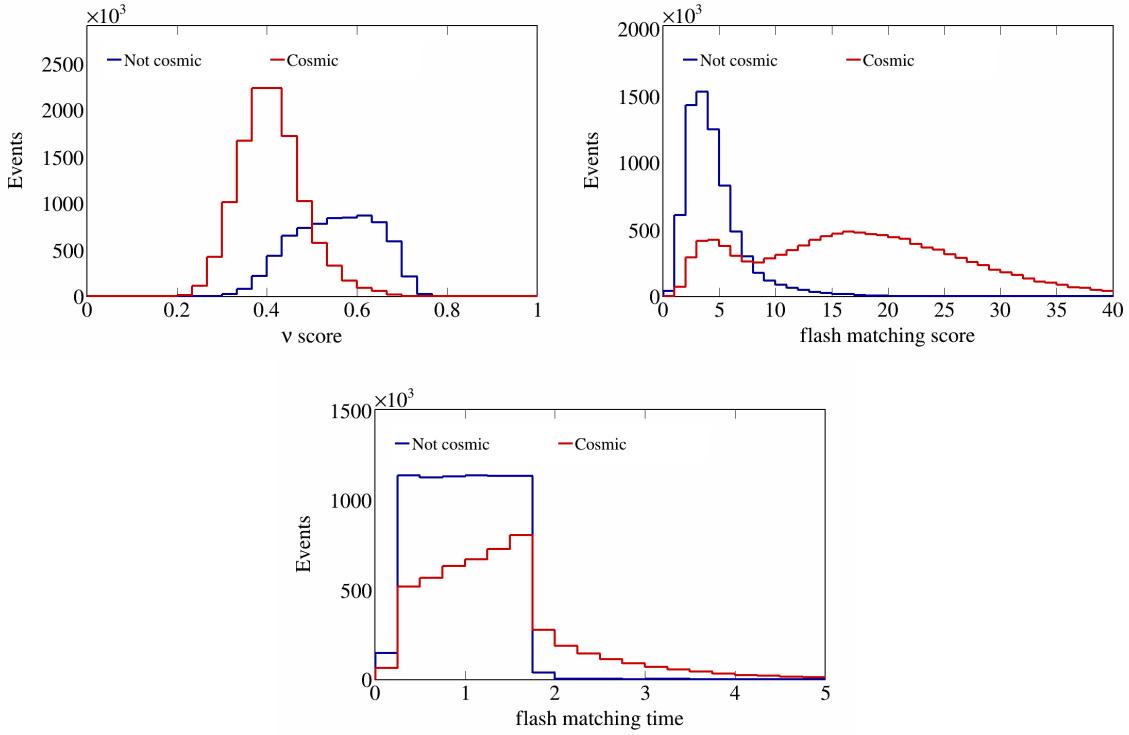


Figure 28: Cosmic cut variables before rejecting cosmic events.

Using these two discriminators on simulated events, the reconstructed events that satisfy the signal definition, and distinguish between true signal events and background events. To get a better sense of what values the variables chosen to do the cuts take on for each true particle, we plot the flash matching score, time, and ν score in Figures 28, and the χ^2 values for muons and protons in Figure 29.

We use a one-bin histogram with lower bound 0 and upper bound of 3 in the true energy variable to get total counts of generated events, true signal events, all reconstructed events, and efficiency and purity data after each of the cuts described above is applied to the reconstructed events. These results are shown in Table 2. Counts are obtained using ROOT’s command `Histo->Integral()`. Global efficiency is defined as the ratio between events that pass the cut and reconstructed events, signal efficiency as the ratio between true events that pass the cut and all true signal events, and purity as the ratio between true signal events that pass the cut and all events that pass the cut. The numbers reported in this table are POT normalized to 6.6×10^{20} .

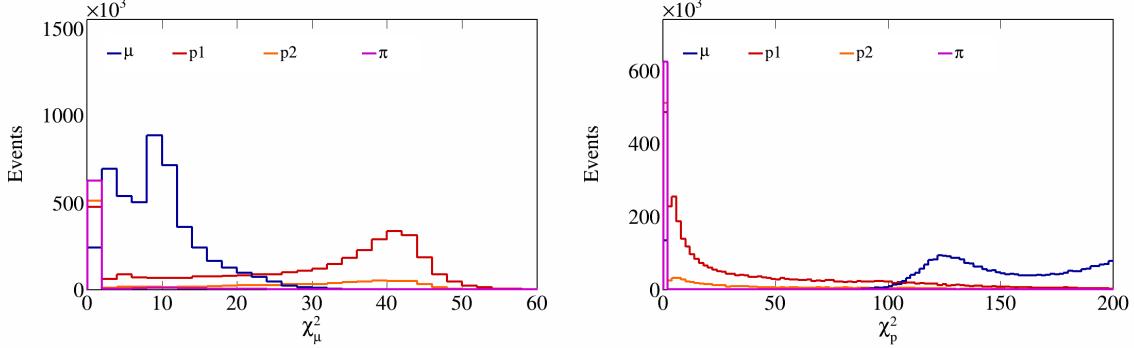


Figure 29: Muon and proton χ^2 values for all particles.

Cut	Number of events	Global efficiency	Signal efficiency	Purity
All	$1.3938 \cdot 10^7$	-	-	-
True signal events	272161	-	-	-
All reco events	$6.82359 \cdot 10^6$	100%	-	-
Cosmic cut	$5.88624 \cdot 10^6$	86.2632%	89.6205%	4.14377%
Vertex in FV cut	$3.29309 \cdot 10^6$	48.2603%	88.2885%	7.29671%
One muon cut	$2.23536 \cdot 10^6$	32.7593%	70.5202%	8.58603%
Two protons cut	146922	2.15315%	17.517%	32.4488%
No charged pions cut	67852.2	0.994377%	12.6665%	50.8065%
No neutral pions cut	54719.5	0.801917%	11.3094%	56.25%

Table 2: Global efficiency, selection efficiency, and purity for cuts made in signal definition.

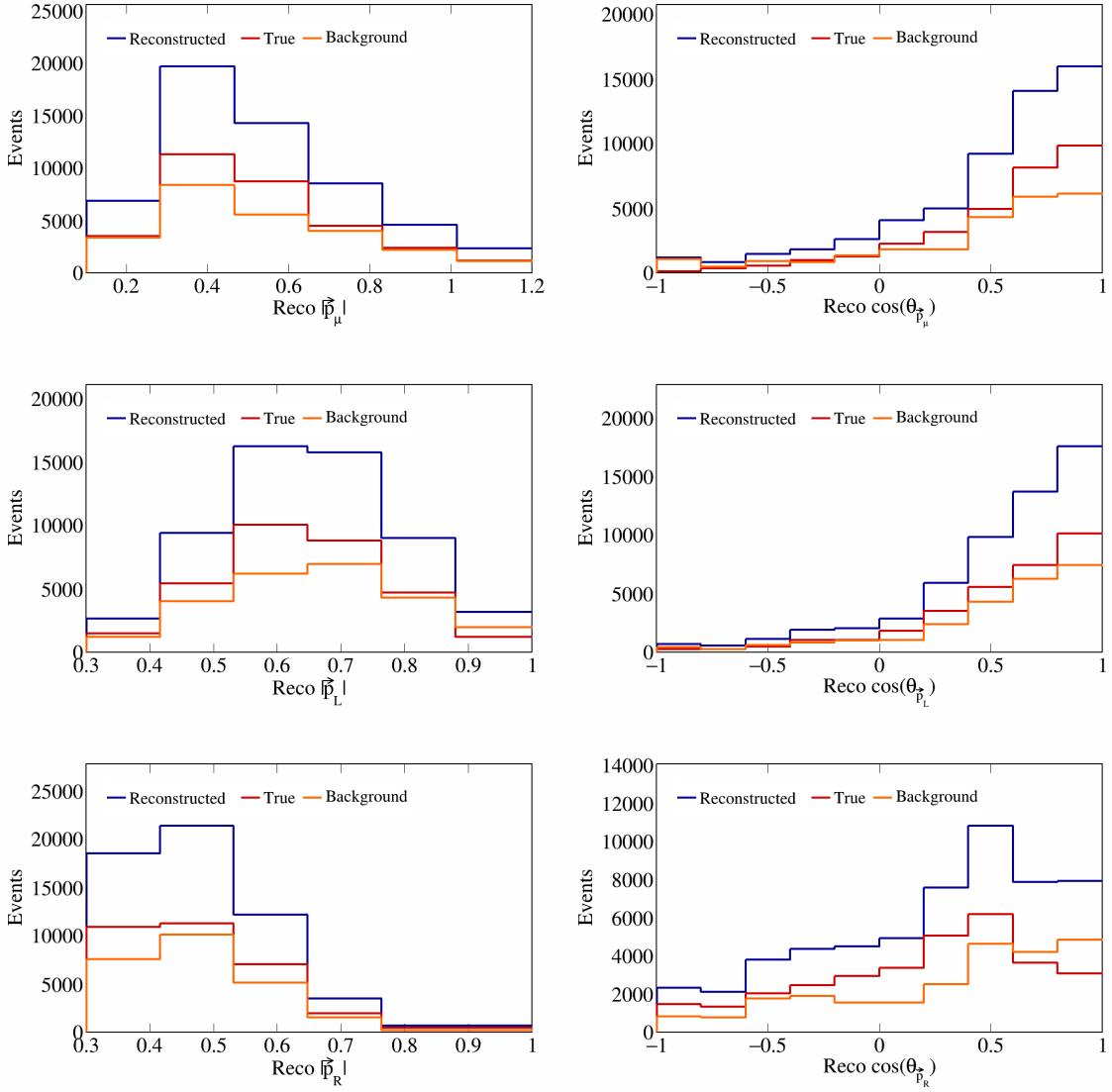


Figure 30: Vector directions and magnitudes for SBND data.

144 3.3 Variable plots

145 Using all the variable definitions as we did when studying the event generators, and the signal definition
 146 based on the cuts described in the previous section, we can generate plots for SBND data. The reconstructed
 147 single differential variables corresponding to vector opening angles and magnitudes are shown in Figure 30.
 148 In these figures, three lines are shown, corresponding to: all reconstructed (all the reconstructed events that
 149 pass our signal definition), signal (reconstructed events that pass signal definition and are true signal events
 150 as determined by the TruthCut from our previous section), and background (reconstructed events that pass
 151 signal definition but are not true signal events) events. Similarly, the variables relating multiple vectors are
 152 shown in Figure 31, and double differential sliced variables are shown in Figure 32.

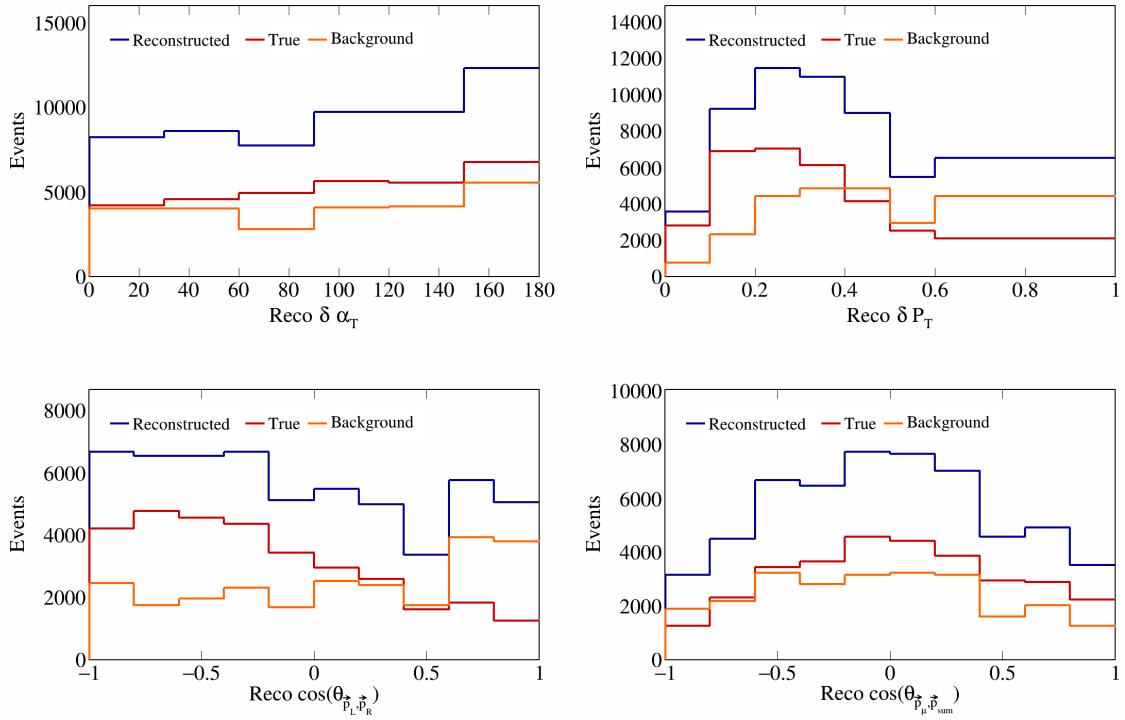


Figure 31: Vector opening angles and transverse momentum for SBND data.

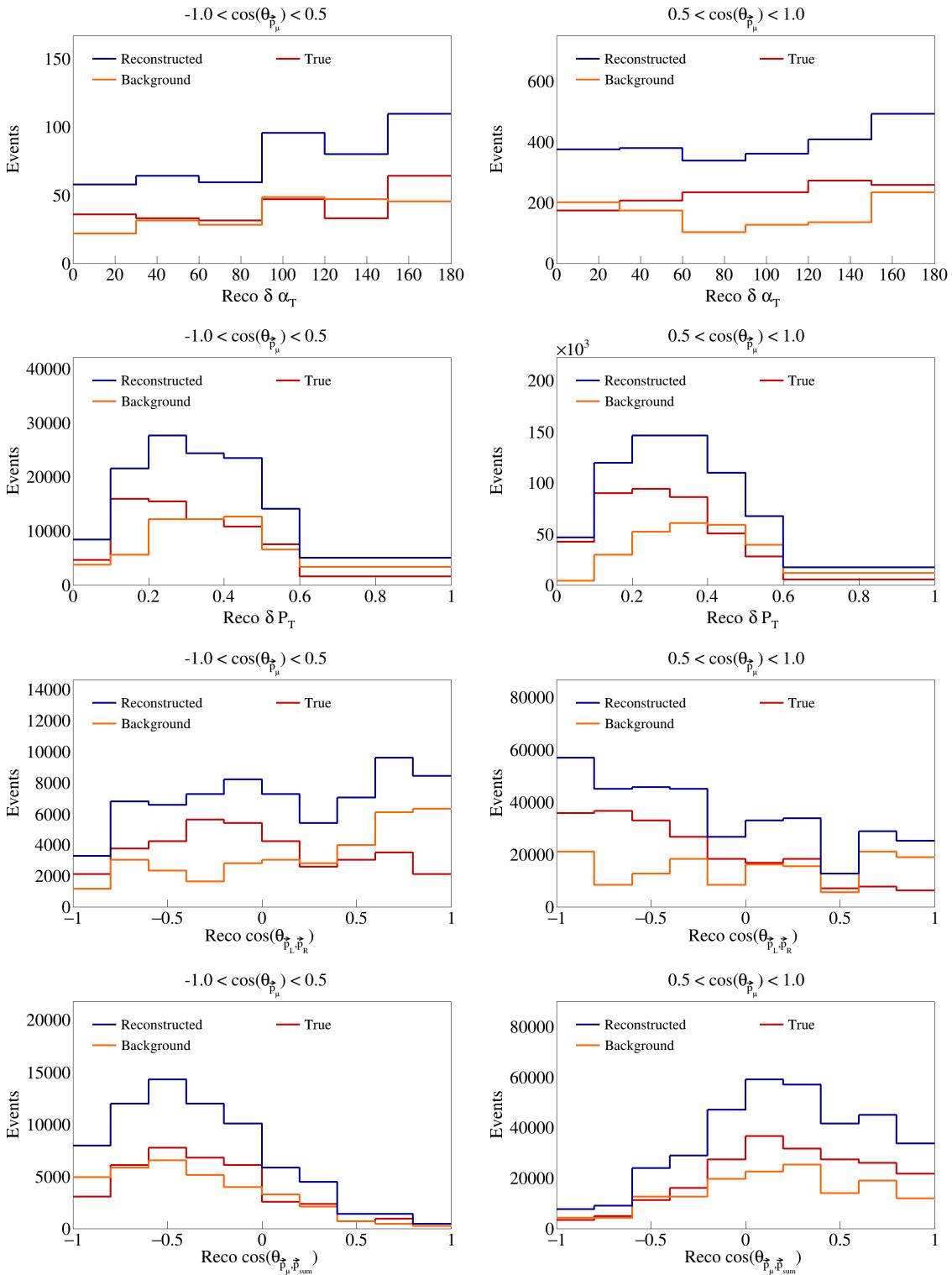


Figure 32: Sliced double differential plots for SBND events.

153 **3.4 Interaction and topology breakdown**

154 We perform an interaction and topology breakdown for the SBND data. For these breakdowns, we look at
155 the reconstructed events that pass our signal definitions cuts and see what percentage of these are generated
156 from different interaction modes and topologies. This helps us get a better idea of what our background
157 signal is composed of. For the interaction breakdown, we look at quasielastic (QE), MEC (meson-exchange
158 current), RES (resonance), and DIS (deep inelastic scattering) events. For the topology breakdown, we look
159 at the number of protons, pions, and muons in the final state. The topologies we label are CC₂p₀pi (our
160 signal definition), CC₁p₀pi, CC($N > 2$)p₀pi, CC($N \geq 0$)p₁pi, and CC₀p₀pi. Any other topology is labeled
161 as “Other”. These breakdowns are shown in Figures 33 to 36.

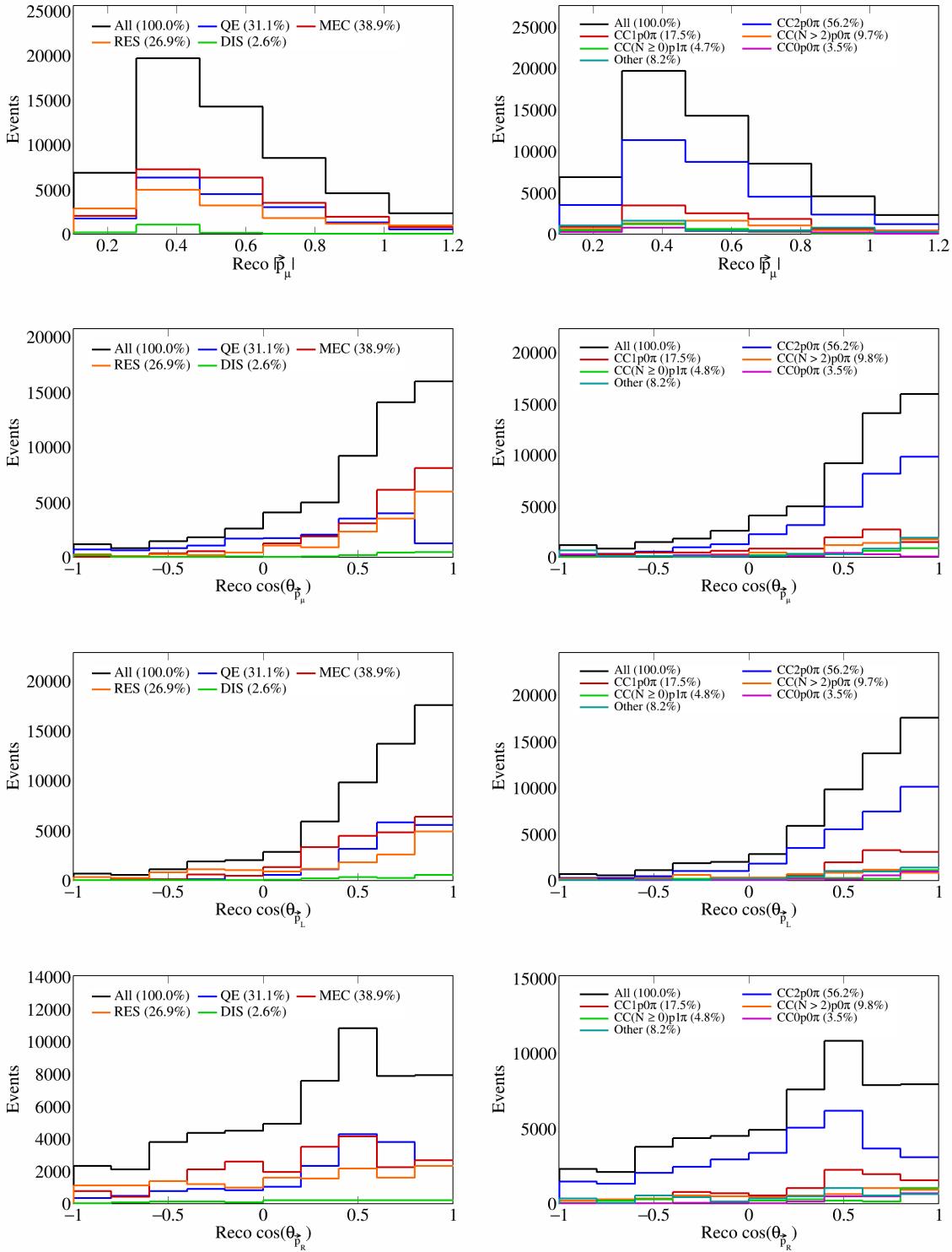


Figure 33: Interaction and topology breakdown for vector directions and magnitudes.

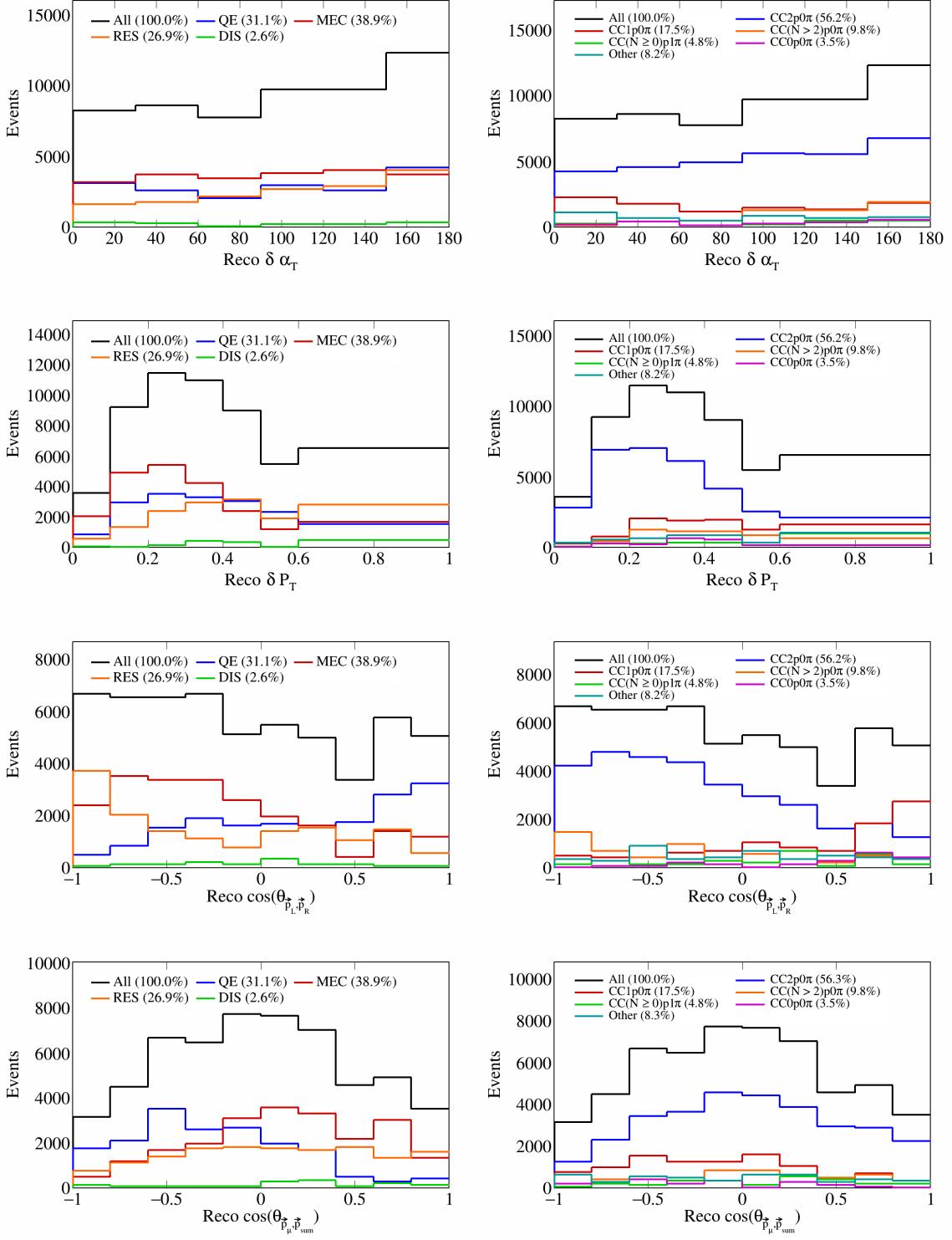


Figure 34: Interaction and topology breakdown for opening angles and transverse variables.

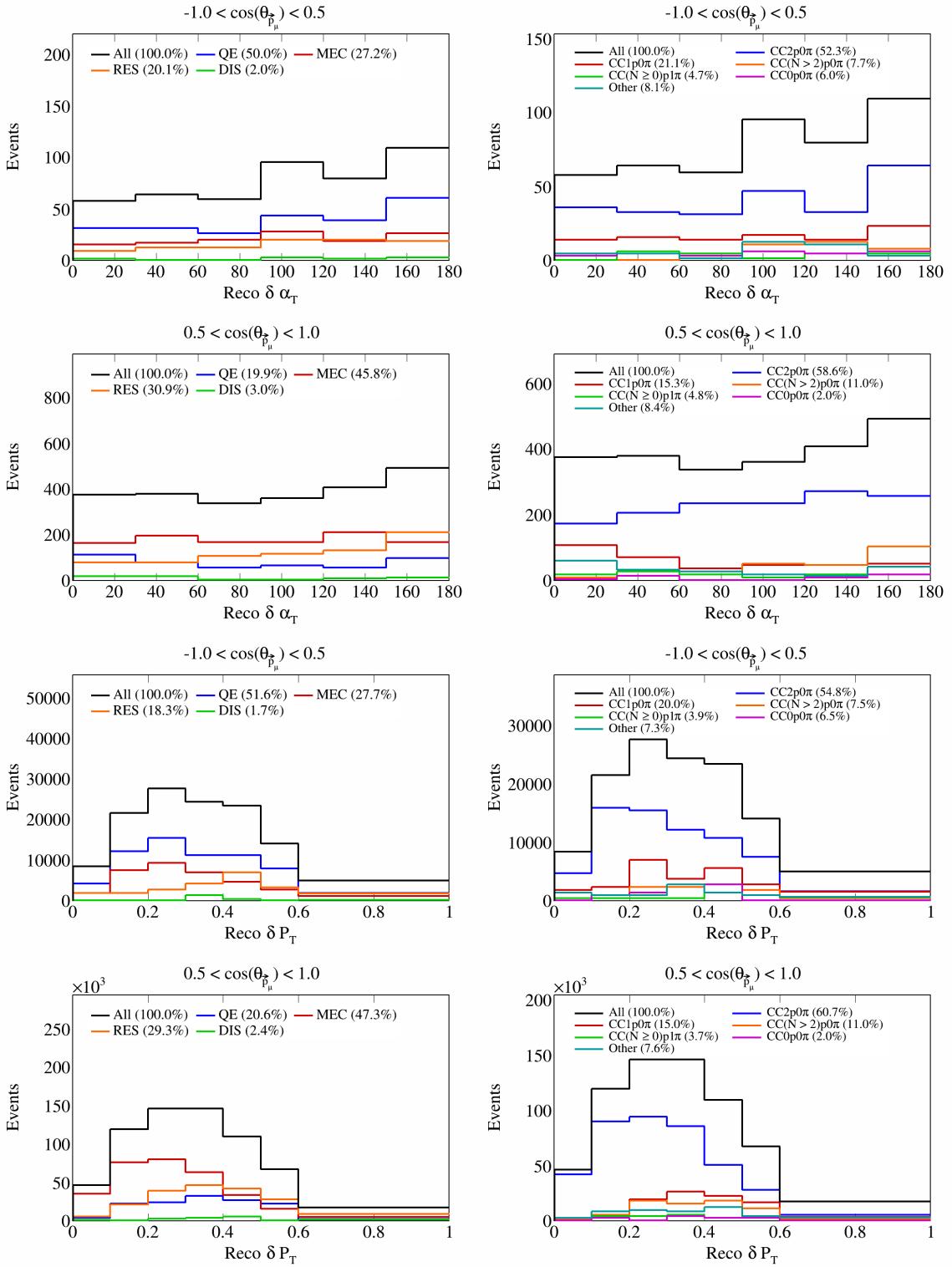


Figure 35: Interaction and topology breakdown for double differential transverse variables.

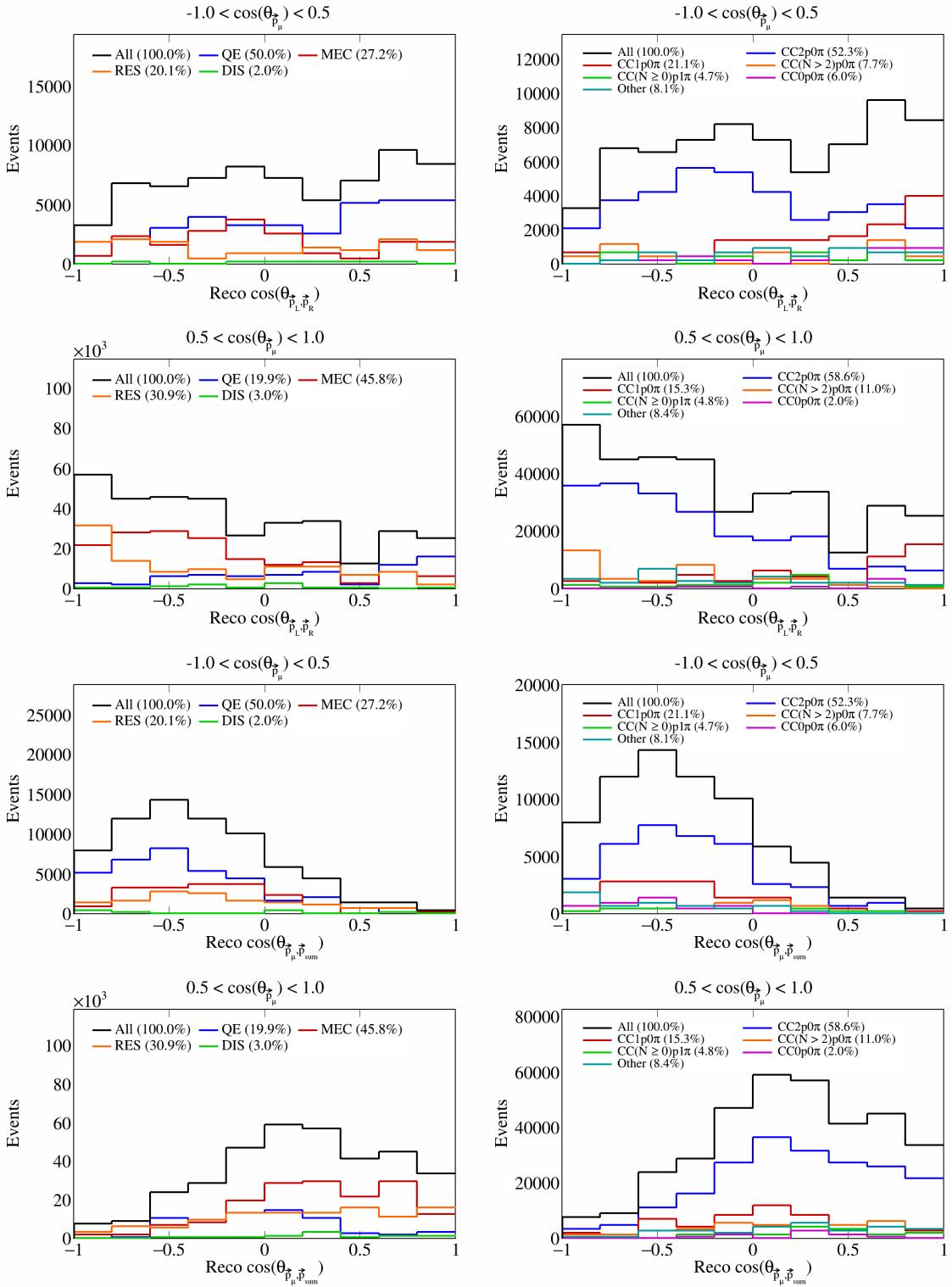


Figure 36: Interaction and topology breakdown for double differential opening angles.

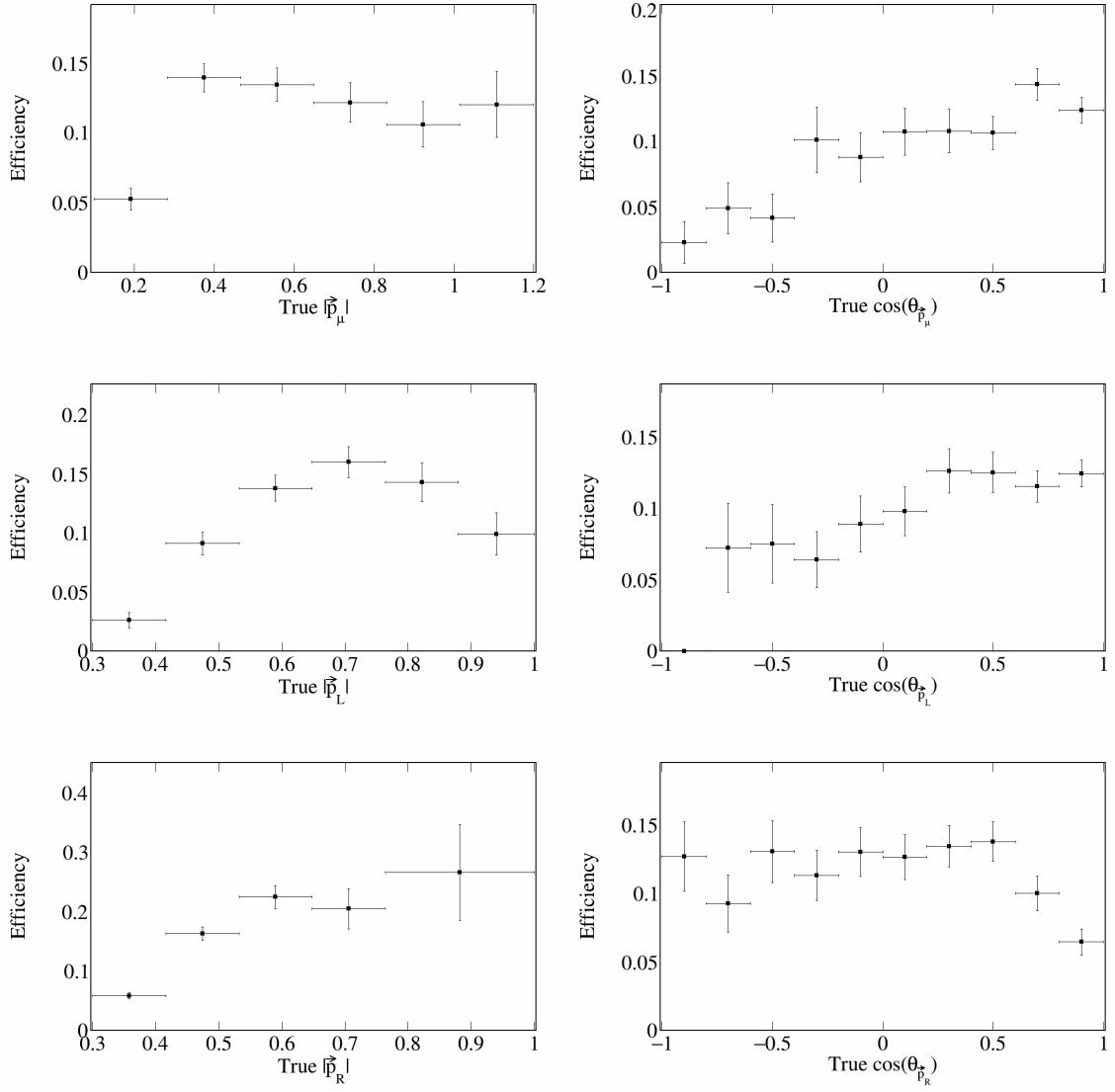


Figure 37: Signal efficiency plots for single differential vector directions and magnitudes.

162 3.5 Signal efficiency

163 Using the truth information about reconstructed events, we can also compute signal efficiency on a bin-by-
 164 bin basis. To be precise, signal definition on a bin i is defined as the ratio between the number of events
 165 generated in bin i and reconstructed in any bin over the number of events generated in bin i . These plots
 166 are shown in Figure 37 and Figure 38 for single-differential variables and Figure 39 for double differential
 167 variables.

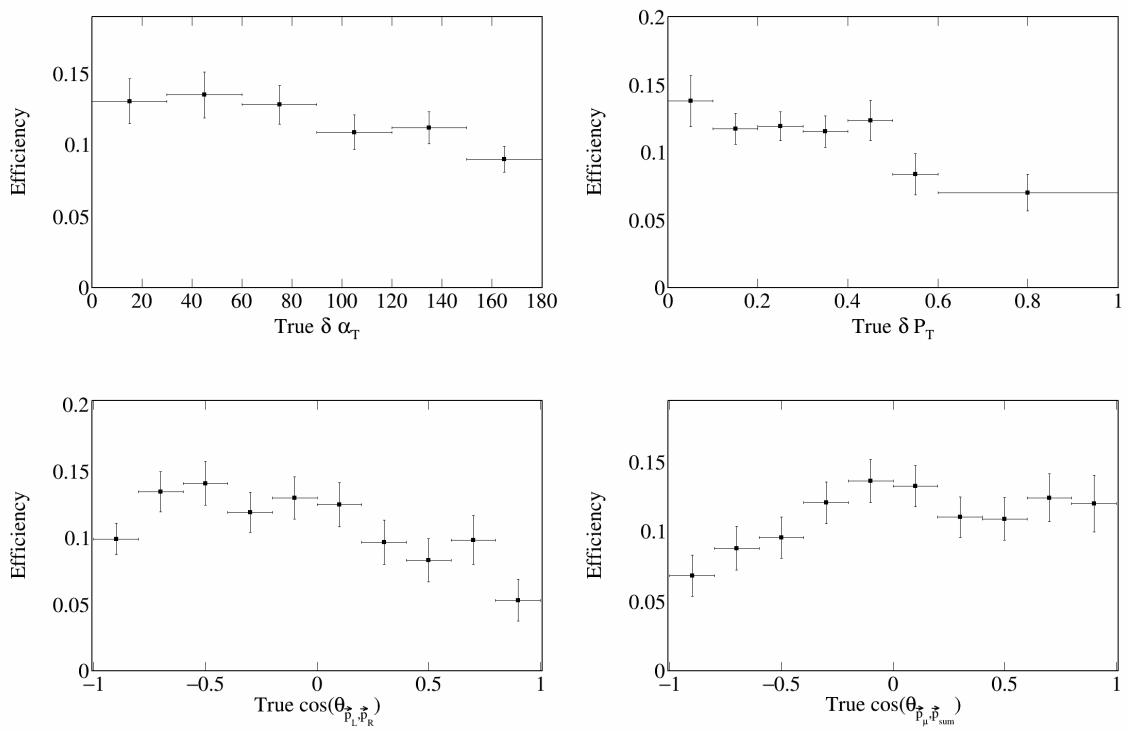


Figure 38: Signal efficiency plots for single differential vector opening angles and transverse momentum.

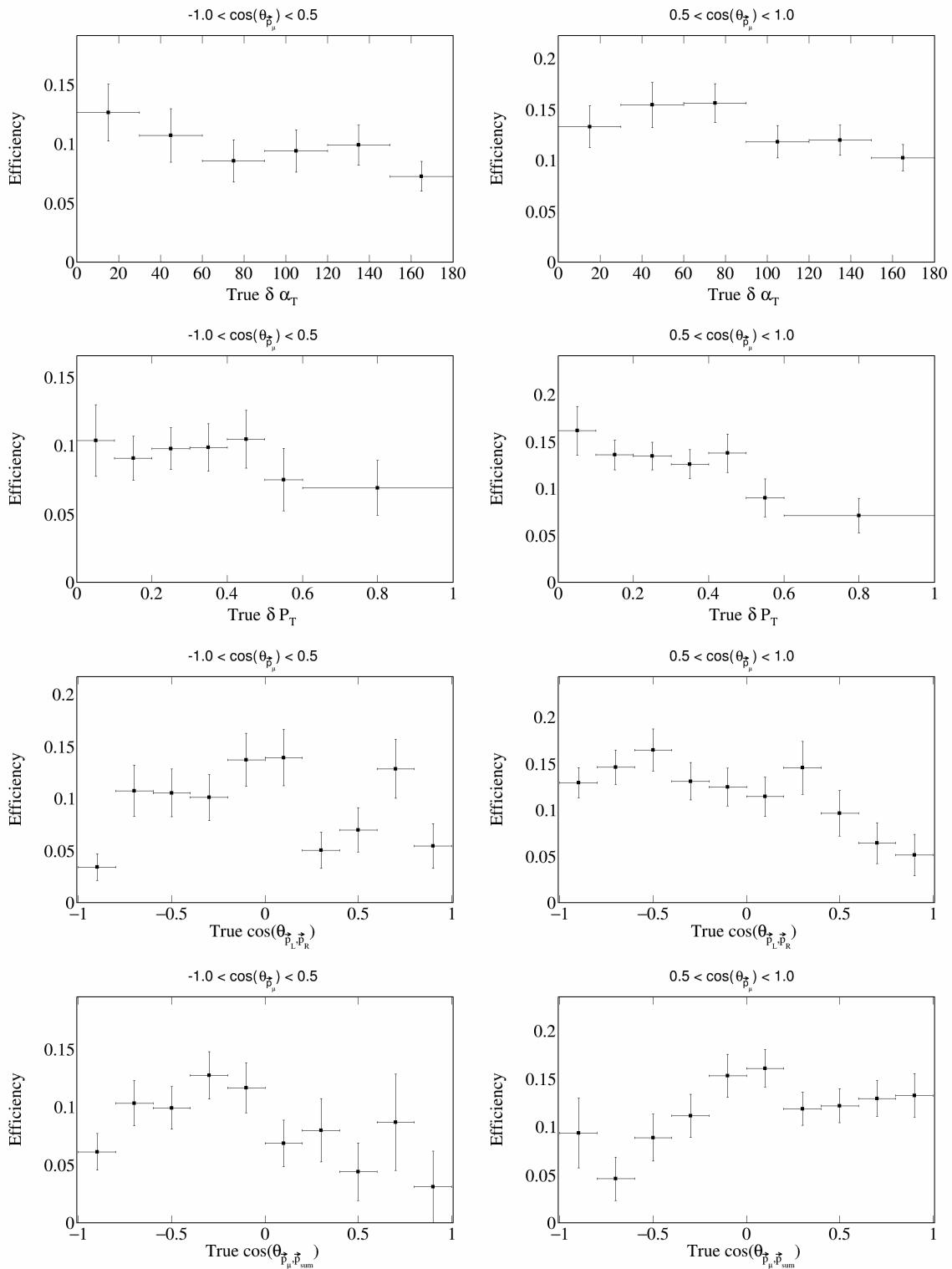


Figure 39: Signal efficiency plots for double differential variables.

168 **3.6 Migration and response matrices**

169 Further, we compute migration matrices which give us a measure of how reliable our reconstructed variables
170 are. A given column in this matrix represents a bin of the truth variable, i.e., the value with which the
171 event was generated. Then, each row corresponds to a reconstructed bin of the same variable, and each cell
172 corresponds to the probability that an event generated with the truth value corresponding to the column gets
173 reconstructed with the value corresponding to the row. For the migration matrix, we consider true signal
174 events that were reconstructed and satisfy our signal definition in the denominator. Therefore, the values in
175 each column must add up to 1. The migration matrices for the single differential variables are presented in
176 Figure 40 and Figure 41. The migration matrices for the double differential variables (given in terms of the
177 bin number) are presented in Figure 42.

178 Response matrices are computed in a similar manner, but using the total number of generated events in the
179 denominator when computing the ratios, i.e., without requiring the events to be successfully reconstructed.
180 Therefore, for these matrices, the columns of the response matrices do not have to add up to 1. The response
181 matrices for single differential variables are presented in Figure 43 and Figure 44, and the double differential
182 response matrices are given in Figure 45. A mathematical definition of the response matrix is given in
183 Equation (10).

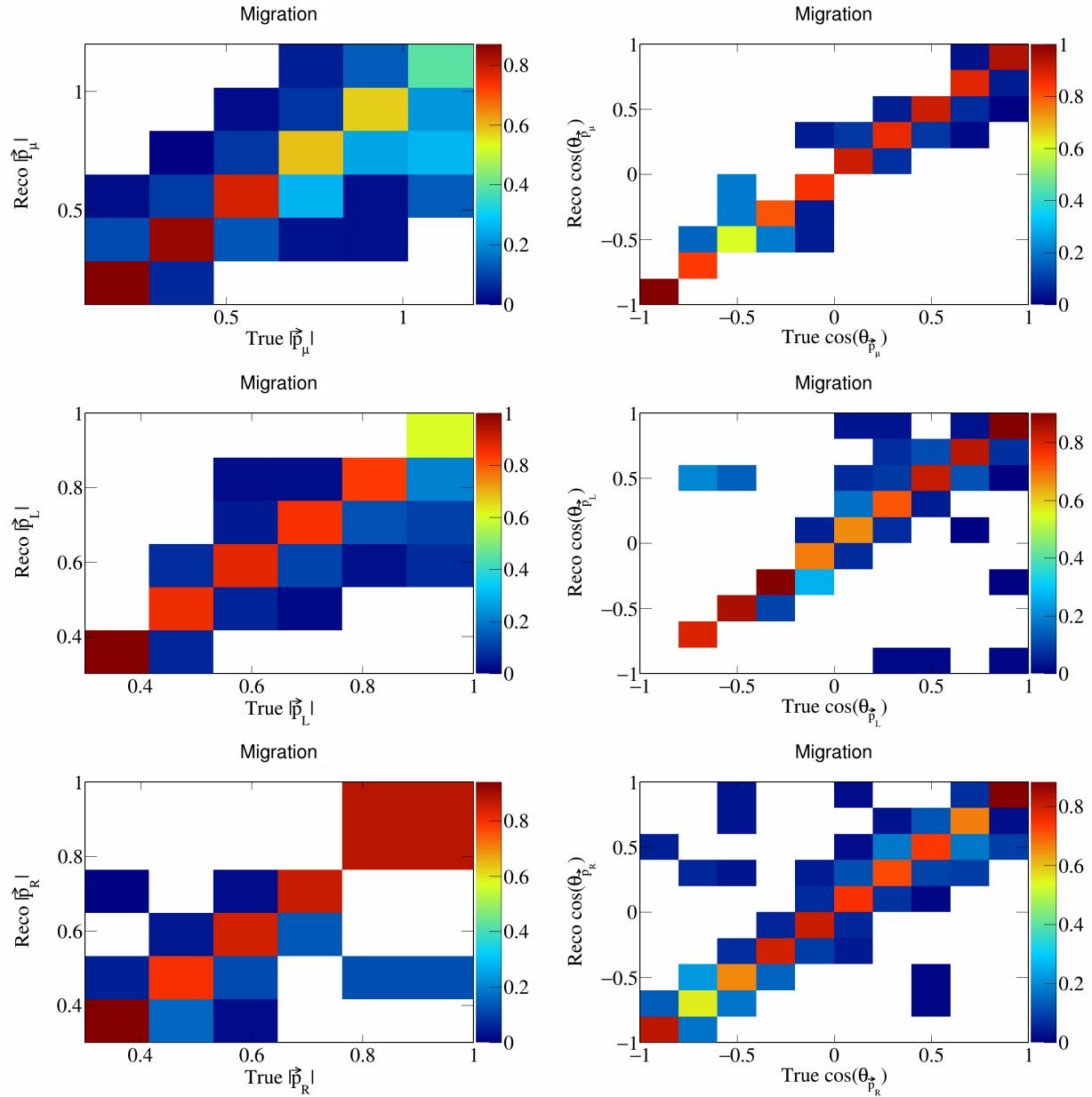


Figure 40: Migration matrices for signal differential vector directions and magnitudes.

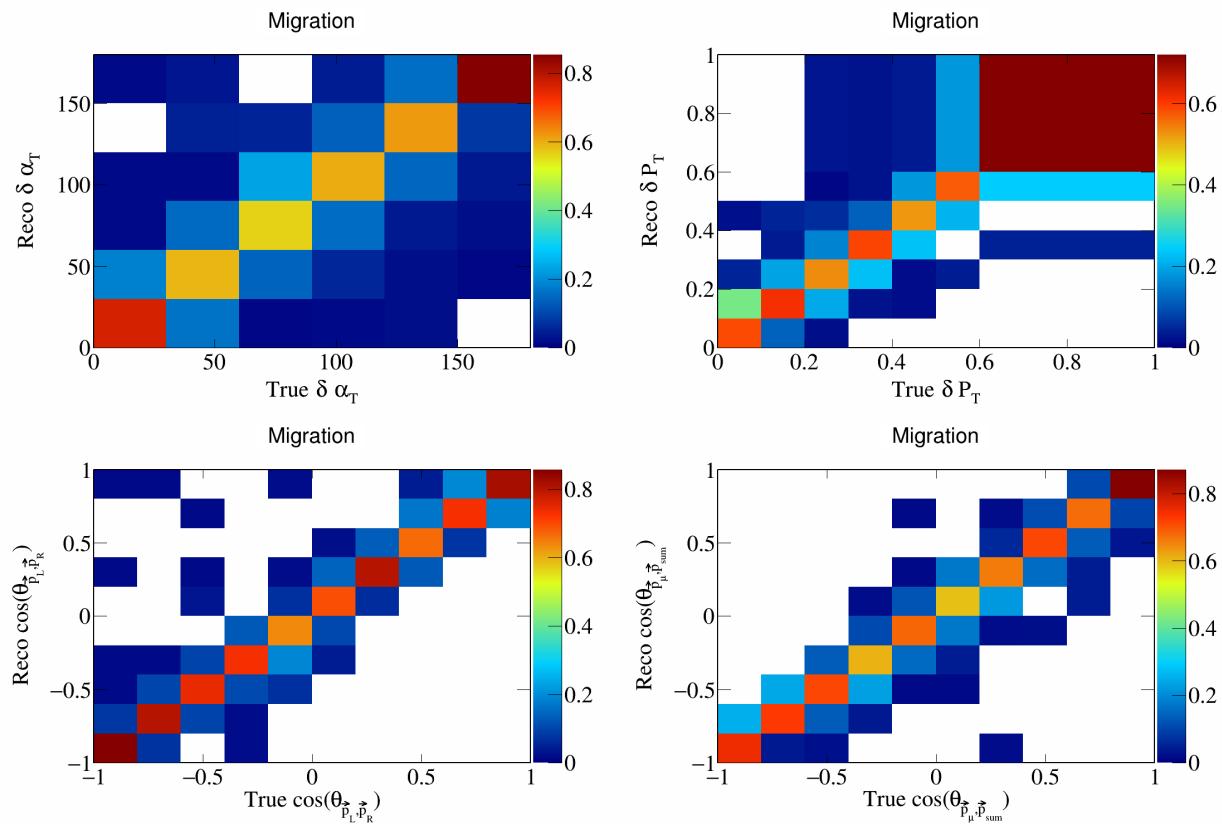


Figure 41: Migration matrices for signal differential vector opening angles and transverse momentum.

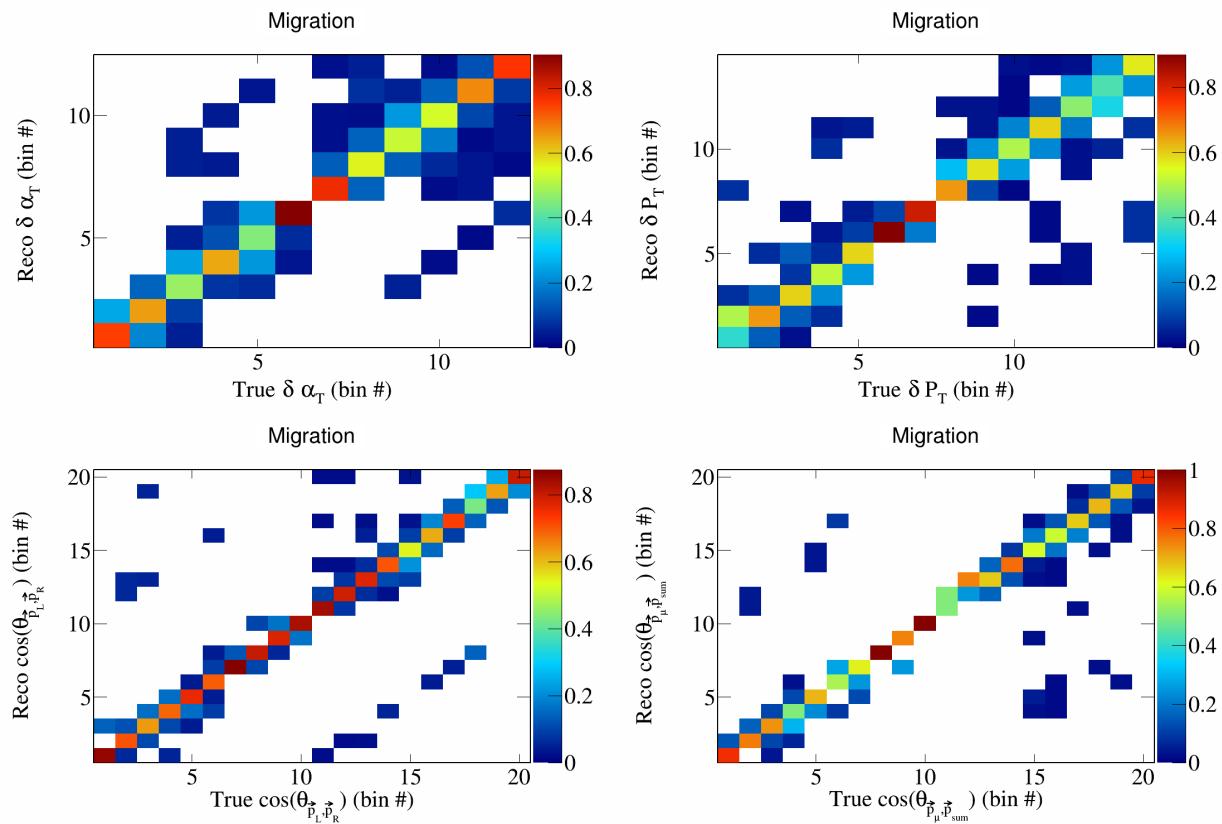


Figure 42: Migration matrices for double differential variables.

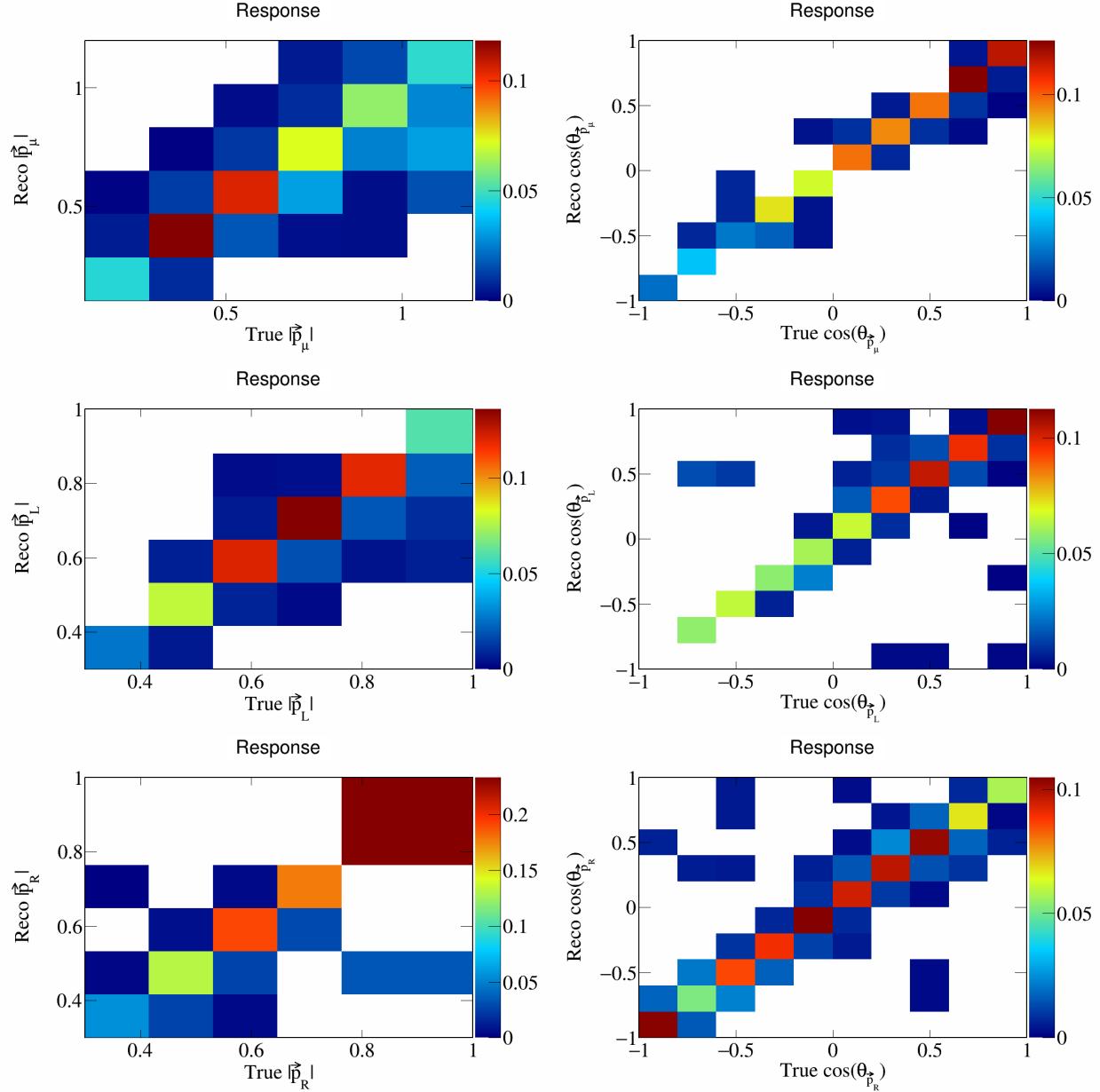


Figure 43: Response matrices for signal differential vector directions and magnitudes.

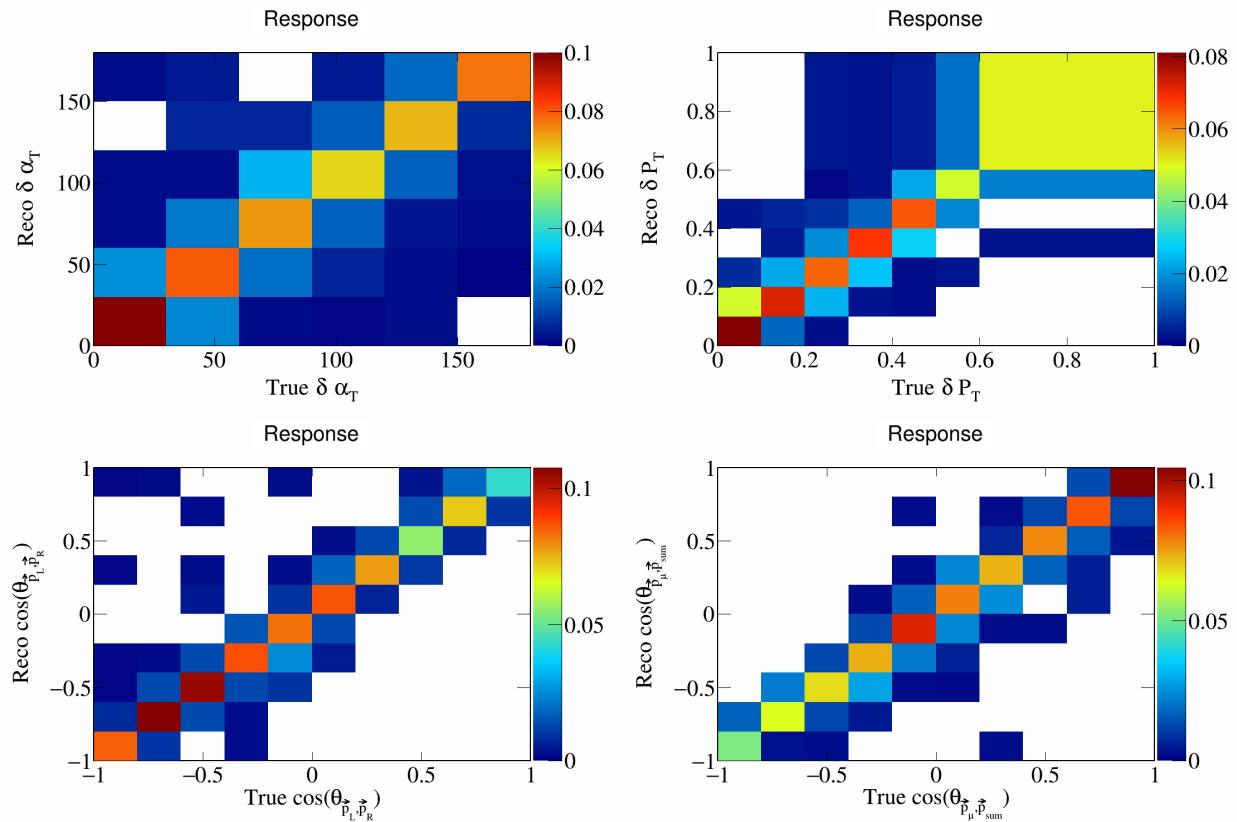


Figure 44: Response matrices for signal differential vector opening angles and transverse momentum.

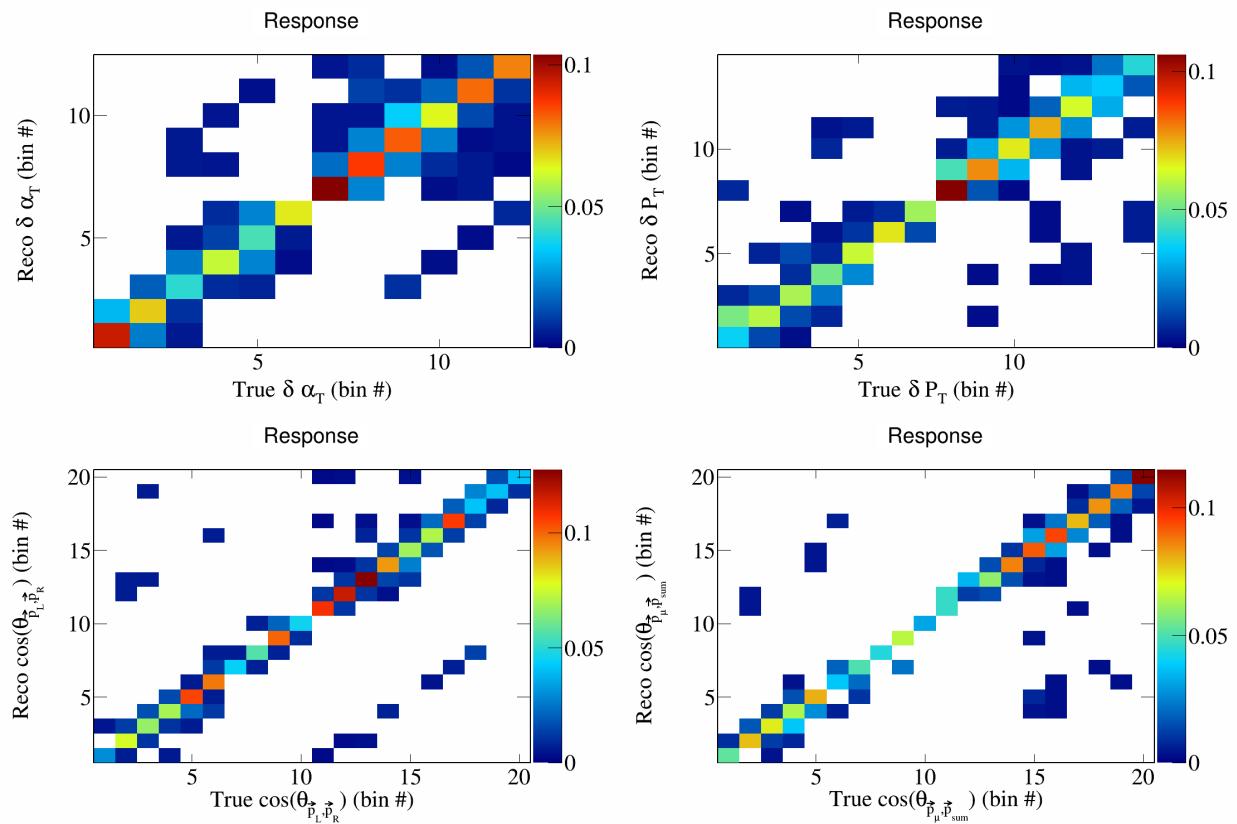


Figure 45: Response matrices for double differential variables.

184 **3.7 Systematics**

185 To include systematic uncertainties in our study, we first consider cross sectional systematics. These are
 186 variations in the cross section models used to generate the events. They can be of two types: multisigma and
 187 multisim. For the former, we consider a 1σ variation of the affected parameters, and in the latter we consider
 188 some number of universes, each with a random variation picked from a Gaussian distribution between 0σ
 189 and 1σ . From these variations, we compute the covariance matrix as

$$E_{i,j} = \frac{1}{N_{\text{Univ}}} \sum_{s=1}^{N_{\text{Univ}}} (\tilde{\sigma}_i^{\text{Var},s} - \tilde{\sigma}_i^{\text{CV}})(\tilde{\sigma}_j^{\text{Var},s} - \tilde{\sigma}_j^{\text{CV}}) \quad (7)$$

190 where $\tilde{\sigma}_i^{\text{Var},s}$ represents the variation flux-integrated event rate of the variable in the i -th bin in the s -th
 191 universe, and $\tilde{\sigma}_i^{\text{CV}}$ is the central value (without any variation) of the flux-integrated event rate in the i -th
 192 bin. More formally,

$$\tilde{\sigma}_i = \frac{N^{\text{reco } i}}{\Phi_\nu^{\text{CV}} \times N_{\text{targets}}}, \quad (8)$$

193 where $N^{\text{reco } i}$ is the number of reconstructed events in bin i , Φ_ν^{CV} is the central value of the neutrino flux
 194 (which remains the same for each variation), and N_{targets} is the number of target Argon nuclei. Further, we
 195 have that $N^{\text{reco } i} = M_{i,j} \times S^{\text{true } j} + B^{\text{reco } i}$, where $M_{i,j}$ is the response matrix corresponding to the true bin j
 196 and reco bin i , $S^{\text{true } j}$ is the number of true signal events in bin j , and $B^{\text{reco } i}$ is the number of reconstructed
 197 background events in bin i . Therefore, we have that

$$\tilde{\sigma}_i = \frac{M_{i,j}^{\text{univ}} \times S^{\text{true } j \text{ CV}} + B^{\text{reco } i \text{ univ}}}{\Phi_\nu^{\text{CV}} \times N_{\text{targets}}}, \quad (9)$$

198 where

$$M_{i,j}^{\text{univ}} = \frac{RS^{\text{true } j, \text{ reco } i \text{ univ}}}{S^{\text{true } j \text{ CV}}}, \quad (10)$$

199 with $RS^{\text{true } j, \text{ reco } i \text{ univ}}$ being the number of signal events generated in bin j and reconstructed in bin i , and
 200 $S^{\text{true } j}$ being the number of signal events generated in bin j . For each variation, terms labeled with **univ**
 201 are modified according to the variation, and terms labeled with **CV** remain the same. When considering the
 202 cross-section variations, the response matrix is modified via the normalization to the true signal in a given
 203 universe as

$$M_{i,j}^{\text{univ}} = \frac{RS^{\text{true } j, \text{ reco } i \text{ univ}}}{S^{\text{true } j \text{ univ}}}. \quad (11)$$

204 Then, the fractional covariance matrix is defined as

$$F_{i,j} = \frac{E_{i,j}}{\tilde{\sigma}_i^{\text{CV}} \tilde{\sigma}_j^{\text{CV}}}. \quad (12)$$

205 And the correlation matrix is defined as

$$\rho_{i,j} = \frac{E_{i,j}}{\sqrt{E_{i,i} E_{j,j}}}. \quad (13)$$

206 In the case of a multisigma systematic, $N_{\text{Univ}} = 1$, and for a multisim systematic, this number varies but is
 207 usually 100 or 1000.

208 The plots for all the individual cross sectional systematics are shown in Appendix 6.1. Flux systematics
 209 are computed in the same way, but each universe varies a flux parameter. The corresponding plots for the
 210 individual flux systematics are shown in Appendix 6.2. We also consider statistical systematics. This are
 211 straightforward to compute, as the covariance matrix is given by the square root of the number of elements
 212 in the corresponding bin in the histogram. These statistical covariance matrices are shown in Appendix 6.3.

213 For POT systematics, we consider a 2% variation in the number of protons on target and treat it as a 1σ
214 variation. The corresponding plots are shown in Appendix [6.4](#). For number of target systematics, we likewise
215 consider a 1% variation in the number of target nuclei and treat it as a 1σ variation. The corresponding
216 plots are shown in Appendix [6.5](#). We consider detector variations of 15% flat for the moment, and these are
217 shown in Appendix [6.6](#). We consider reinteraction systematics as a 2% flat variation, and these are shown
218 in Appendix [6.7](#). The total covariance matrices for each variable are shown in Figures [46](#) and [47](#).

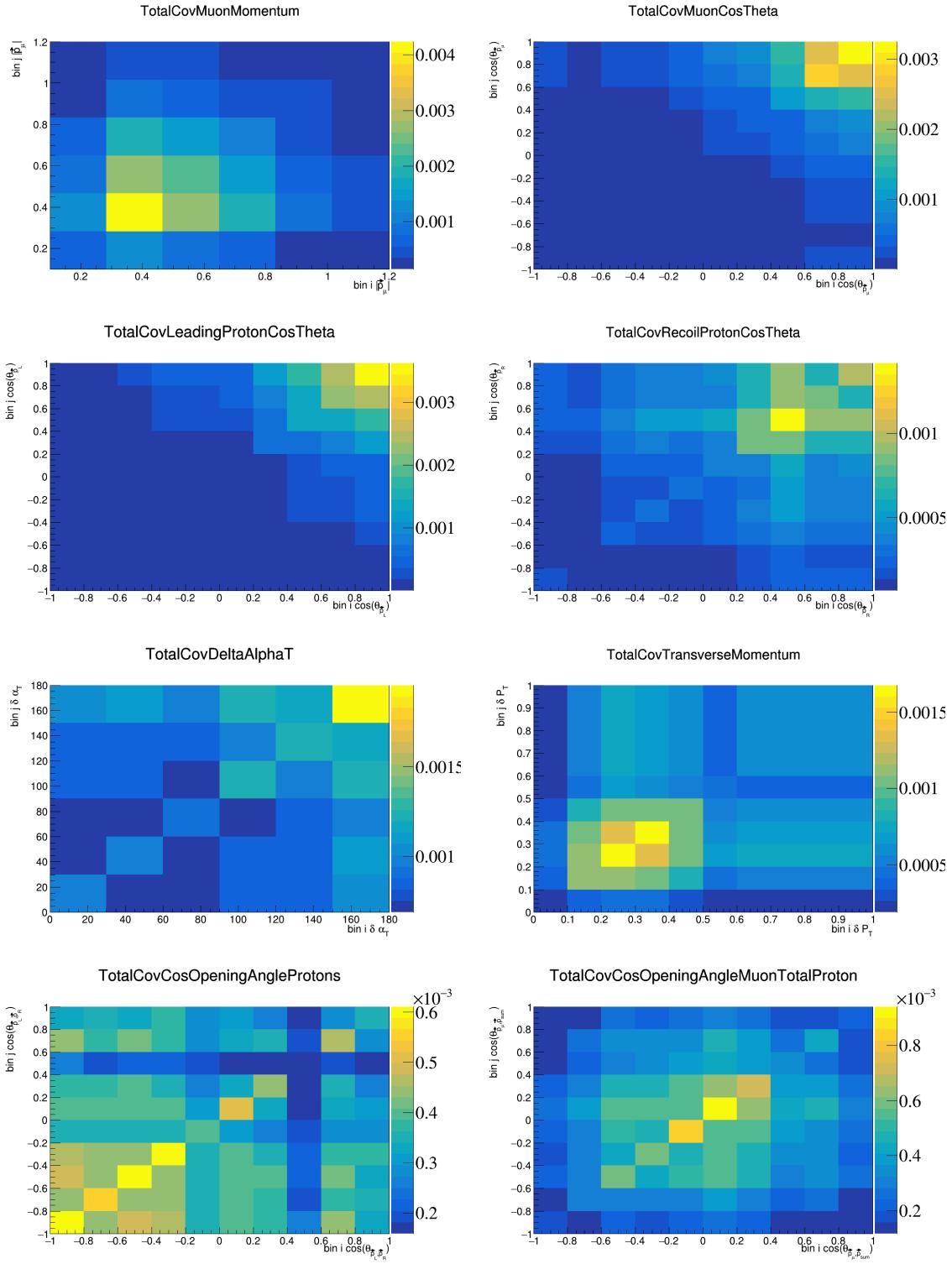


Figure 46: Total covariance matrices for single differential variables.

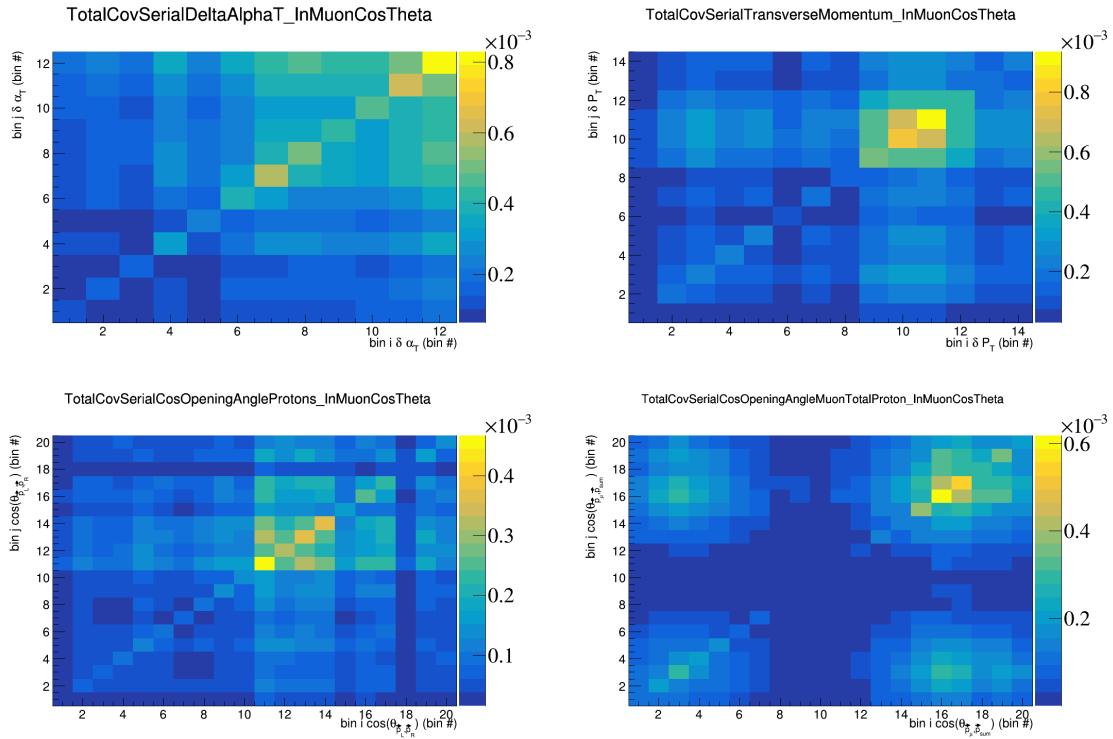


Figure 47: Total covariance matrices for double differential variables.

219 **3.8 Wiener-SVD unfolding**

220 We use the total covariance matrices obtained from all the systematics and shown in the previous section
221 to unfold our data. We perform this unfolding following the Wiener-SVD method [27], which for a given
222 variable takes as input a response matrix, true signal histogram, a reconstructed signal histogram, and the
223 covariance matrix.

224 The output is the unfolded spectrum, a smearing matrix that can be used to smear true signal histograms,
225 and a covariance rotation matrix to consider uncertainties in the regularized space as opposed to the true
226 space. The additional smearing matrices obtained from the Wiener-SVD unfolding are shown in Figures 48
227 and 49.

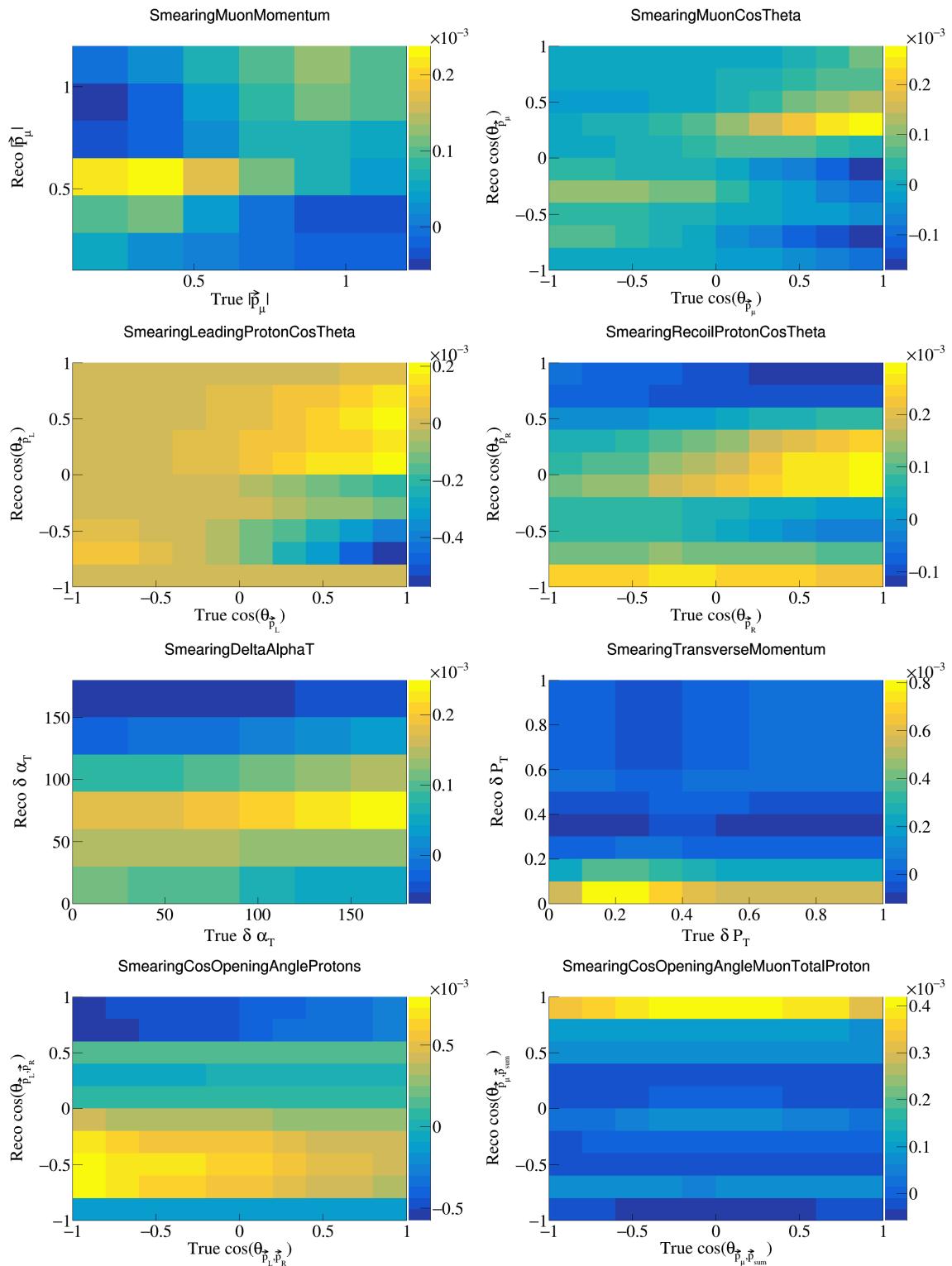


Figure 48: Additional smearing matrices for single differential variables.

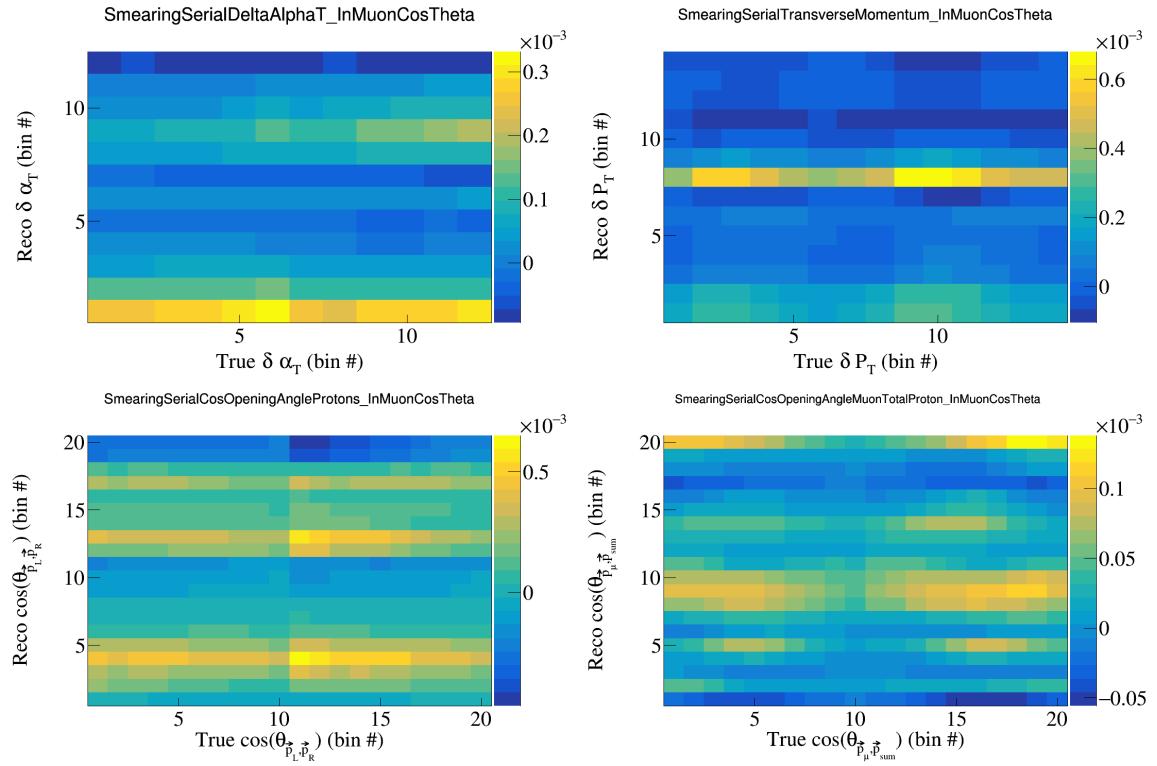


Figure 49: Additional smearing matrices for double differential variables.

228 **3.9 Closure test**

229 To ensure that the unfolding techniques implemented work correctly, we use the true signal part of our
230 Monte-Carlo data as our signal, and compare it to the truth level signal prediction to see that they are
231 identical. The plots showing they are identical are in Figure 50 and Figure 51. We also note that the overall
232 shape and magnitude of our histograms match previously reported MicroBooNE analyses.

233 The error bands for the unfolded spectra are given by the cross-section uncertainties, which are shown
234 in a bin-by-bin basis in the Section 4.1. For the sliced double differential measurements, we make sure to
235 divide by the slice and bin widths to obtain the correct error bands. In the single differential measurements,
236 we only have to divide by the bin width.

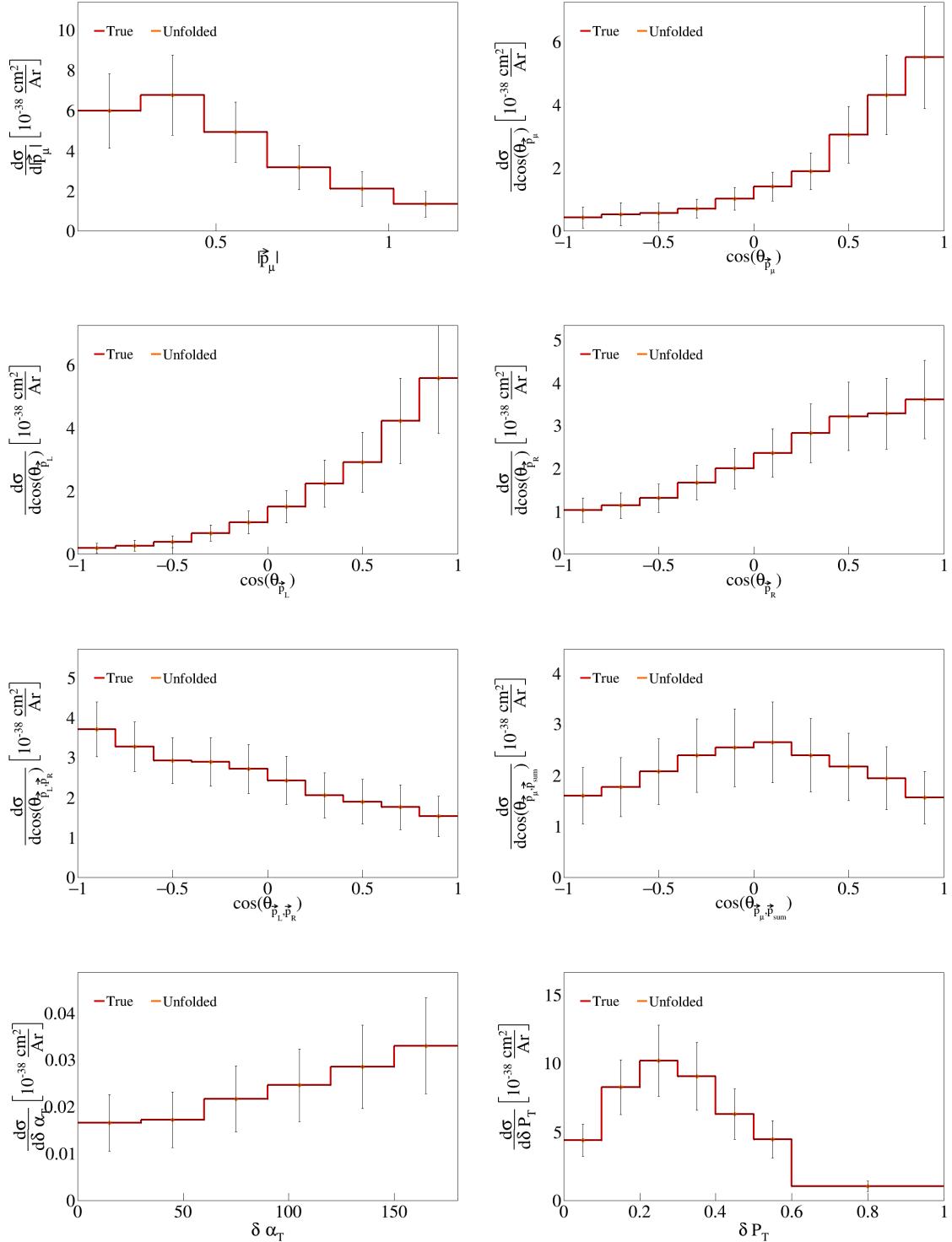


Figure 50: Closure test for single differential plots.

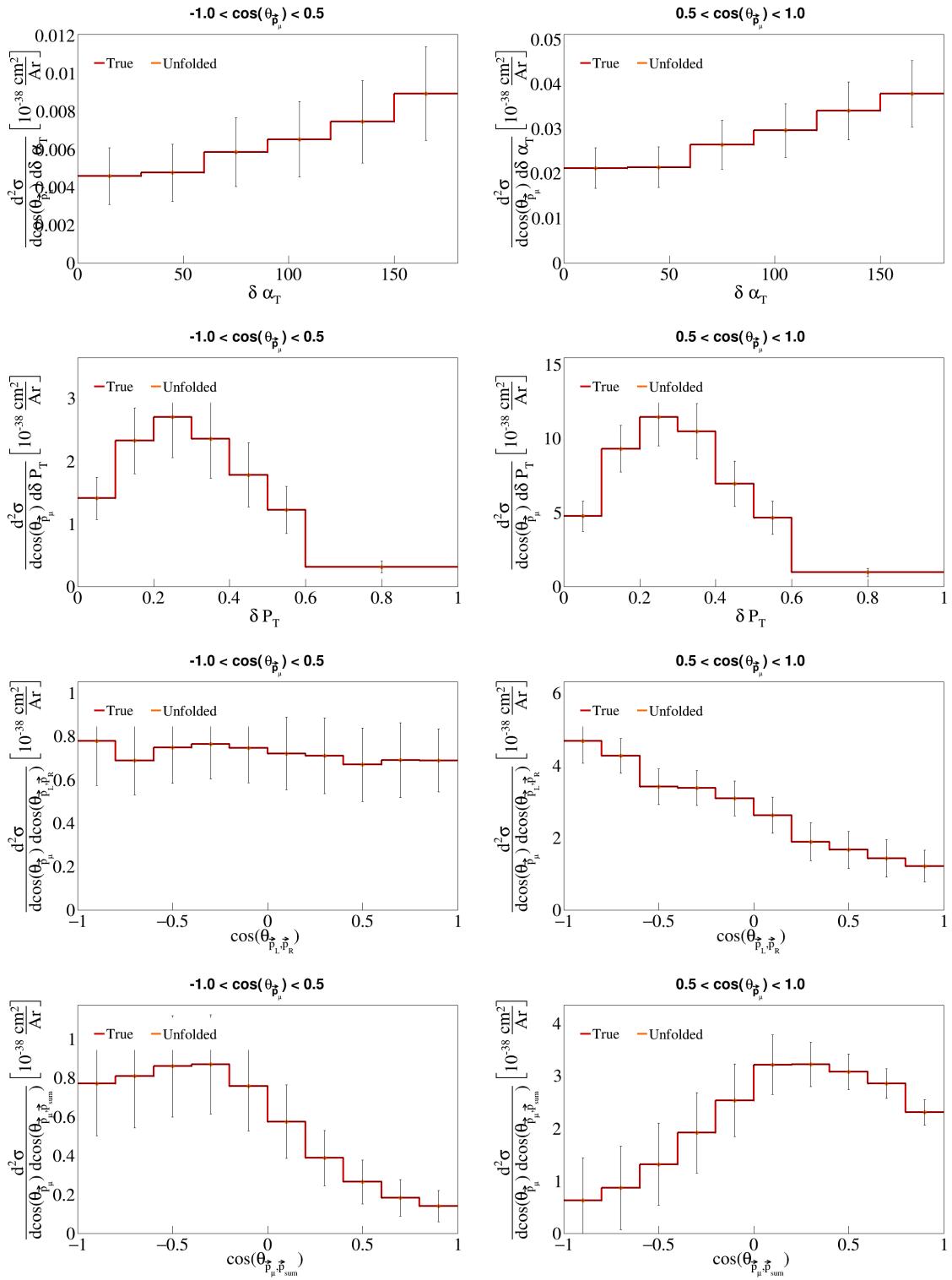


Figure 51: Closure test for double differential plots.

²³⁷ **3.10 Event rate uncertainties**

²³⁸ Figure 52 shows the single bin uncertainty breakdown using the event rates. We used the square root of
²³⁹ the relevant fractional covariance matrix for each of the outlined sources of uncertainty to obtain the figure.
²⁴⁰ The bin by bin event rate uncertainties for all our variables are shown in Figures 53 to 55.

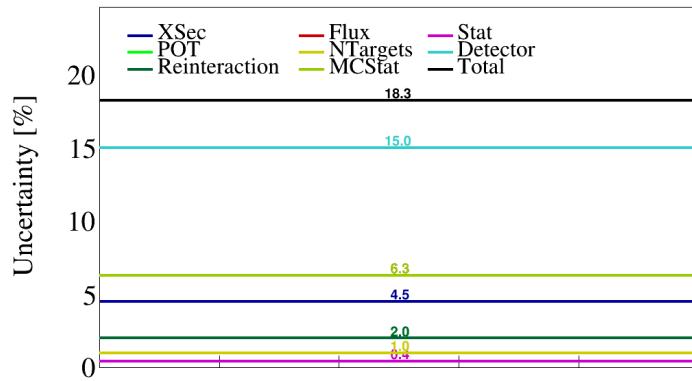


Figure 52: Fractional contribution for the sources of uncertainty using the event rates.

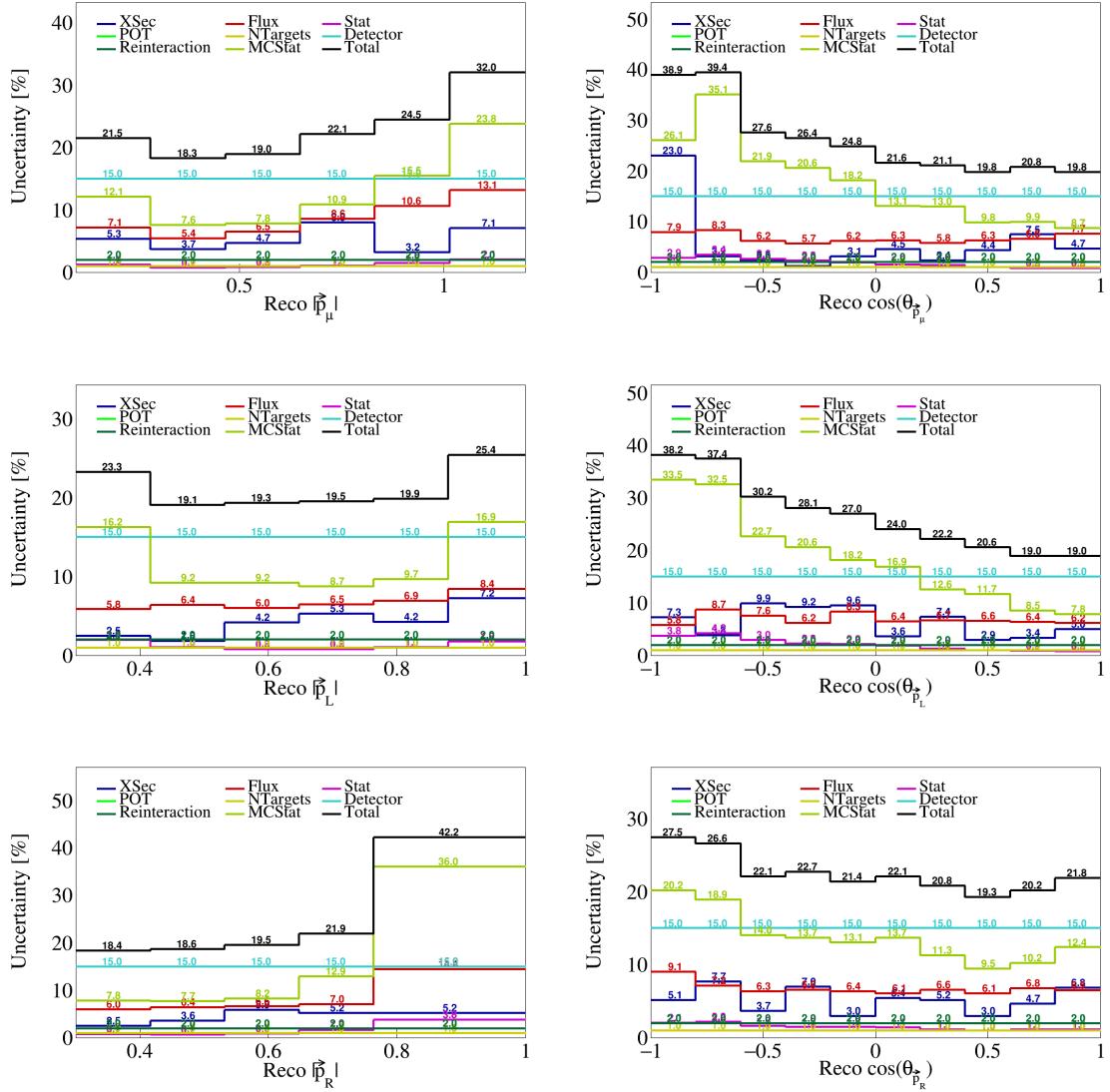


Figure 53: Bin by bin event rate uncertainties for single differential vector directions and magnitudes.

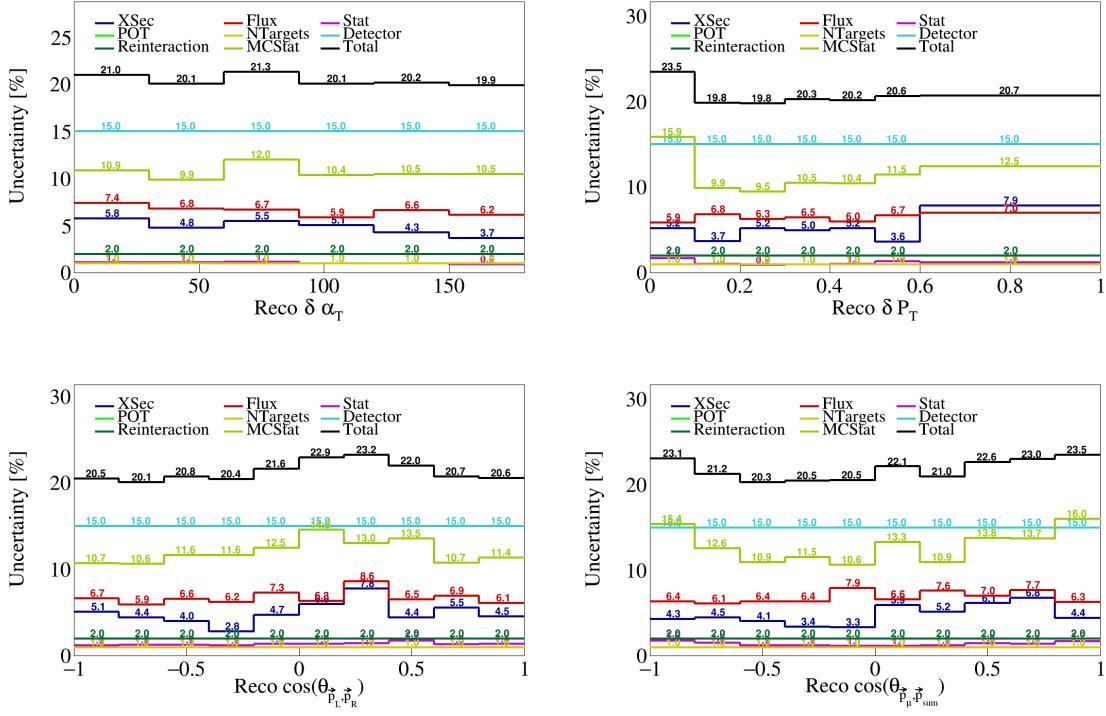


Figure 54: Bin by bin event rate uncertainties for single differential vector opening angles and transverse momentum.

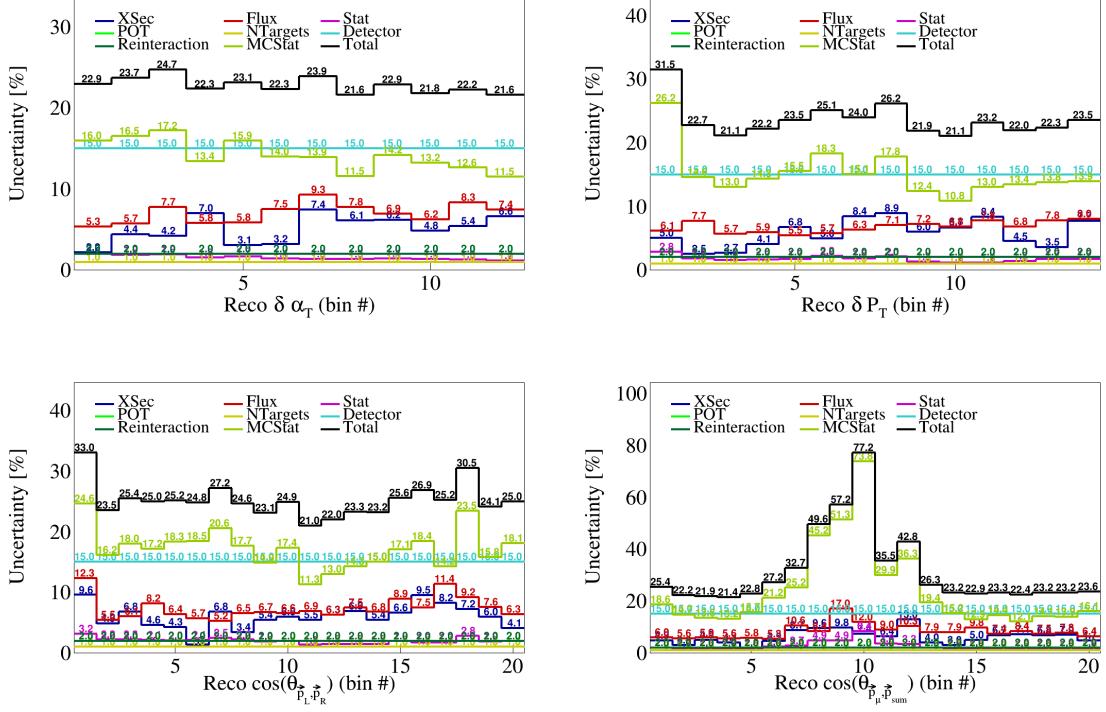


Figure 55: Bin by bin event rate uncertainties for double differential variables.

²⁴¹ **4 Cross-section results**

²⁴² Placeholder.

²⁴³ **4.1 Cross-section uncertainties**

²⁴⁴ Figure 56 shows the single bin uncertainty breakdown using the cross sections. We used the unfolded
²⁴⁵ covariances obtained with the Wiener-SVD filter for each of the sources of uncertainty. The square root of the
²⁴⁶ corresponding fractional covariance matrix is normalized to the CV cross-section value for the uncertainties
²⁴⁷ to be obtained. The bin by bin cross section uncertainties for all our variables are shown in Figures 57 to 59.

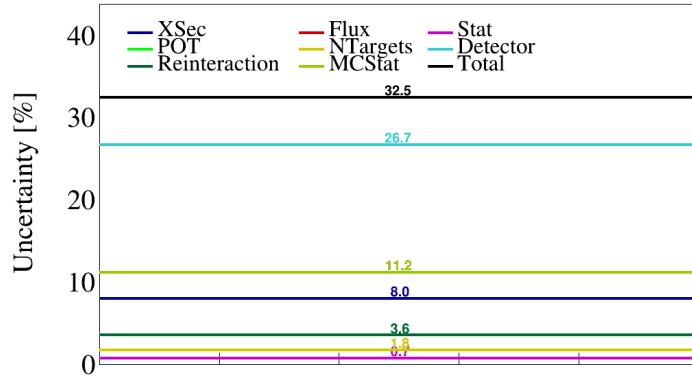


Figure 56: Fractional contribution for the sources of uncertainty using the cross sections.

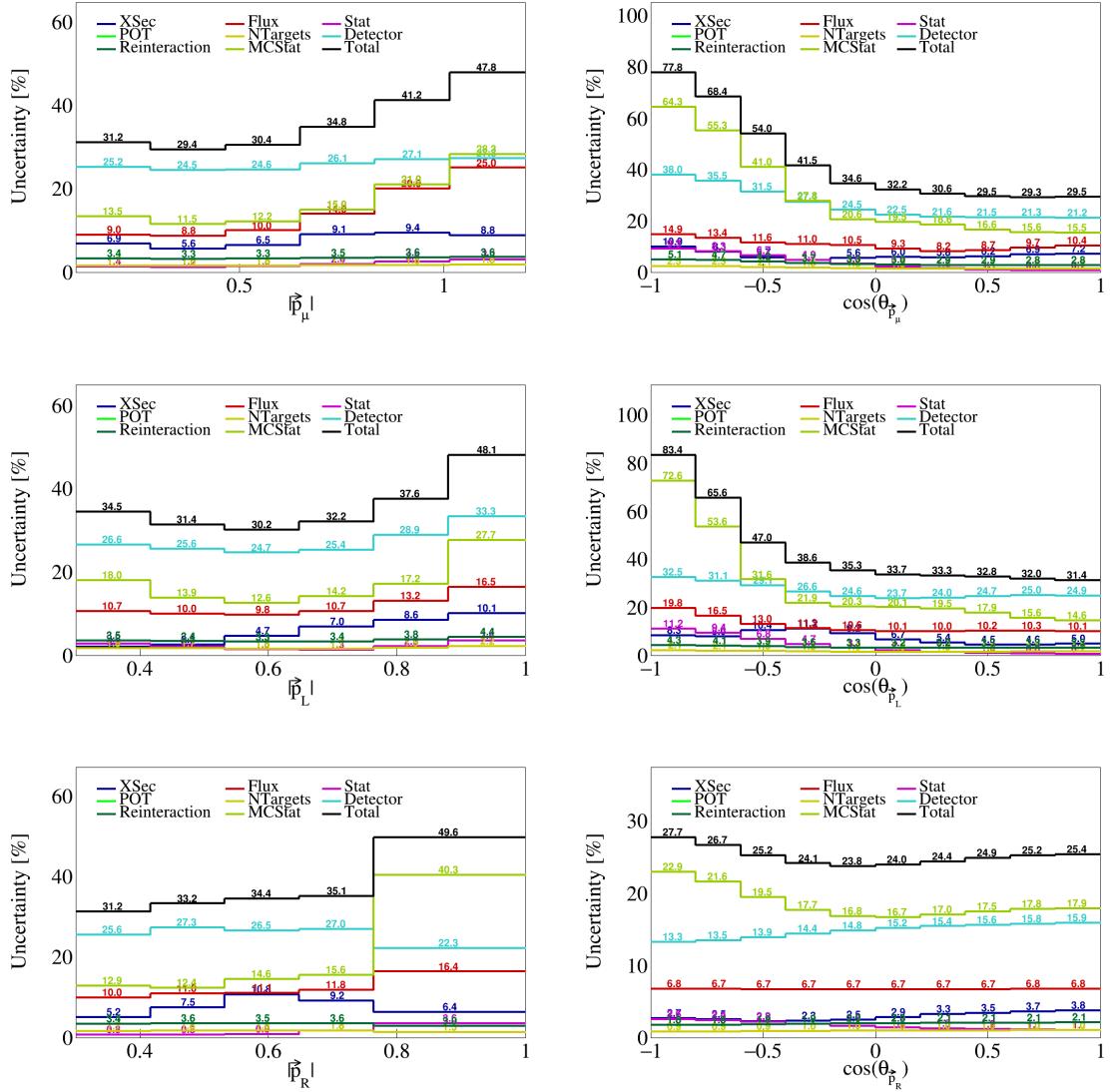


Figure 57: Bin by bin event cross-section uncertainties for single differential vector directions and magnitudes.

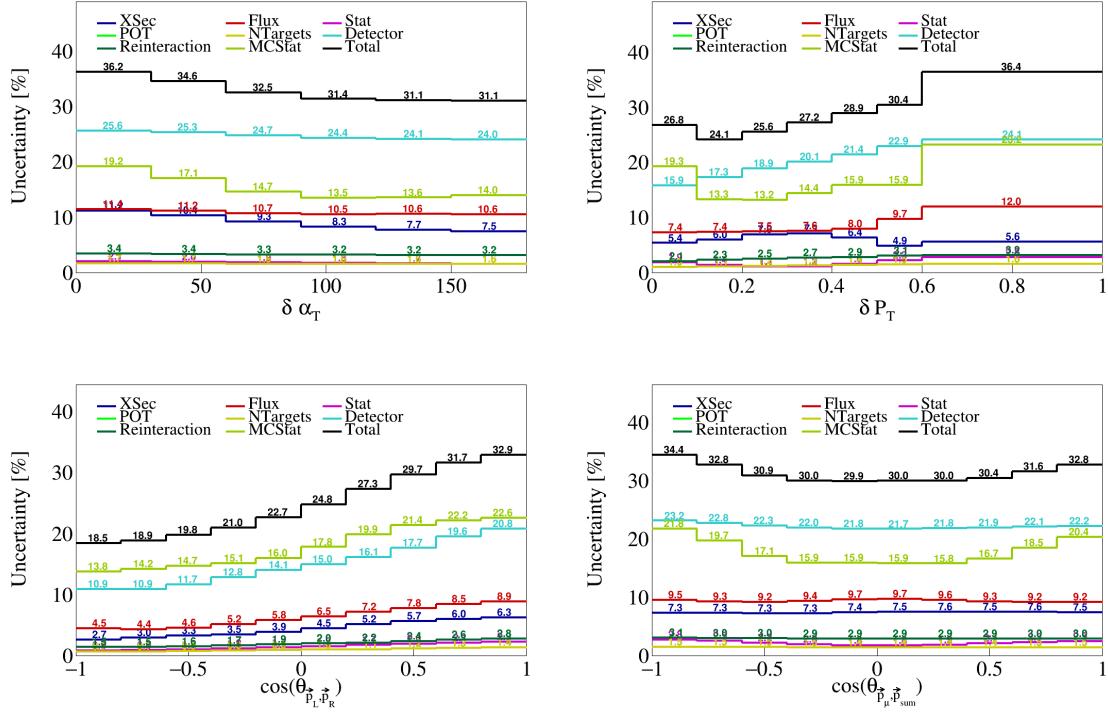


Figure 58: Bin by bin cross-section uncertainties for single differential vector opening angles and transverse momentum.

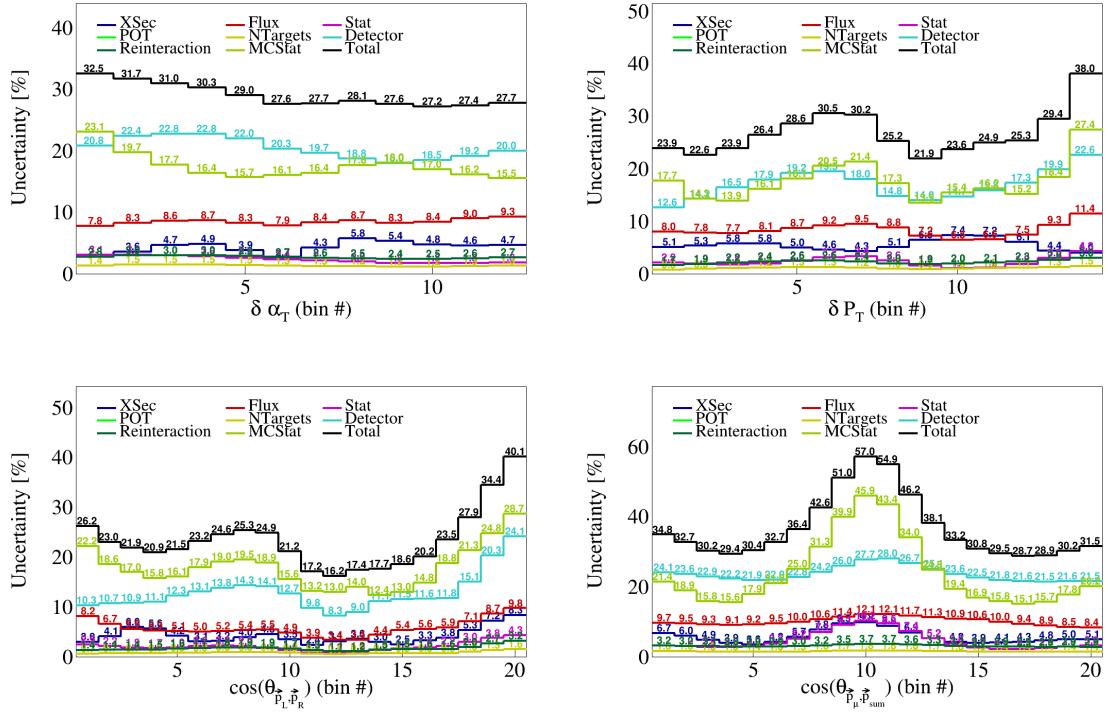


Figure 59: Bin by bin cross-section uncertainties for double differential variables.

248 **5 Fake data studies**

249 To test our unfolding procedure, we generate fake data by increasing the weight of certain events in our
250 Monte Carlo simulations. We give meson exchange current (MEC) events a weight of 2 in Section 5.1,
251 and quasi-elastic (QE) events a weight of 2 in Section 5.2. We then unfold these fake data using the
252 nominal Monte-Carlo predictions from the GENIE AR23 generator. Therefore, the input to the Wiener-
253 SVD unfolding are: the response matrix constructed with the nominal predictions, the true nominal signal,
254 the reconstructed signal from the fake data (this is the only input that changes), and the total covariance
255 matrix, which in this case was the statistical covariance matrix for the fake data added to the MC statistical
256 and cross-section covariance matrices obtained with the nominal predictions.

257 After unfolding the fake data, we compare the unfolded fake data to the smeared fake signal and the
258 smeared nominal signal, using the additional smearing matrix obtained from the Wiener-SVD unfolding. We
259 then perform a χ^2 test to see if the unfolded fake data agrees with the smeared fake signal. Additionally, we
260 also report the p - and σ -values for the distributions. We expect to see good agreement between the smeared
261 fake signal and the unfolded fake data, while the smeared nominal signal should not agree with the unfolded
262 fake data. In other words, we expect below 1σ agreement between the smeared fake signal and unfolded fake
263 data.

264 **5.1 MEC 2x weight**

265 In this first fake data study, we give MEC events a weight of 2, while keeping all other events with a weight
266 of 1. We see that we are under 1σ agreement between the smeared fake signal and the unfolded fake data
267 for all our variables, while on or above 2.9σ with the smeared nominal signal, as expected. Therefore, we
268 can conclude that this fake data study was successful. The unfolded fake data along with the two smeared
269 signals is shown in Figures 60 to 63.

270 **5.2 QE 2x weight**

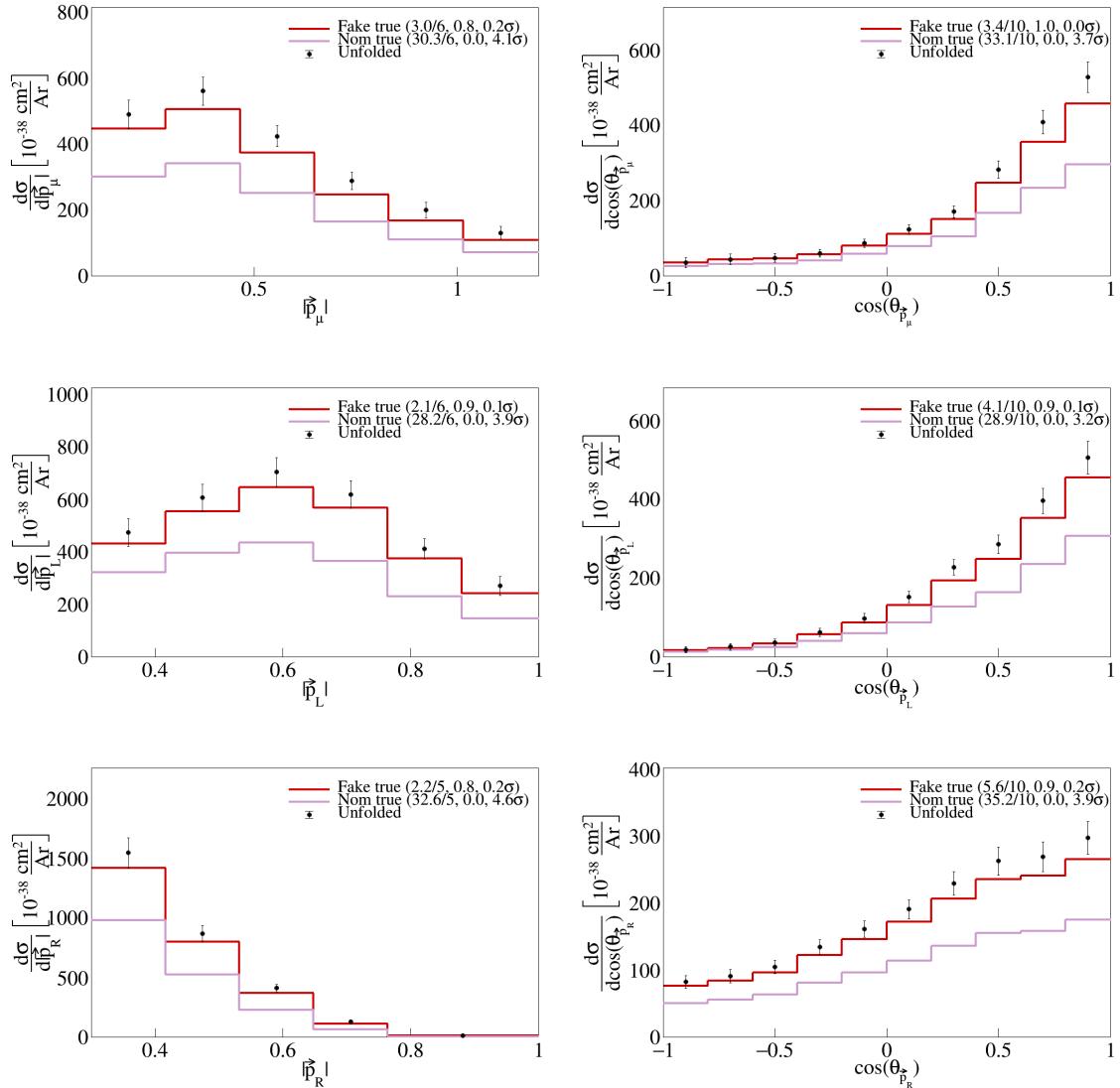


Figure 60: Unfolded fake data showing agreement with smeared fake signal data for single differential vector directions and magnitudes.

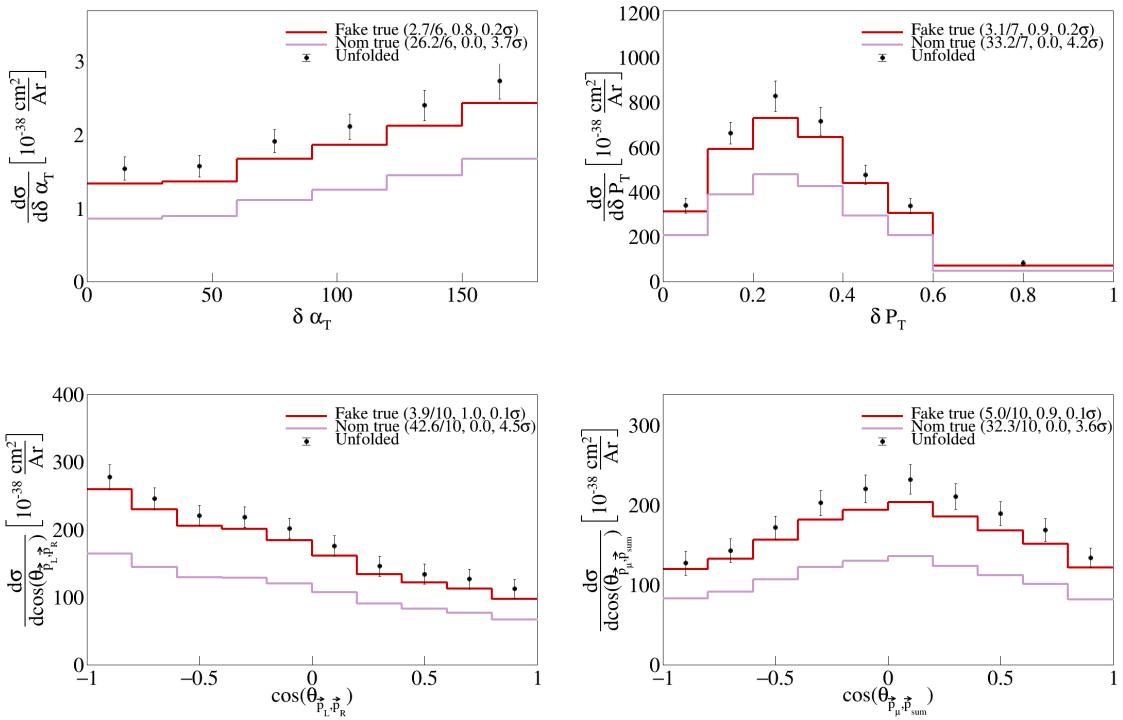


Figure 61: Unfolded fake data showing agreement with smeared fake signal data for single differential vector opening angles and transverse momentum.

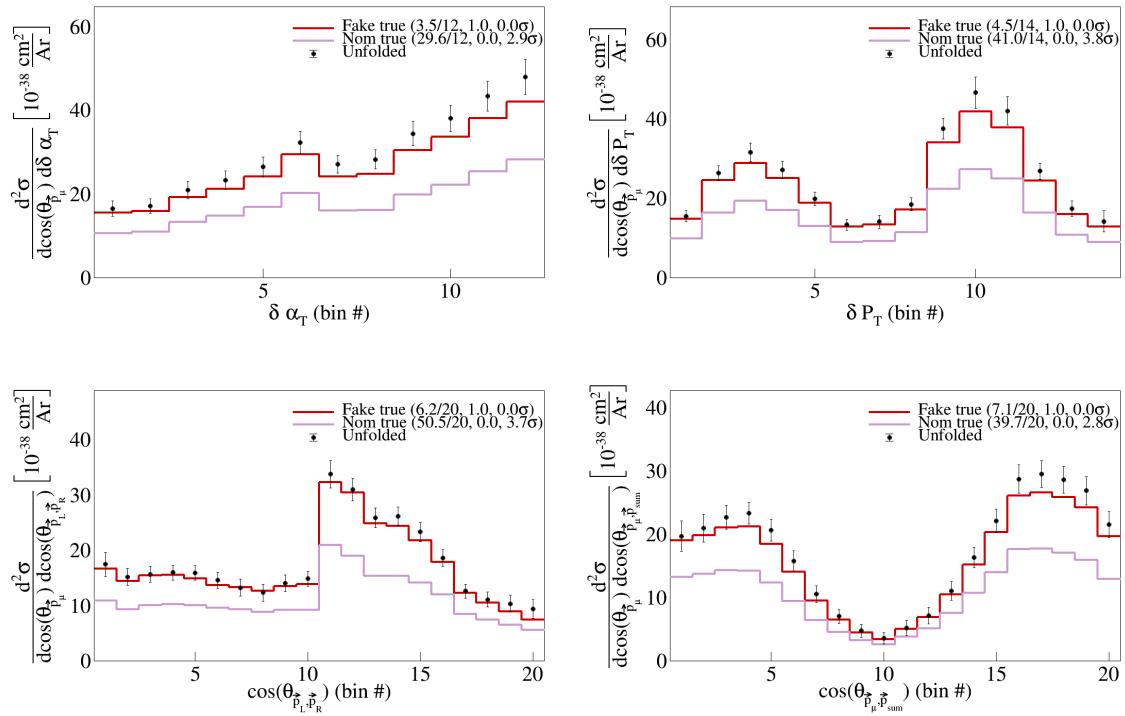


Figure 62: Unfolded fake data showing agreement with smeared fake signal data for serial double differential variables.

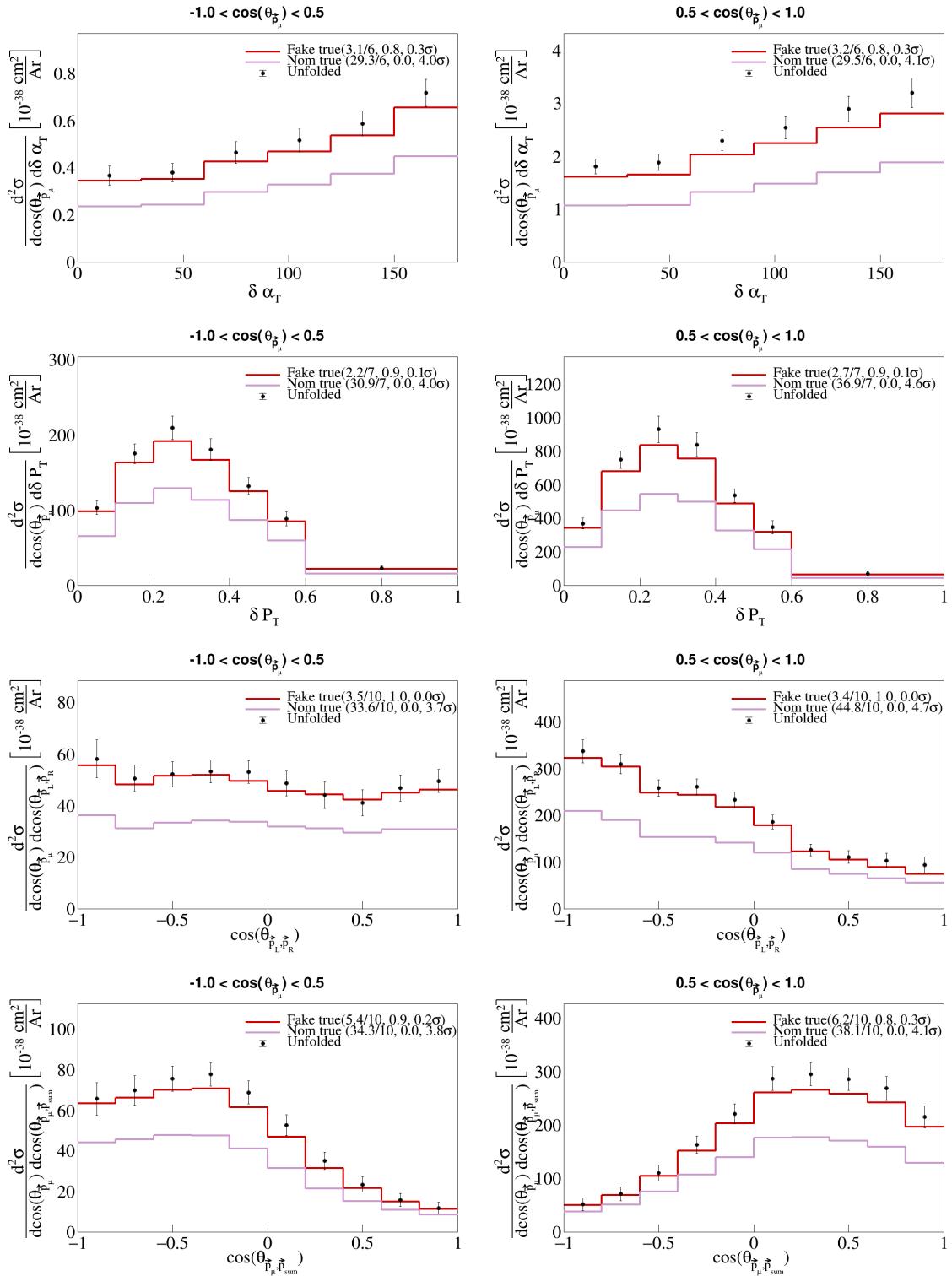


Figure 63: Unfolded fake data showing agreement with smeared fake signal data for sliced double differential variables.

271 6 Appendices

272 6.1 Cross section systematics

273 In this appendix, the variations, covariance matrices, fractional covariance matrices, and correlation matrices
 274 are plotted for all of the cross section systematics and variables.

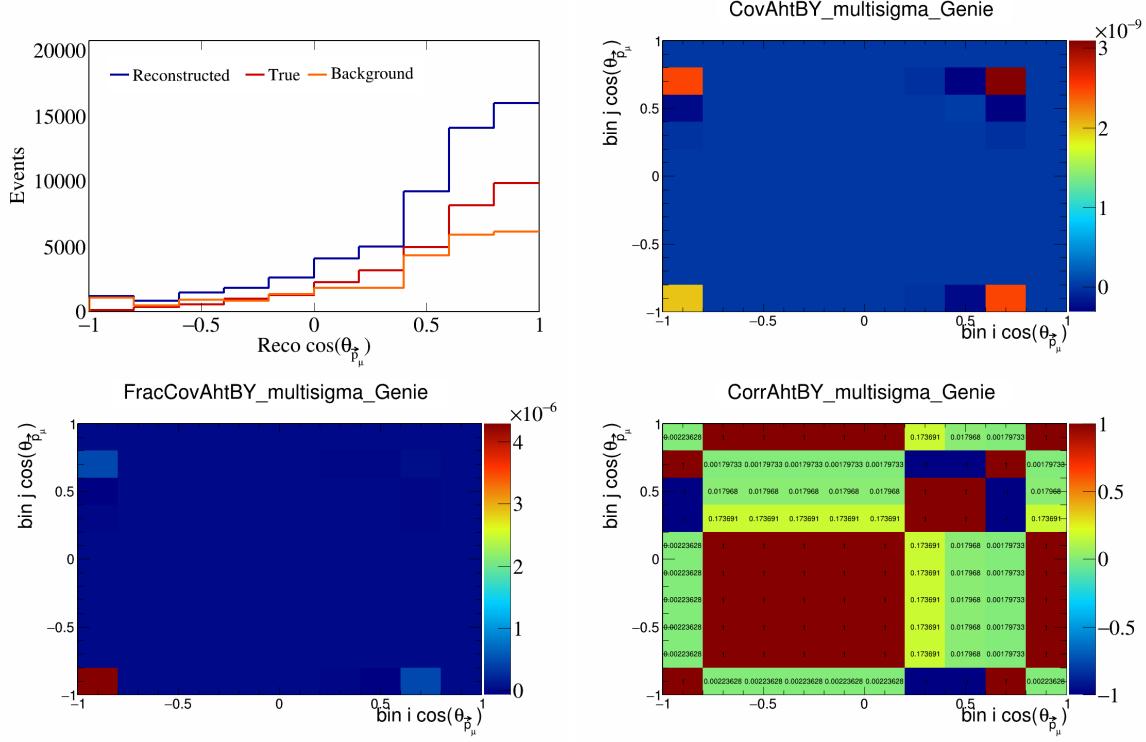


Figure 64: AhtBY variations for $\cos(\theta_{\vec{p}_\mu})$.

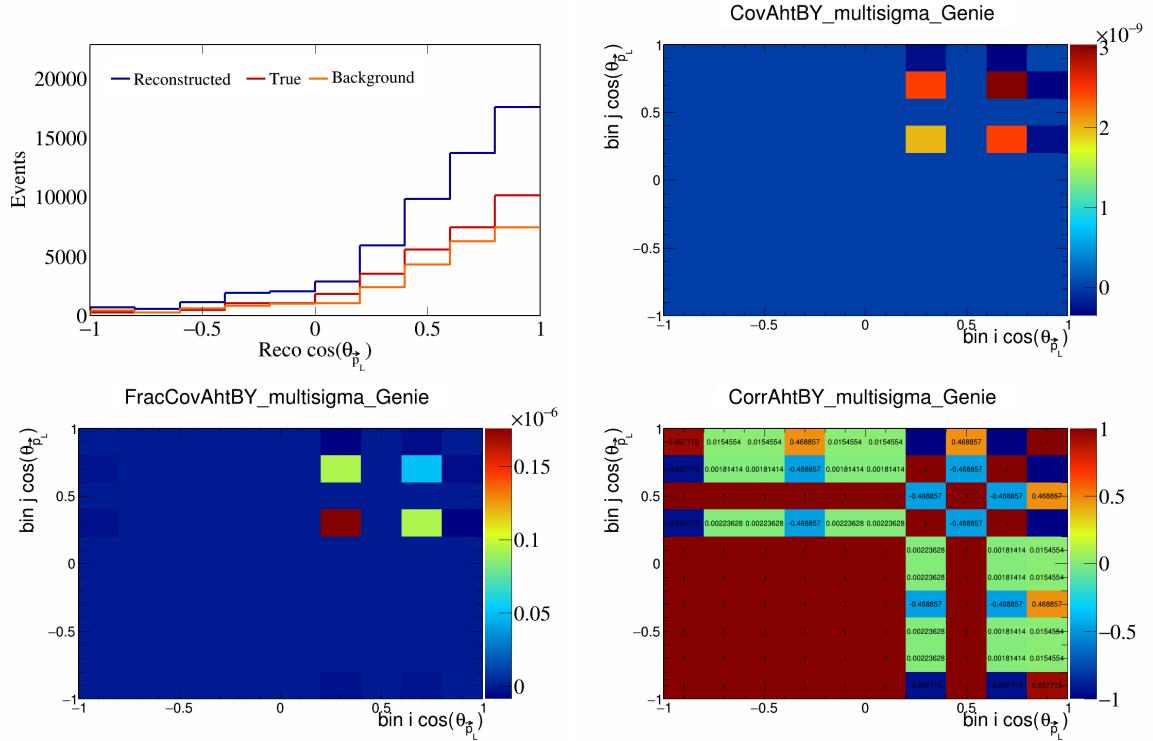


Figure 65: AhtBY variations for $\cos(\theta_{\vec{p}_L})$.

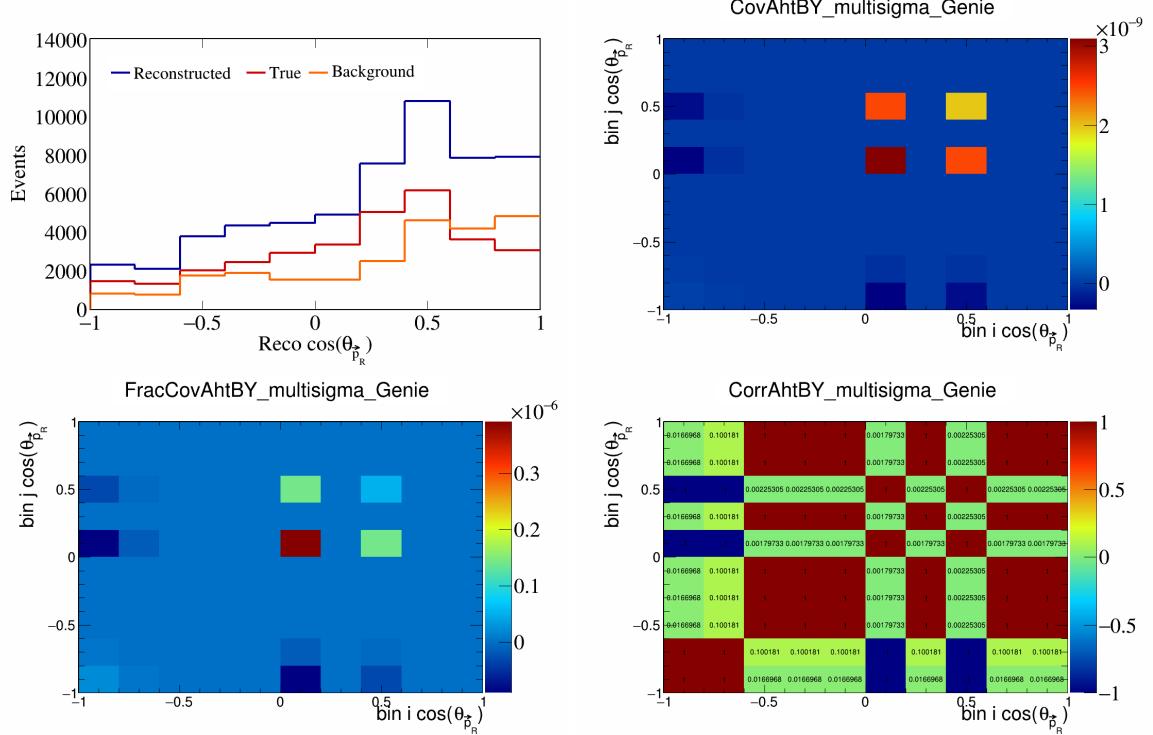


Figure 66: AhtBY variations for $\cos(\theta_{\vec{p}_R})$.

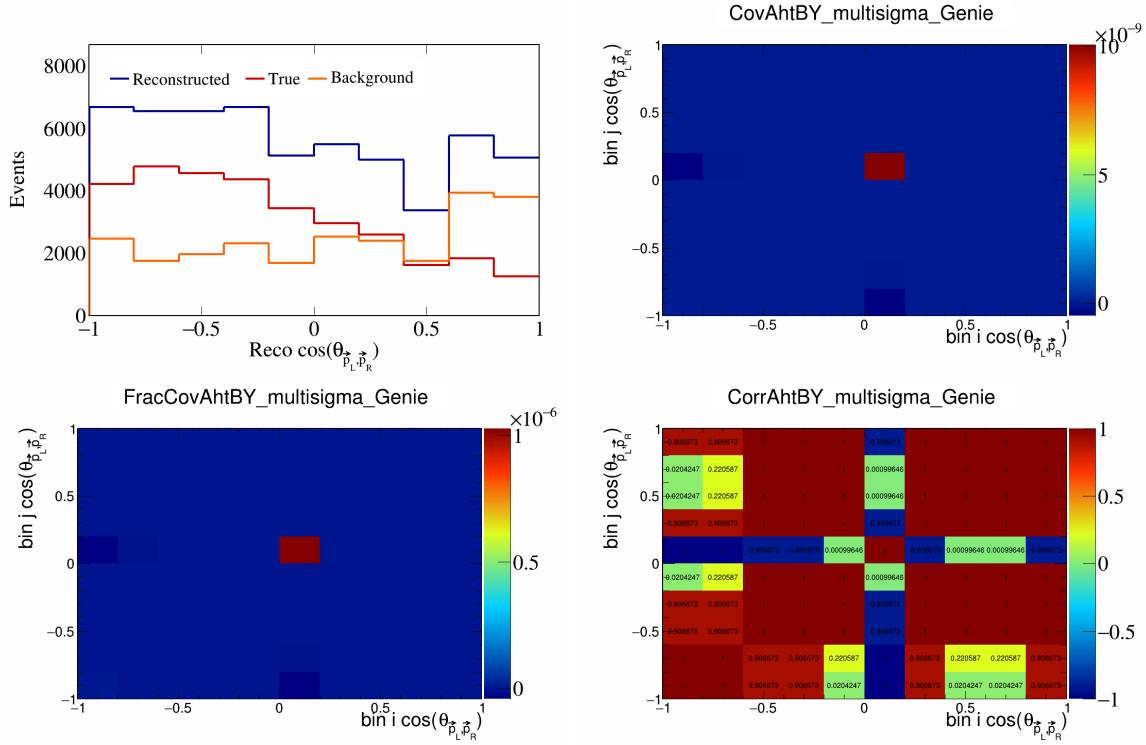


Figure 67: AhtBY variations for $\cos(\theta_{\vec{p}_L, \vec{p}_R})$.

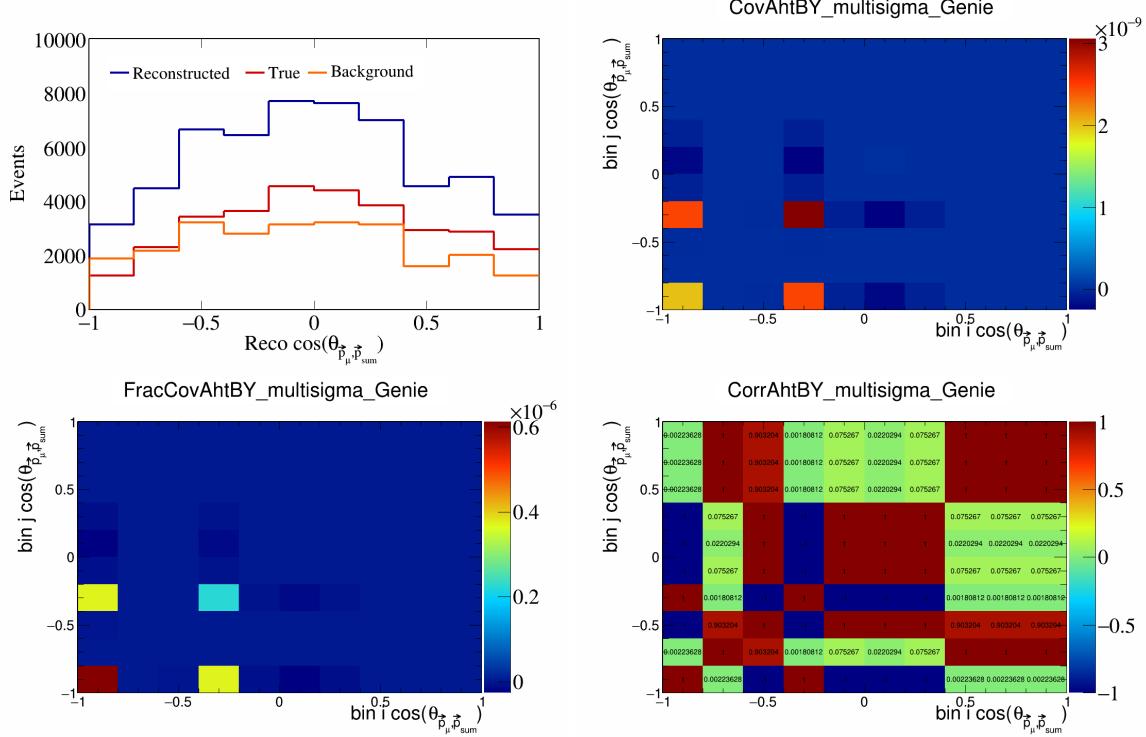


Figure 68: AhtBY variations for $\cos(\theta_{\vec{p}_\mu, \vec{p}_{\text{sum}}})$.

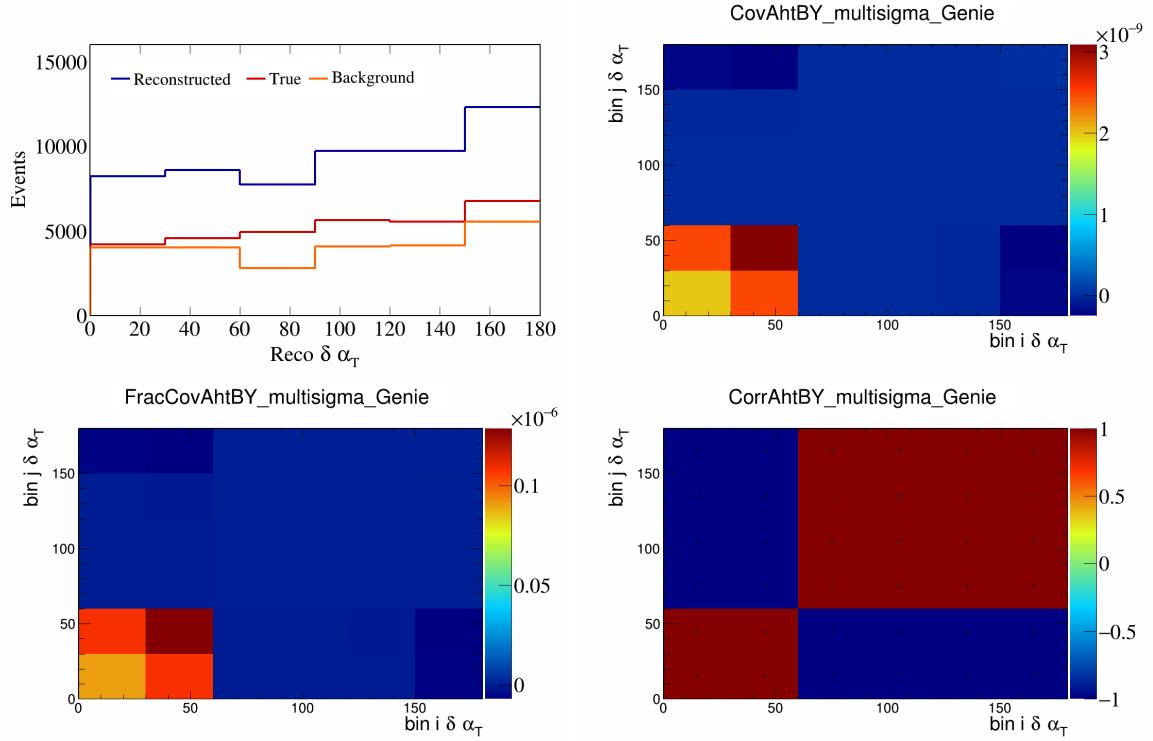


Figure 69: AhtBY variations for $\delta\alpha_T$.

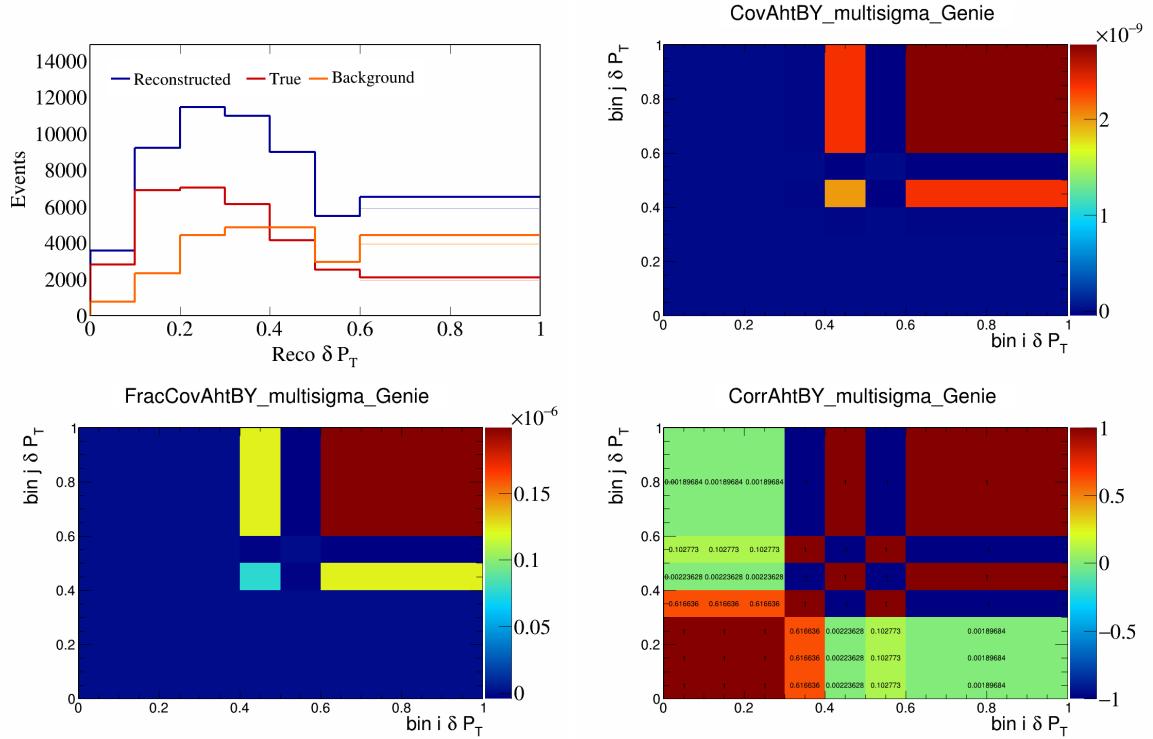


Figure 70: AhtBY variations for δP_T .

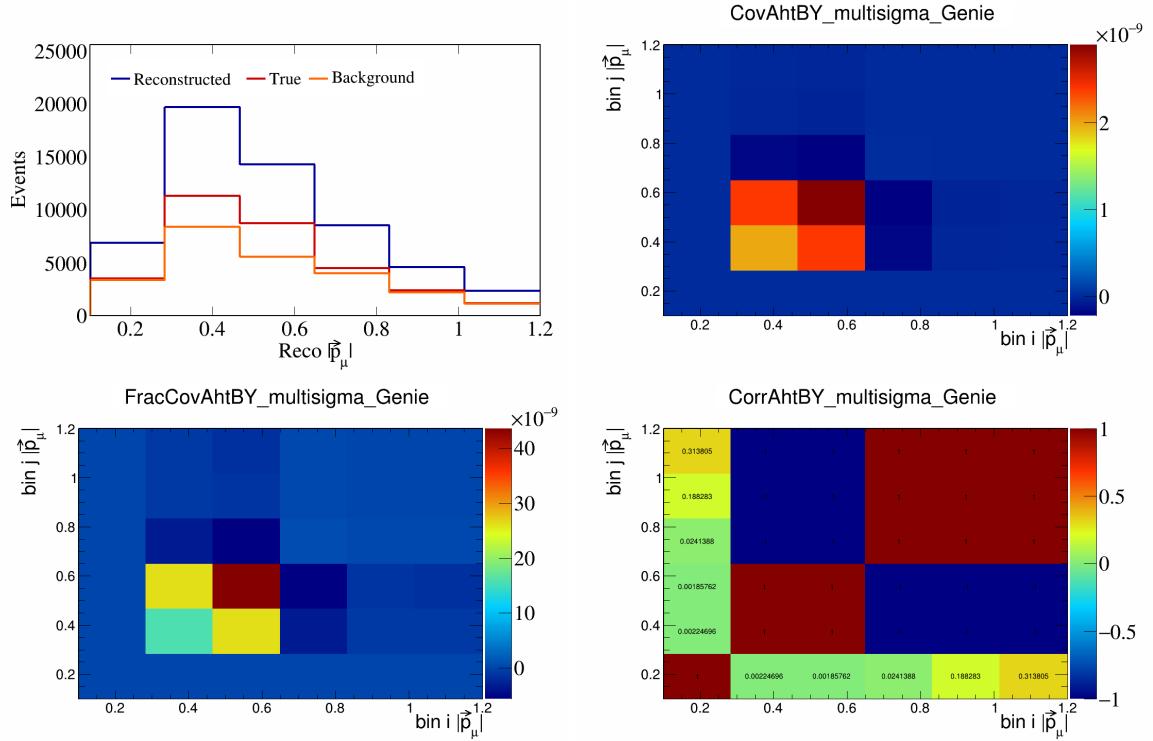


Figure 71: AhtBY variations for $|\vec{p}_\mu|$.

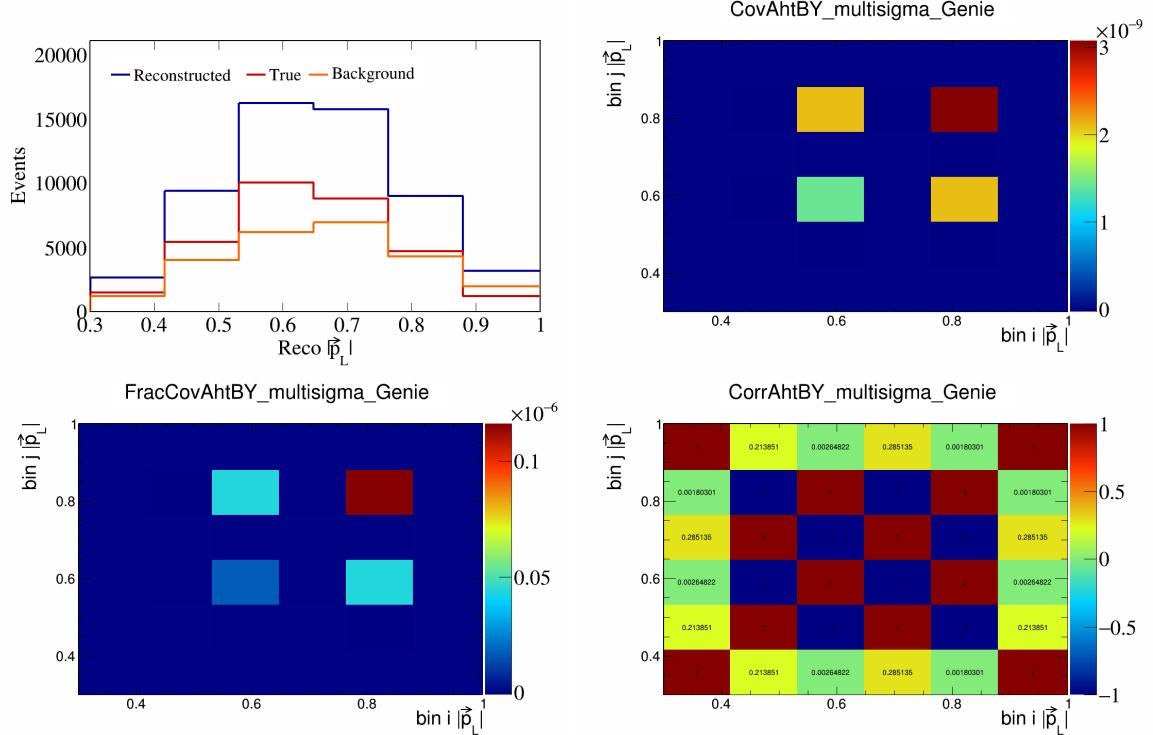


Figure 72: AhtBY variations for $|\vec{p}_L|$.

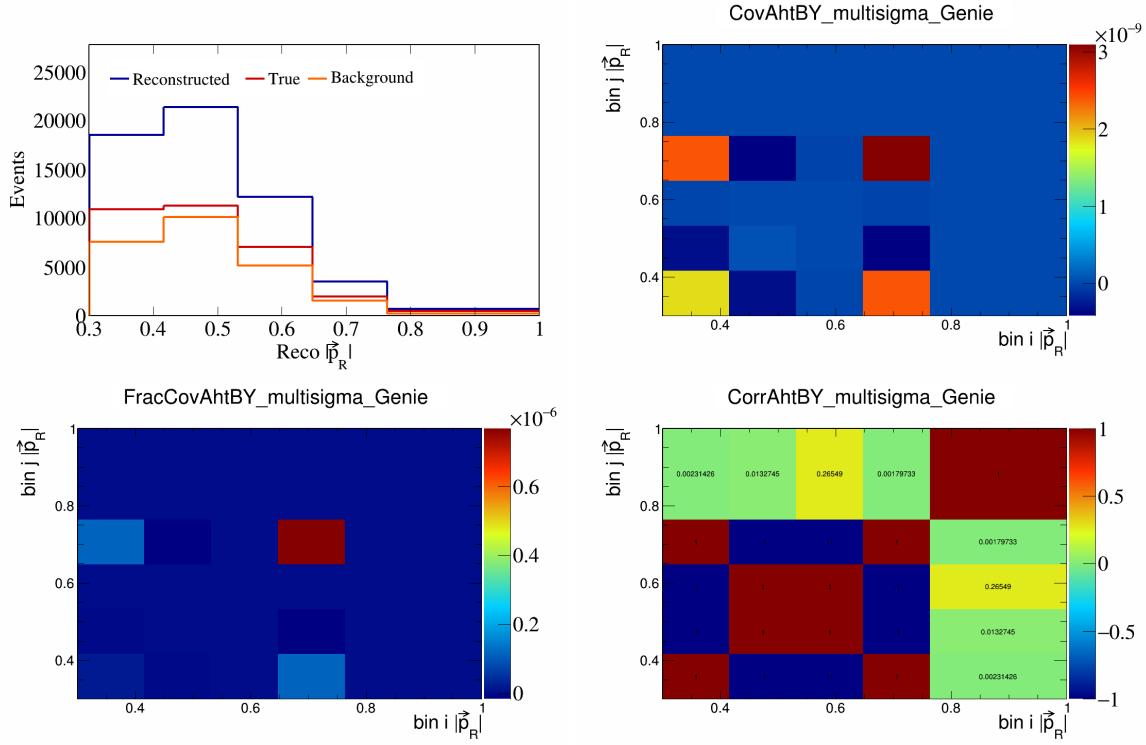


Figure 73: AhtBY variations for $|\vec{p}_R|$.

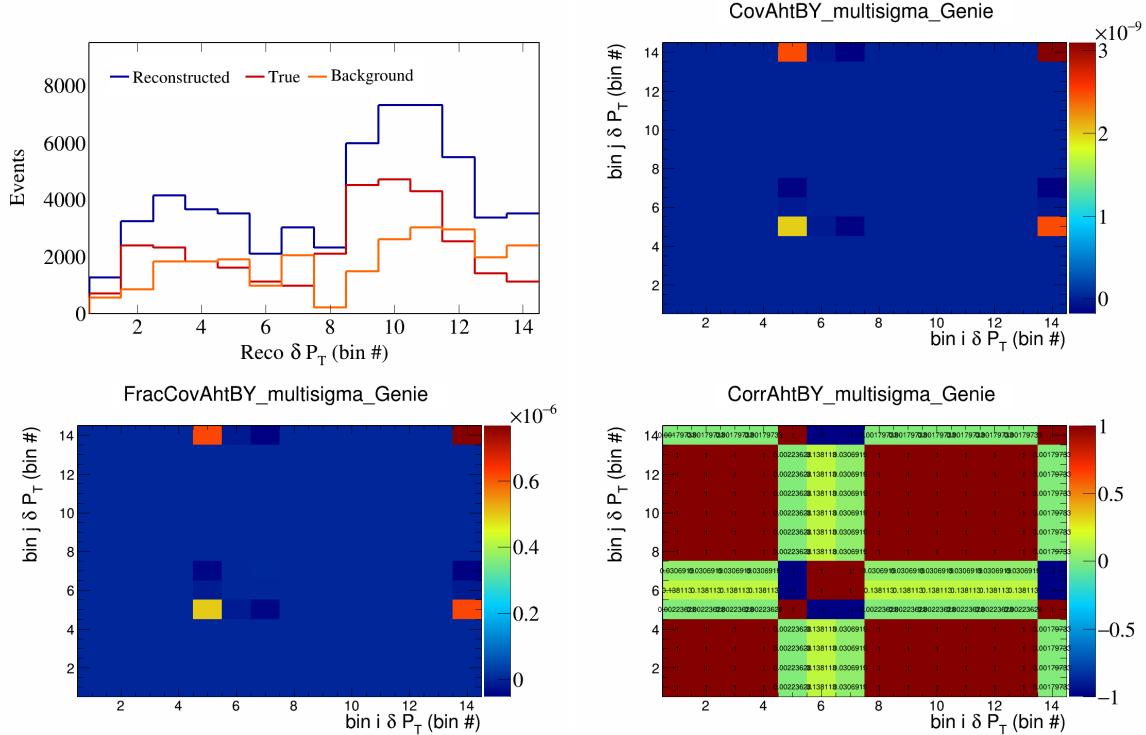


Figure 74: AhtBY variations for δP_T in $\cos(\theta_{\vec{p}_\mu})$.

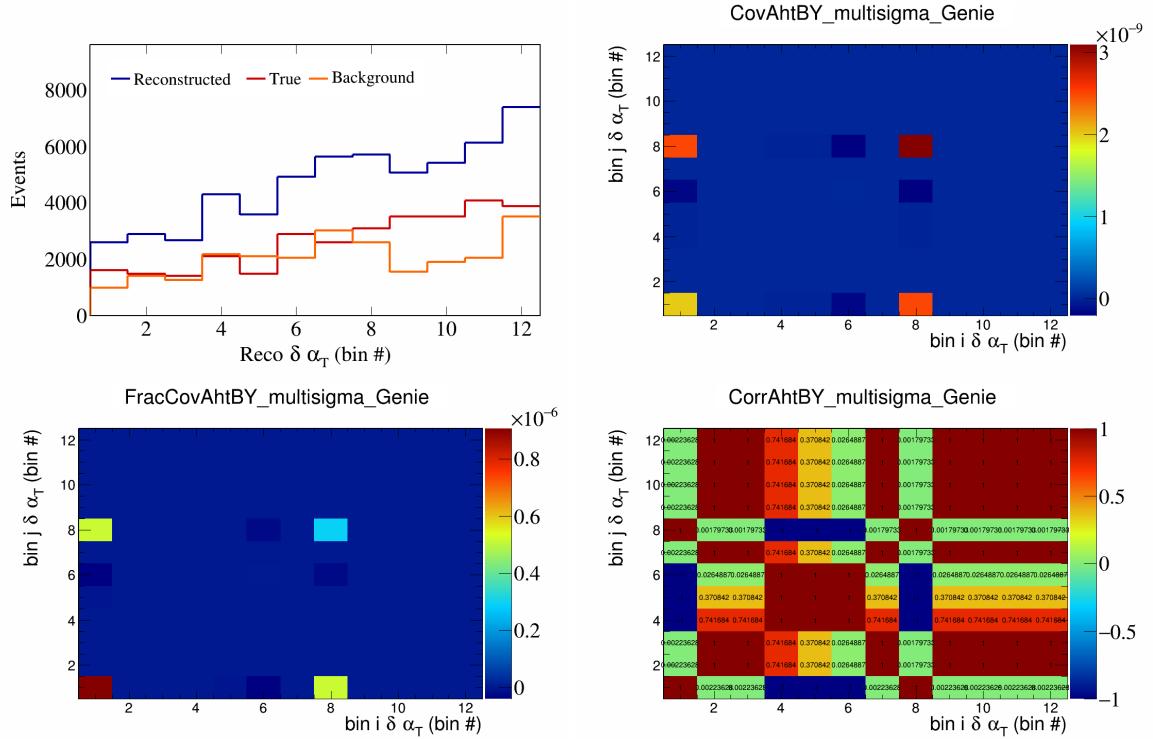


Figure 75: AhtBY variations for $\delta\alpha_T$ in $\cos(\theta_{\vec{p}_\mu})$.

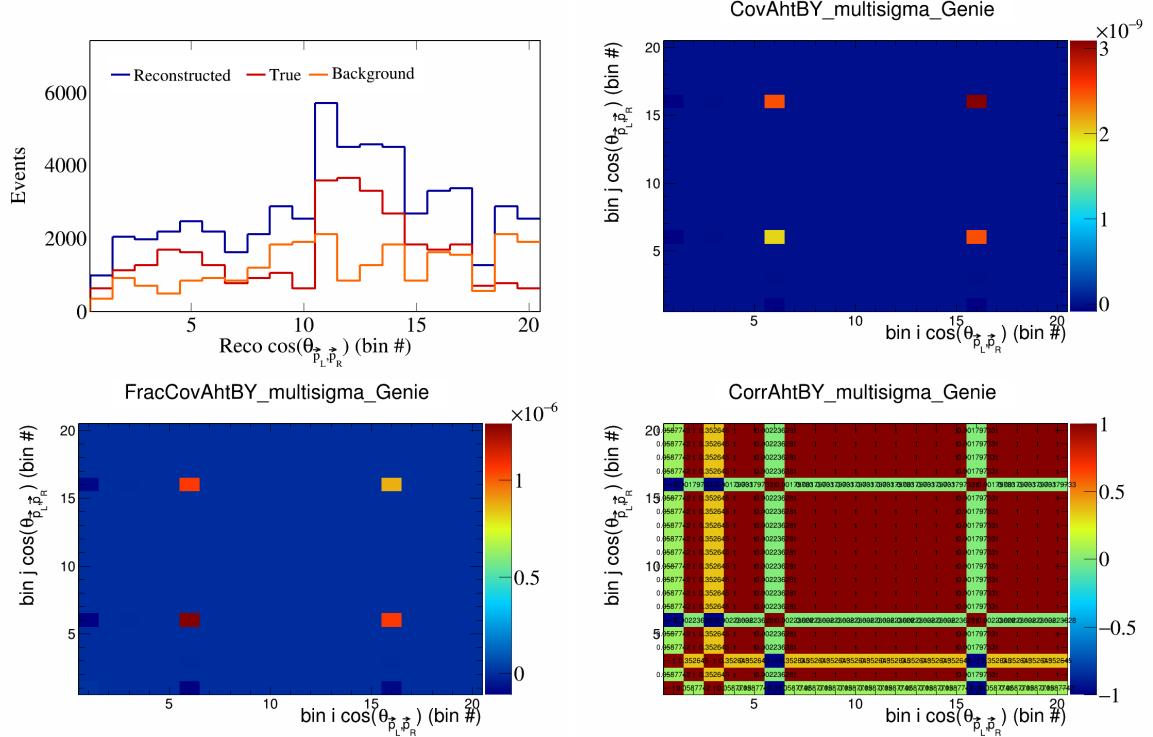


Figure 76: AhtBY variations for $\cos(\theta_{\vec{p}_L, \vec{p}_R})$ in $\cos(\theta_{\vec{p}_\mu})$.

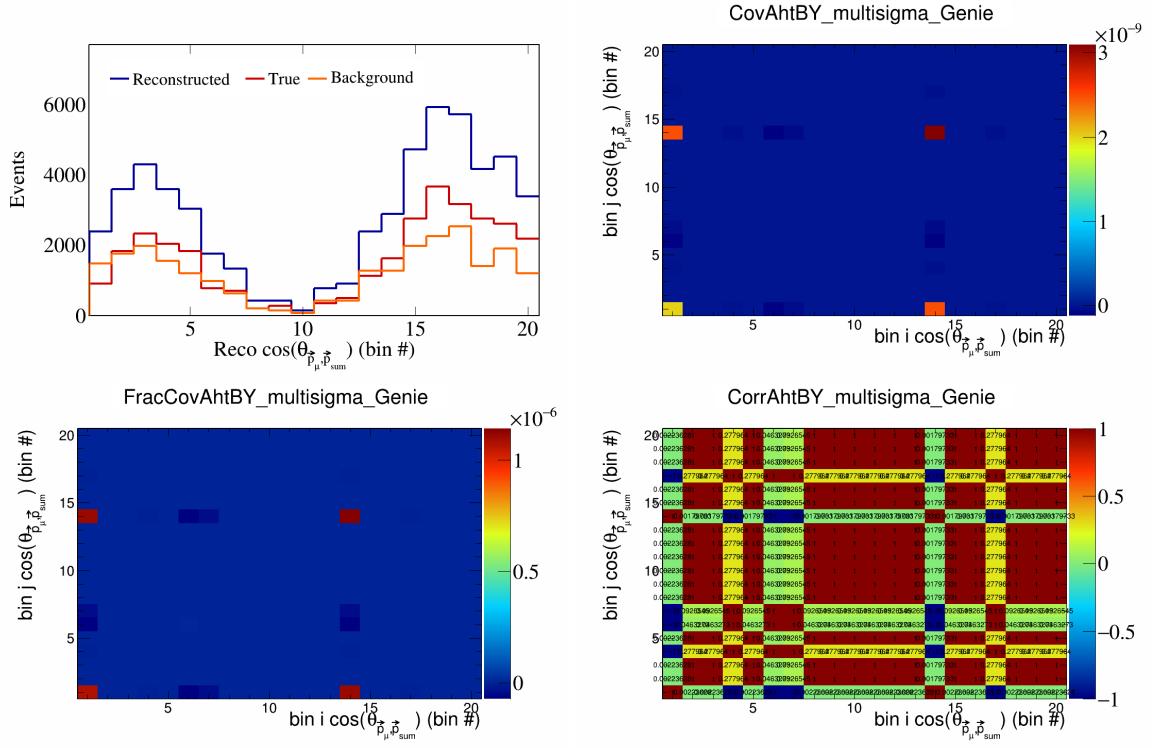


Figure 77: AhtBY variations for $\cos(\theta_{\vec{p}_\mu, \vec{p}_{\text{sum}}})$ in $\cos(\theta_{\vec{p}_\mu})$.

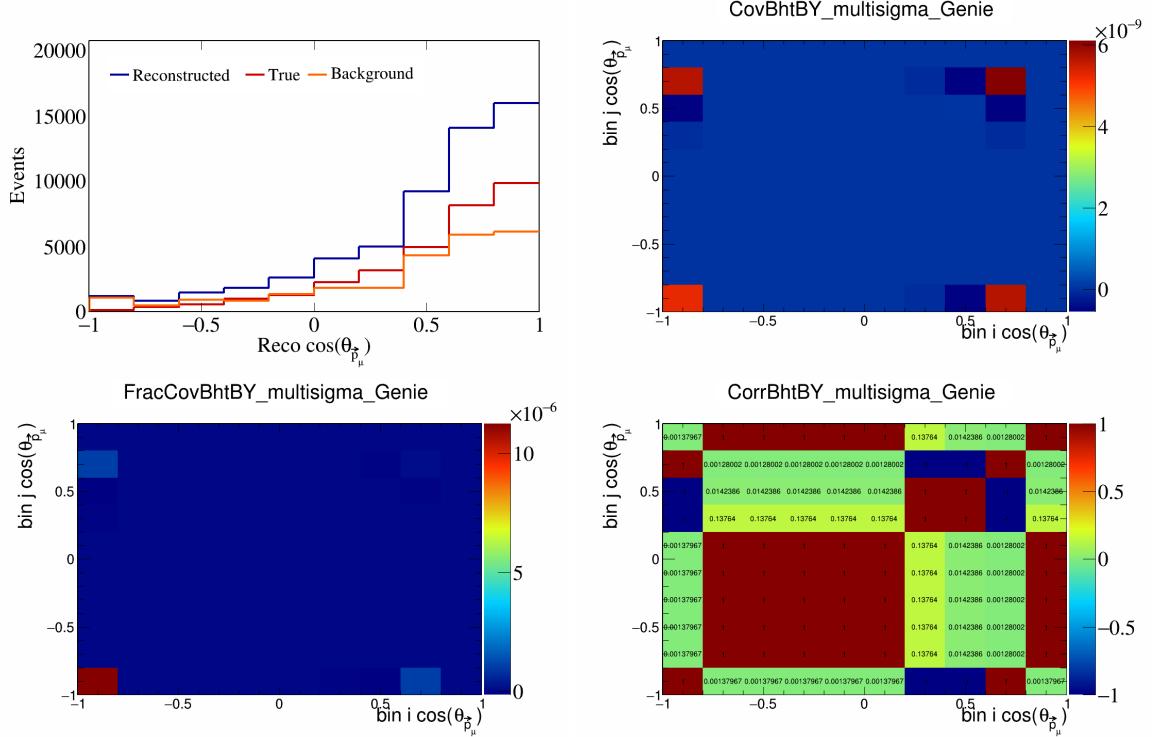


Figure 78: BhtBY variations for $\cos(\theta_{\vec{p}_\mu})$.

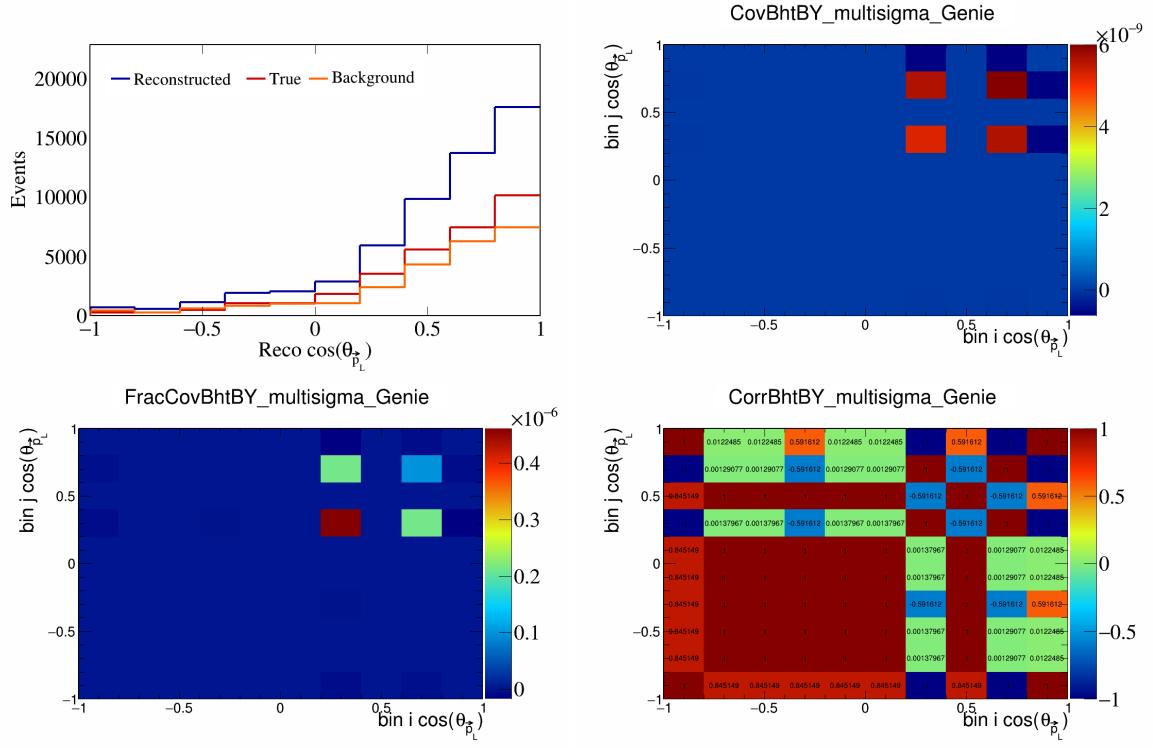


Figure 79: BhtBY variations for $\cos(\theta_{\vec{p}_L})$.

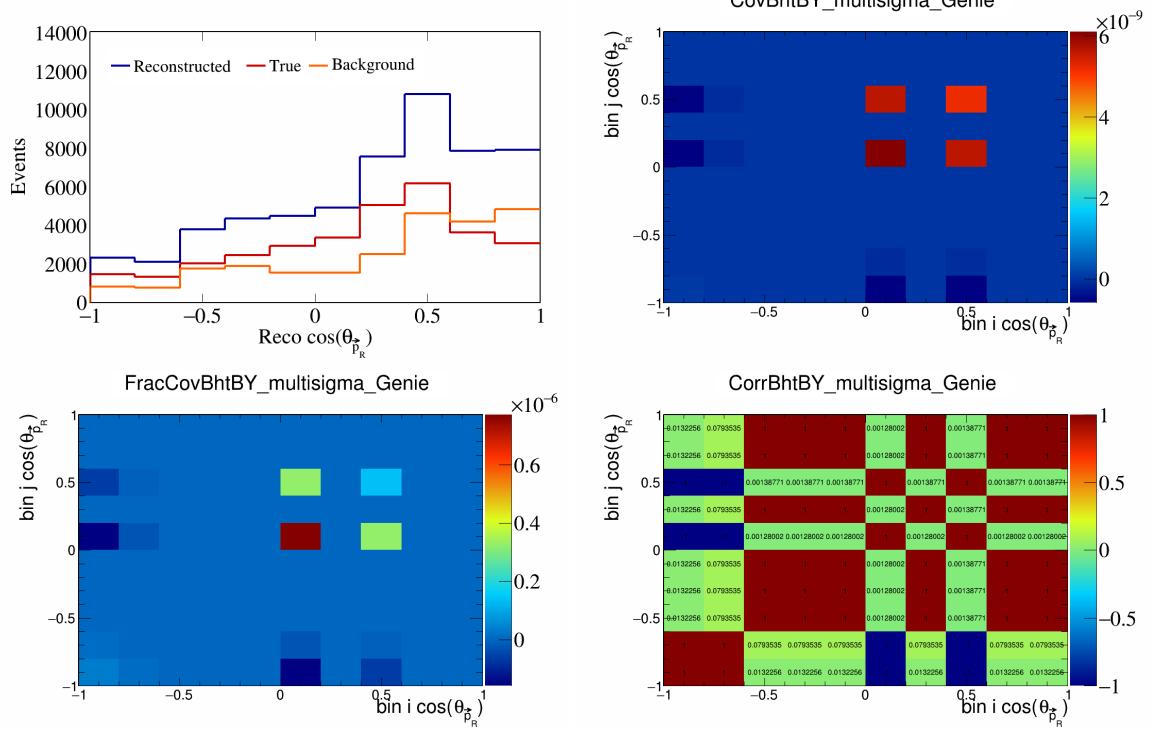


Figure 80: BhtBY variations for $\cos(\theta_{\vec{p}_R})$.

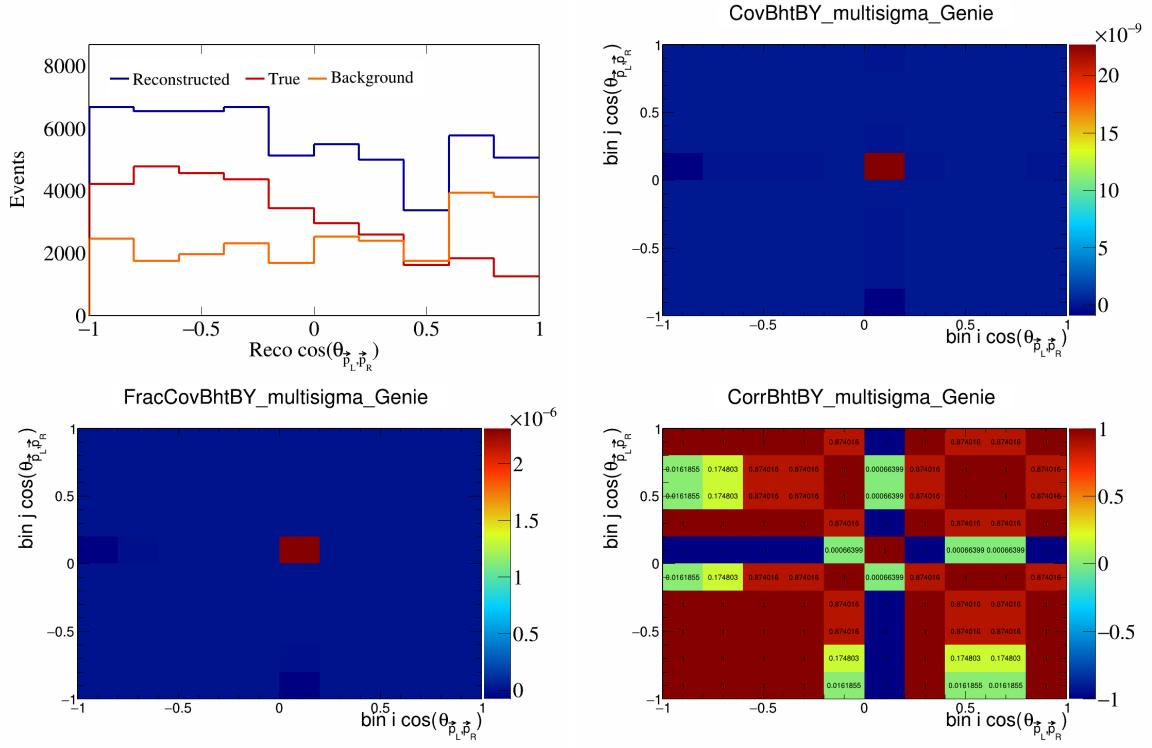


Figure 81: BhtBY variations for $\cos(\theta_{\vec{p}_L, \vec{p}_R})$.

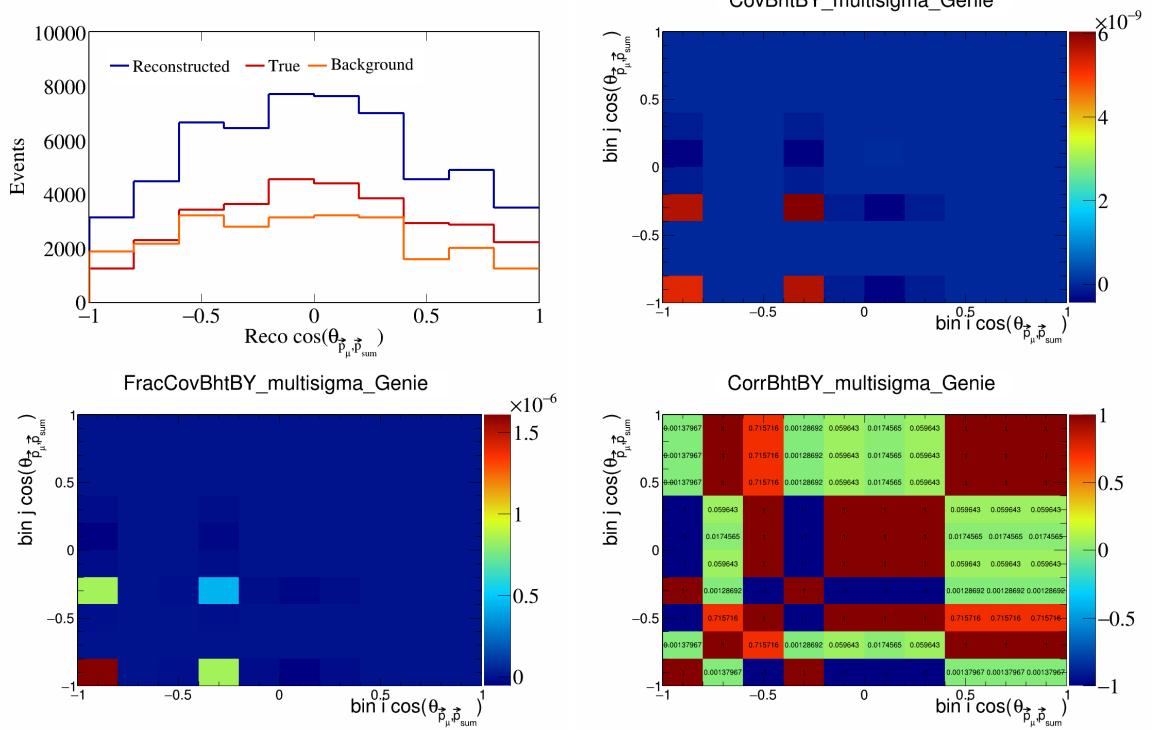


Figure 82: BhtBY variations for $\cos(\theta_{\vec{p}_\mu, \vec{p}_{\text{sum}}})$.

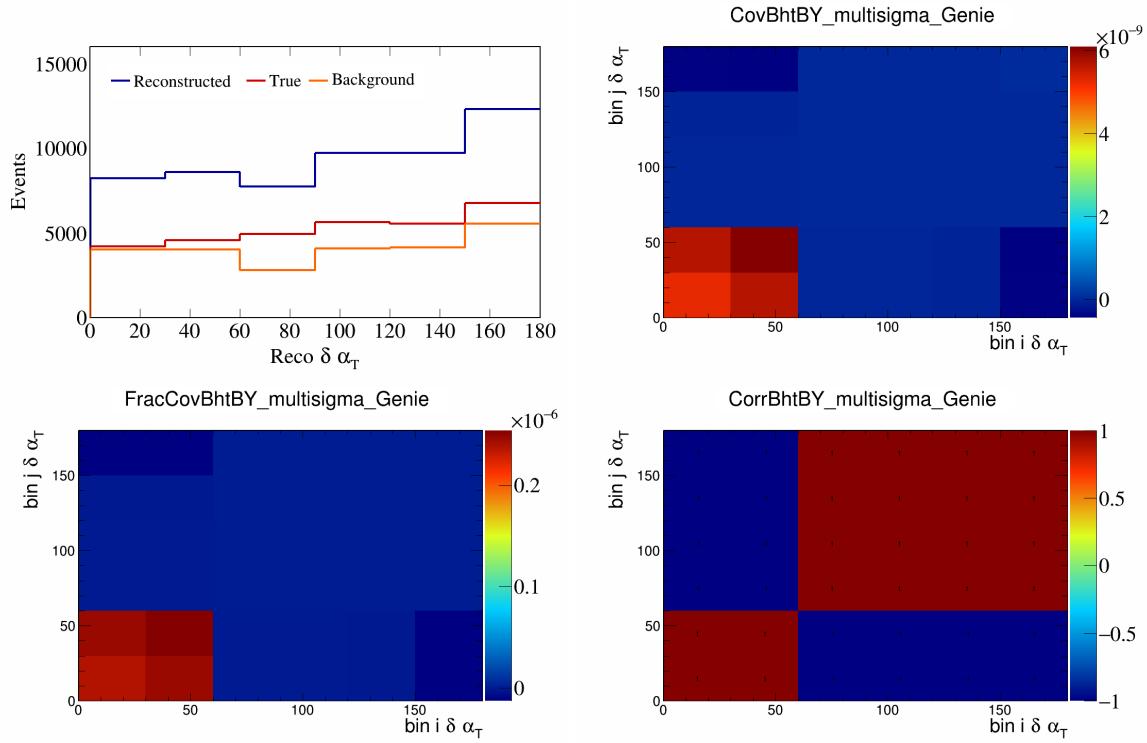


Figure 83: BhtBY variations for $\delta\alpha_T$.

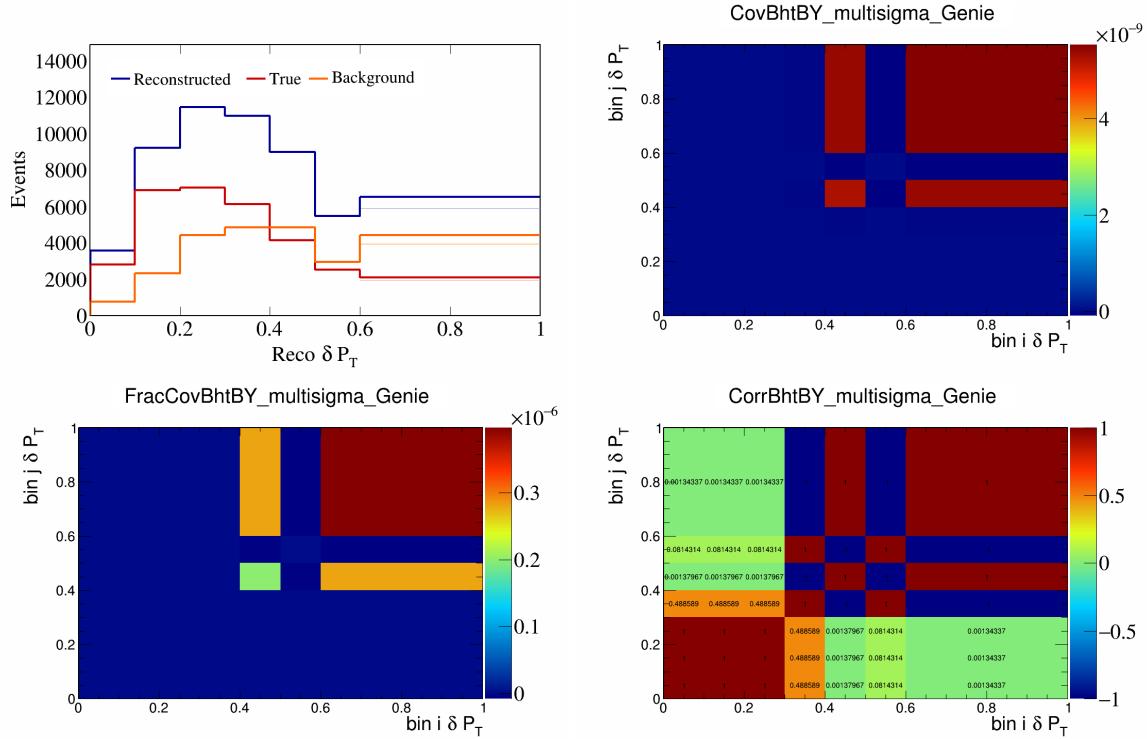


Figure 84: BhtBY variations for δP_T .

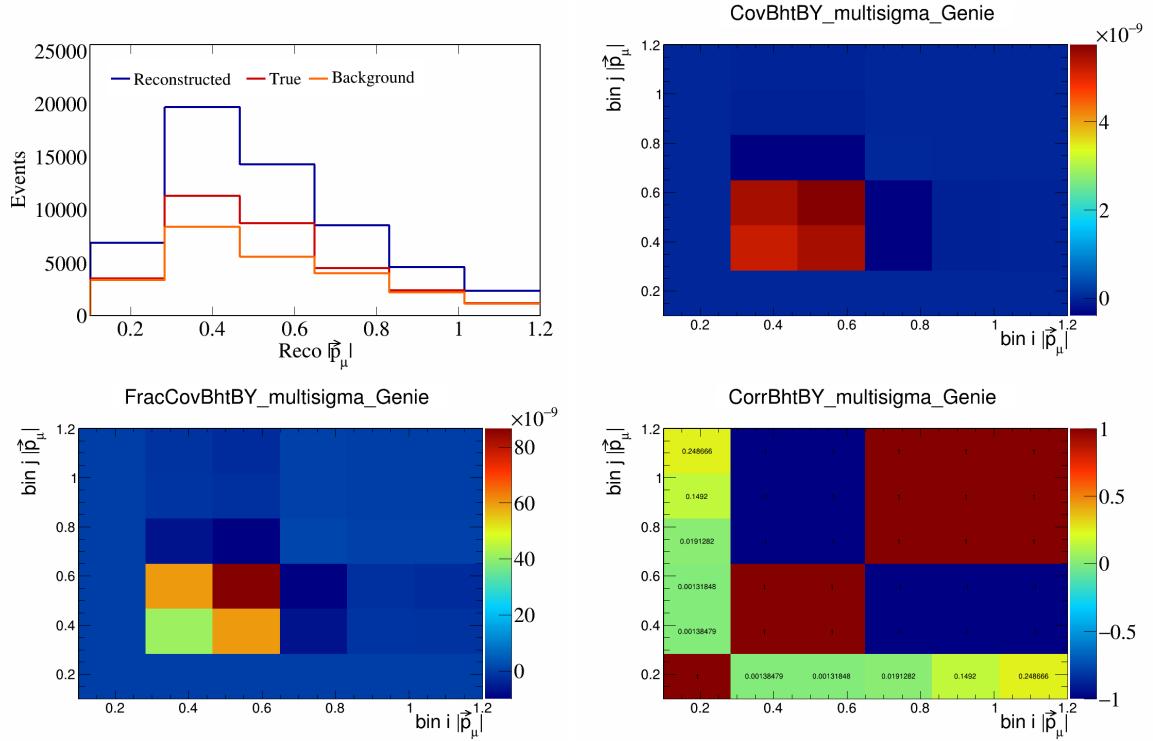


Figure 85: BhtBY variations for $|\vec{p}_\mu|$.

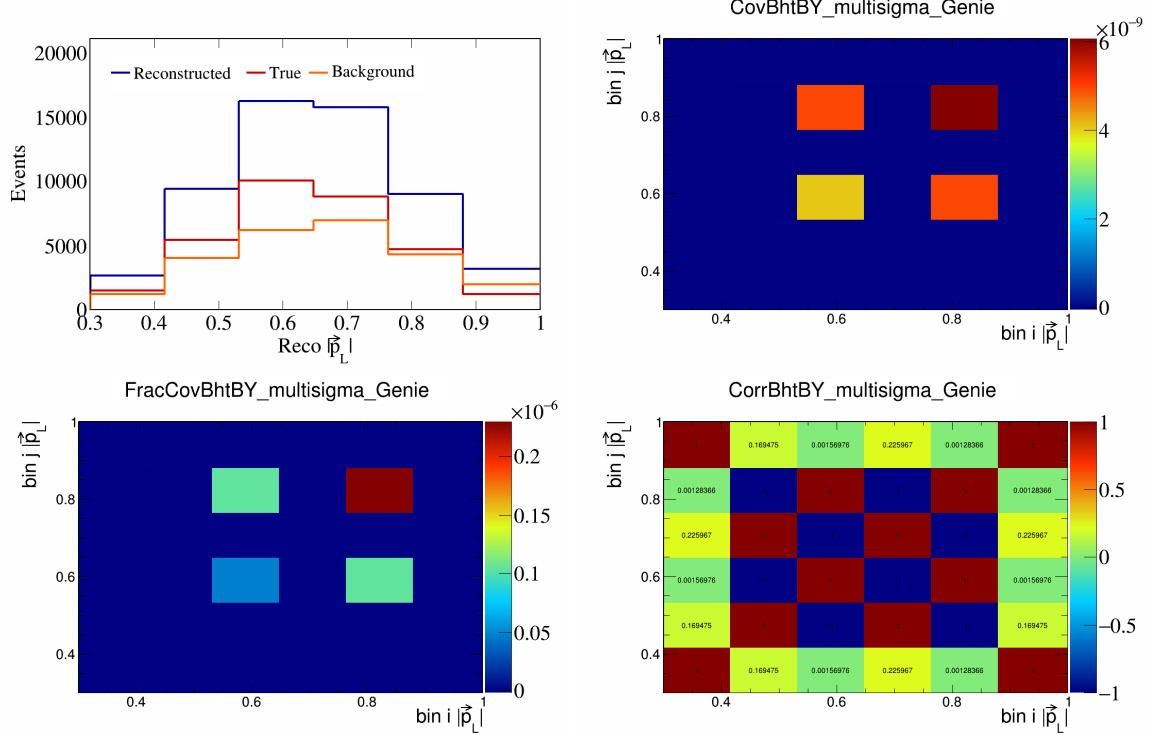


Figure 86: BhtBY variations for $|\vec{p}_L|$.

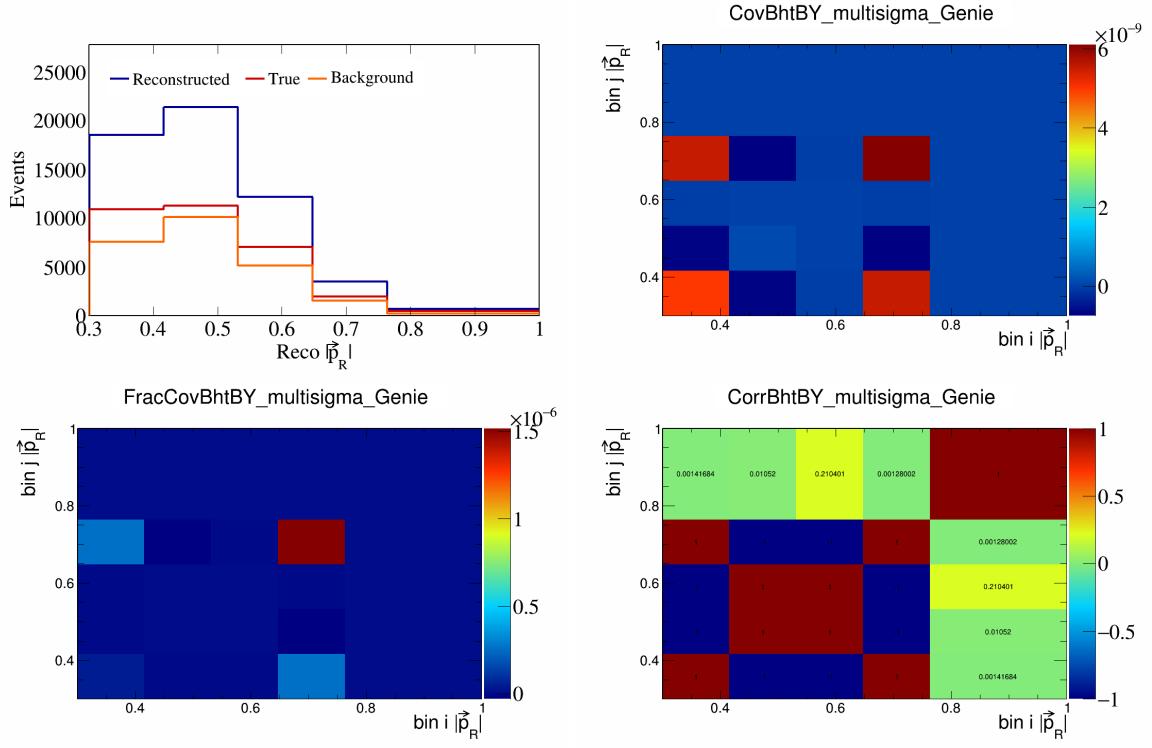


Figure 87: BhtBY variations for $|\vec{p}_R|$.

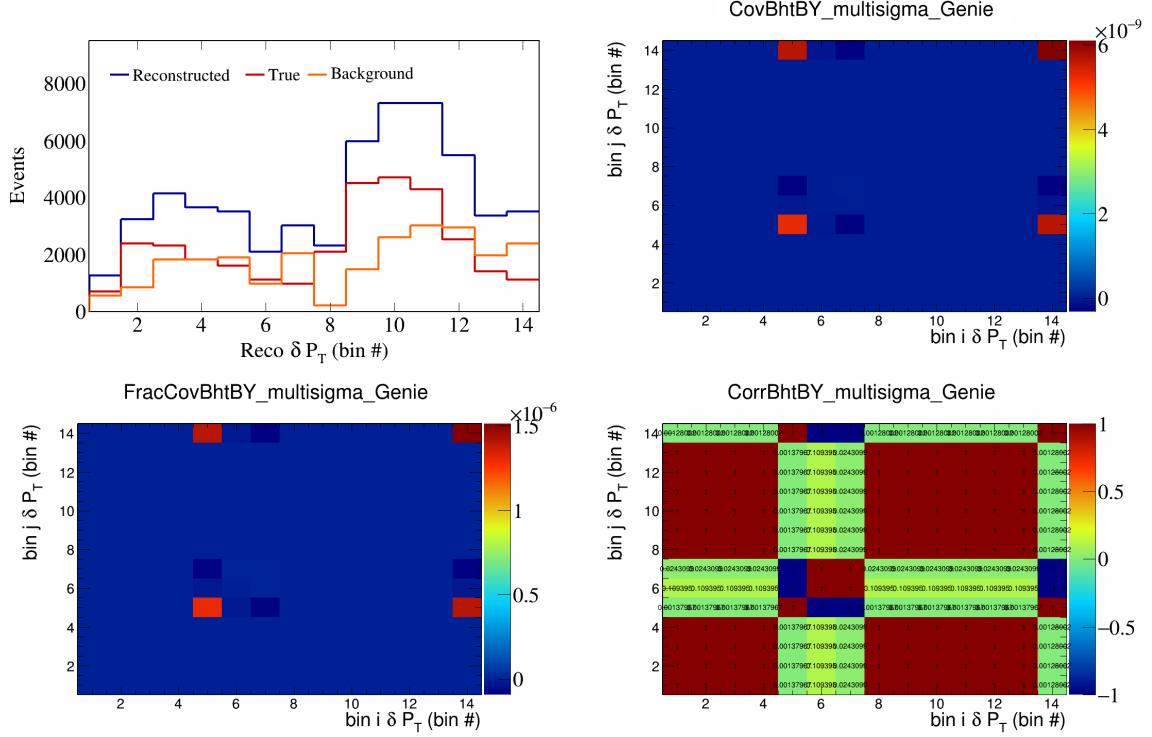


Figure 88: BhtBY variations for δP_T in $\cos(\theta_{\vec{p}_\mu})$.

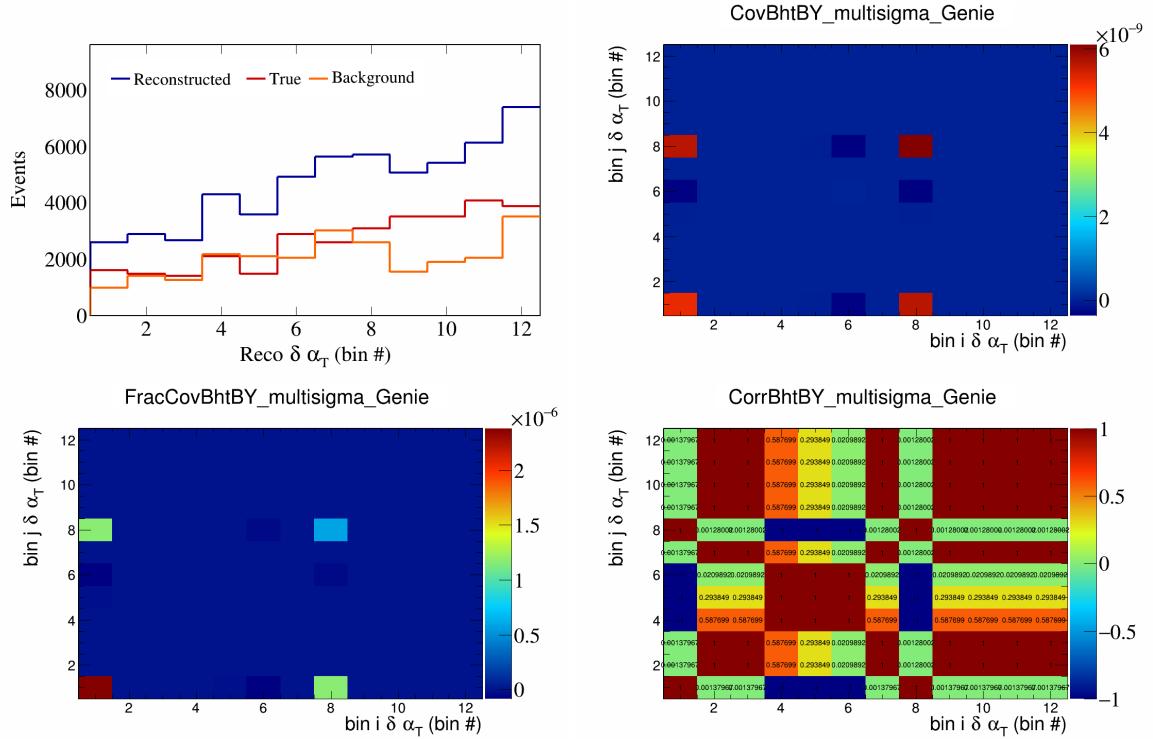


Figure 89: BhtBY variations for $\delta\alpha_T$ in $\cos(\theta_{\vec{p}_\mu})$.

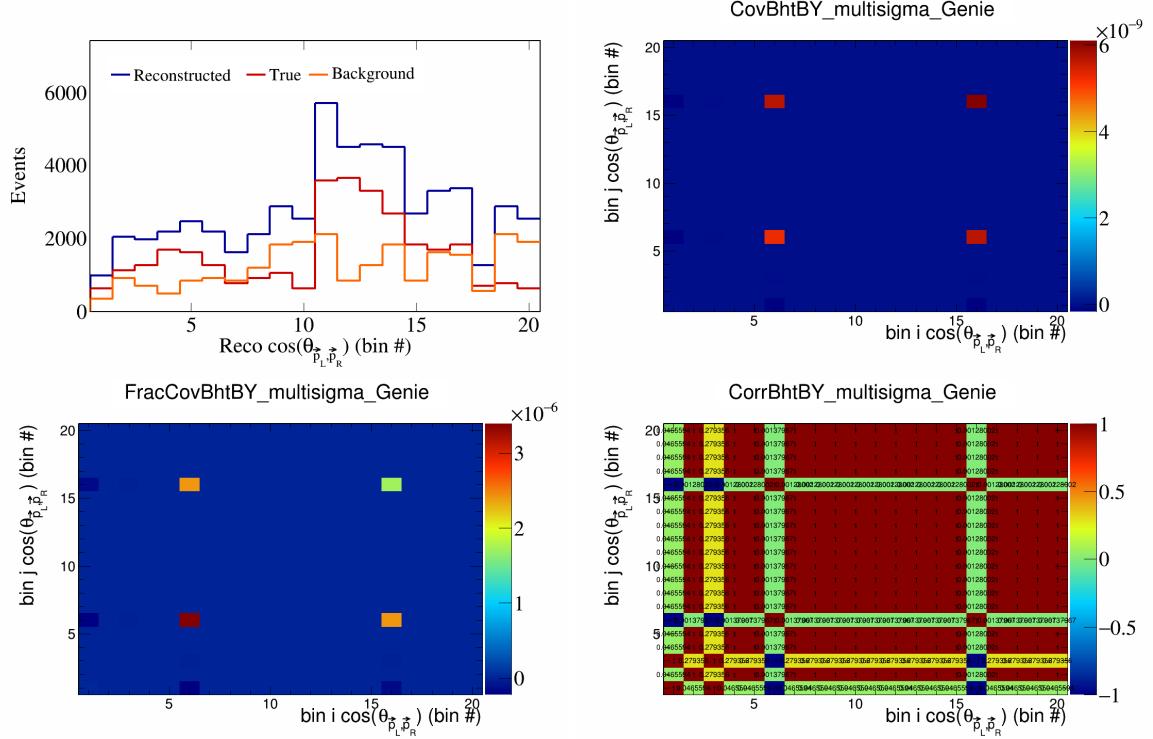


Figure 90: BhtBY variations for $\cos(\theta_{\vec{p}_L, \vec{p}_R})$ in $\cos(\theta_{\vec{p}_\mu})$.

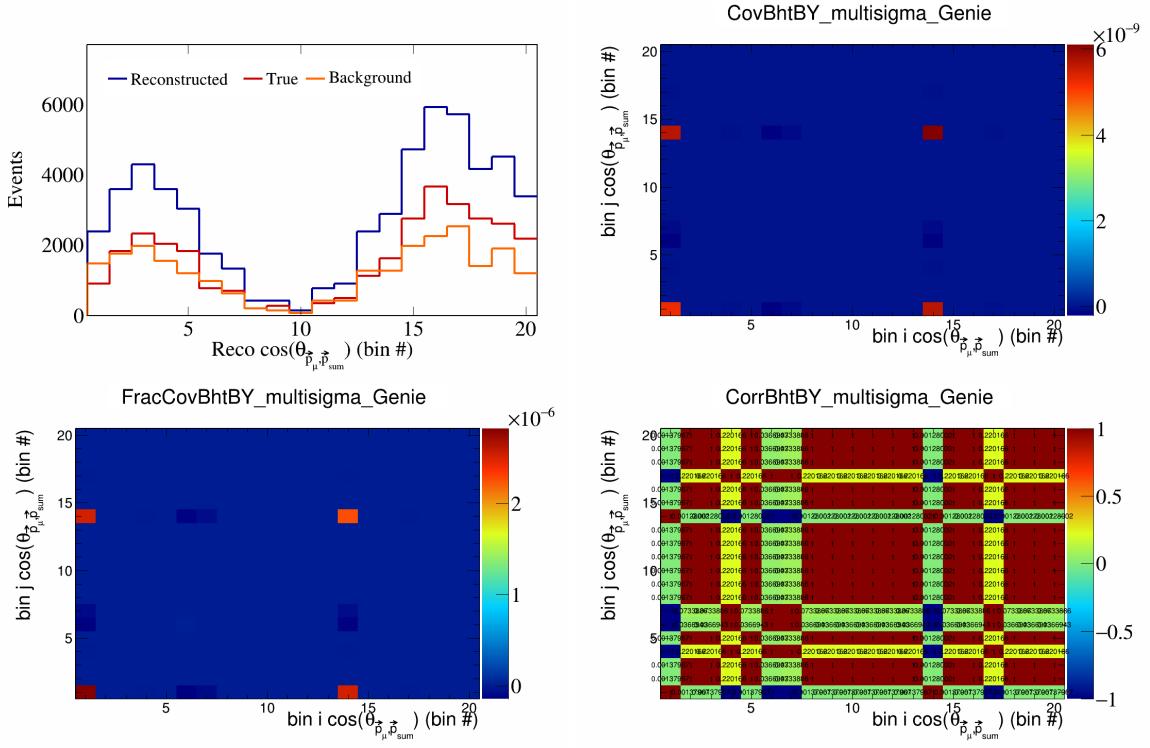


Figure 91: BhtBY variations for $\cos(\theta_{\vec{p}_\mu, \vec{p}_{\text{sum}}})$ in $\cos(\theta_{\vec{p}_\mu})$.

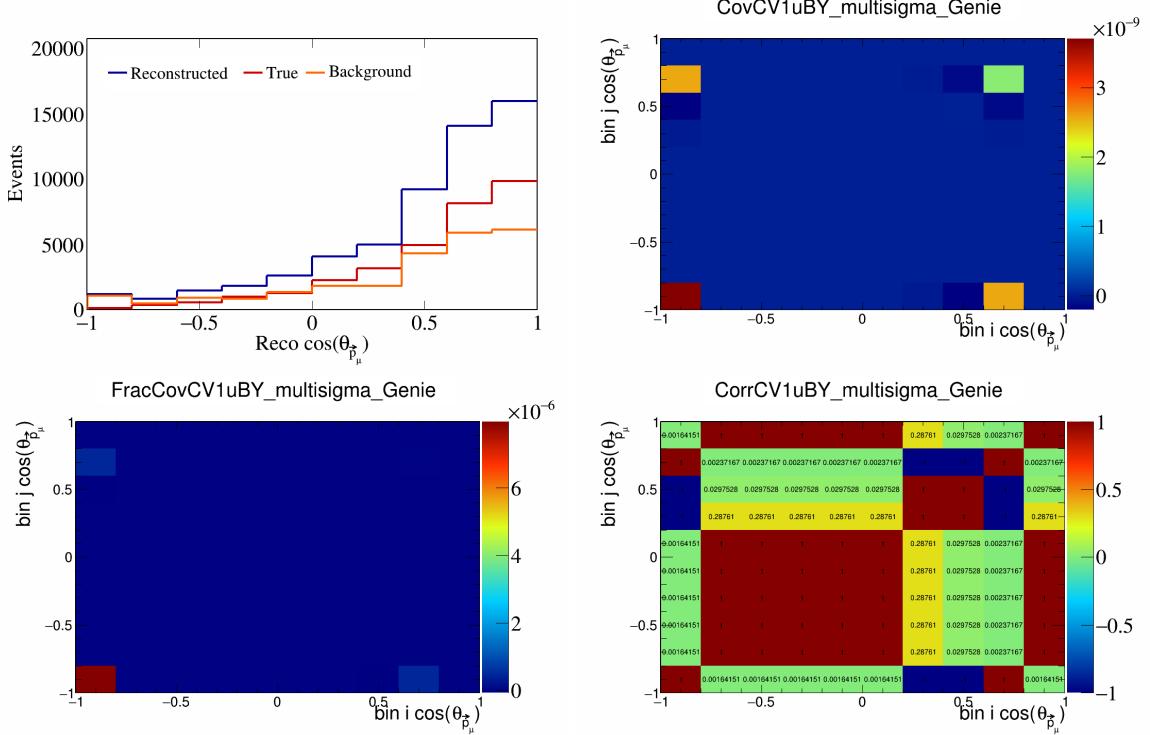


Figure 92: CV1uBY variations for $\cos(\theta_{\vec{p}_\mu})$.

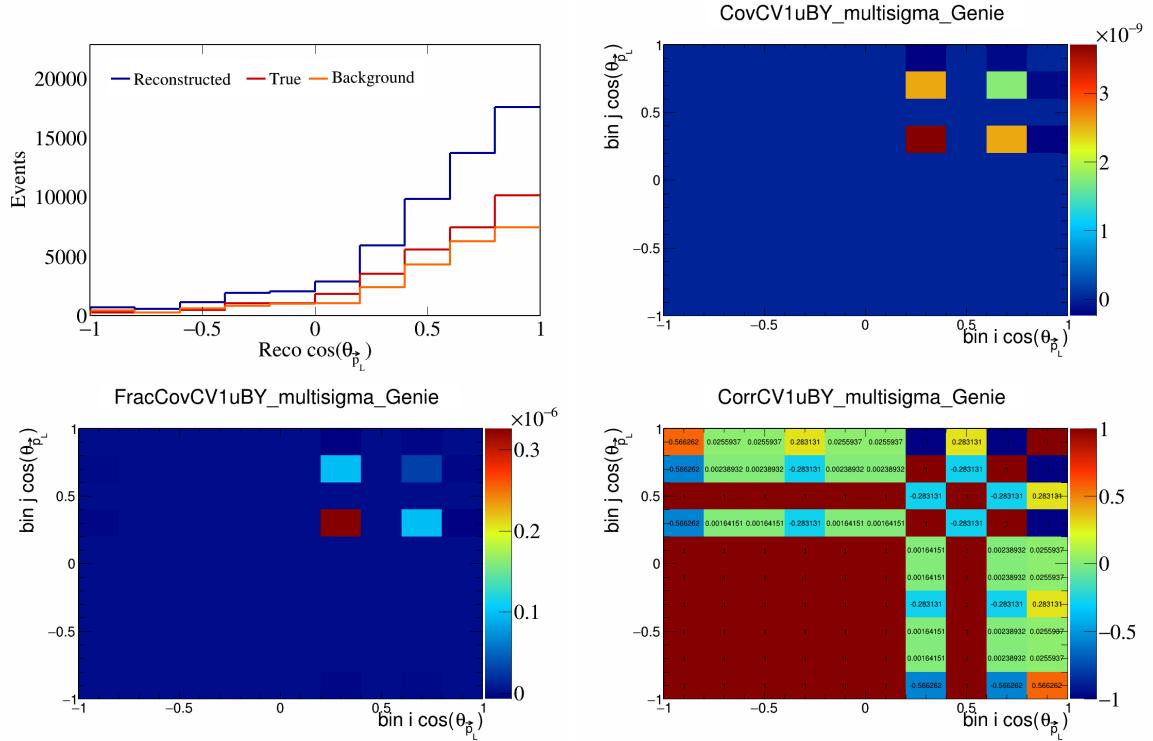


Figure 93: CV1uBY variations for $\cos(\theta_{\vec{p}_L})$.

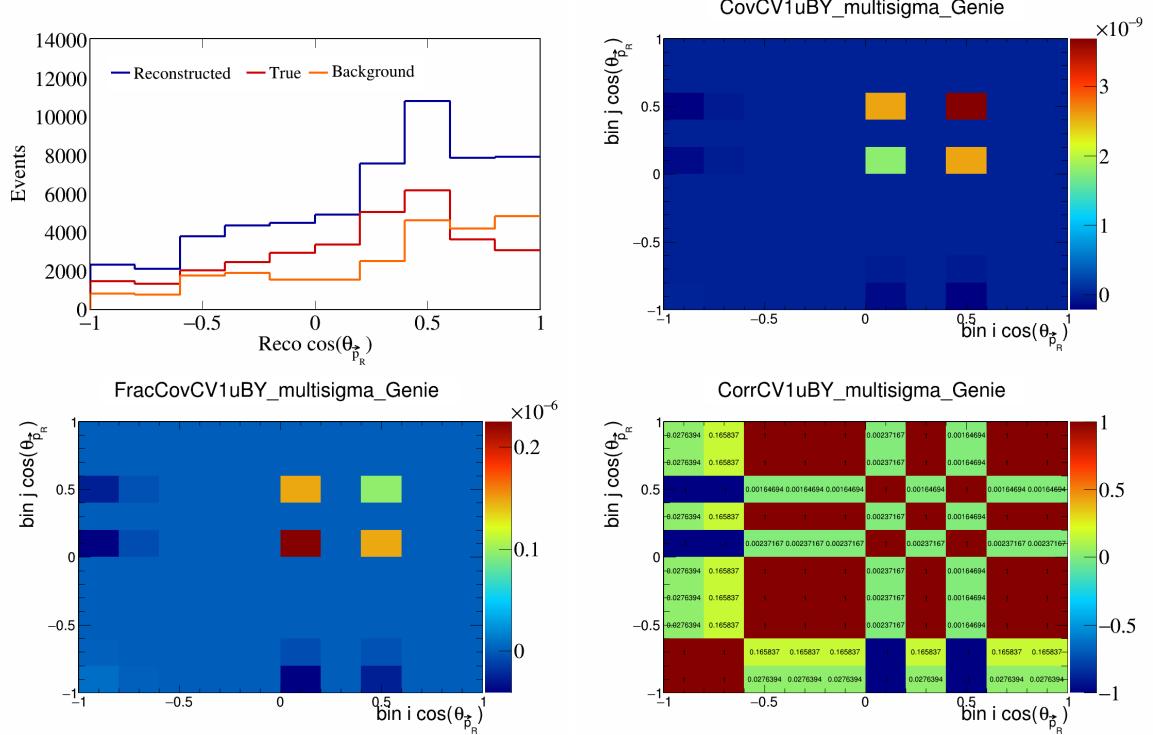


Figure 94: CV1uBY variations for $\cos(\theta_{\vec{p}_R})$.

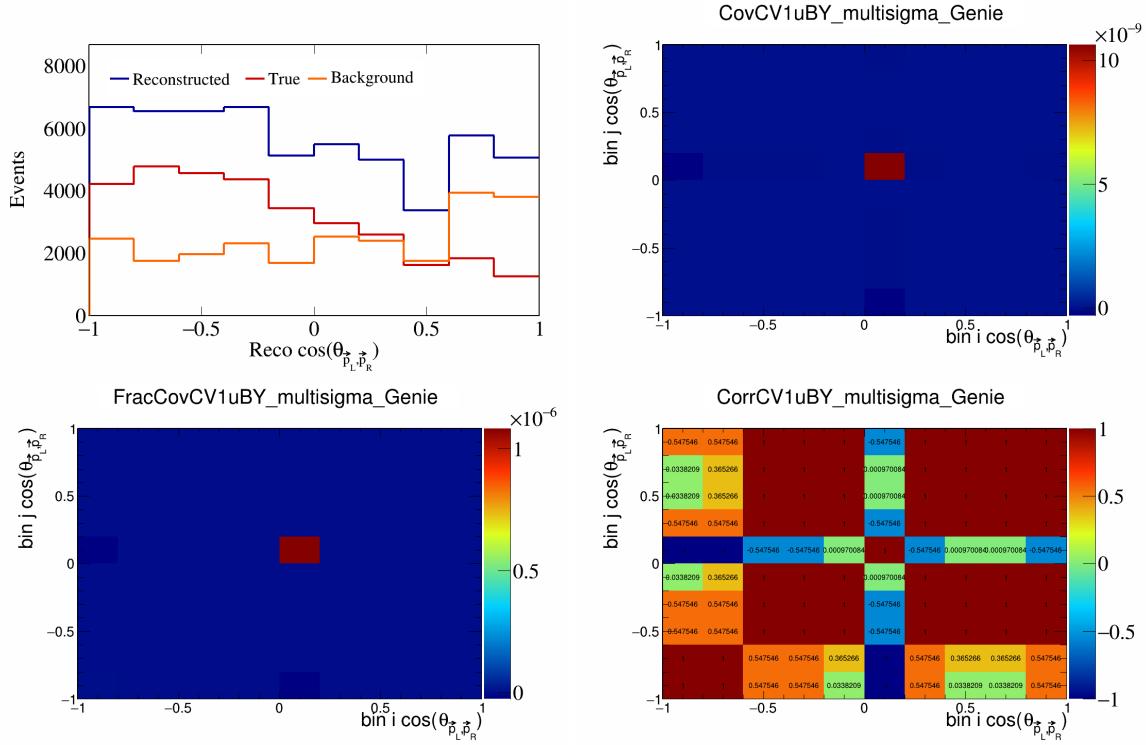


Figure 95: CV1uBY variations for $\cos(\theta_{\vec{p}_L, \vec{p}_R})$.

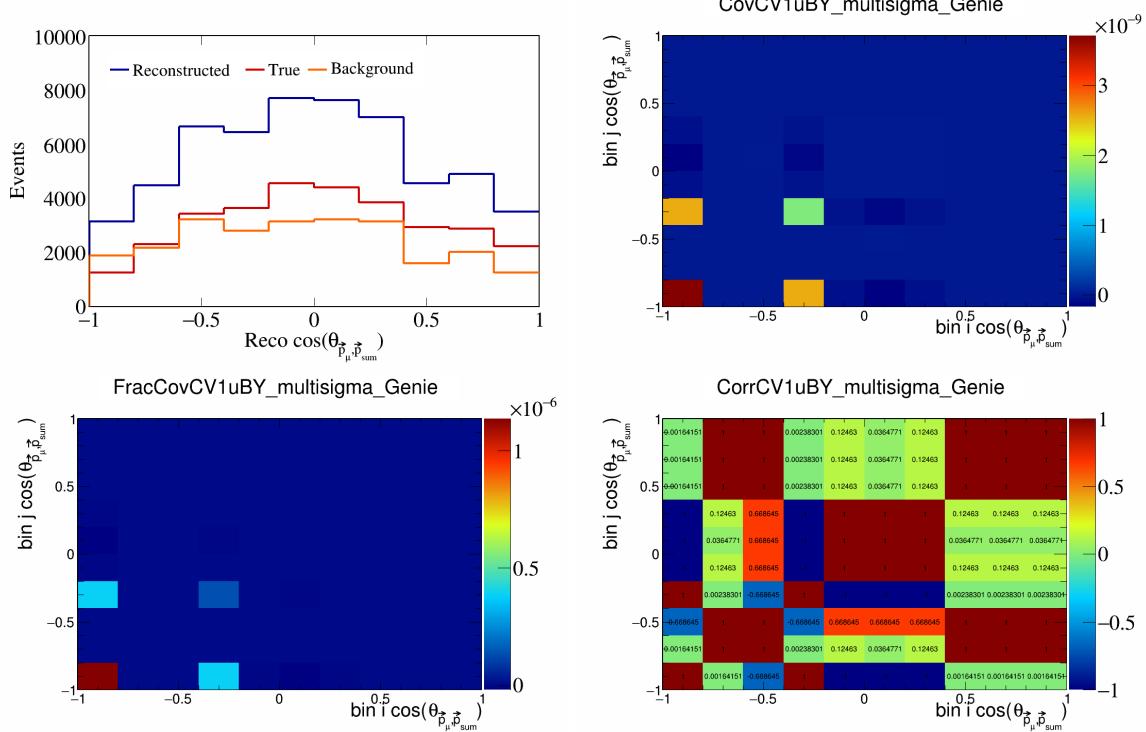


Figure 96: CV1uBY variations for $\cos(\theta_{\vec{p}_\mu, \vec{p}_{\text{sum}}})$.

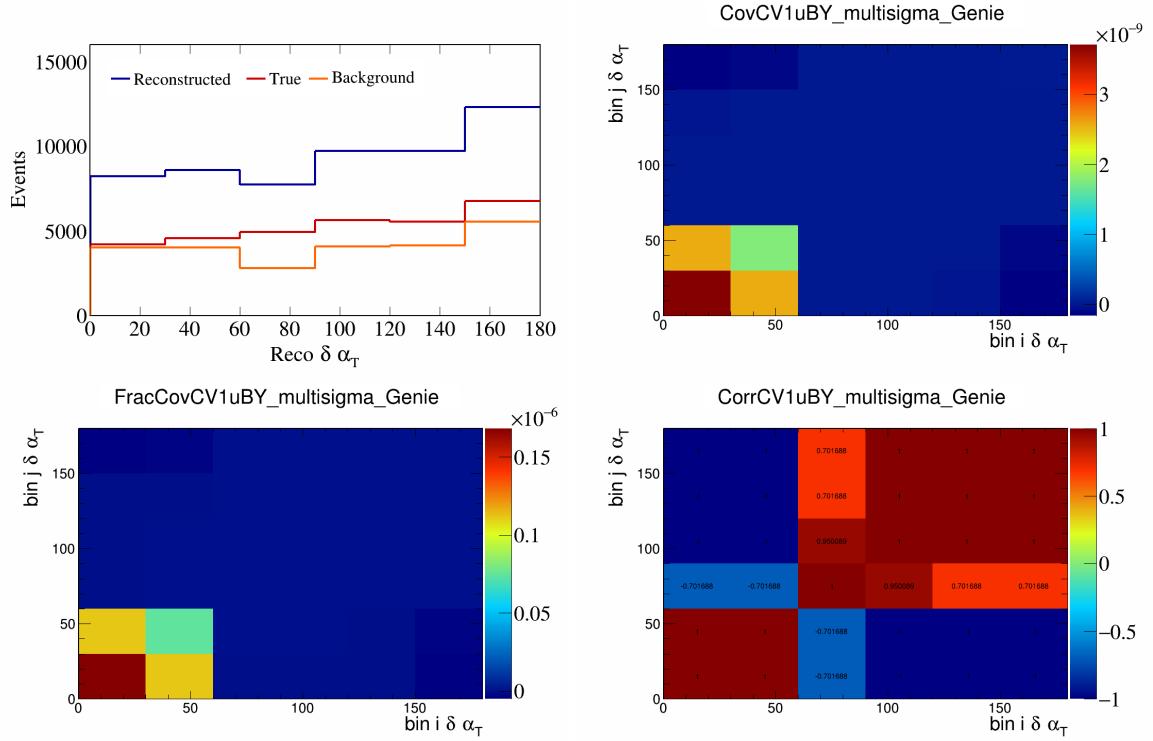


Figure 97: CV1uBY variations for $\delta\alpha_T$.

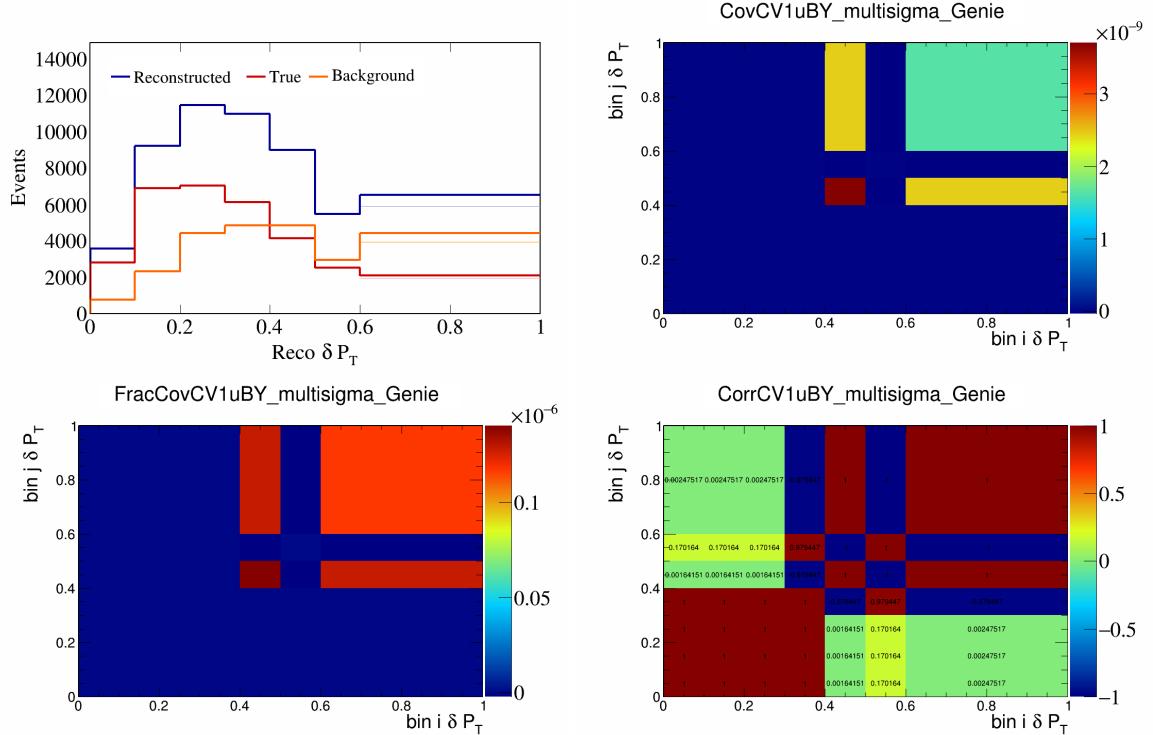


Figure 98: CV1uBY variations for δP_T .

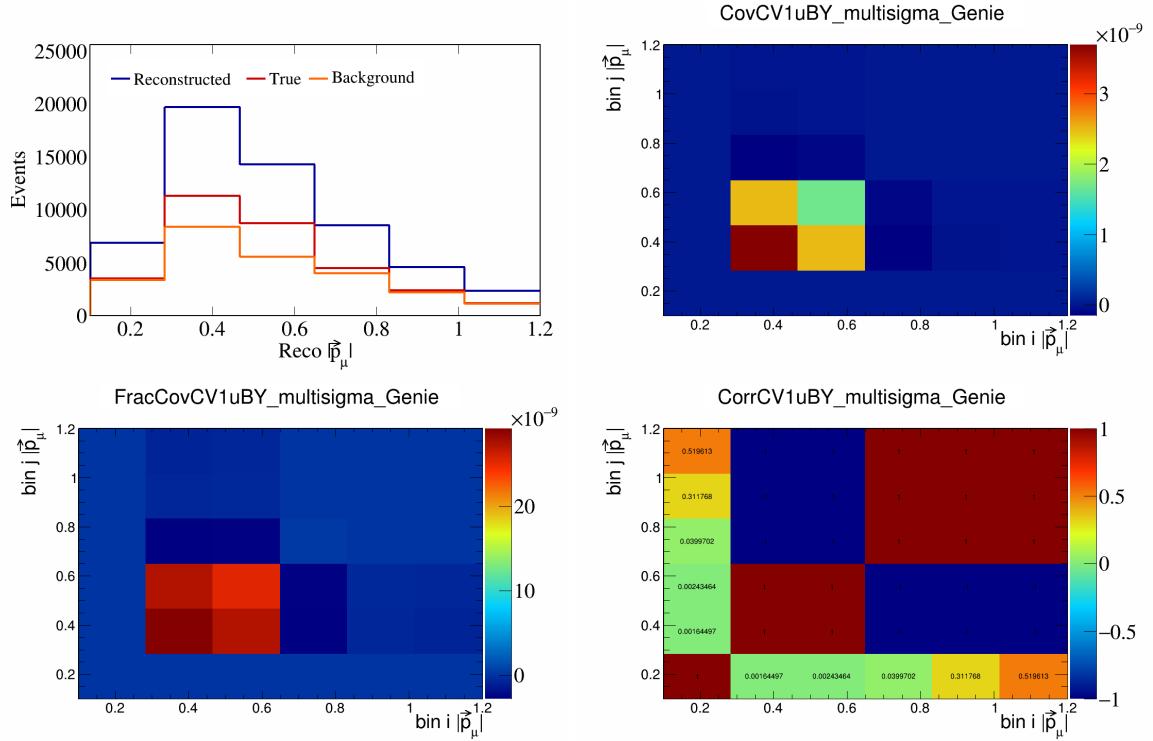


Figure 99: CV1uBY variations for $|\vec{p}_\mu|$.

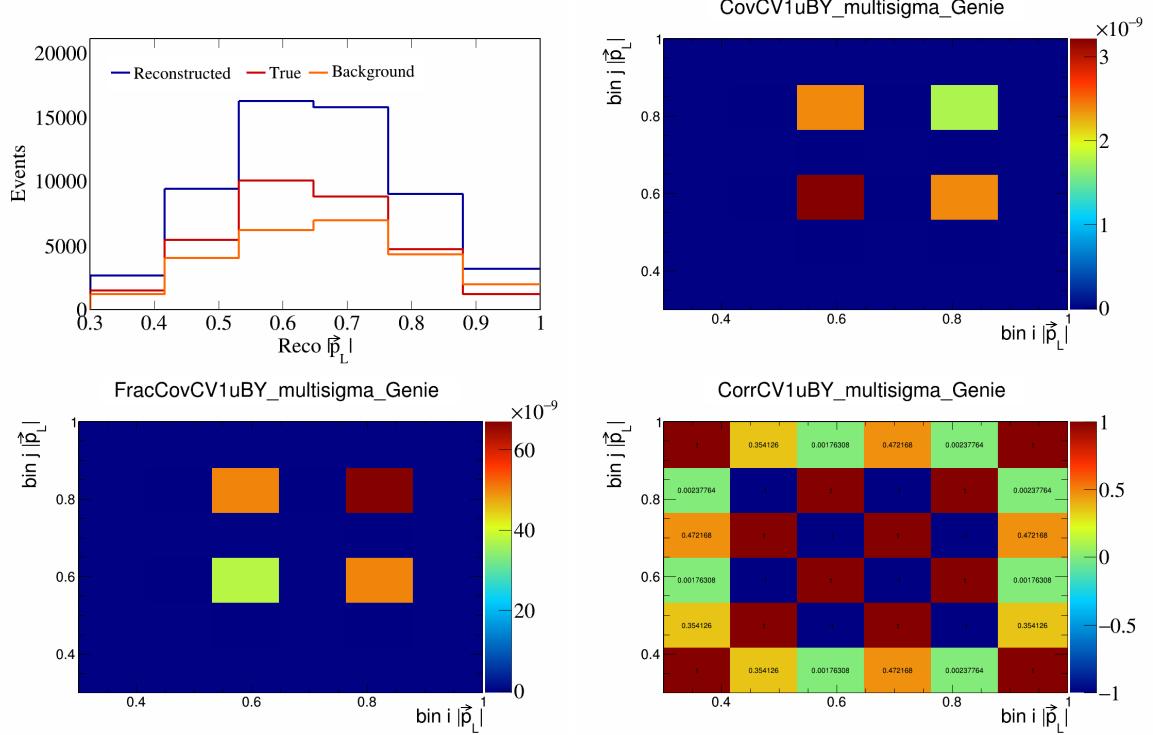


Figure 100: CV1uBY variations for $|\vec{p}_L|$.

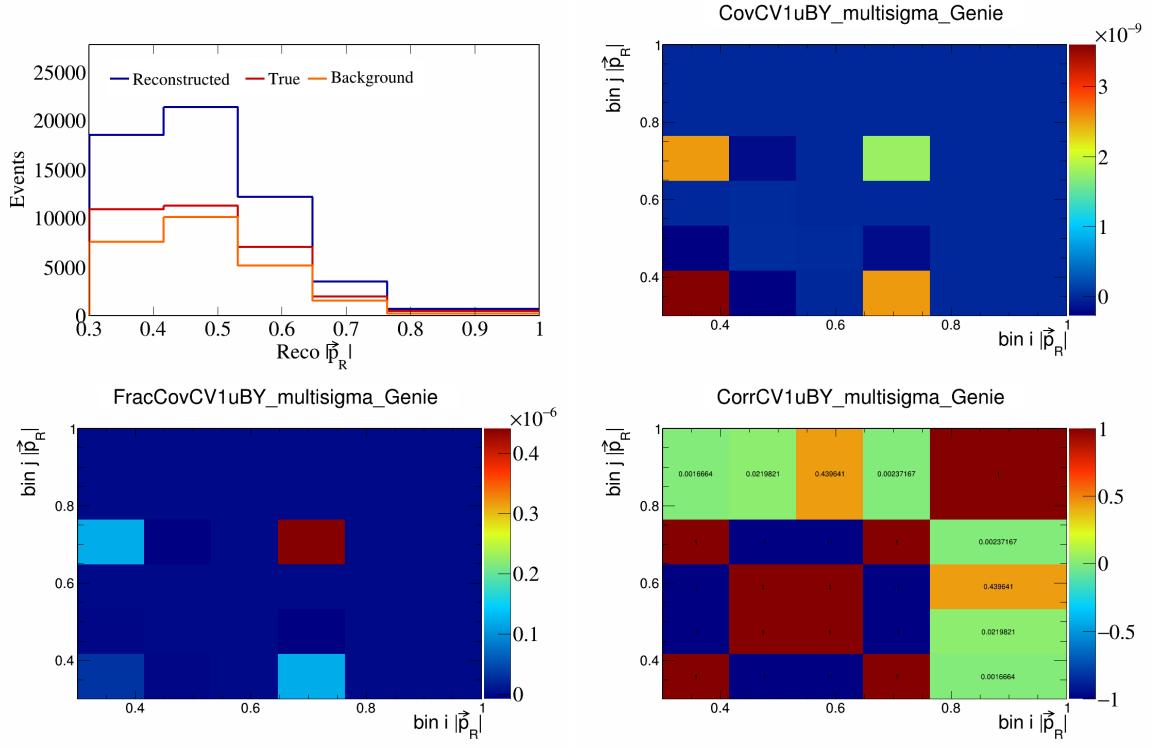


Figure 101: CV1uBY variations for $|\vec{p}_R|$.

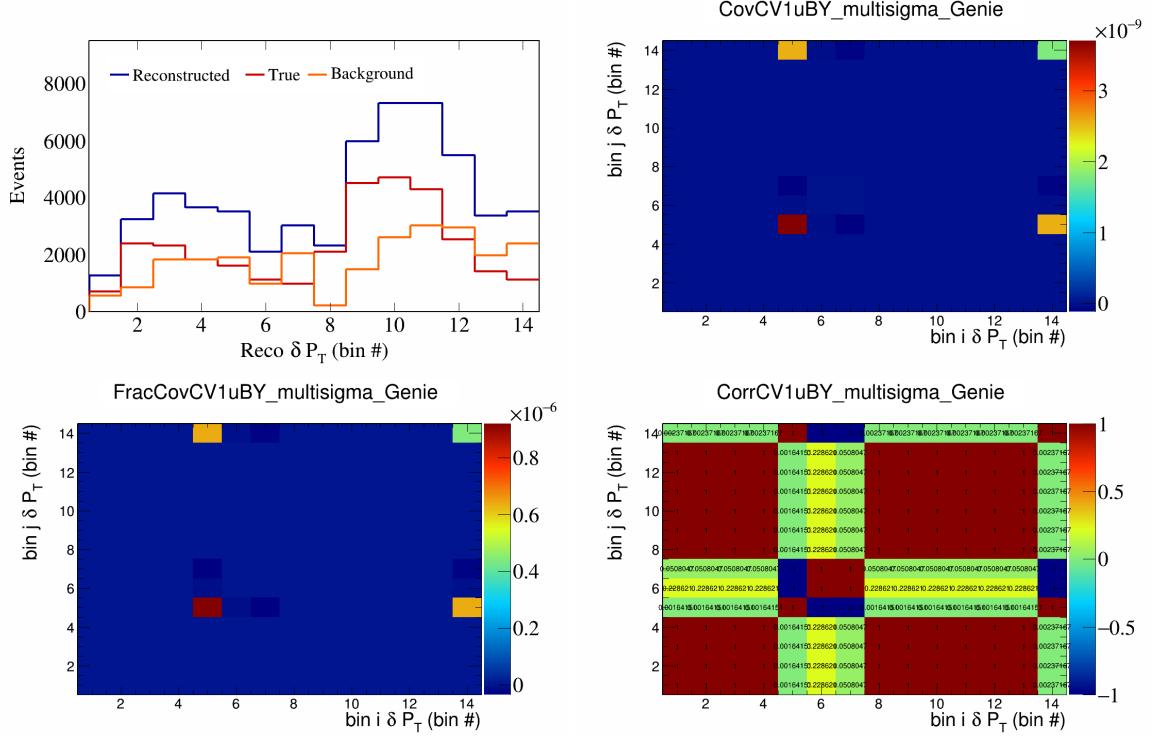


Figure 102: CV1uBY variations for δP_T in $\cos(\theta_{\vec{p}_\mu})$.

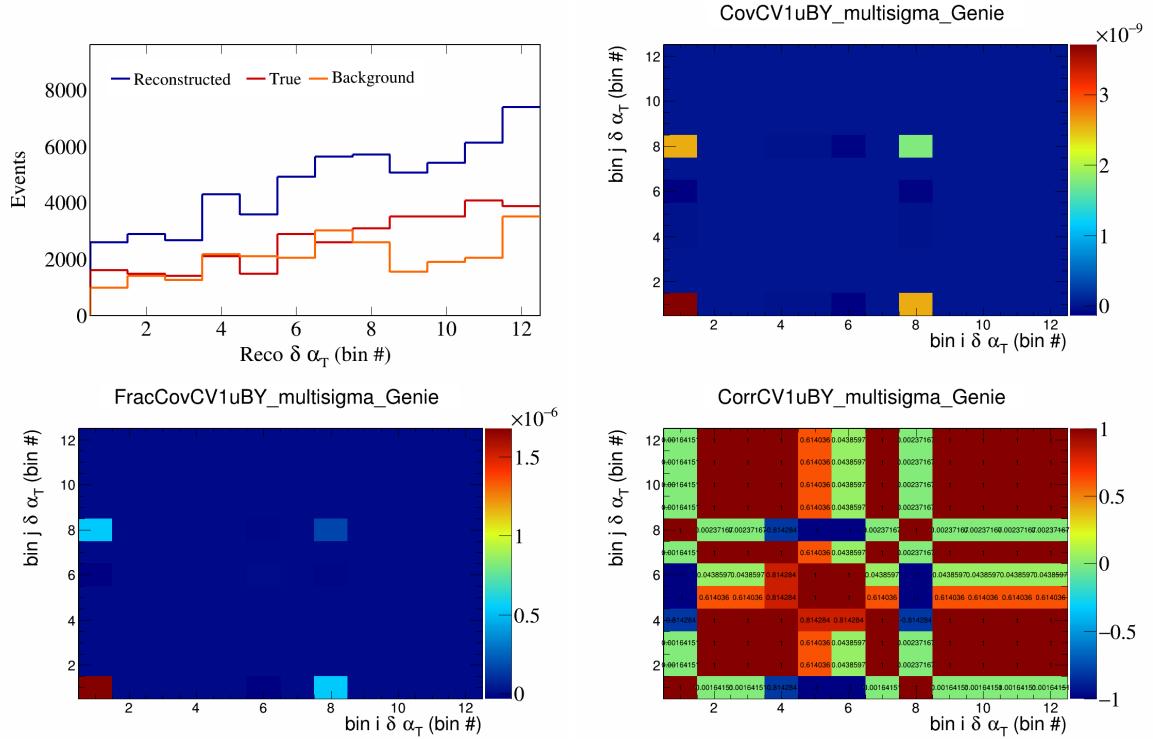


Figure 103: CV1uBY variations for $\delta \alpha_T$ in $\cos(\theta_{\vec{p}_\mu})$.

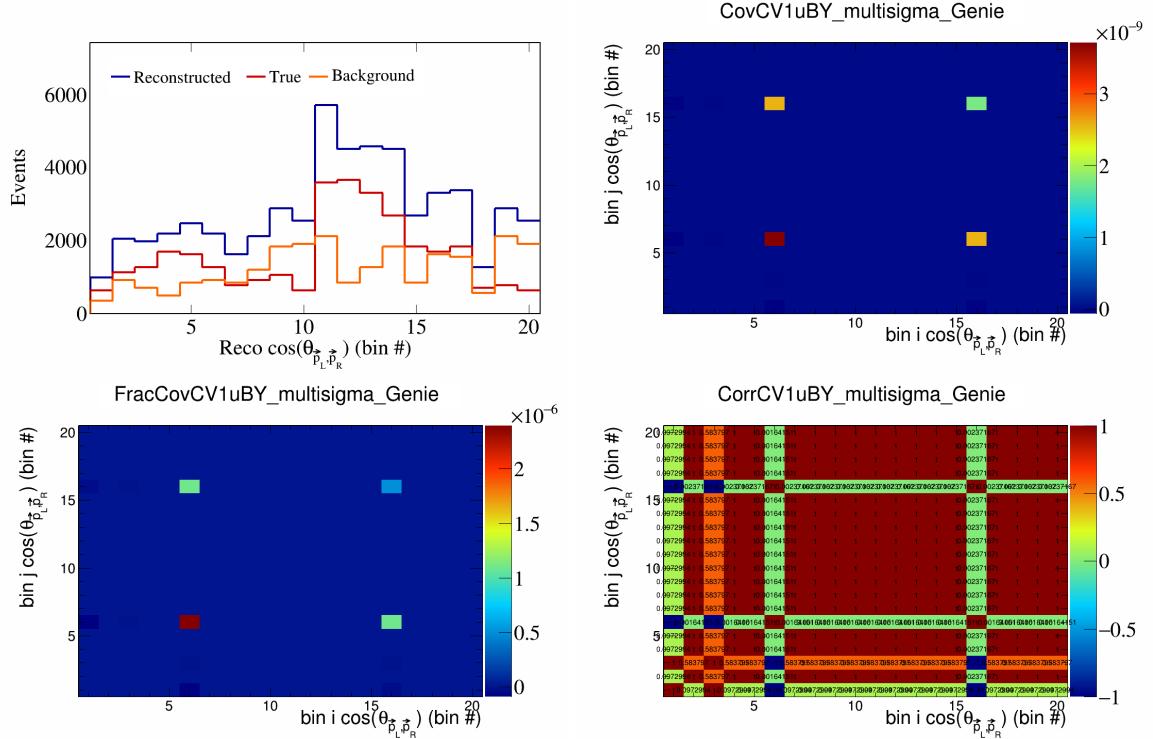


Figure 104: CV1uBY variations for $\cos(\theta_{\vec{p}_L, \vec{p}_R})$ in $\cos(\theta_{\vec{p}_\mu})$.

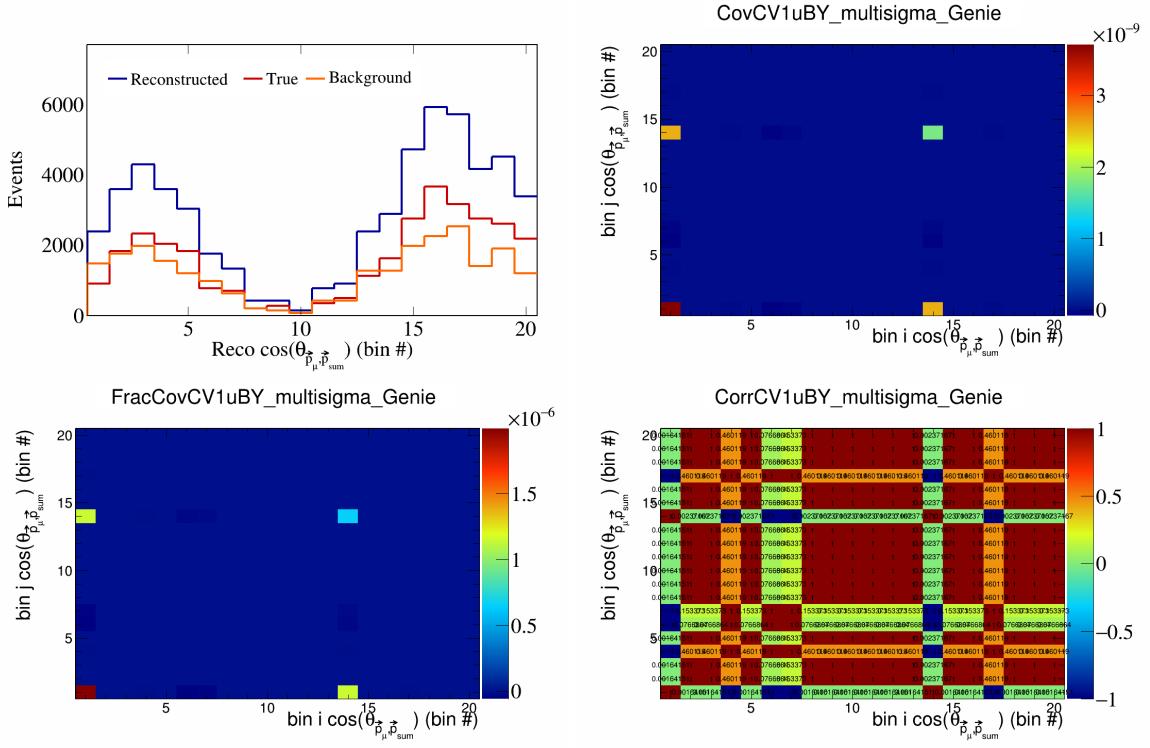


Figure 105: CV1uBY variations for $\cos(\theta_{\vec{p}_\mu, \vec{p}_{\text{sum}}})$ in $\cos(\theta_{\vec{p}_\mu})$.

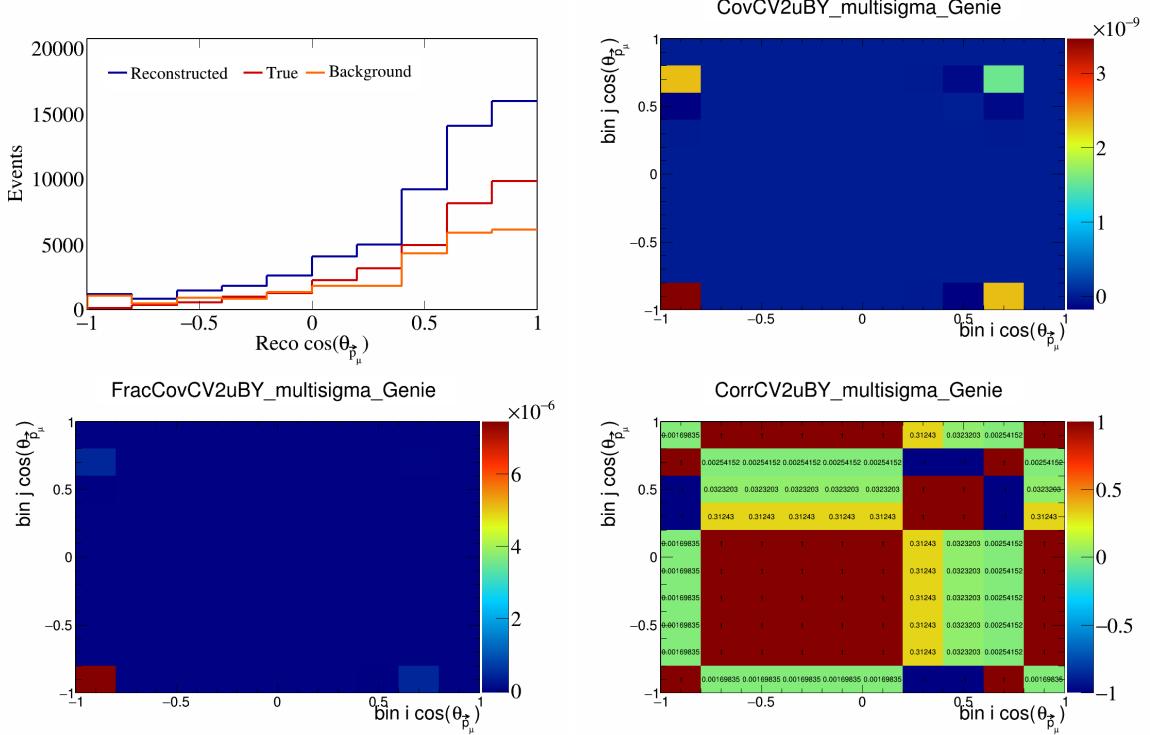


Figure 106: CV2uBY variations for $\cos(\theta_{\vec{p}_\mu})$.

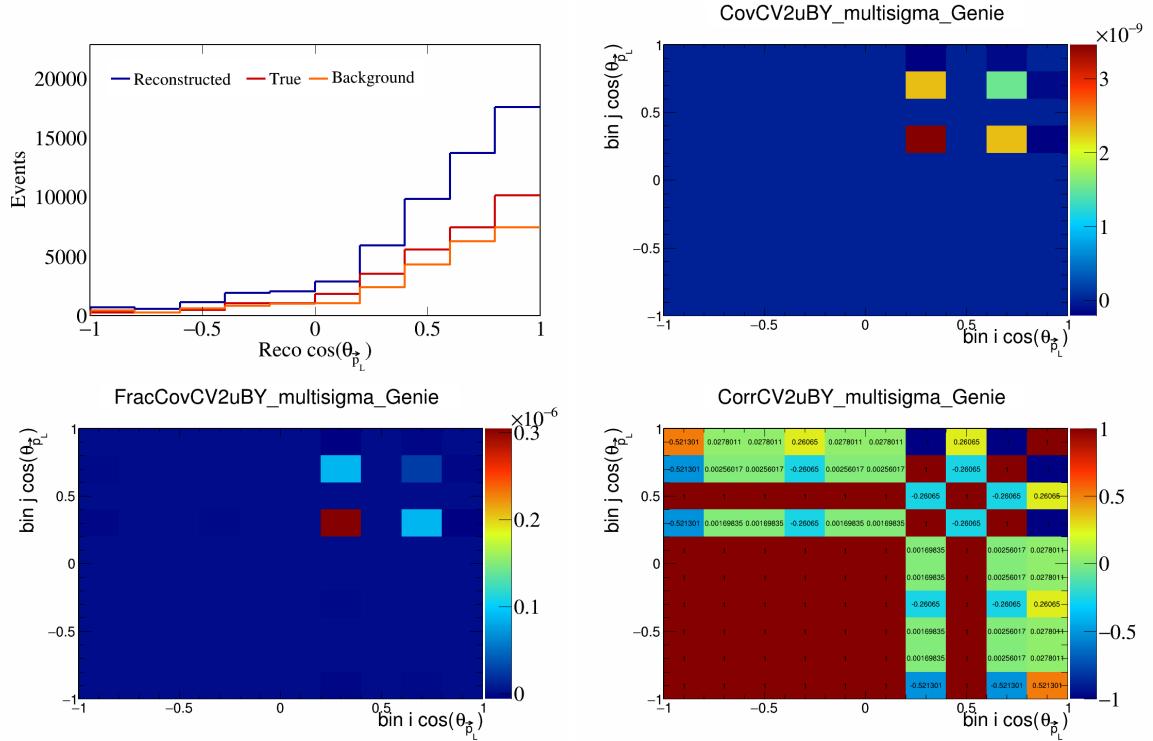


Figure 107: CV2uBY variations for $\cos(\theta_{\vec{p}_L})$.

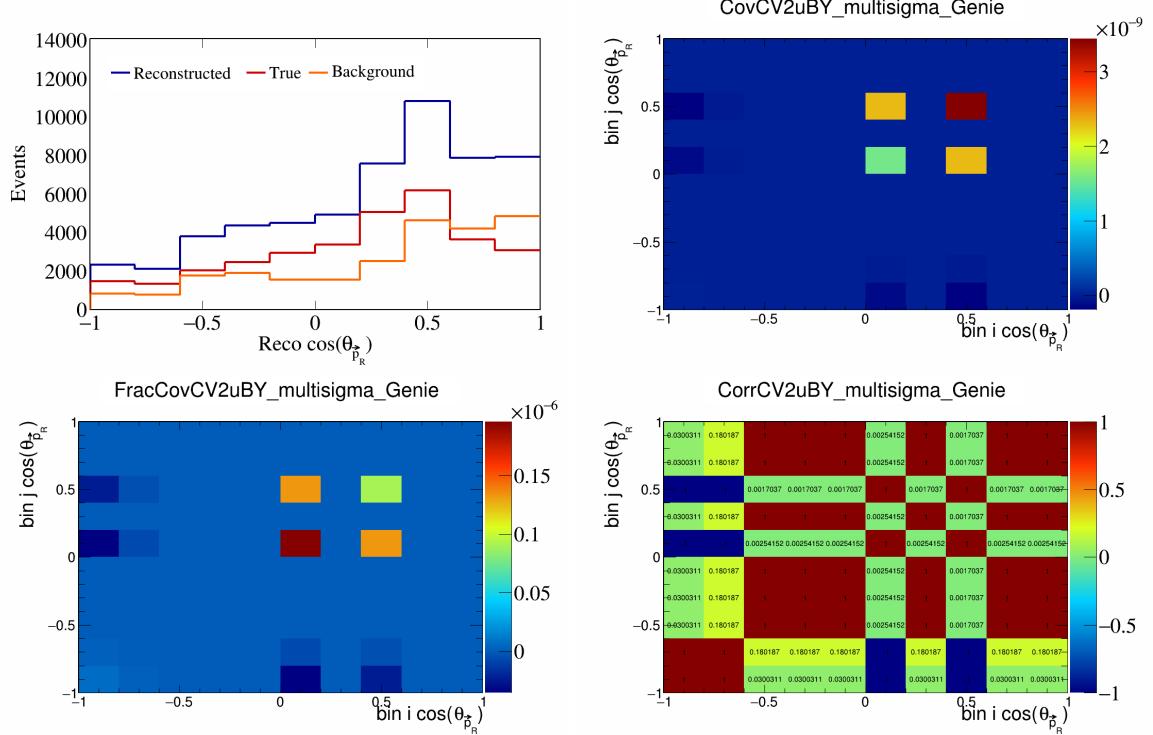


Figure 108: CV2uBY variations for $\cos(\theta_{\vec{p}_R})$.

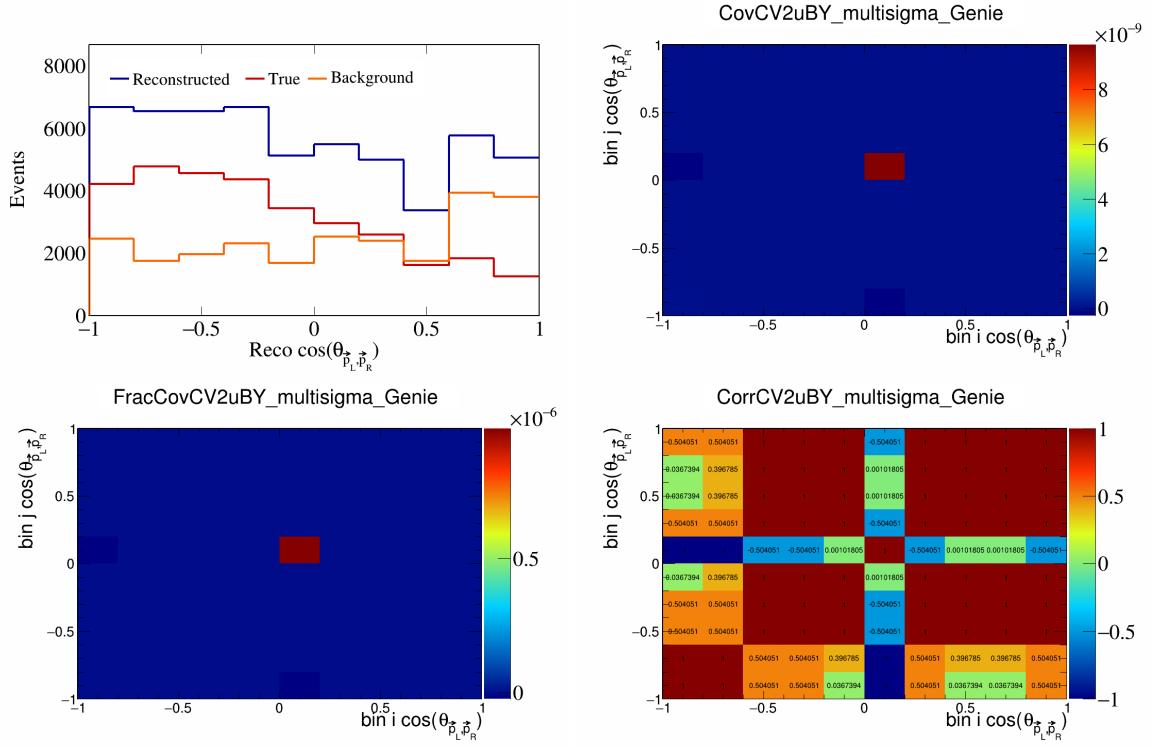


Figure 109: CV2uBY variations for $\cos(\theta_{\vec{p}_L, \vec{p}_R})$.

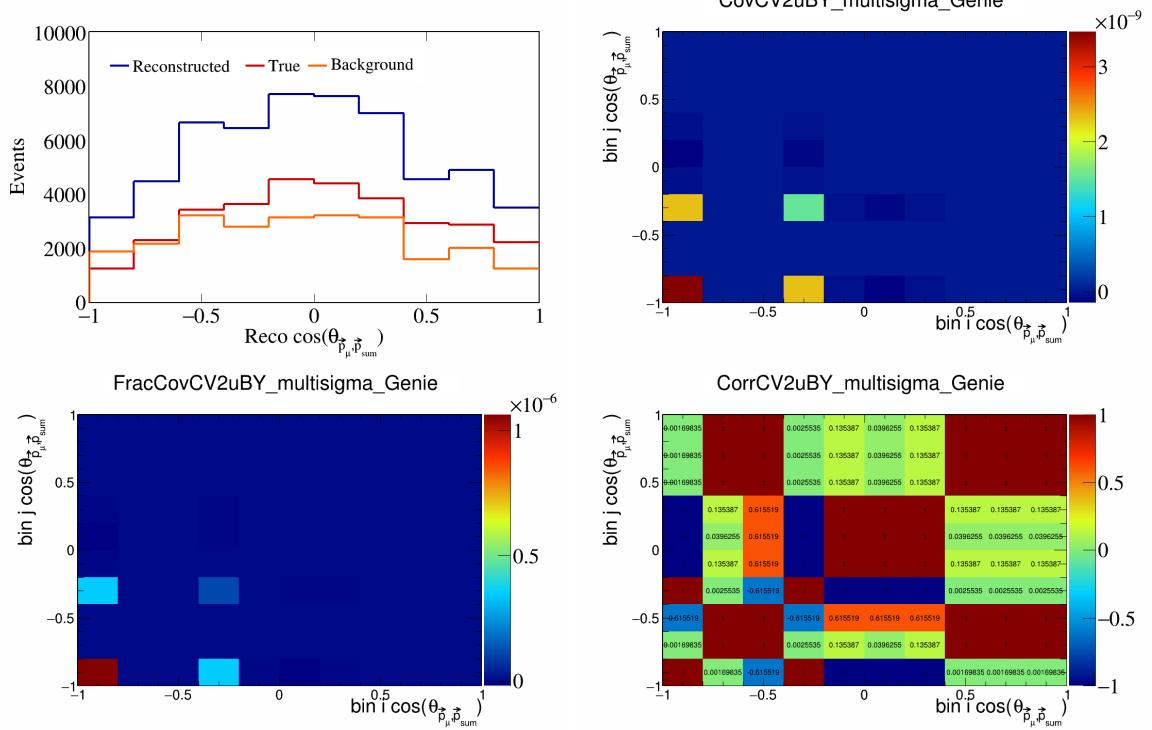


Figure 110: CV2uBY variations for $\cos(\theta_{\vec{p}_\mu, \vec{p}_{\text{sum}}})$.

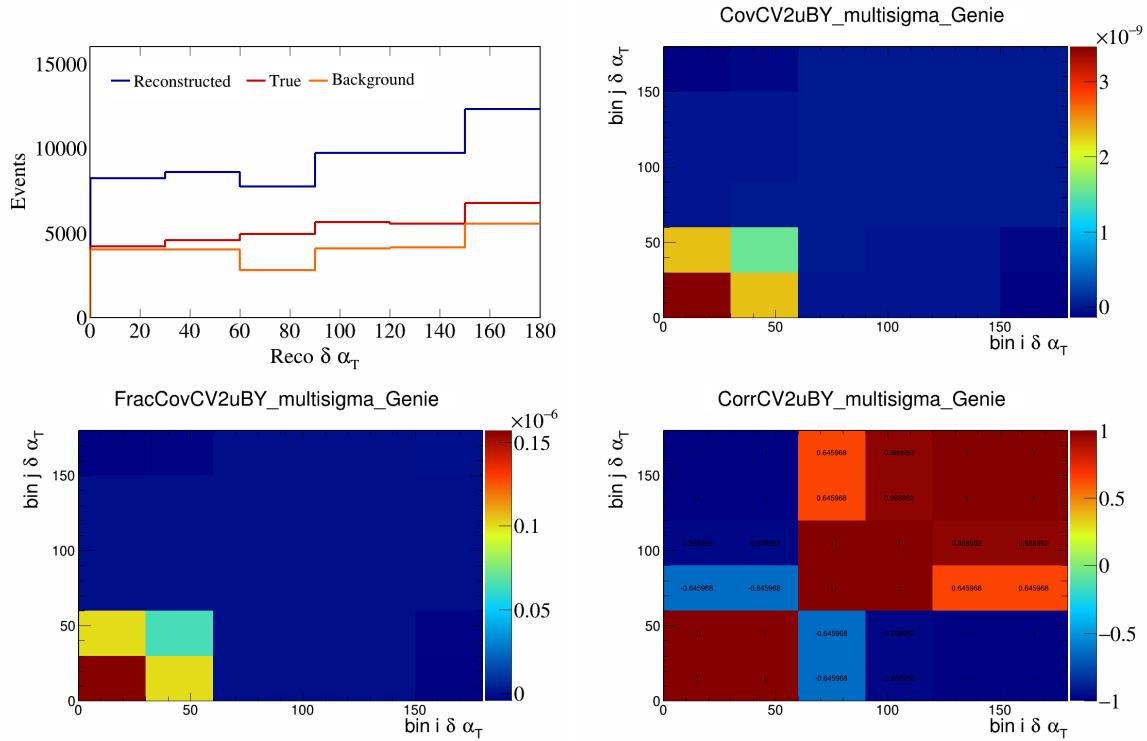


Figure 111: CV2uBY variations for $\delta\alpha_T$.

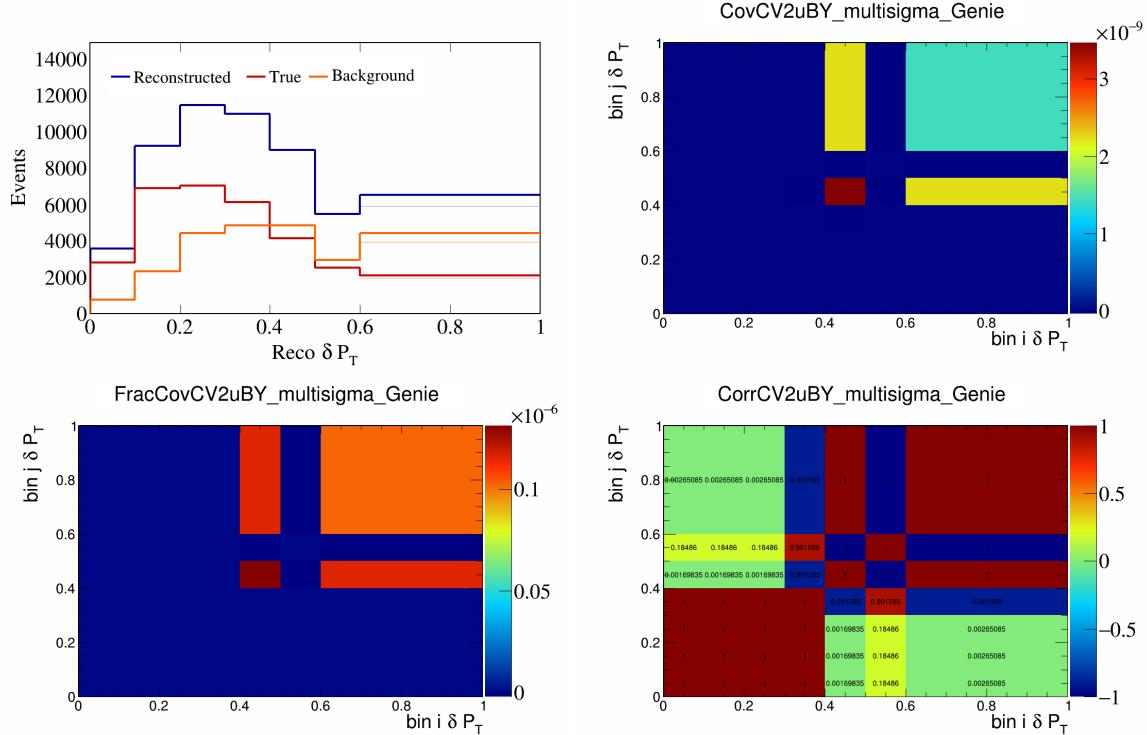


Figure 112: CV2uBY variations for δP_T .

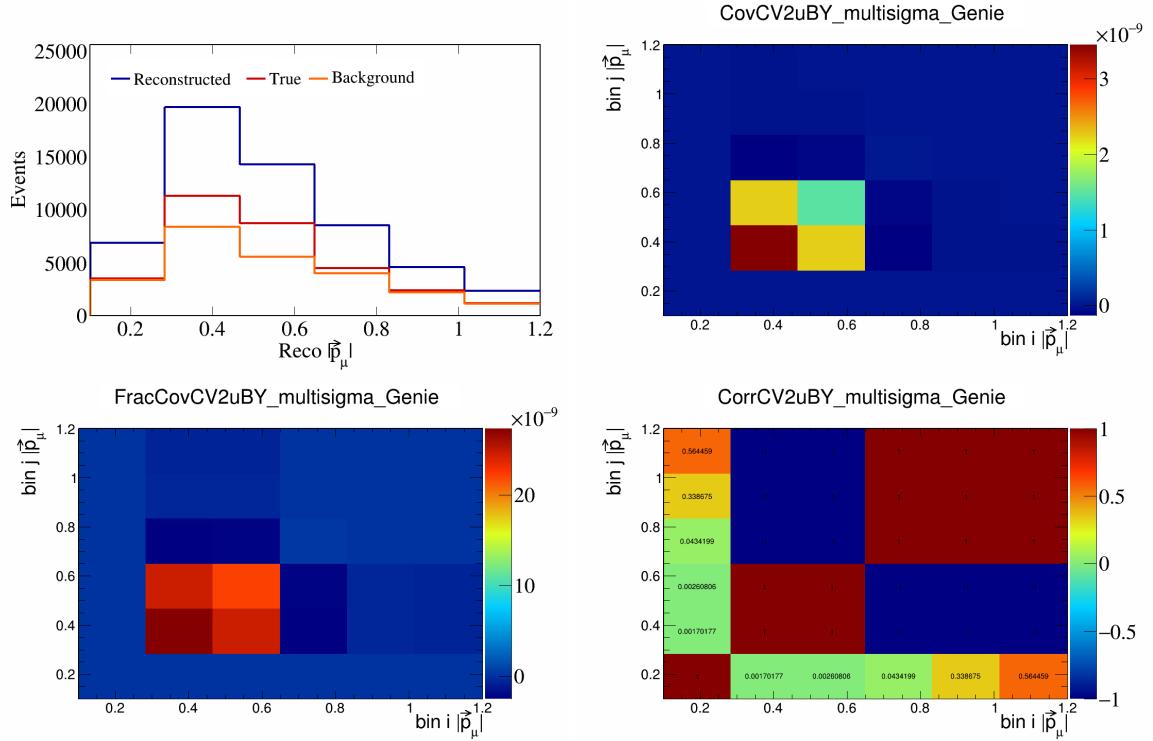


Figure 113: CV2uBY variations for $|\vec{p}_\mu|$.

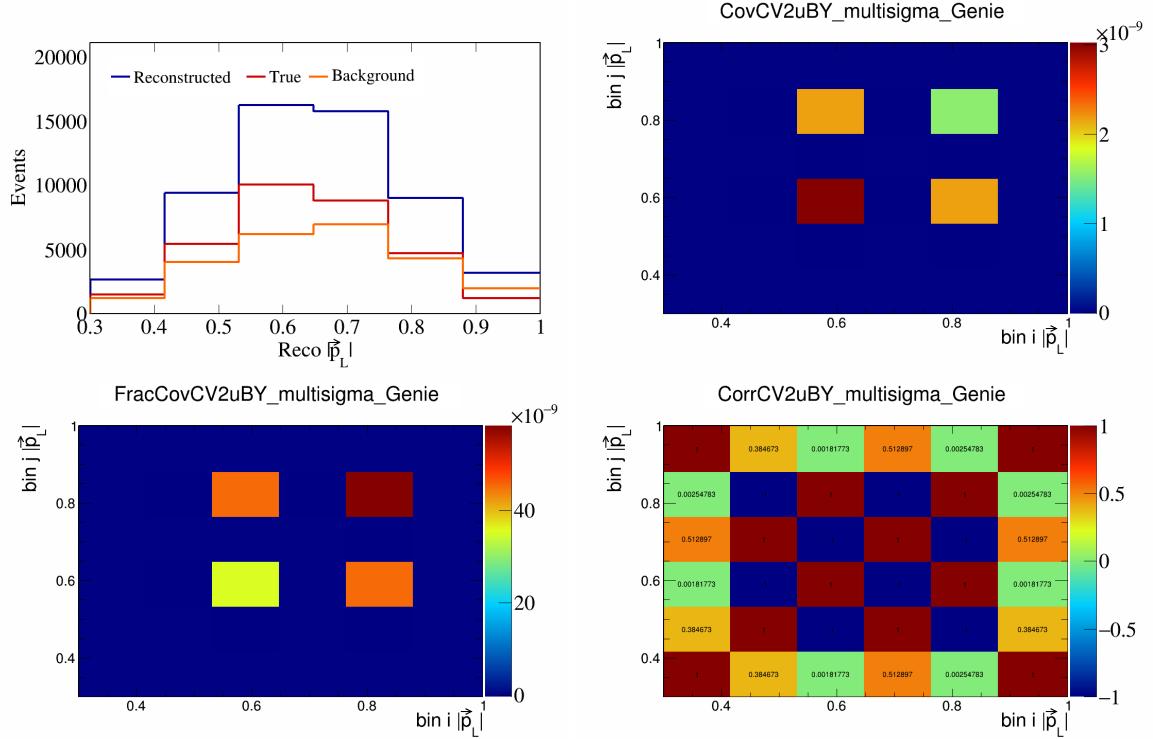


Figure 114: CV2uBY variations for $|\vec{p}_L|$.

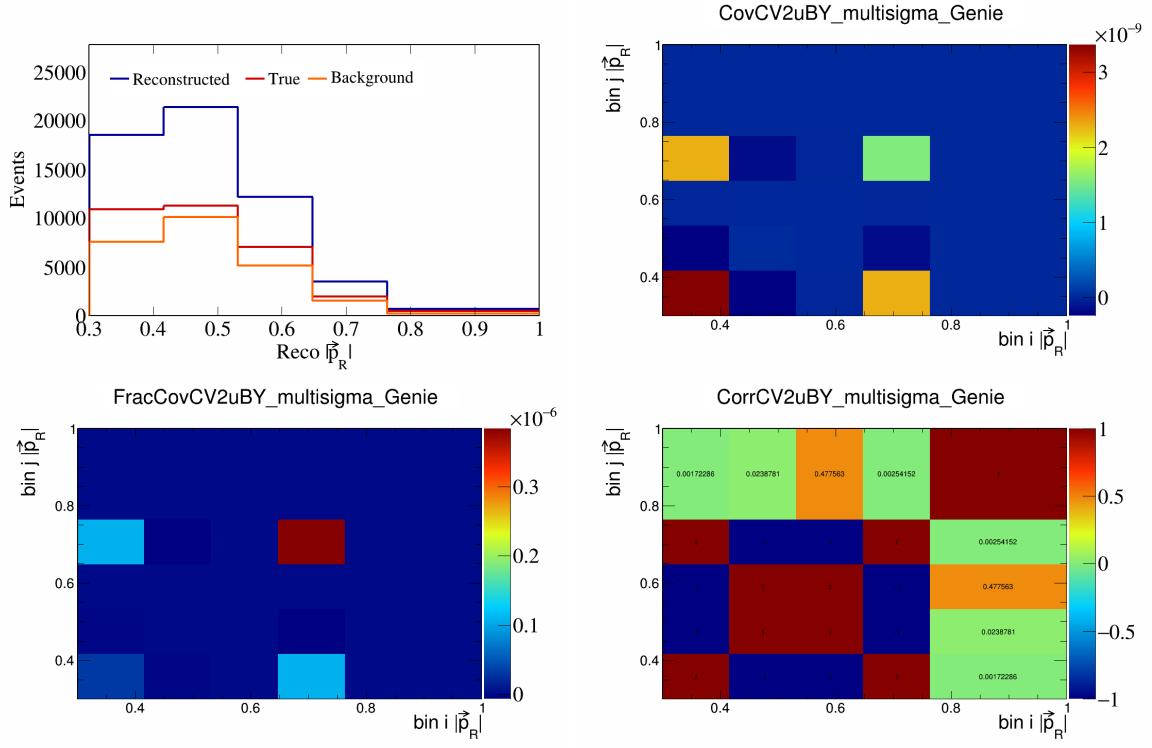


Figure 115: CV2uBY variations for $|\vec{p}_R|$.

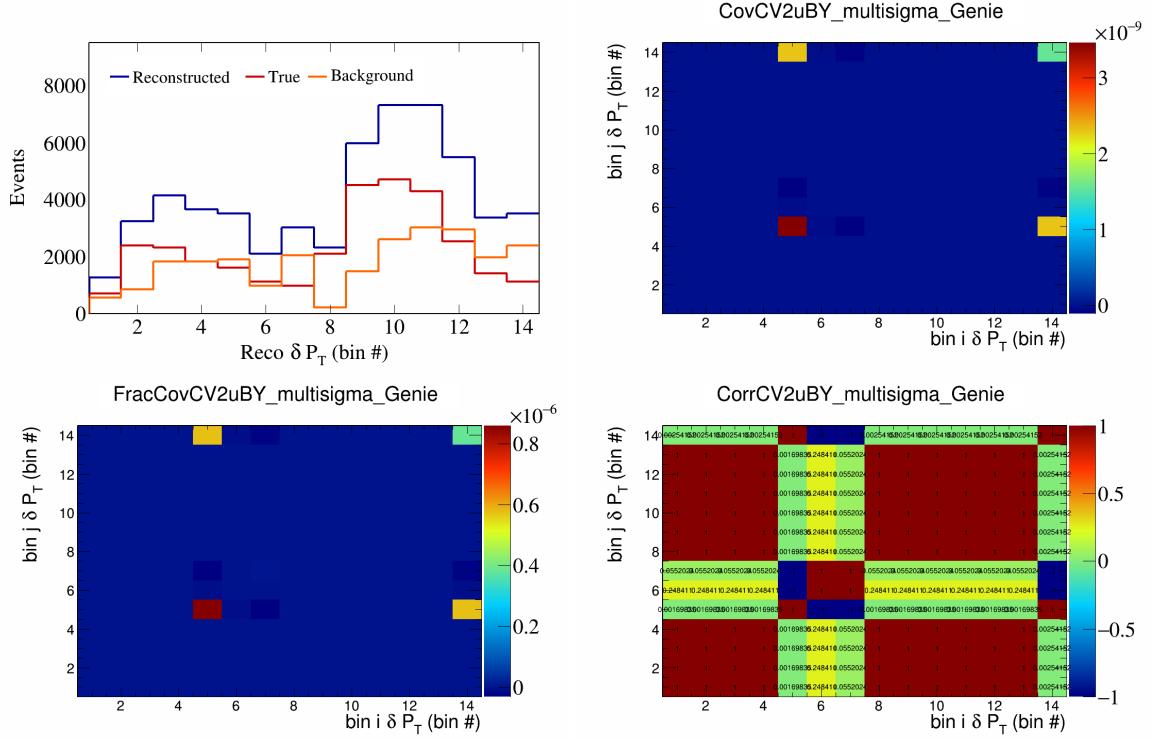


Figure 116: CV2uBY variations for δP_T in $\cos(\theta_{\vec{p}_\mu})$.

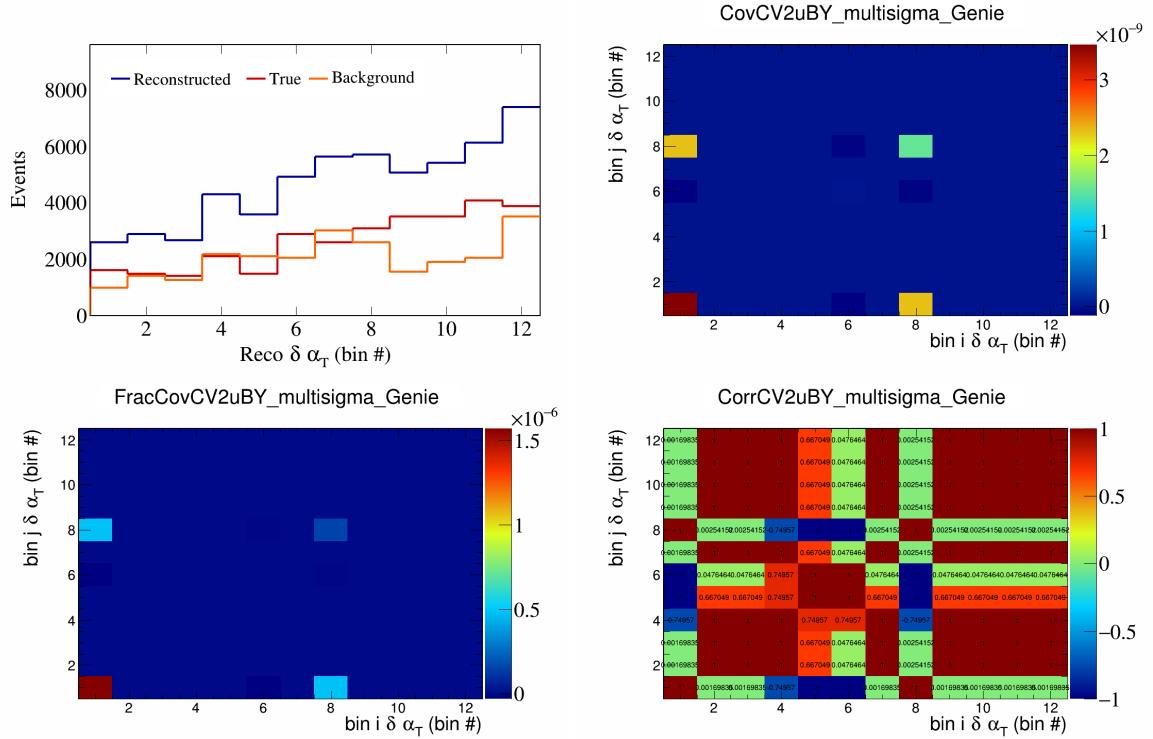


Figure 117: CV2uBY variations for $\delta\alpha_T$ in $\cos(\theta_{\vec{p}_\mu})$.

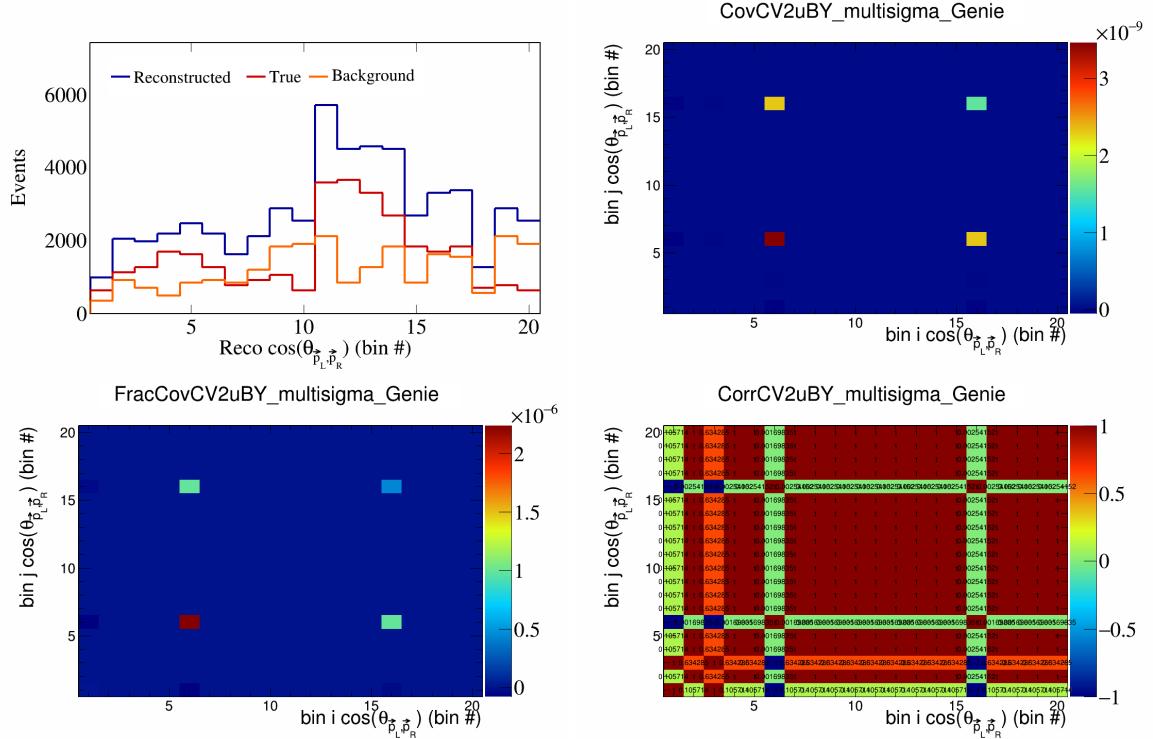


Figure 118: CV2uBY variations for $\cos(\theta_{\vec{p}_L, \vec{p}_R})$ in $\cos(\theta_{\vec{p}_\mu})$.

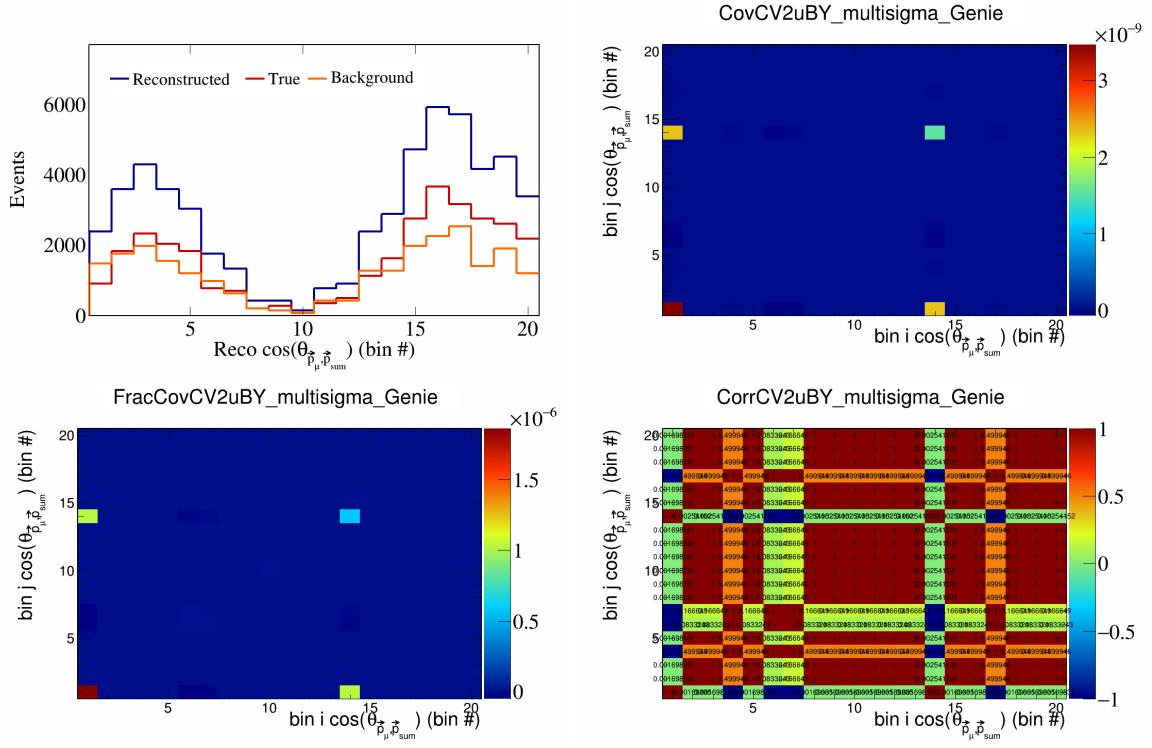


Figure 119: CV2uBY variations for $\cos(\theta_{\vec{p}_\mu, \vec{p}_{\text{sum}}})$ in $\cos(\theta_{\vec{p}_\mu})$.

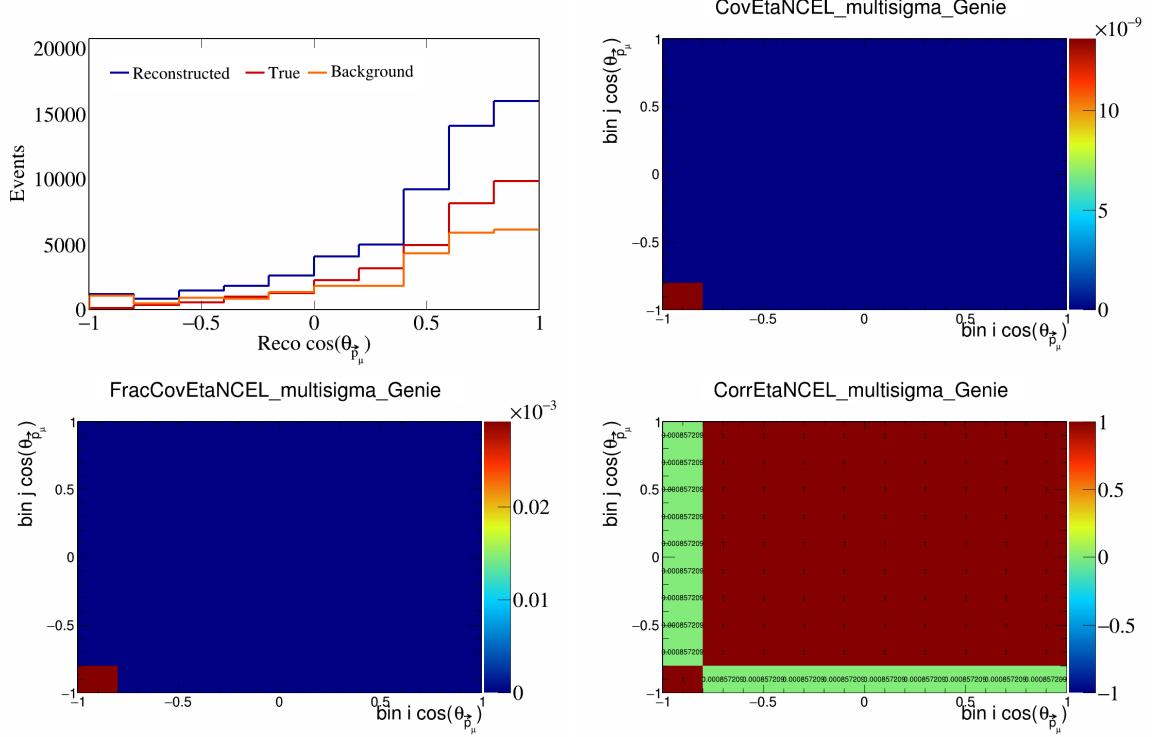


Figure 120: EtaNCEL variations for $\cos(\theta_{\vec{p}_\mu})$.

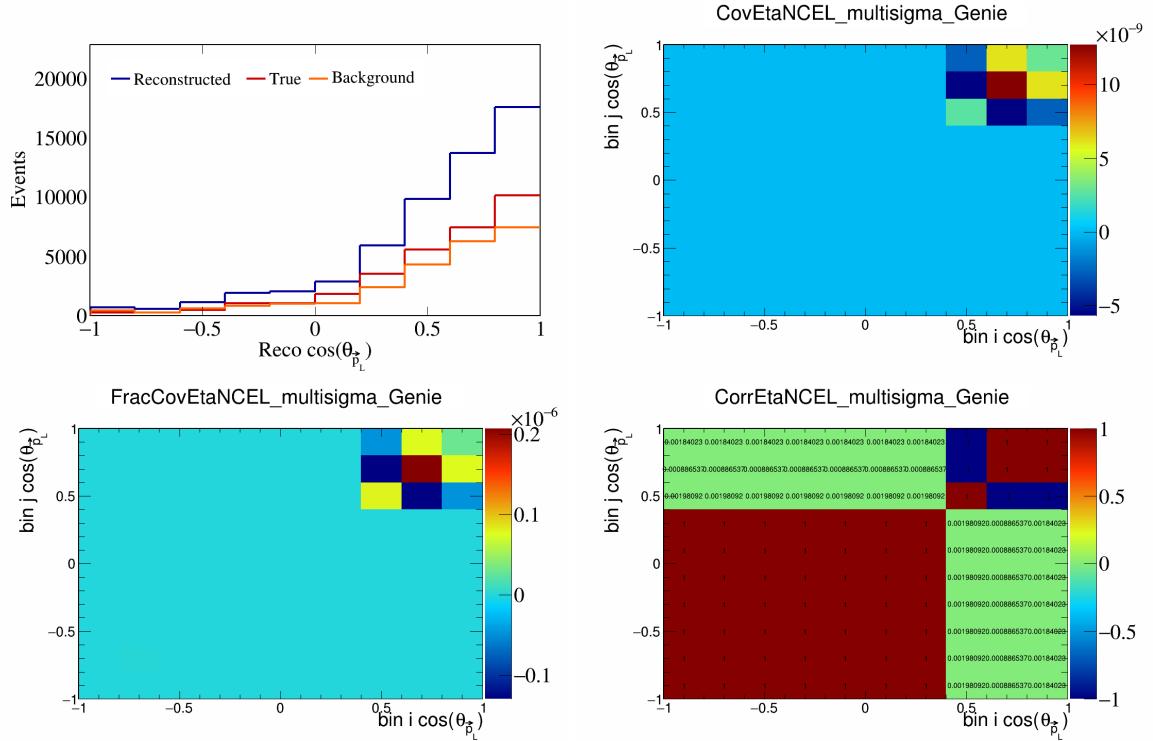


Figure 121: EtaNCEL variations for $\cos(\theta_{\vec{p}_L})$.

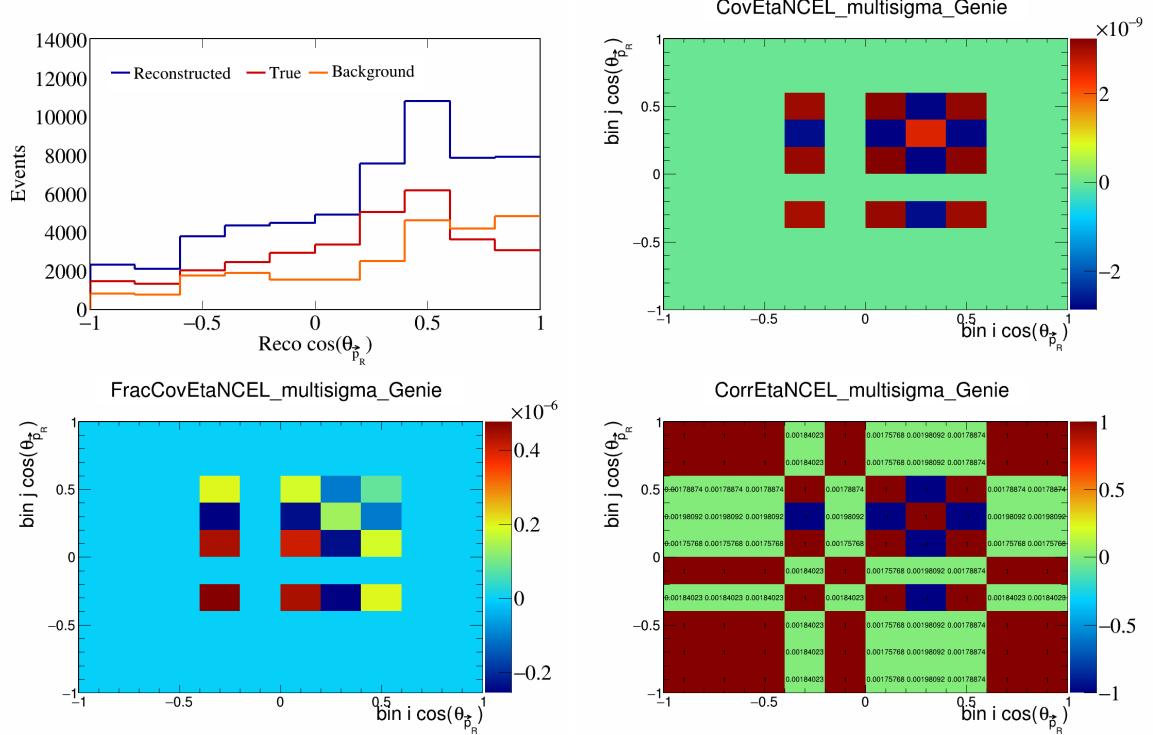


Figure 122: EtaNCEL variations for $\cos(\theta_{\vec{p}_R})$.

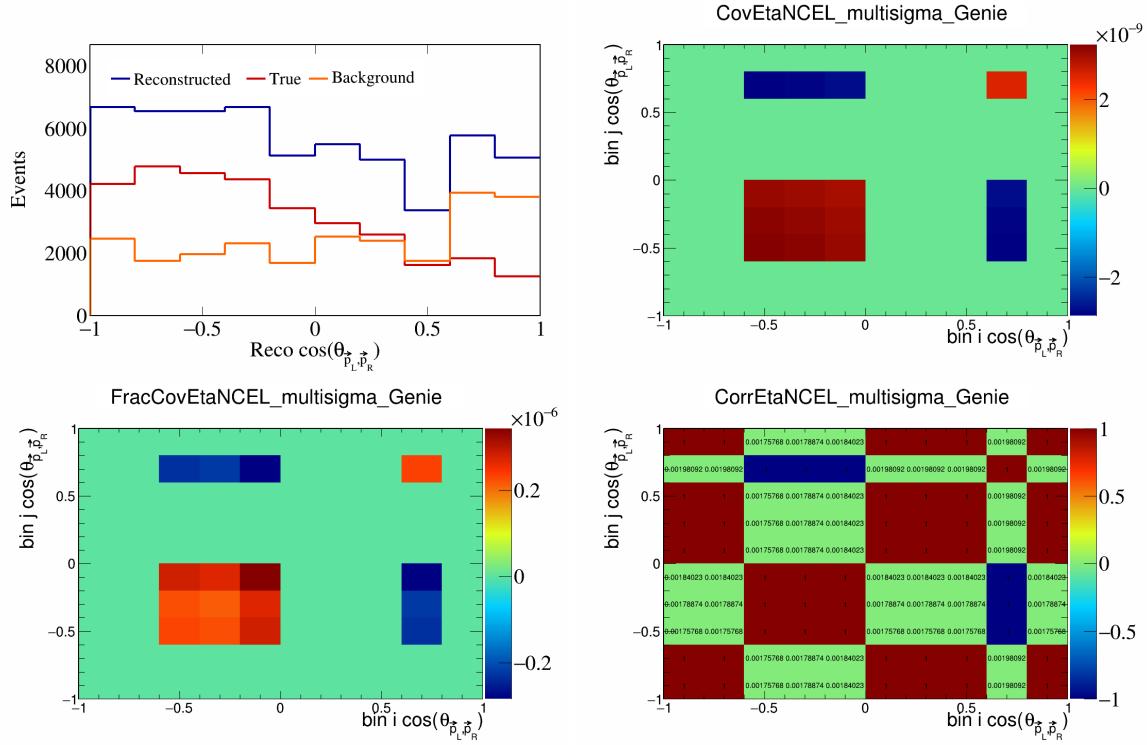


Figure 123: EtaNCEL variations for $\cos(\theta_{\vec{p}_L, \vec{p}_R})$.

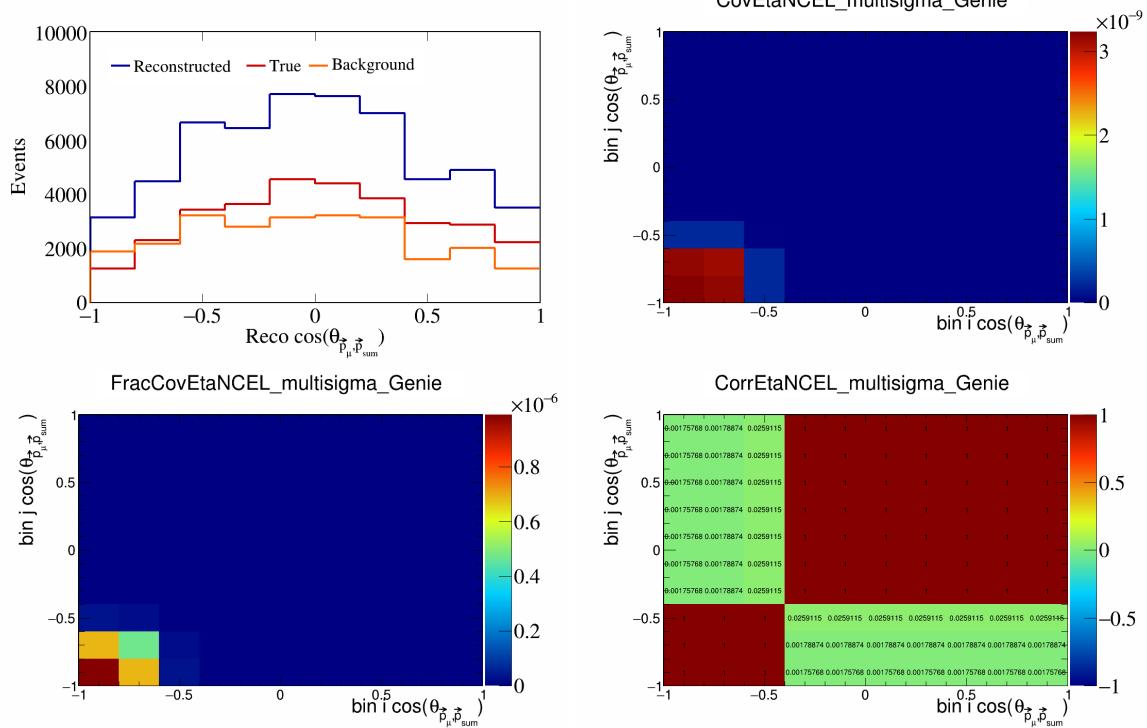


Figure 124: EtaNCEL variations for $\cos(\theta_{\vec{p}_\mu, \vec{p}_{\text{sum}}})$.

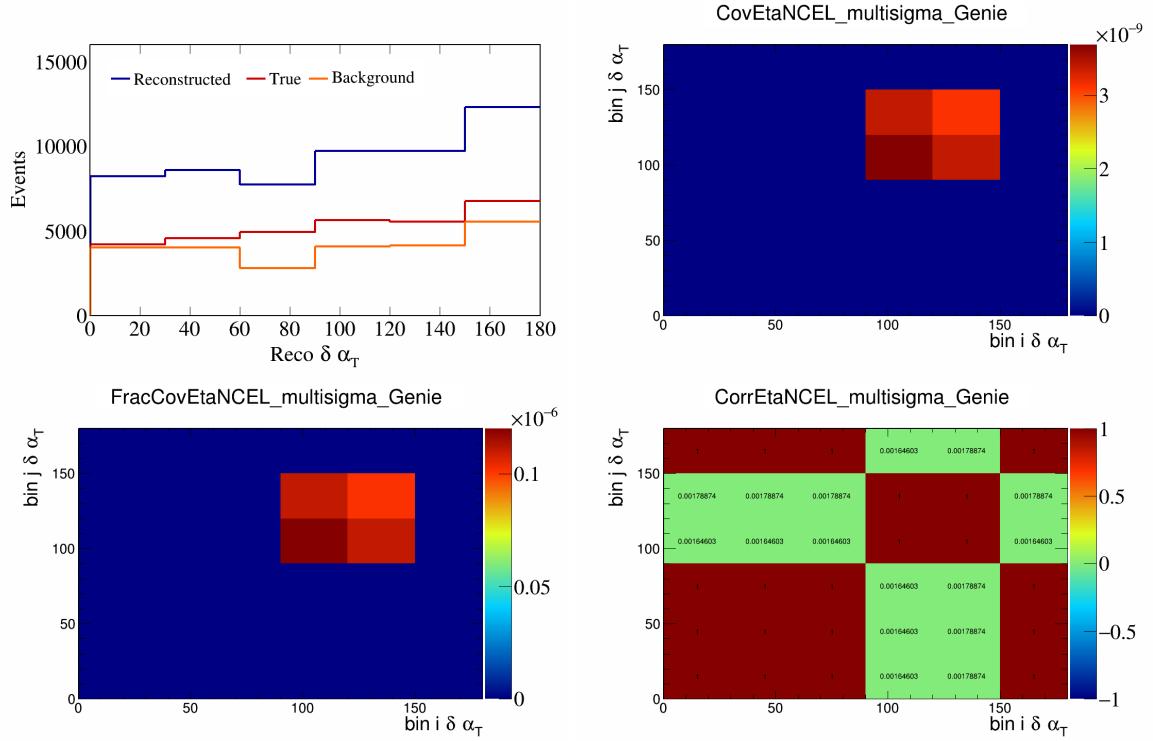


Figure 125: EtaNCEL variations for $\delta\alpha_T$.

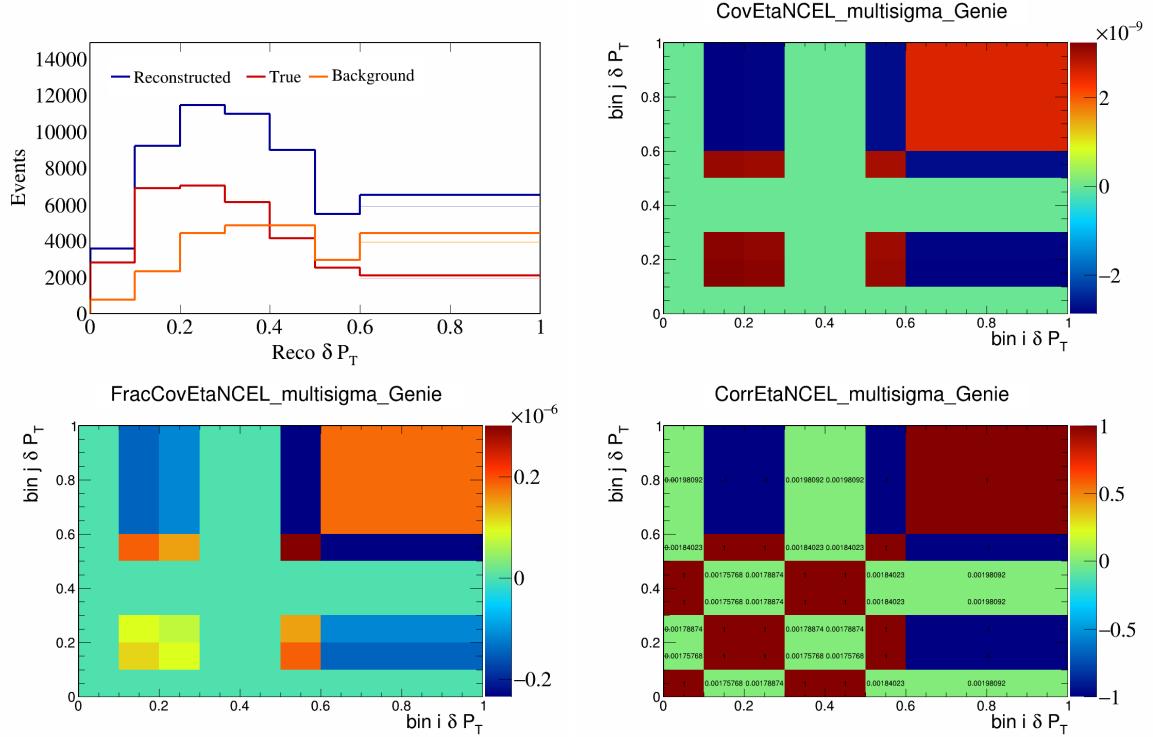


Figure 126: EtaNCEL variations for δP_T .

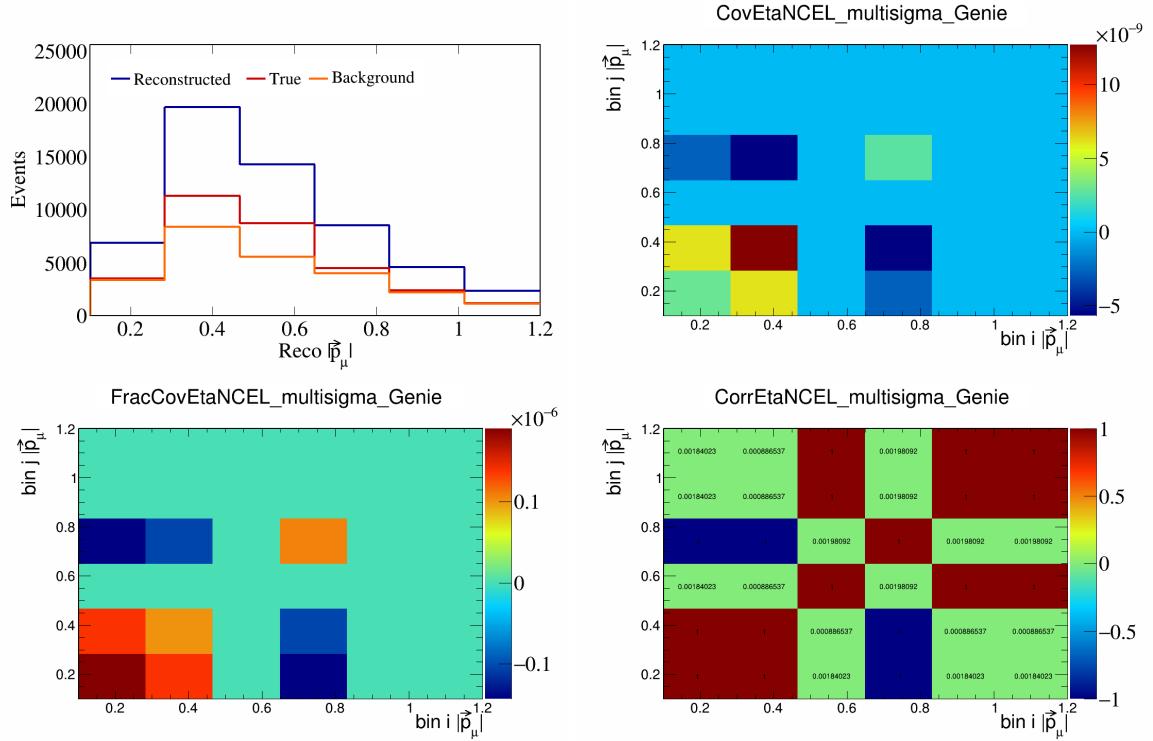


Figure 127: EtaNCEL variations for $|\vec{p}_\mu|$.

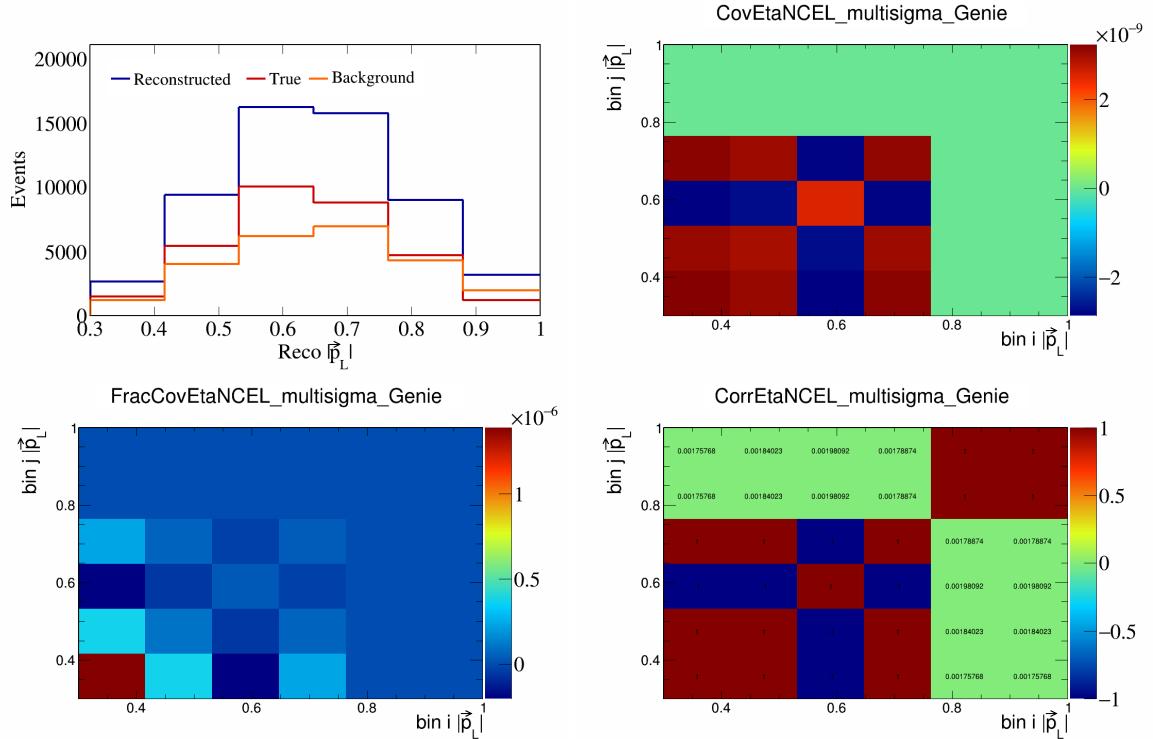


Figure 128: EtaNCEL variations for $|\vec{p}_L|$.

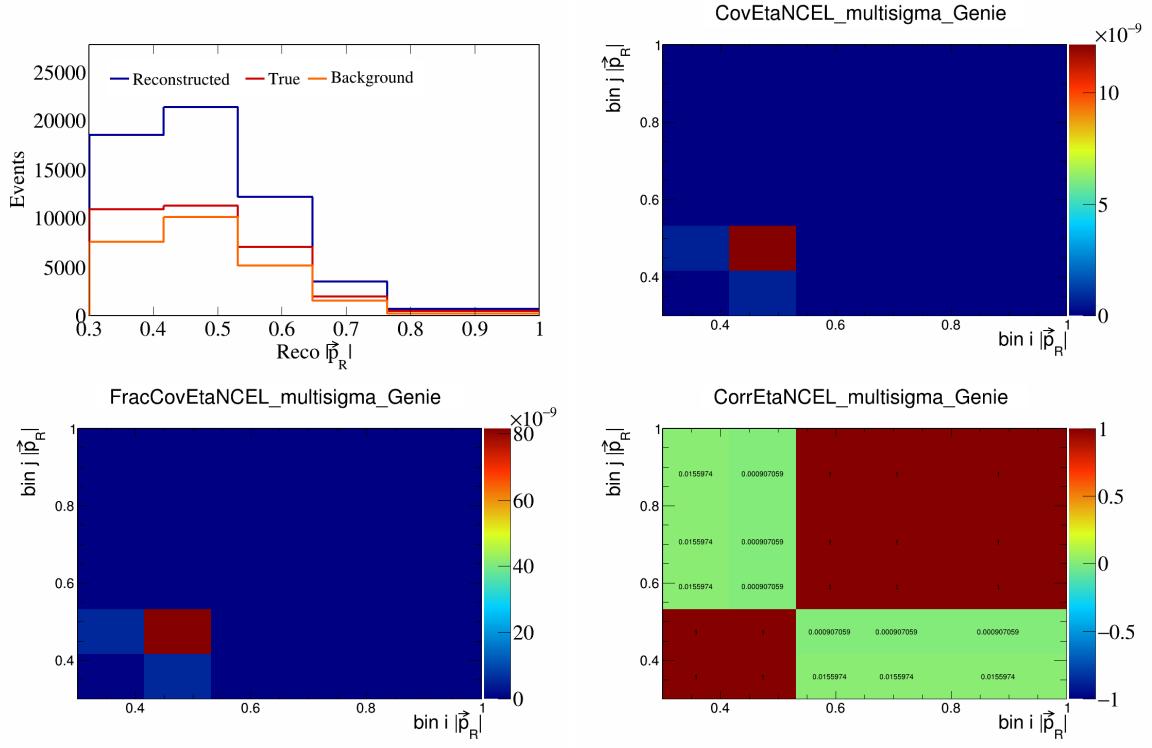


Figure 129: EtaNCEL variations for $|\vec{p}_R|$.

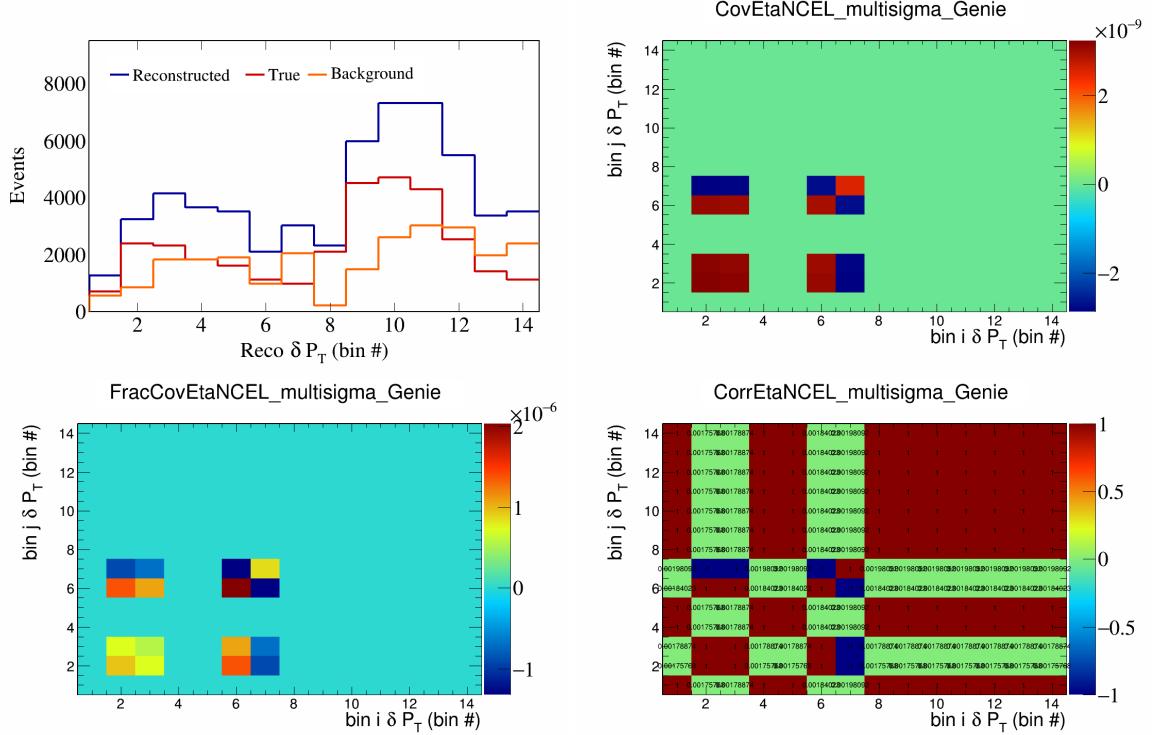


Figure 130: EtaNCEL variations for δP_T in $\cos(\theta_{\vec{p}_\mu})$.

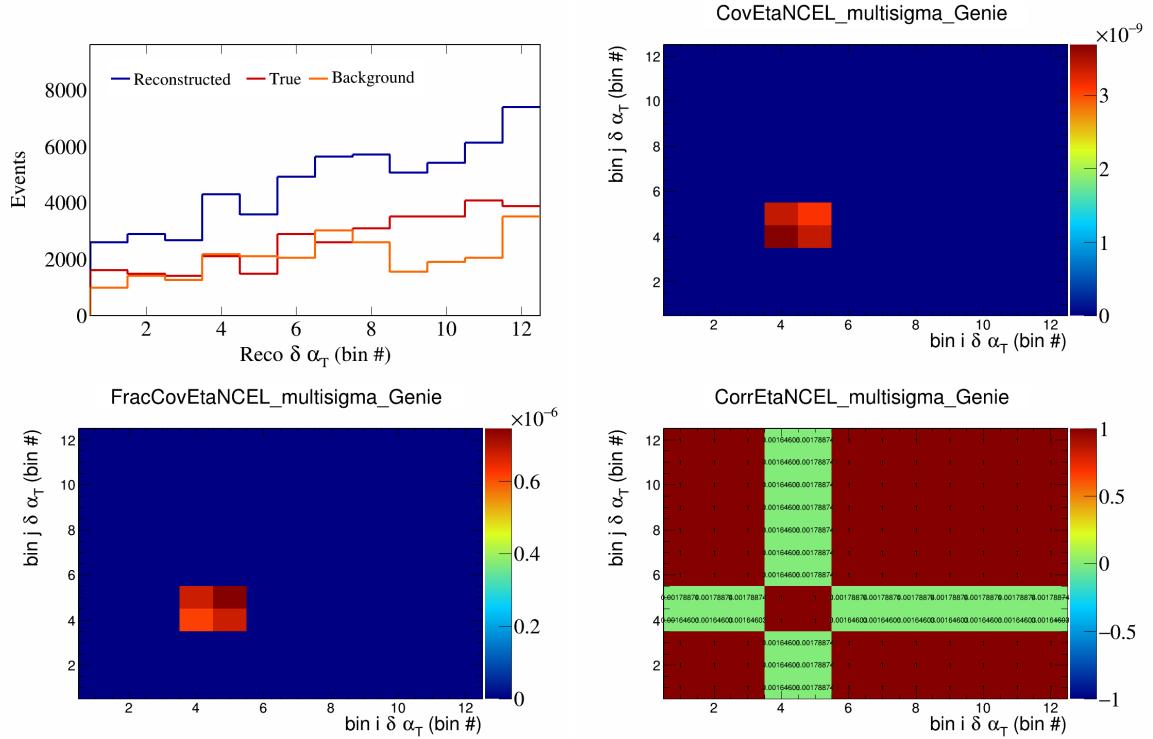


Figure 131: EtaNCEL variations for $\delta\alpha_T$ in $\cos(\theta_{\vec{p}_\mu})$.

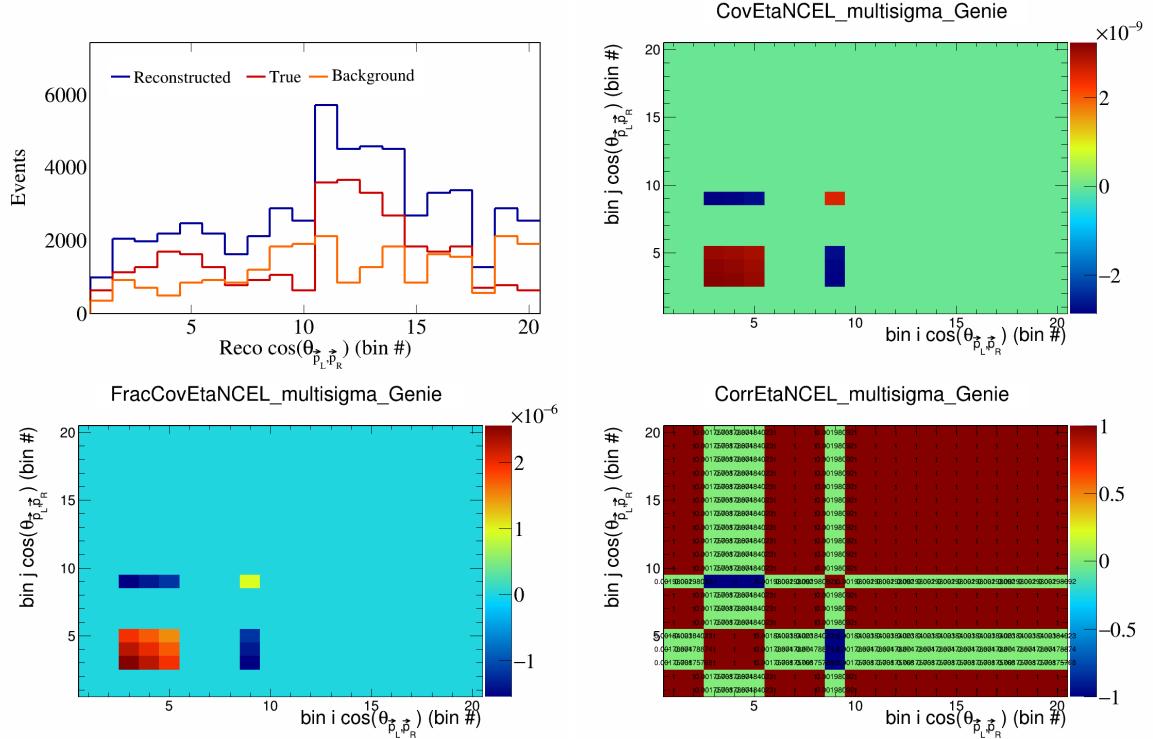


Figure 132: EtaNCEL variations for $\cos(\theta_{\vec{p}_L, \vec{p}_R})$ in $\cos(\theta_{\vec{p}_\mu})$.

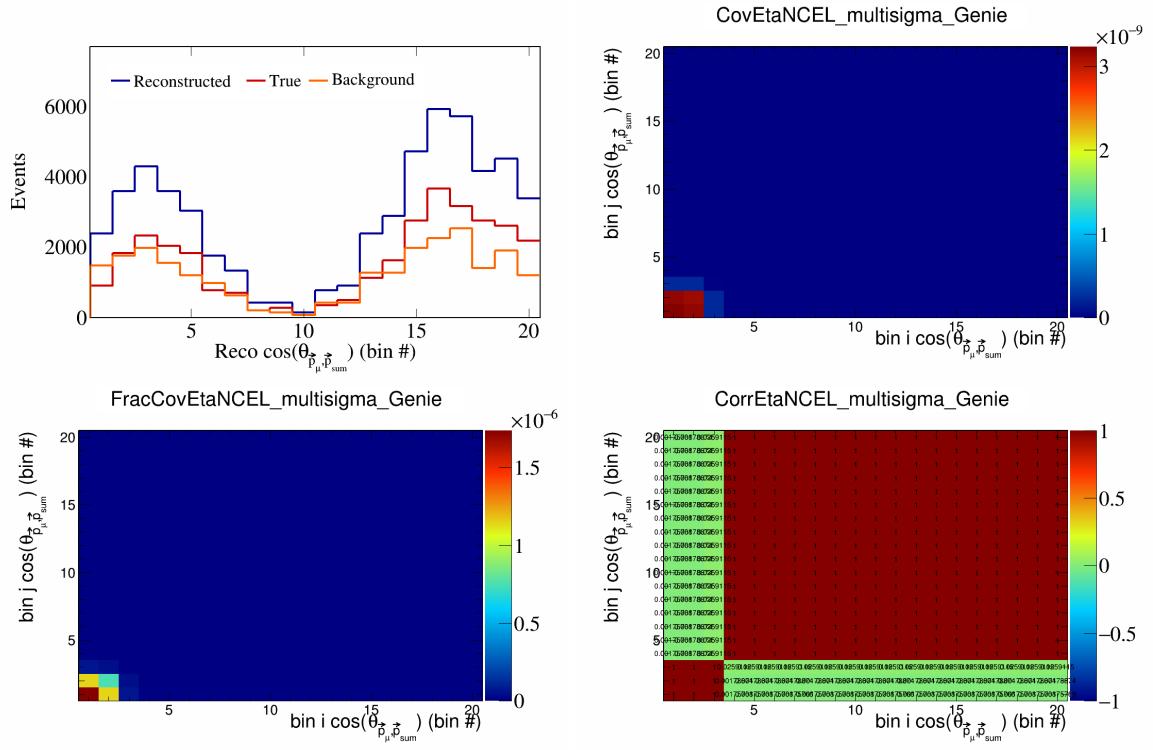


Figure 133: EtaNCEL variations for $\cos(\theta_{\vec{p}_\mu} \cdot \vec{p}_{\text{sum}})$ in $\cos(\theta_{\vec{p}_\mu})$.

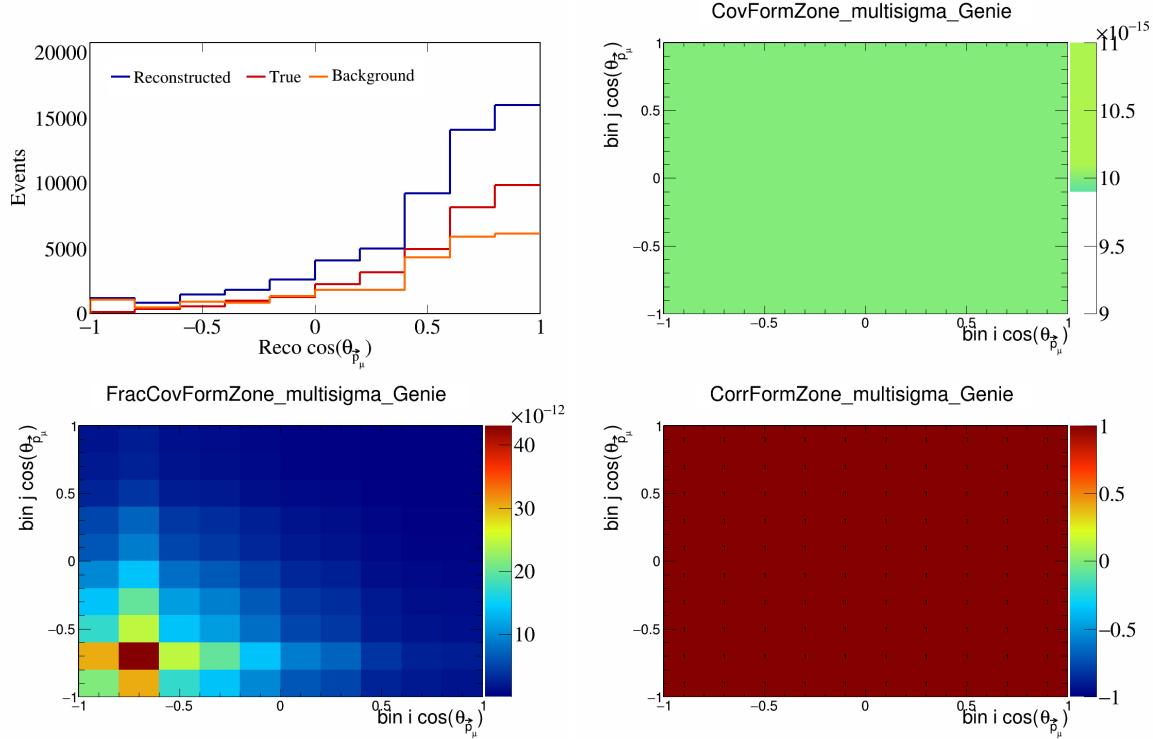


Figure 134: FormZone variations for $\cos(\theta_{\vec{p}_\mu})$.

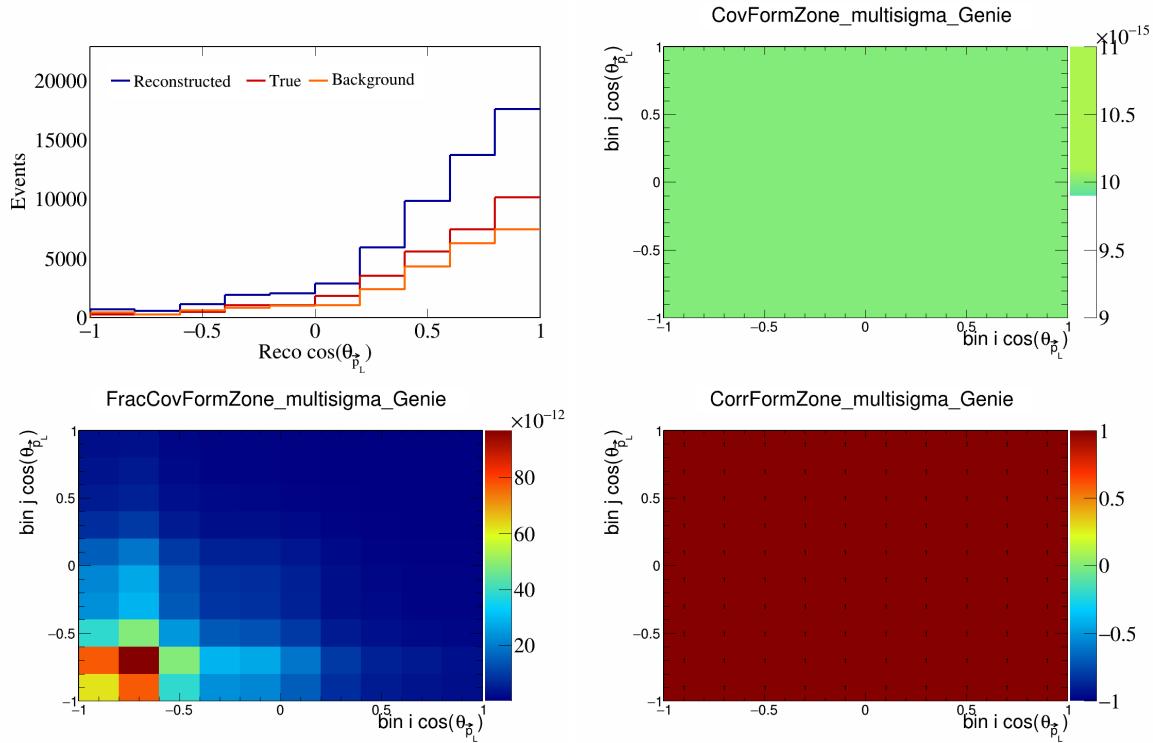


Figure 135: FormZone variations for $\cos(\theta_{\vec{p}_L})$.

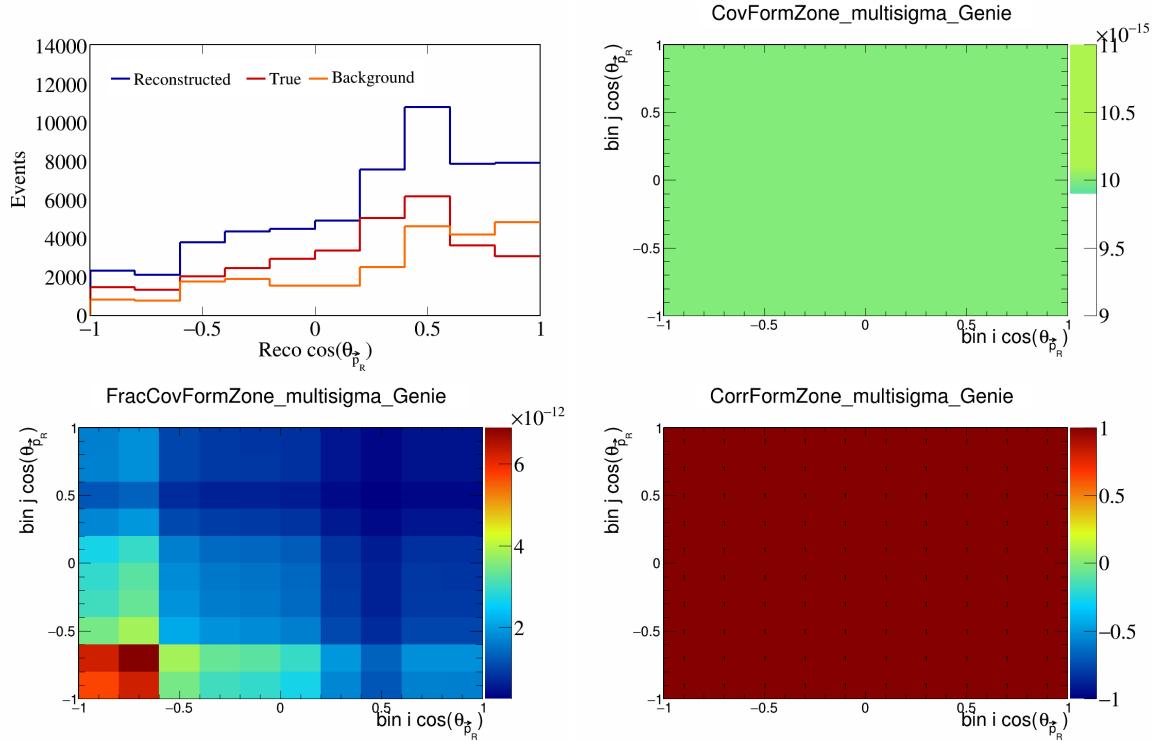


Figure 136: FormZone variations for $\cos(\theta_{\vec{p}_R})$.

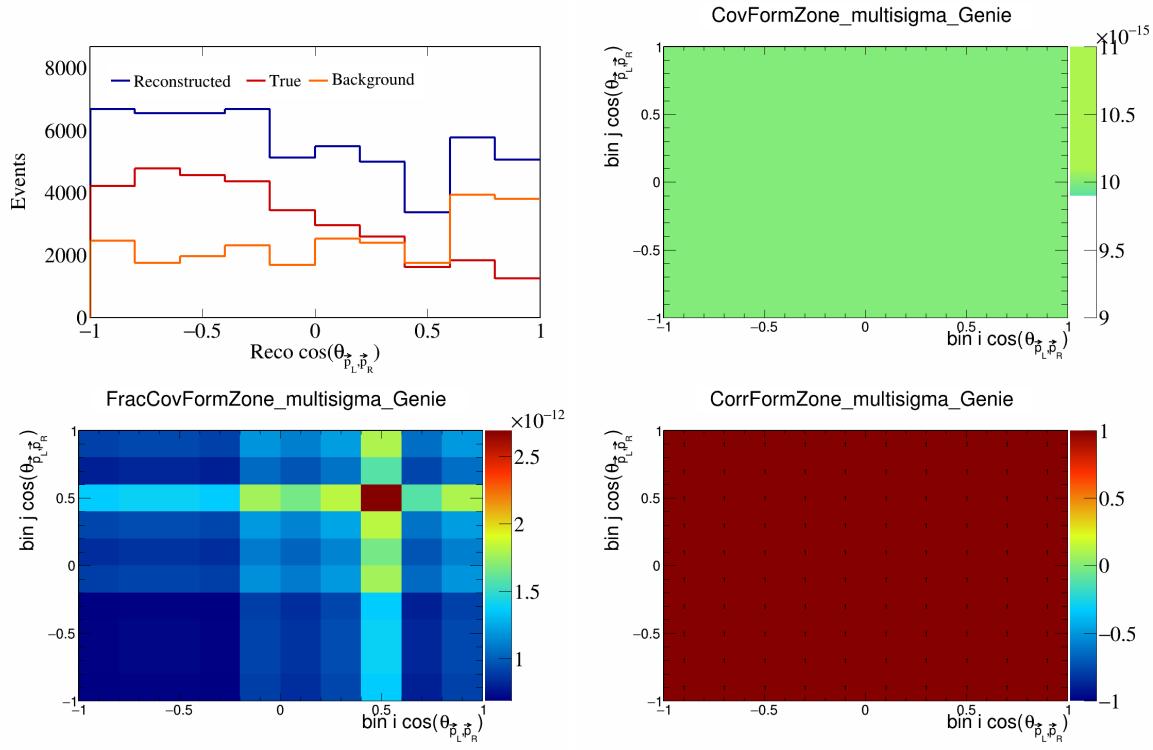


Figure 137: FormZone variations for $\cos(\theta_{\vec{p}_L, \vec{p}_R})$.

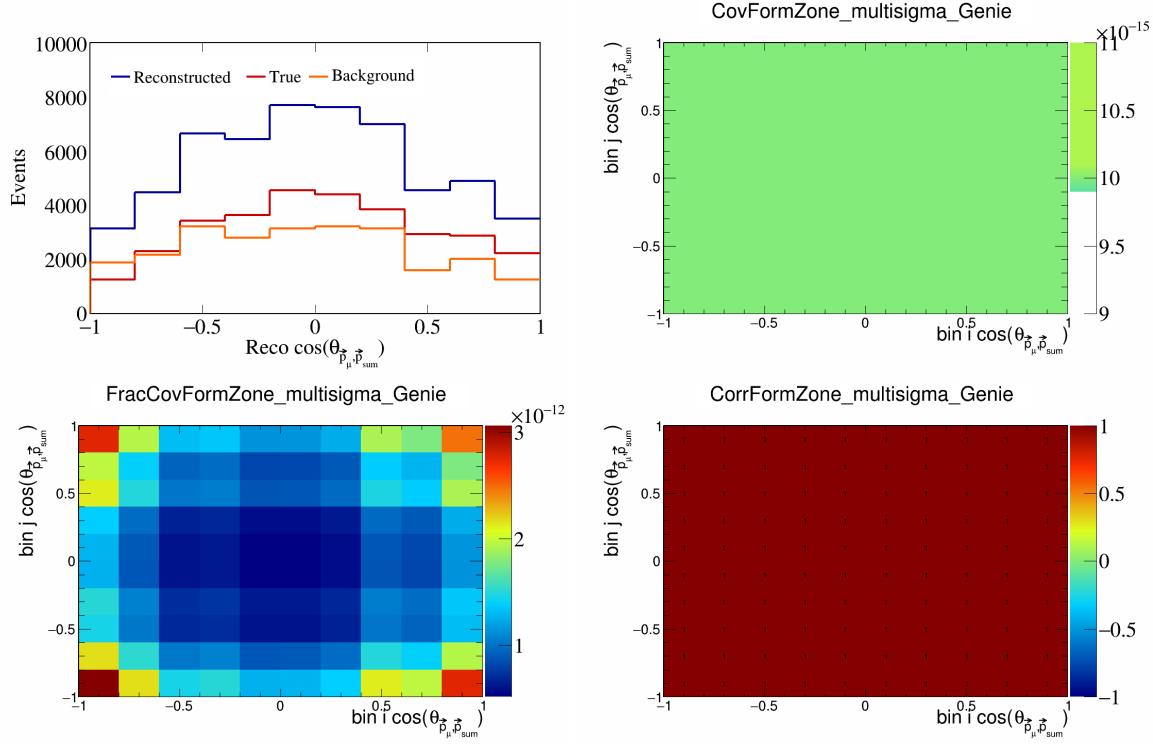


Figure 138: FormZone variations for $\cos(\theta_{\vec{p}_\mu, \vec{p}_{\text{sum}}})$.

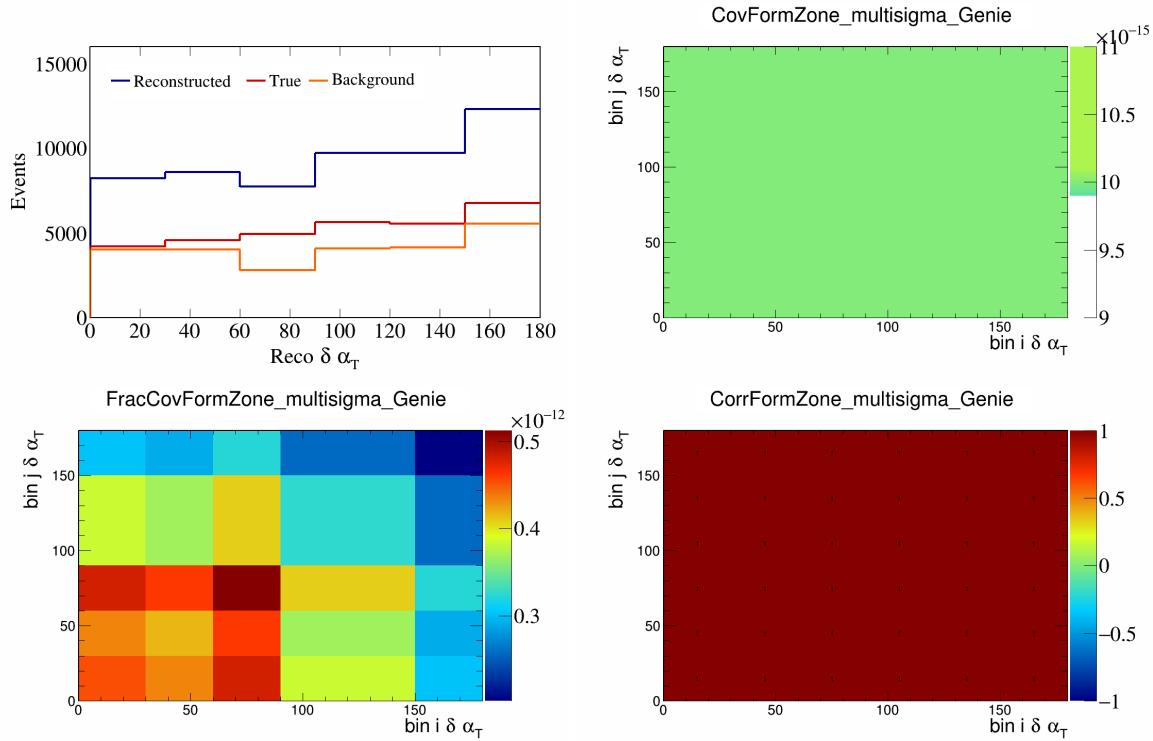


Figure 139: FormZone variations for $\delta\alpha_T$.

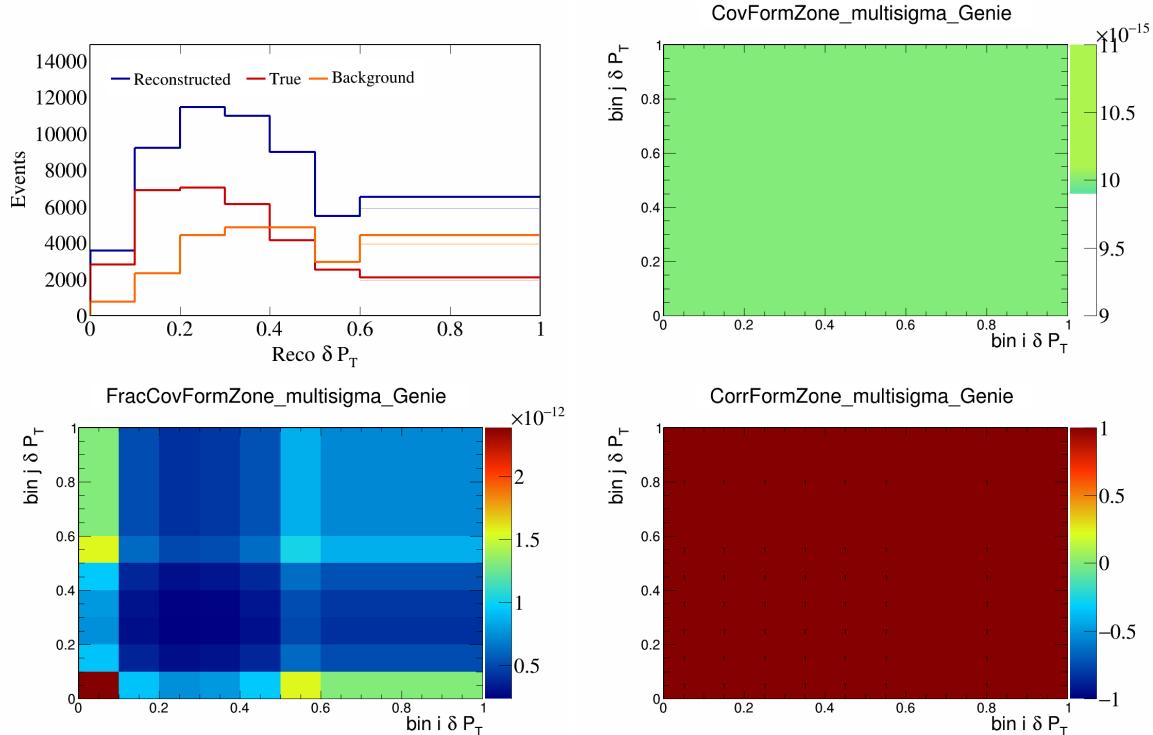


Figure 140: FormZone variations for δP_T .

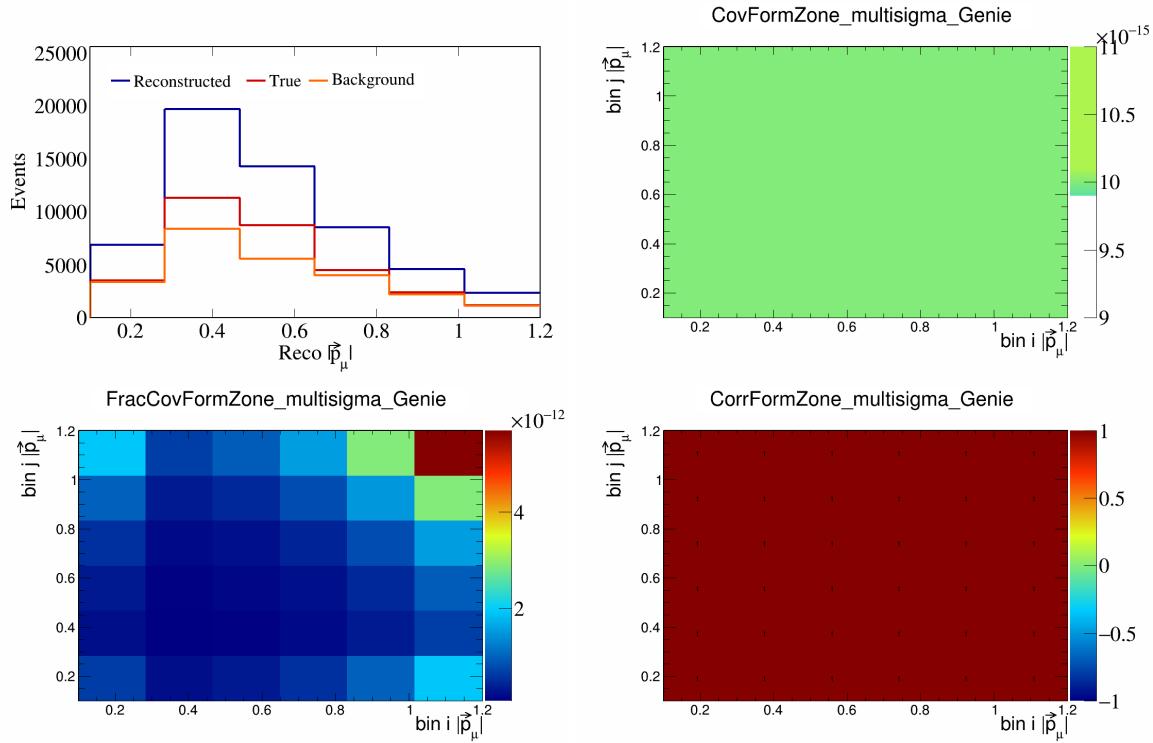


Figure 141: FormZone variations for $|\vec{p}_\mu|$.

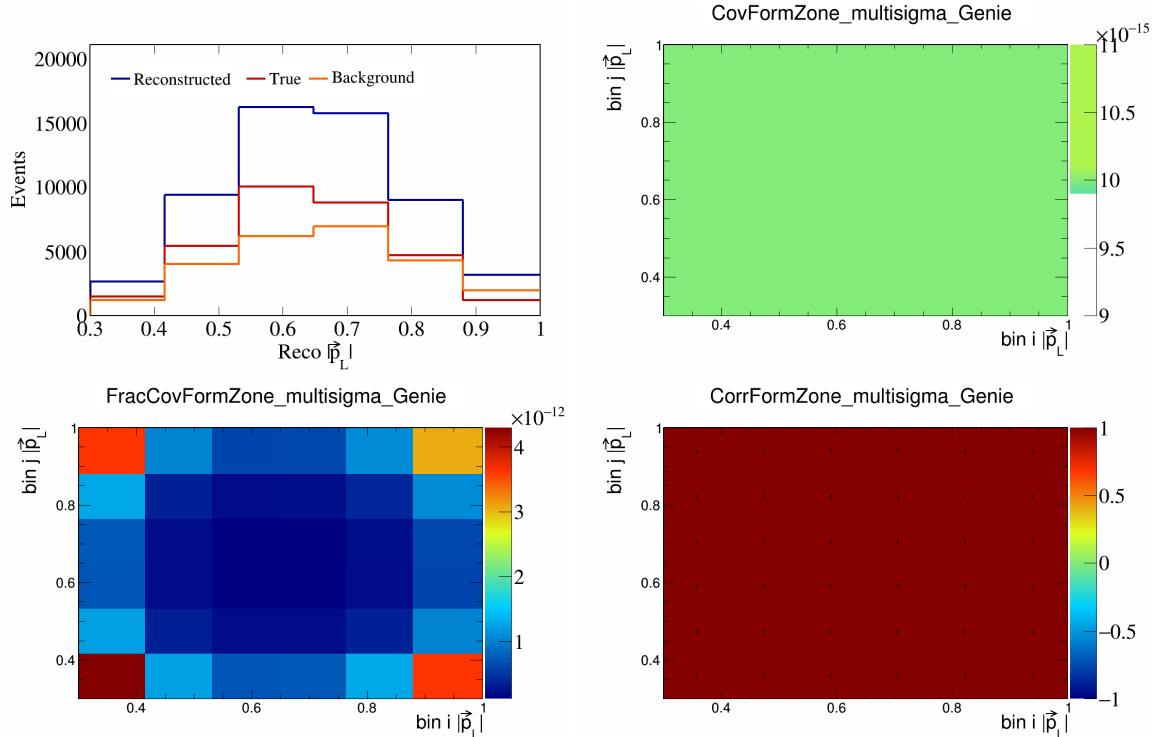


Figure 142: FormZone variations for $|\vec{p}_L|$.

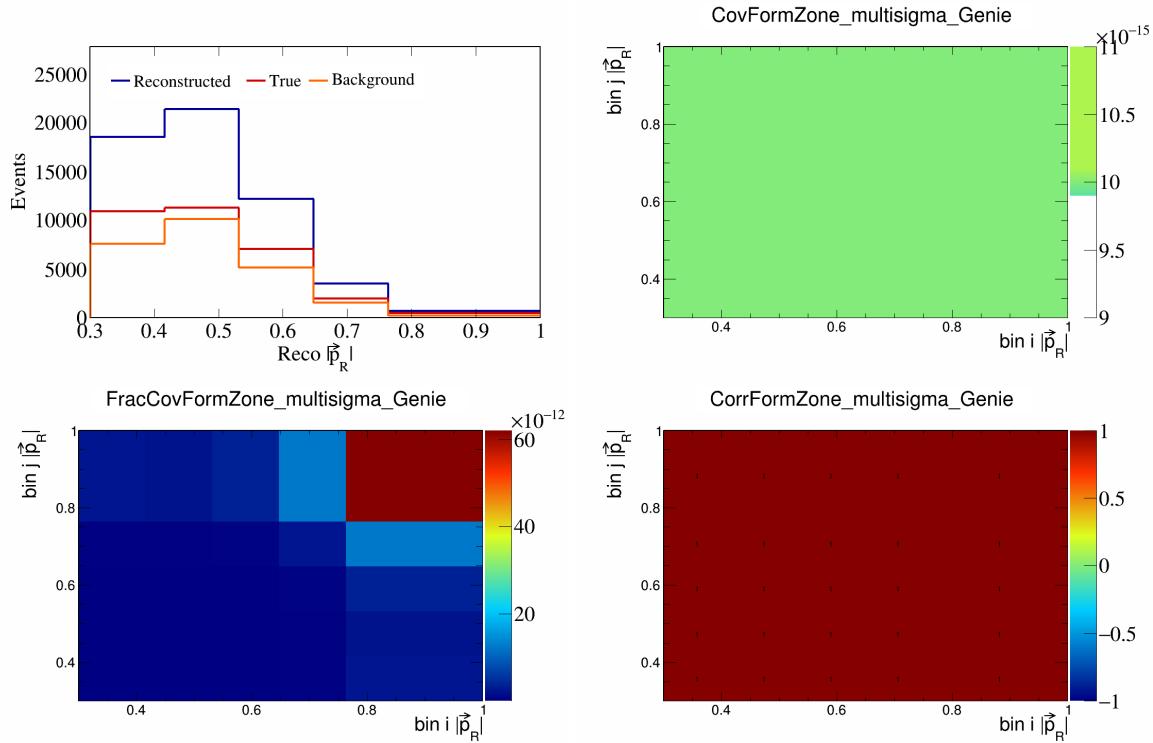


Figure 143: FormZone variations for $|\vec{p}_R|$.

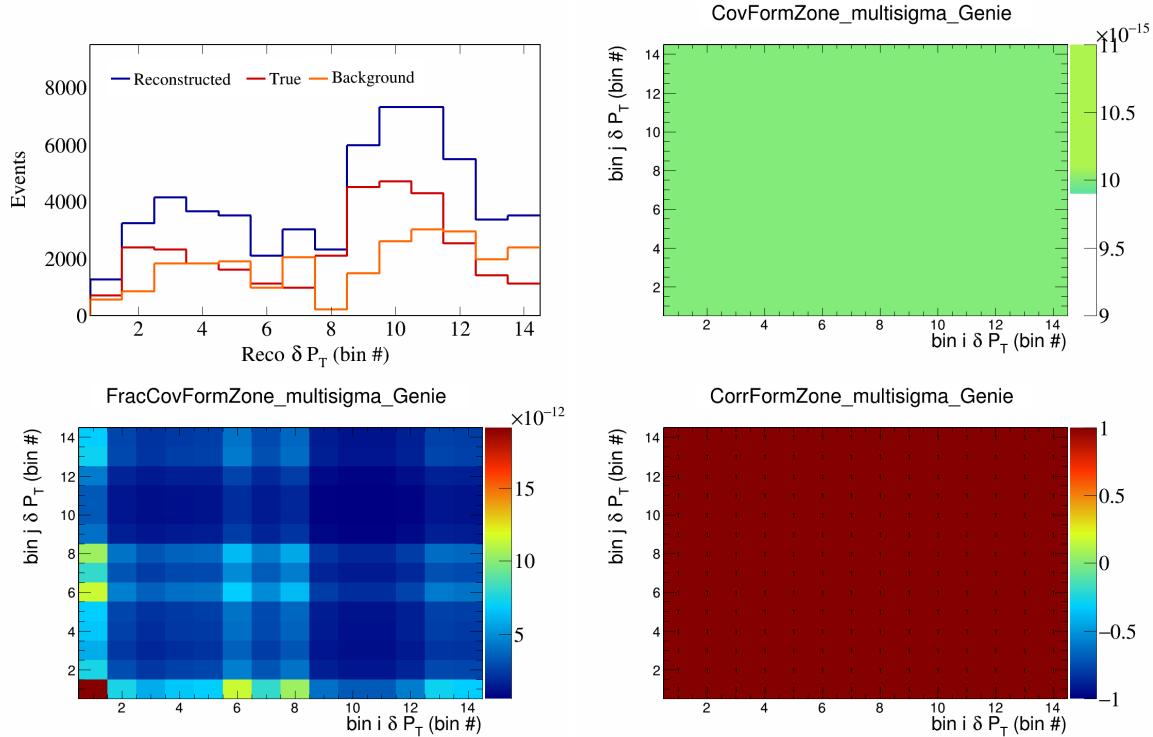


Figure 144: FormZone variations for δP_T in $\cos(\theta_{\vec{p}_\mu})$.

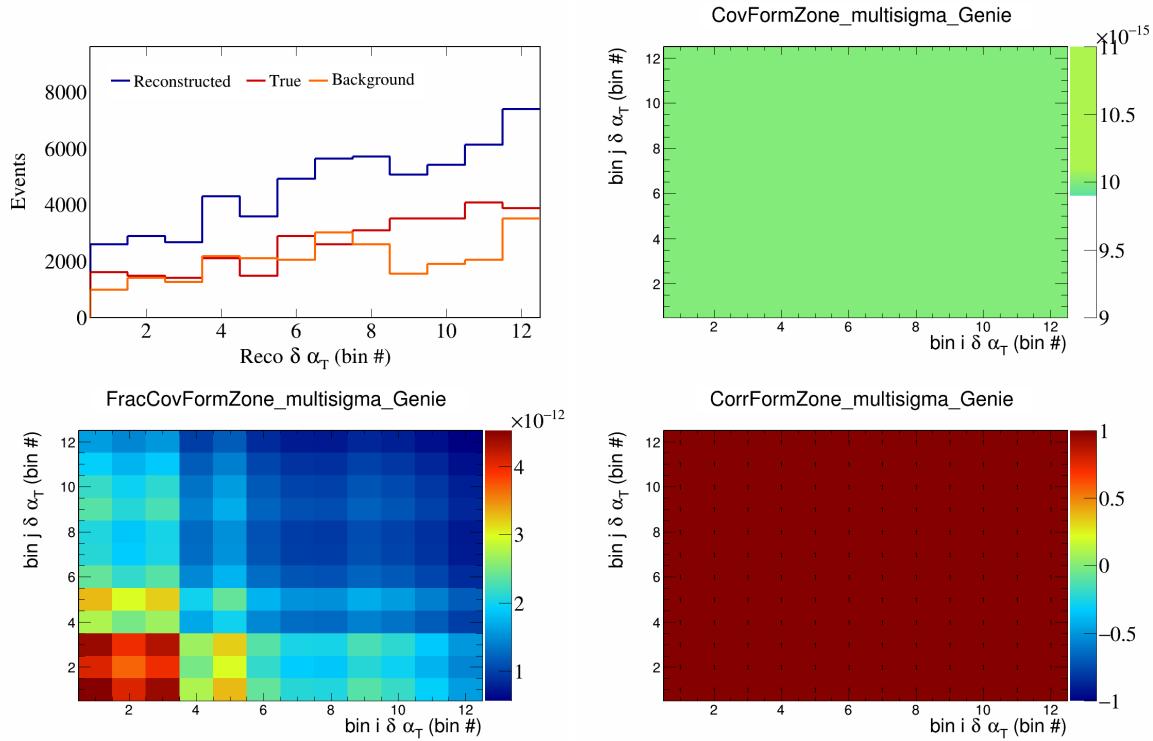


Figure 145: FormZone variations for $\delta\alpha_T$ in $\cos(\theta_{\vec{p}_\mu})$.

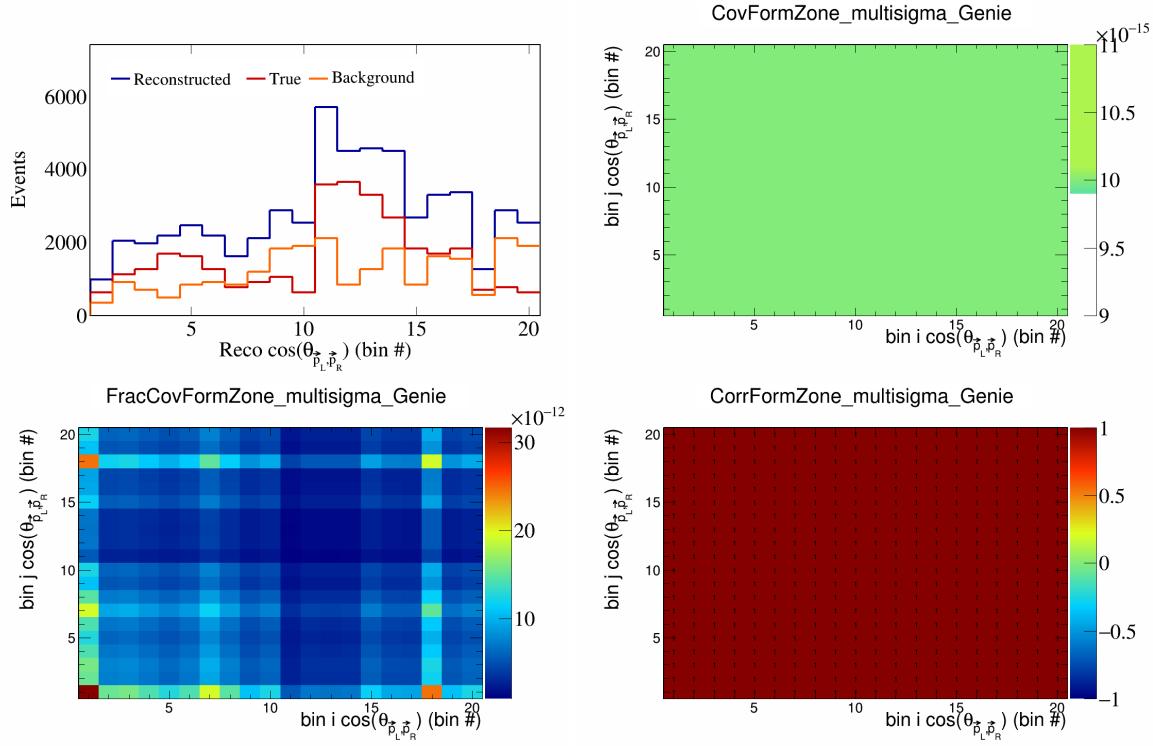


Figure 146: FormZone variations for $\cos(\theta_{\vec{p}_L, \vec{p}_R})$ in $\cos(\theta_{\vec{p}_\mu})$.

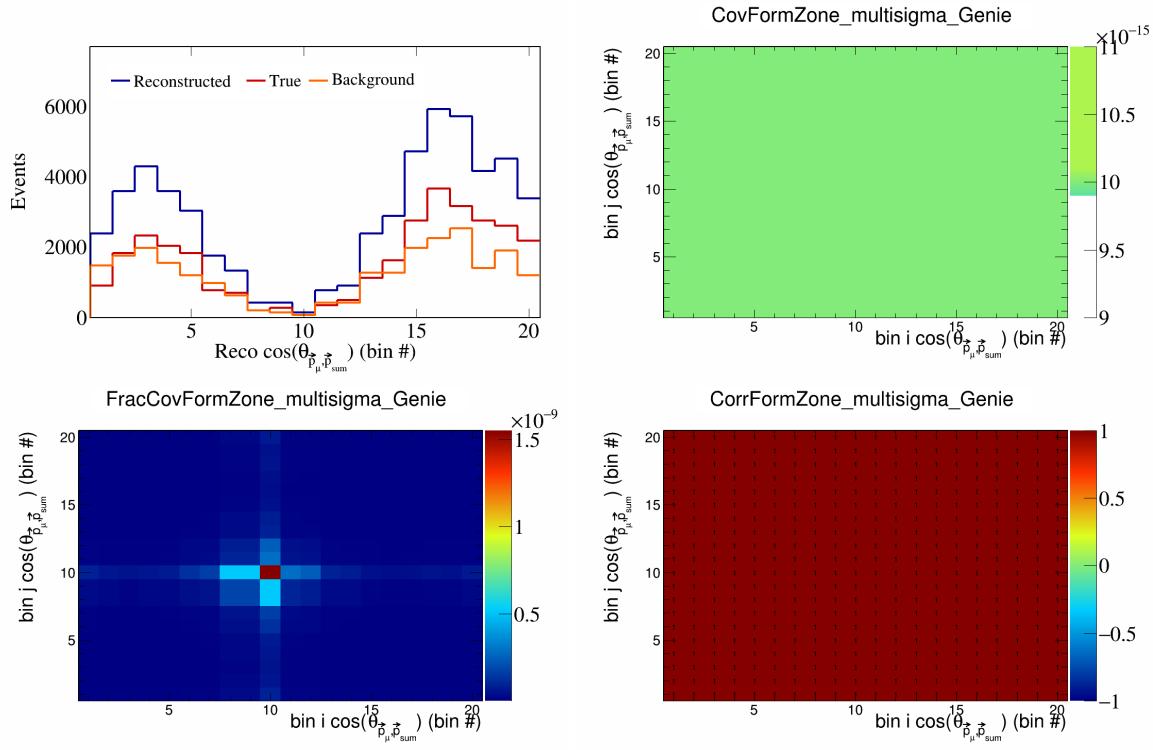


Figure 147: FormZone variations for $\cos(\theta_{\vec{p}_\mu \vec{p}_{\text{sum}}})$ in $\cos(\theta_{\vec{p}_\mu})$.

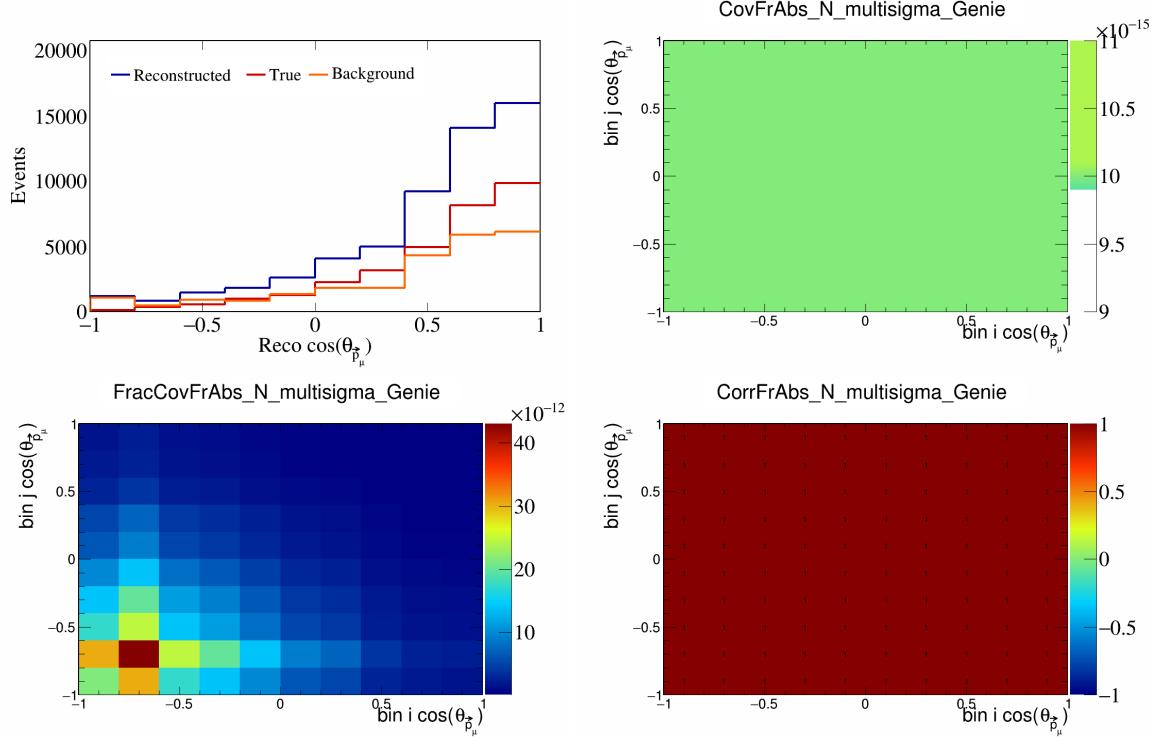


Figure 148: FrAbsN variations for $\cos(\theta_{\vec{p}_\mu})$.

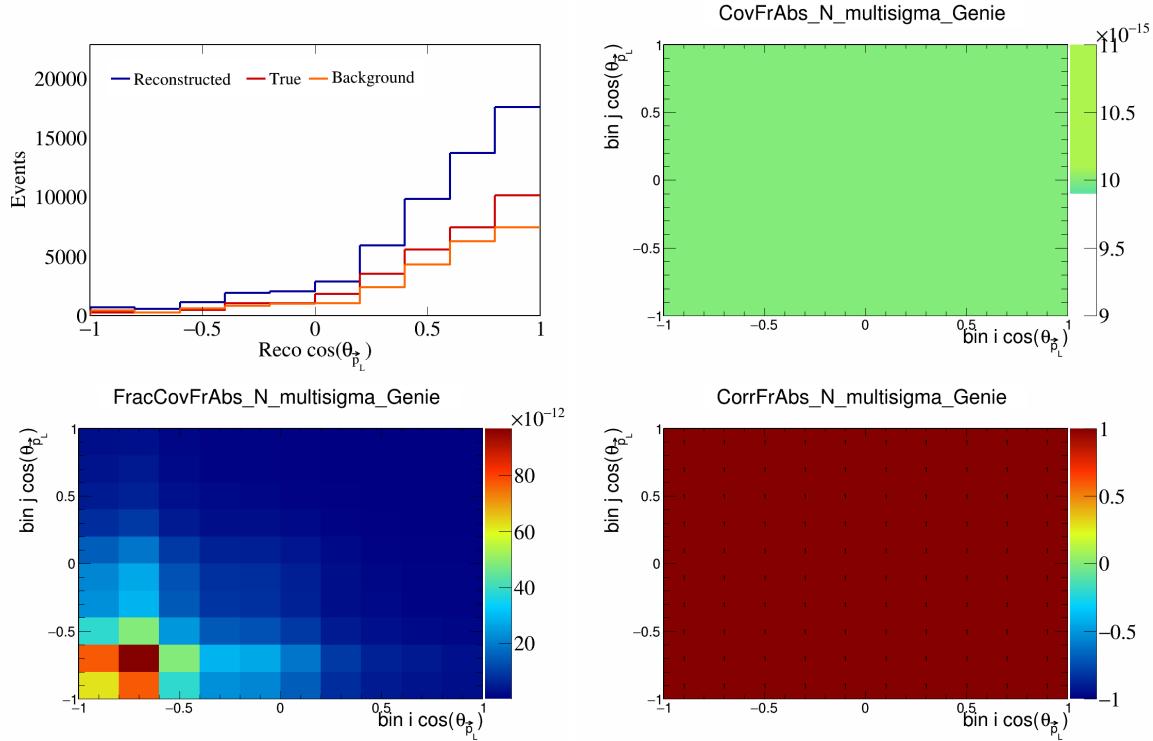


Figure 149: FrAbsN variations for $\cos(\theta_{\vec{p}_L})$.

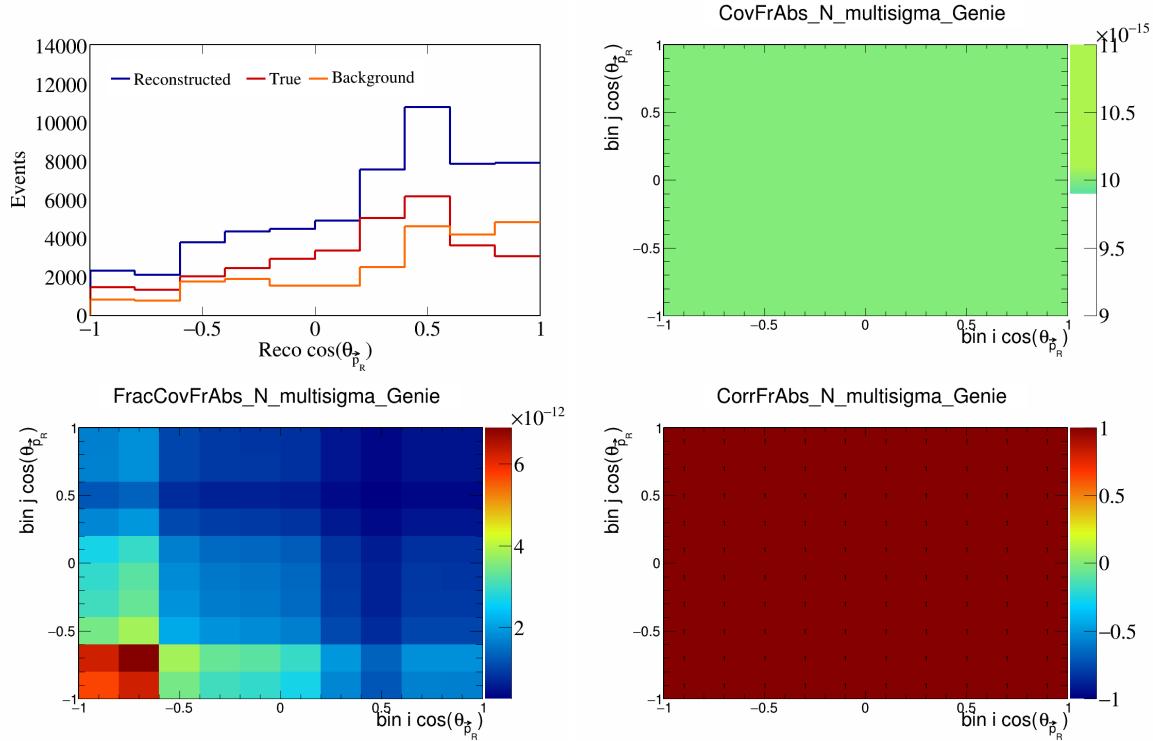


Figure 150: FrAbsN variations for $\cos(\theta_{\vec{p}_R})$.

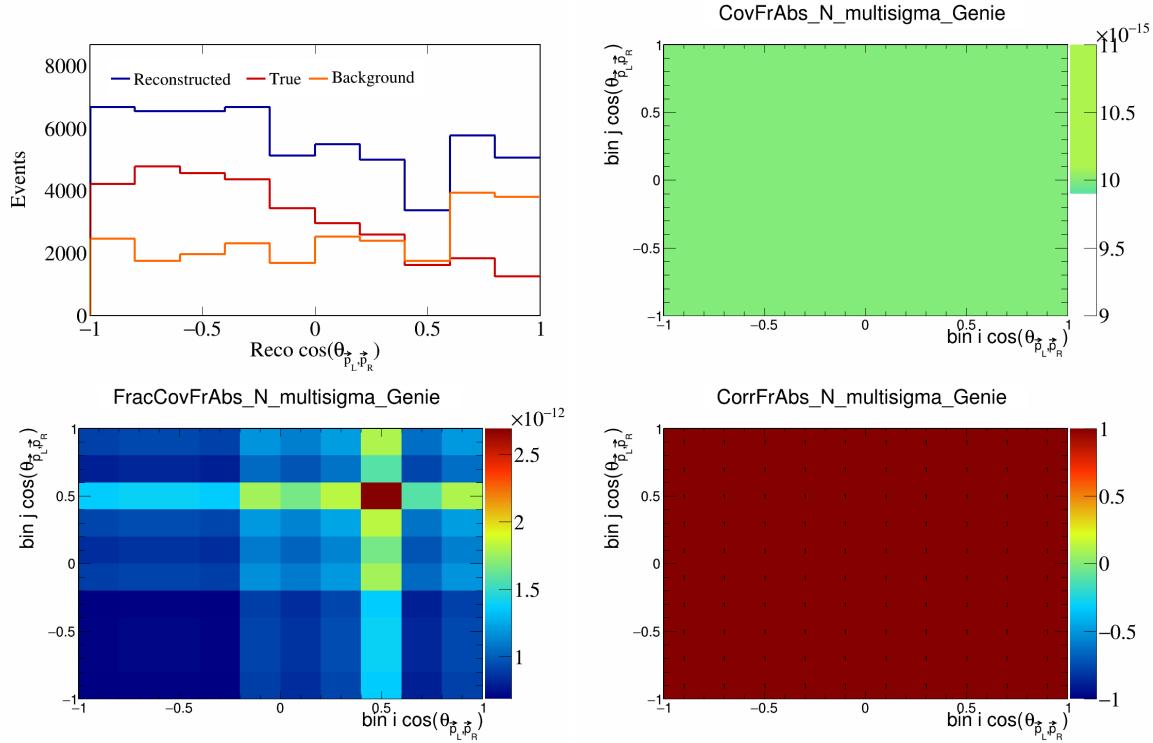


Figure 151: FrAbsN variations for $\cos(\theta_{\vec{p}_L, \vec{p}_R})$.

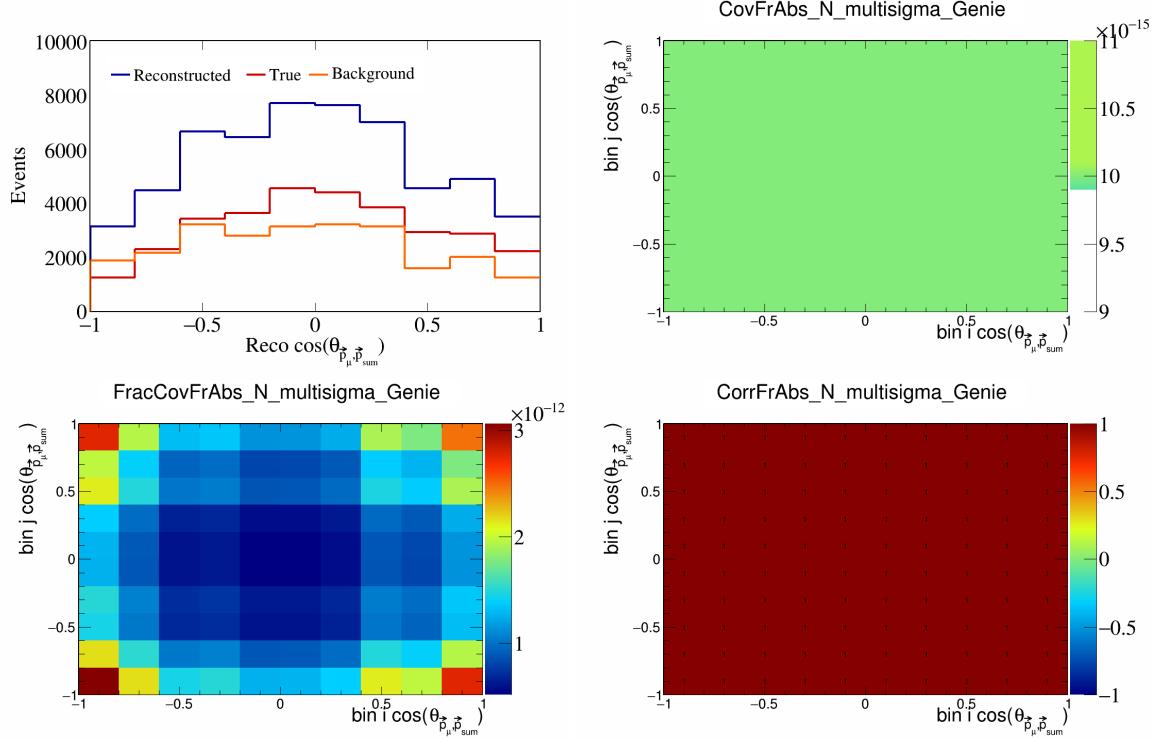


Figure 152: FrAbsN variations for $\cos(\theta_{\vec{p}_\mu, \vec{p}_{\text{sum}}})$.

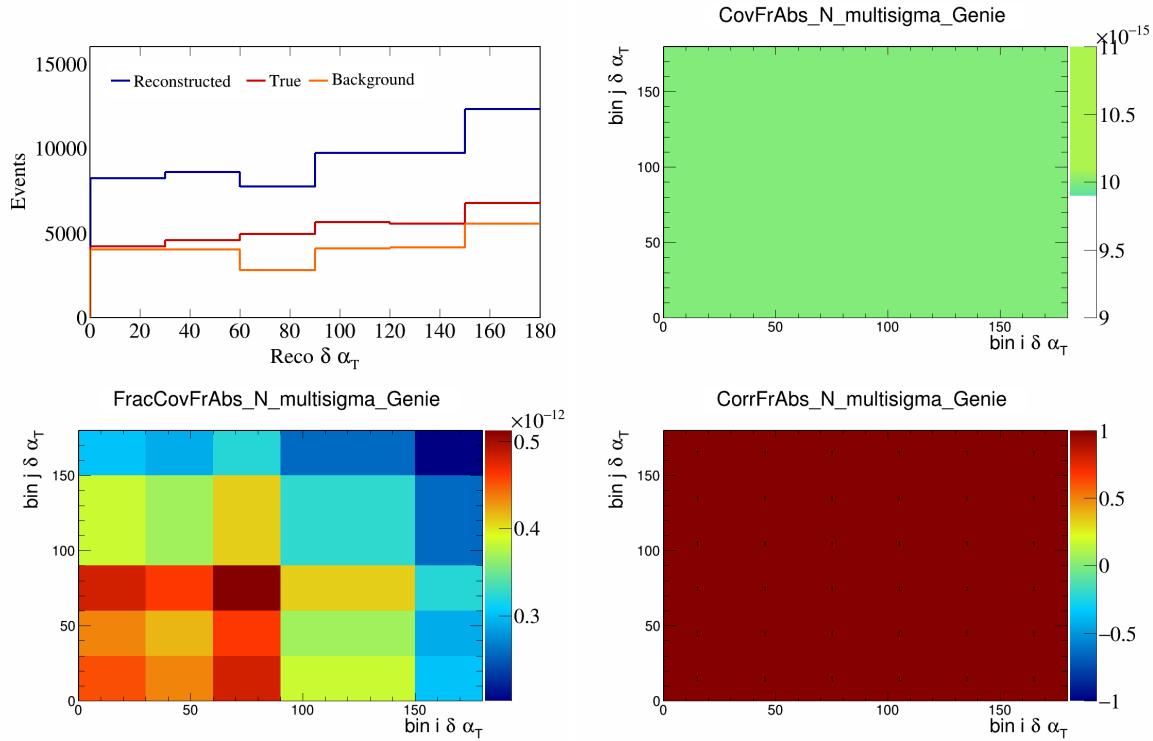


Figure 153: FrAbsN variations for $\delta\alpha_T$.

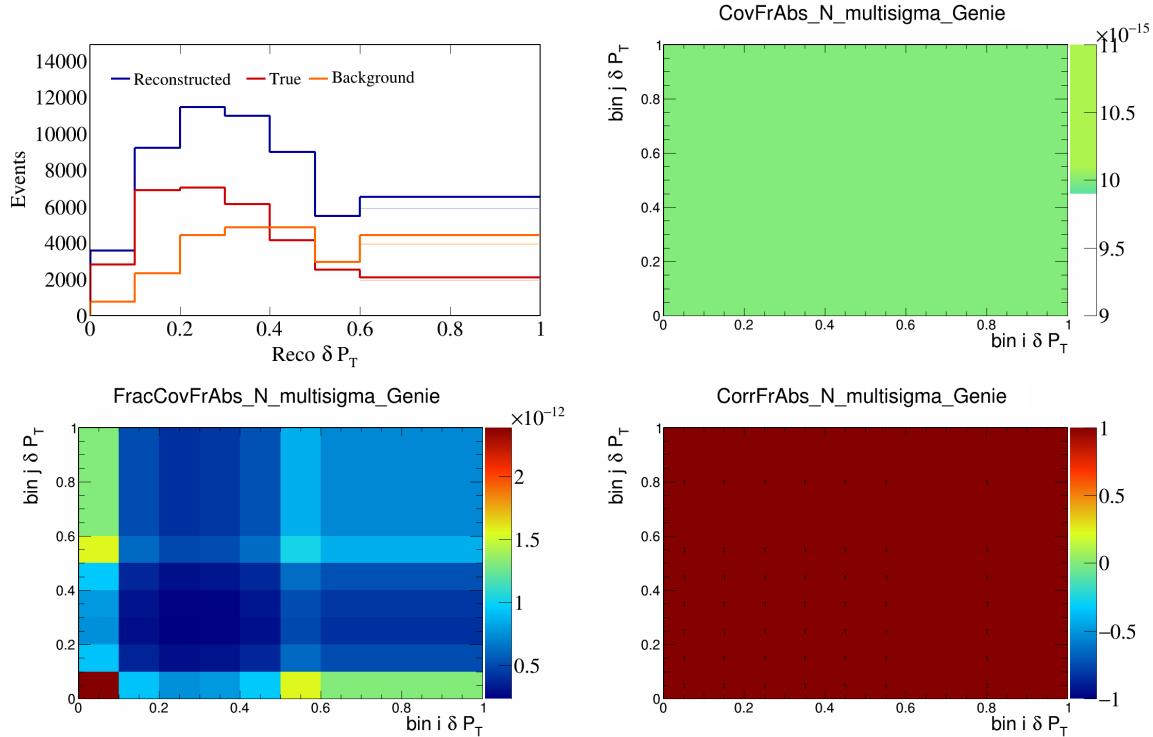


Figure 154: FrAbsN variations for δP_T .

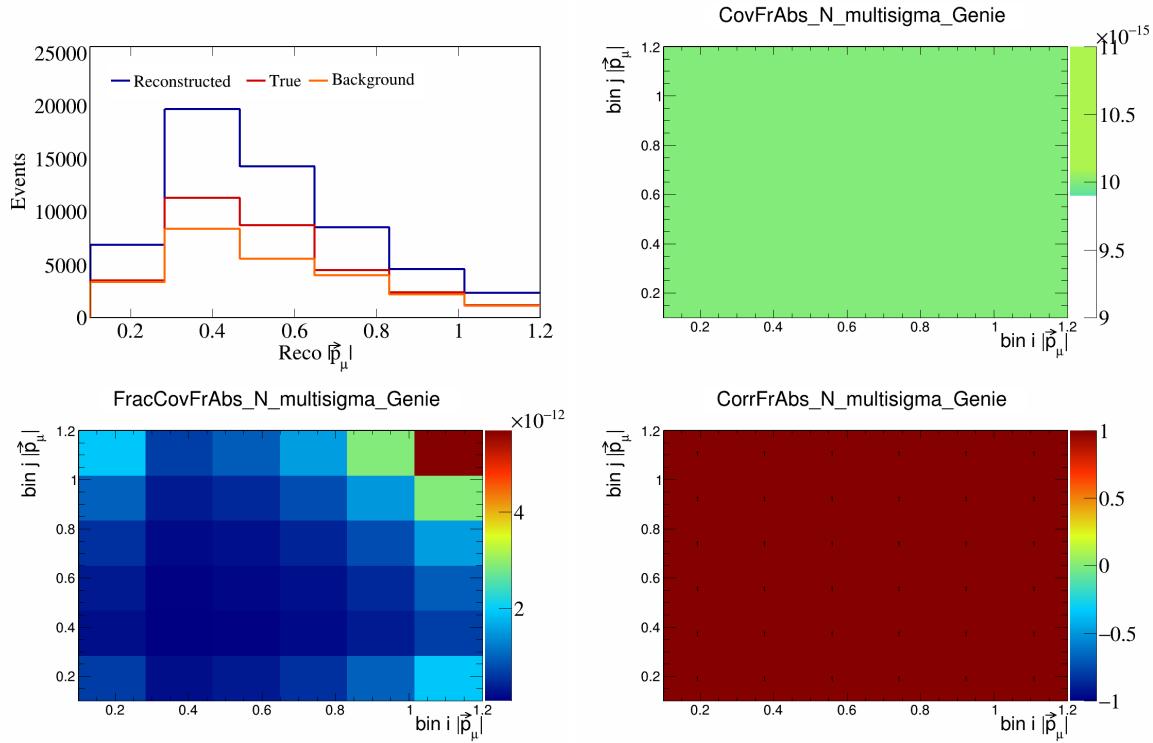


Figure 155: FrAbsN variations for $|\vec{p}_\mu|$.

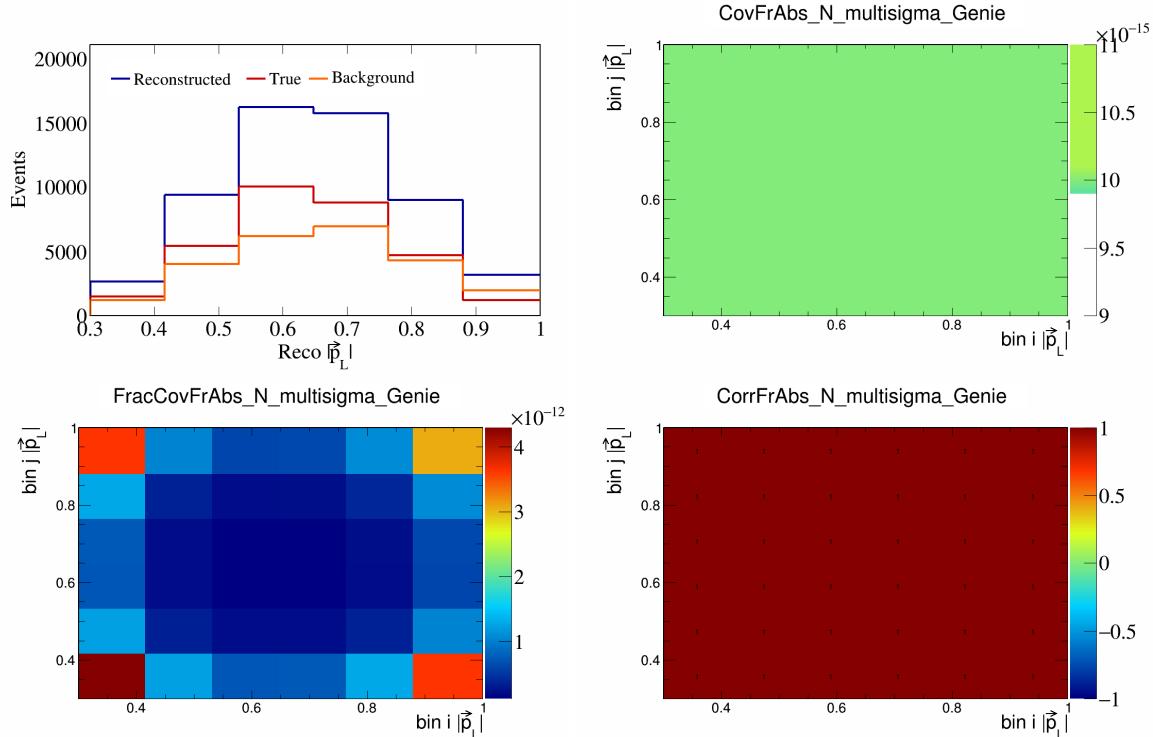


Figure 156: FrAbsN variations for $|\vec{p}_L|$.

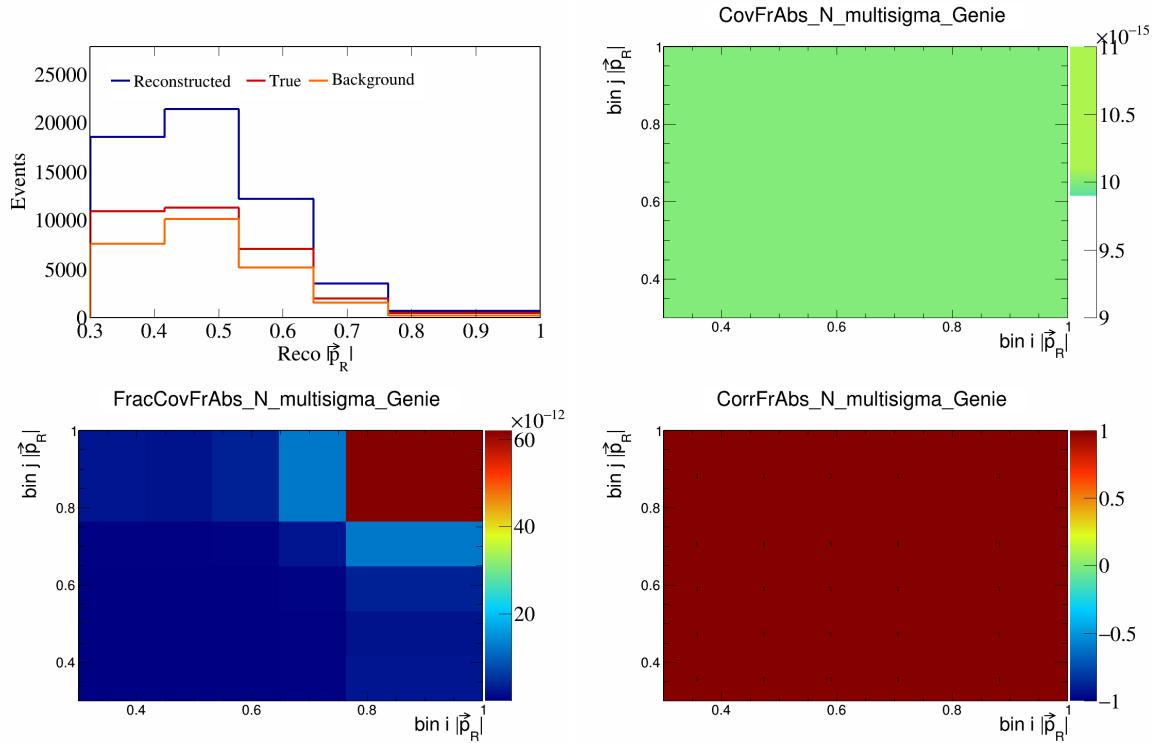


Figure 157: FrAbsN variations for $|\vec{p}_R|$.

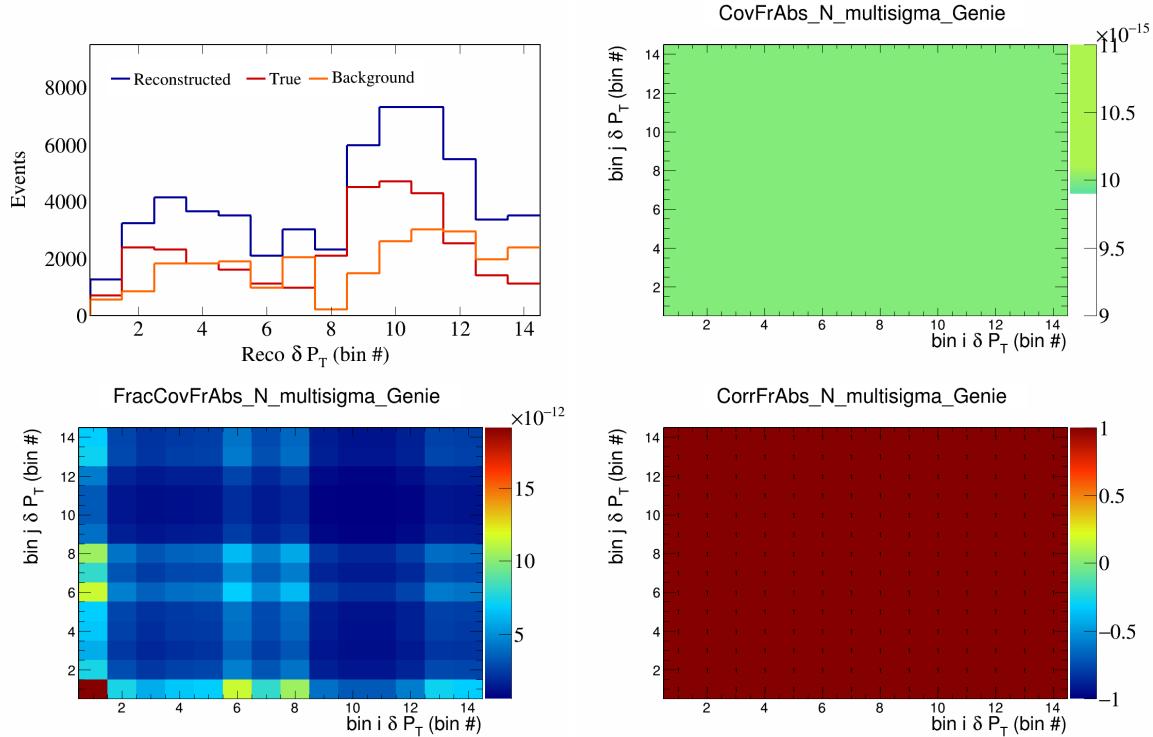


Figure 158: FrAbsN variations for δP_T in $\cos(\theta_{\vec{p}_\mu})$.

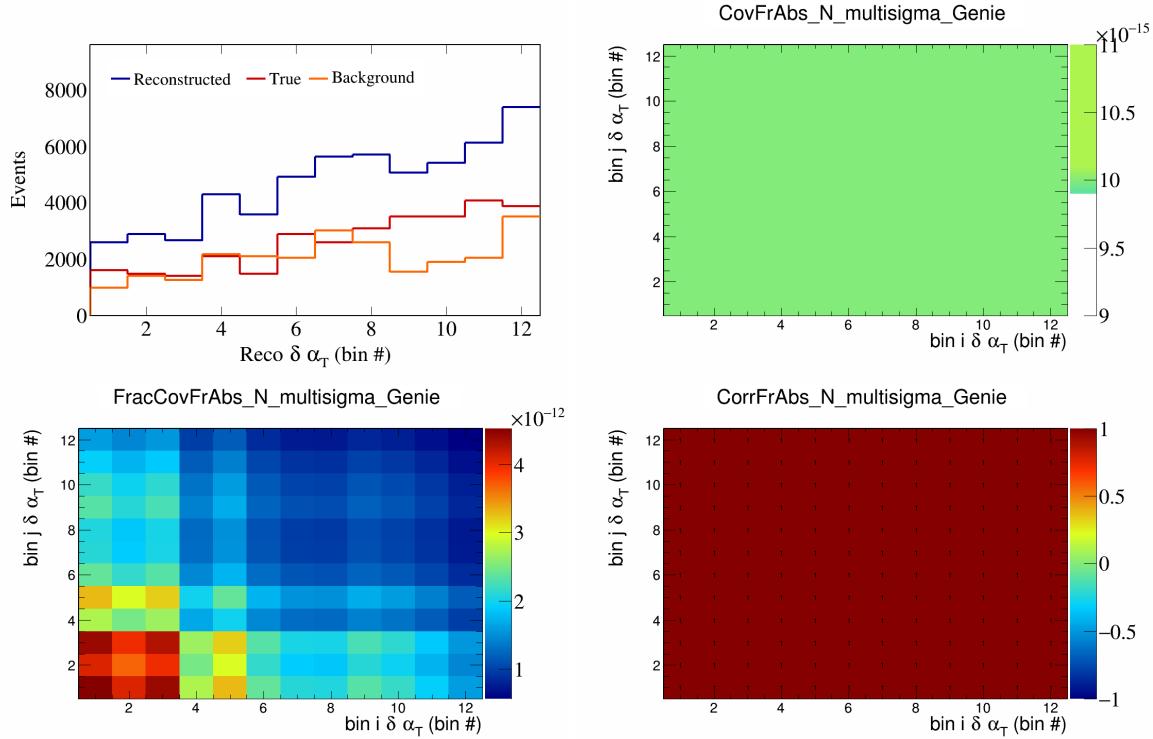


Figure 159: FrAbsN variations for $\delta \alpha_T$ in $\cos(\theta_{\vec{p}_\mu})$.

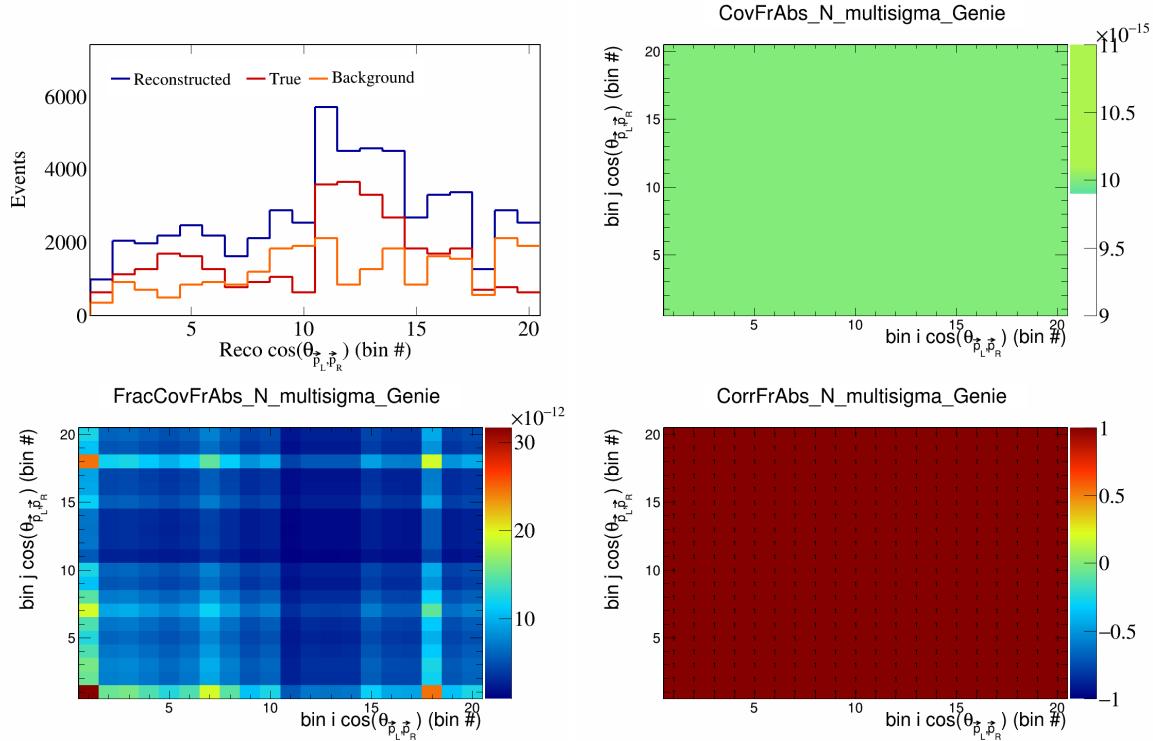


Figure 160: FrAbsN variations for $\cos(\theta_{\vec{p}_L, \vec{p}_R})$ in $\cos(\theta_{\vec{p}_\mu})$.

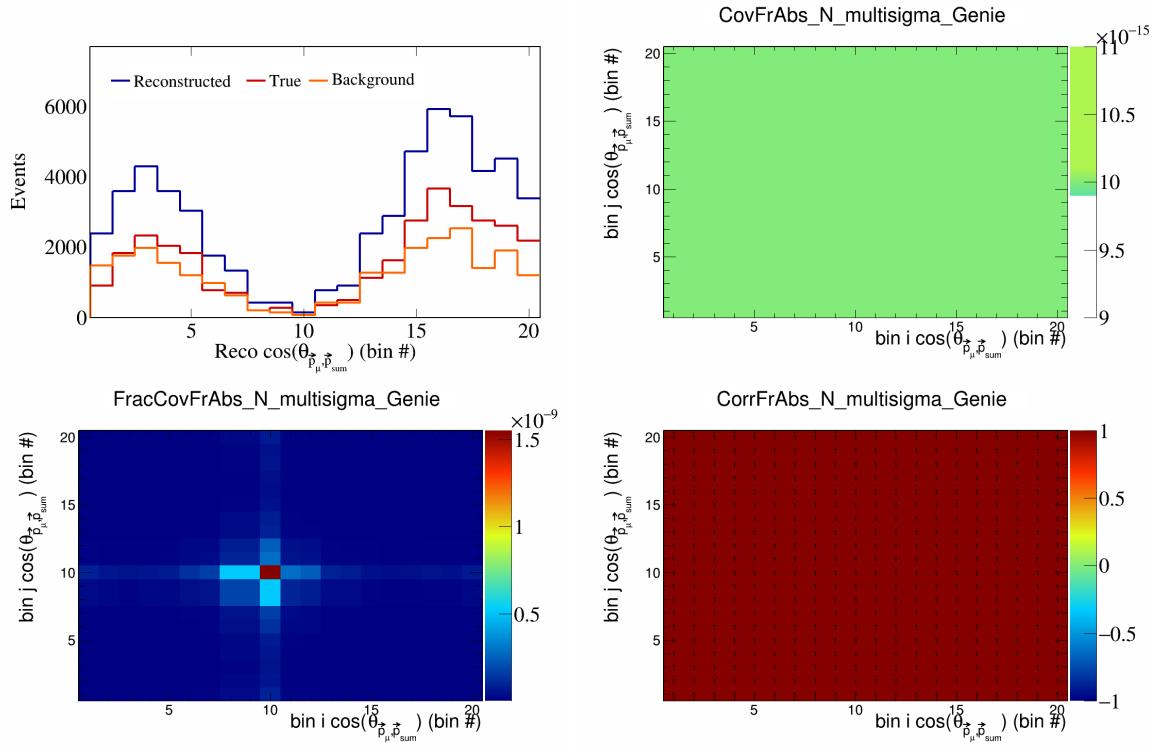


Figure 161: FrAbsN variations for $\cos(\theta_{\vec{p}_\mu}^{\text{sum}})$ in $\cos(\theta_{\vec{p}_\mu})$.

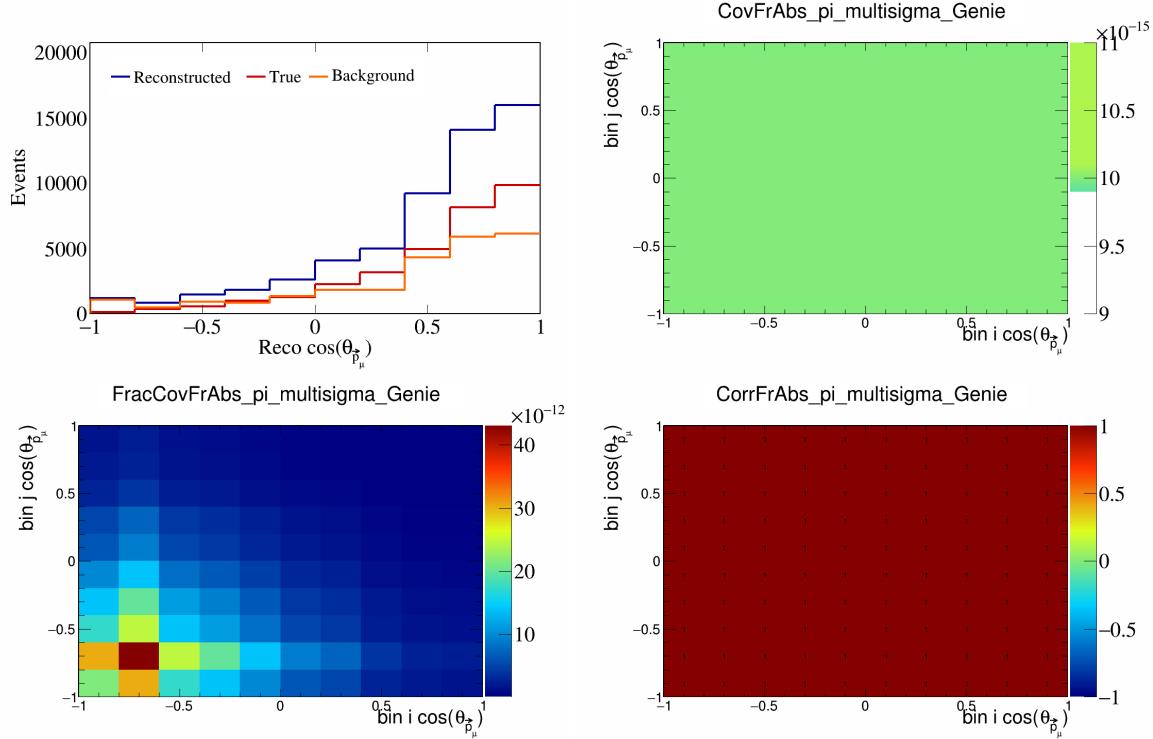


Figure 162: FrAbspi variations for $\cos(\theta_{\vec{p}_\mu})$.

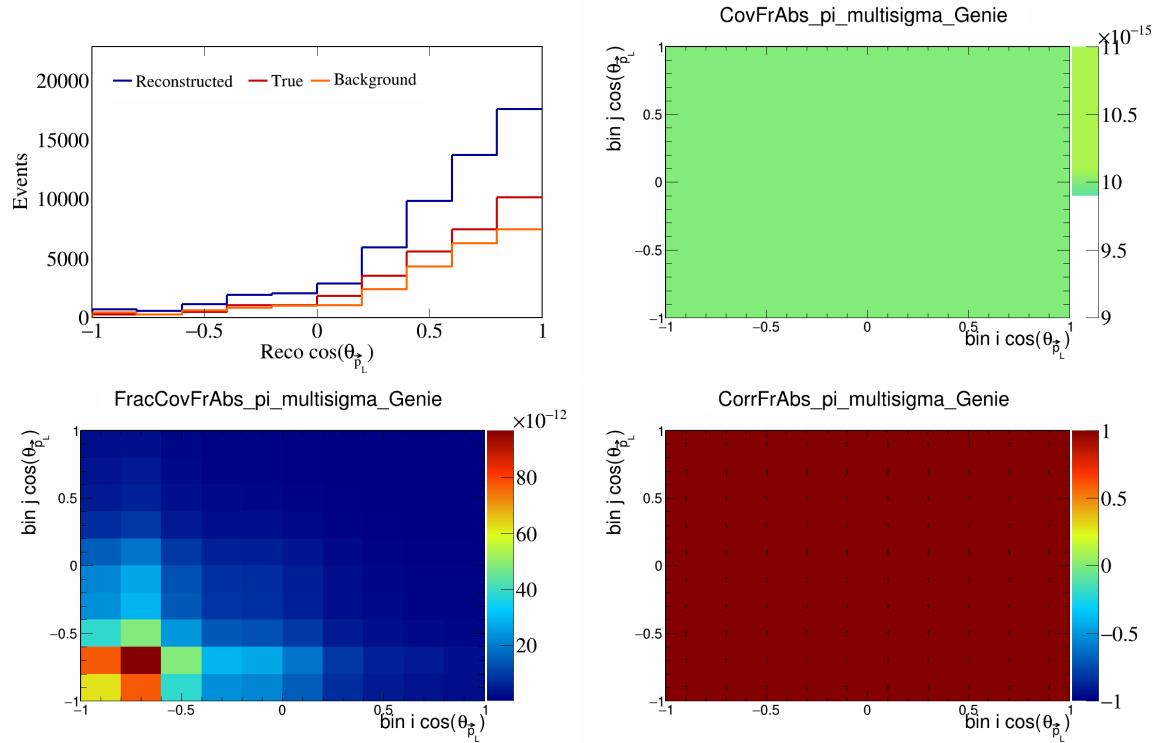


Figure 163: FrAbspi variations for $\cos(\theta_{\vec{p}_L})$.

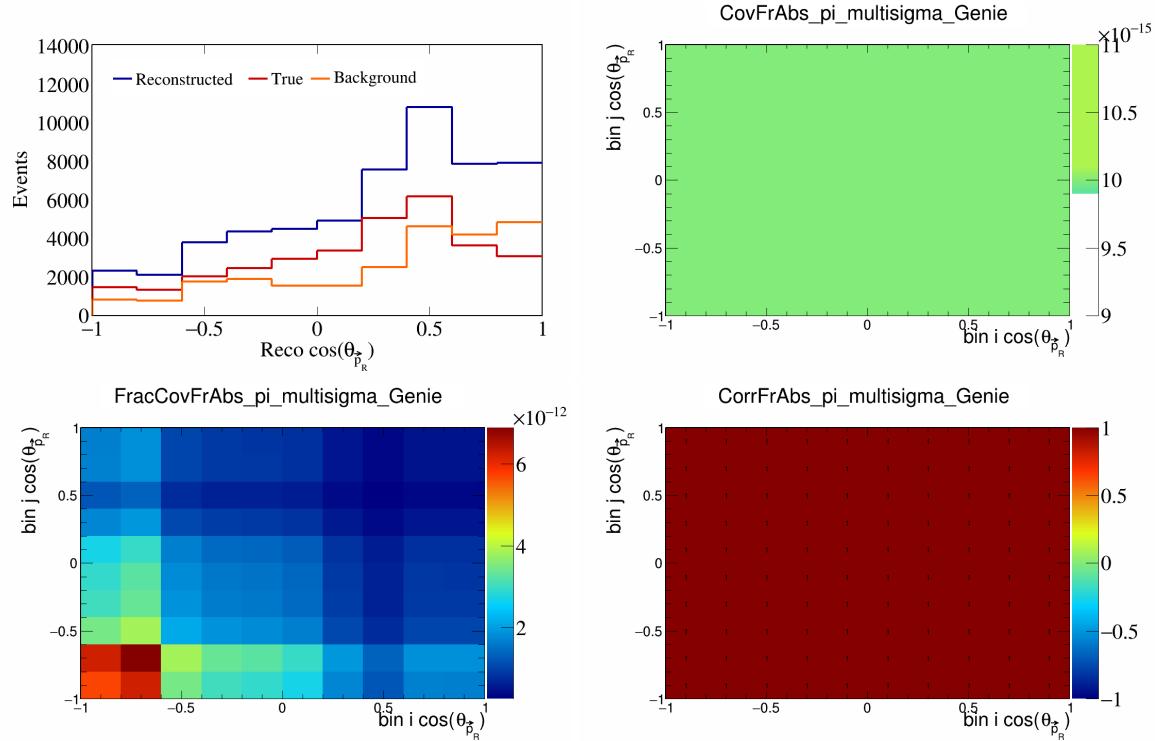


Figure 164: FrAbspi variations for $\cos(\theta_{\vec{p}_R})$.

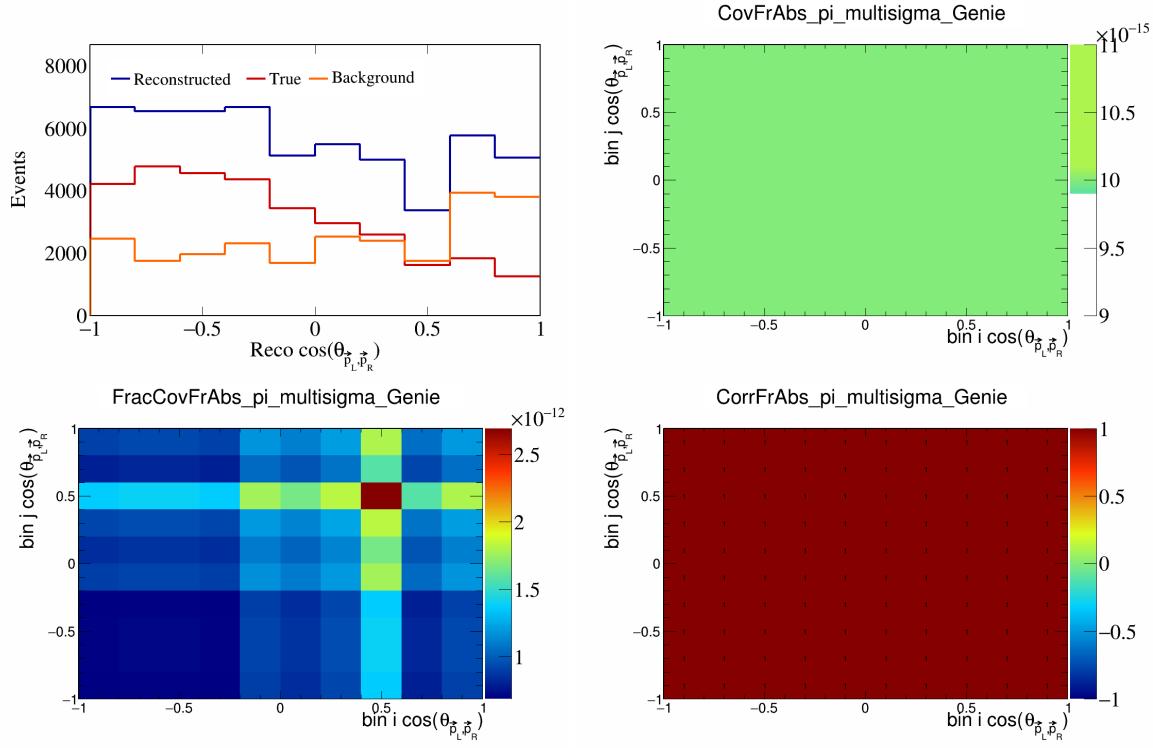


Figure 165: FrAbspi variations for $\cos(\theta_{\vec{p}_L, \vec{p}_R})$.

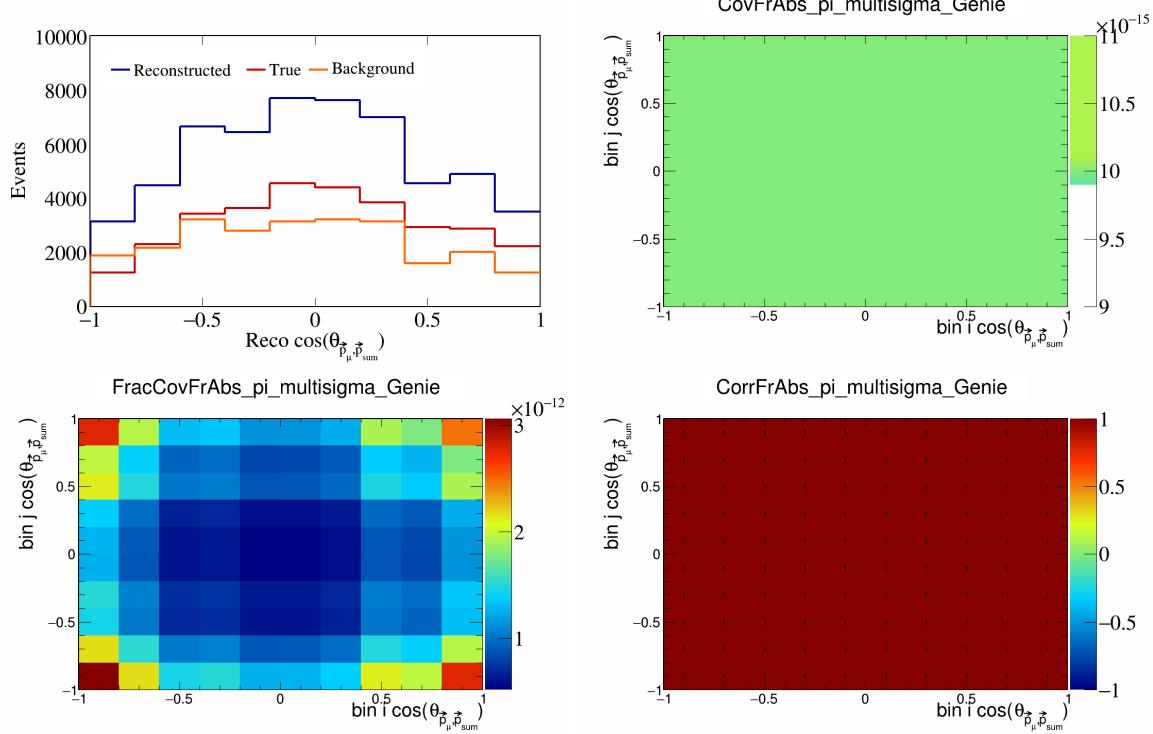


Figure 166: FrAbspi variations for $\cos(\theta_{\vec{p}_\mu, \vec{p}_{\text{sum}}})$.

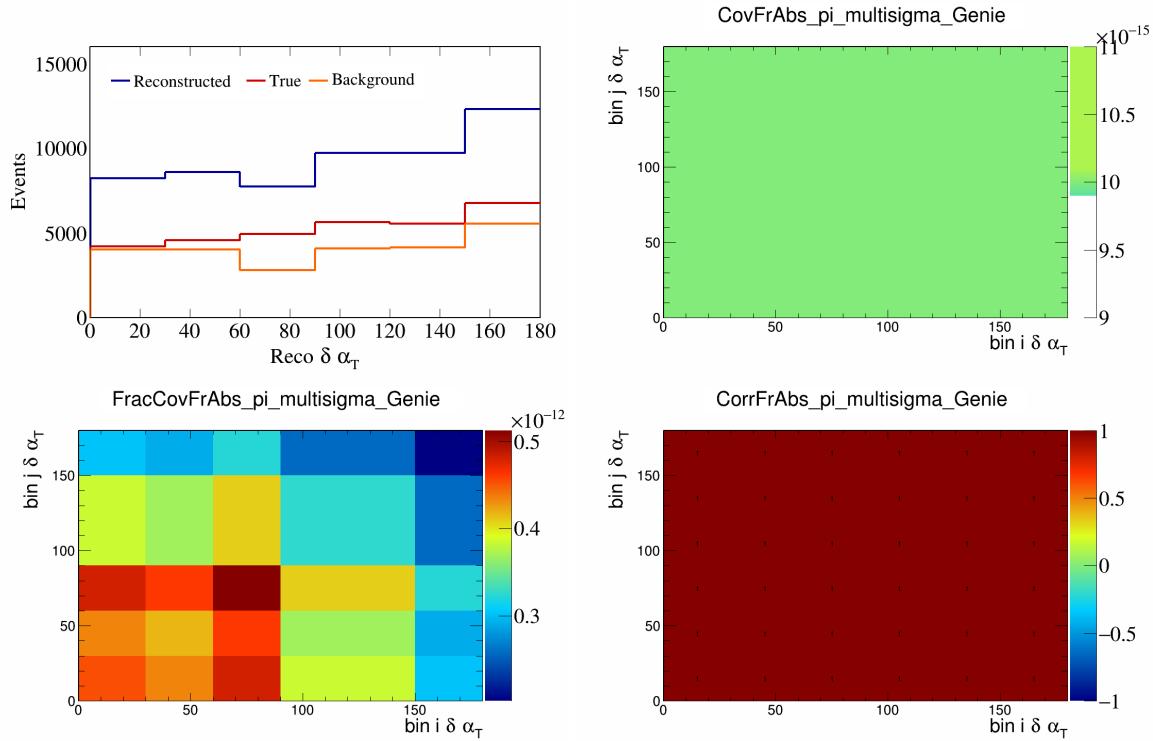


Figure 167: FrAbspi variations for $\delta \alpha_T$.

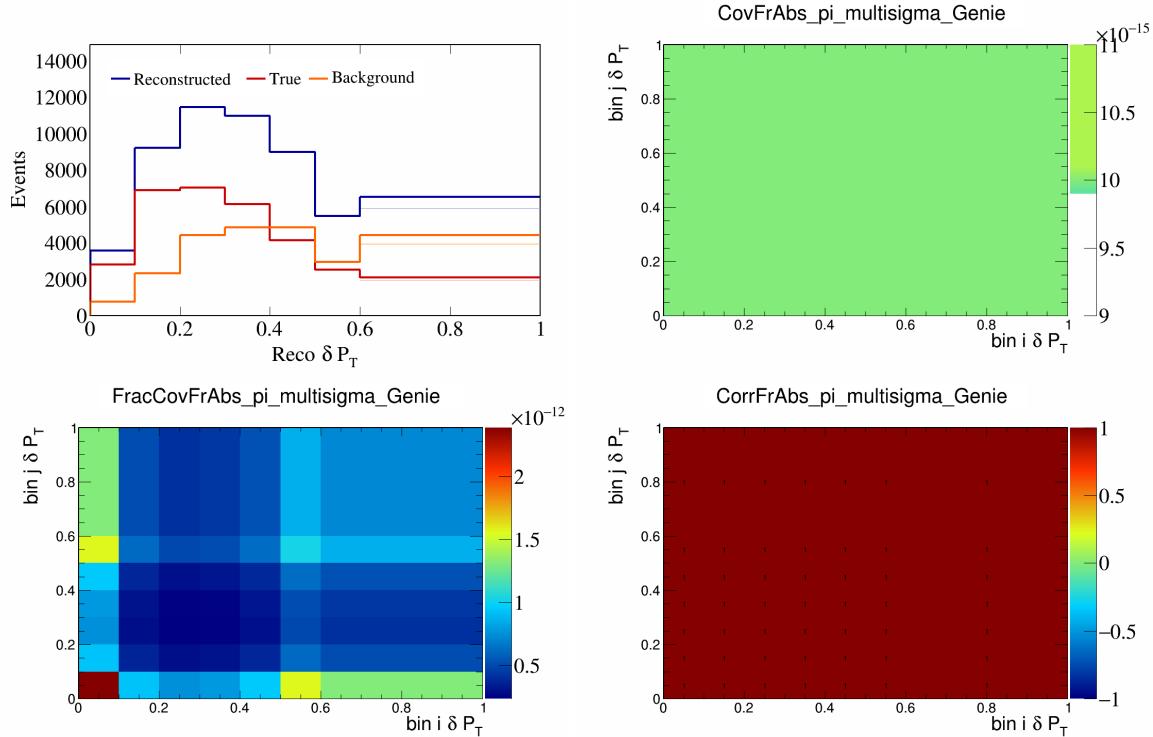


Figure 168: FrAbspi variations for δP_T .

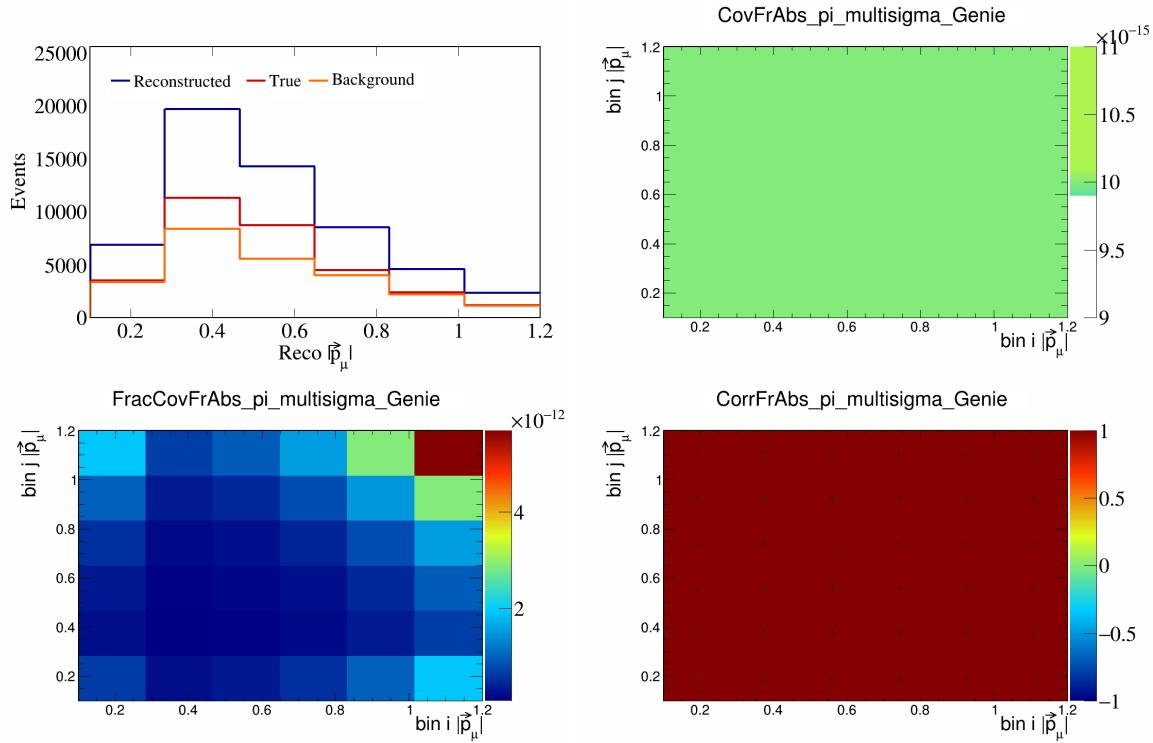


Figure 169: FrAbspi variations for $|\vec{p}_\mu|$.

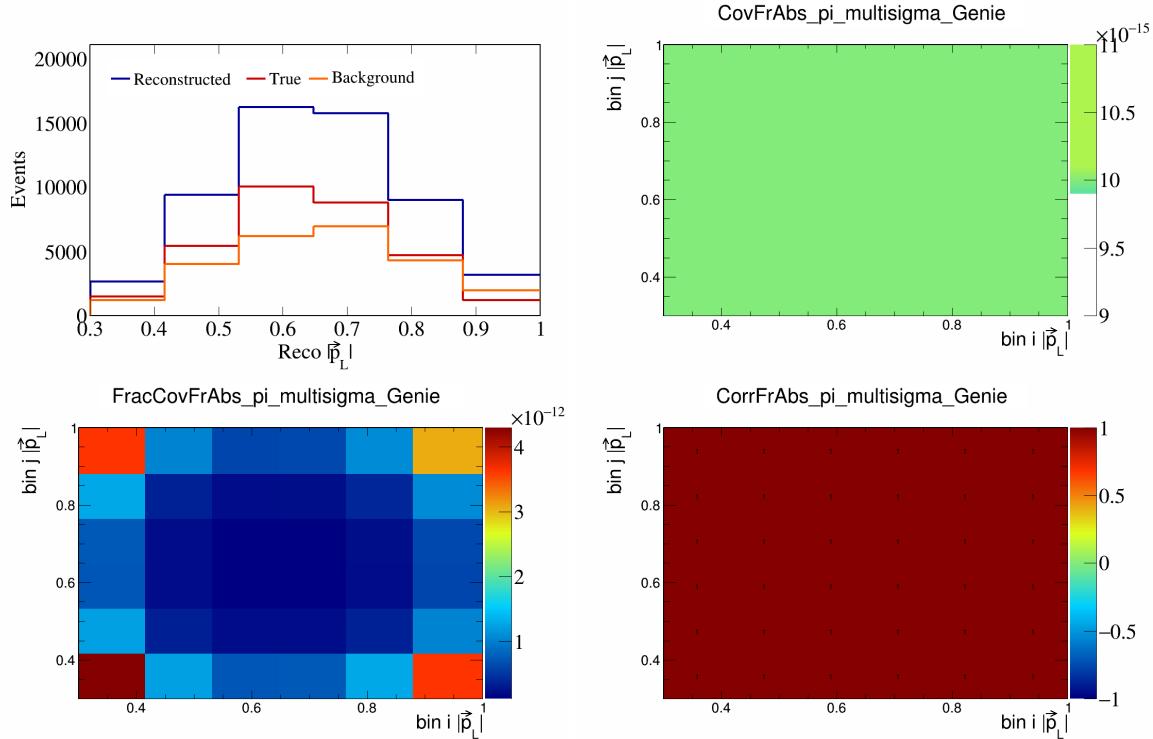


Figure 170: FrAbspi variations for $|\vec{p}_L|$.

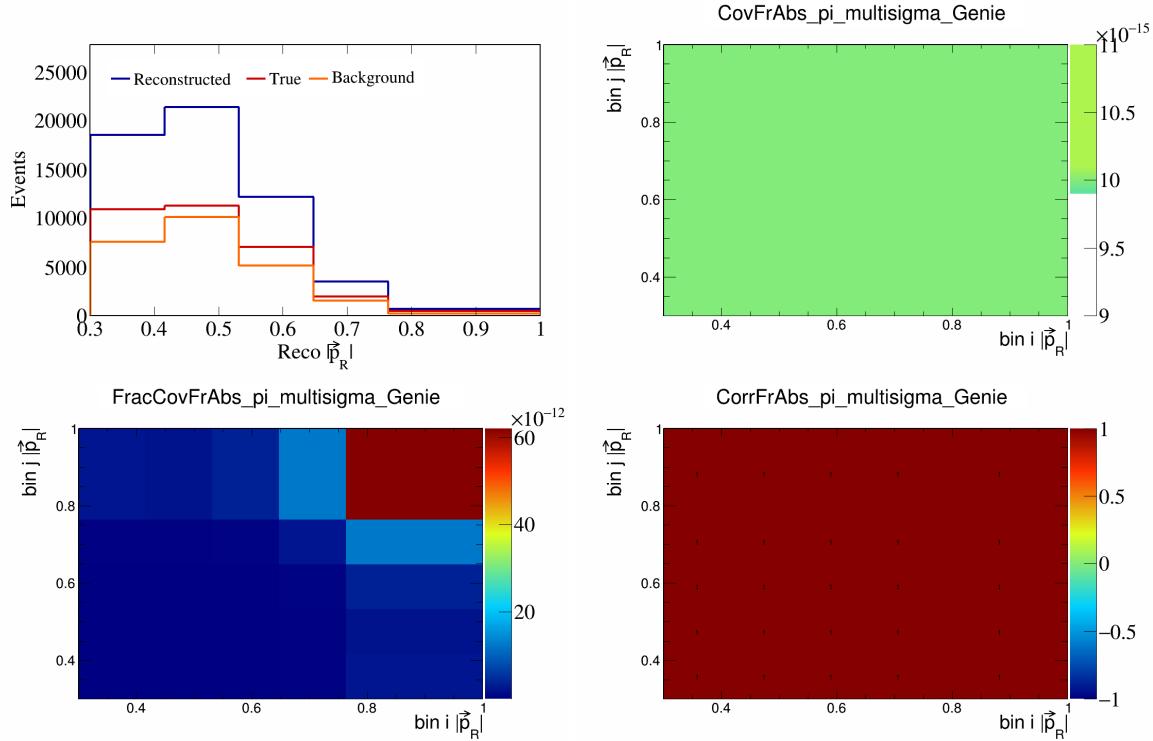


Figure 171: FrAbspi variations for $|\vec{p}_R|$.

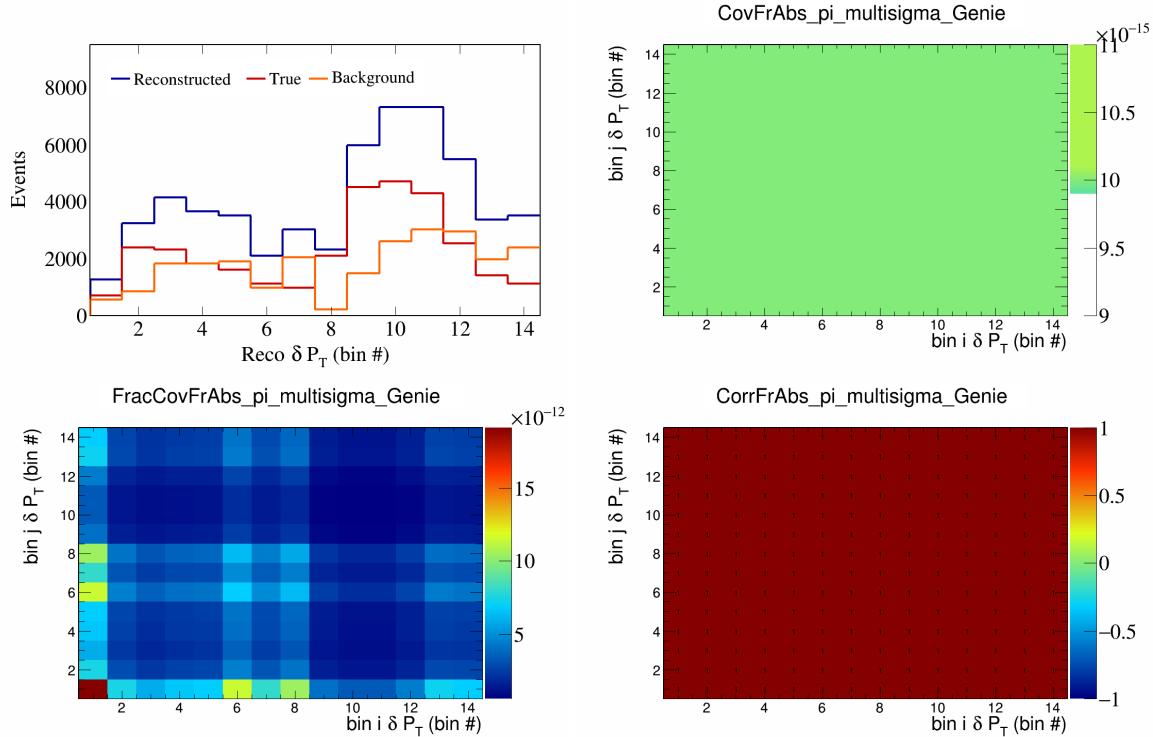


Figure 172: FrAbspi variations for δP_T in $\cos(\theta_{\vec{p}_\mu})$.

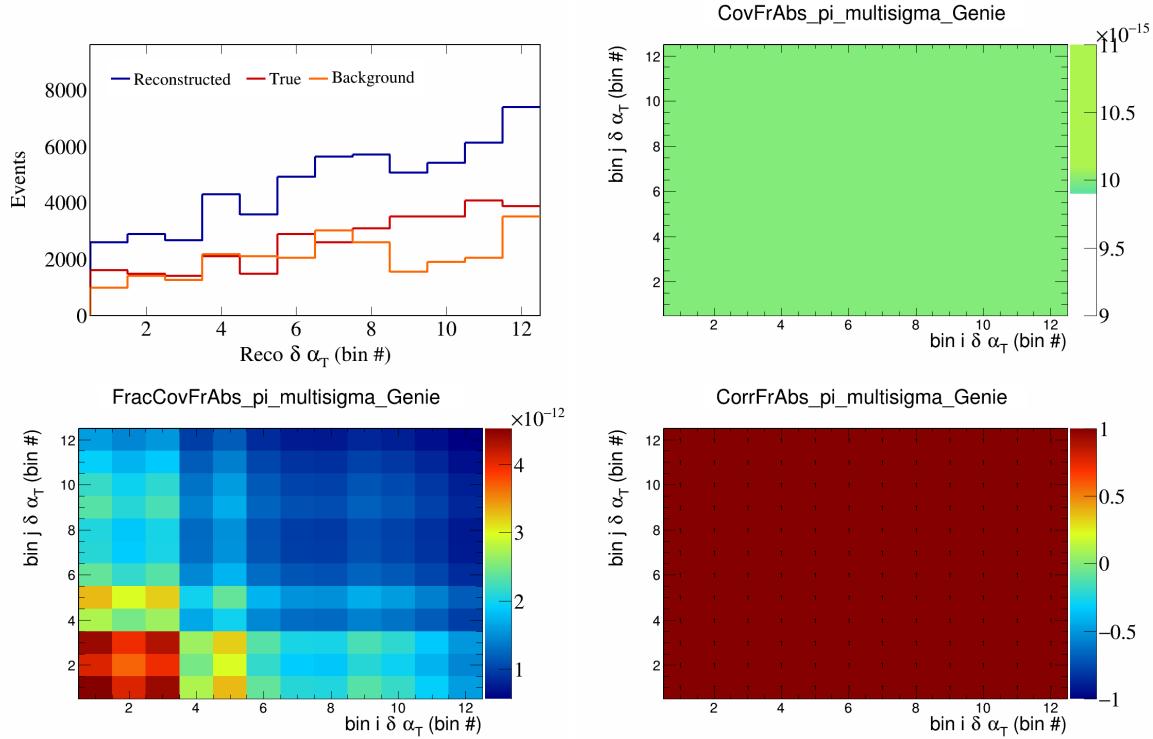


Figure 173: FrAbspi variations for $\delta\alpha_T$ in $\cos(\theta_{\vec{p}_\mu})$.

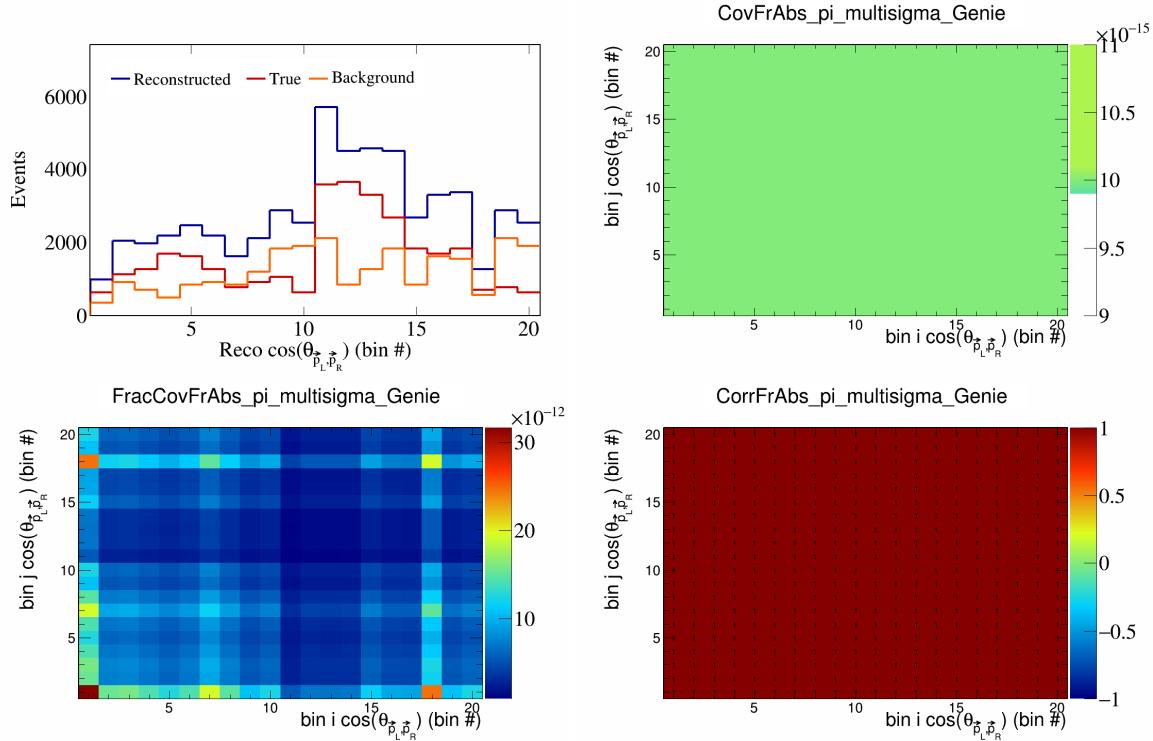


Figure 174: FrAbspi variations for $\cos(\theta_{\vec{p}_L, \vec{p}_R})$ in $\cos(\theta_{\vec{p}_\mu})$.

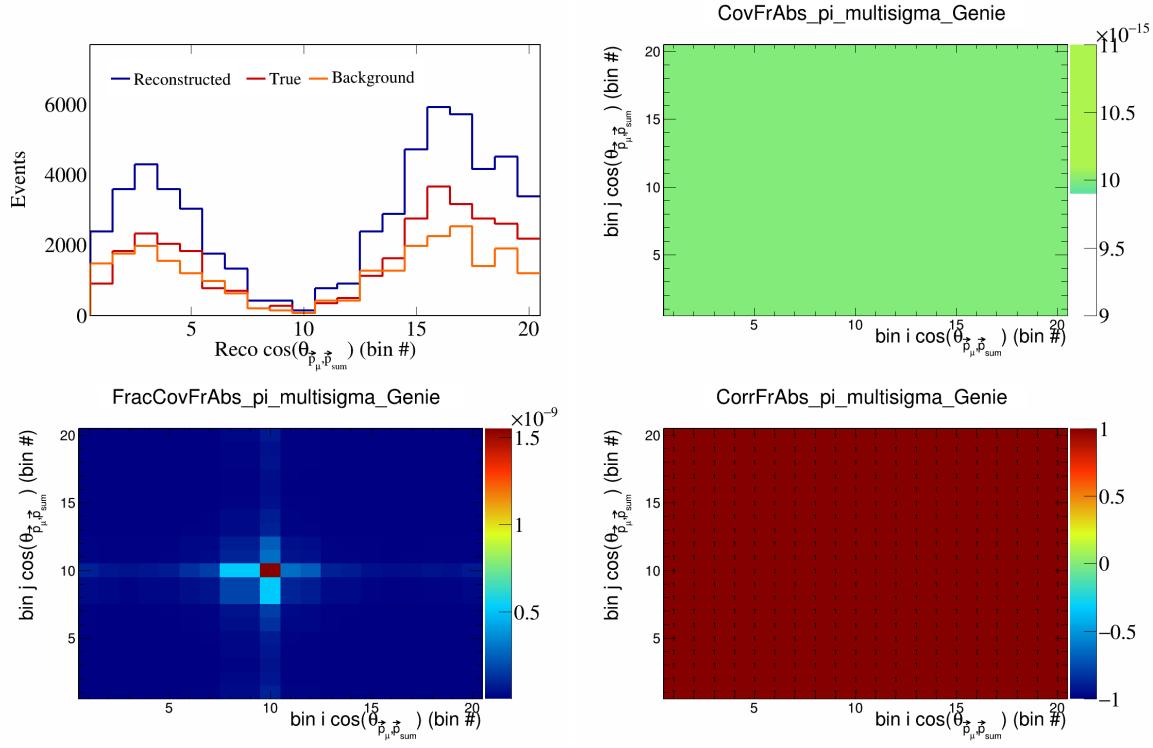


Figure 175: FrAbspi variations for $\cos(\theta_{\vec{p}_\mu, \vec{p}_{\text{sum}}})$ in $\cos(\theta_{\vec{p}_\mu})$.

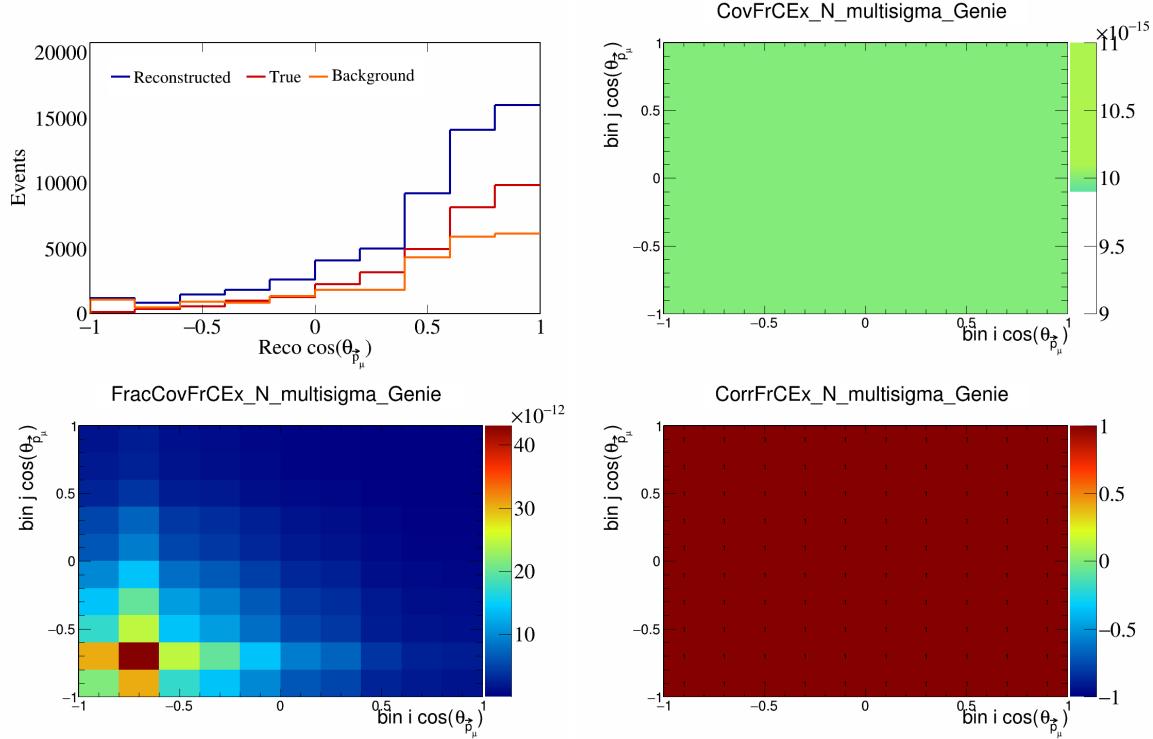


Figure 176: FrCExN variations for $\cos(\theta_{\vec{p}_\mu})$.

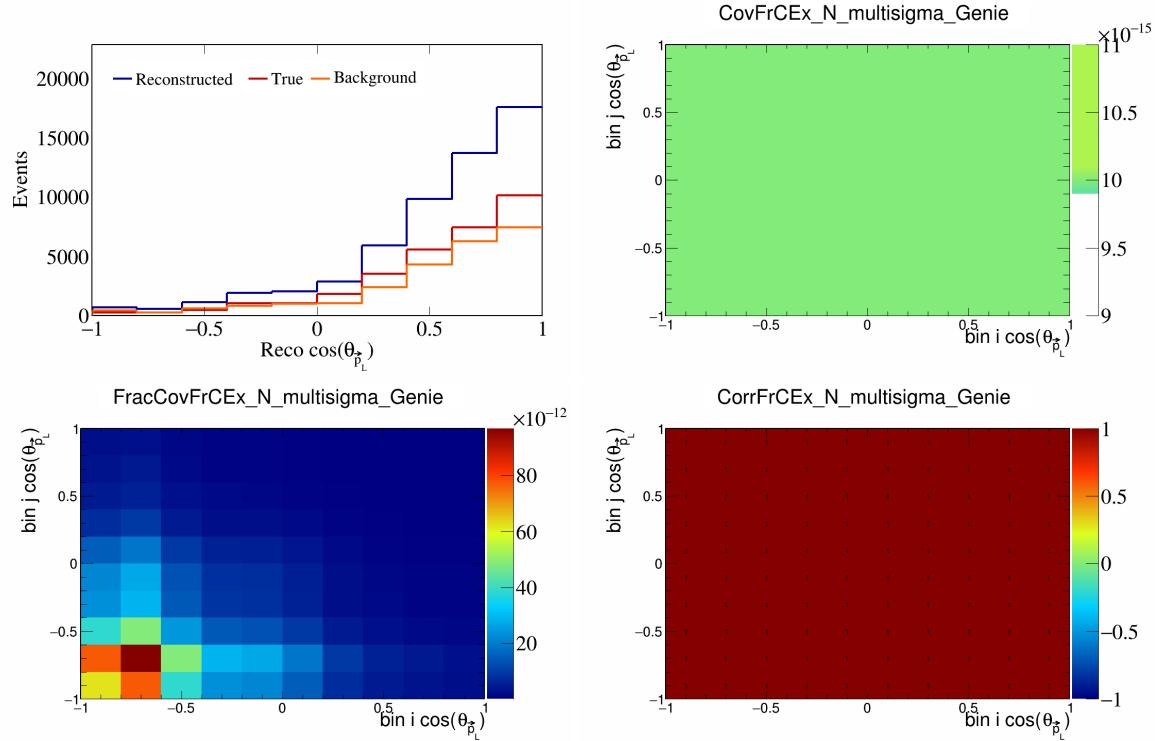


Figure 177: FrCExN variations for $\cos(\theta_{\vec{p}_L})$.

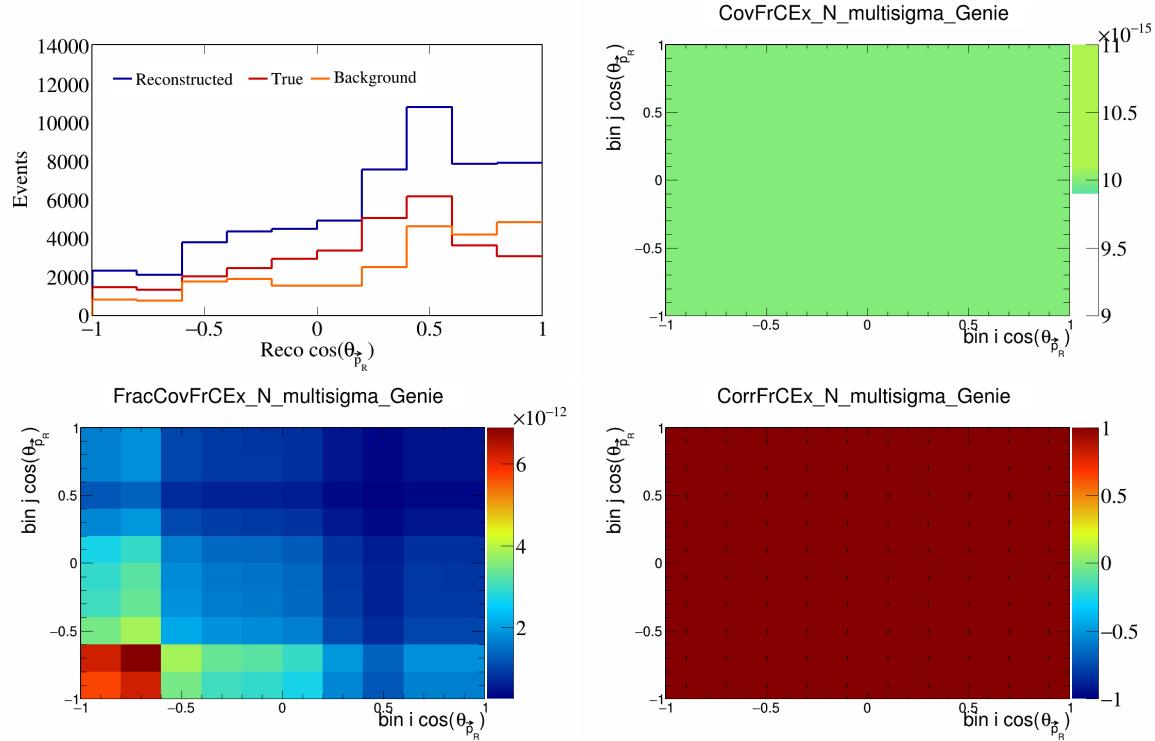


Figure 178: FrCExN variations for $\cos(\theta_{\vec{p}_R})$.

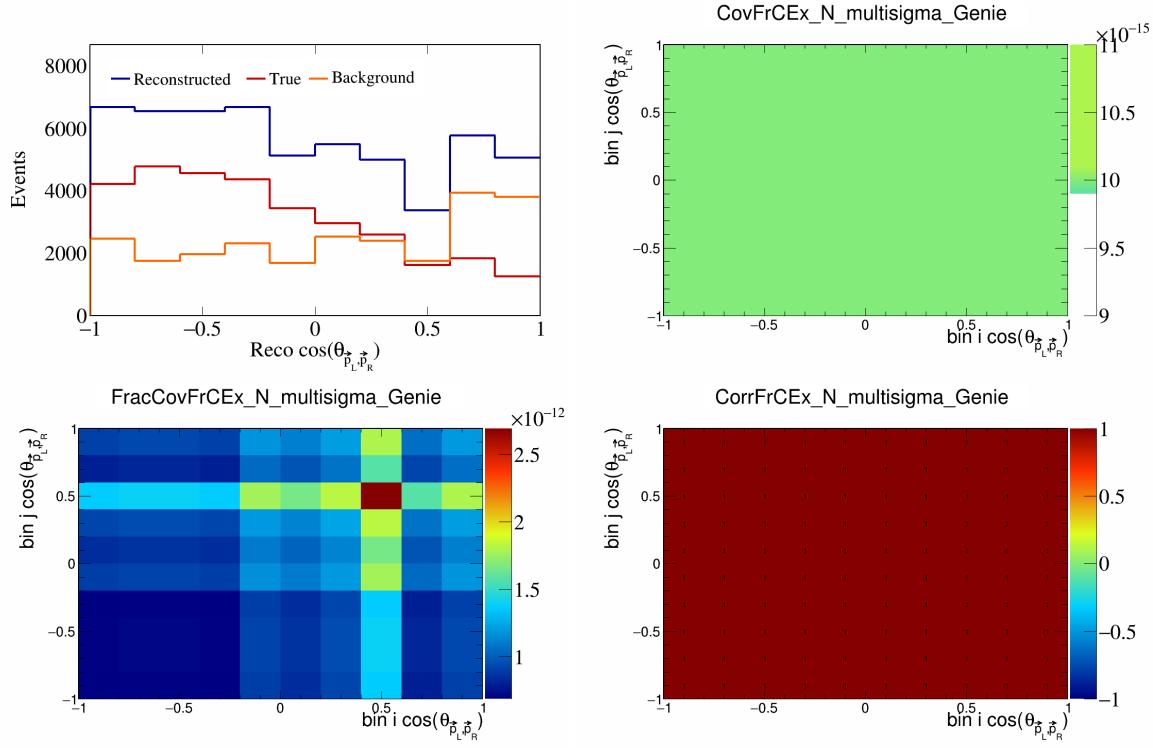


Figure 179: FrCEExN variations for $\cos(\theta_{\vec{p}_L, \vec{p}_R})$.

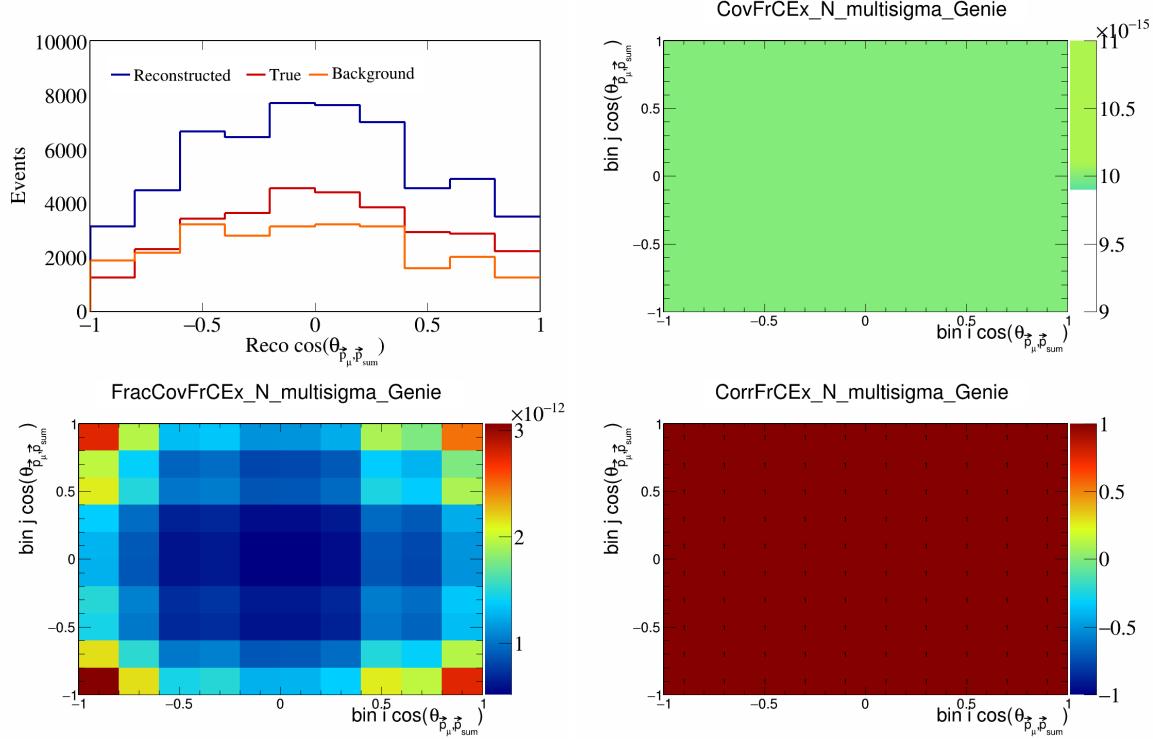


Figure 180: FrCEExN variations for $\cos(\theta_{\vec{p}_\mu, \vec{p}_{\text{sum}}})$.

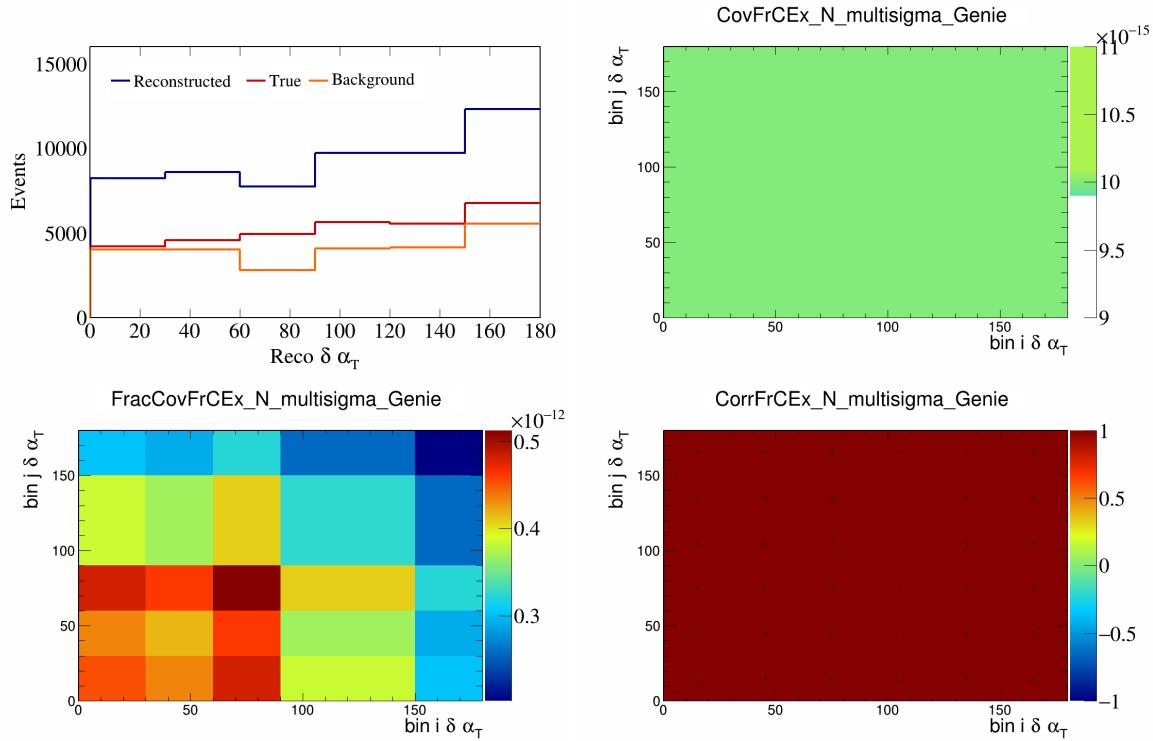


Figure 181: FrCEExN variations for $\delta\alpha_T$.

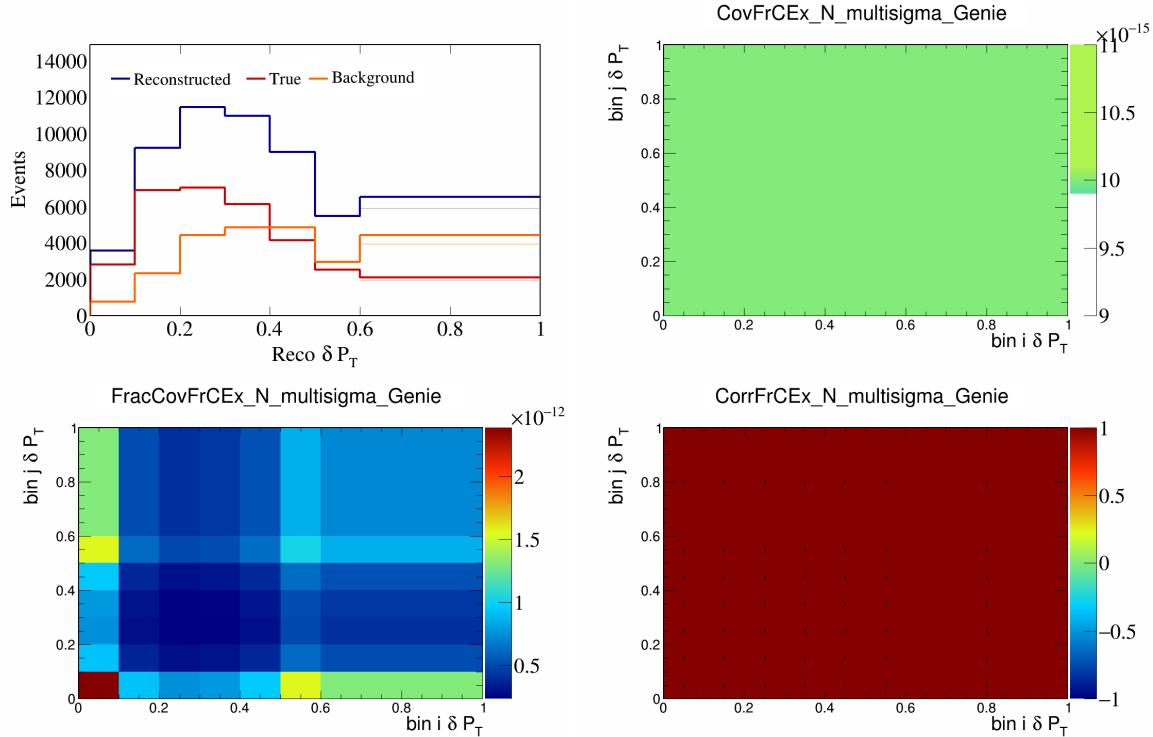


Figure 182: FrCEExN variations for δP_T .

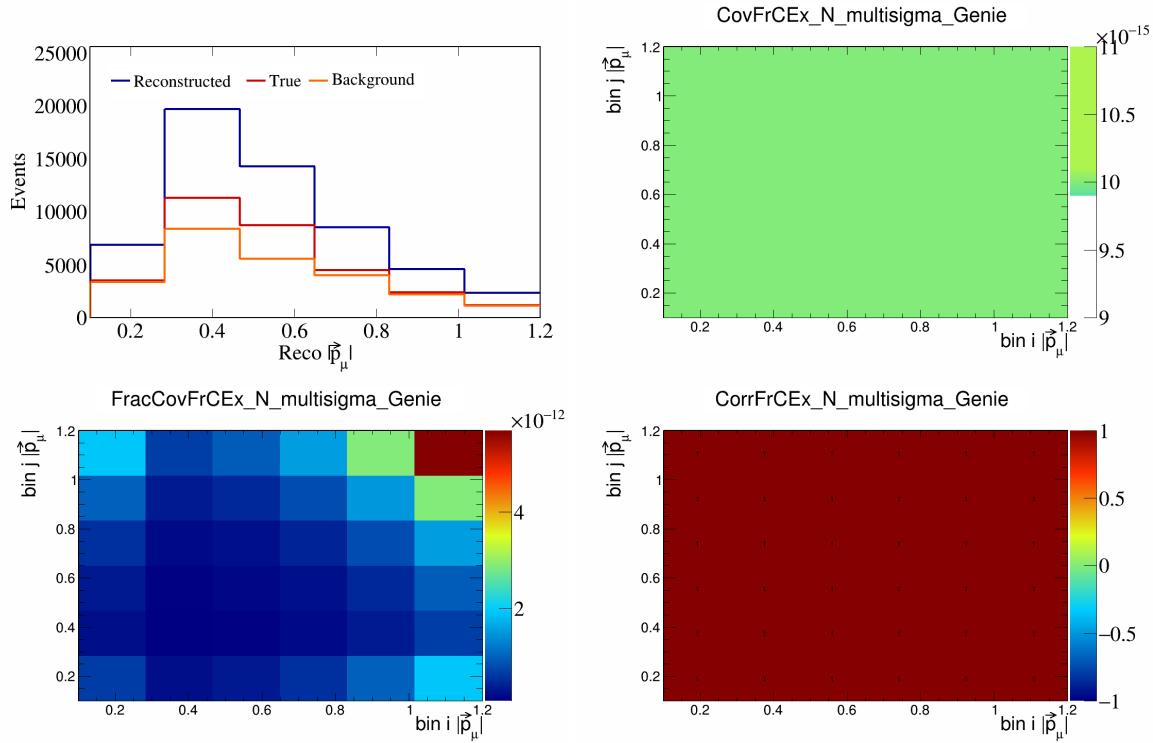


Figure 183: FrCEExN variations for $|\vec{p}_\mu|$.

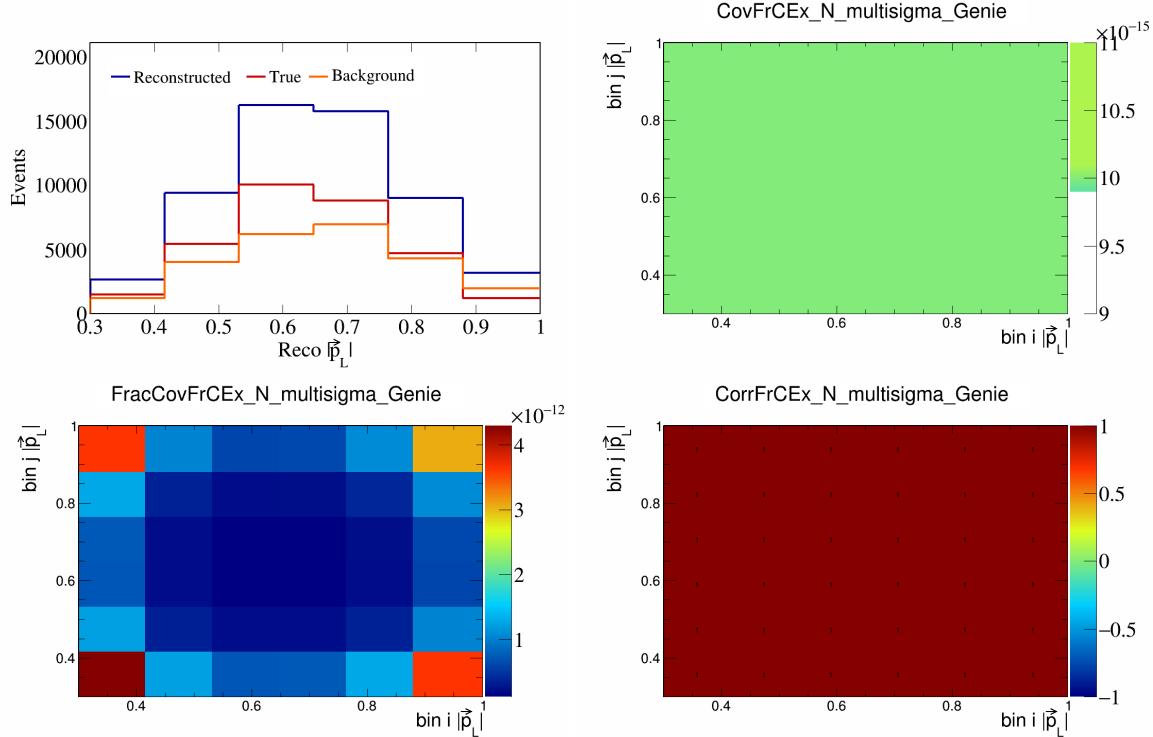


Figure 184: FrCEExN variations for $|\vec{p}_L|$.

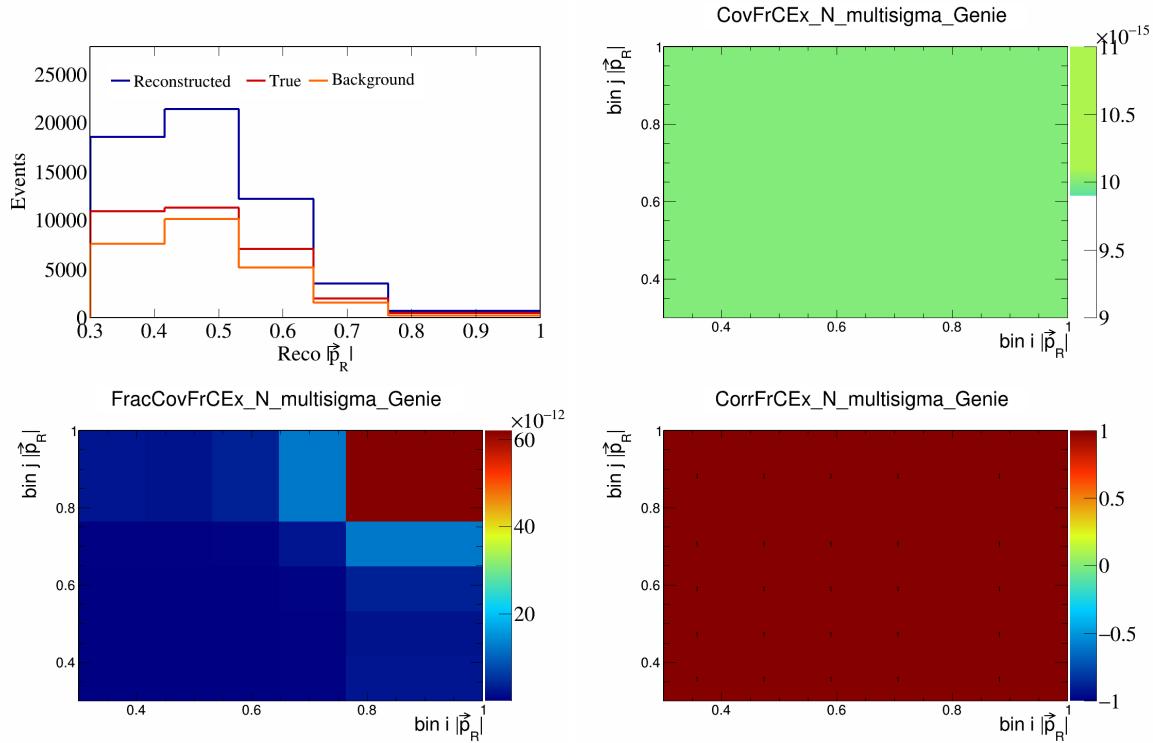


Figure 185: FrCEExN variations for $|\vec{p}_R|$.

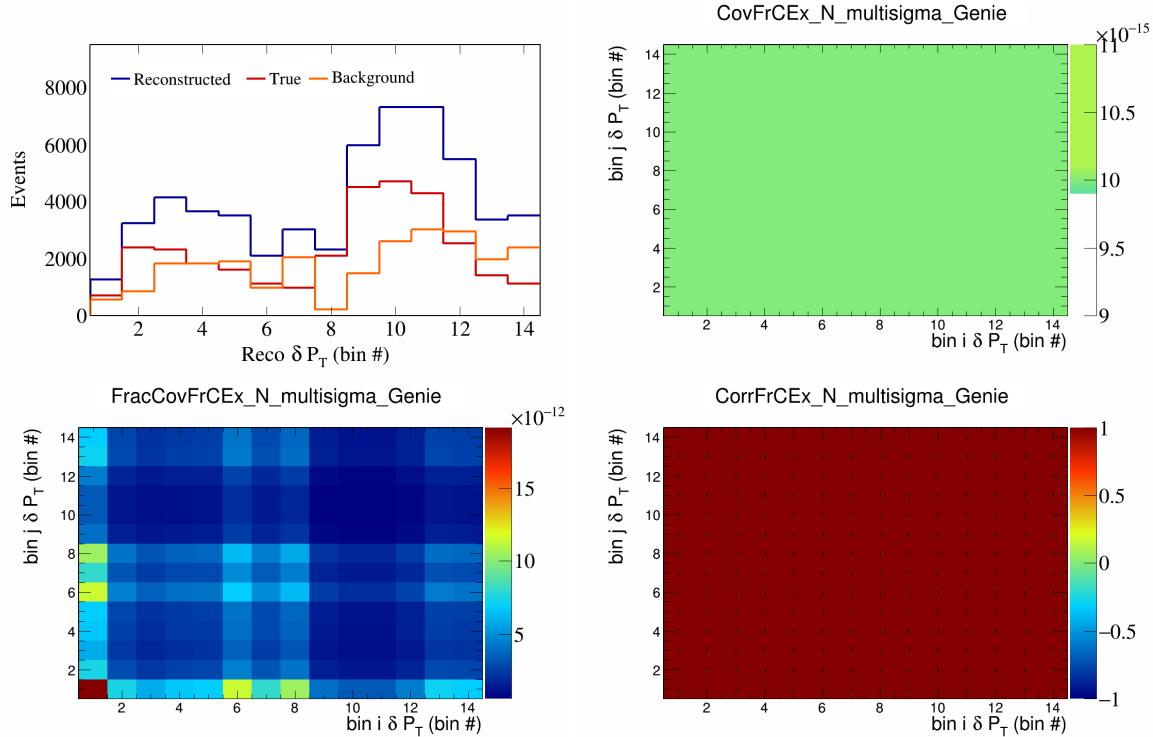


Figure 186: FrCEExN variations for δP_T in $\cos(\theta_{\vec{p}_\mu})$.

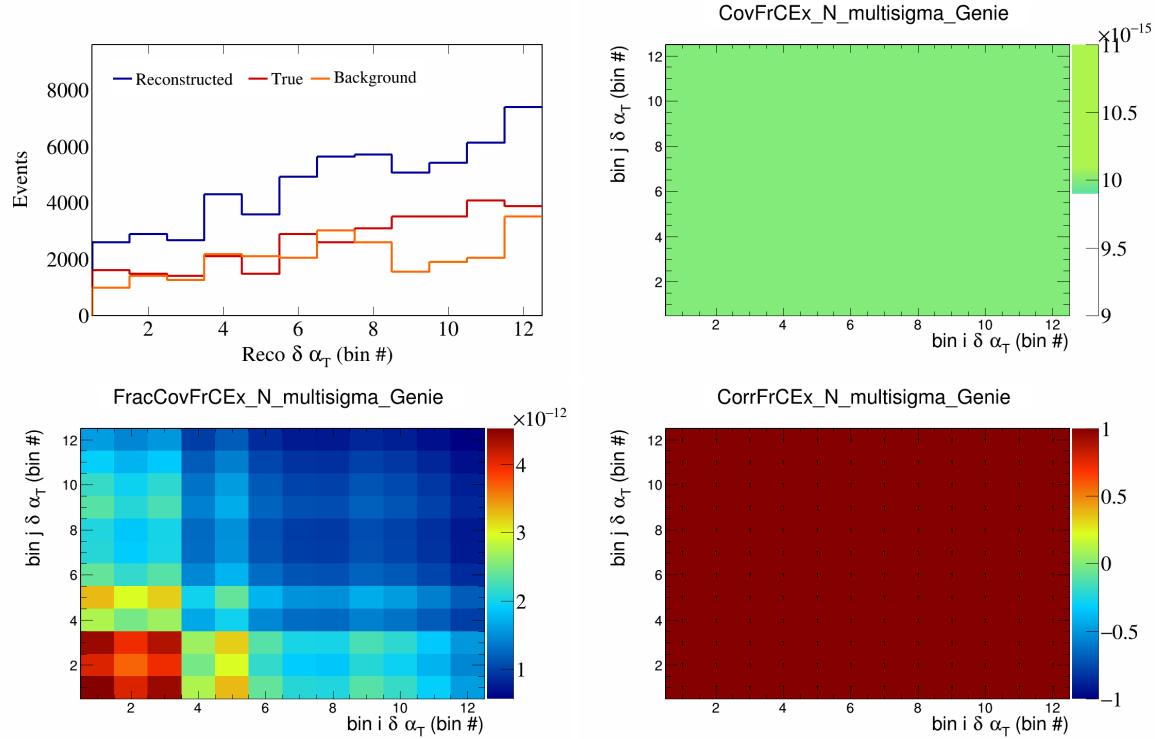


Figure 187: FrCEExN variations for $\delta\alpha_T$ in $\cos(\theta_{\vec{p}_\mu})$.

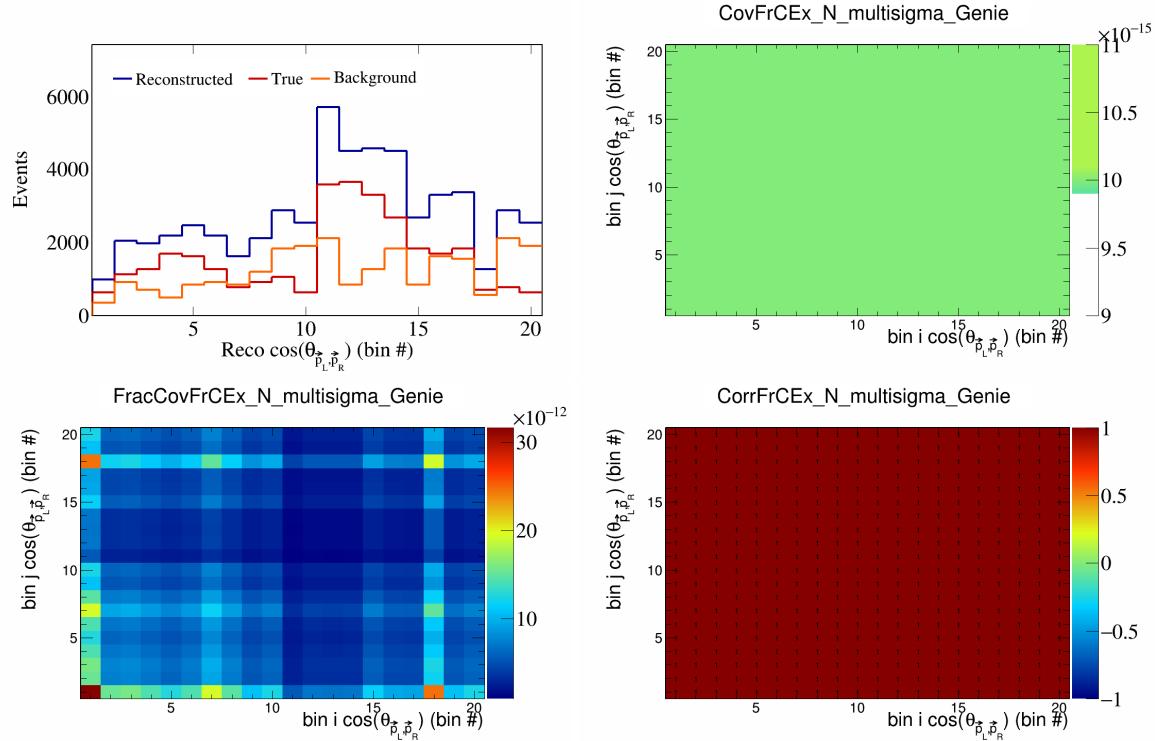


Figure 188: FrCEExN variations for $\cos(\theta_{\vec{p}_L, \vec{p}_R})$ in $\cos(\theta_{\vec{p}_\mu})$.

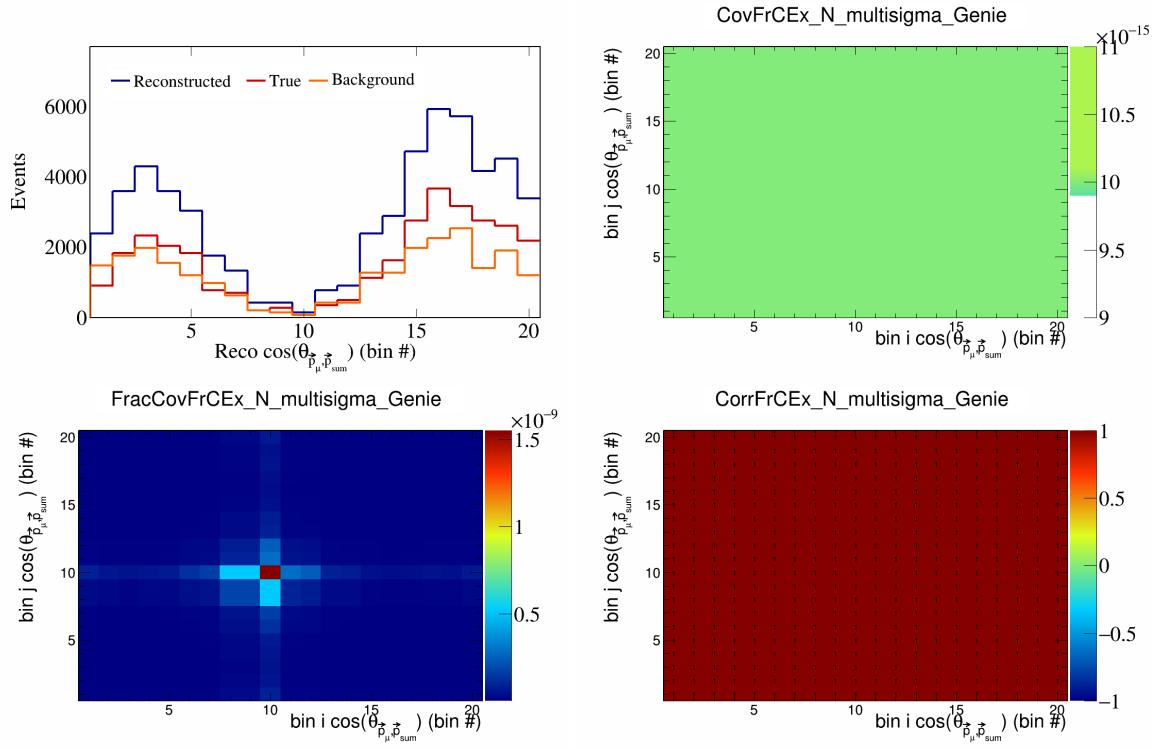


Figure 189: FrCEExN variations for $\cos(\theta_{\vec{p}_\mu, \vec{p}_{\text{sum}}})$ in $\cos(\theta_{\vec{p}_\mu})$.

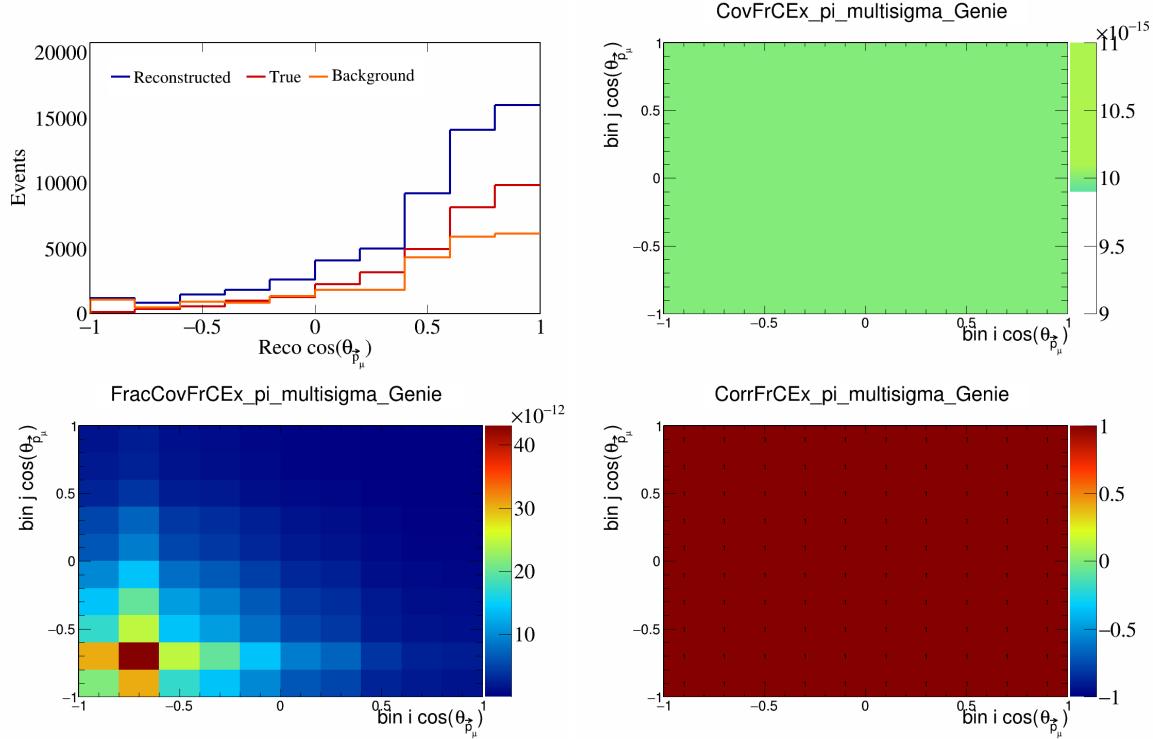


Figure 190: FrCEExpi variations for $\cos(\theta_{\vec{p}_\mu})$.

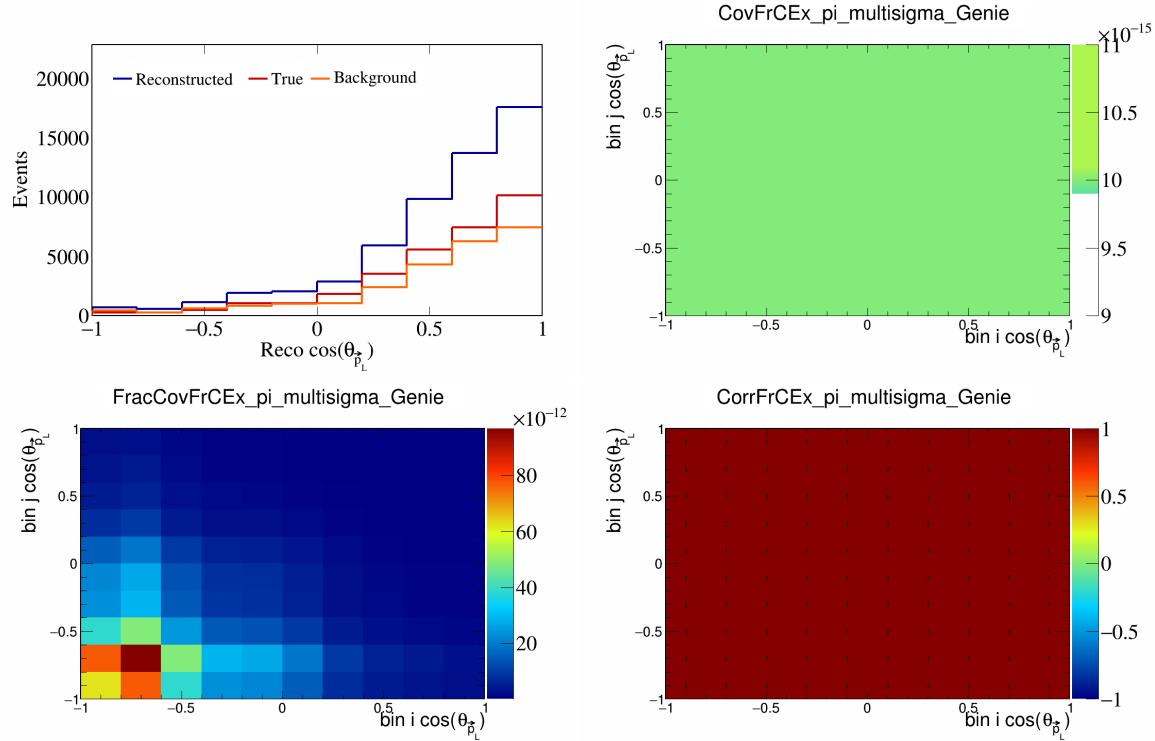


Figure 191: FrCExpi variations for $\cos(\theta_{\vec{p}_L})$.

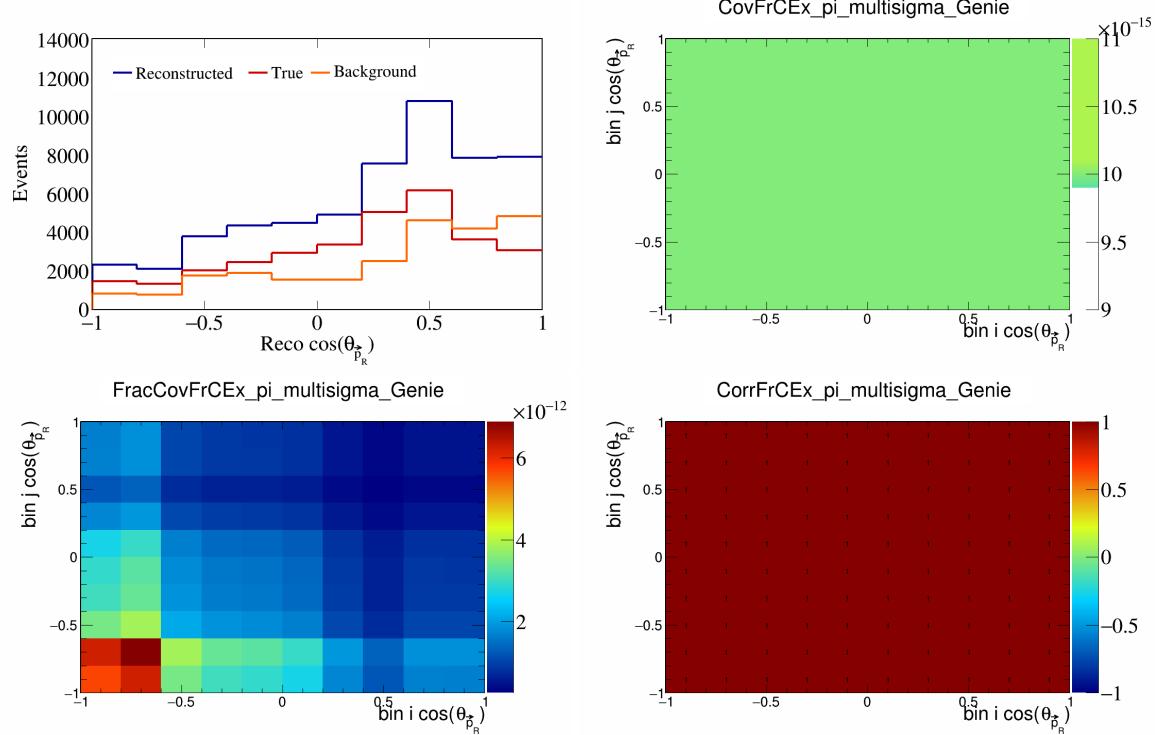


Figure 192: FrCExpi variations for $\cos(\theta_{\vec{p}_R})$.

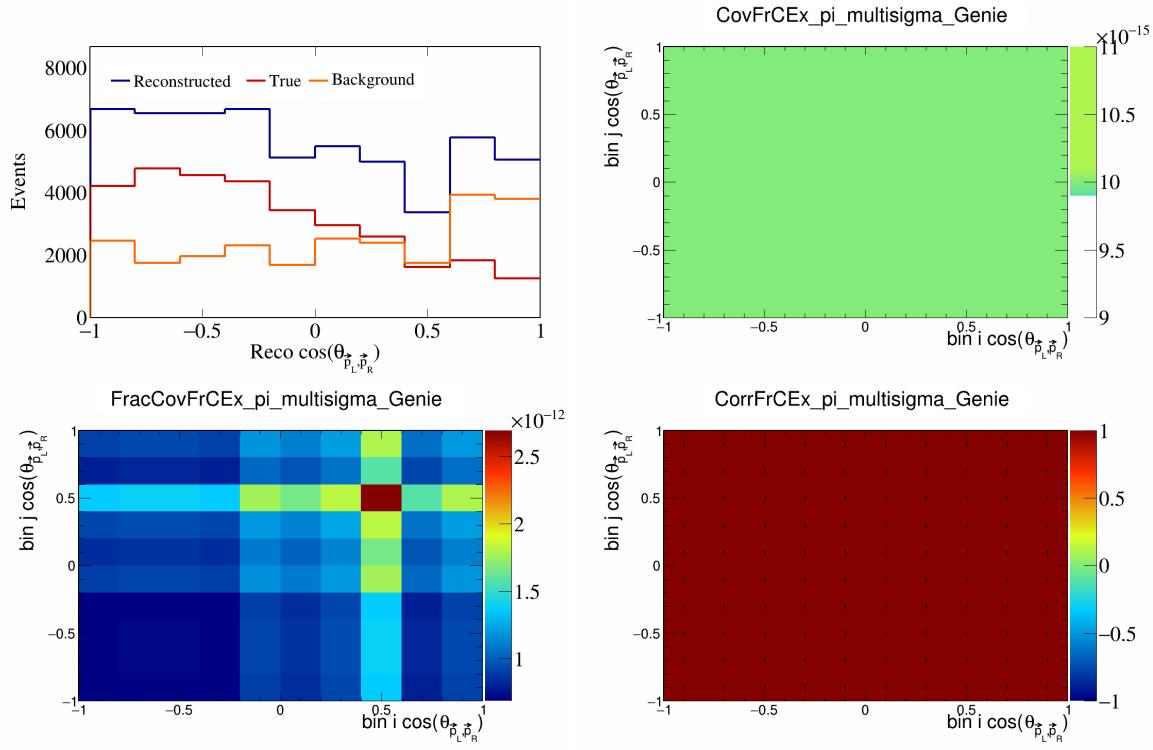


Figure 193: FrCEpi variations for $\cos(\theta_{\vec{p}_L, \vec{p}_R})$.

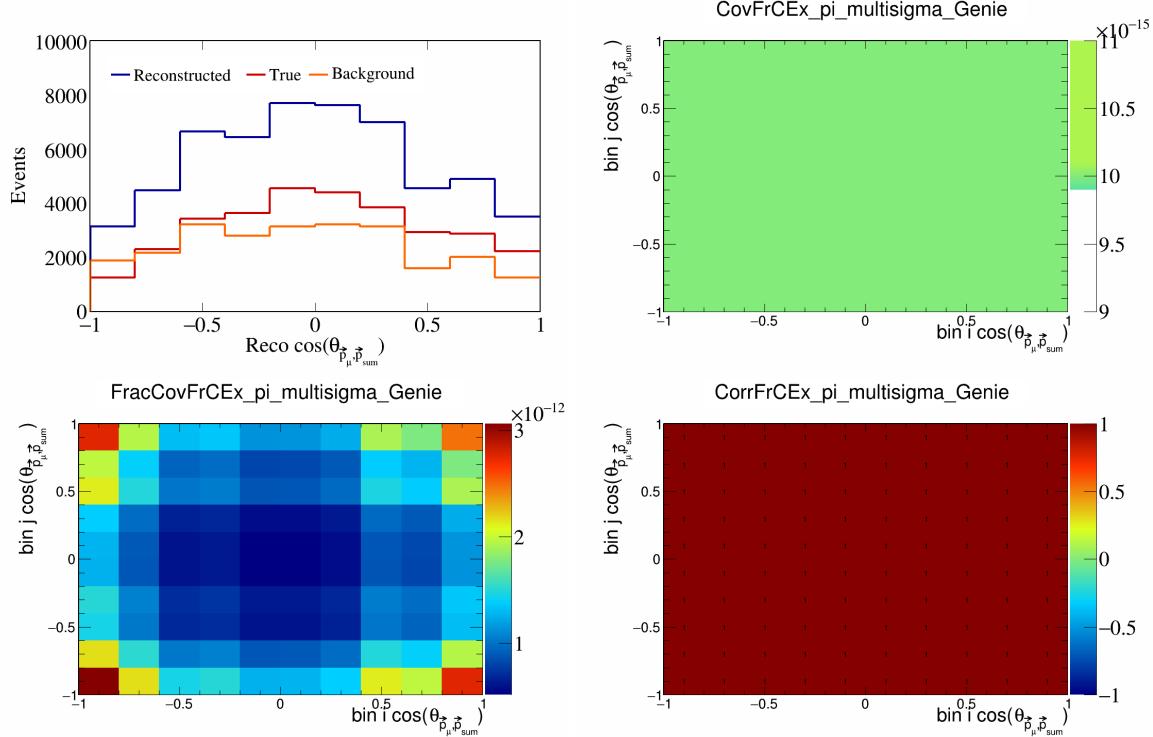


Figure 194: FrCEpi variations for $\cos(\theta_{\vec{p}_\mu, \vec{p}_{\text{sum}}})$.

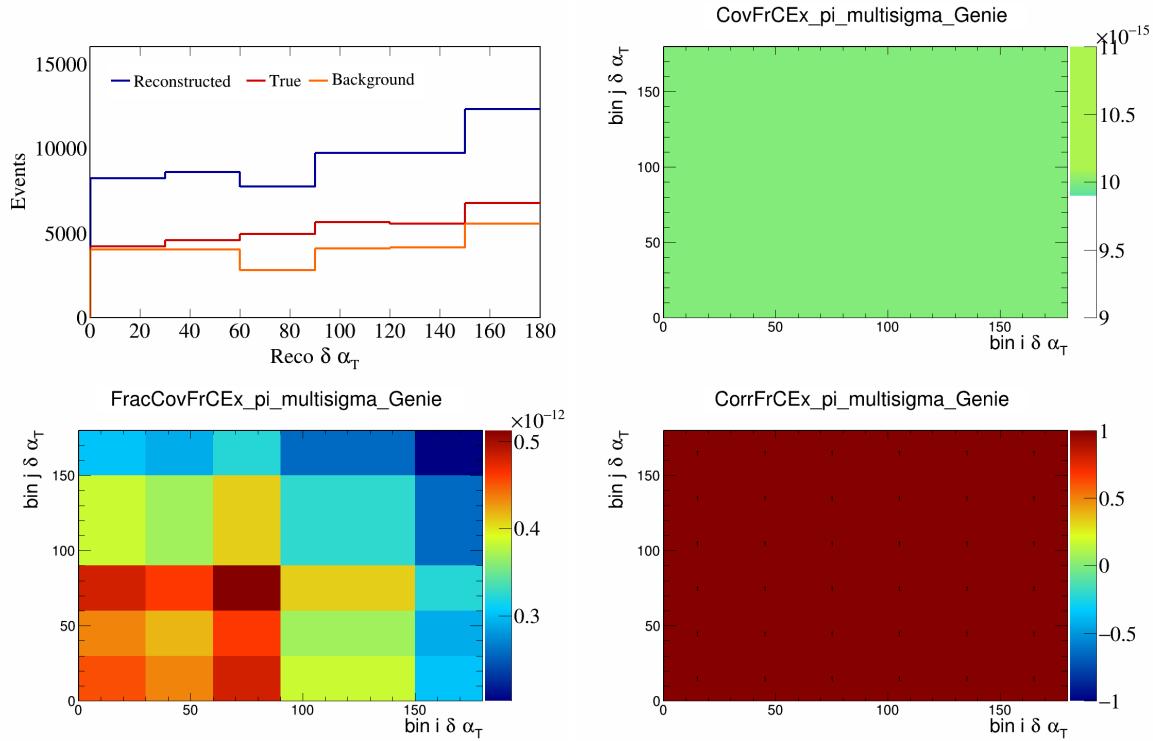


Figure 195: FrCEExpi variations for $\delta\alpha_T$.

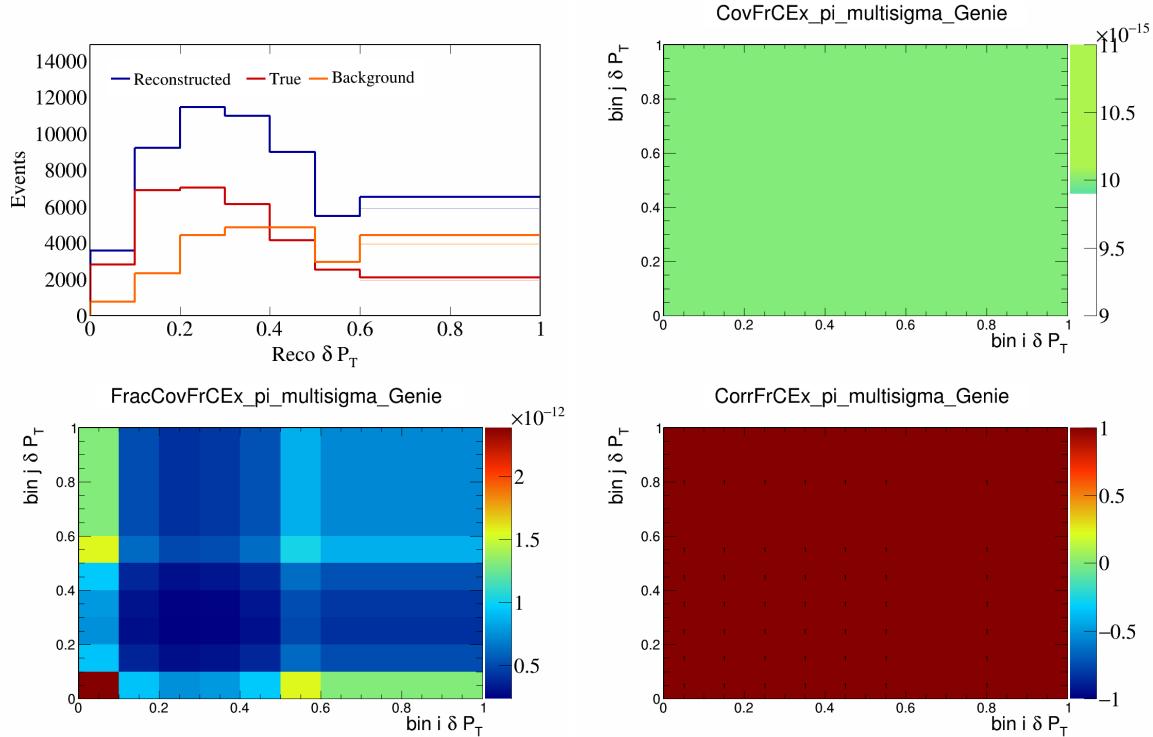


Figure 196: FrCEExpi variations for δP_T .

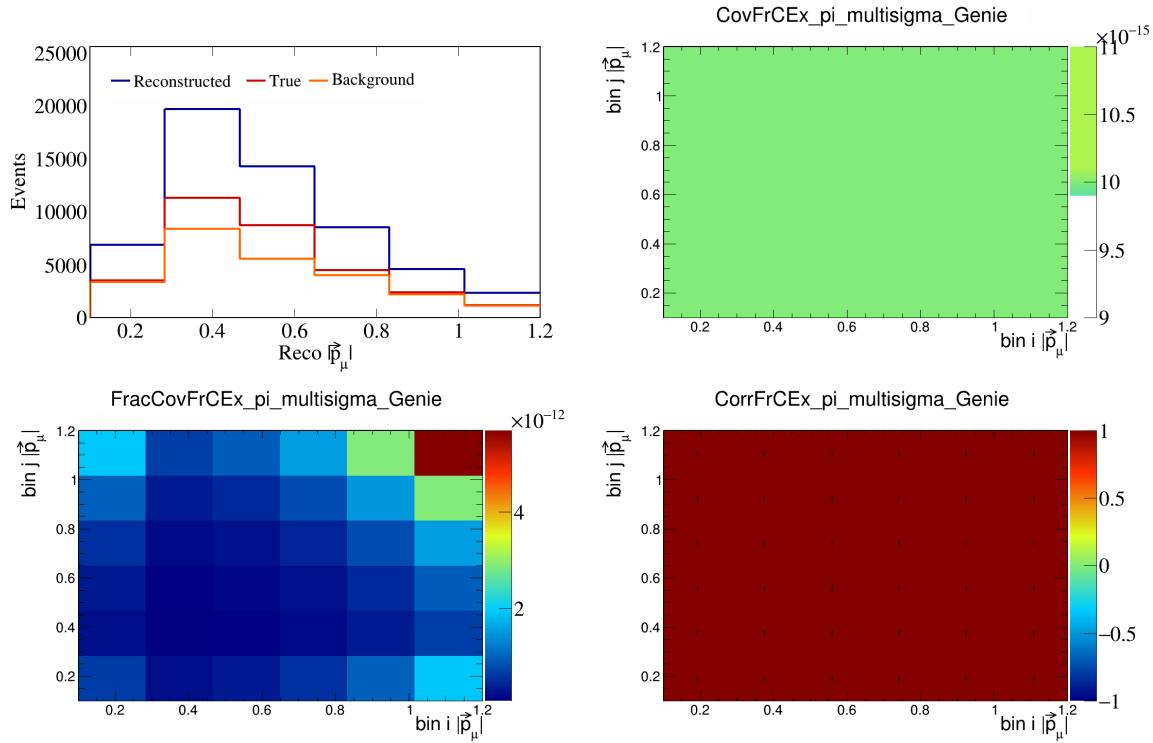


Figure 197: FrCEExpi variations for $|\vec{p}_\mu|$.

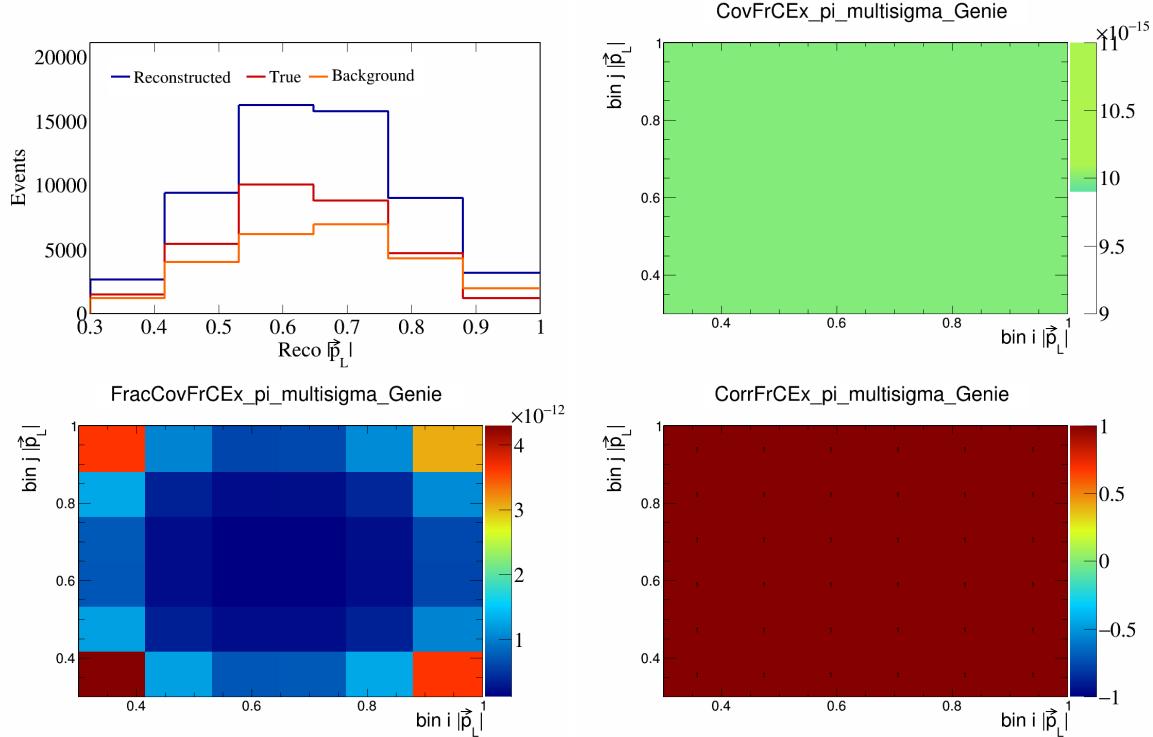


Figure 198: FrCEExpi variations for $|\vec{p}_L|$.

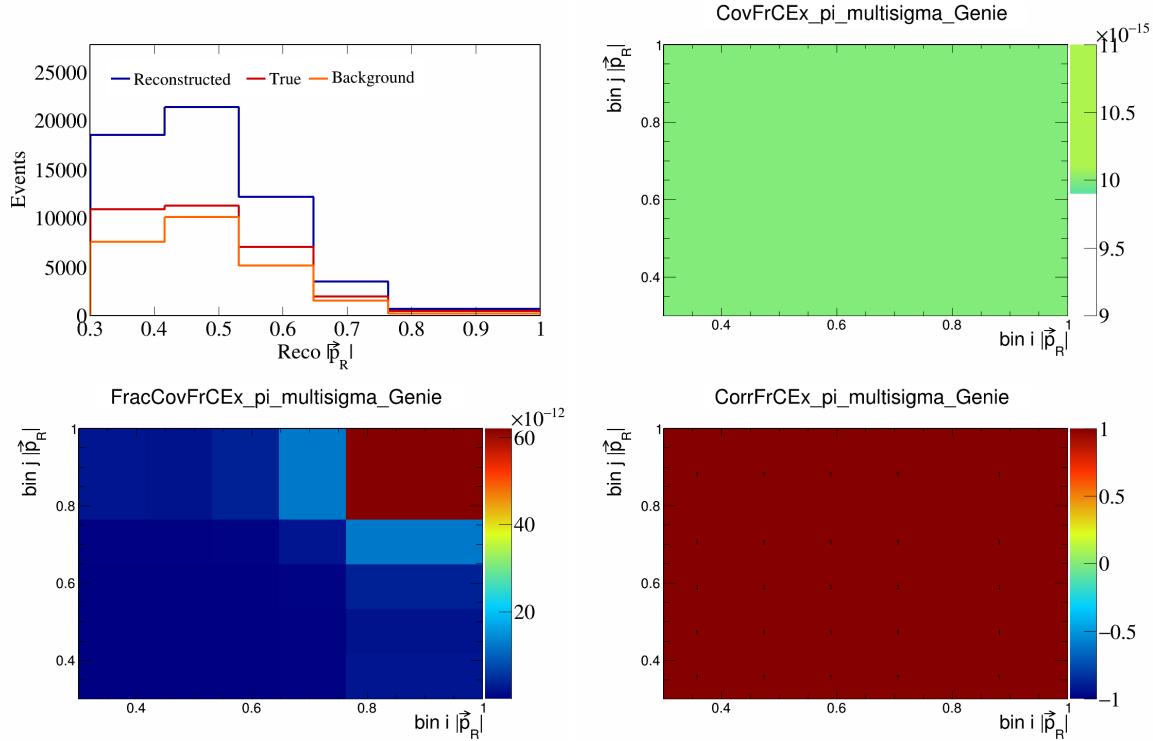


Figure 199: FrCEExpi variations for $|\vec{p}_R|$.

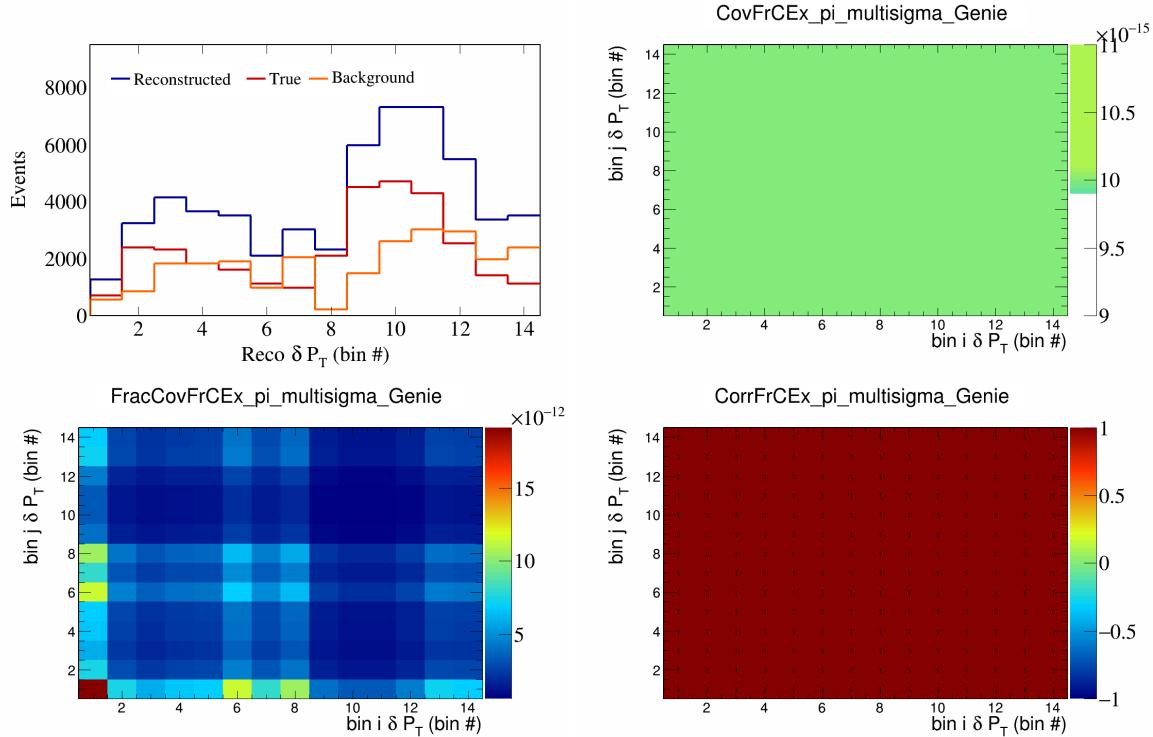


Figure 200: FrCEExpi variations for δP_T in $\cos(\theta_{\vec{p}_\mu})$.

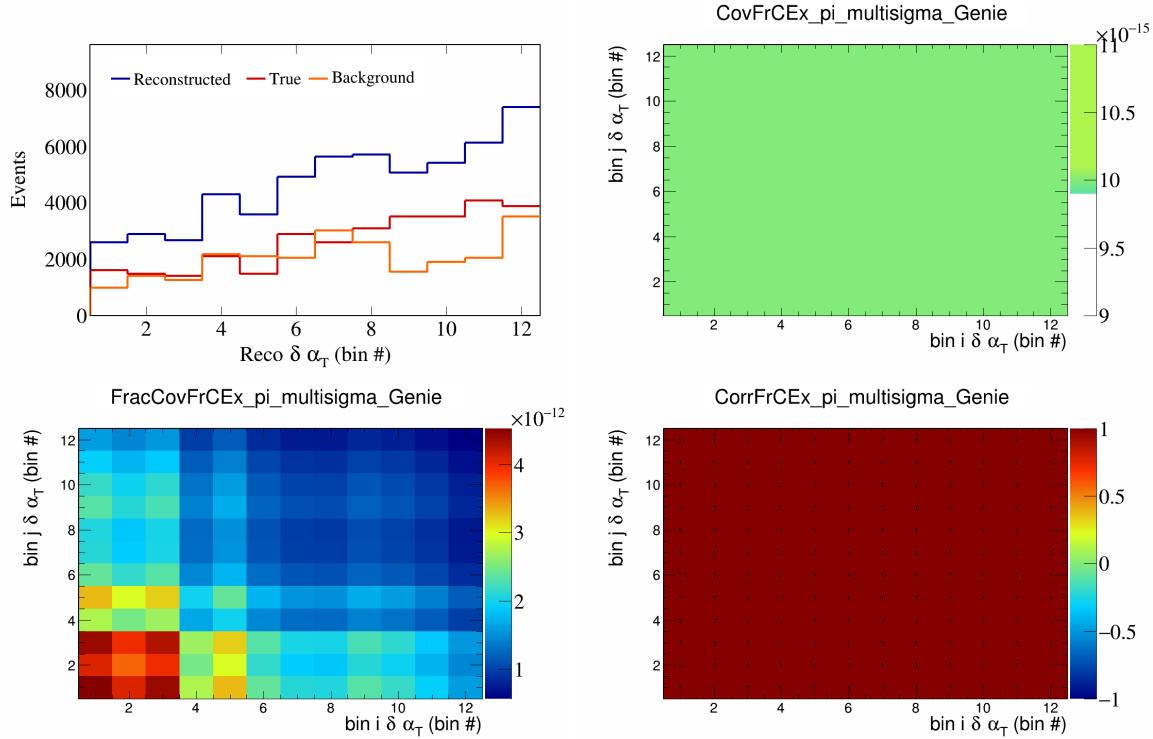


Figure 201: FrCEpi variations for $\delta\alpha_T$ in $\cos(\theta_{\vec{p}_\mu})$.

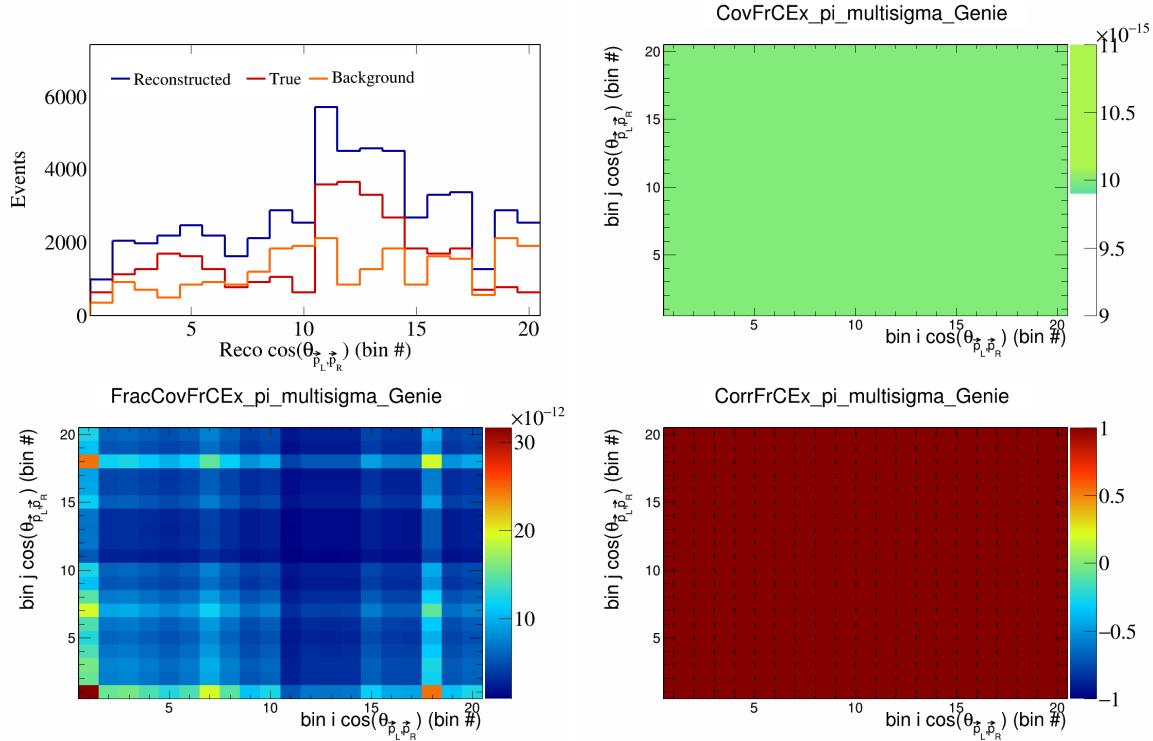


Figure 202: FrCEpi variations for $\cos(\theta_{\vec{p}_L, \vec{p}_R})$ in $\cos(\theta_{\vec{p}_\mu})$.

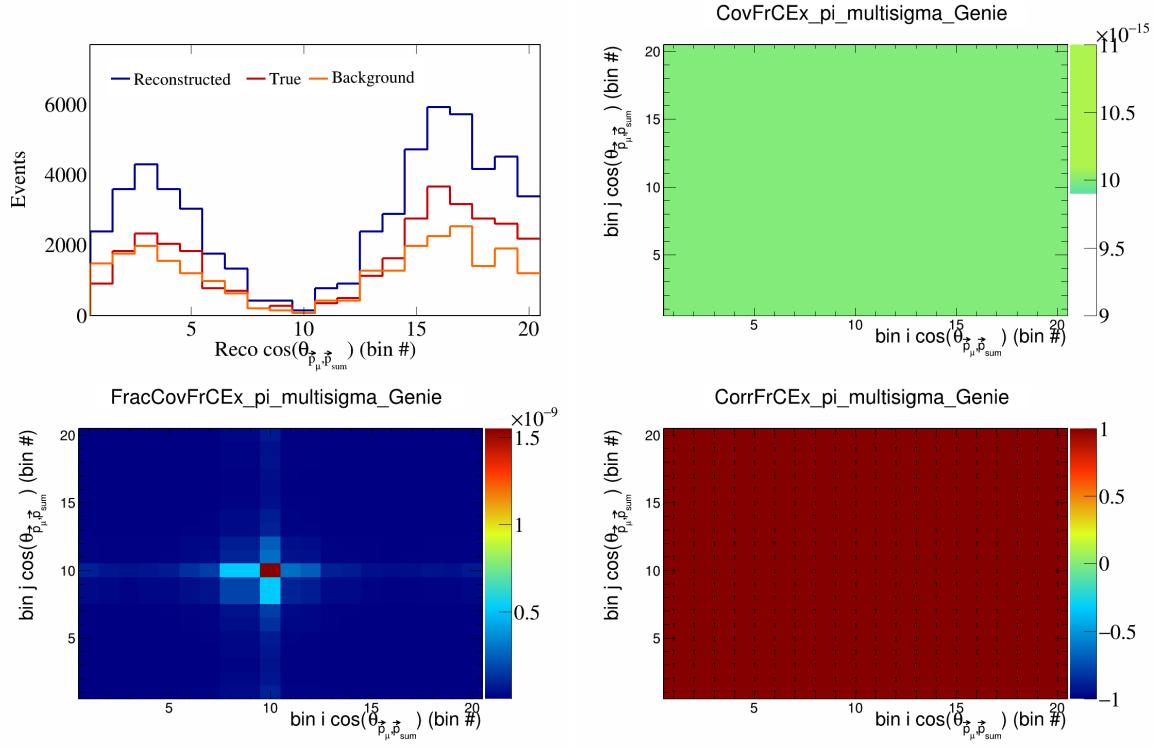


Figure 203: FrCEExpi variations for $\cos(\theta_{\vec{p}_\mu, \vec{p}_{\text{sum}}})$ in $\cos(\theta_{\vec{p}_\mu})$.

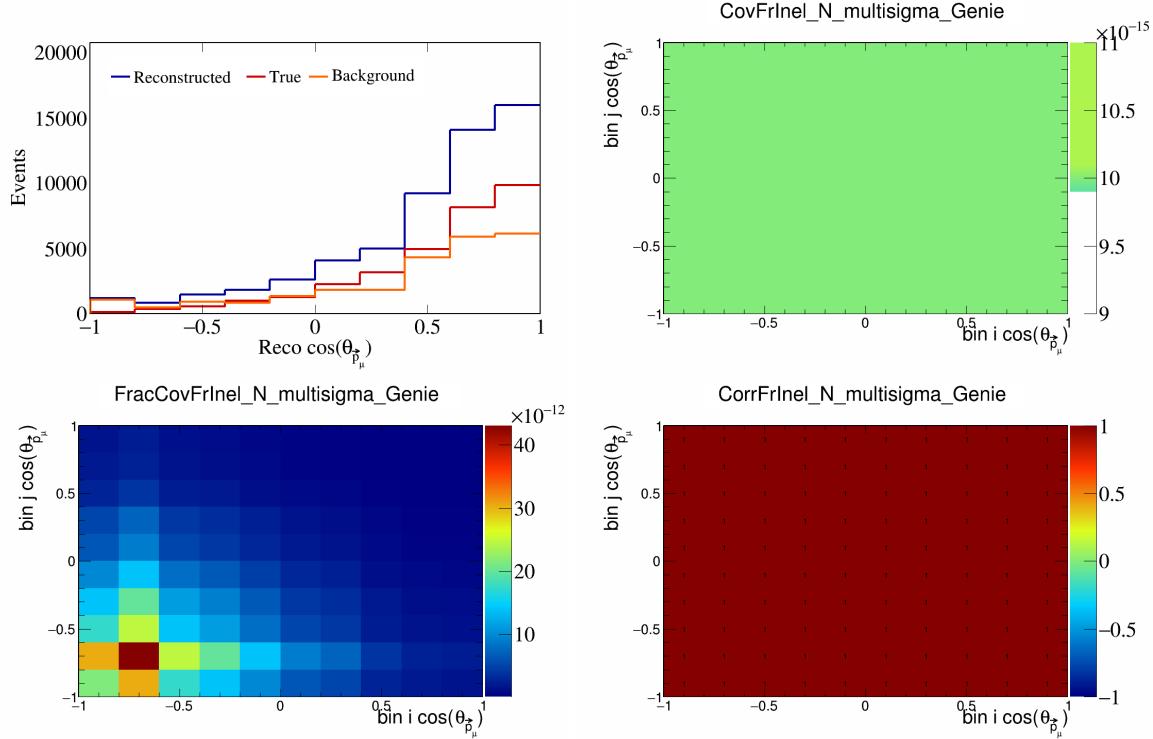


Figure 204: FrInelN variations for $\cos(\theta_{\vec{p}_\mu})$.

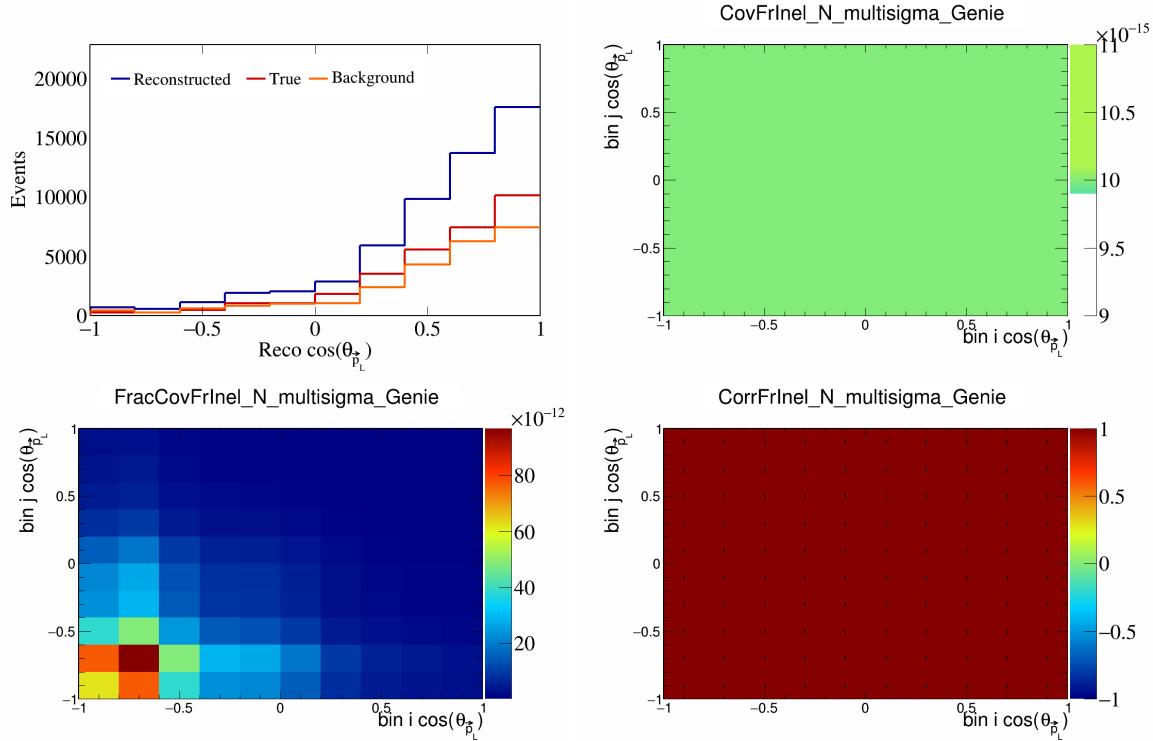


Figure 205: FrInelN variations for $\cos(\theta_{\vec{p}_L})$.

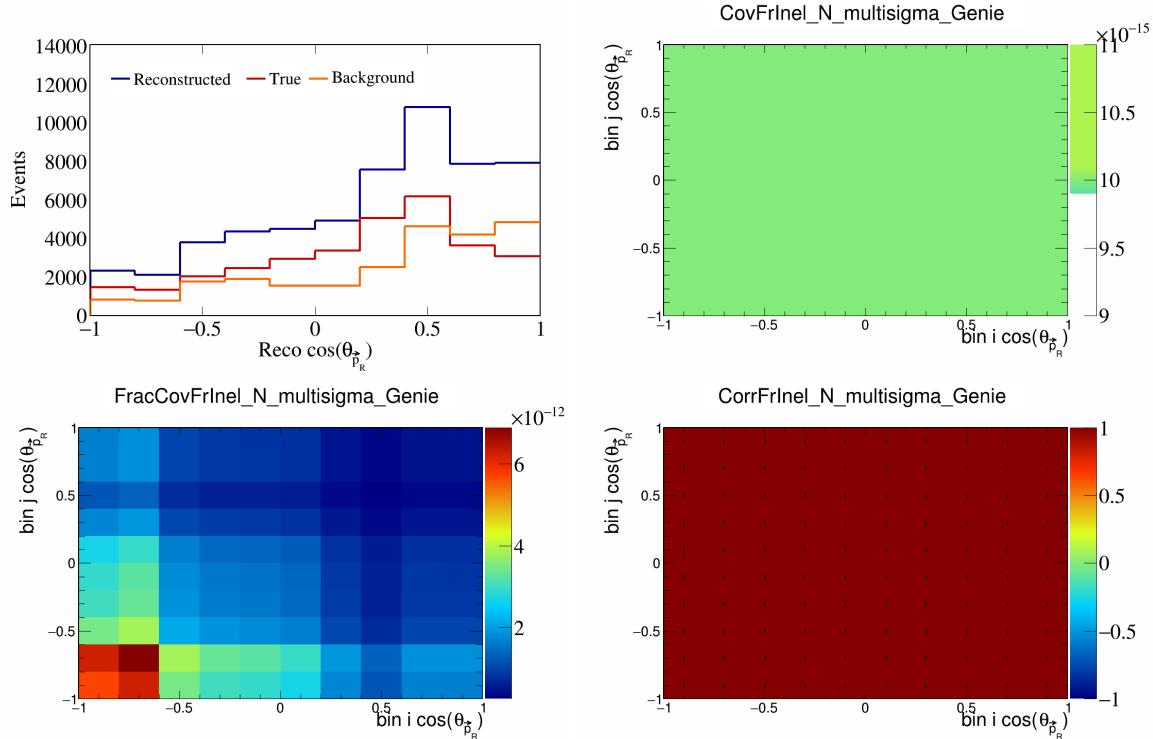


Figure 206: FrInelN variations for $\cos(\theta_{\vec{p}_R})$.

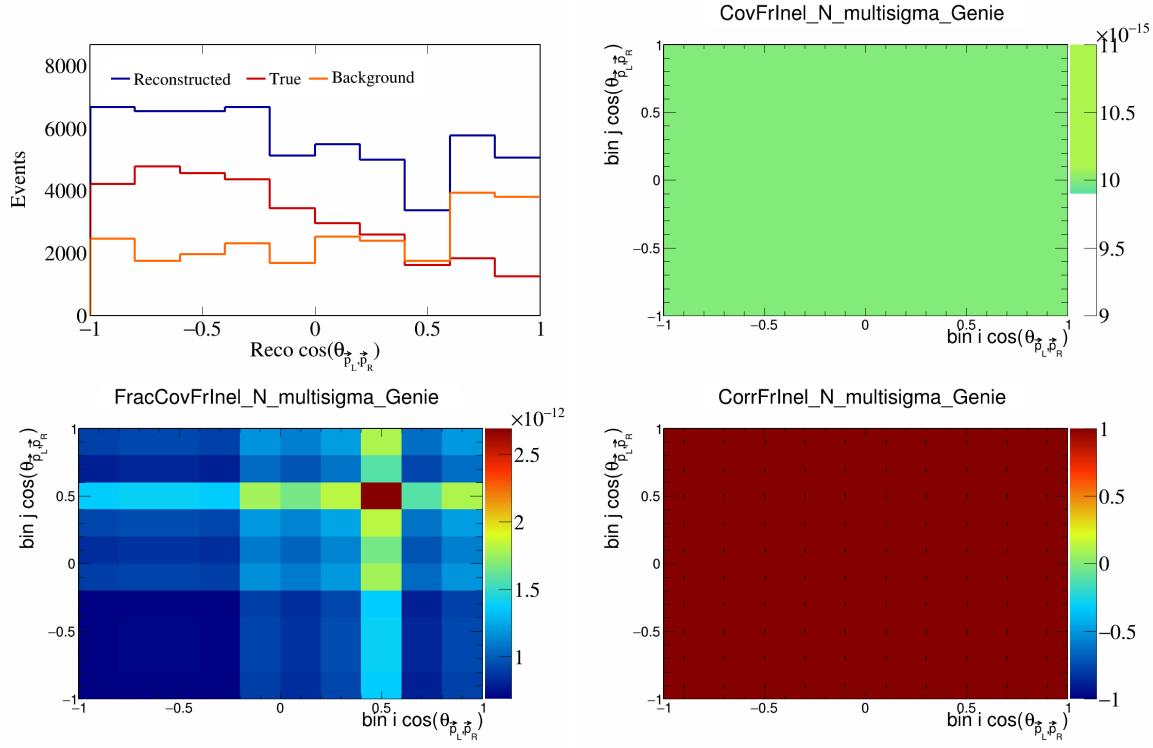


Figure 207: FrInelN variations for $\cos(\theta_{\vec{p}_L, \vec{p}_R})$.

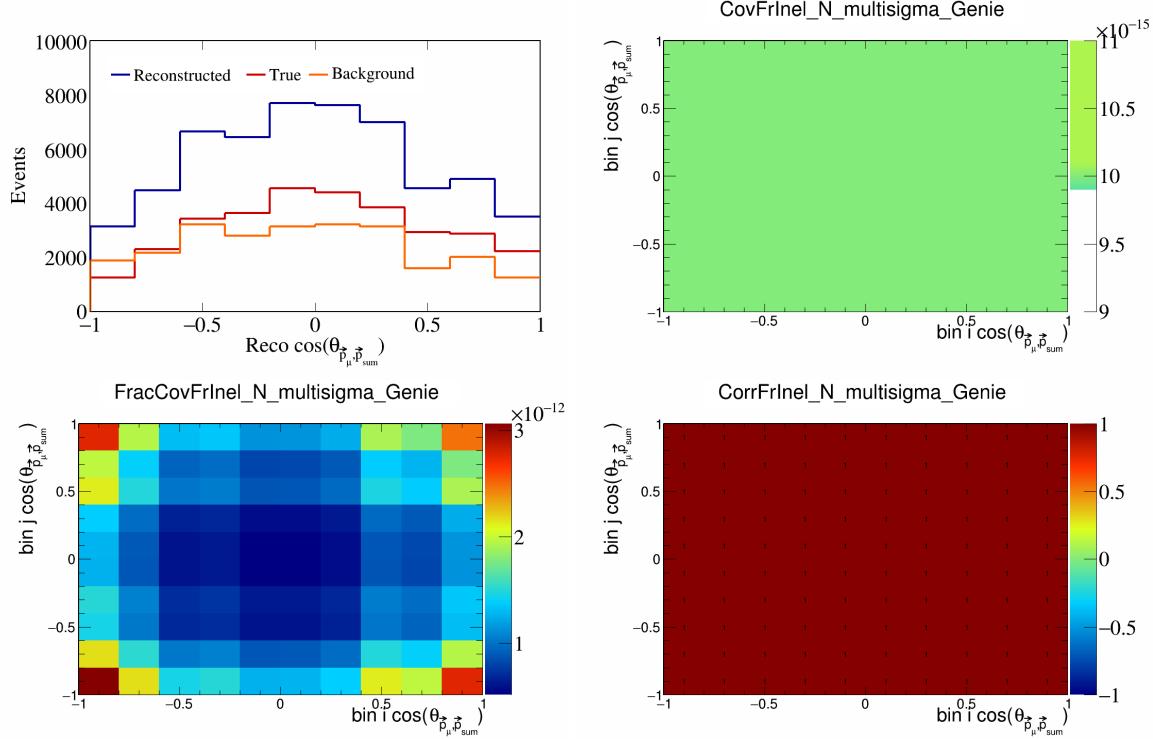


Figure 208: FrInelN variations for $\cos(\theta_{\vec{p}_\mu, \vec{p}_{\text{sum}}})$.

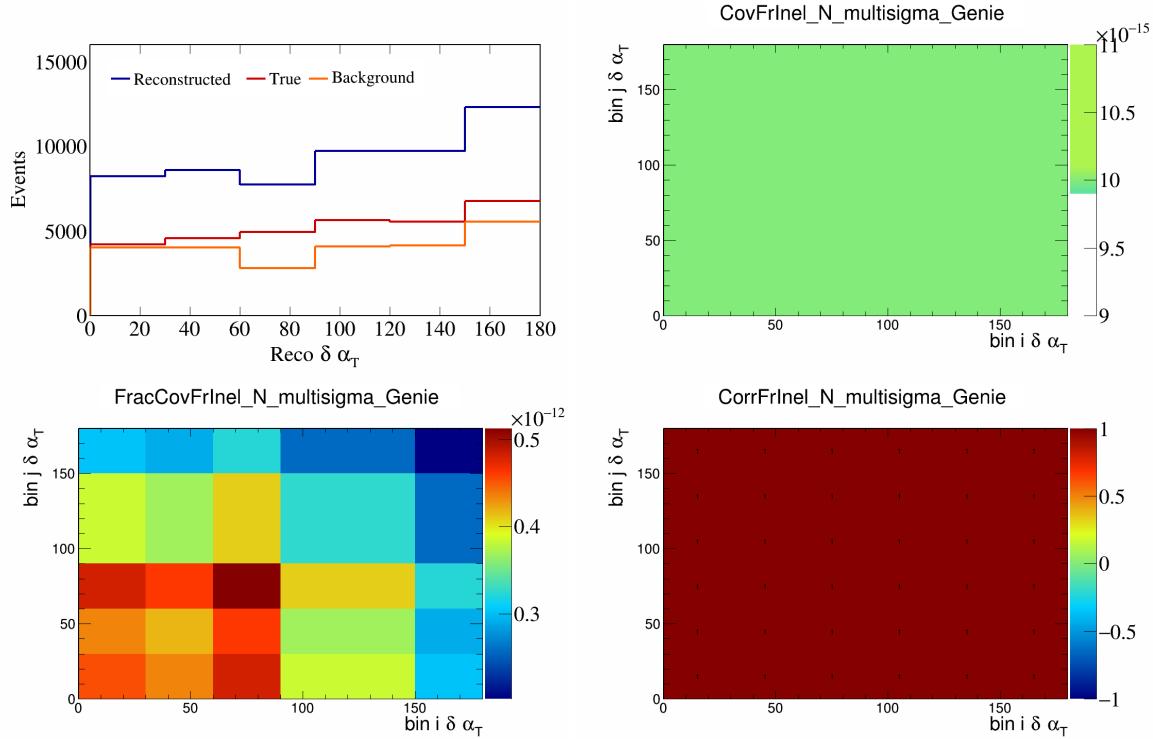


Figure 209: FrInelN variations for $\delta\alpha_T$.

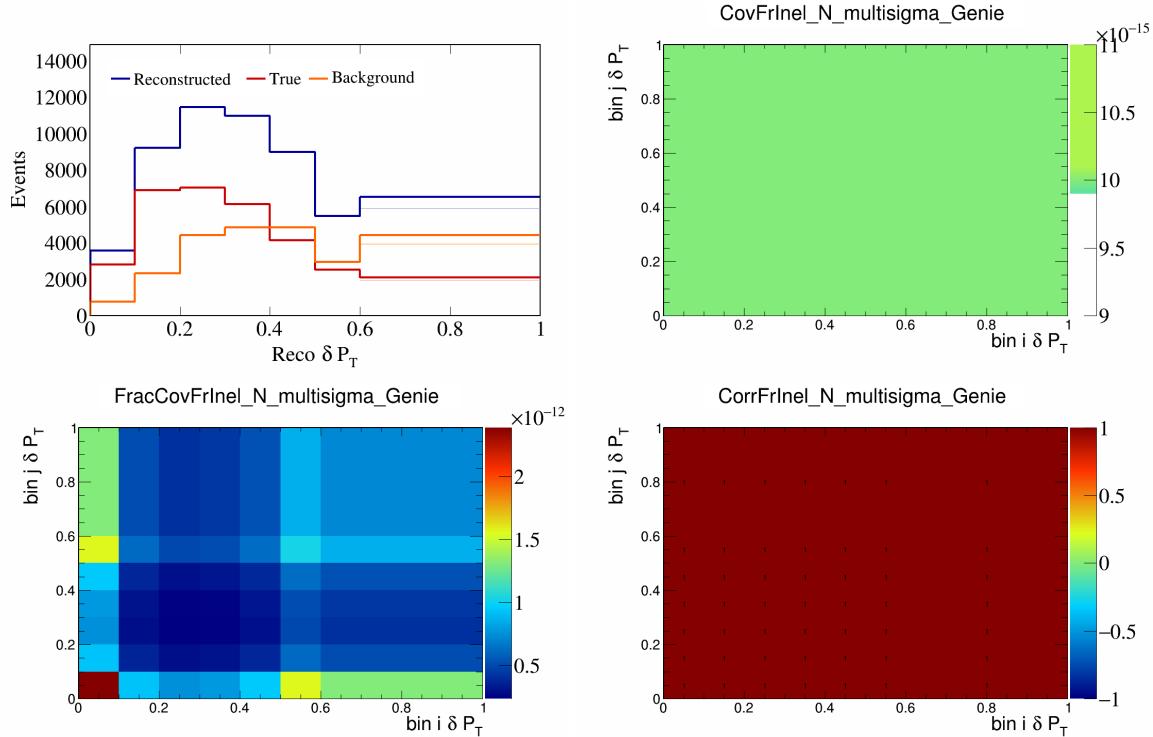


Figure 210: FrInelN variations for δP_T .

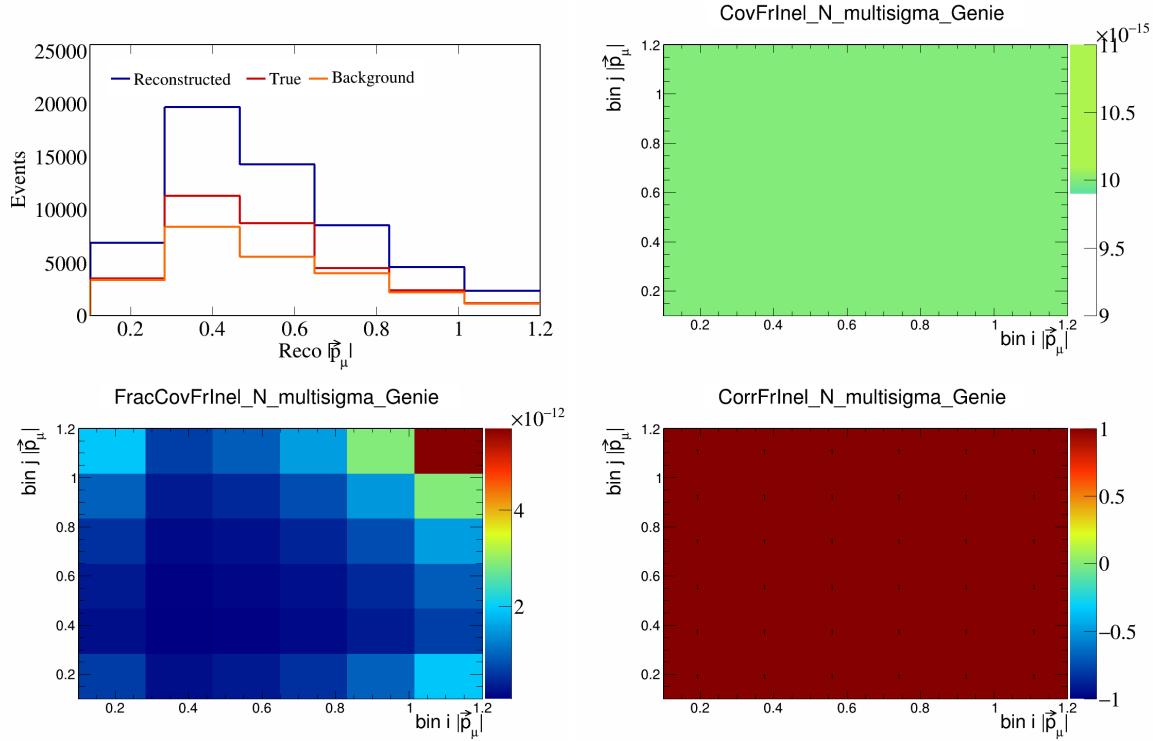


Figure 211: FrInelN variations for $|\vec{p}_\mu|$.

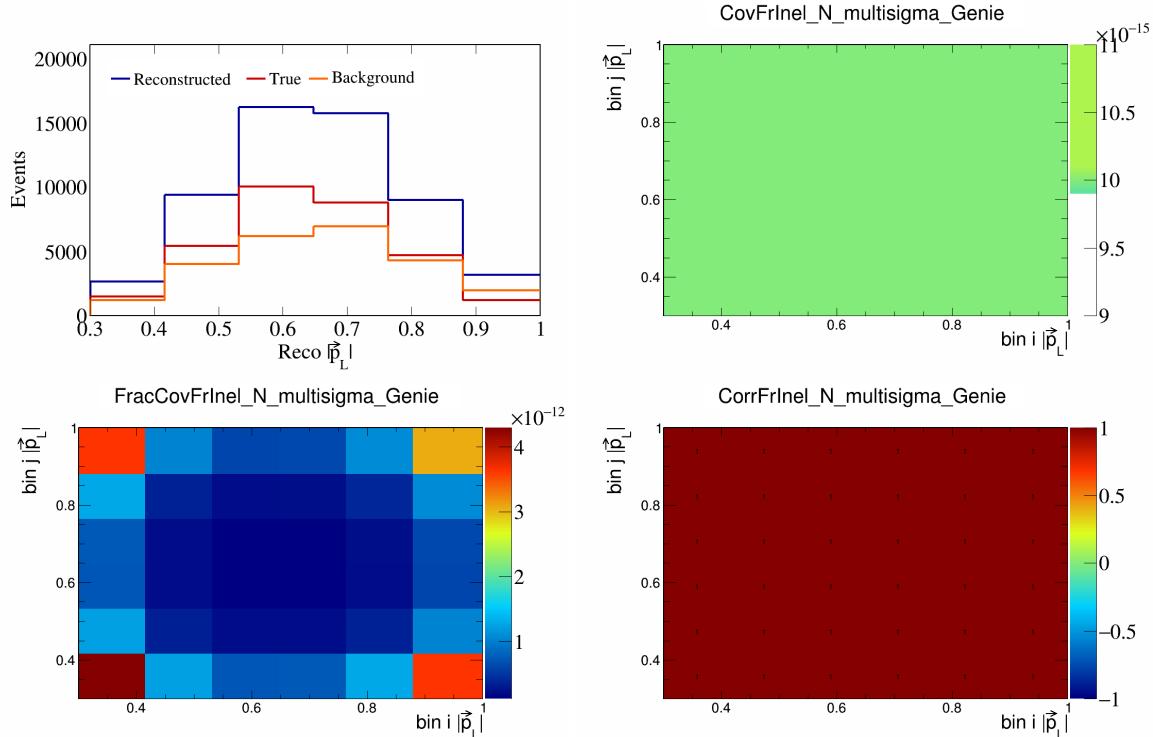


Figure 212: FrInelN variations for $|\vec{p}_L|$.

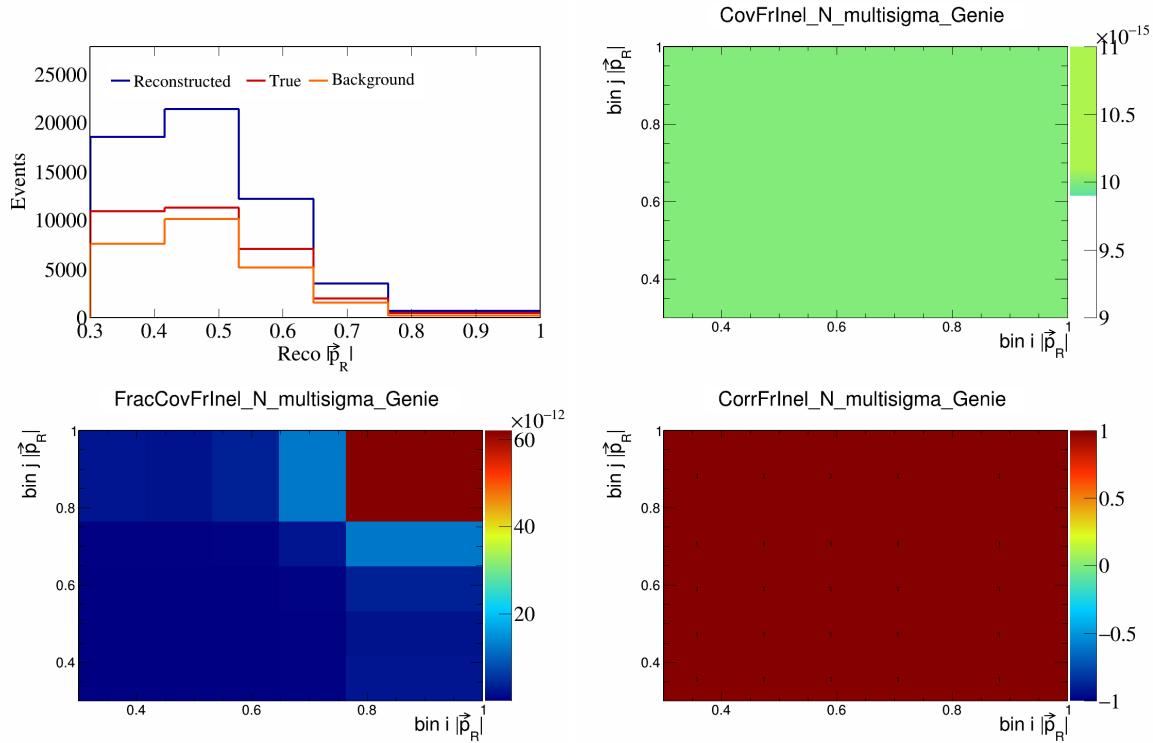


Figure 213: FrInelN variations for $|\vec{p}_R|$.

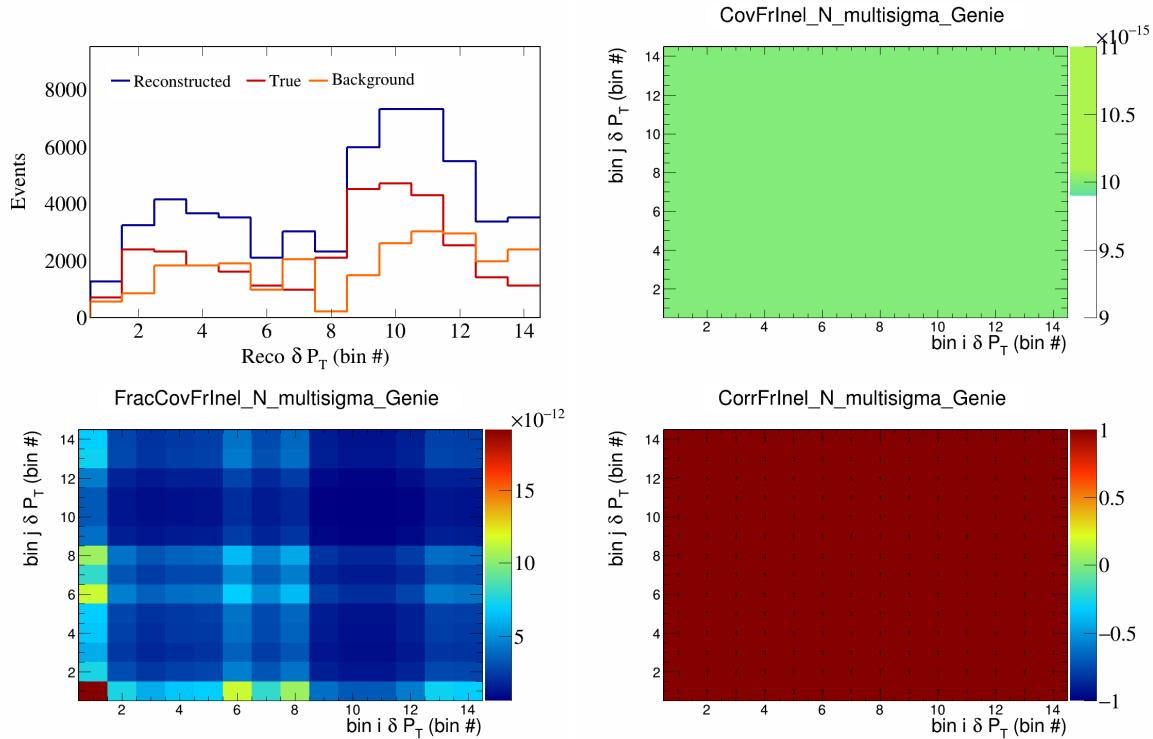


Figure 214: FrInelN variations for δP_T in $\cos(\theta_{\vec{p}_\mu})$.

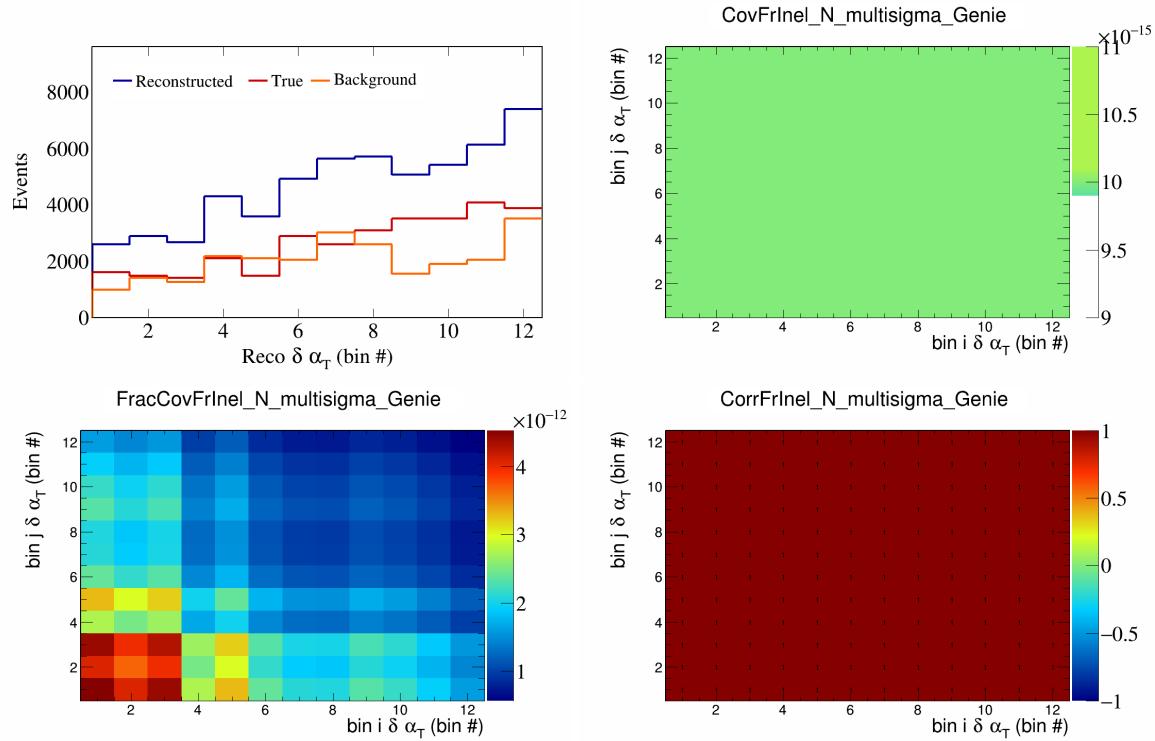


Figure 215: FrInelN variations for $\delta\alpha_T$ in $\cos(\theta_{\vec{p}_\mu})$.

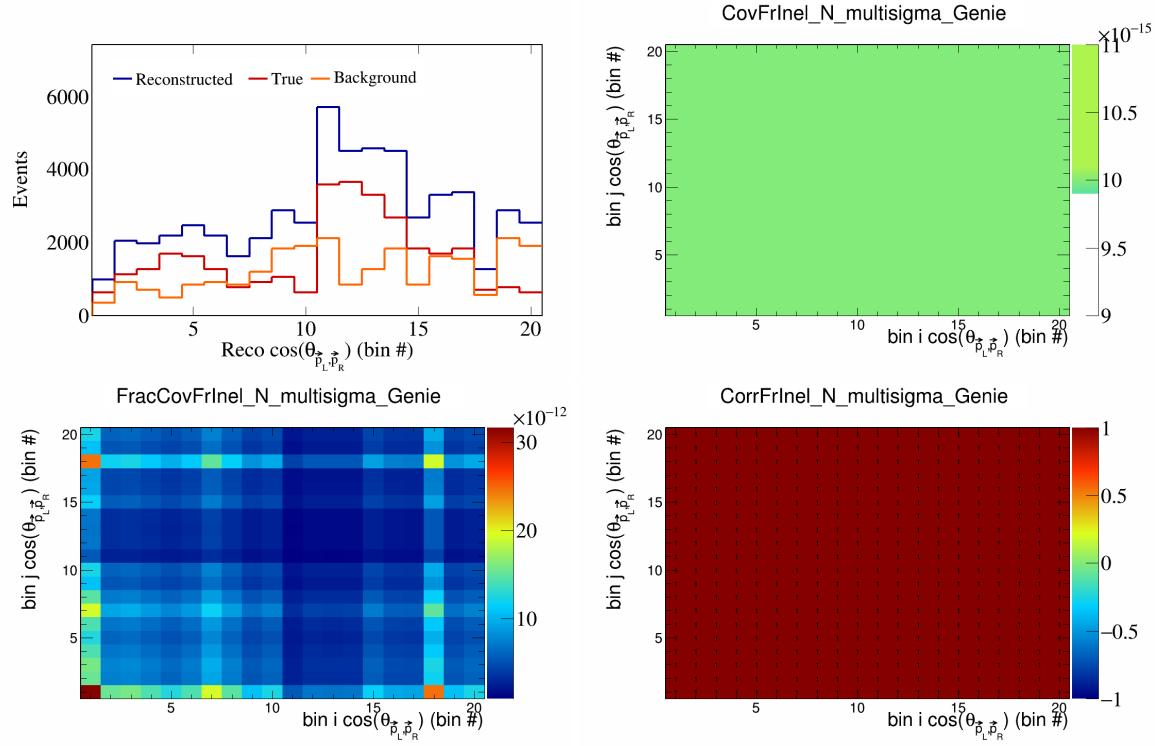


Figure 216: FrInelN variations for $\cos(\theta_{\vec{p}_L, \vec{p}_R})$ in $\cos(\theta_{\vec{p}_\mu})$.

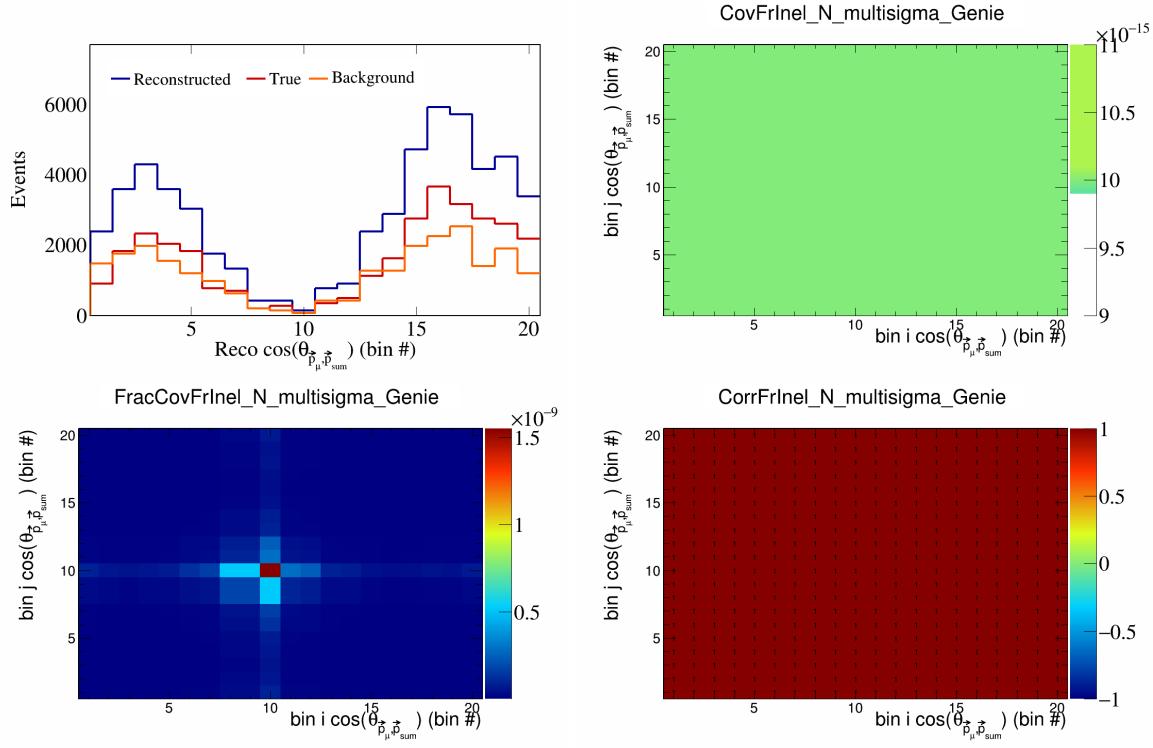


Figure 217: FrInelN variations for $\cos(\theta_{\vec{p}_\mu, \vec{p}_{\text{sum}}})$ in $\cos(\theta_{\vec{p}_\mu})$.

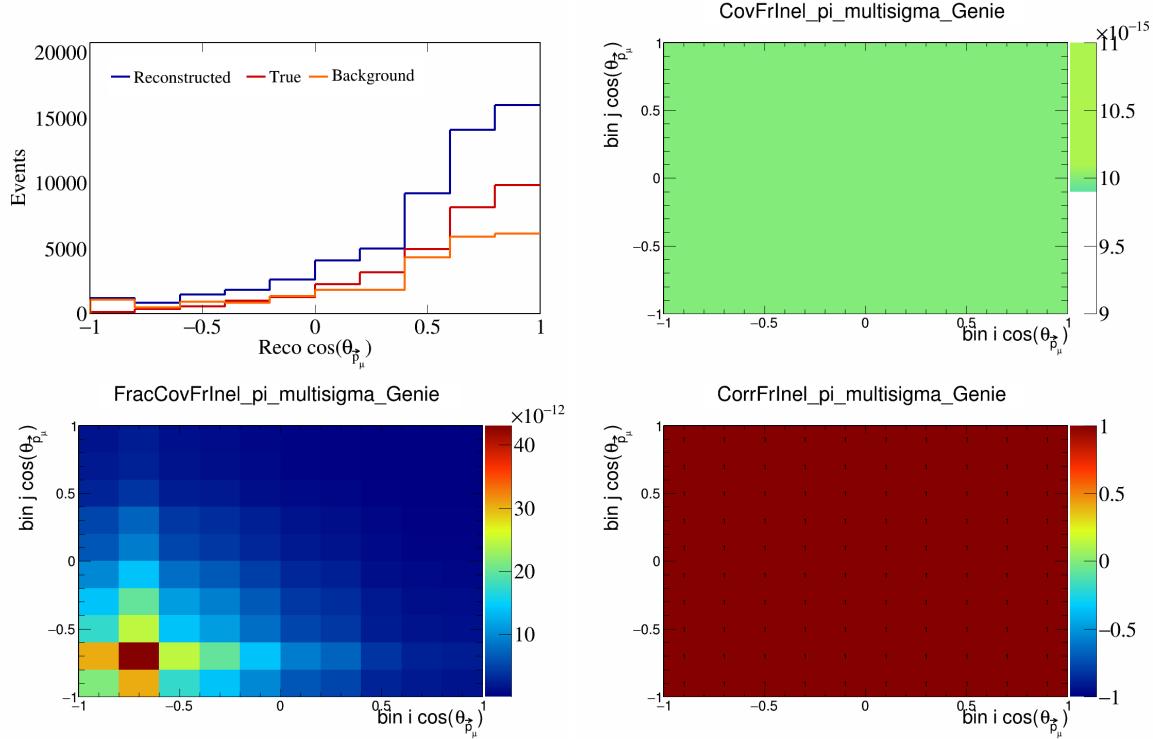


Figure 218: FrInelpi variations for $\cos(\theta_{\vec{p}_\mu})$.

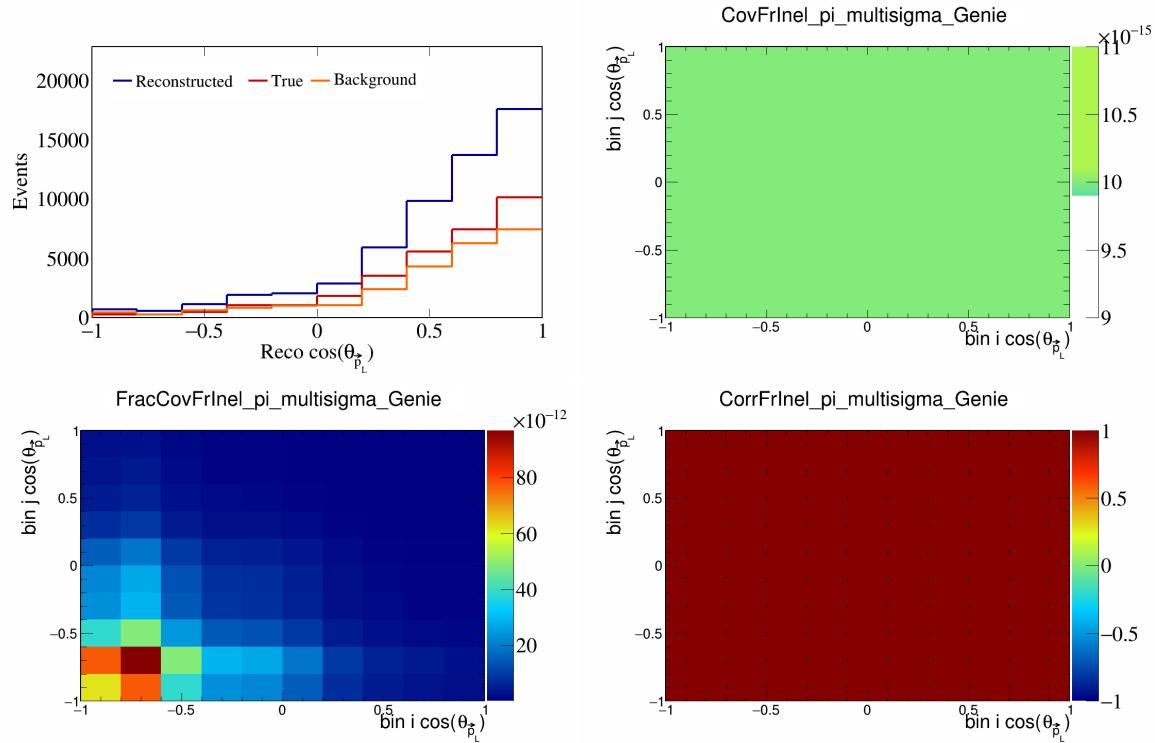


Figure 219: FrInelpi variations for $\cos(\theta_{\vec{p}_L})$.

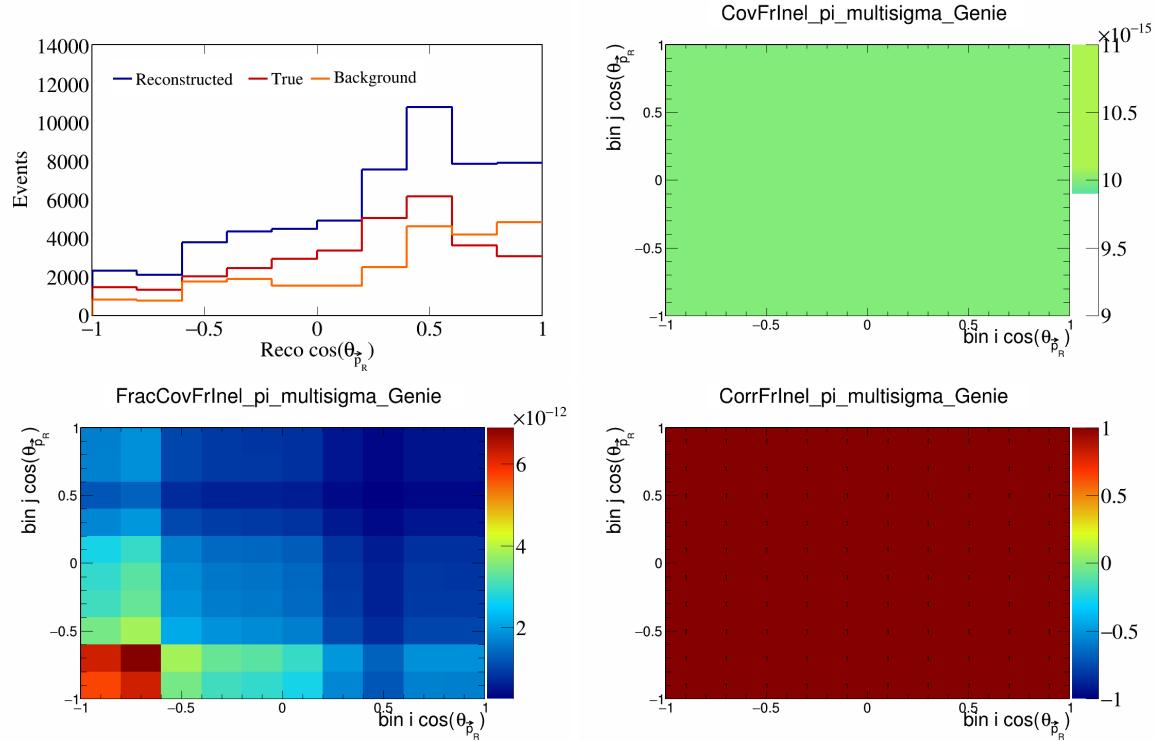


Figure 220: FrInelpi variations for $\cos(\theta_{\vec{p}_R})$.

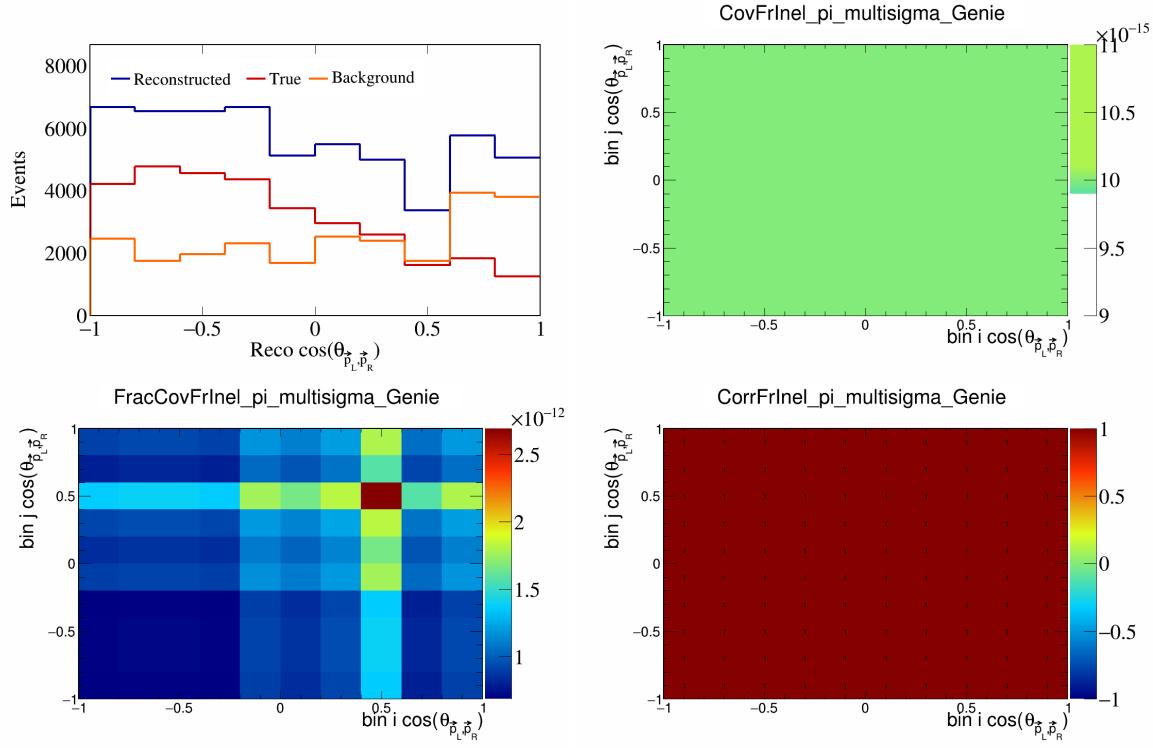


Figure 221: FrInelpi variations for $\cos(\theta_{\vec{p}_L, \vec{p}_R})$.

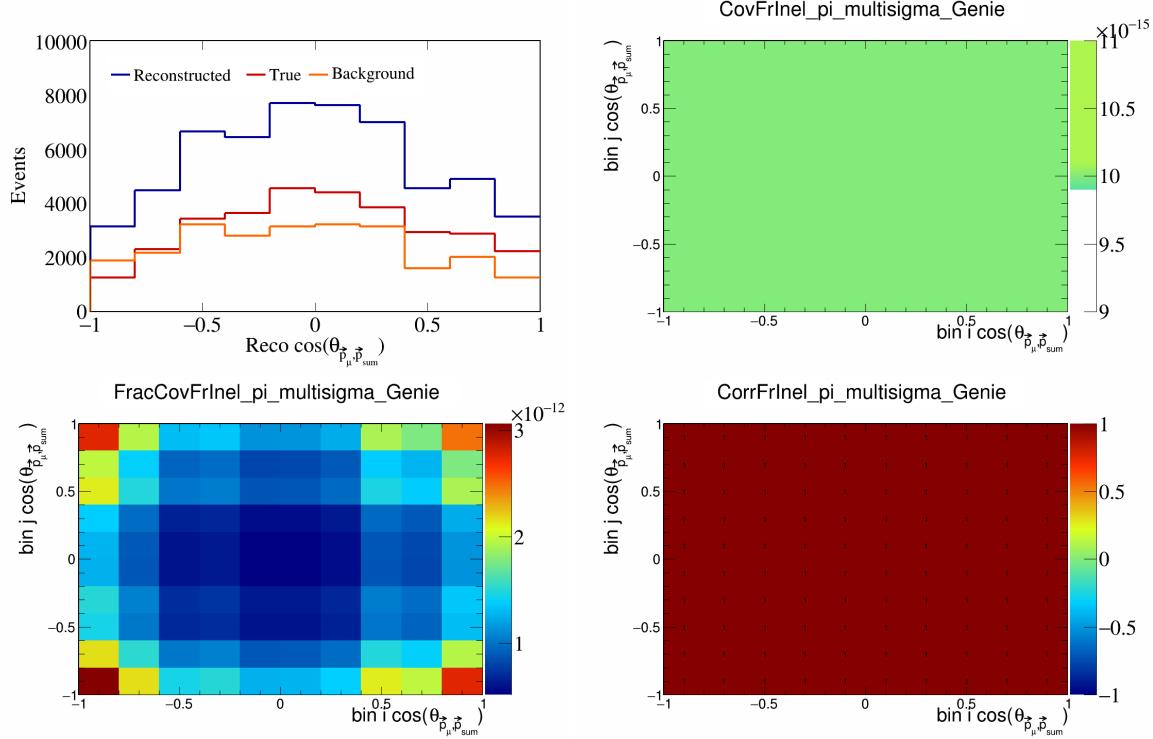


Figure 222: FrInelpi variations for $\cos(\theta_{\vec{p}_\mu, \vec{p}_{\text{sum}}})$.

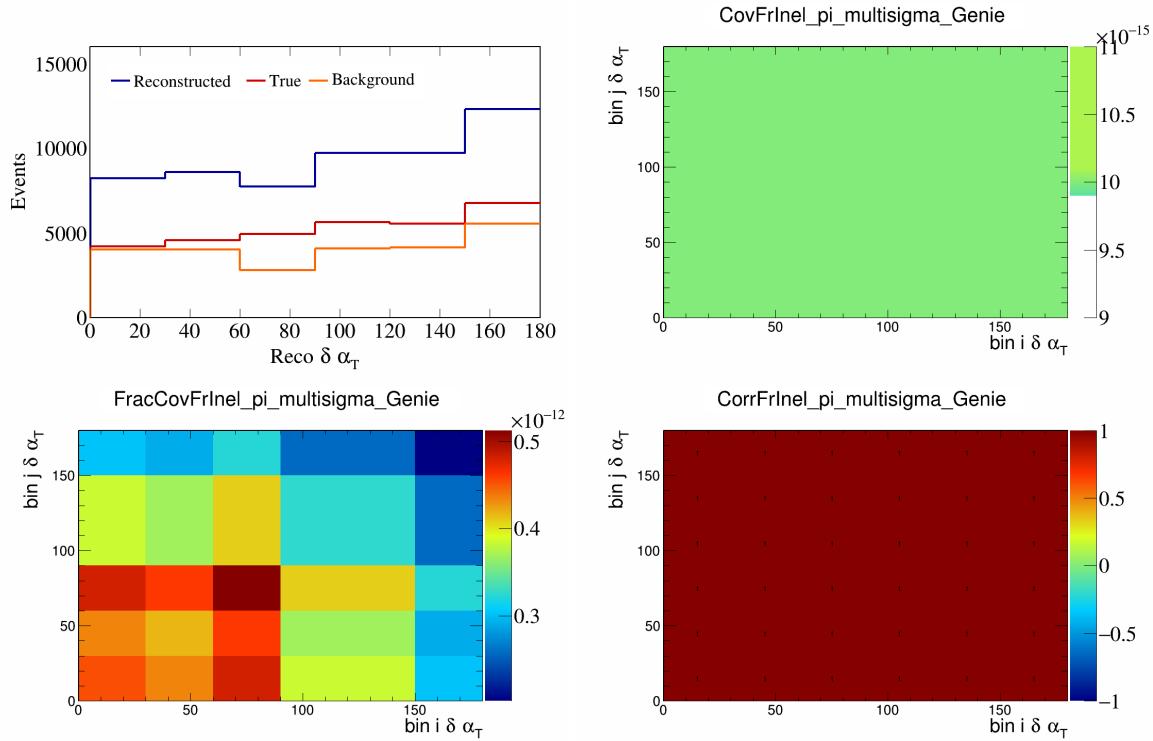


Figure 223: FrInelpi variations for $\delta\alpha_T$.

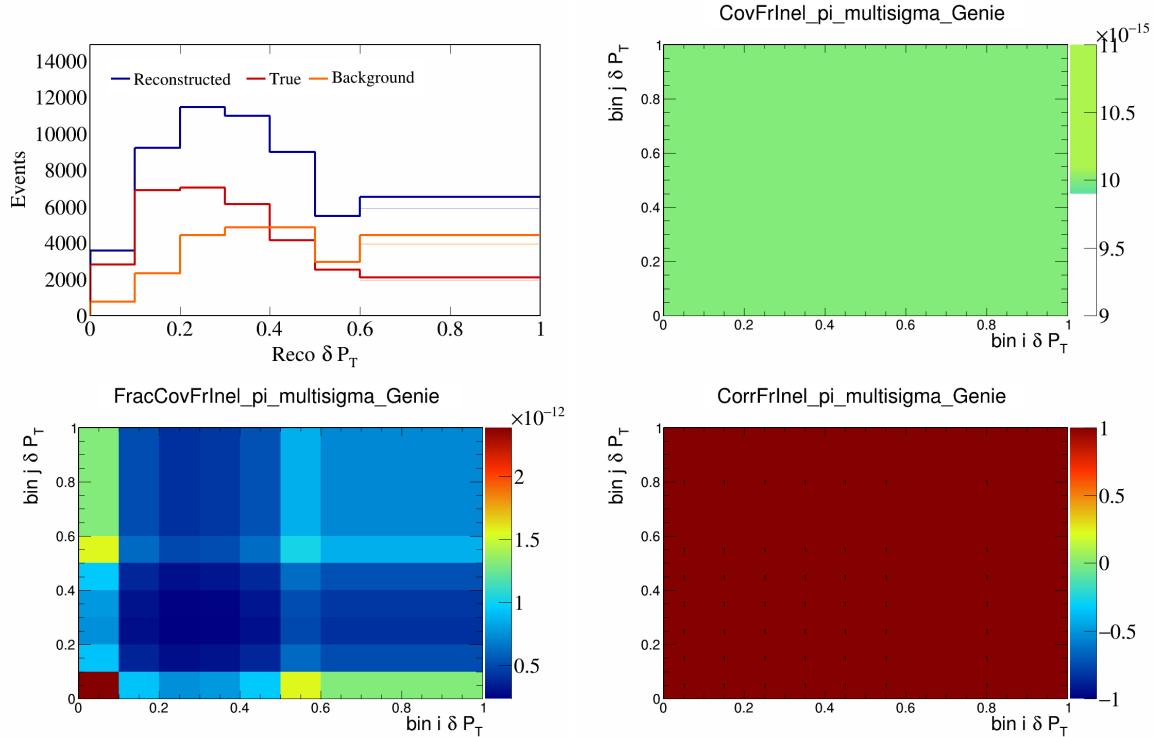


Figure 224: FrInelpi variations for δP_T .

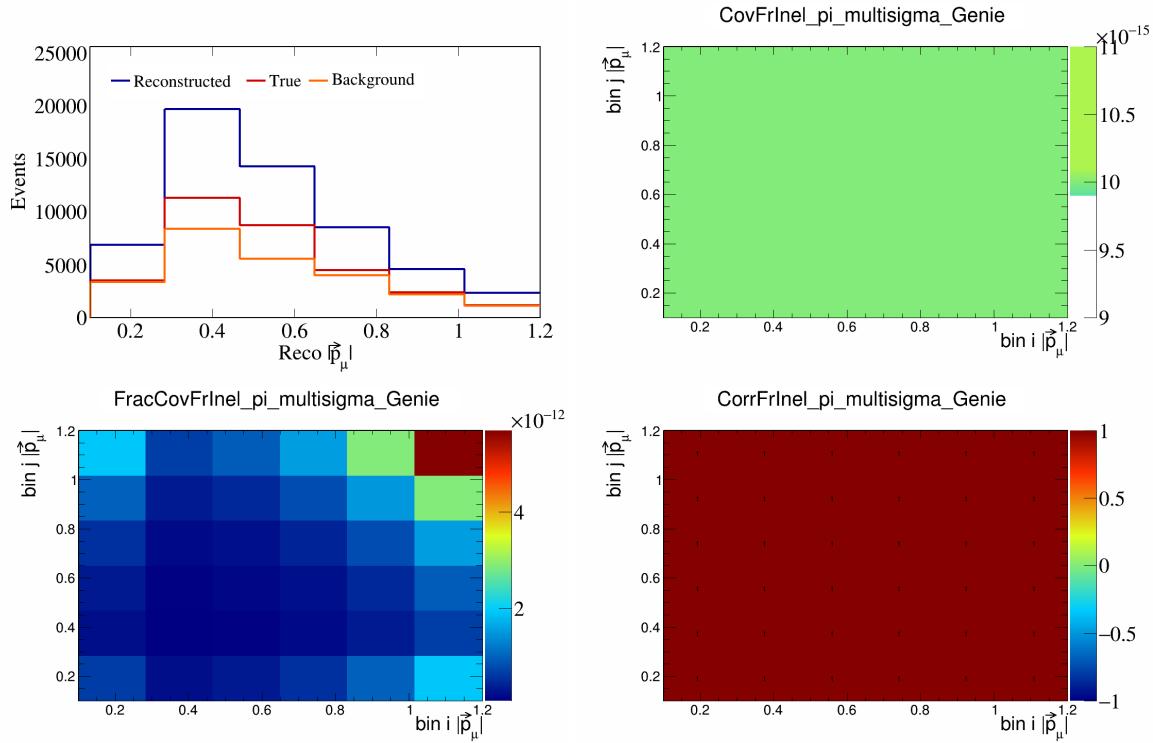


Figure 225: FrInelpi variations for $|\vec{p}_\mu|$.

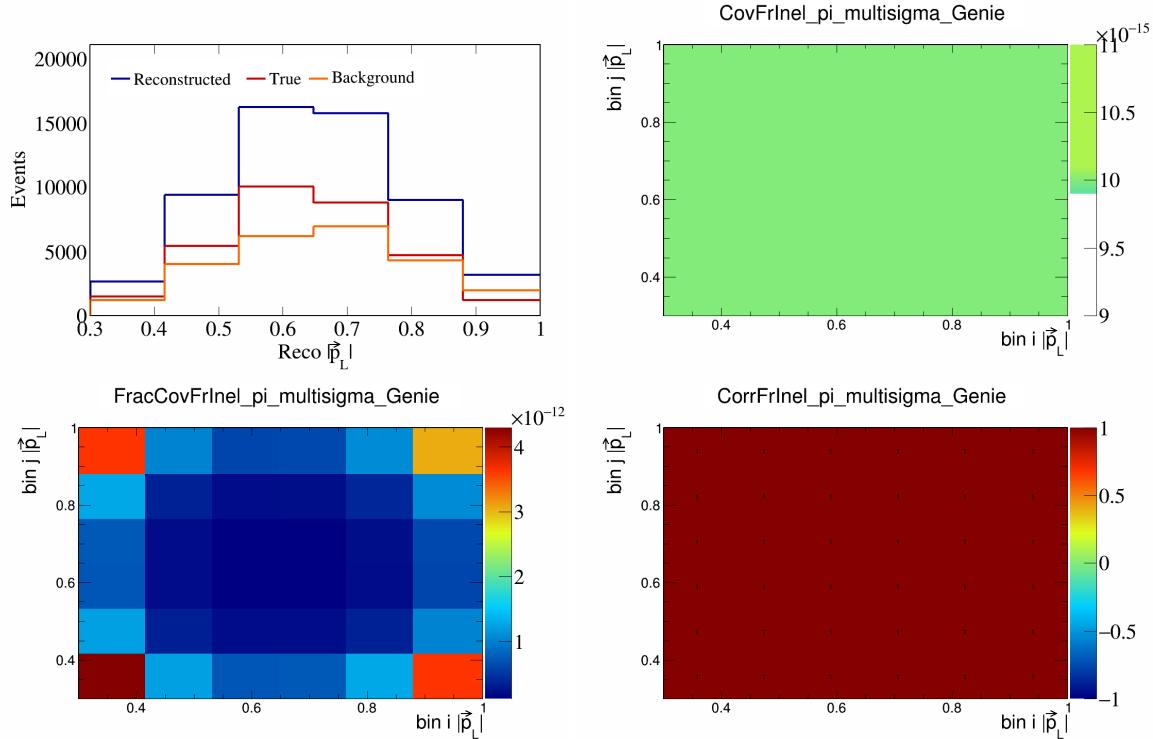


Figure 226: FrInelpi variations for $|\vec{p}_L|$.

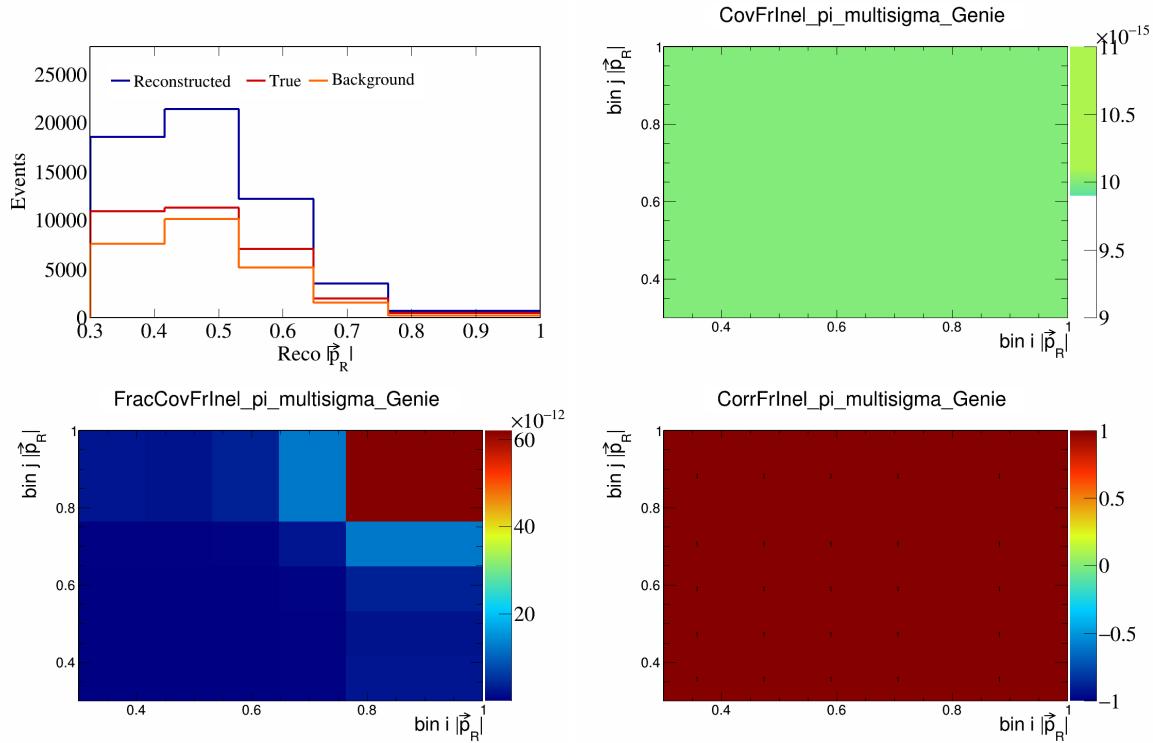


Figure 227: FrInelpi variations for $|\vec{p}_R|$.

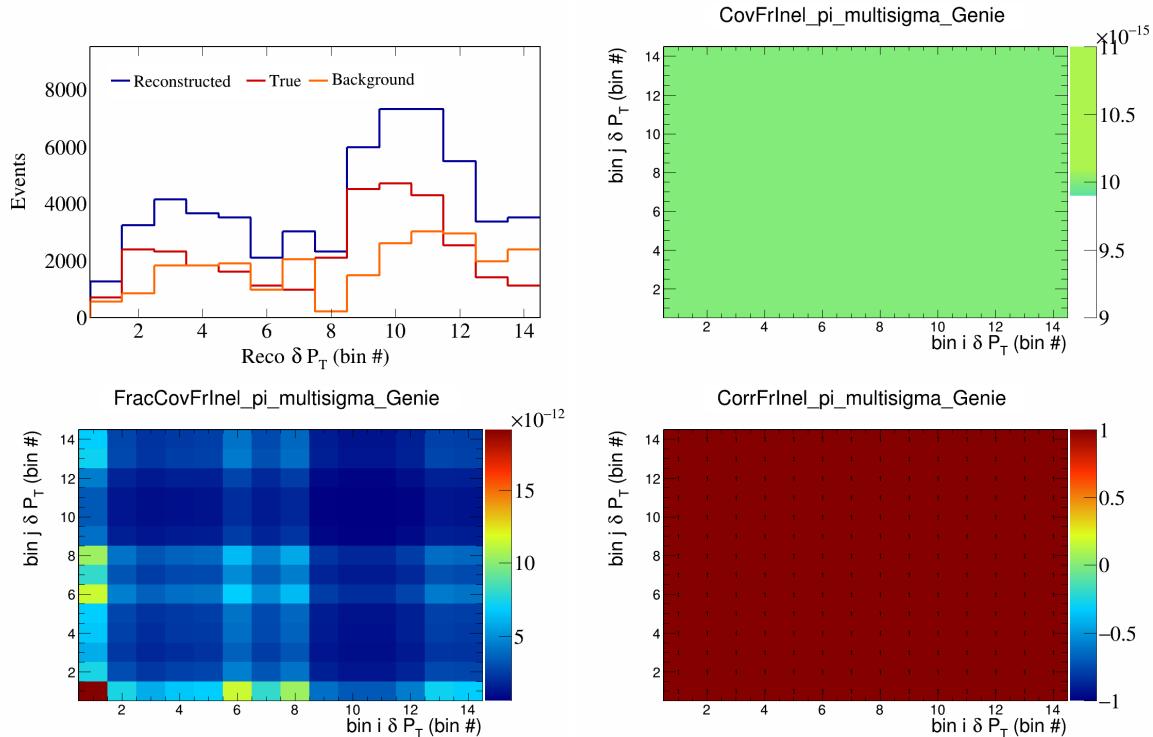


Figure 228: FrInelpi variations for δP_T in $\cos(\theta_{\vec{p}_\mu})$.

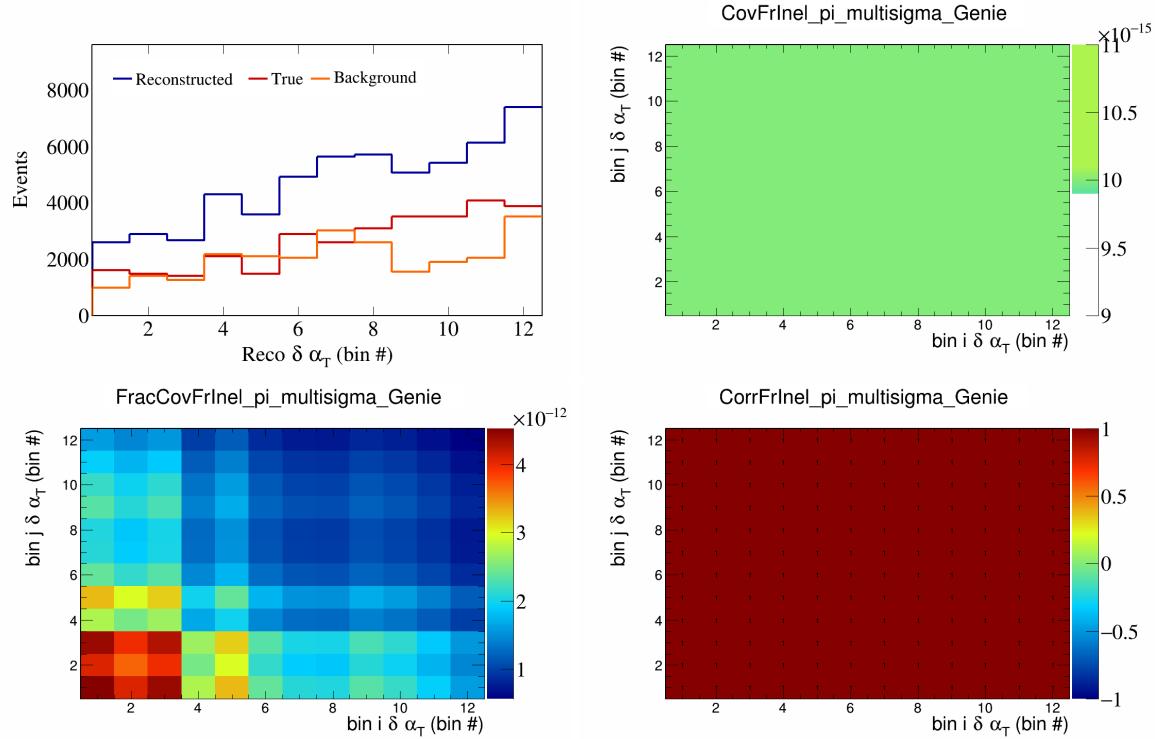


Figure 229: FrInelpi variations for $\delta\alpha_T$ in $\cos(\theta_{\vec{p}_\mu})$.

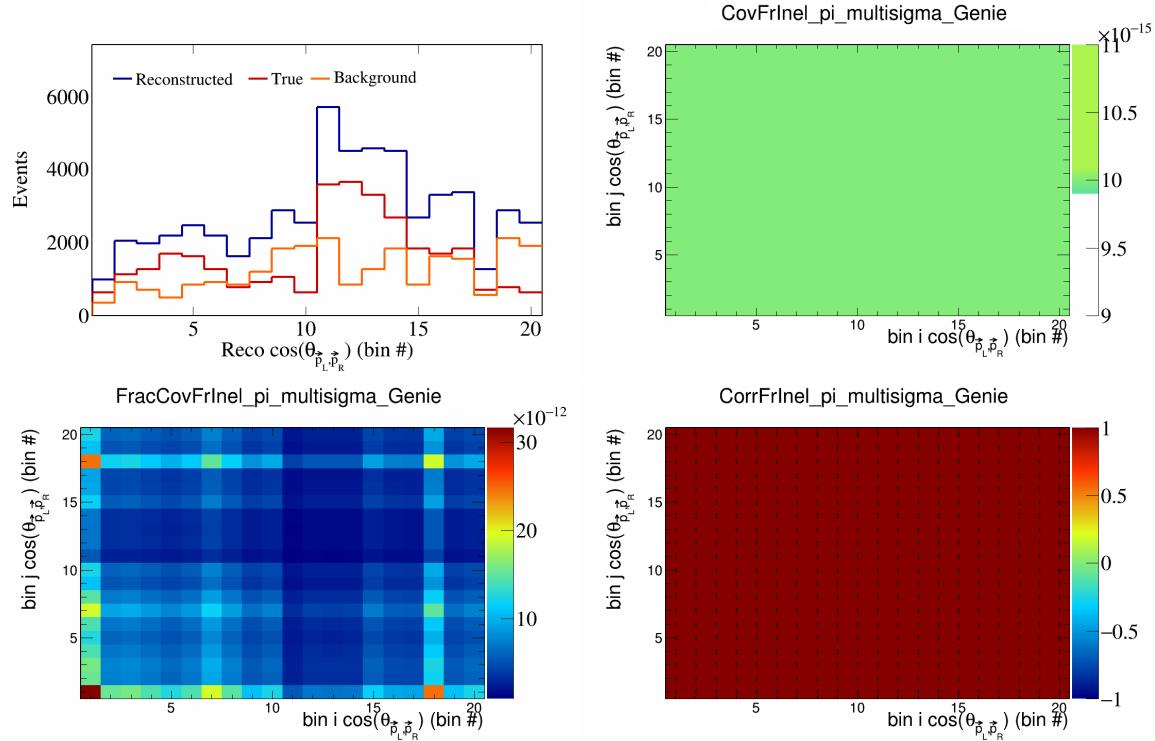


Figure 230: FrInelpi variations for $\cos(\theta_{\vec{p}_L, \vec{p}_R})$ in $\cos(\theta_{\vec{p}_\mu})$.

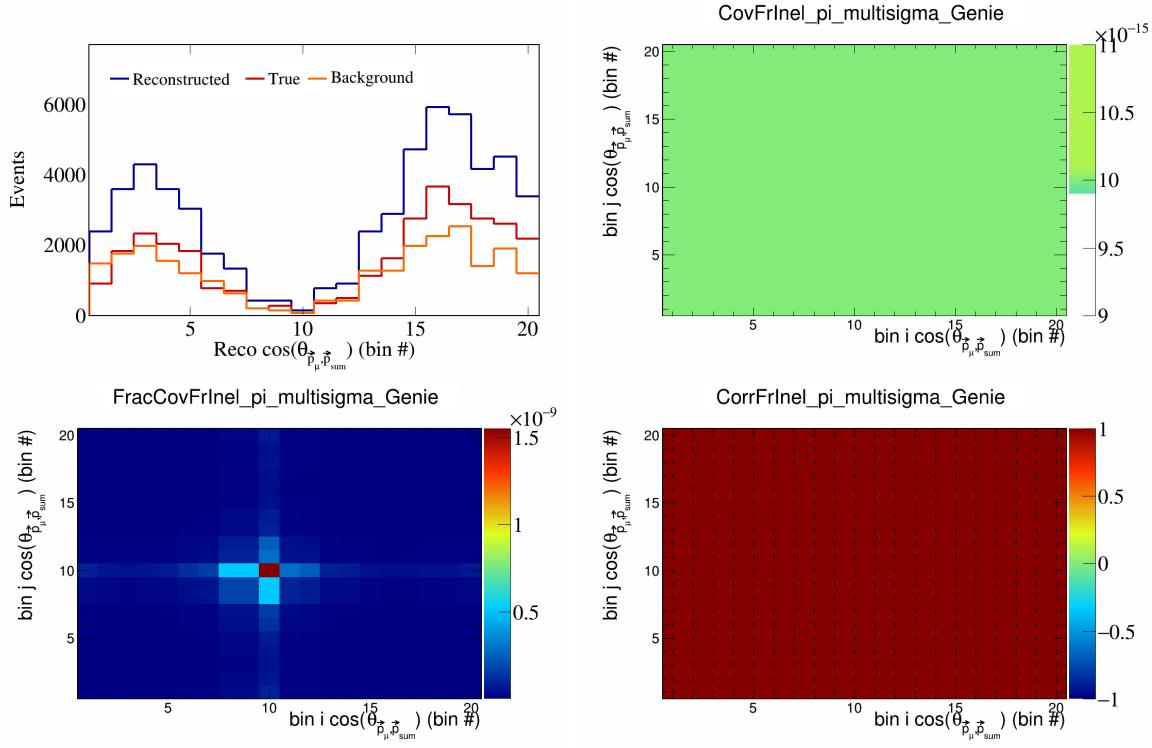


Figure 231: FrInelpi variations for $\cos(\theta_{\vec{p}_\mu, \vec{p}_{\text{sum}}})$ in $\cos(\theta_{\vec{p}_\mu})$.

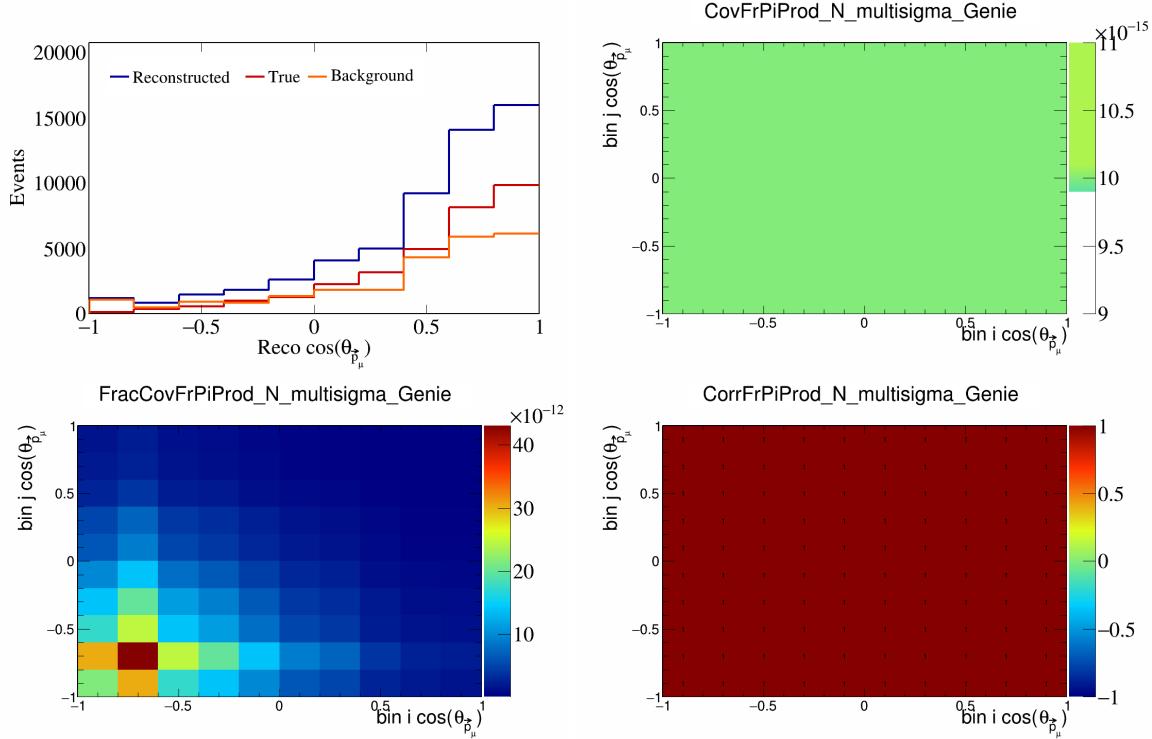


Figure 232: FrPiProdN variations for $\cos(\theta_{\vec{p}_\mu})$.

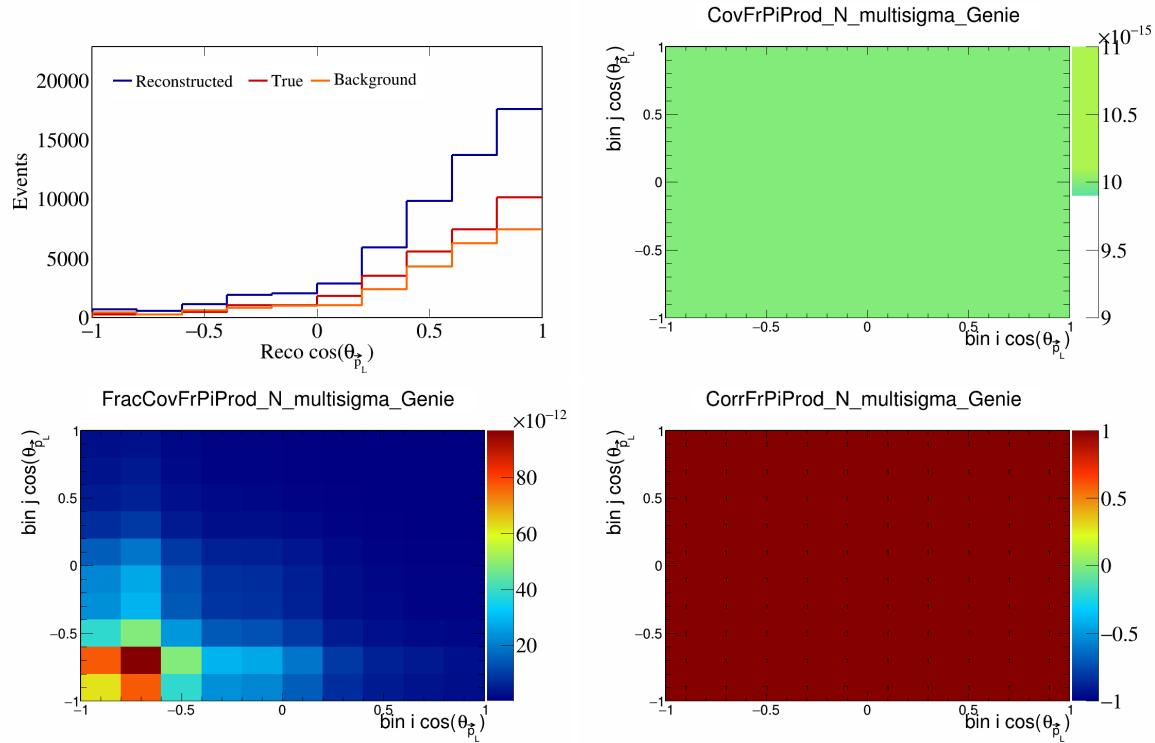


Figure 233: FrPiProdN variations for $\cos(\theta_{\vec{p}_L})$.

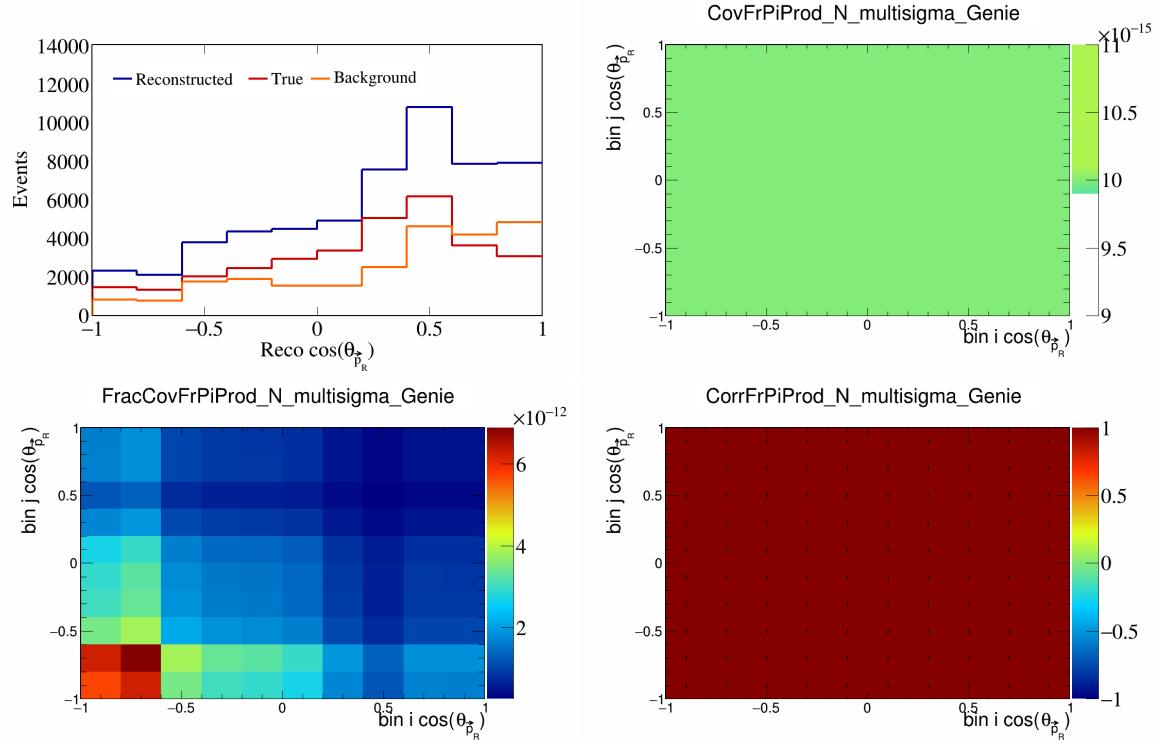


Figure 234: FrPiProdN variations for $\cos(\theta_{\vec{p}_R})$.

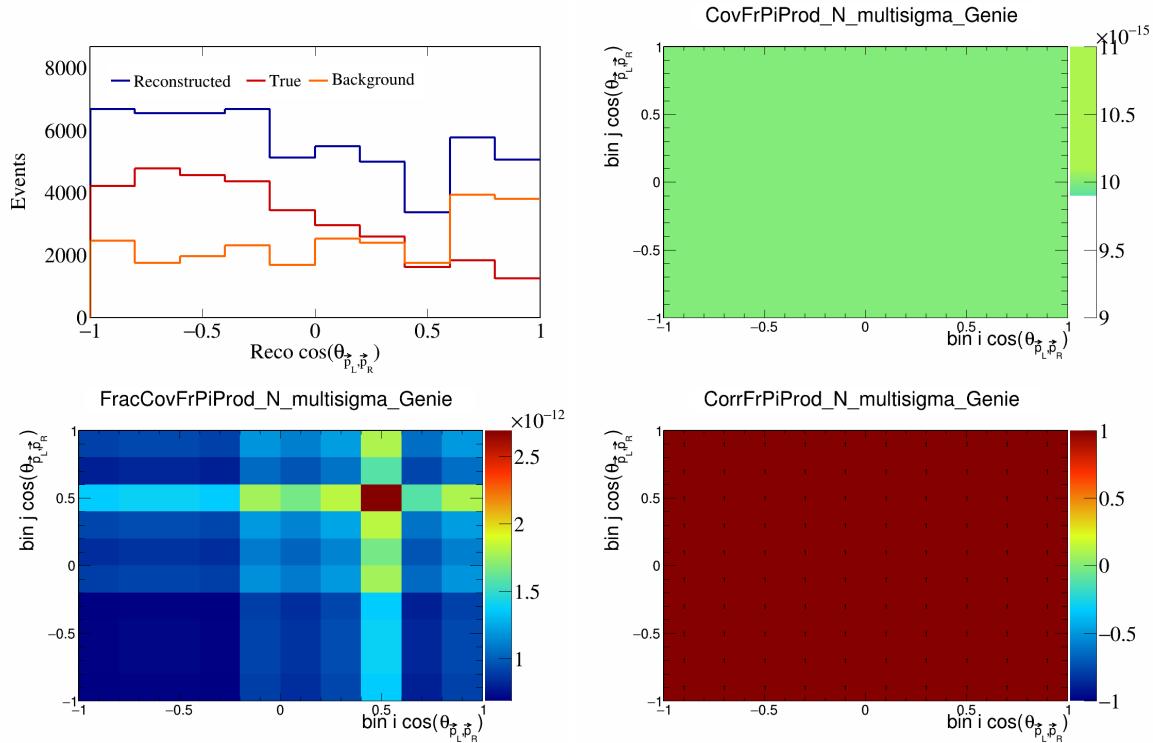


Figure 235: FrPiProdN variations for $\cos(\theta_{\vec{p}_L, \vec{p}_R})$.

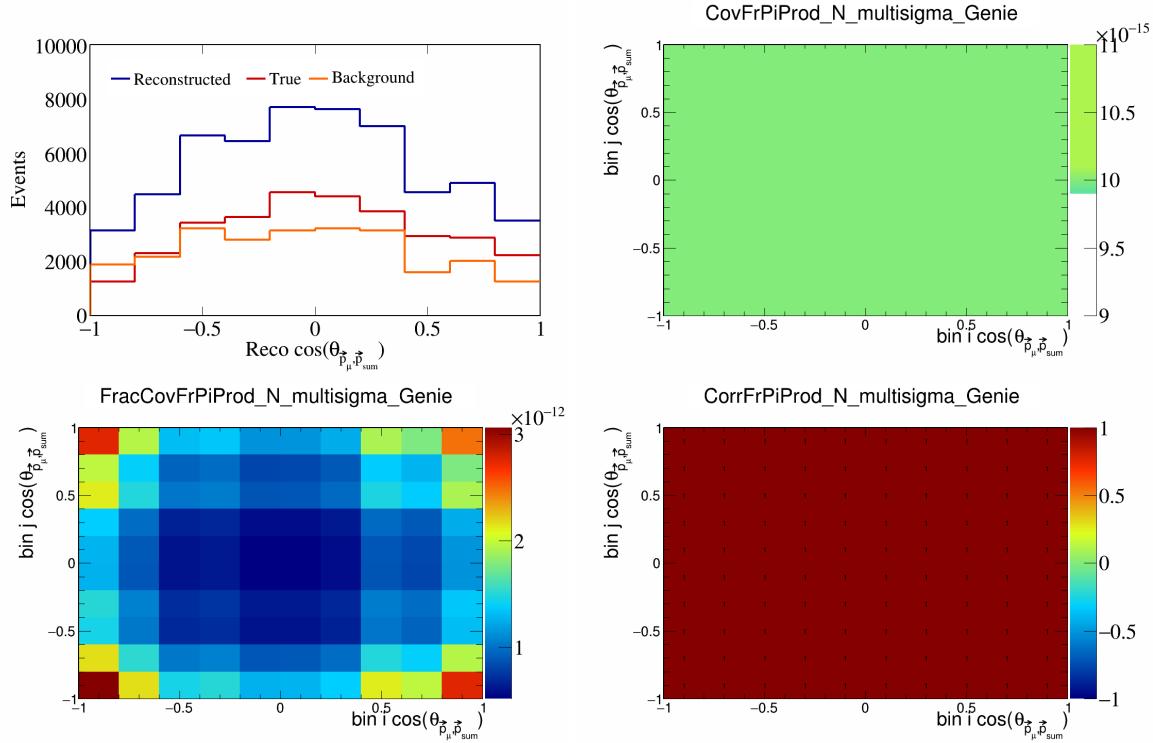


Figure 236: FrPiProdN variations for $\cos(\theta_{\vec{p}_\mu, \vec{p}_{\text{sum}}})$.

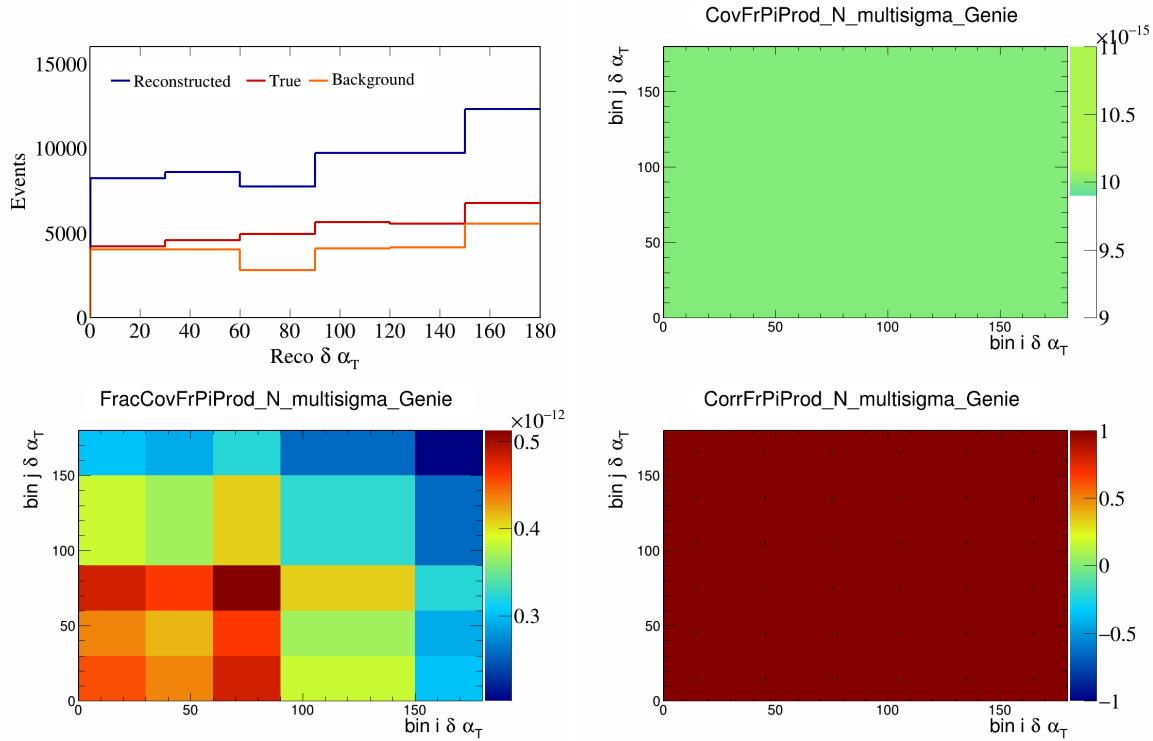


Figure 237: FrPiProdN variations for $\delta\alpha_T$.

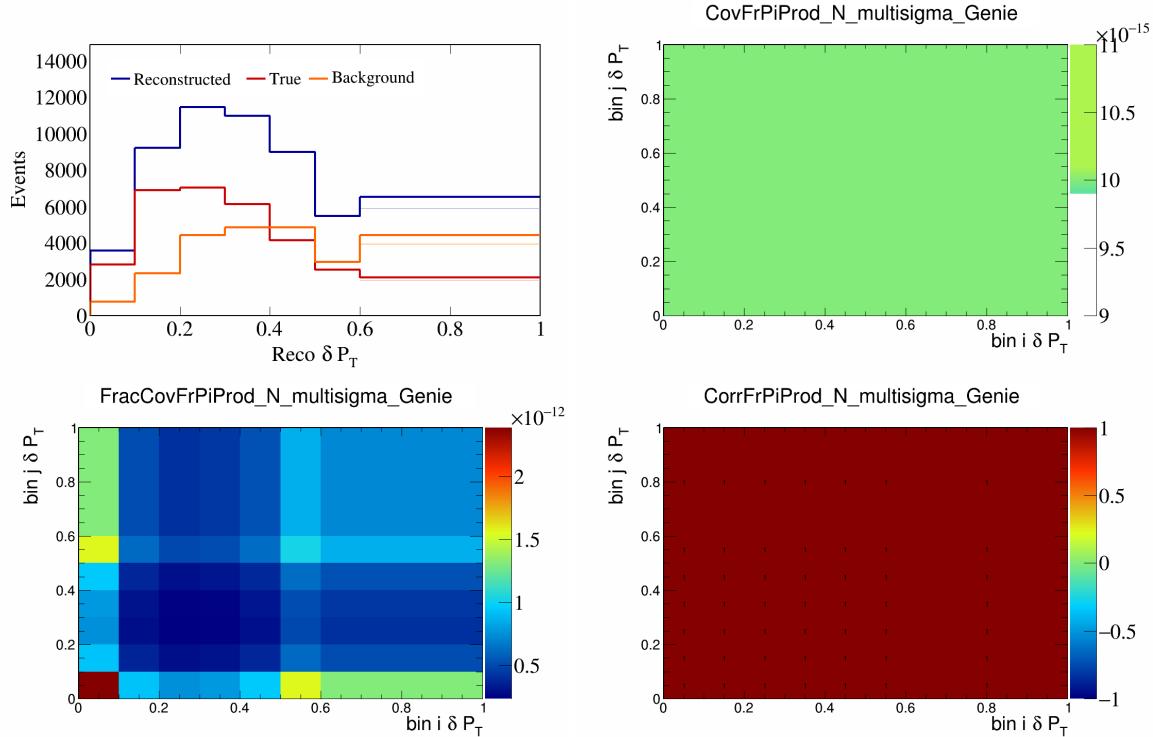


Figure 238: FrPiProdN variations for δP_T .

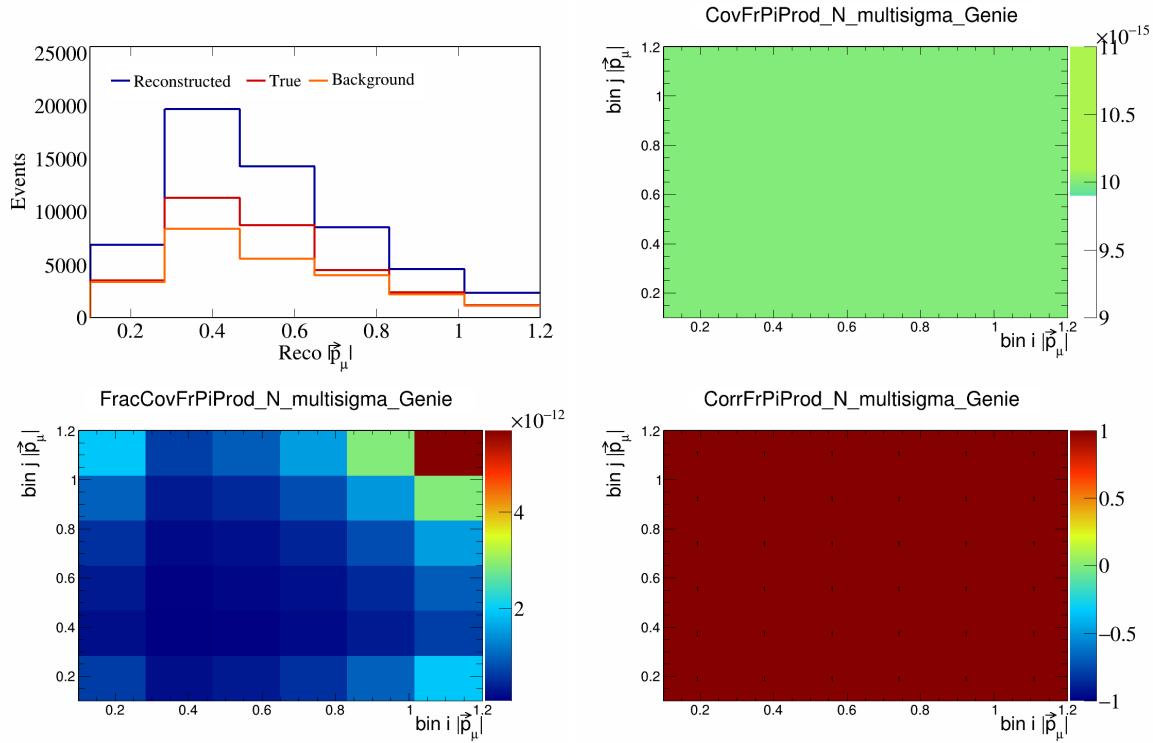


Figure 239: FrPiProdN variations for $|\vec{p}_\mu|$.

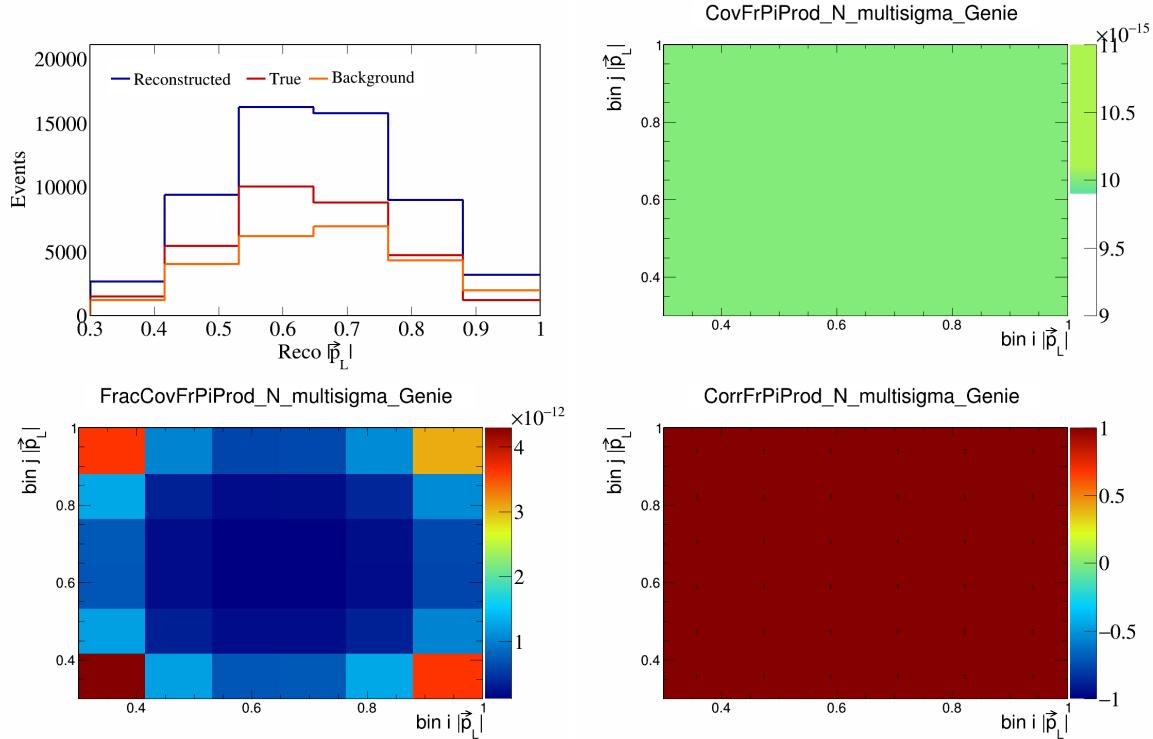


Figure 240: FrPiProdN variations for $|\vec{p}_L|$.

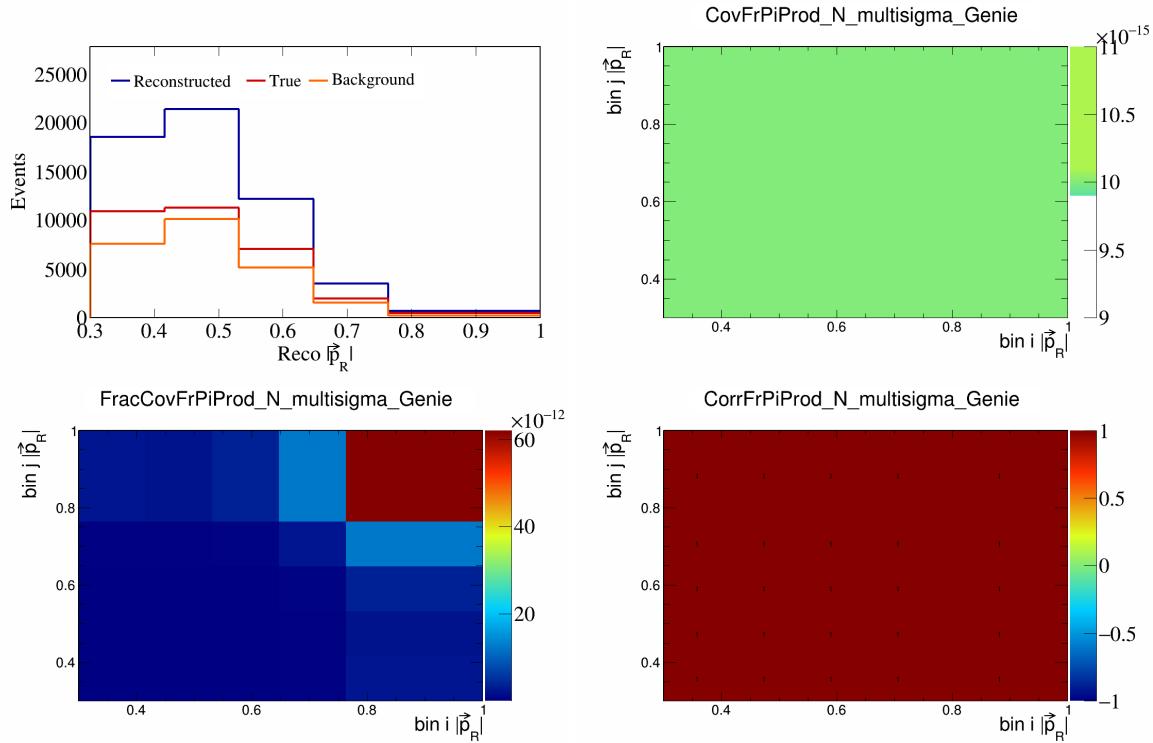


Figure 241: FrPiProdN variations for $|\vec{p}_R|$.

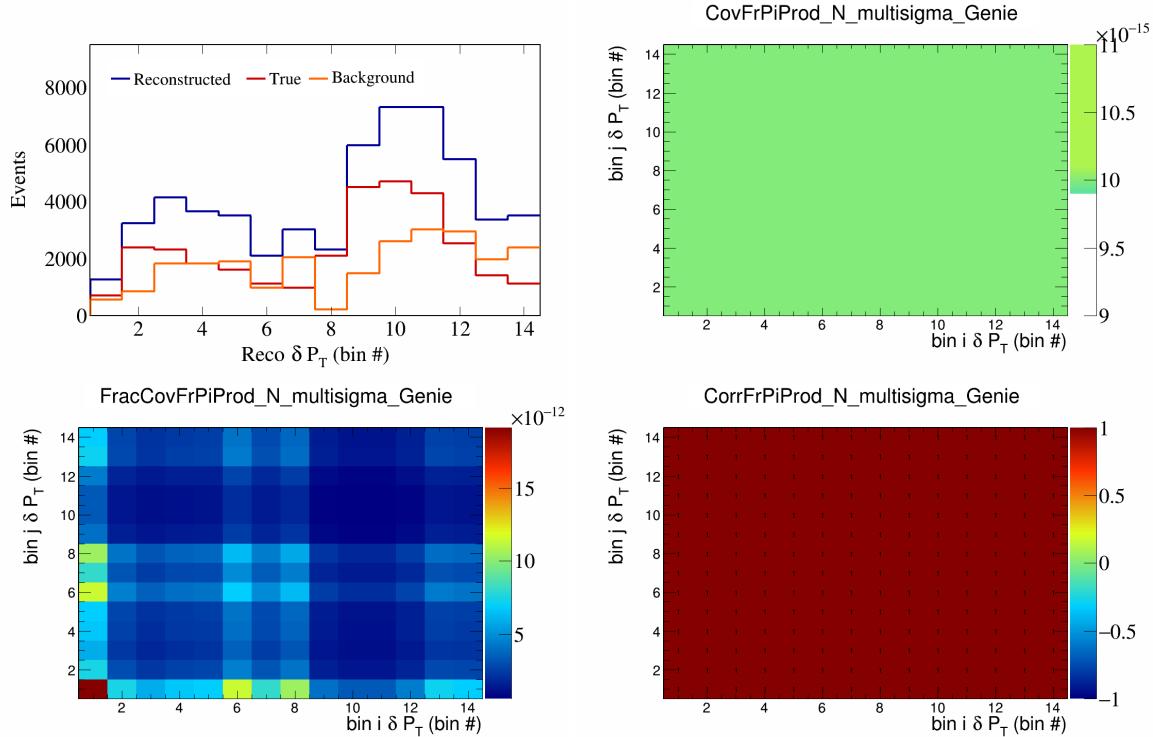


Figure 242: FrPiProdN variations for δP_T in $\cos(\theta_{\vec{p}_\mu})$.

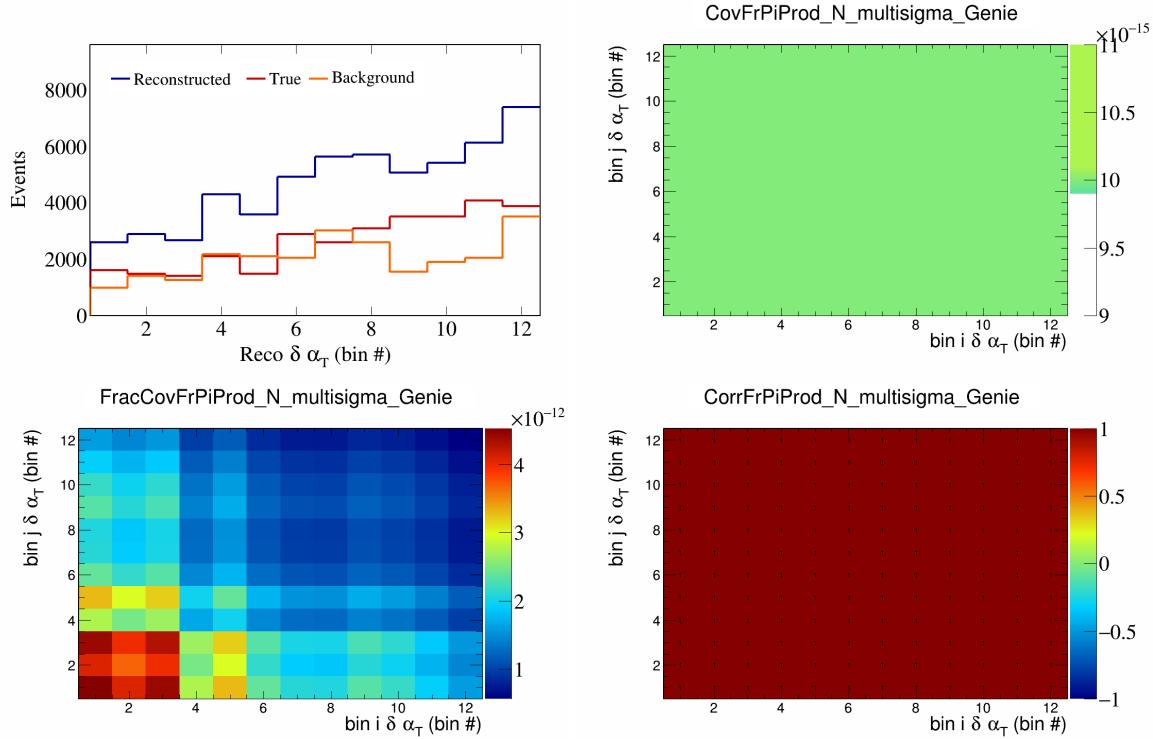


Figure 243: FrPiProdN variations for $\delta\alpha_T$ in $\cos(\theta_{\vec{p}_\mu})$.

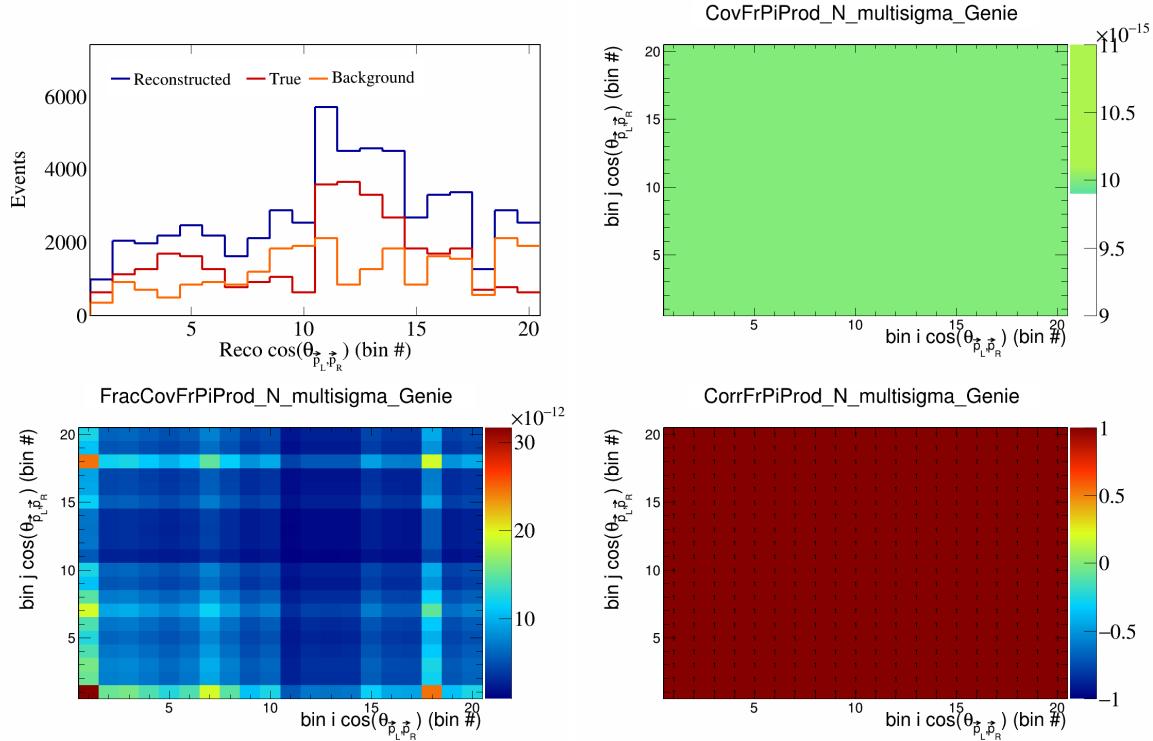


Figure 244: FrPiProdN variations for $\cos(\theta_{\vec{p}_L, \vec{p}_R})$ in $\cos(\theta_{\vec{p}_\mu})$.

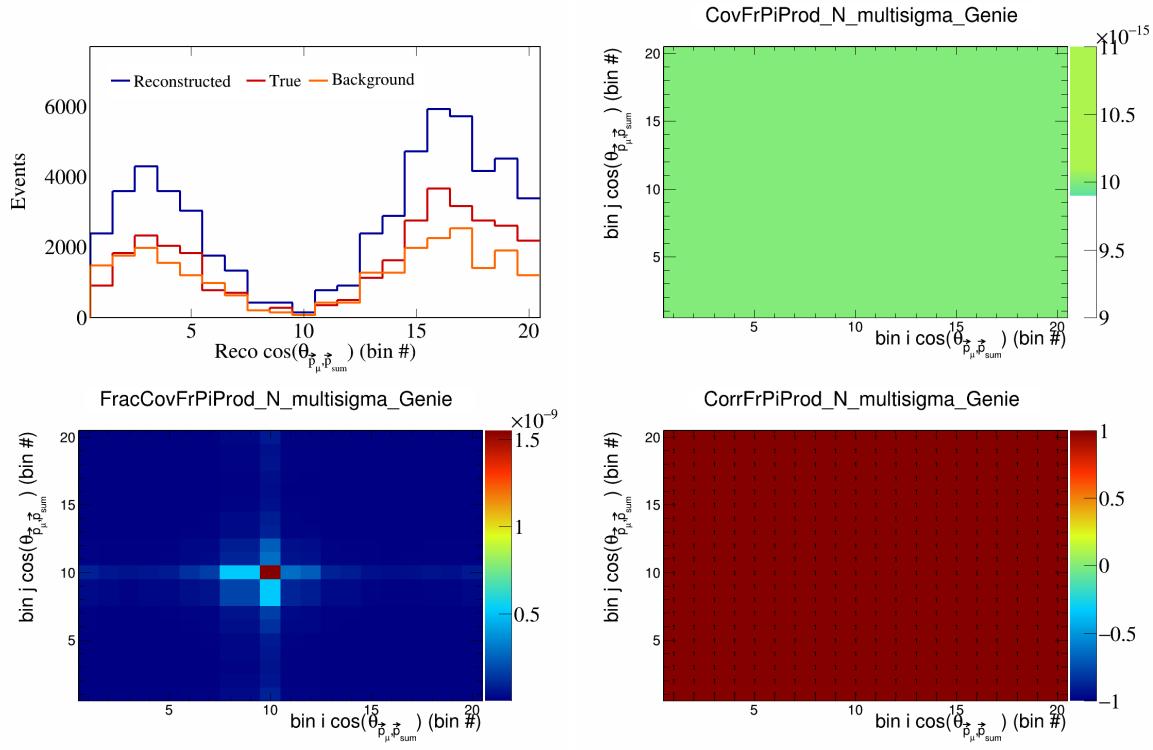


Figure 245: FrPiProdN variations for $\cos(\theta_{\vec{p}_\mu, \vec{p}_{\text{sum}}})$ in $\cos(\theta_{\vec{p}_\mu})$.

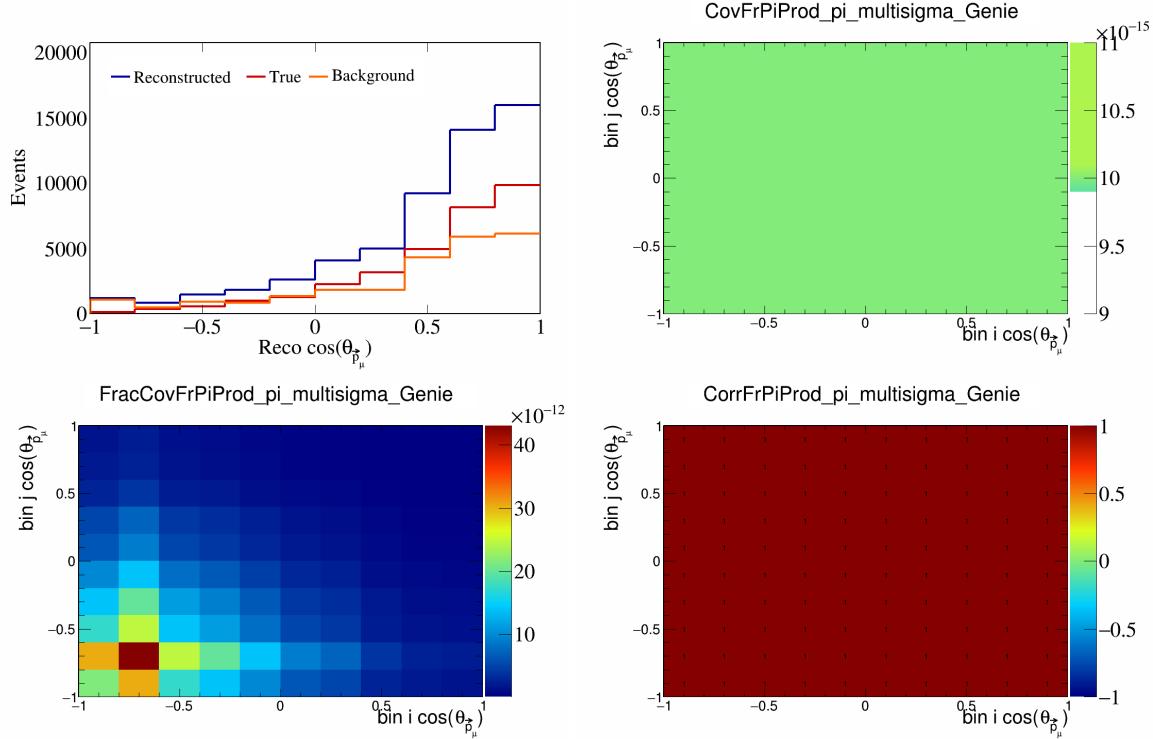


Figure 246: FrPiProdpi variations for $\cos(\theta_{\vec{p}_\mu})$.

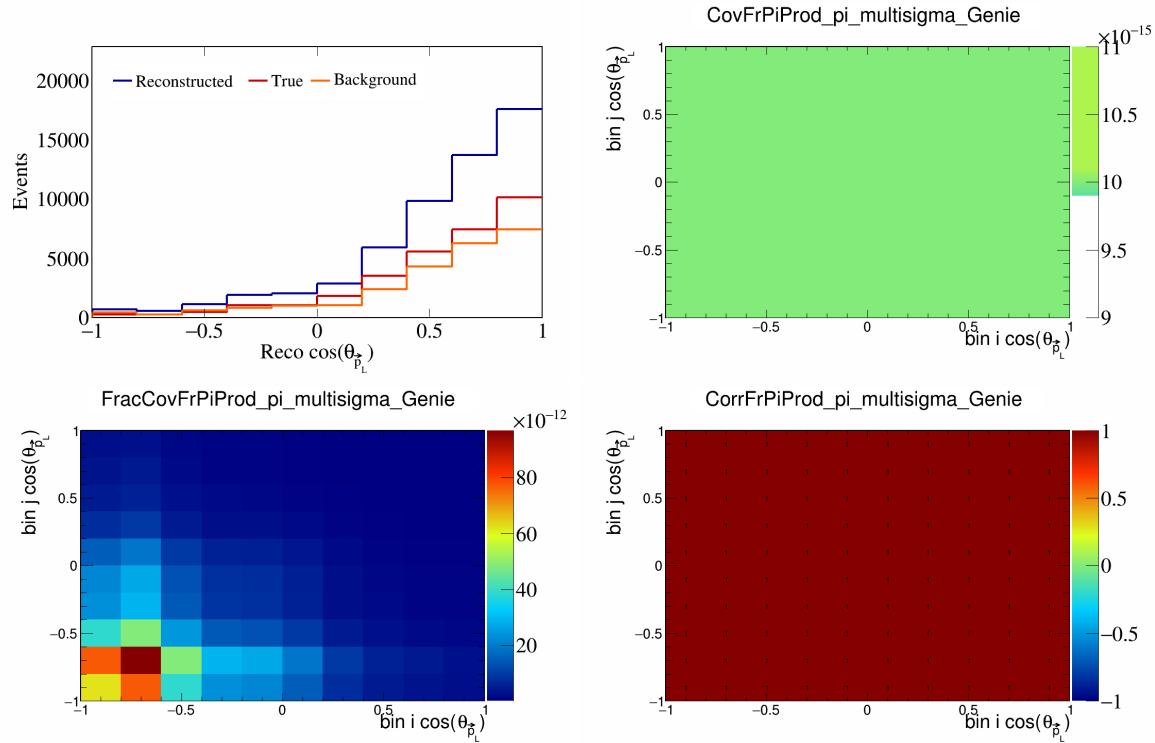


Figure 247: FrPiProdpi variations for $\cos(\theta_{\vec{p}_L})$.

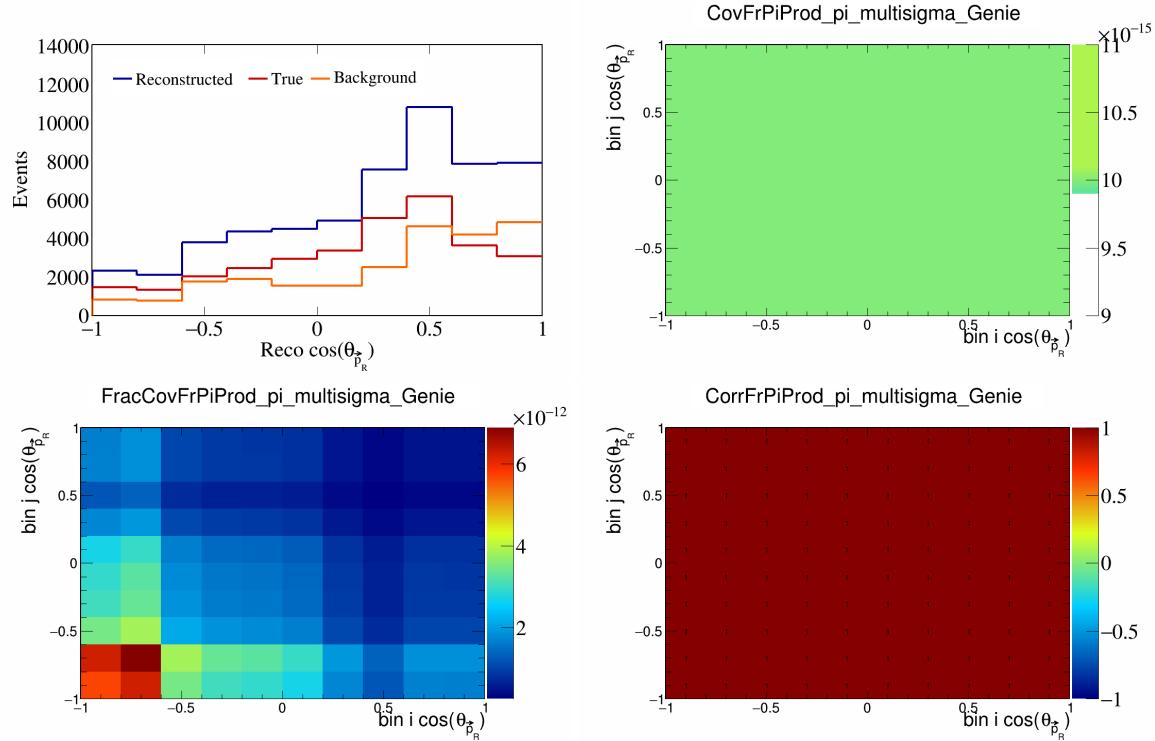


Figure 248: FrPiProdpi variations for $\cos(\theta_{\vec{p}_R})$.

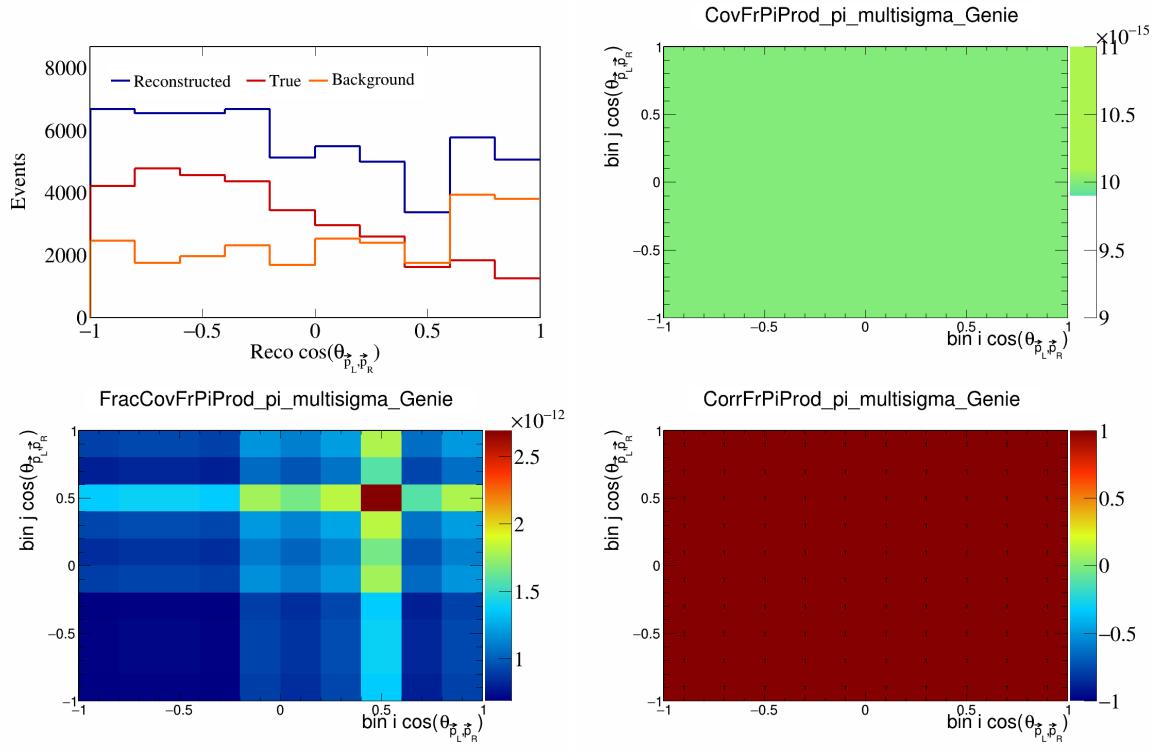


Figure 249: FrPiProdpi variations for $\cos(\theta_{\vec{p}_L, \vec{p}_R})$.

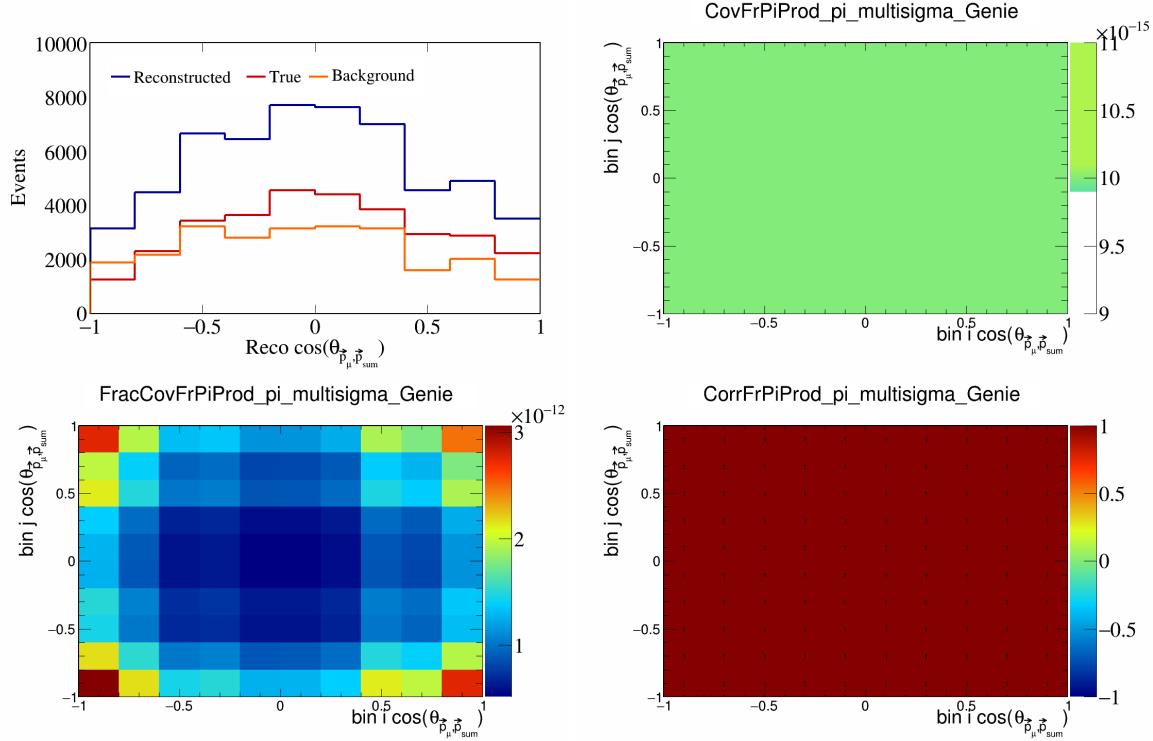


Figure 250: FrPiProdpi variations for $\cos(\theta_{\vec{p}_\mu, \vec{p}_{\text{sum}}})$.

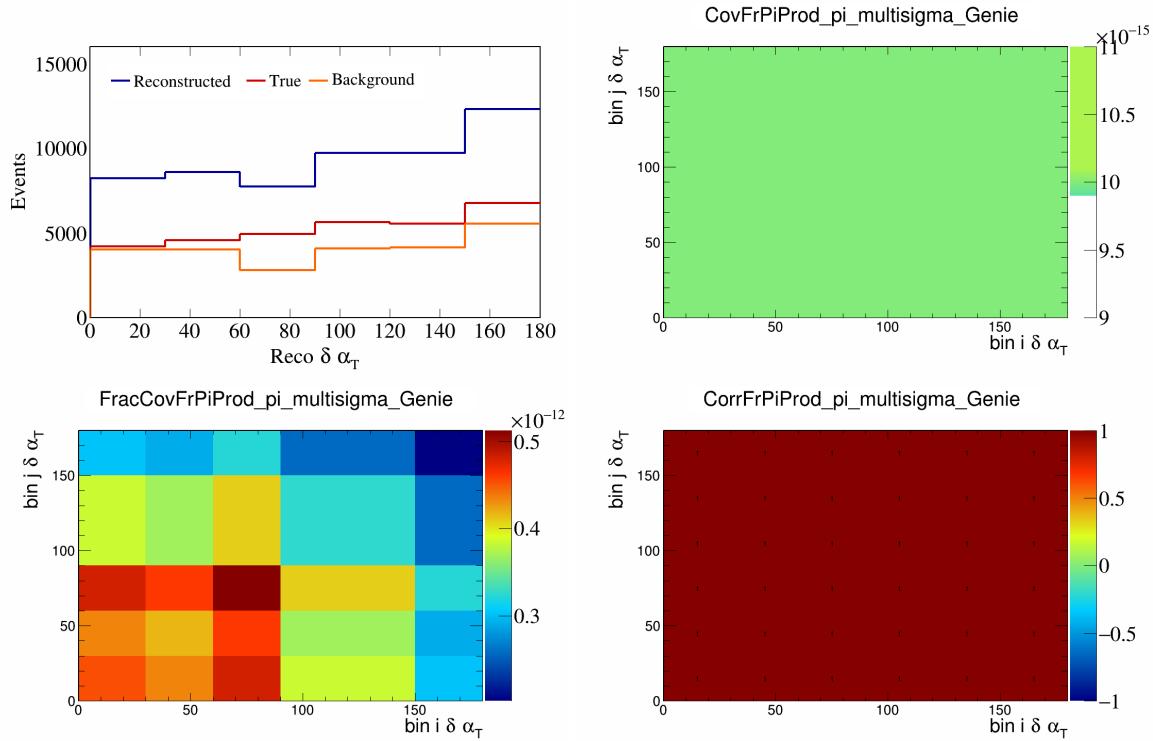


Figure 251: FrPiProdpi variations for $\delta\alpha_T$.

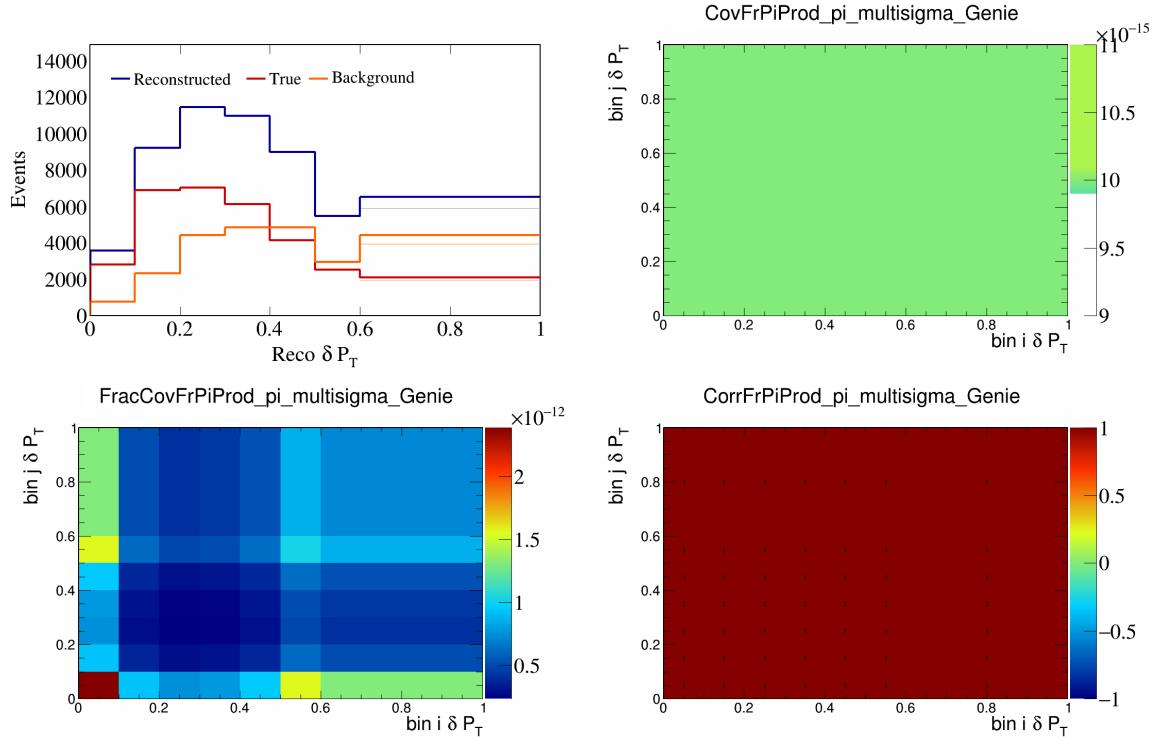


Figure 252: FrPiProdpi variations for δP_T .

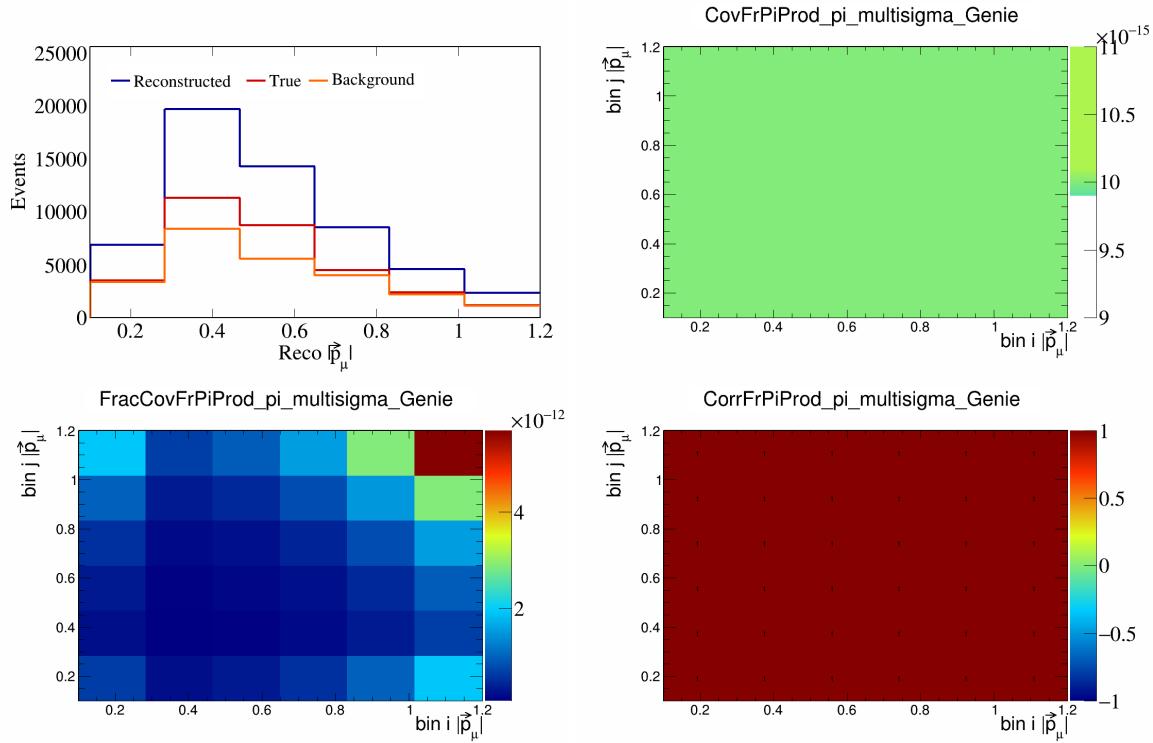


Figure 253: FrPiProdpi variations for $|\vec{p}_\mu|$.

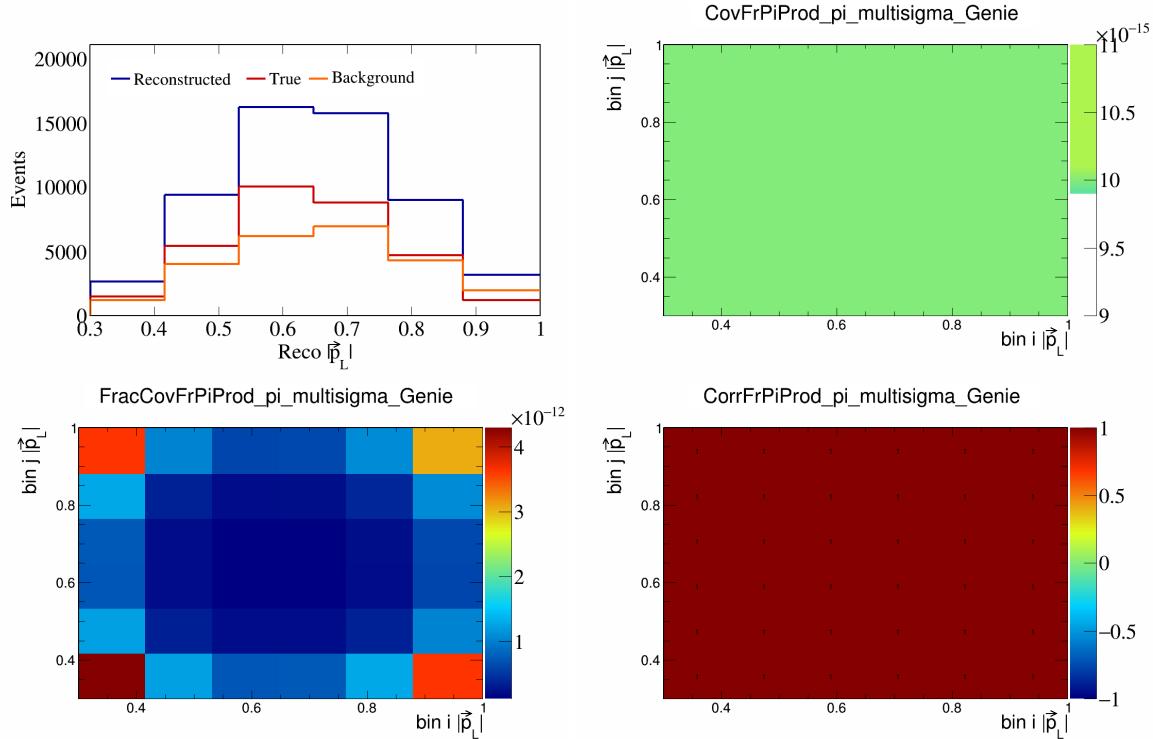


Figure 254: FrPiProdpi variations for $|\vec{p}_L|$.

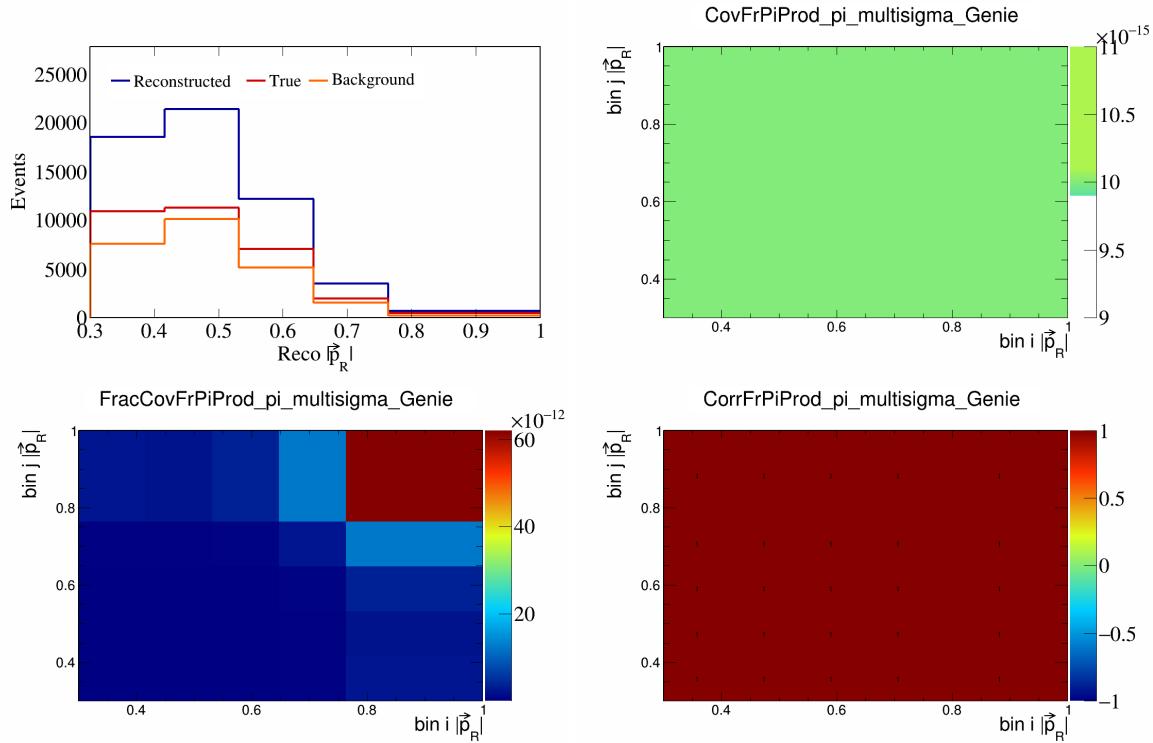


Figure 255: FrPiProdpi variations for $|\vec{p}_R|$.

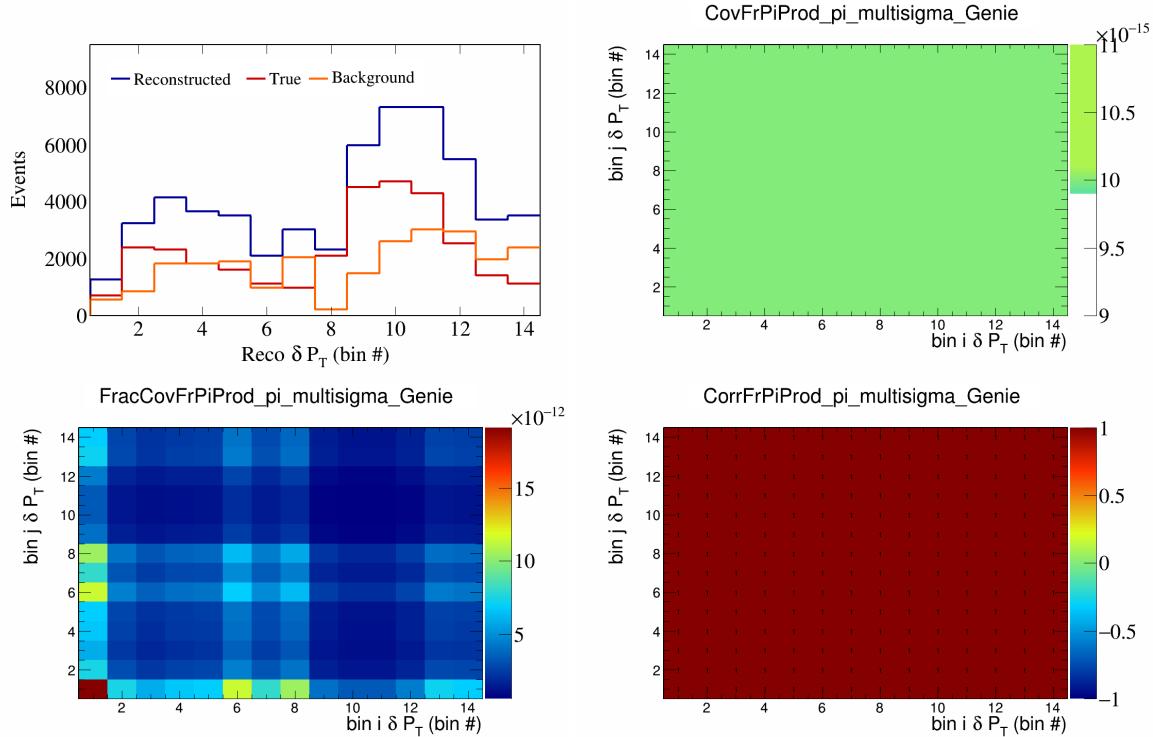


Figure 256: FrPiProdpi variations for δP_T in $\cos(\theta_{\vec{p}_\mu})$.

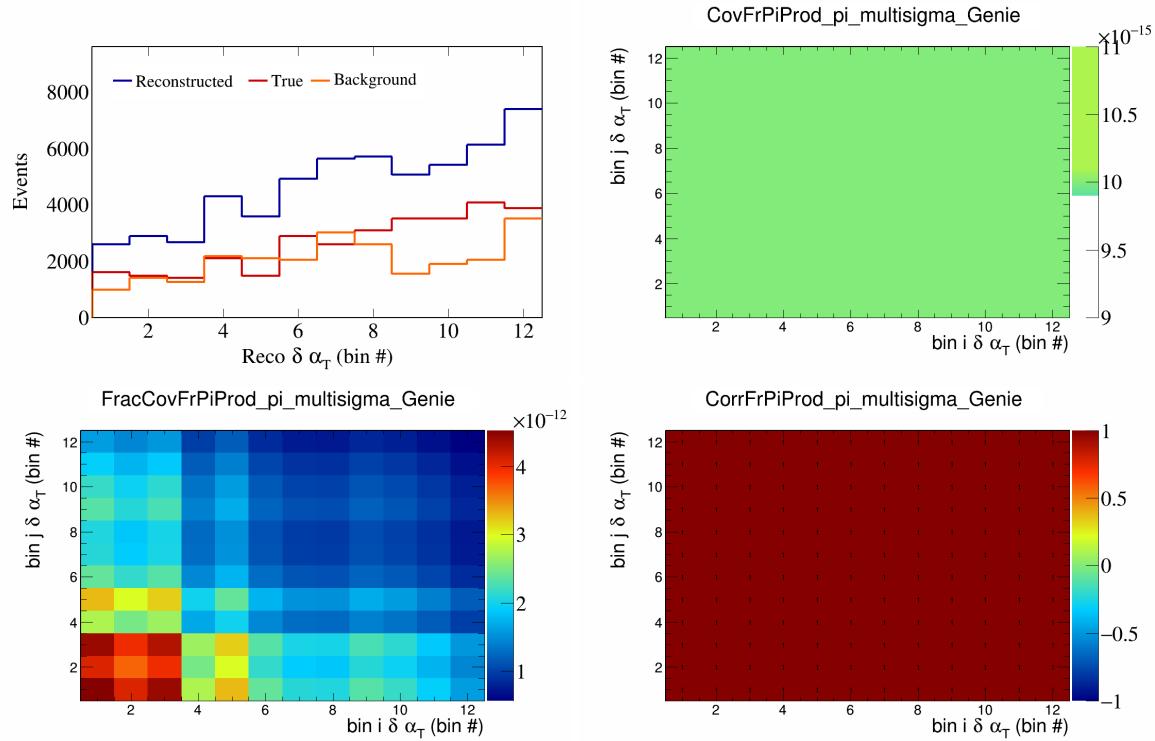


Figure 257: FrPiProdpi variations for $\delta\alpha_T$ in $\cos(\theta_{\vec{p}_\mu})$.

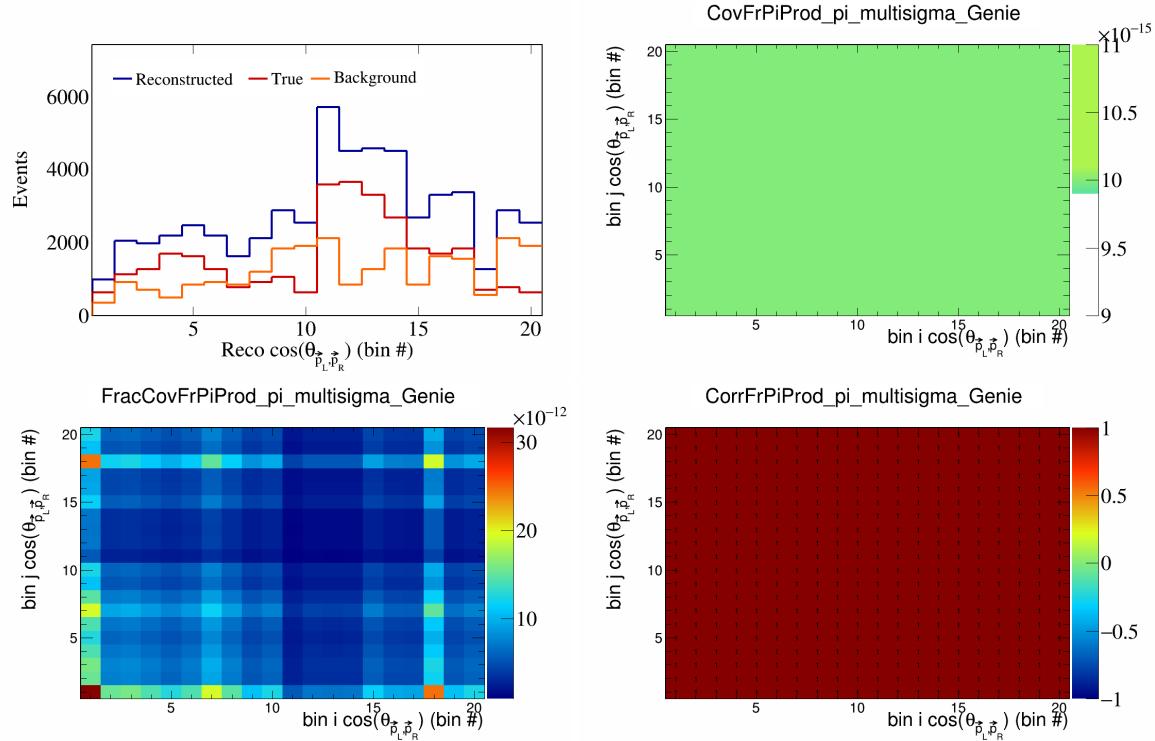


Figure 258: FrPiProdpi variations for $\cos(\theta_{\vec{p}_L, \vec{p}_R})$ in $\cos(\theta_{\vec{p}_\mu})$.

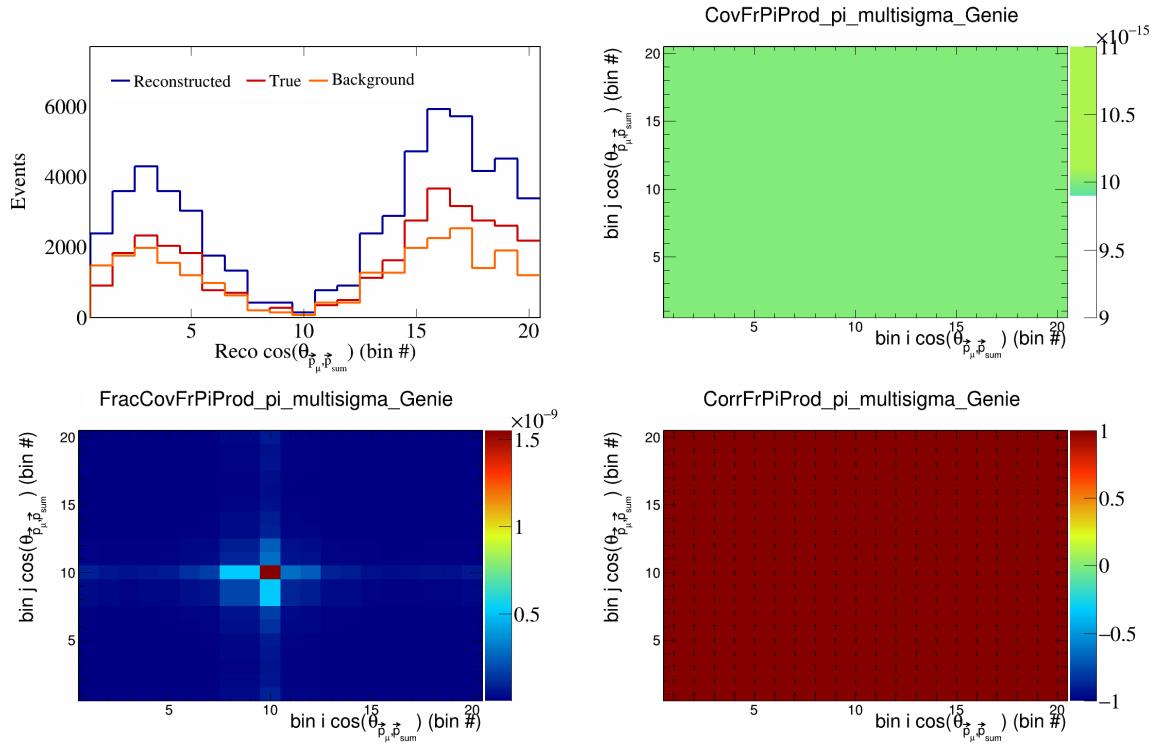


Figure 259: FrPiProdpi variations for $\cos(\theta_{\vec{p}_\mu, \vec{p}_{\text{sum}}})$ in $\cos(\theta_{\vec{p}_\mu})$.

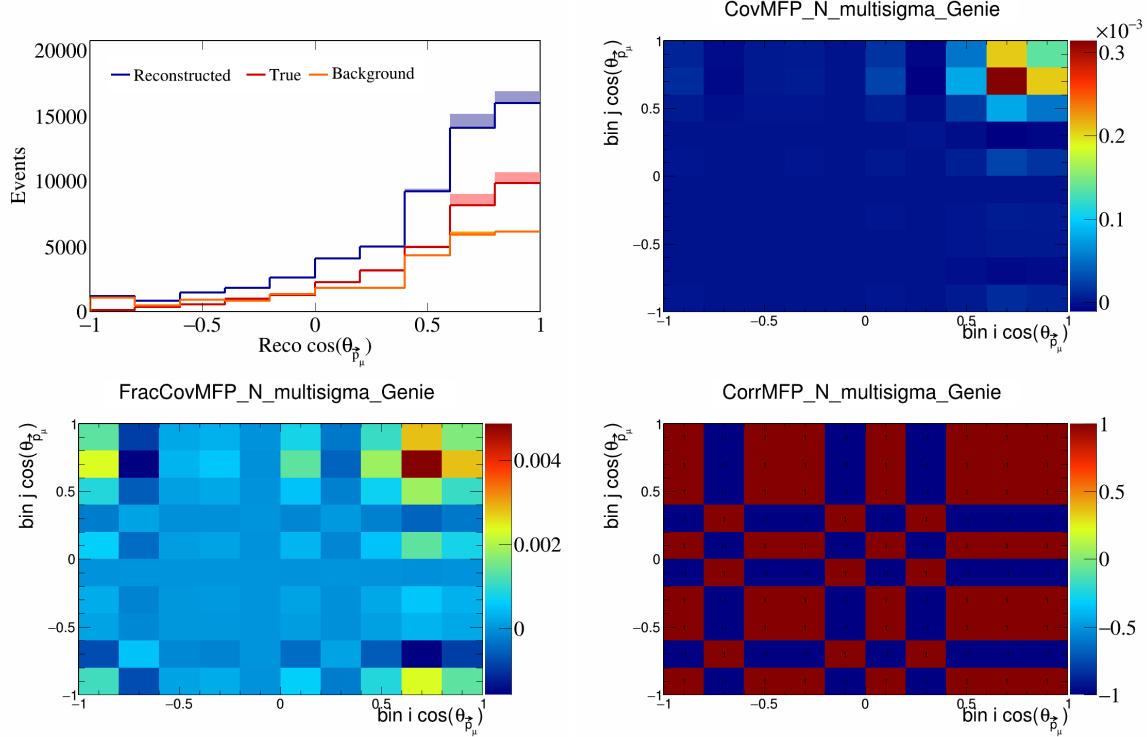


Figure 260: MFPN variations for $\cos(\theta_{\vec{p}_\mu})$.

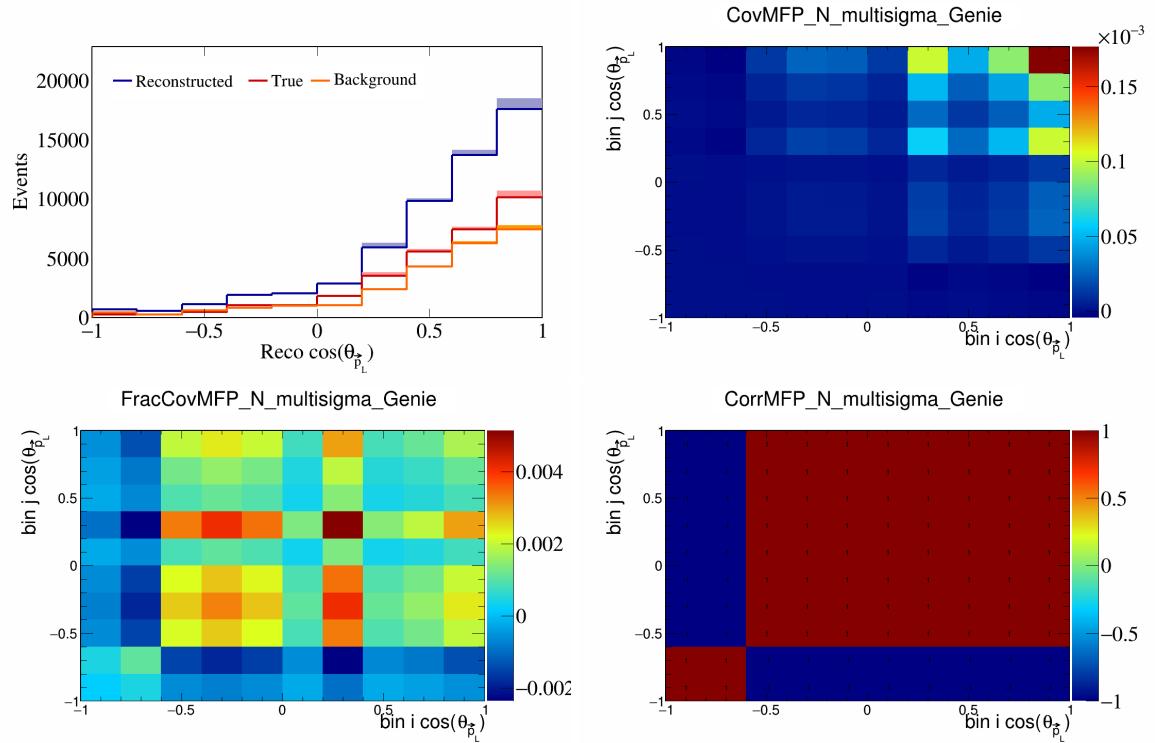


Figure 261: MFPN variations for $\cos(\theta_{\vec{p}_L})$.

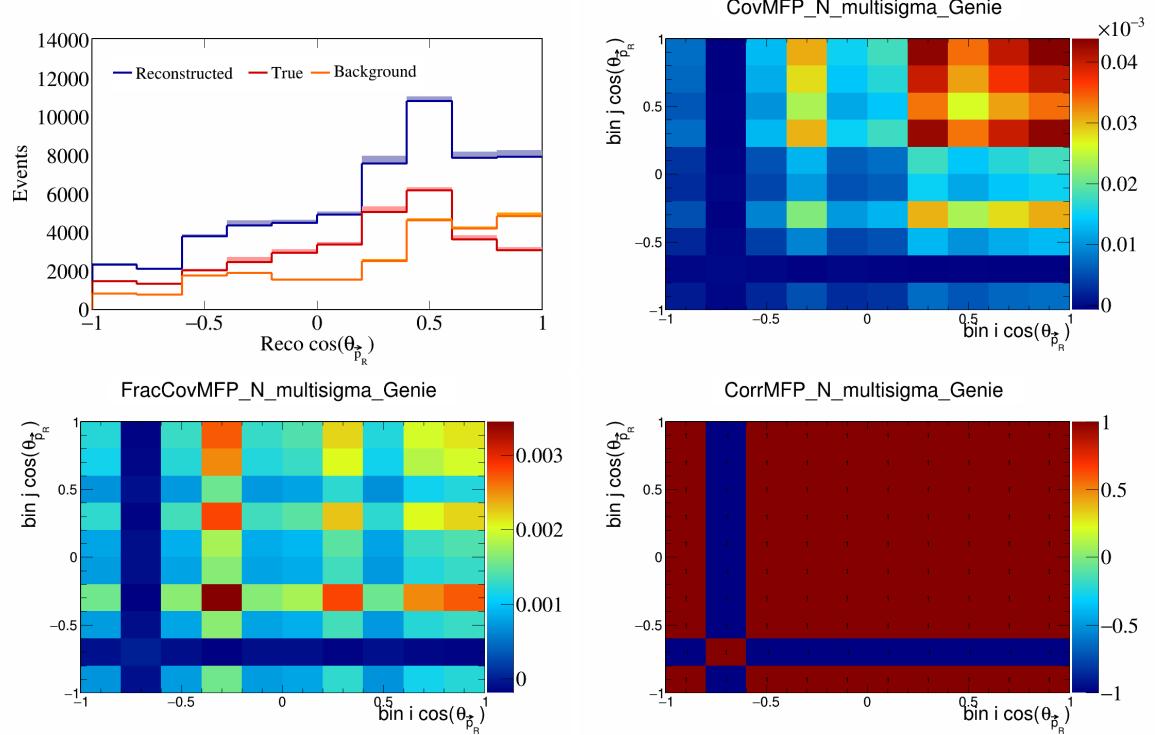


Figure 262: MFPN variations for $\cos(\theta_{\vec{p}_R})$.

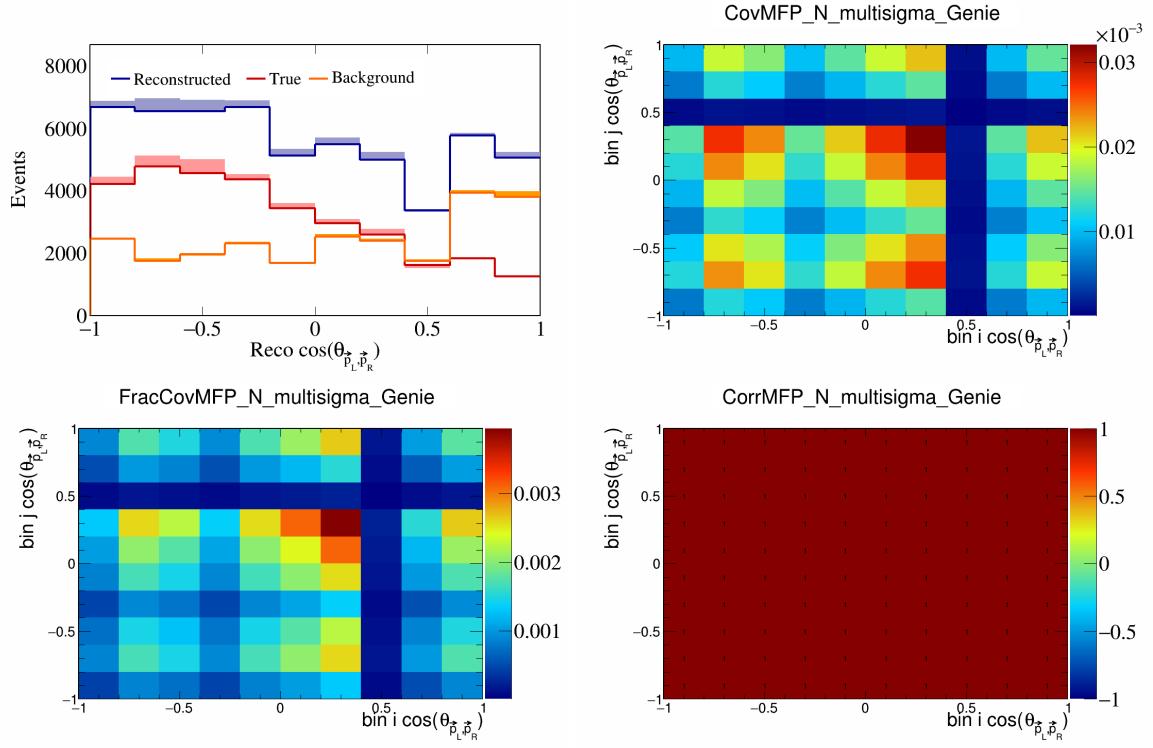


Figure 263: MFPN variations for $\cos(\theta_{\vec{p}_L, \vec{p}_R})$.

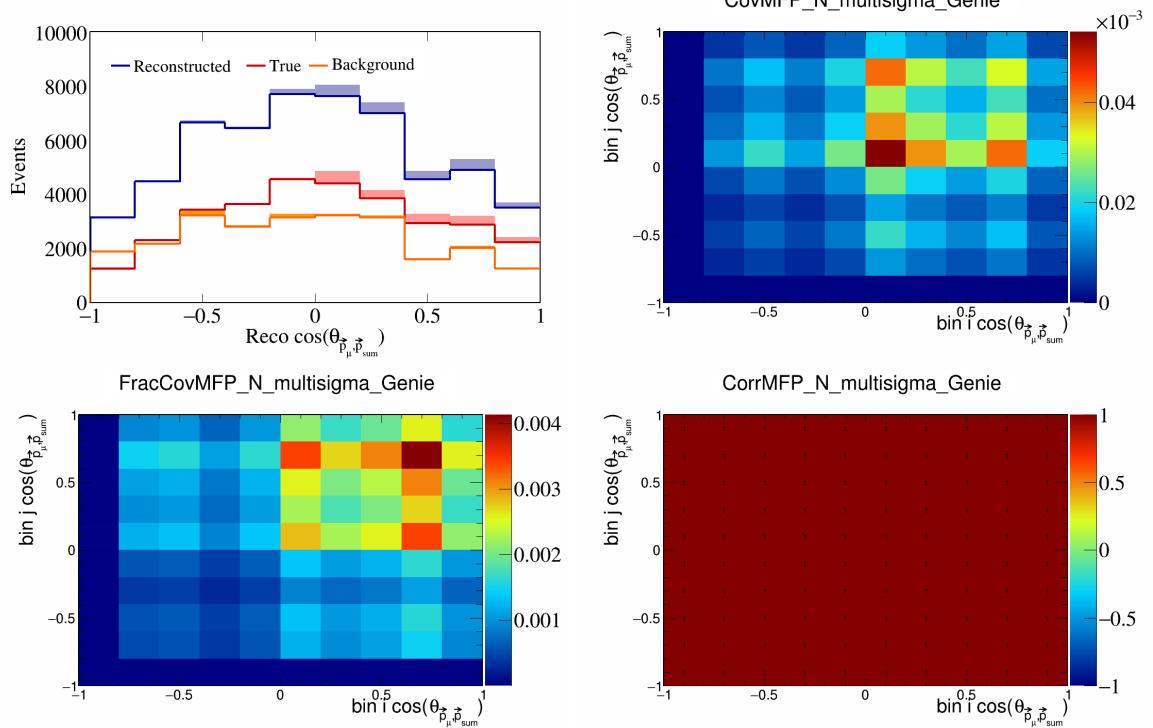


Figure 264: MFPN variations for $\cos(\theta_{\vec{p}_\mu, \vec{p}_{\text{sum}}})$.

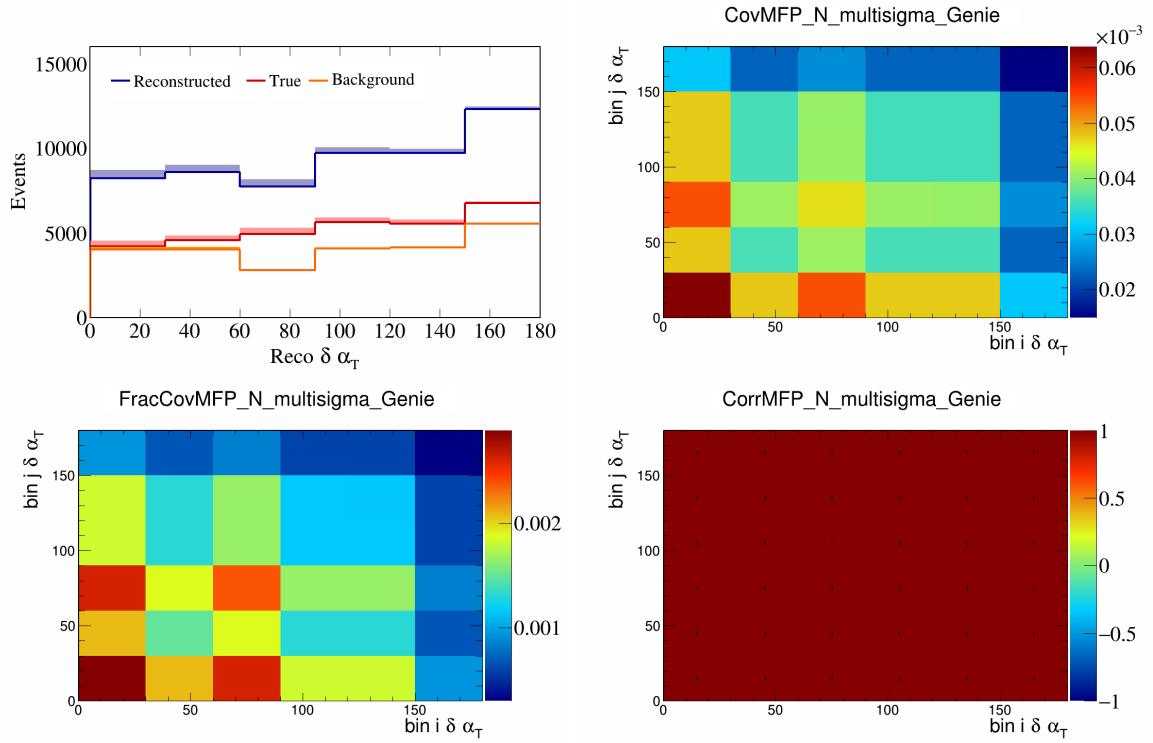


Figure 265: MFPN variations for $\delta\alpha_T$.

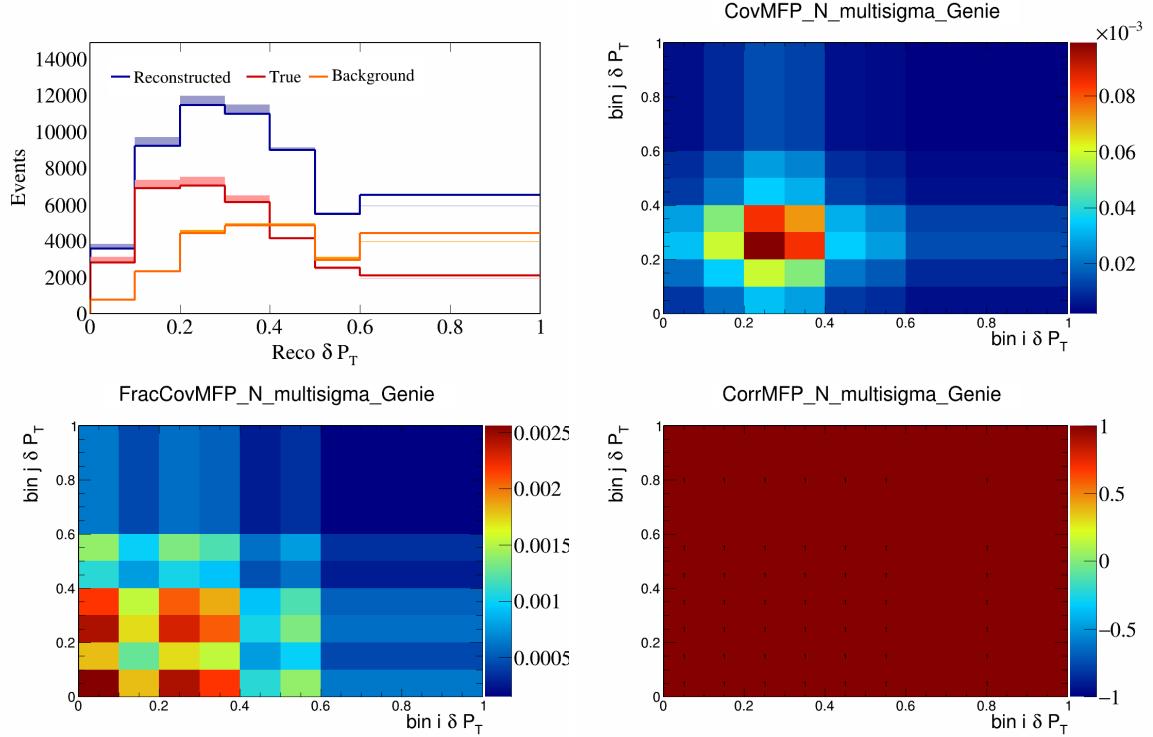


Figure 266: MFPN variations for δP_T .

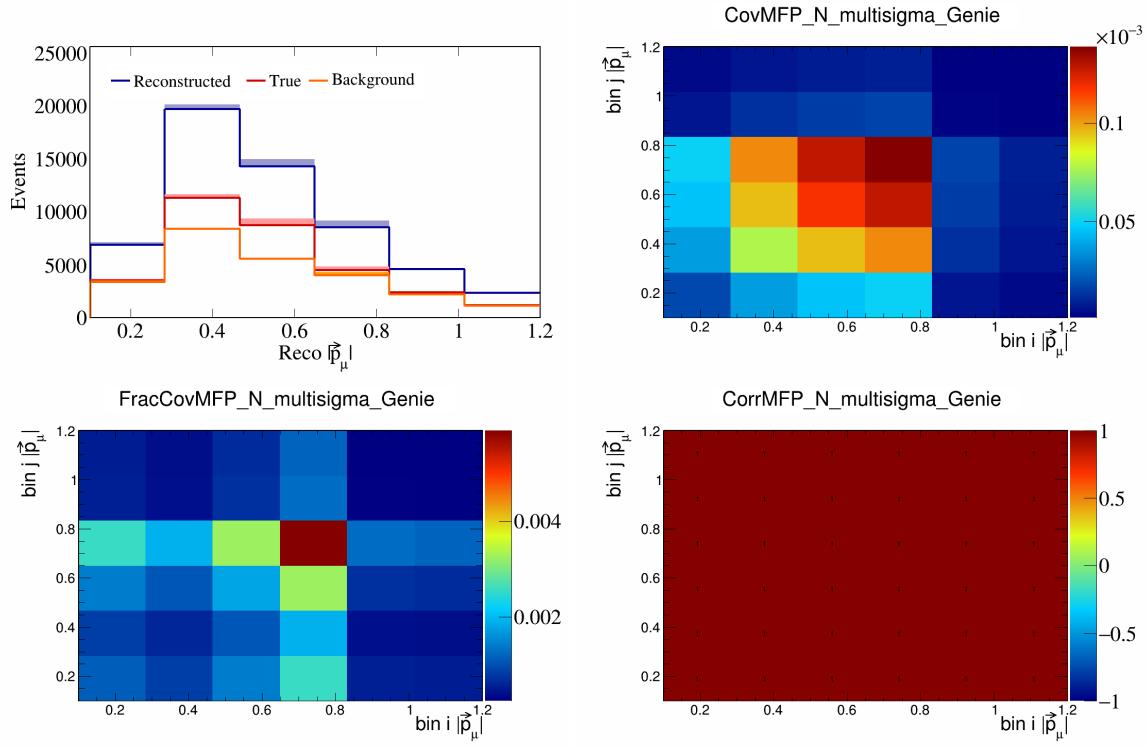


Figure 267: MFPN variations for $|\vec{p}_\mu|$.

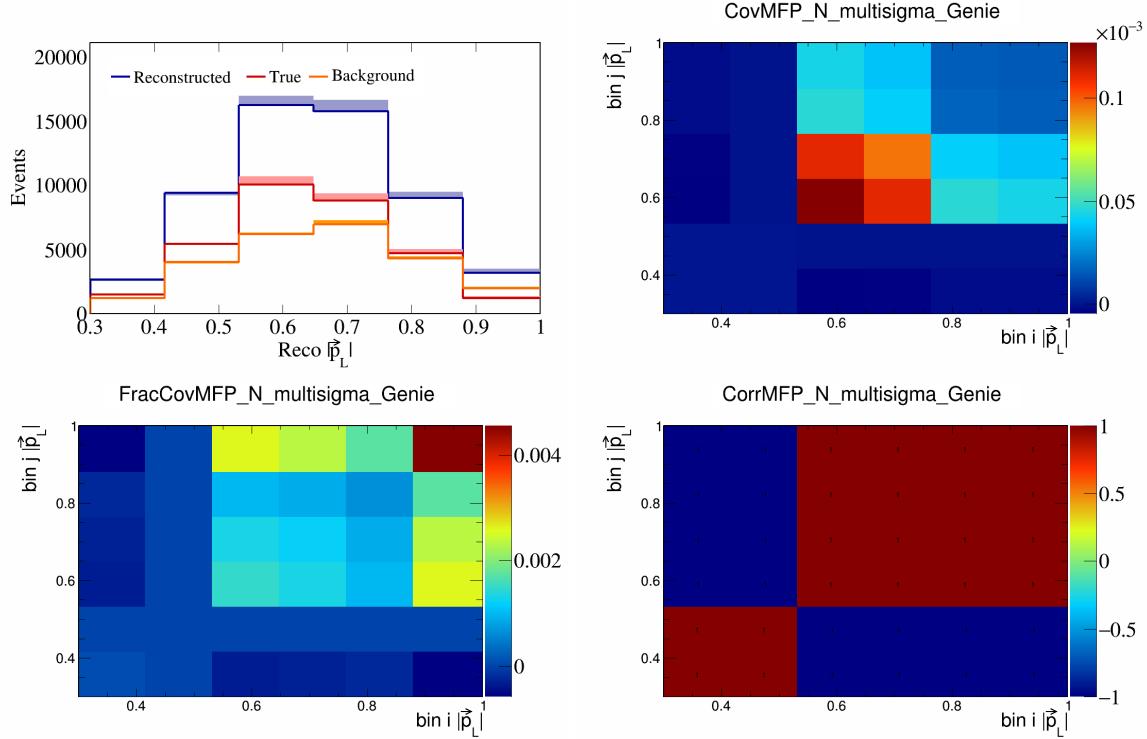


Figure 268: MFPN variations for $|\vec{p}_L|$.

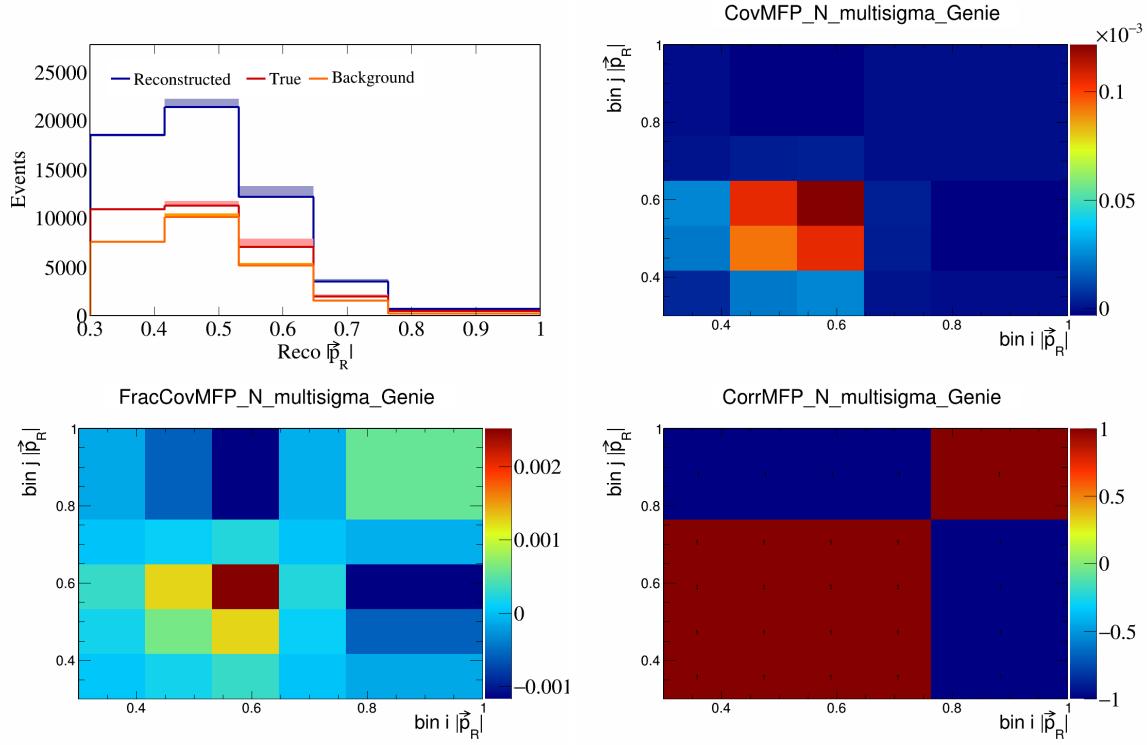


Figure 269: MFPN variations for $|\vec{p}_R|$.

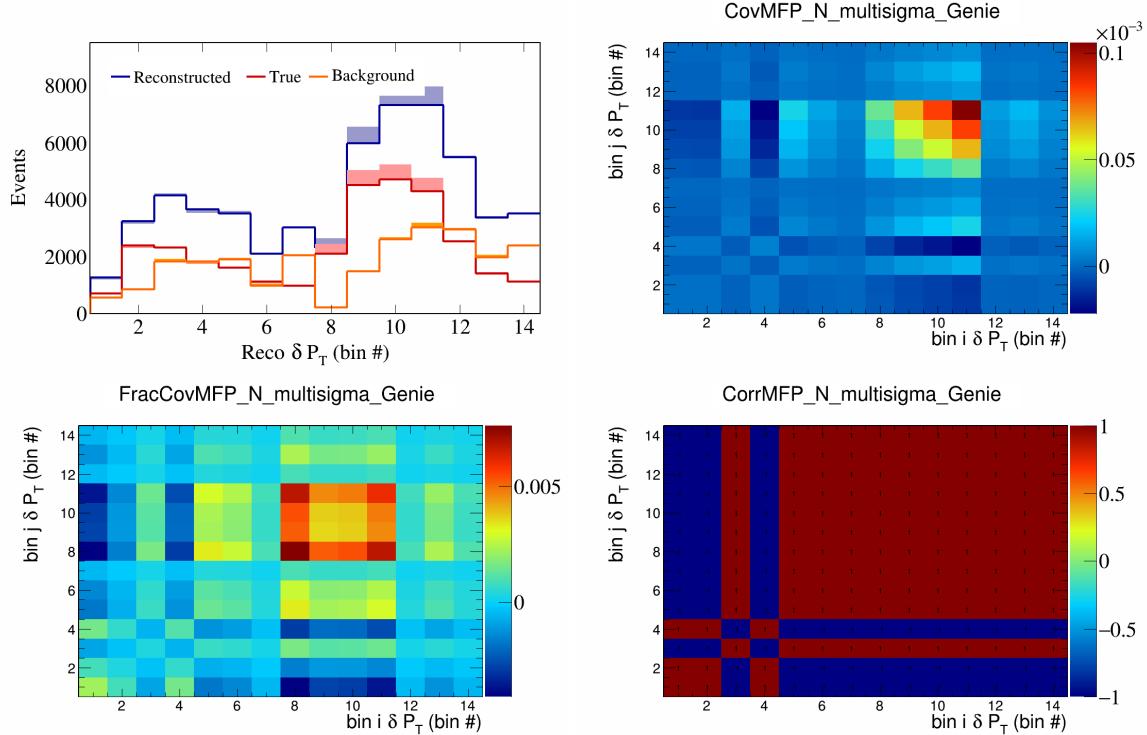


Figure 270: MFPN variations for δP_T in $\cos(\theta_{\vec{p}_\mu})$.

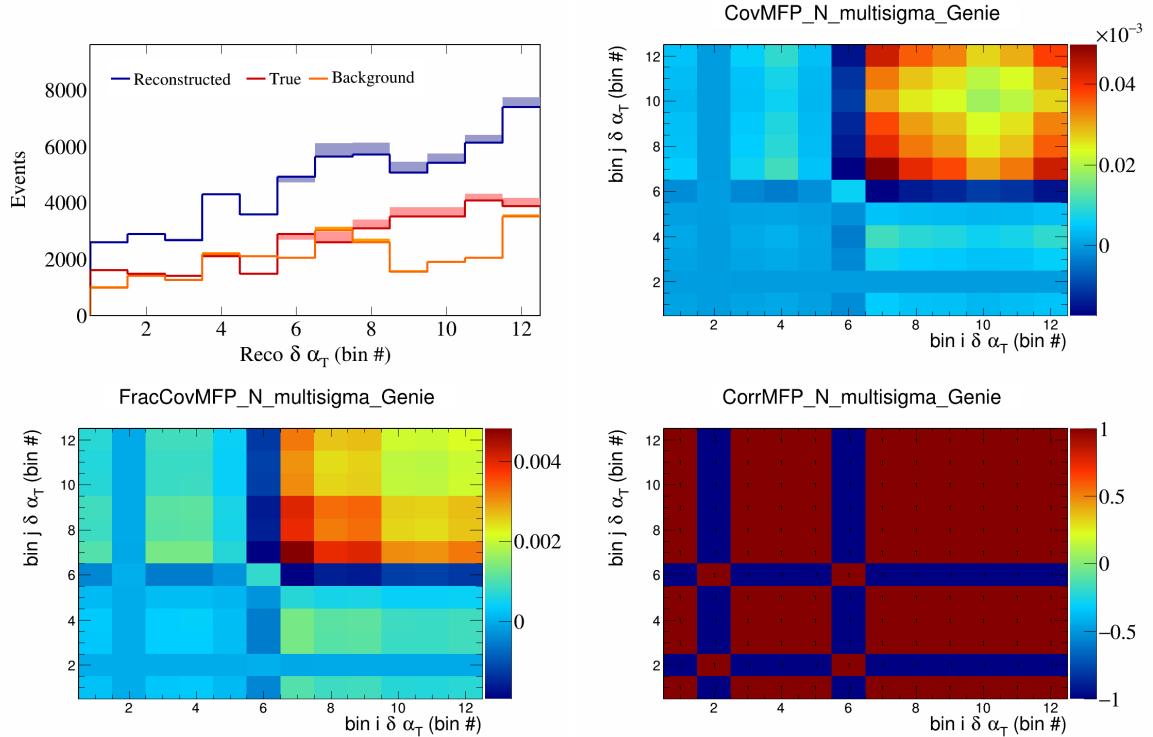


Figure 271: MFPN variations for $\delta\alpha_T$ in $\cos(\theta_{\vec{p}_\mu})$.

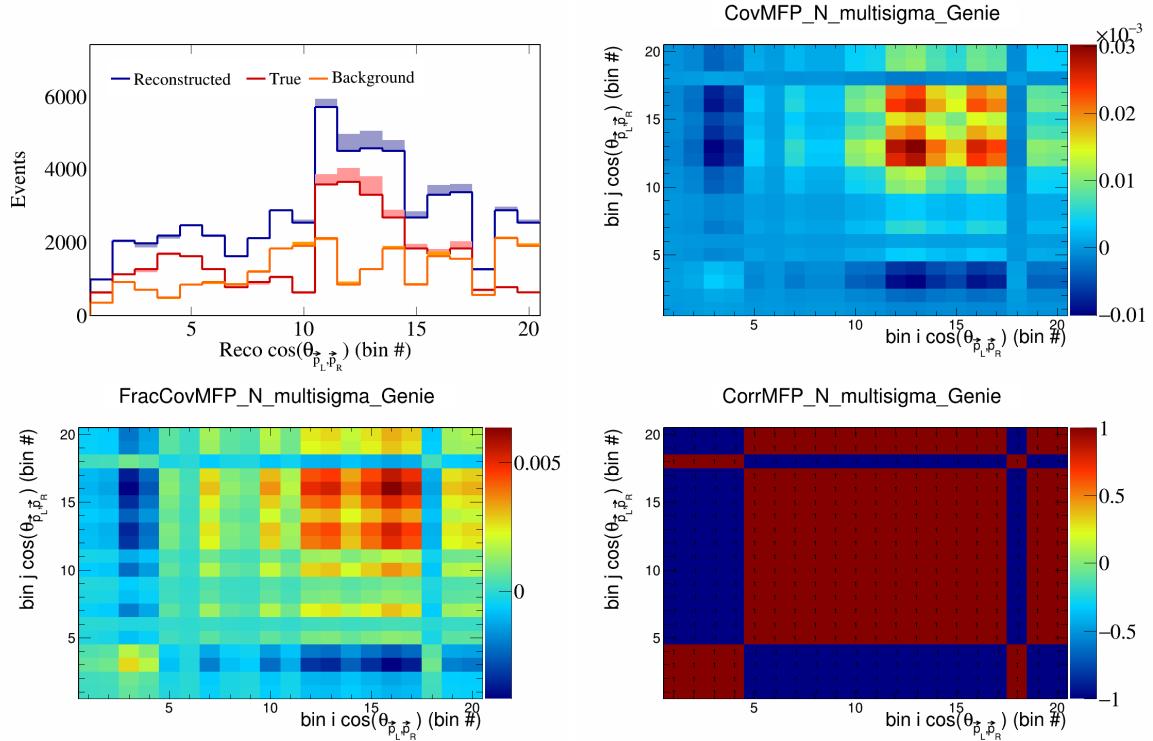


Figure 272: MFPN variations for $\cos(\theta_{\vec{p}_L, \vec{p}_R})$ in $\cos(\theta_{\vec{p}_\mu})$.

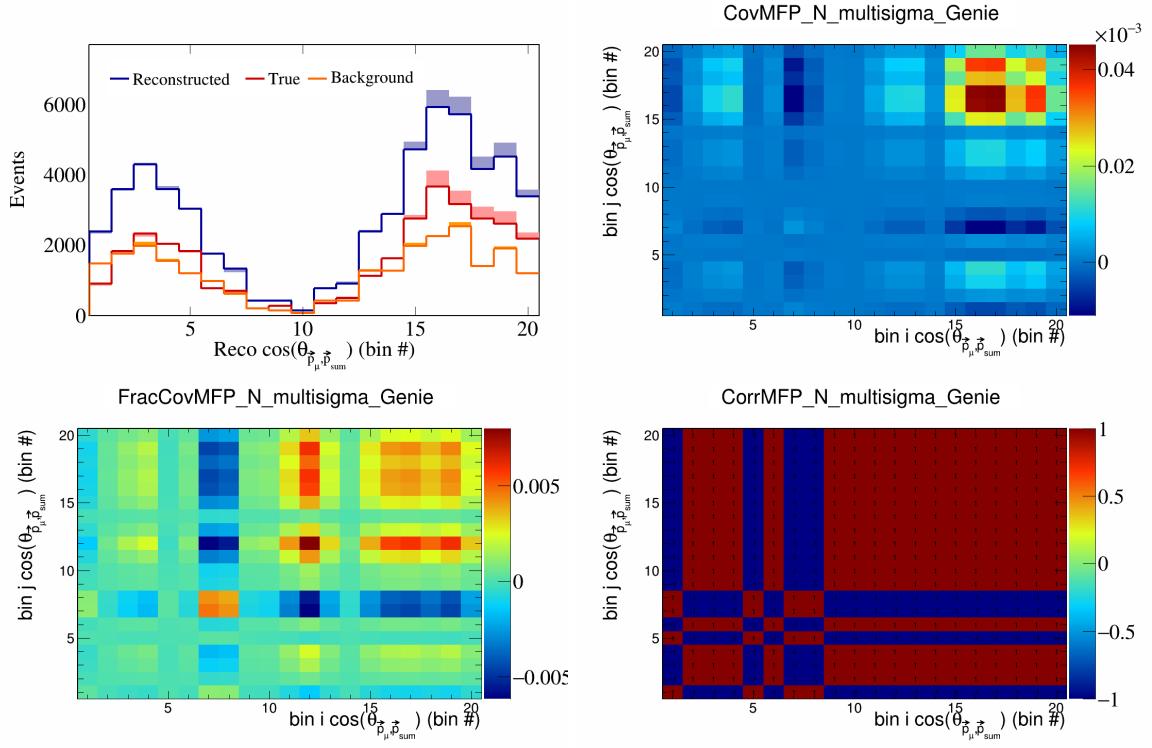


Figure 273: MFPN variations for $\cos(\theta_{\vec{p}_\mu, \vec{p}_{\text{sum}}})$ in $\cos(\theta_{\vec{p}_\mu})$.

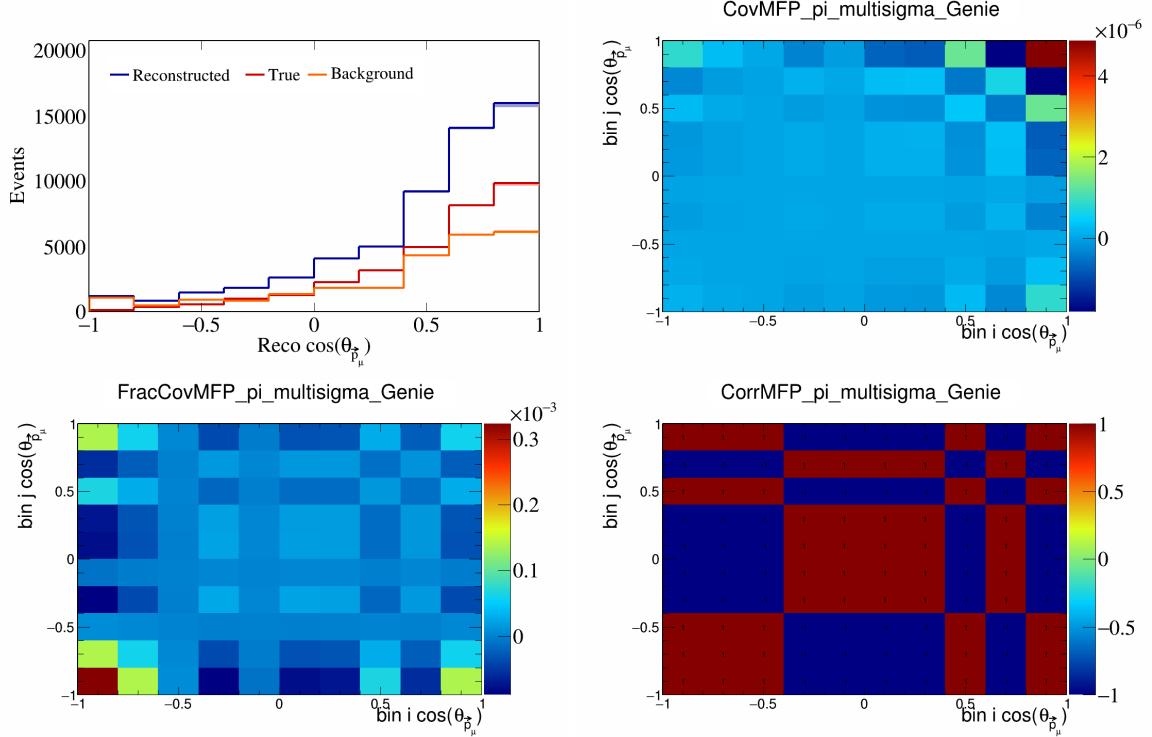


Figure 274: MFPPi variations for $\cos(\theta_{\vec{p}_\mu})$.

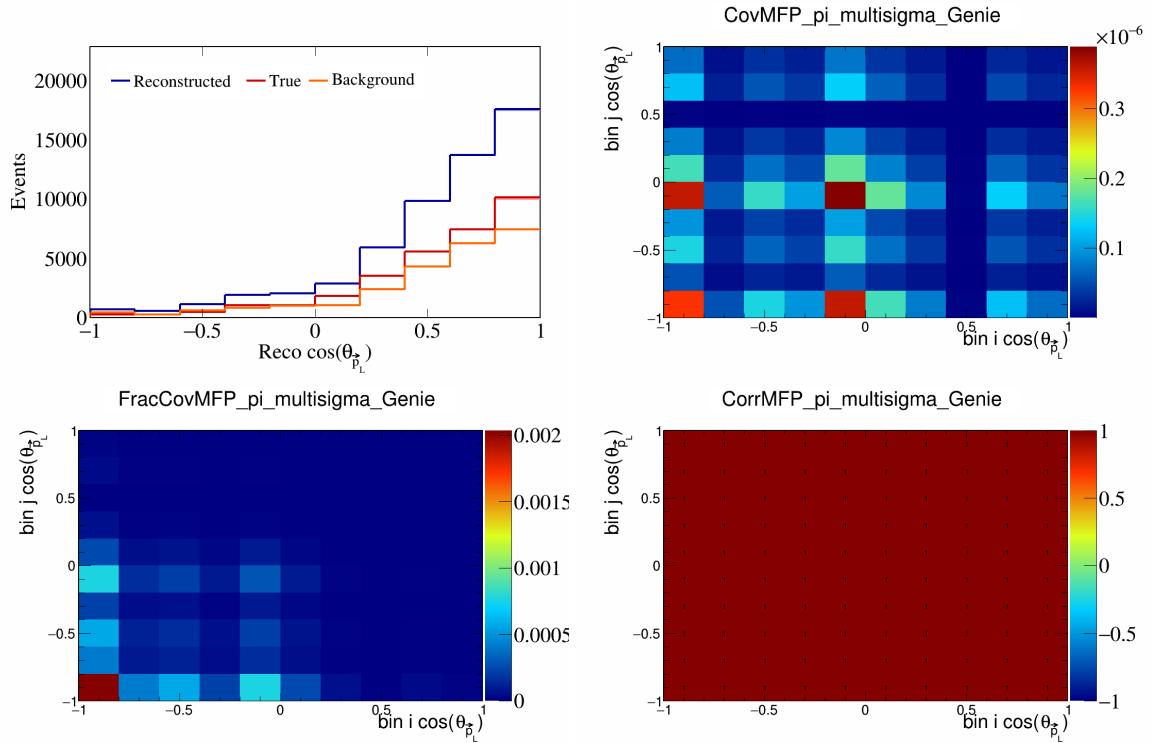


Figure 275: MFPPi variations for $\cos(\theta_{\vec{p}_L})$.

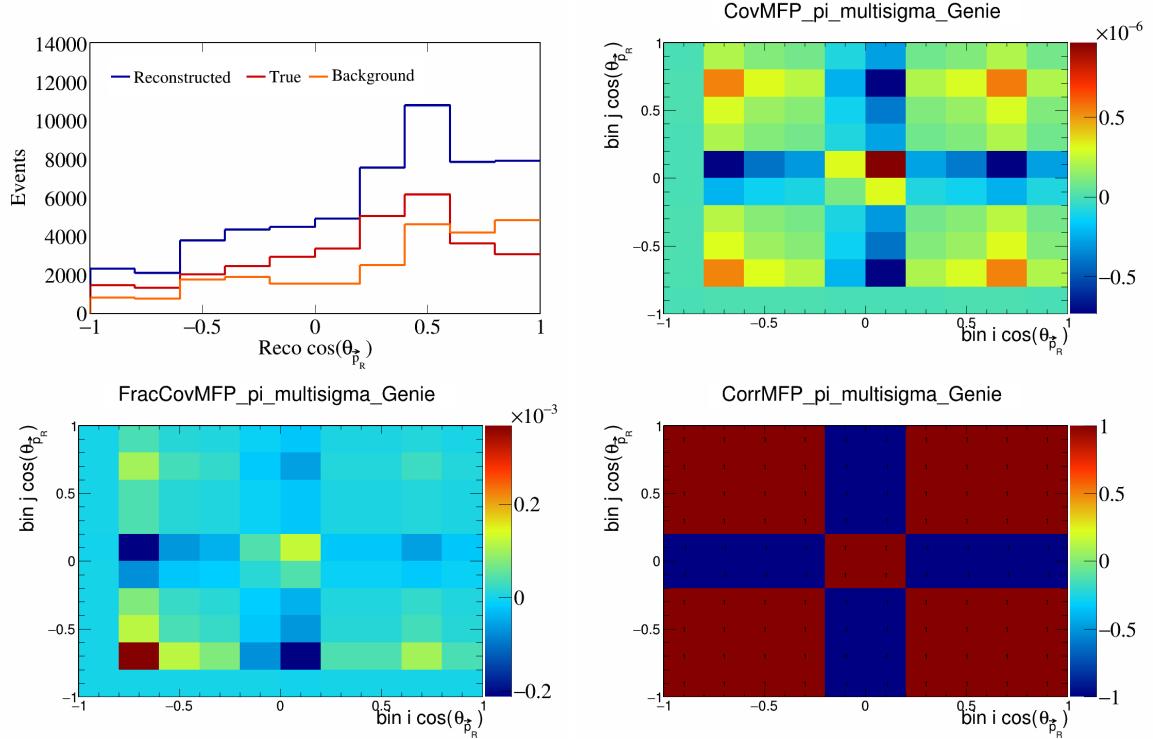


Figure 276: MFPPi variations for $\cos(\theta_{\vec{p}_R})$.

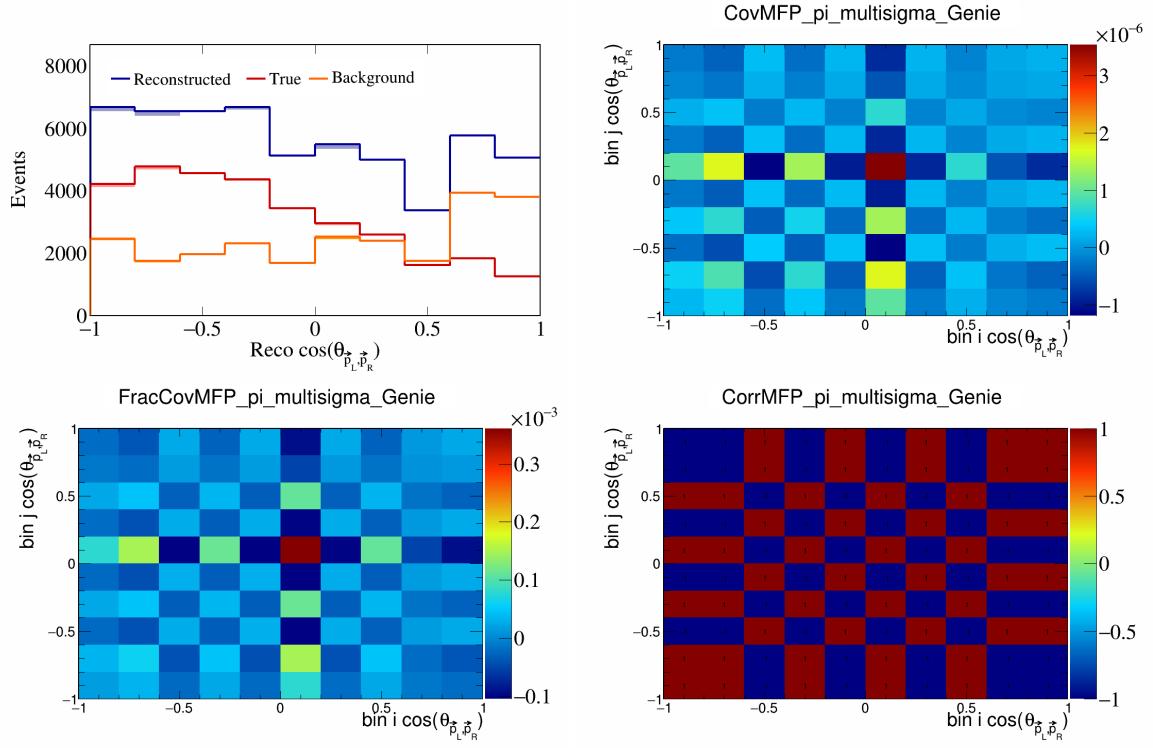


Figure 277: MFPpi variations for $\cos(\theta_{\vec{p}_L, \vec{p}_R})$.

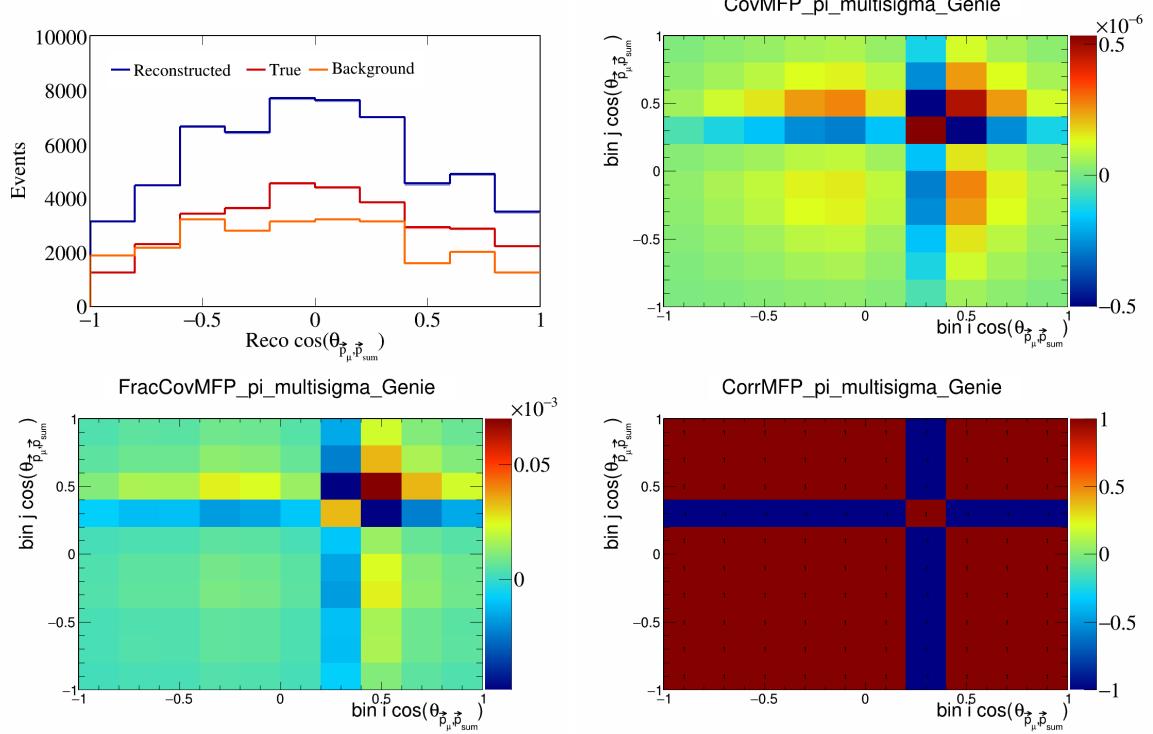


Figure 278: MFPpi variations for $\cos(\theta_{\vec{p}_\mu, \vec{p}_{\text{sum}}})$.

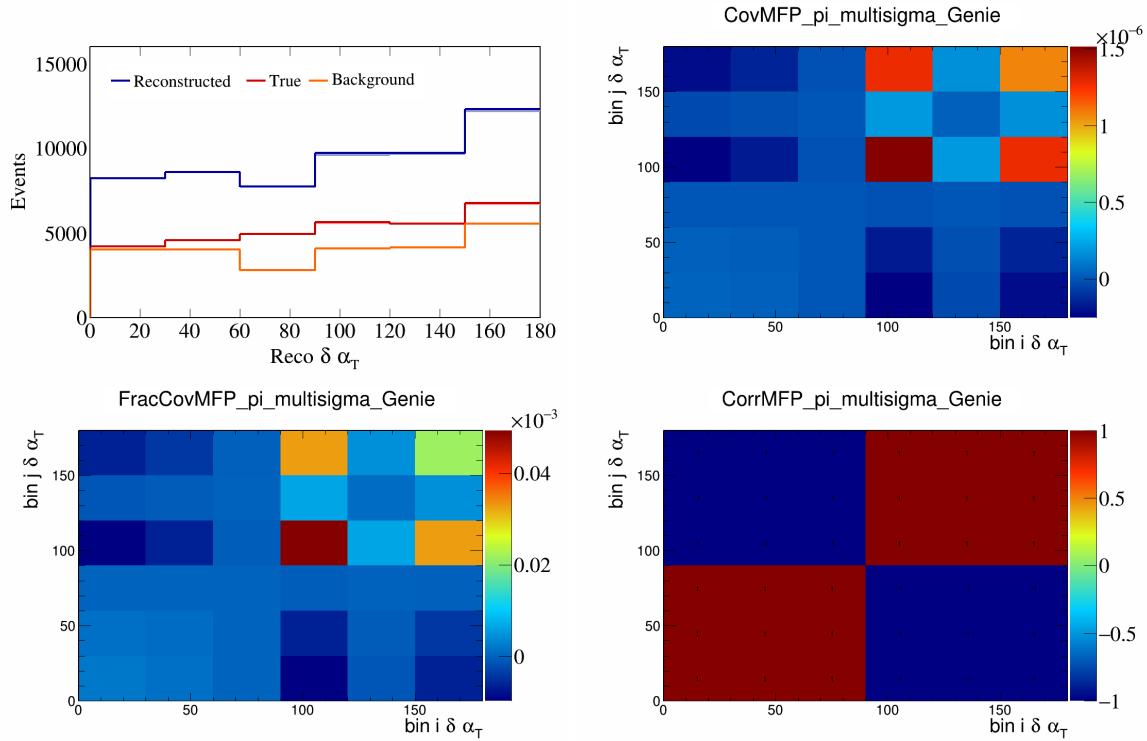


Figure 279: MFPPi variations for $\delta\alpha_T$.

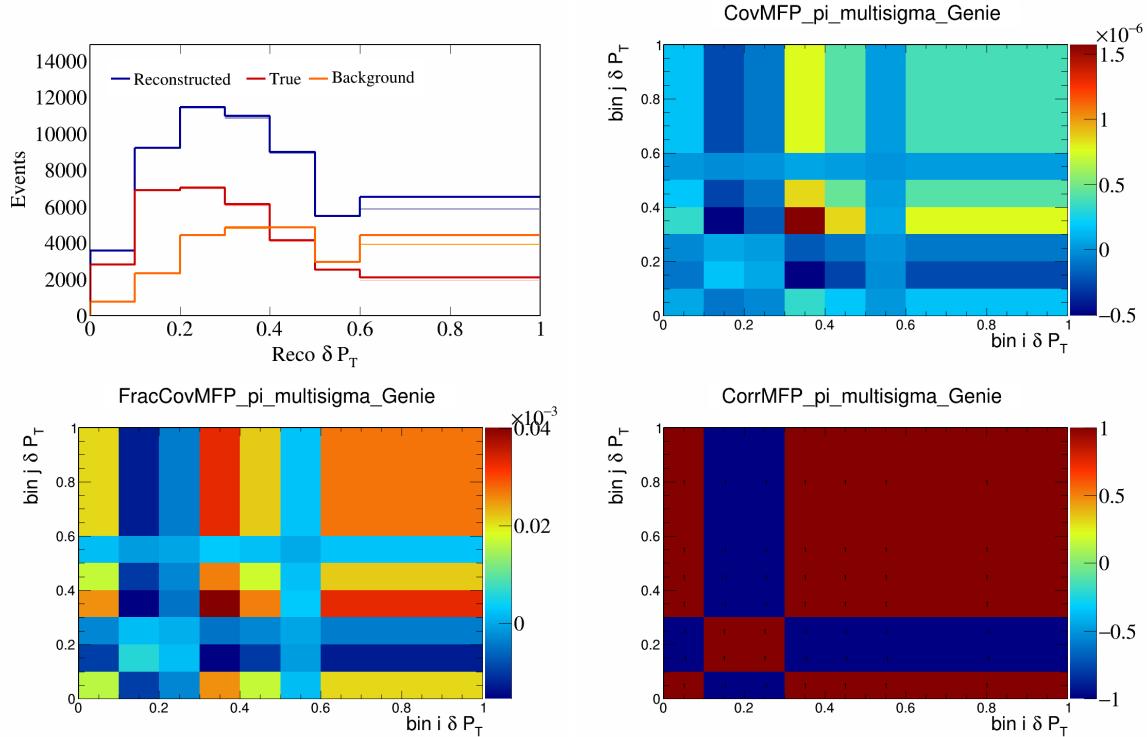


Figure 280: MFPPi variations for δP_T .

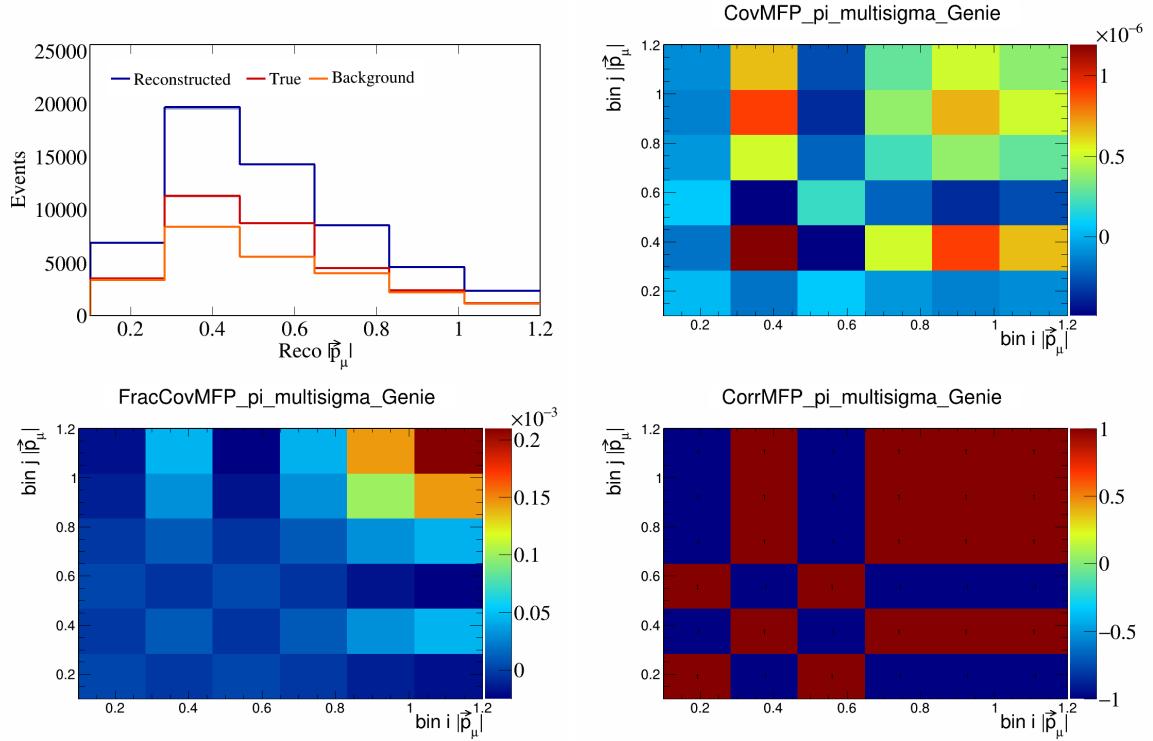


Figure 281: MFPpi variations for $|\vec{p}_\mu|$.

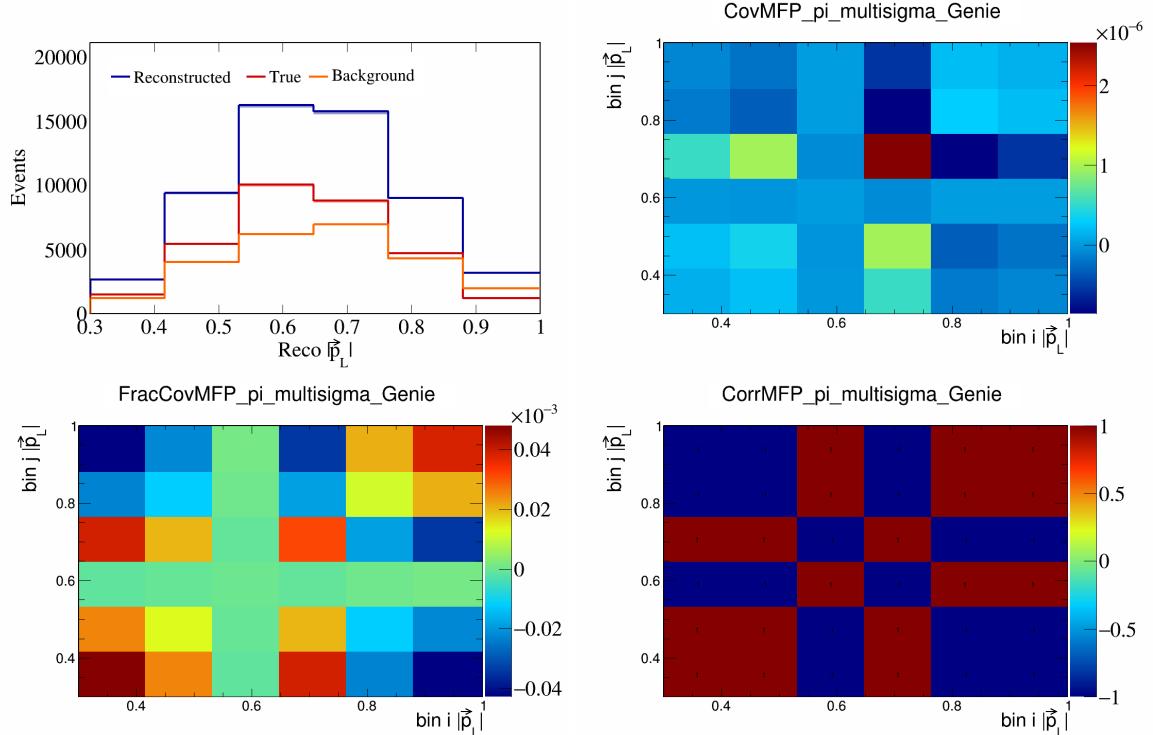


Figure 282: MFPpi variations for $|\vec{p}_L|$.

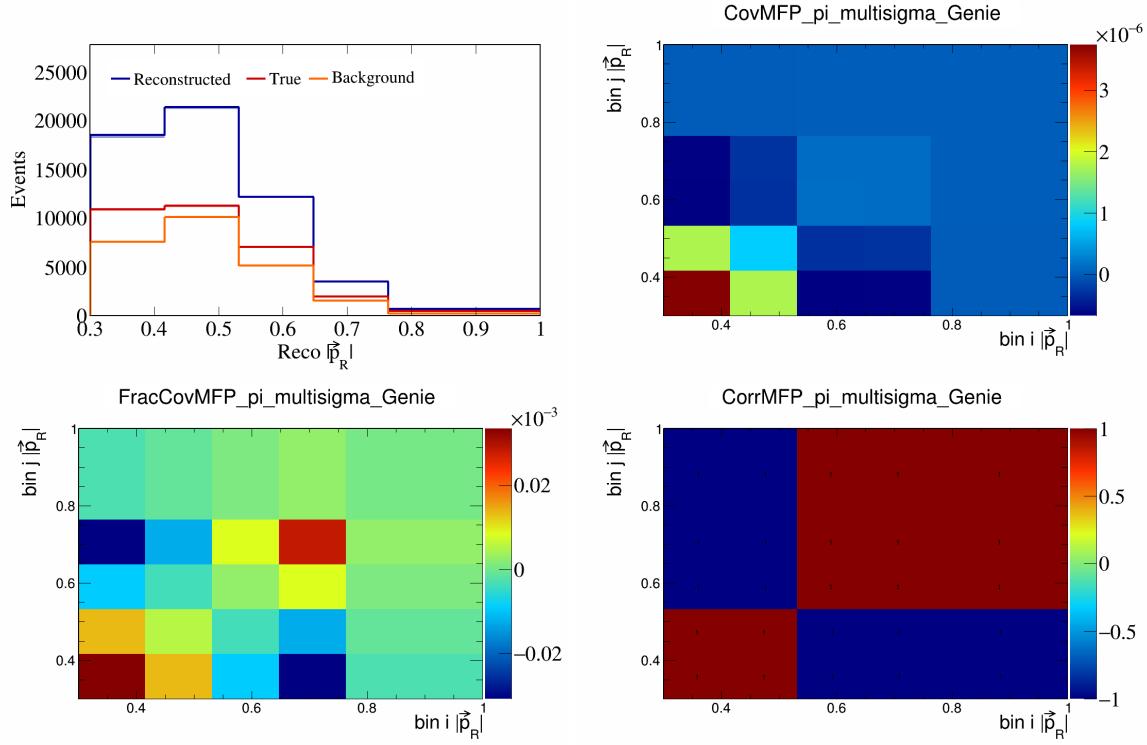


Figure 283: MFPPi variations for $|\vec{p}_R|$.

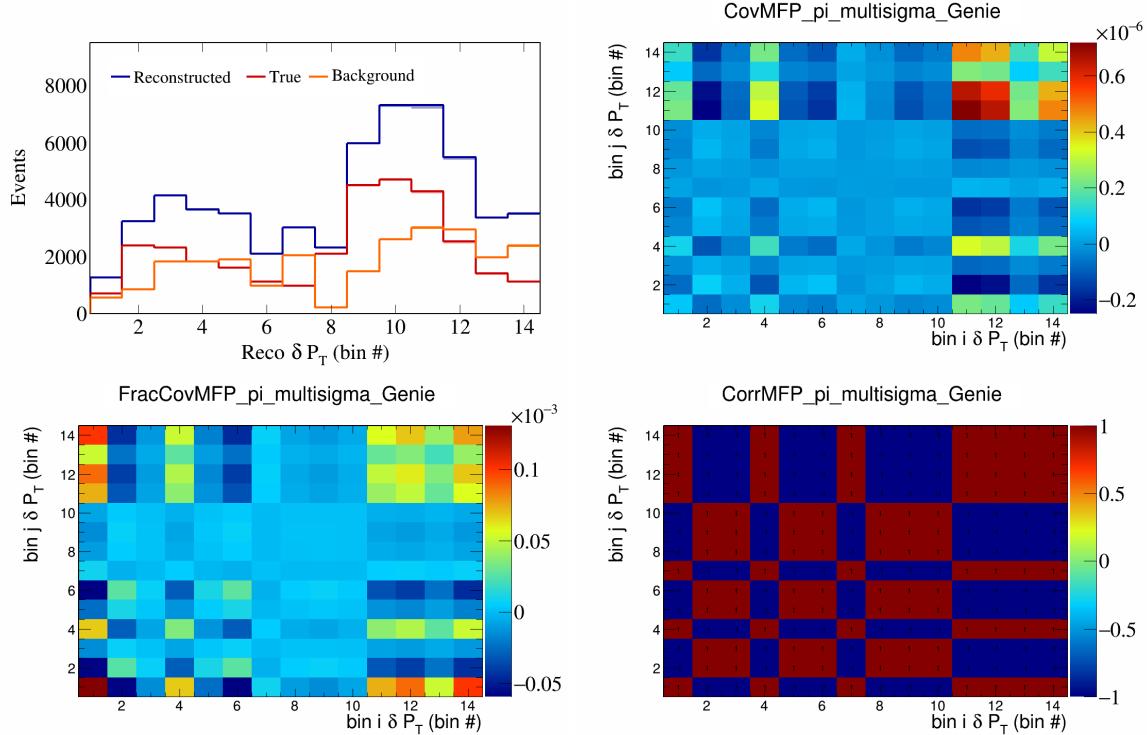


Figure 284: MFPPi variations for δP_T in $\cos(\theta_{\vec{p}_\mu})$.

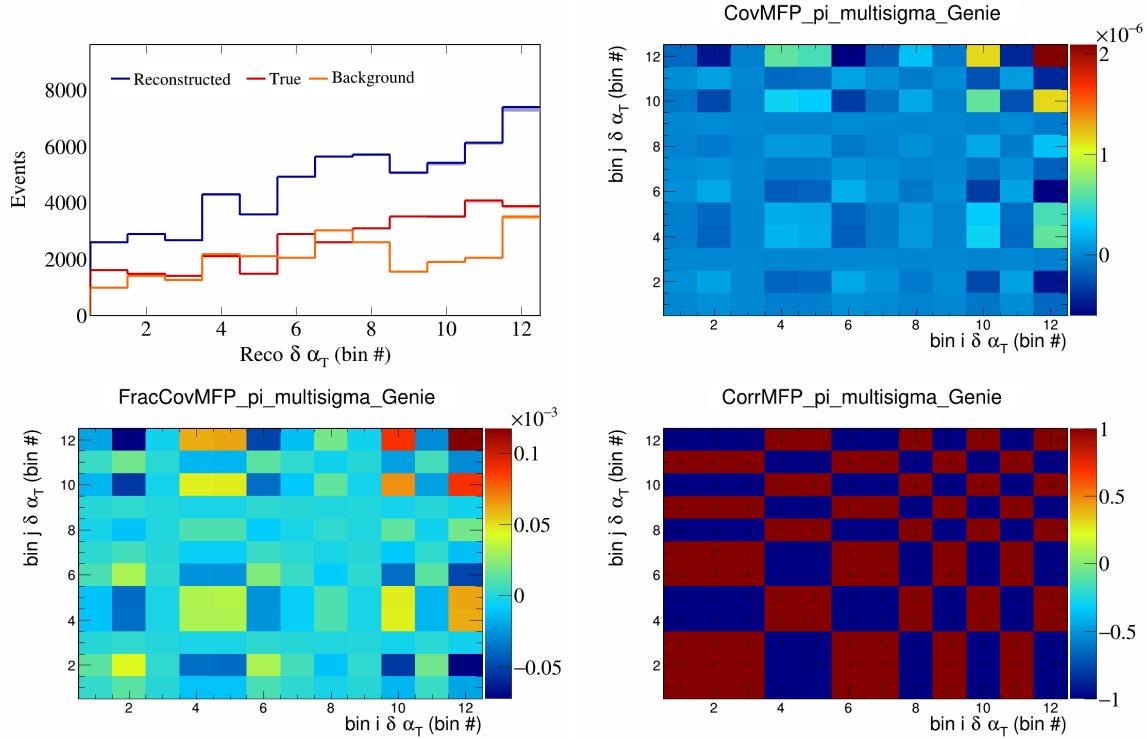


Figure 285: MFPpi variations for $\delta\alpha_T$ in $\cos(\theta_{\vec{p}_\mu})$.

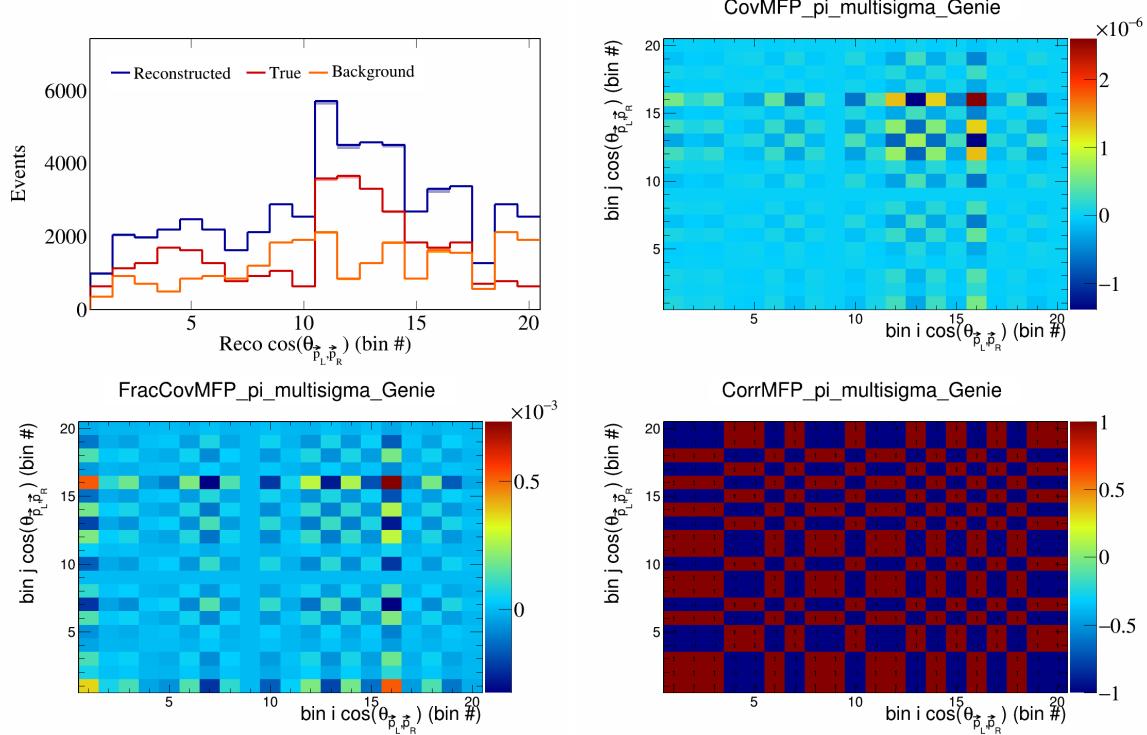


Figure 286: MFPpi variations for $\cos(\theta_{\vec{p}_L, \vec{p}_R})$ in $\cos(\theta_{\vec{p}_\mu})$.

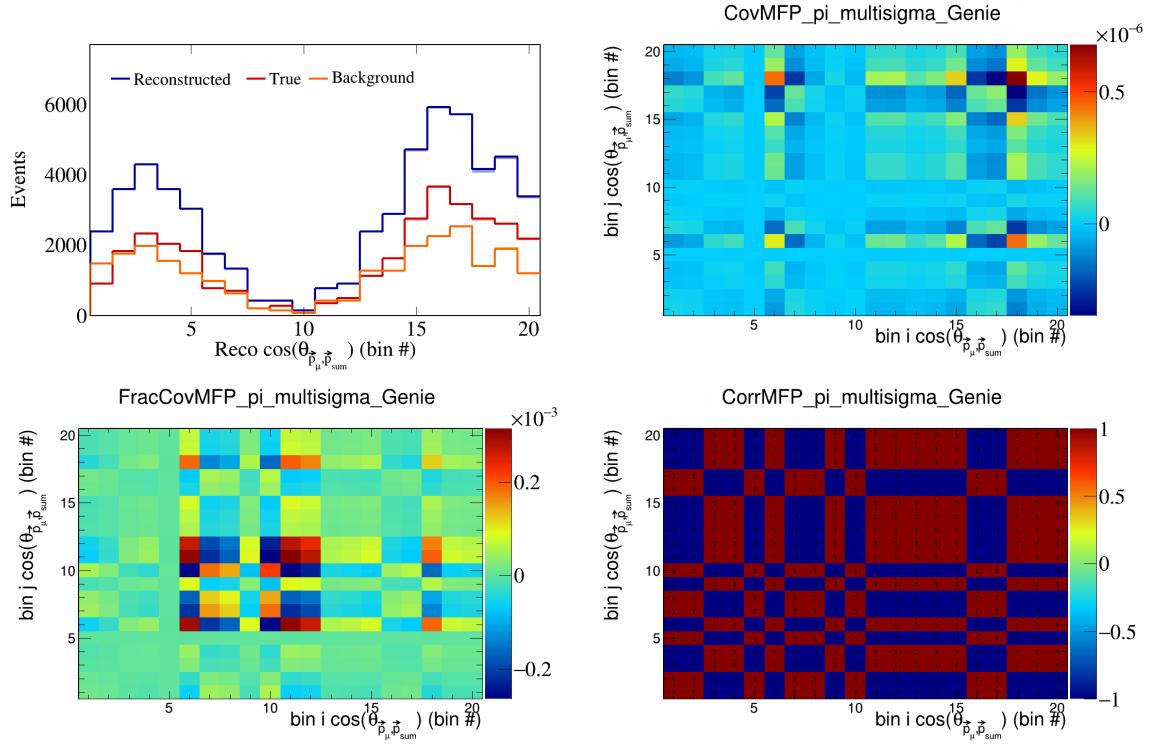


Figure 287: MFPpi variations for $\cos(\theta_{\vec{p}_\mu, \vec{p}_{\text{sum}}})$ in $\cos(\theta_{\vec{p}_\mu})$.

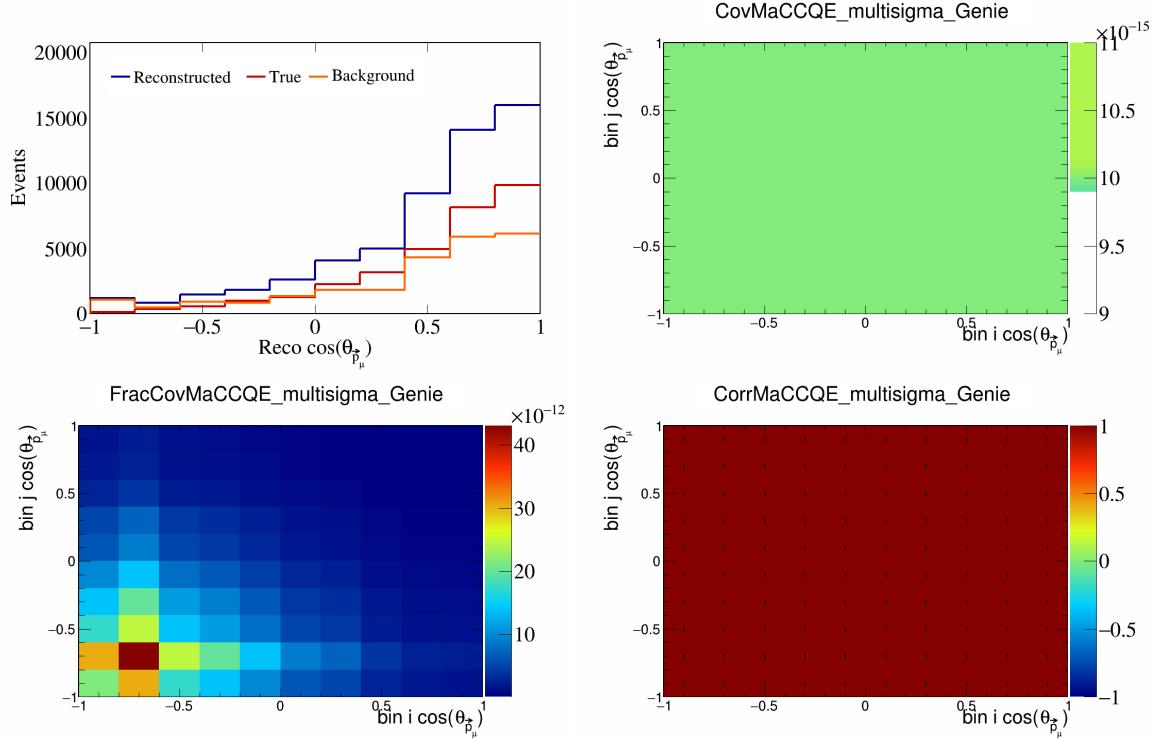


Figure 288: MaCCQE variations for $\cos(\theta_{\vec{p}_\mu})$.

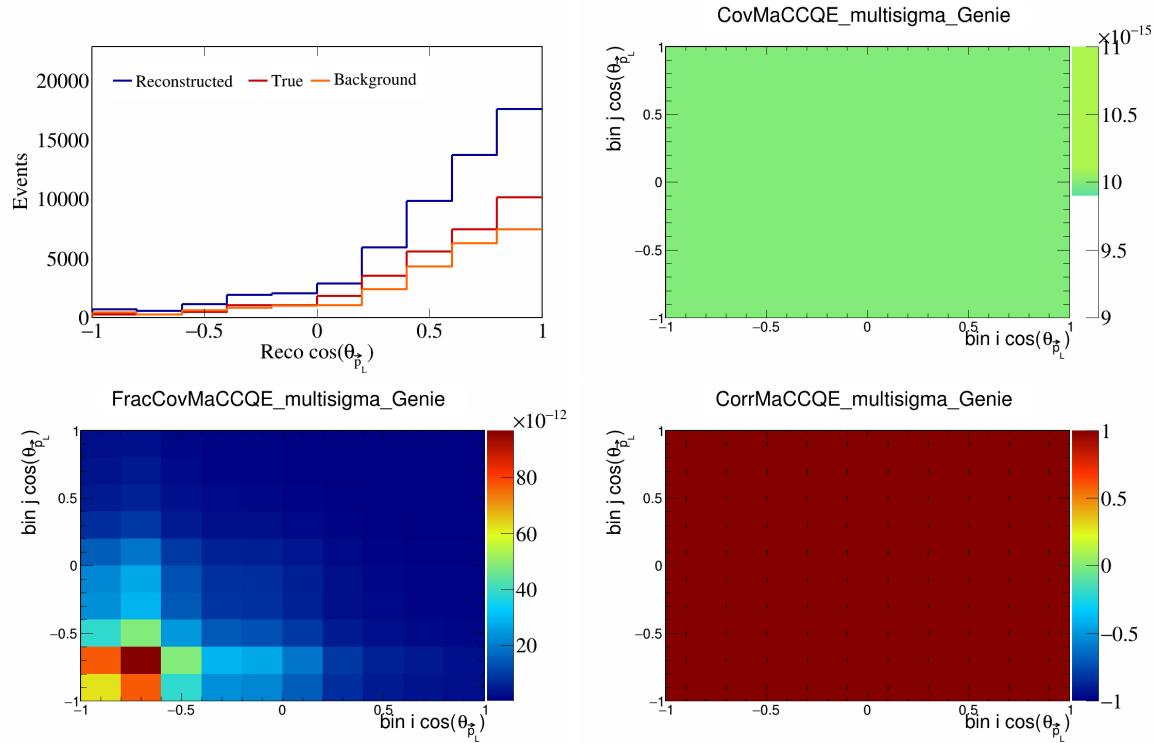


Figure 289: MaCCQE variations for $\cos(\theta_{\vec{p}_L})$.

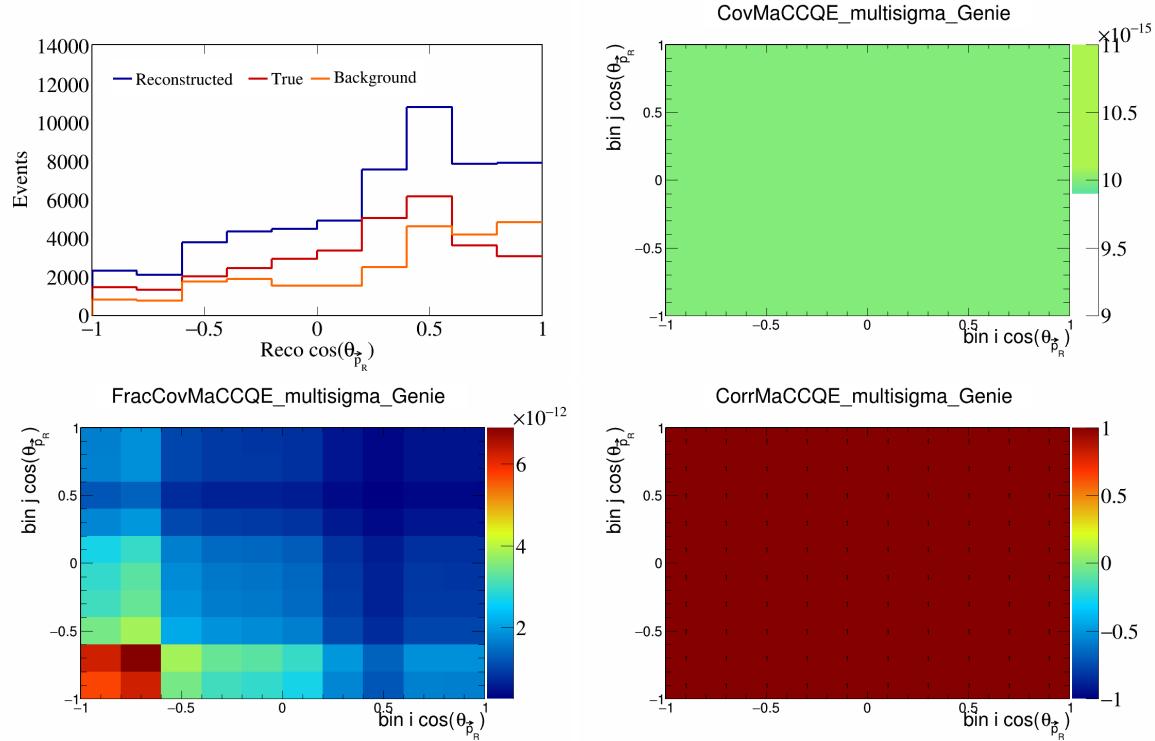


Figure 290: MaCCQE variations for $\cos(\theta_{\vec{p}_R})$.

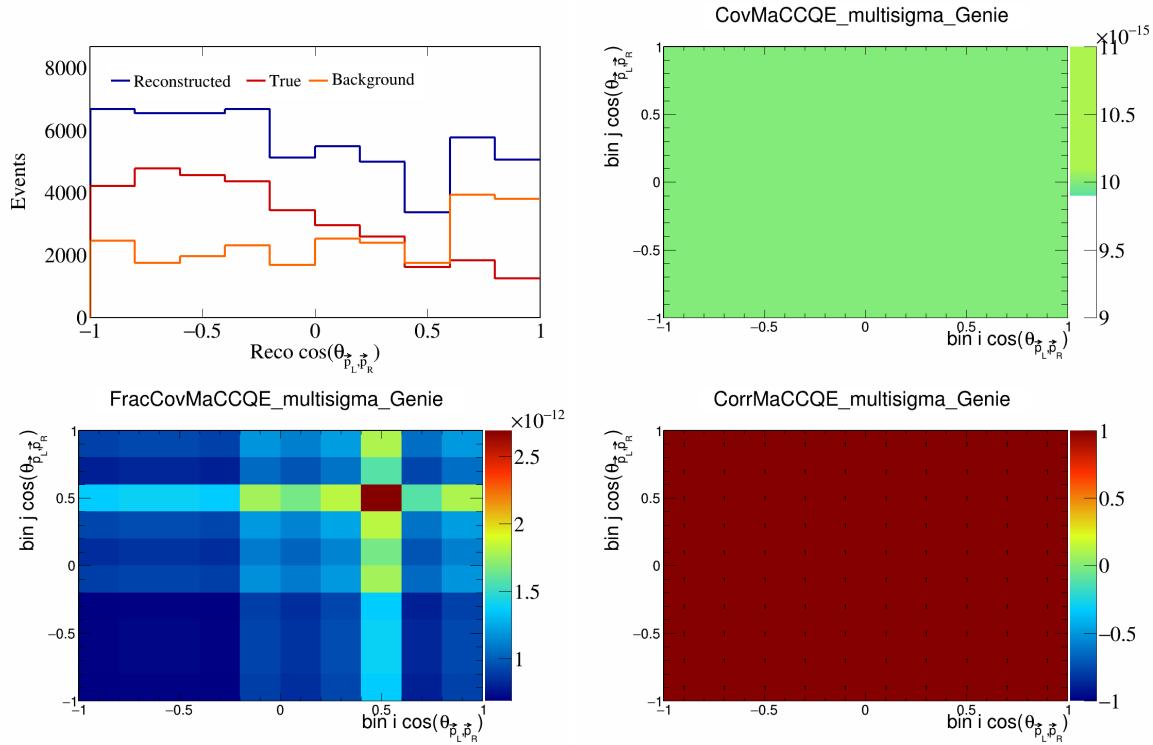


Figure 291: MaCCQE variations for $\cos(\theta_{\vec{p}_L, \vec{p}_R})$.

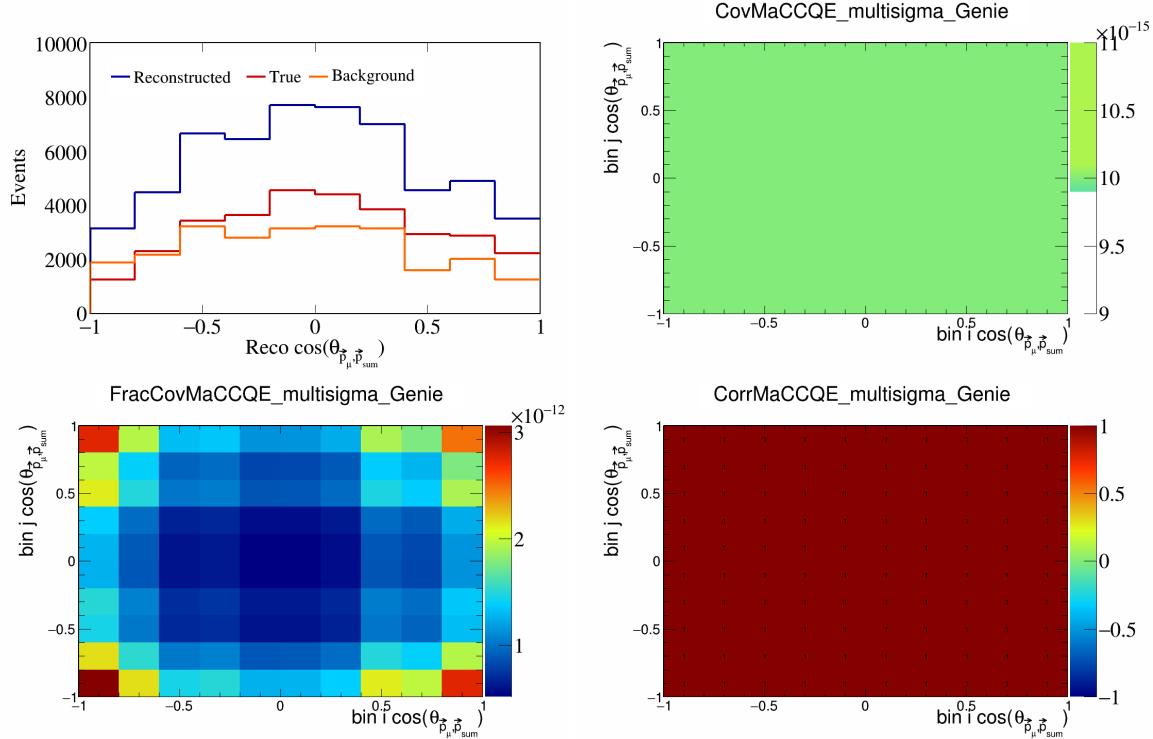


Figure 292: MaCCQE variations for $\cos(\theta_{\vec{p}_\mu, \vec{p}_{\text{sum}}})$.

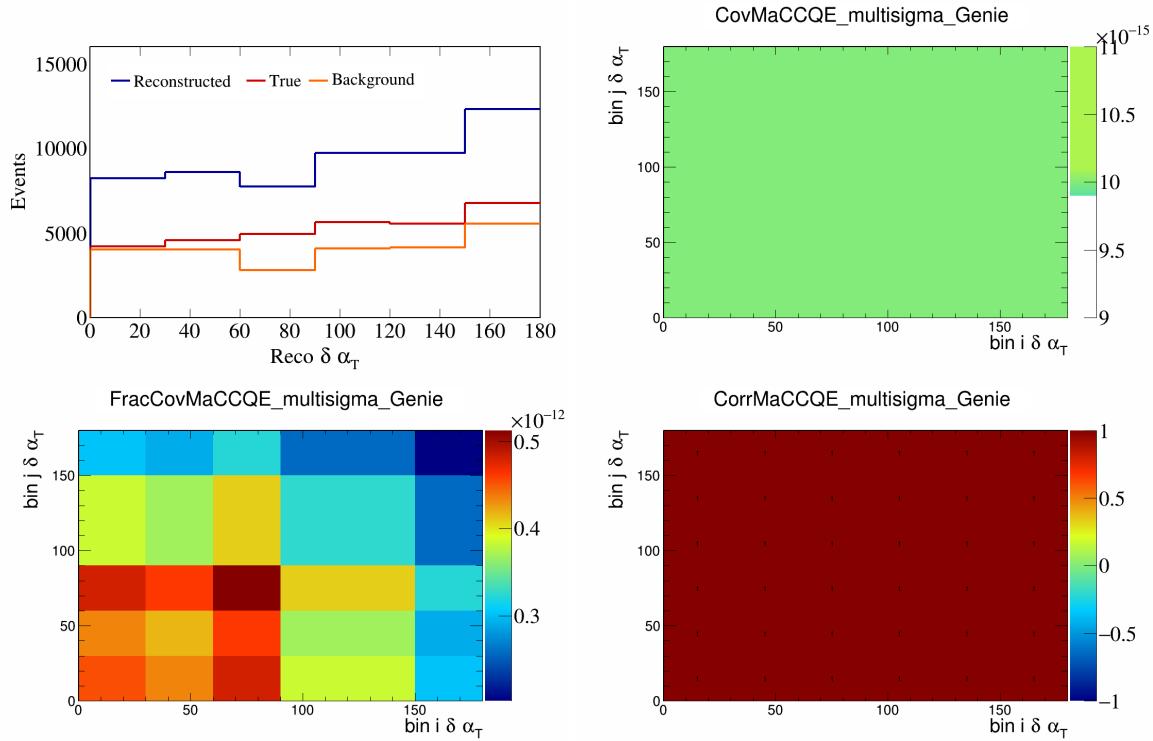


Figure 293: MaCCQE variations for $\delta\alpha_T$.

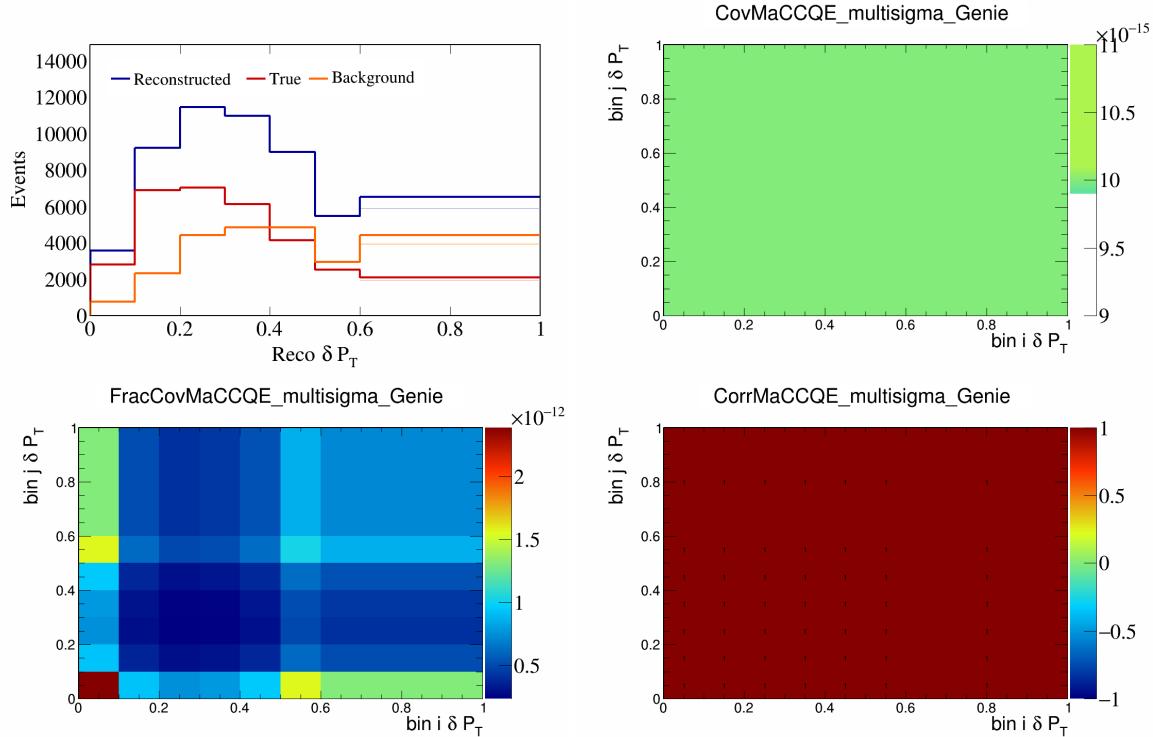


Figure 294: MaCCQE variations for δP_T .

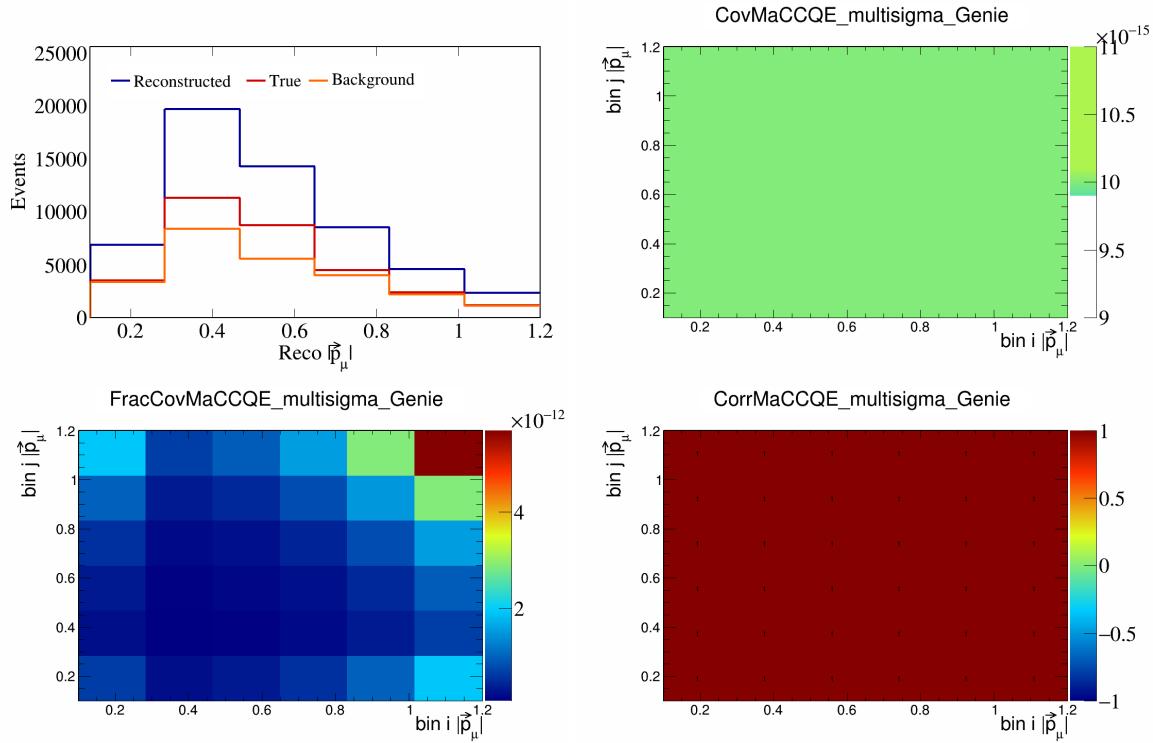


Figure 295: MaCCQE variations for $|\vec{p}_\mu|$.

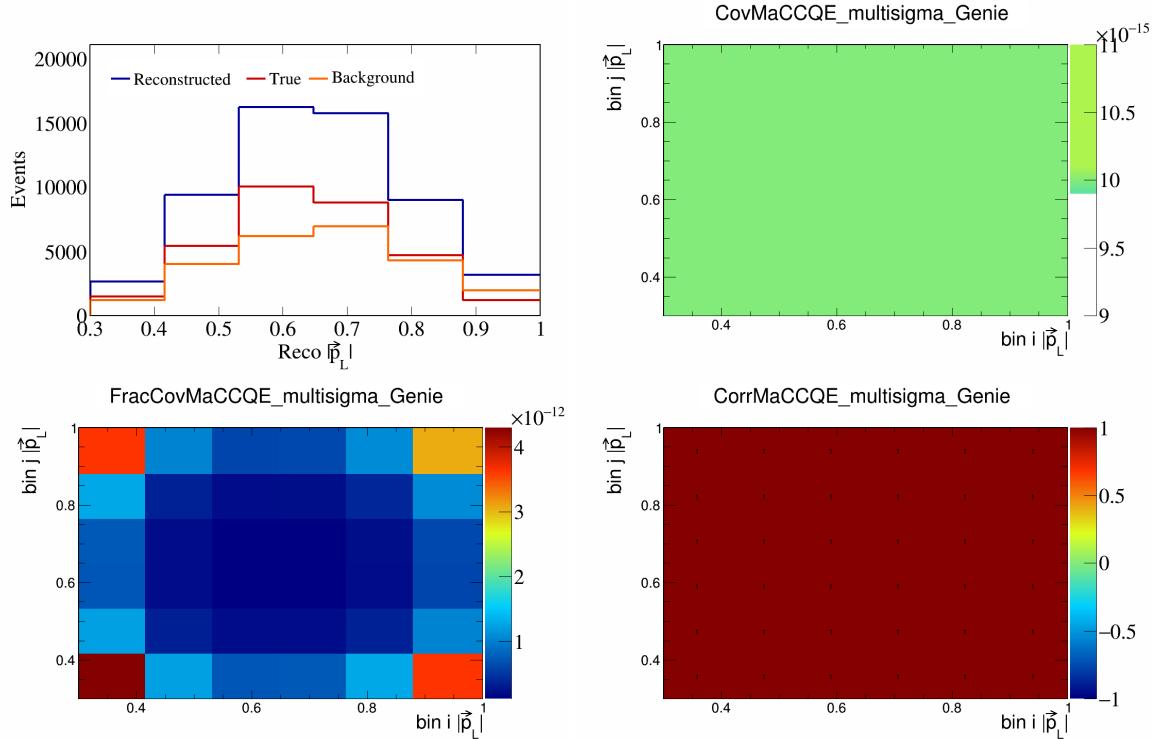


Figure 296: MaCCQE variations for $|\vec{p}_L|$.

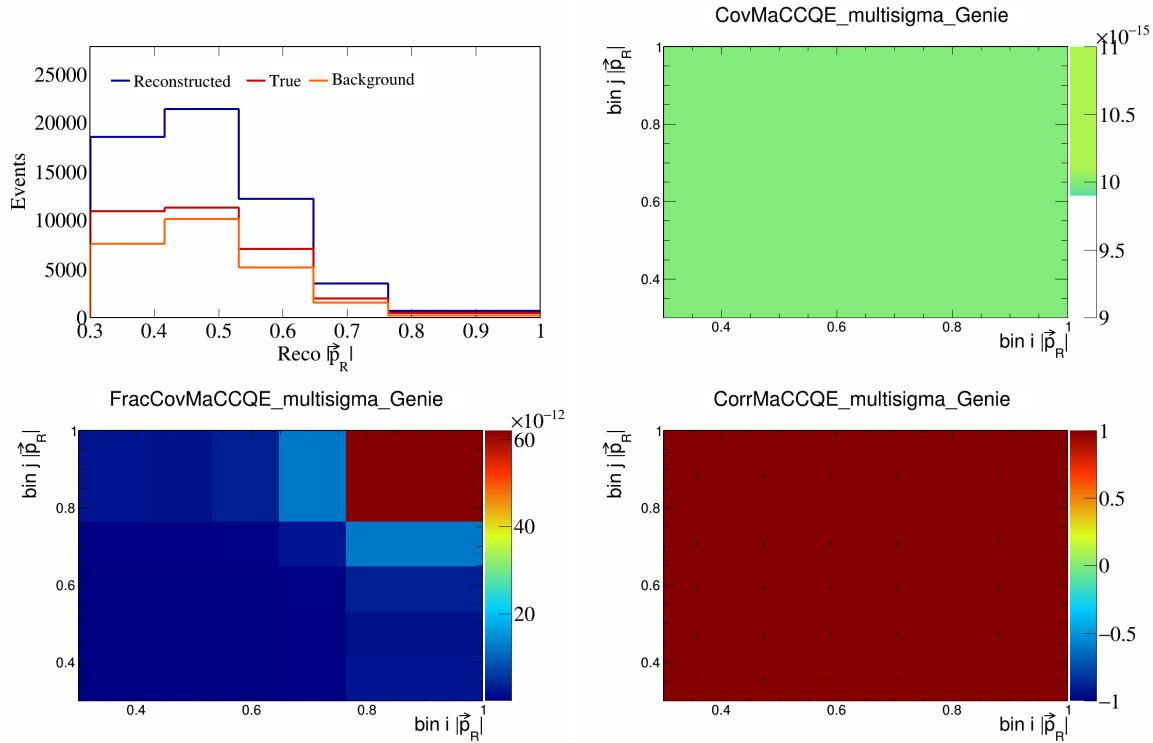


Figure 297: MaCCQE variations for $|\vec{p}_R|$.

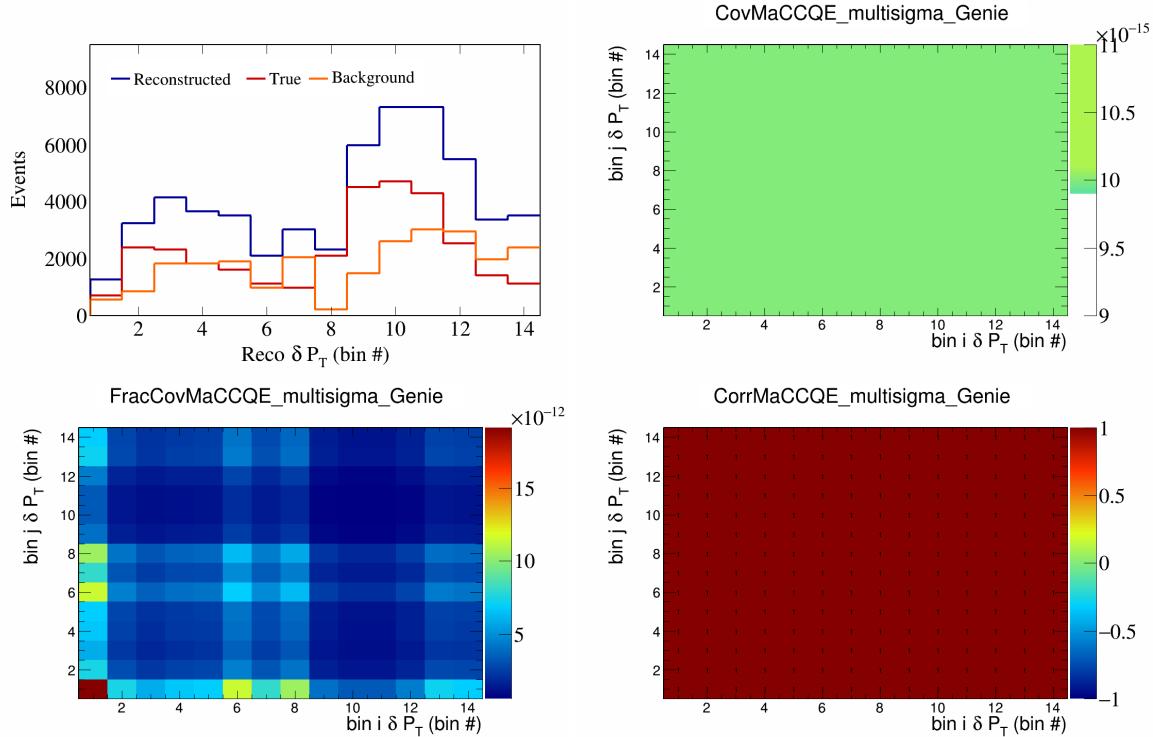


Figure 298: MaCCQE variations for δP_T in $\cos(\theta_{\vec{p}_\mu})$.

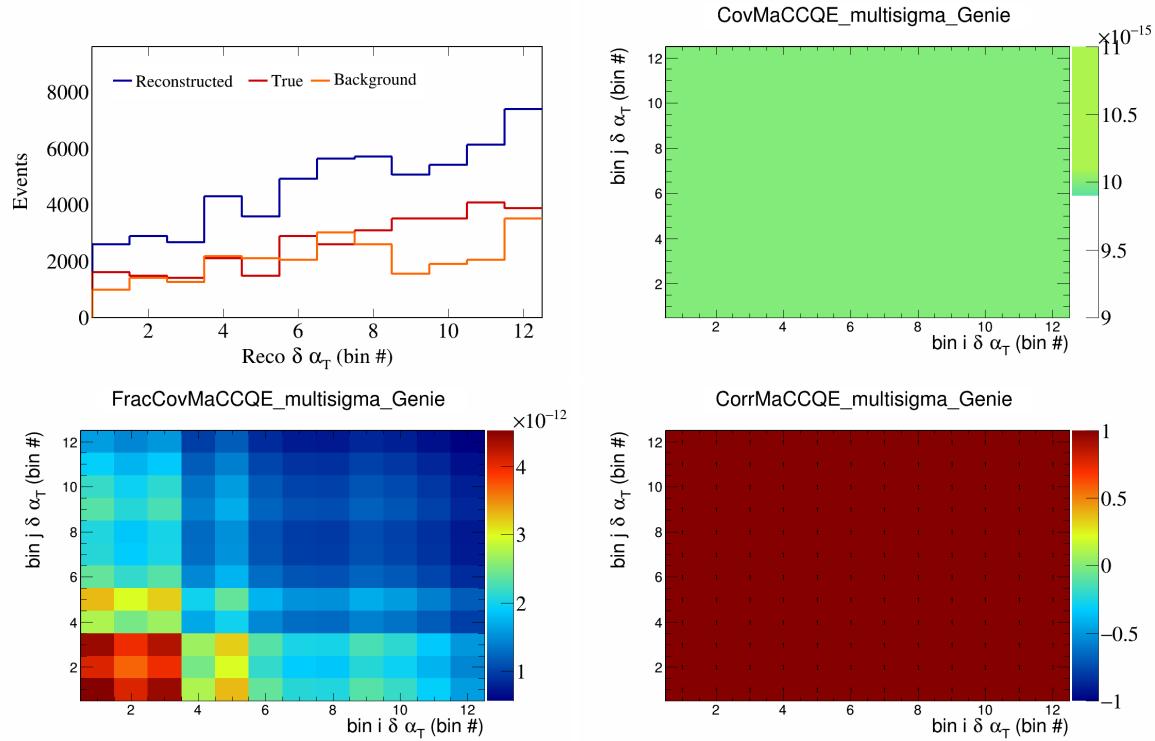


Figure 299: MaCCQE variations for $\delta\alpha_T$ in $\cos(\theta_{\vec{p}_\mu})$.

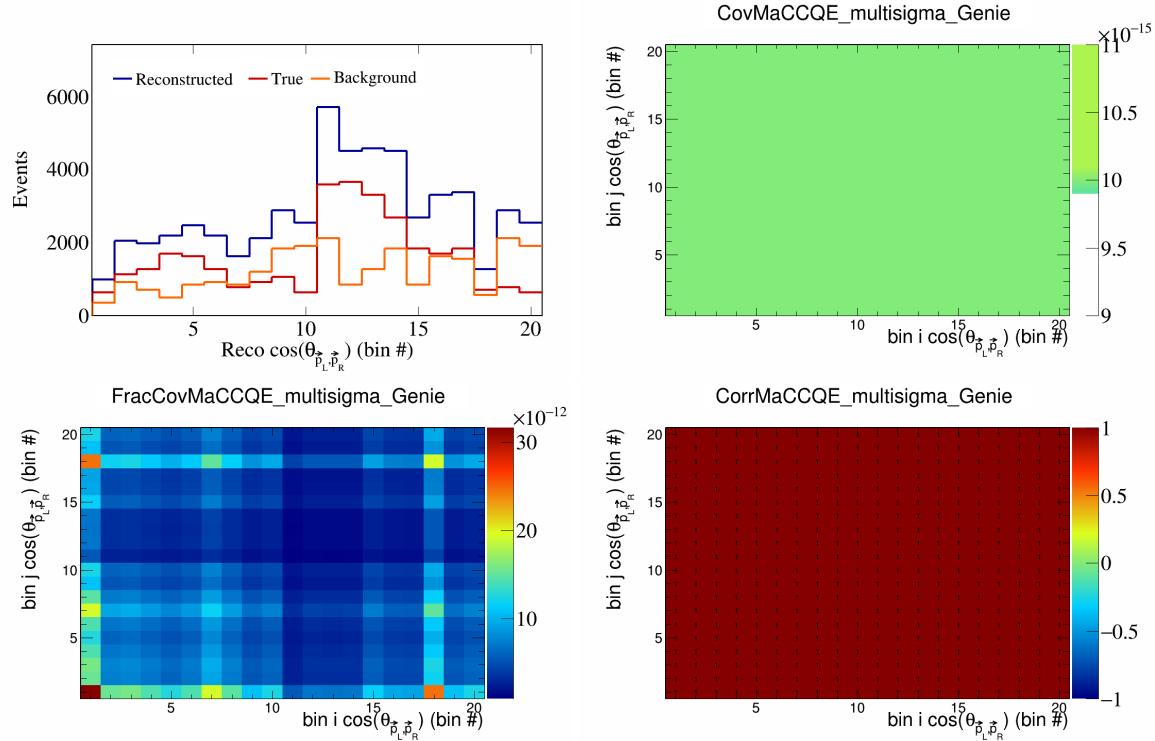


Figure 300: MaCCQE variations for $\cos(\theta_{\vec{p}_L, \vec{p}_R})$ in $\cos(\theta_{\vec{p}_\mu})$.

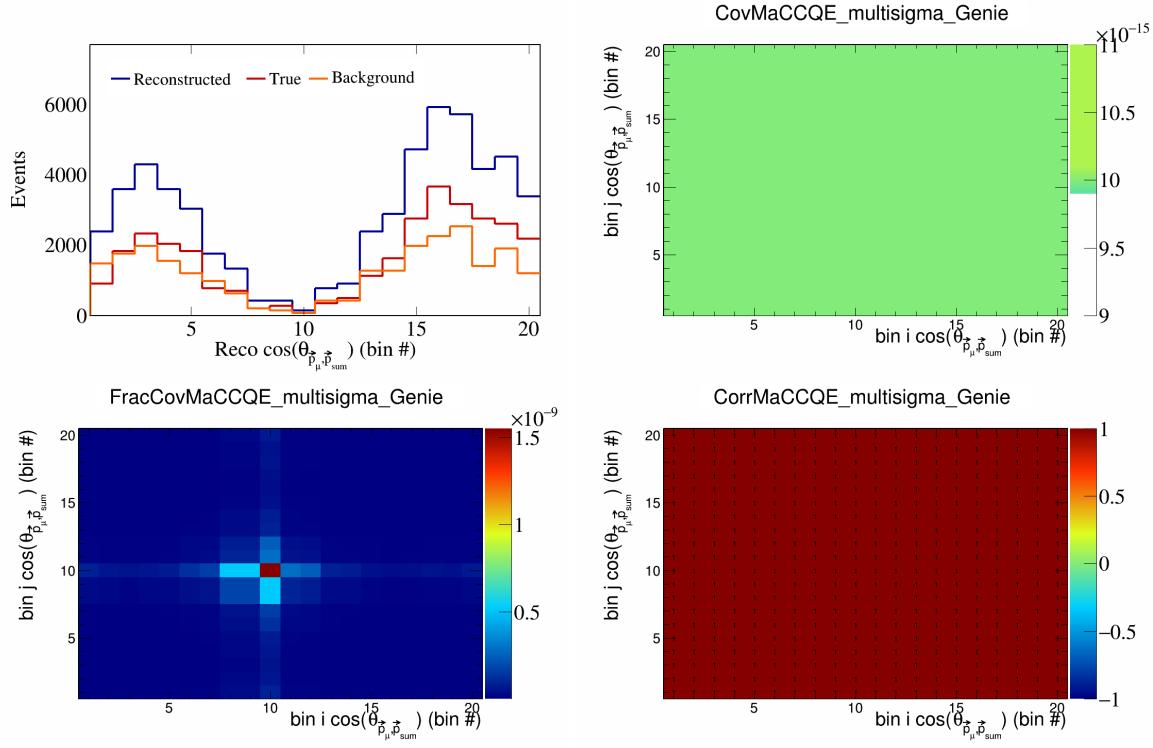


Figure 301: MaCCQE variations for $\cos(\theta_{\vec{p}_\mu} \vec{p}_{\text{sum}})$ in $\cos(\theta_{\vec{p}_\mu})$.

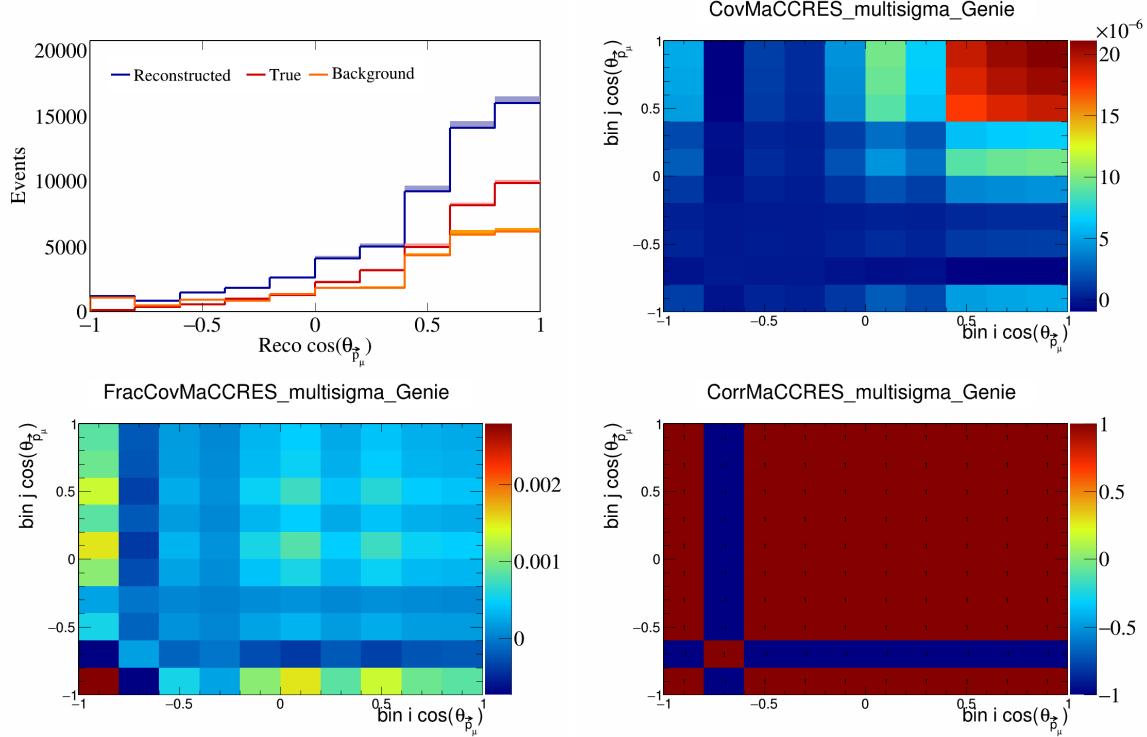


Figure 302: MaCCRES variations for $\cos(\theta_{\vec{p}_\mu})$.

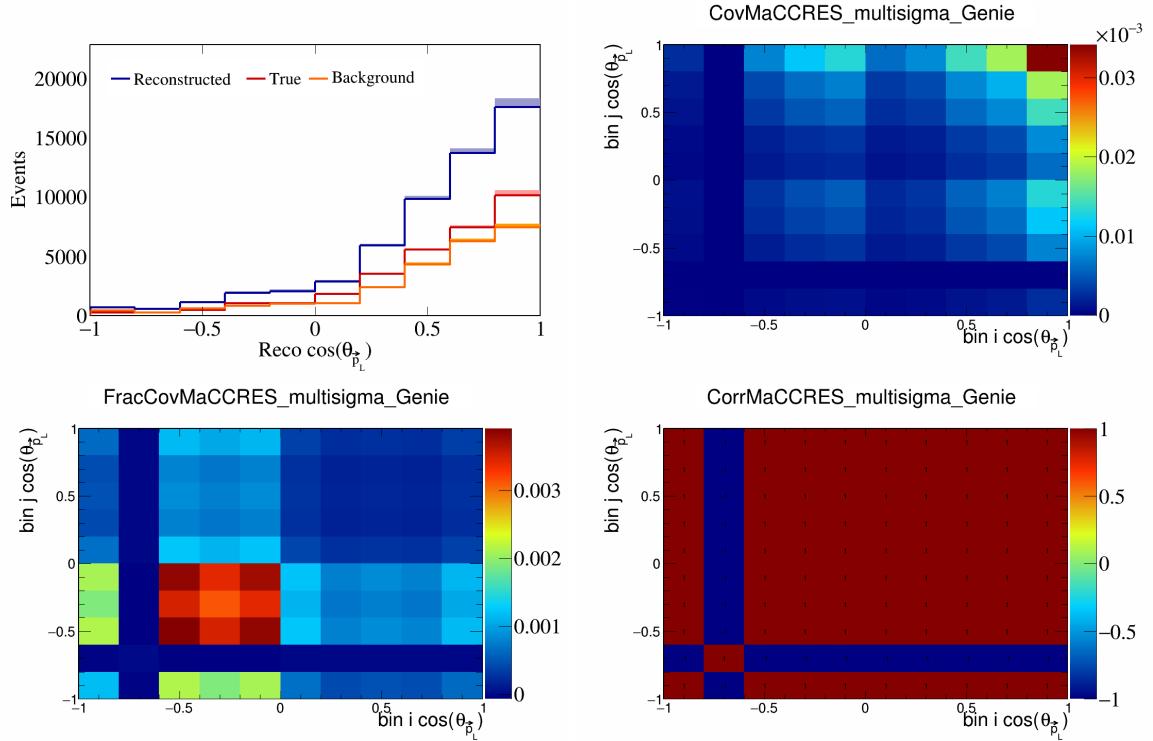


Figure 303: MaCCRES variations for $\cos(\theta_{\vec{p}_L})$.

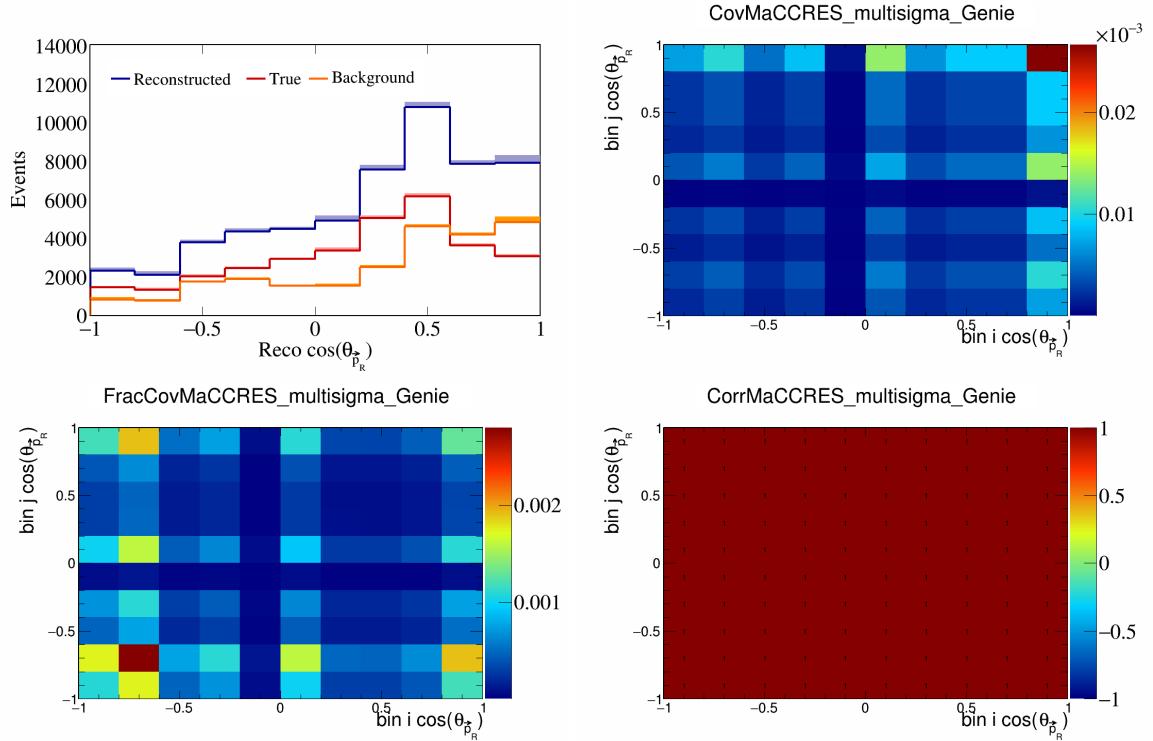


Figure 304: MaCCRES variations for $\cos(\theta_{\vec{p}_R})$.

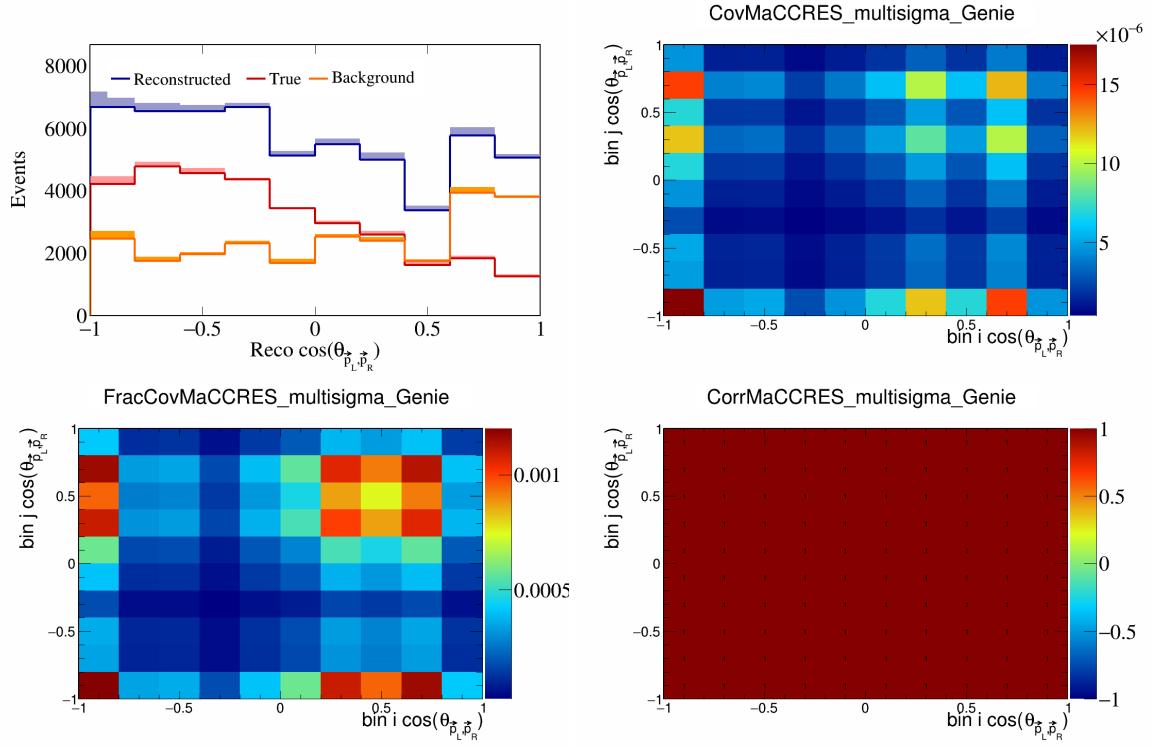


Figure 305: MaCCRES variations for $\cos(\theta_{\vec{p}_L, \vec{p}_R})$.

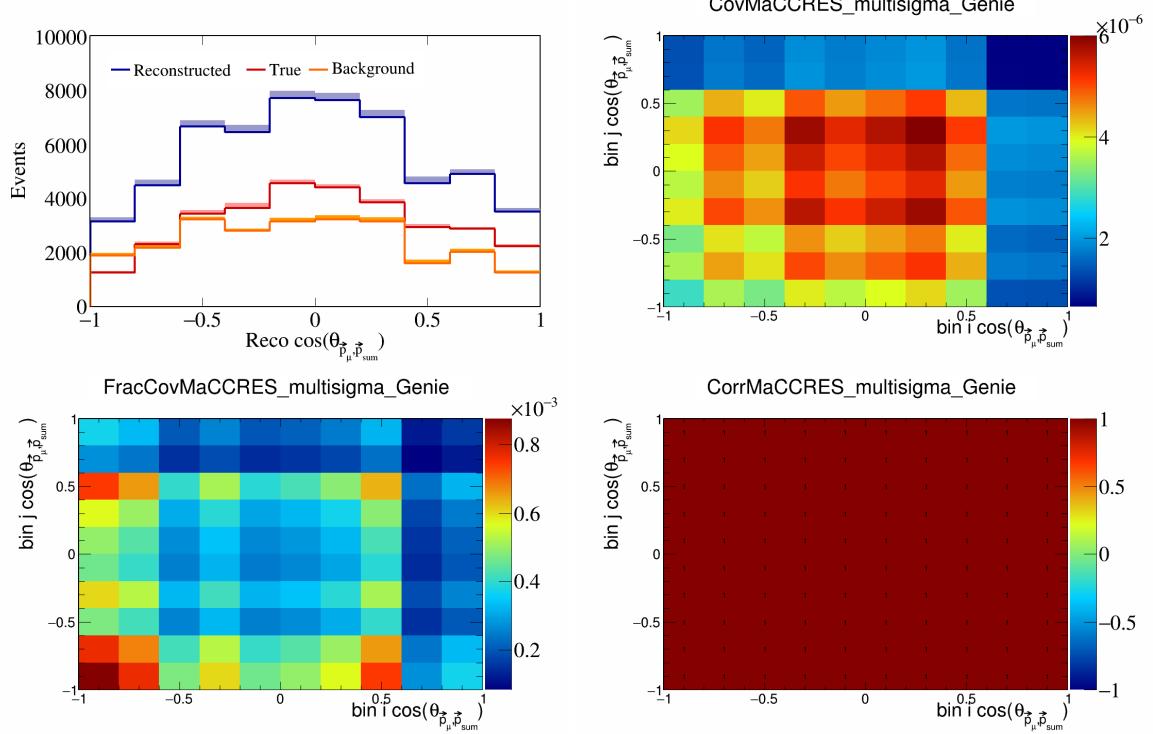


Figure 306: MaCCRES variations for $\cos(\theta_{\vec{p}_\mu, \vec{p}_{\text{sum}}})$.

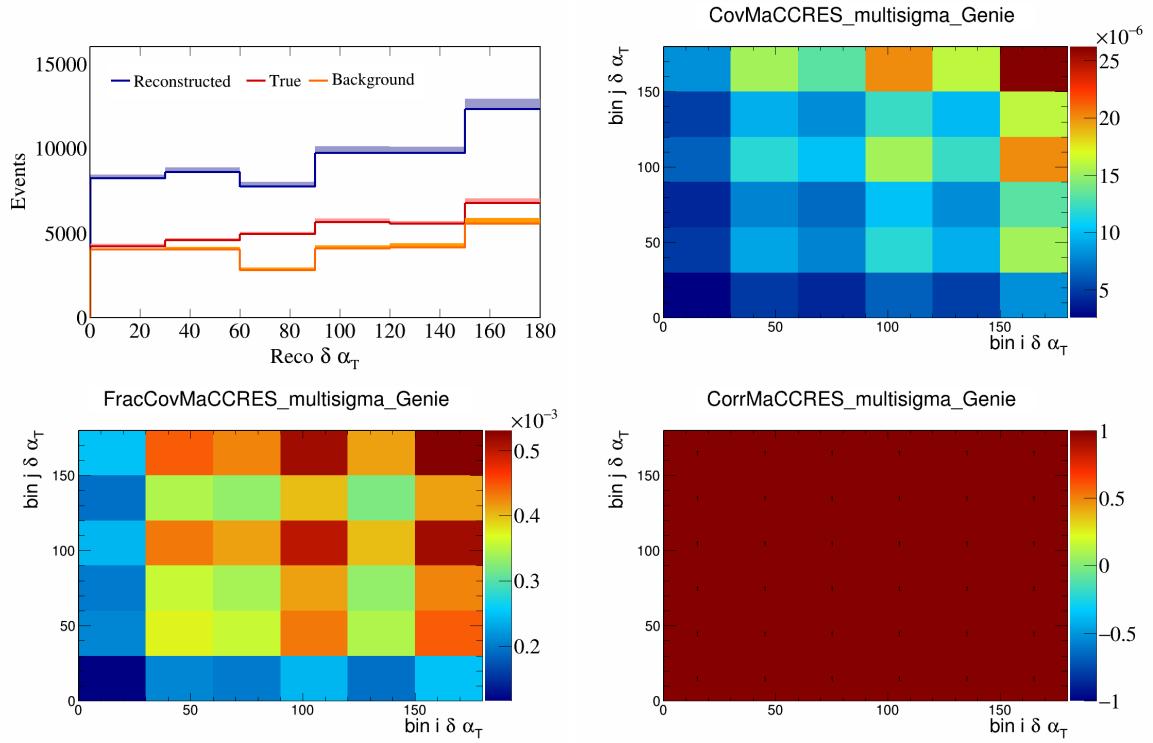


Figure 307: MaCCRES variations for $\delta\alpha_T$.

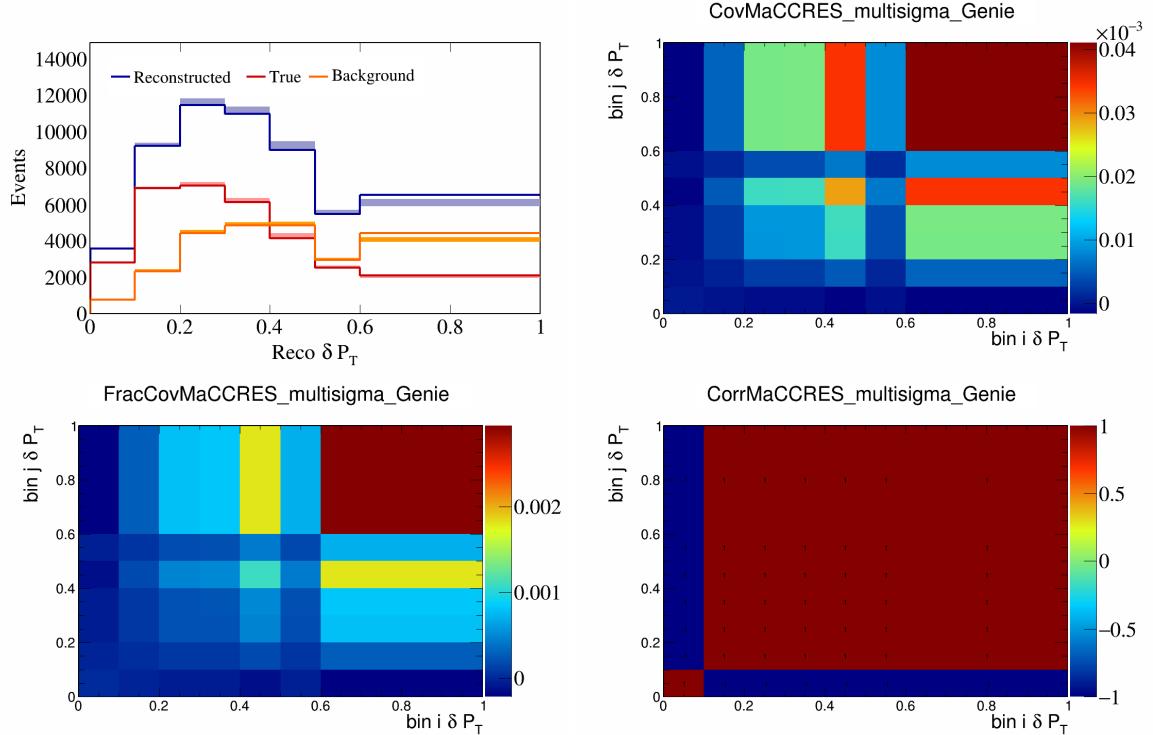


Figure 308: MaCCRES variations for δP_T .

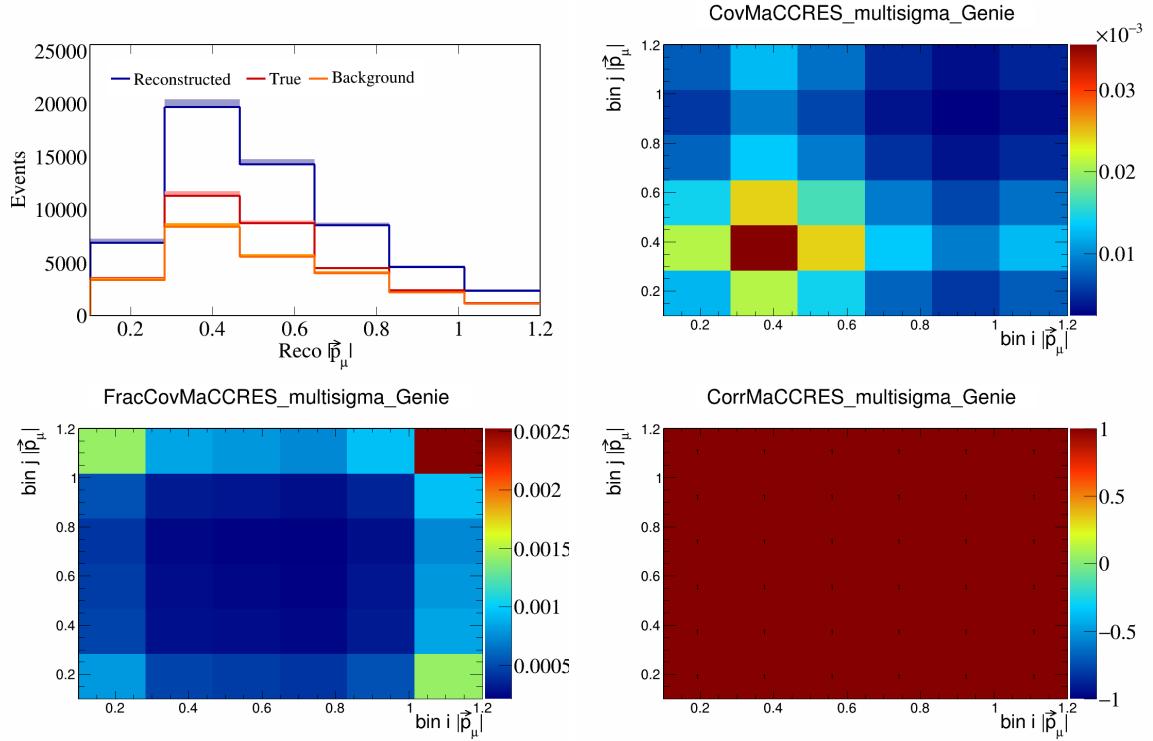


Figure 309: MaCCRES variations for $|\vec{p}_\mu|$.

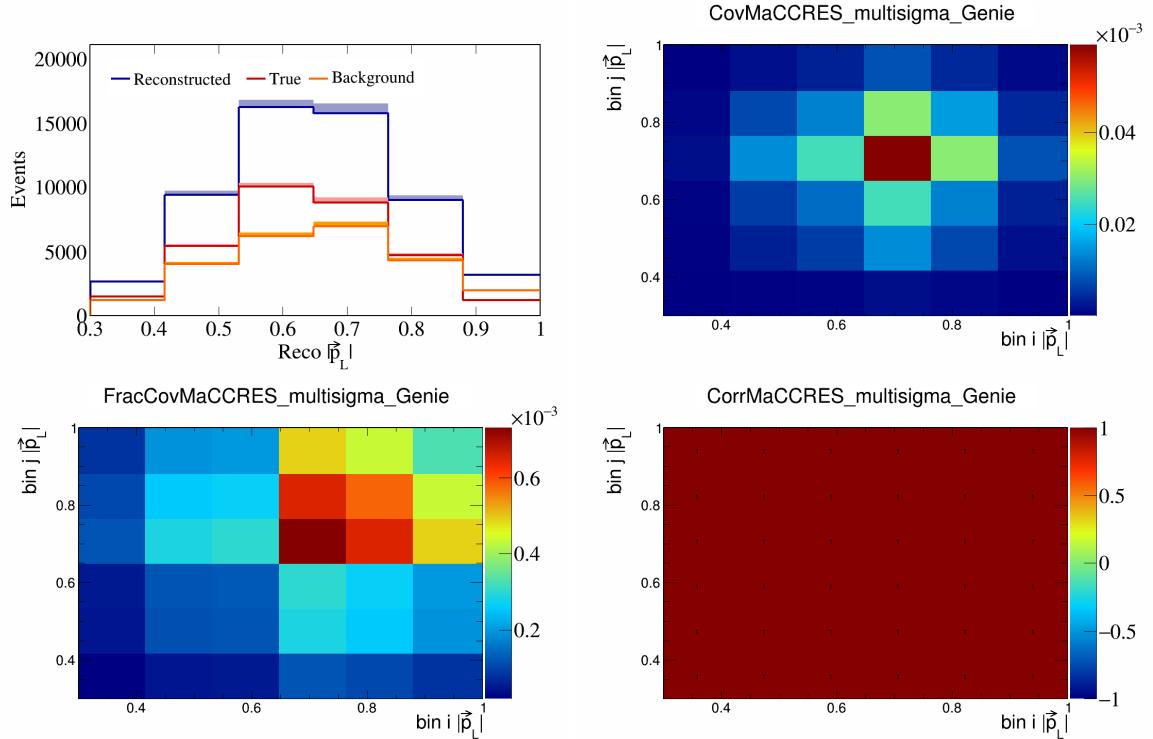


Figure 310: MaCCRES variations for $|\vec{p}_L|$.

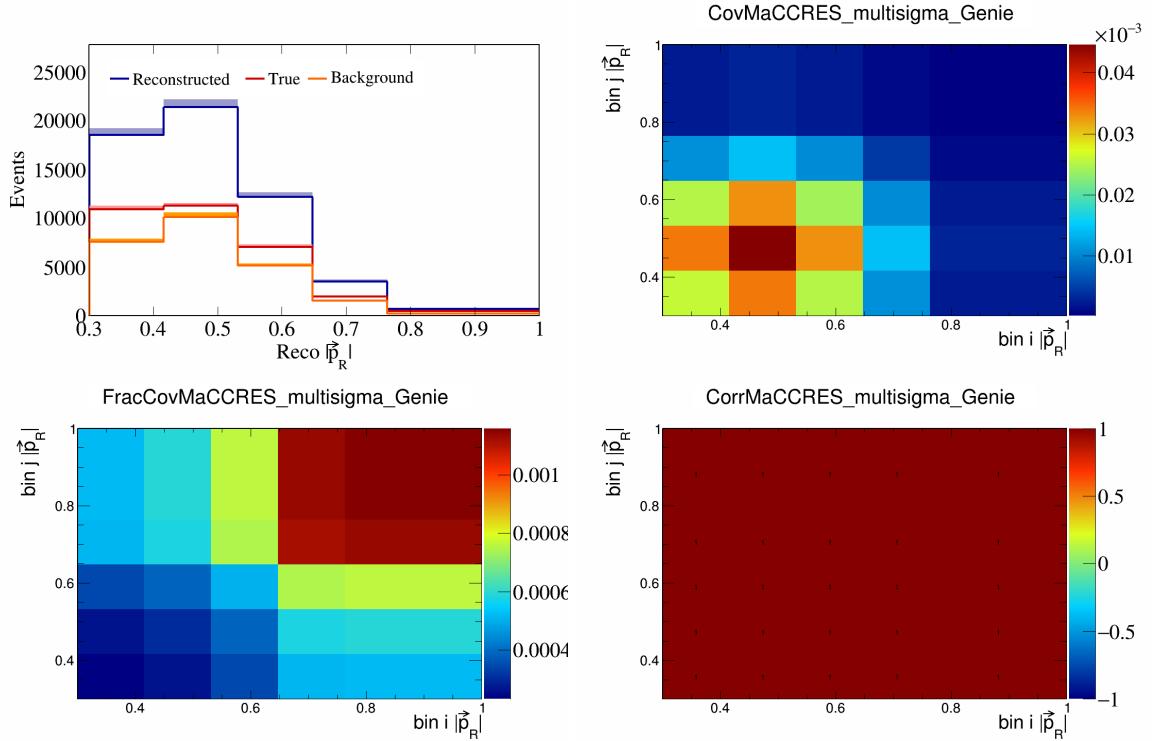


Figure 311: MaCCRES variations for $|\vec{p}_R|$.

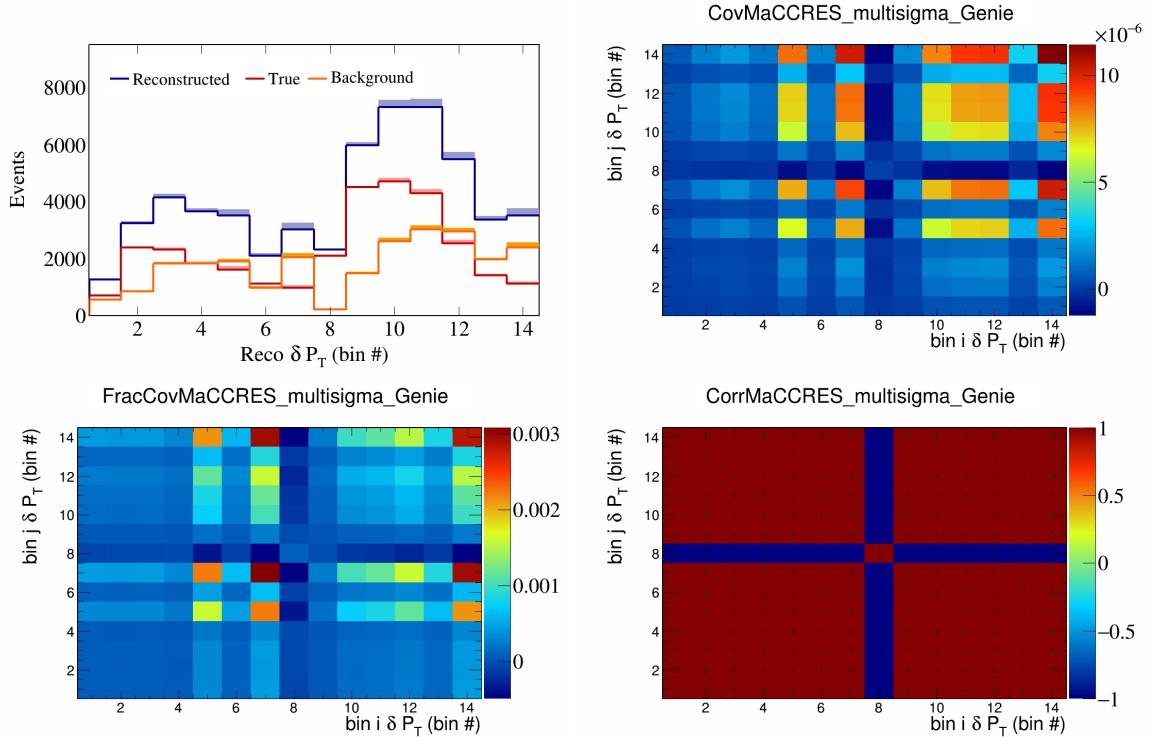


Figure 312: MaCCRES variations for δP_T in $\cos(\theta_{\vec{p}_\mu})$.

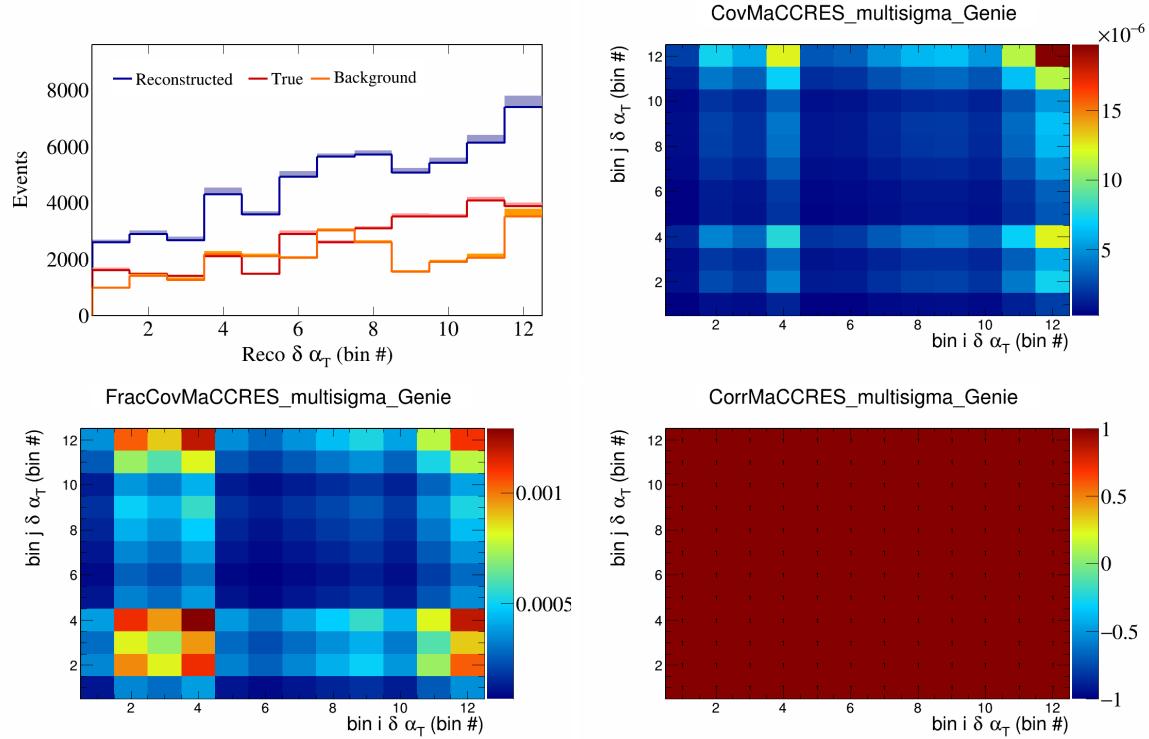


Figure 313: MaCCRES variations for $\delta \alpha_T$ in $\cos(\theta_{\vec{p}_\mu})$.

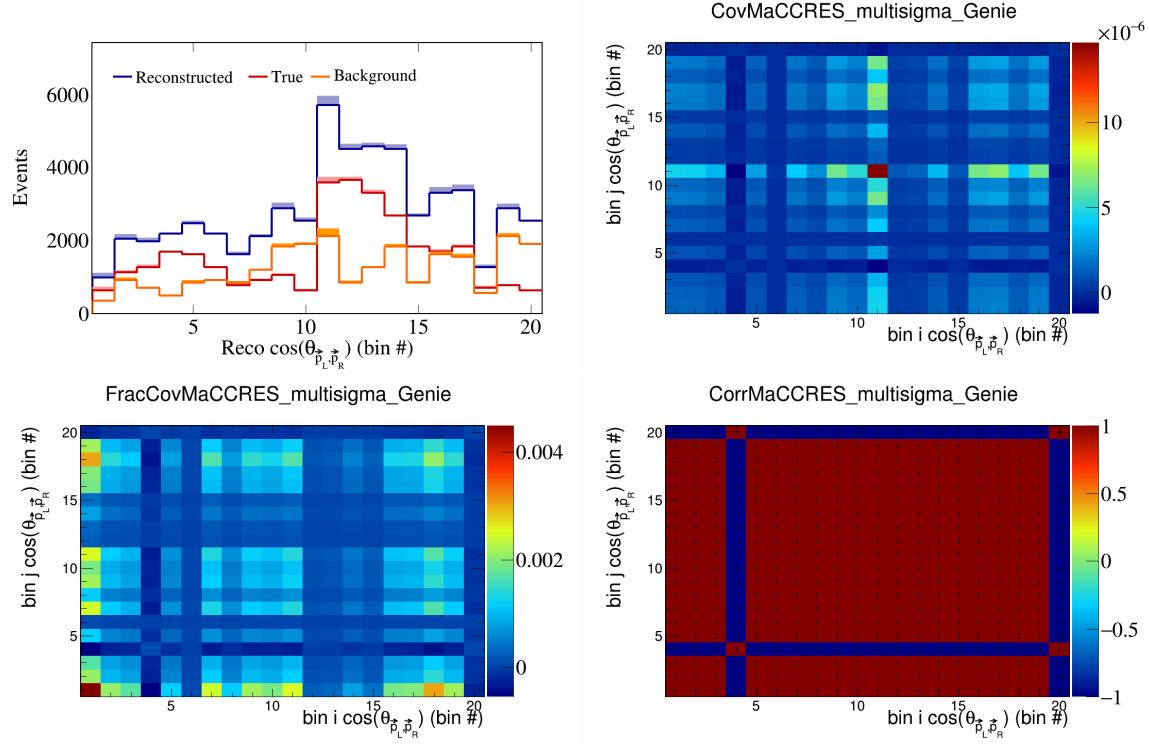


Figure 314: MaCCRES variations for $\cos(\theta_{\vec{p}_L, \vec{p}_R})$ in $\cos(\theta_{\vec{p}_\mu})$.

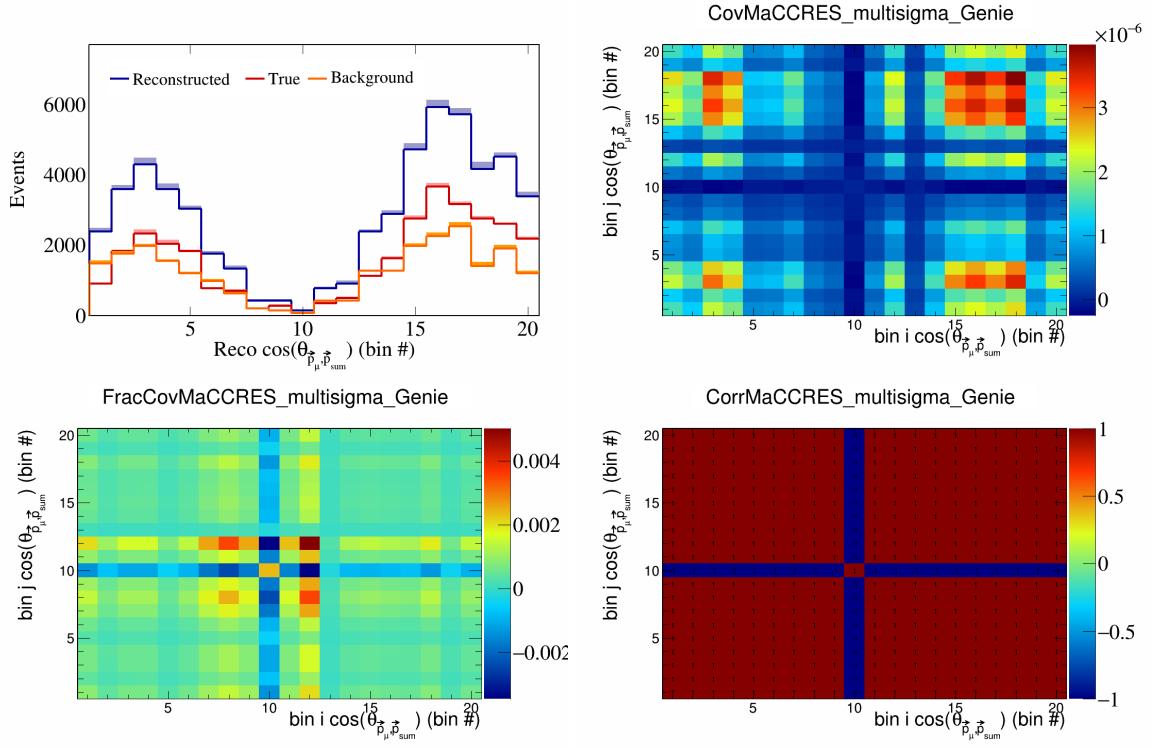


Figure 315: MaCCRES variations for $\cos(\theta_{\vec{p}_\mu, \vec{p}_{\text{sum}}})$ in $\cos(\theta_{\vec{p}_\mu})$.

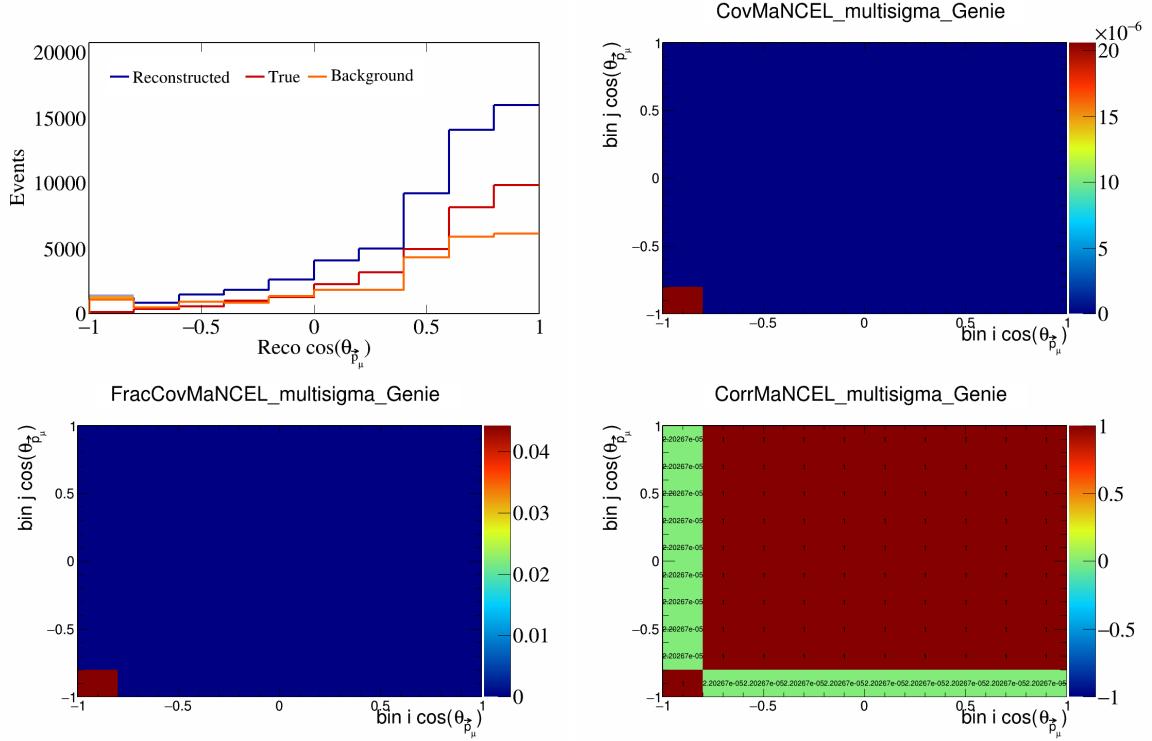


Figure 316: MaNCEL variations for $\cos(\theta_{\vec{p}_\mu})$.

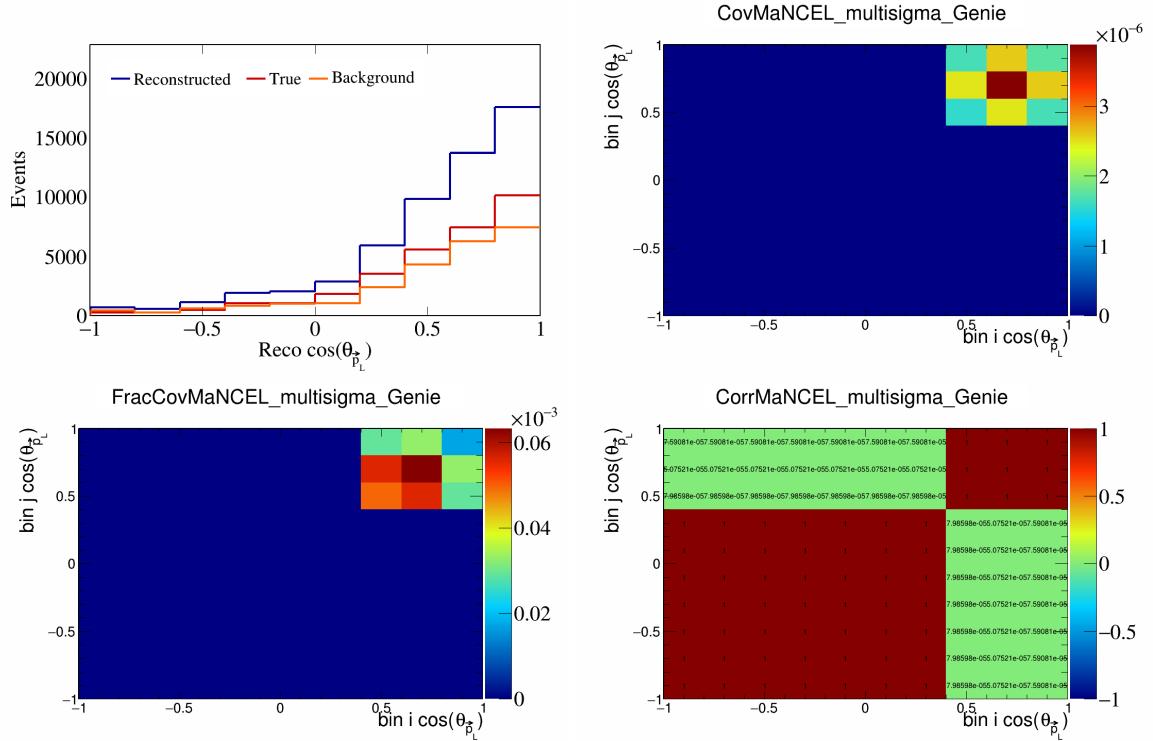


Figure 317: MaNCEL variations for $\cos(\theta_{\vec{p}_L})$.

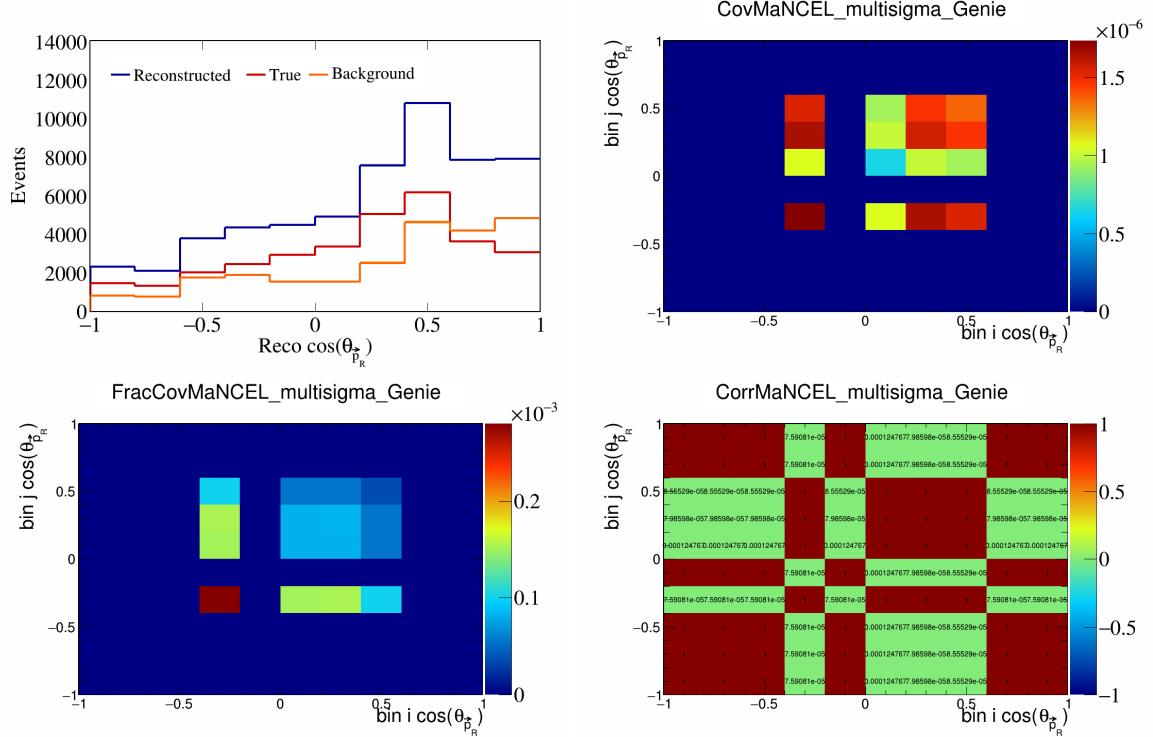


Figure 318: MaNCEL variations for $\cos(\theta_{\vec{p}_R})$.

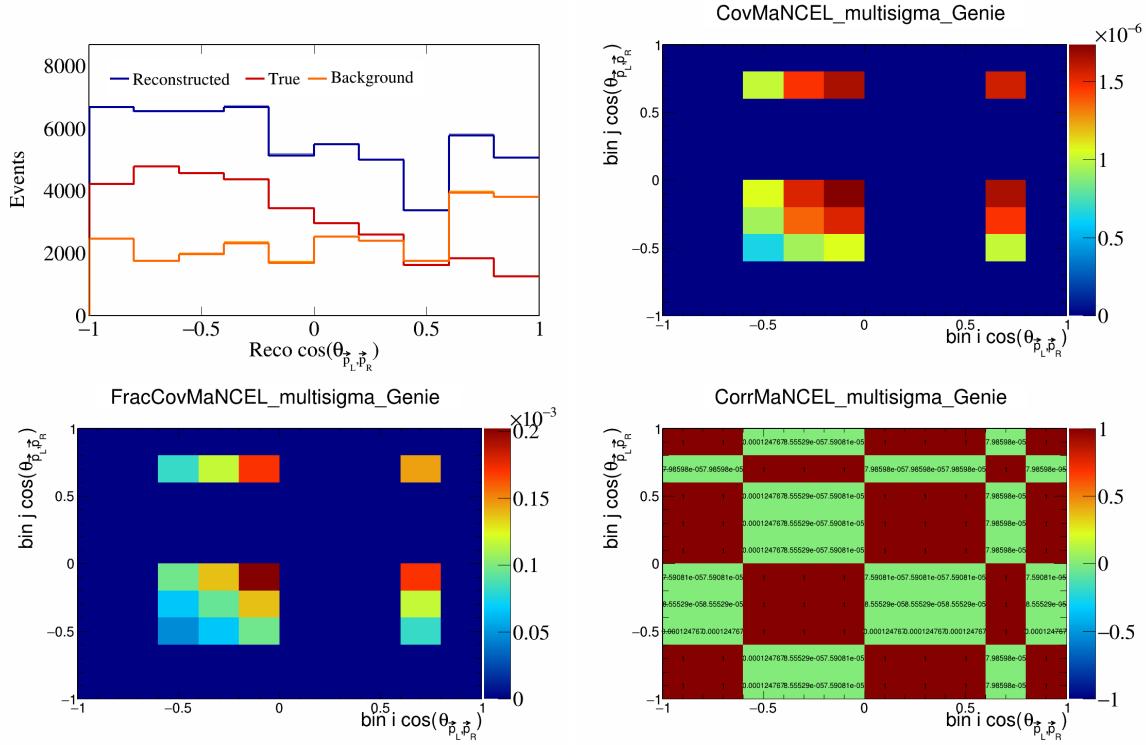


Figure 319: MaNCEL variations for $\cos(\theta_{\vec{p}_L, \vec{p}_R})$.

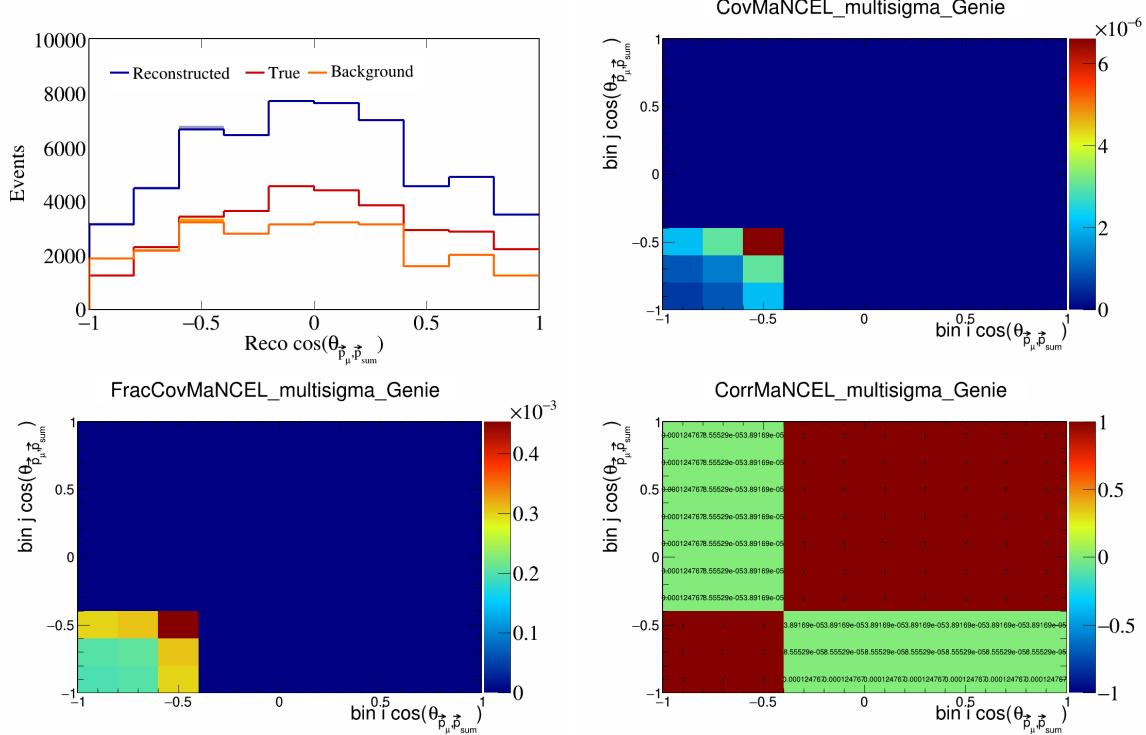


Figure 320: MaNCEL variations for $\cos(\theta_{\vec{p}_\mu, \vec{p}_{\text{sum}}})$.

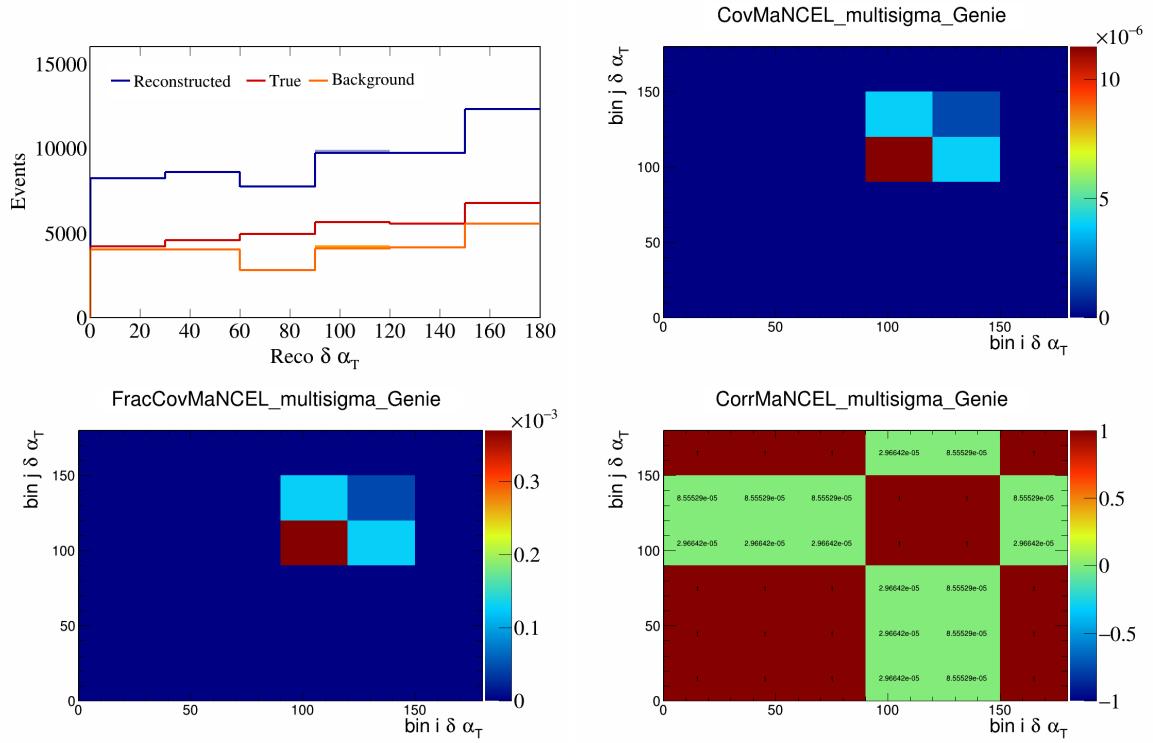


Figure 321: MaNCEL variations for $\delta\alpha_T$.

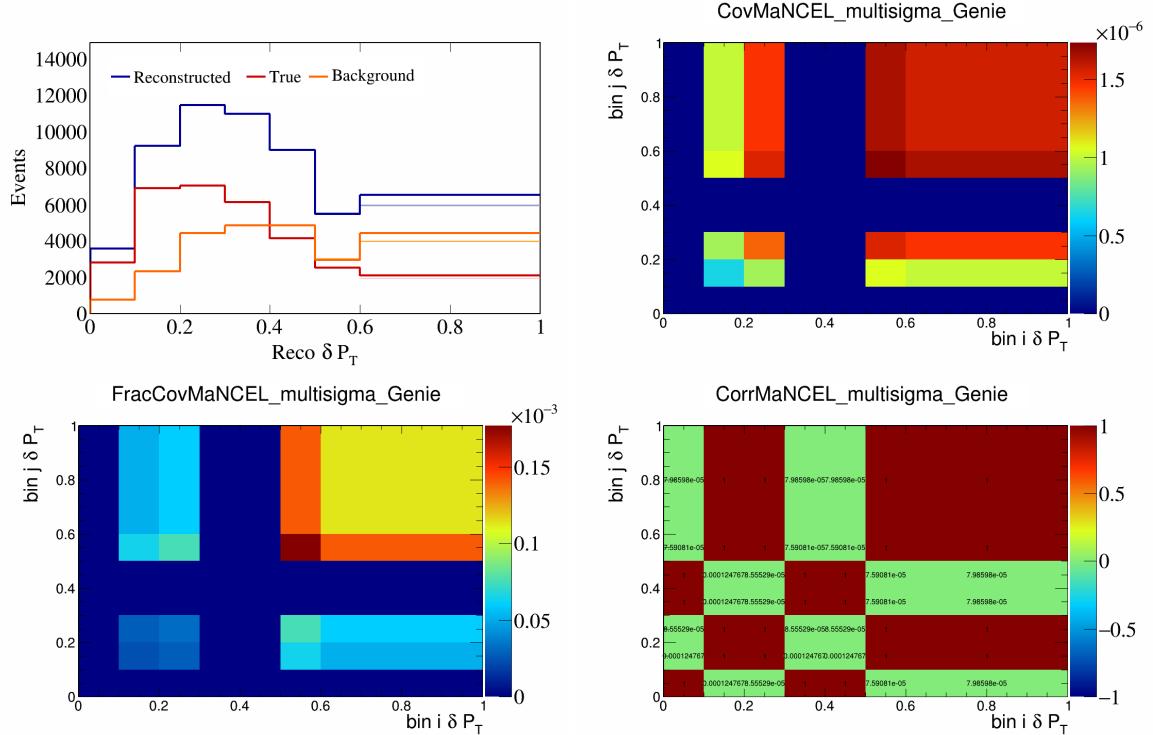


Figure 322: MaNCEL variations for δP_T .

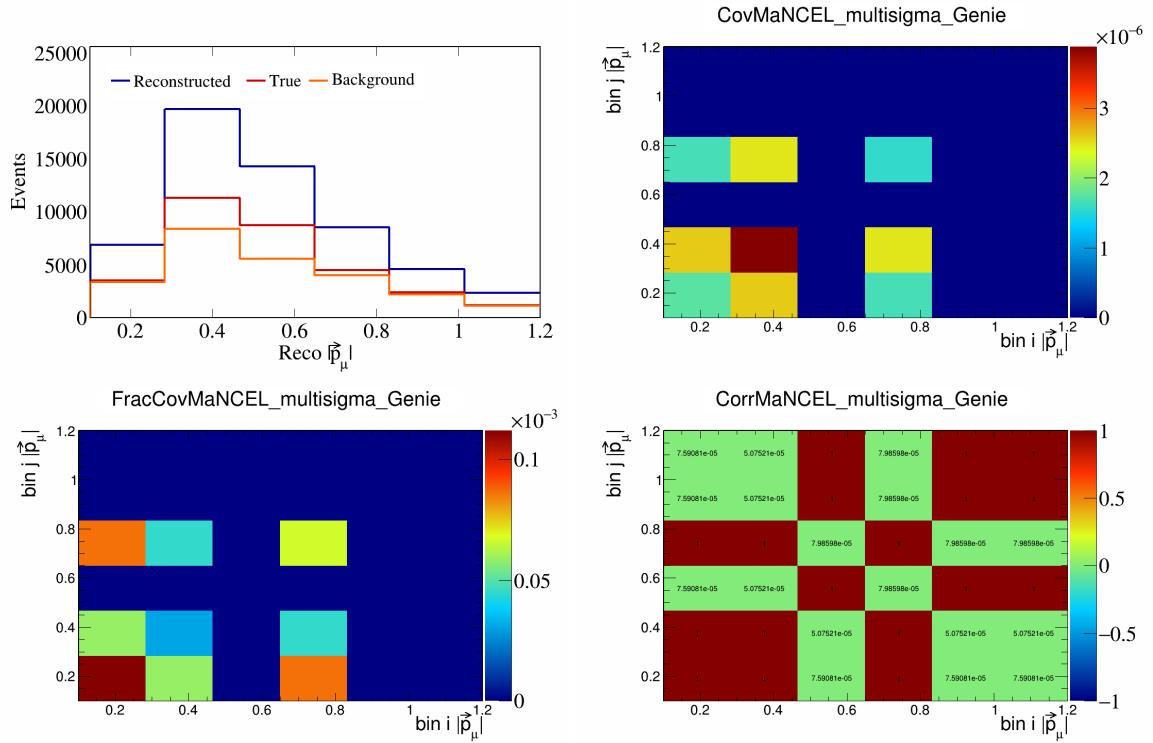


Figure 323: MaNCEL variations for $|\vec{p}_\mu|$.

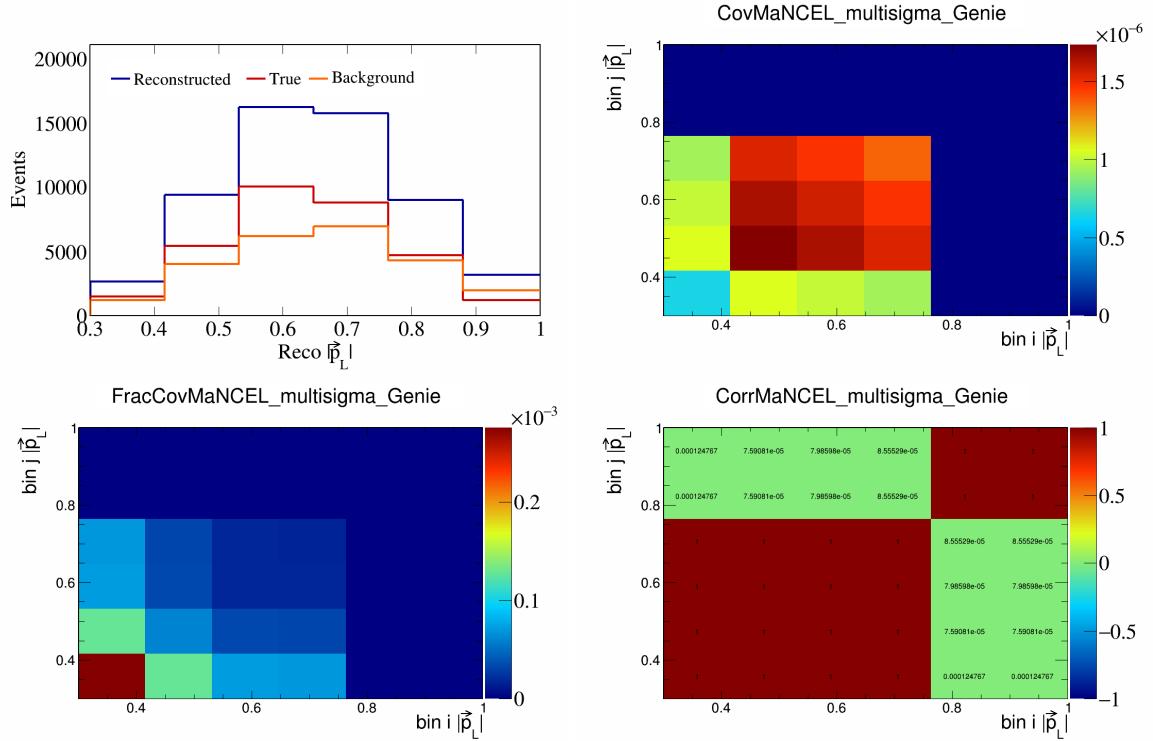


Figure 324: MaNCEL variations for $|\vec{p}_L|$.

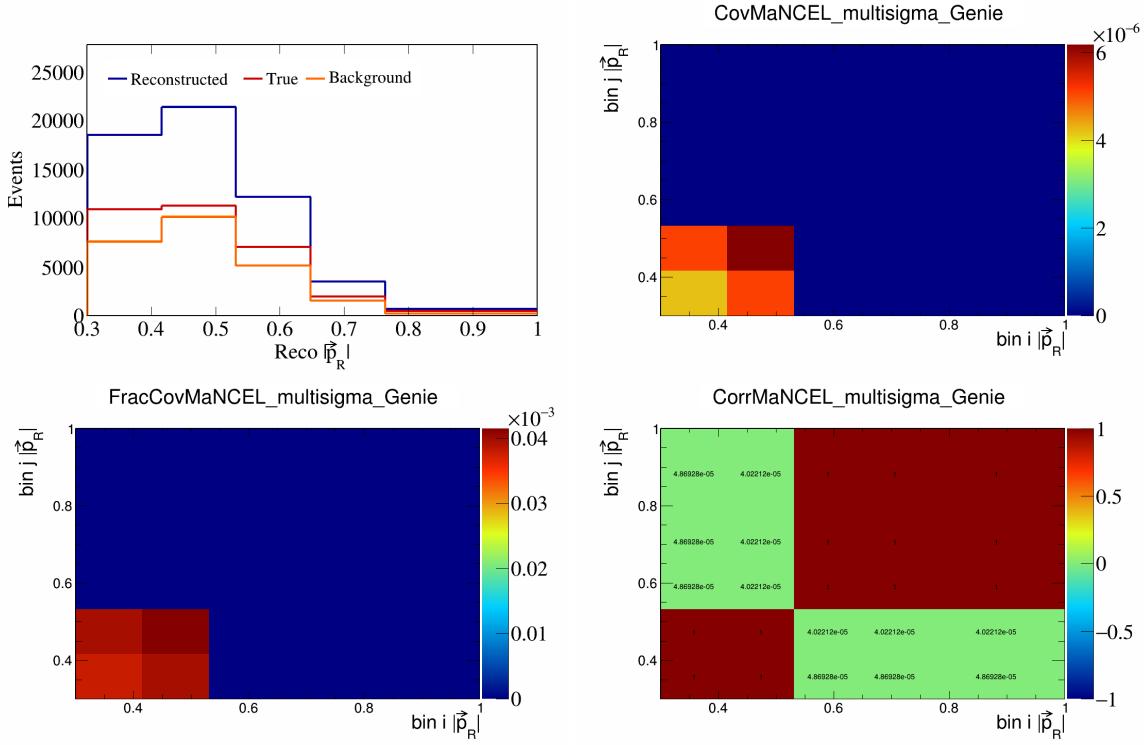


Figure 325: MaNCEL variations for $|\vec{p}_R|$.

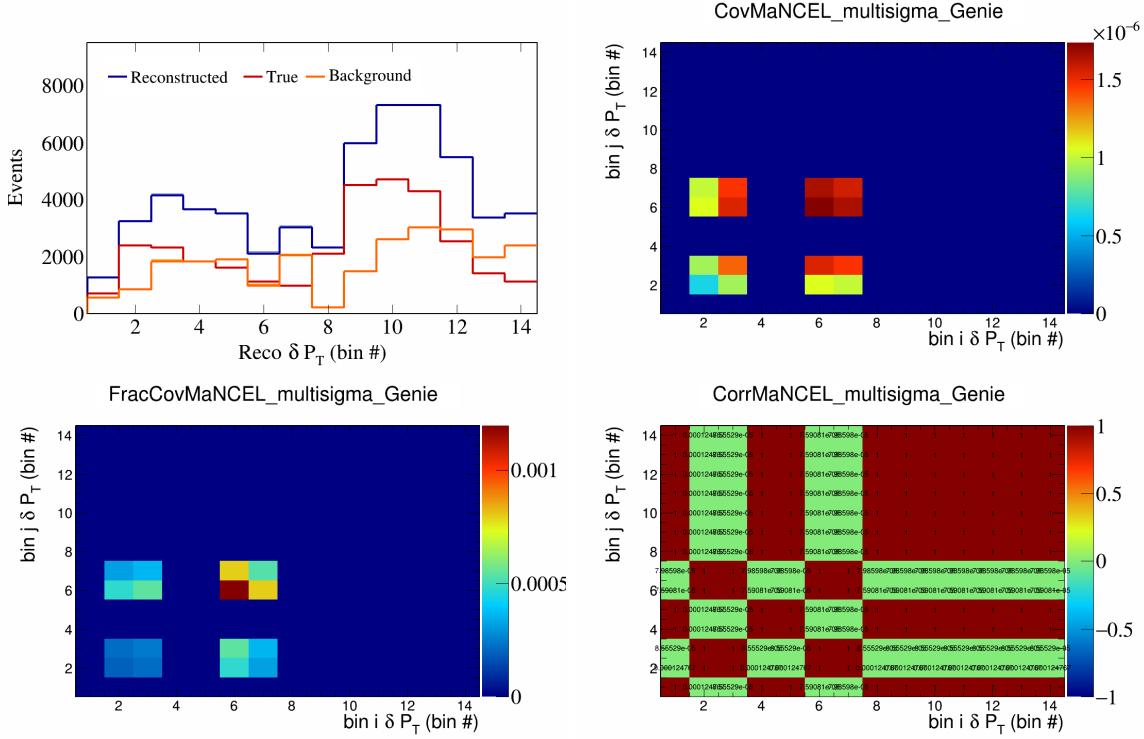


Figure 326: MaNCEL variations for δP_T in $\cos(\theta_{\vec{p}_\mu})$.

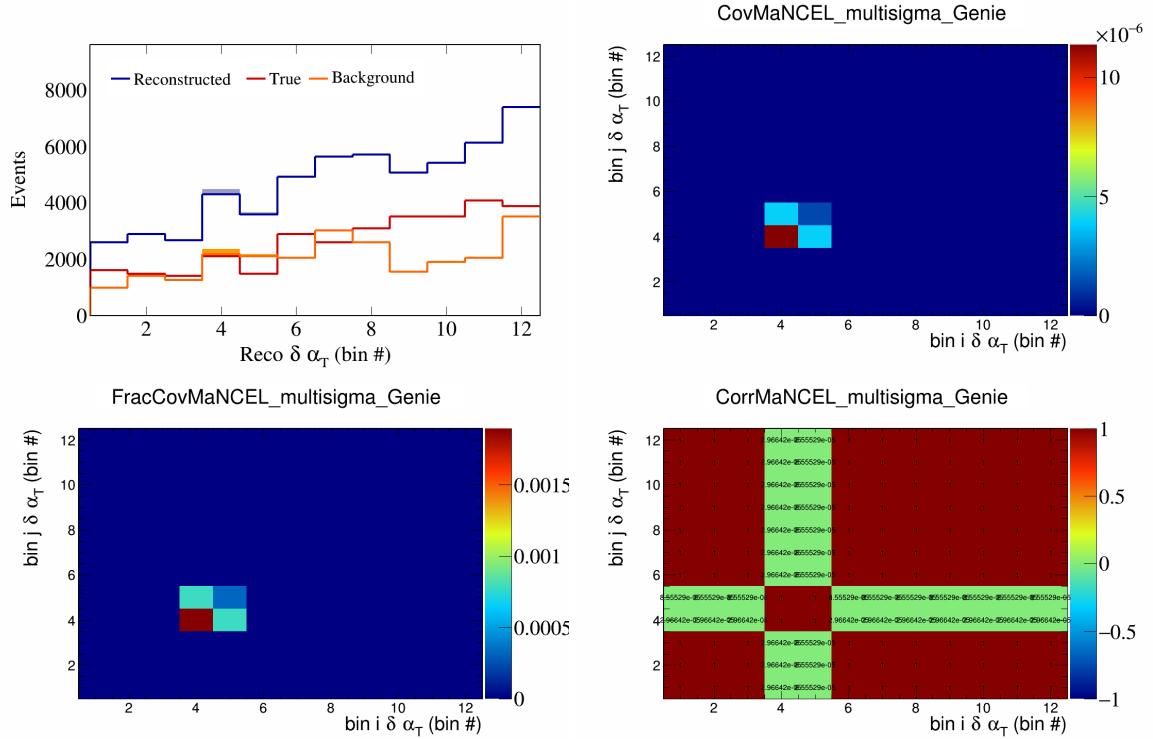


Figure 327: MaNCEL variations for $\delta\alpha_T$ in $\cos(\theta_{\vec{p}_\mu})$.

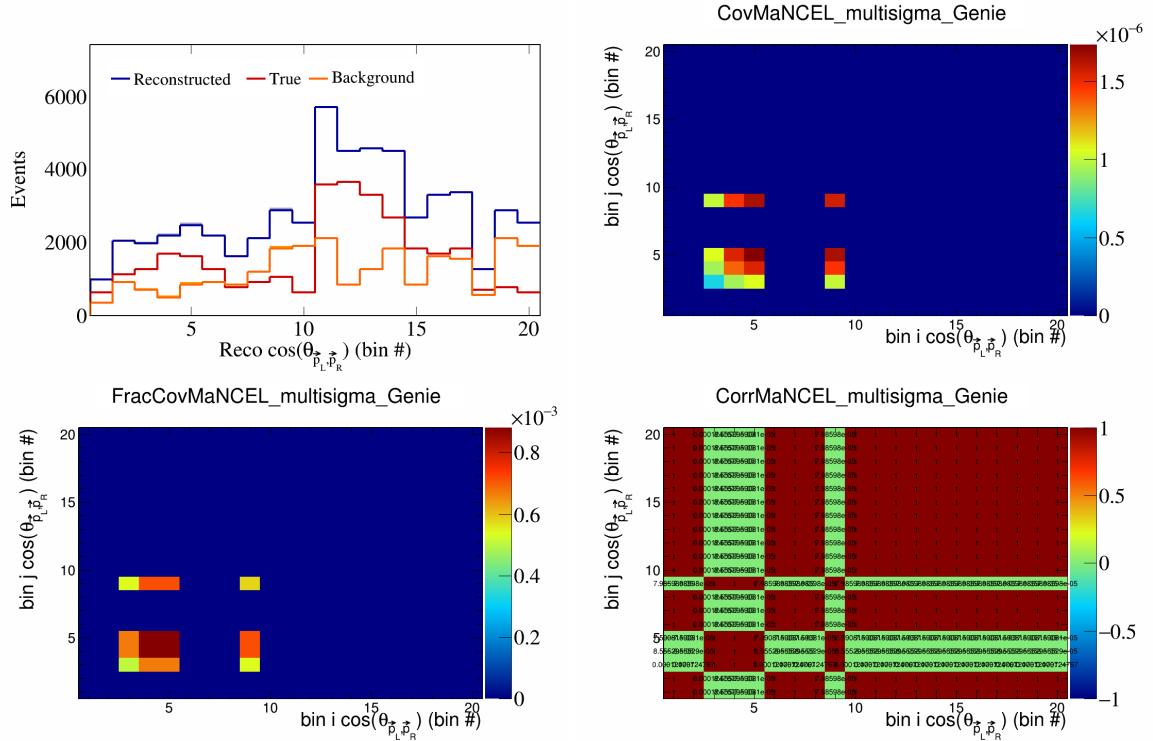


Figure 328: MaNCEL variations for $\cos(\theta_{\vec{p}_L, \vec{p}_R})$ in $\cos(\theta_{\vec{p}_\mu})$.

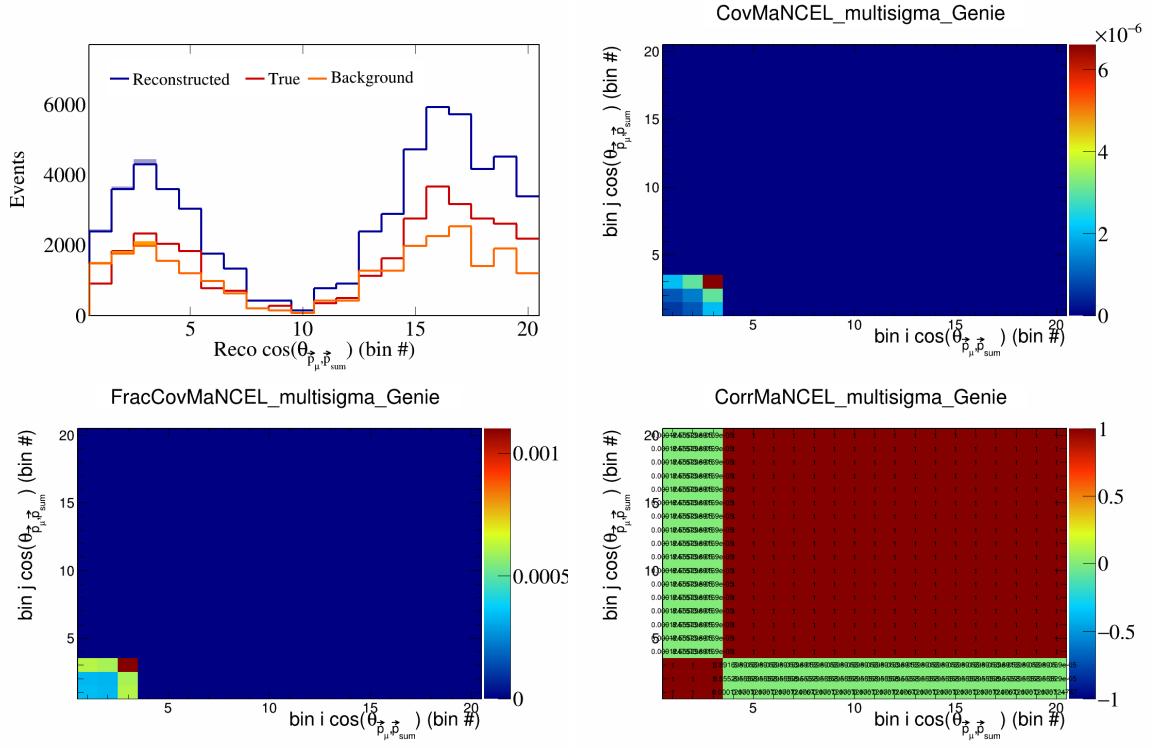


Figure 329: MaNCEL variations for $\cos(\theta_{\vec{p}_\mu, \vec{p}_{\text{sum}}})$ in $\cos(\theta_{\vec{p}_\mu})$.

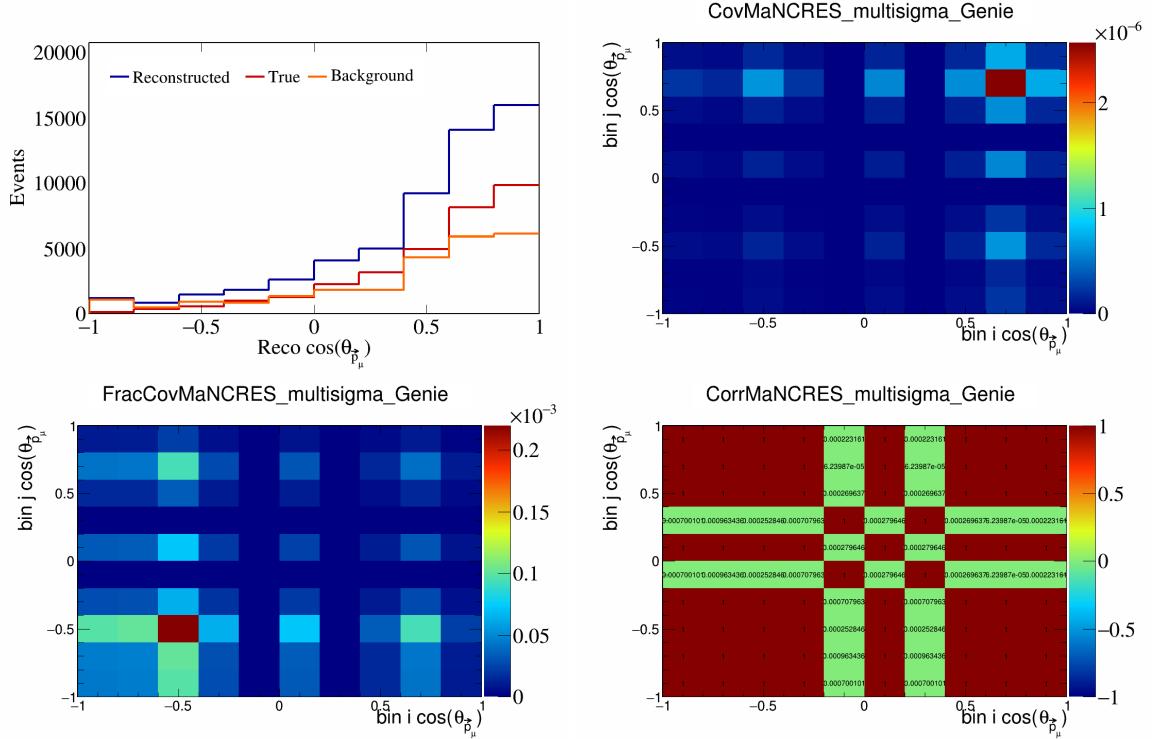


Figure 330: MaNCRES variations for $\cos(\theta_{\vec{p}_\mu, \vec{p}_{\text{sum}}})$ in $\cos(\theta_{\vec{p}_\mu})$.

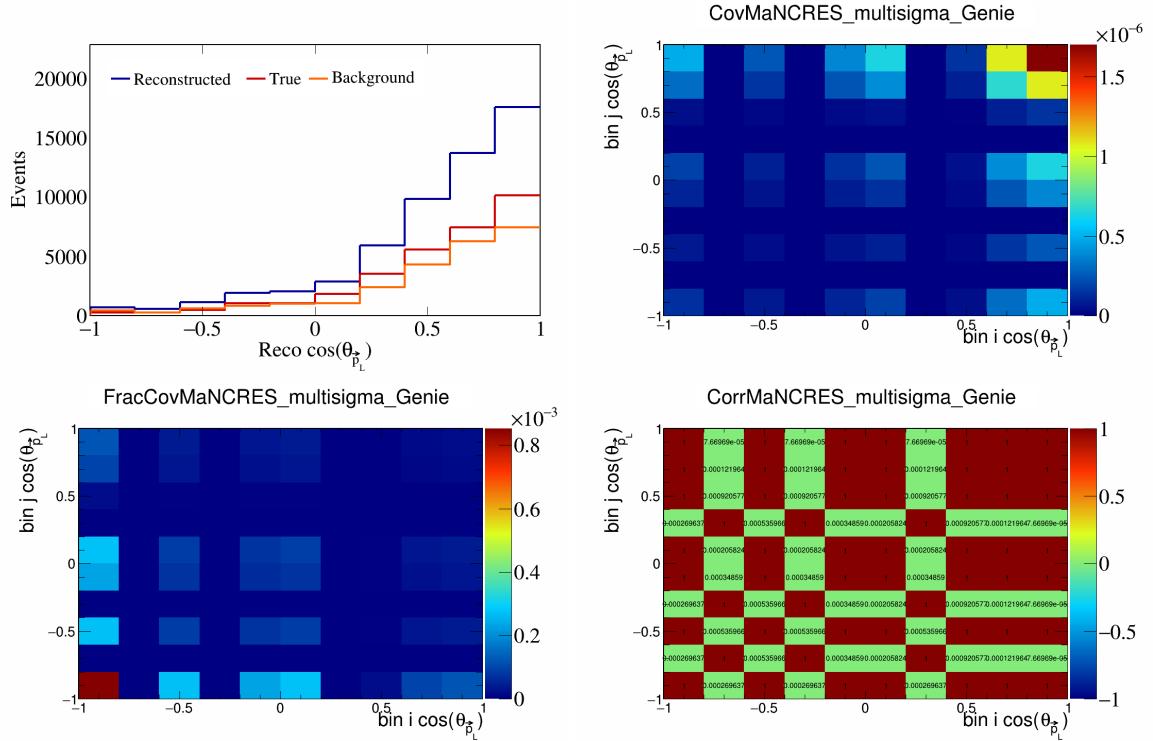


Figure 331: MaNCRES variations for $\cos(\theta_{\vec{p}_L})$.

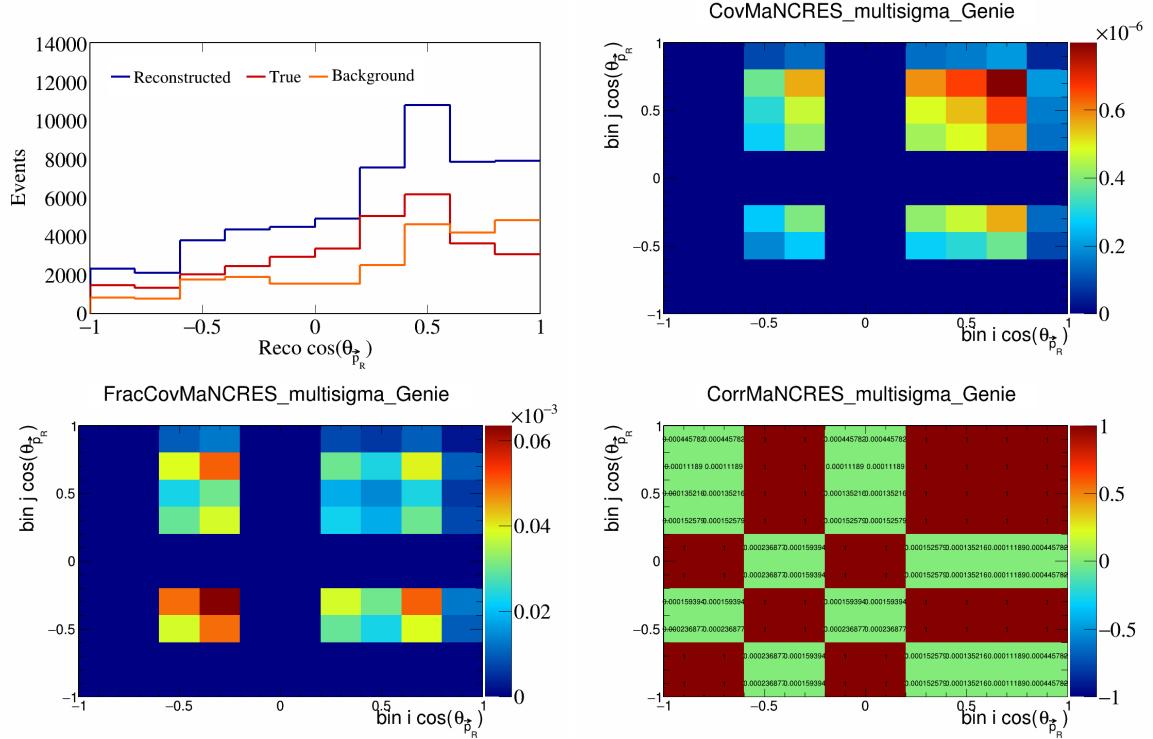


Figure 332: MaNCRES variations for $\cos(\theta_{\vec{p}_R})$.

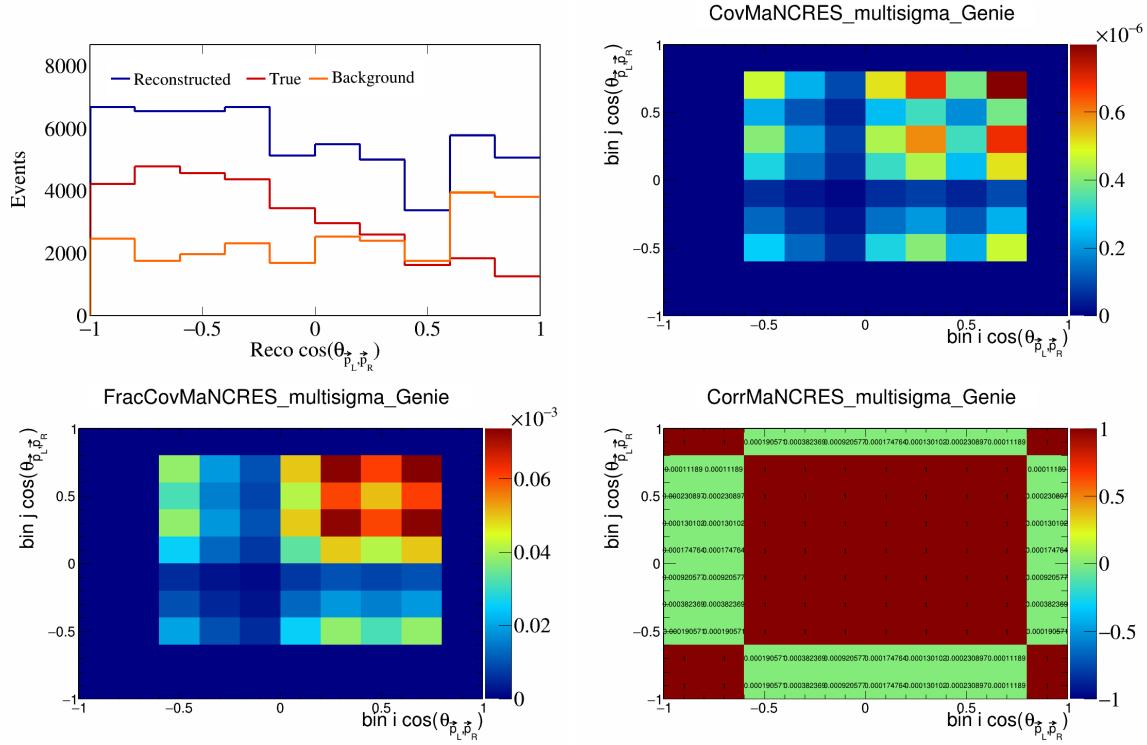


Figure 333: MaNCRES variations for $\cos(\theta_{\vec{p}_L, \vec{p}_R})$.

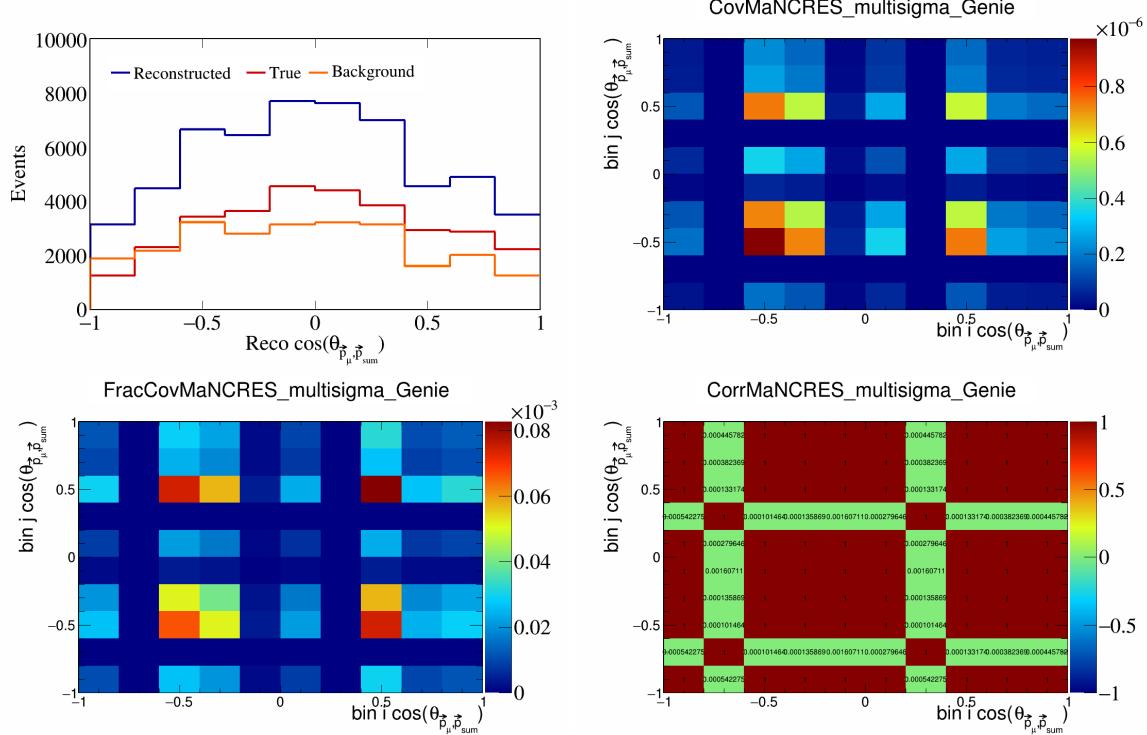


Figure 334: MaNCRES variations for $\cos(\theta_{\vec{p}_\mu, \vec{p}_{\text{sum}}})$.

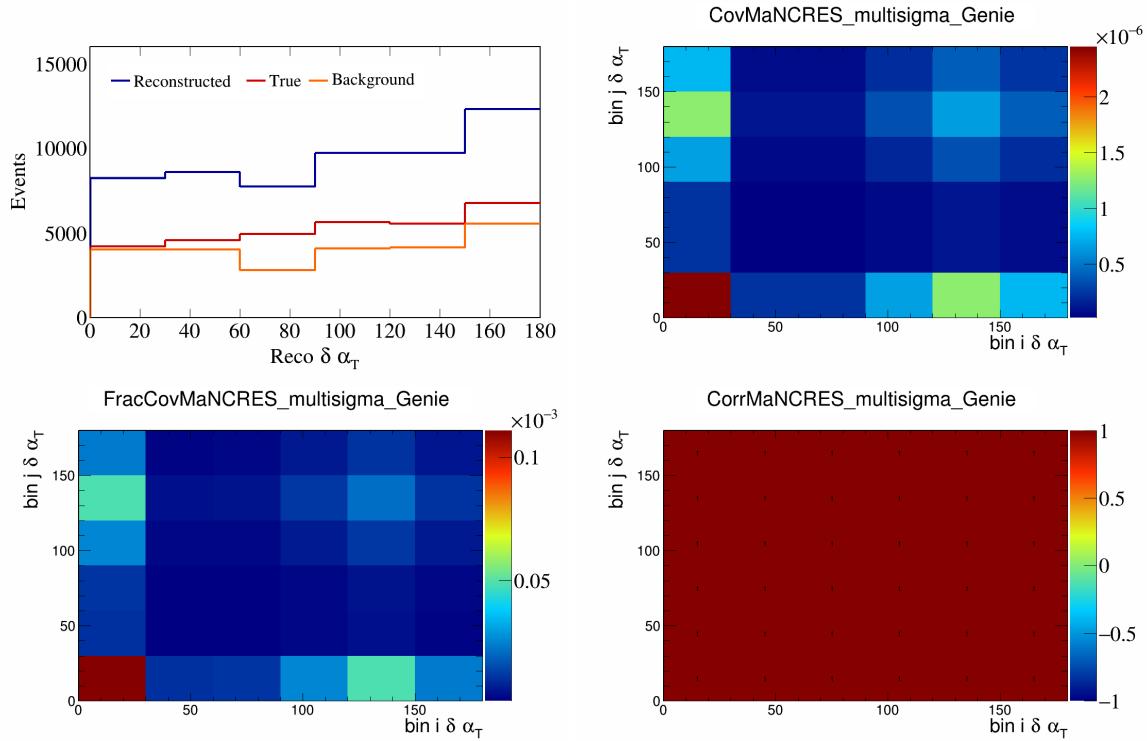


Figure 335: MaNCRES variations for $\delta\alpha_T$.

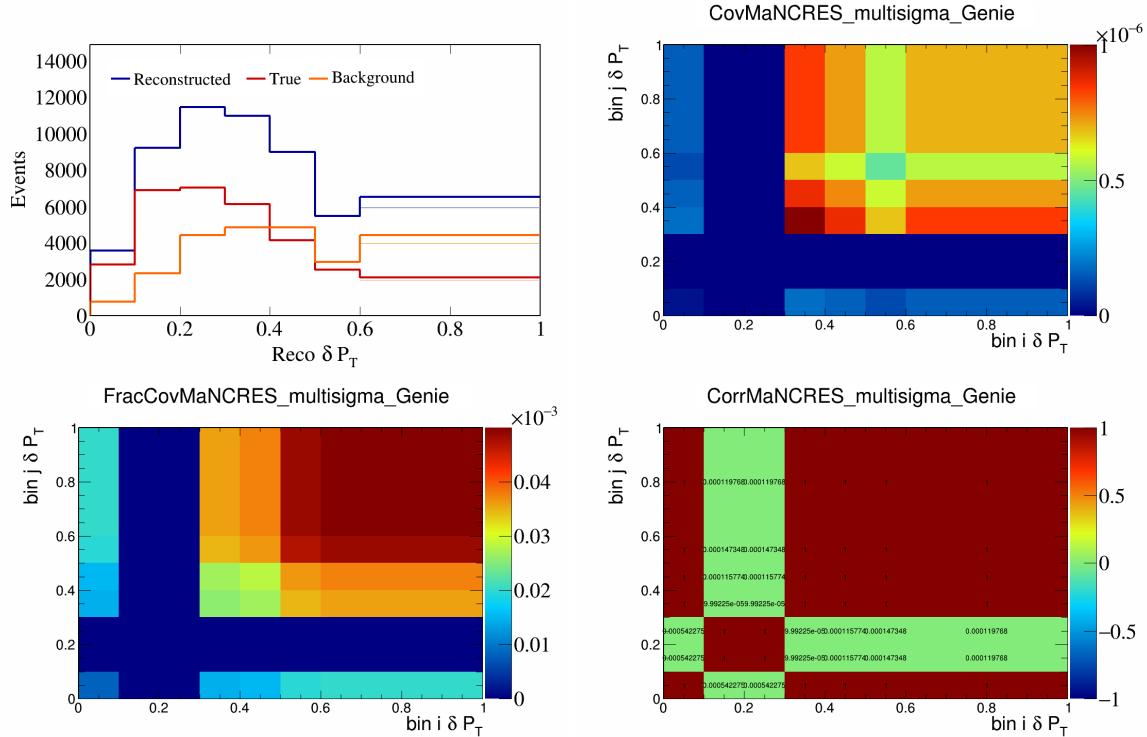


Figure 336: MaNCRES variations for δP_T .

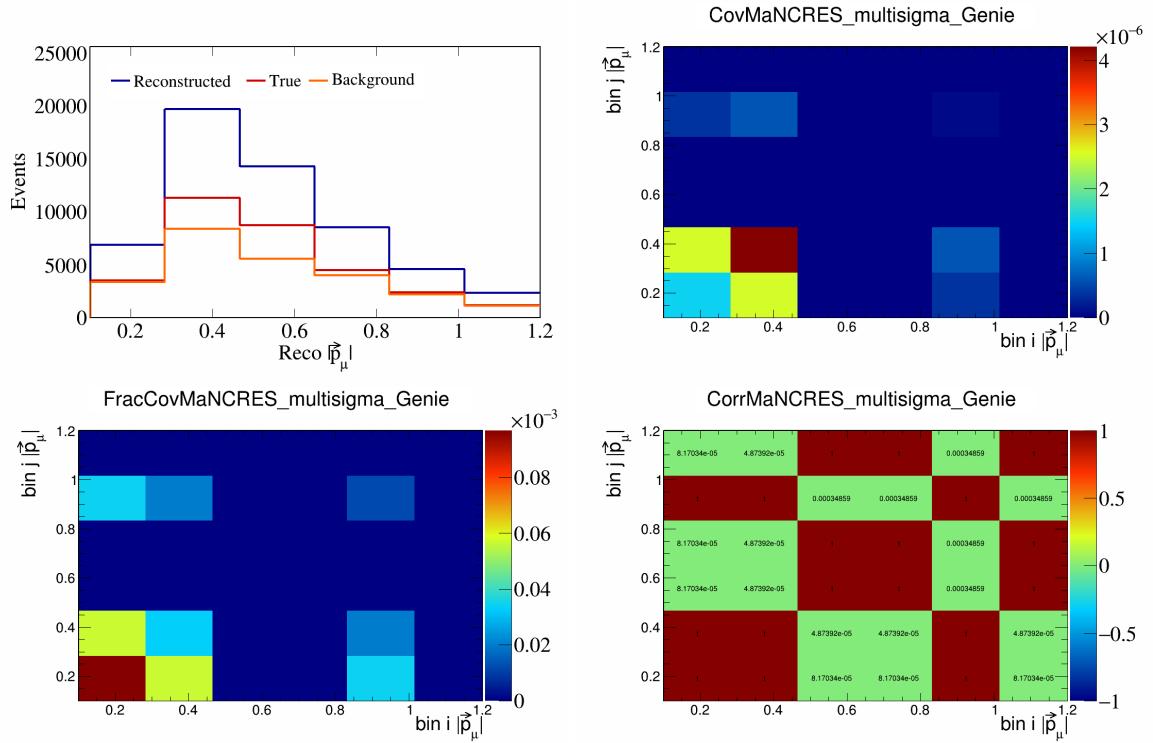


Figure 337: MaNCRES variations for $|\vec{p}_\mu|$.

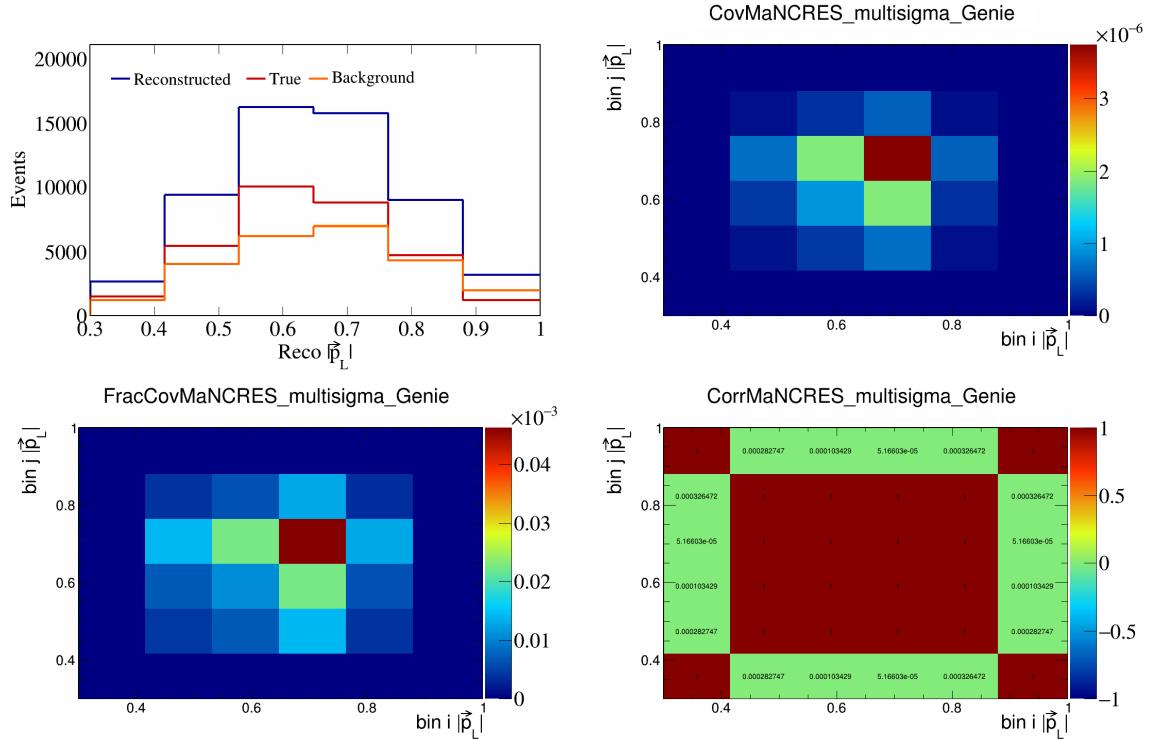


Figure 338: MaNCRES variations for $|\vec{p}_L|$.

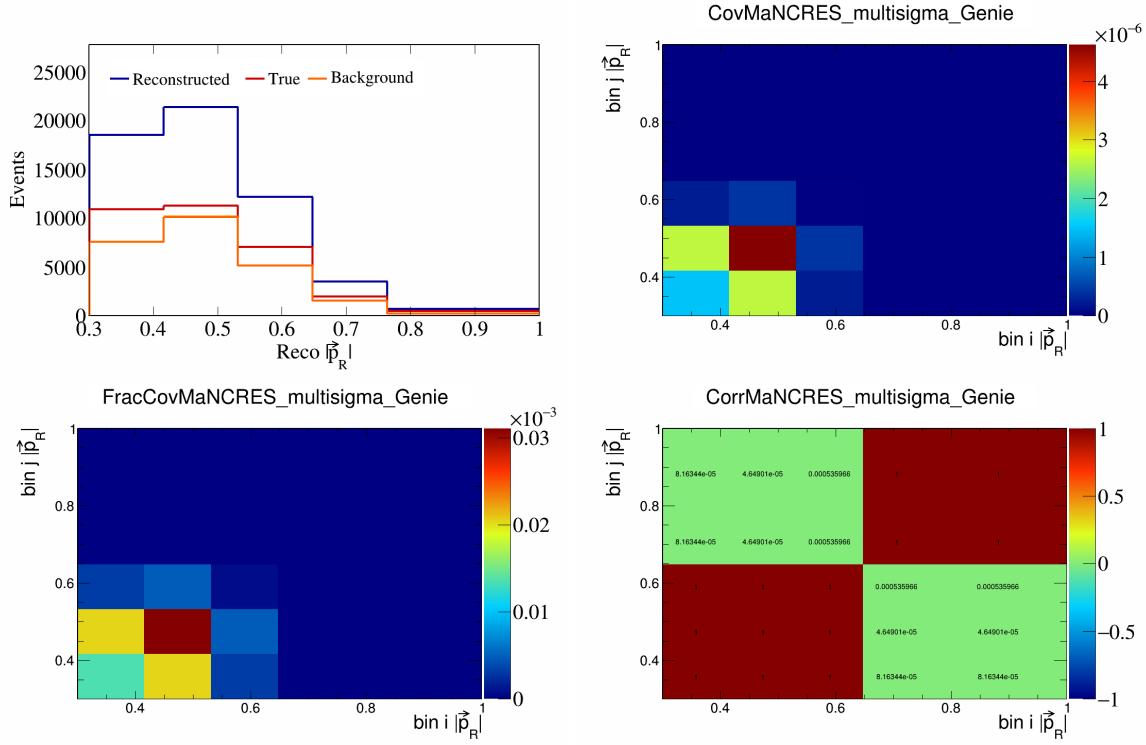


Figure 339: MaNCRES variations for $|\vec{p}_R|$.

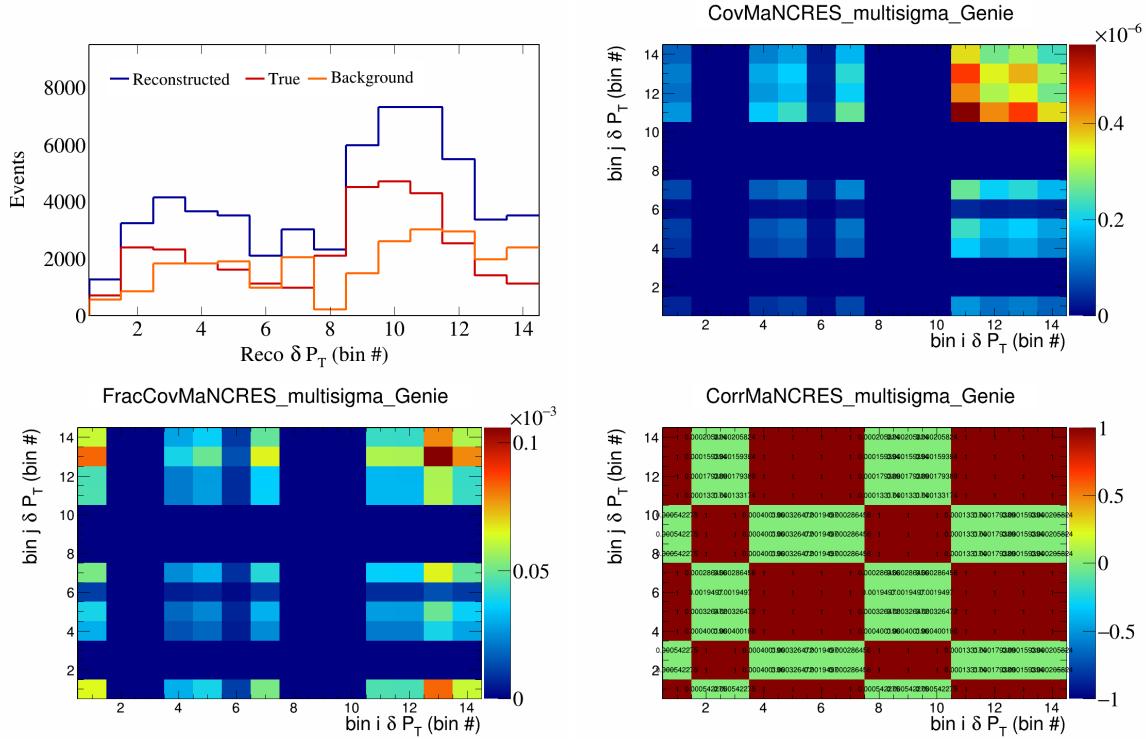


Figure 340: MaNCRES variations for δP_T in $\cos(\theta_{\vec{p}_\mu})$.

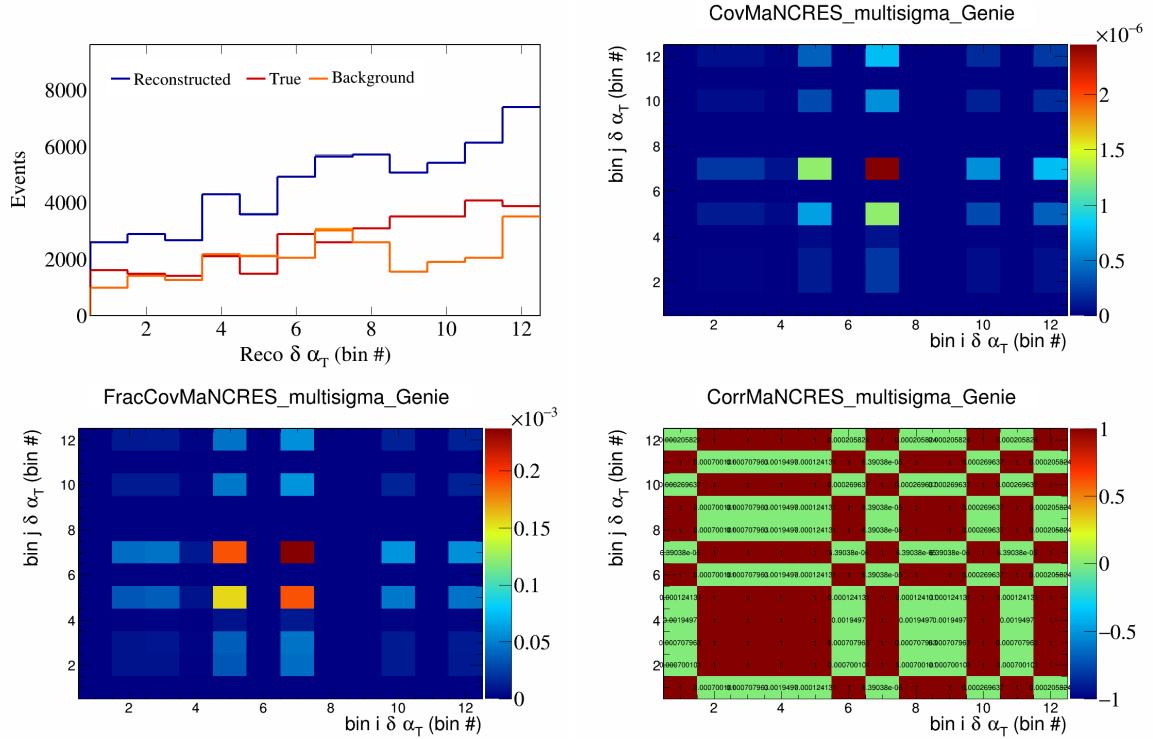


Figure 341: MaNCRES variations for $\delta\alpha_T$ in $\cos(\theta_{\vec{p}_\mu})$.

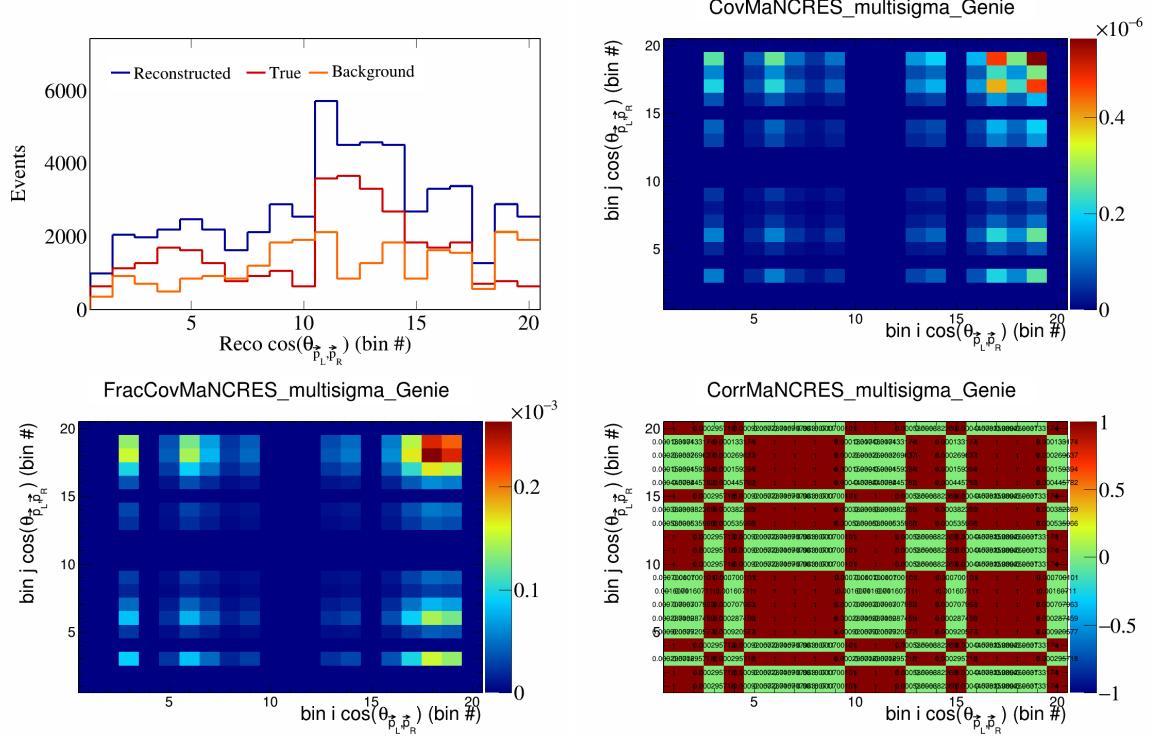


Figure 342: MaNCRES variations for $\cos(\theta_{p_L, p_R})$ in $\cos(\theta_{\vec{p}_\mu})$.

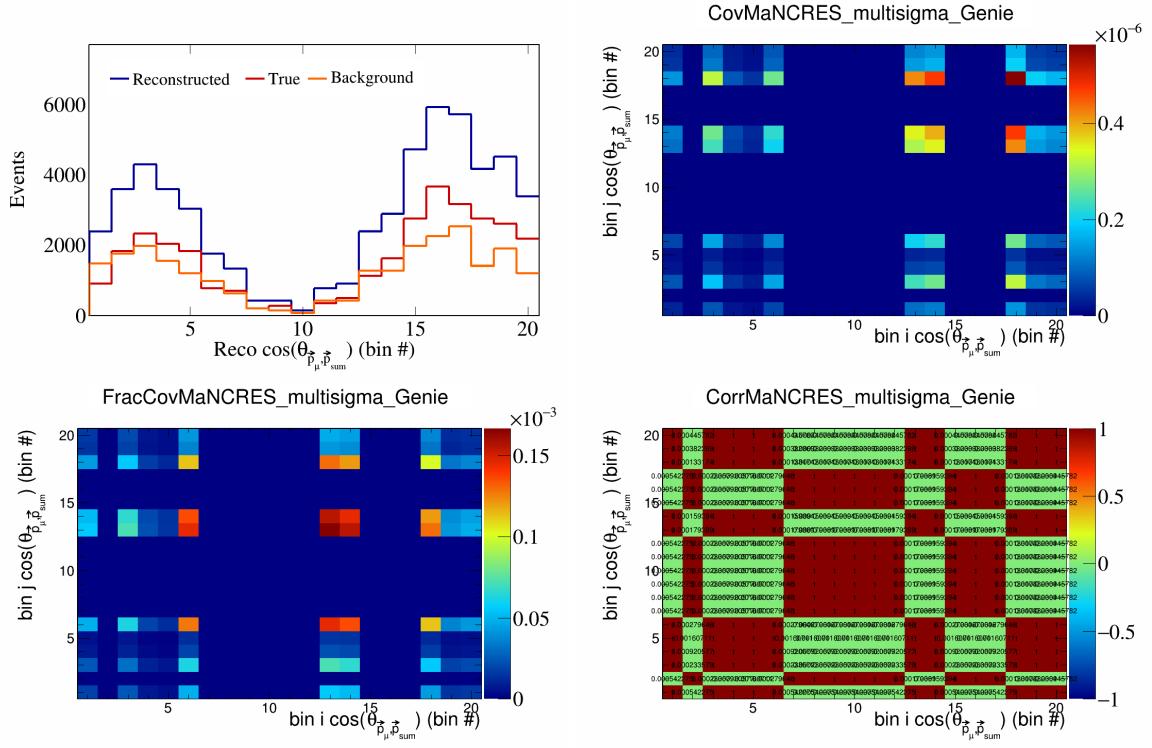


Figure 343: MaNCRES variations for $\cos(\theta_{\vec{p}_\mu, \vec{p}_{\text{sum}}})$ in $\cos(\theta_{\vec{p}_\mu})$.

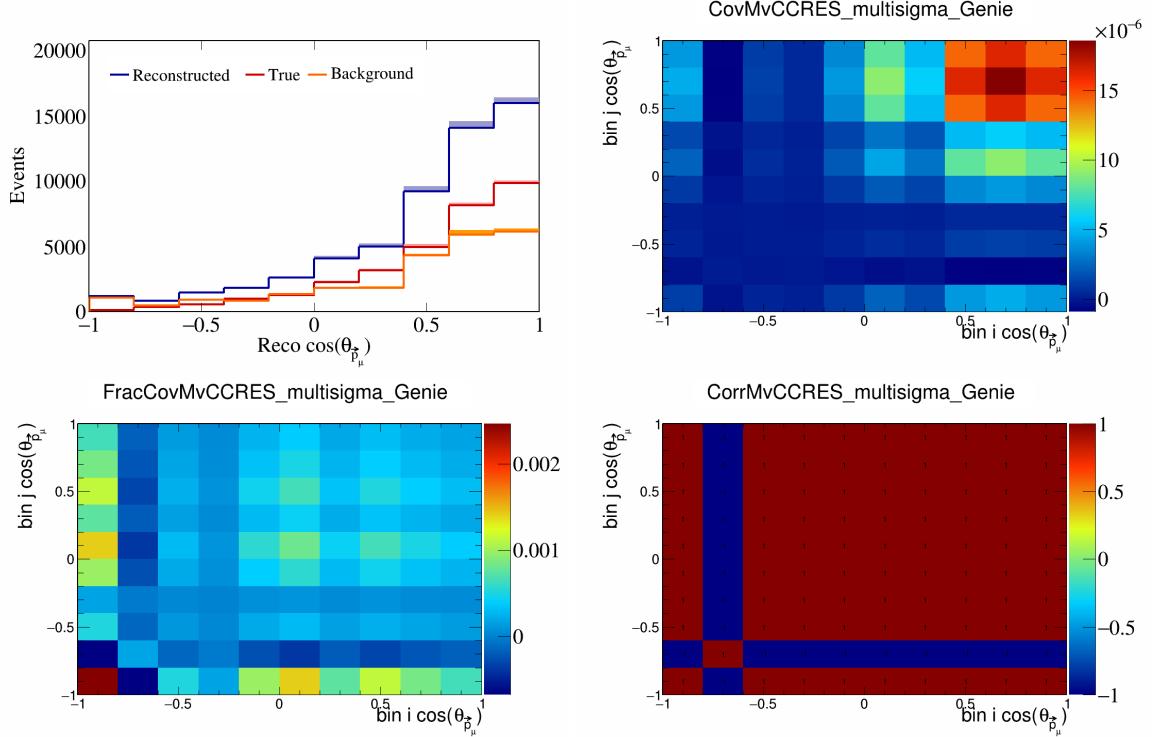


Figure 344: MvCCRES variations for $\cos(\theta_{\vec{p}_\mu})$.

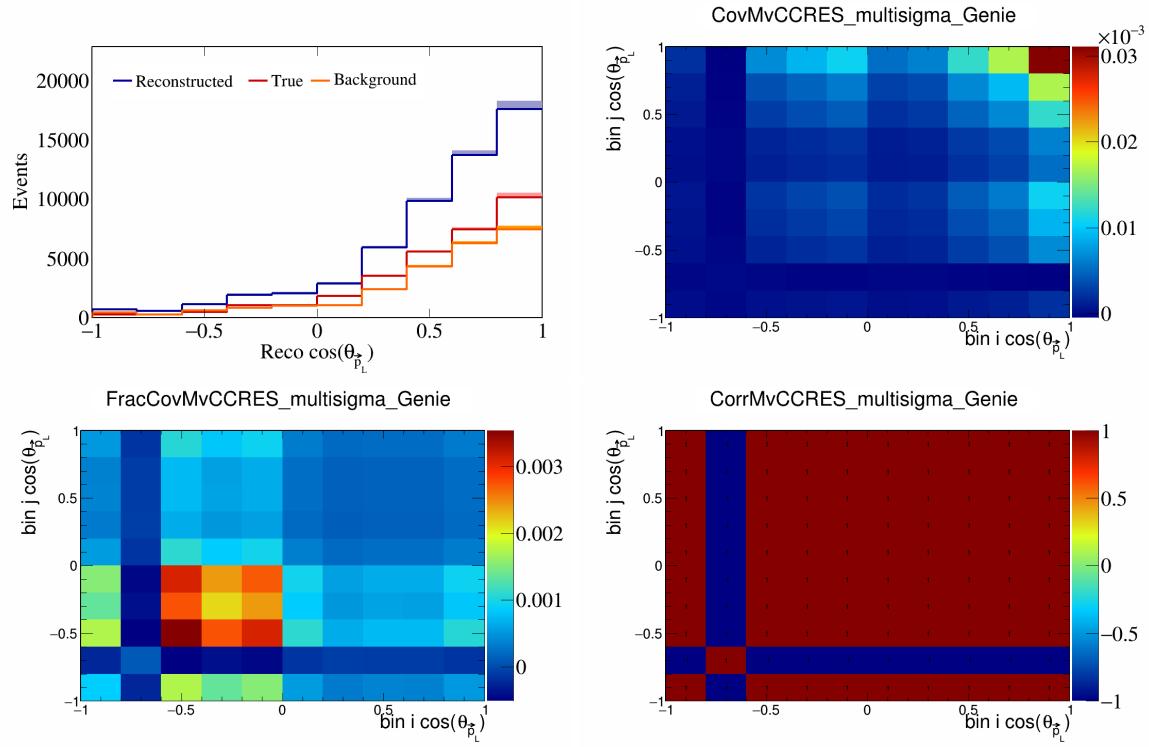


Figure 345: MvCCRES variations for $\cos(\theta_{\vec{p}_L})$.

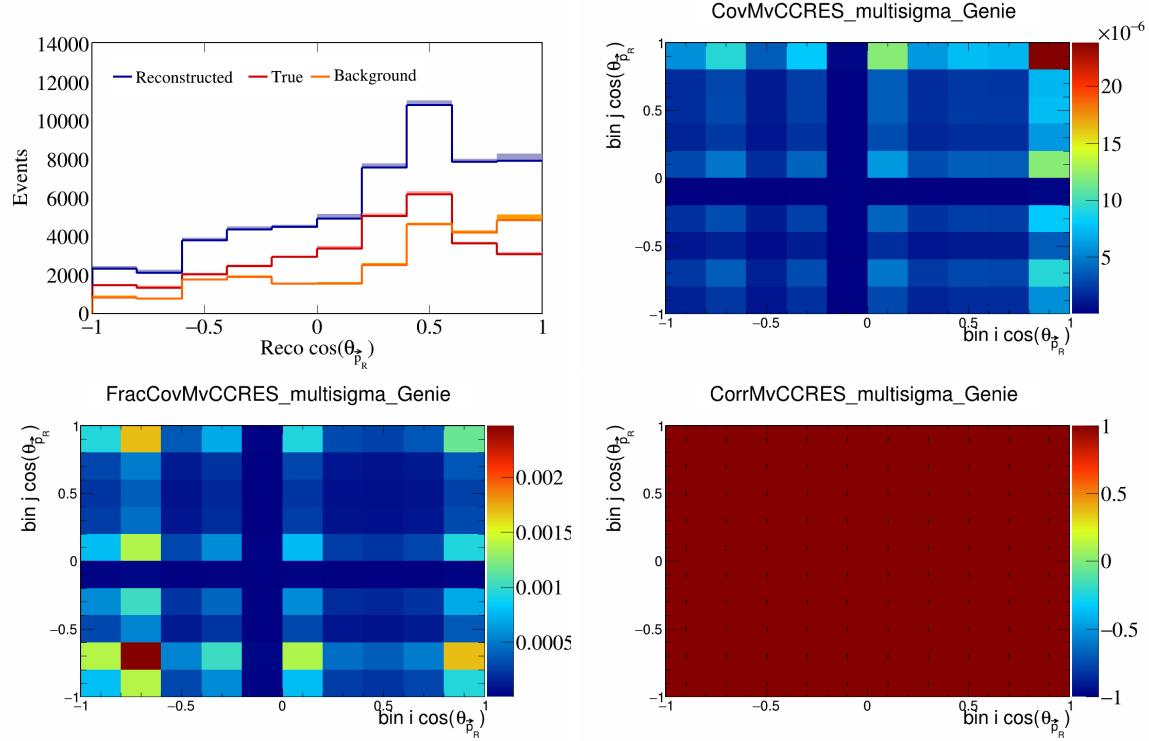


Figure 346: MvCCRES variations for $\cos(\theta_{\vec{p}_R})$.

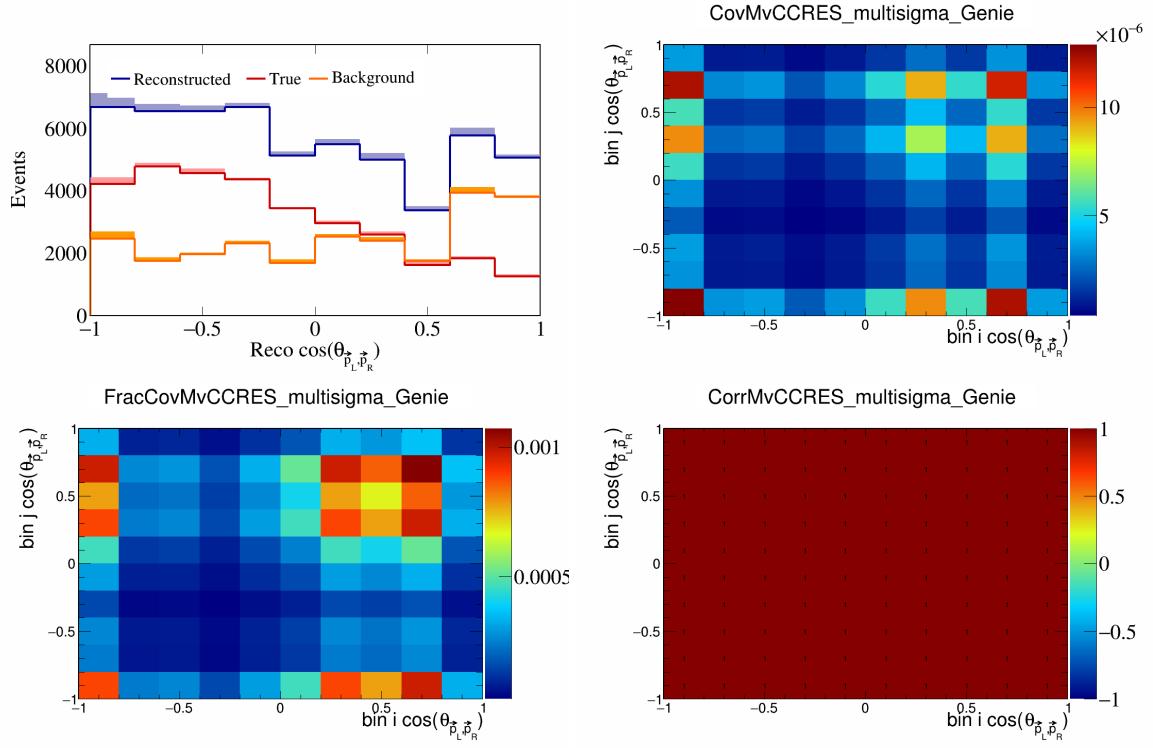


Figure 347: MvCCRES variations for $\cos(\theta_{\vec{p}_L, \vec{p}_R})$.

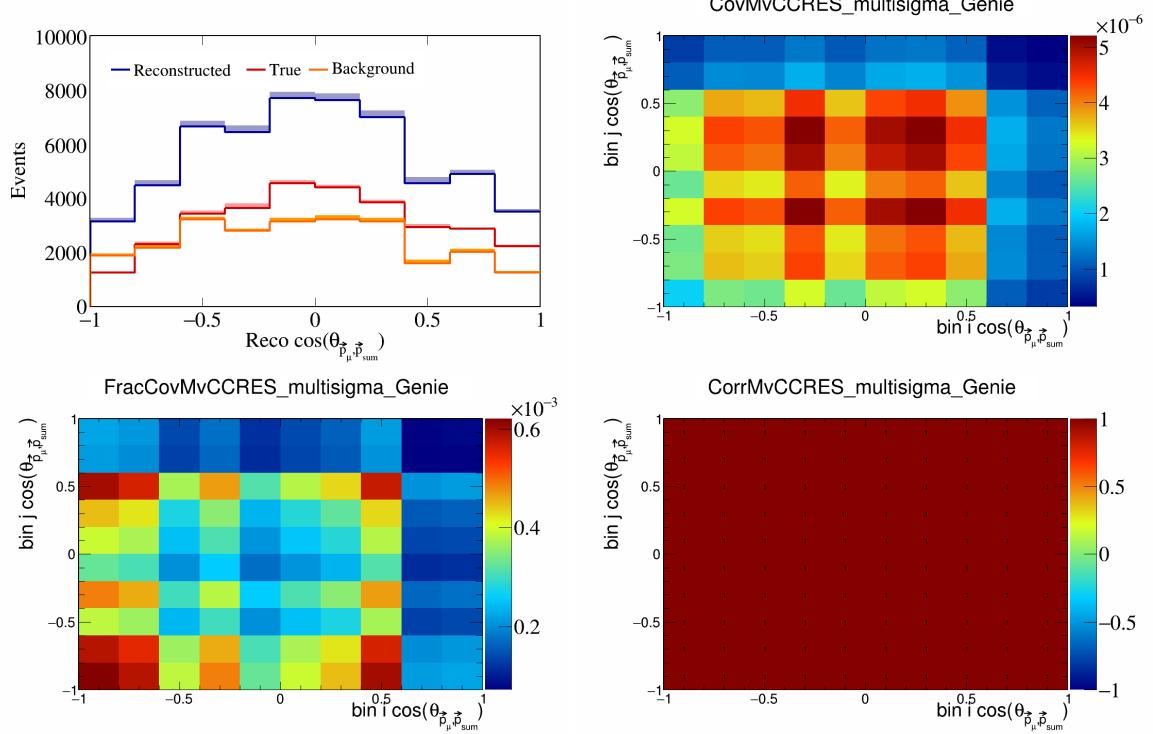


Figure 348: MvCCRES variations for $\cos(\theta_{\vec{p}_\mu, \vec{p}_{\text{sum}}})$.

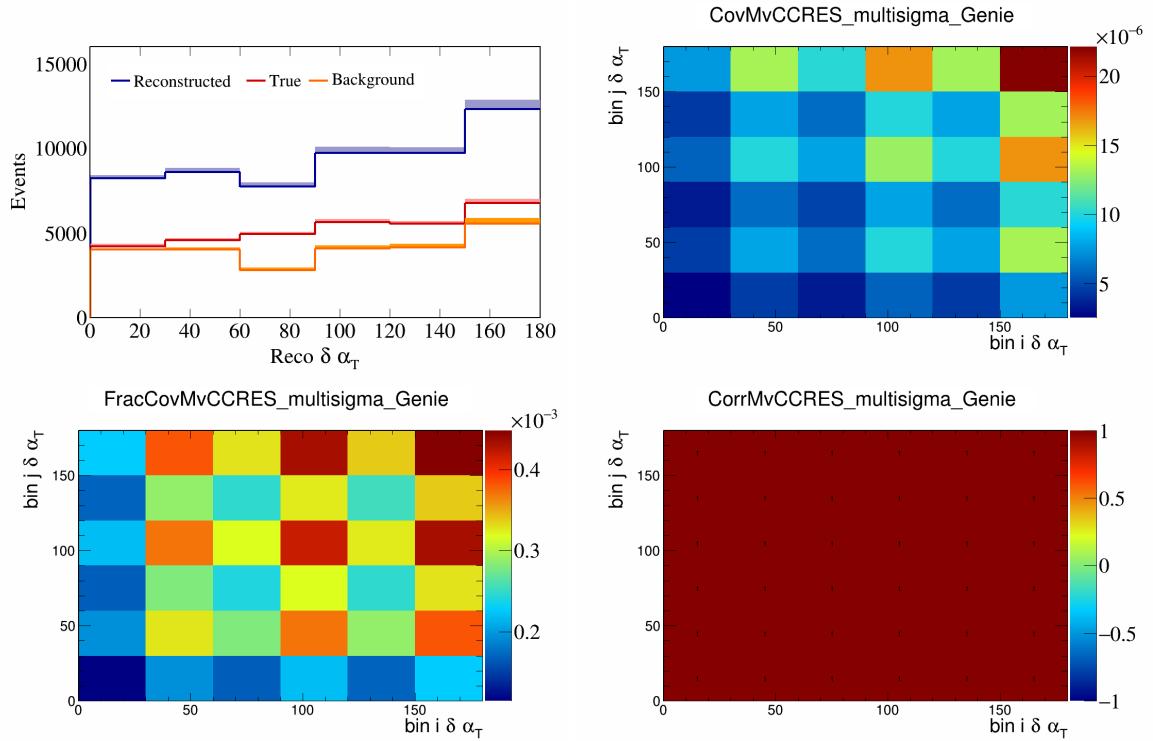


Figure 349: MvCCRES variations for $\delta\alpha_T$.

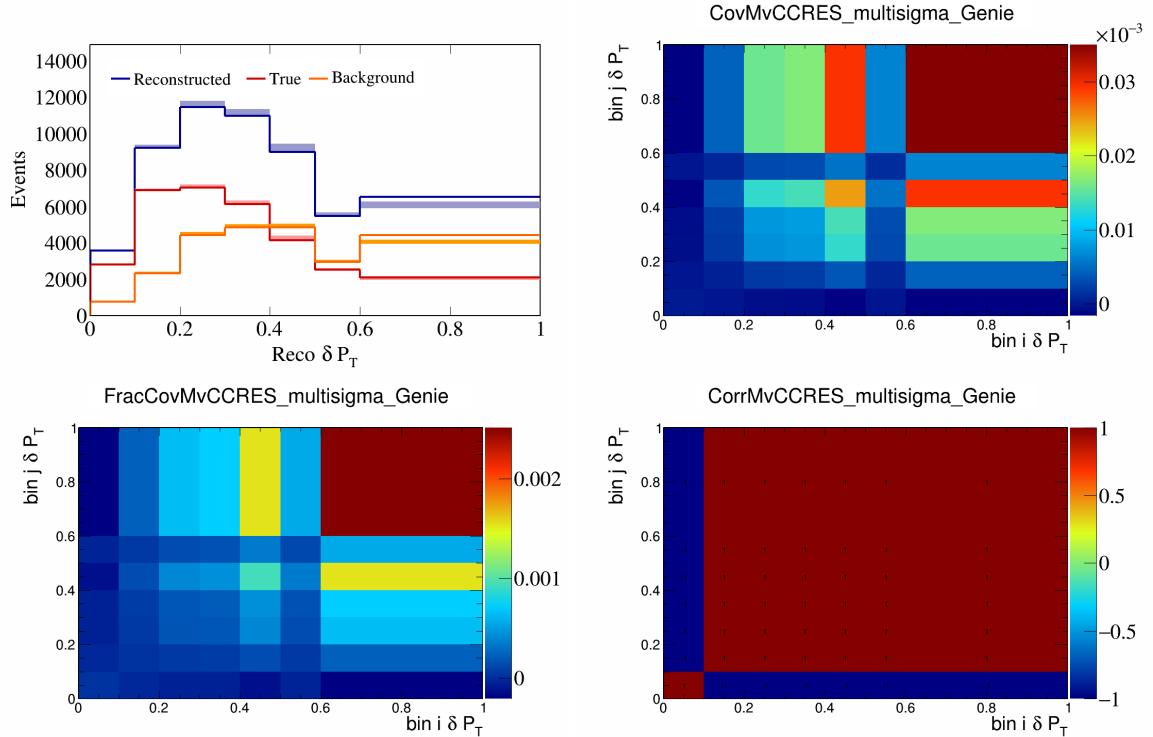


Figure 350: MvCCRES variations for δP_T .

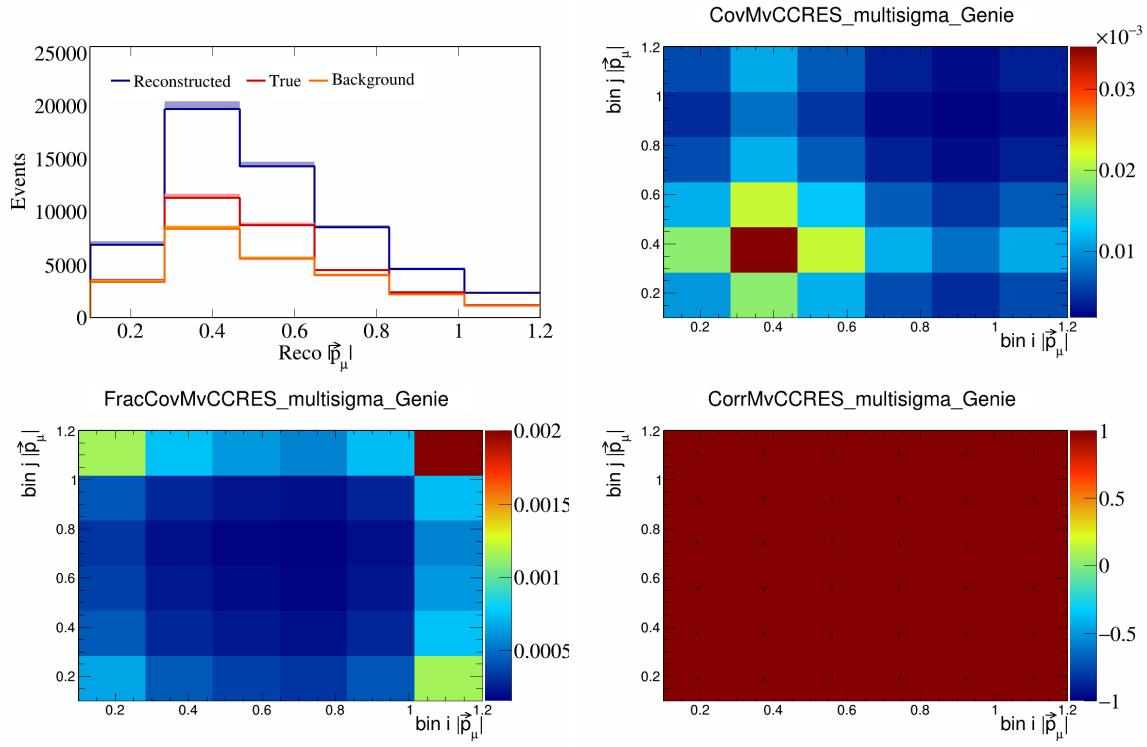


Figure 351: MvCCRES variations for $|\vec{p}_\mu|$.

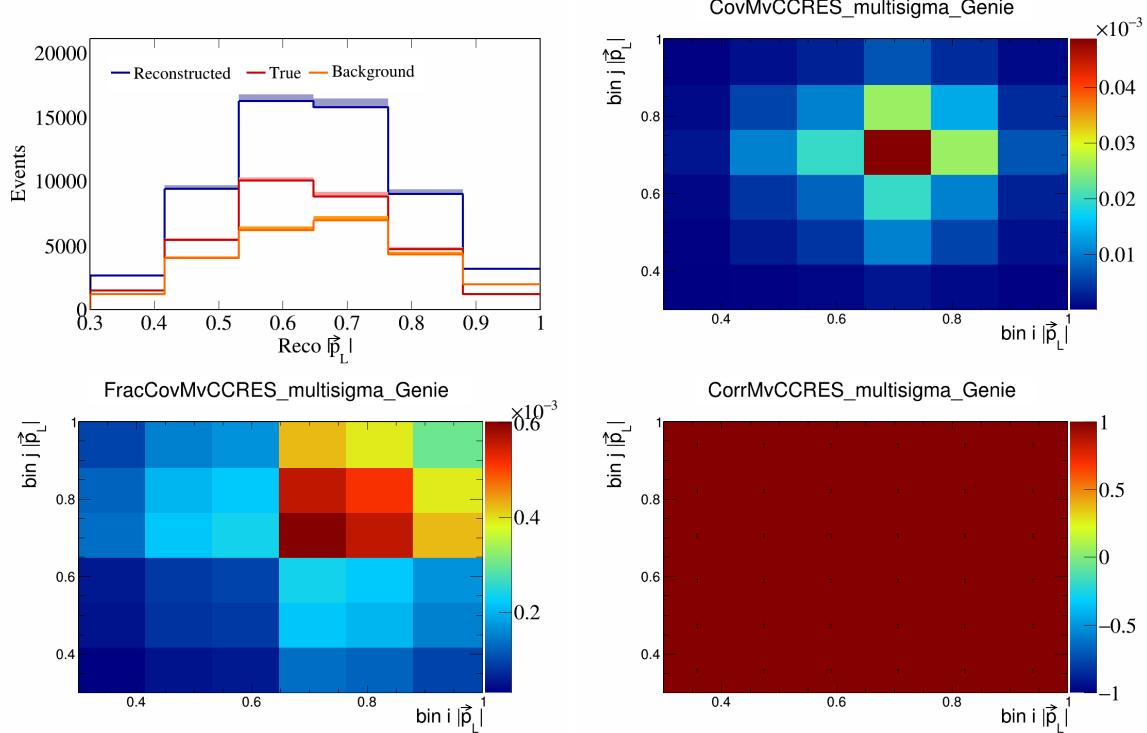


Figure 352: MvCCRES variations for $|\vec{p}_L|$.

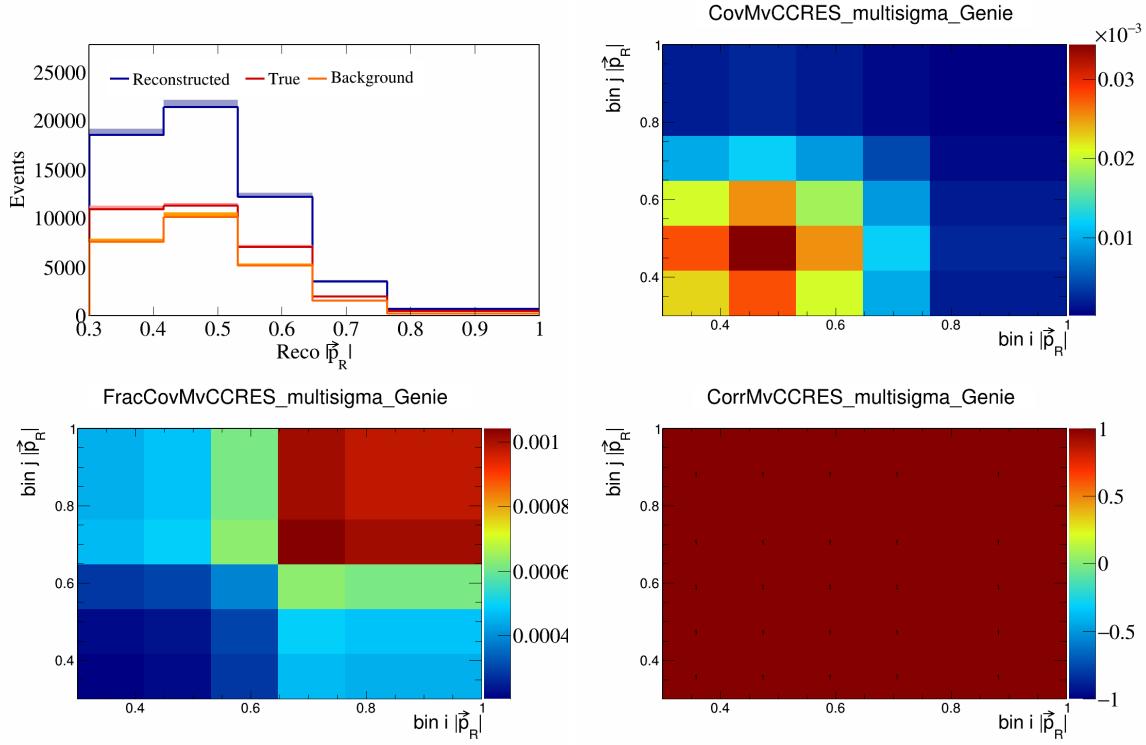


Figure 353: MvCCRES variations for $|\vec{p}_R|$.

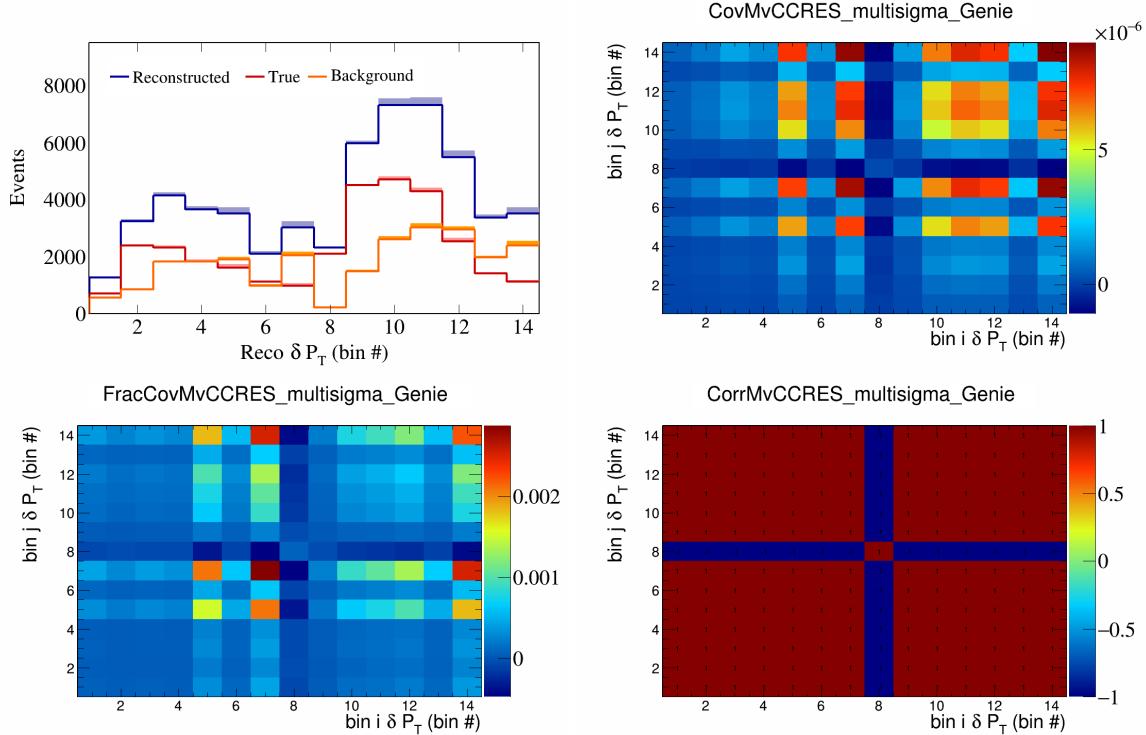


Figure 354: MvCCRES variations for δP_T in $\cos(\theta_{\vec{p}_\mu})$.

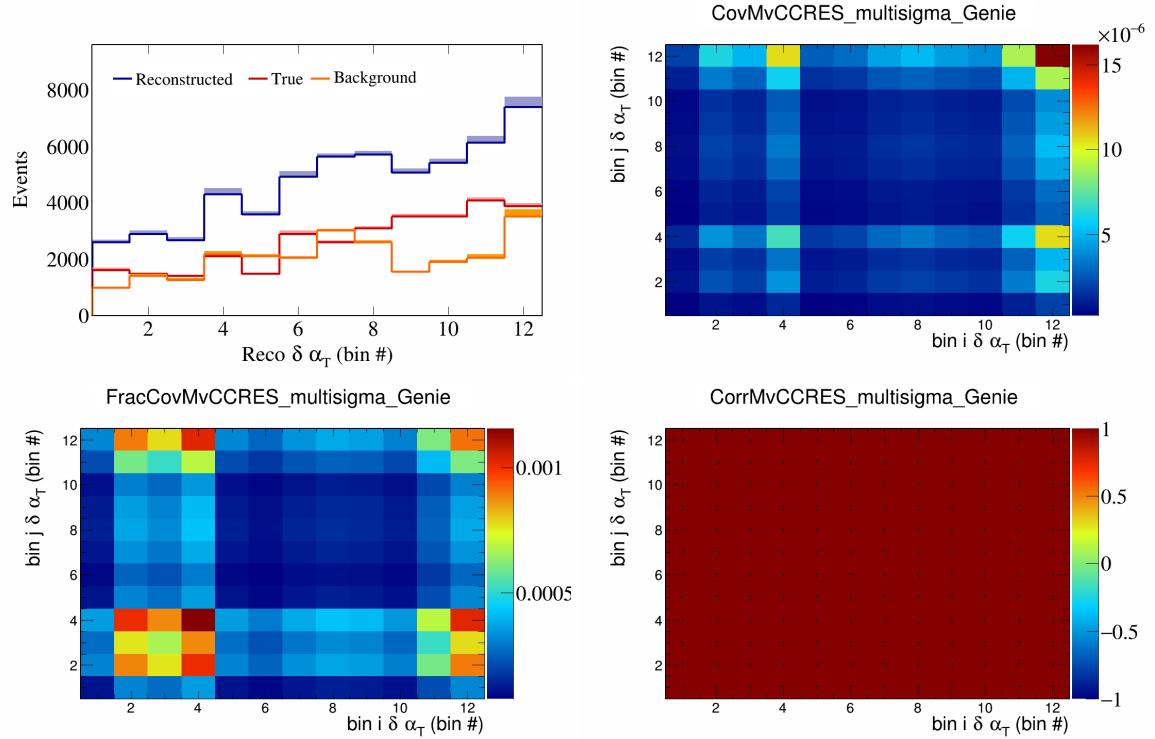


Figure 355: MvCCRES variations for $\delta \alpha_T$ in $\cos(\theta_{\vec{p}_\mu})$.

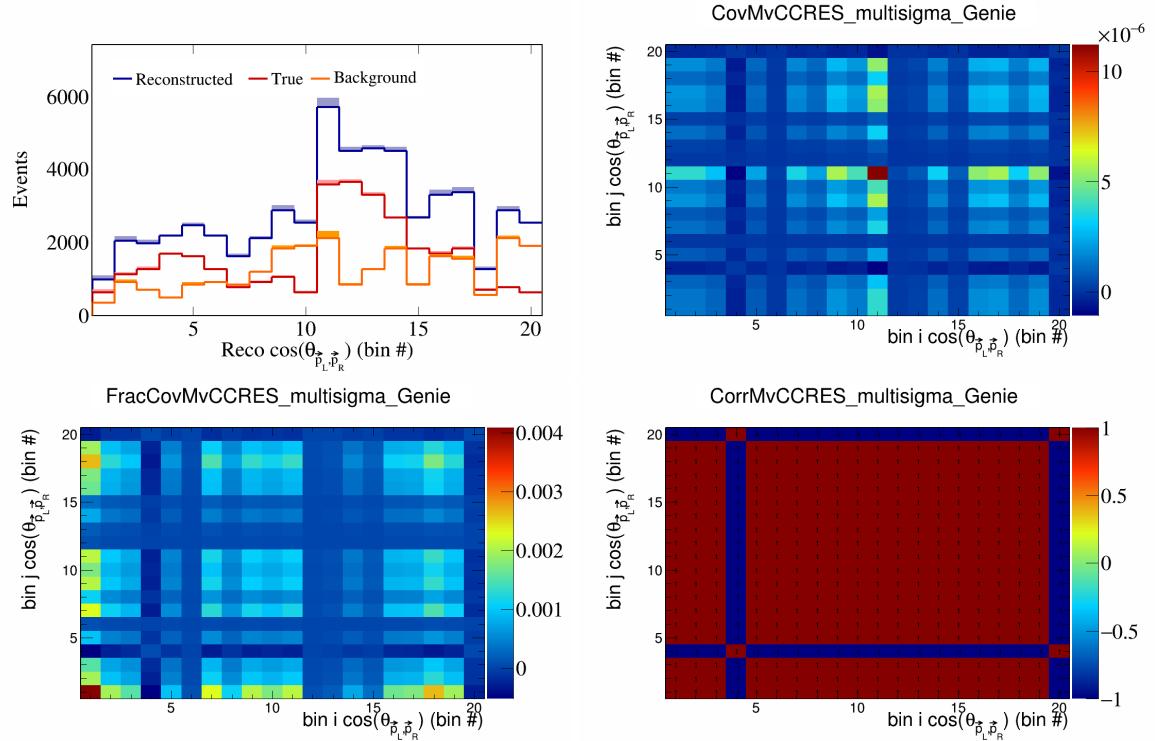


Figure 356: MvCCRES variations for $\cos(\theta_{\vec{p}_L, \vec{p}_R})$ in $\cos(\theta_{\vec{p}_\mu})$.

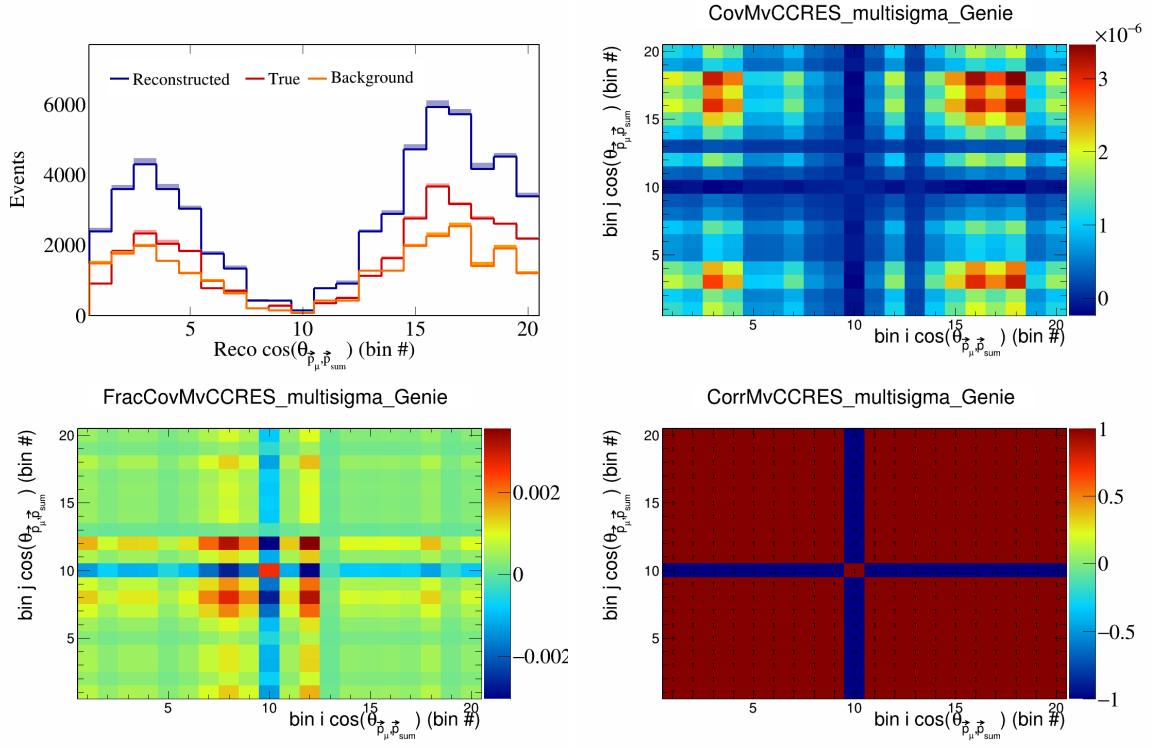


Figure 357: MvCCRES variations for $\cos(\theta_{\vec{p}_\mu, \vec{p}_{\text{sum}}})$ in $\cos(\theta_{\vec{p}_\mu})$.

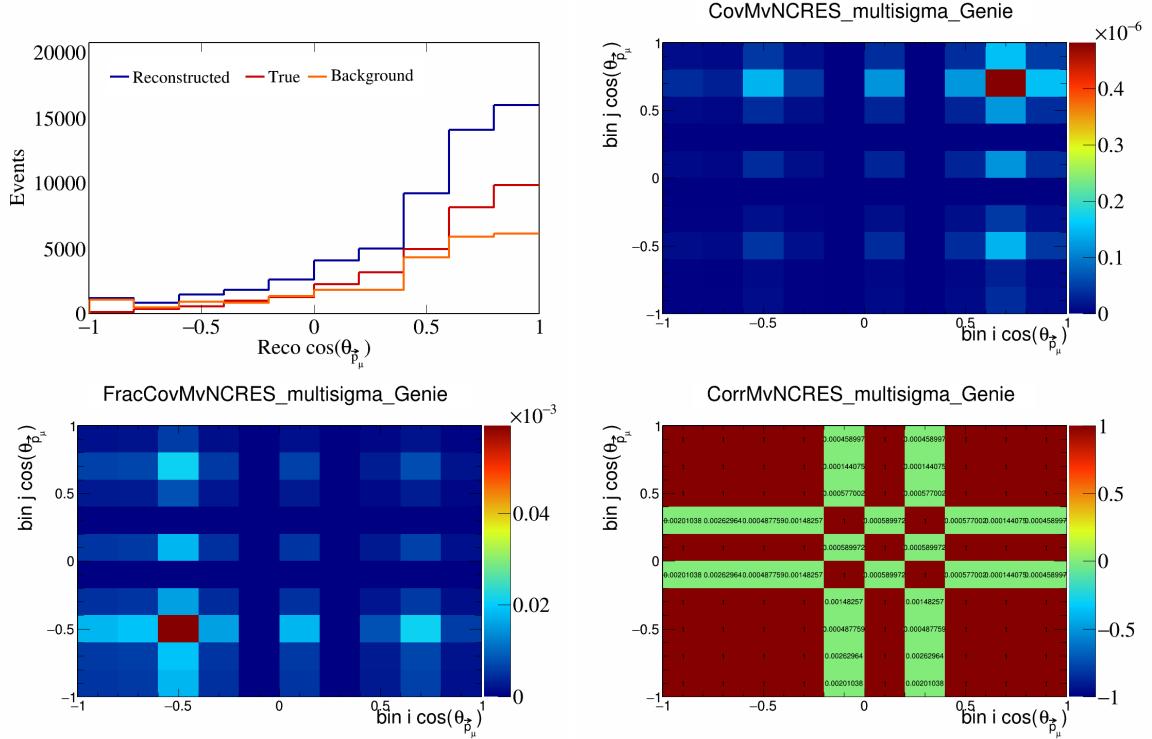


Figure 358: MvNCRES variations for $\cos(\theta_{\vec{p}_\mu, \vec{p}_{\text{sum}}})$.

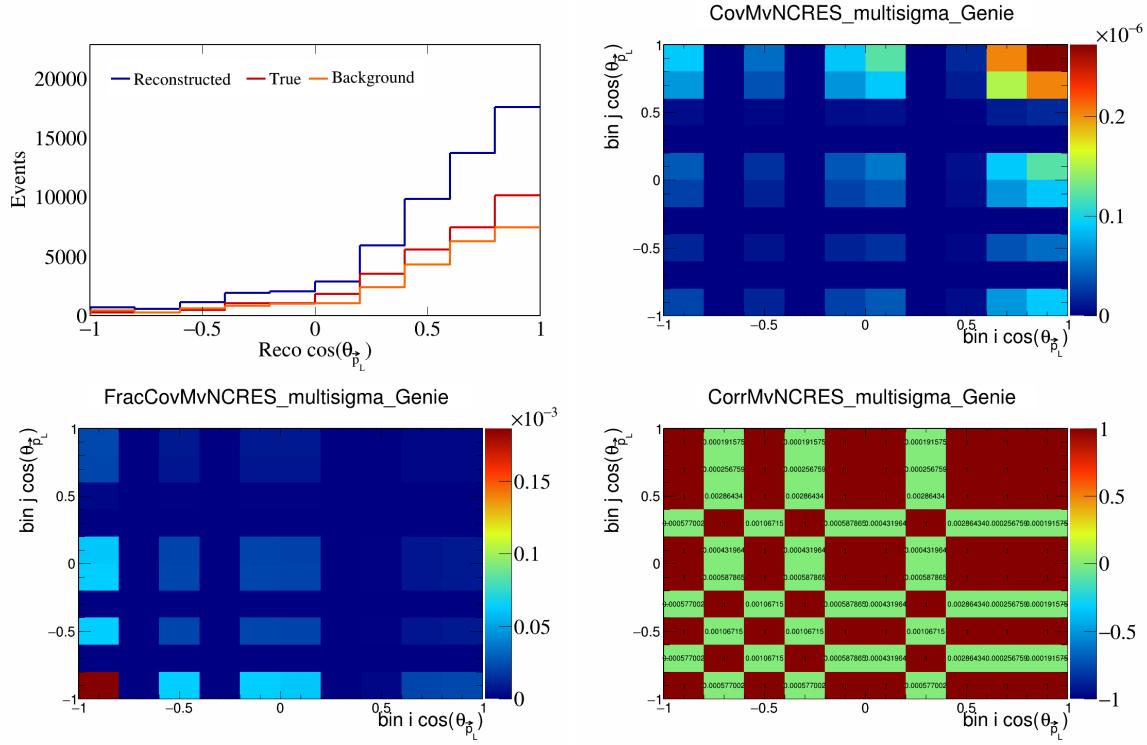


Figure 359: MvNCRES variations for $\cos(\theta_{\vec{p}_L})$.

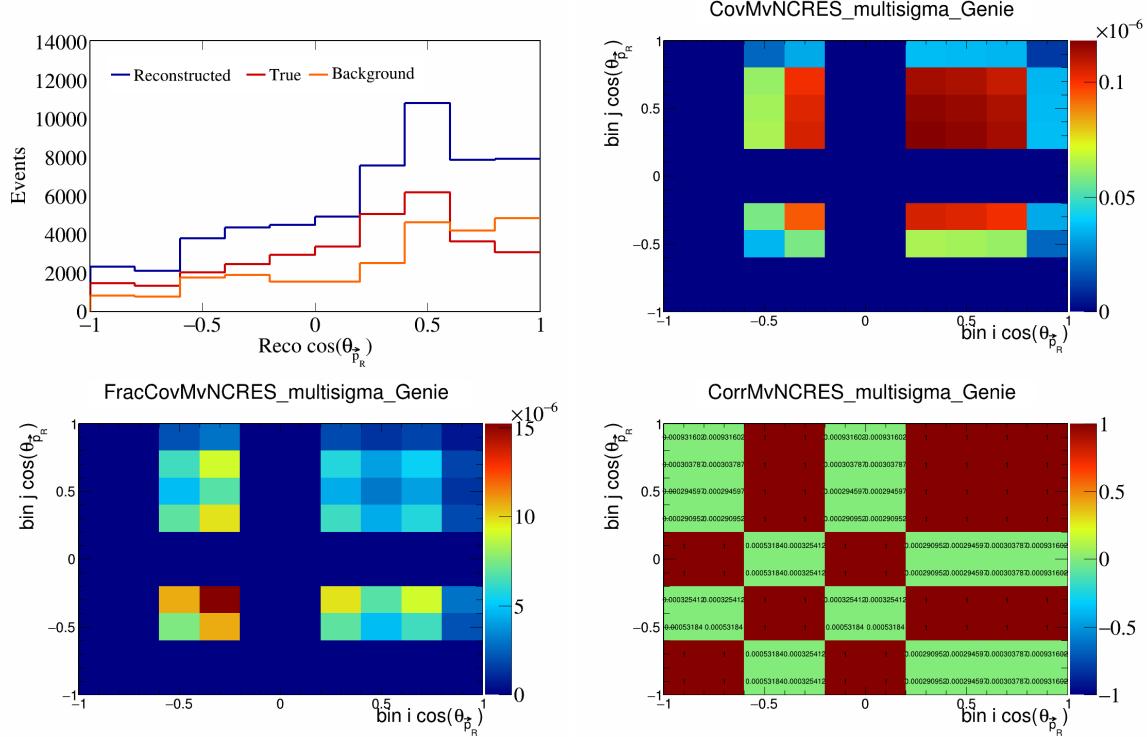


Figure 360: MvNCRES variations for $\cos(\theta_{\vec{p}_R})$.

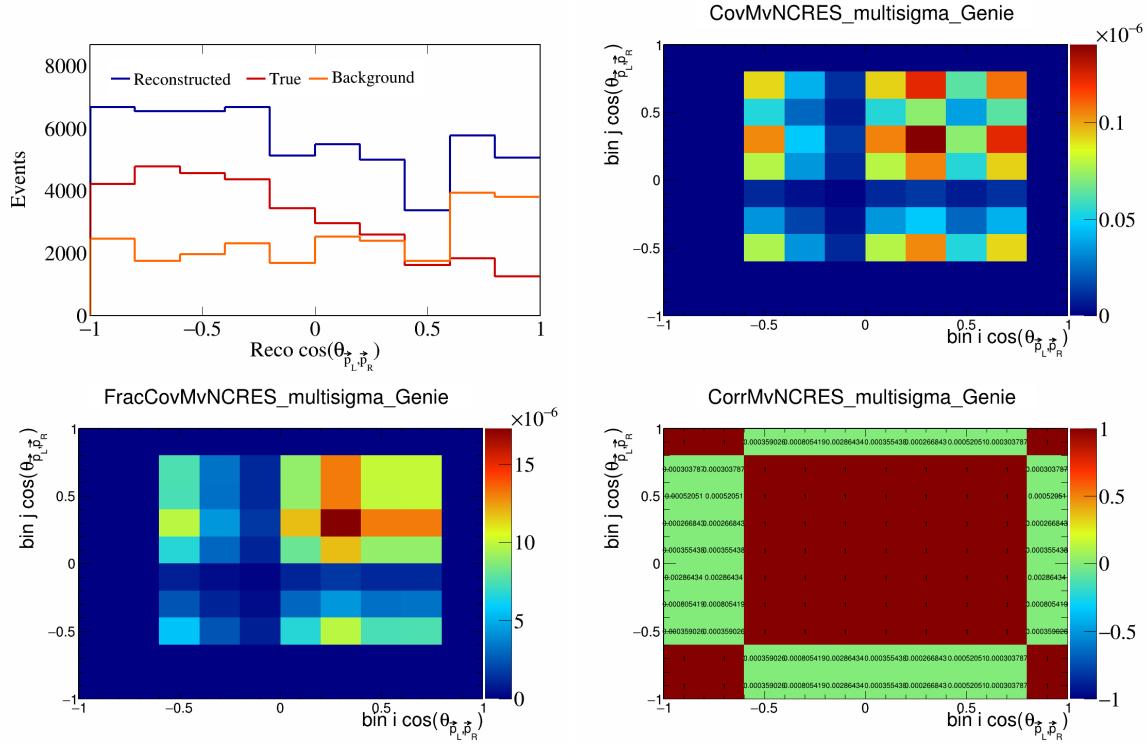


Figure 361: MvNCRES variations for $\cos(\theta_{\vec{p}_L, \vec{p}_R})$.

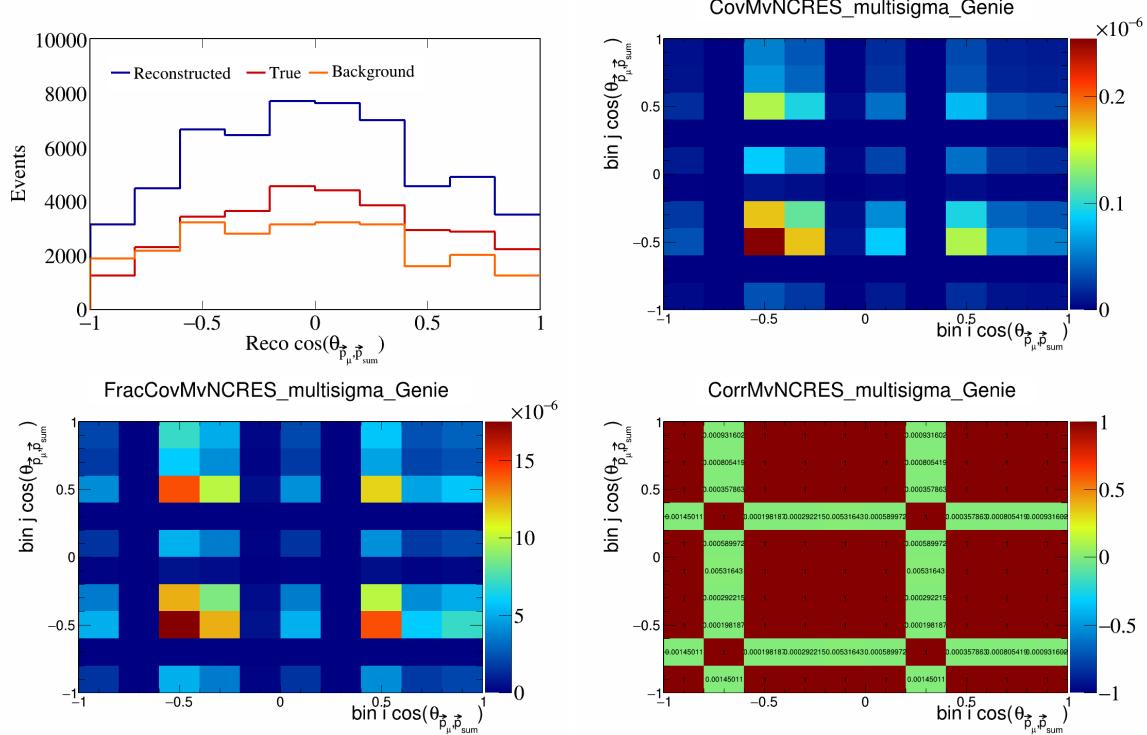


Figure 362: MvNCRES variations for $\cos(\theta_{\vec{p}_\mu, \vec{p}_{\text{sum}}})$.

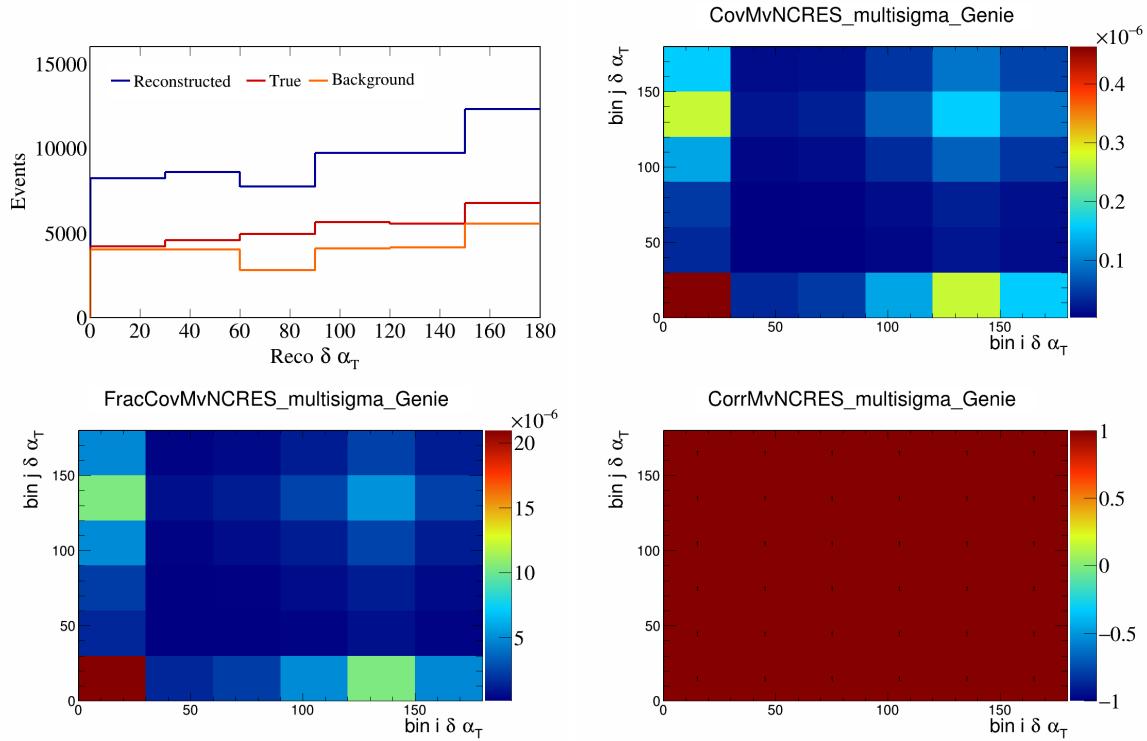


Figure 363: MvNCRES variations for $\delta\alpha_T$.

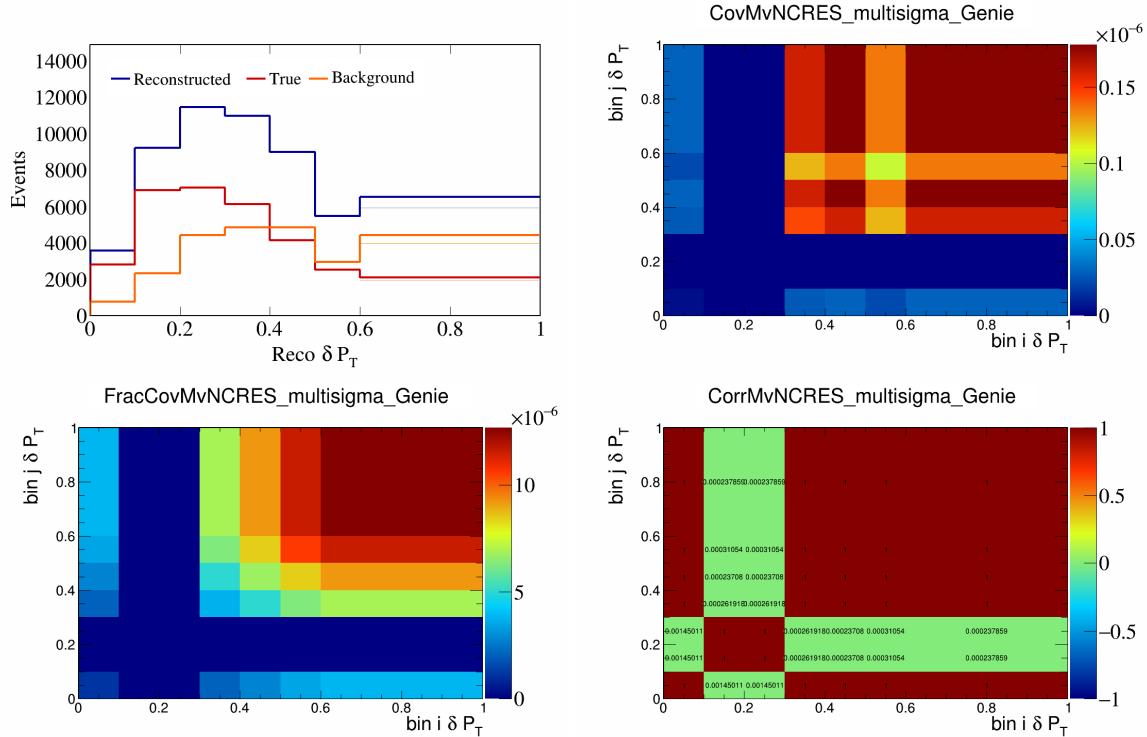


Figure 364: MvNCRES variations for δP_T .

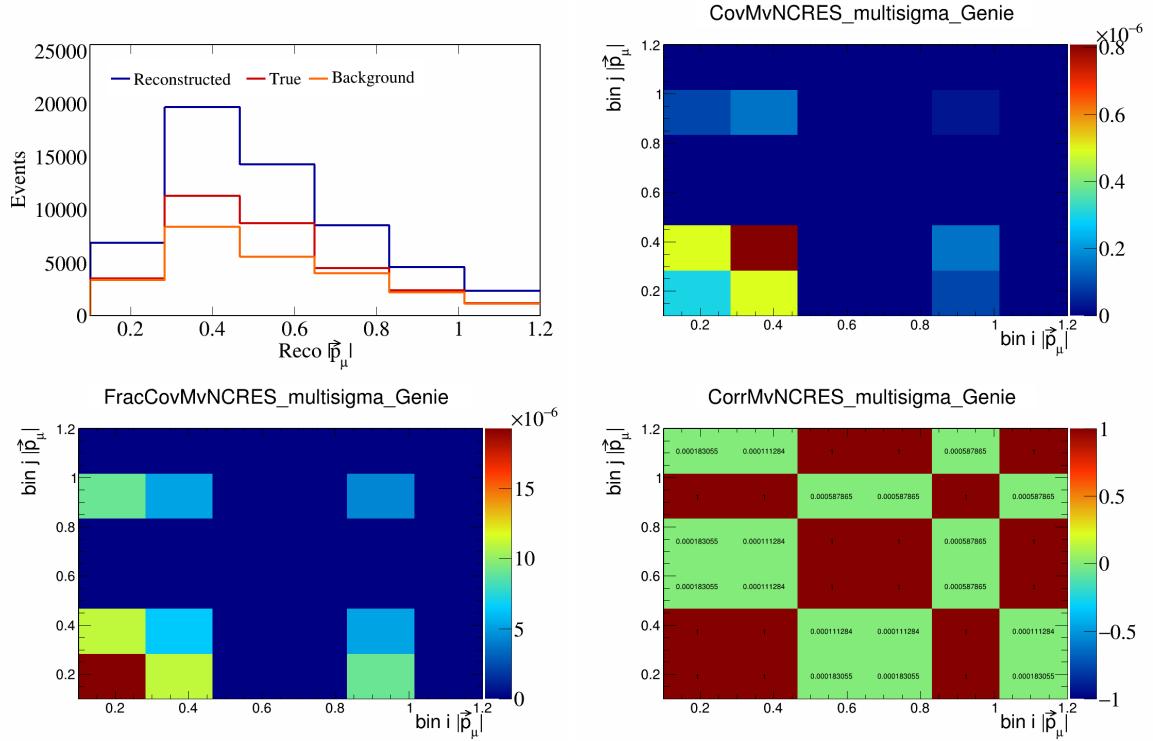


Figure 365: MvNCRES variations for $|\vec{p}_\mu|$.

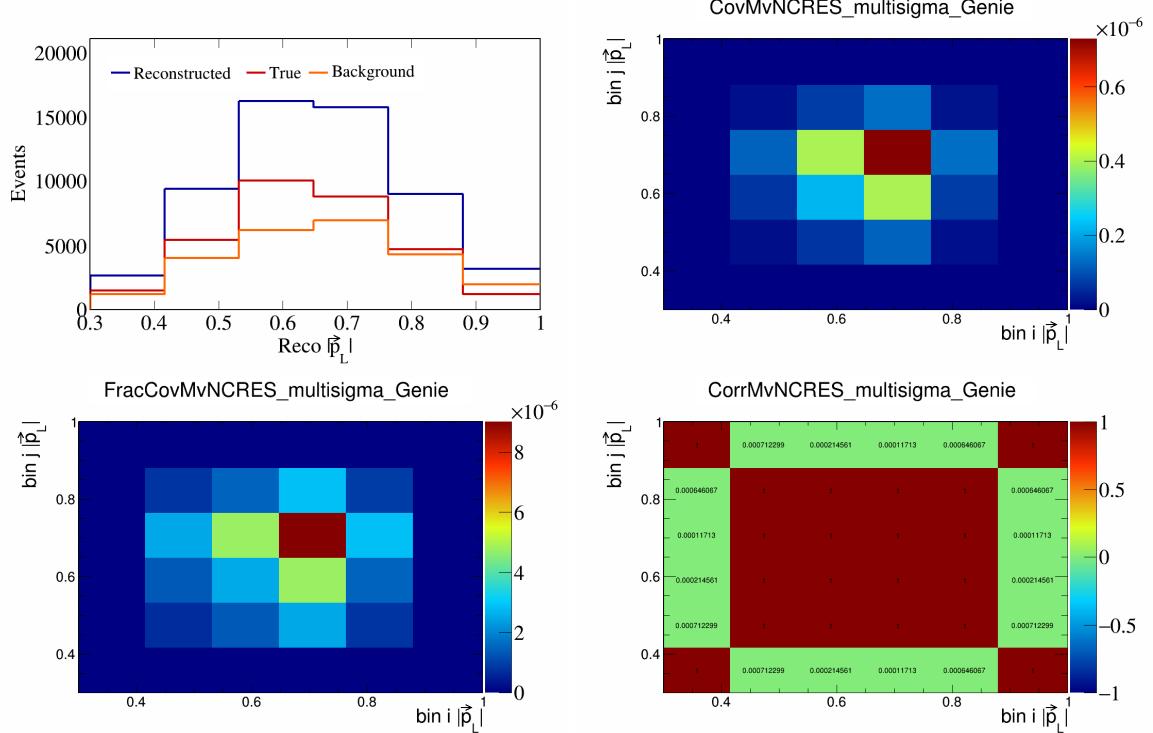


Figure 366: MvNCRES variations for $|\vec{p}_L|$.

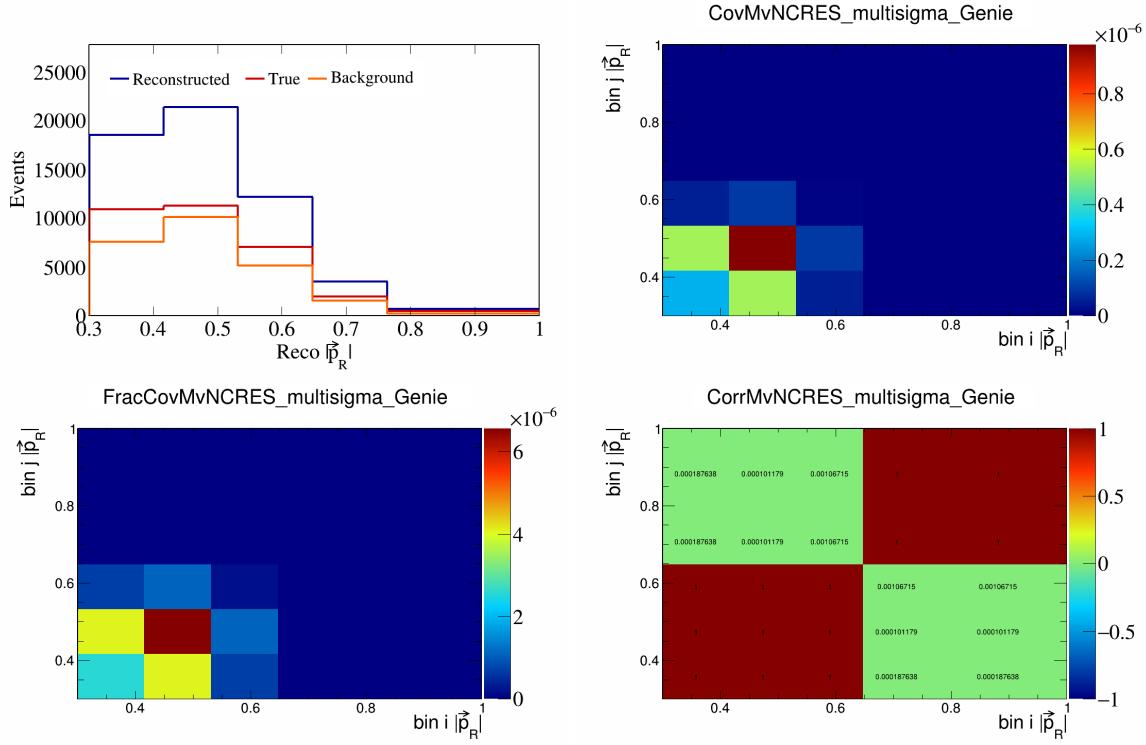


Figure 367: MvNCRES variations for $|\vec{p}_R|$.

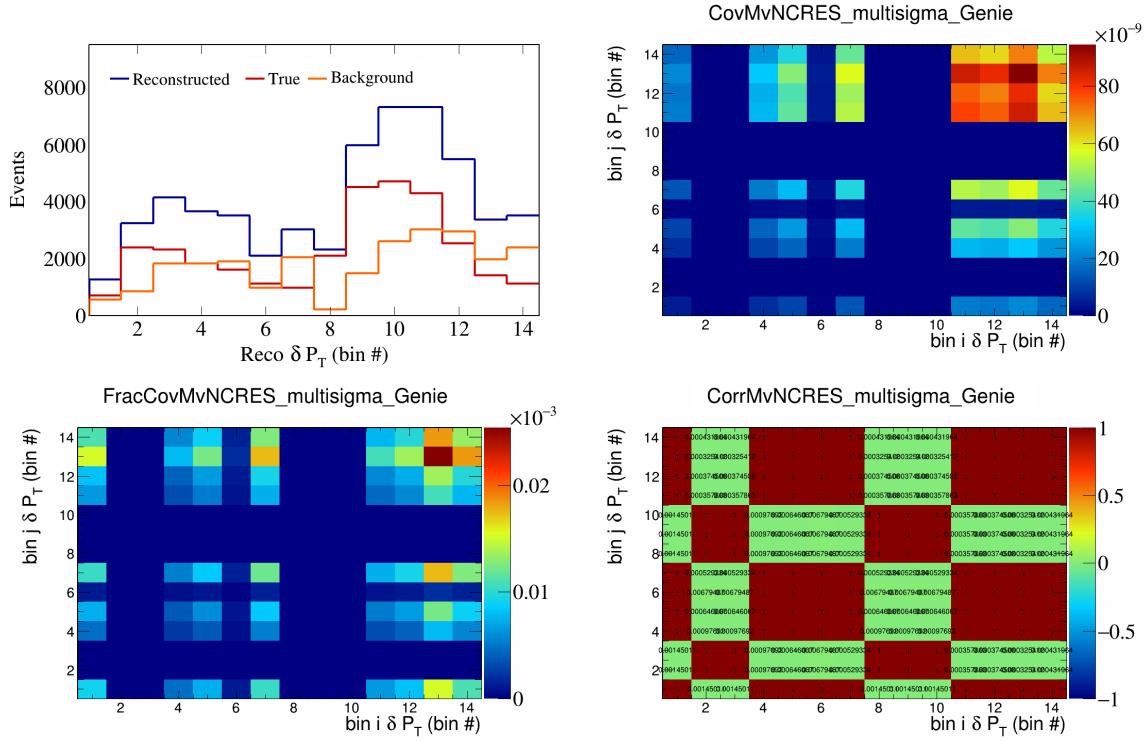


Figure 368: MvNCRES variations for δP_T in $\cos(\theta_{\vec{p}_\mu})$.

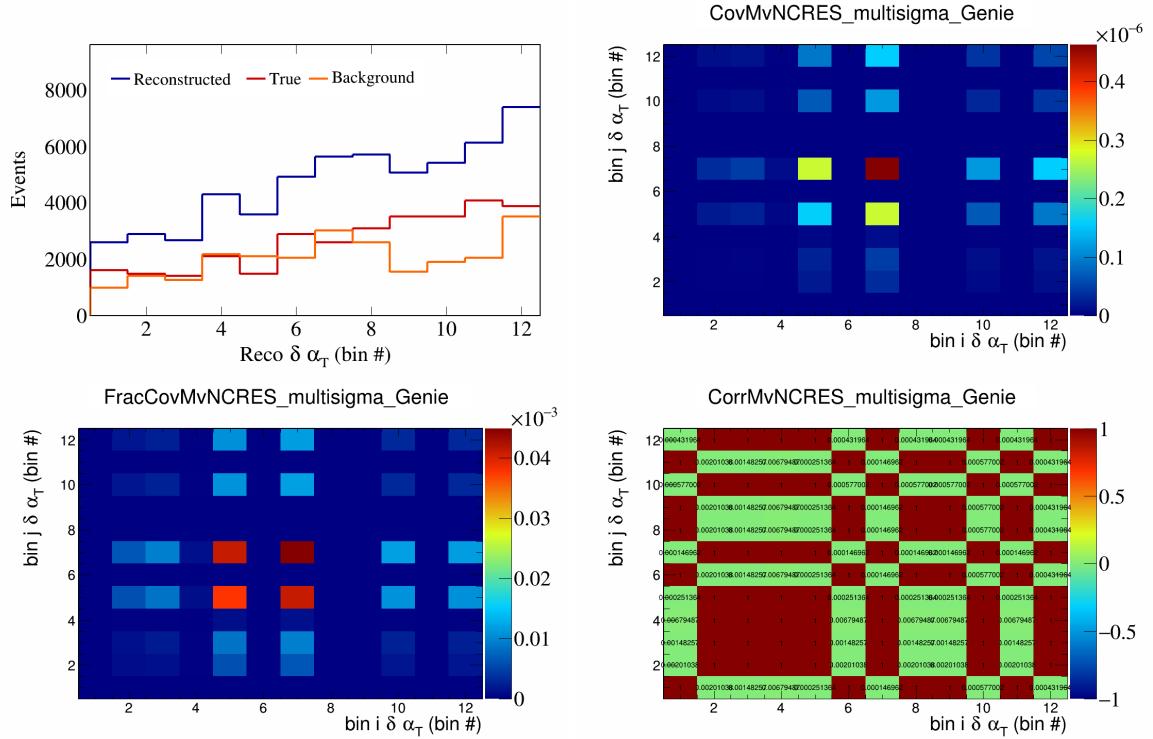


Figure 369: MvNCRES variations for $\delta\alpha_T$ in $\cos(\theta_{\vec{p}_\mu})$.

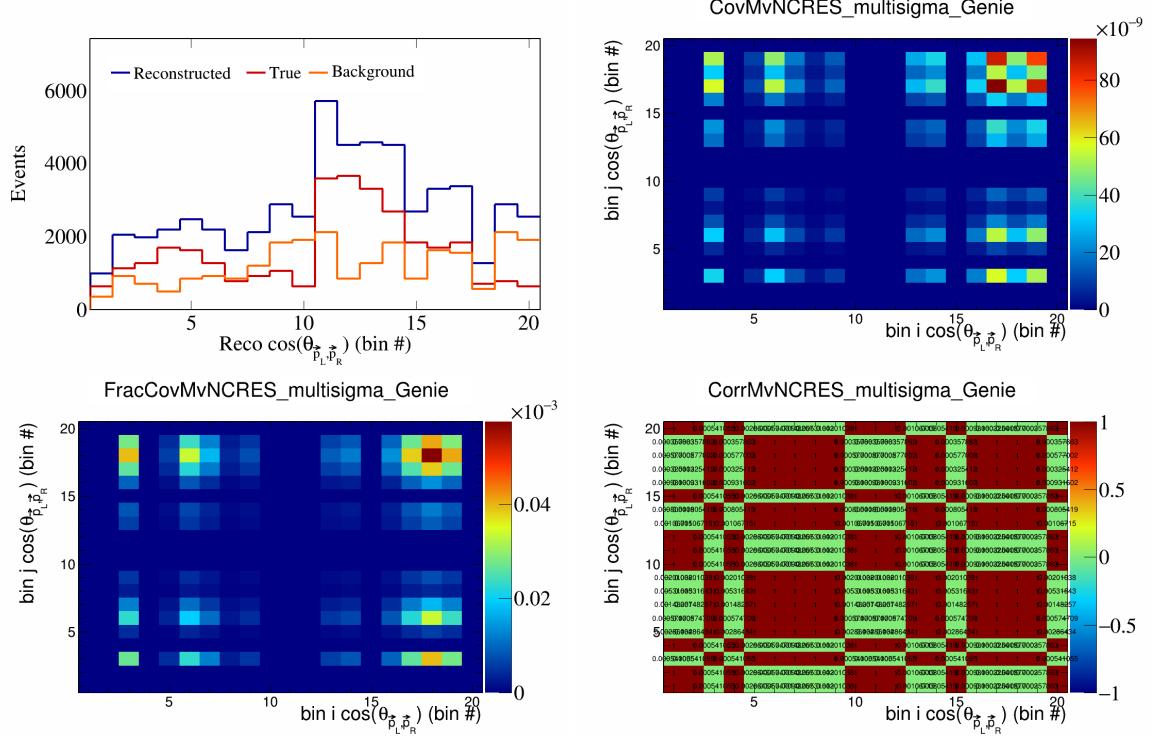


Figure 370: MvNCRES variations for $\cos(\theta_{p_L, p_R})$ in $\cos(\theta_{\vec{p}_\mu})$.

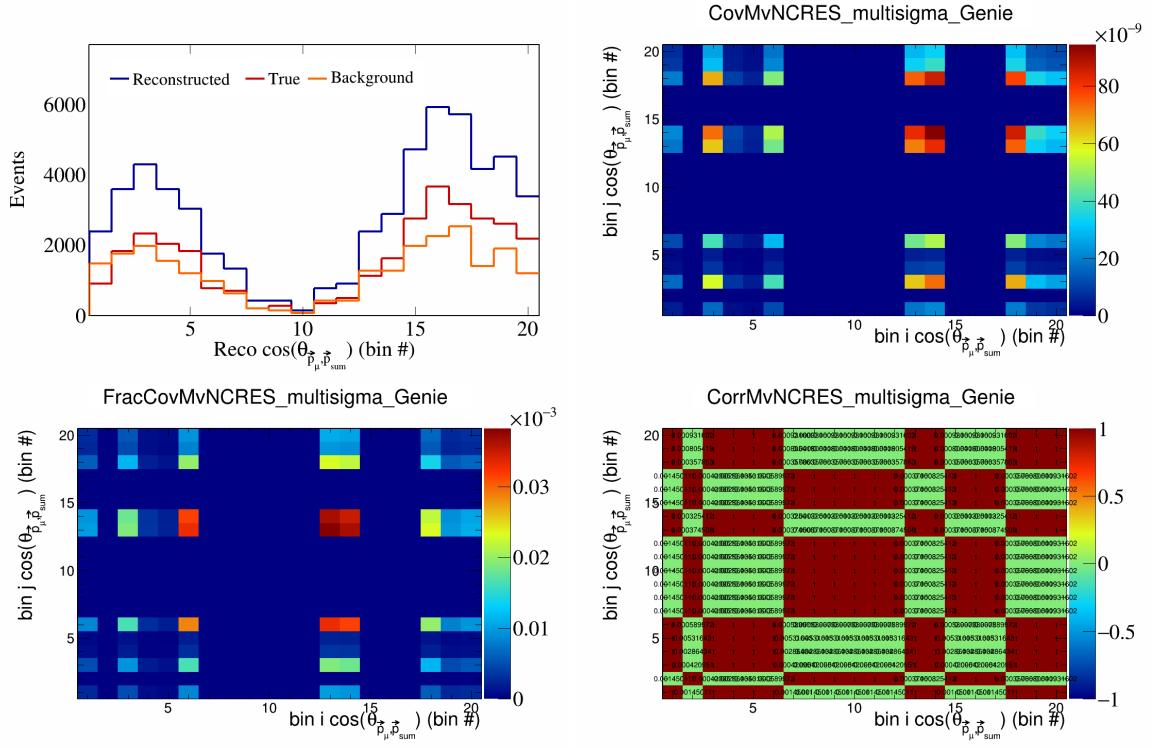


Figure 371: MyNCRES variations for $\cos(\theta_{\vec{p}_\mu, \vec{p}_{\text{sum}}})$ in $\cos(\theta_{\vec{p}_\mu})$.

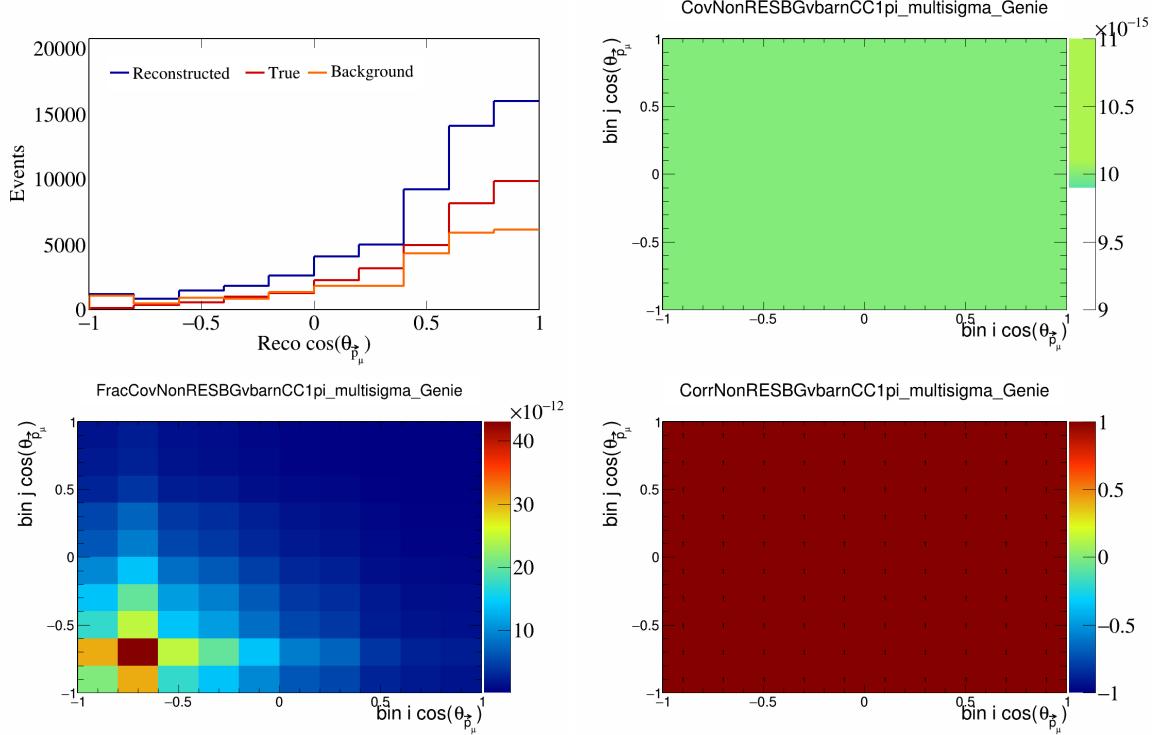


Figure 372: NonRESBGvbarCC1pi variations for $\cos(\theta_{\vec{p}_\mu})$.

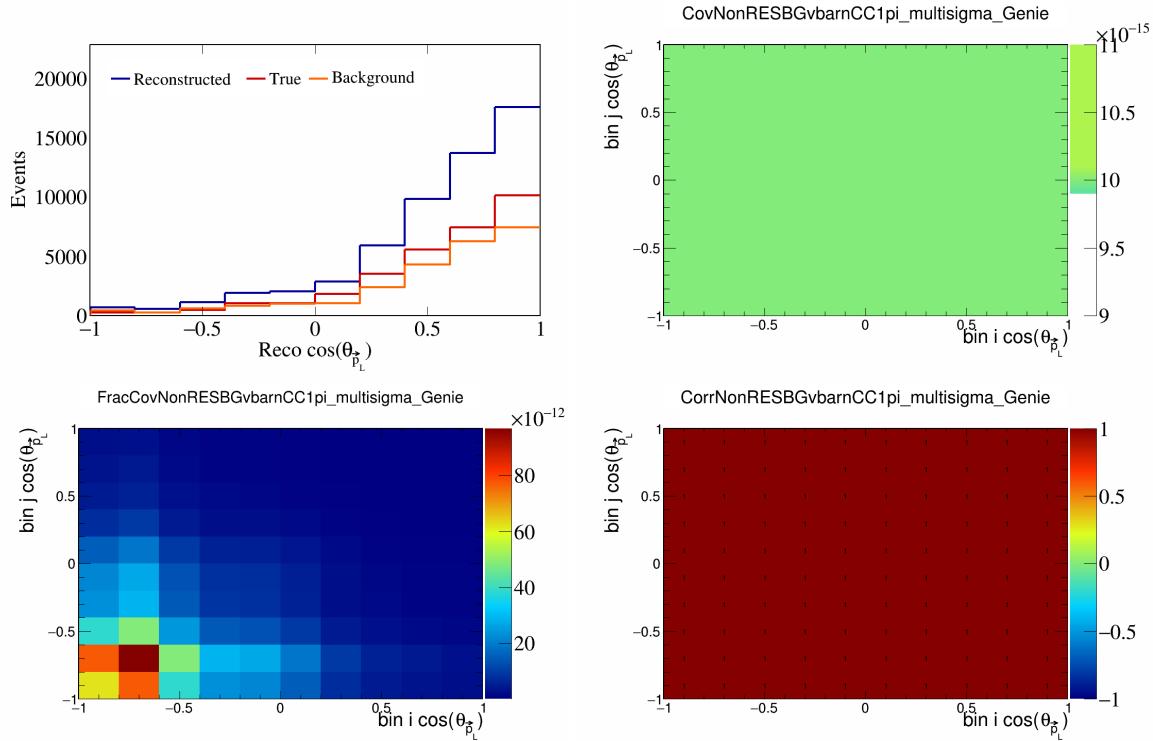


Figure 373: NonRESBGvbarCC1pi variations for $\cos(\theta_{\vec{p}_L})$.

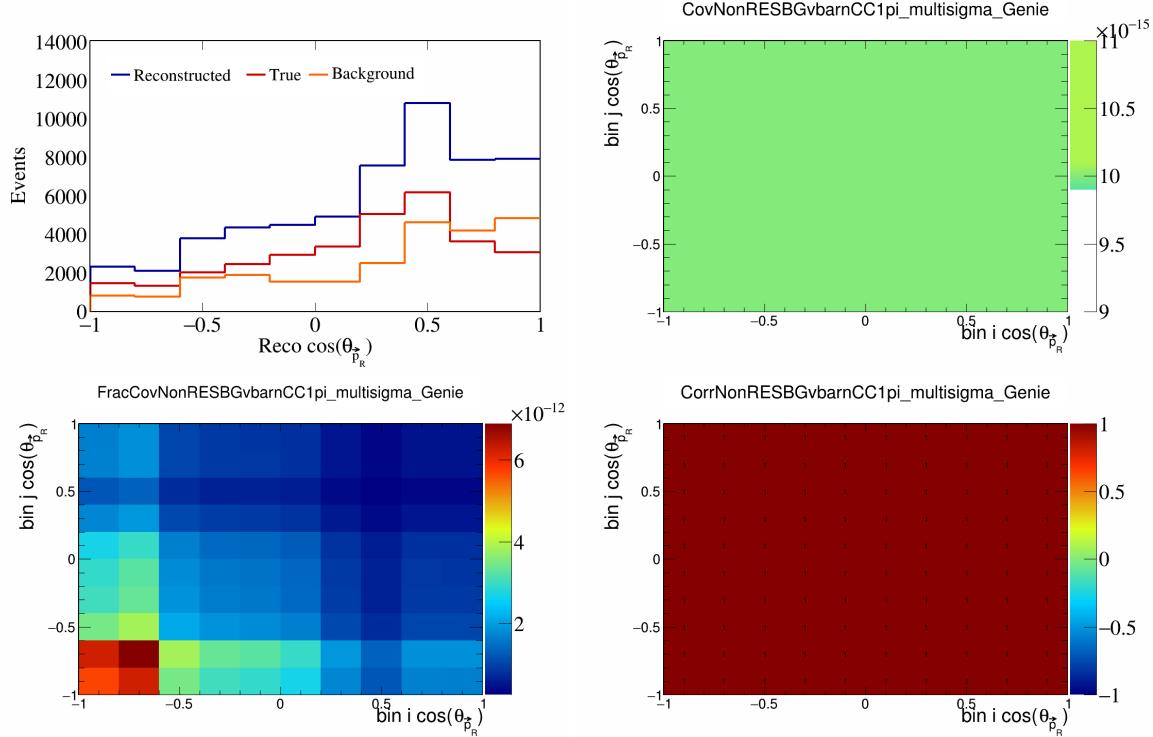


Figure 374: NonRESBGvbarCC1pi variations for $\cos(\theta_{\vec{p}_R})$.

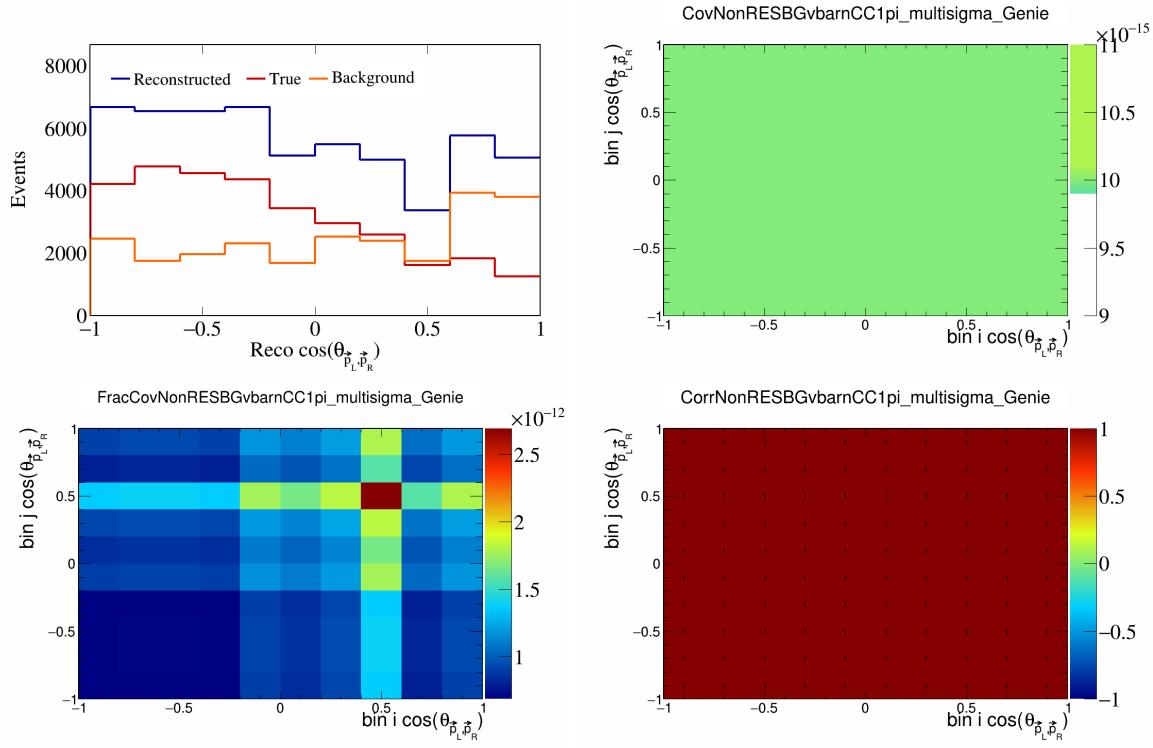


Figure 375: NonRESBGvbarCC1pi variations for $\cos(\theta_{\vec{p}_L, \vec{p}_R})$.

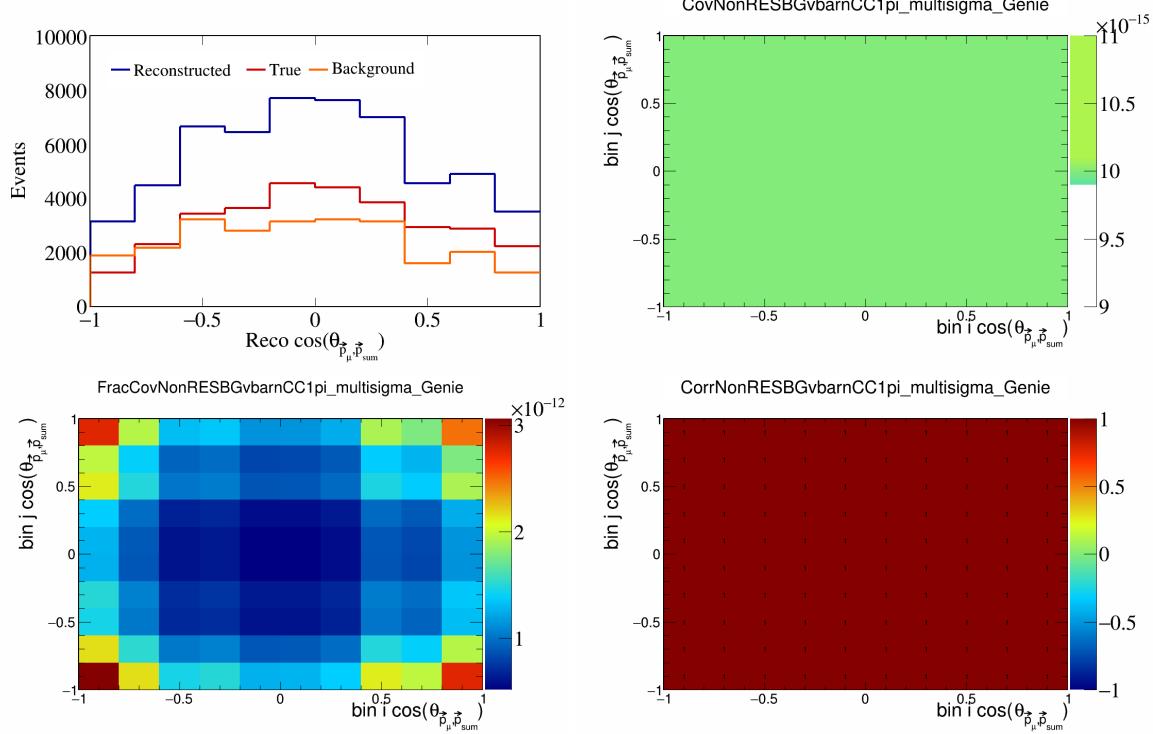


Figure 376: NonRESBGvbarCC1pi variations for $\cos(\theta_{\vec{p}_\mu, \vec{p}_{\text{sum}}})$.

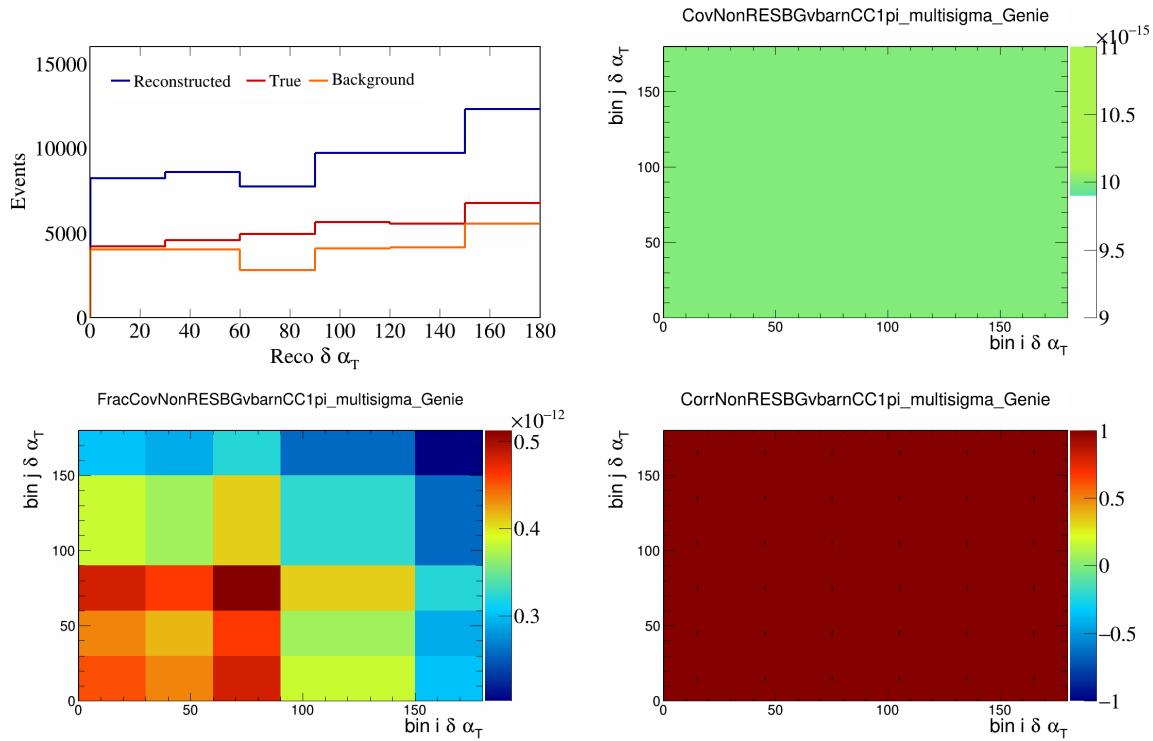


Figure 377: NonRESBGvbarCC1pi variations for $\delta\alpha_T$.

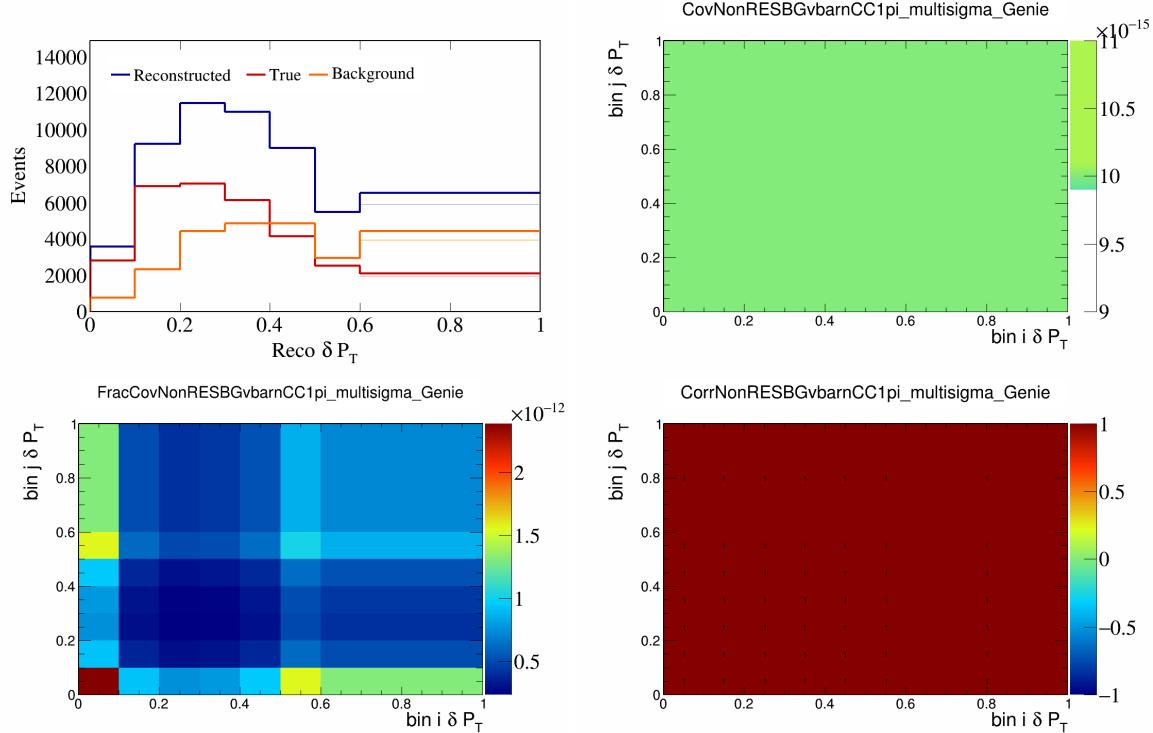


Figure 378: NonRESBGvbarCC1pi variations for δP_T .

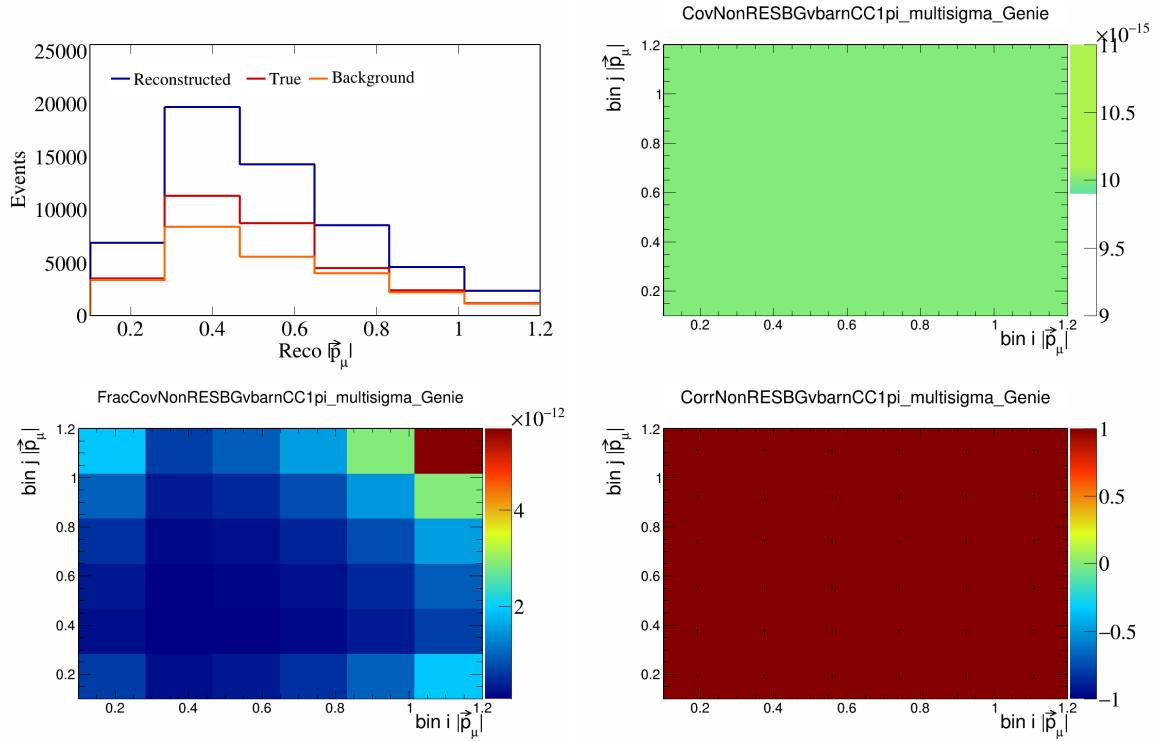


Figure 379: NonRESBGvbarCC1pi variations for $|\vec{p}_\mu|$.

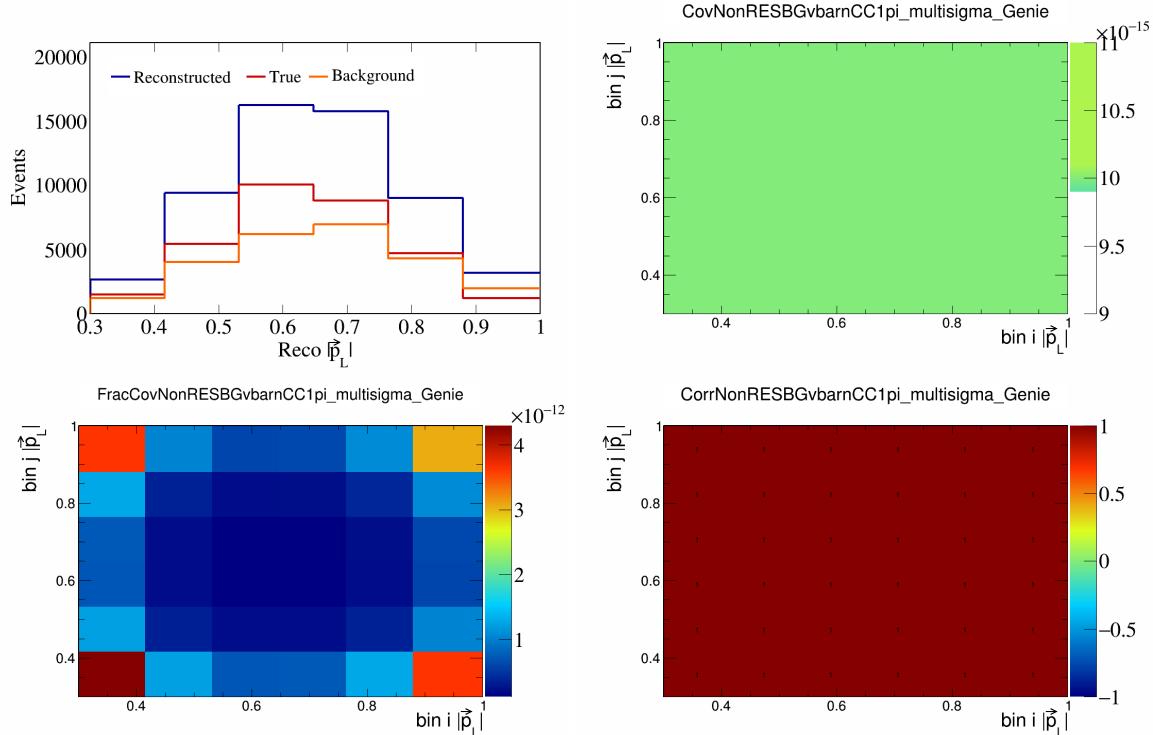


Figure 380: NonRESBGvbarCC1pi variations for $|\vec{p}_L|$.

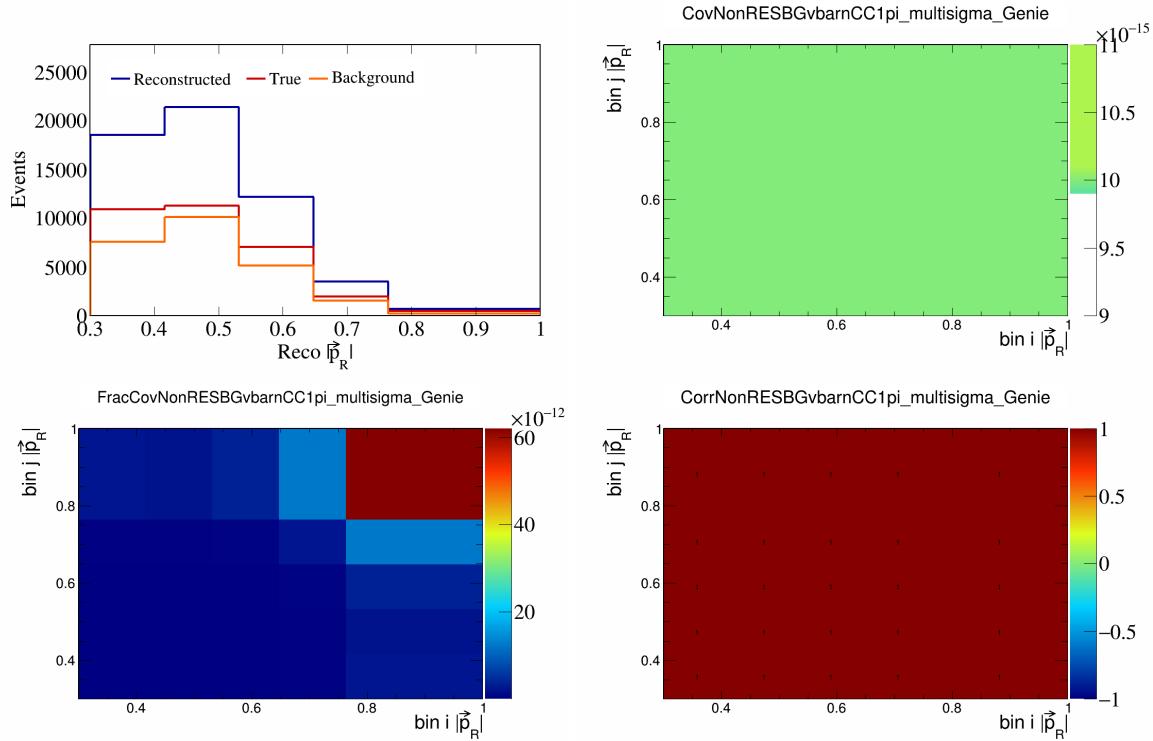


Figure 381: NonRESBGvbarCC1pi variations for $|\vec{p}_R|$.

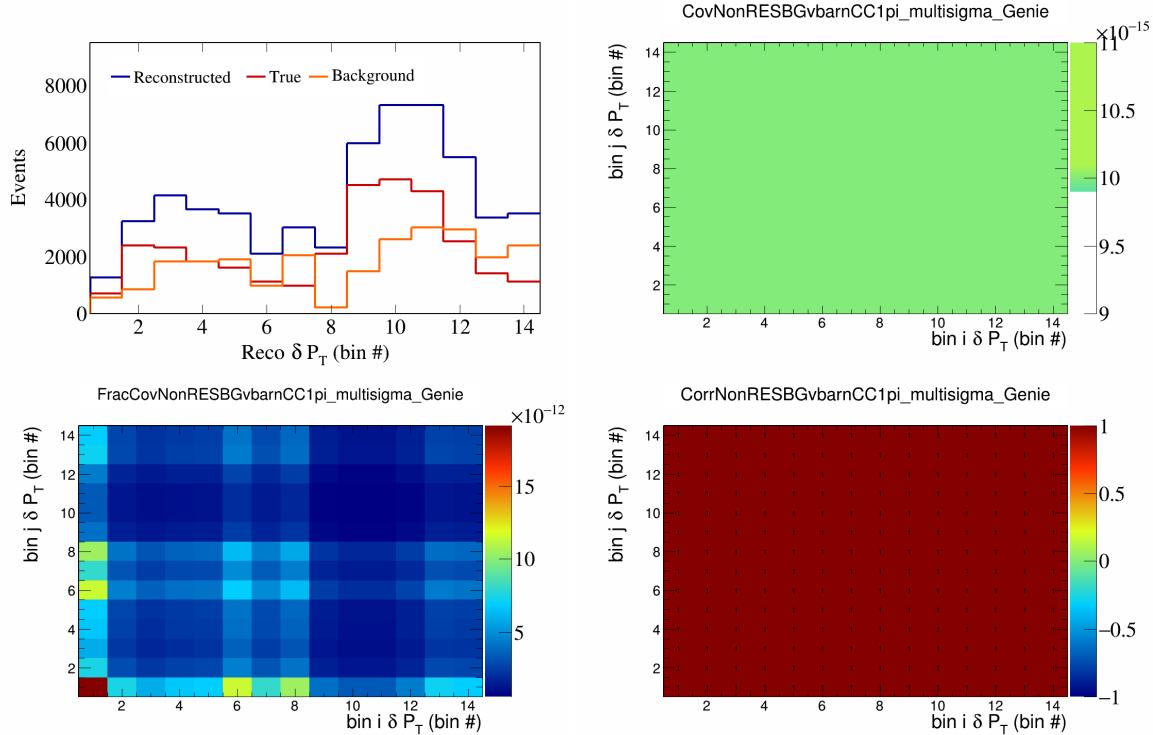


Figure 382: NonRESBGvbarCC1pi variations for δP_T in $\cos(\theta_{\vec{p}_\mu})$.

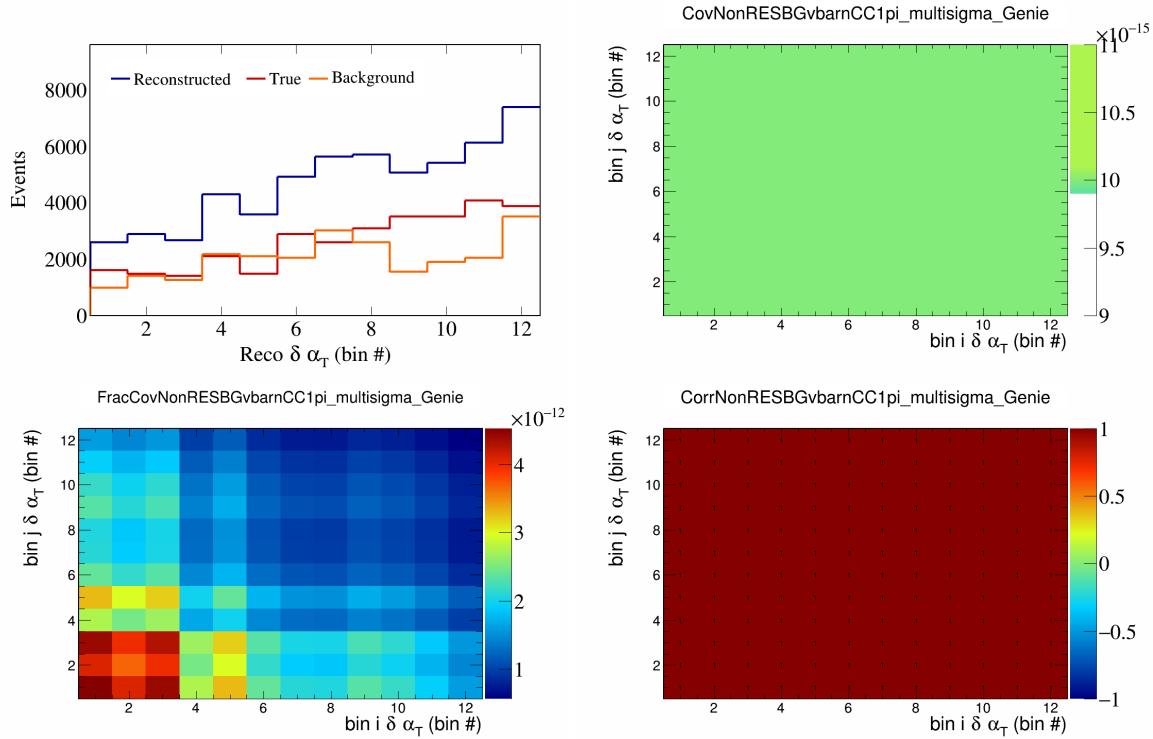


Figure 383: NonRESBGvbarCC1pi variations for $\delta\alpha_T$ in $\cos(\theta_{\vec{p}_\mu})$.

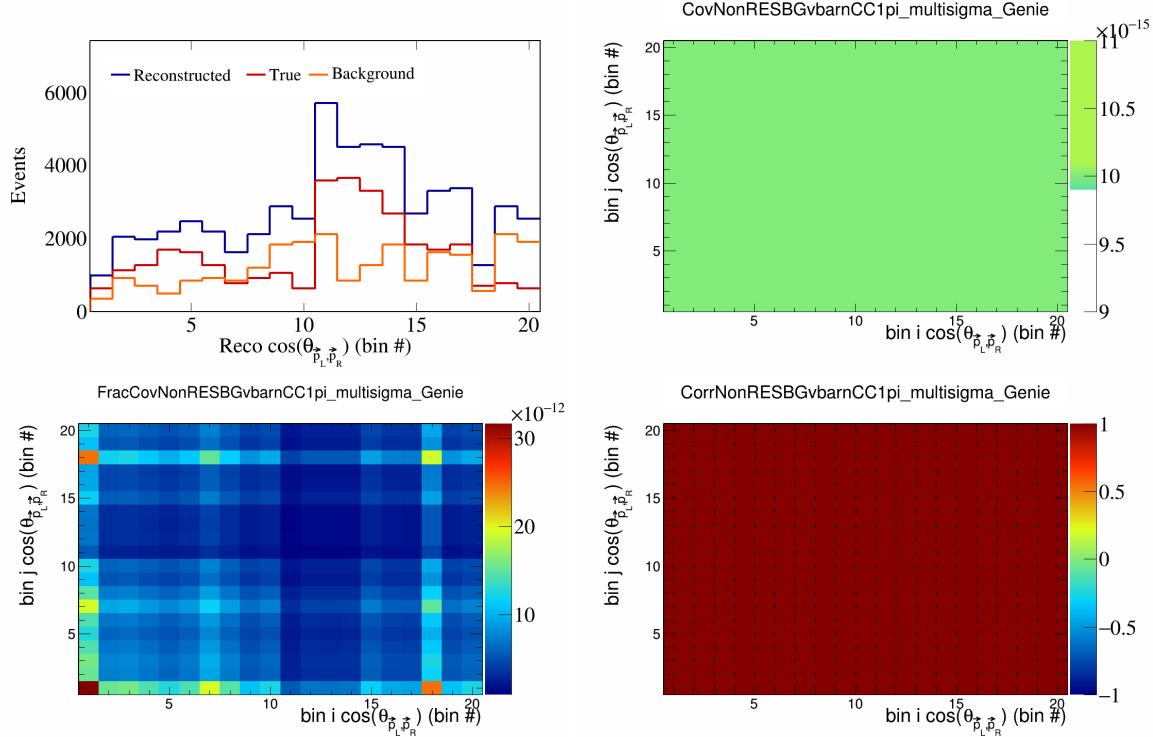


Figure 384: NonRESBGvbarCC1pi variations for $\cos(\theta_{\vec{p}_L, \vec{p}_R})$ in $\cos(\theta_{\vec{p}_\mu})$.

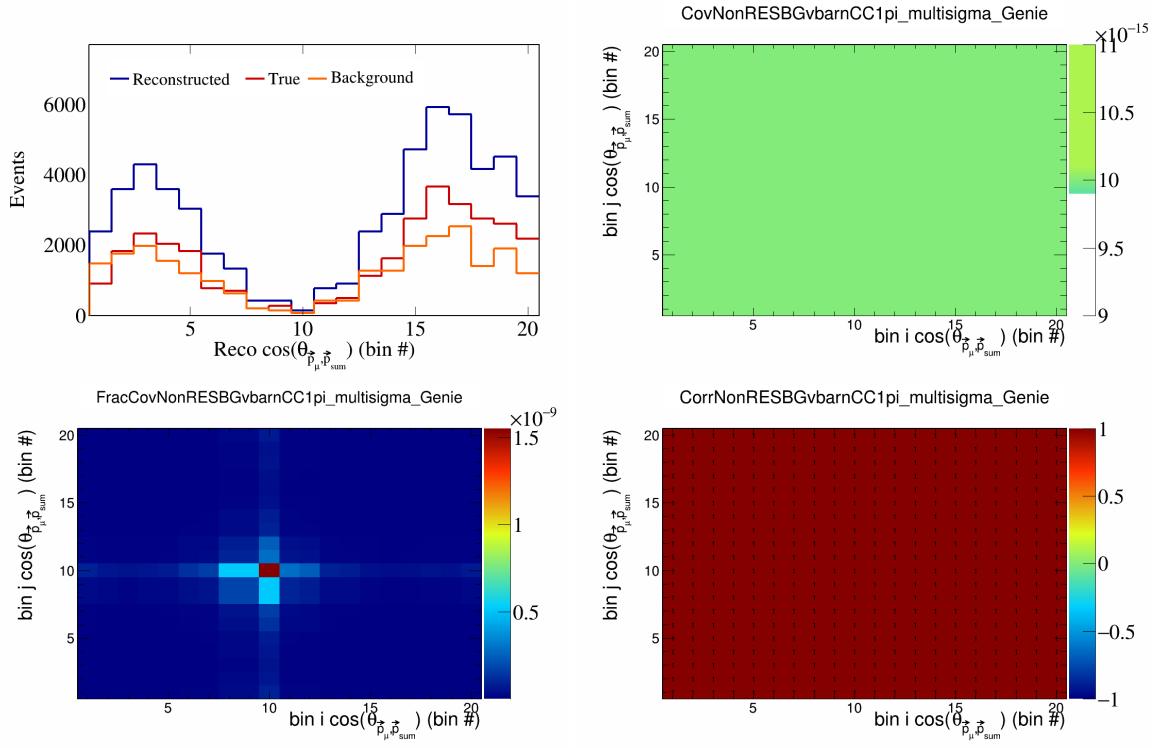


Figure 385: NonRESBGvbarCC1pi variations for $\cos(\theta_{\vec{p}_\mu, \vec{p}_{\text{sum}}})$.

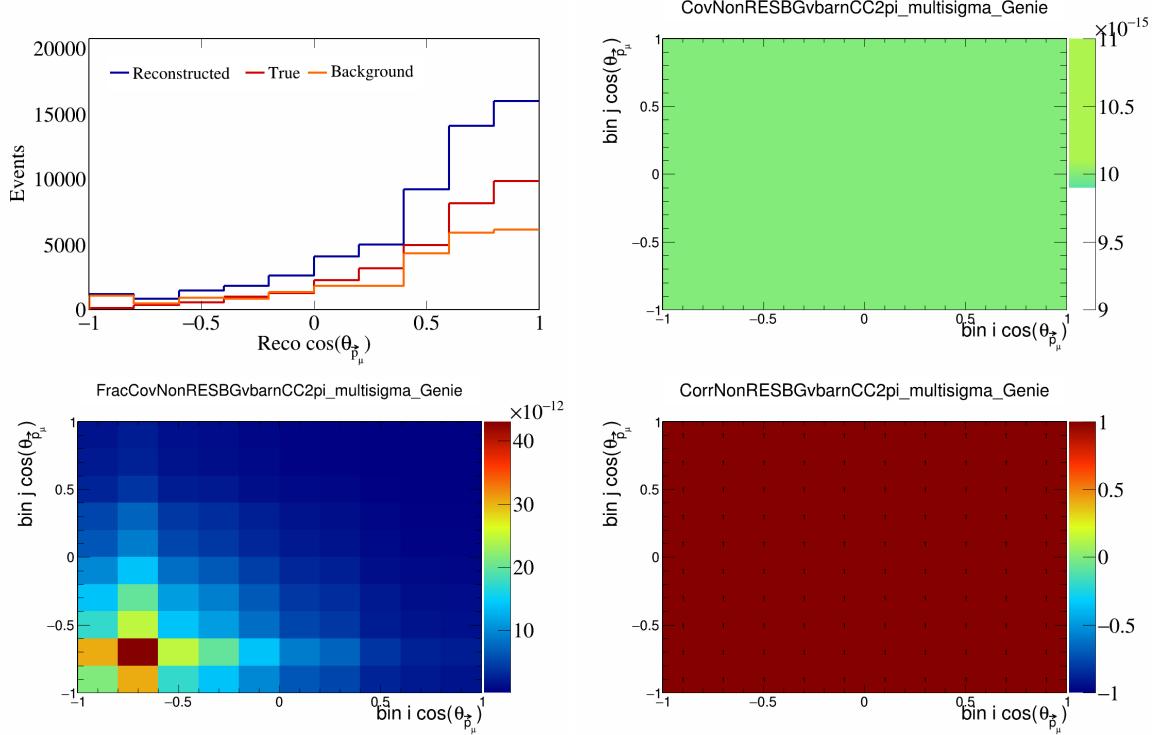


Figure 386: NonRESBGvbarCC2pi variations for $\cos(\theta_{\vec{p}_\mu})$.

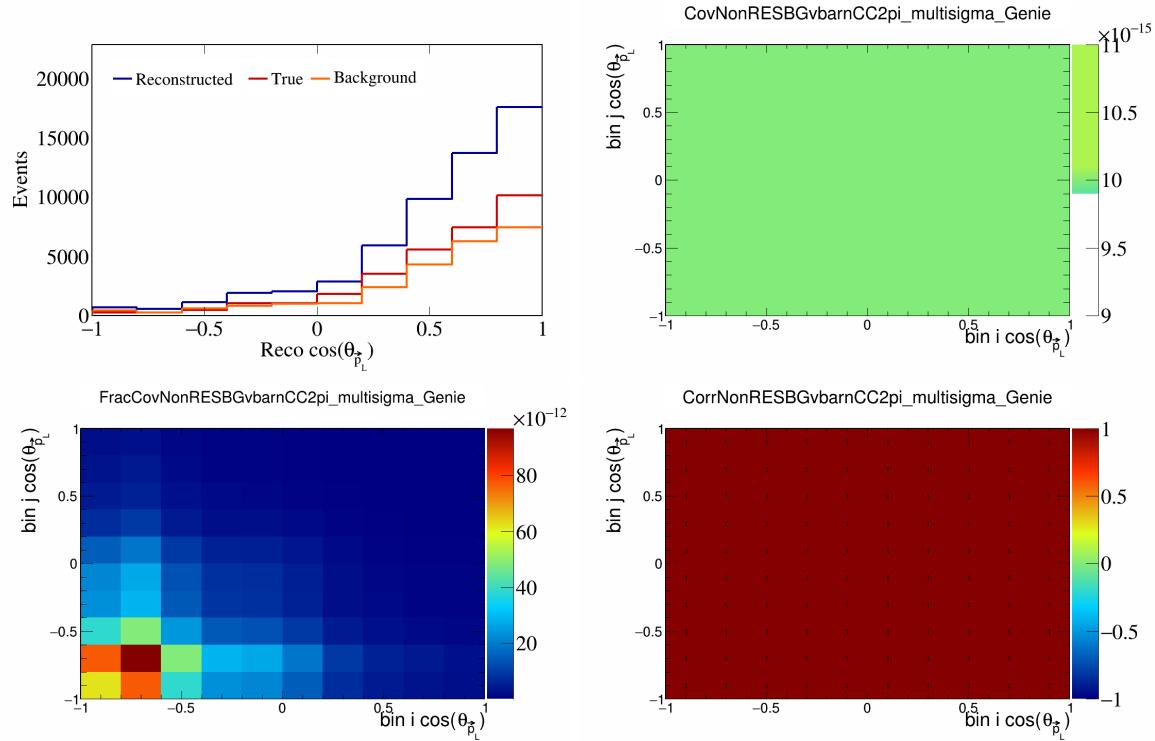


Figure 387: NonRESBGvbarCC2pi variations for $\cos(\theta_{\vec{p}_L})$.

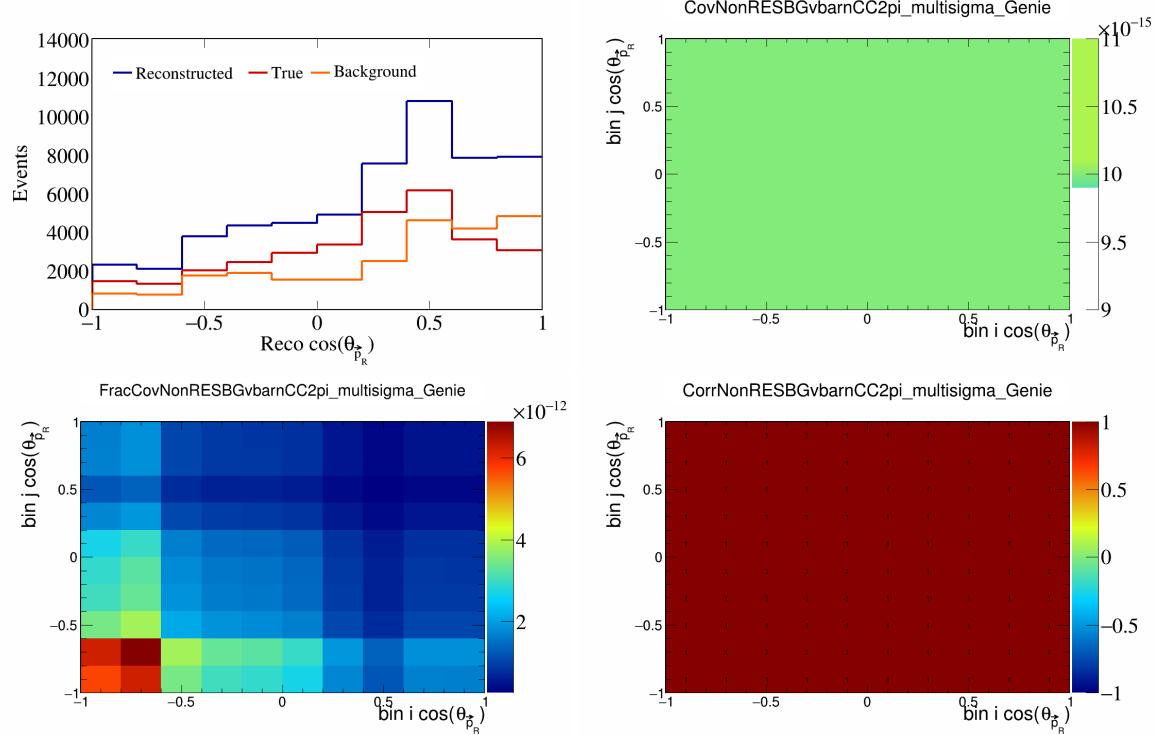


Figure 388: NonRESBGvbarCC2pi variations for $\cos(\theta_{\vec{p}_R})$.

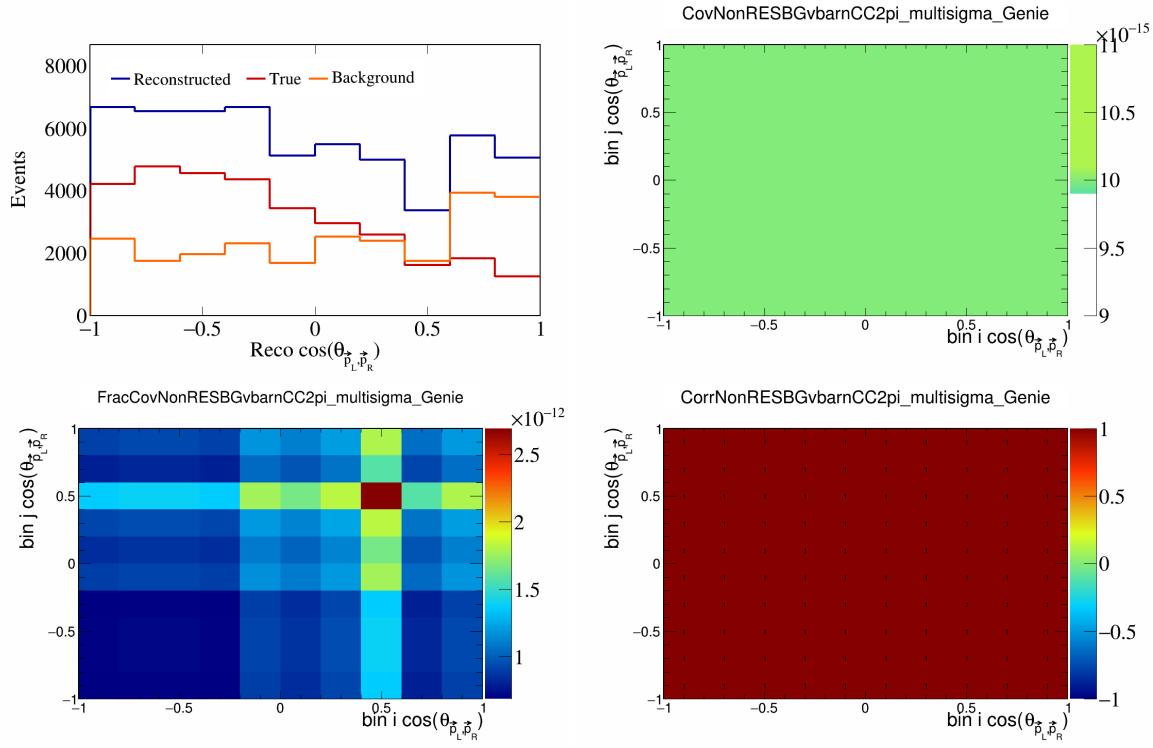


Figure 389: NonRESBGvbarCC2pi variations for $\cos(\theta_{\vec{p}_L, \vec{p}_R})$.

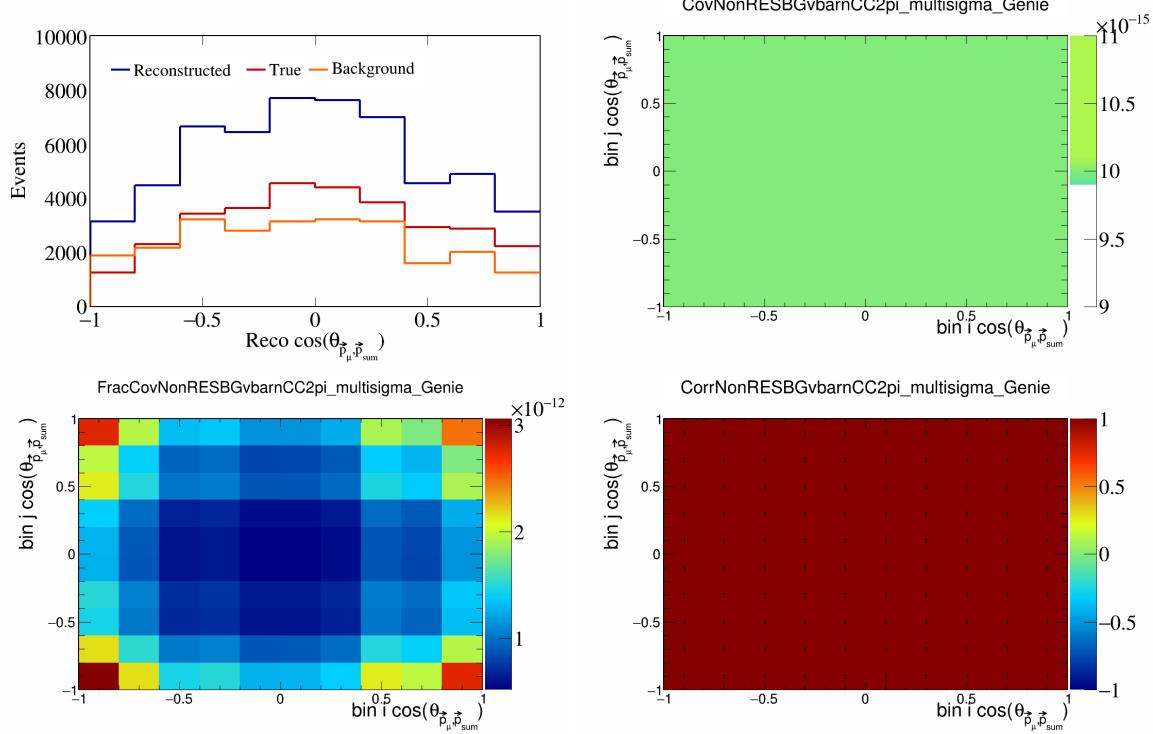


Figure 390: NonRESBGvbarCC2pi variations for $\cos(\theta_{\vec{p}_\mu, \vec{p}_{\text{sum}}})$.

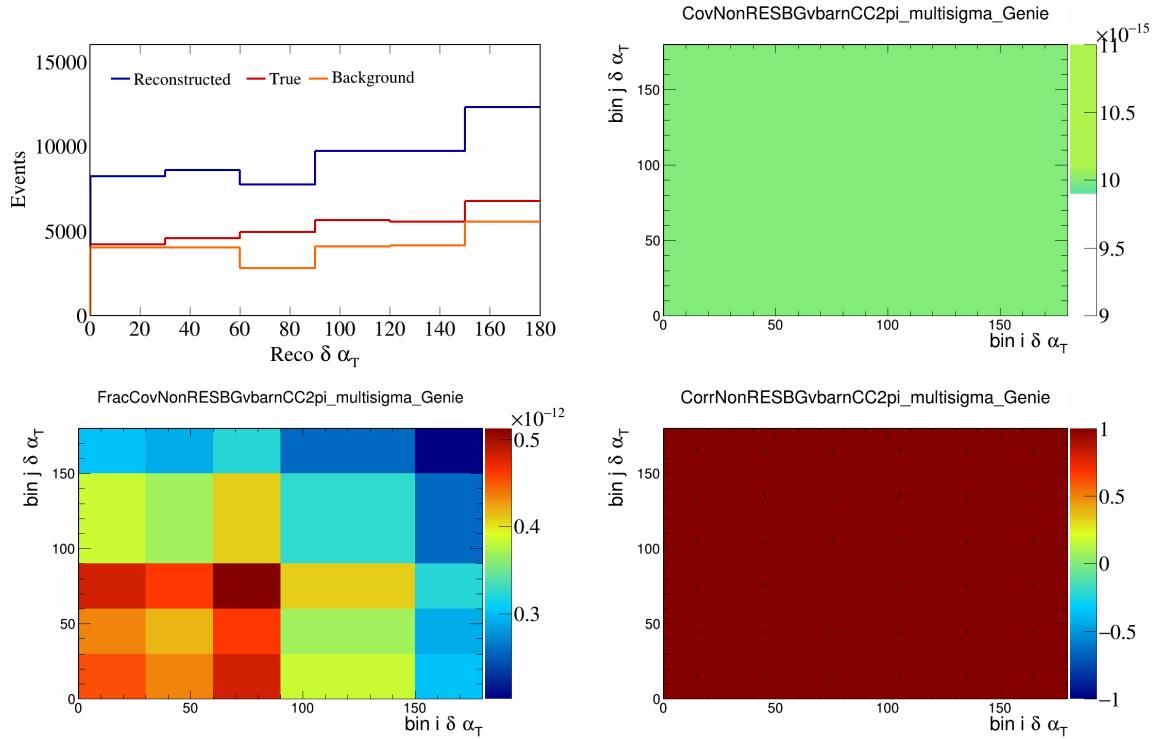


Figure 391: NonRESBGvbarCC2pi variations for $\delta\alpha_T$.

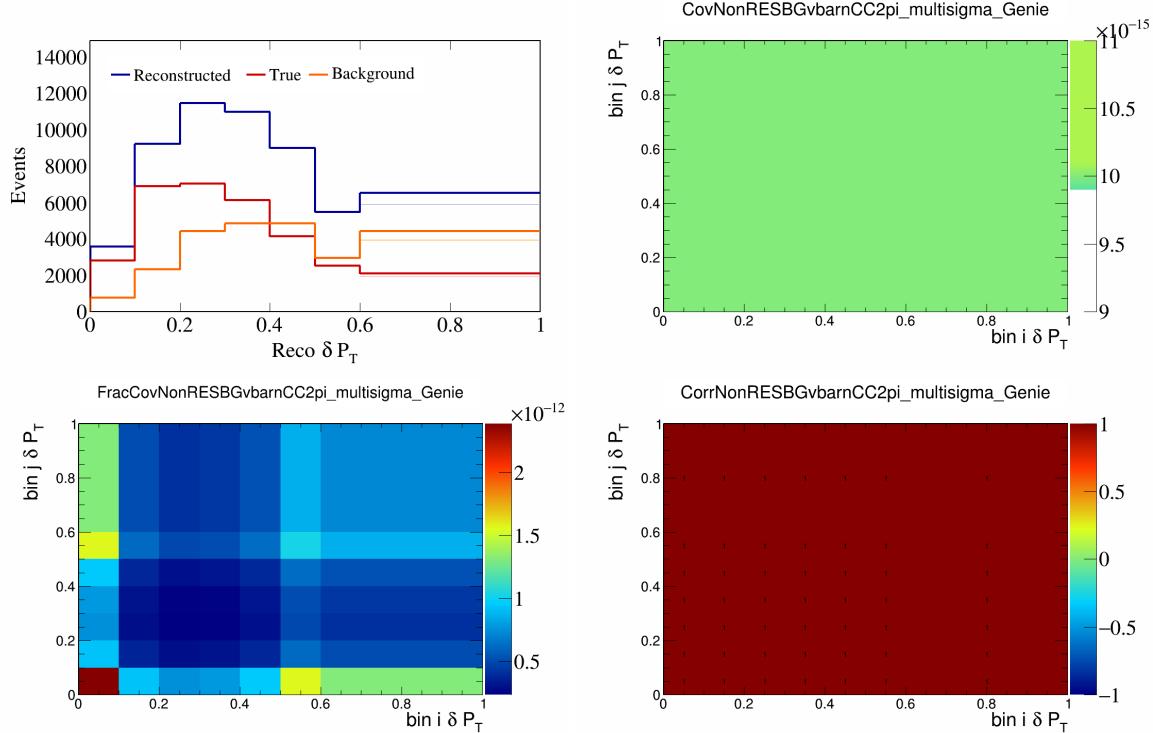


Figure 392: NonRESBGvbarCC2pi variations for δP_T .

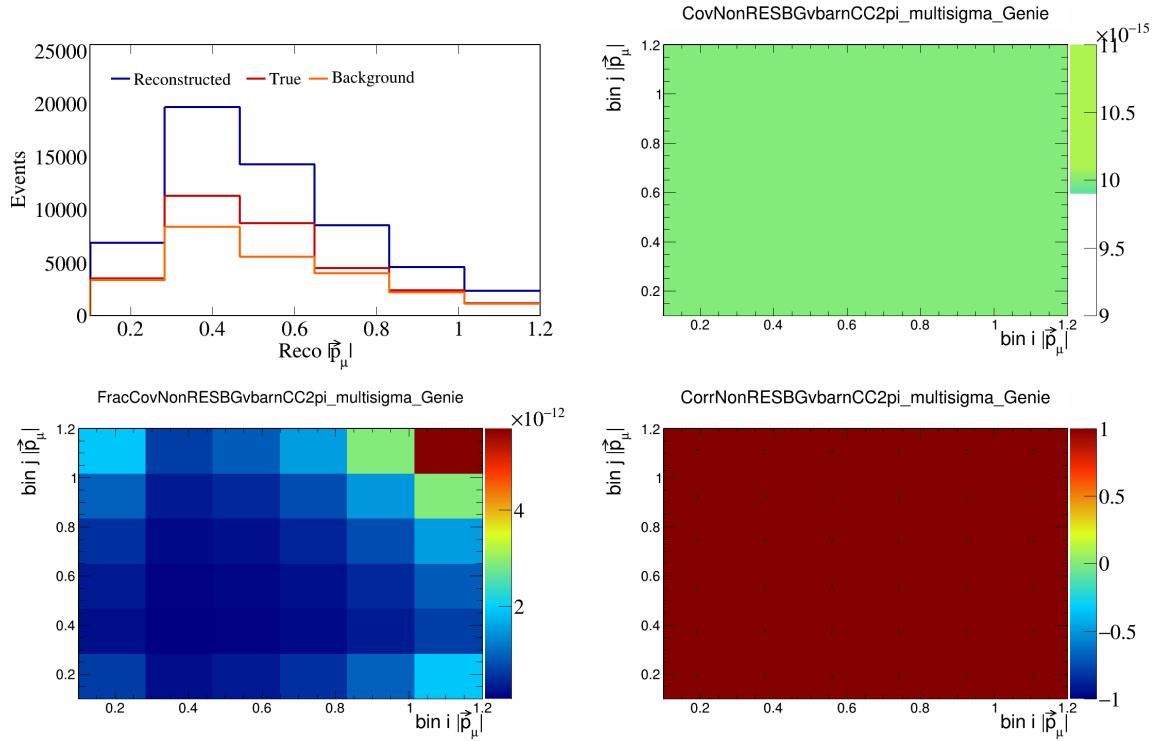


Figure 393: NonRESBGvbarCC2pi variations for $|\vec{p}_\mu|$.

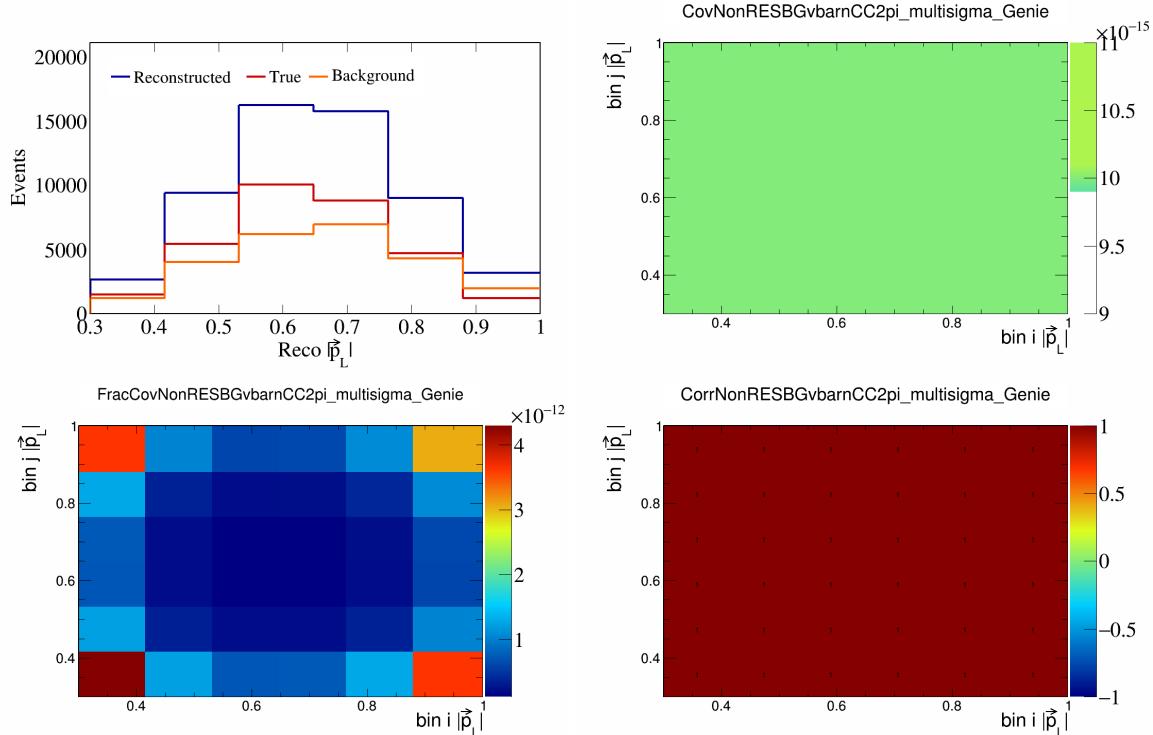


Figure 394: NonRESBGvbarCC2pi variations for $|\vec{p}_L|$.

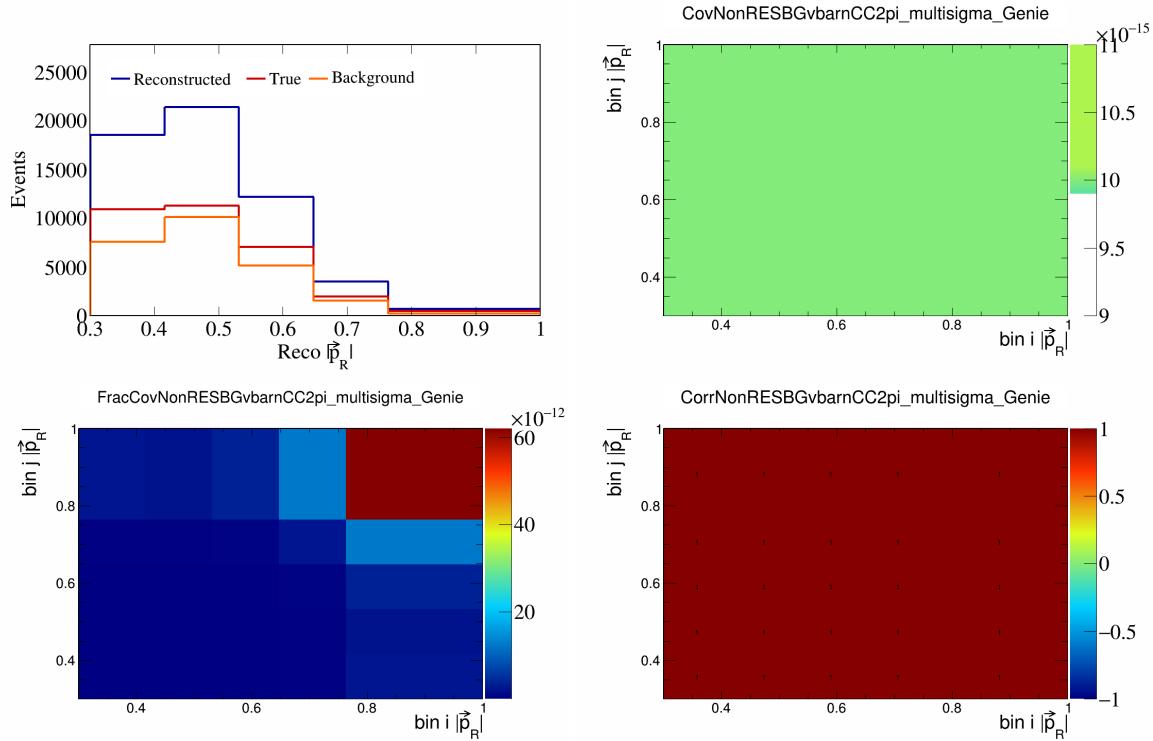


Figure 395: NonRESBGvbarCC2pi variations for $|\vec{p}_R|$.

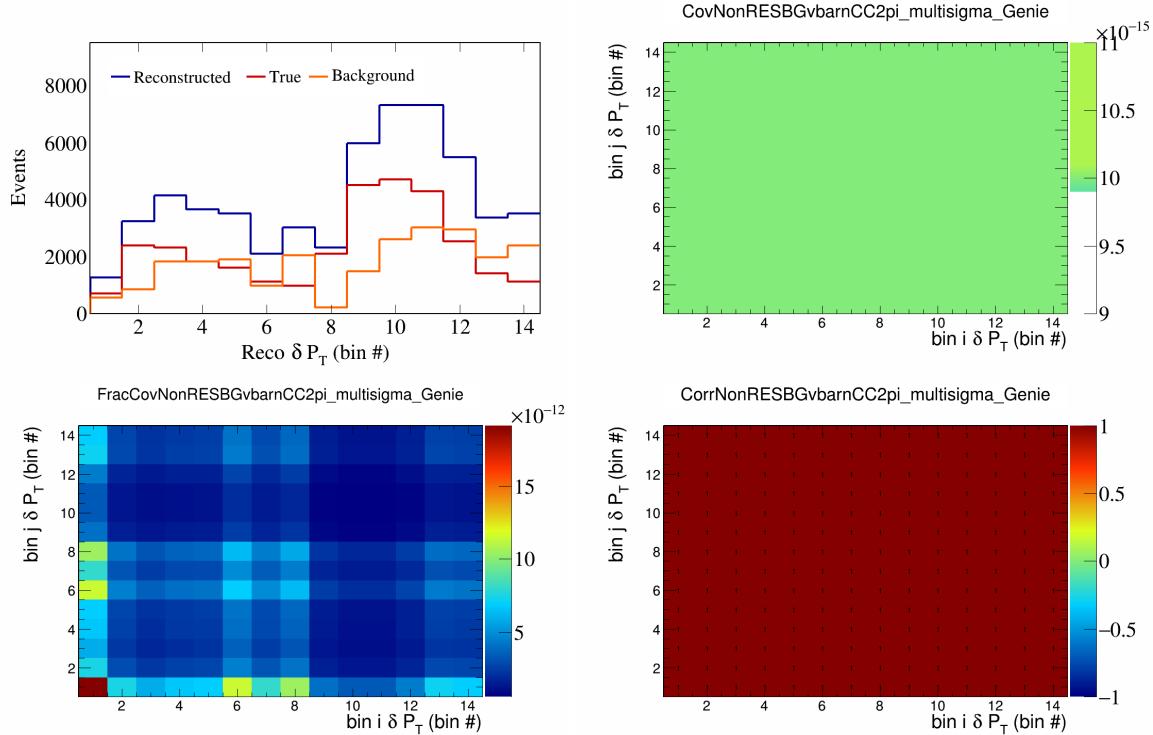


Figure 396: NonRESBGvbarCC2pi variations for δP_T in $\cos(\theta_{\vec{p}_\mu})$.

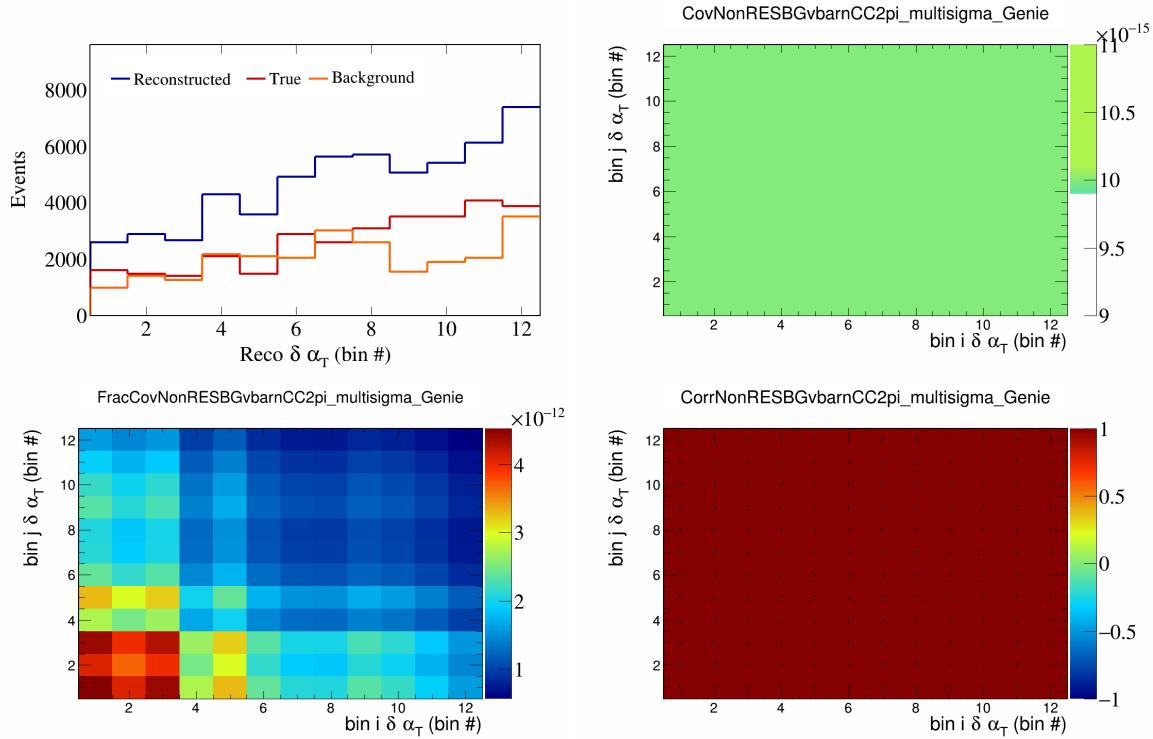


Figure 397: NonRESBGvbarCC2pi variations for $\delta\alpha_T$ in $\cos(\theta_{\vec{p}_\mu})$.

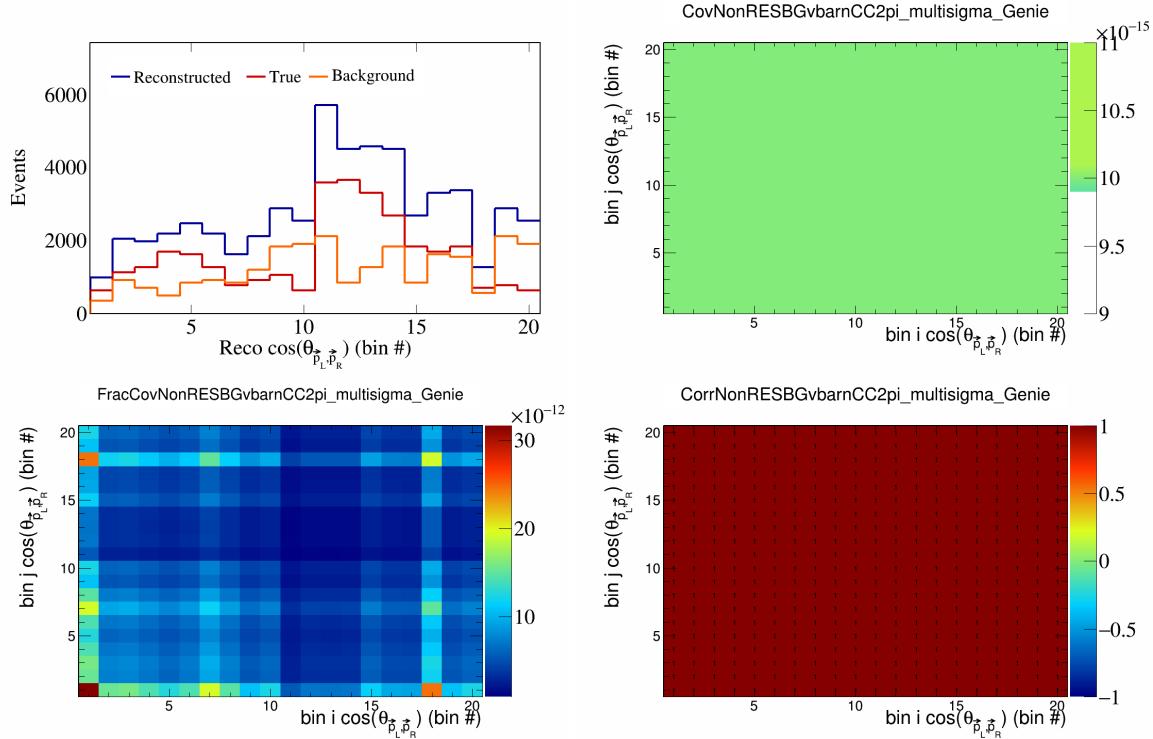


Figure 398: NonRESBGvbarCC2pi variations for $\cos(\theta_{\vec{p}_L, \vec{p}_R})$ in $\cos(\theta_{\vec{p}_\mu})$.

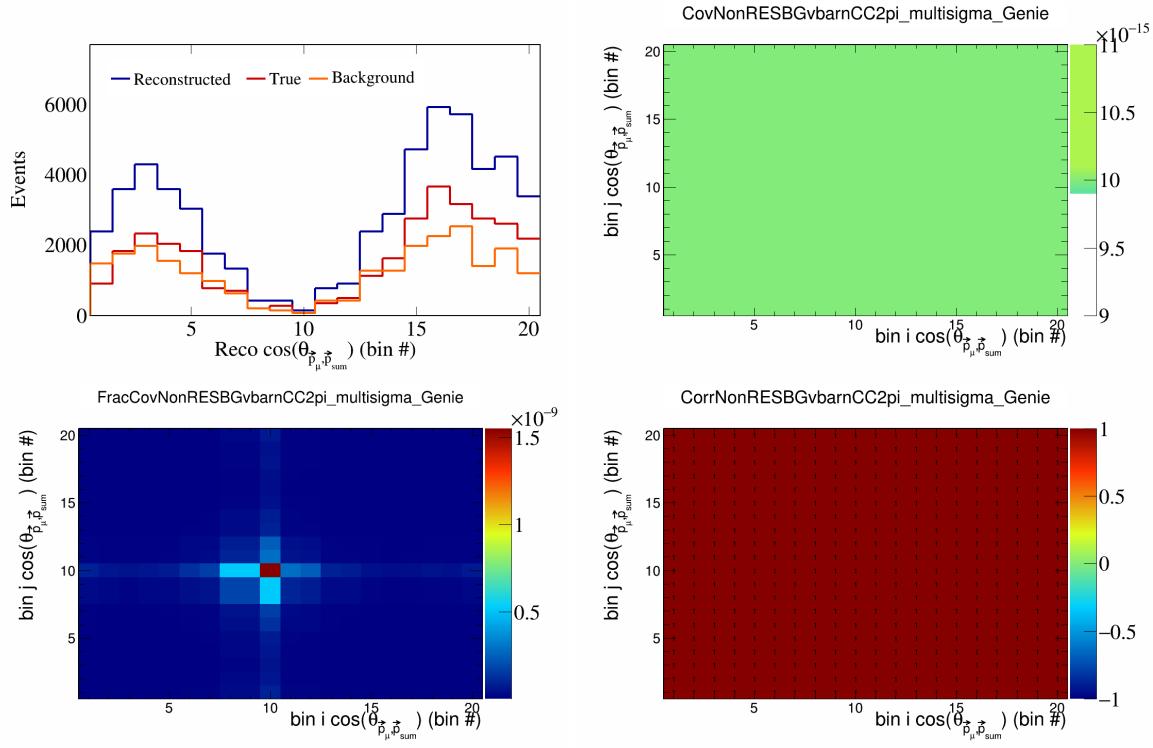


Figure 399: NonRESBGvbarCC2pi variations for $\cos(\theta_{\vec{p}_\mu})$ in $\cos(\theta_{\vec{p}_\mu})$.

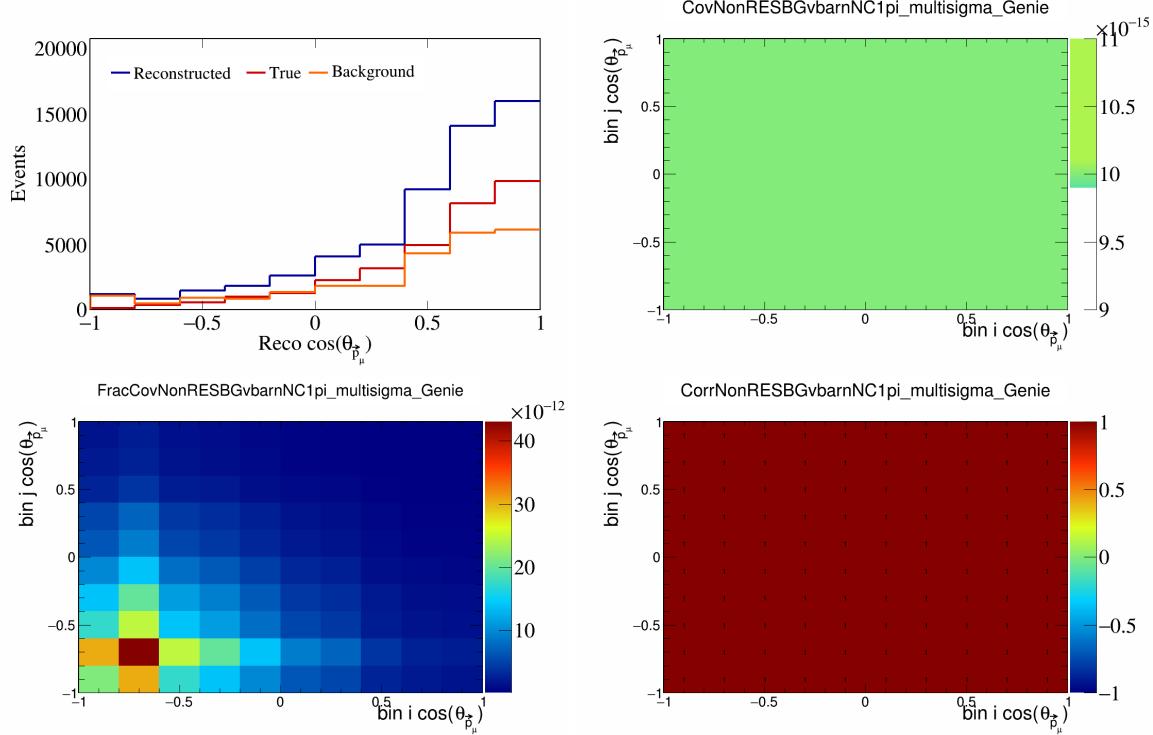


Figure 400: NonRESBGvbarNC1pi variations for $\cos(\theta_{\vec{p}_\mu})$.

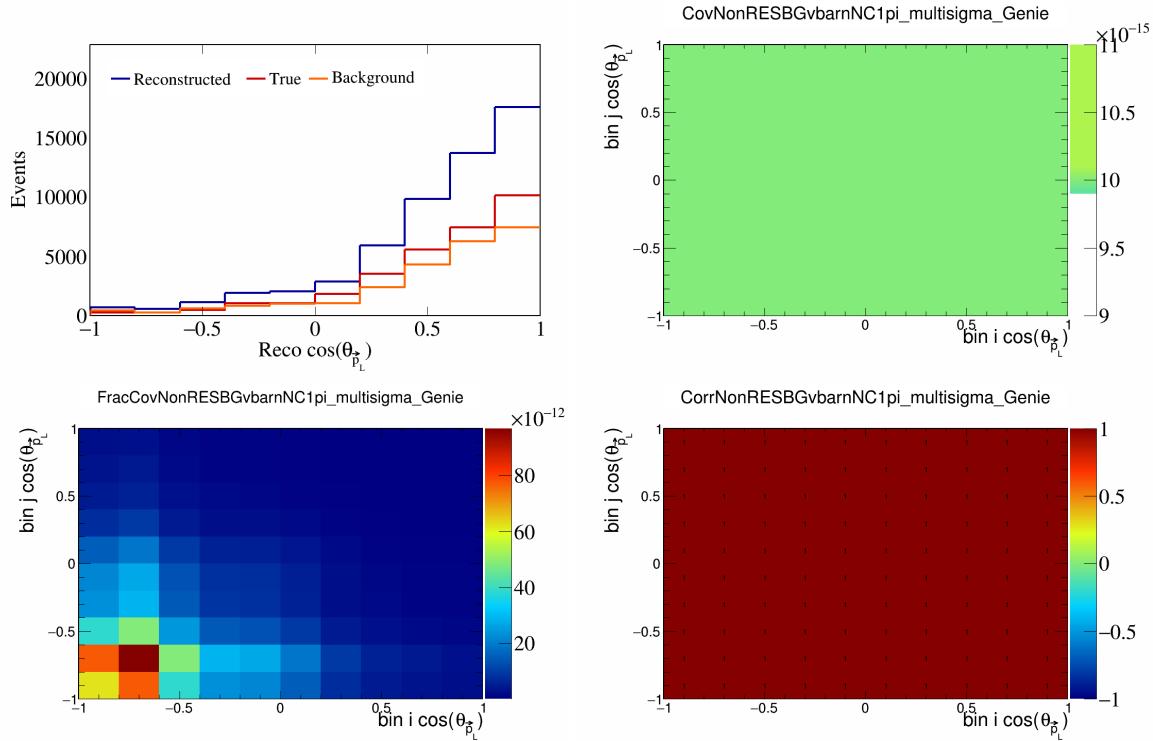


Figure 401: NonRESBGvbarNC1pi variations for $\cos(\theta_{\vec{p}_L})$.

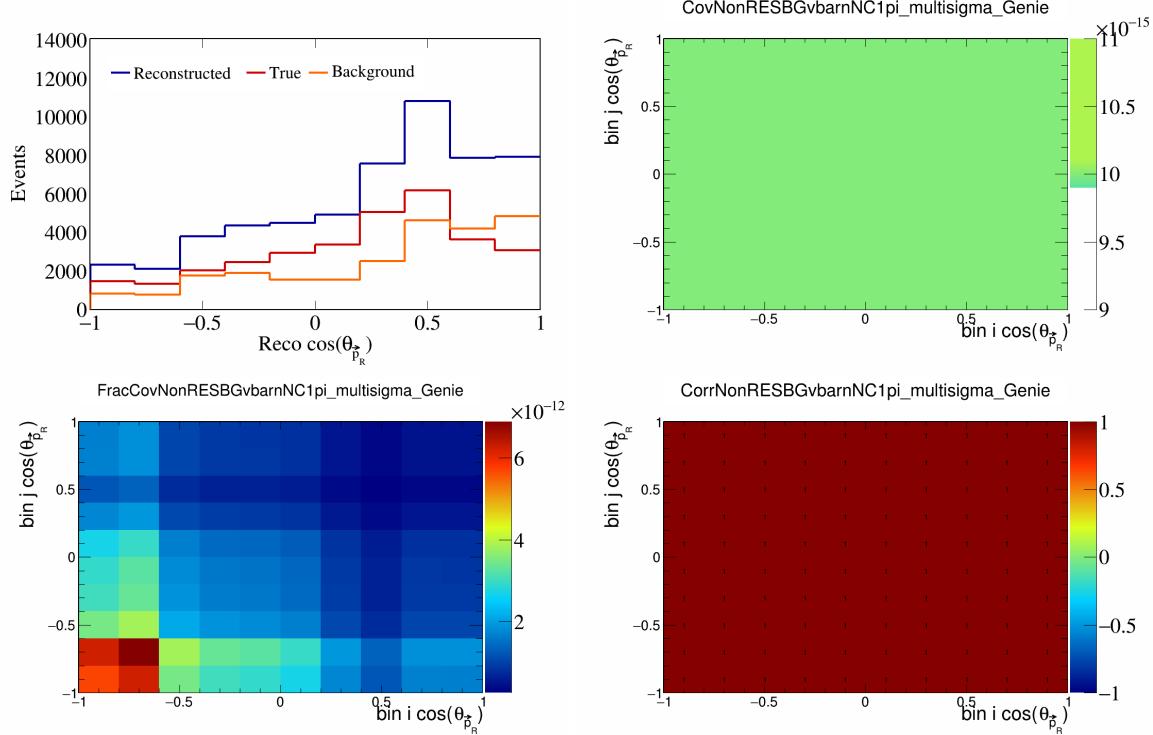


Figure 402: NonRESBGvbarNC1pi variations for $\cos(\theta_{\vec{p}_R})$.

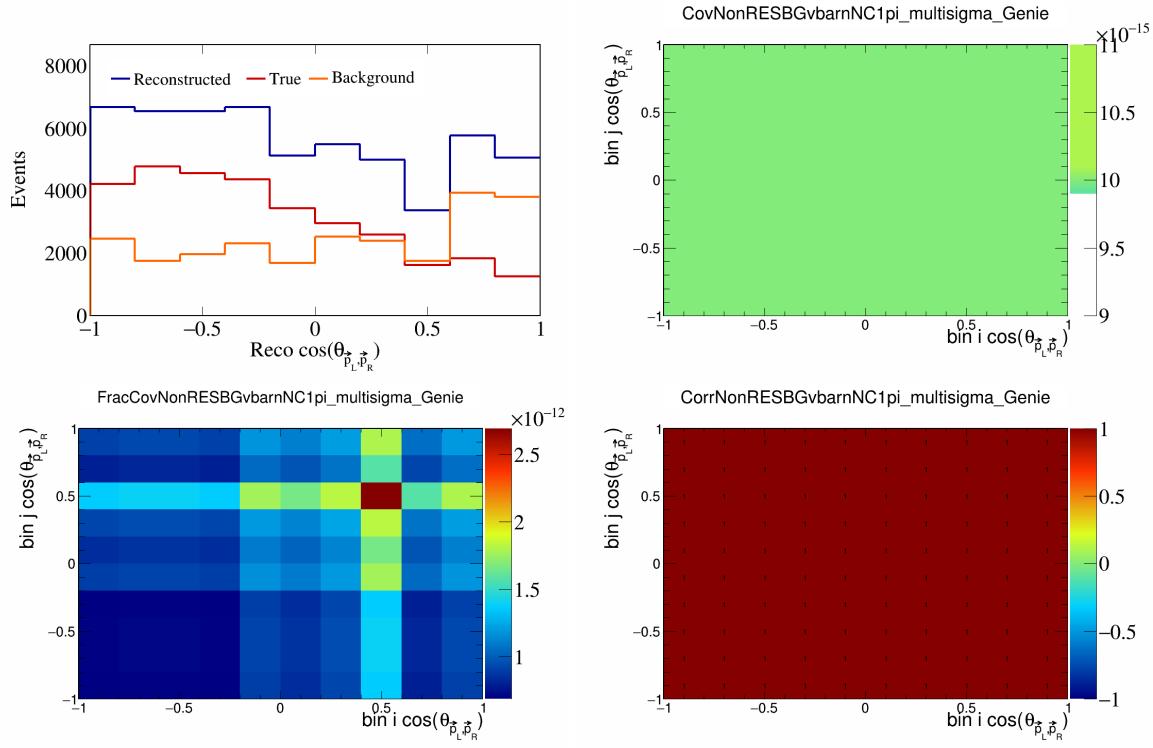


Figure 403: NonRESBGvbarNC1pi variations for $\cos(\theta_{\vec{p}_L, \vec{p}_R})$.

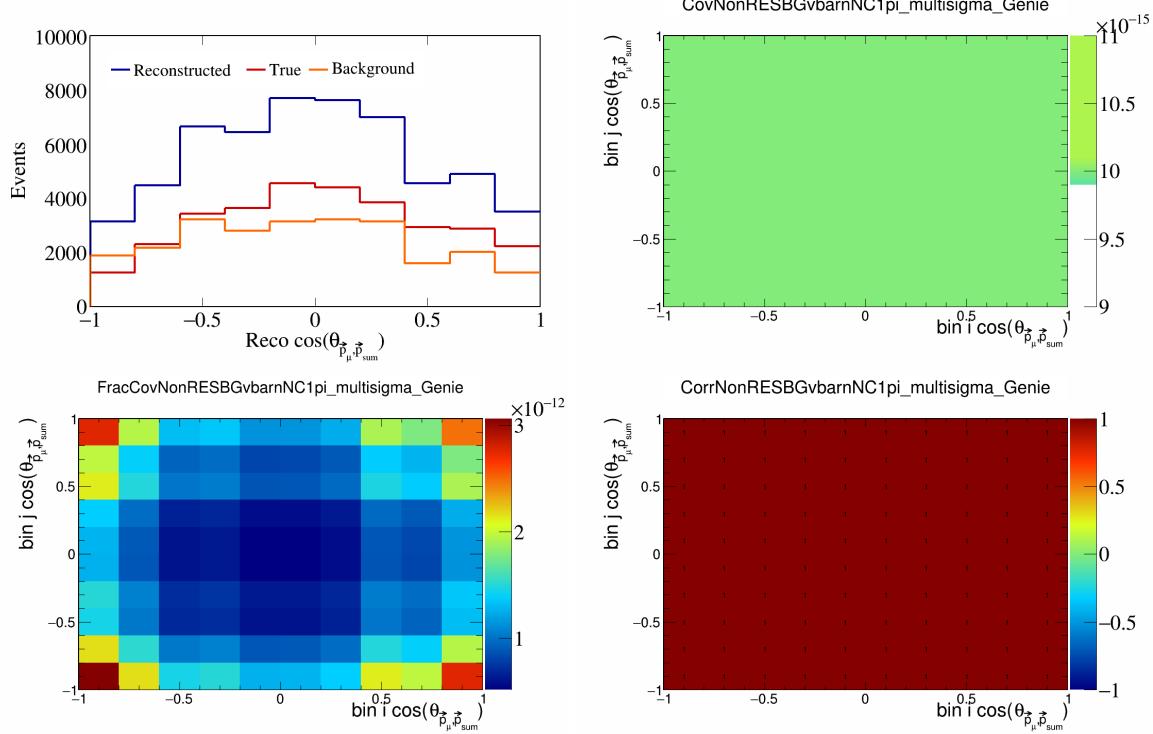


Figure 404: NonRESBGvbarNC1pi variations for $\cos(\theta_{\vec{p}_\mu, \vec{p}_{\text{sum}}})$.

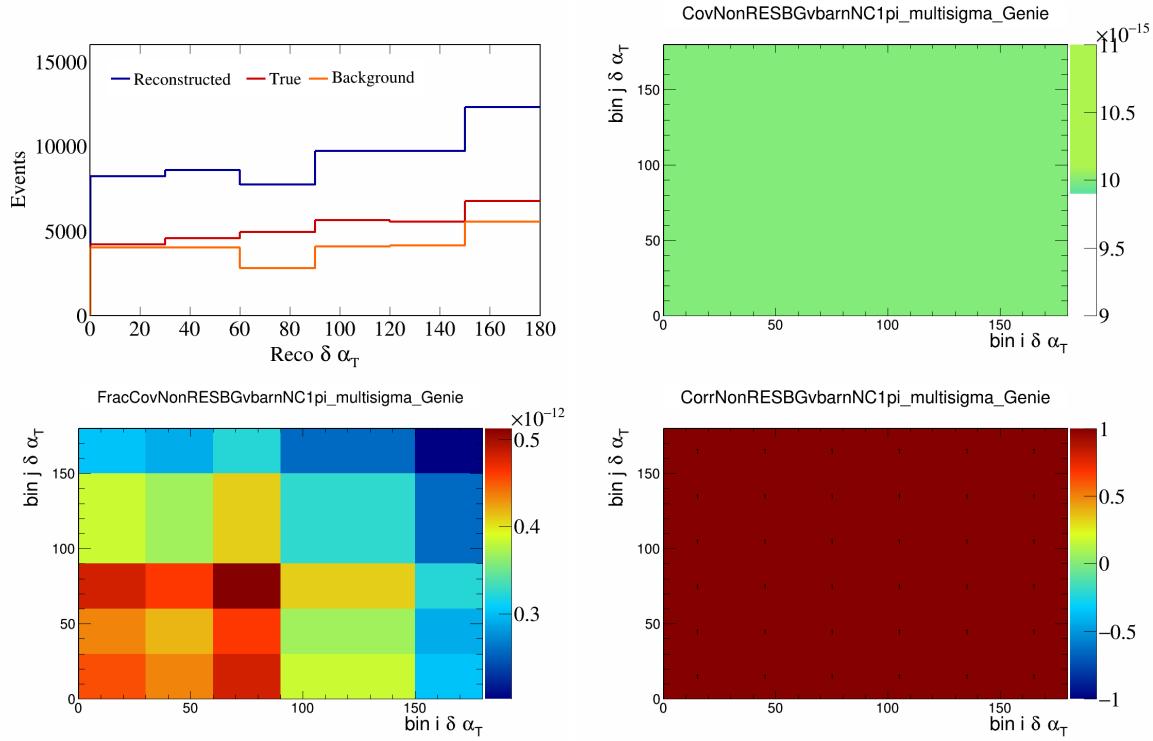


Figure 405: NonRESBGvbarNC1pi variations for $\delta\alpha_T$.

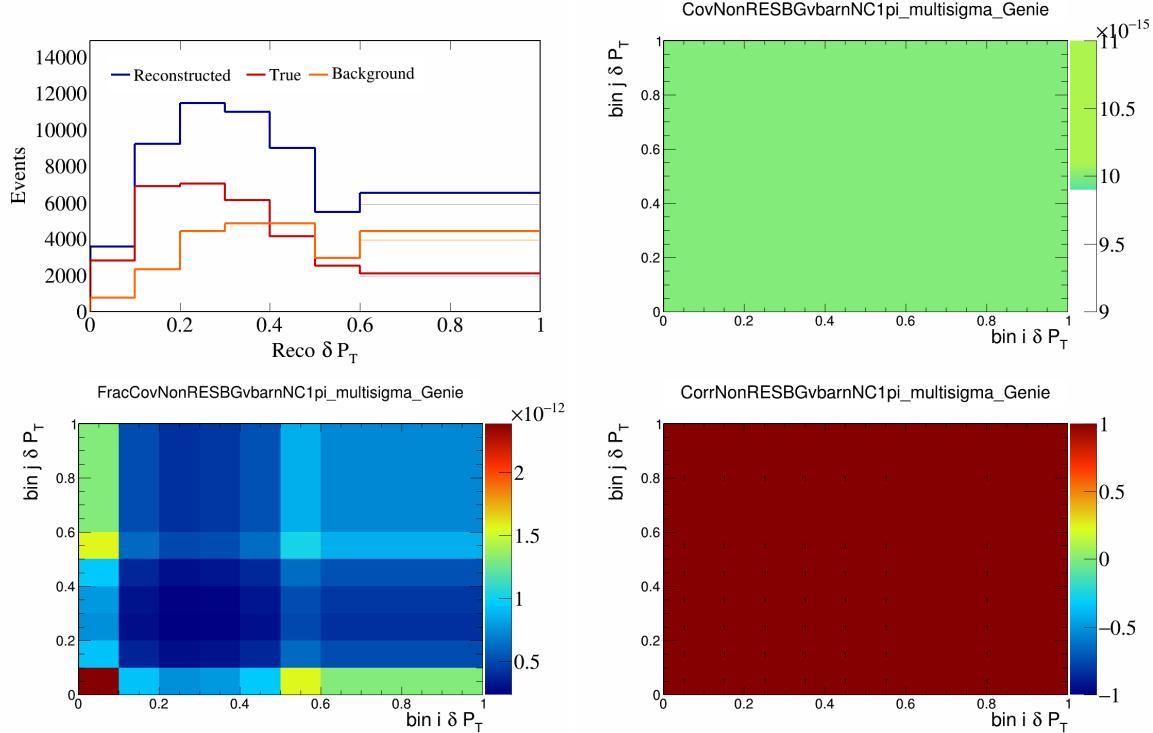


Figure 406: NonRESBGvbarNC1pi variations for δP_T .

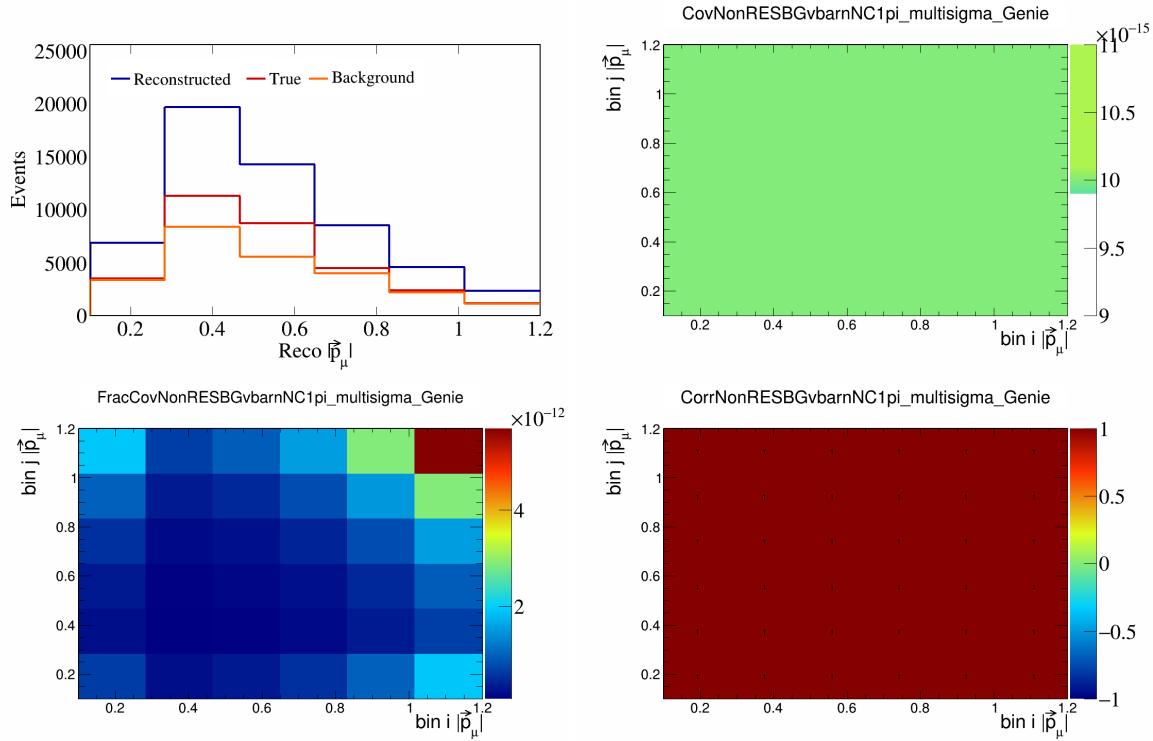


Figure 407: NonRESBGvbarNC1pi variations for $|\vec{p}_\mu|$.

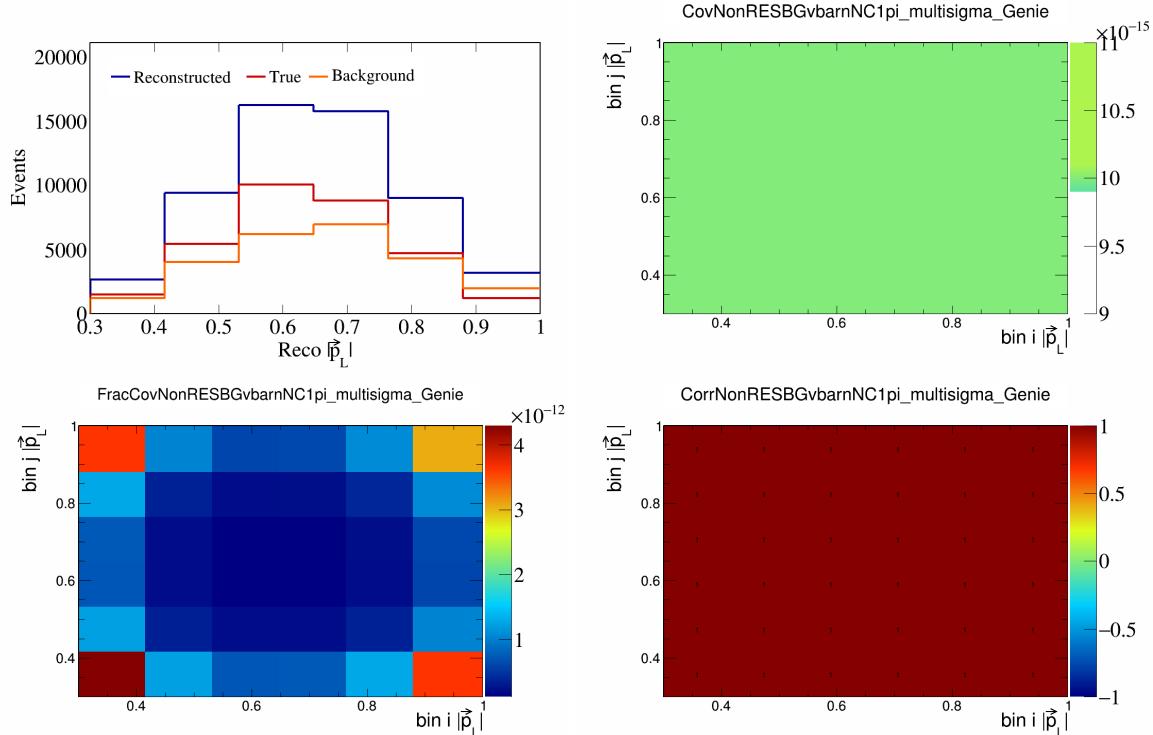


Figure 408: NonRESBGvbarNC1pi variations for $|\vec{p}_L|$.

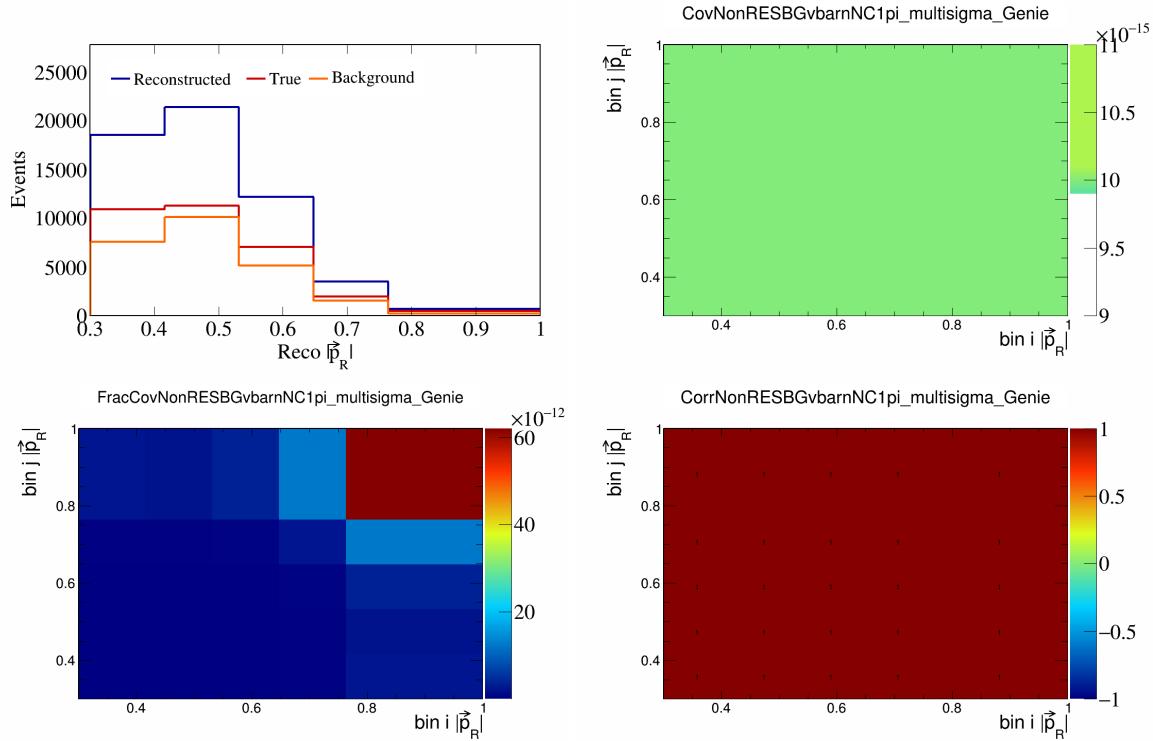


Figure 409: NonRESBGvbarNC1pi variations for $|\vec{p}_R|$.

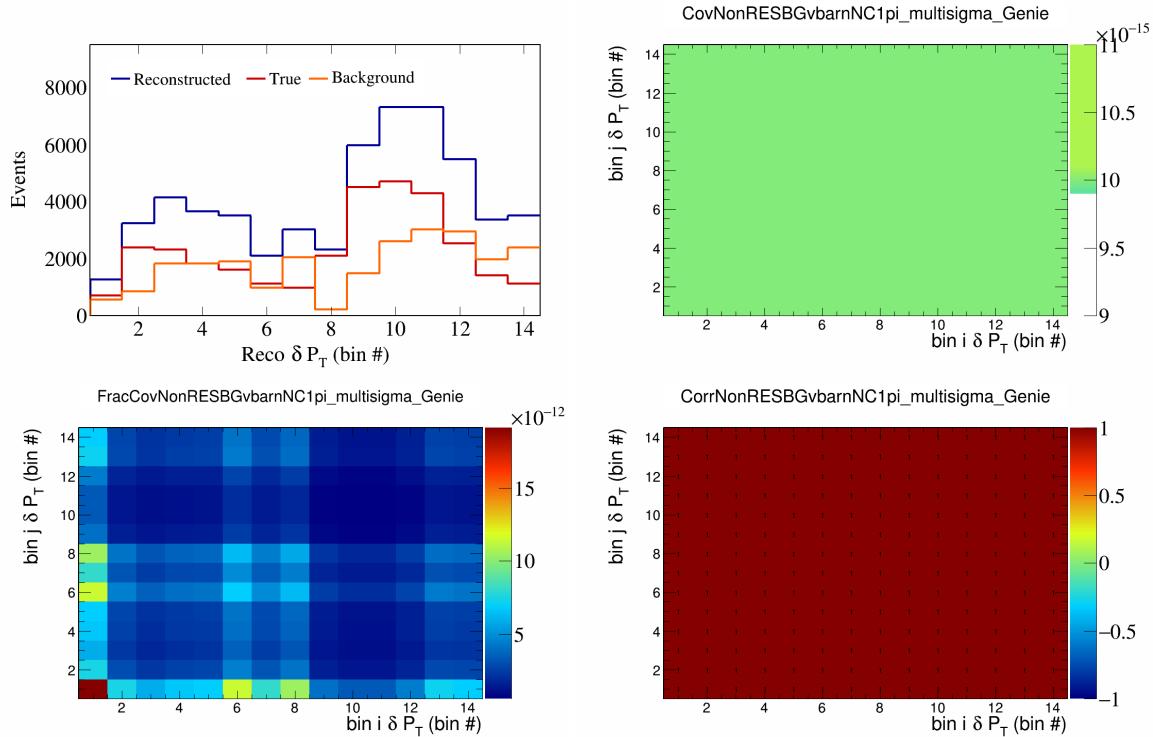


Figure 410: NonRESBGvbarNC1pi variations for δP_T in $\cos(\theta_{\vec{p}_\mu})$.

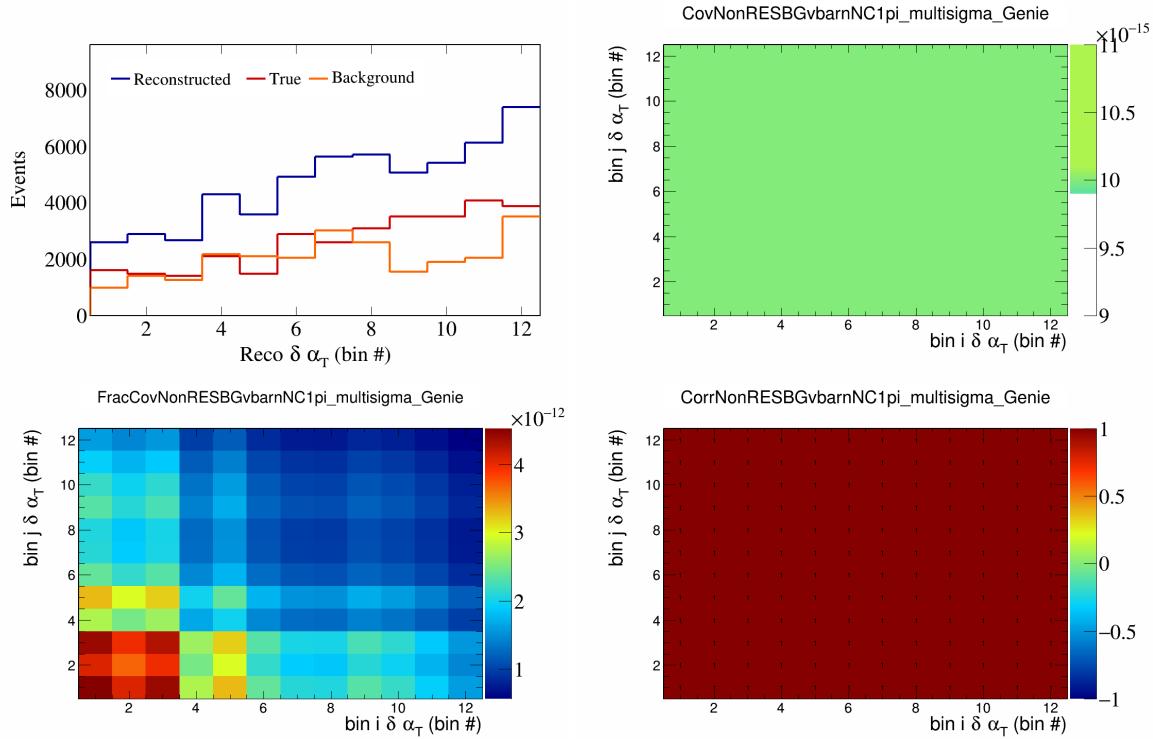


Figure 411: NonRESBGvbarNC1pi variations for $\delta\alpha_T$ in $\cos(\theta_{\vec{p}_\mu})$.

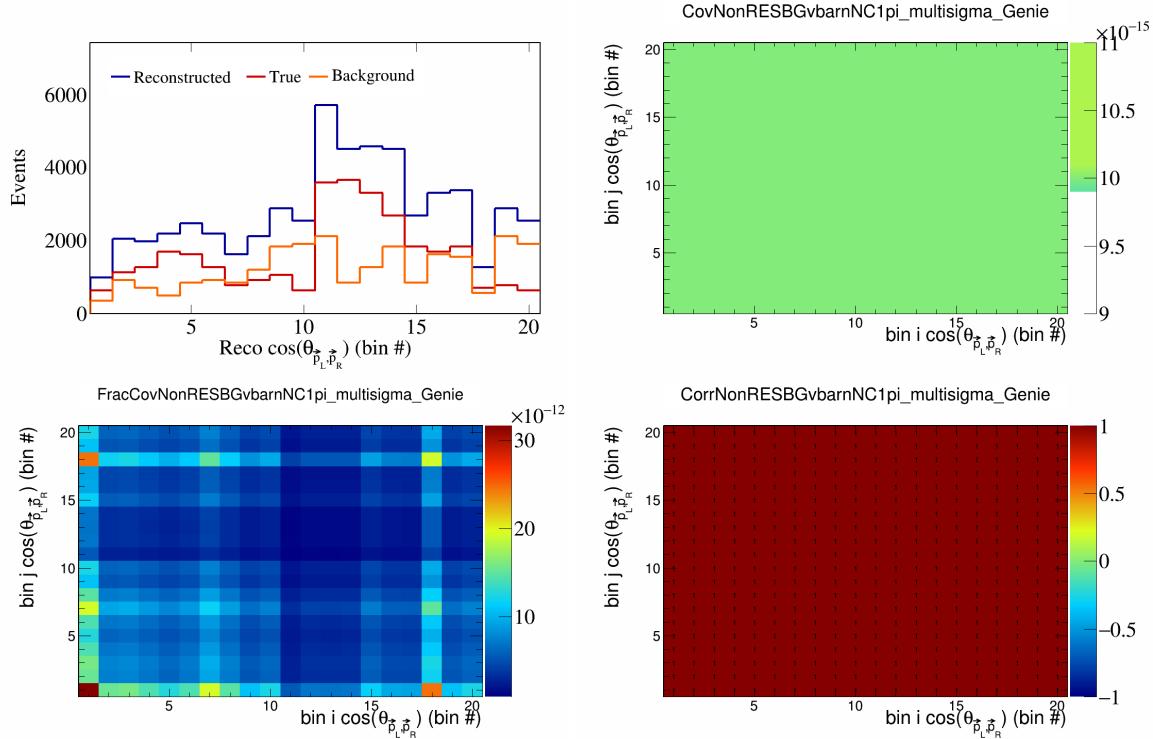


Figure 412: NonRESBGvbarNC1pi variations for $\cos(\theta_{\vec{p}_L, \vec{p}_R})$ in $\cos(\theta_{\vec{p}_\mu})$.

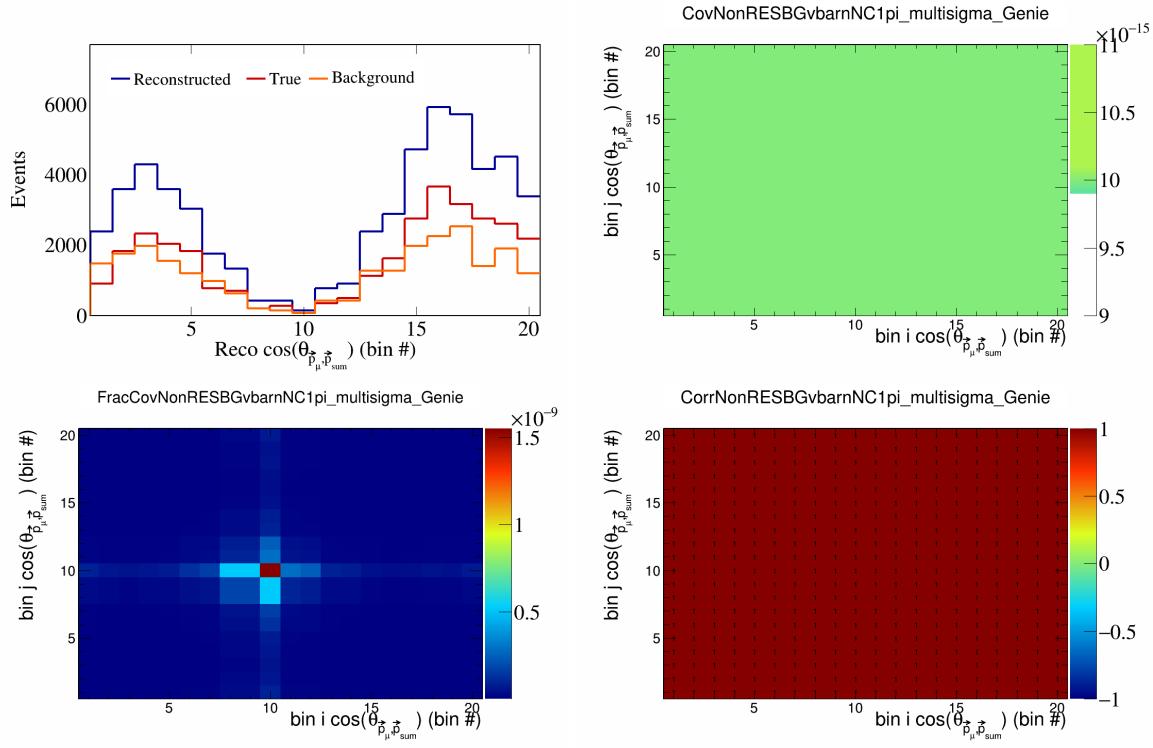


Figure 413: NonRESBGvbarNC1pi variations for $\cos(\theta_{\vec{p}_\mu})$ in $\cos(\theta_{\vec{p}_\mu})$.

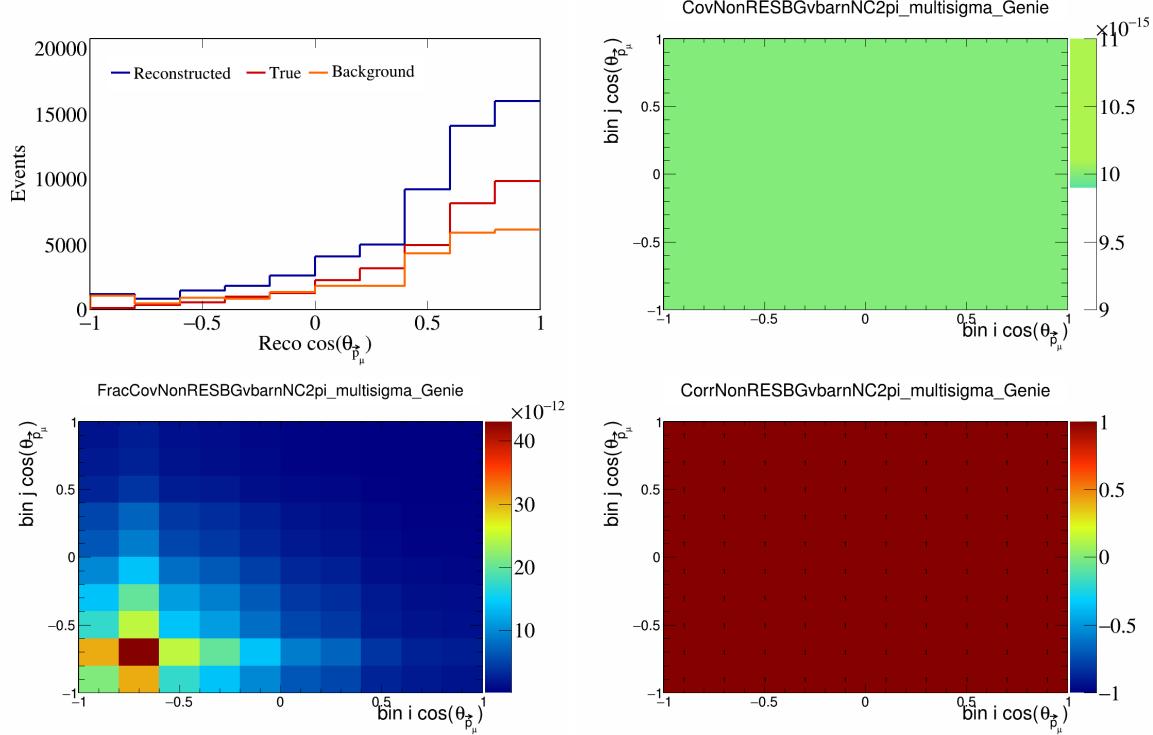


Figure 414: NonRESBGvbarNC2pi variations for $\cos(\theta_{\vec{p}_\mu})$.

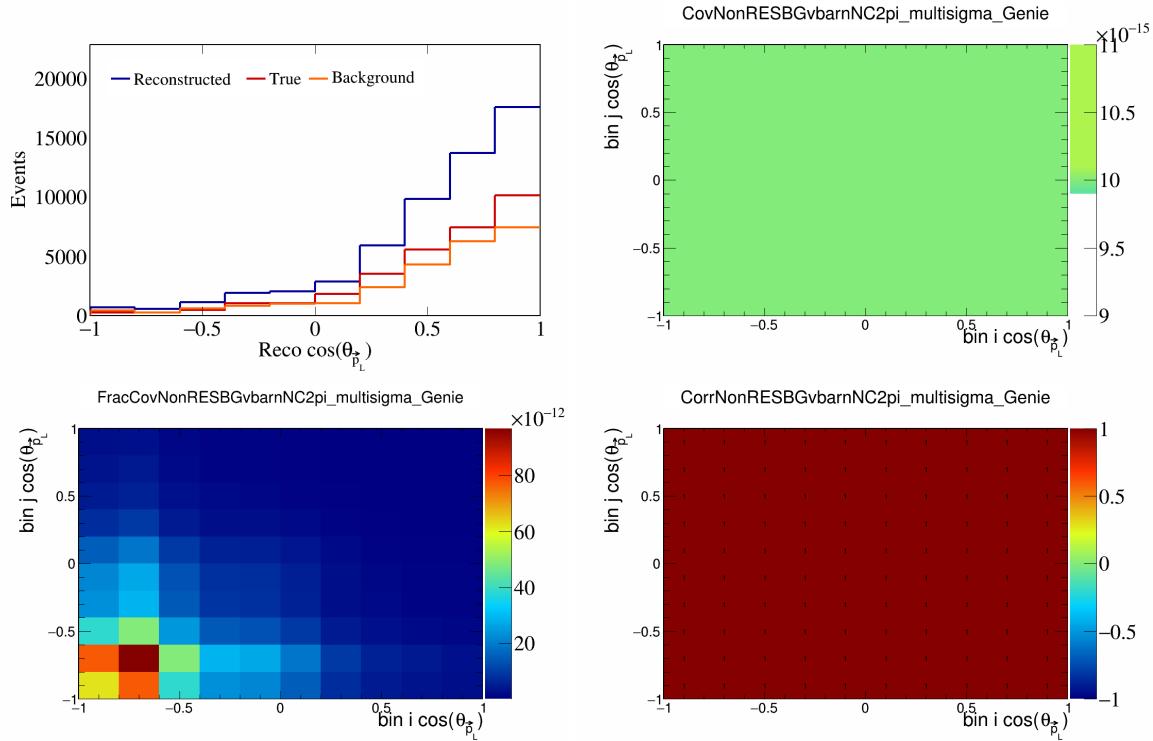


Figure 415: NonRESBGvbarNC2pi variations for $\cos(\theta_{\vec{p}_L})$.

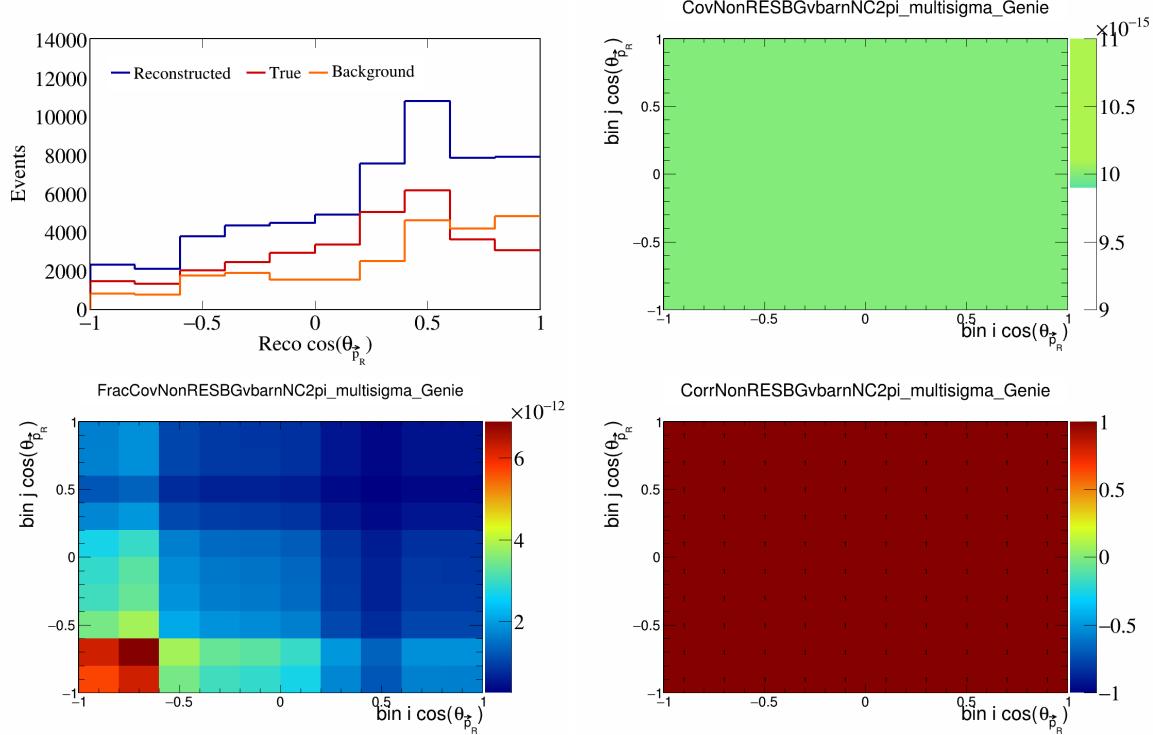


Figure 416: NonRESBGvbarNC2pi variations for $\cos(\theta_{\vec{p}_R})$.

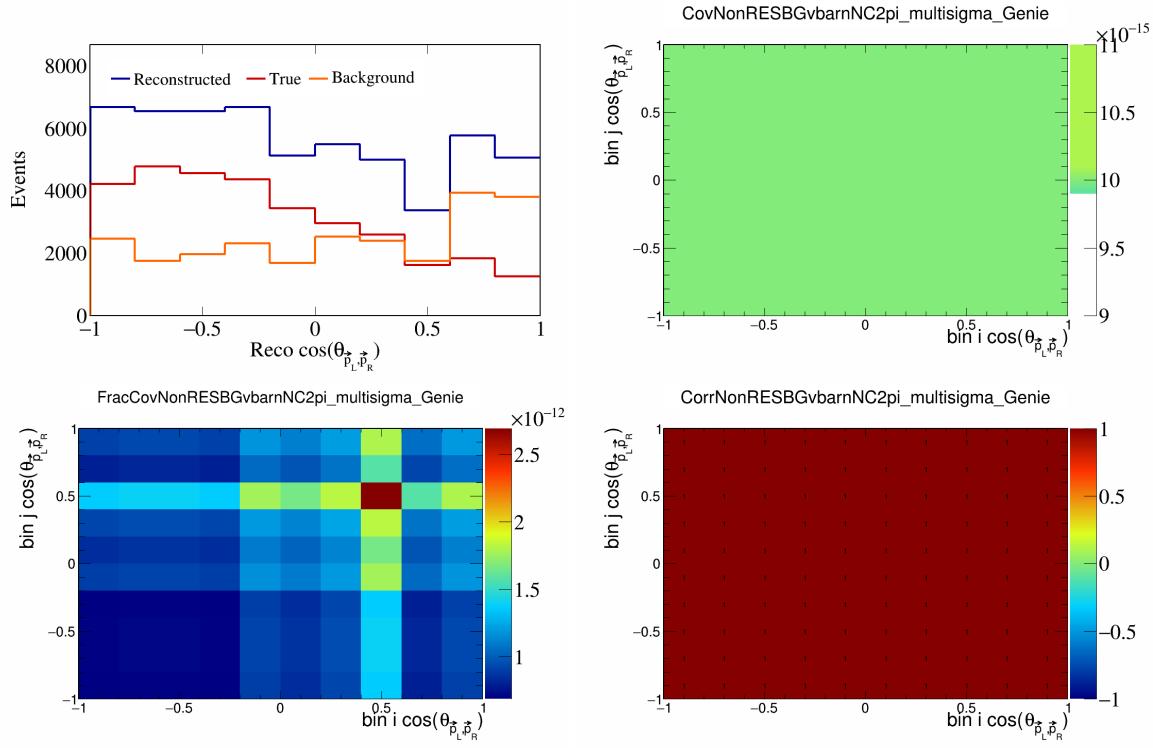


Figure 417: NonRESBGvbarNC2pi variations for $\cos(\theta_{\vec{p}_L, \vec{p}_R})$.

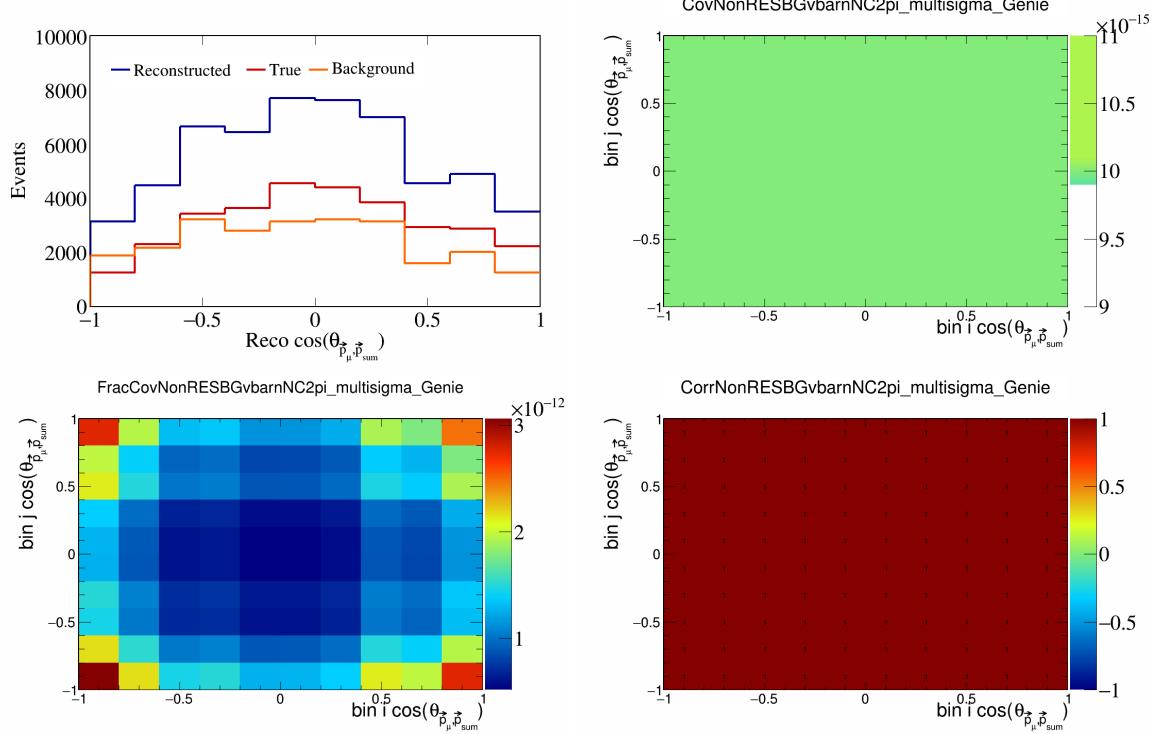


Figure 418: NonRESBGvbarNC2pi variations for $\cos(\theta_{\vec{p}_\mu, \vec{p}_{\text{sum}}})$.

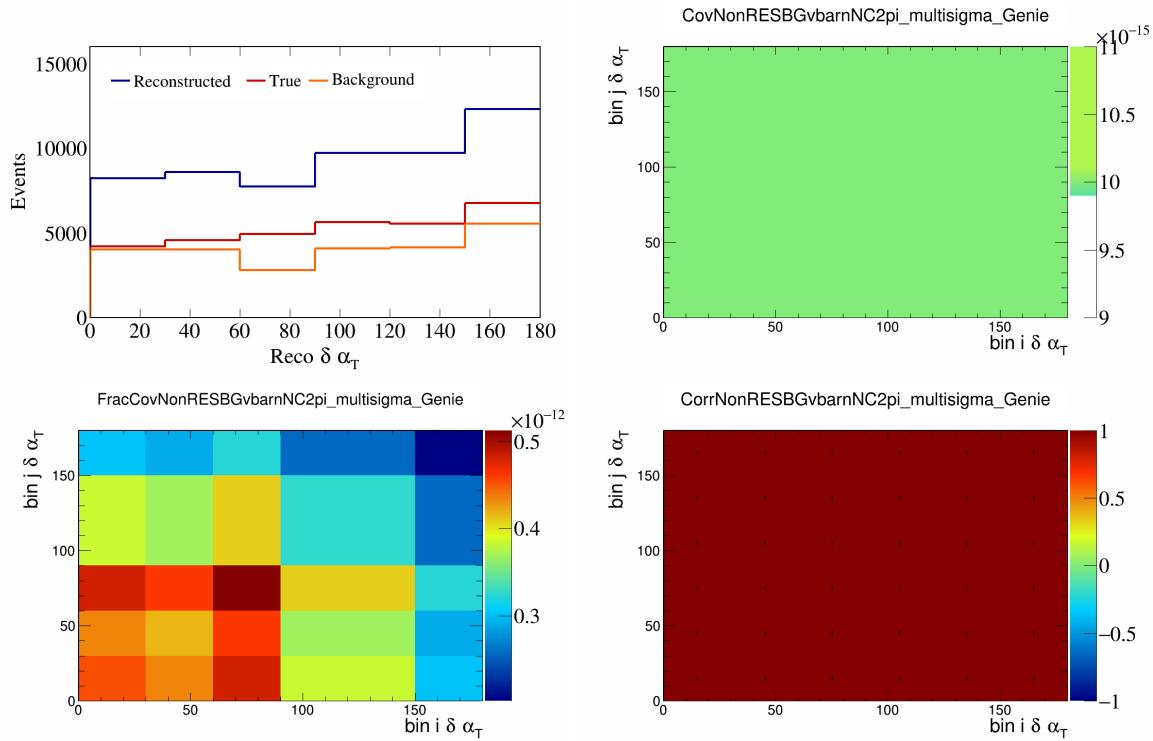


Figure 419: NonRESBGvbarNC2pi variations for $\delta\alpha_T$.

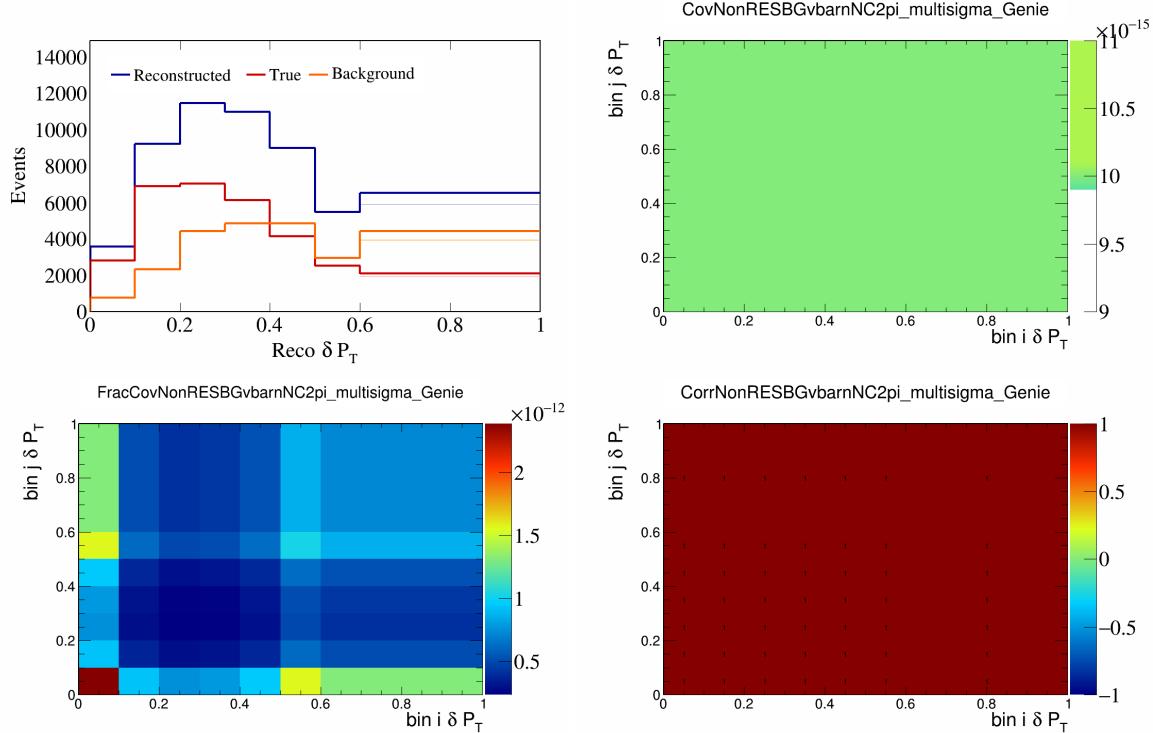


Figure 420: NonRESBGvbarNC2pi variations for δP_T .

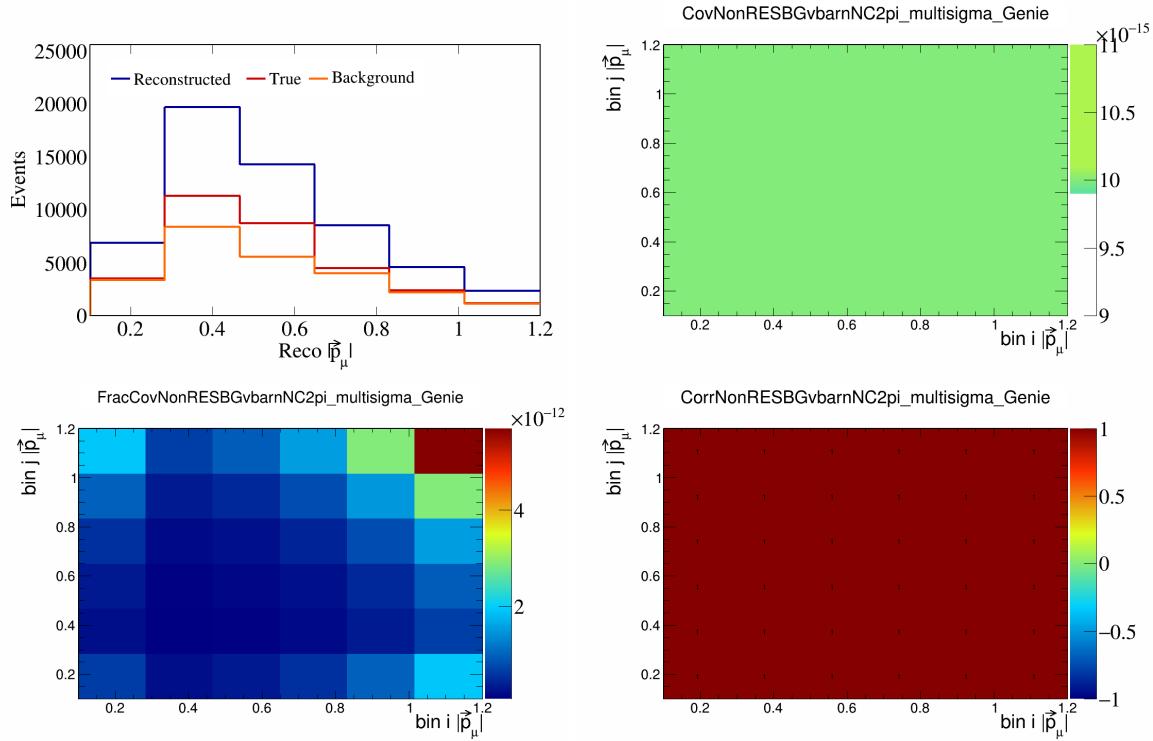


Figure 421: NonRESBGvbarNC2pi variations for $|\vec{p}_\mu|$.

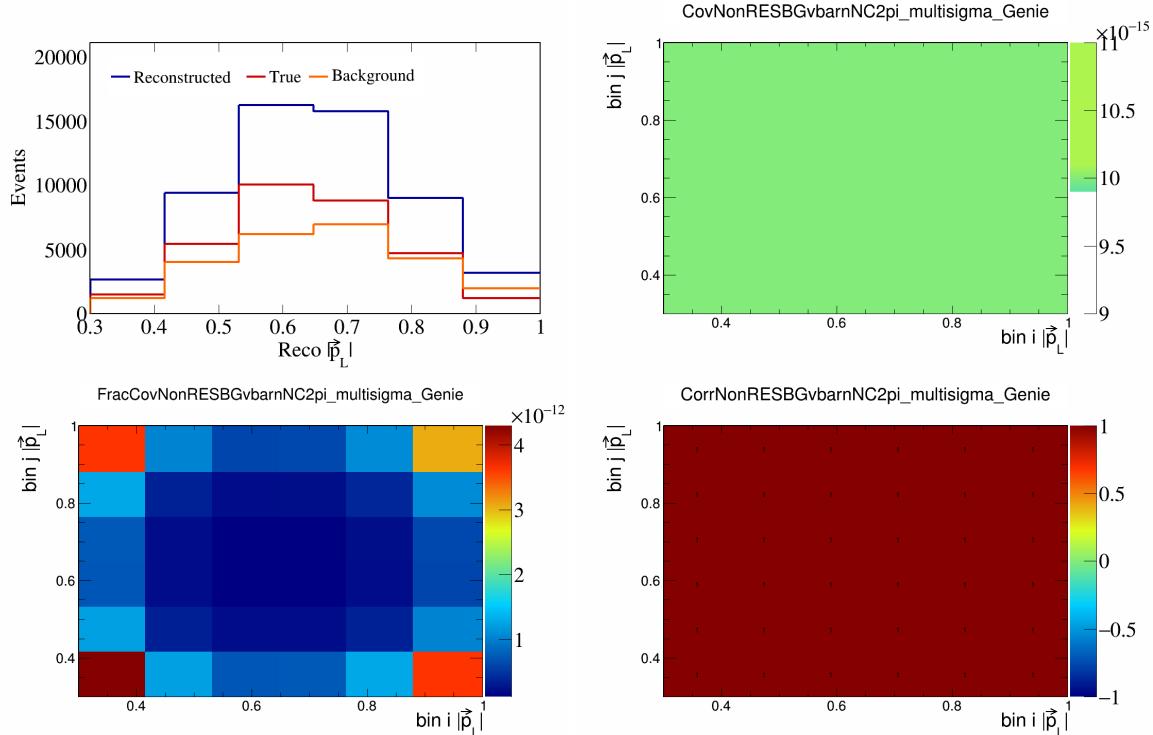


Figure 422: NonRESBGvbarNC2pi variations for $|\vec{p}_L|$.

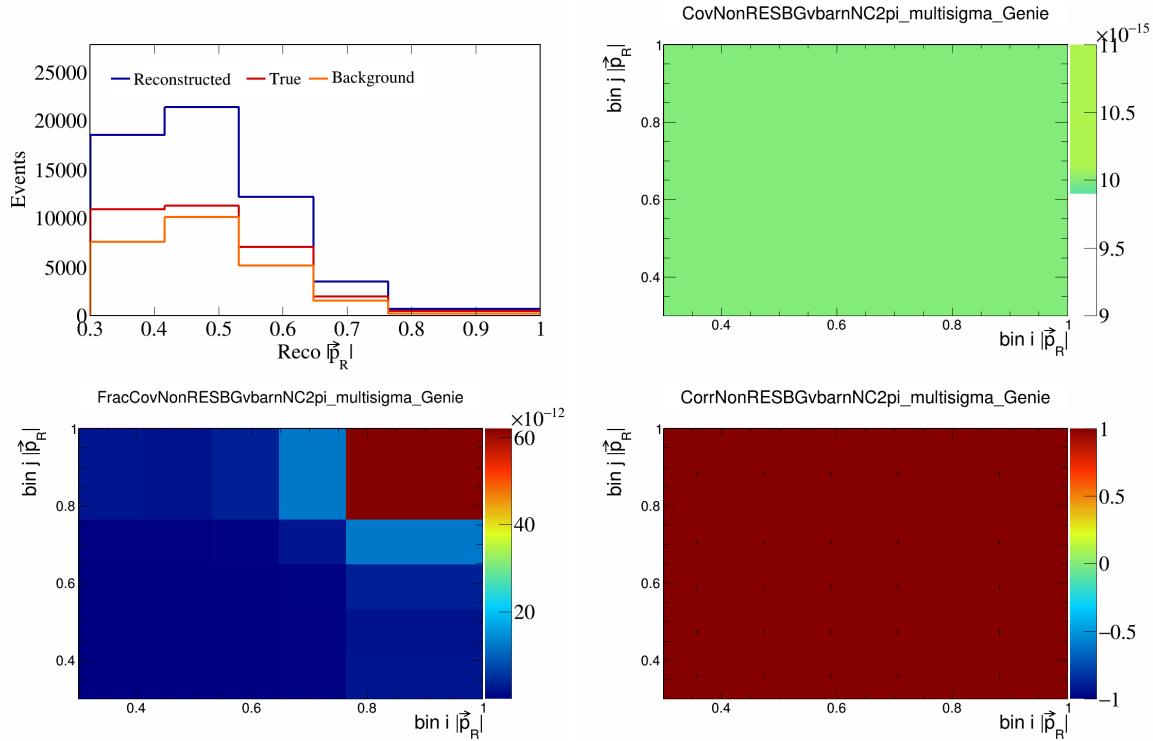


Figure 423: NonRESBGvbarNC2pi variations for $|\vec{p}_R|$.

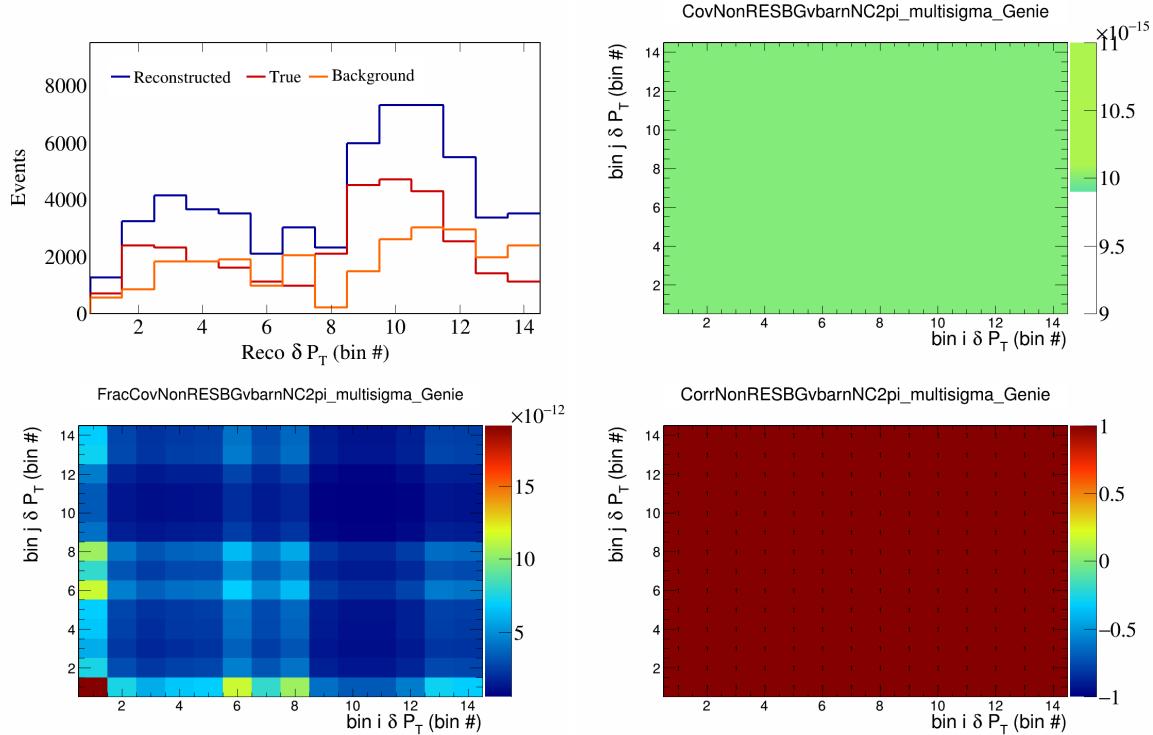


Figure 424: NonRESBGvbarNC2pi variations for δP_T in $\cos(\theta_{\vec{p}_\mu})$.

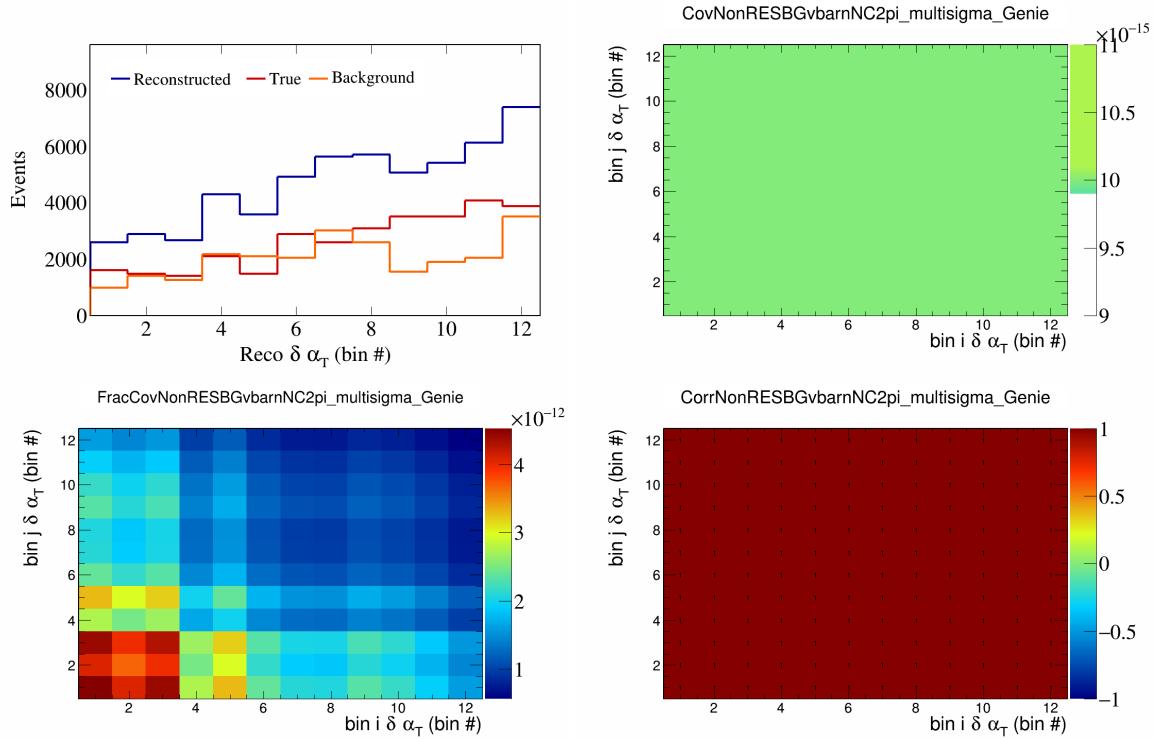


Figure 425: NonRESBGvbarNC2pi variations for $\delta\alpha_T$ in $\cos(\theta_{\vec{p}_\mu})$.

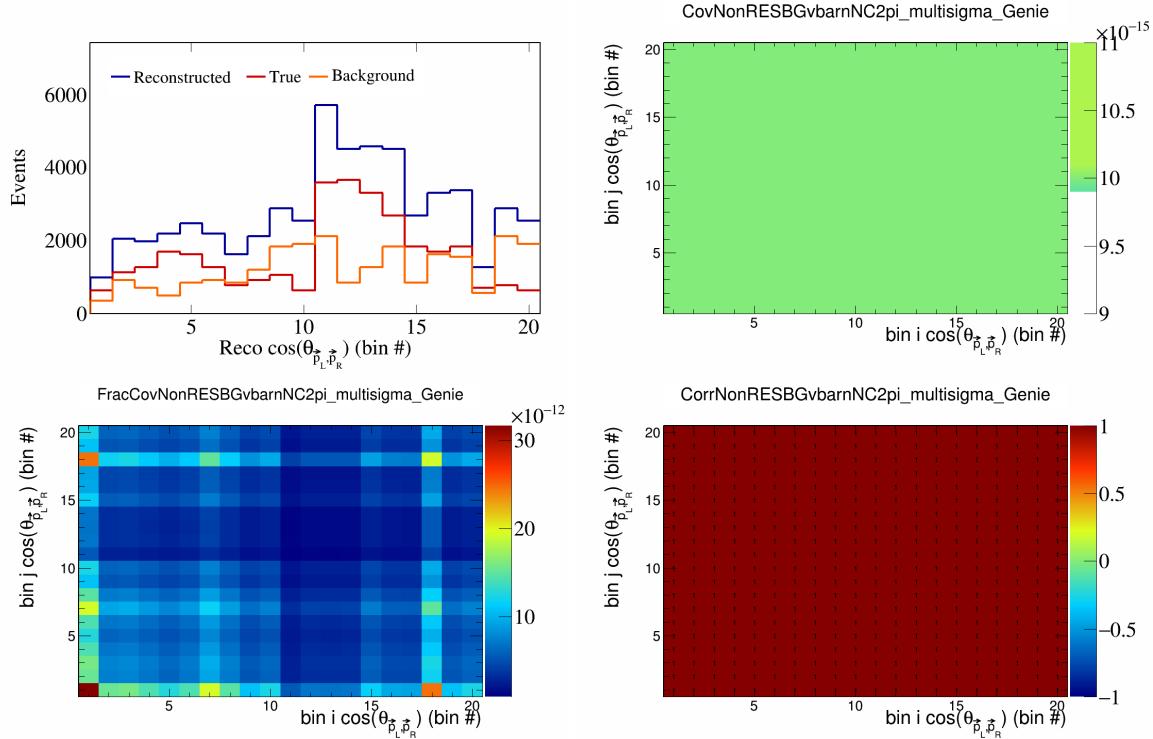


Figure 426: NonRESBGvbarNC2pi variations for $\cos(\theta_{\vec{p}_L, \vec{p}_R})$ in $\cos(\theta_{\vec{p}_\mu})$.

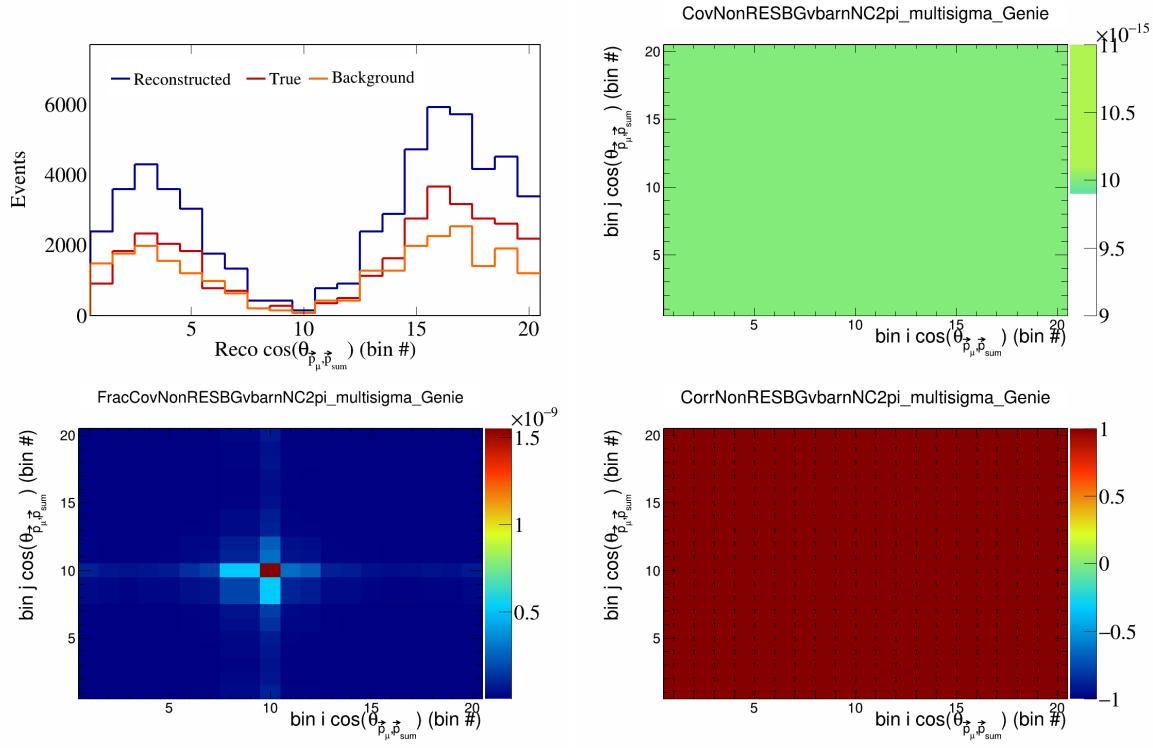


Figure 427: NonRESBGvbarNC2pi variations for $\cos(\theta_{\vec{p}_\mu, \vec{p}_{\text{sum}}})$ in $\cos(\theta_{\vec{p}_\mu})$.

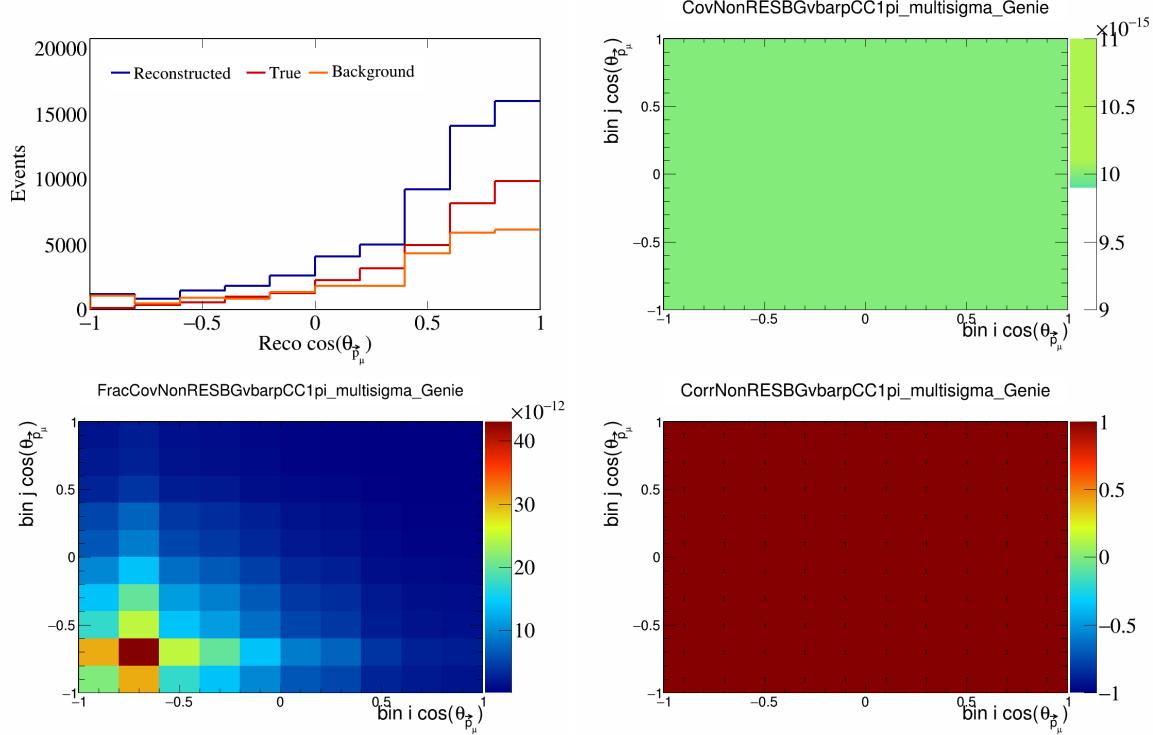


Figure 428: NonRESBGvbarCC1pi variations for $\cos(\theta_{\vec{p}_\mu})$.

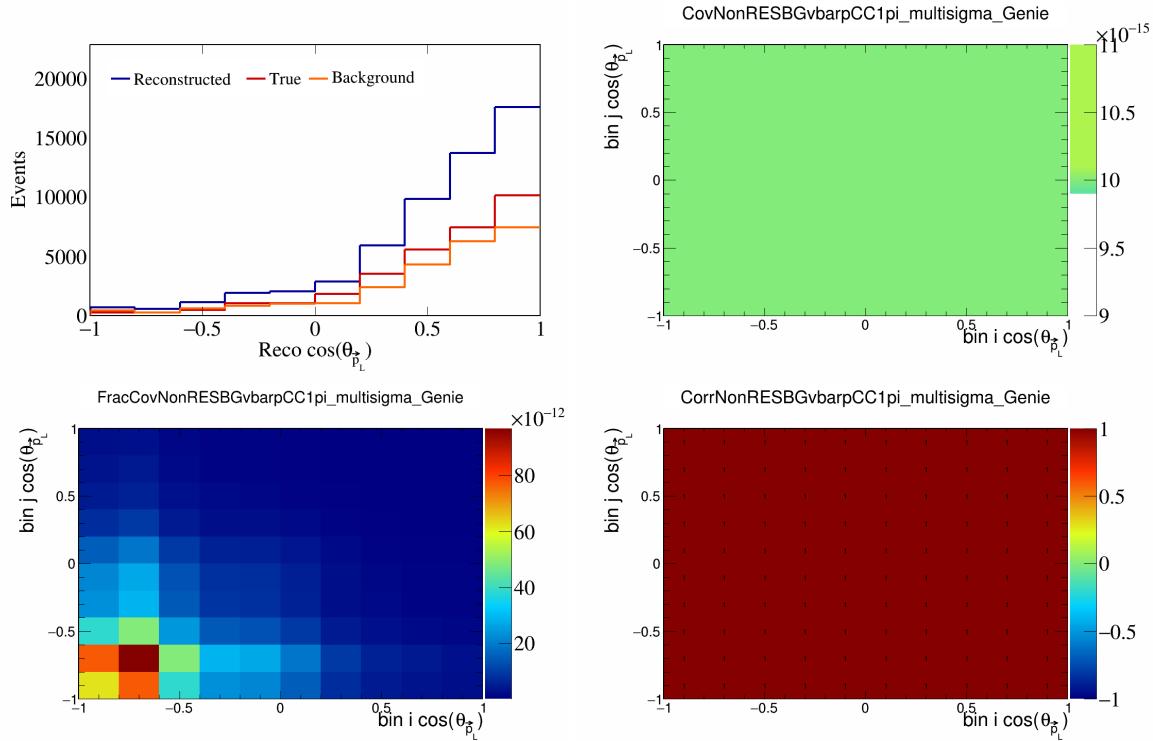


Figure 429: NonRESBGvbarpCC1pi variations for $\cos(\theta_{\vec{p}_L})$.

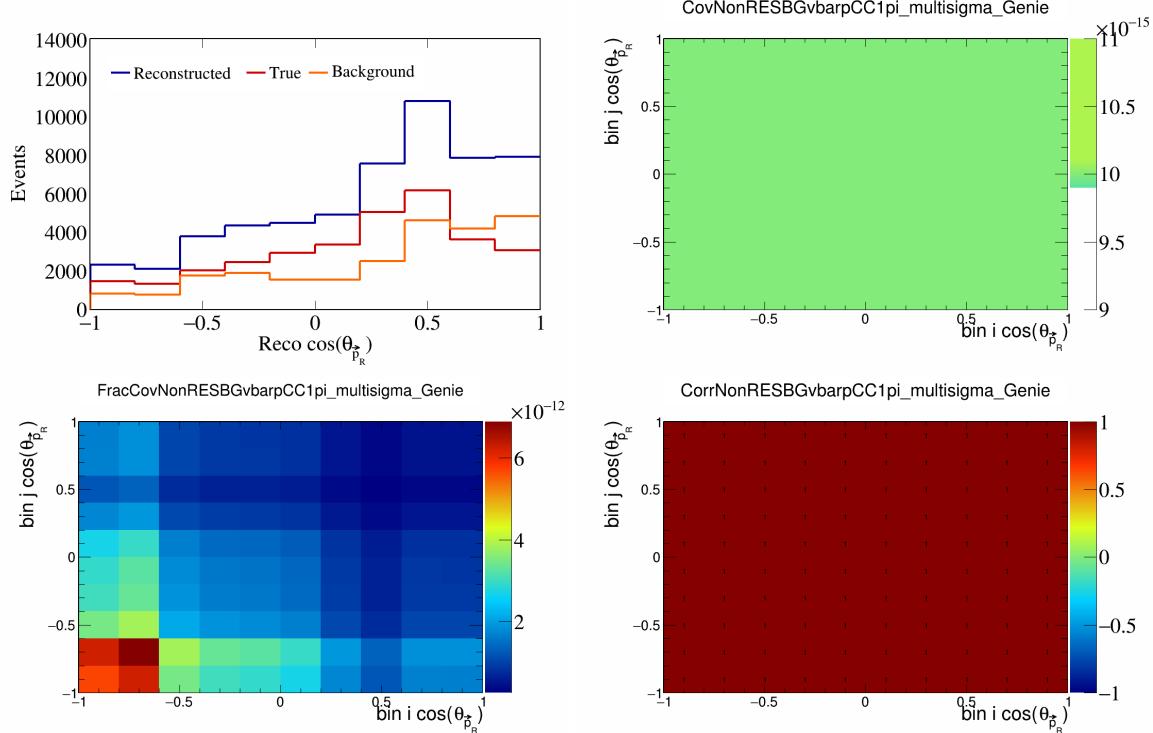


Figure 430: NonRESBGvbarpCC1pi variations for $\cos(\theta_{\vec{p}_R})$.

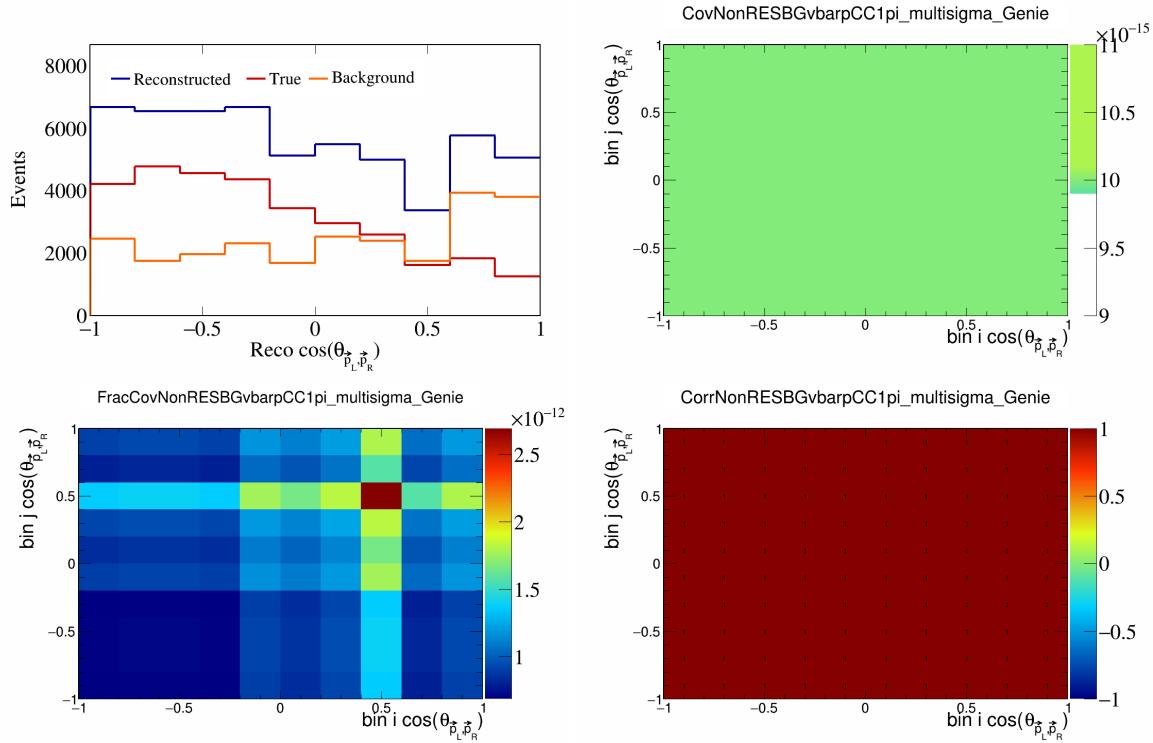


Figure 431: NonRESBGvbarpCC1pi variations for $\cos(\theta_{\vec{p}_L, \vec{p}_R})$.

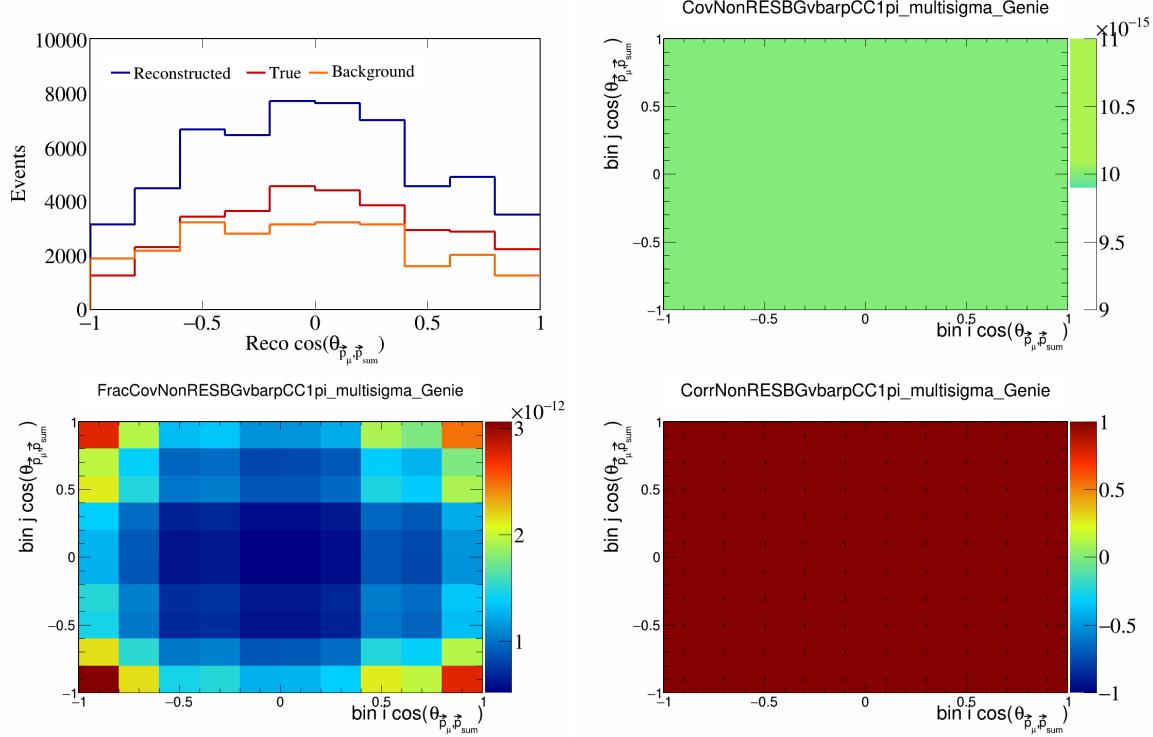


Figure 432: NonRESBGvbarpCC1pi variations for $\cos(\theta_{\vec{p}_\mu, \vec{p}_{\text{sum}}})$.

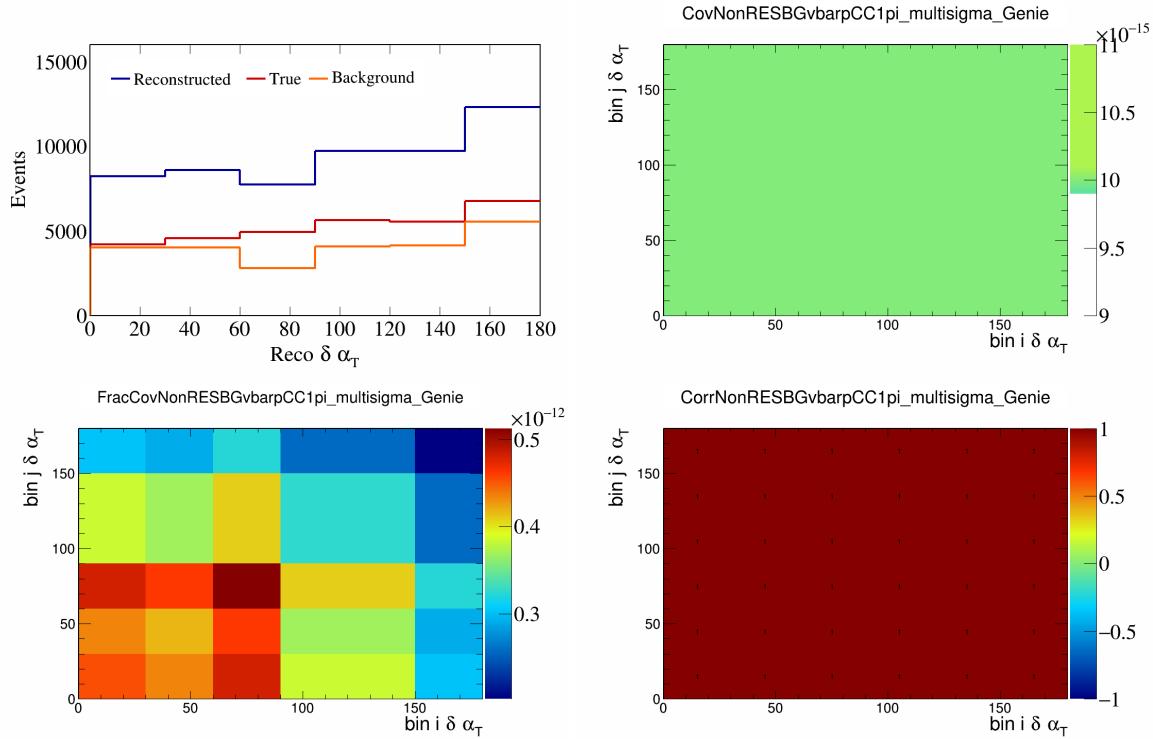


Figure 433: NonRESBGvbarpCC1pi variations for $\delta\alpha_T$.

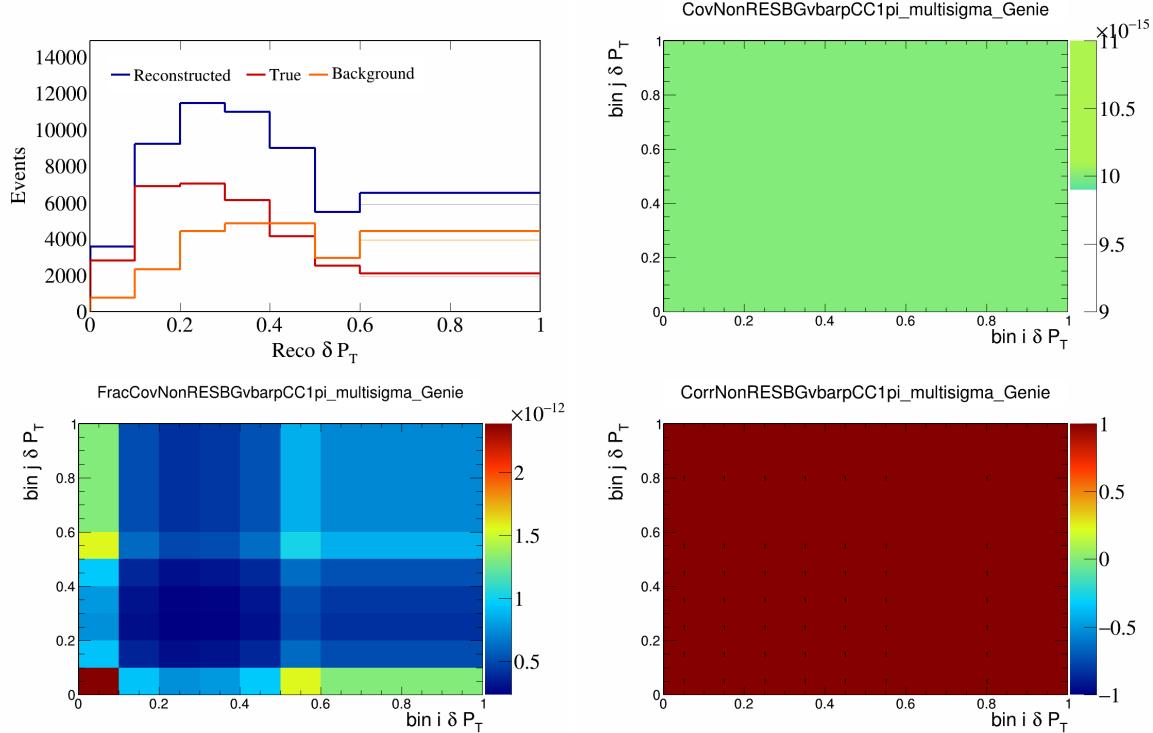


Figure 434: NonRESBGvbarpCC1pi variations for δP_T .

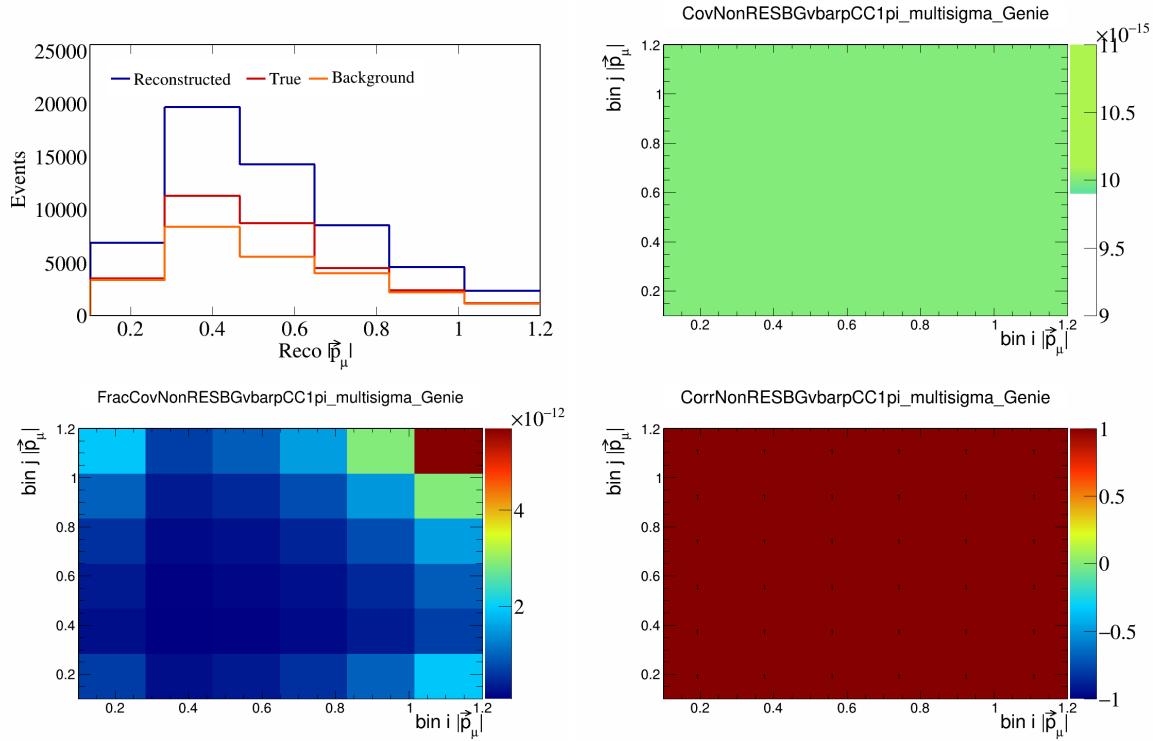


Figure 435: NonRESBGvbarpCC1pi variations for $|\vec{p}_\mu|$.

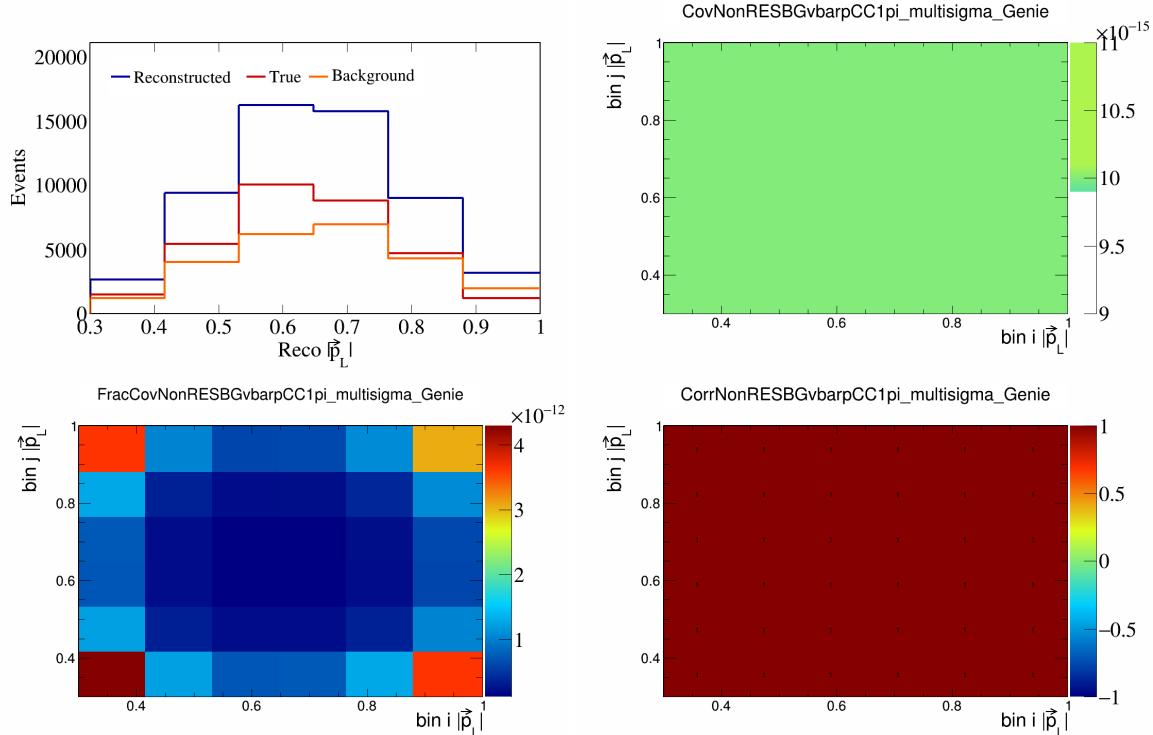


Figure 436: NonRESBGvbarpCC1pi variations for $|\vec{p}_L|$.

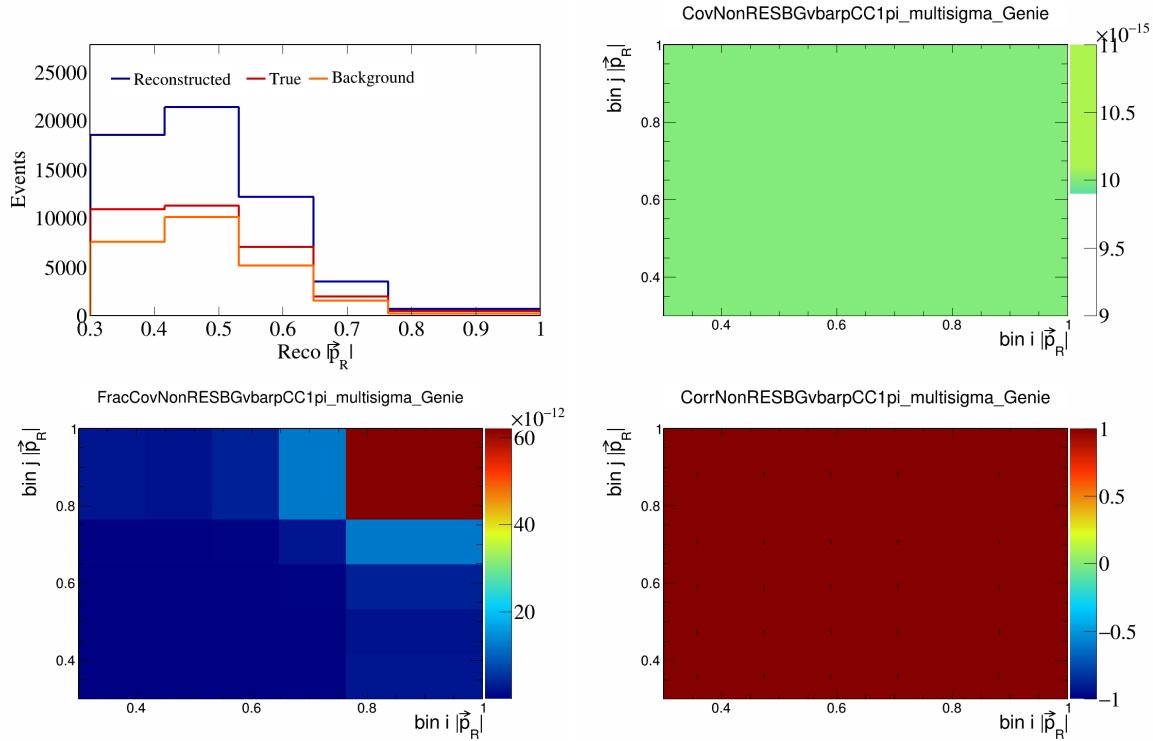


Figure 437: NonRESBGvbarpCC1pi variations for $|\vec{p}_R|$.

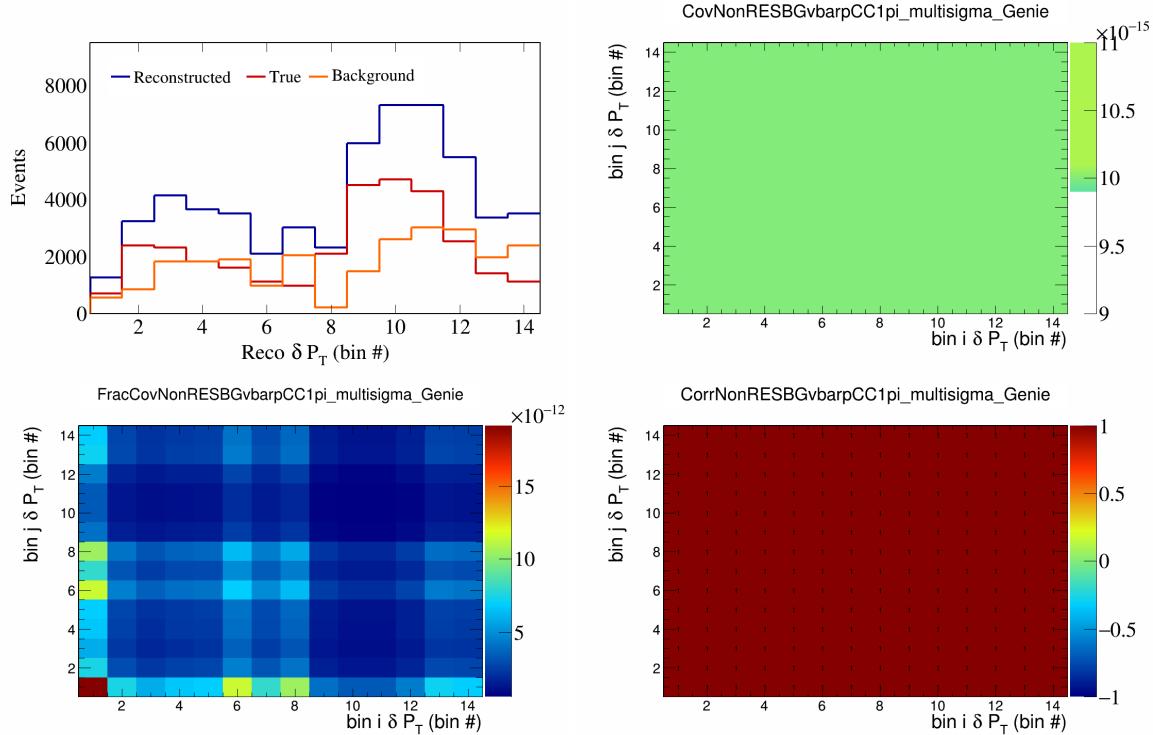


Figure 438: NonRESBGvbarpCC1pi variations for δP_T in $\cos(\theta_{\vec{p}_\mu})$.

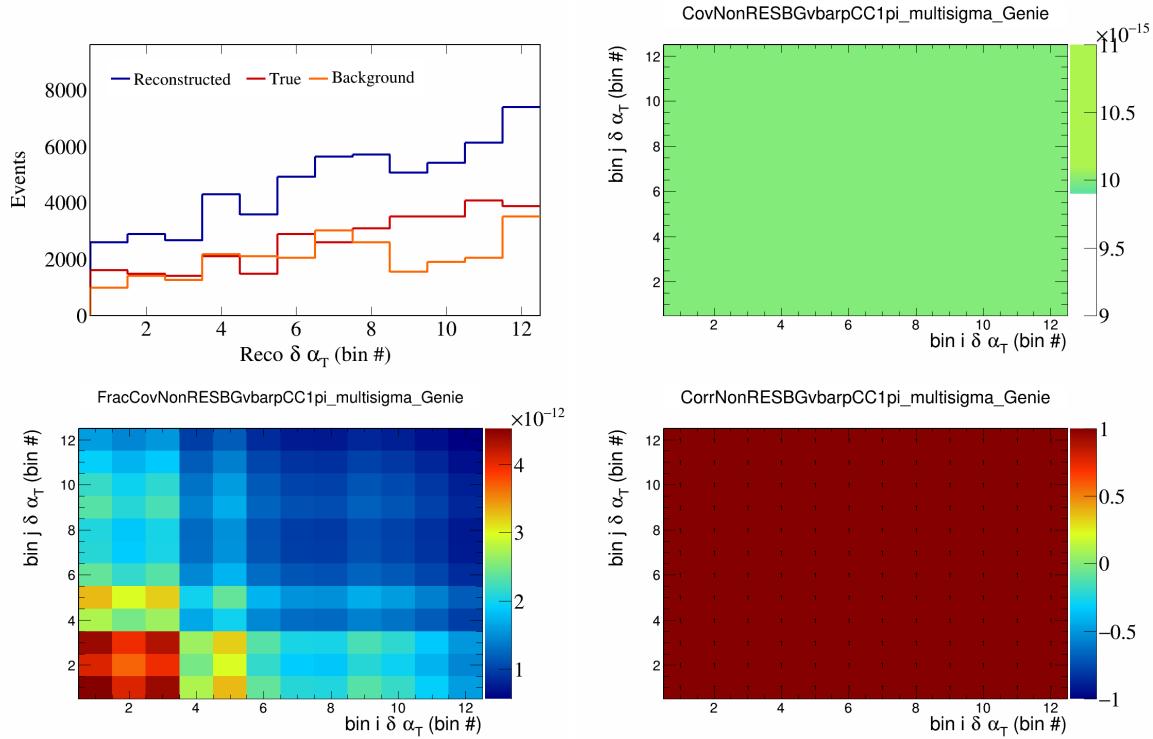


Figure 439: NonRESBGvbarpCC1pi variations for $\delta\alpha_T$ in $\cos(\theta_{\vec{p}_\mu})$.

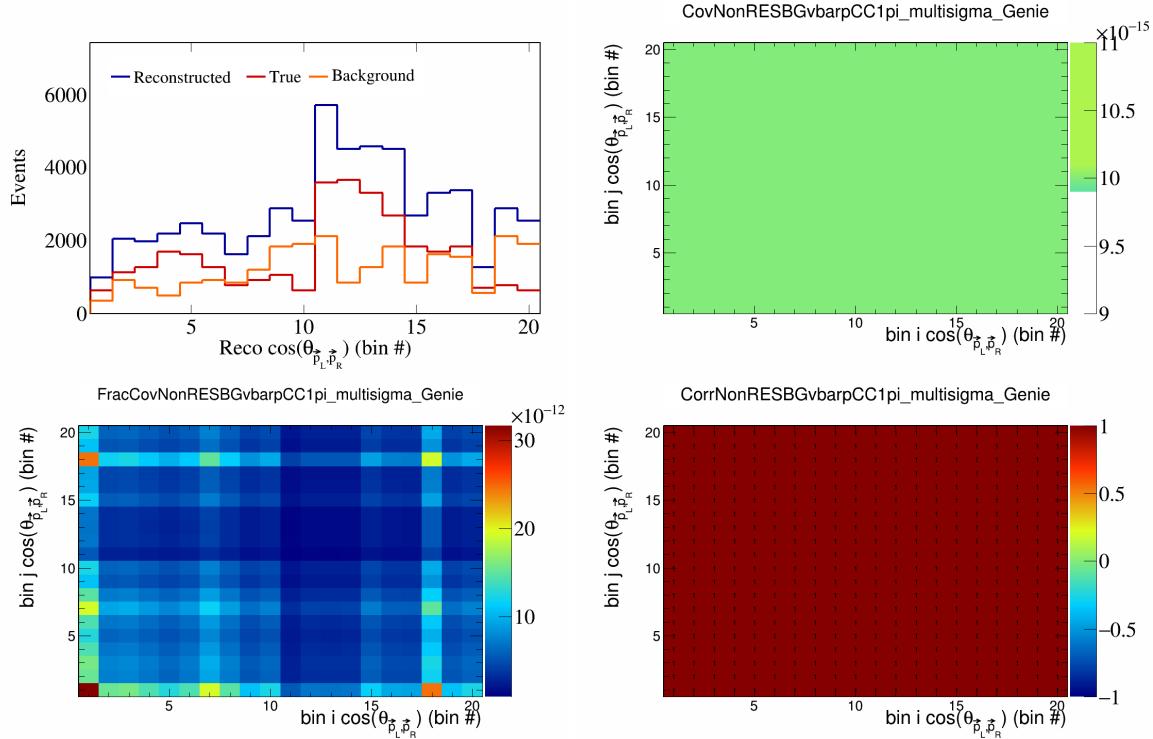


Figure 440: NonRESBGvbarpCC1pi variations for $\cos(\theta_{\vec{p}_L, \vec{p}_R})$ in $\cos(\theta_{\vec{p}_\mu})$.

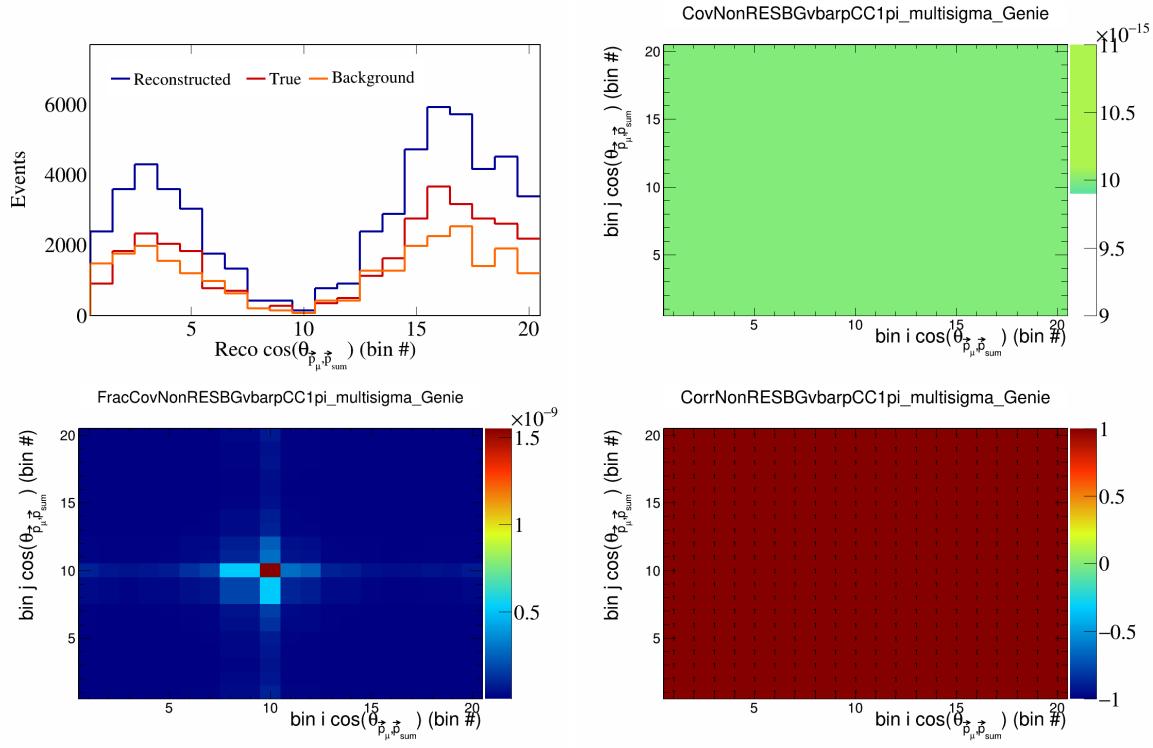


Figure 441: NonRESBGvbarpCC1pi variations for $\cos(\theta_{\vec{p}_\mu})$ in $\cos(\theta_{\vec{p}_\mu})$.

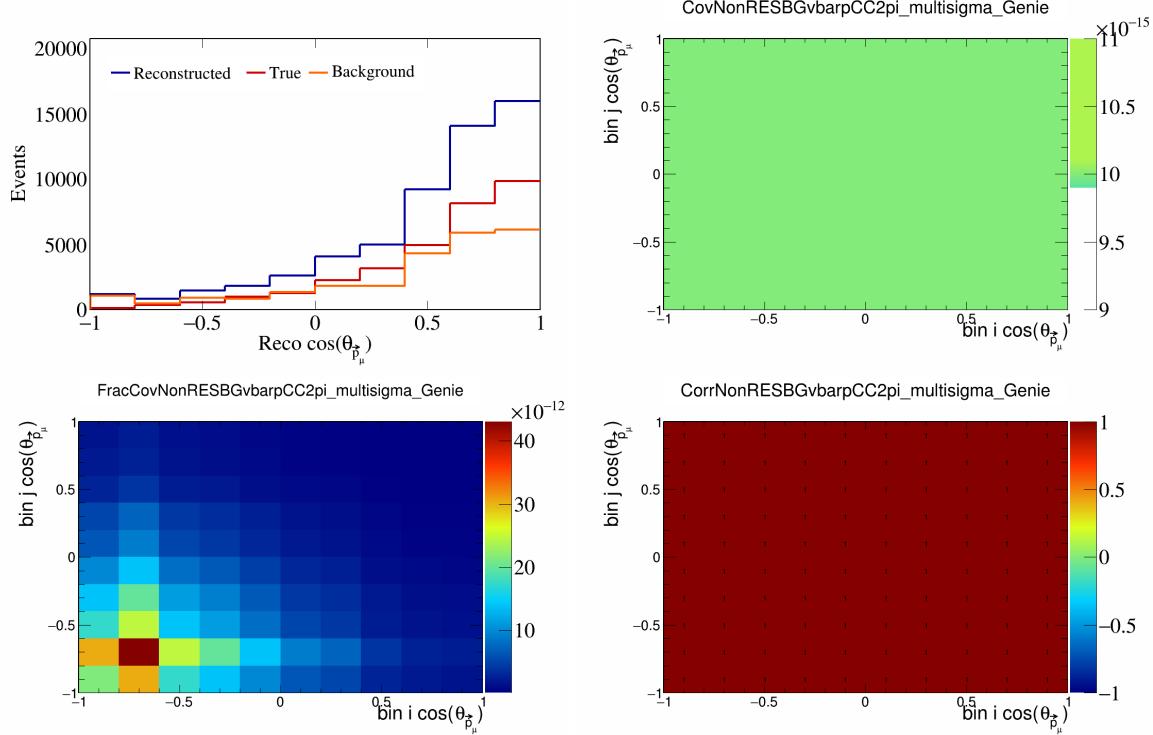


Figure 442: NonRESBGvbarpCC2pi variations for $\cos(\theta_{\vec{p}_\mu})$.

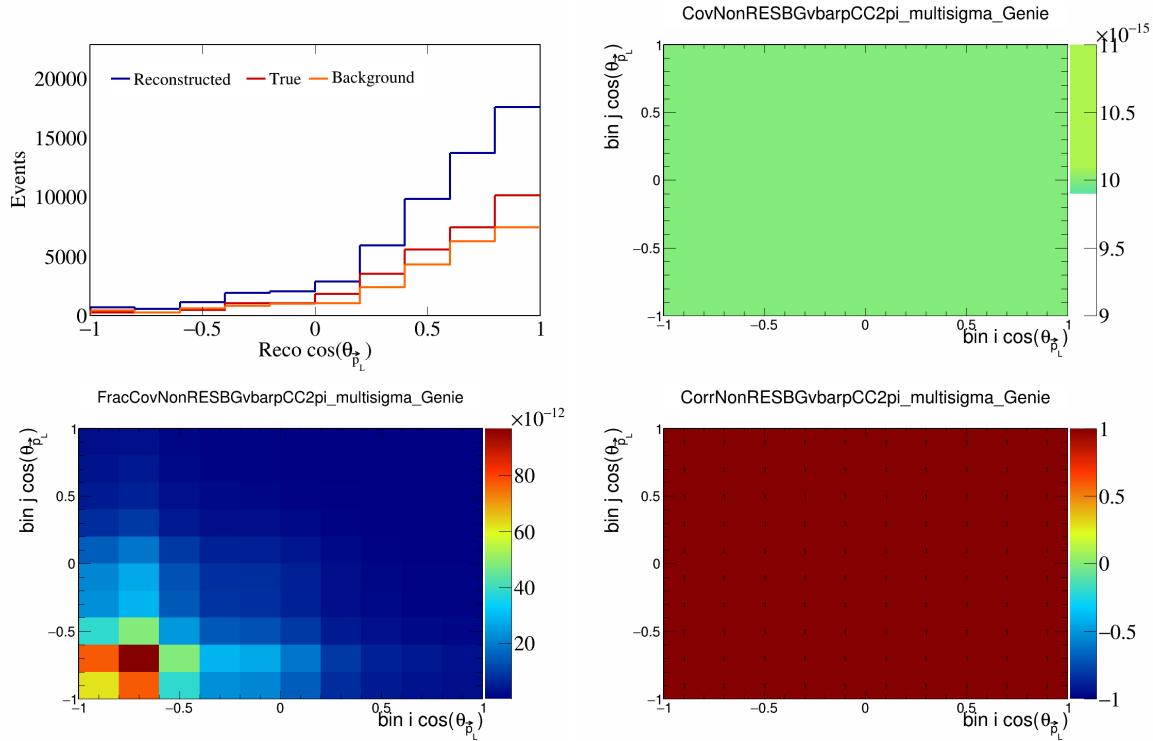


Figure 443: NonRESBGvbarpCC2pi variations for $\cos(\theta_{\vec{p}_L})$.

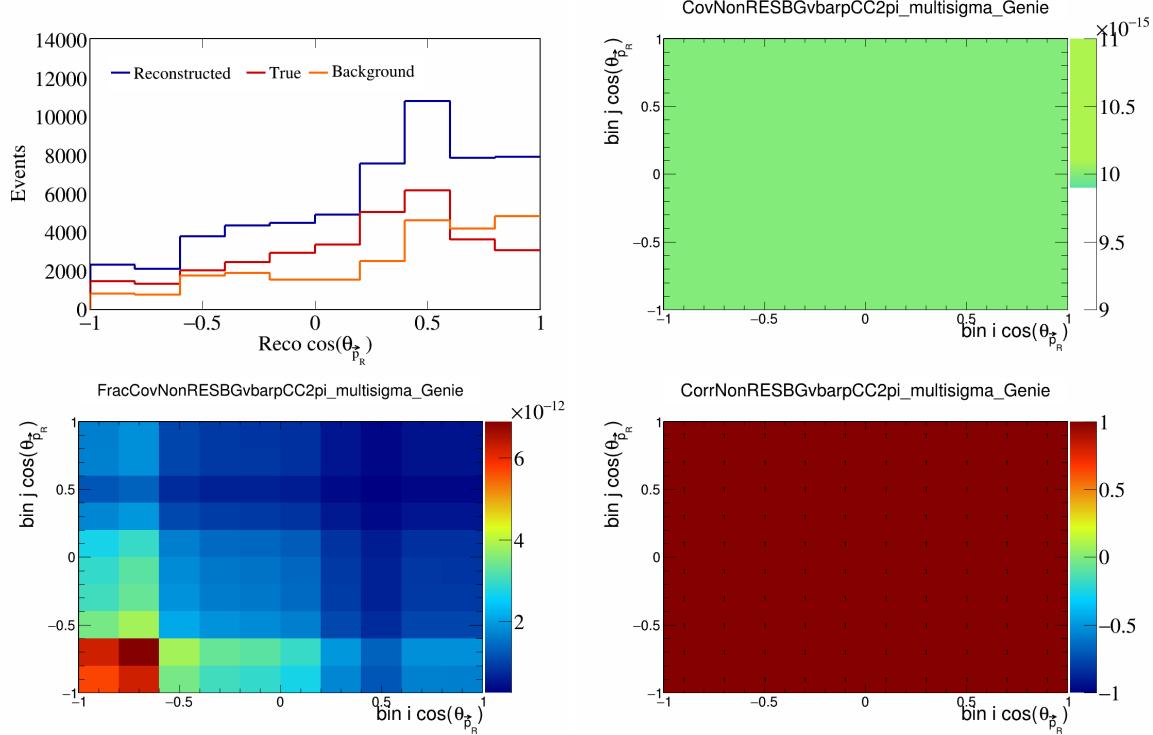


Figure 444: NonRESBGvbarpCC2pi variations for $\cos(\theta_{\vec{p}_R})$.

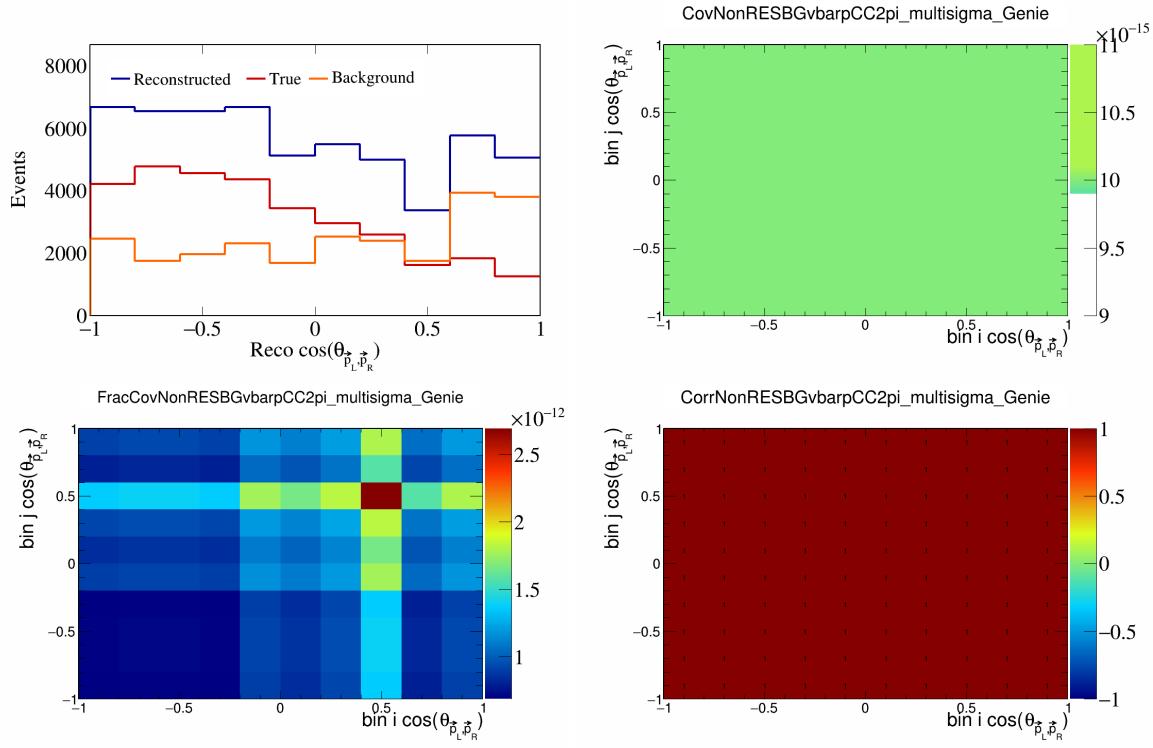


Figure 445: NonRESBGvbarpCC2pi variations for $\cos(\theta_{\vec{p}_L, \vec{p}_R})$.

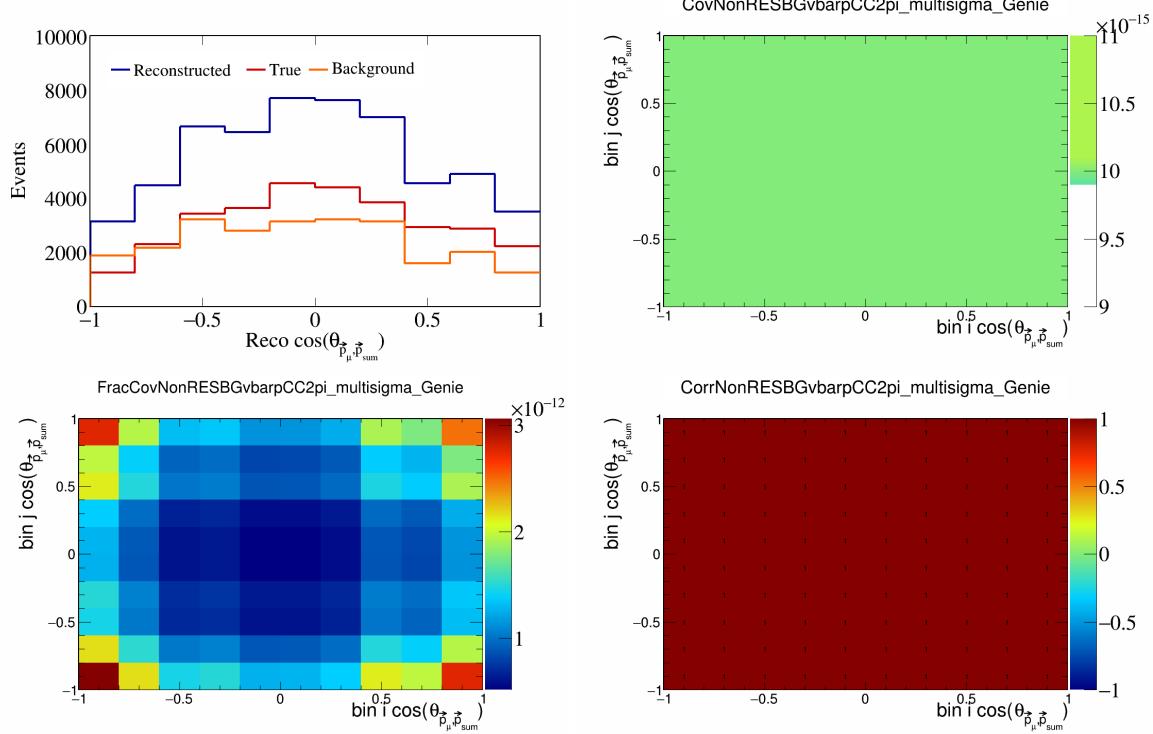


Figure 446: NonRESBGvbarpCC2pi variations for $\cos(\theta_{\vec{p}_\mu, \vec{p}_{\text{sum}}})$.

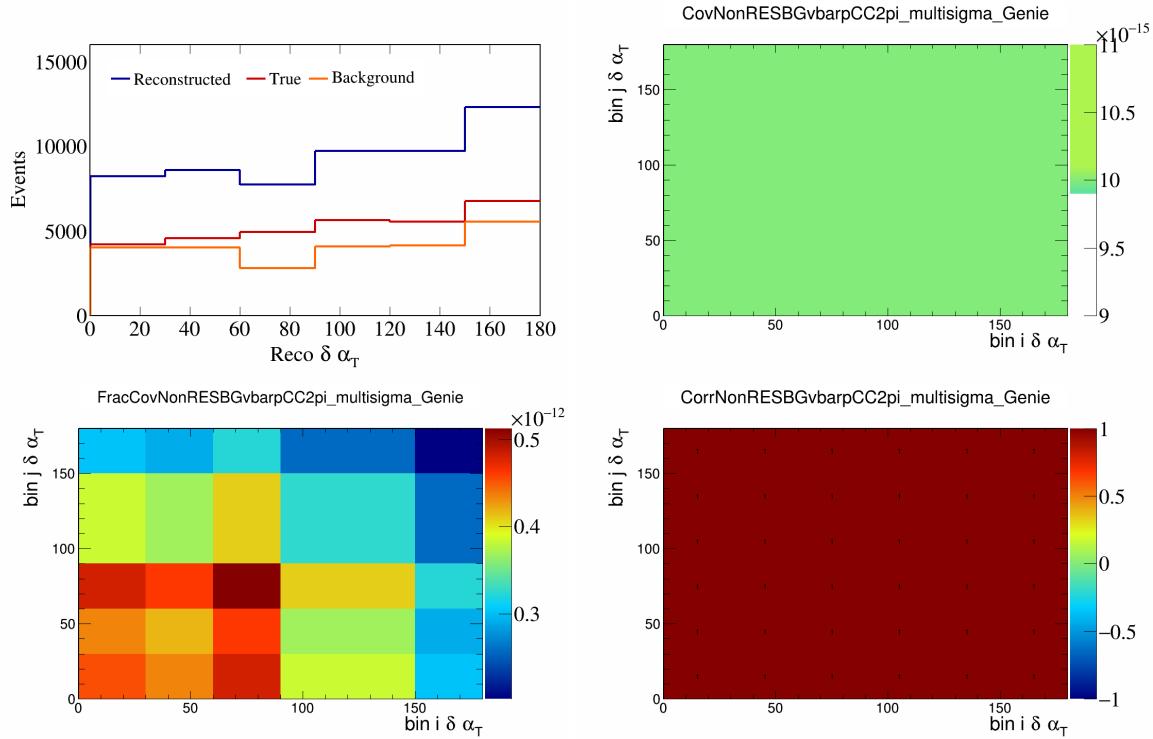


Figure 447: NonRESBGvbarpCC2pi variations for $\delta\alpha_T$.

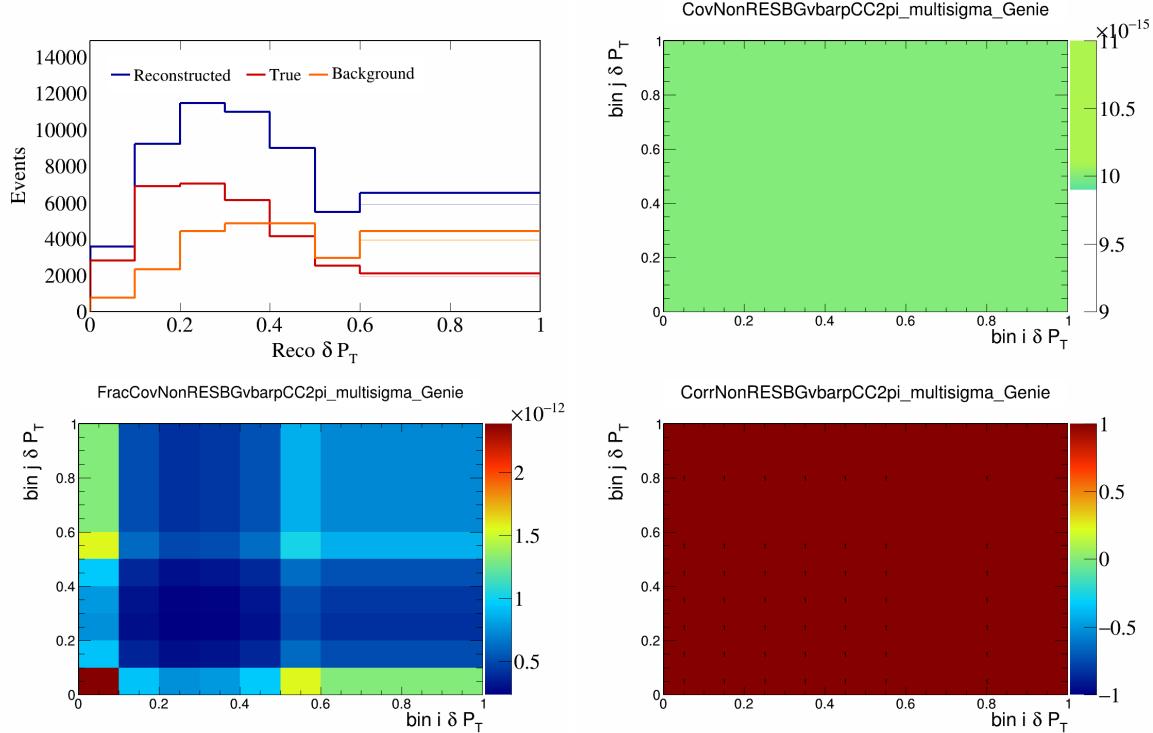


Figure 448: NonRESBGvbarpCC2pi variations for δP_T .

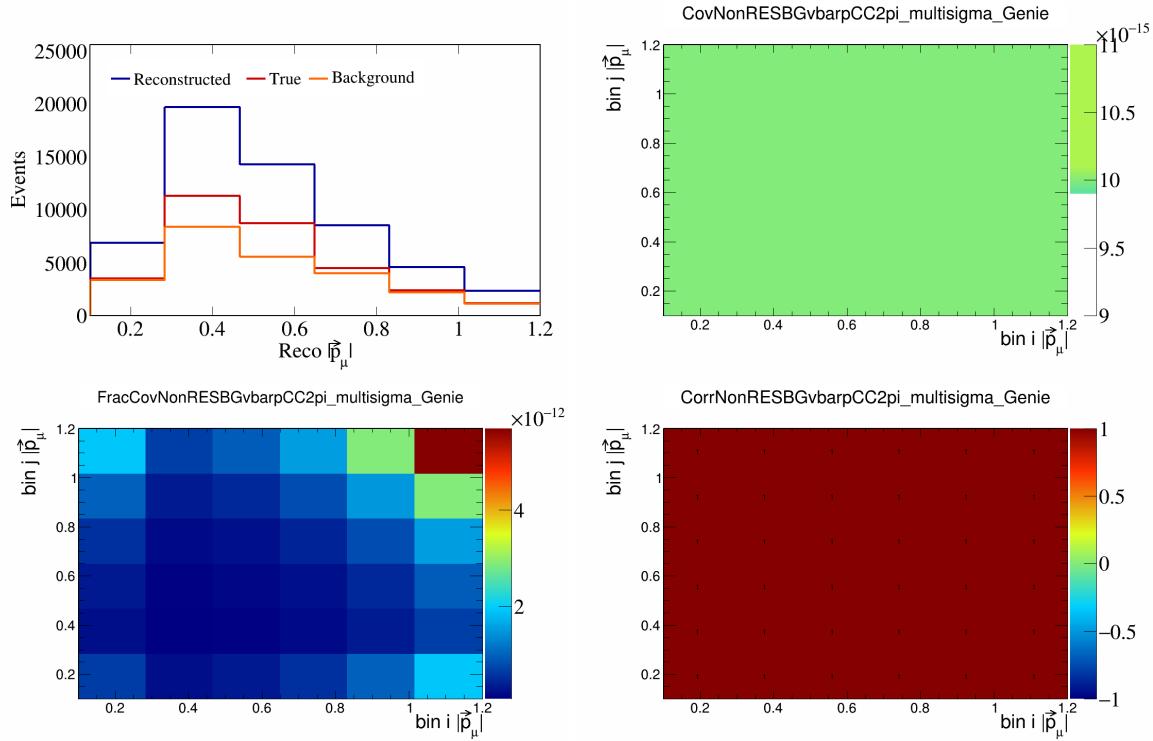


Figure 449: NonRESBGvbarpCC2pi variations for $|\vec{p}_\mu|$.

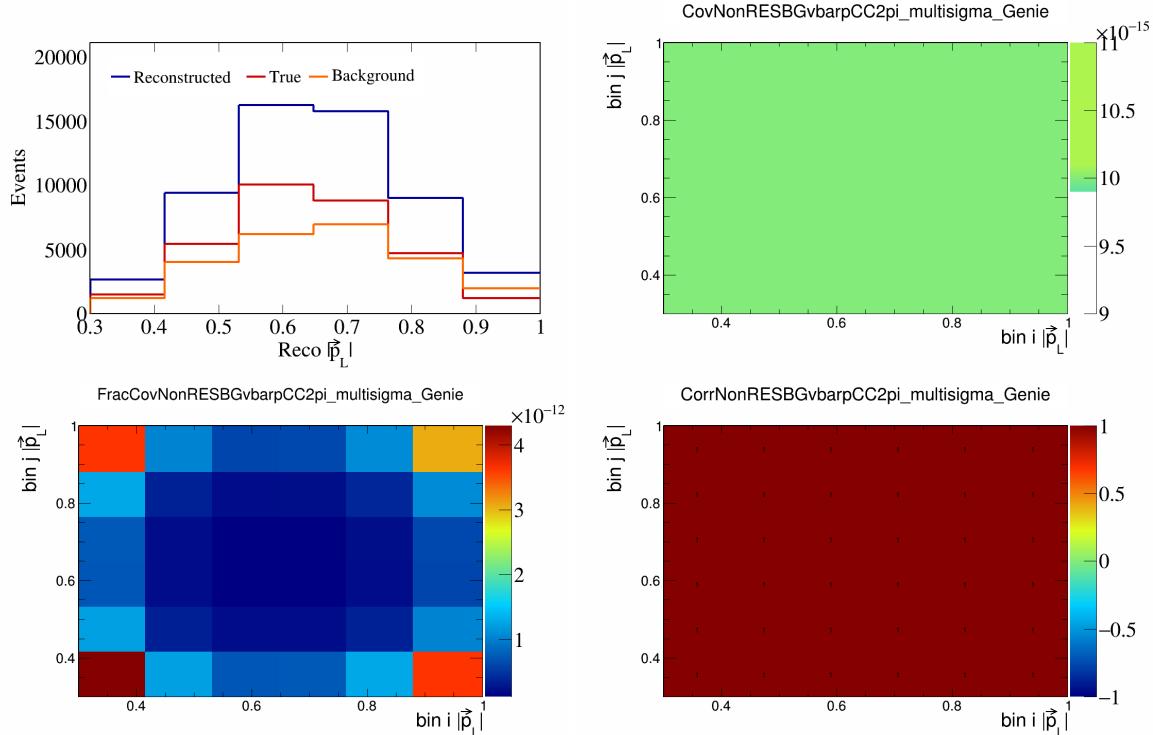


Figure 450: NonRESBGvbarpCC2pi variations for $|\vec{p}_L|$.

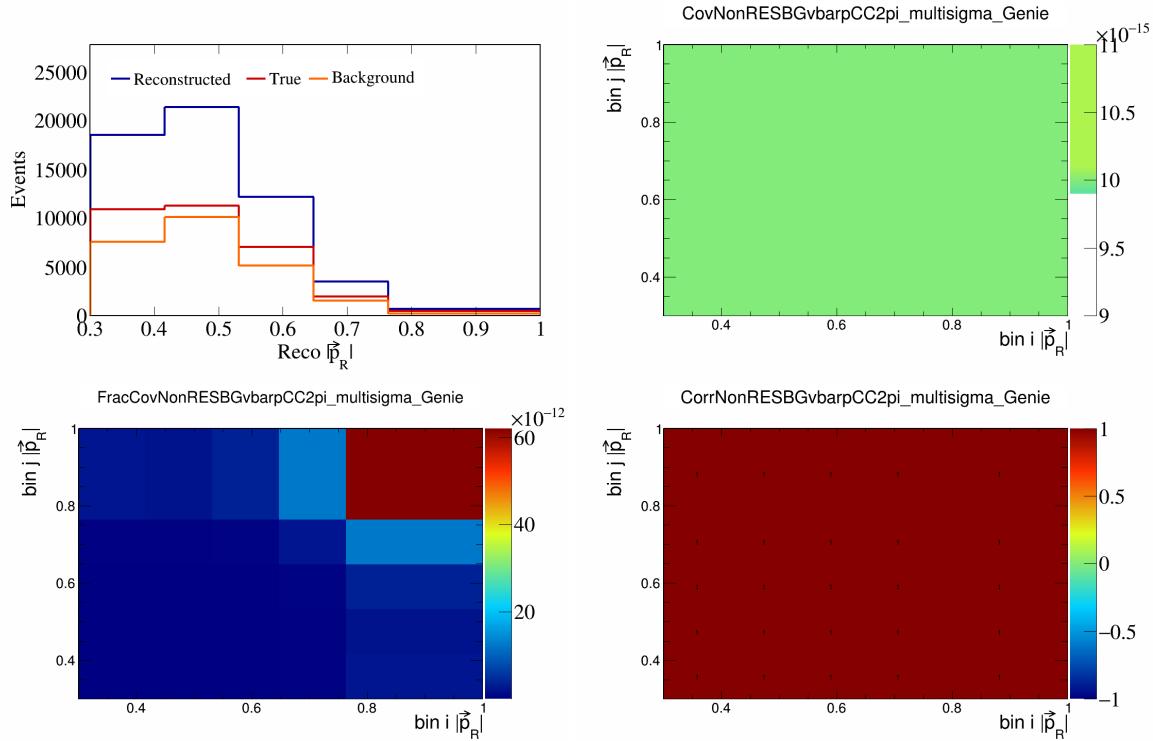


Figure 451: NonRESBGvbarpCC2pi variations for $|\vec{p}_R|$.

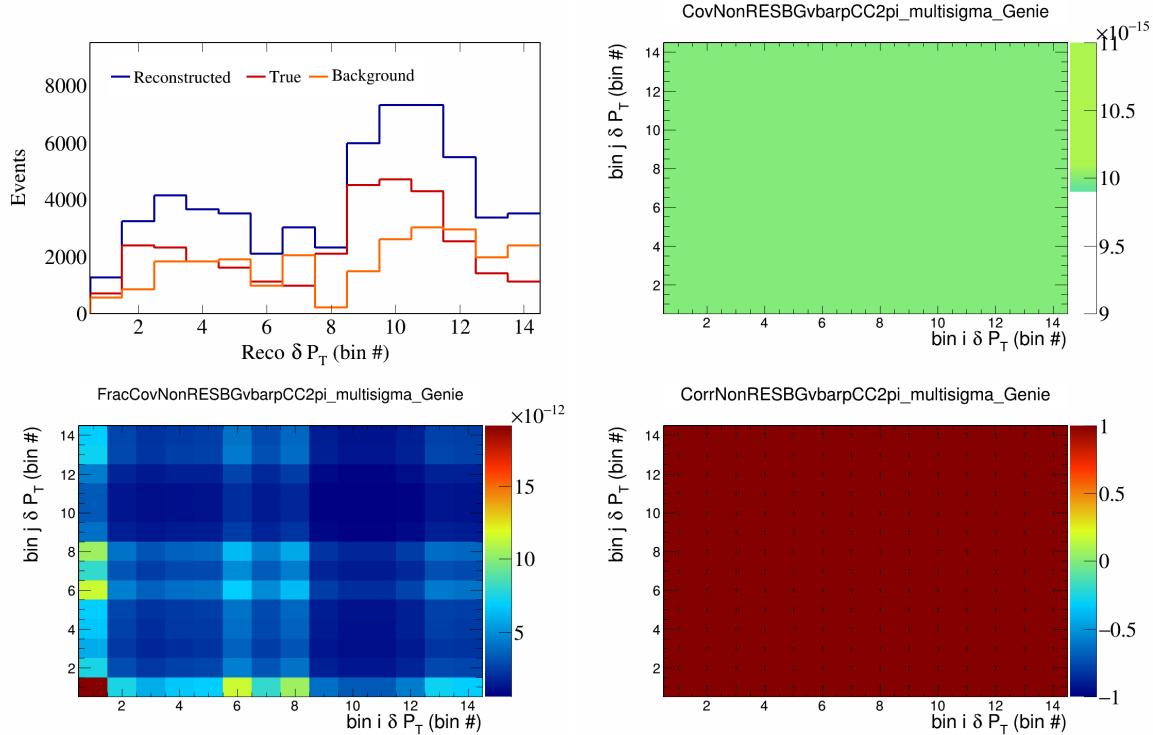


Figure 452: NonRESBGvbarpCC2pi variations for δP_T in $\cos(\theta_{\vec{p}_\mu})$.

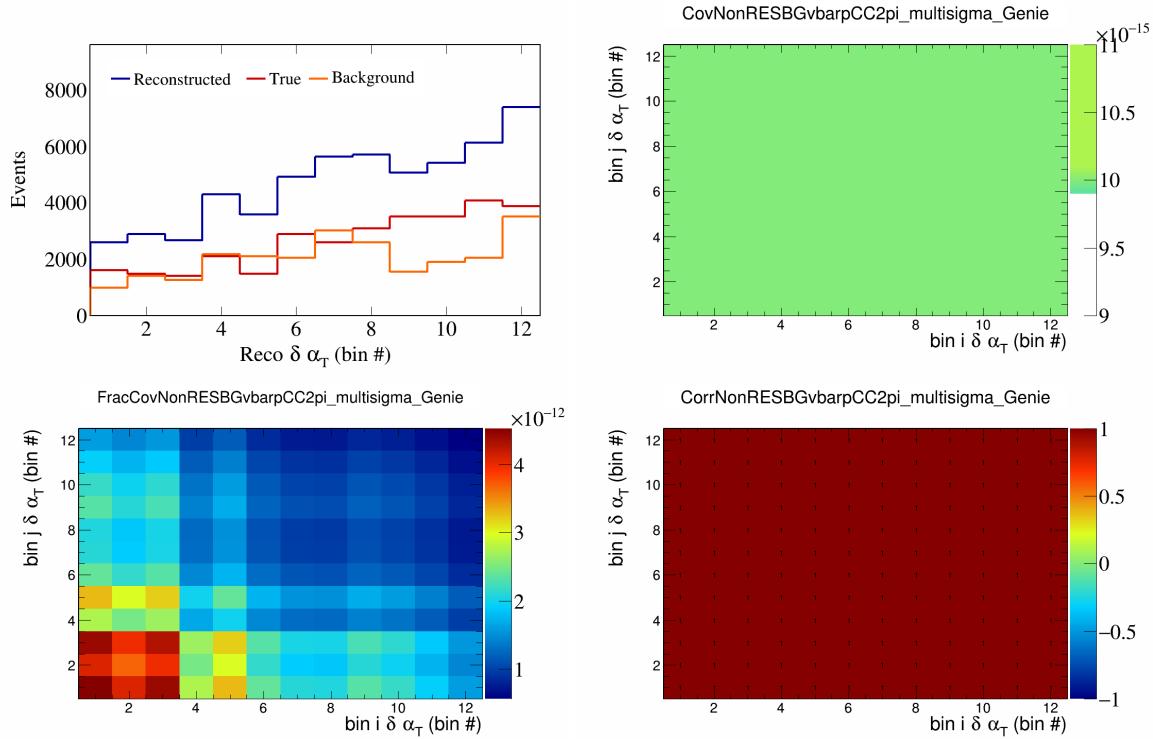


Figure 453: NonRESBGvbarpCC2pi variations for $\delta\alpha_T$ in $\cos(\theta_{\vec{p}_\mu})$.

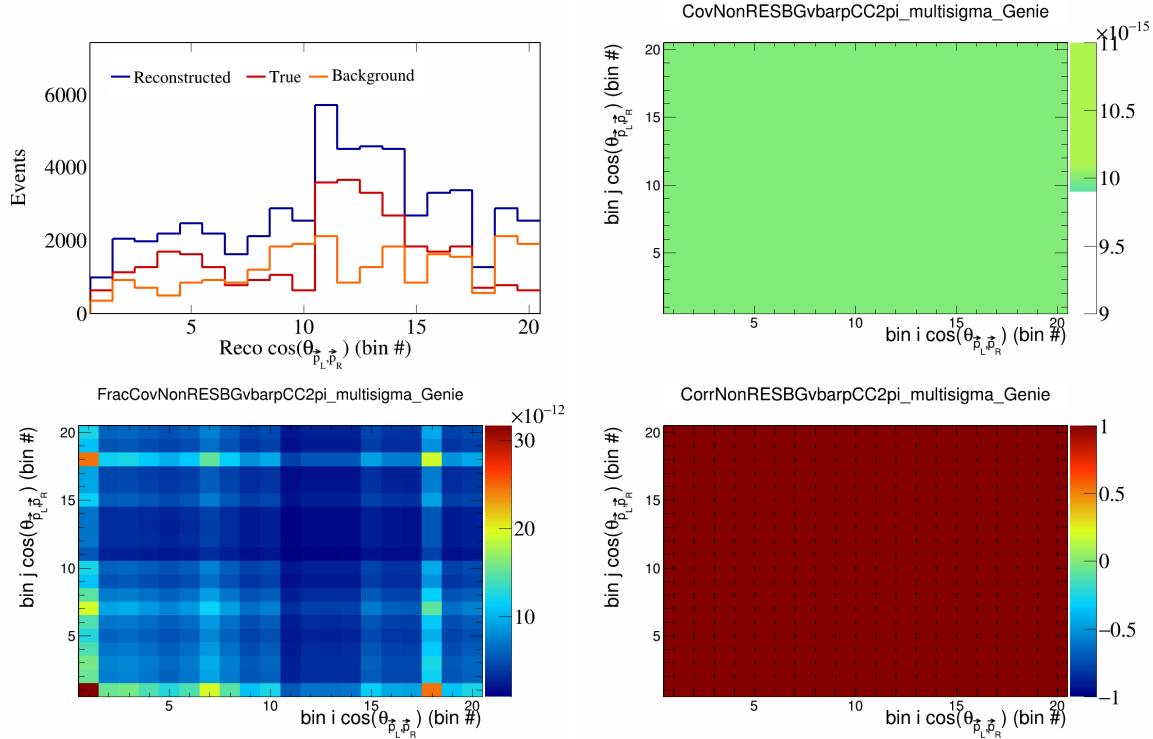


Figure 454: NonRESBGvbarpCC2pi variations for $\cos(\theta_{\vec{p}_L, \vec{p}_R})$ in $\cos(\theta_{\vec{p}_\mu})$.

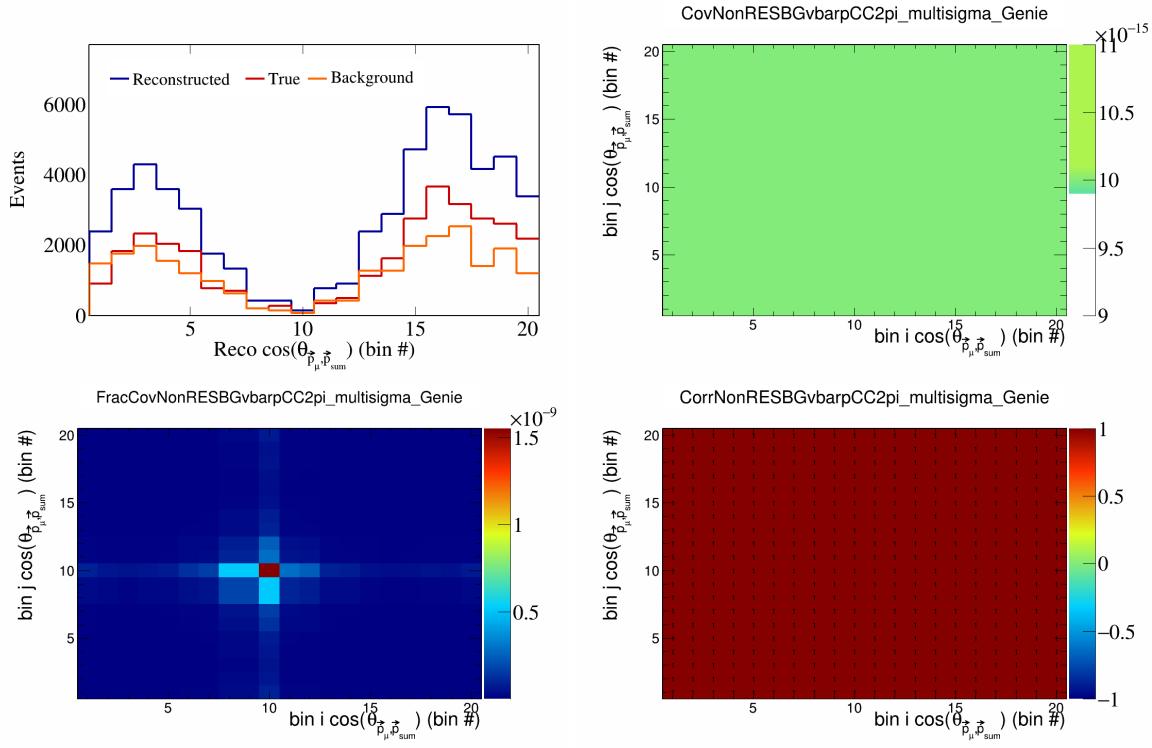


Figure 455: NonRESBGvbarpCC2pi variations for $\cos(\theta_{\vec{p}_\mu})$ in $\cos(\theta_{\vec{p}_\mu})$.

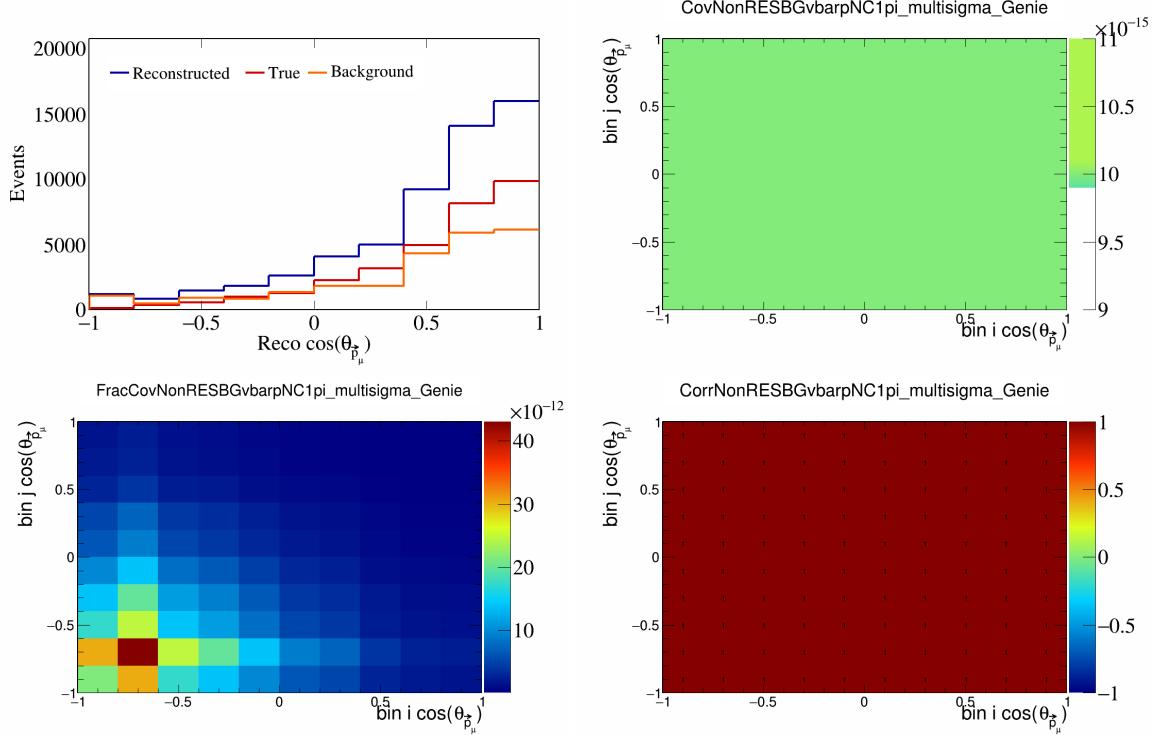


Figure 456: NonRESBGvbarpNC1pi variations for $\cos(\theta_{\vec{p}_\mu})$.

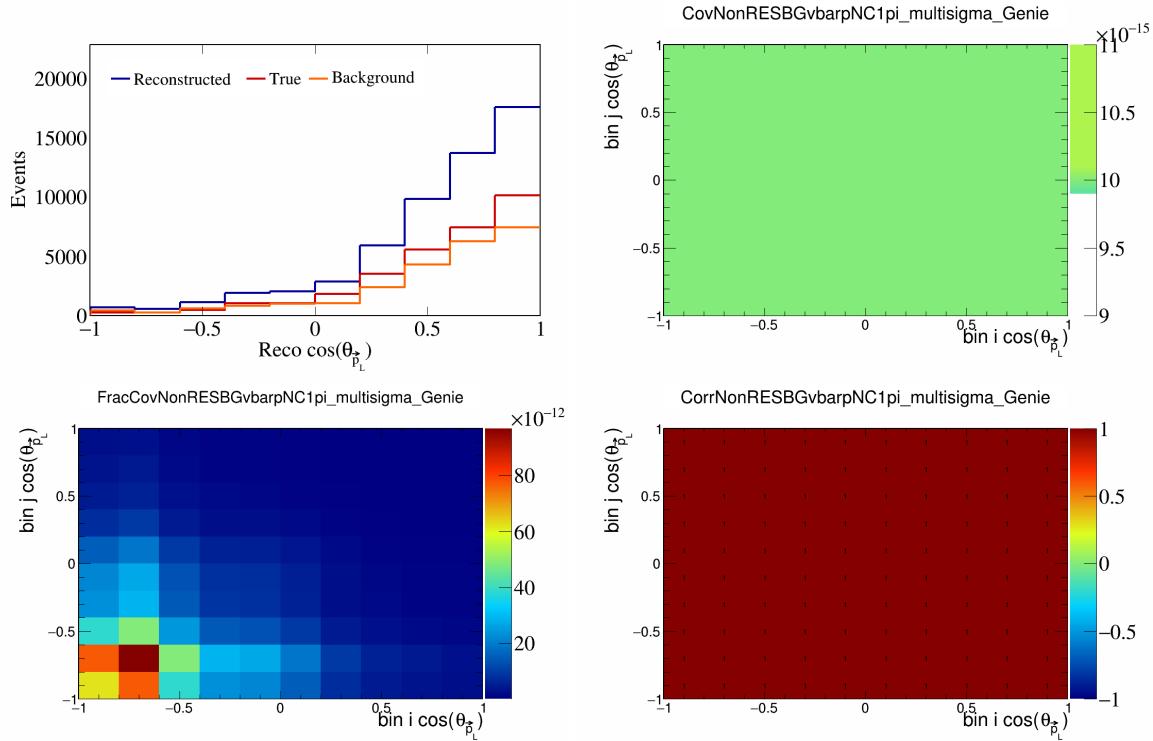


Figure 457: NonRESBGvbarpi variations for $\cos(\theta_{\vec{p}_L})$.

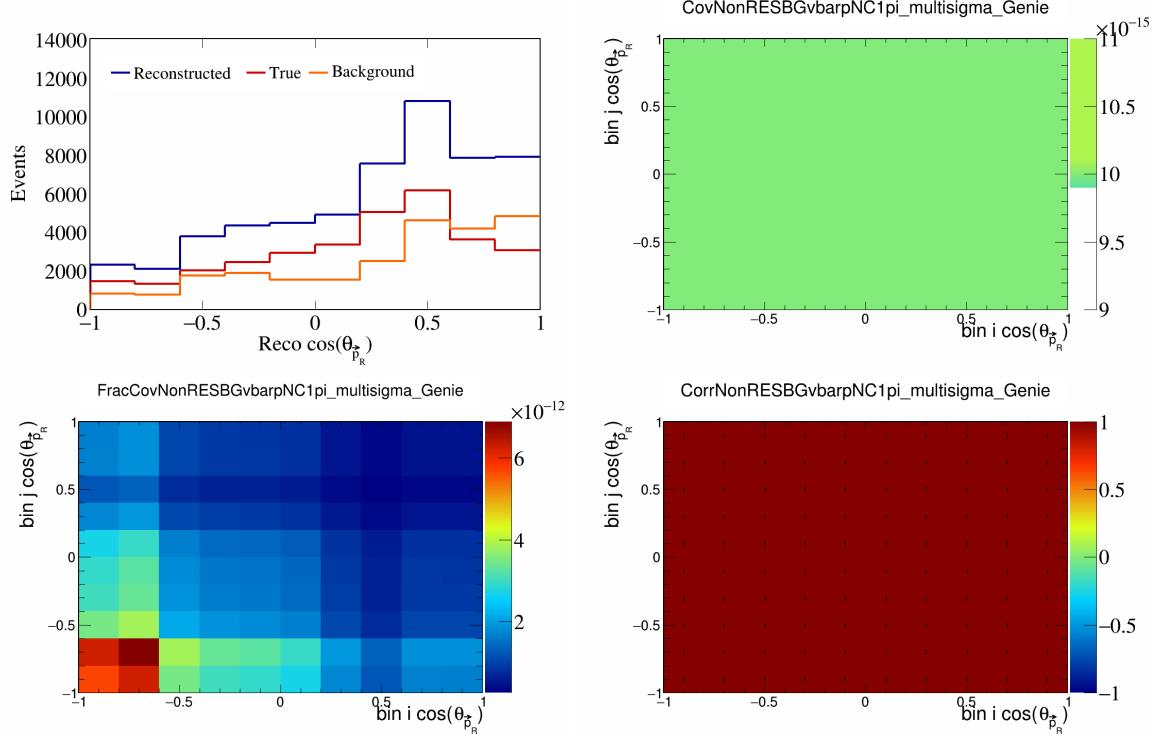


Figure 458: NonRESBGvbarpi variations for $\cos(\theta_{\vec{p}_R})$.

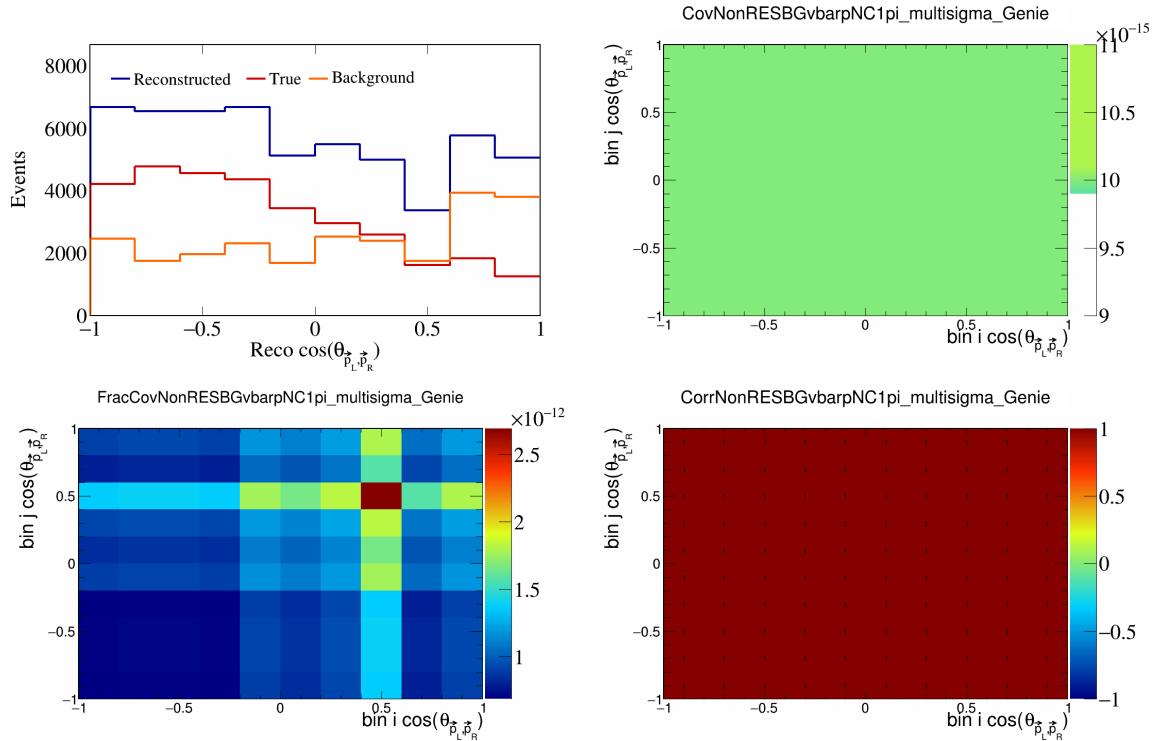


Figure 459: NonRESBGvbarpNC1pi variations for $\cos(\theta_{\vec{p}_L, \vec{p}_R})$.

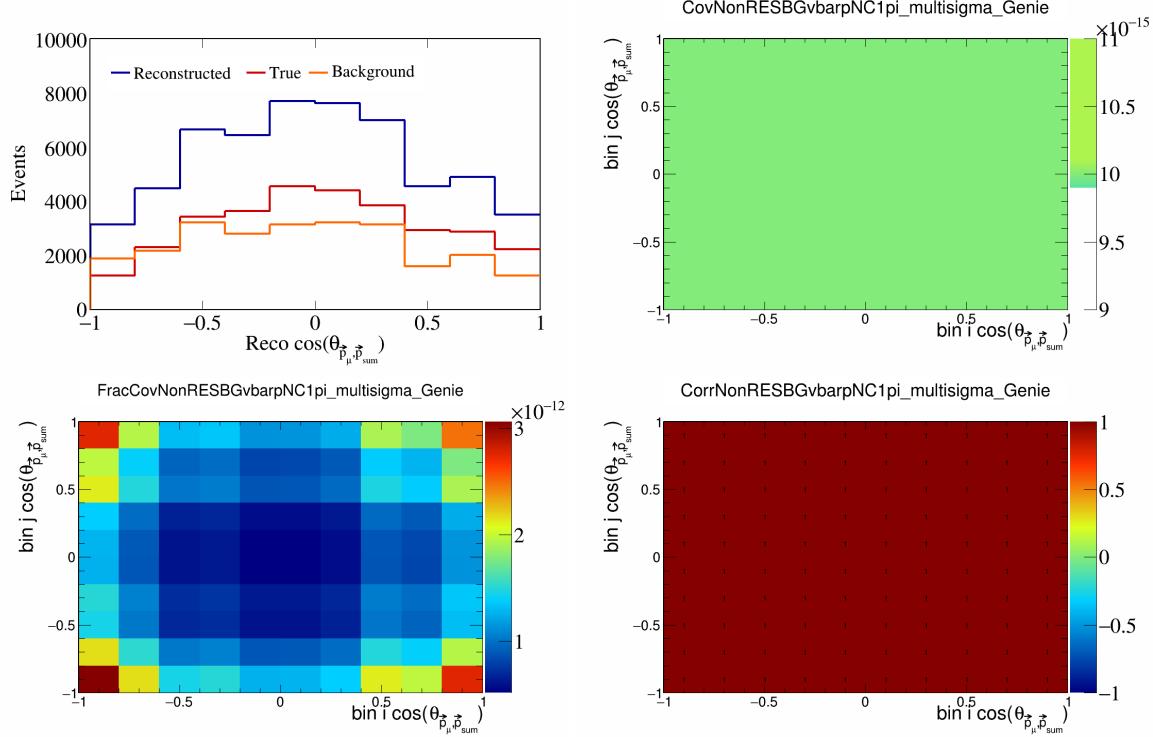


Figure 460: NonRESBGvbarpNC1pi variations for $\cos(\theta_{\vec{p}_\mu, \vec{p}_{\text{sum}}})$.

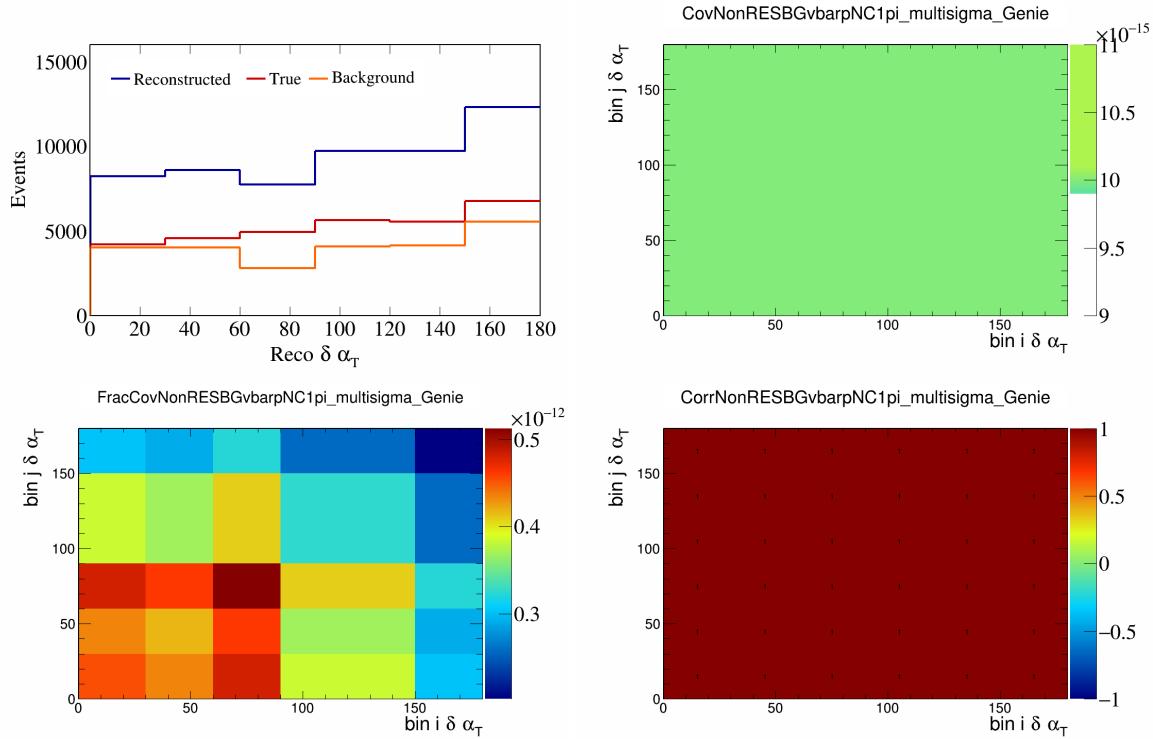


Figure 461: NonRESBGvbarpNC1pi variations for $\delta\alpha_T$.

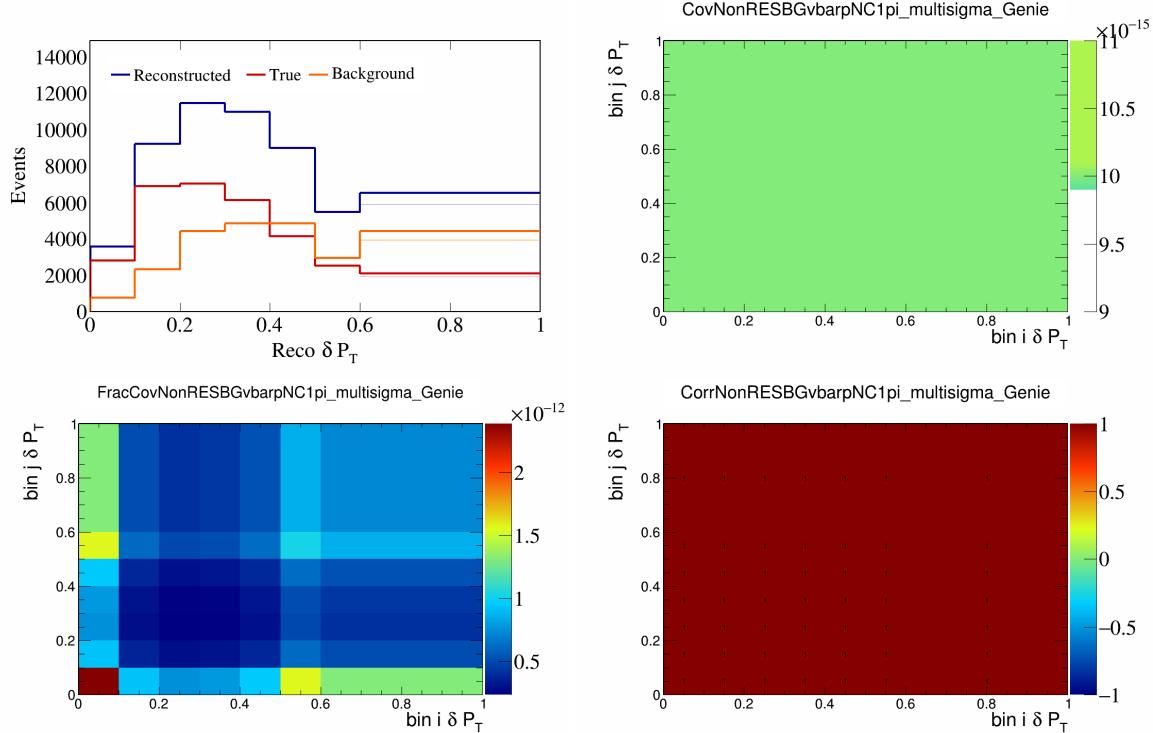


Figure 462: NonRESBGvbarpNC1pi variations for δP_T .

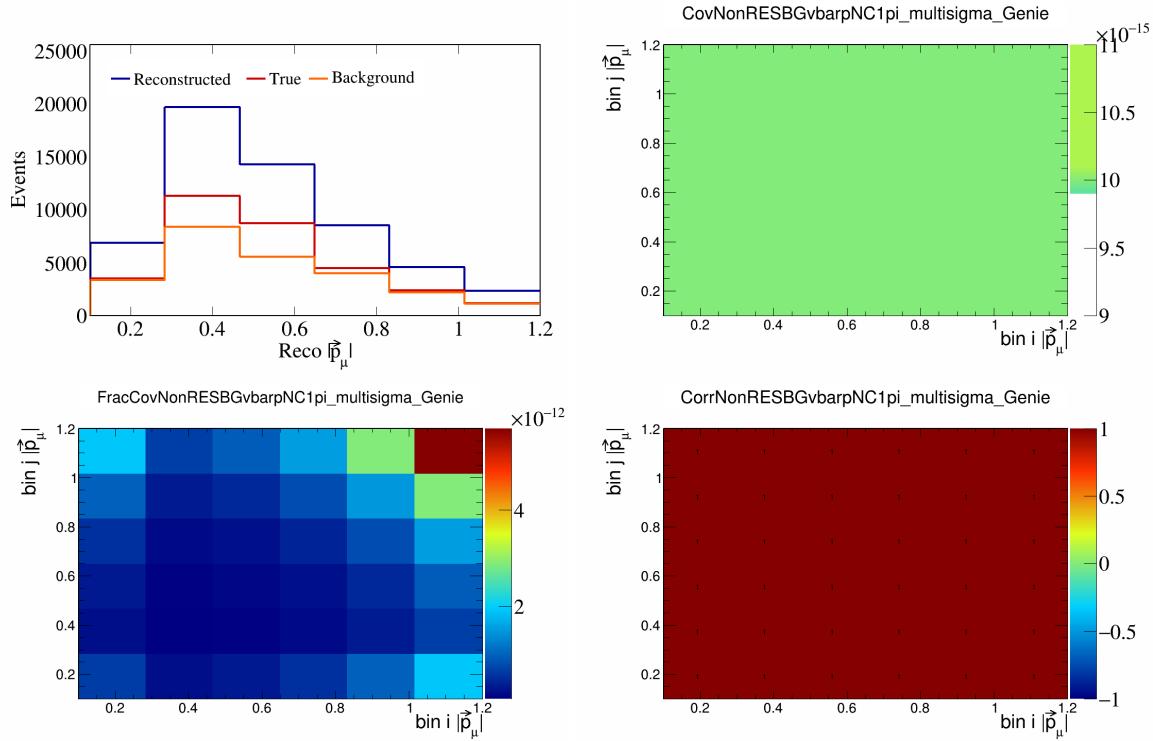


Figure 463: NonRESBGvbarpNC1pi variations for $|\vec{p}_\mu|$.

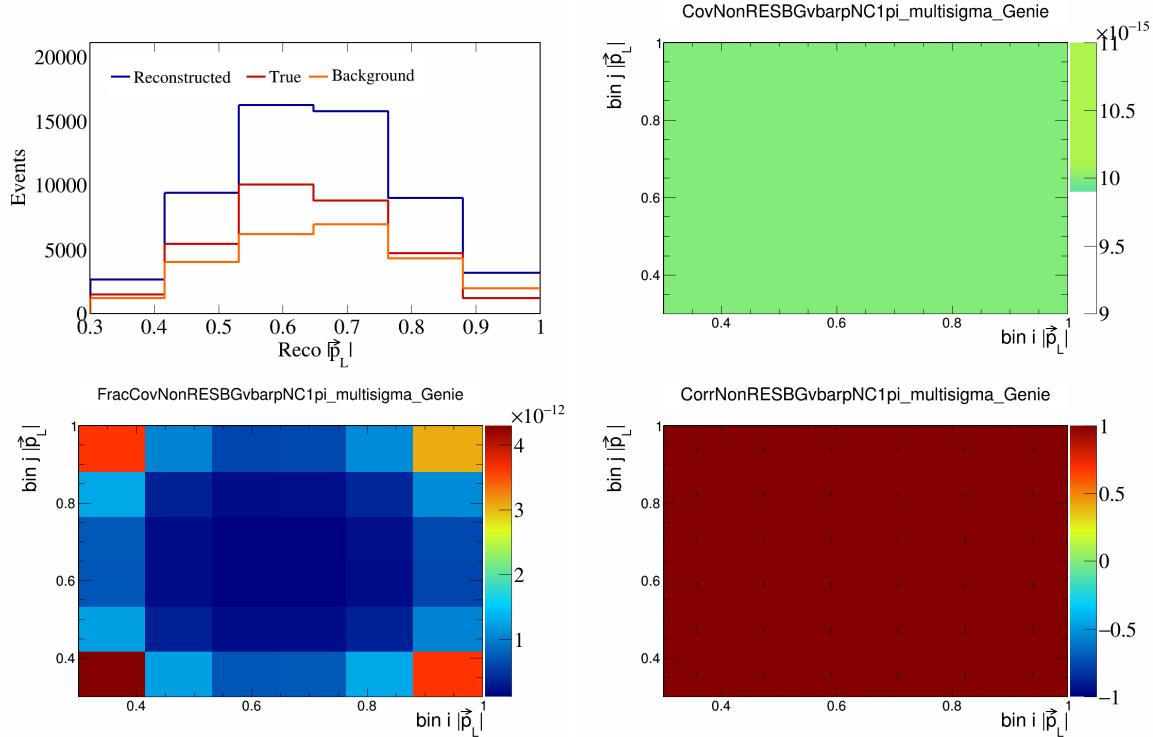


Figure 464: NonRESBGvbarpNC1pi variations for $|\vec{p}_L|$.

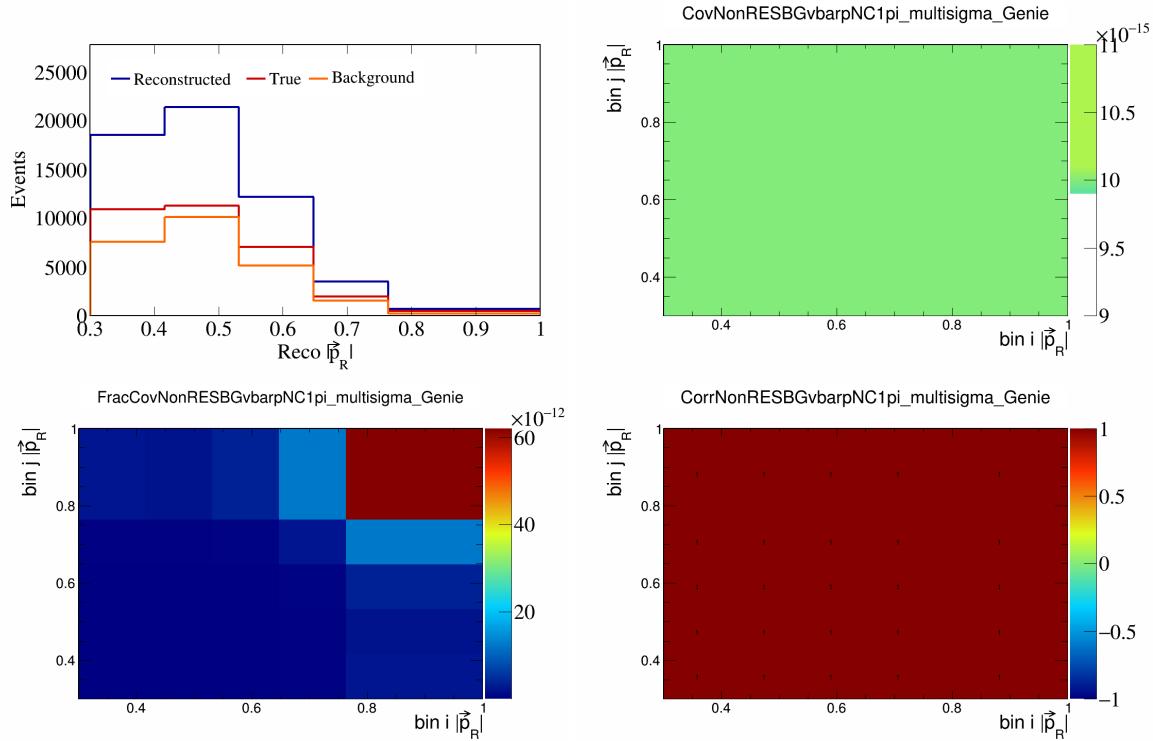


Figure 465: NonRESBGvbarpNC1pi variations for $|\vec{p}_R|$.

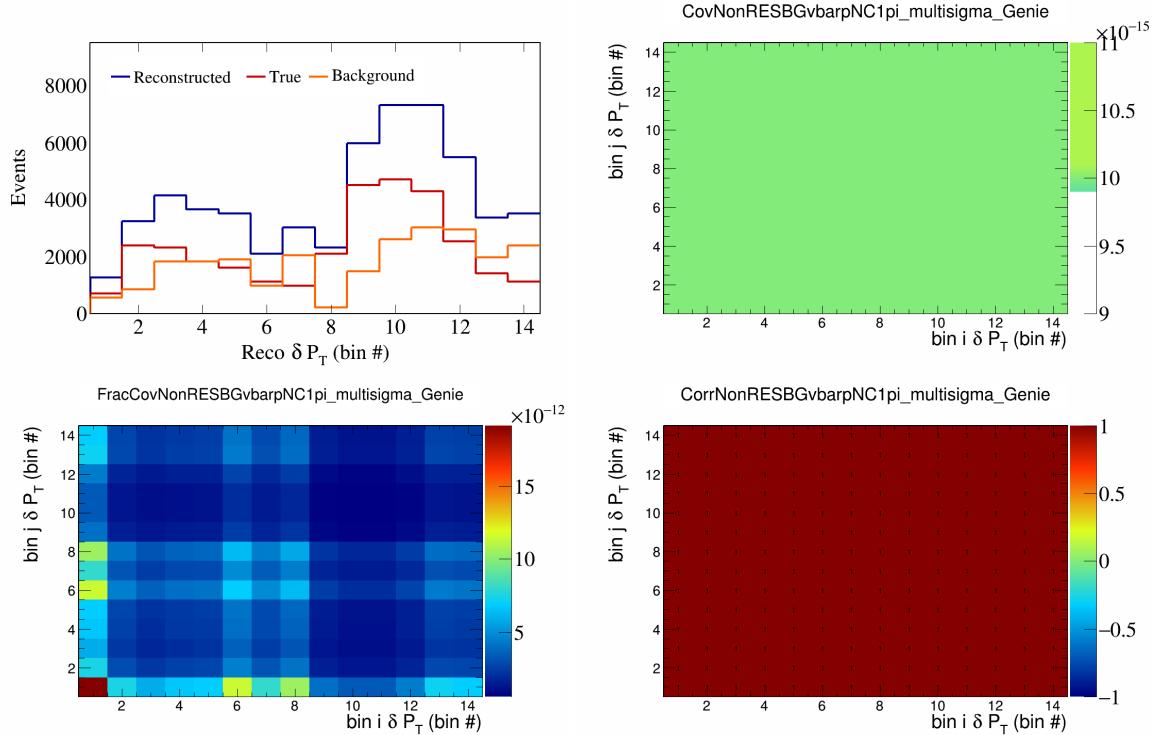


Figure 466: NonRESBGvbarpNC1pi variations for δP_T in $\cos(\theta_{\vec{p}_\mu})$.

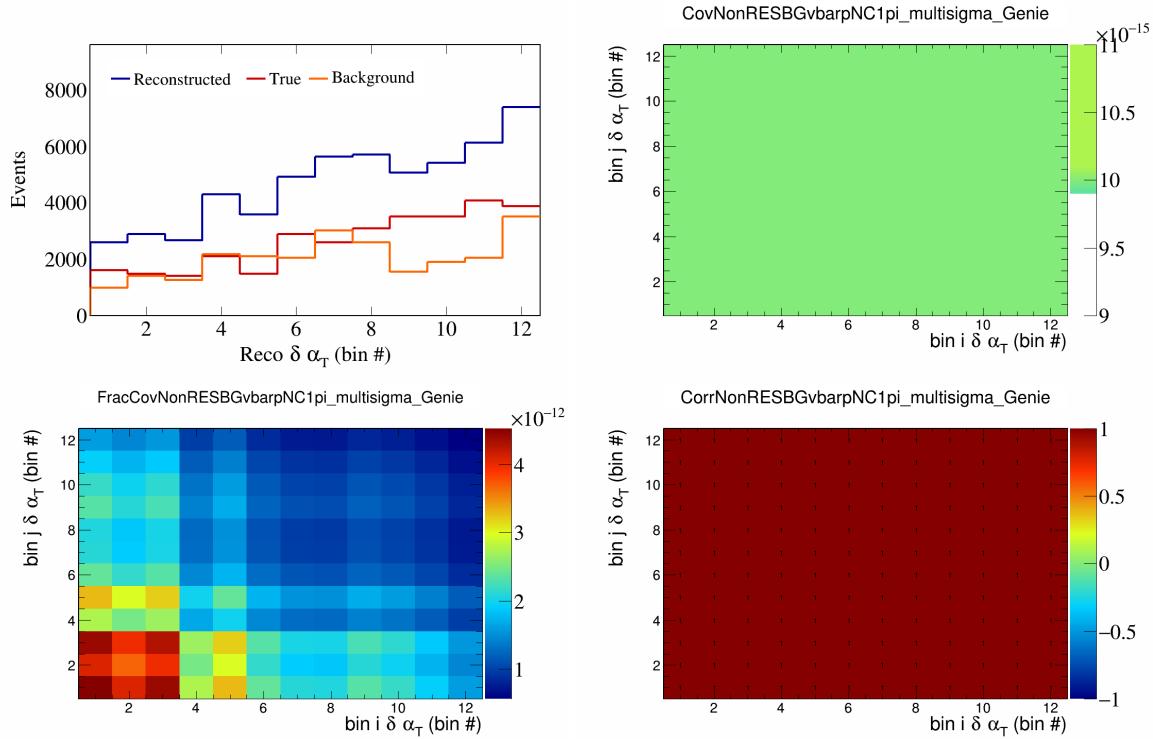


Figure 467: NonRESBGvbarpNC1pi variations for $\delta\alpha_T$ in $\cos(\theta_{\vec{p}_\mu})$.

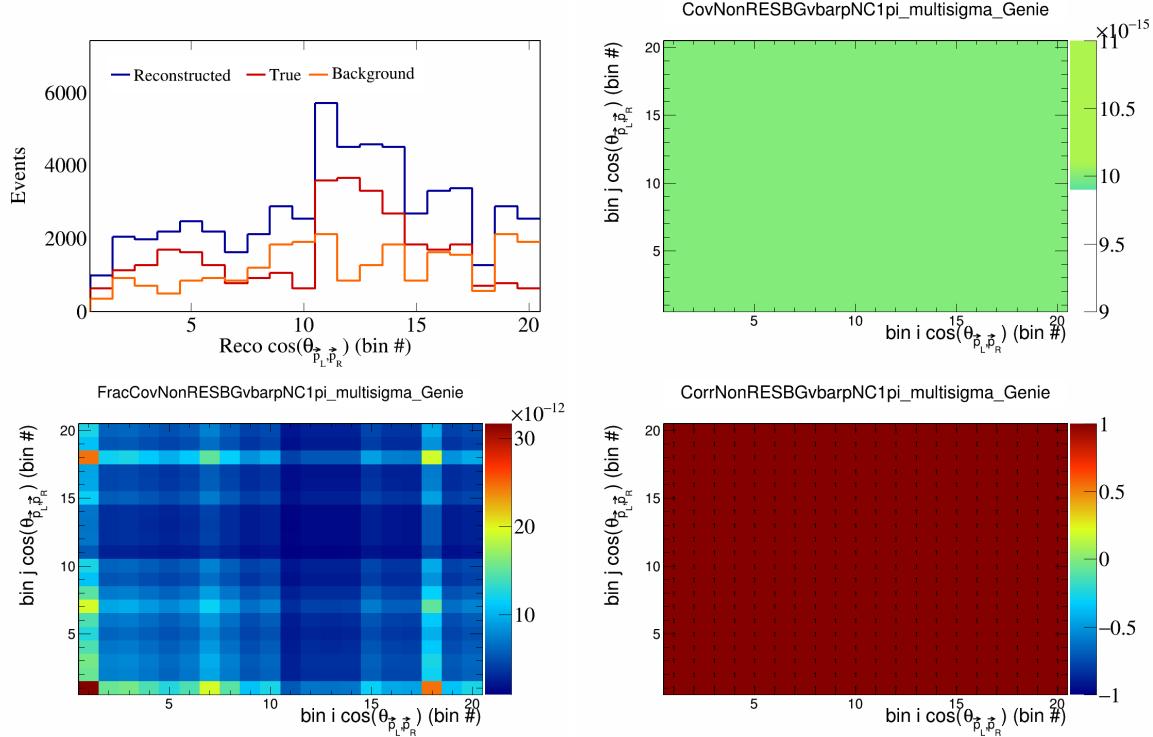


Figure 468: NonRESBGvbarpNC1pi variations for $\cos(\theta_{\vec{p}_L, \vec{p}_R})$ in $\cos(\theta_{\vec{p}_\mu})$.

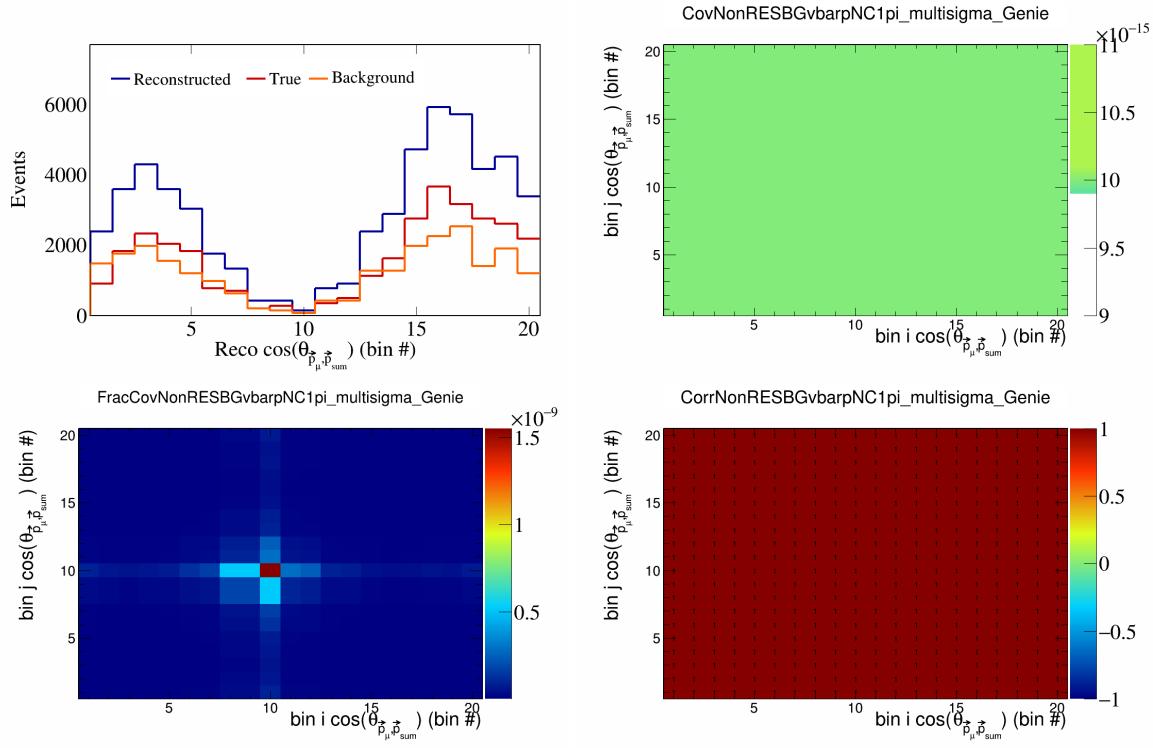


Figure 469: NonRESBGvbarpNC1pi variations for $\cos(\theta_{\vec{p}_\mu})$ in $\cos(\theta_{\vec{p}_\mu})$.

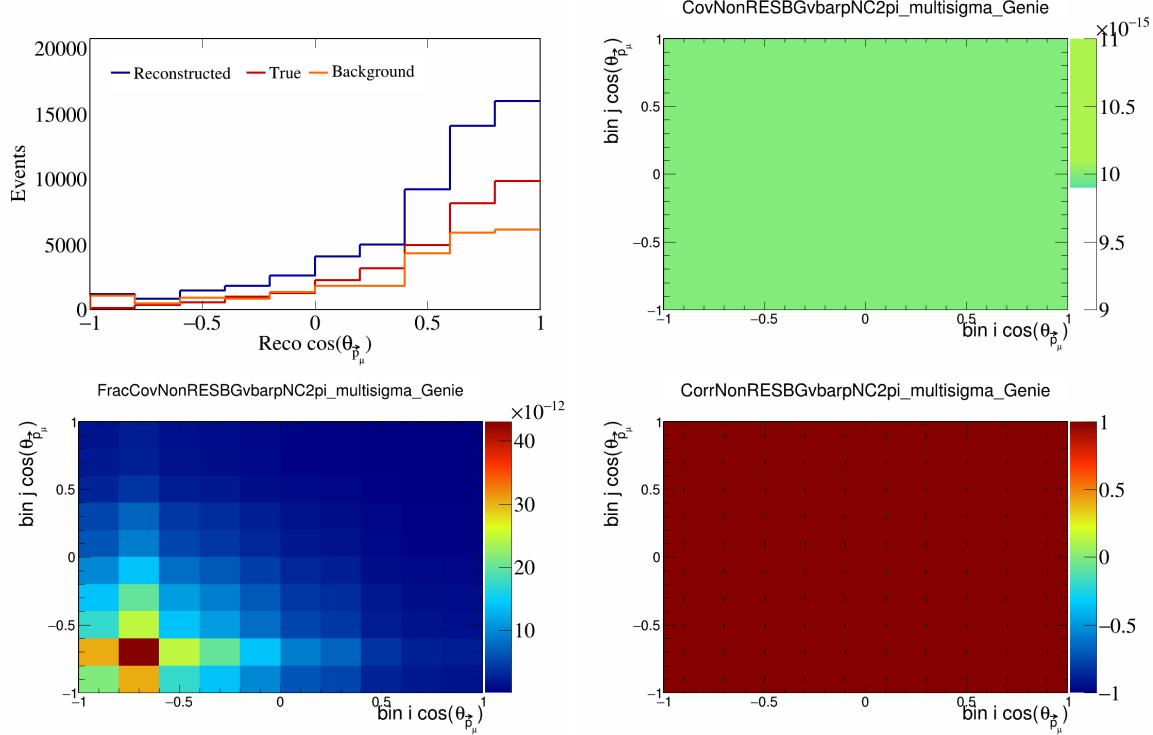


Figure 470: NonRESBGvbarpNC2pi variations for $\cos(\theta_{\vec{p}_\mu})$.

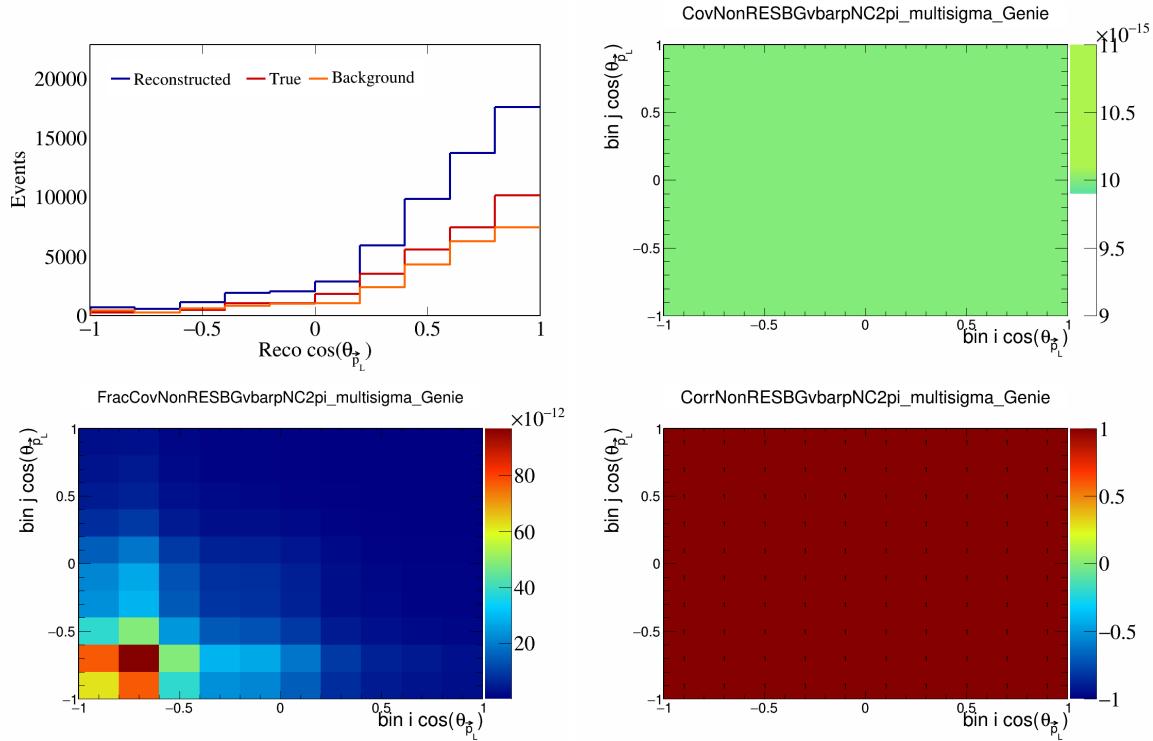


Figure 471: NonRESBGvbarpiNC2pi variations for $\cos(\theta_{\vec{p}_L})$.

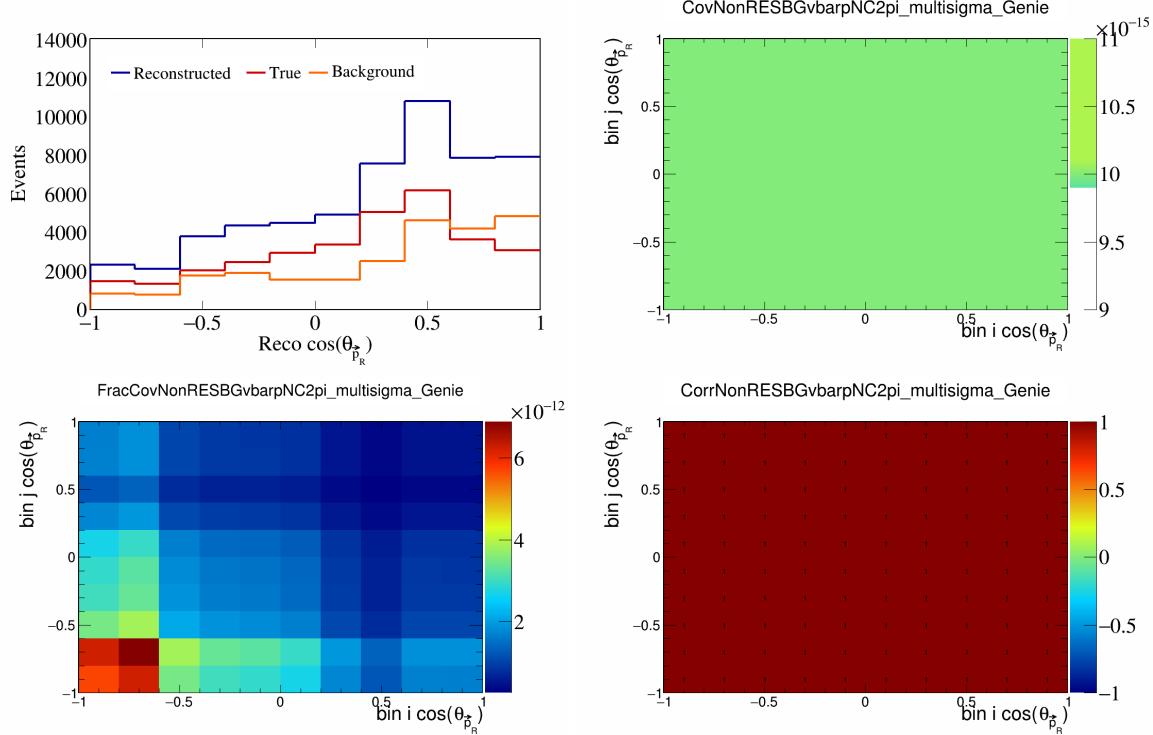


Figure 472: NonRESBGvbarpiNC2pi variations for $\cos(\theta_{\vec{p}_R})$.

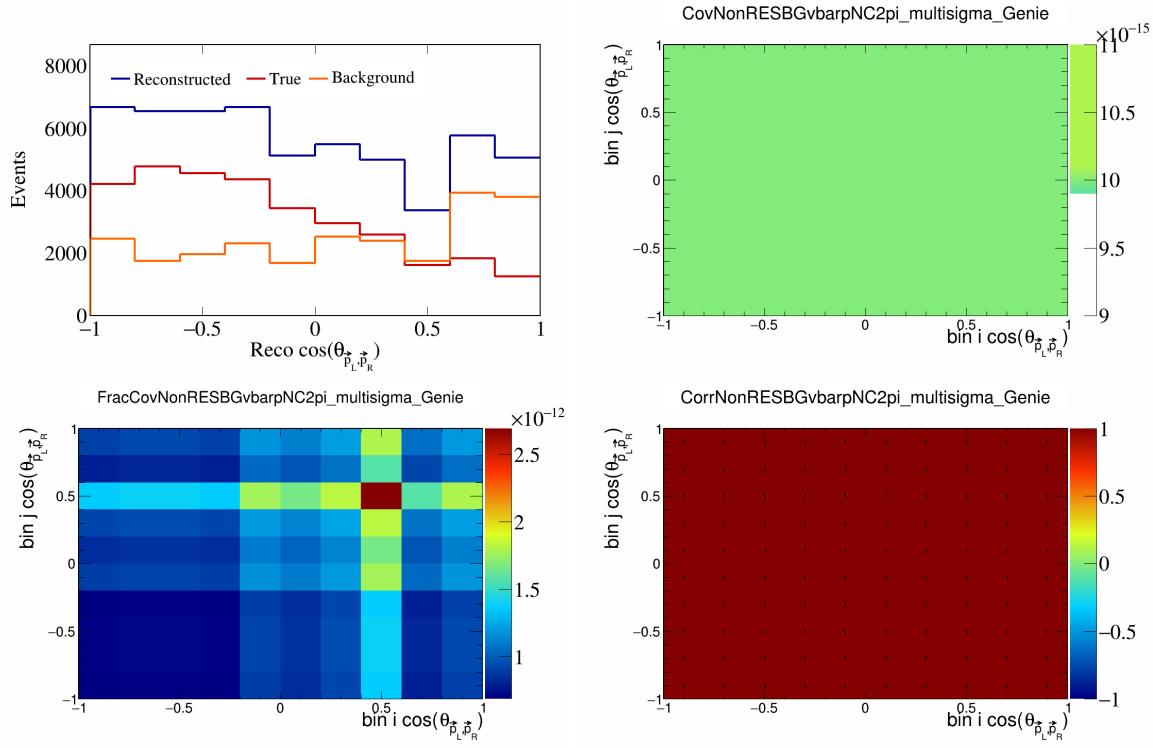


Figure 473: NonRESBGvbarpNC2pi variations for $\cos(\theta_{\vec{p}_L, \vec{p}_R})$.

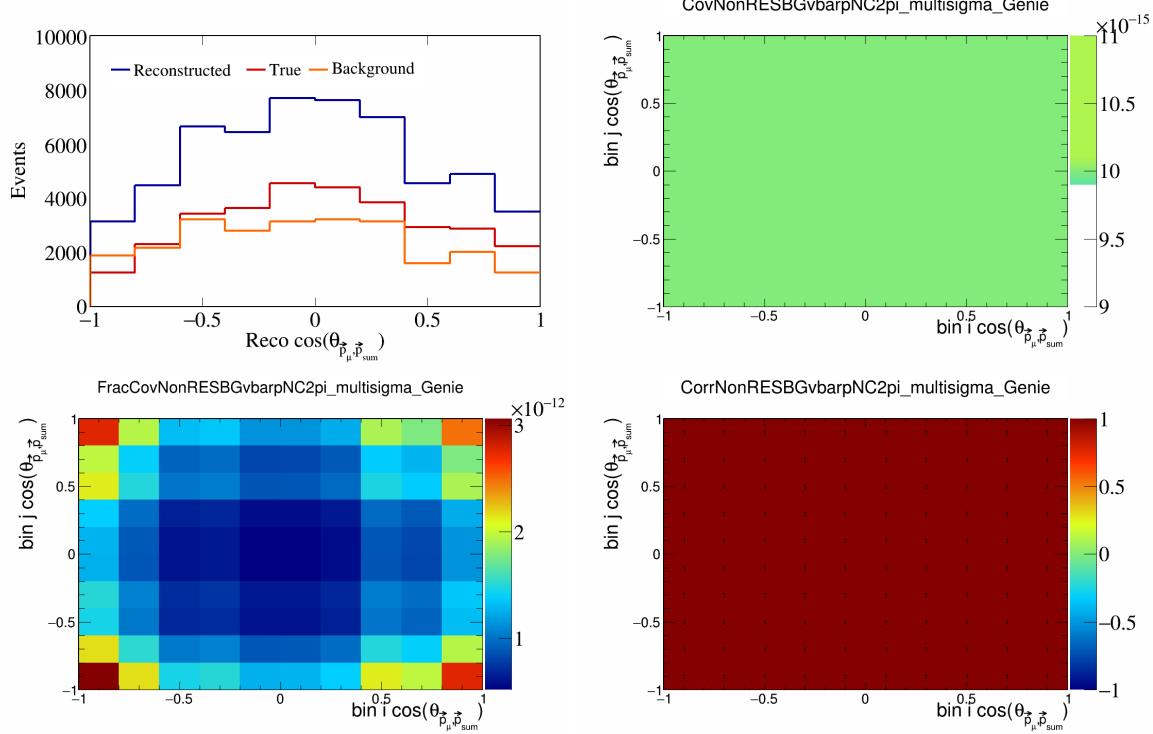


Figure 474: NonRESBGvbarpNC2pi variations for $\cos(\theta_{\vec{p}_\mu, \vec{p}_{\text{sum}}})$.

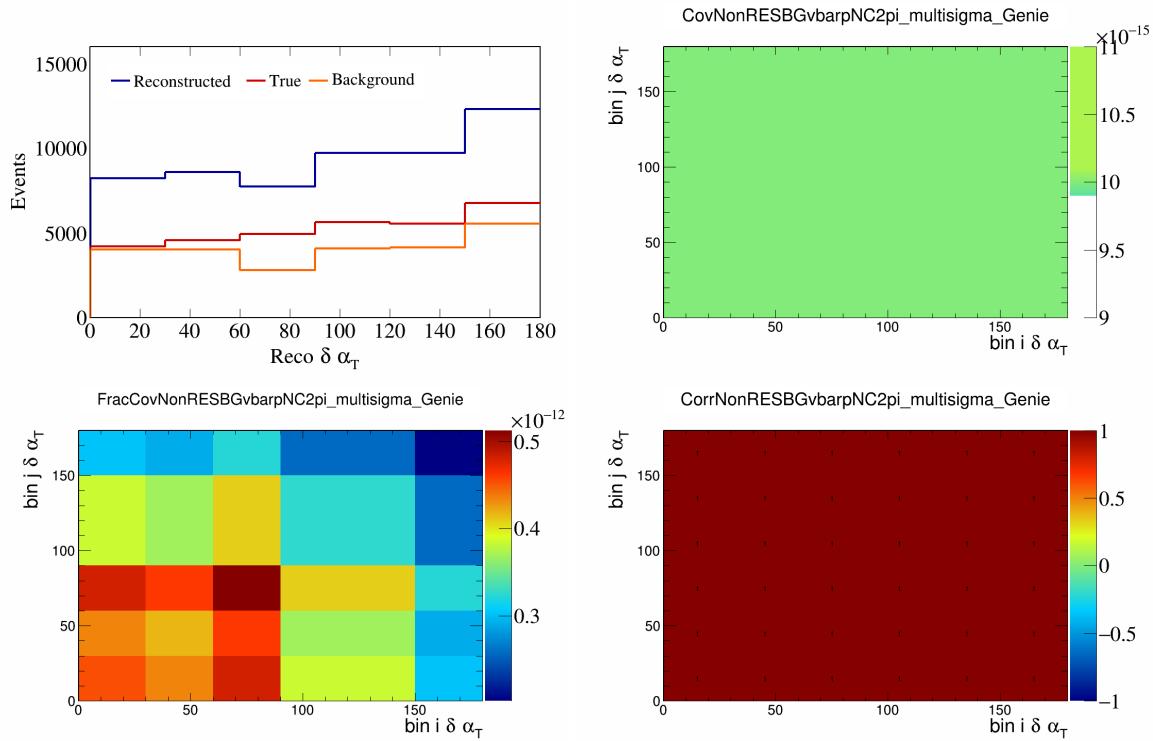


Figure 475: NonRESBGvbarpNC2pi variations for $\delta\alpha_T$.

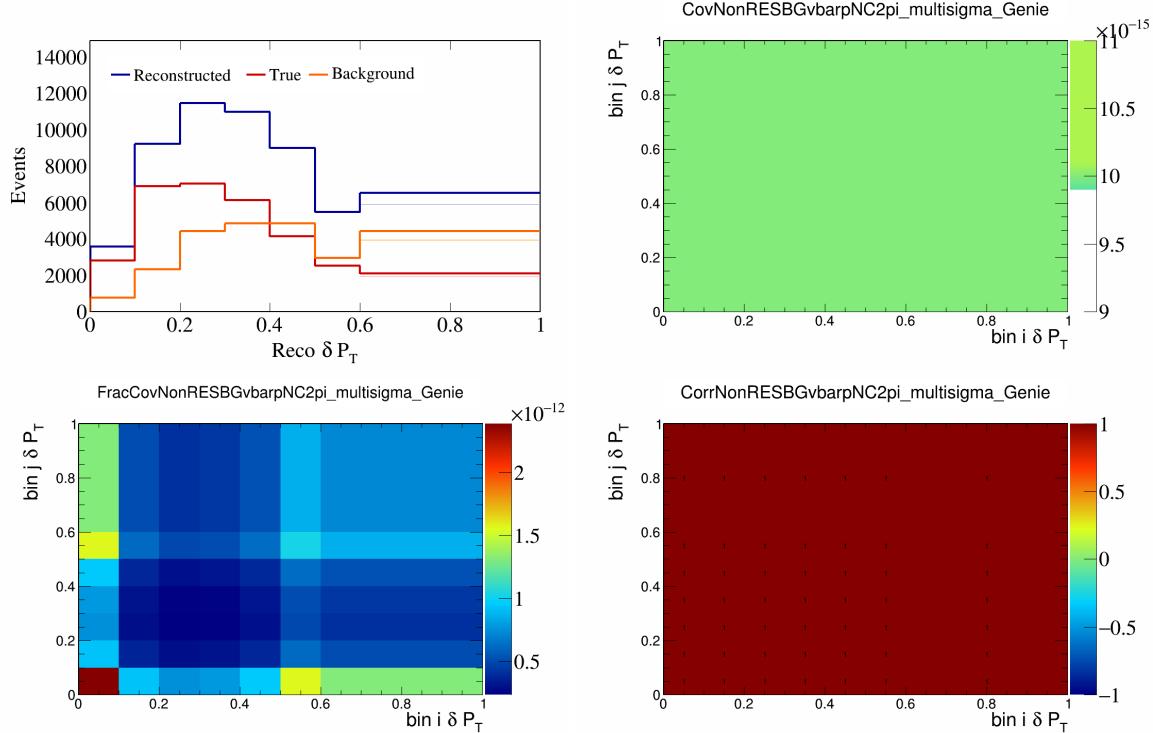


Figure 476: NonRESBGvbarpNC2pi variations for δP_T .

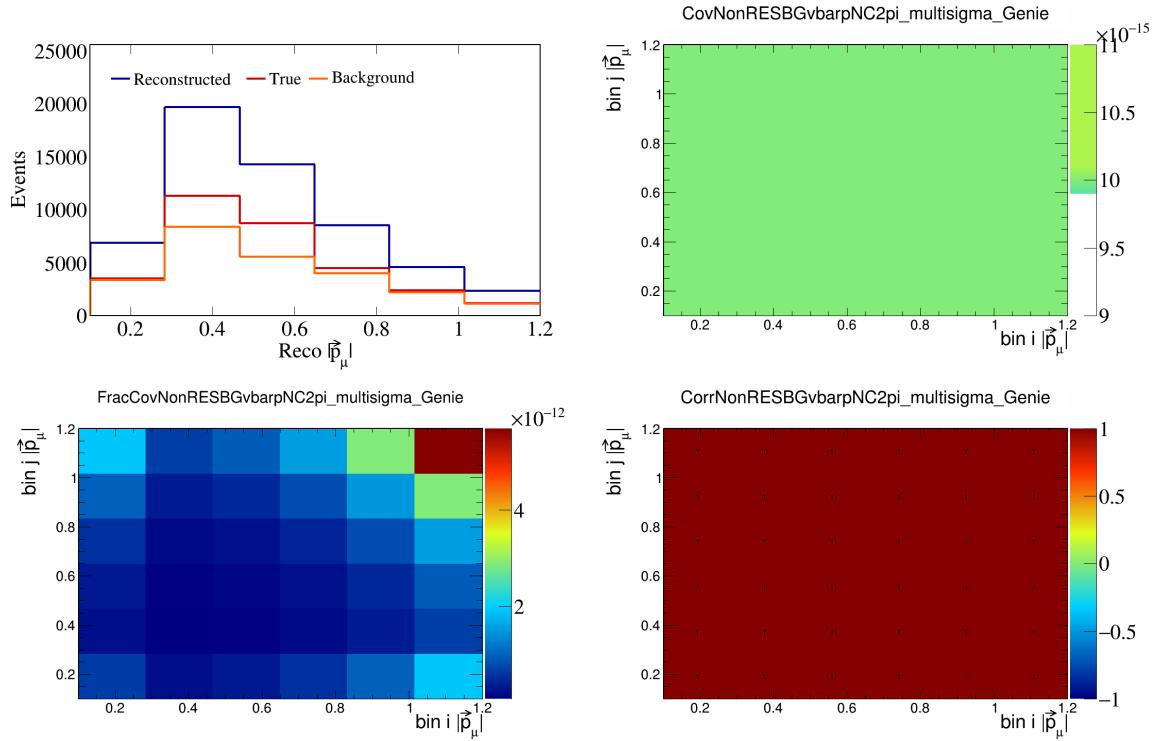


Figure 477: NonRESBGvbarpNC2pi variations for $|\vec{p}_\mu|$.

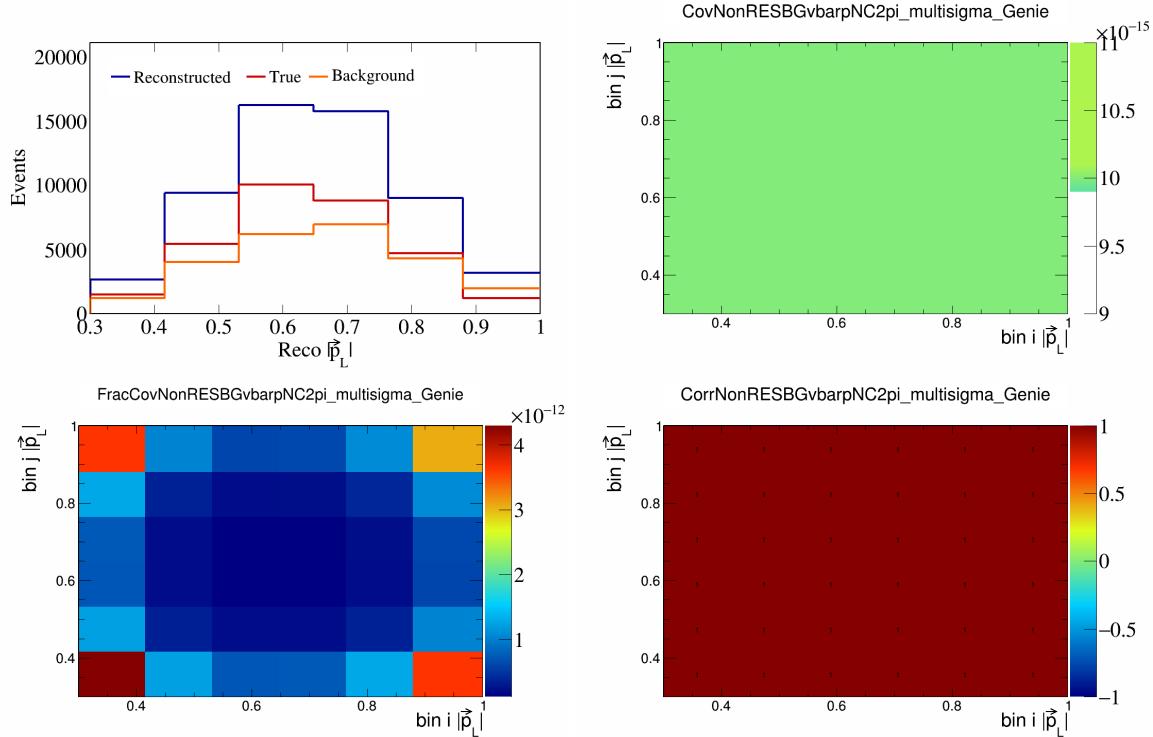


Figure 478: NonRESBGvbarpNC2pi variations for $|\vec{p}_L|$.

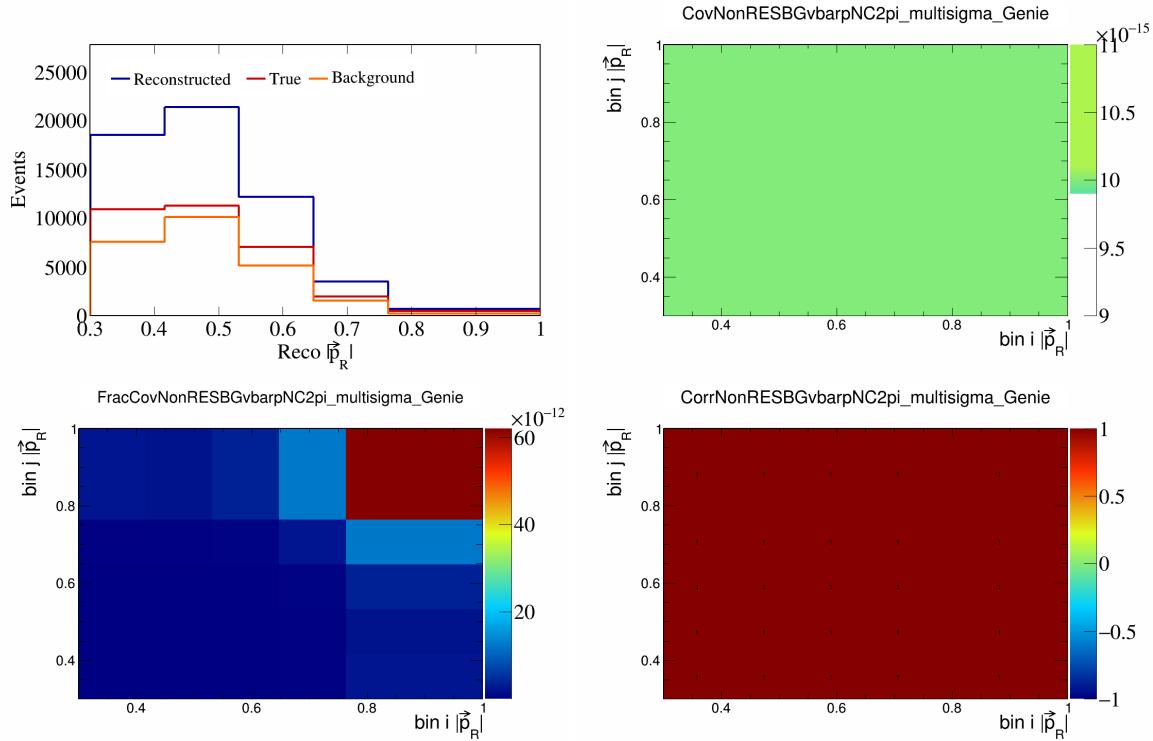


Figure 479: NonRESBGvbarpNC2pi variations for $|\vec{p}_R|$.

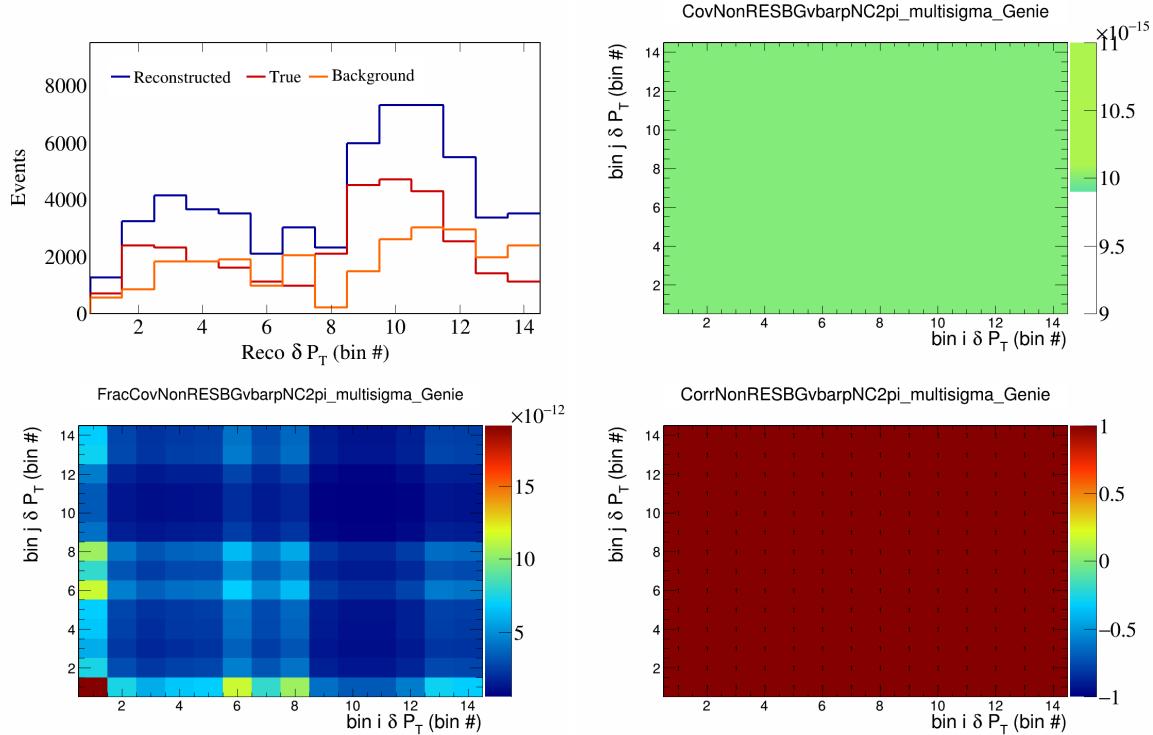


Figure 480: NonRESBGvbarpNC2pi variations for δP_T in $\cos(\theta_{\vec{p}_\mu})$.

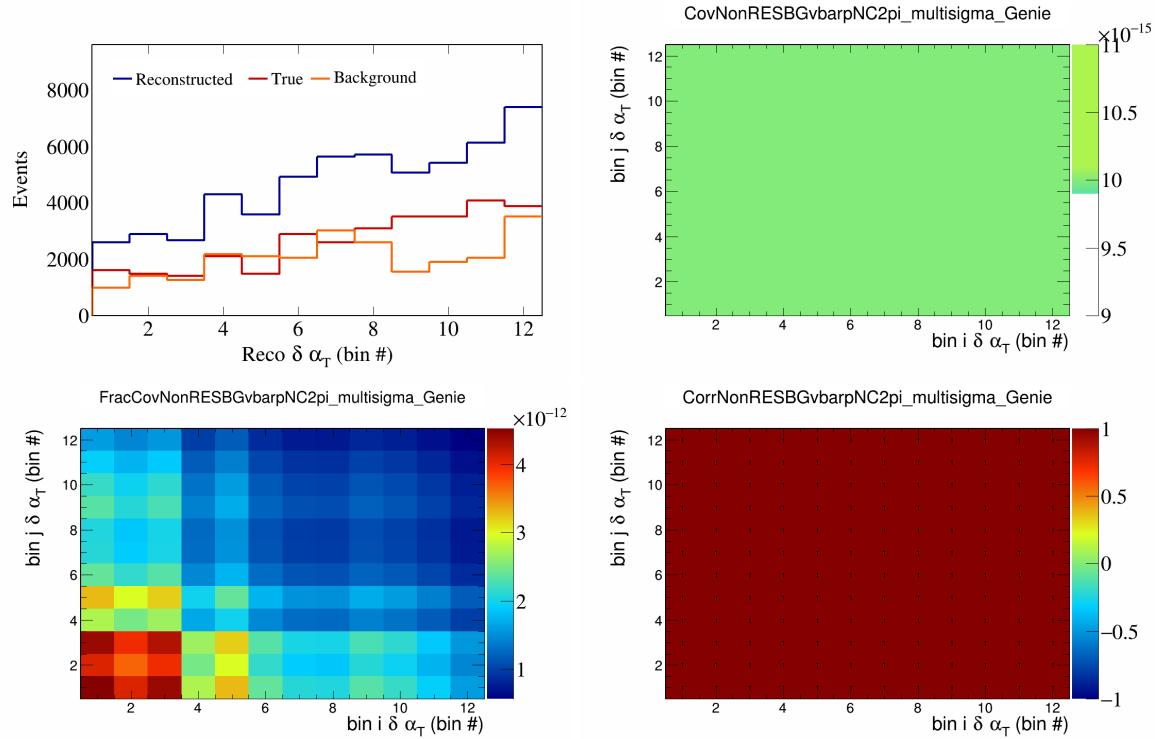


Figure 481: NonRESBGvbarNC2pi variations for $\delta\alpha_T$ in $\cos(\theta_{\vec{p}_\mu})$.

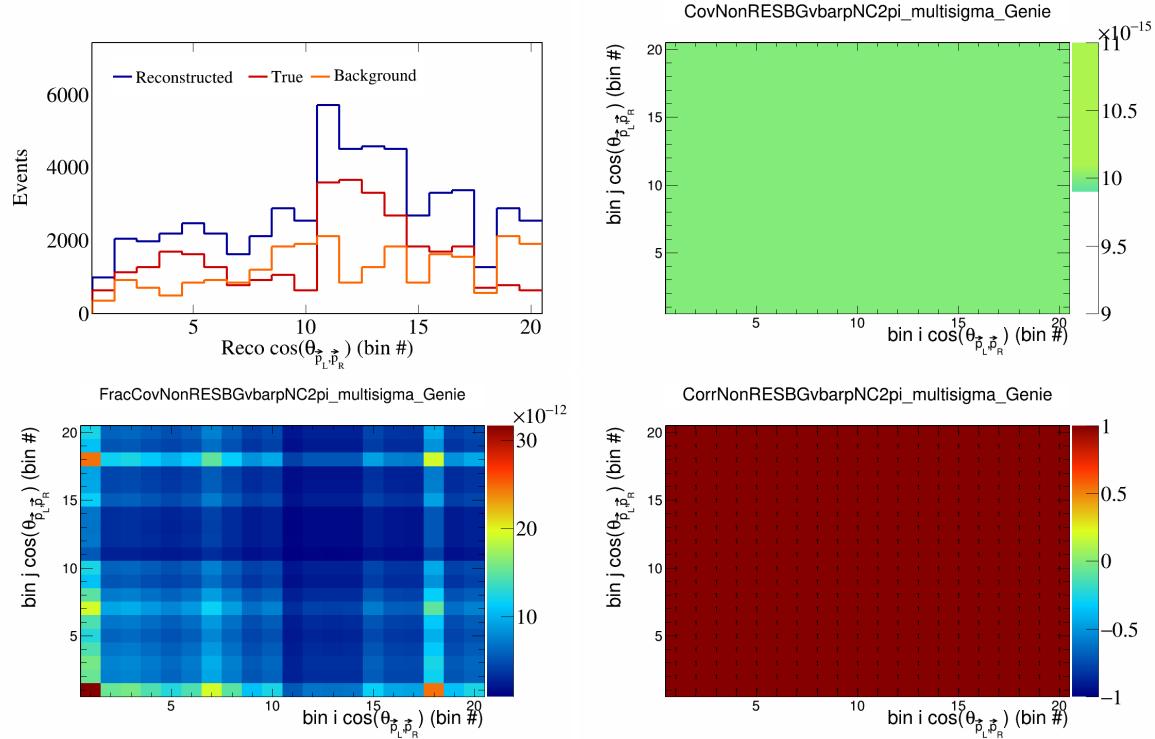


Figure 482: NonRESBGvbarNC2pi variations for $\cos(\theta_{\vec{p}_L, \vec{p}_R})$ in $\cos(\theta_{\vec{p}_\mu})$.

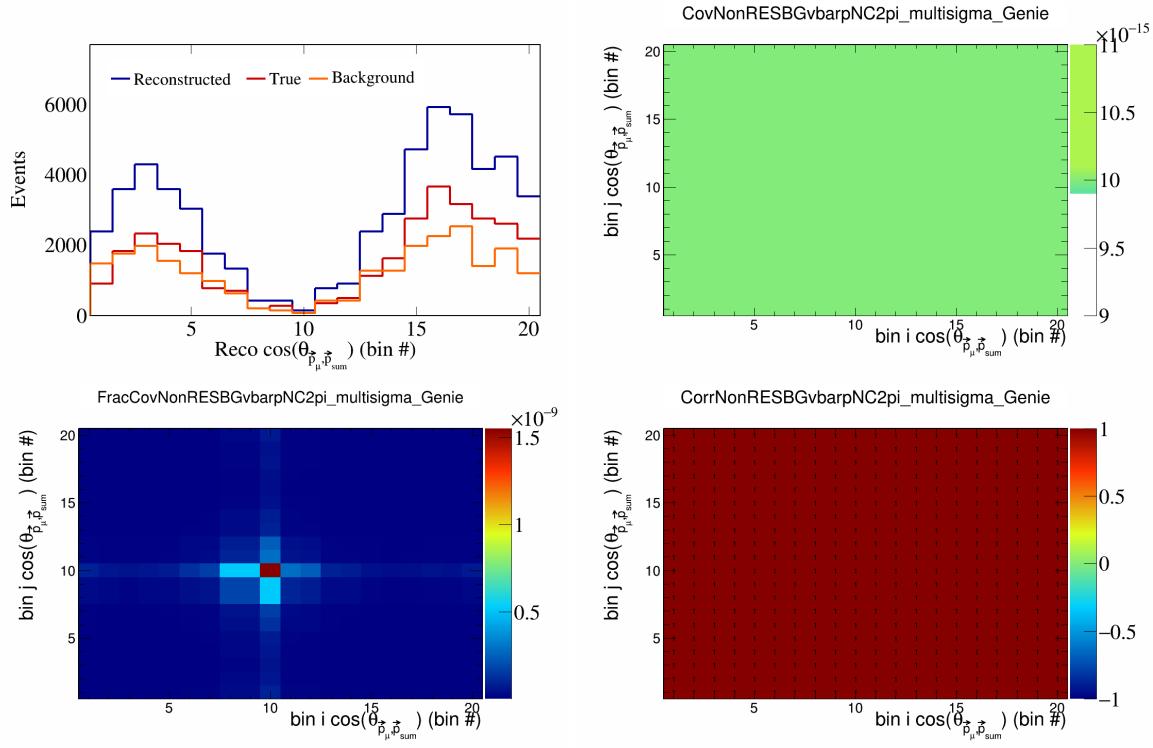


Figure 483: NonRESBGvbarpNC2pi variations for $\cos(\theta_{\vec{p}_\mu} \cdot \vec{p}_{\text{sum}})$ in $\cos(\theta_{\vec{p}_\mu})$.

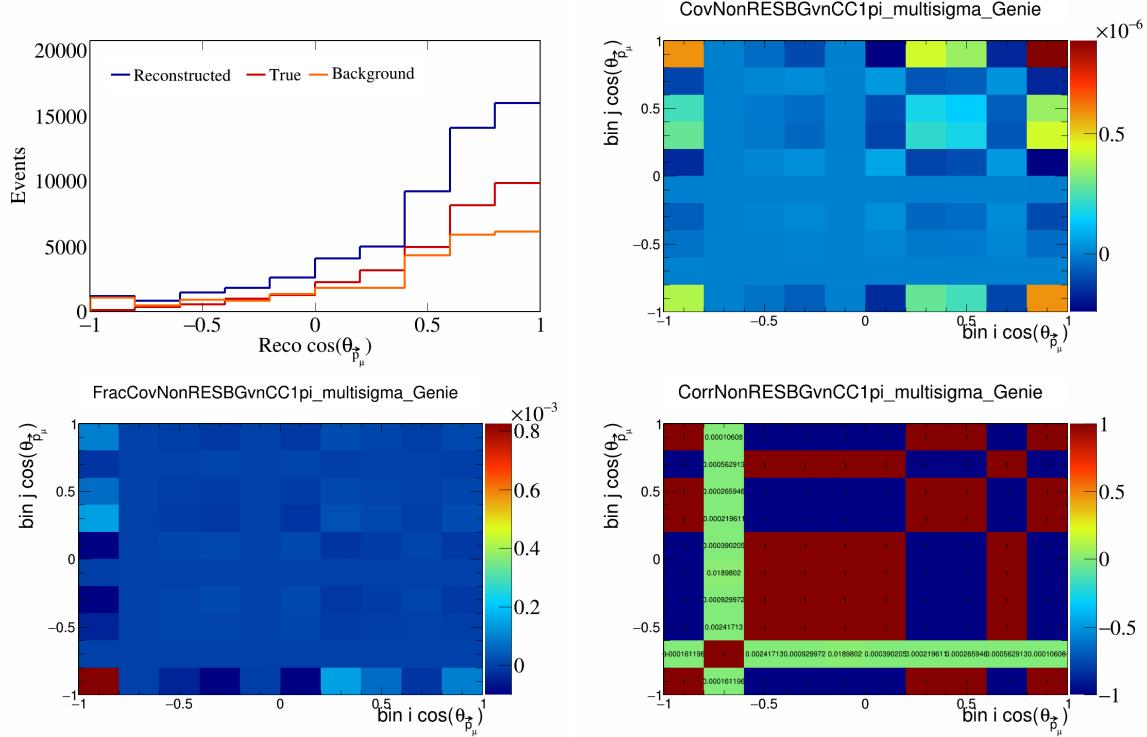


Figure 484: NonRESBGvnCC1pi variations for $\cos(\theta_{\vec{p}_\mu})$.

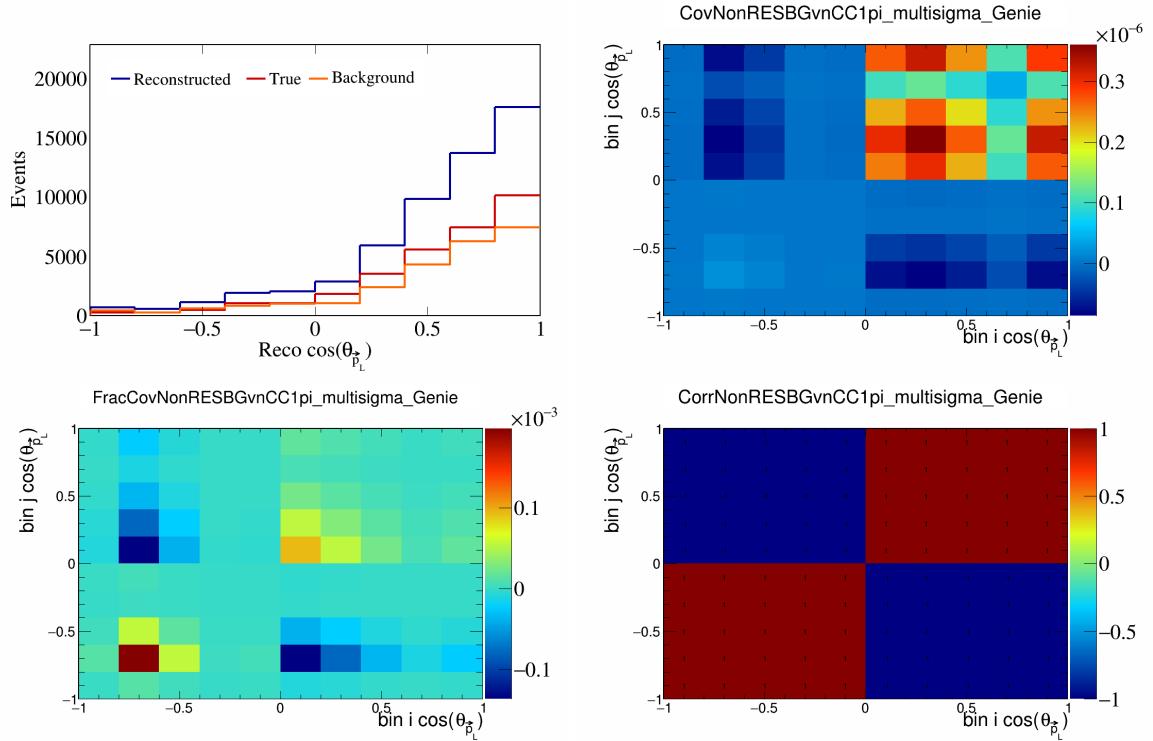


Figure 485: NonRESBGvnCC1pi variations for $\cos(\theta_{\vec{p}_L})$.

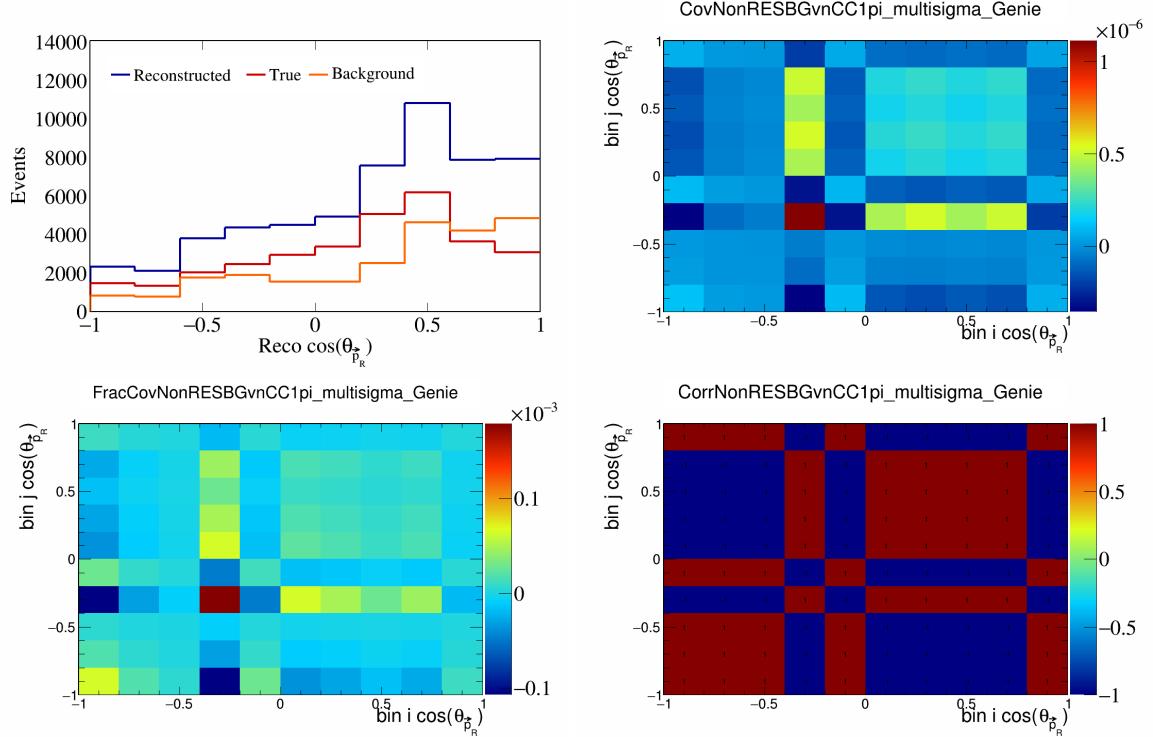


Figure 486: NonRESBGvnCC1pi variations for $\cos(\theta_{\vec{p}_R})$.

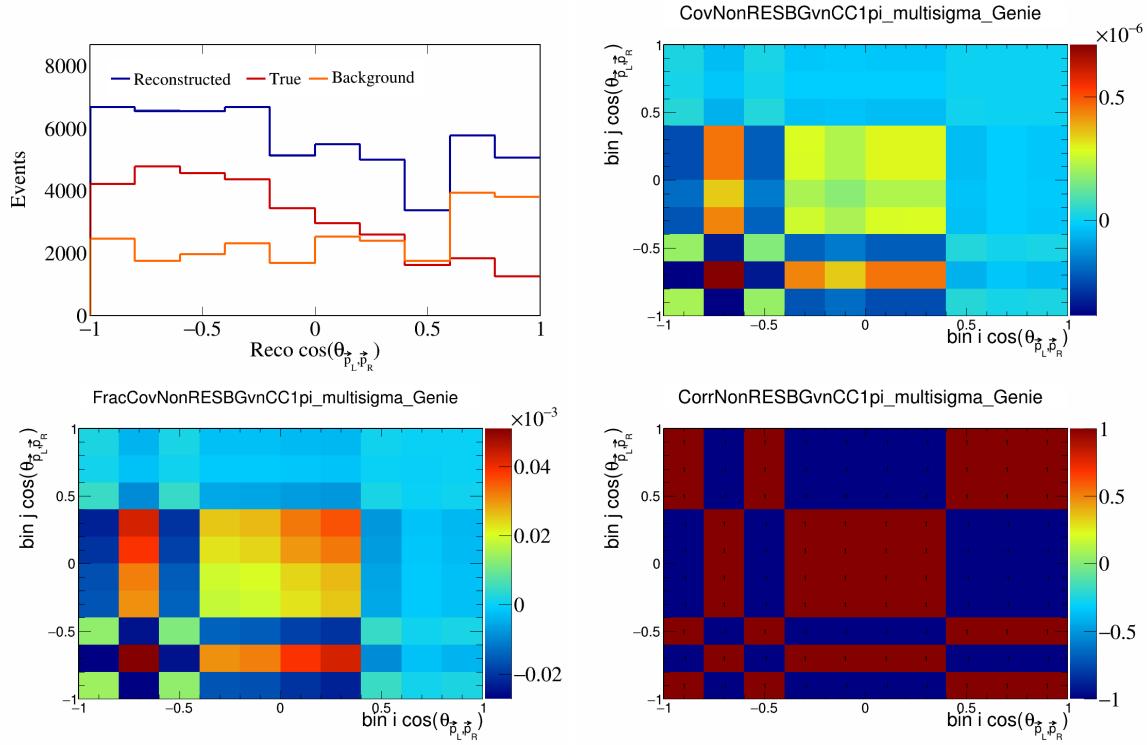


Figure 487: NonRESBGvnCC1pi variations for $\cos(\theta_{\vec{p}_L, \vec{p}_R})$.

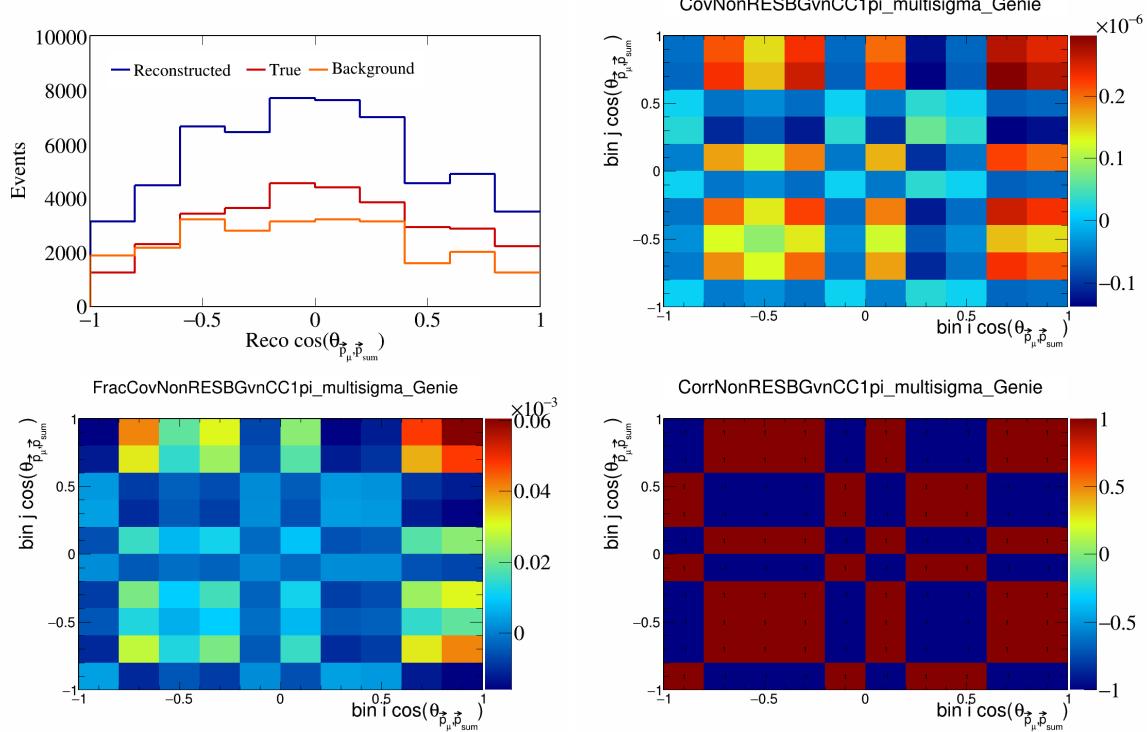


Figure 488: NonRESBGvnCC1pi variations for $\cos(\theta_{\vec{p}_\mu, \vec{p}_{\text{sum}}})$.

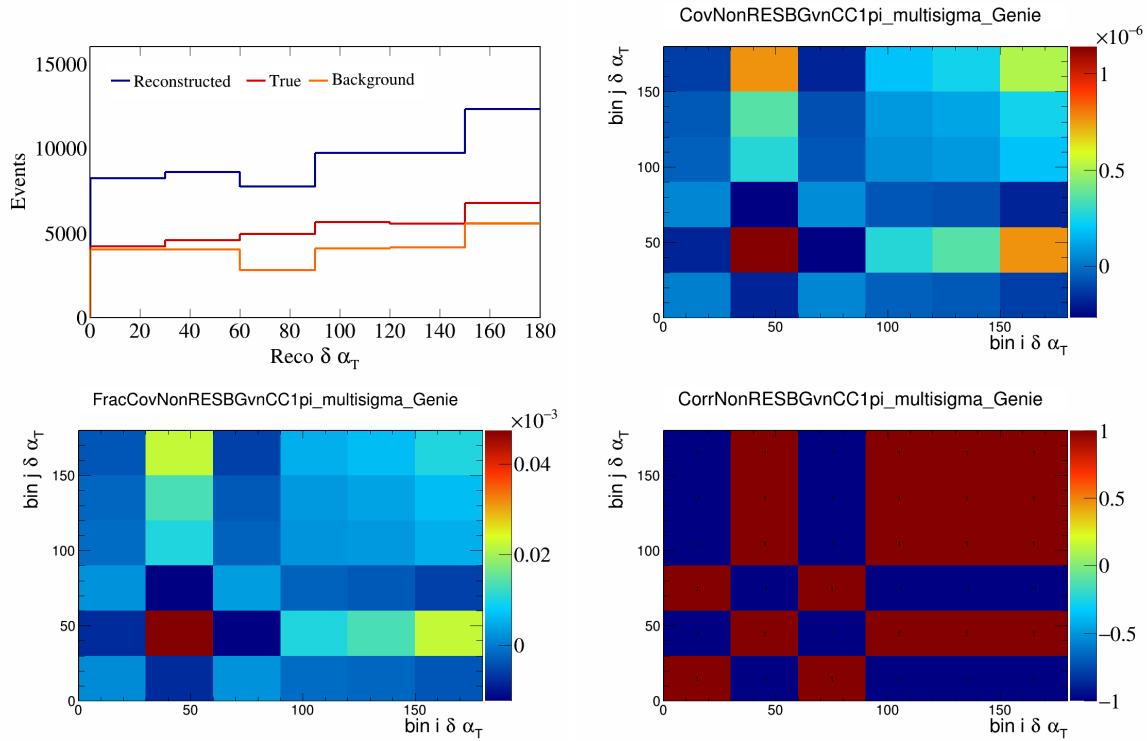


Figure 489: NonRESBGvnCC1pi variations for $\delta\alpha_T$.

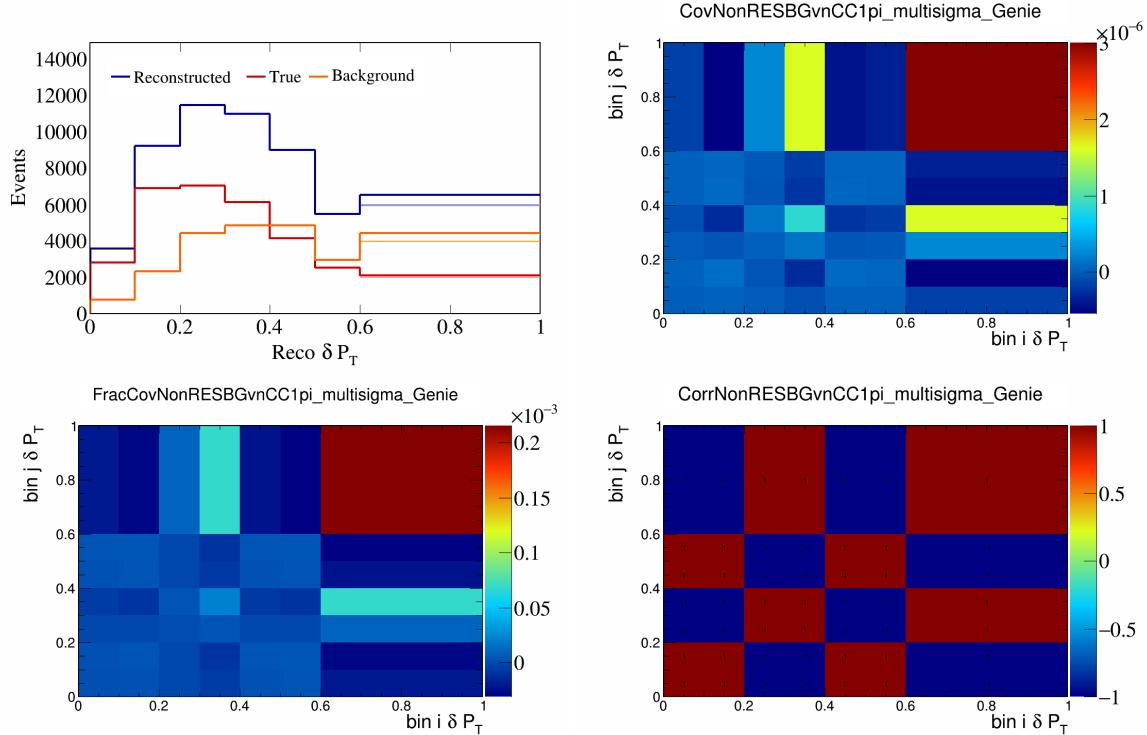


Figure 490: NonRESBGvnCC1pi variations for δP_T .

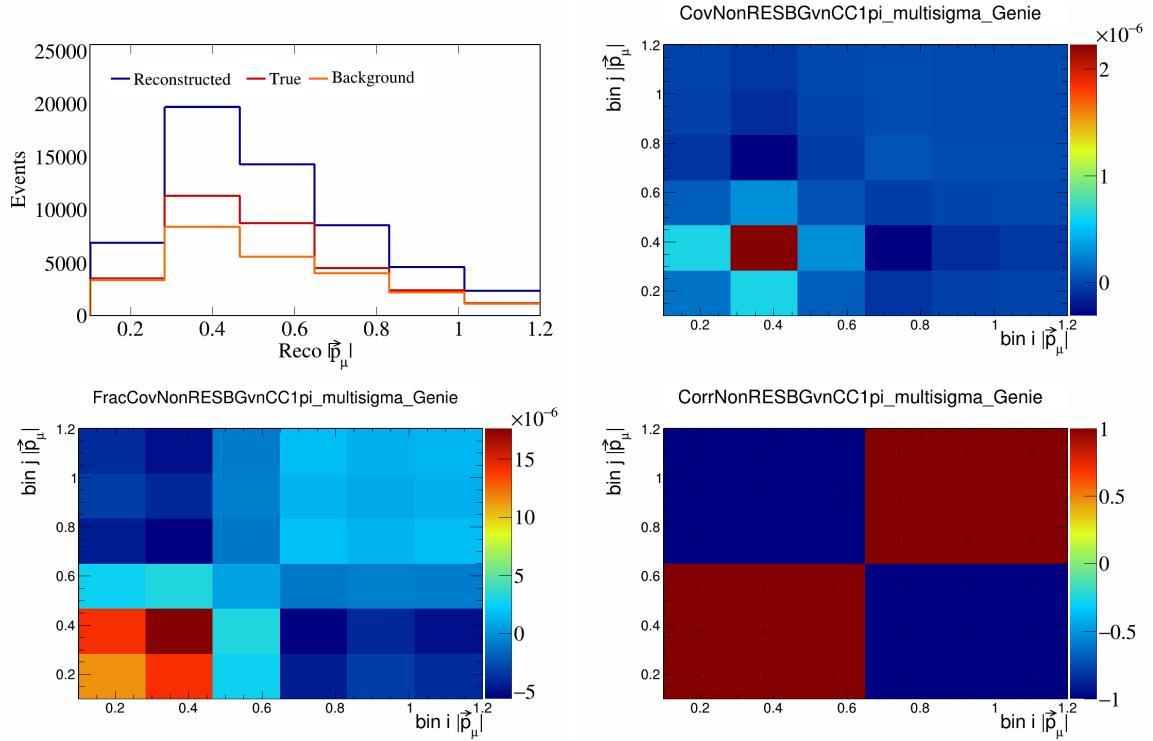


Figure 491: NonRESBGvnCC1pi variations for $|\vec{p}_\mu|$.

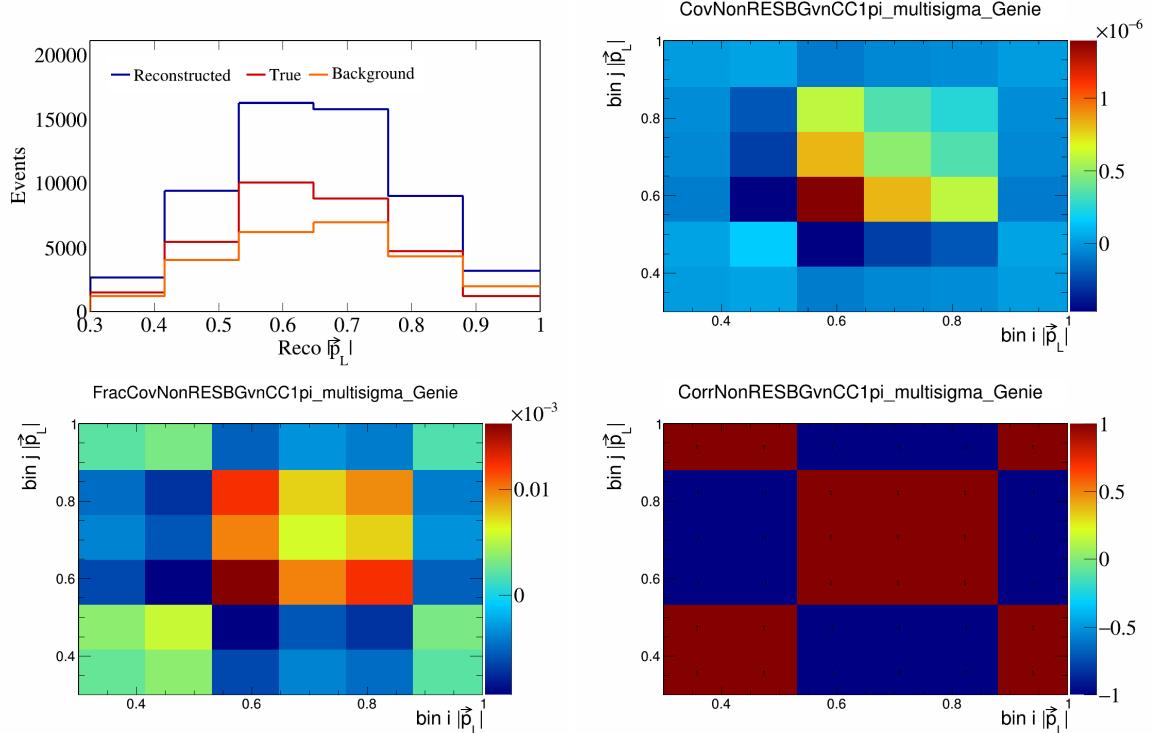


Figure 492: NonRESBGvnCC1pi variations for $|\vec{p}_L|$.

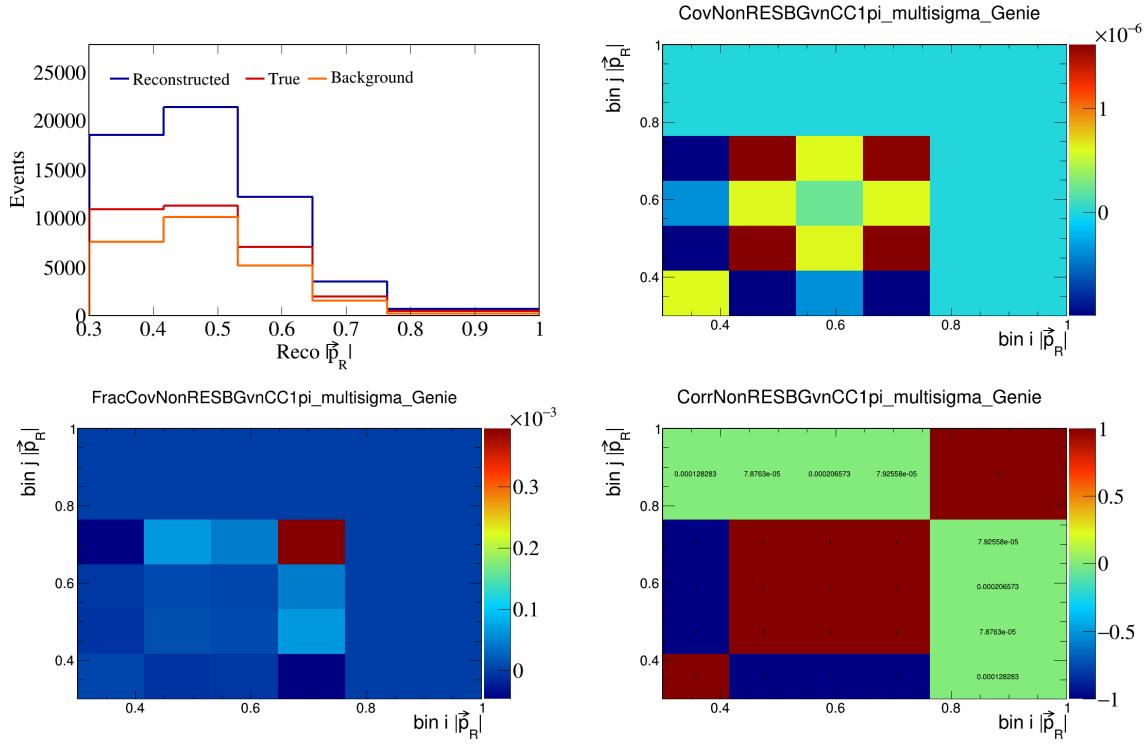


Figure 493: NonRESBGvnCC1pi variations for $|\vec{p}_R|$.

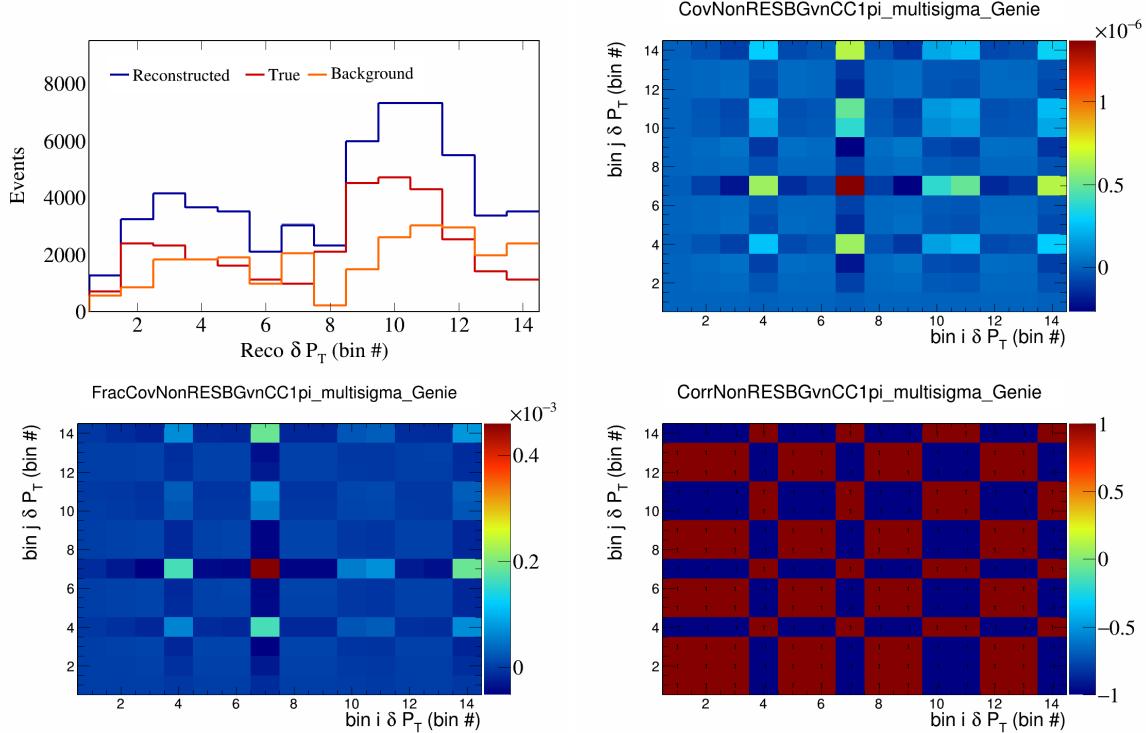


Figure 494: NonRESBGvnCC1pi variations for δP_T in $\cos(\theta_{\vec{p}_\mu})$.

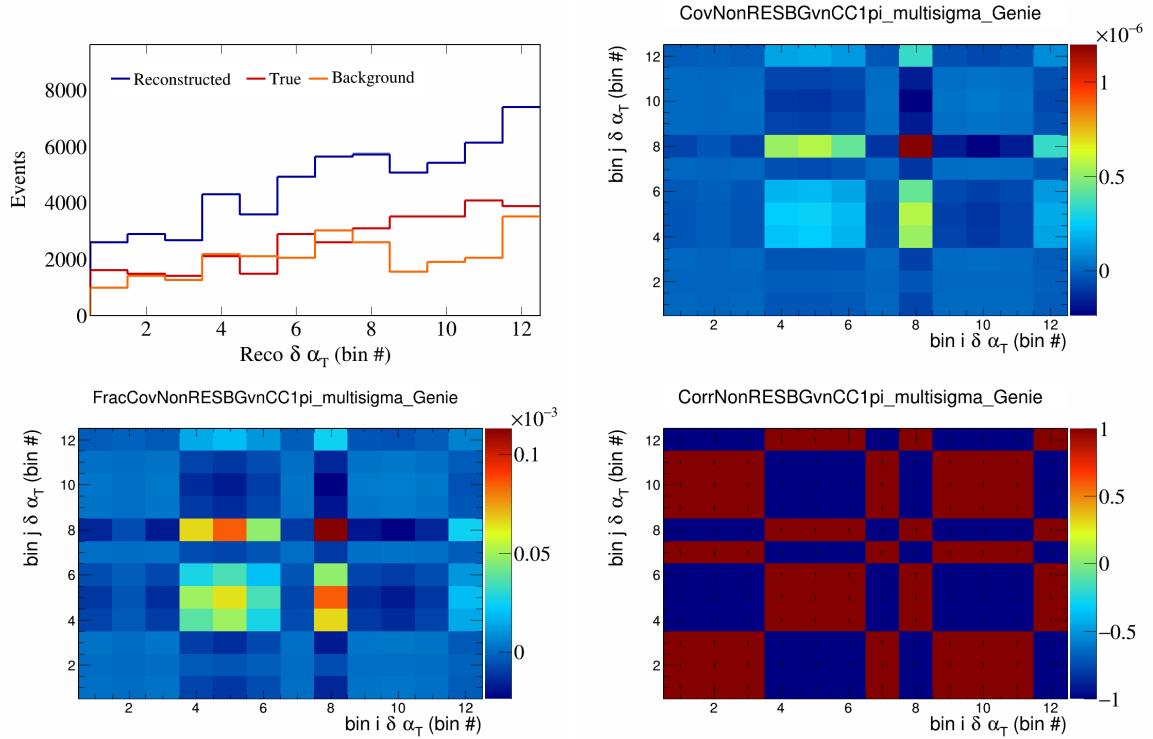


Figure 495: NonRESBGvnCC1pi variations for $\delta\alpha_T$ in $\cos(\theta_{\vec{p}_\mu})$.

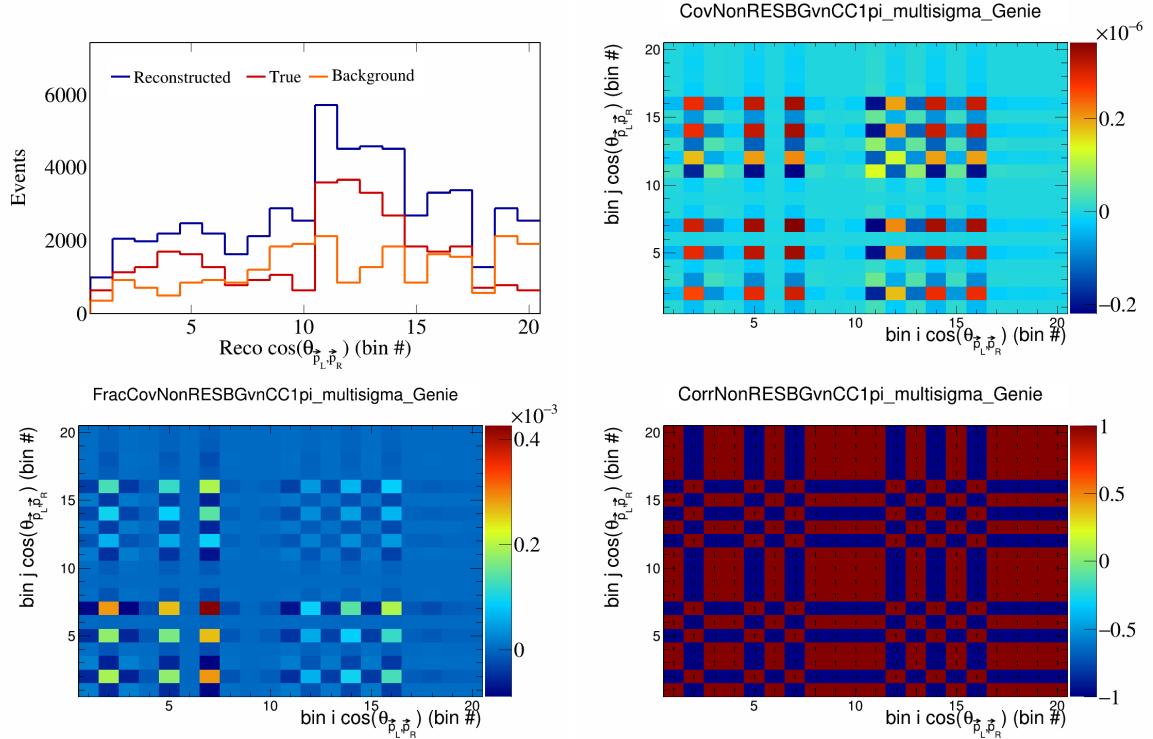


Figure 496: NonRESBGvnCC1pi variations for $\cos(\theta_{\vec{p}_L, \vec{p}_R})$ in $\cos(\theta_{\vec{p}_\mu})$.

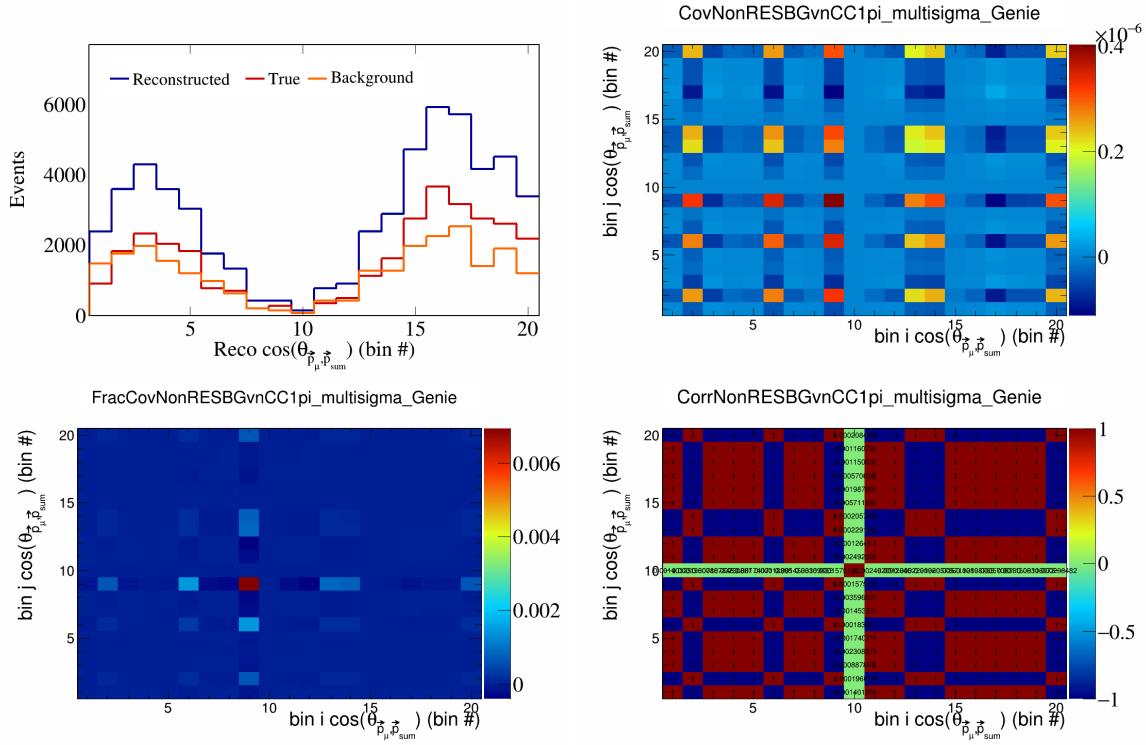


Figure 497: NonRESBGvnCC1pi variations for $\cos(\theta_{\vec{p}_\mu, \vec{p}_{\text{sum}}})$ in $\cos(\theta_{\vec{p}_\mu})$.

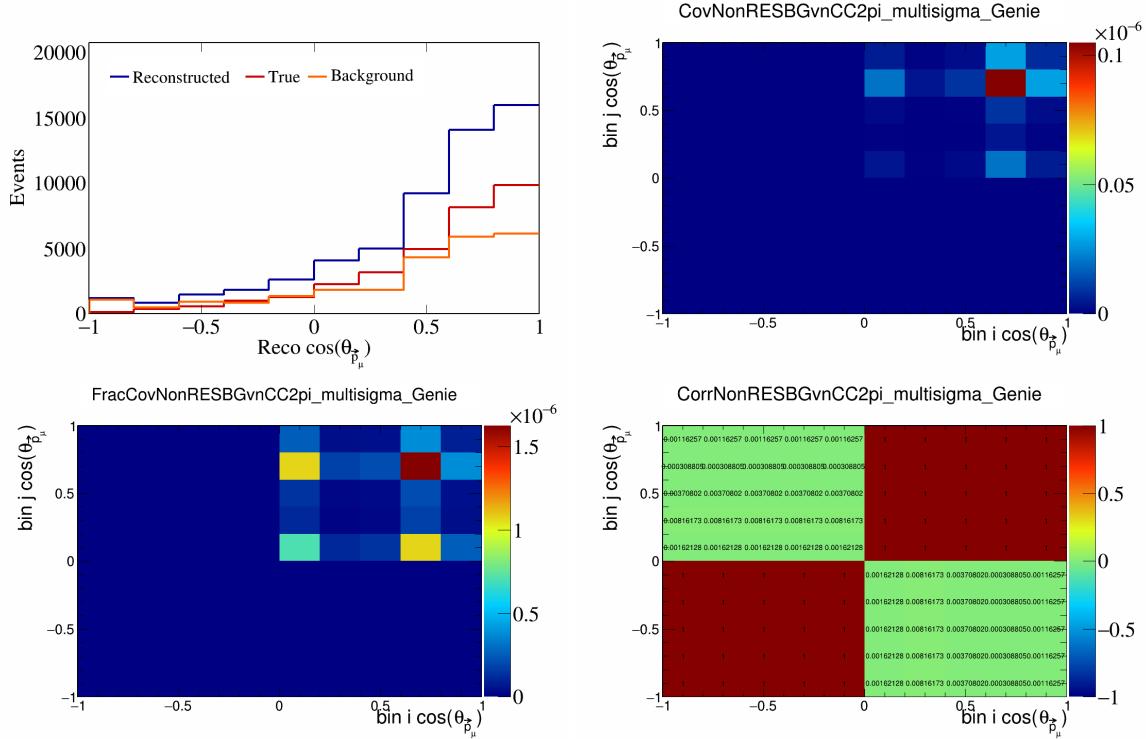


Figure 498: NonRESBGvnCC2pi variations for $\cos(\theta_{\vec{p}_\mu})$.

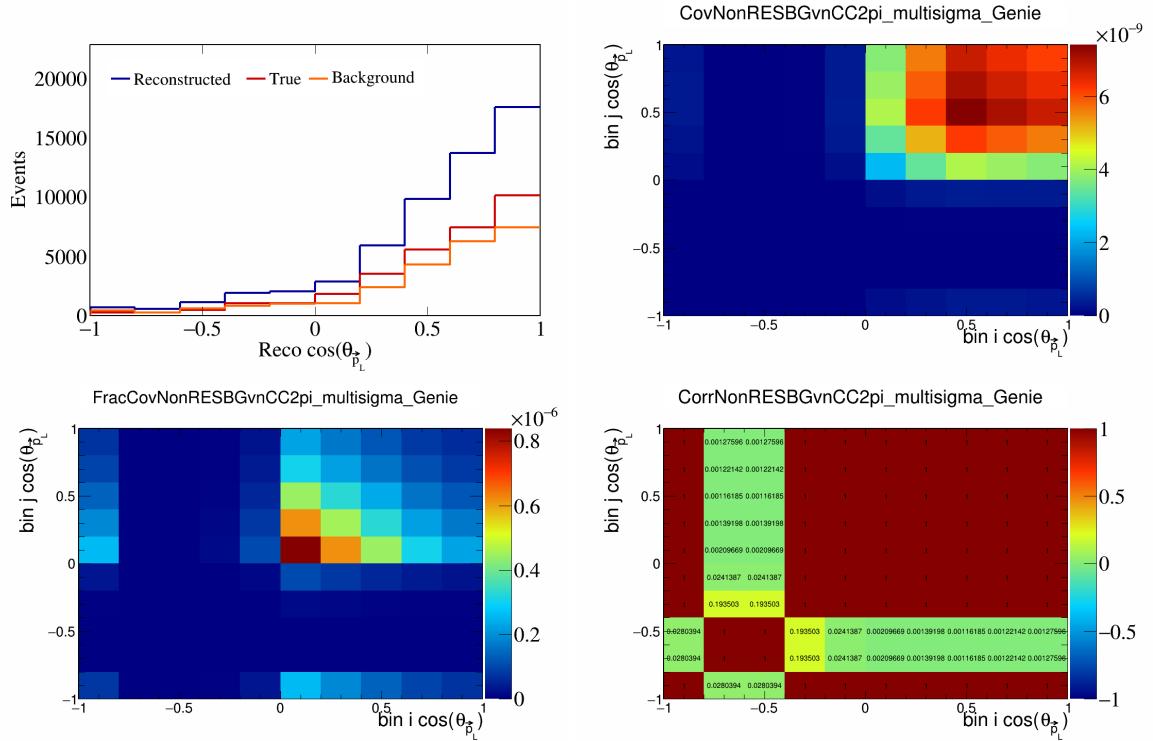


Figure 499: NonRESBGvnCC2pi variations for $\cos(\theta_{\vec{p}_L})$.

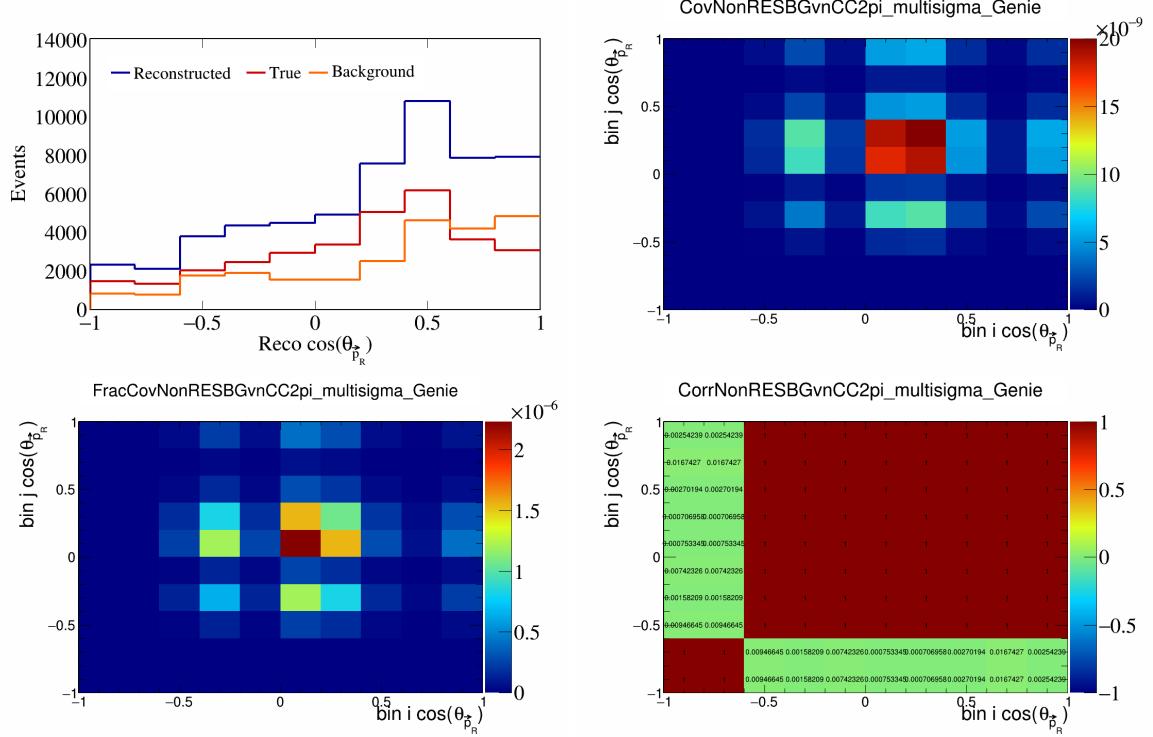


Figure 500: NonRESBGvnCC2pi variations for $\cos(\theta_{\vec{p}_R})$.

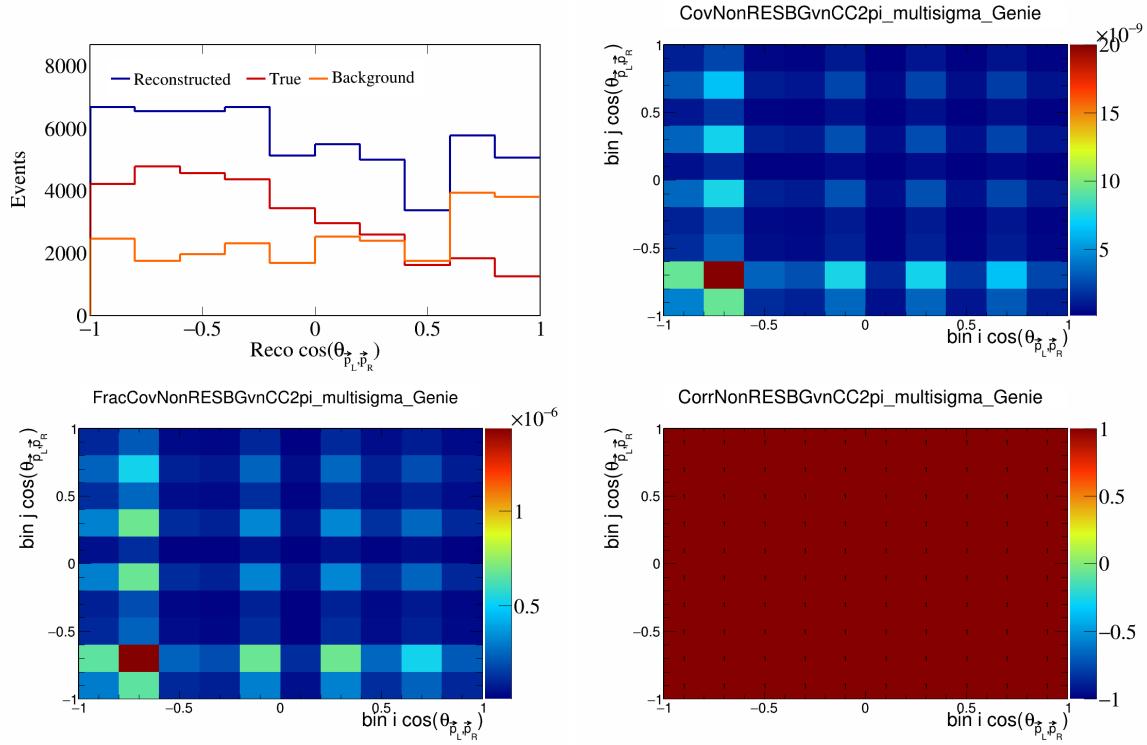


Figure 501: NonRESBGvnCC2pi variations for $\cos(\theta_{\vec{p}_L, \vec{p}_R})$.

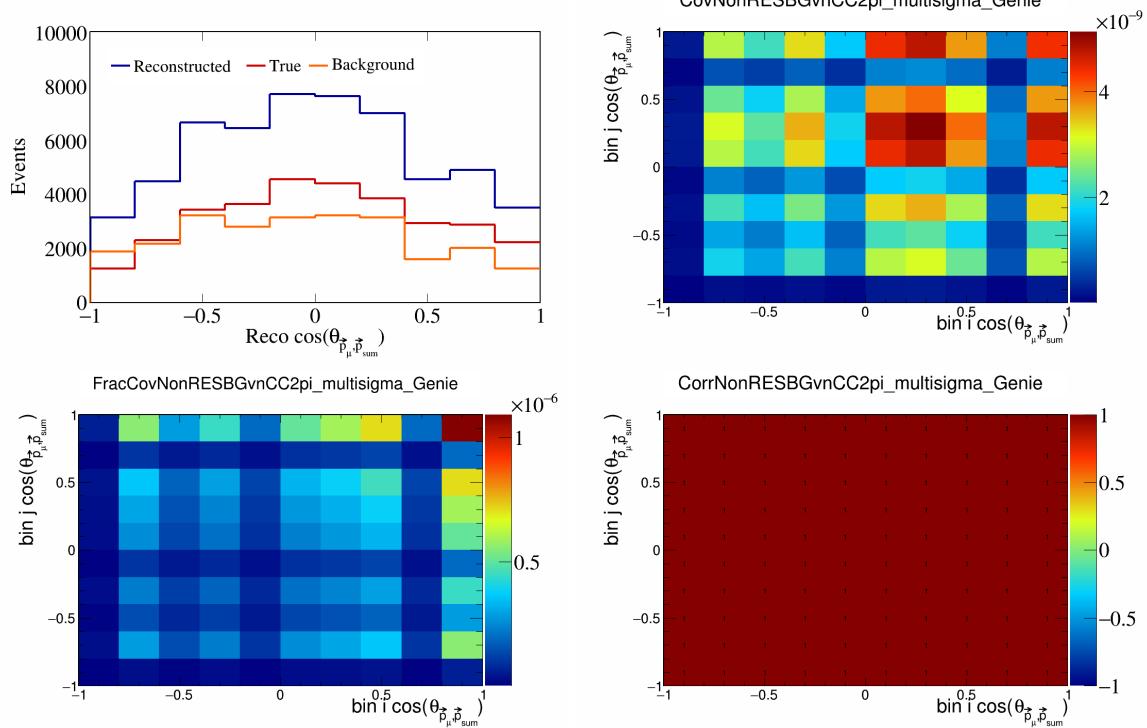


Figure 502: NonRESBGvnCC2pi variations for $\cos(\theta_{\vec{p}_\mu, \vec{p}_{\text{sum}}})$.

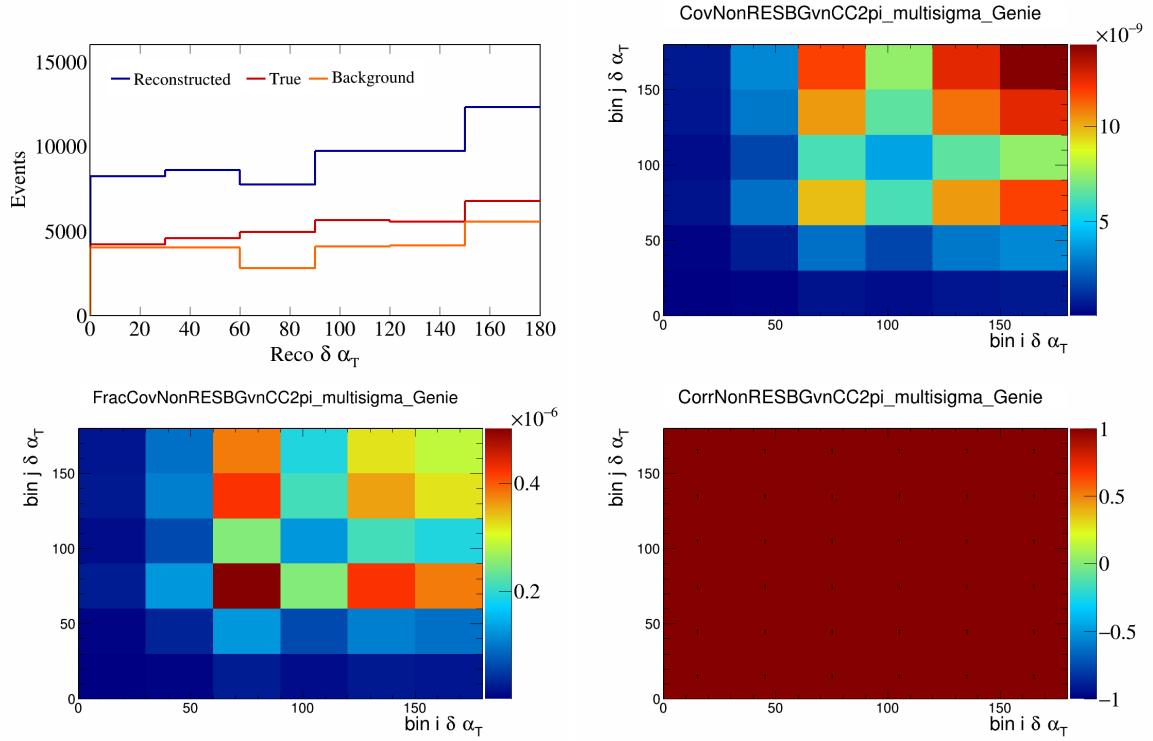


Figure 503: NonRESBGvnCC2pi variations for $\delta\alpha_T$.

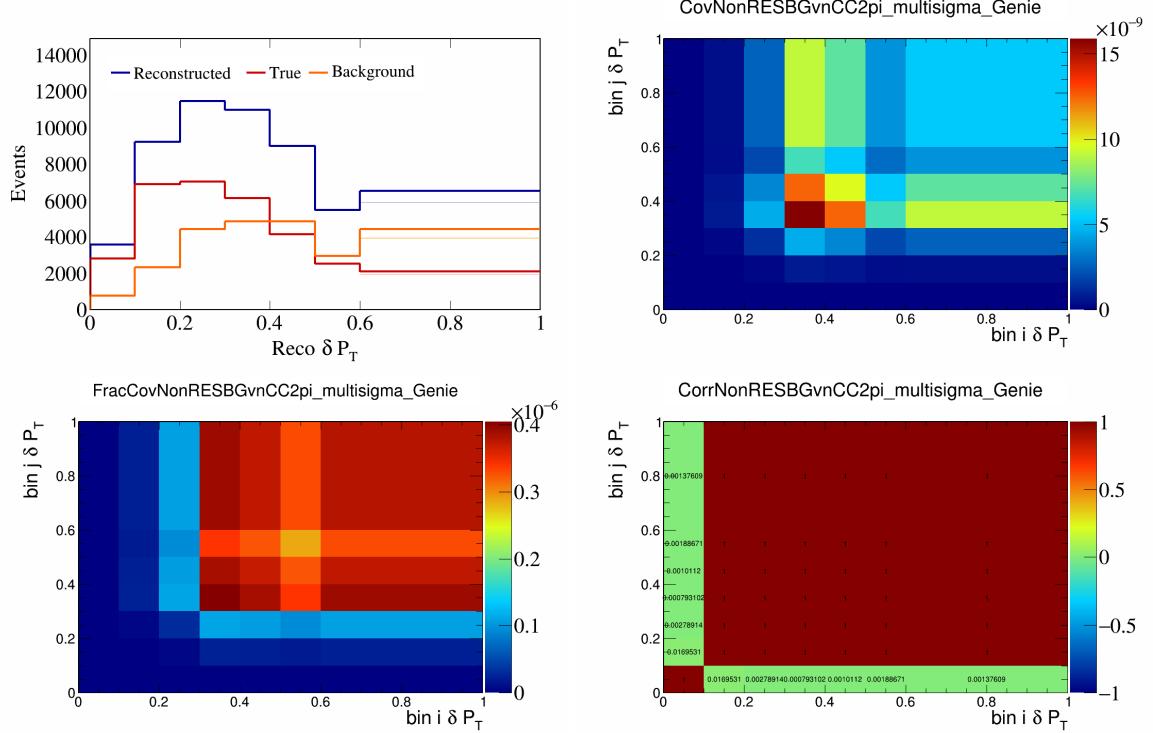


Figure 504: NonRESBGvnCC2pi variations for δP_T .

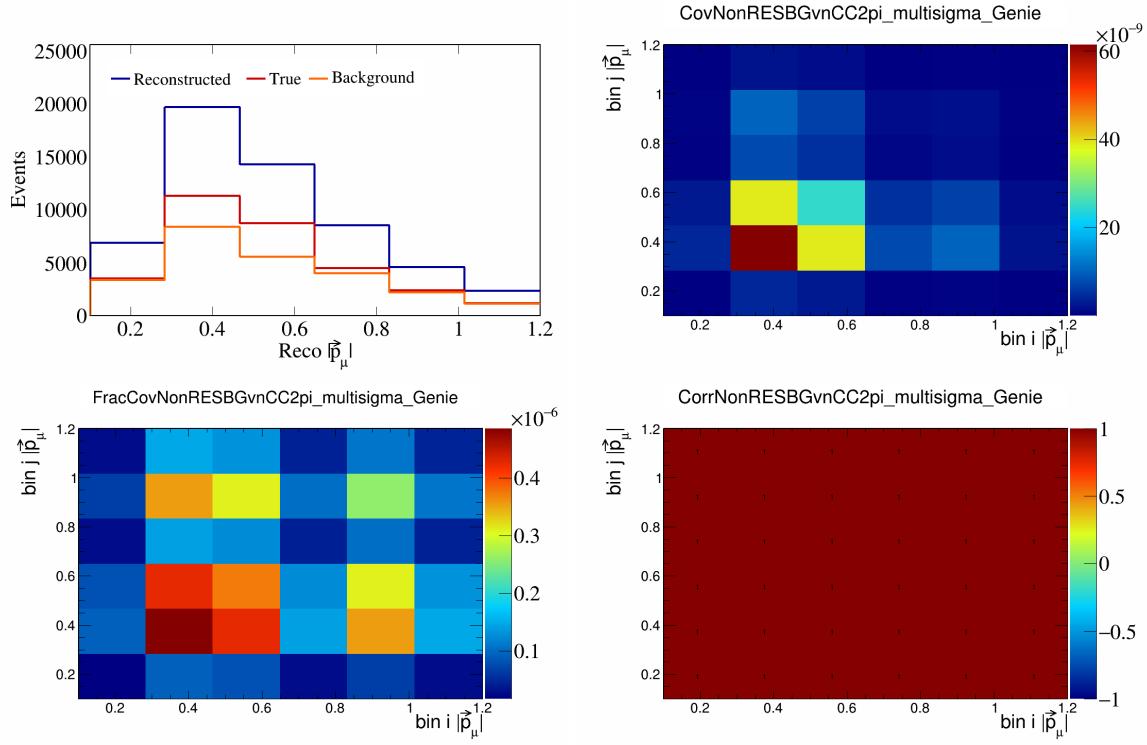


Figure 505: NonRESBGvnCC2pi variations for $|\vec{p}_\mu|$.

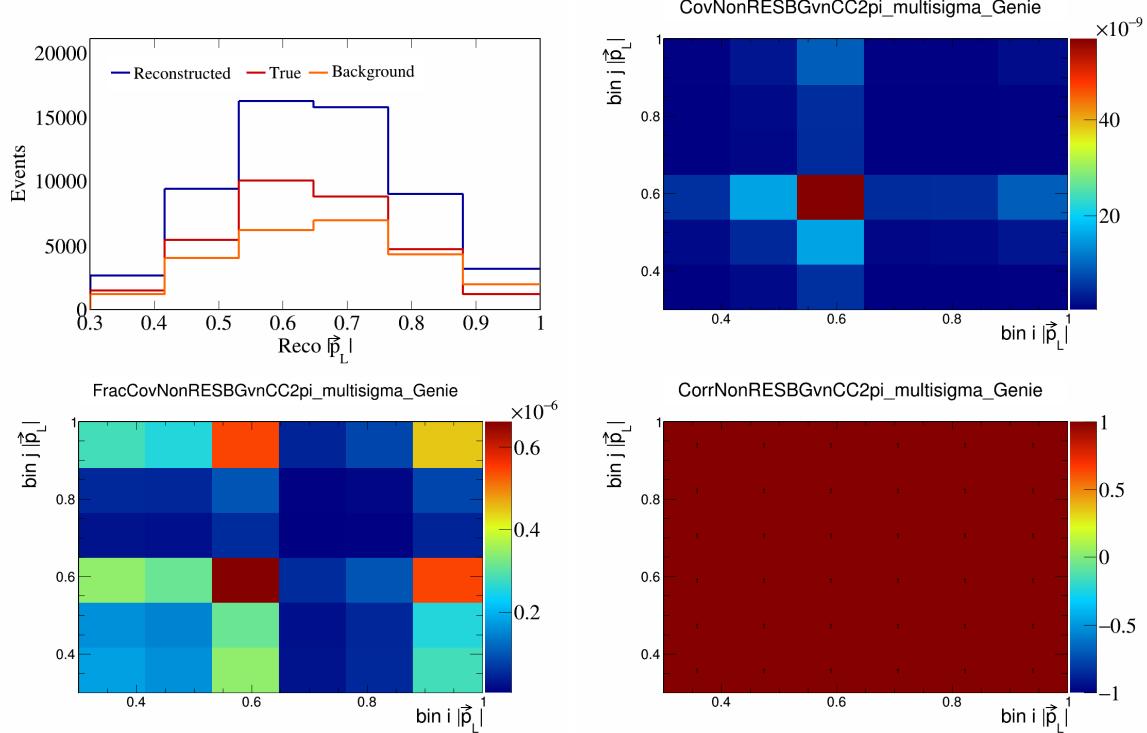


Figure 506: NonRESBGvnCC2pi variations for $|\vec{p}_L|$.

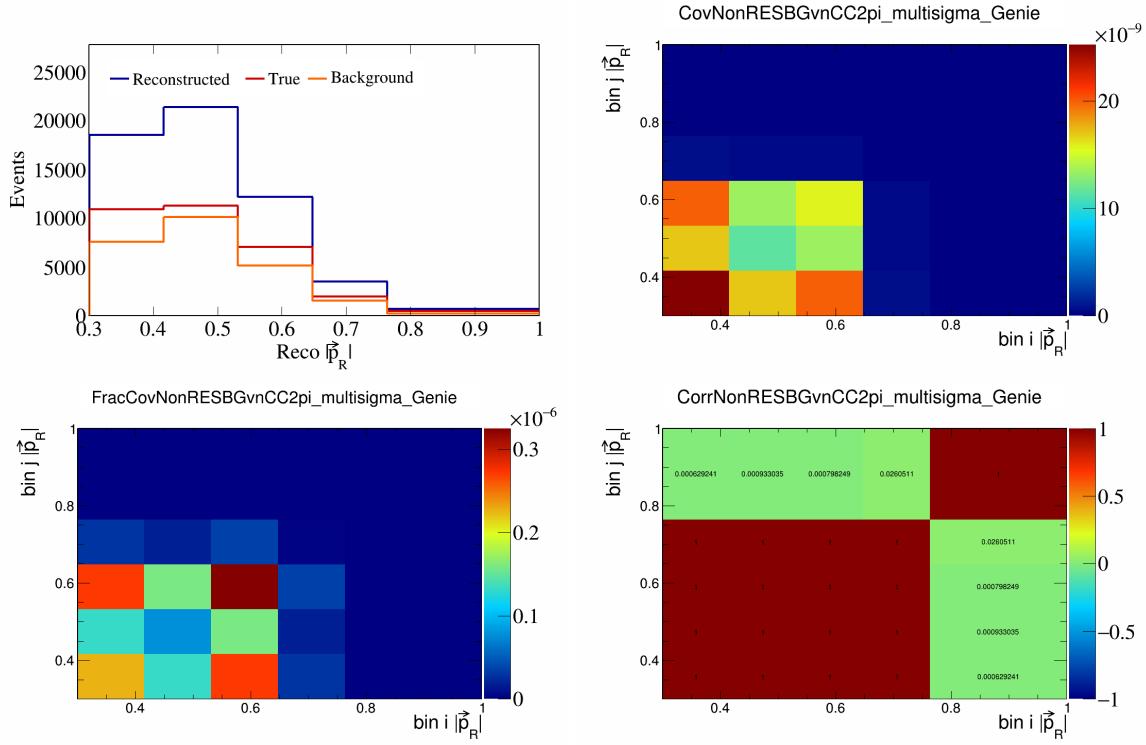


Figure 507: NonRESBGvnCC2pi variations for $|\vec{p}_R|$.

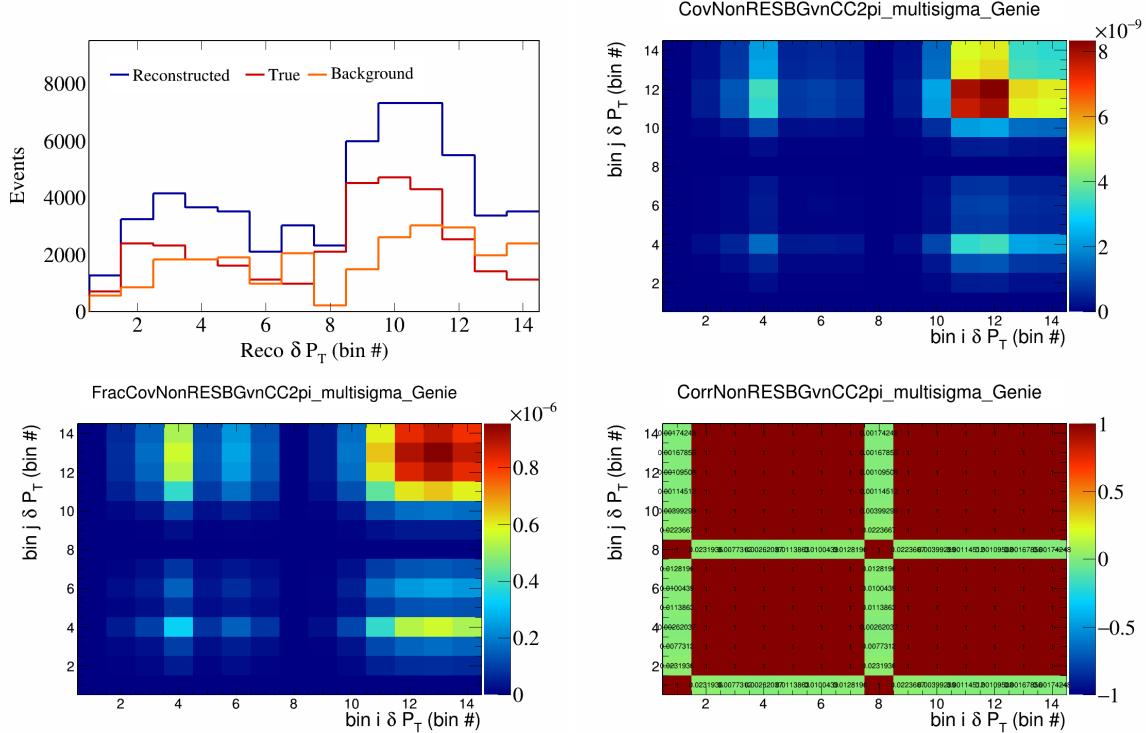


Figure 508: NonRESBGvnCC2pi variations for δP_T in $\cos(\theta_{\vec{p}_\mu})$.

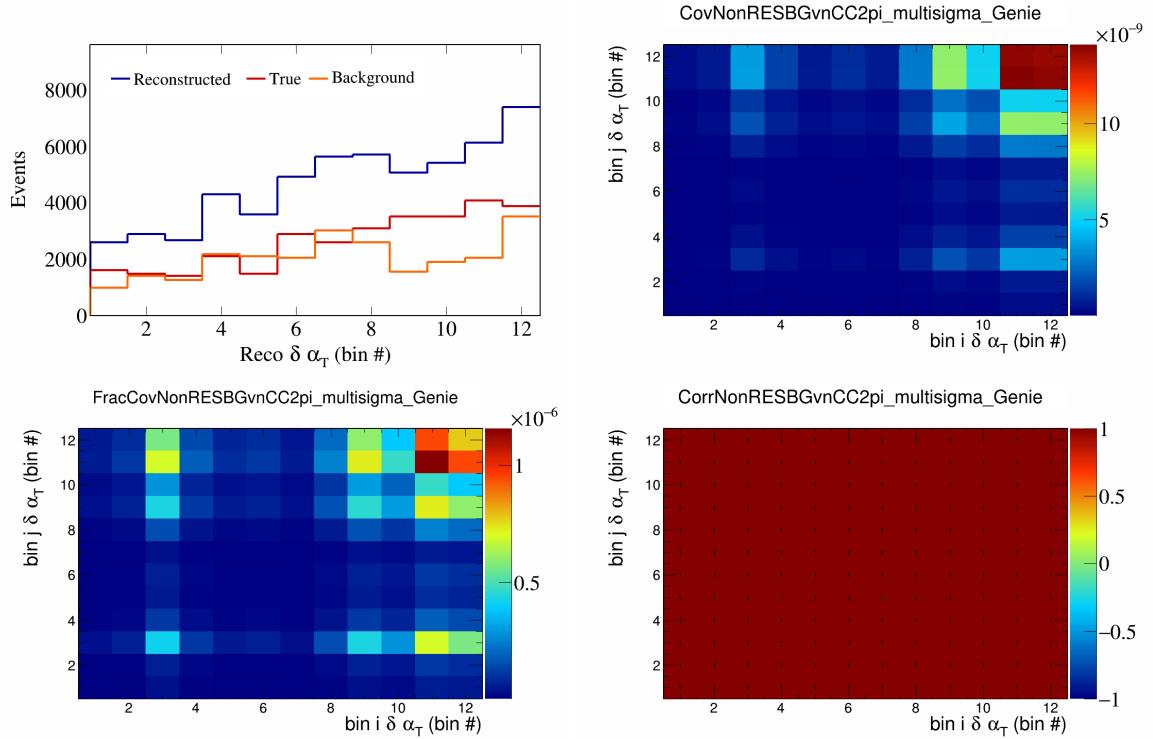


Figure 509: NonRESBGvnCC2pi variations for $\delta \alpha_T$ in $\cos(\theta_{\vec{p}_\mu})$.

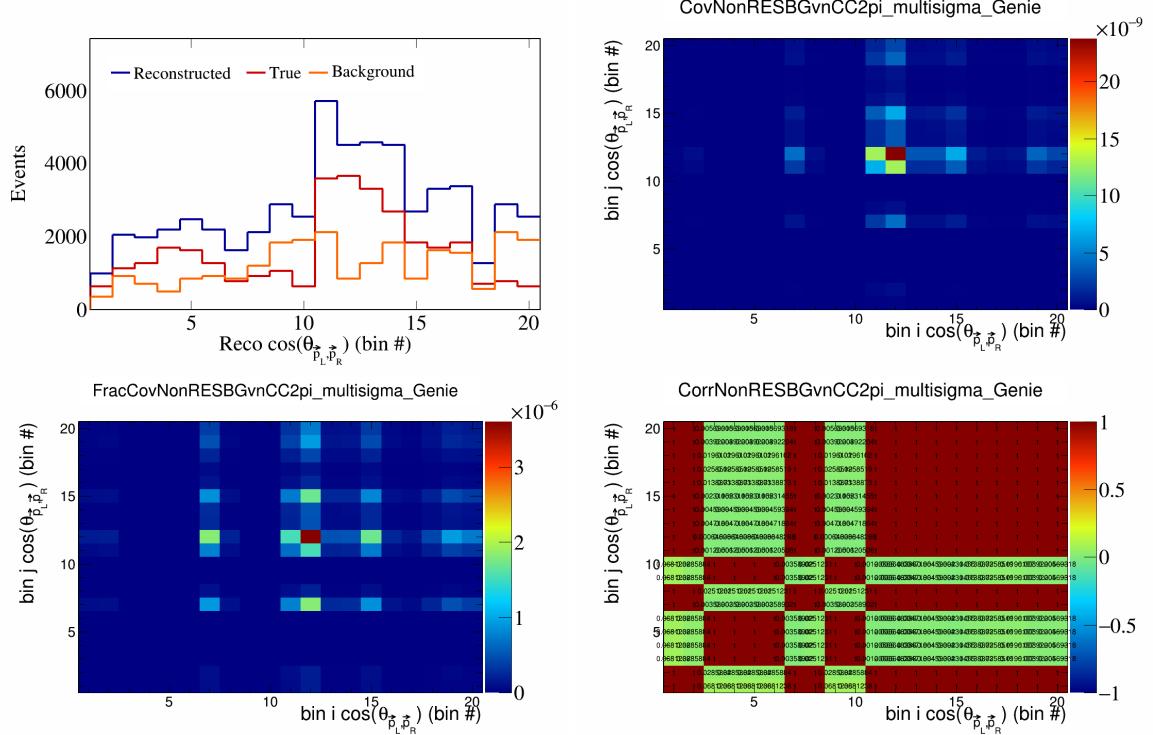


Figure 510: NonRESBGvnCC2pi variations for $\cos(\theta_{\vec{p}_L, \vec{p}_R})$ in $\cos(\theta_{\vec{p}_\mu})$.

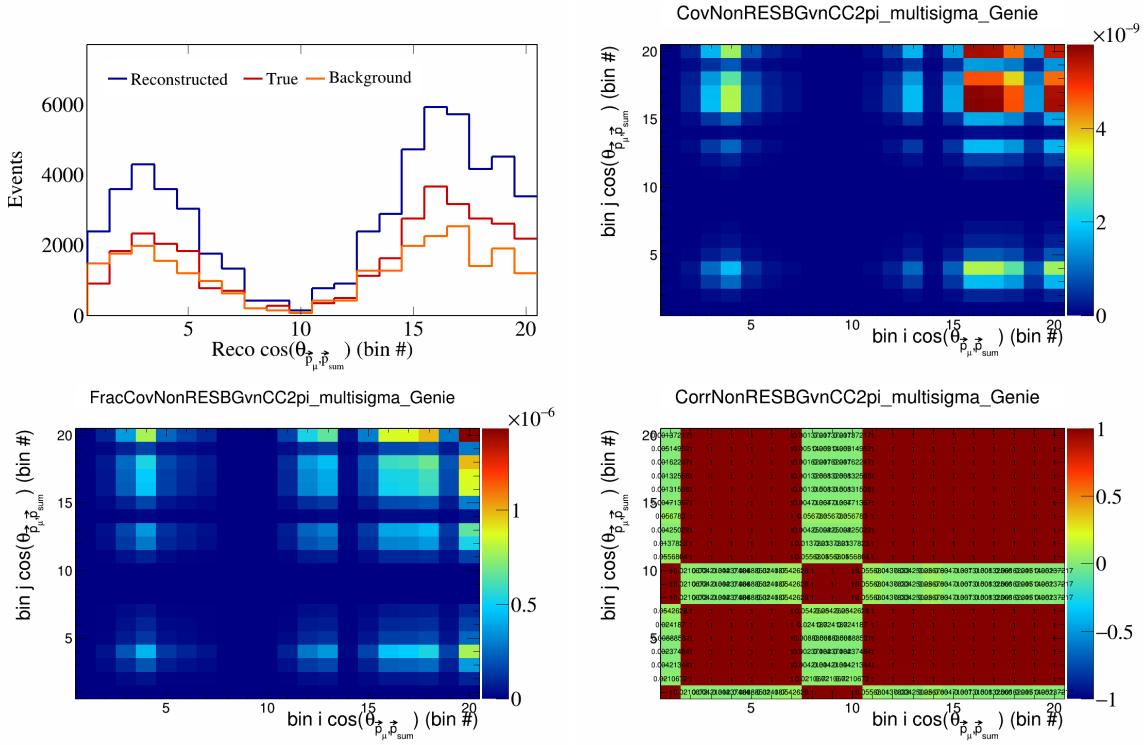


Figure 511: NonRESBGvnCC2pi variations for $\cos(\theta_{\vec{p}_\mu, \vec{p}_{\text{sum}}})$ in $\cos(\theta_{\vec{p}_\mu})$.

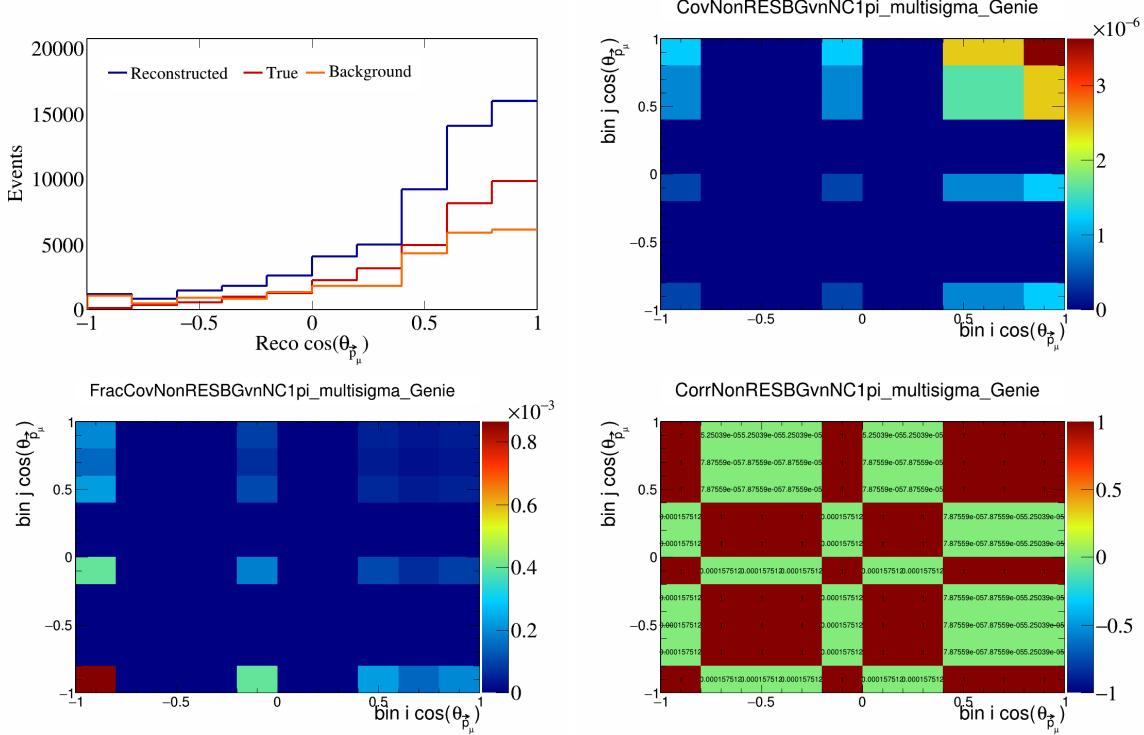


Figure 512: NonRESBGvnNC1pi variations for $\cos(\theta_{\vec{p}_\mu})$.

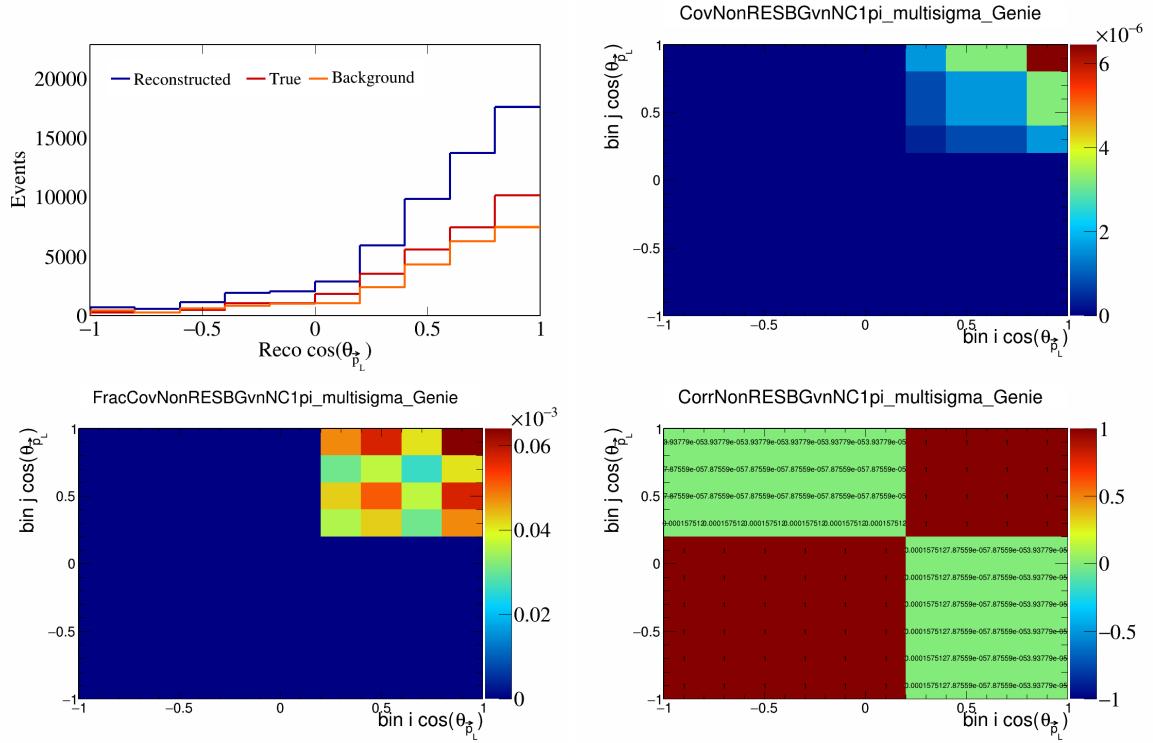


Figure 513: NonRESBGvnNC1pi variations for $\cos(\theta_{\vec{p}_L})$.

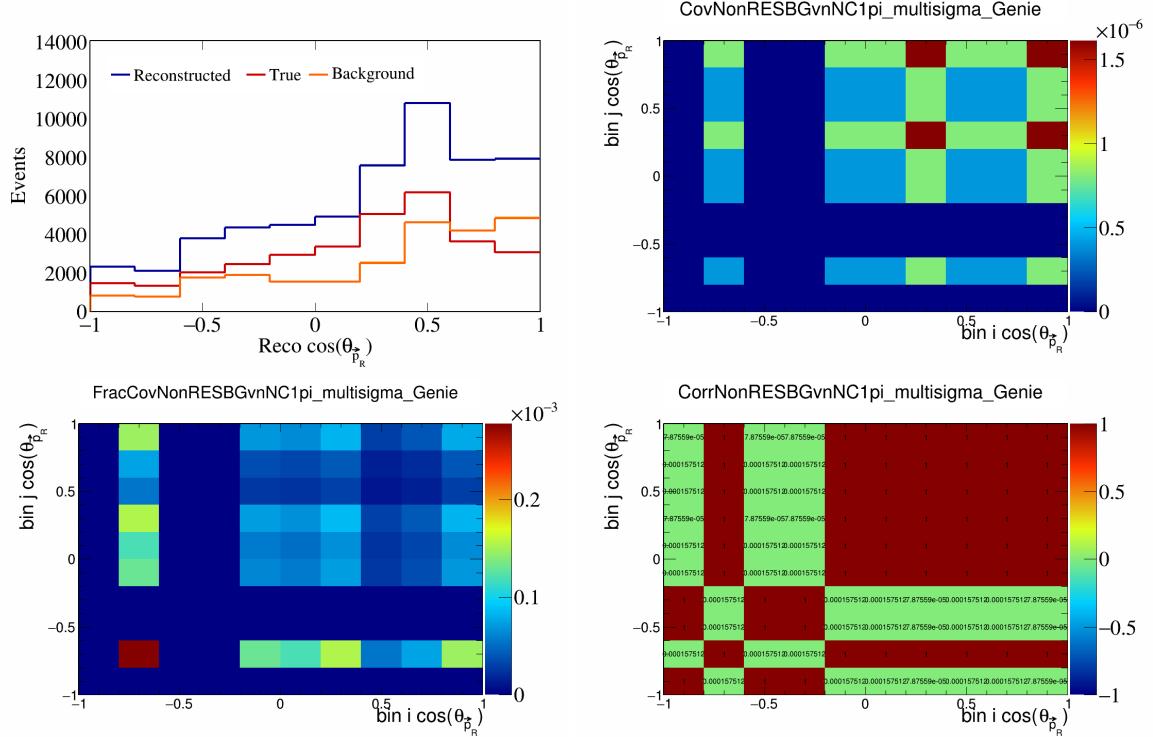


Figure 514: NonRESBGvnNC1pi variations for $\cos(\theta_{\vec{p}_R})$.

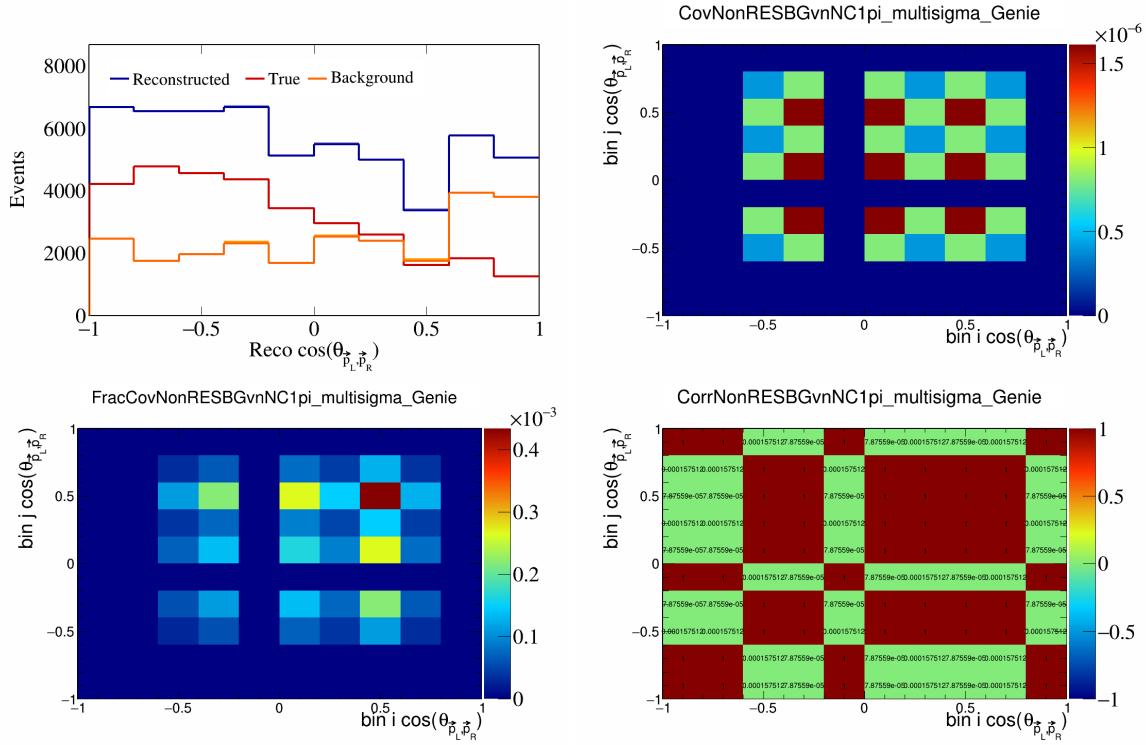


Figure 515: NonRESBGvnNC1pi variations for $\cos(\theta_{\vec{p}_L, \vec{p}_R})$.

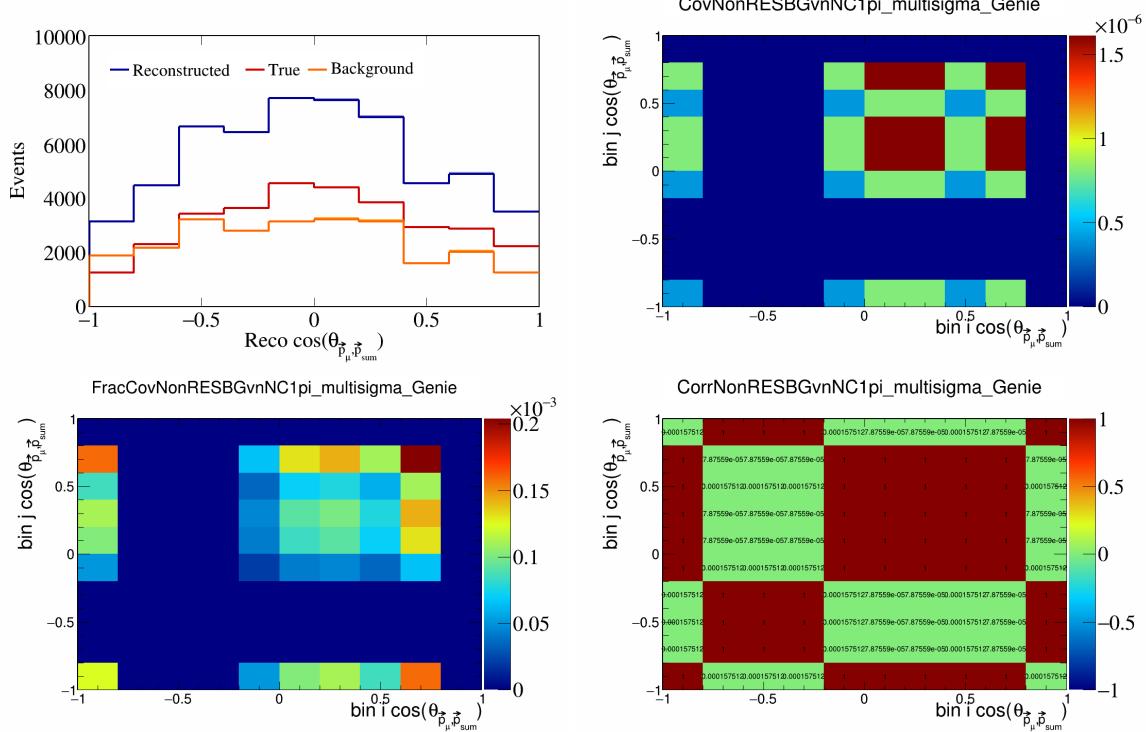


Figure 516: NonRESBGvnNC1pi variations for $\cos(\theta_{\vec{p}_\mu, \vec{p}_{\text{sum}}})$.

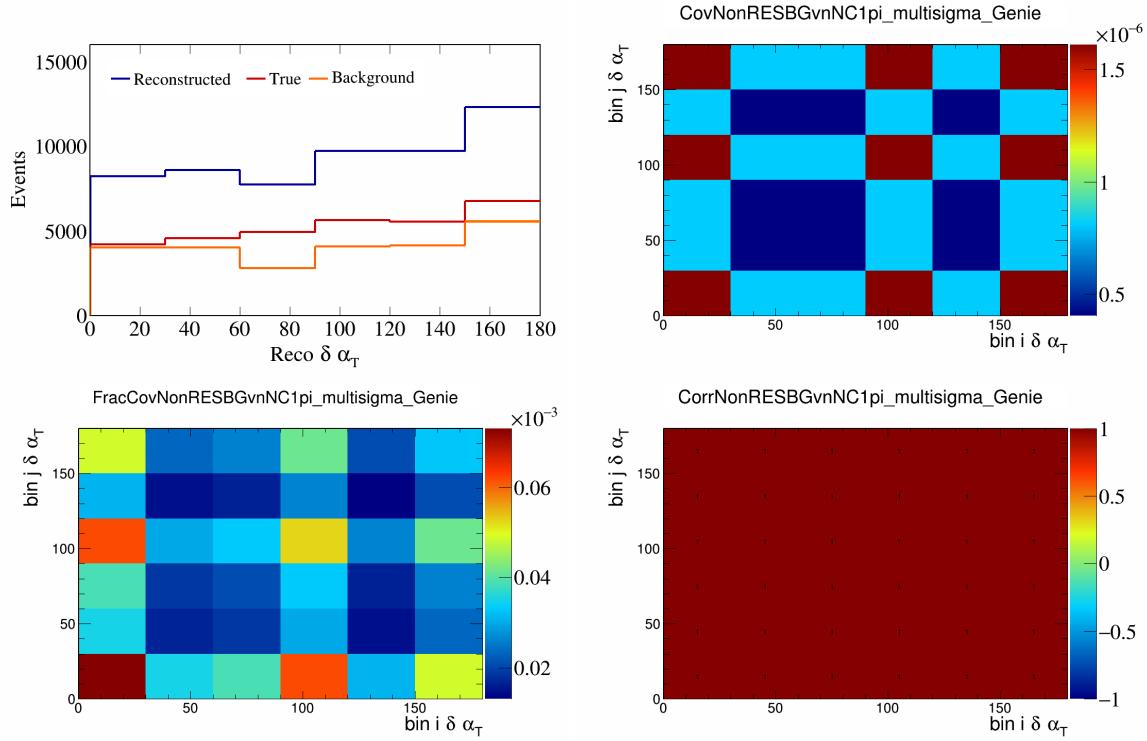


Figure 517: NonRESBGvnNC1pi variations for $\delta\alpha_T$.

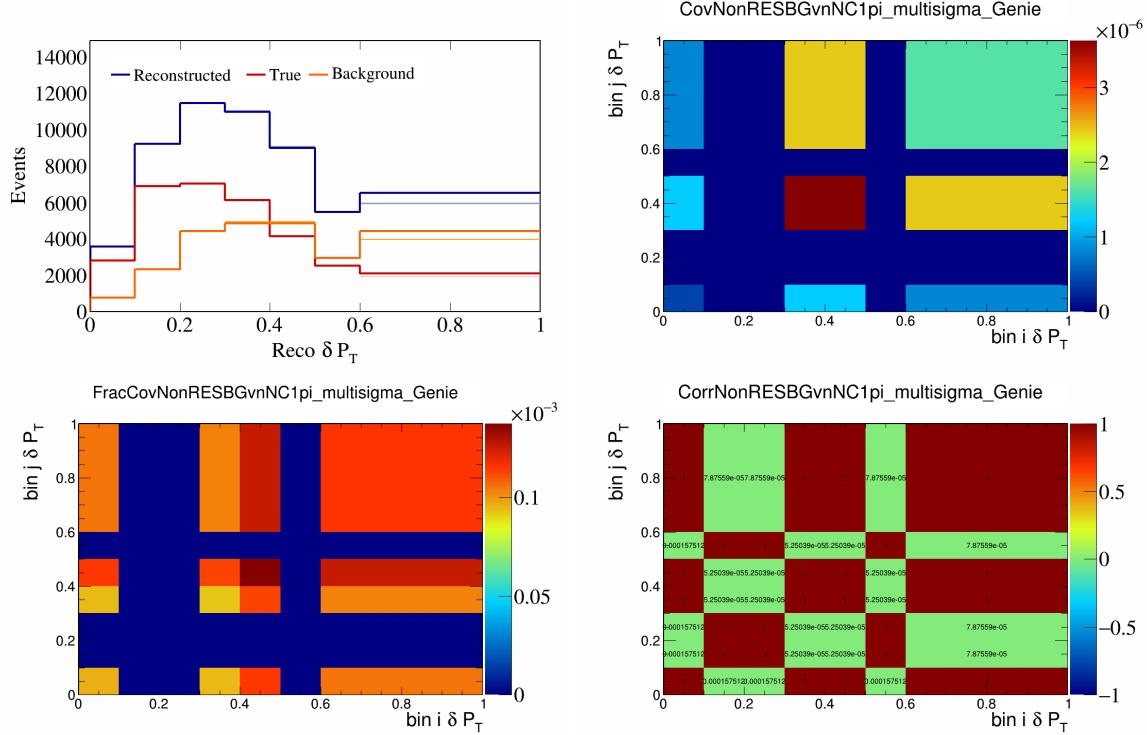


Figure 518: NonRESBGvnNC1pi variations for δP_T .

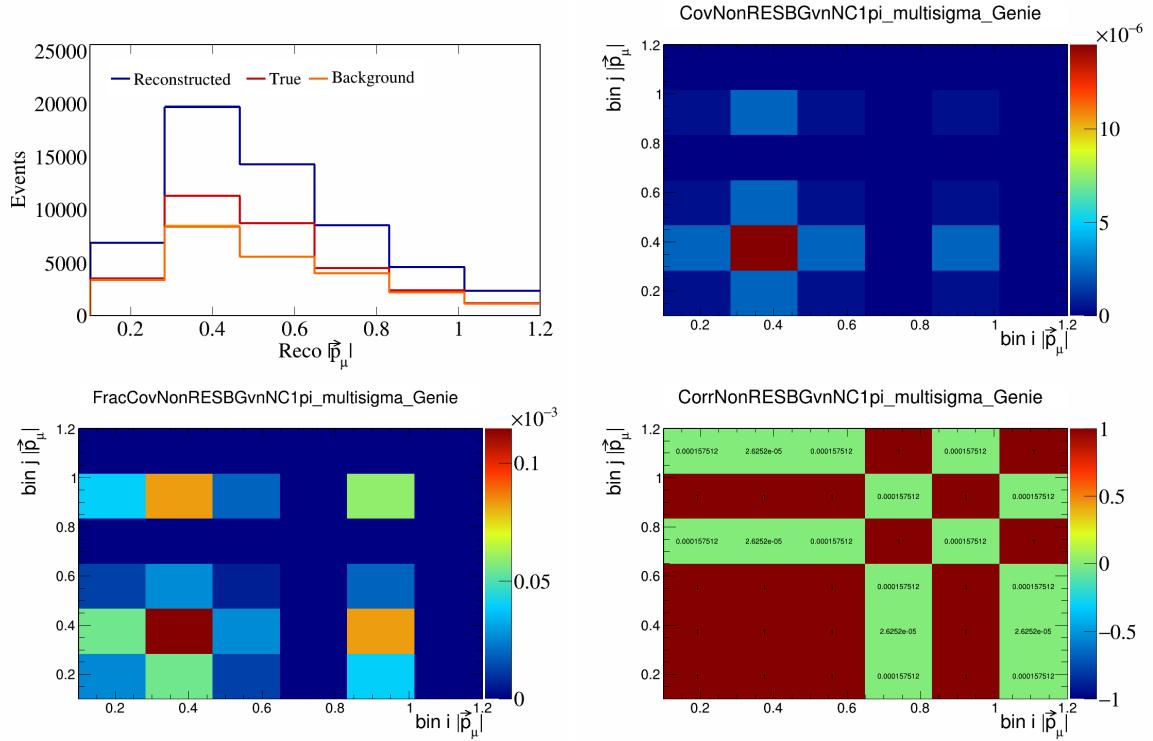


Figure 519: NonRESBGvnNC1pi variations for $|\vec{p}_\mu|$.

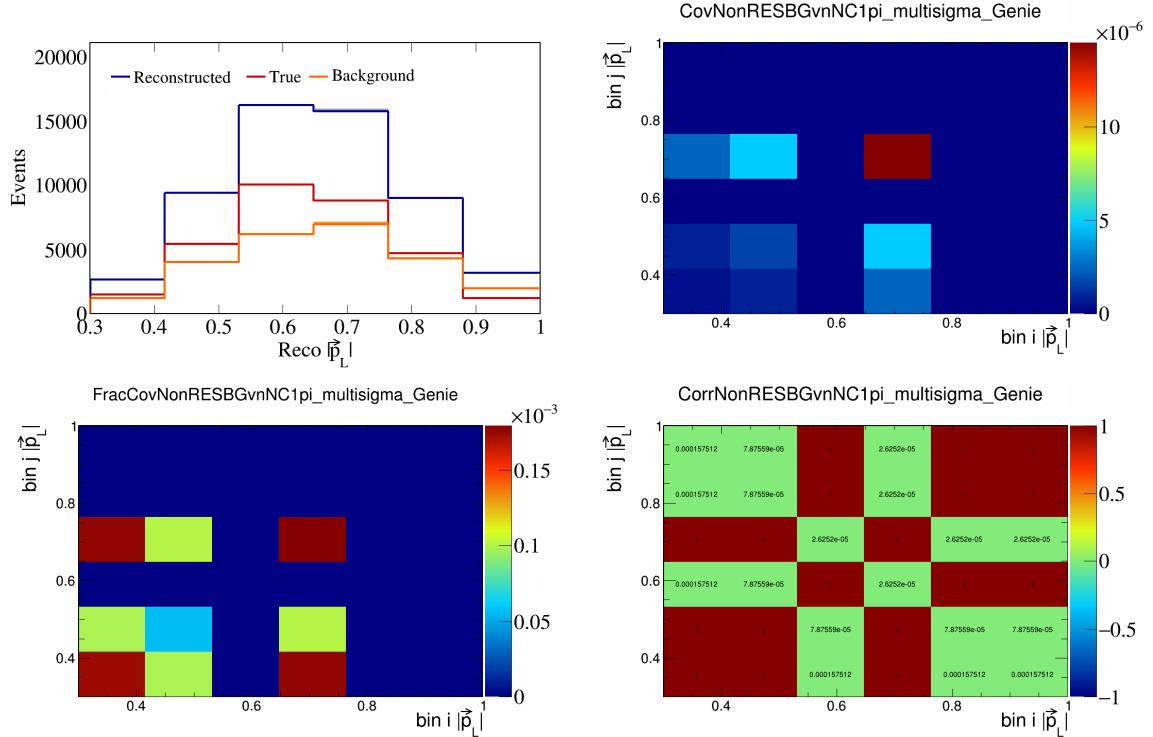


Figure 520: NonRESBGvnNC1pi variations for $|\vec{p}_L|$.

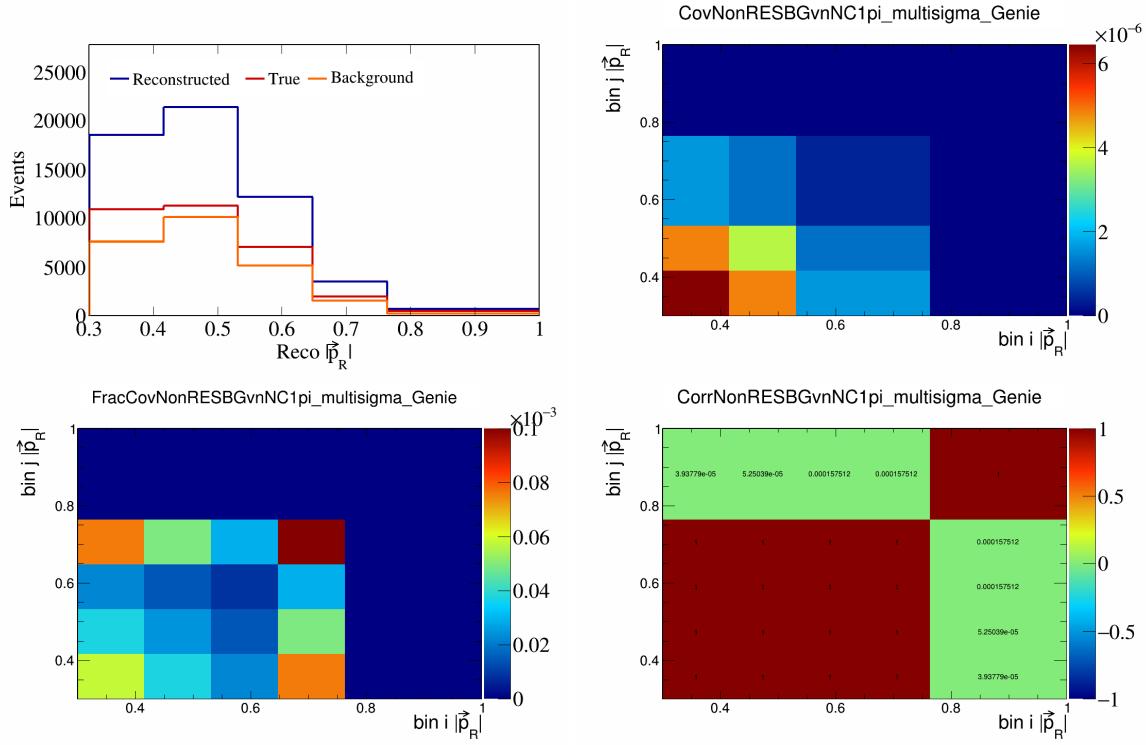


Figure 521: NonRESBGvnNC1pi variations for $|\vec{p}_R|$.

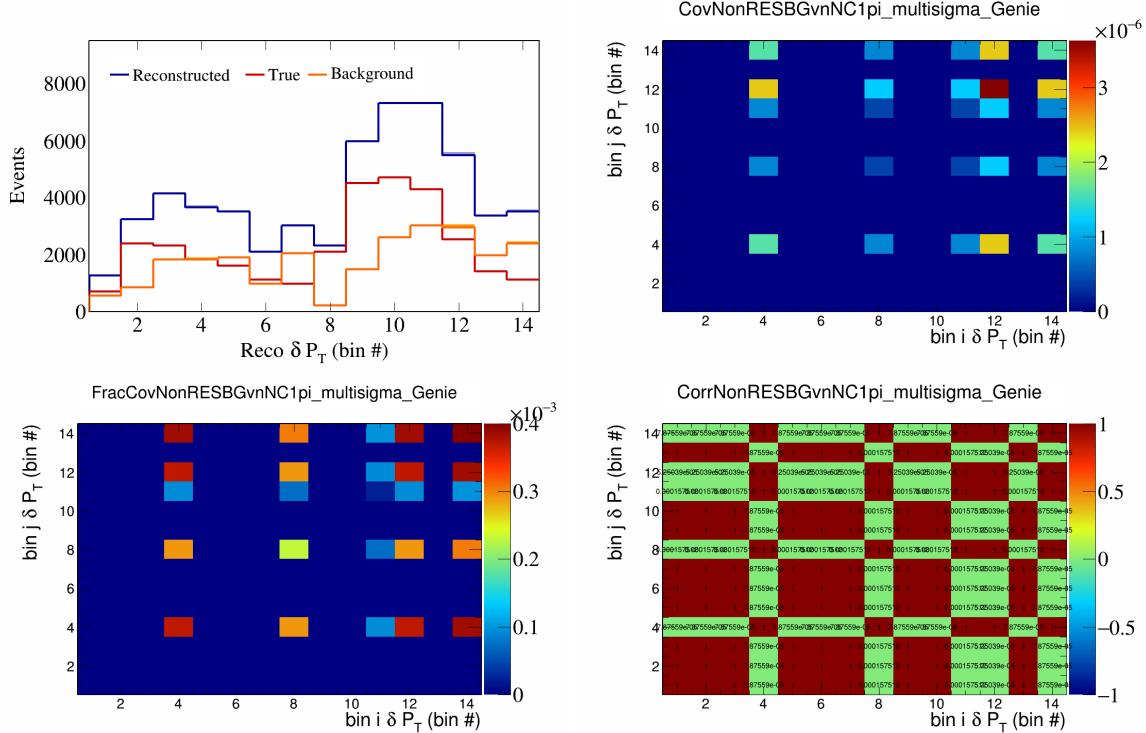


Figure 522: NonRESBGvnNC1pi variations for δP_T in $\cos(\theta_{\vec{p}_\mu})$.

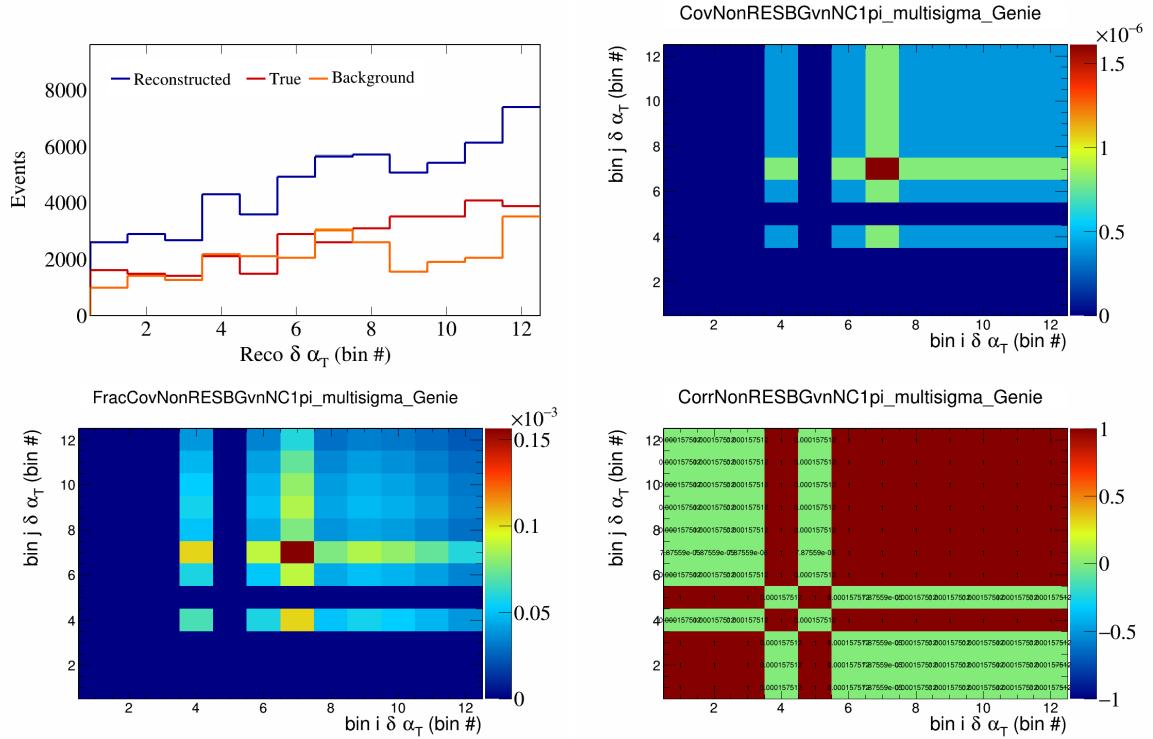


Figure 523: NonRESBGvnNC1pi variations for $\delta \alpha_T$ in $\cos(\theta_{\vec{p}_\mu})$.

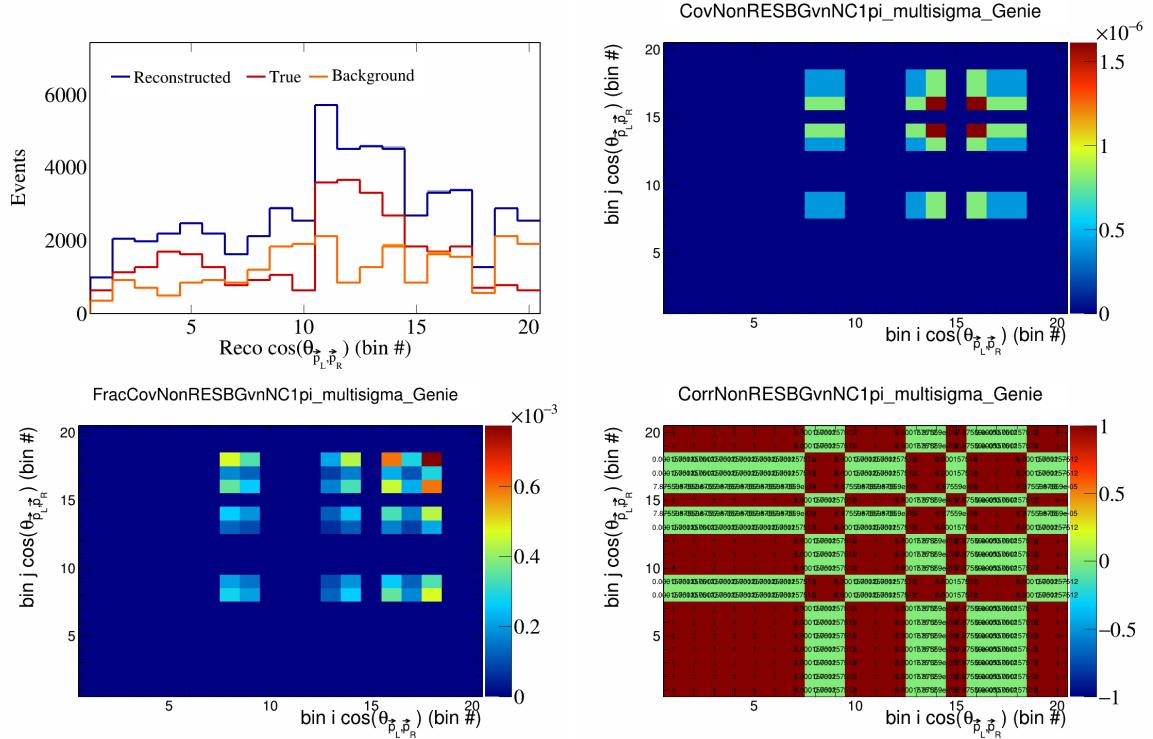


Figure 524: NonRESBGvnNC1pi variations for $\cos(\theta_{\vec{p}_L, \vec{p}_R})$ in $\cos(\theta_{\vec{p}_\mu})$.

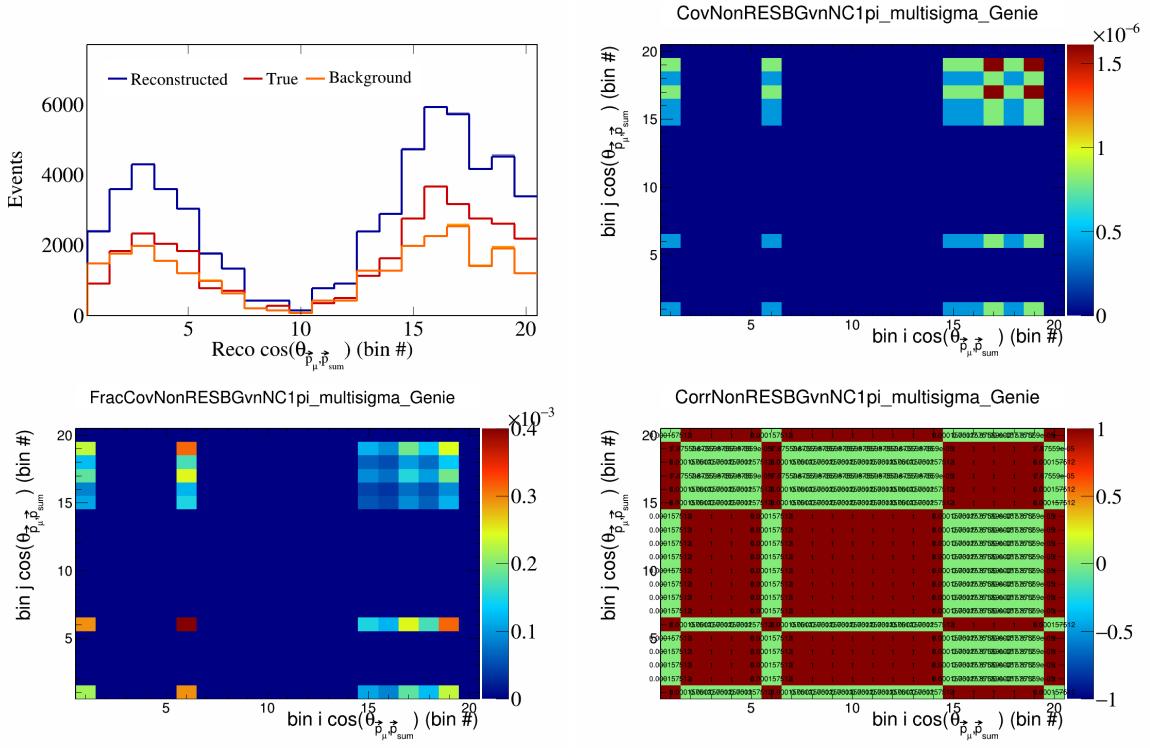


Figure 525: NonRESBGvnNC1pi variations for $\cos(\theta_{\vec{p}_\mu})$ in $\cos(\theta_{\vec{p}_\mu})$.

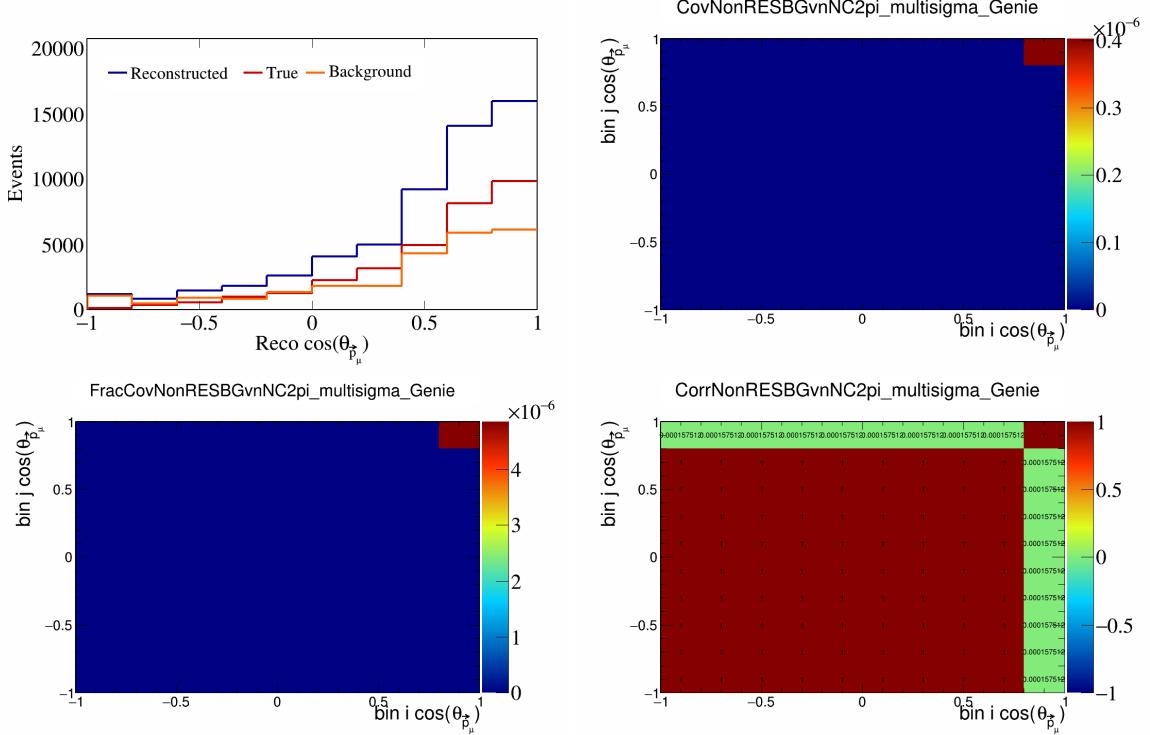


Figure 526: NonRESBGvnNC2pi variations for $\cos(\theta_{\vec{p}_\mu})$.

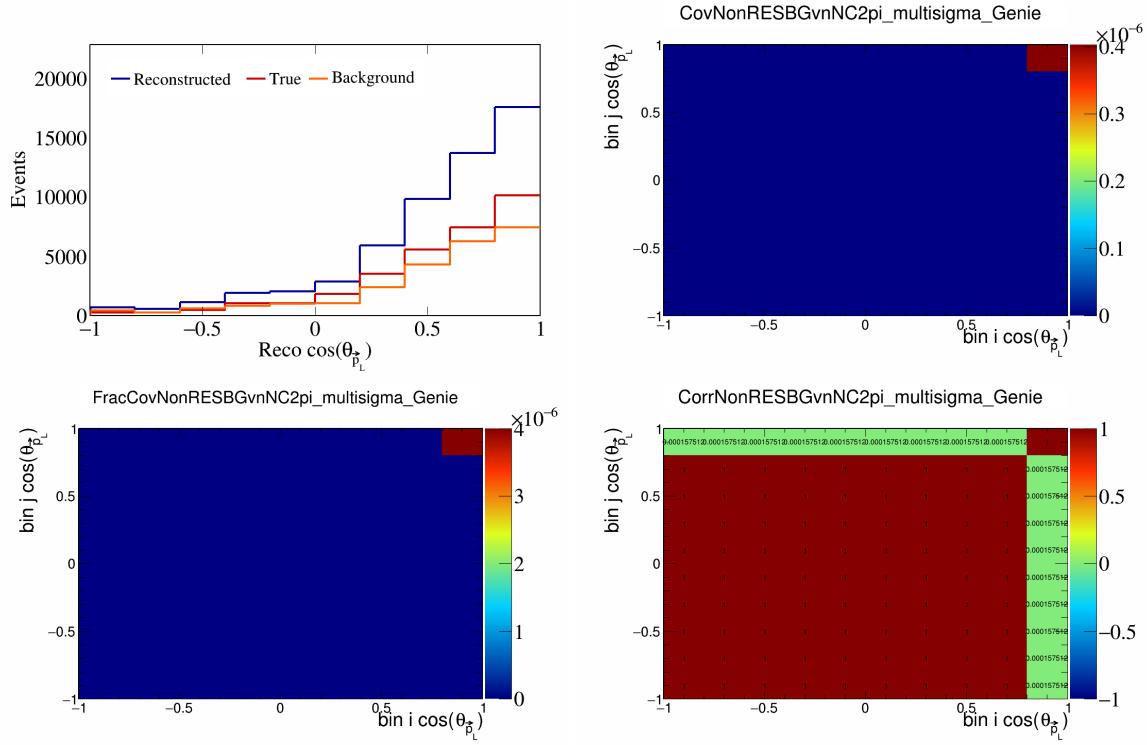


Figure 527: NonRESBGvnNC2pi variations for $\cos(\theta_{\vec{p}_L})$.

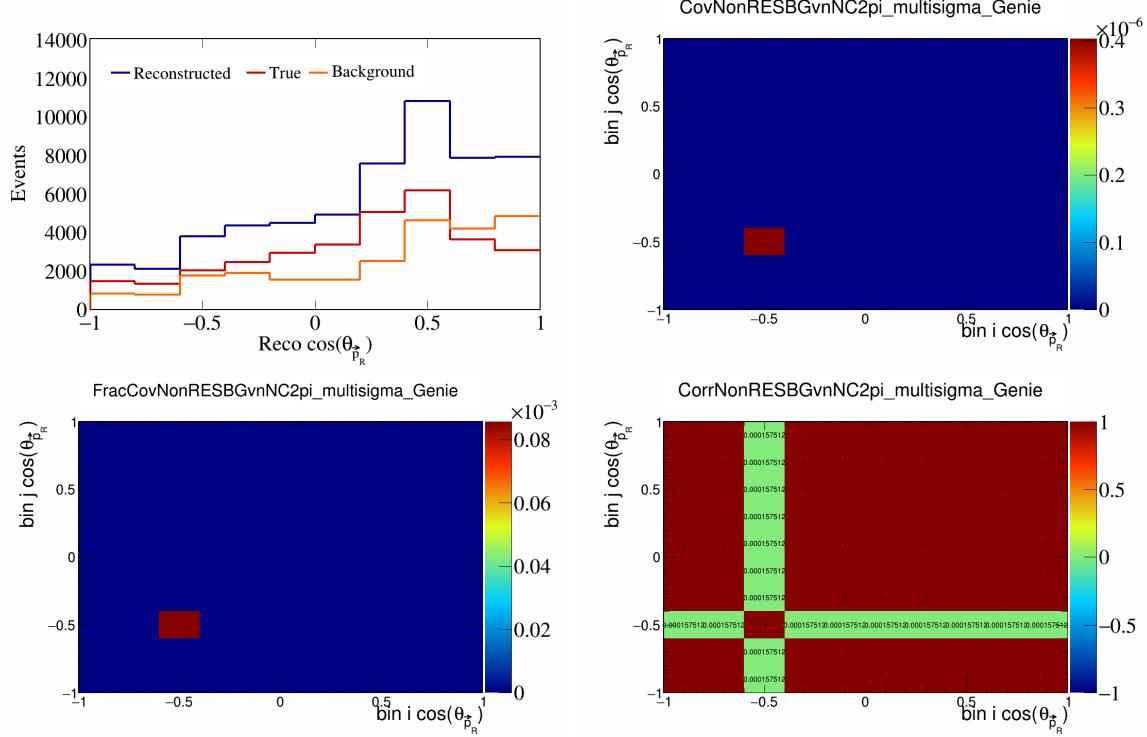


Figure 528: NonRESBGvnNC2pi variations for $\cos(\theta_{\vec{p}_R})$.

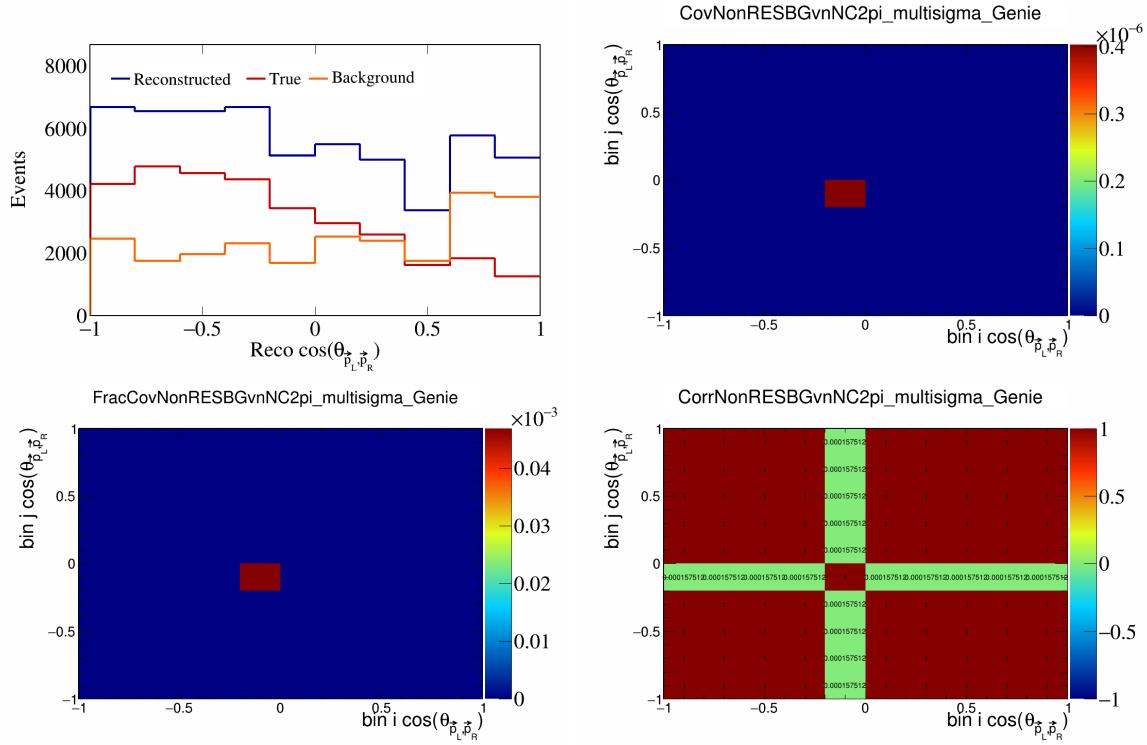


Figure 529: NonRESBGvnNC2pi variations for $\cos(\theta_{\vec{p}_L, \vec{p}_R})$.

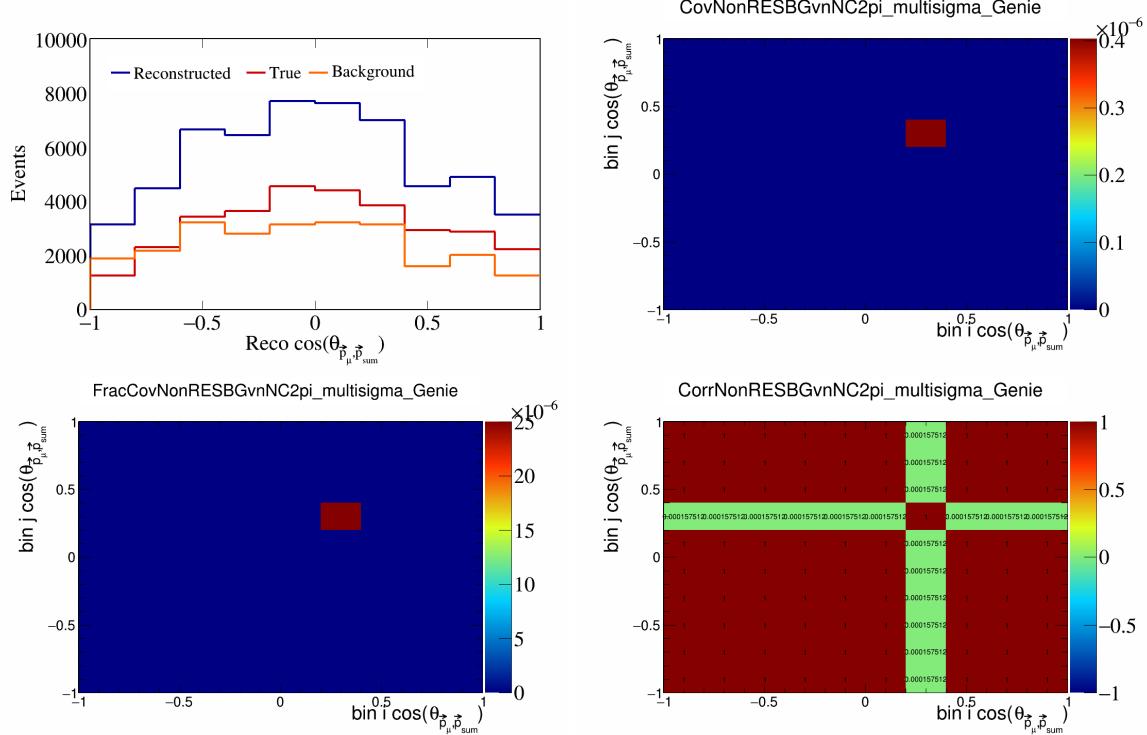


Figure 530: NonRESBGvnNC2pi variations for $\cos(\theta_{\vec{p}_\mu, \vec{p}_{\text{sum}}})$.

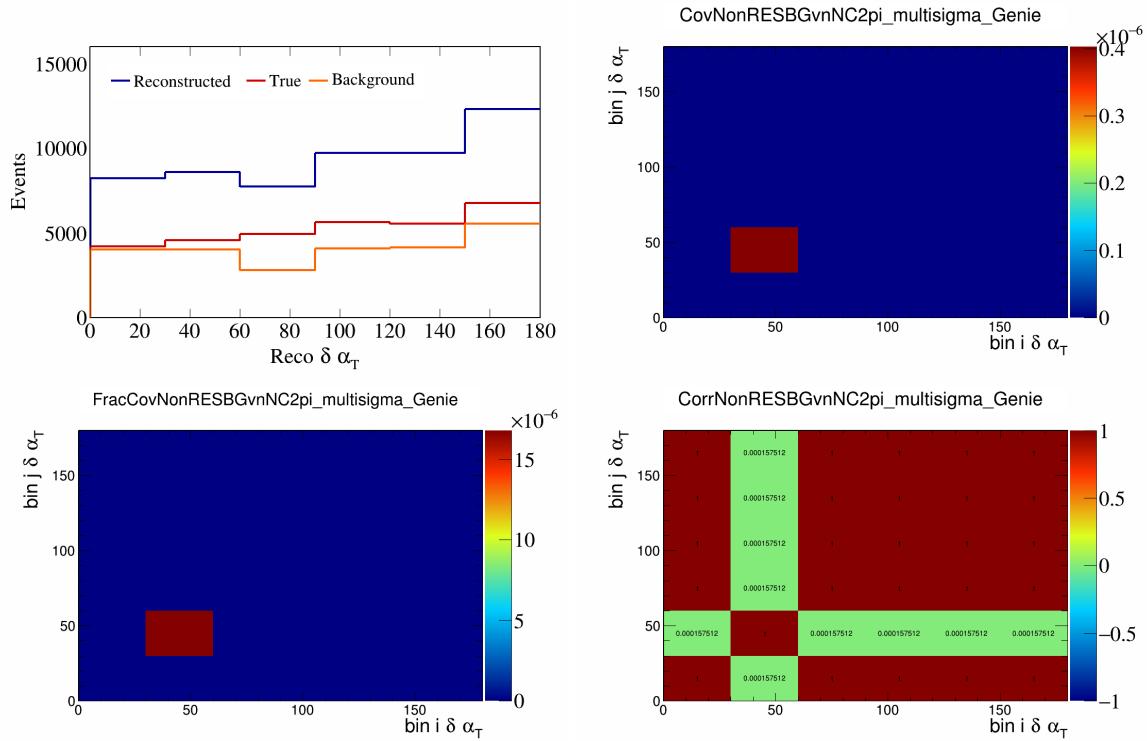


Figure 531: NonRESBGvnNC2pi variations for $\delta \alpha_T$.

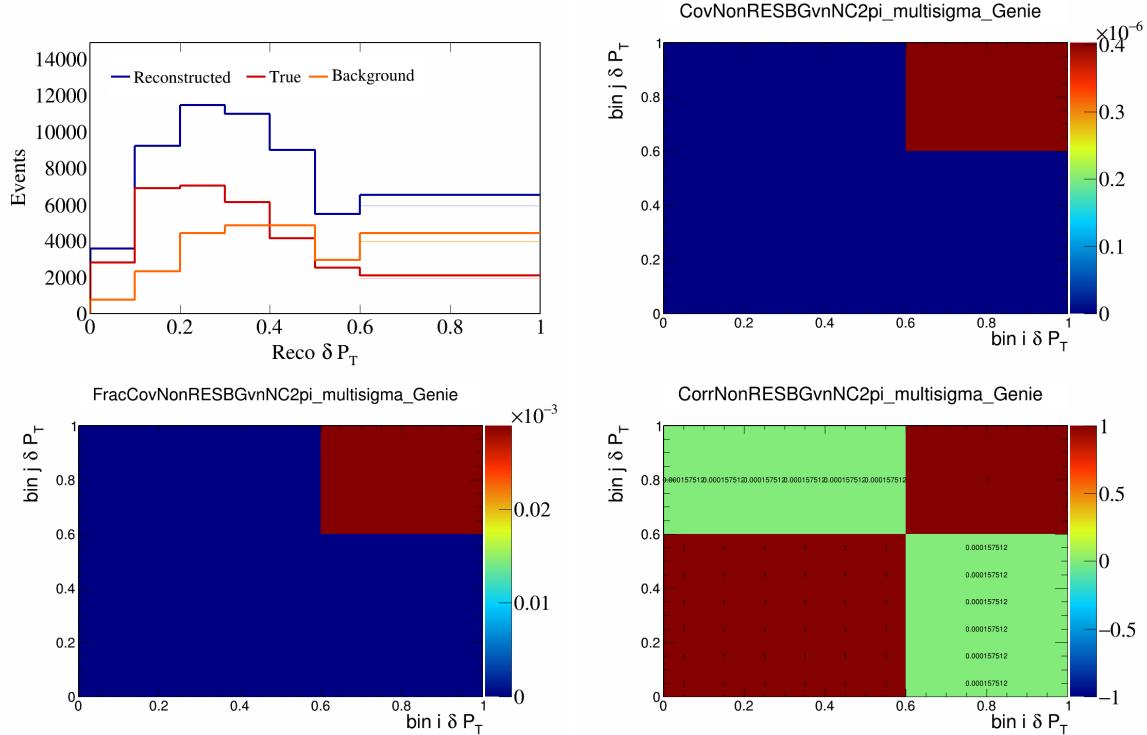


Figure 532: NonRESBGvnNC2pi variations for δP_T .

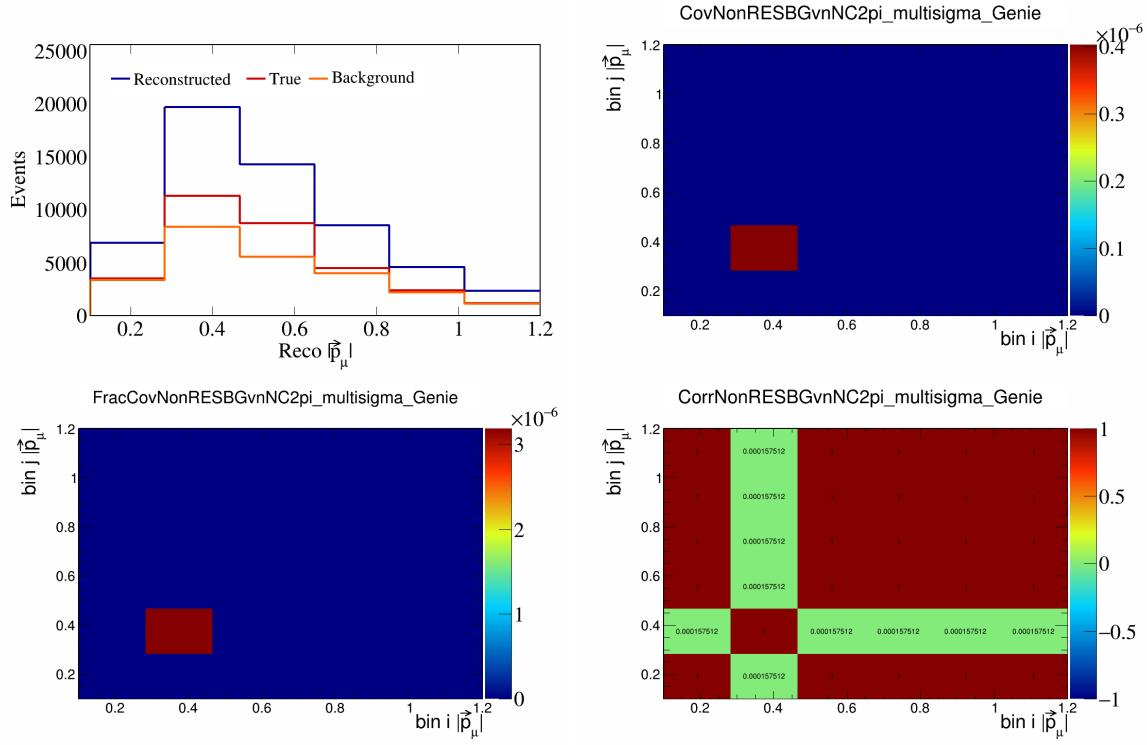


Figure 533: NonRESBGvnNC2pi variations for $|\vec{p}_\mu|$.

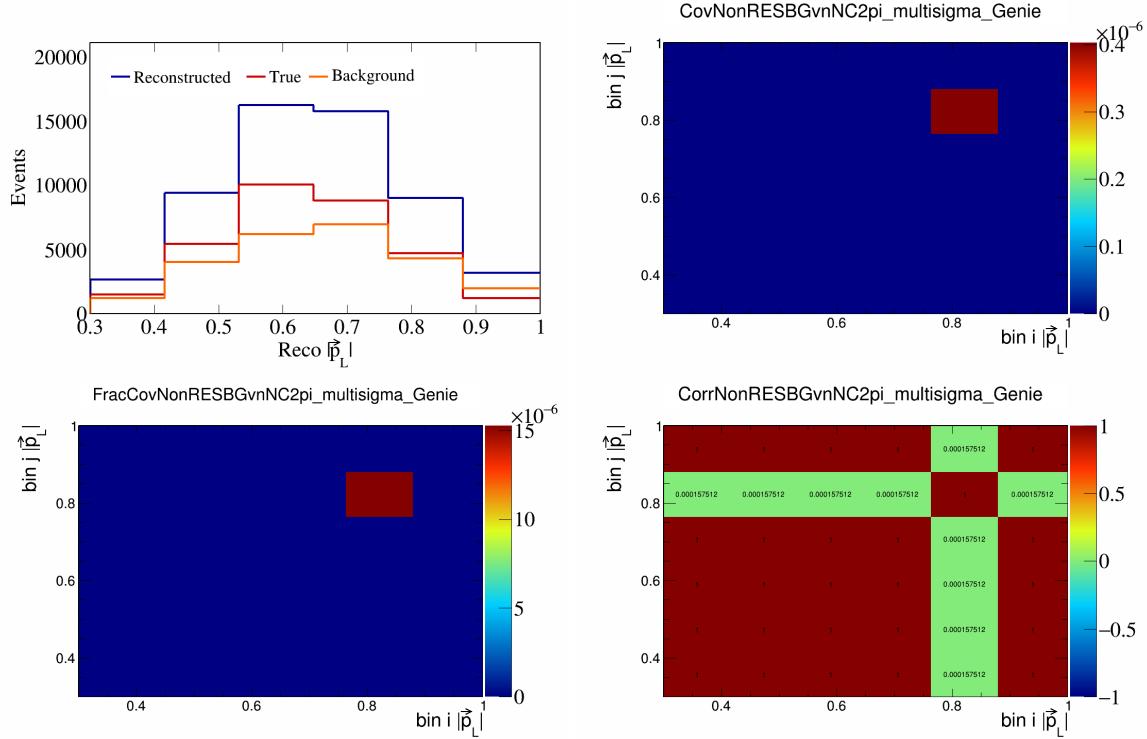


Figure 534: NonRESBGvnNC2pi variations for $|\vec{p}_L|$.

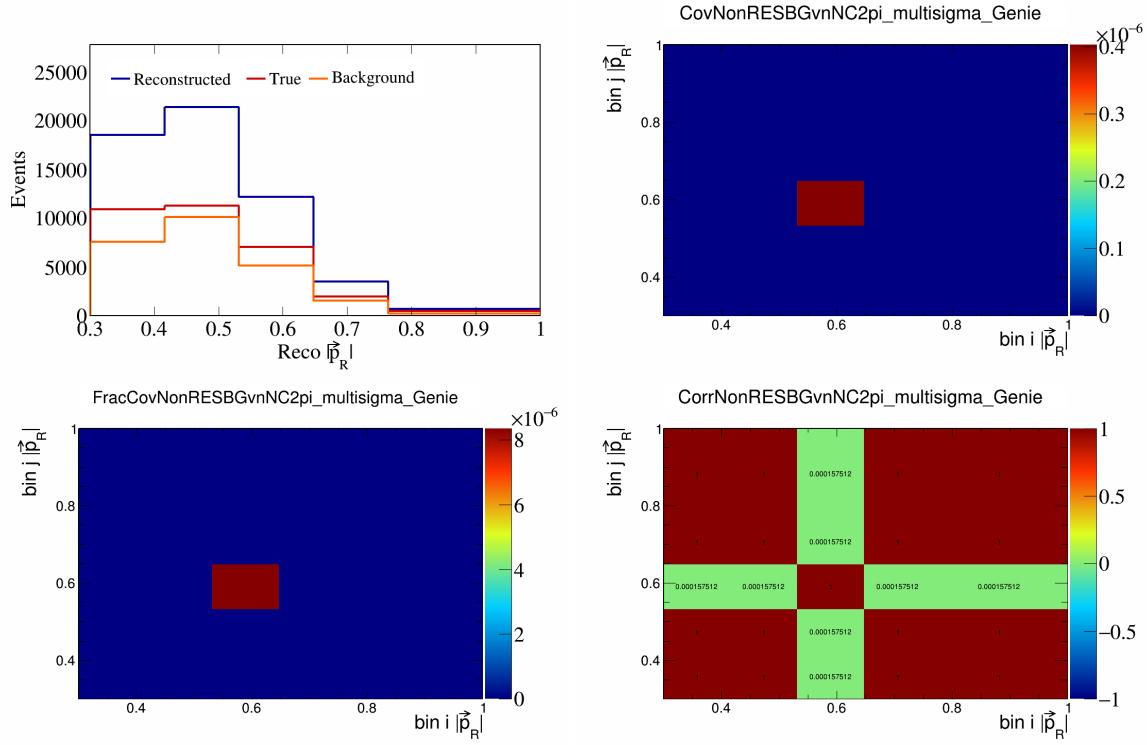


Figure 535: NonRESBGvnNC2pi variations for $|\vec{p}_R|$.

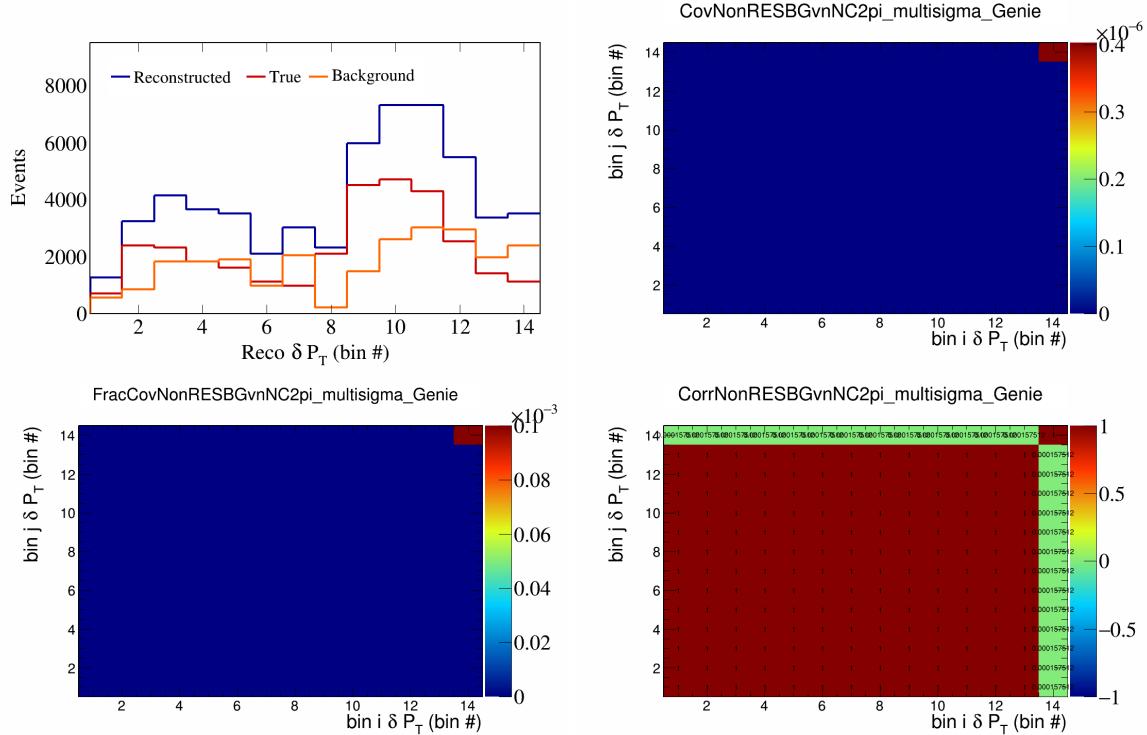


Figure 536: NonRESBGvnNC2pi variations for δP_T in $\cos(\theta_{\vec{p}_\mu})$.

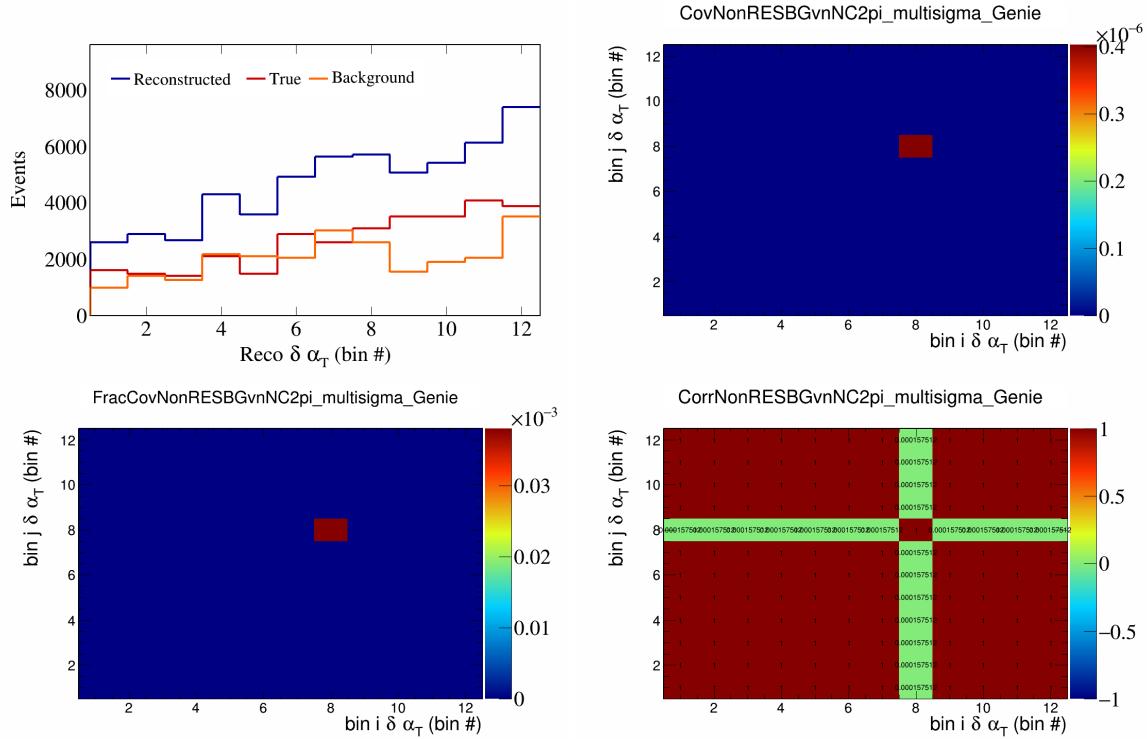


Figure 537: NonRESBGvnNC2pi variations for $\delta\alpha_T$ in $\cos(\theta_{\vec{p}_\mu})$.

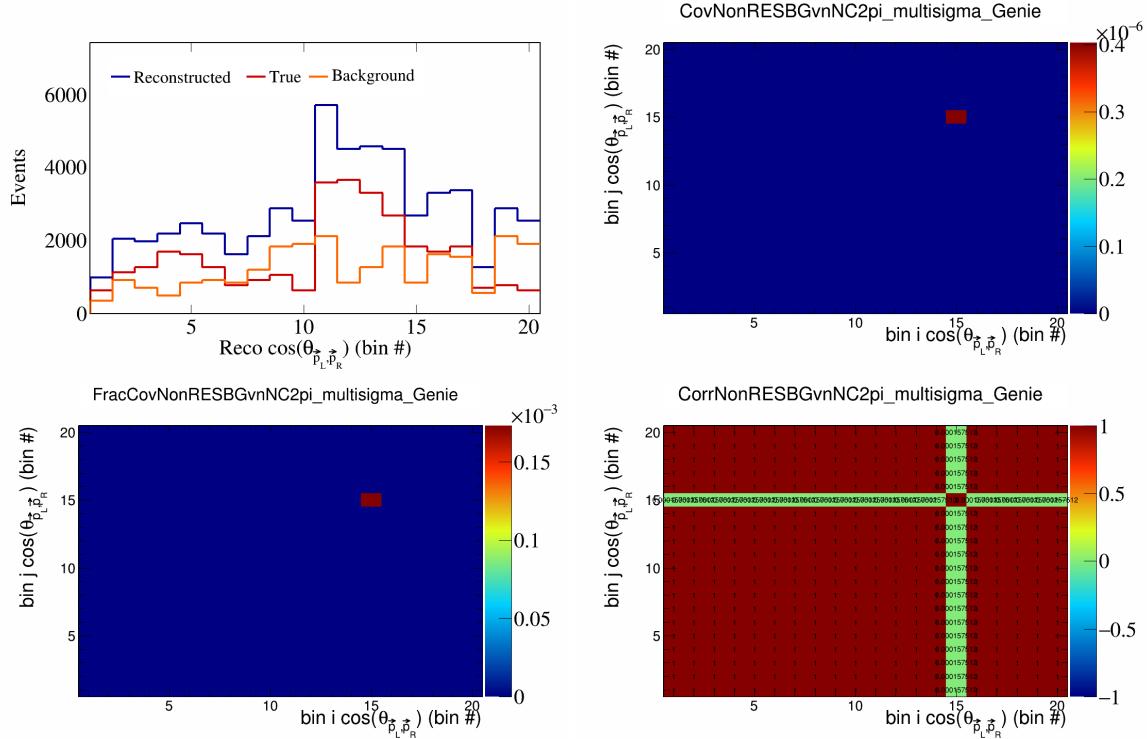


Figure 538: NonRESBGvnNC2pi variations for $\cos(\theta_{\vec{p}_L, \vec{p}_R})$ in $\cos(\theta_{\vec{p}_\mu})$.

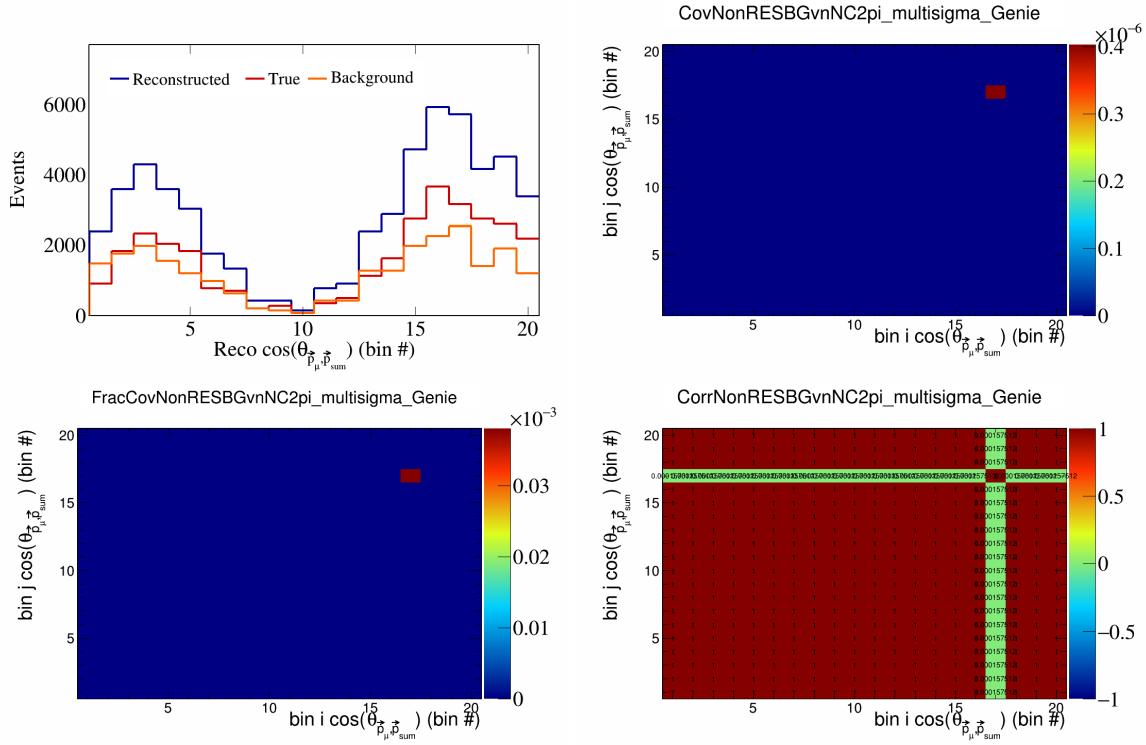


Figure 539: NonRESBGvnNC2pi variations for $\cos(\theta_{\vec{p}_\mu, \vec{p}_{\text{sum}}})$ in $\cos(\theta_{\vec{p}_\mu})$.

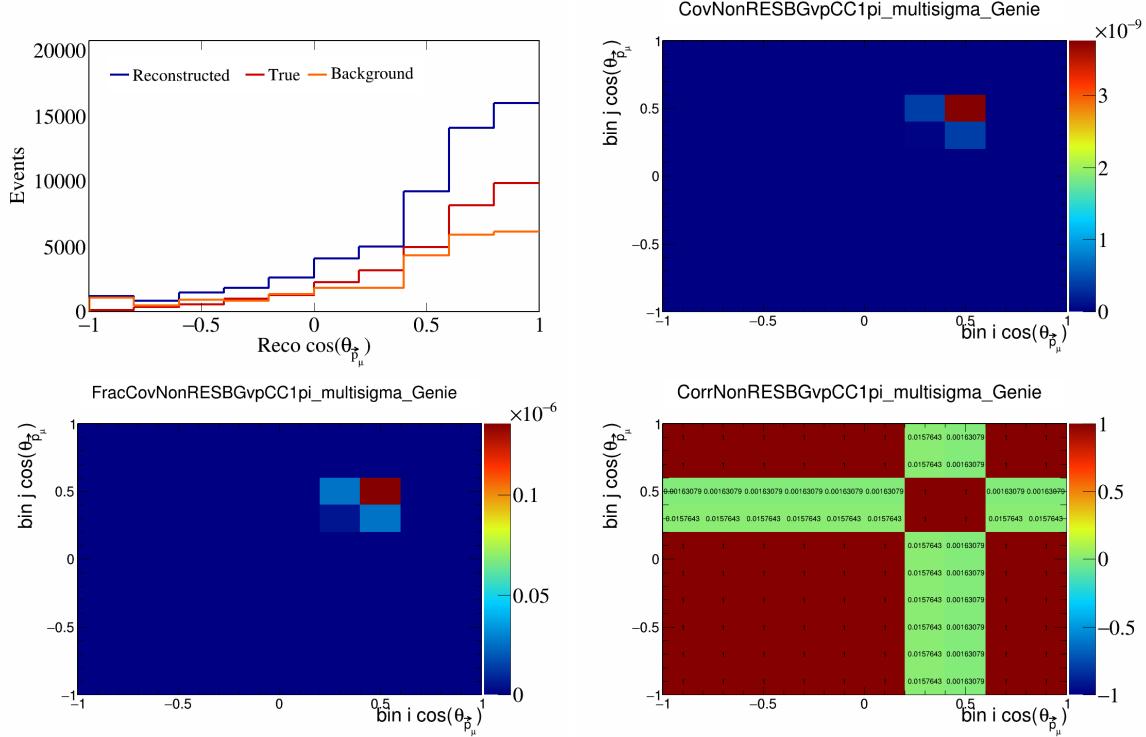


Figure 540: NonRESBGvpCC1pi variations for $\cos(\theta_{\vec{p}_\mu})$.

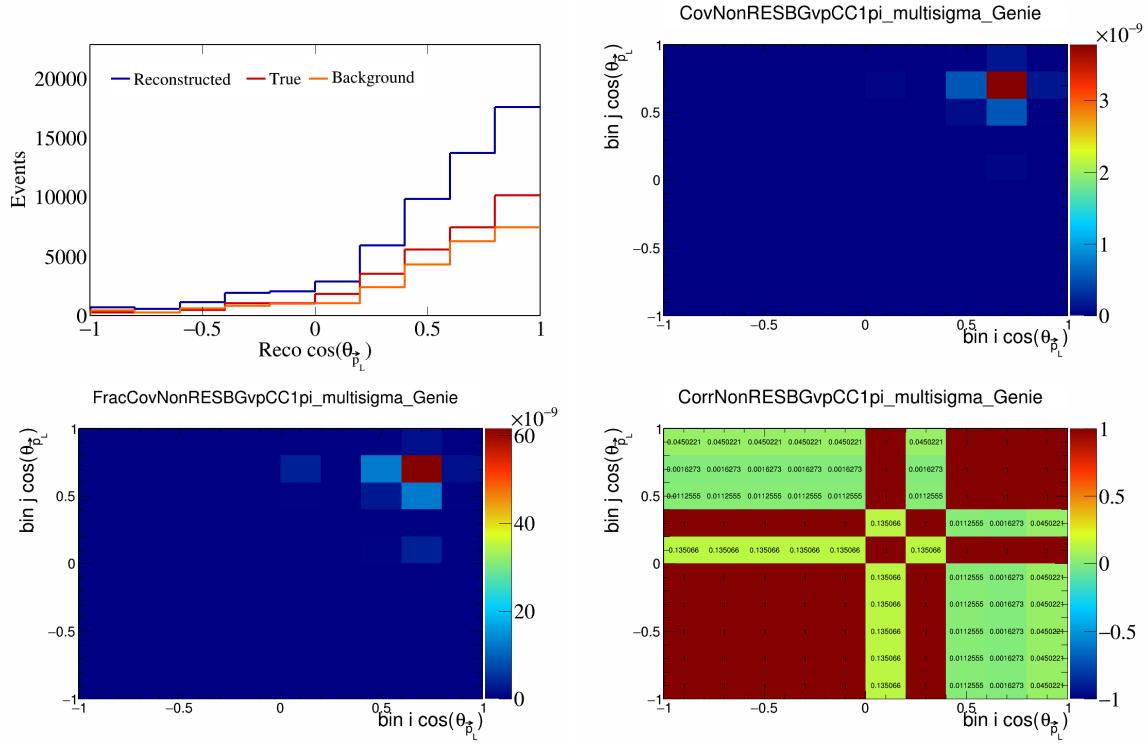


Figure 541: NonRESBGvpCC1pi variations for $\cos(\theta_{\vec{p}_L})$.

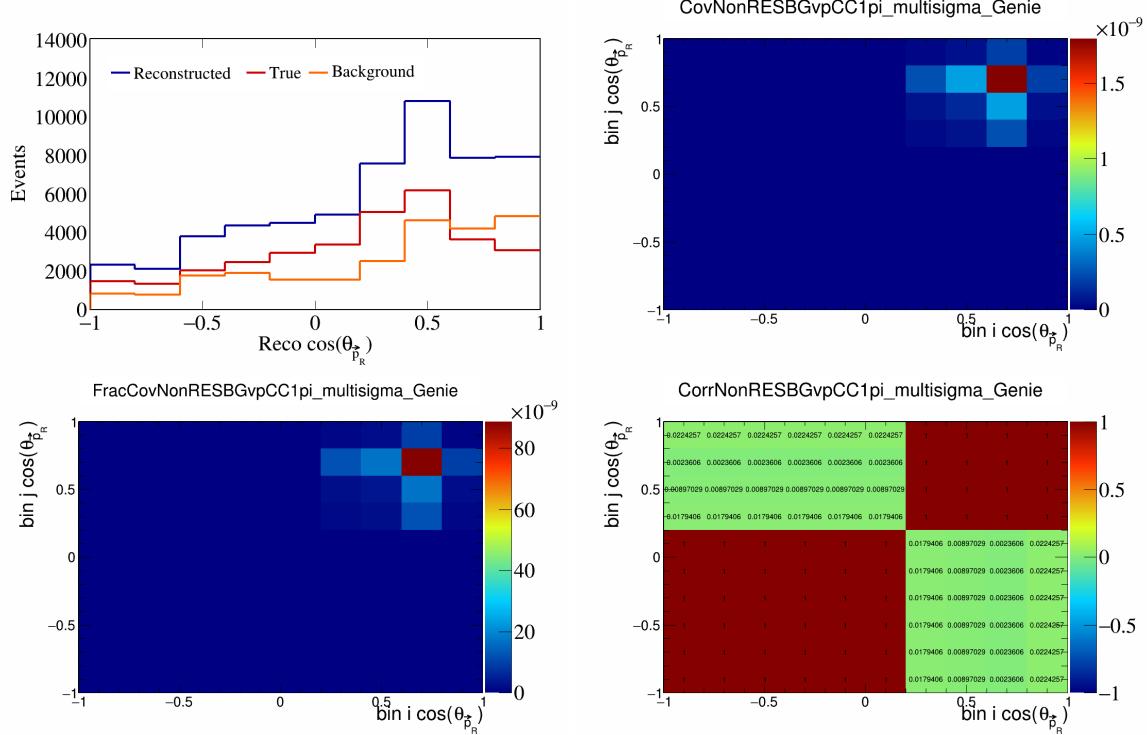


Figure 542: NonRESBGvpCC1pi variations for $\cos(\theta_{\vec{p}_R})$.

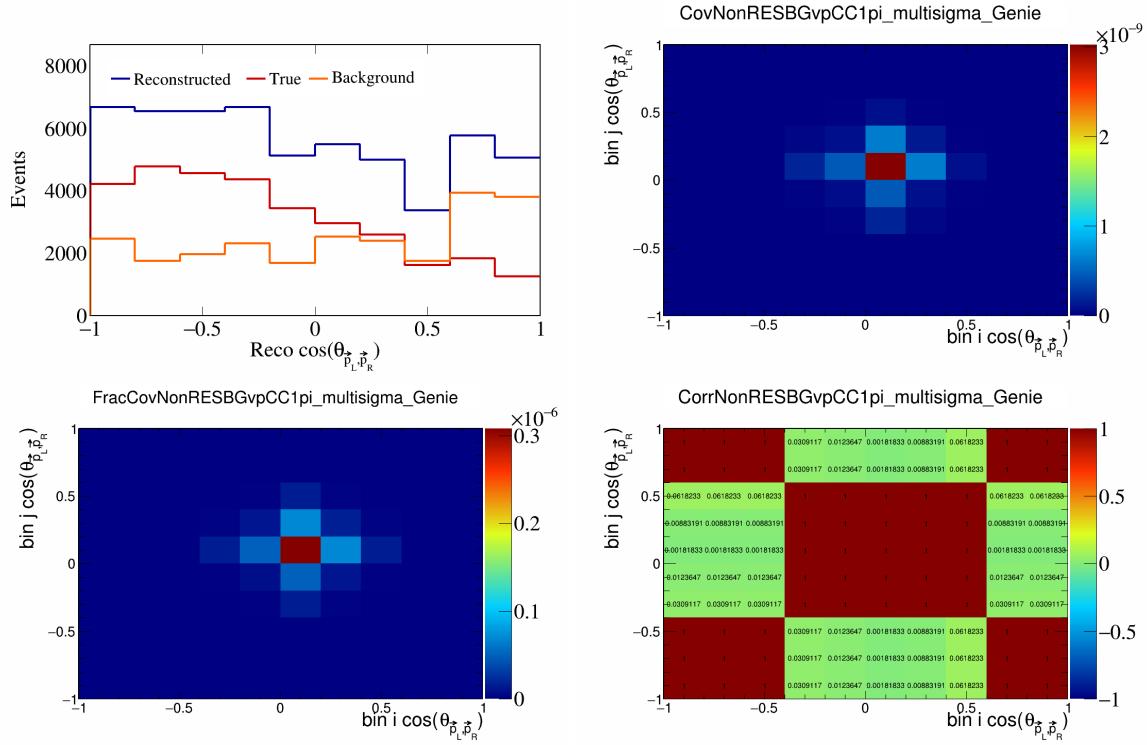


Figure 543: NonRESBGvpCC1pi variations for $\cos(\theta_{\vec{p}_L, \vec{p}_R})$.

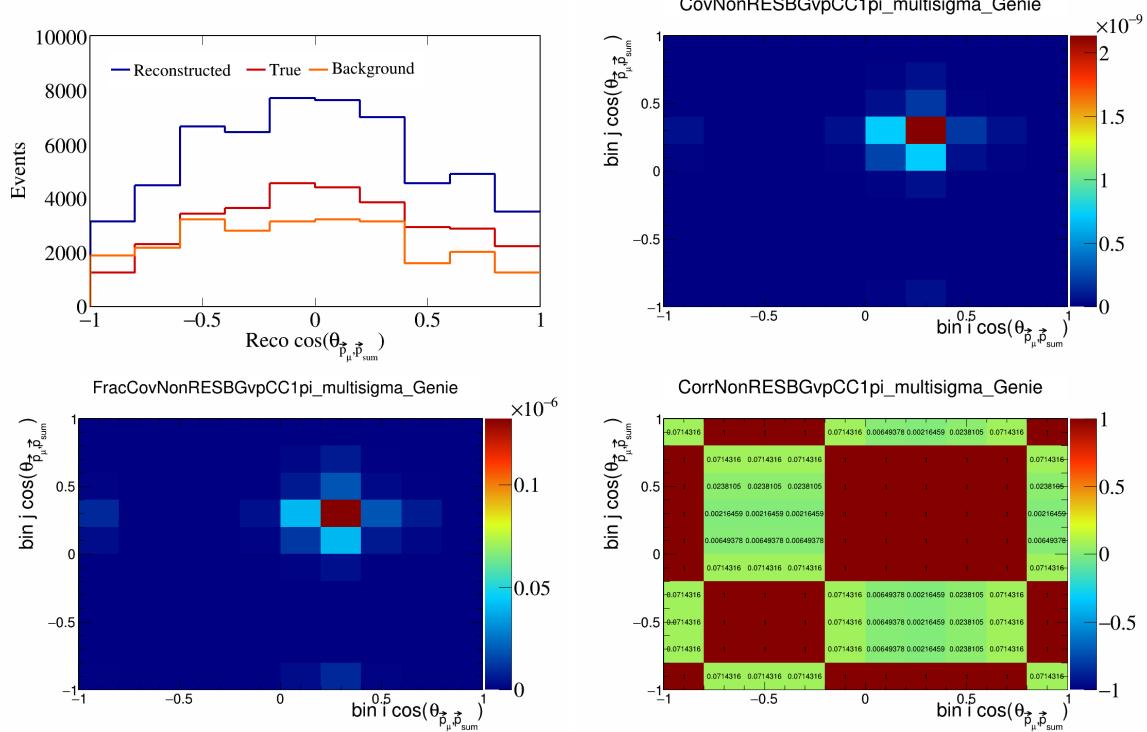


Figure 544: NonRESBGvpCC1pi variations for $\cos(\theta_{\vec{p}_\mu, \vec{p}_{\text{sum}}})$.

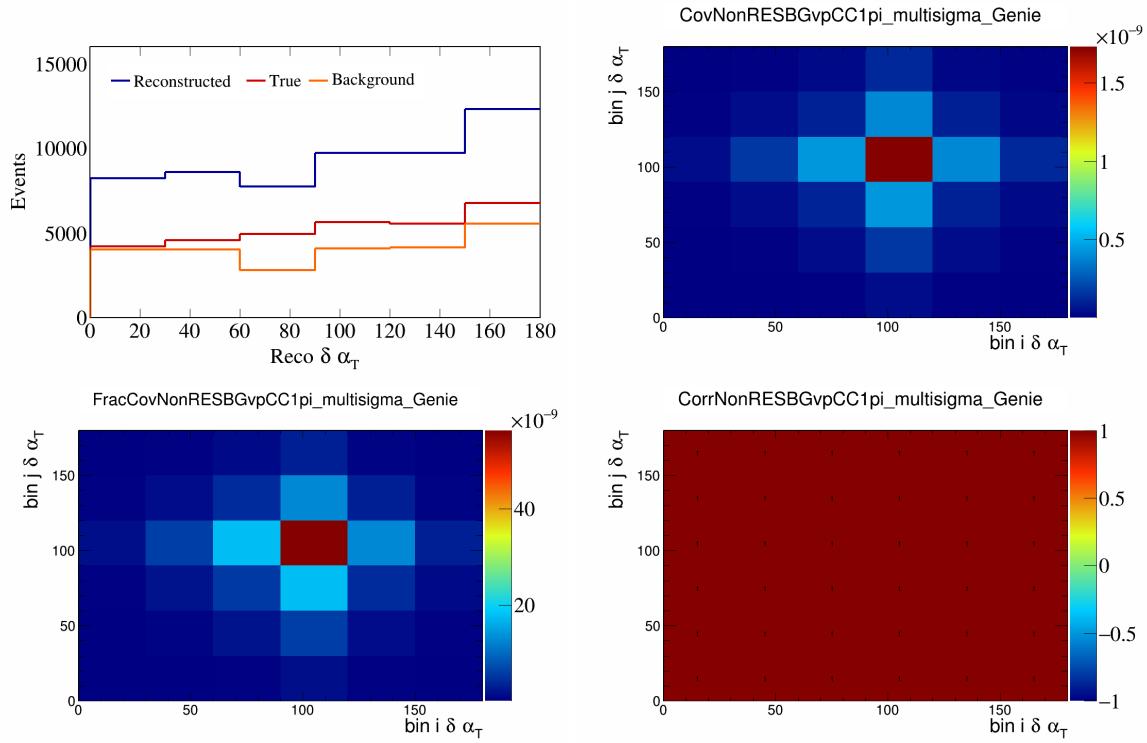


Figure 545: NonRESBGvpCC1pi variations for $\delta\alpha_T$.

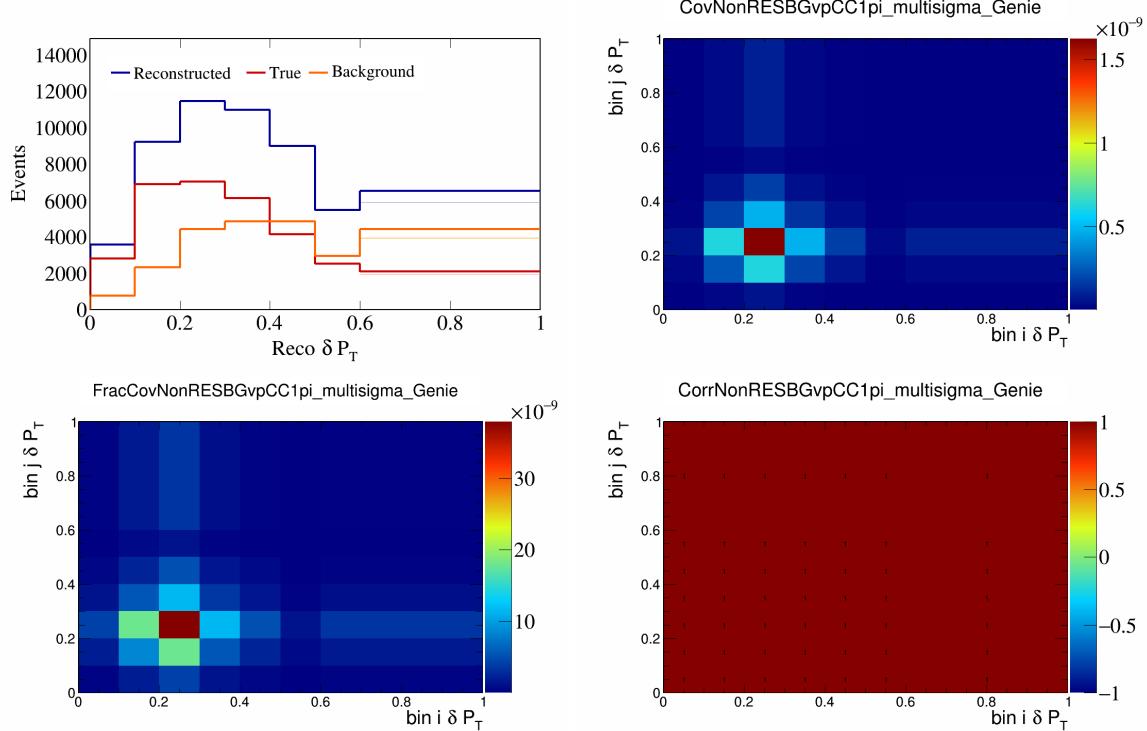


Figure 546: NonRESBGvpCC1pi variations for δP_T .

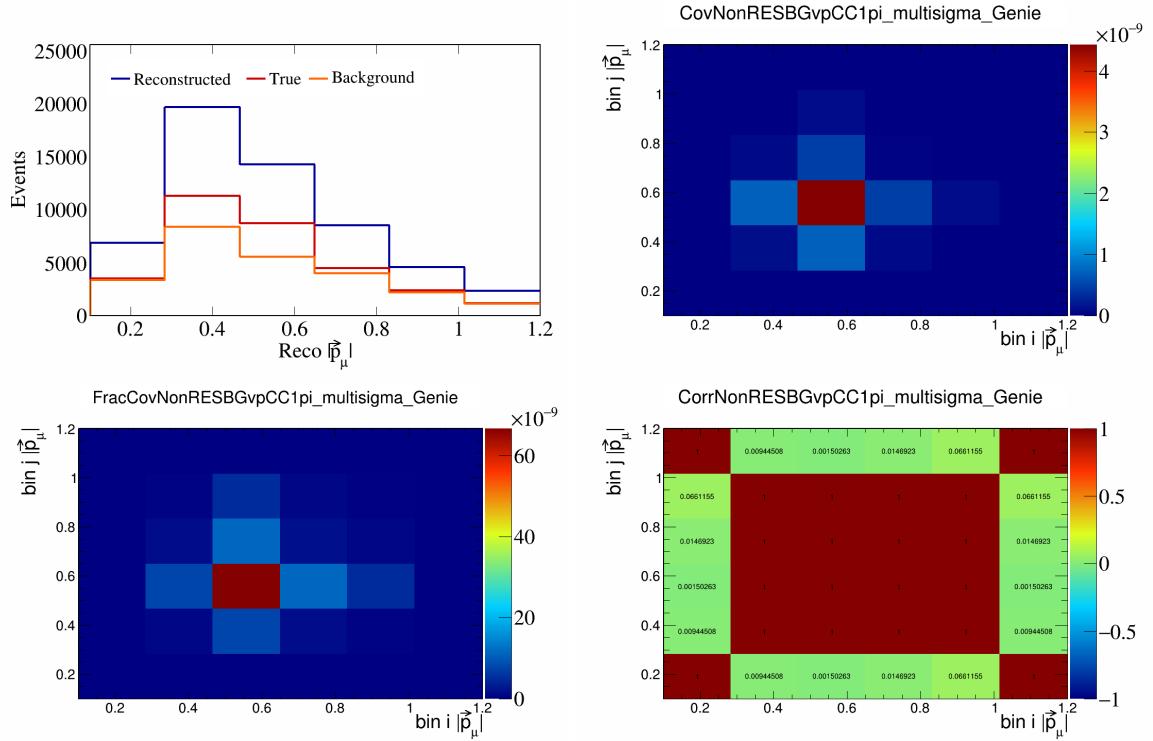


Figure 547: NonRESBGvpCC1pi variations for $|\vec{p}_\mu|$.

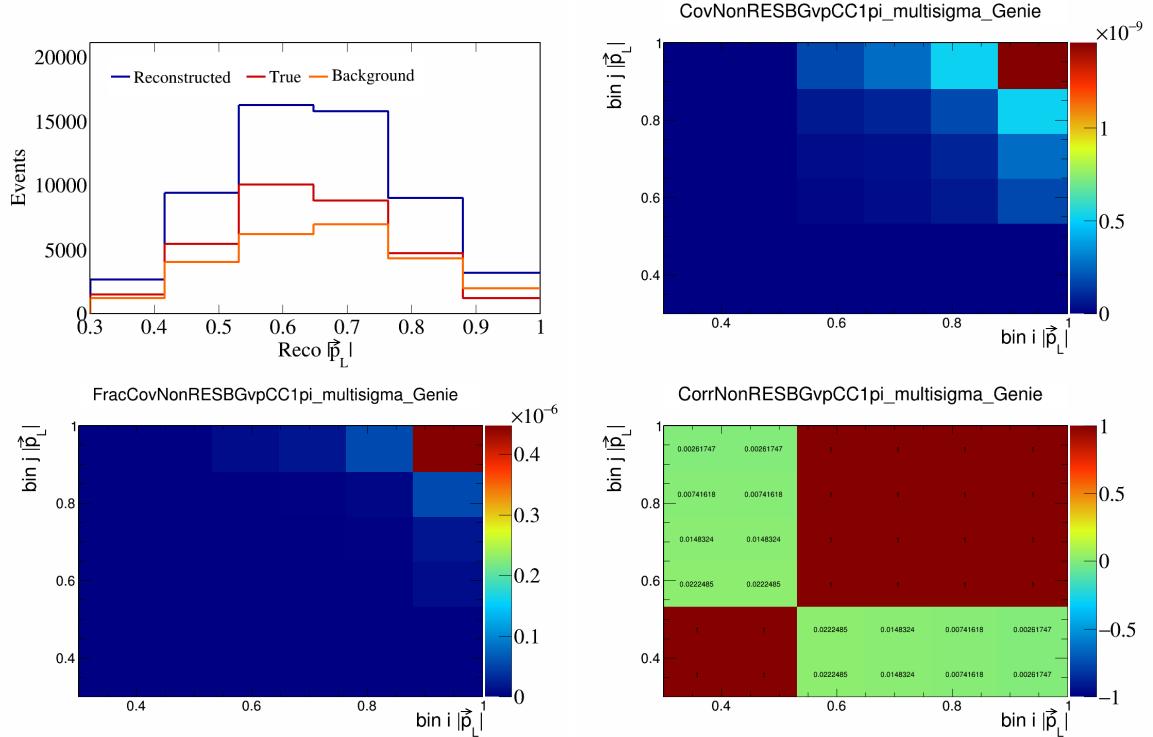


Figure 548: NonRESBGvpCC1pi variations for $|\vec{p}_L|$.

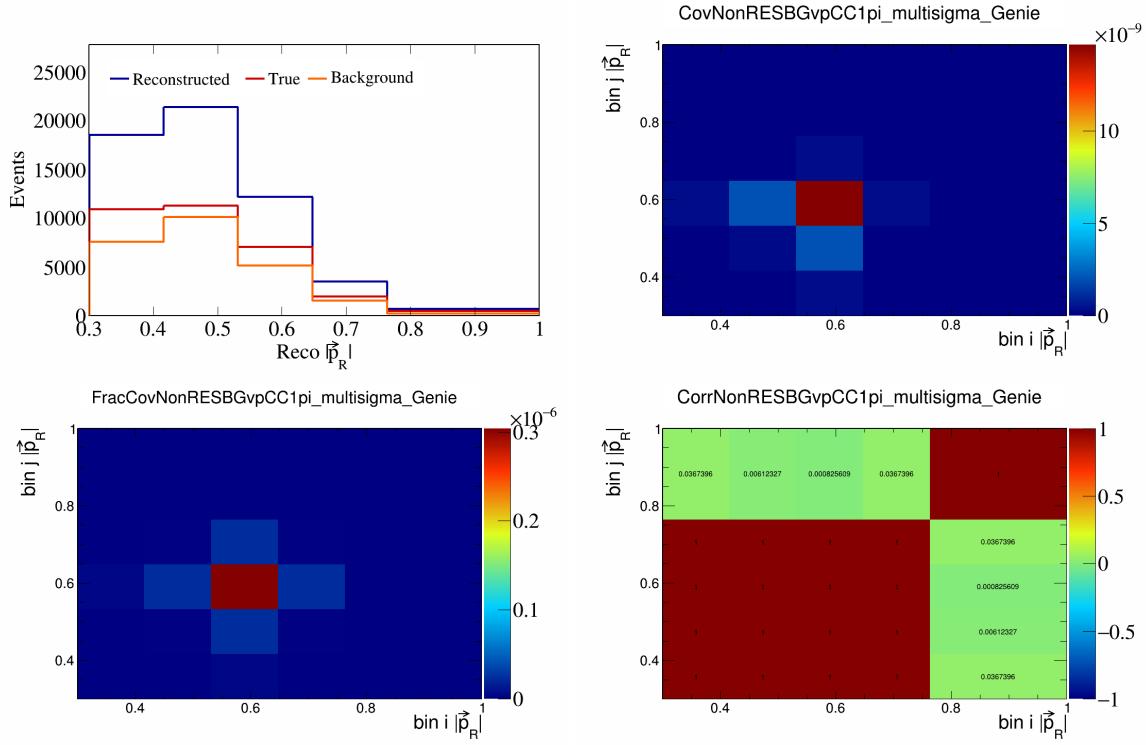


Figure 549: NonRESBGvpCC1pi variations for $|\vec{p}_R|$.

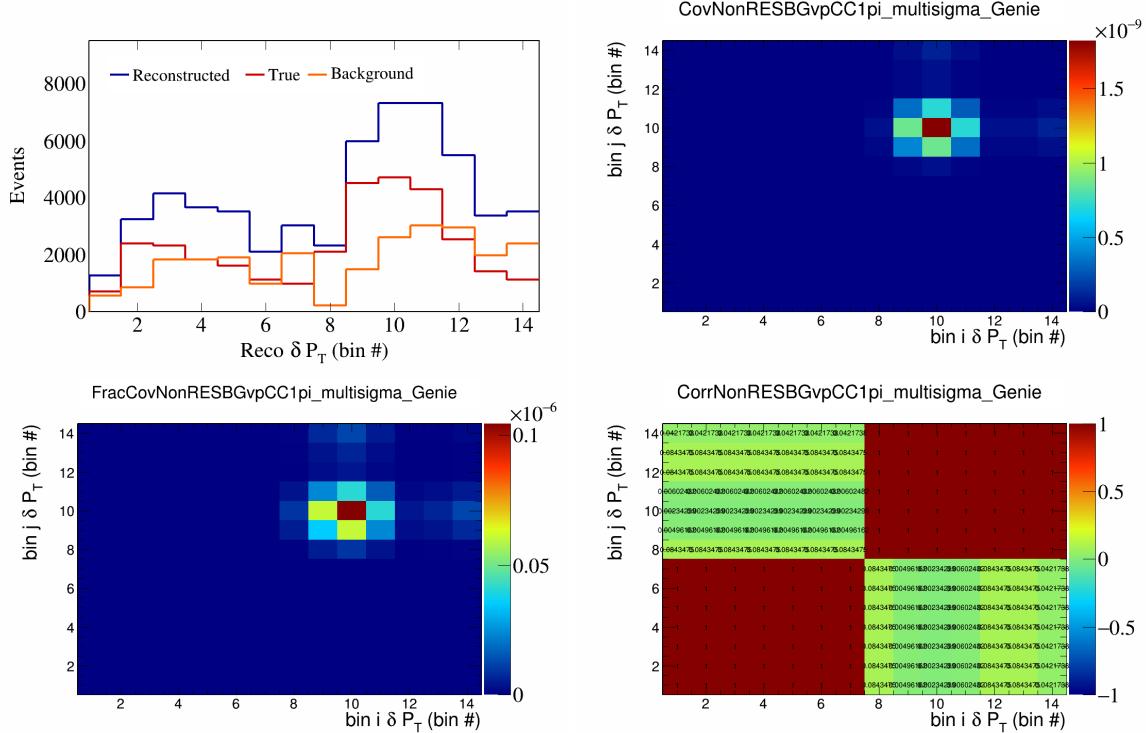


Figure 550: NonRESBGvpCC1pi variations for δP_T in $\cos(\theta_{\vec{p}_\mu})$.

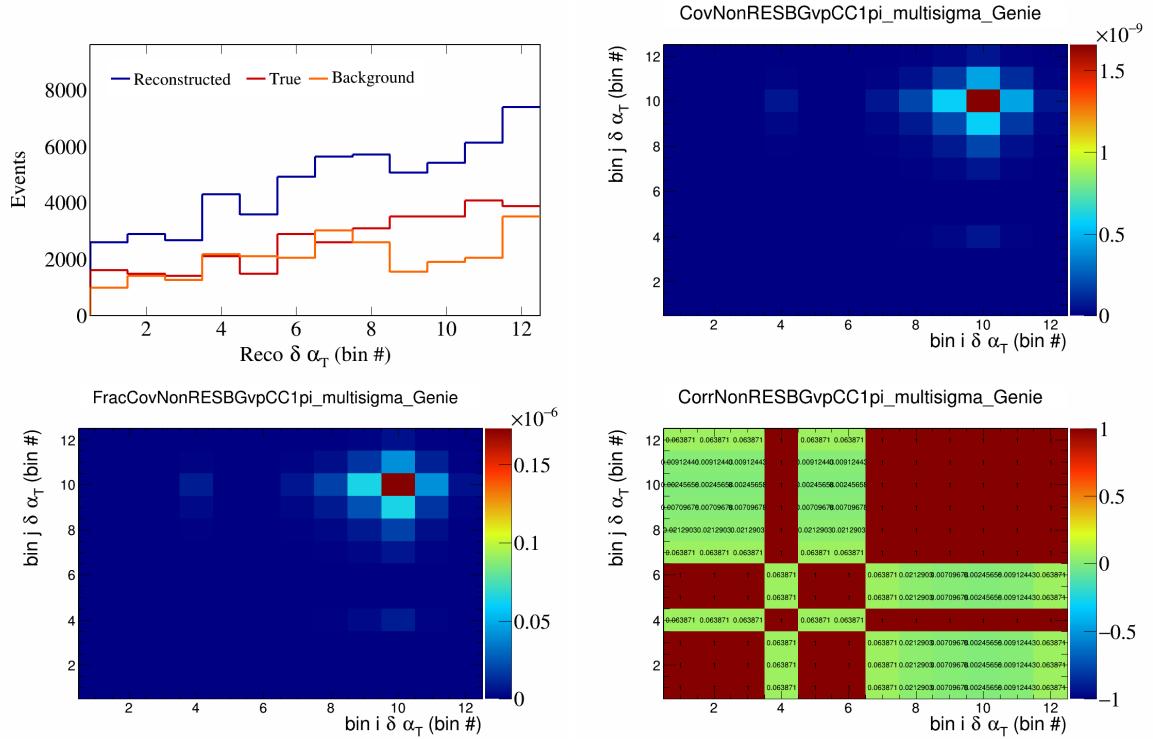


Figure 551: NonRESBGvpCC1pi variations for $\delta\alpha_T$ in $\cos(\theta_{\vec{p}_\mu})$.

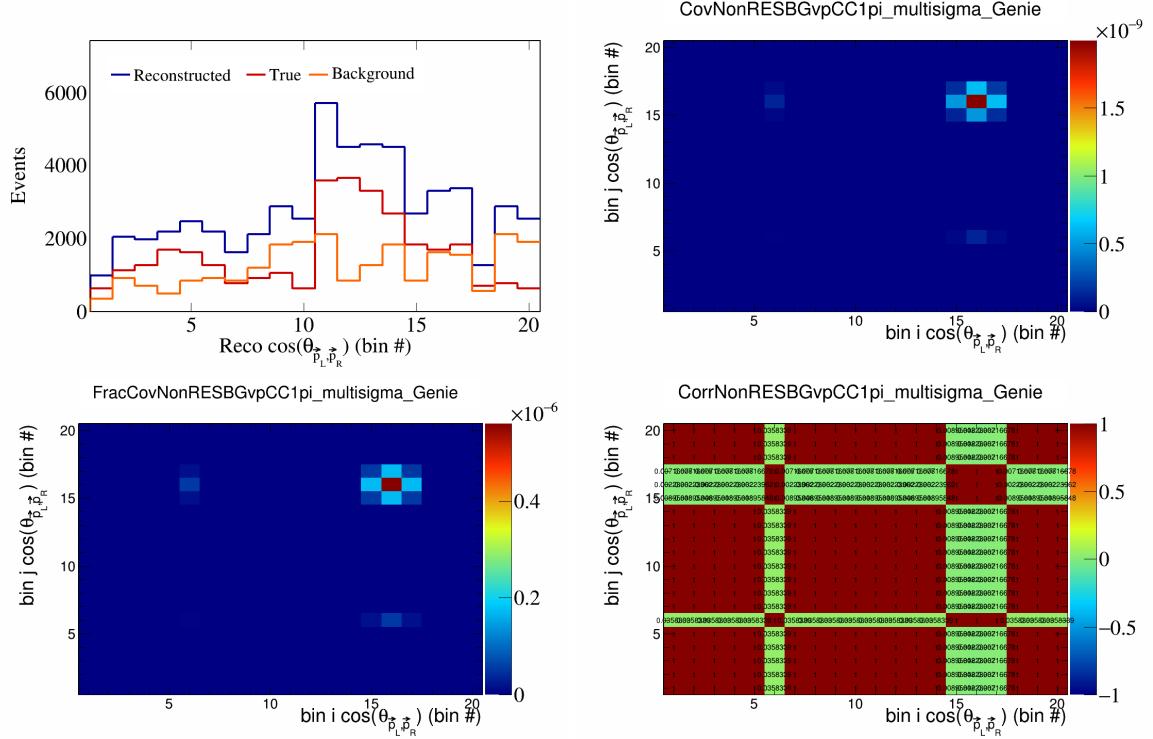


Figure 552: NonRESBGvpCC1pi variations for $\cos(\theta_{\vec{p}_L, \vec{p}_R})$ in $\cos(\theta_{\vec{p}_\mu})$.

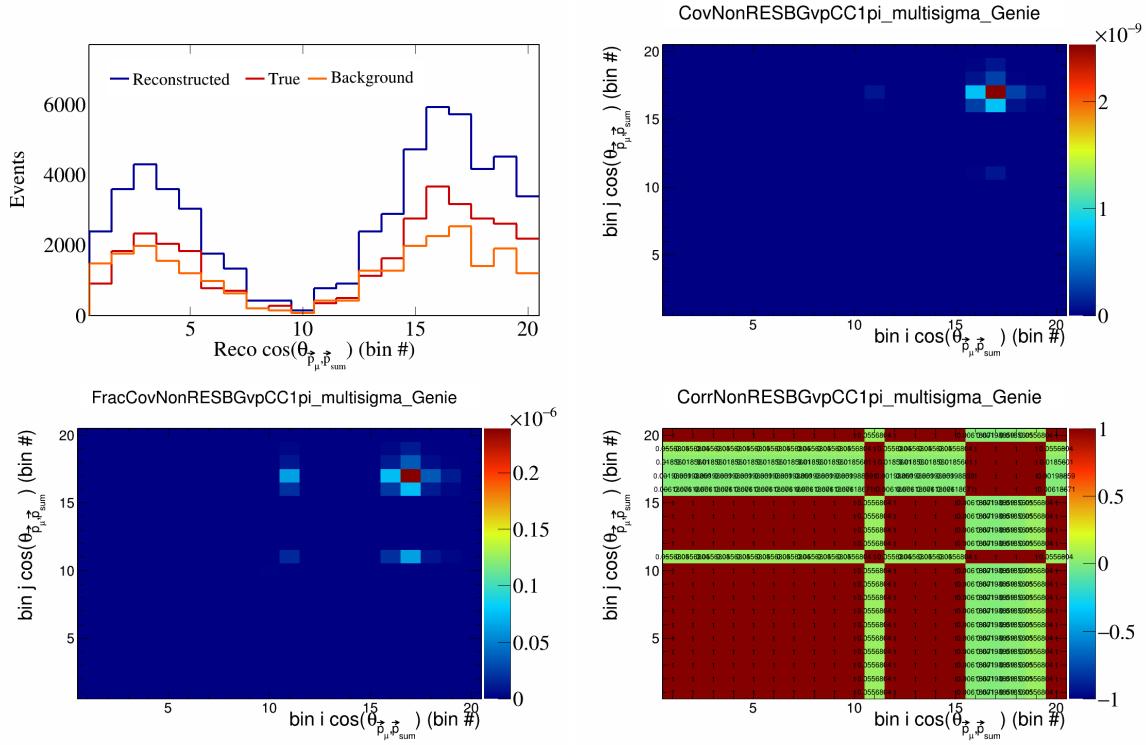


Figure 553: NonRESBGvpCC1pi variations for $\cos(\theta_{\vec{p}_\mu})$ in $\cos(\theta_{\vec{p}_\mu})$.

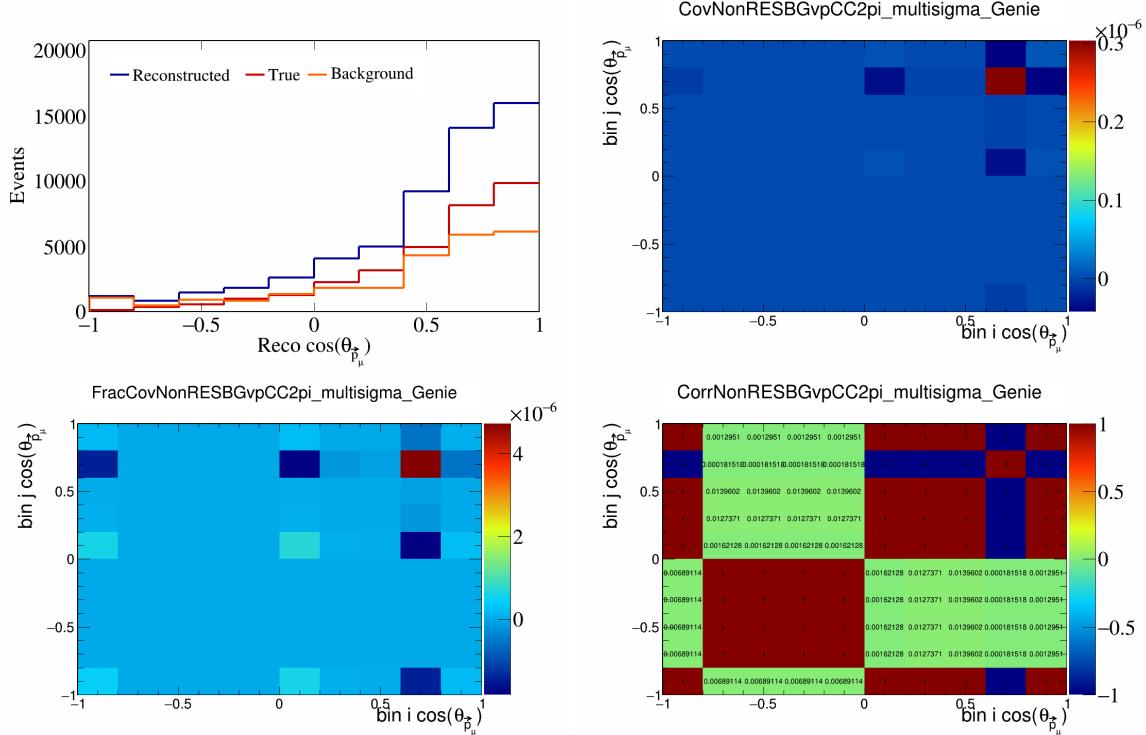


Figure 554: NonRESBGvpCC2pi variations for $\cos(\theta_{\vec{p}_\mu})$.

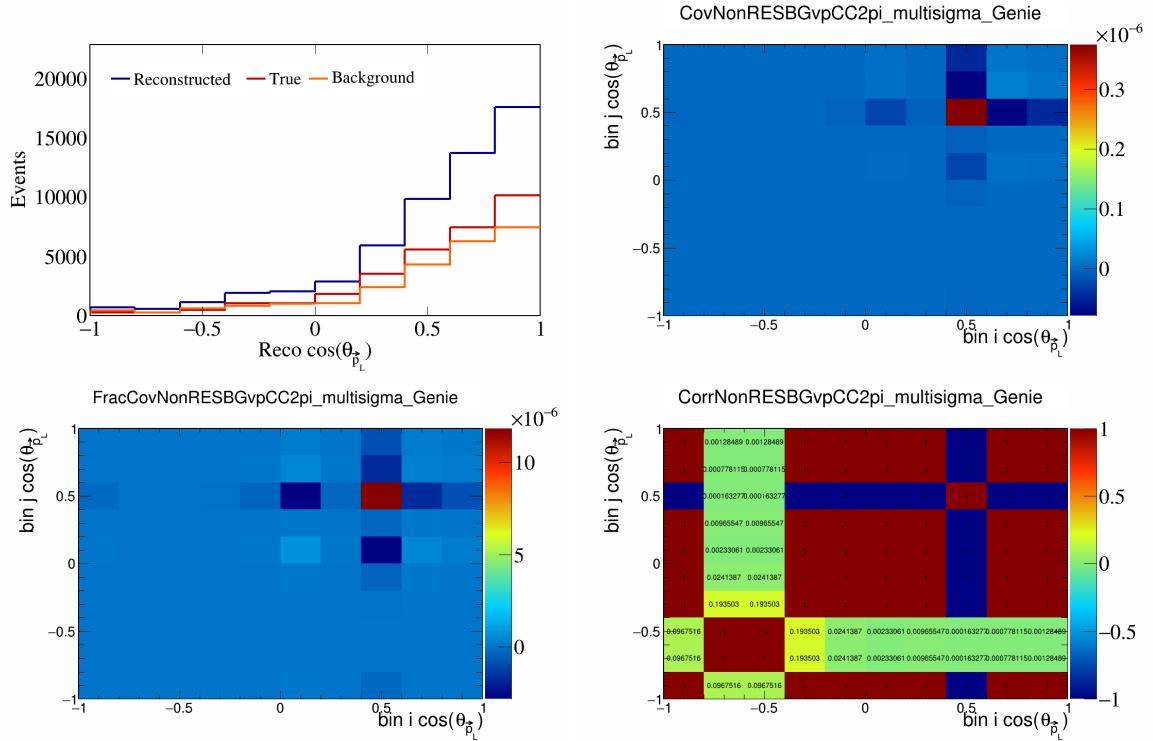


Figure 555: NonRESBGvpCC2pi variations for $\cos(\theta_{\vec{p}_L})$.

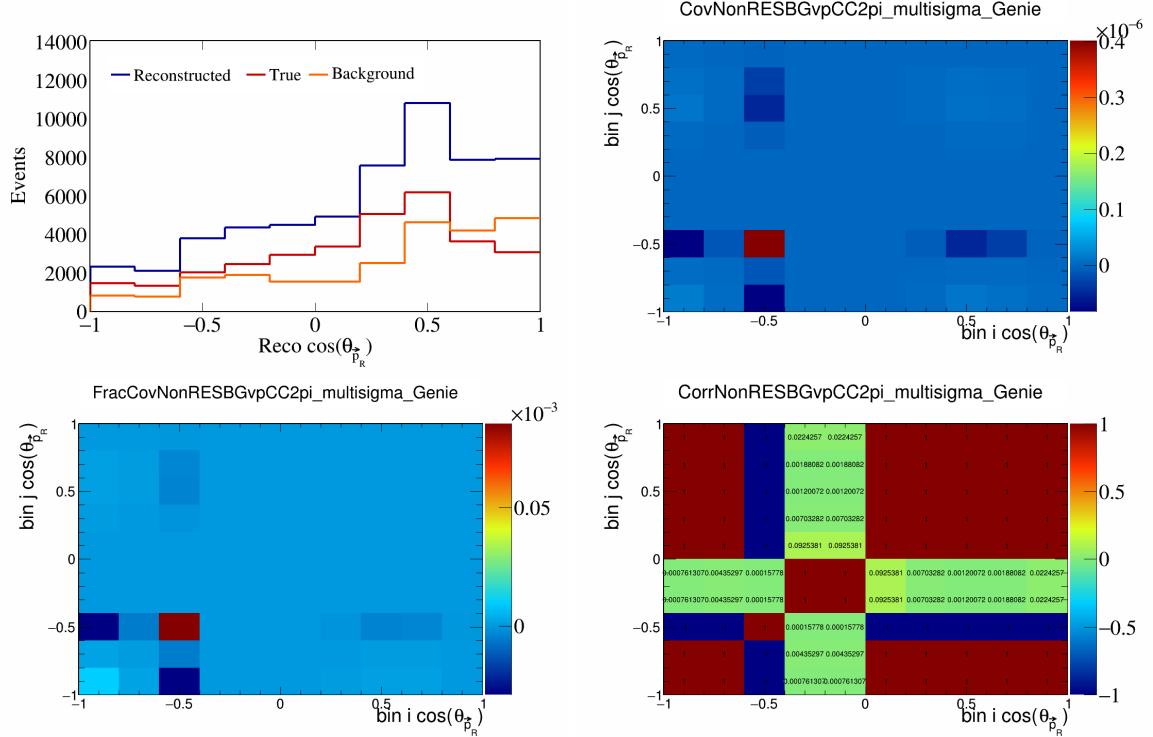


Figure 556: NonRESBGvpCC2pi variations for $\cos(\theta_{\vec{p}_R})$.

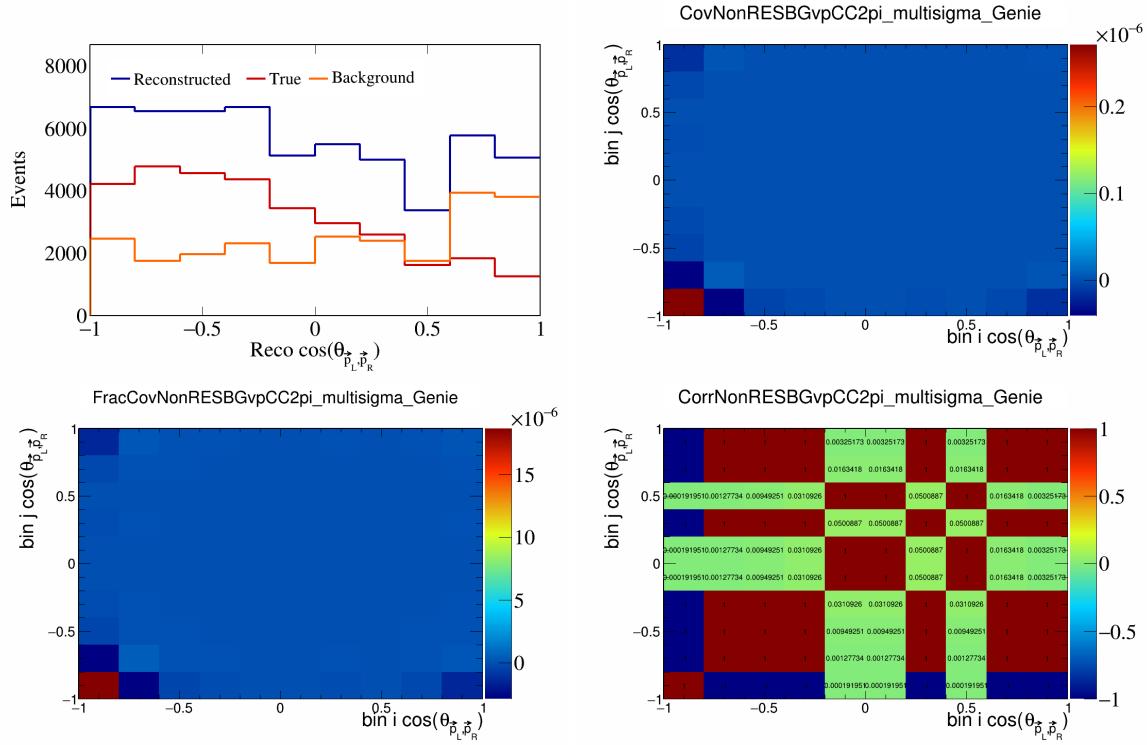


Figure 557: NonRESBGvpCC2pi variations for $\cos(\theta_{\vec{p}_L, \vec{p}_R})$.

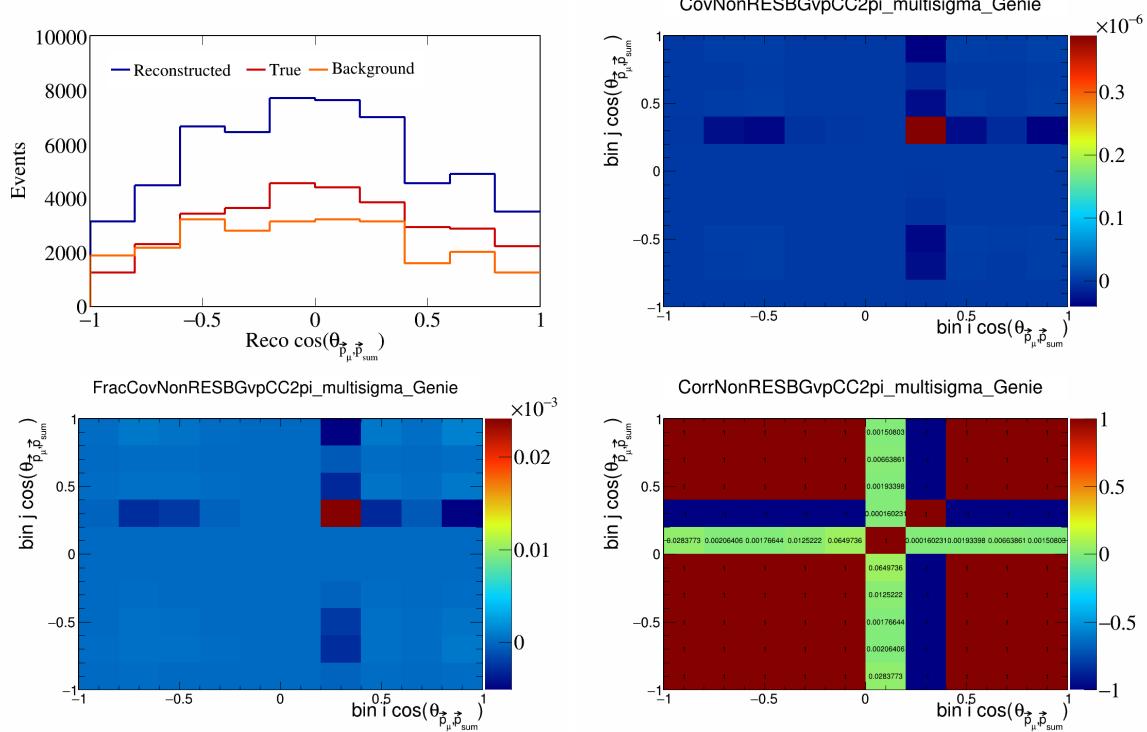


Figure 558: NonRESBGvpCC2pi variations for $\cos(\theta_{\vec{p}_\mu, \vec{p}_{\text{sum}}})$.

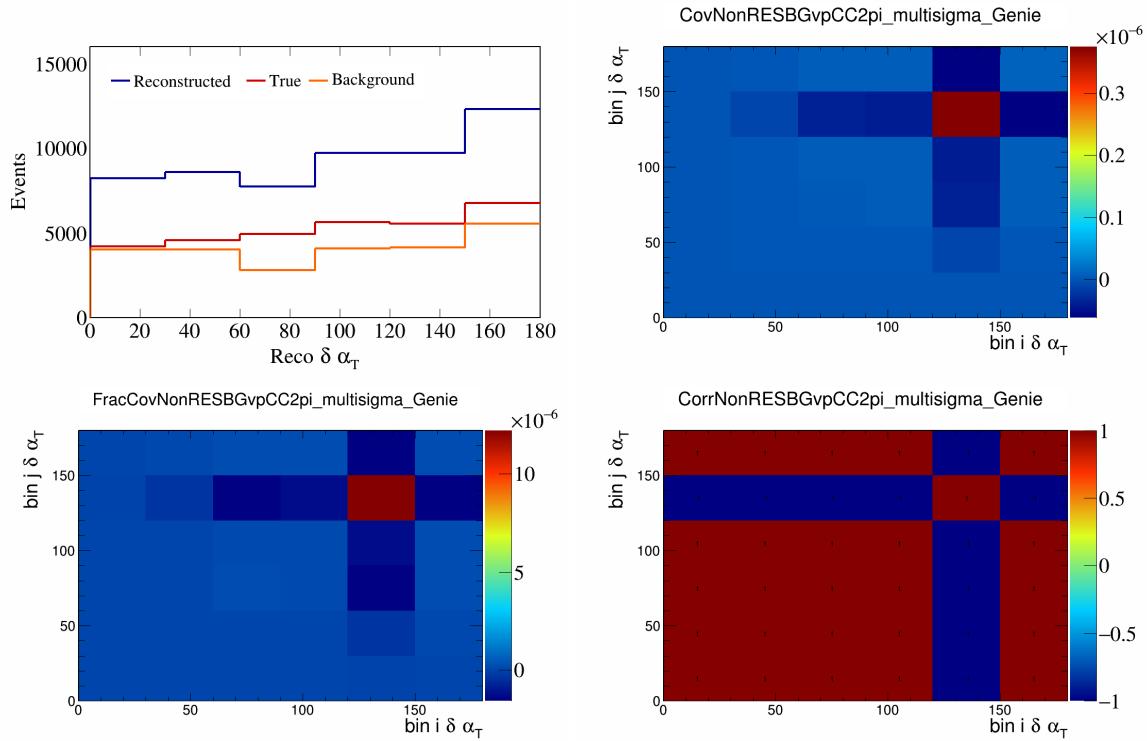


Figure 559: NonRESBGvpCC2pi variations for $\delta\alpha_T$.

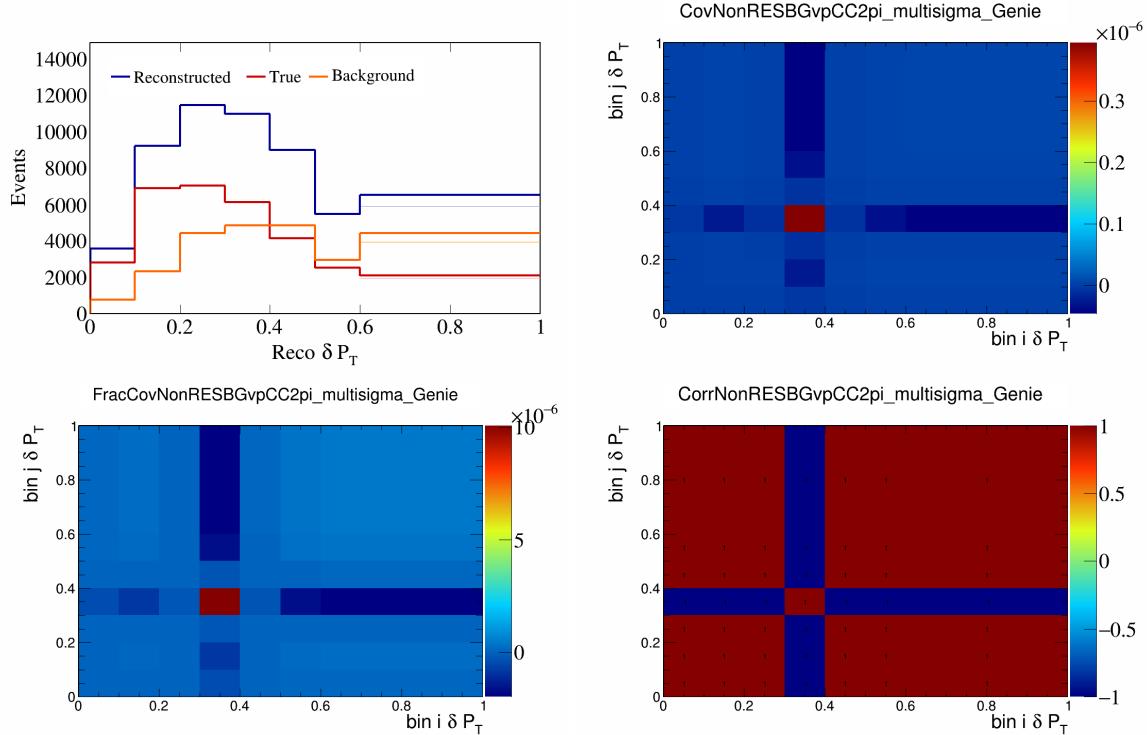


Figure 560: NonRESBGvpCC2pi variations for δP_T .

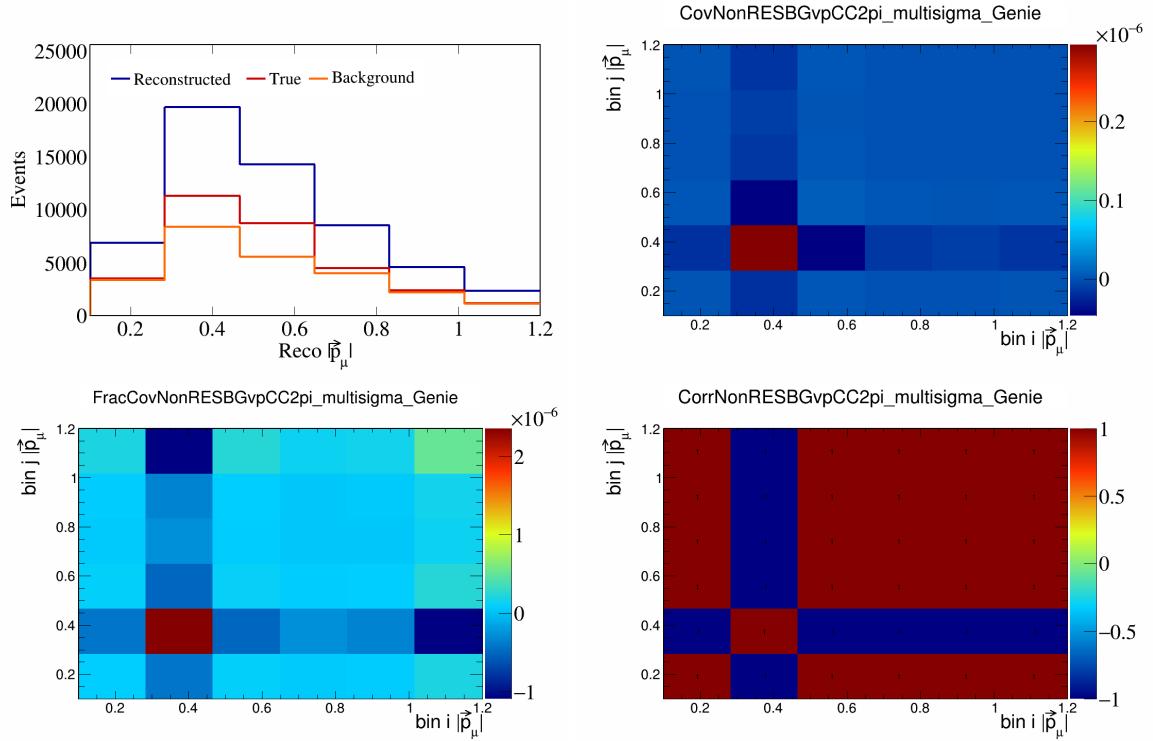


Figure 561: NonRESBGvpCC2pi variations for $|\vec{p}_\mu|$.

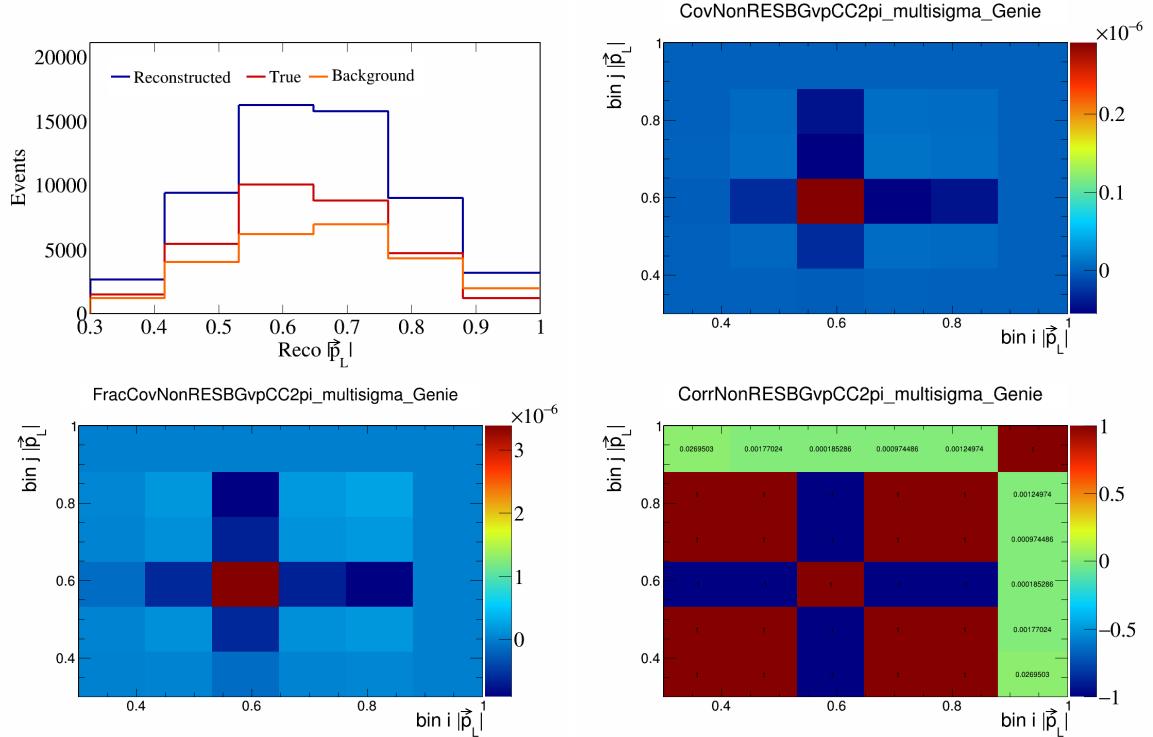


Figure 562: NonRESBGvpCC2pi variations for $|\vec{p}_L|$.

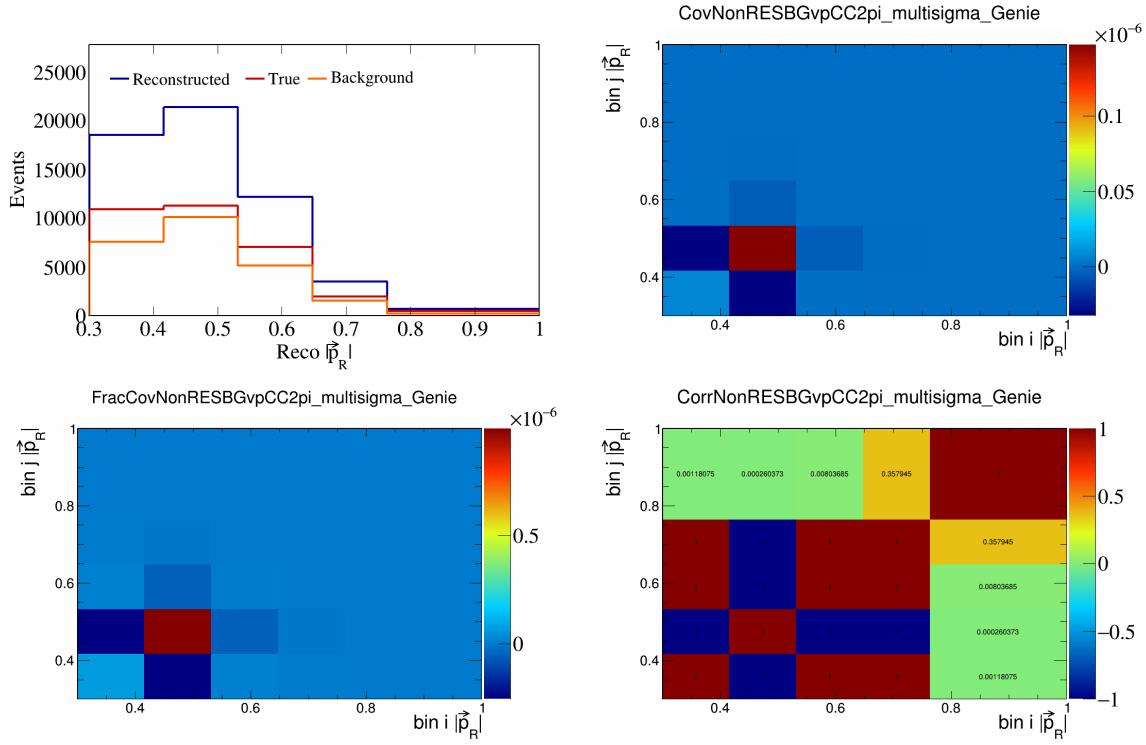


Figure 563: NonRESBGvpCC2pi variations for $|\vec{p}_R|$.

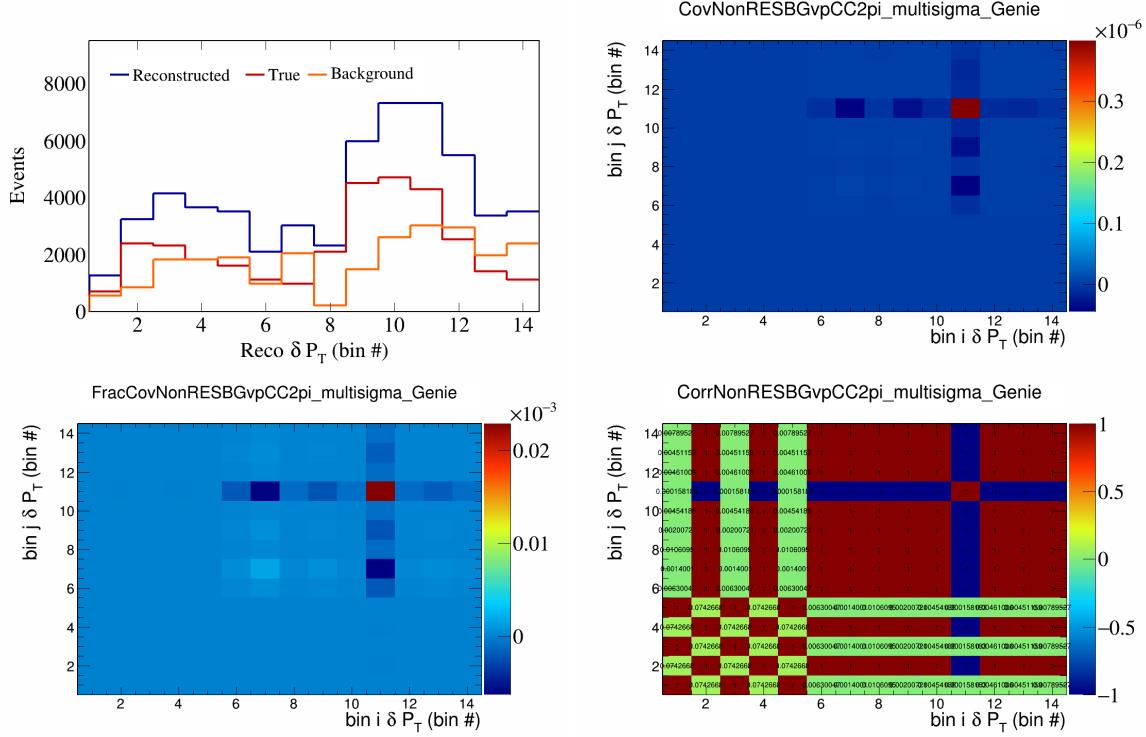


Figure 564: NonRESBGvpCC2pi variations for δP_T in $\cos(\theta_{\vec{p}_\mu})$.

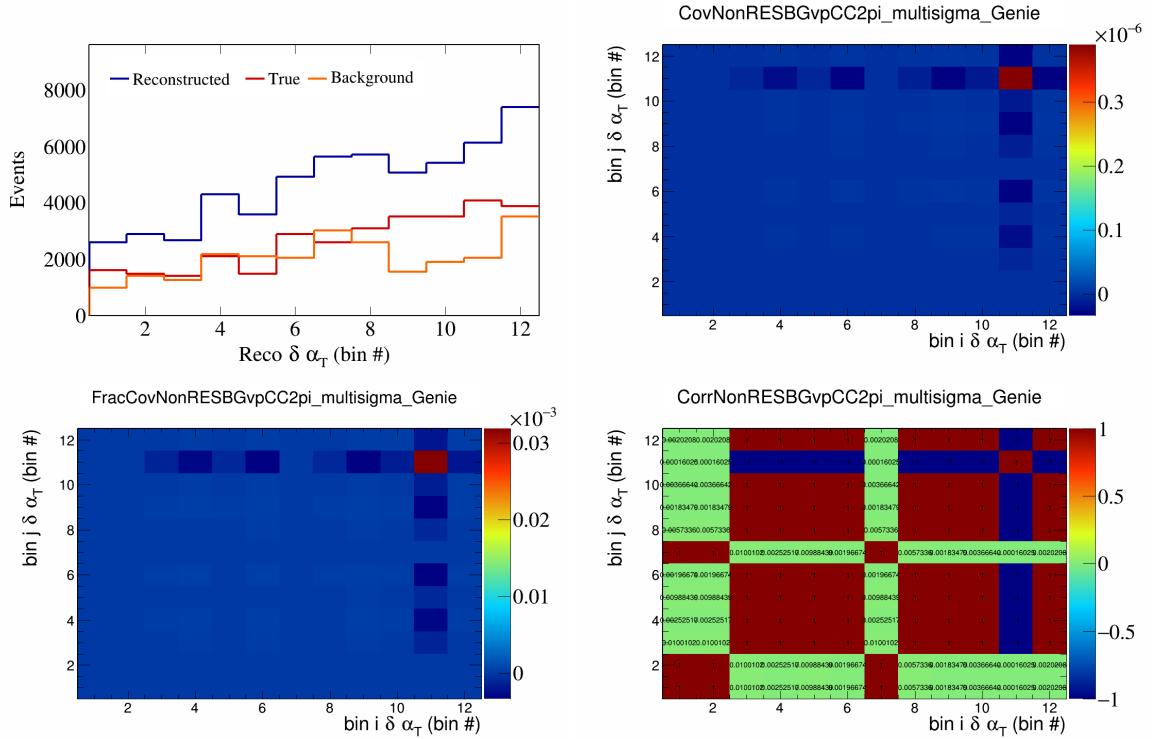


Figure 565: NonRESBGvpCC2pi variations for $\delta\alpha_T$ in $\cos(\theta_{\vec{p}_\mu})$.

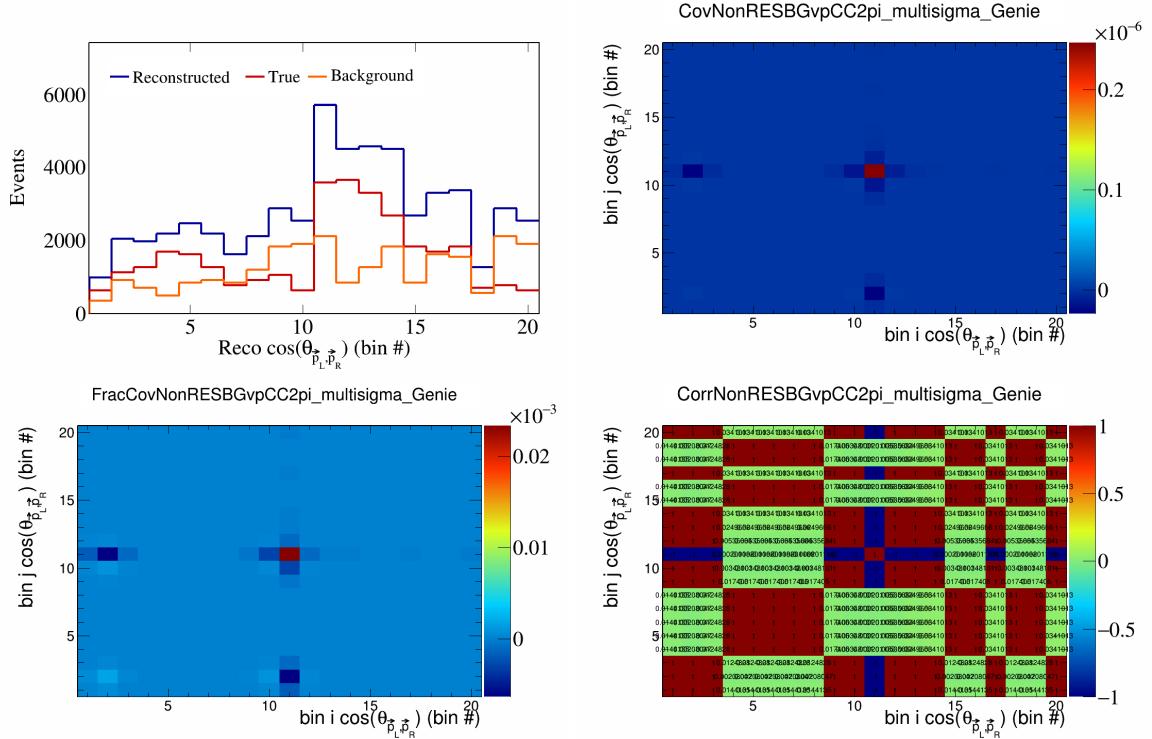


Figure 566: NonRESBGvpCC2pi variations for $\cos(\theta_{\vec{p}_L, \vec{p}_R})$ in $\cos(\theta_{\vec{p}_\mu})$.

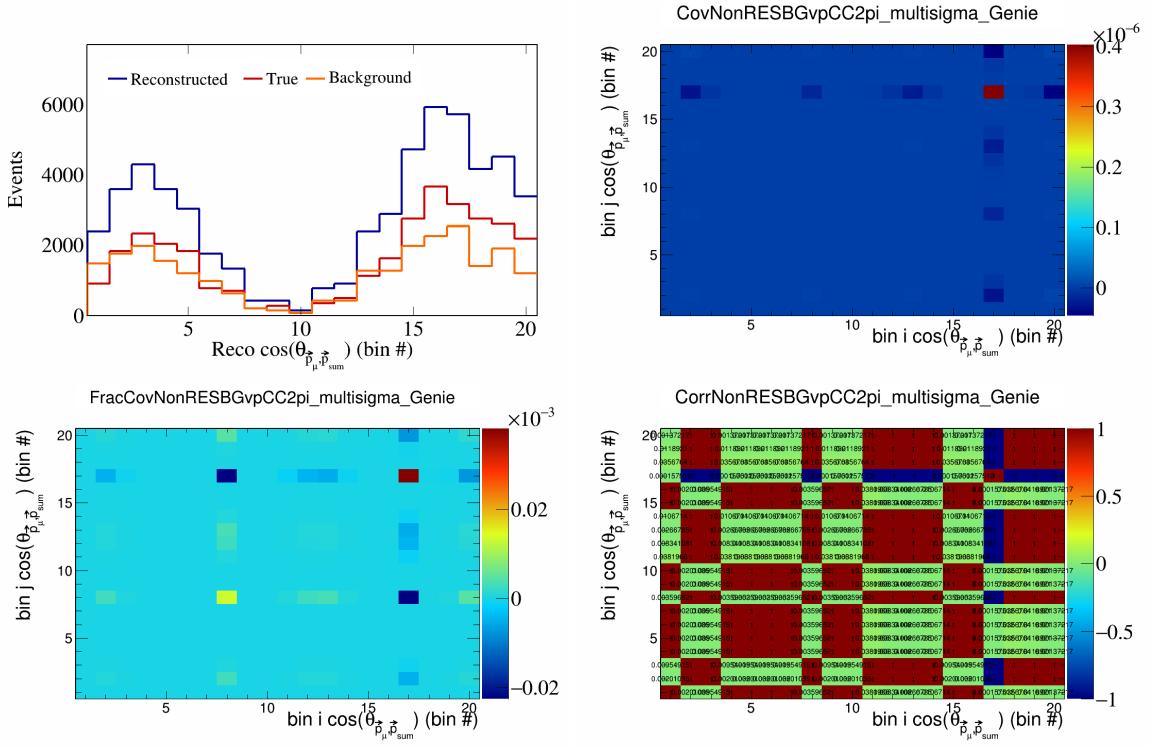


Figure 567: NonRESBGvpCC2pi variations for $\cos(\theta_{\vec{p}_\mu, \vec{p}_{\text{sum}}})$ in $\cos(\theta_{\vec{p}_\mu})$.

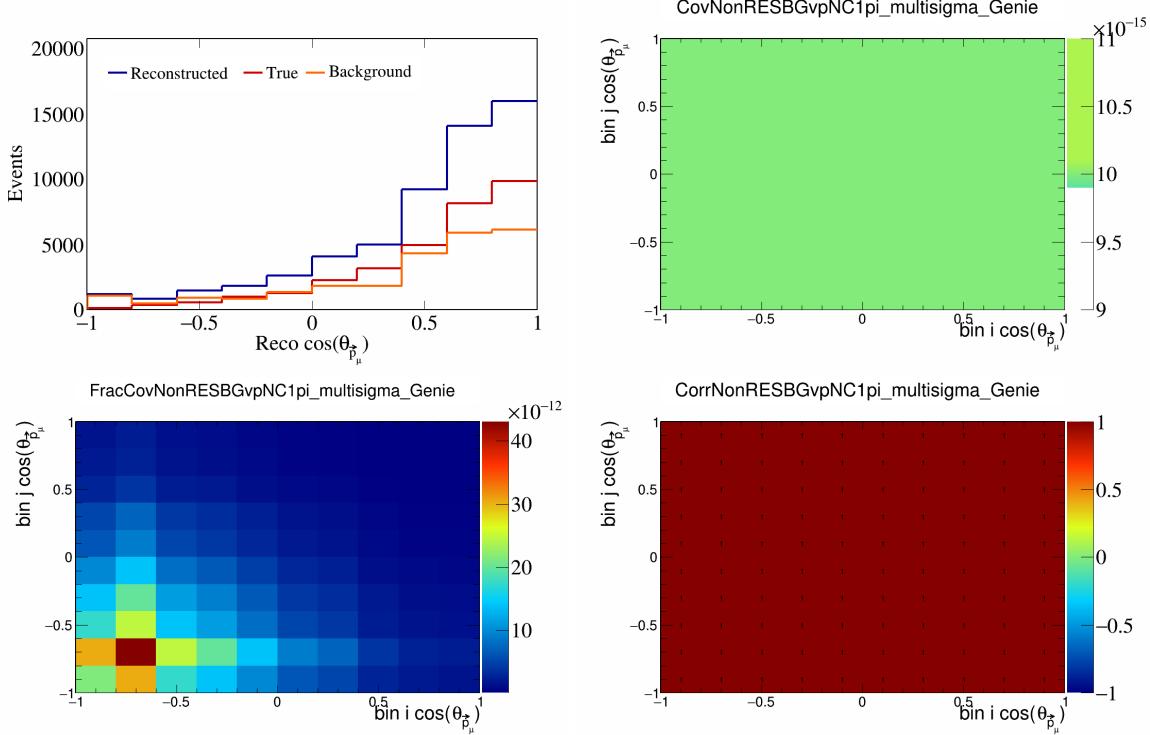


Figure 568: NonRESBGvpNC1pi variations for $\cos(\theta_{\vec{p}_\mu})$.

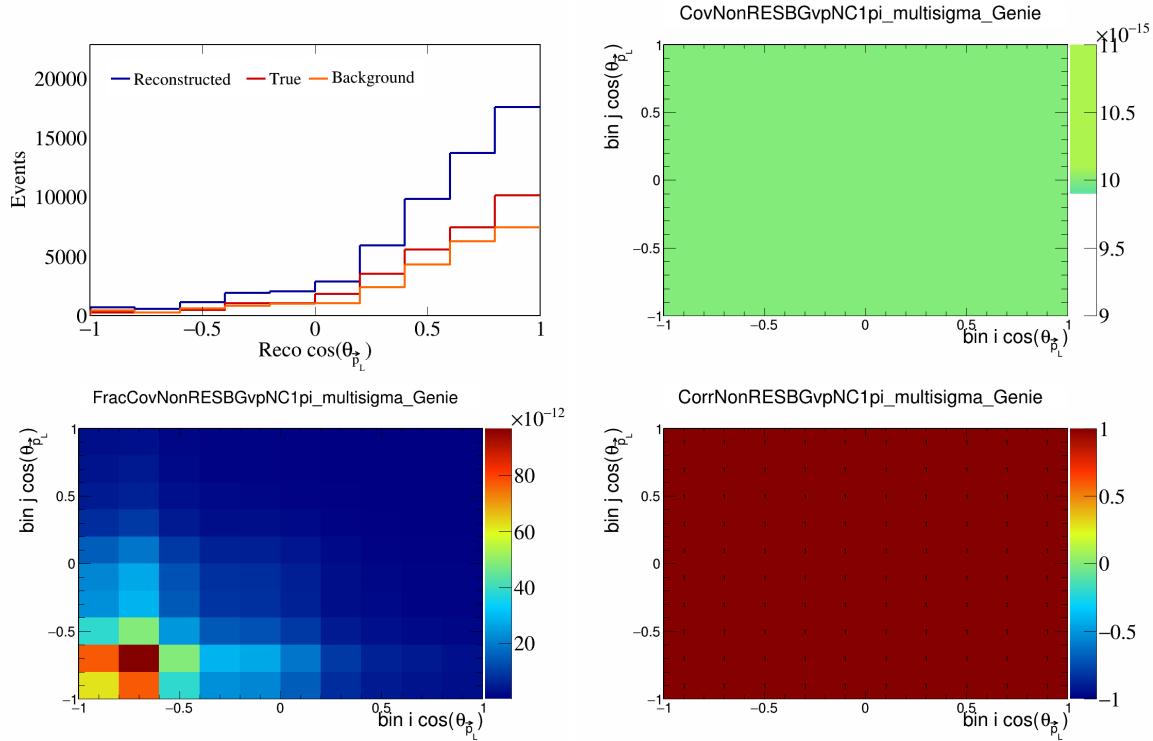


Figure 569: NonRESBGvpNC1pi variations for $\cos(\theta_{\vec{p}_L})$.

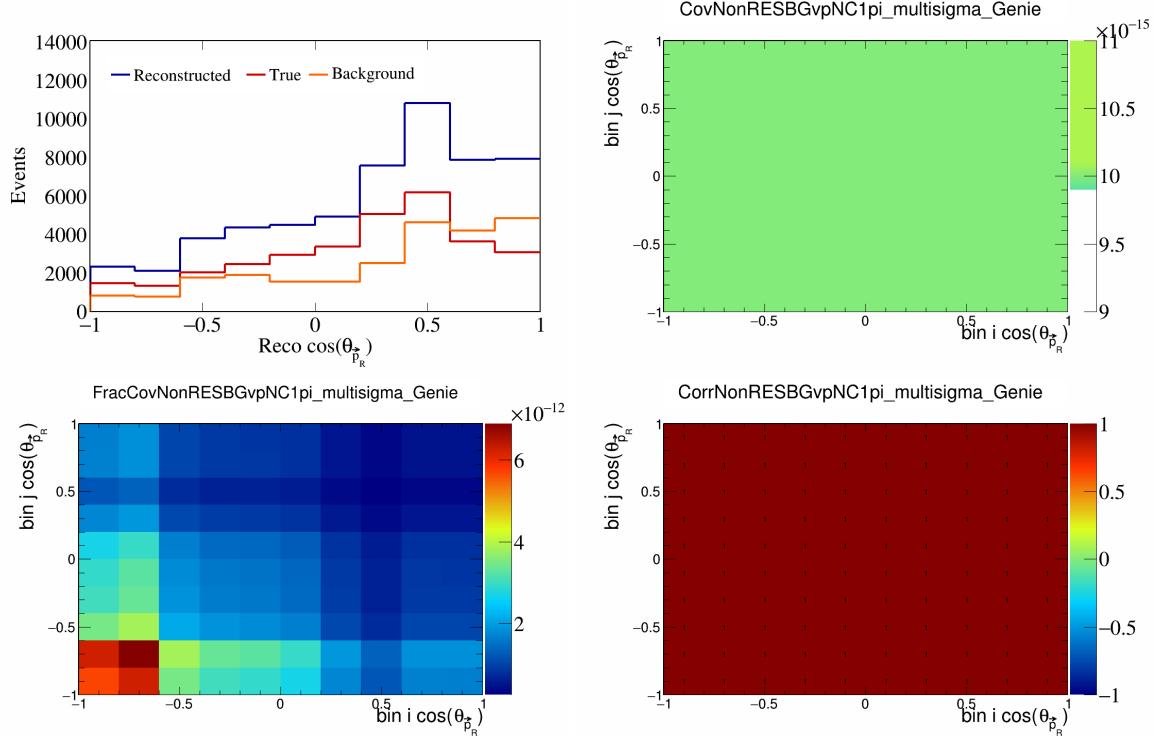


Figure 570: NonRESBGvpNC1pi variations for $\cos(\theta_{\vec{p}_R})$.

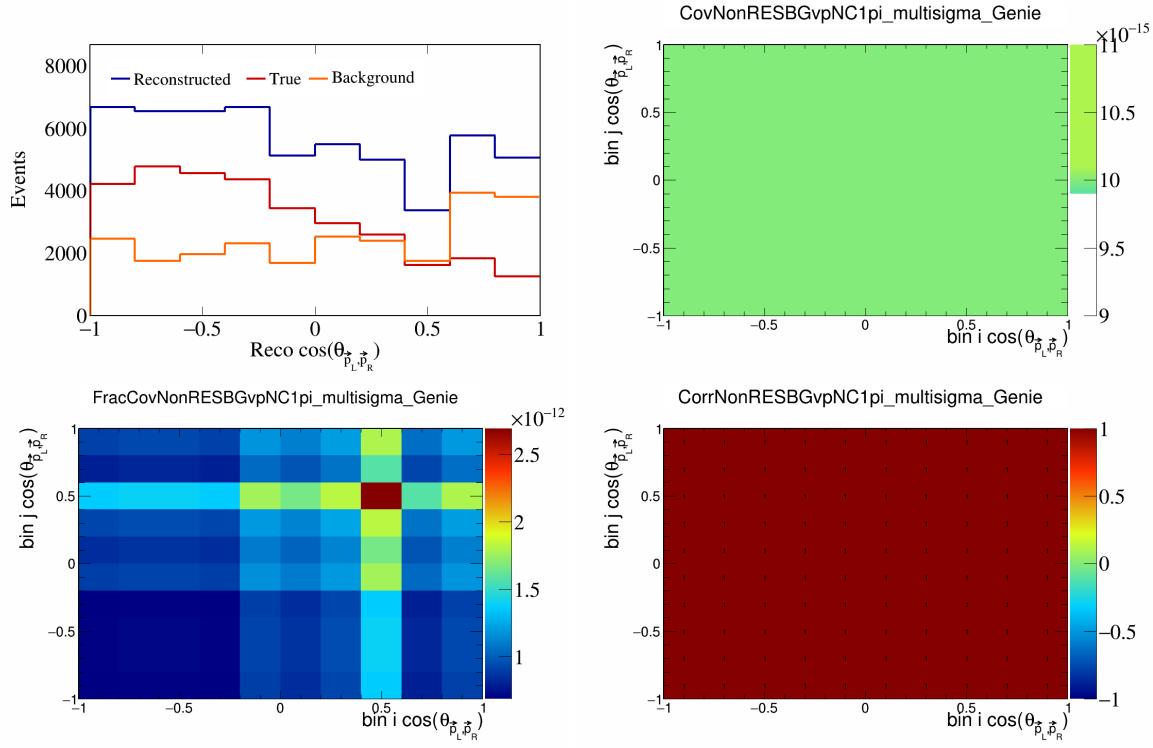


Figure 571: NonRESBGvNC1pi variations for $\cos(\theta_{\vec{p}_L, \vec{p}_R})$.

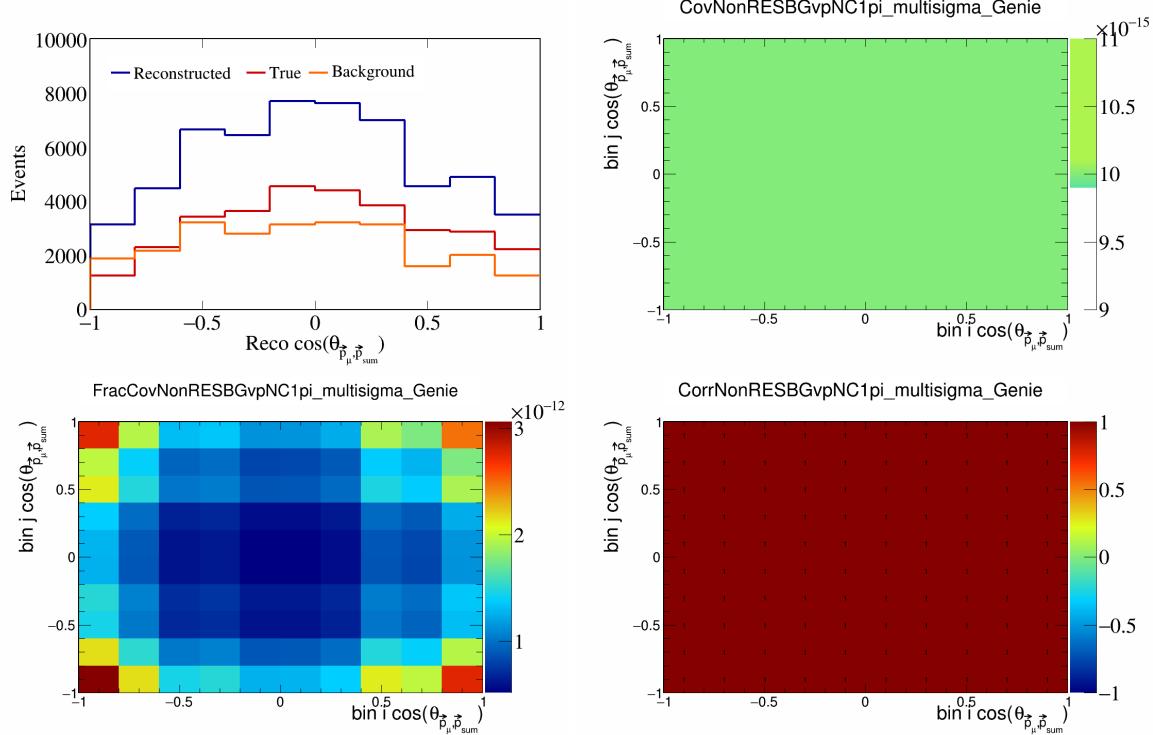


Figure 572: NonRESBGvNC1pi variations for $\cos(\theta_{\vec{p}_\mu, \vec{p}_{\text{sum}}})$.

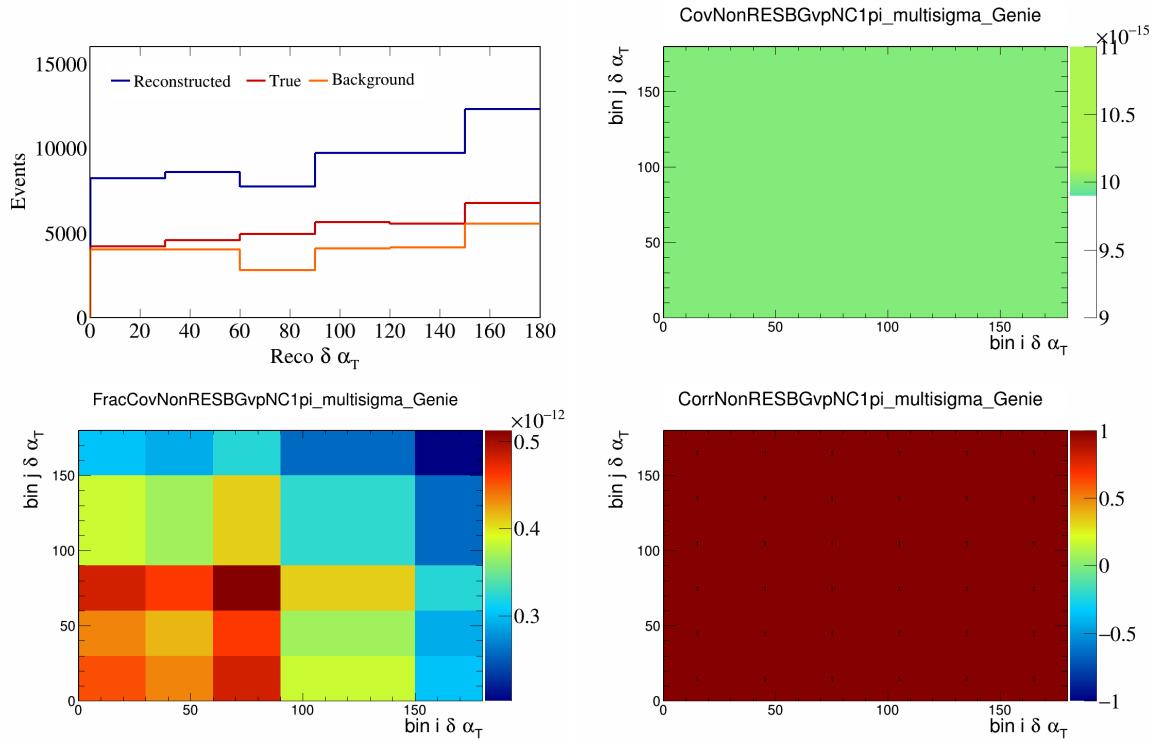


Figure 573: NonRESBGvpNC1pi variations for $\delta\alpha_T$.

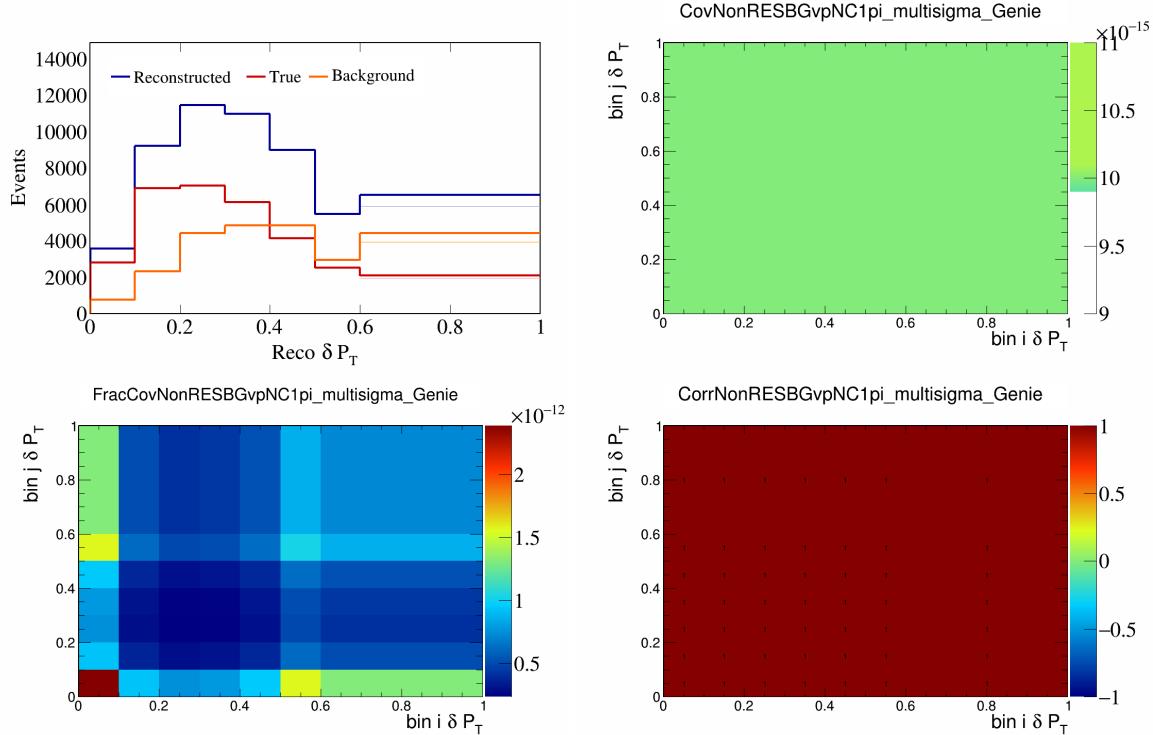


Figure 574: NonRESBGvpNC1pi variations for δP_T .

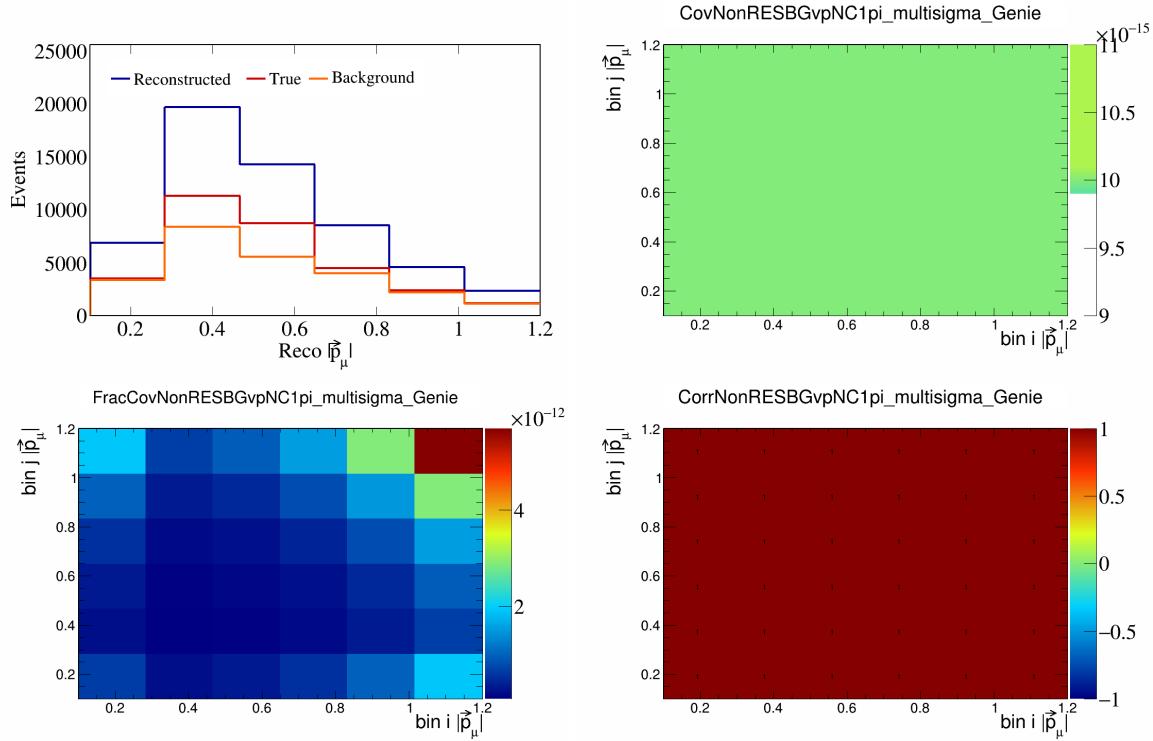


Figure 575: NonRESBGvpNC1pi variations for $|\vec{p}_\mu|$.

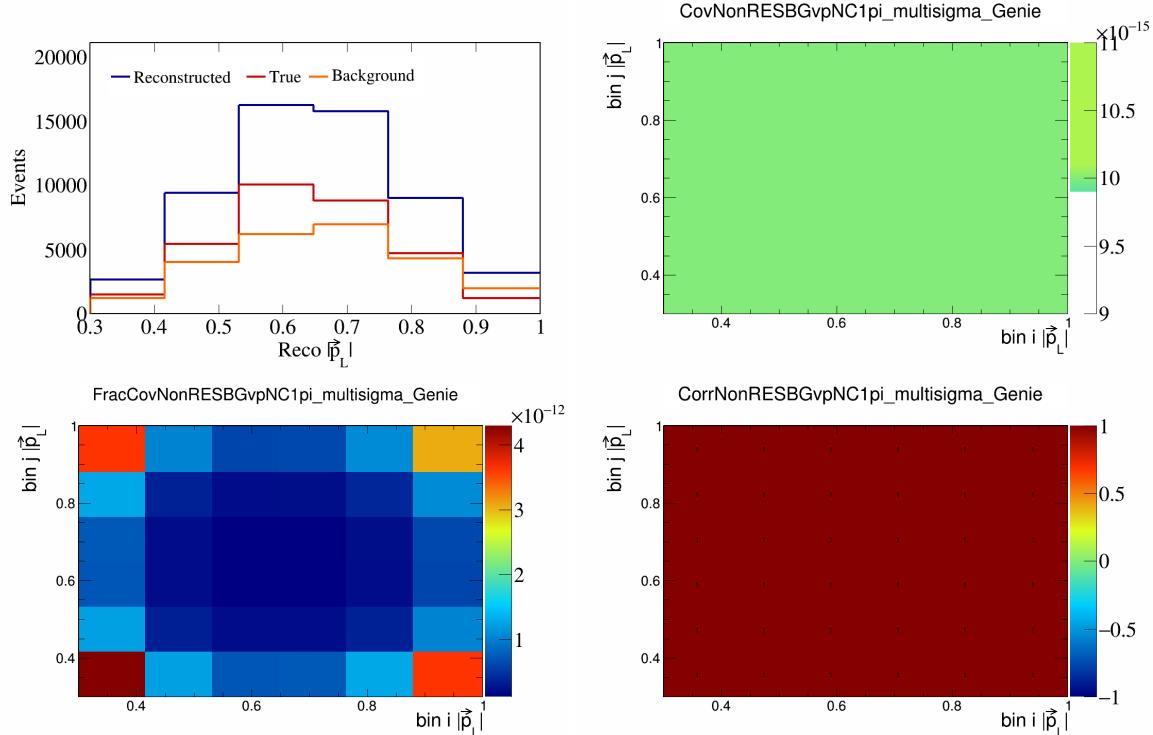


Figure 576: NonRESBGvpNC1pi variations for $|\vec{p}_L|$.

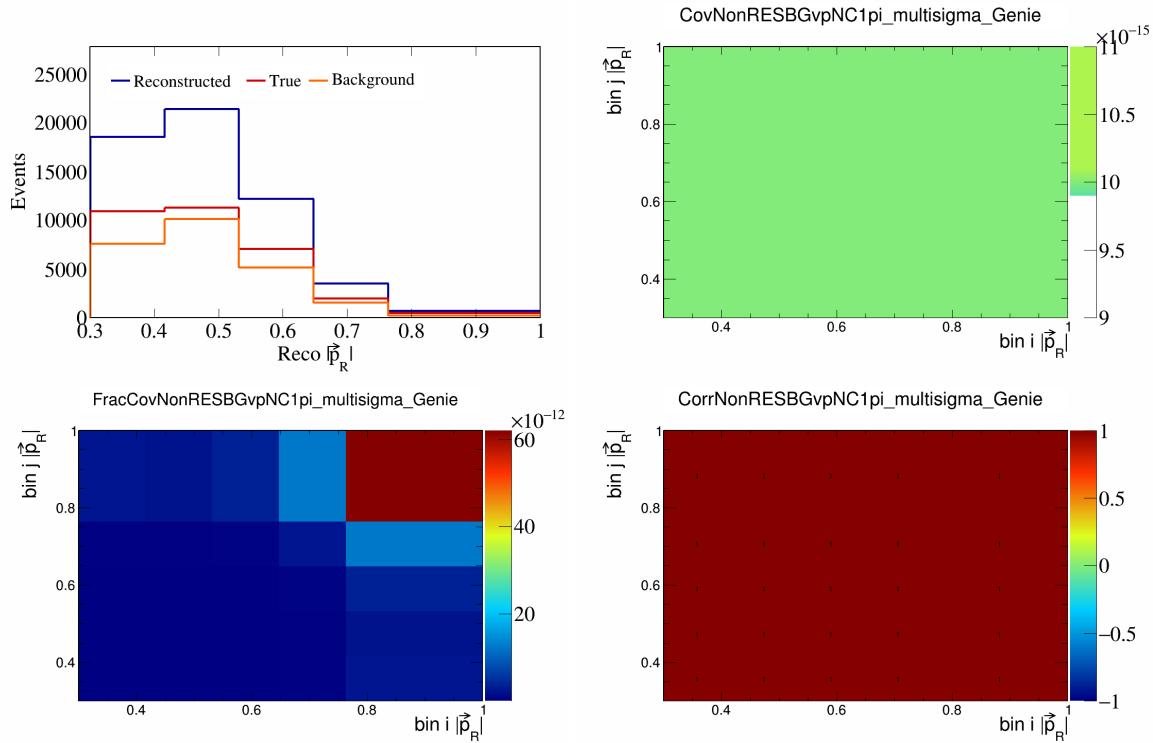


Figure 577: NonRESBGvpNC1pi variations for $|\vec{p}_R|$.

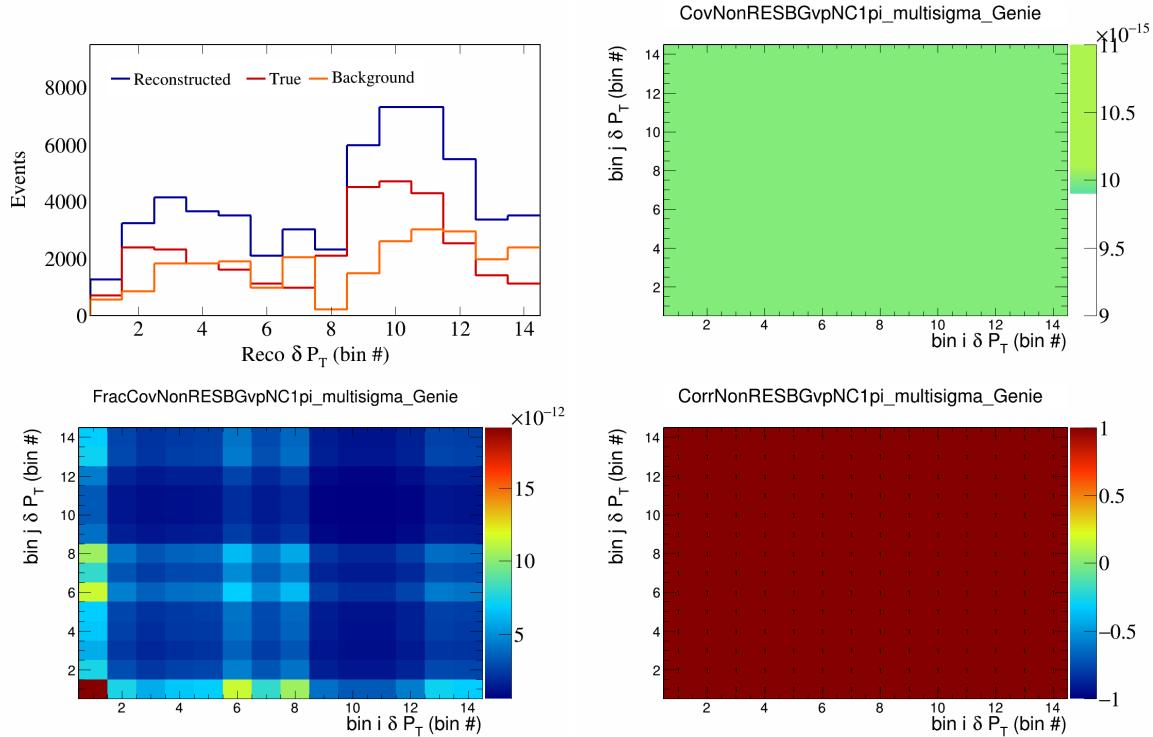


Figure 578: NonRESBGvpNC1pi variations for δP_T in $\cos(\theta_{\vec{p}_\mu})$.

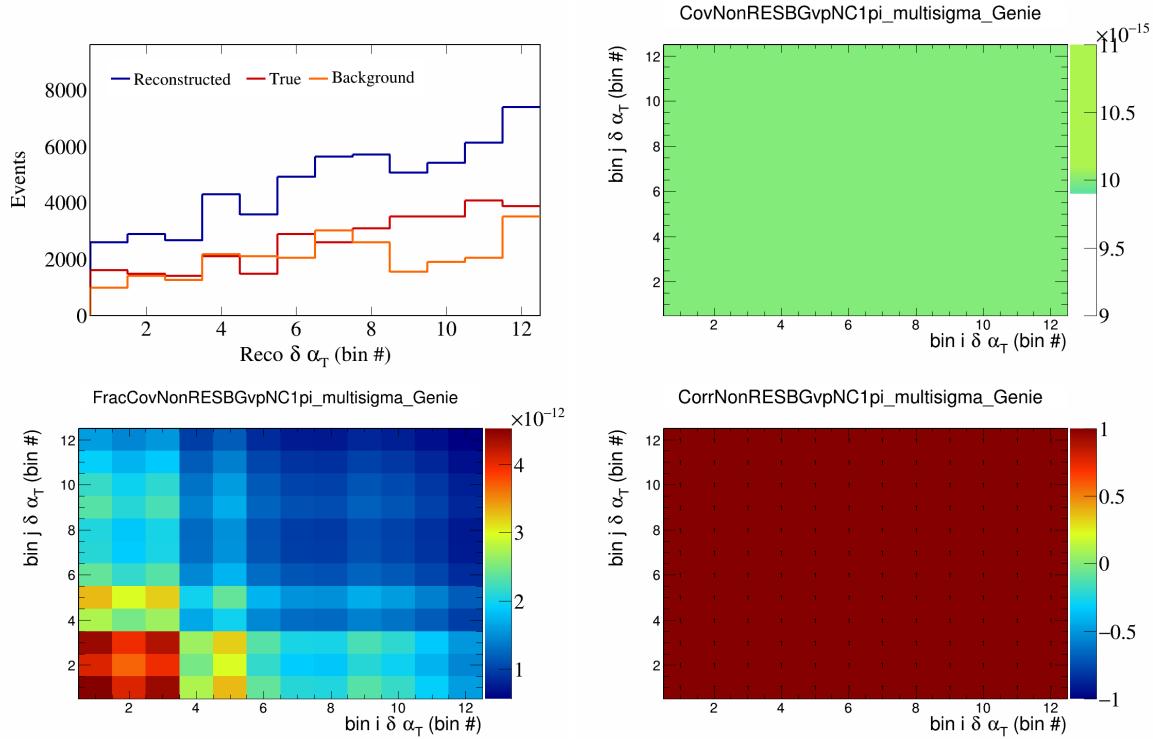


Figure 579: NonRESBGvpNC1pi variations for $\delta\alpha_T$ in $\cos(\theta_{\vec{p}_\mu})$.

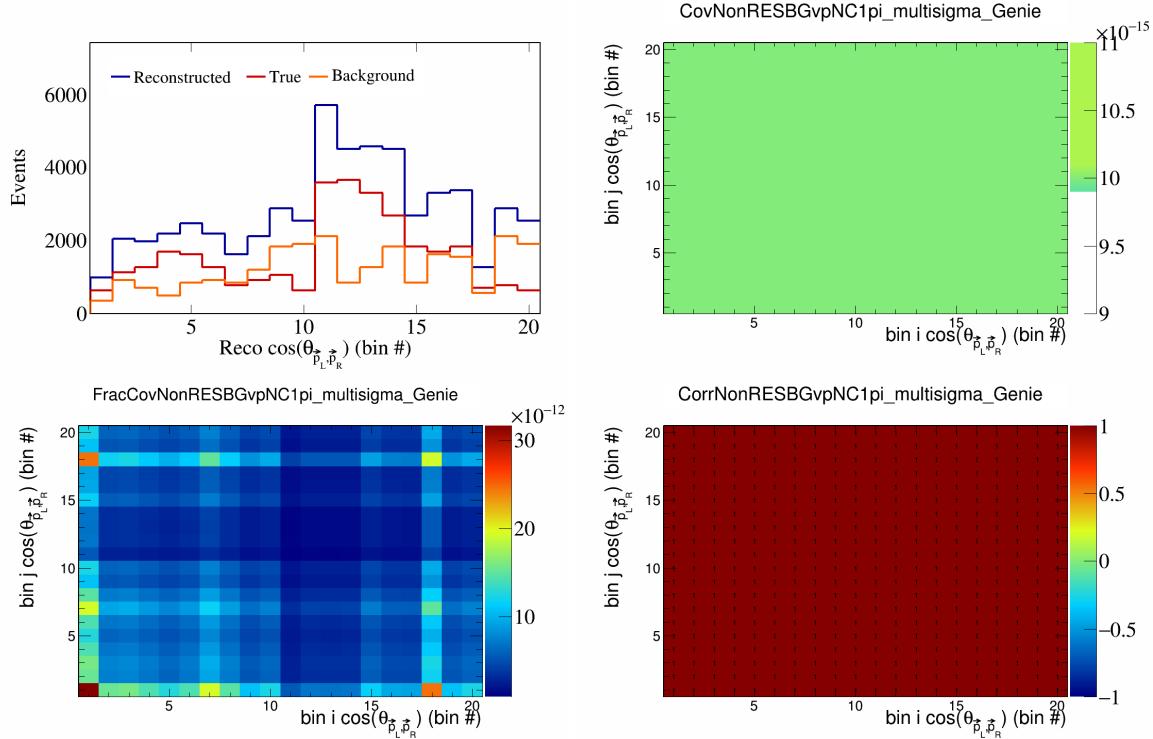


Figure 580: NonRESBGvpNC1pi variations for $\cos(\theta_{\vec{p}_L, \vec{p}_R})$ in $\cos(\theta_{\vec{p}_\mu})$.

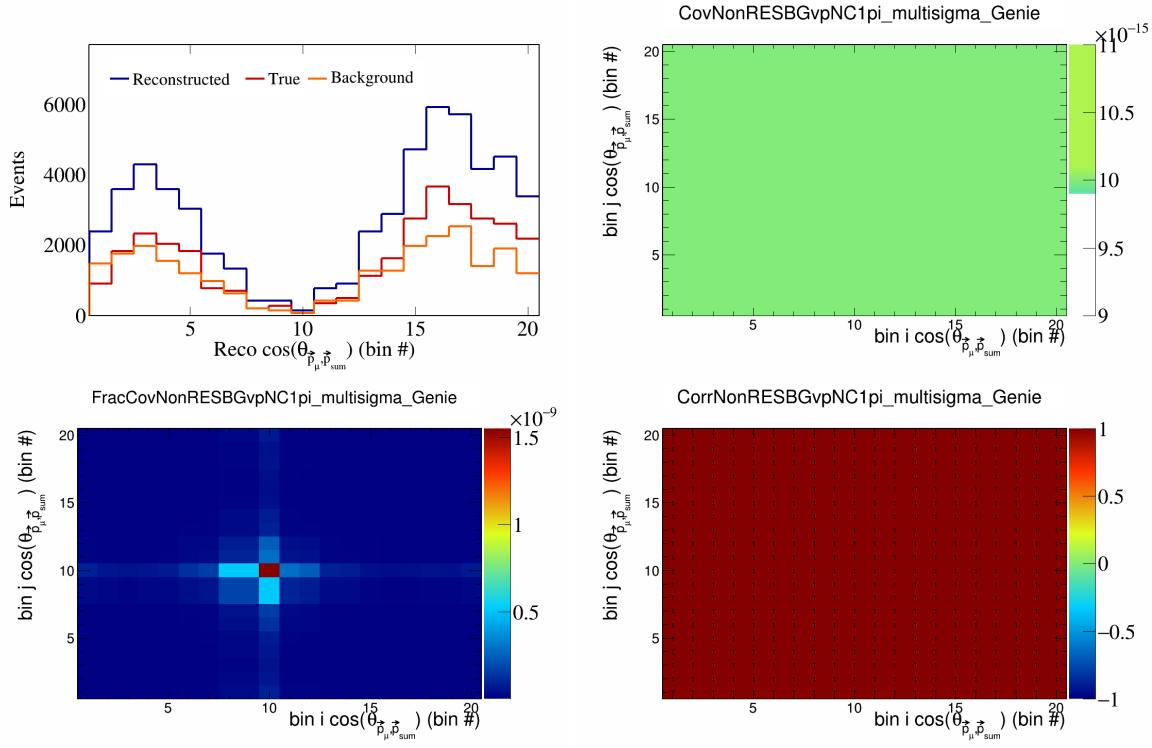


Figure 581: NonRESBGvpNC1pi variations for $\cos(\theta_{\vec{p}_\mu, \vec{p}_{\text{sum}}})$ in $\cos(\theta_{\vec{p}_\mu})$.

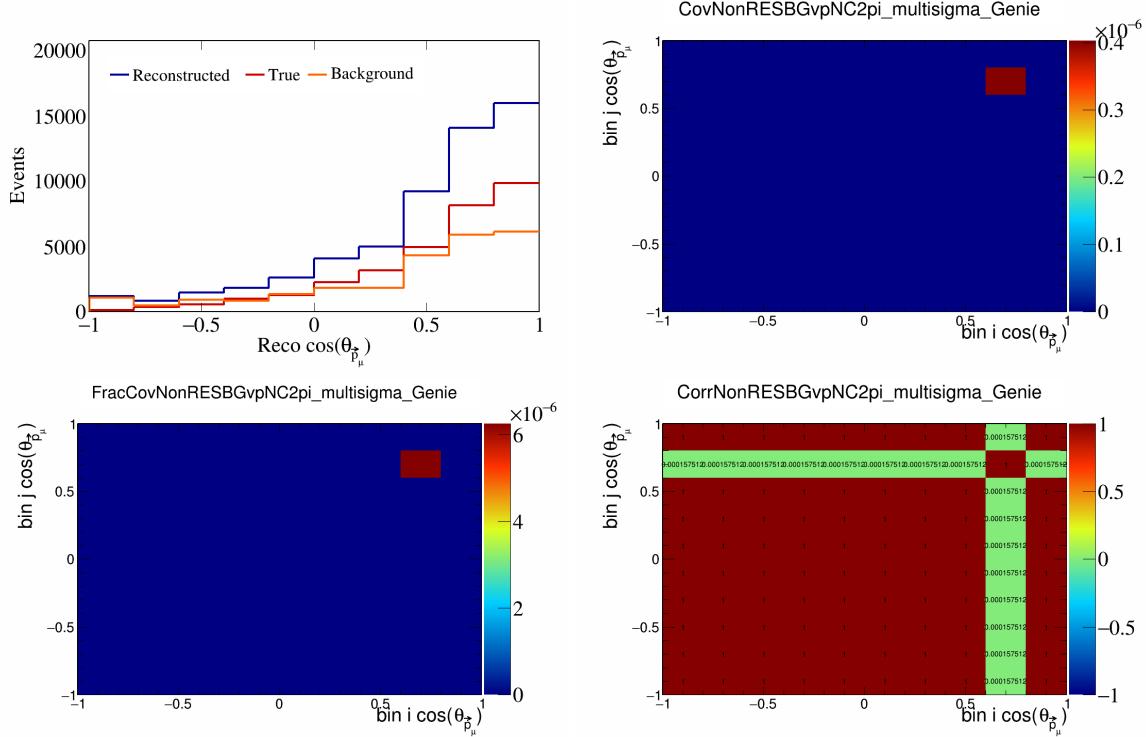


Figure 582: NonRESBGvpNC2pi variations for $\cos(\theta_{\vec{p}_\mu})$.

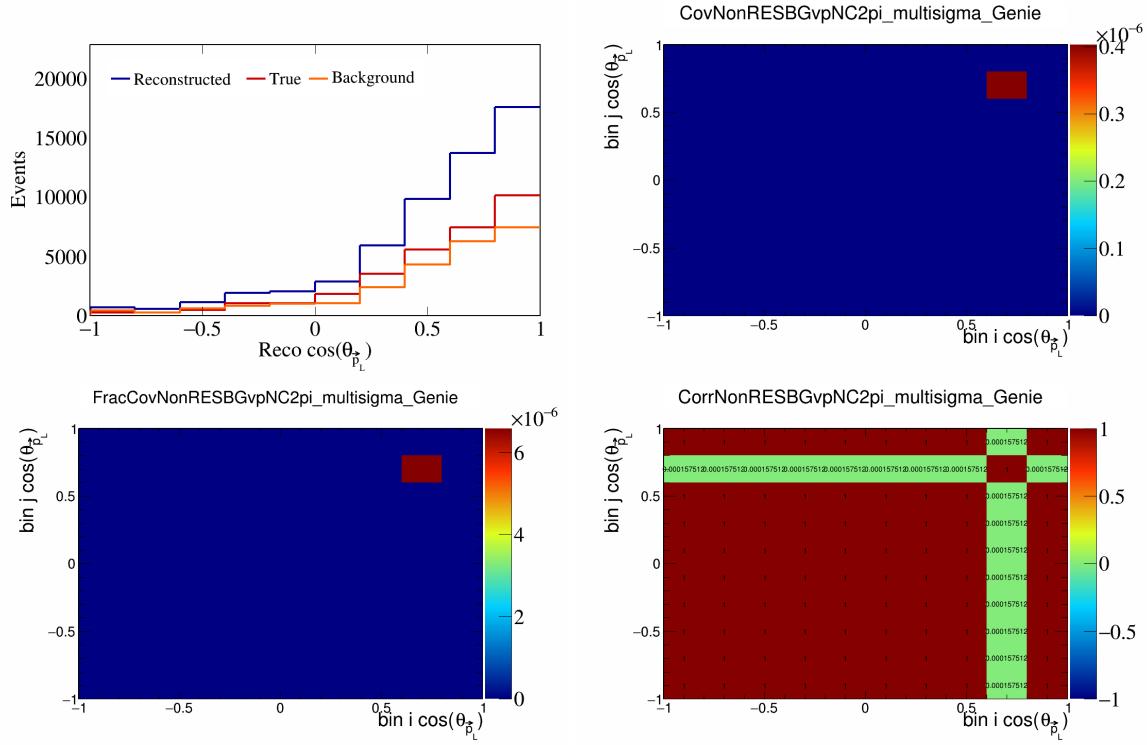


Figure 583: NonRESBGvpNC2pi variations for $\cos(\theta_{\vec{p}_L})$.

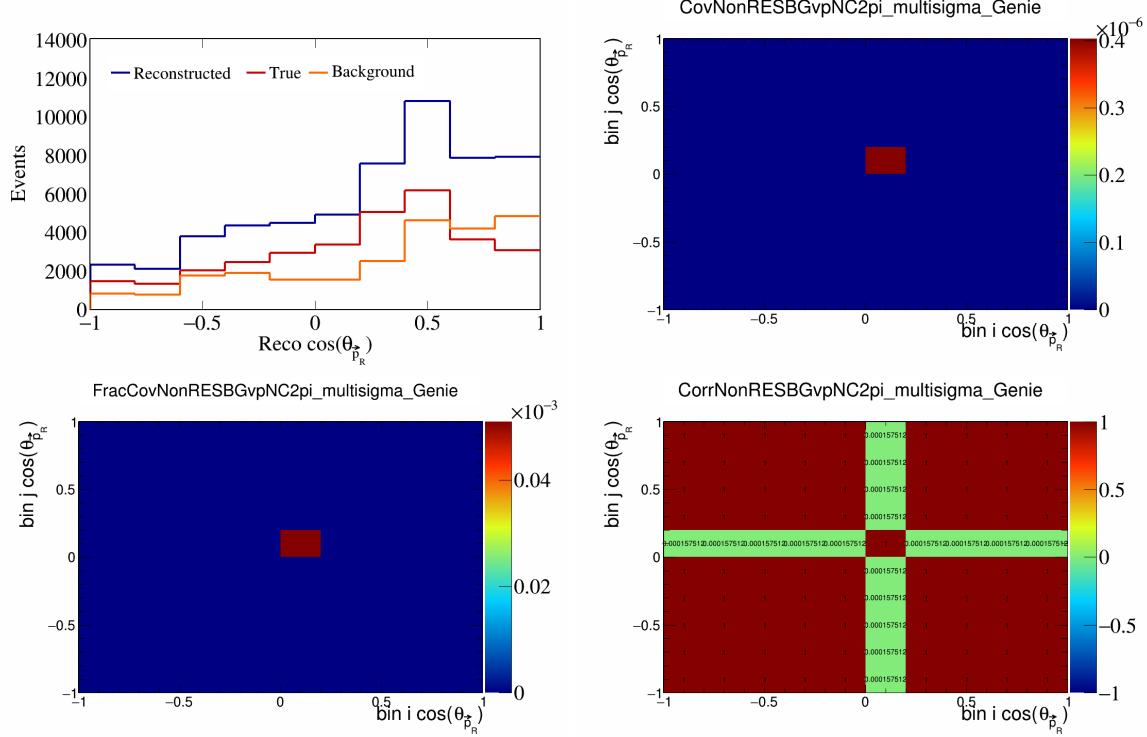


Figure 584: NonRESBGvpNC2pi variations for $\cos(\theta_{\vec{p}_R})$.

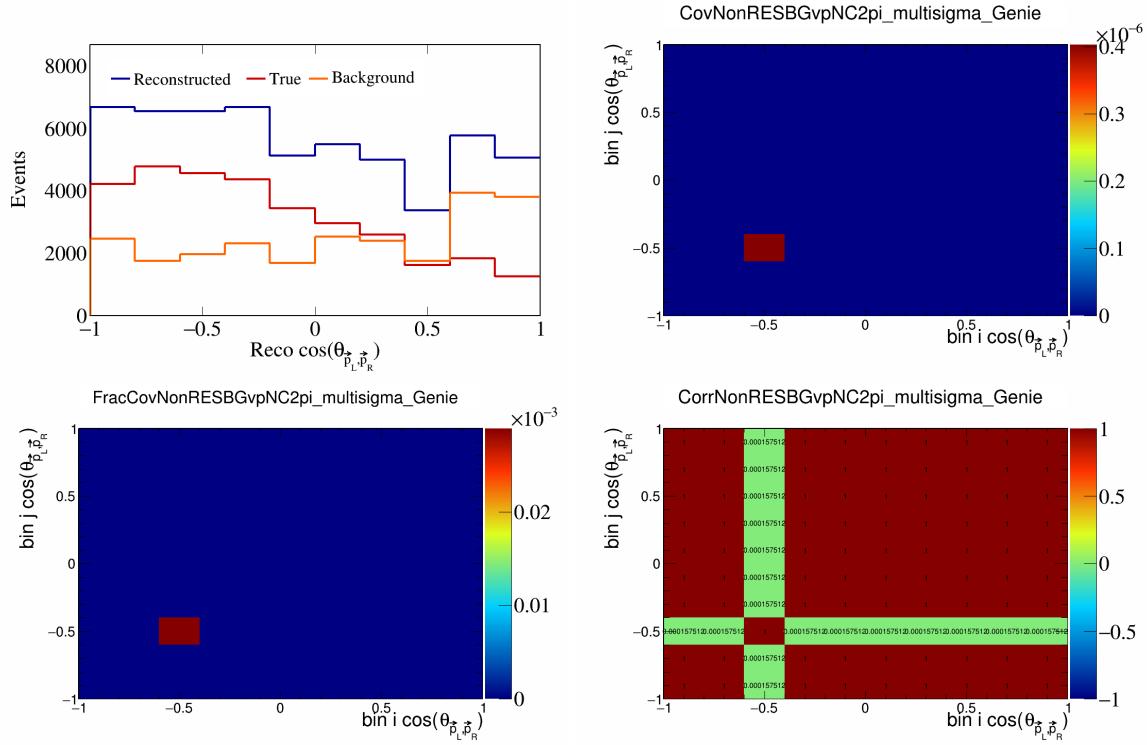


Figure 585: NonRESBGvpNC2pi variations for $\cos(\theta_{\vec{p}_L, \vec{p}_R})$.

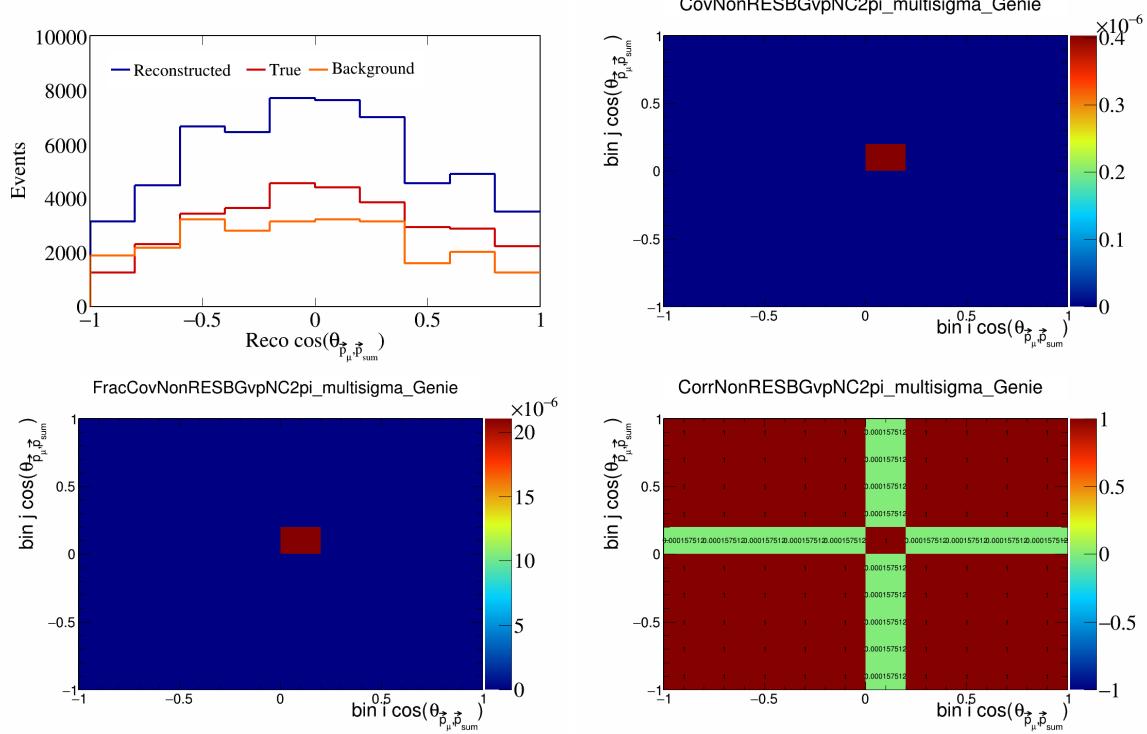


Figure 586: NonRESBGvpNC2pi variations for $\cos(\theta_{\vec{p}_\mu, \vec{p}_{\text{sum}}})$.

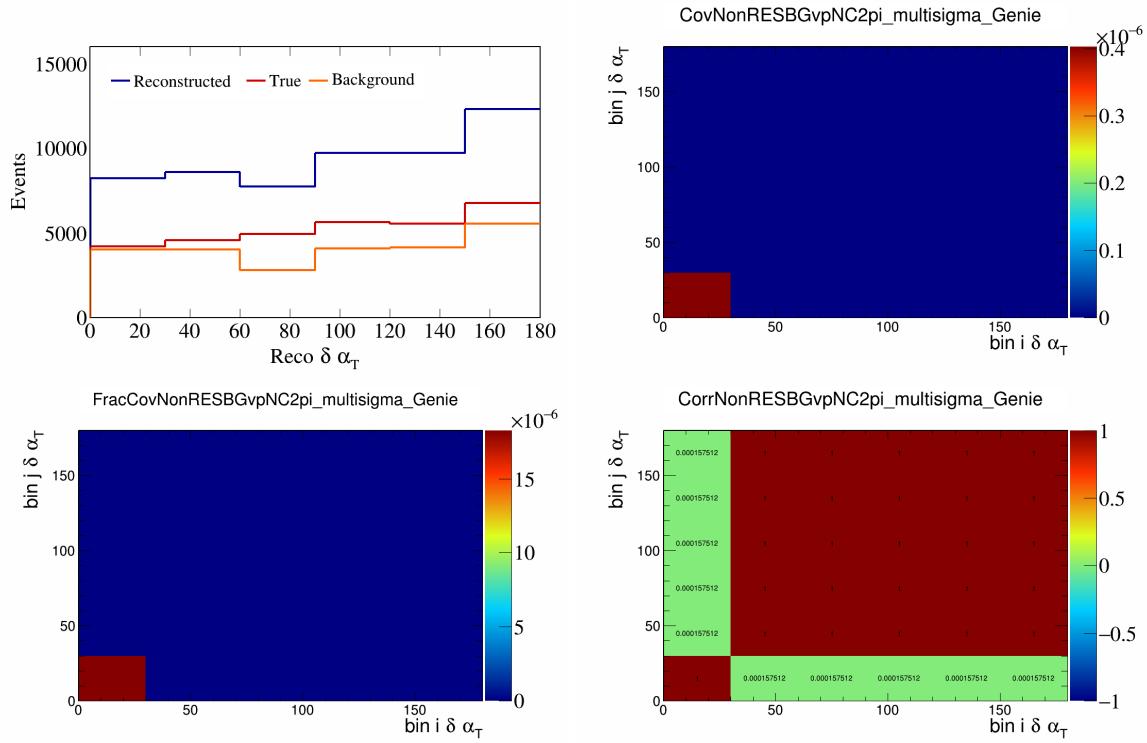


Figure 587: NonRESBGvpNC2pi variations for $\delta\alpha_T$.

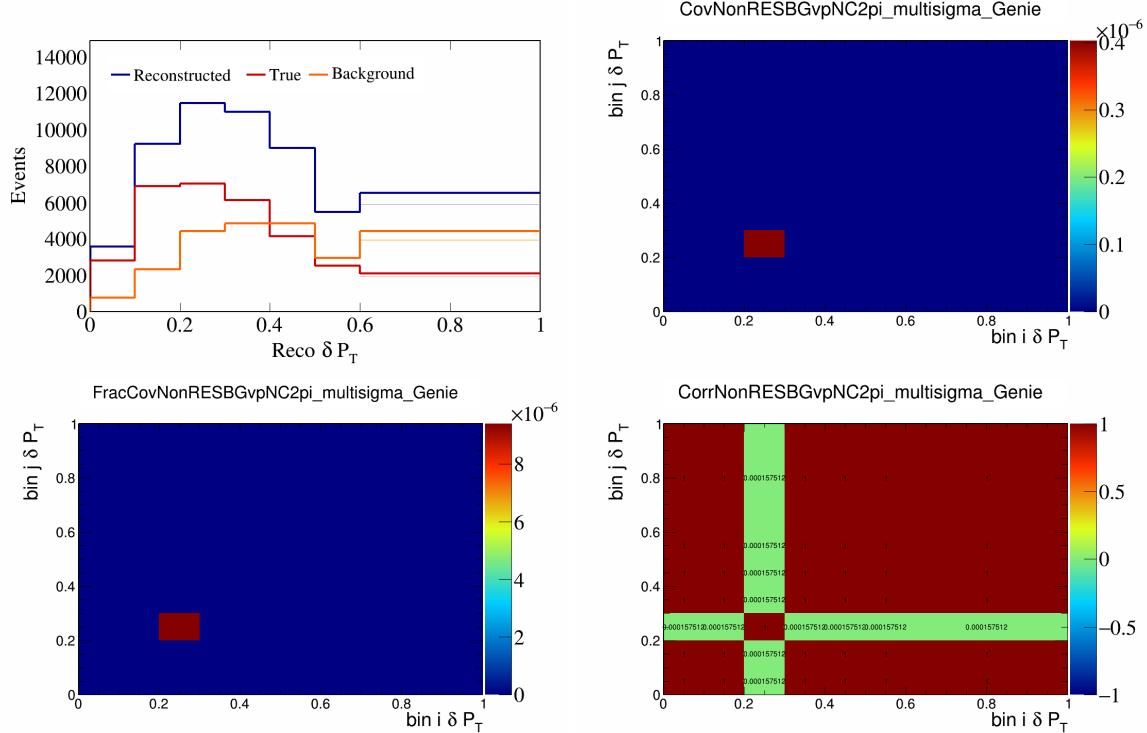


Figure 588: NonRESBGvpNC2pi variations for δP_T .

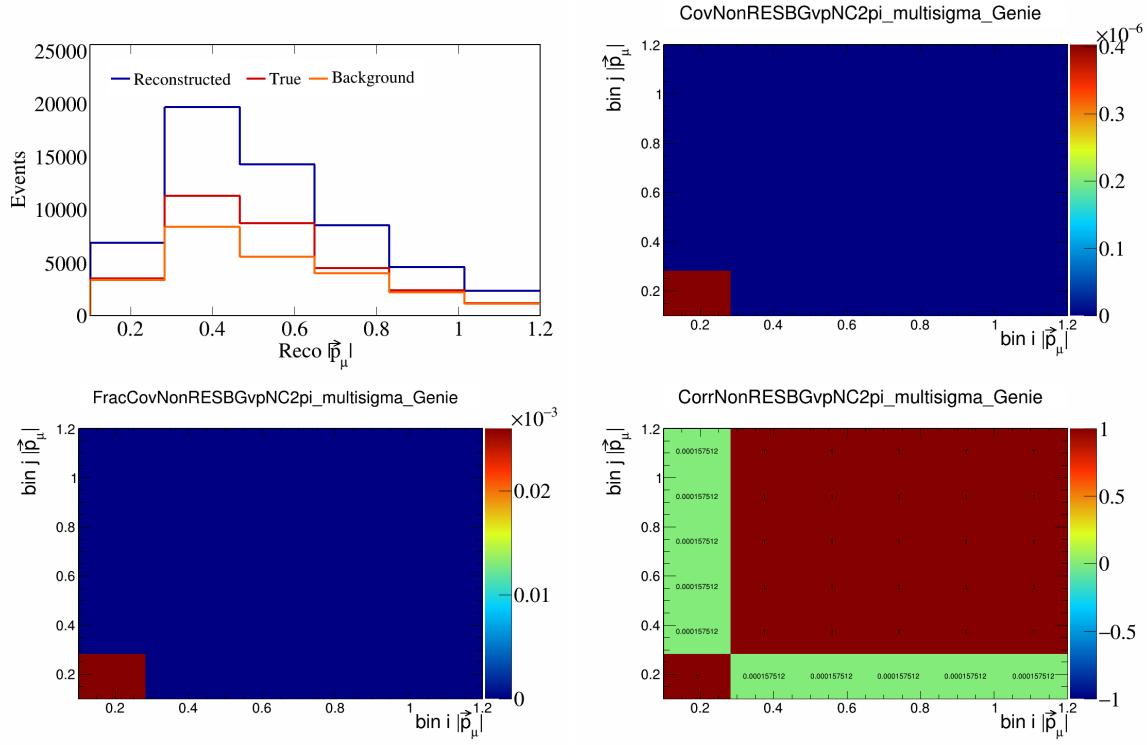


Figure 589: NonRESBGvpNC2pi variations for $|\vec{p}_\mu|$.

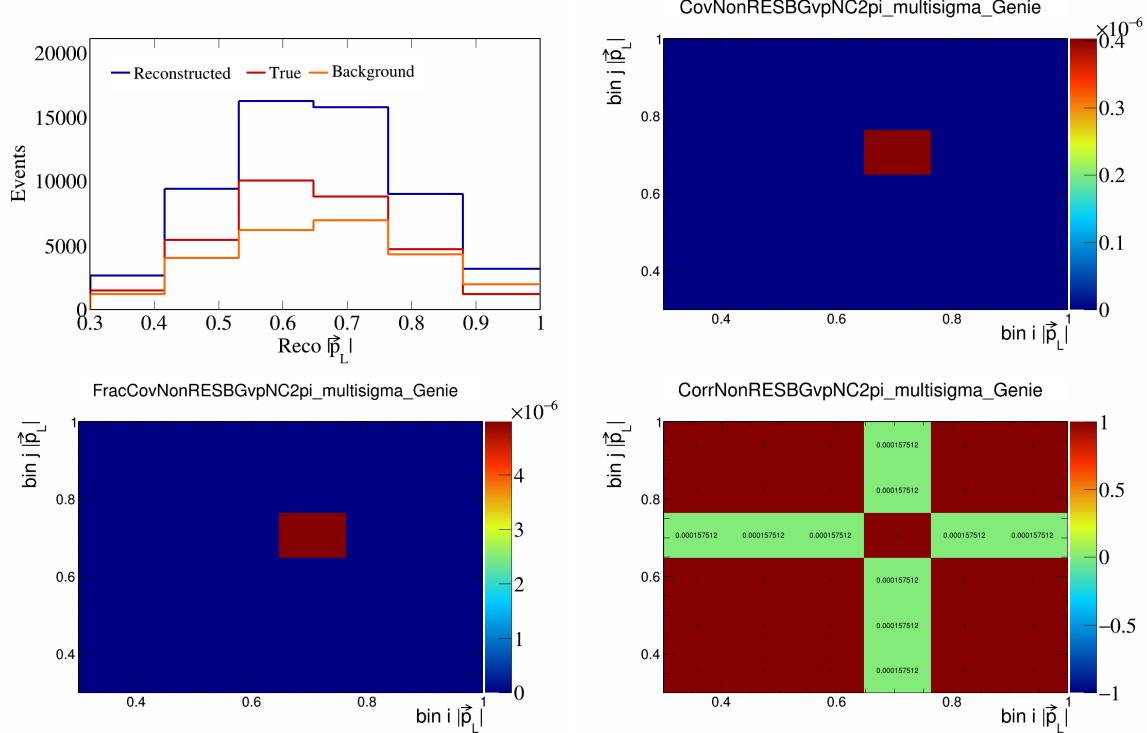


Figure 590: NonRESBGvpNC2pi variations for $|\vec{p}_L|$.

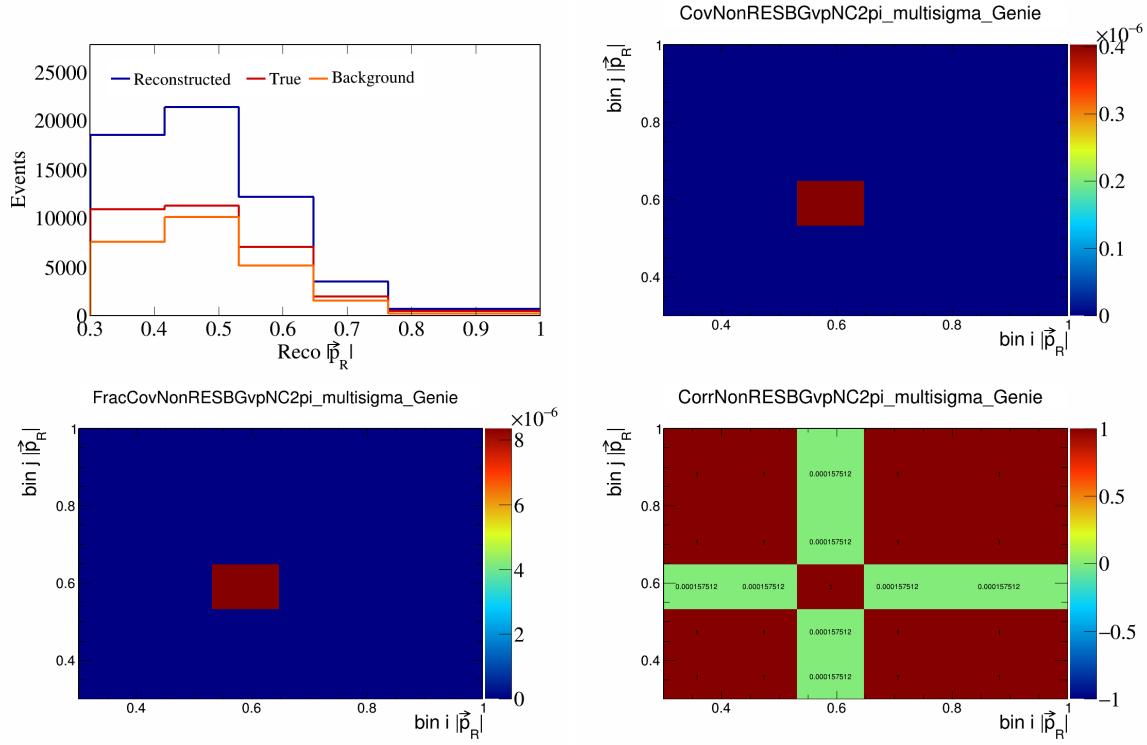


Figure 591: NonRESBGvpNC2pi variations for $|\vec{p}_R|$.

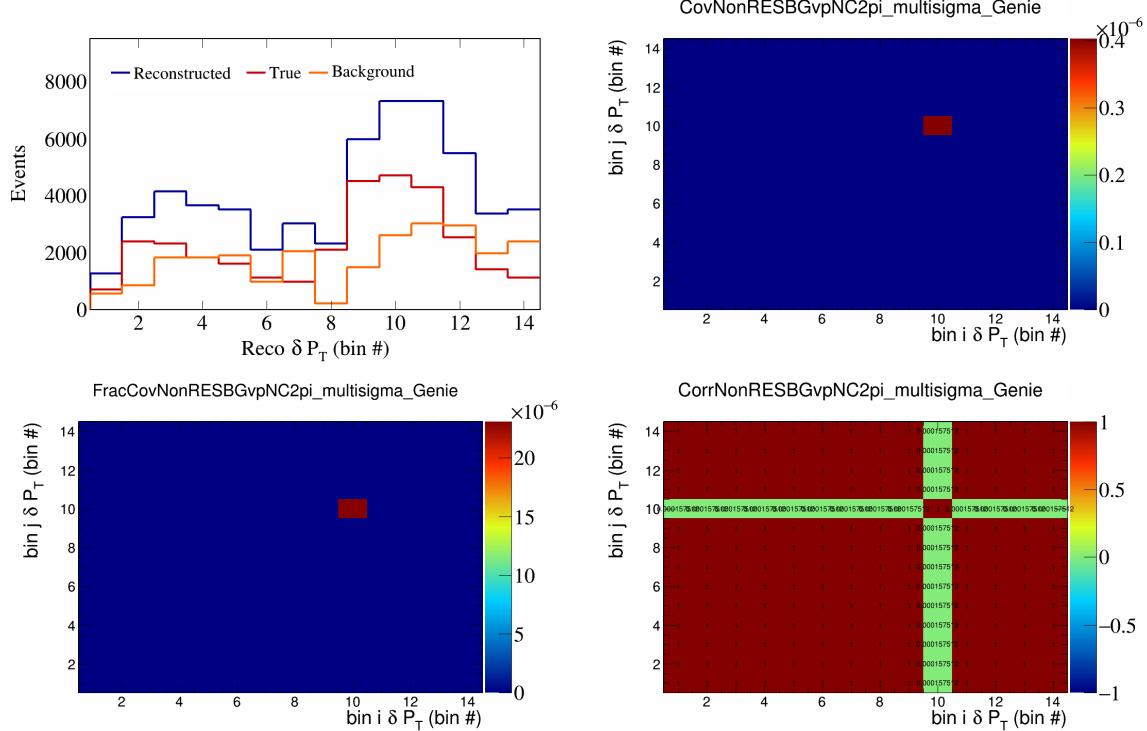


Figure 592: NonRESBGvpNC2pi variations for δP_T in $\cos(\theta_{\vec{p}_\mu})$.

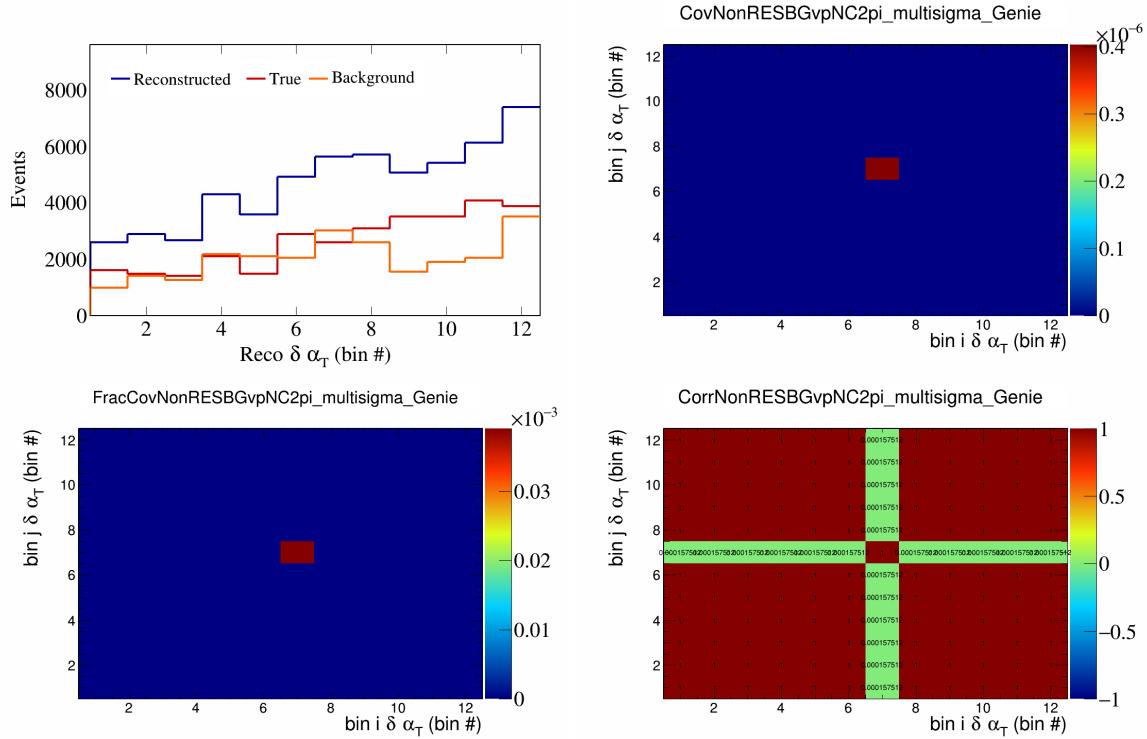


Figure 593: NonRESBGvpNC2pi variations for $\delta\alpha_T$ in $\cos(\theta_{\vec{p}_\mu})$.

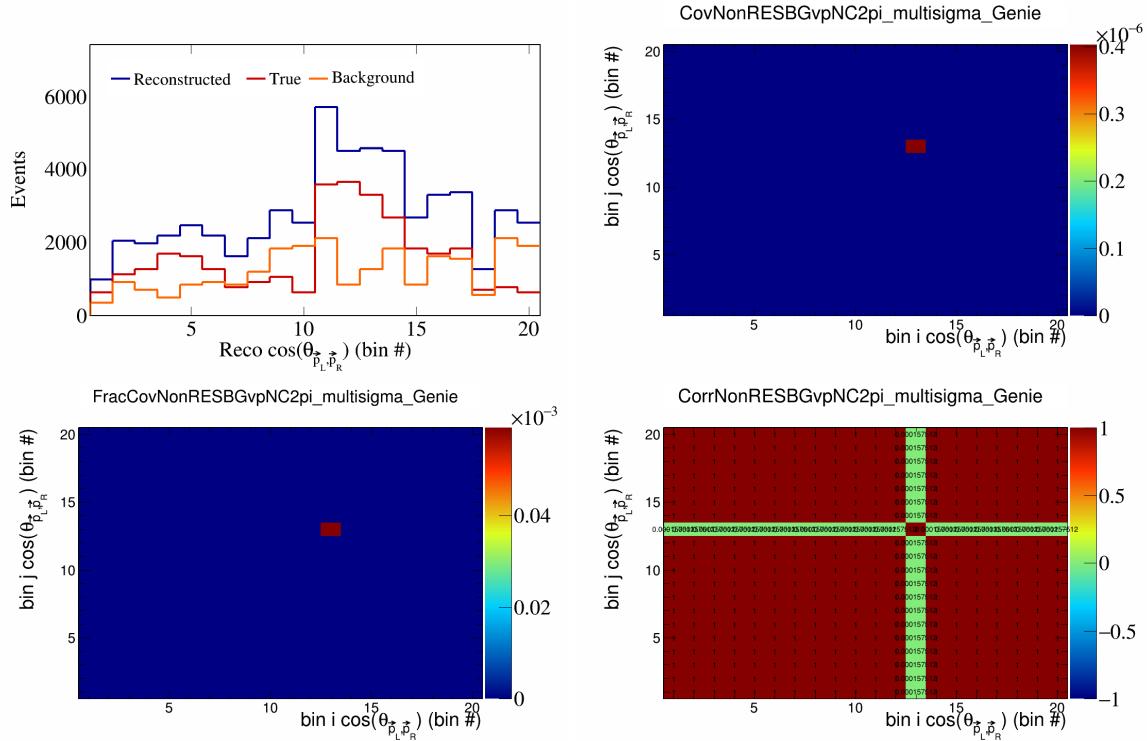


Figure 594: NonRESBGvpNC2pi variations for $\cos(\theta_{\vec{p}_L, \vec{p}_R})$ in $\cos(\theta_{\vec{p}_\mu})$.

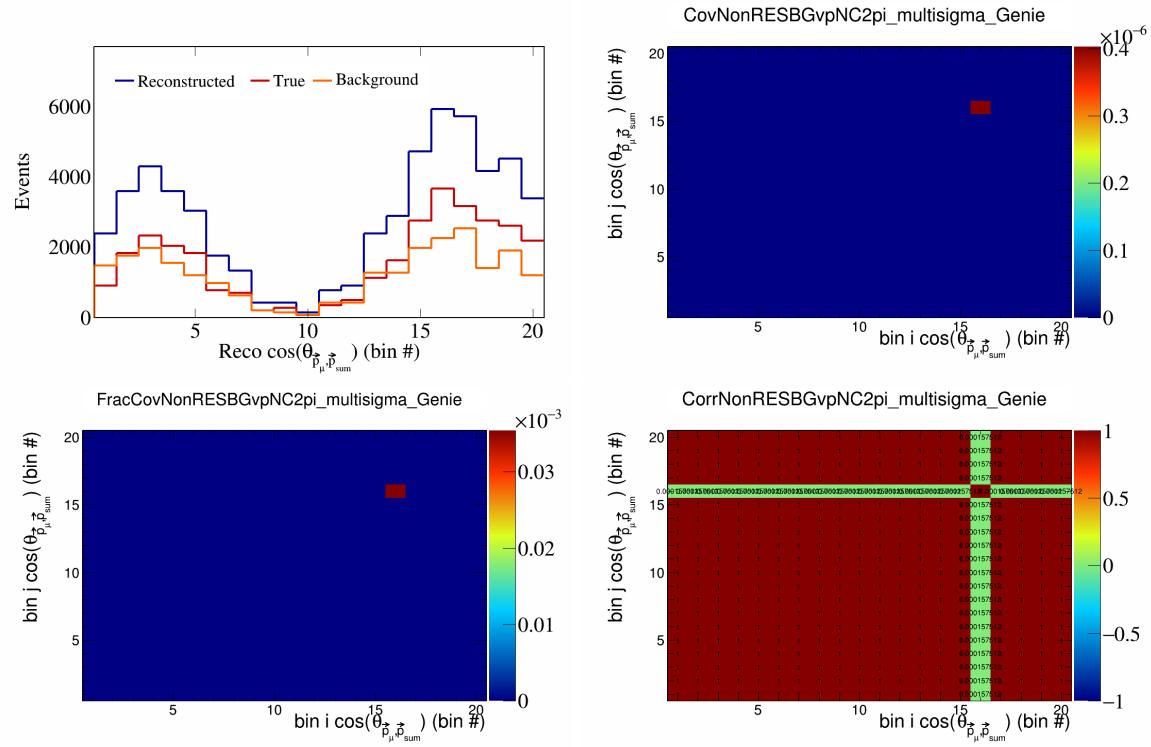


Figure 595: NonRESBGvpNC2pi variations for $\cos(\theta_{\vec{p}_\mu, \vec{p}_{\text{sum}}})$ in $\cos(\theta_{\vec{p}_\mu})$.

275 **6.2 Flux systematics**

276 In this appendix, the variations, covariance matrices, fractional covariance matrices, and correlation matrices
 277 are plotted for all of the flux systematics and variables.

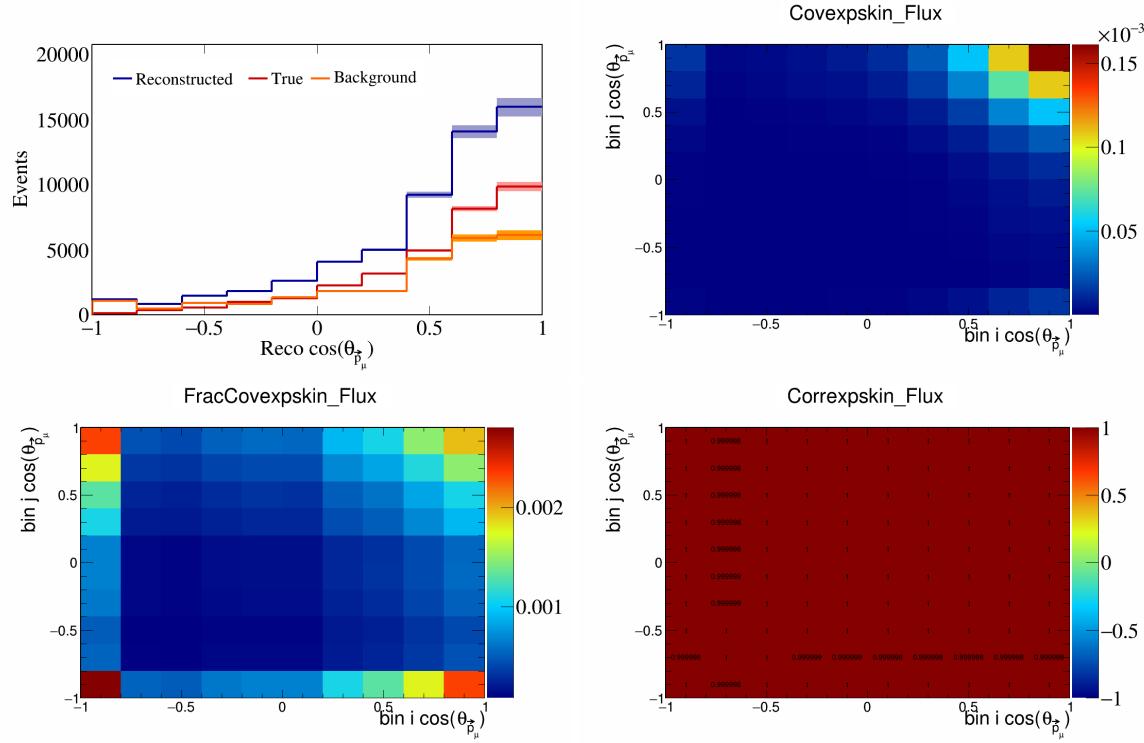


Figure 596: Epskin variations for $\cos(\theta_{\vec{p}_\mu})$.

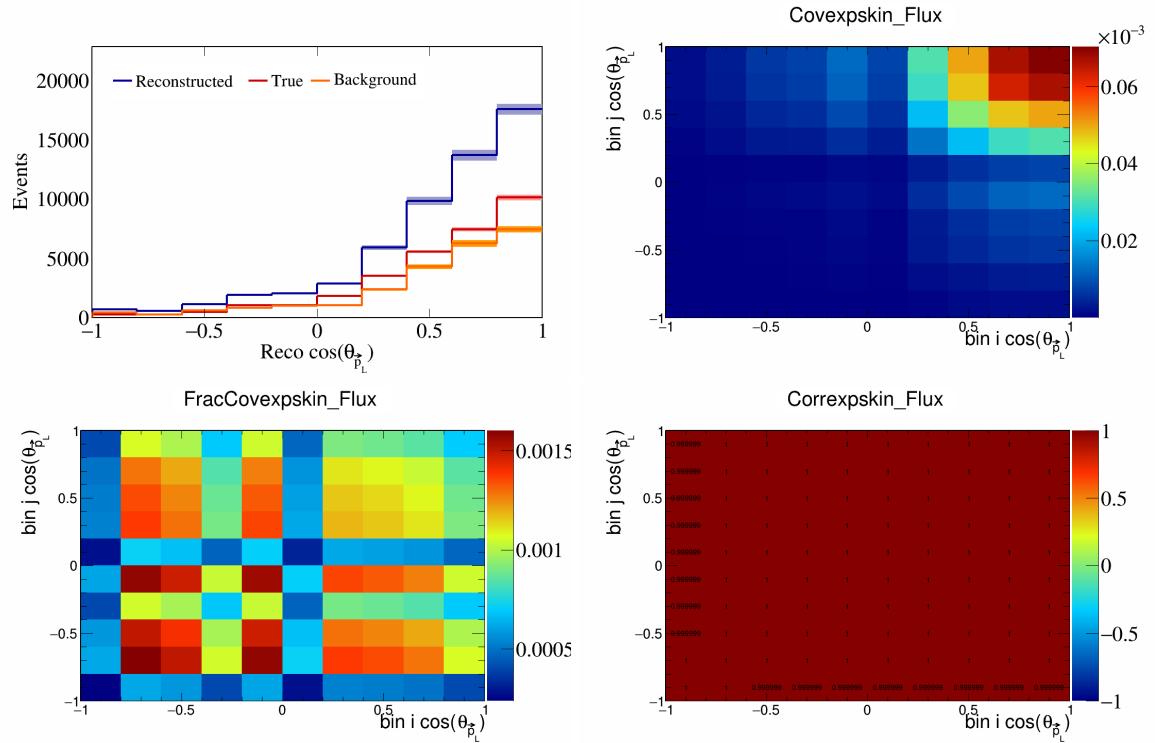


Figure 597: Expskin variations for $\cos(\theta_{\vec{p}_L})$.

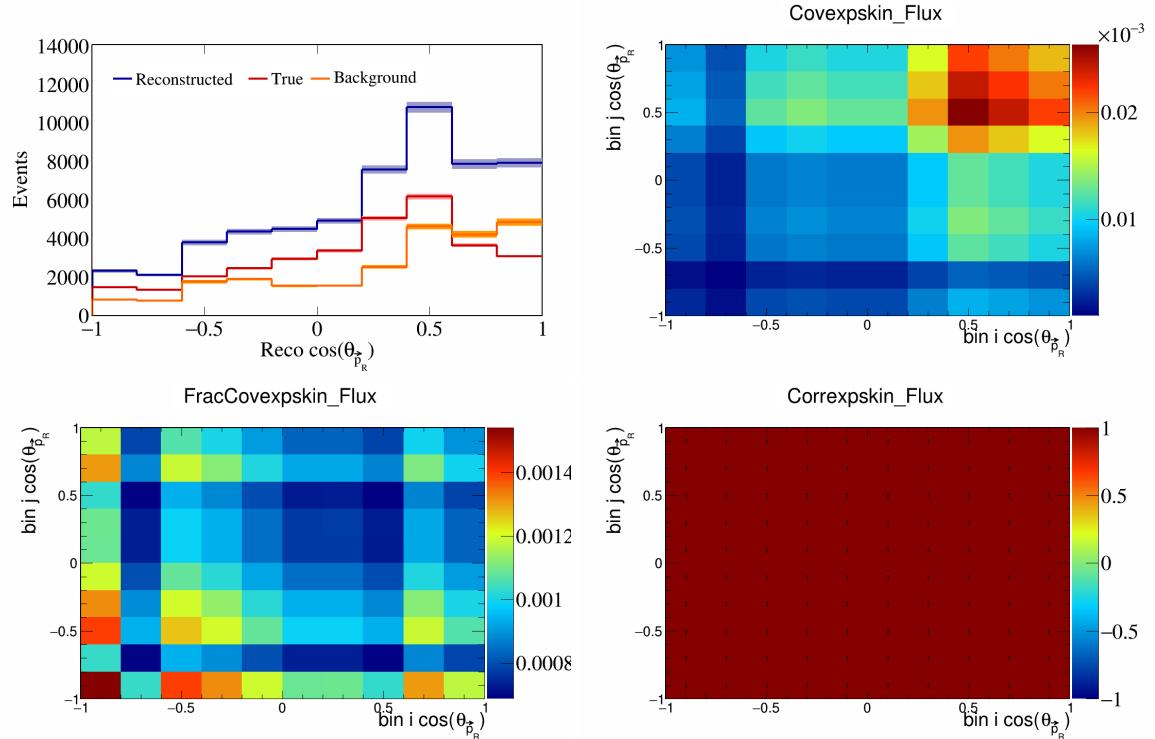


Figure 598: Expskin variations for $\cos(\theta_{\vec{p}_R})$.

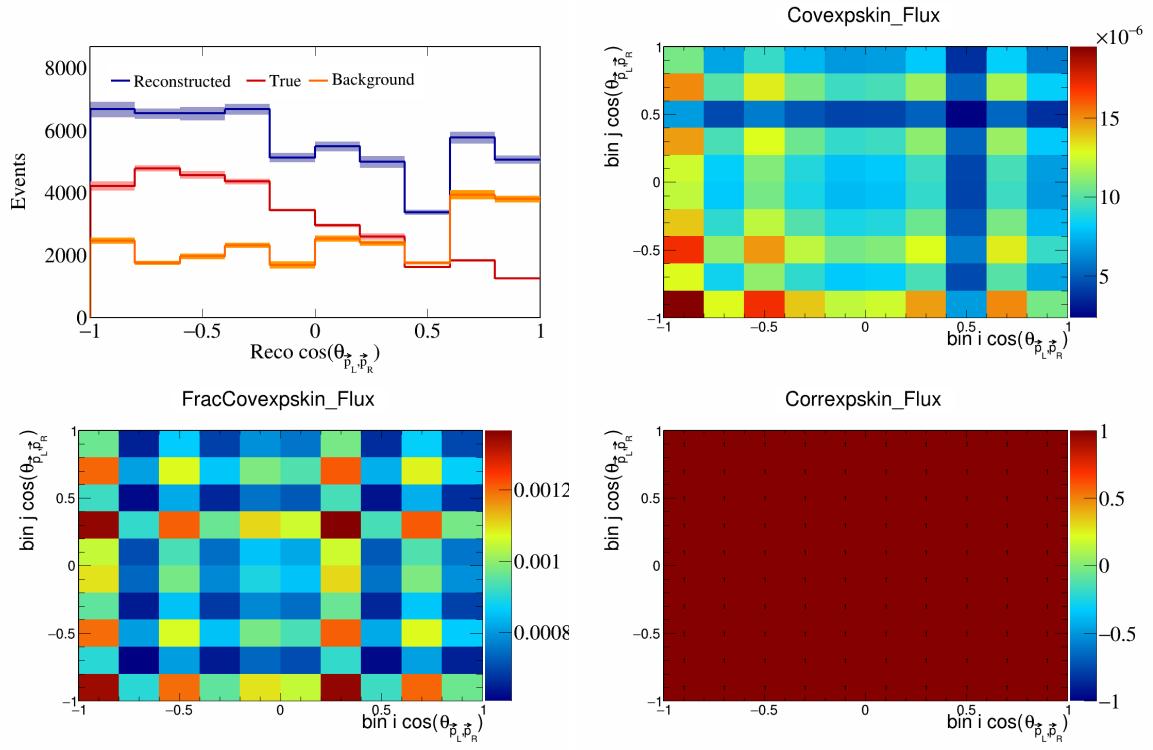


Figure 599: ExpSkin variations for $\cos(\theta_{\vec{p}_L, \vec{p}_R})$.

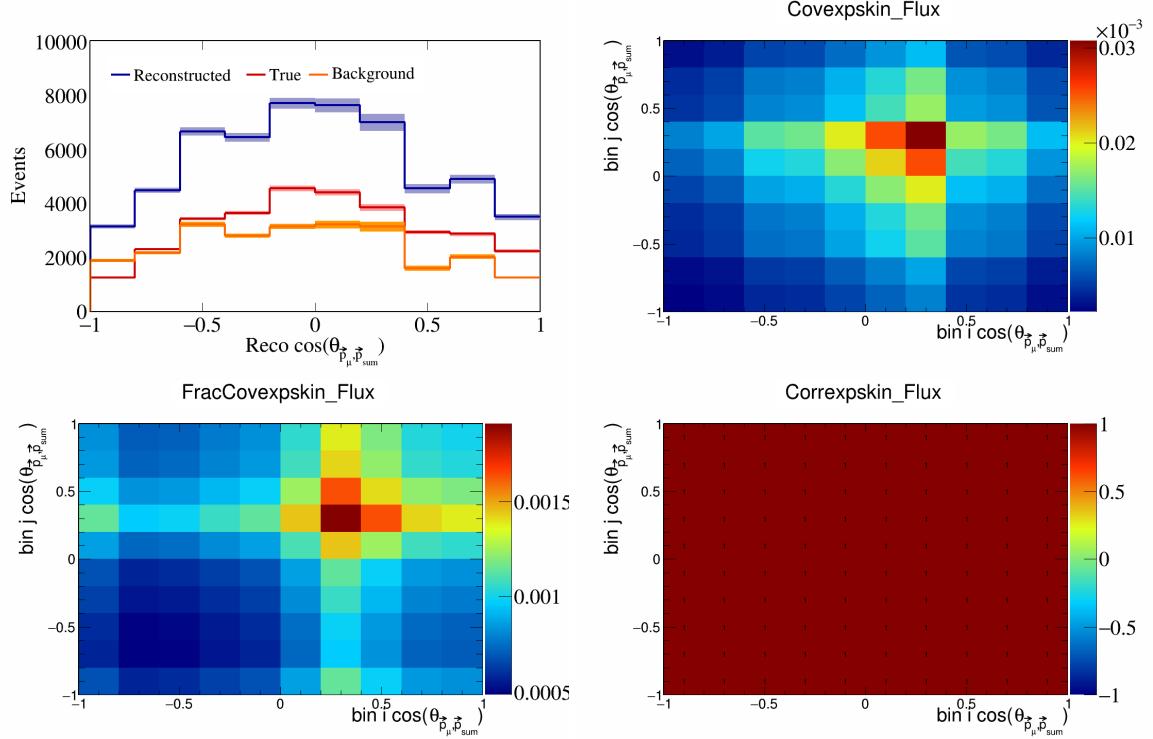


Figure 600: ExpSkin variations for $\cos(\theta_{\vec{p}_\mu, \vec{p}_{\text{sum}}})$.

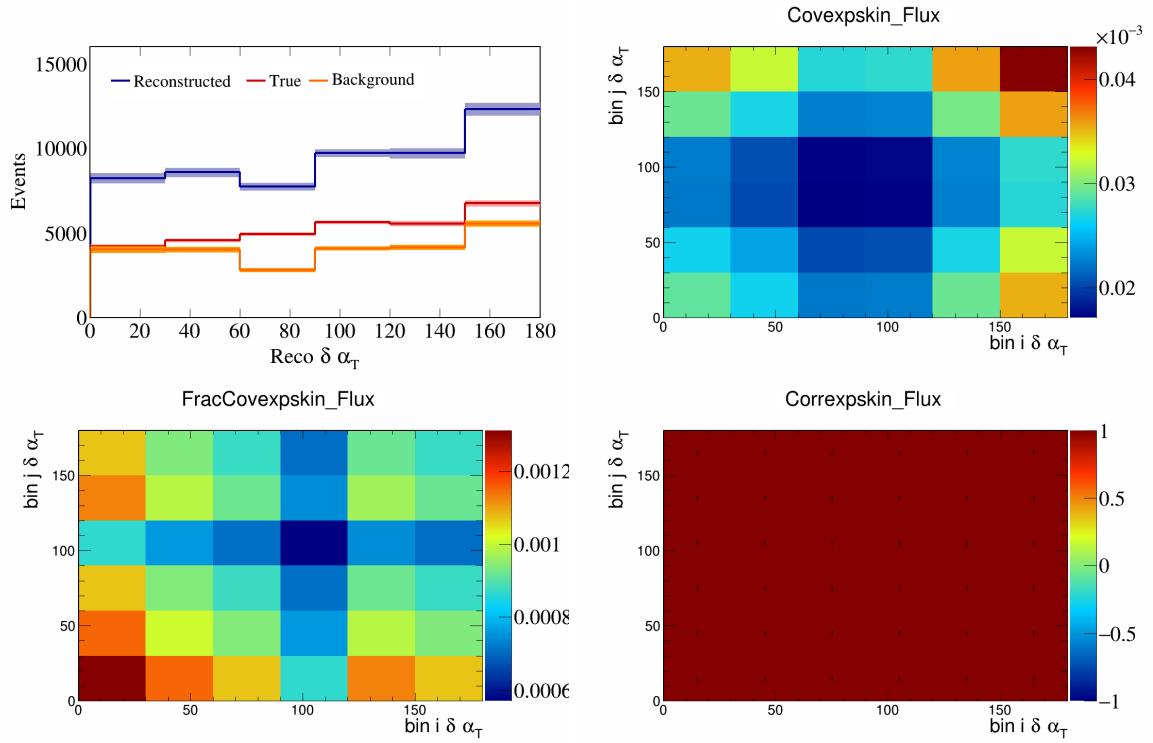


Figure 601: Expskin variations for $\delta \alpha_T$.

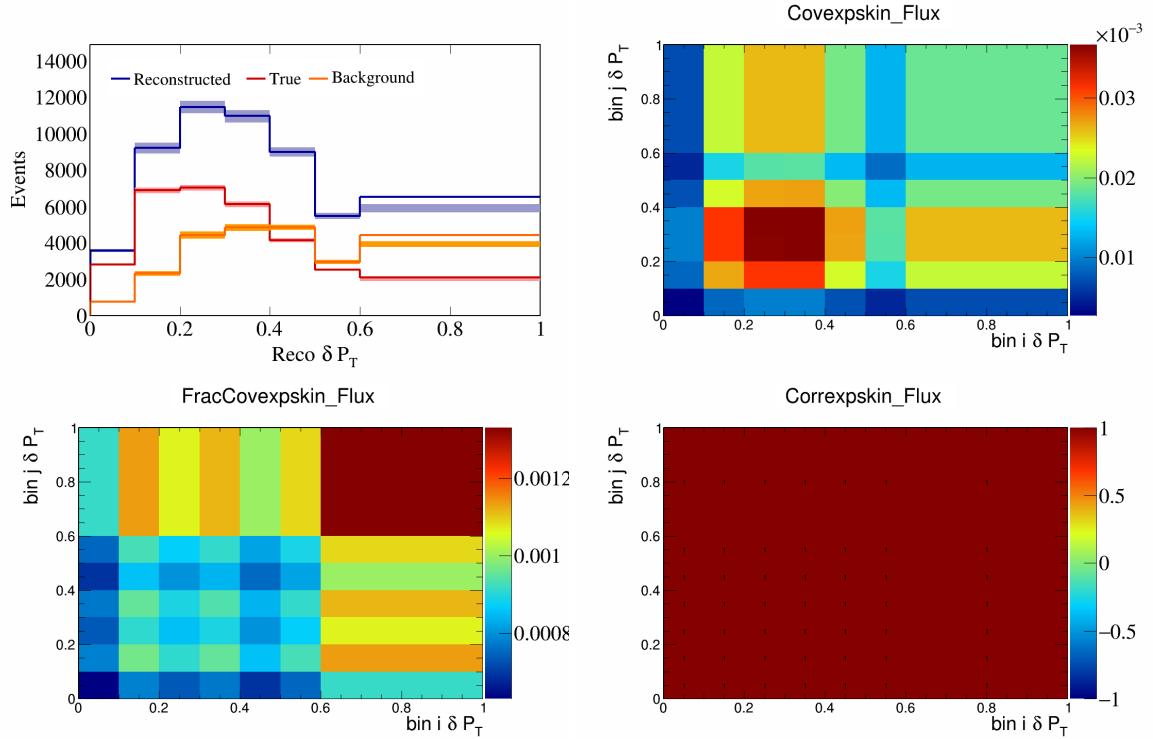


Figure 602: Expskin variations for δP_T .

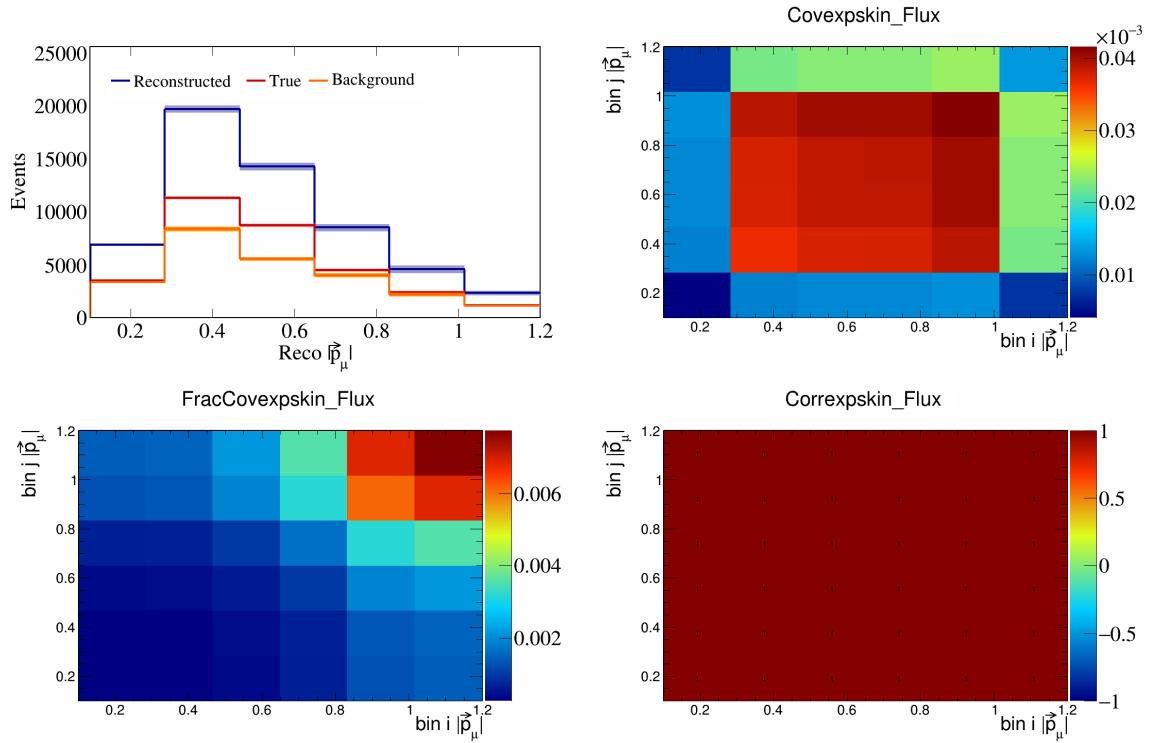


Figure 603: Expskin variations for $|\vec{p}_\mu|$.

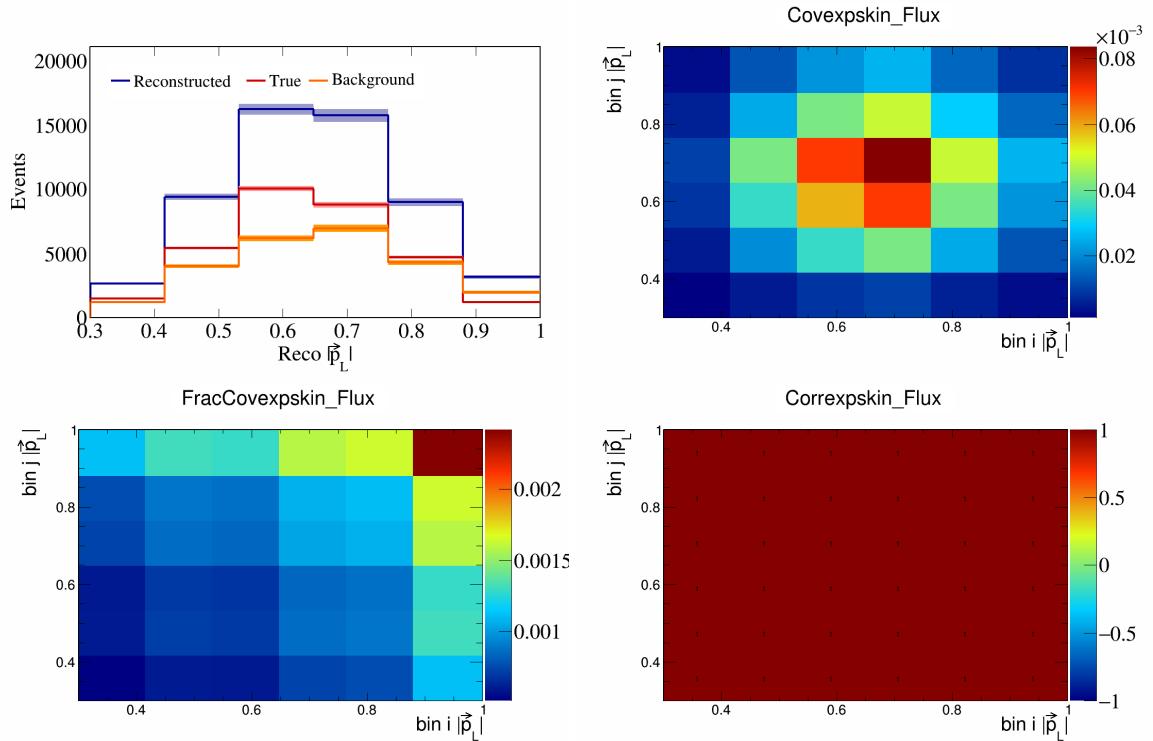


Figure 604: Expskin variations for $|\vec{p}_L|$.

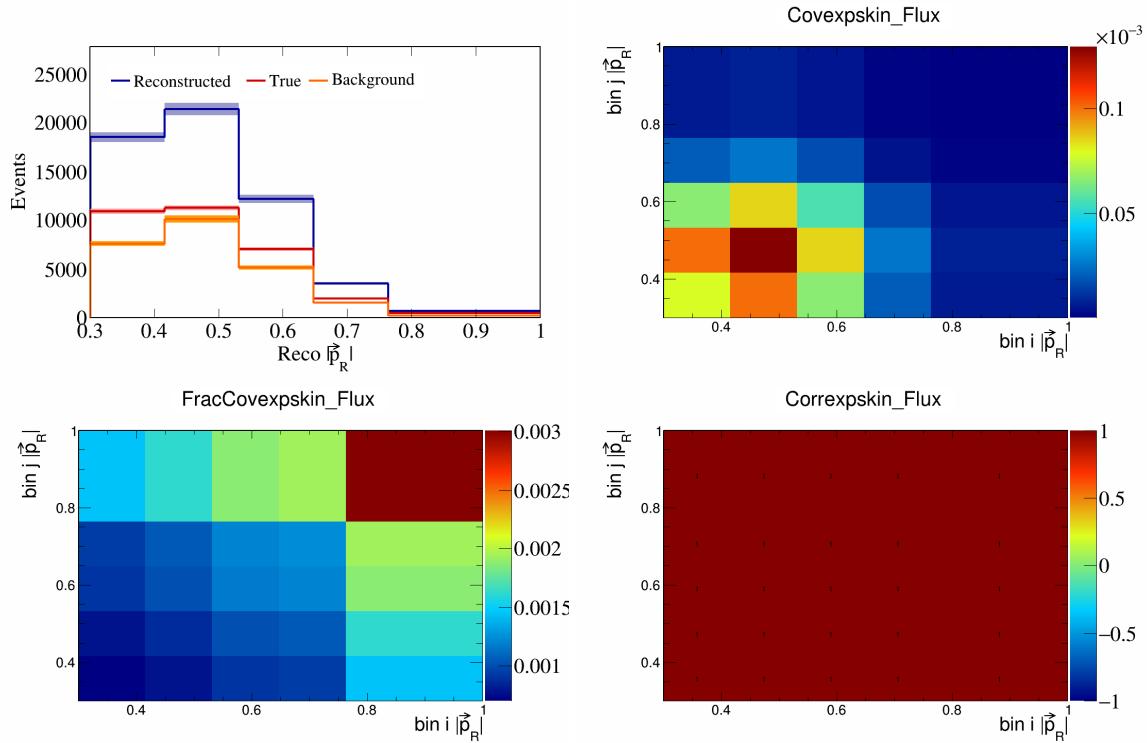


Figure 605: Expskin variations for $|\vec{p}_R|$.

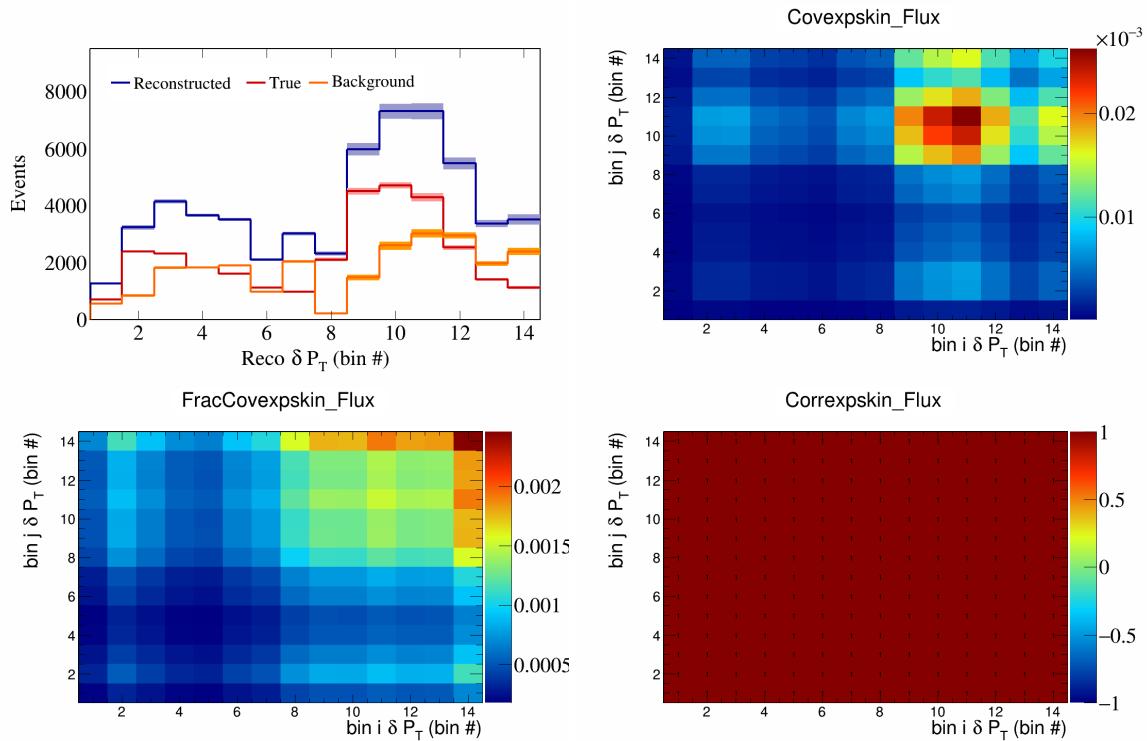


Figure 606: Expskin variations for δP_T in $\cos(\theta_{\vec{p}_\mu})$.

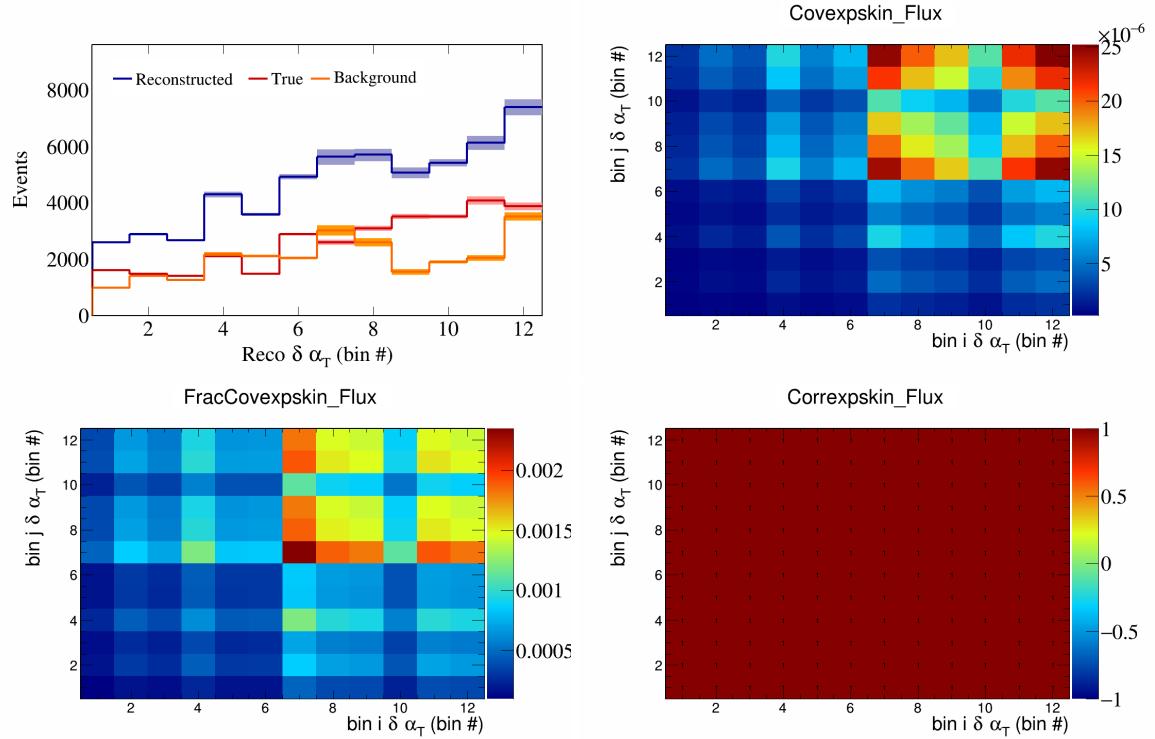


Figure 607: Expskin variations for $\delta\alpha_T$ in $\cos(\theta_{\vec{p}_\mu})$.

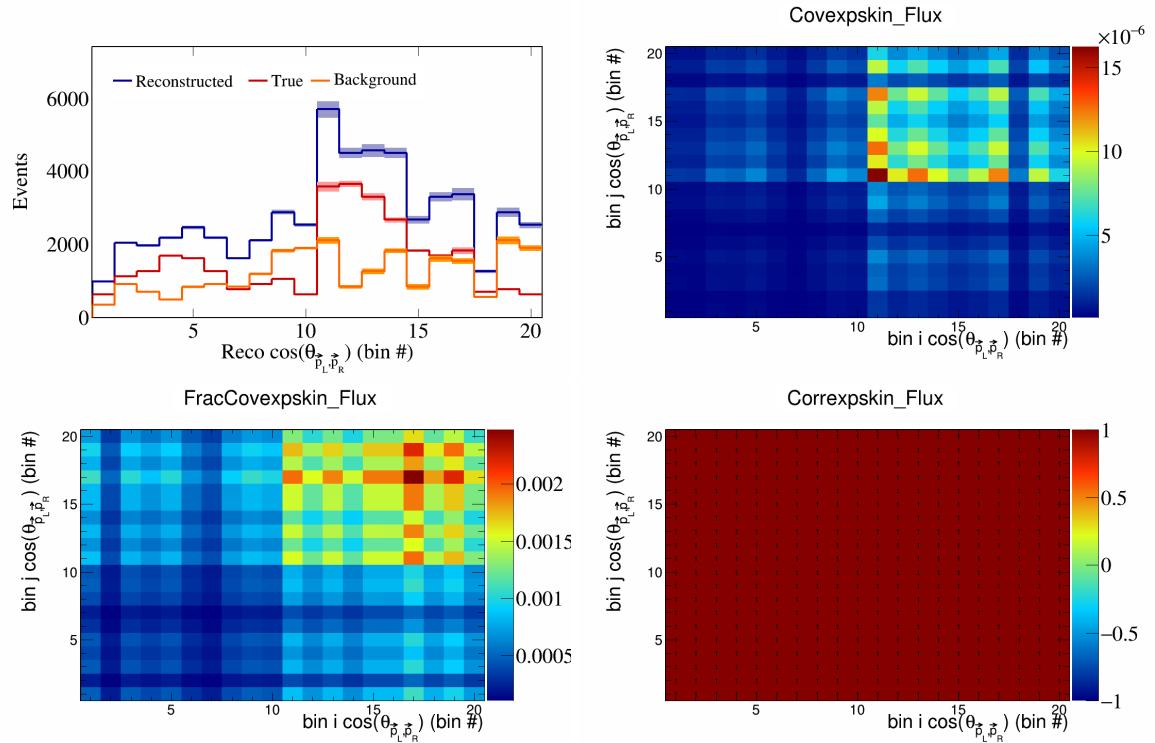


Figure 608: Expskin variations for $\cos(\theta_{\vec{p}_L, \vec{p}_R})$ in $\cos(\theta_{\vec{p}_\mu})$.

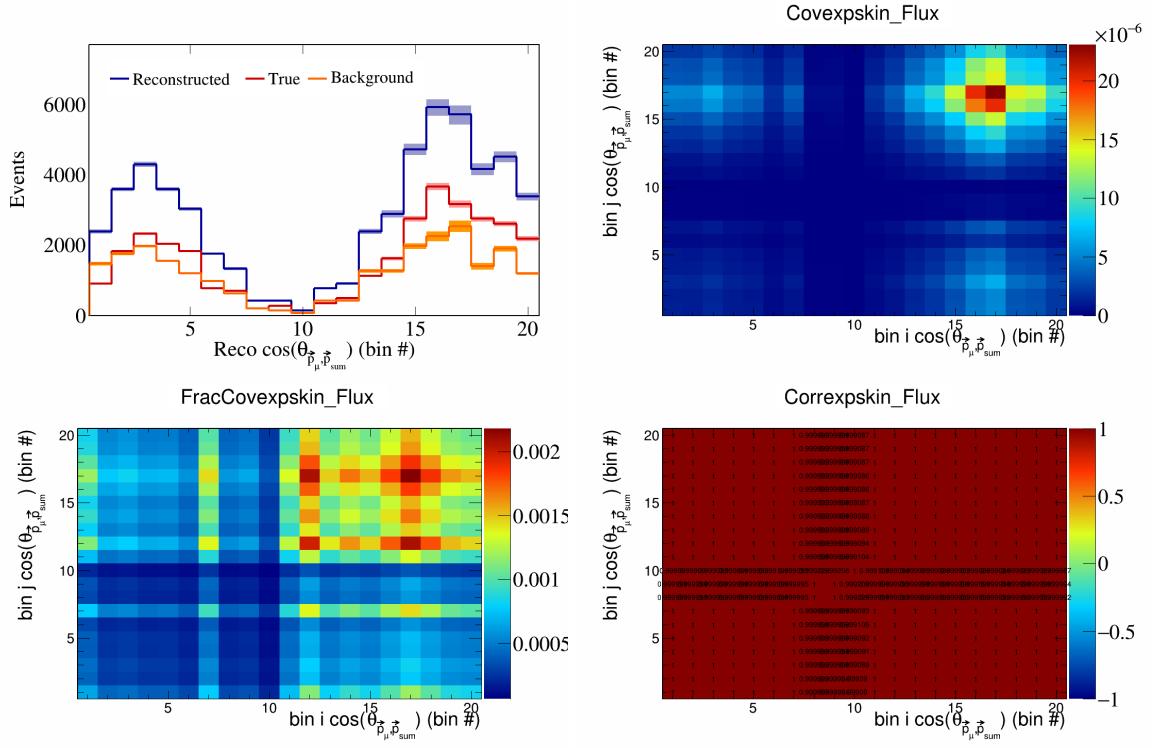


Figure 609: Expskin variations for $\cos(\theta_{\vec{p}_\mu}, \vec{p}_{\text{sum}})$ in $\cos(\theta_{\vec{p}_\mu})$.

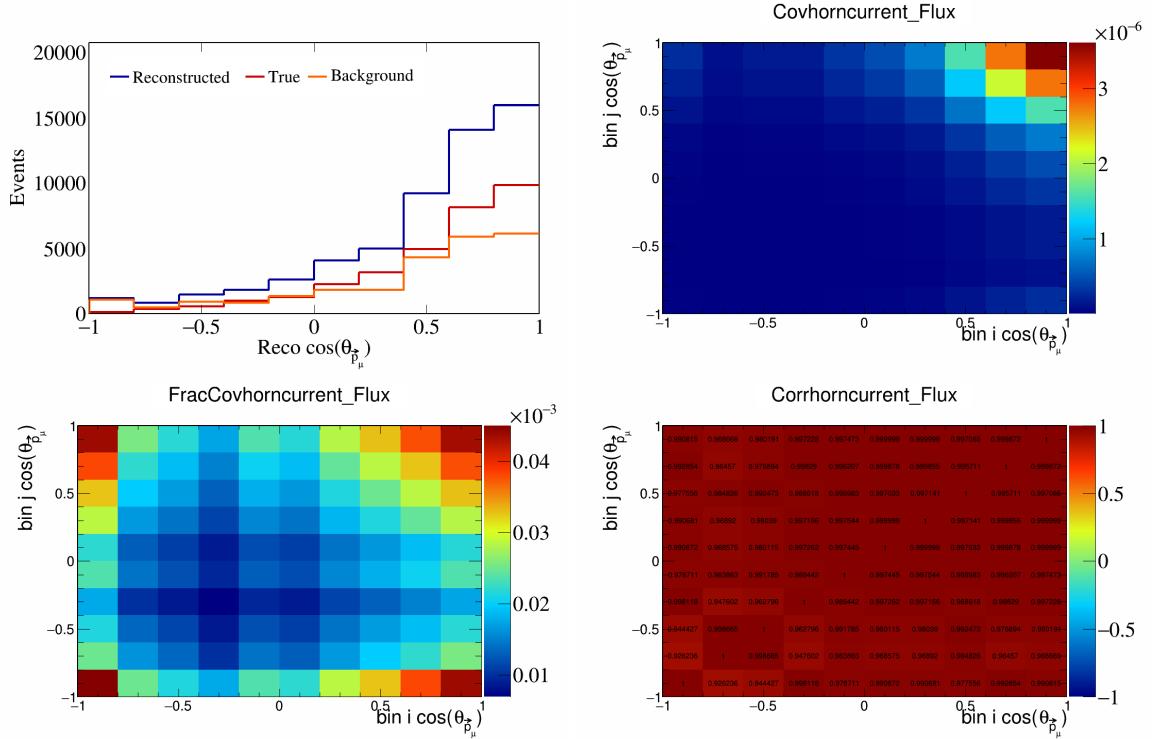


Figure 610: HornCurrent variations for $\cos(\theta_{\vec{p}_\mu})$.

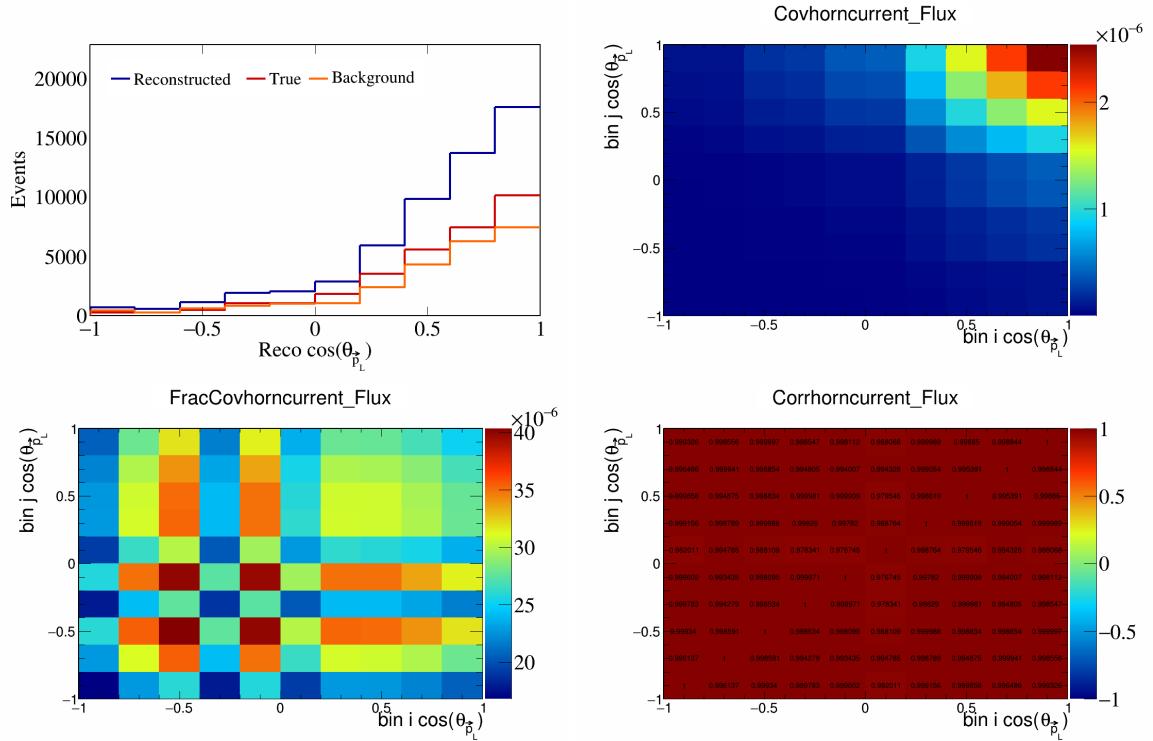


Figure 611: HornCurrent variations for $\cos(\theta_{\vec{p}_L})$.

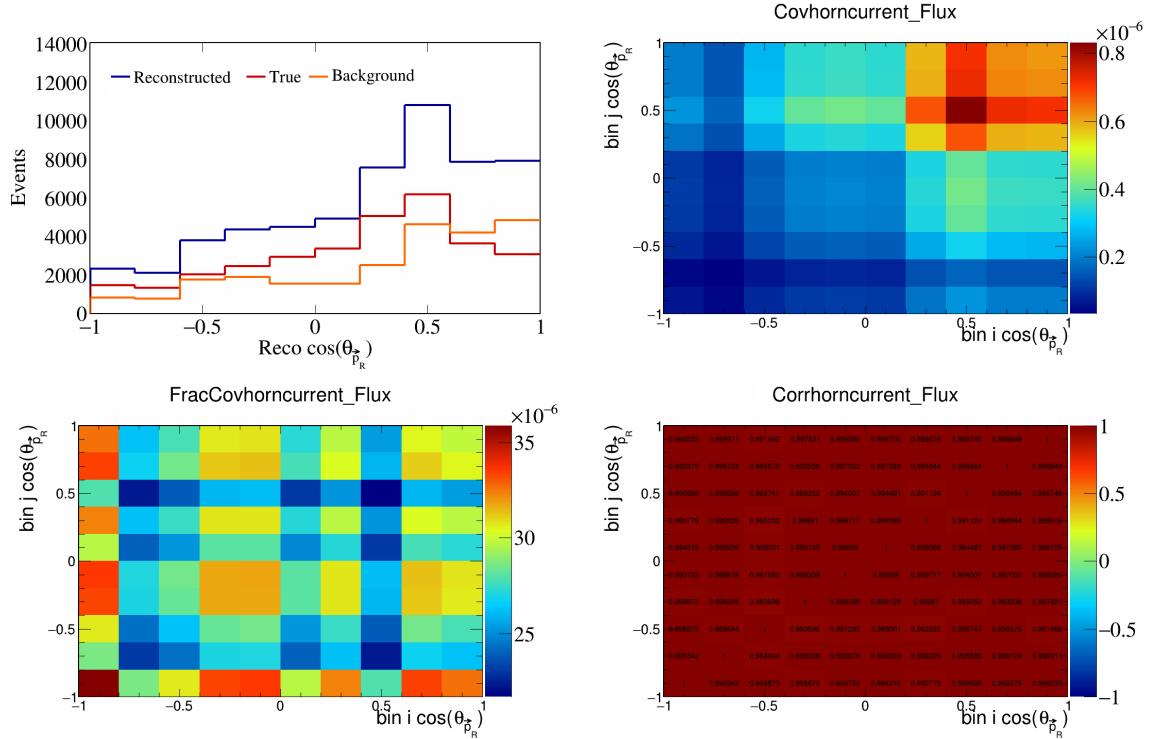


Figure 612: HornCurrent variations for $\cos(\theta_{\vec{p}_R})$.

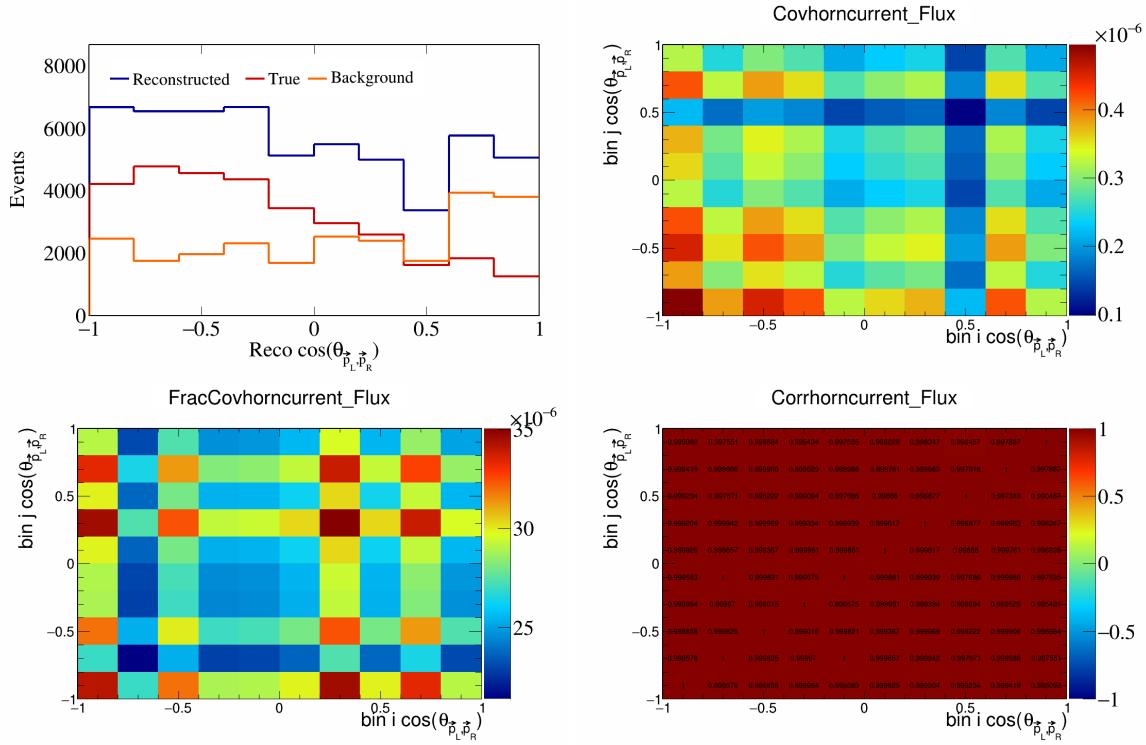


Figure 613: HornCurrent variations for $\cos(\theta_{\vec{p}_L, \vec{p}_R})$.

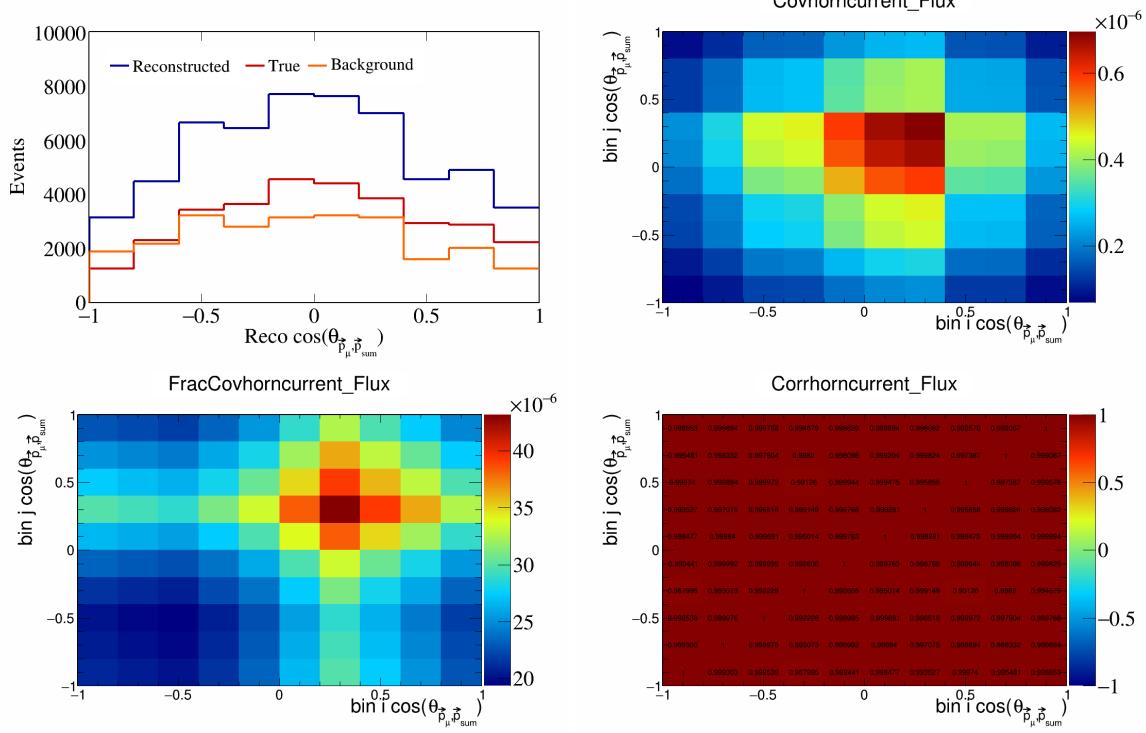


Figure 614: HornCurrent variations for $\cos(\theta_{\vec{p}_\mu, \vec{p}_{\text{sum}}})$.

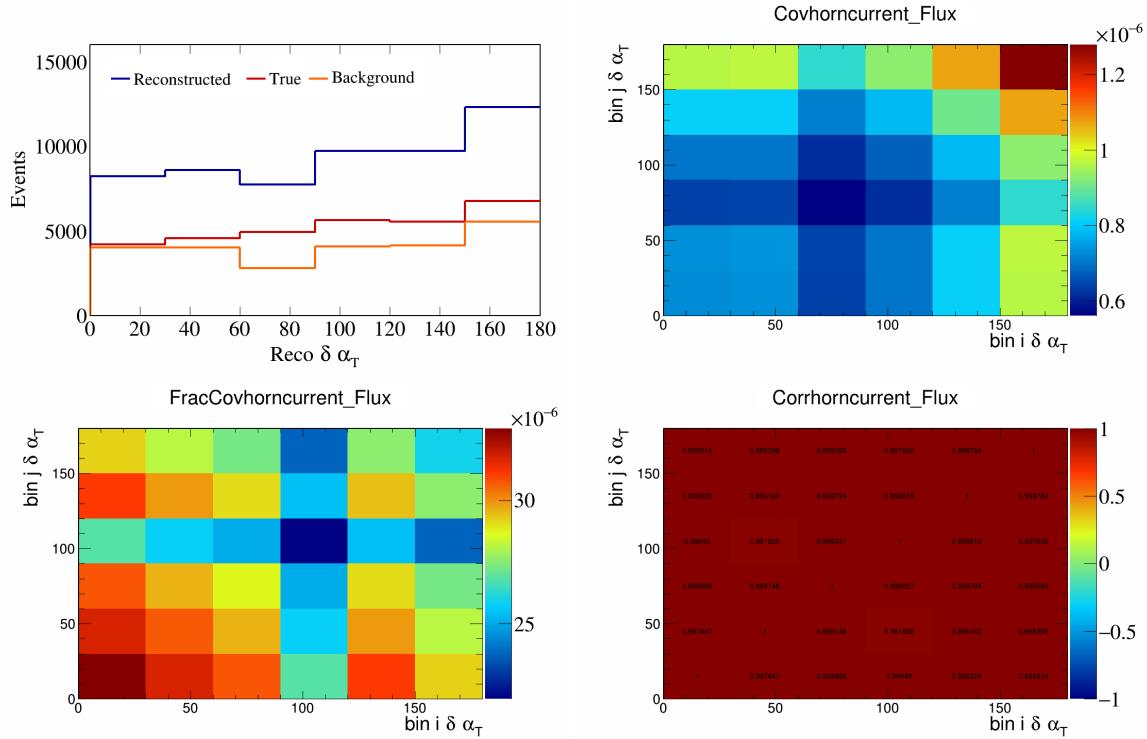


Figure 615: HornCurrent variations for $\delta\alpha_T$.

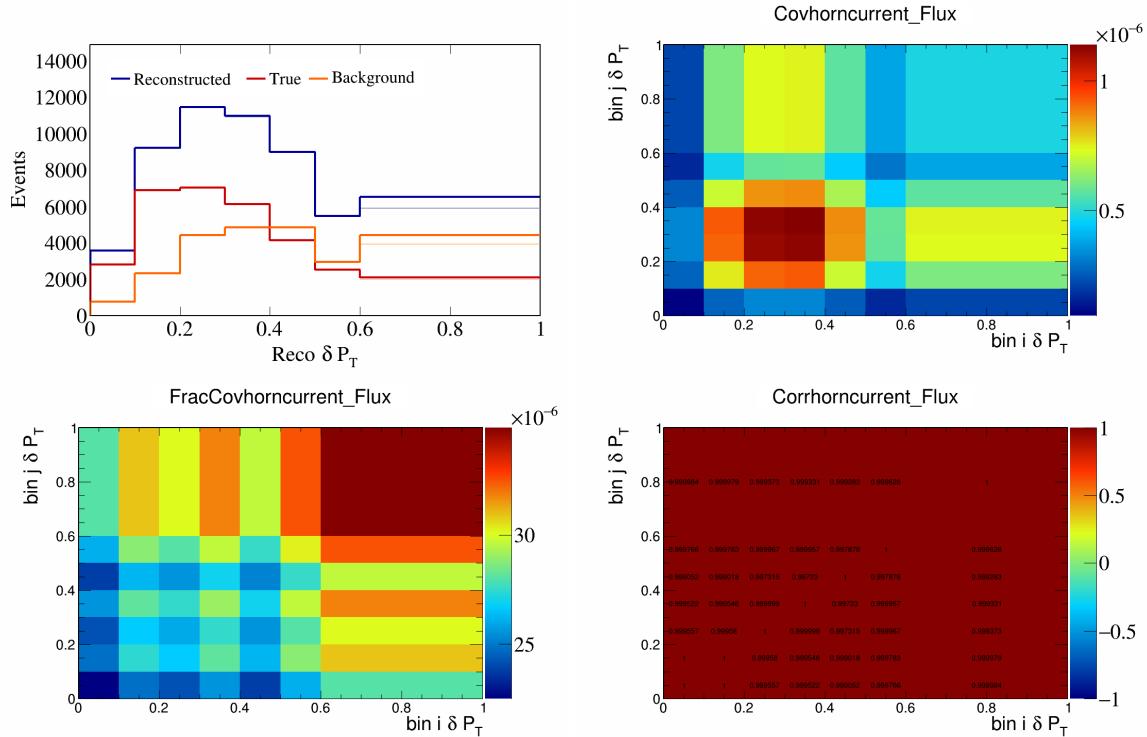


Figure 616: HornCurrent variations for δP_T .

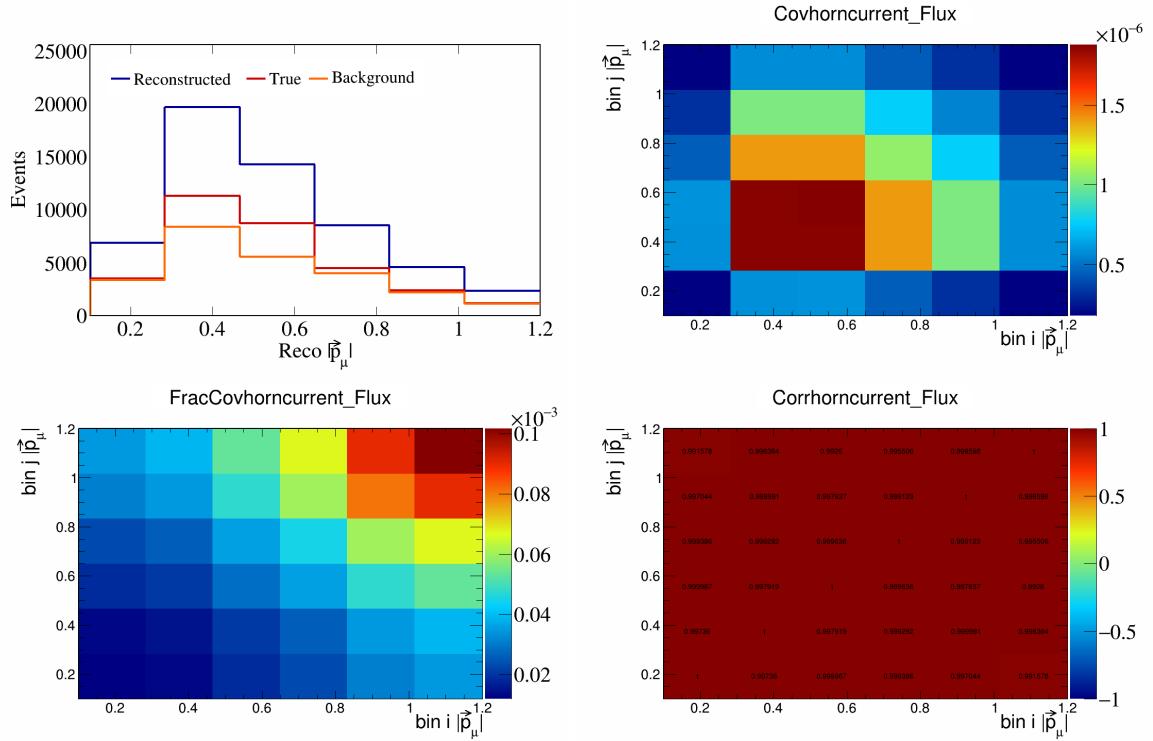


Figure 617: HornCurrent variations for $|\vec{p}_\mu|$.

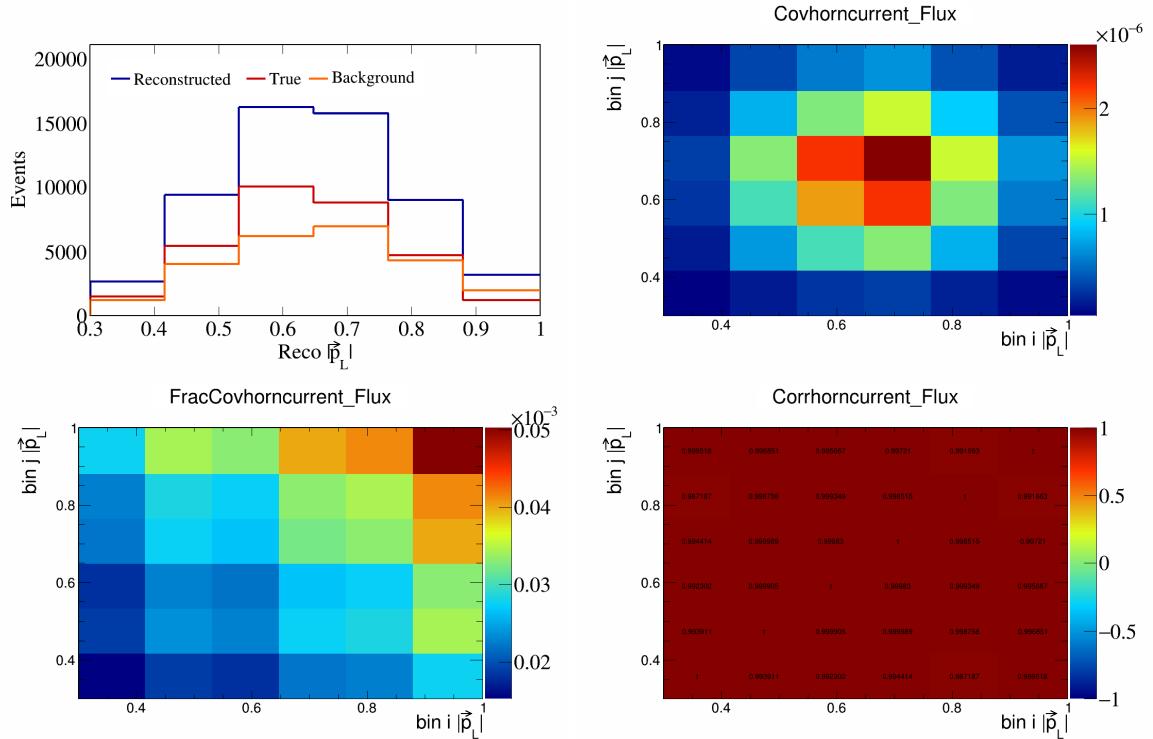


Figure 618: HornCurrent variations for $|\vec{p}_L|$.

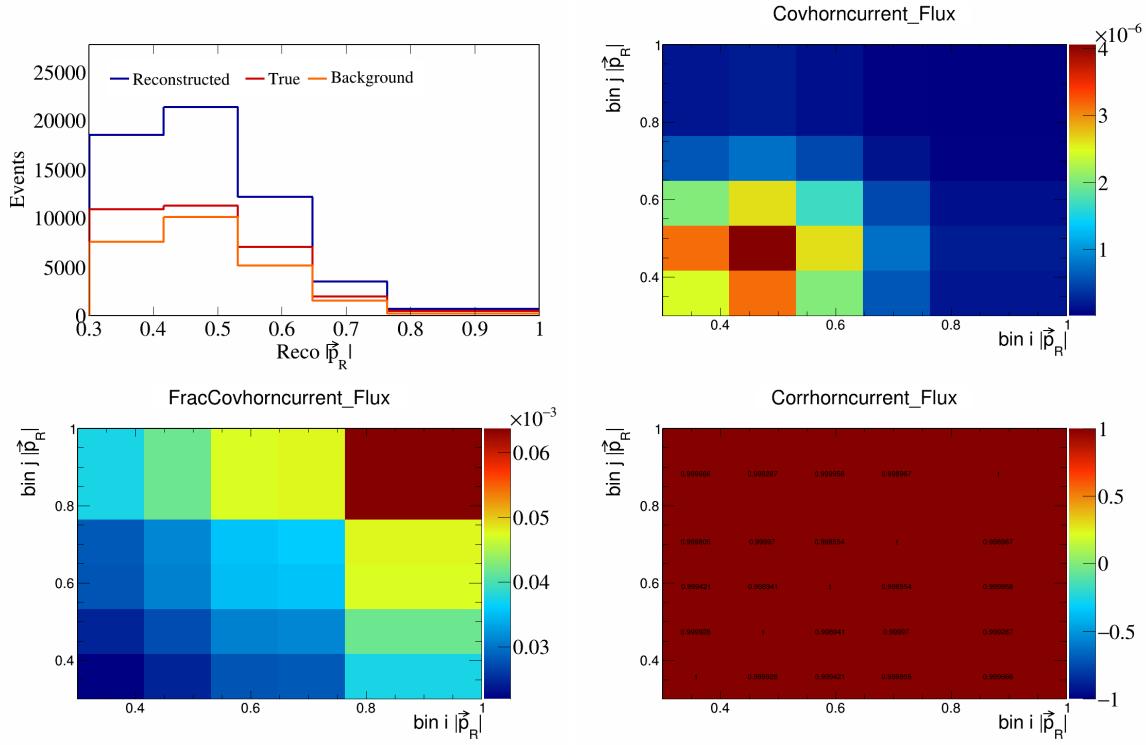


Figure 619: HornCurrent variations for $|\vec{p}_R|$.

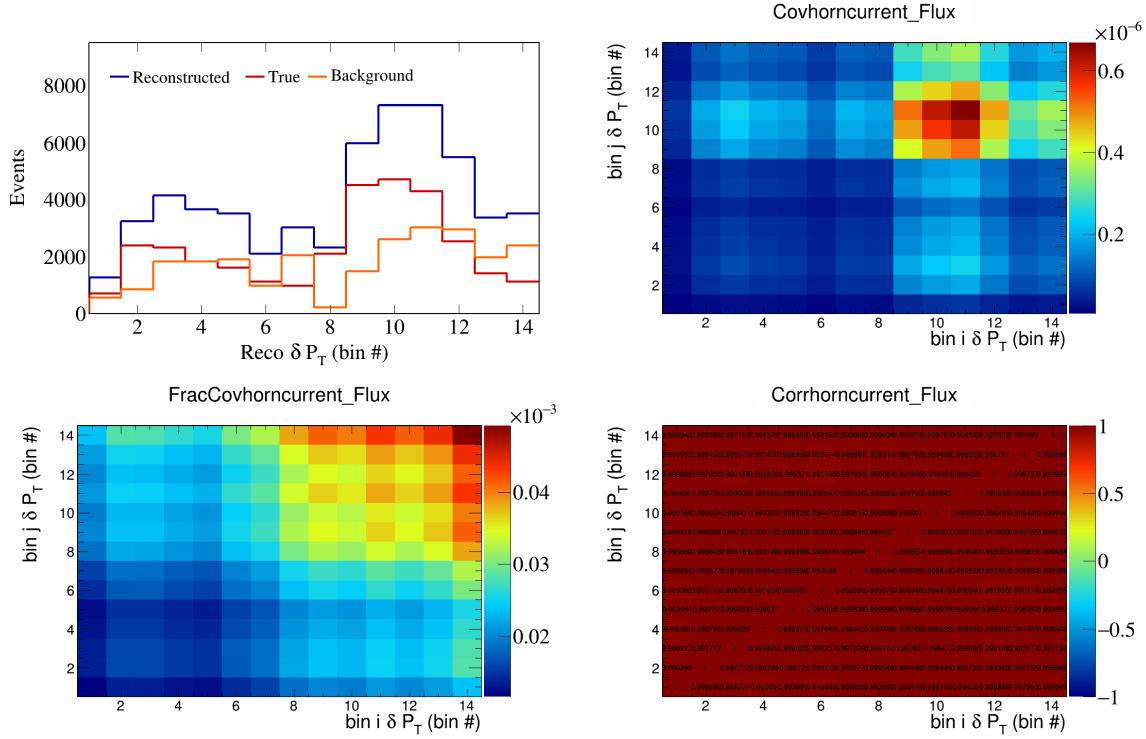


Figure 620: HornCurrent variations for δP_T in $\cos(\theta_{\vec{p}_\mu})$.

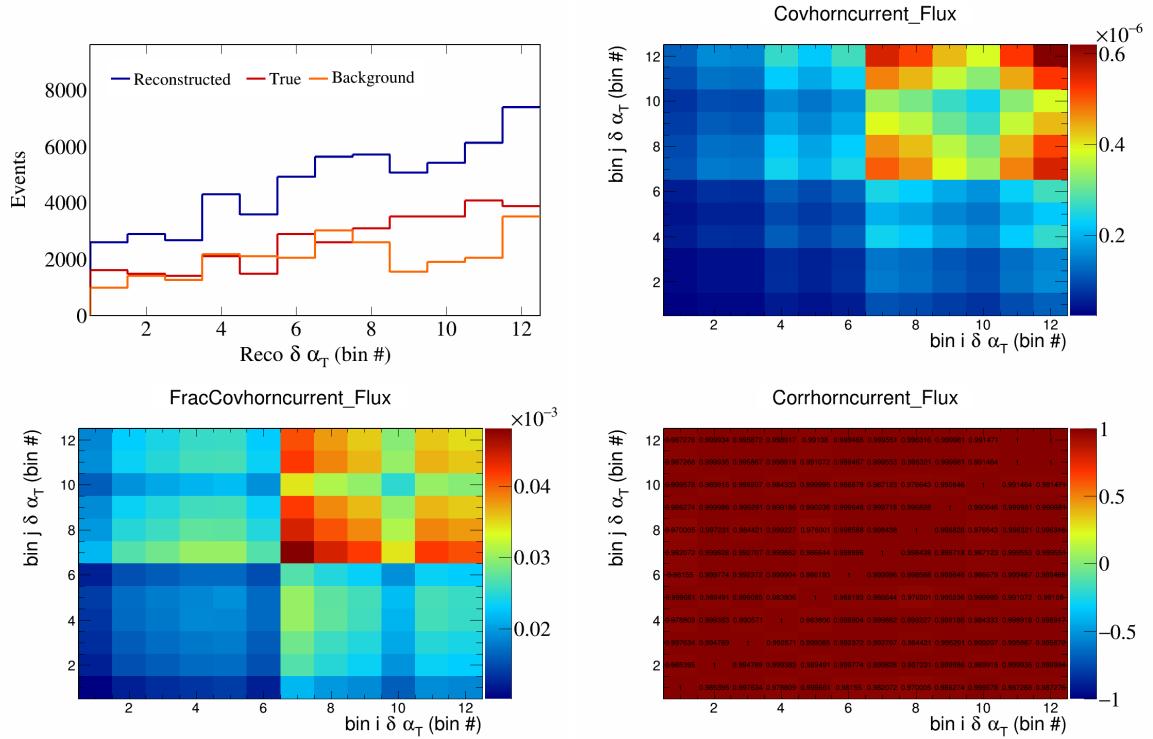


Figure 621: HornCurrent variations for $\delta \alpha_T$ in $\cos(\theta_{\vec{p}_\mu})$.

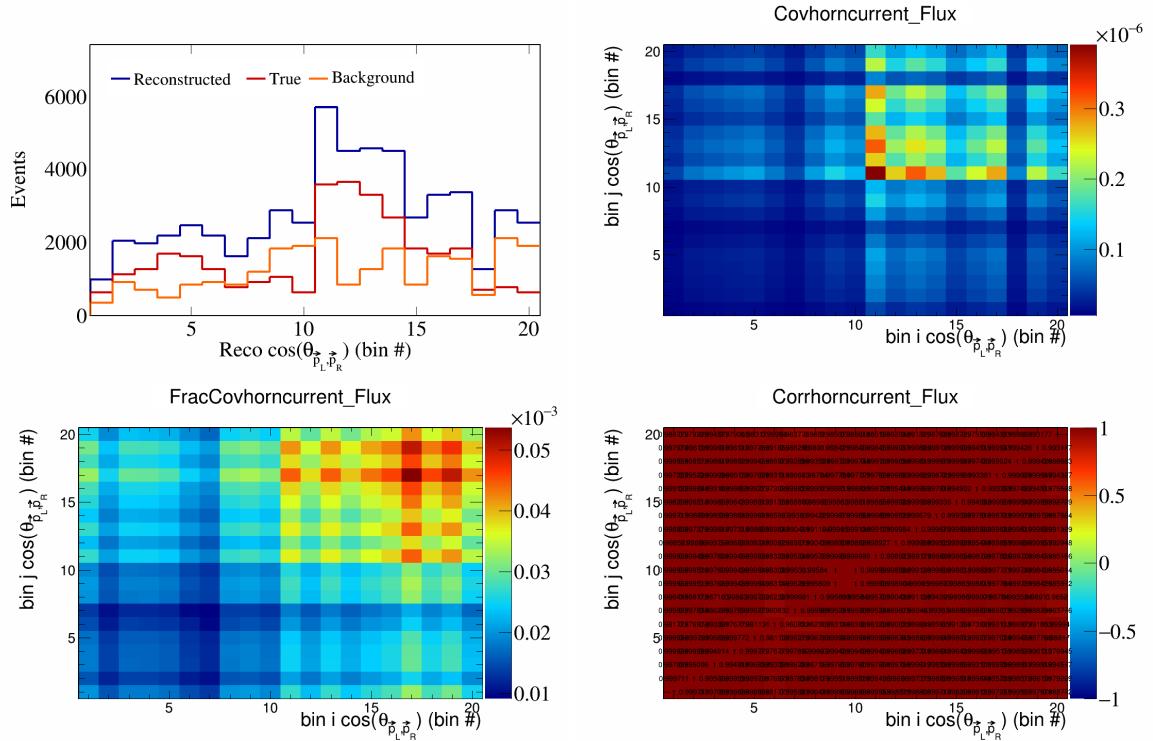


Figure 622: HornCurrent variations for $\cos(\theta_{\vec{p}_L, \vec{p}_R})$ in $\cos(\theta_{\vec{p}_\mu})$.

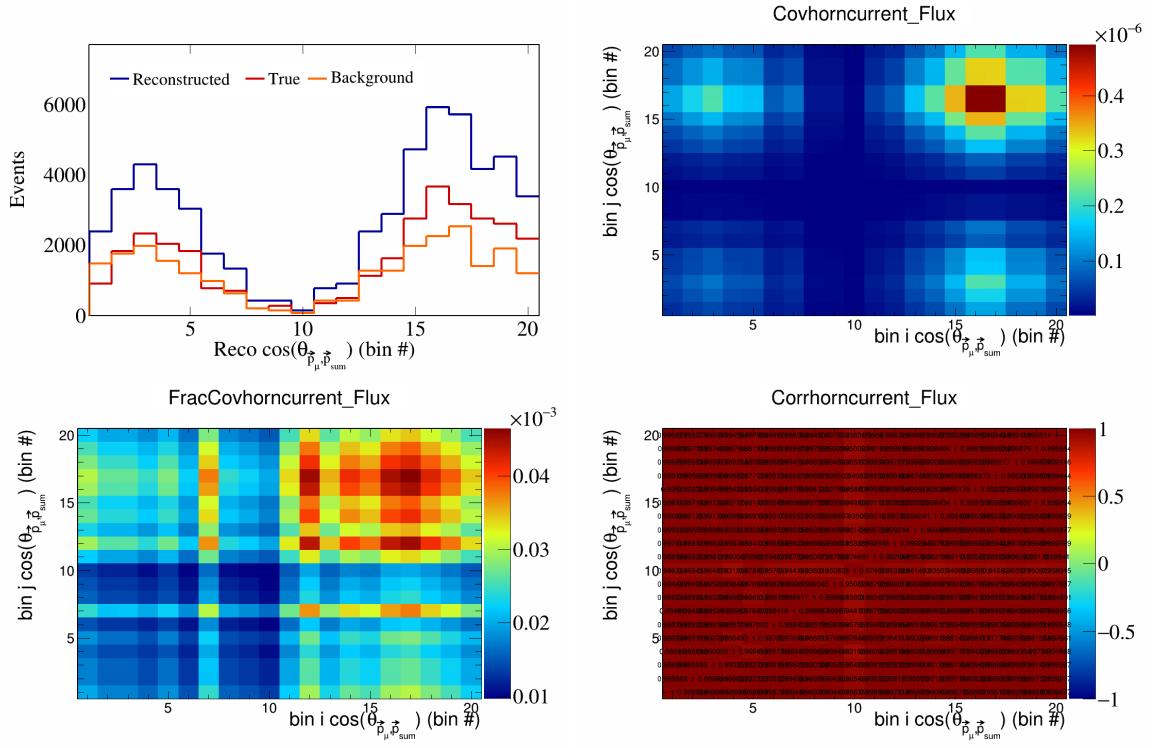


Figure 623: HornCurrent variations for $\cos(\theta_{\vec{p}_\mu, \vec{p}_{\text{sum}}})$ in $\cos(\theta_{\vec{p}_\mu})$.

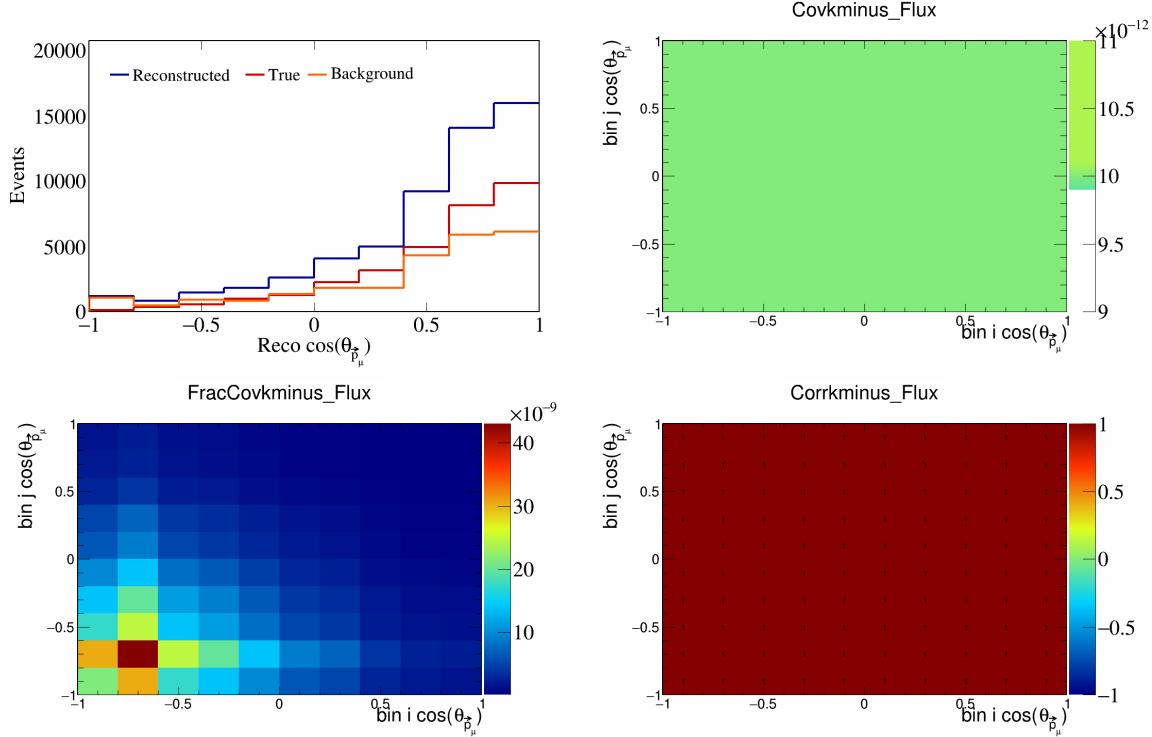


Figure 624: KMinus variations for $\cos(\theta_{\vec{p}_\mu})$.

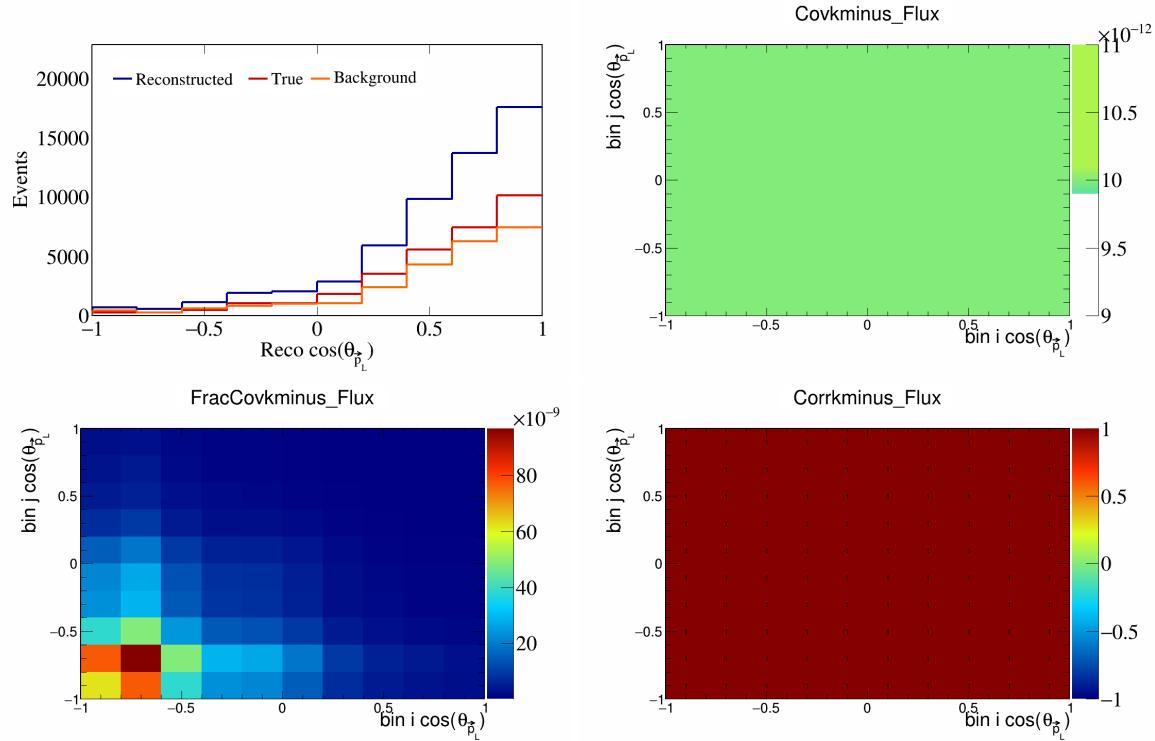


Figure 625: KMinus variations for $\cos(\theta_{\vec{p}_L})$.

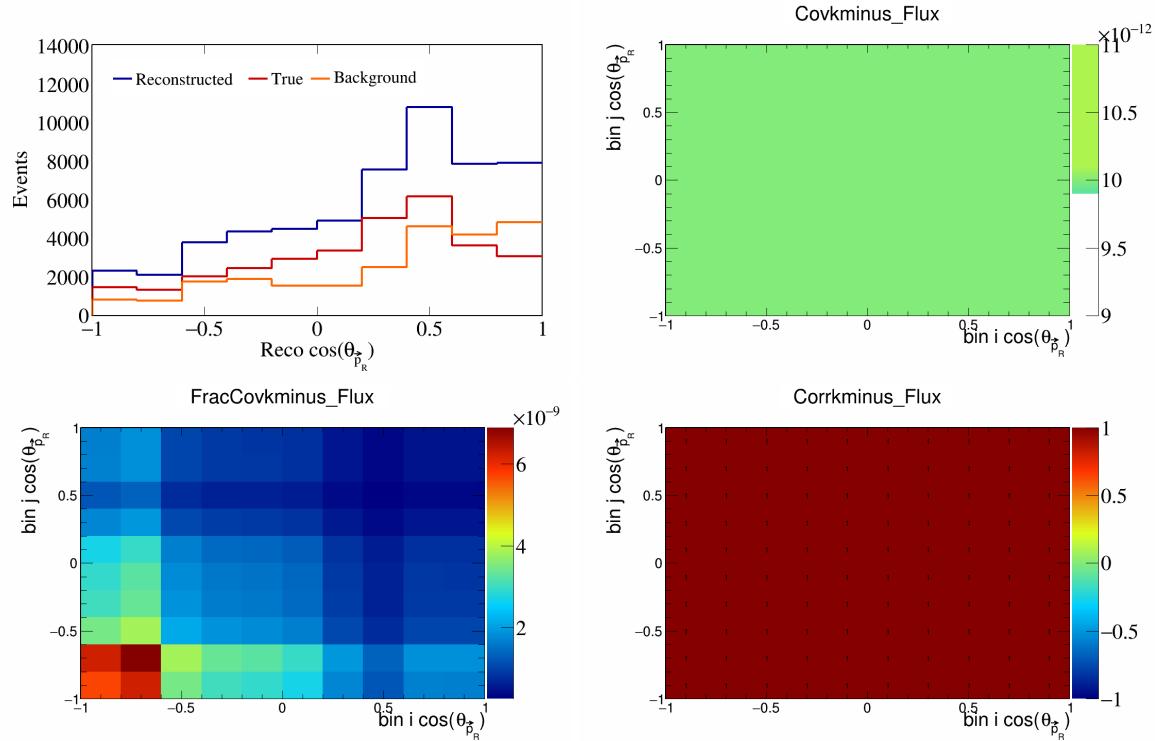


Figure 626: KMinus variations for $\cos(\theta_{\vec{p}_R})$.

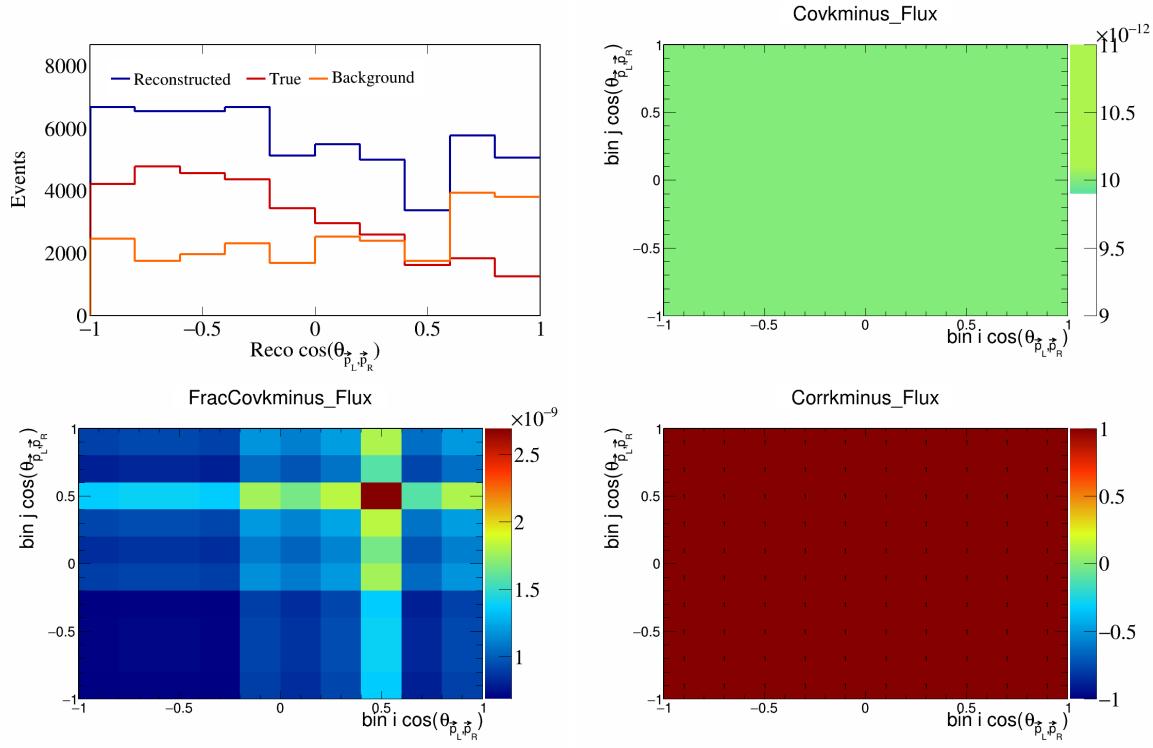


Figure 627: KMinus variations for $\cos(\theta_{\vec{p}_L, \vec{p}_R})$.

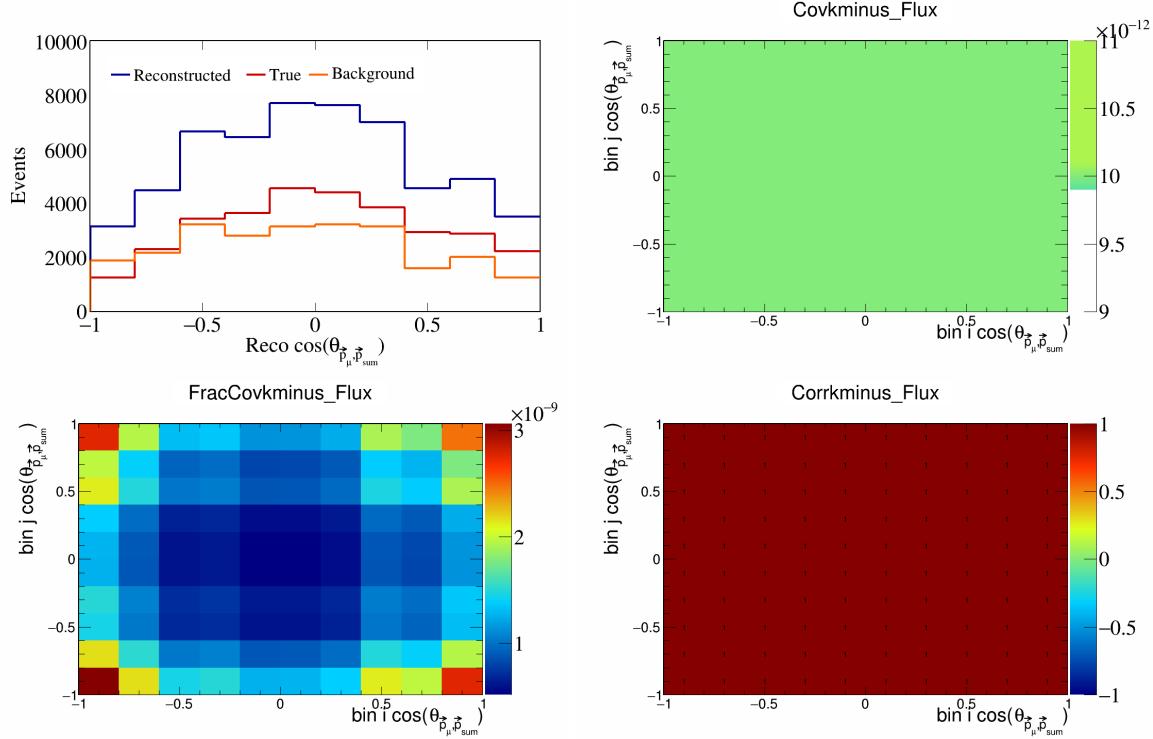


Figure 628: KMinus variations for $\cos(\theta_{\vec{p}_\mu, \vec{p}_{\text{sum}}})$.

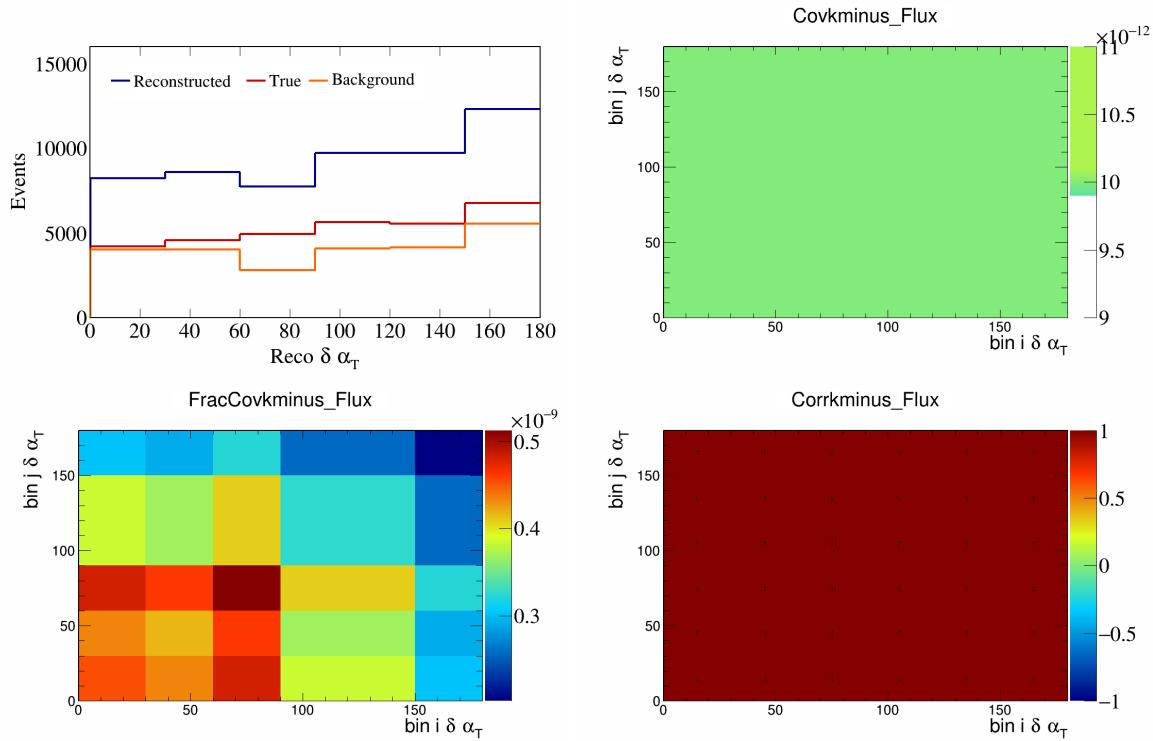


Figure 629: KMinus variations for $\delta\alpha_T$.

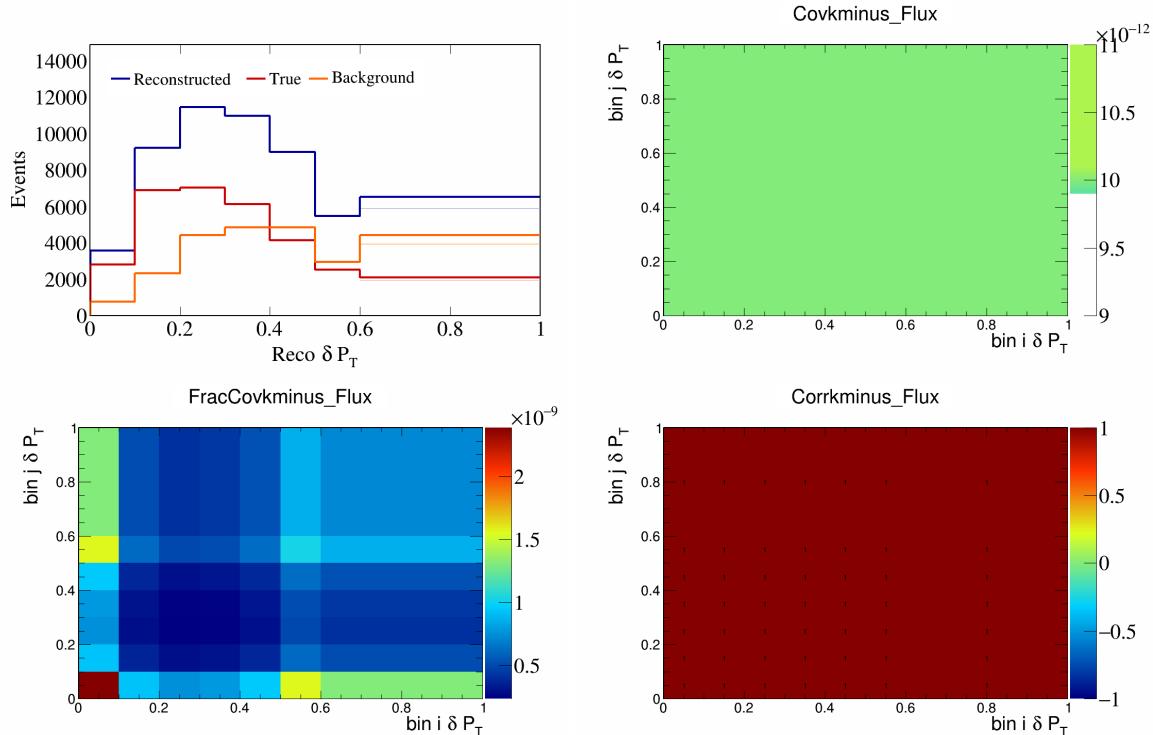


Figure 630: KMinus variations for δP_T .

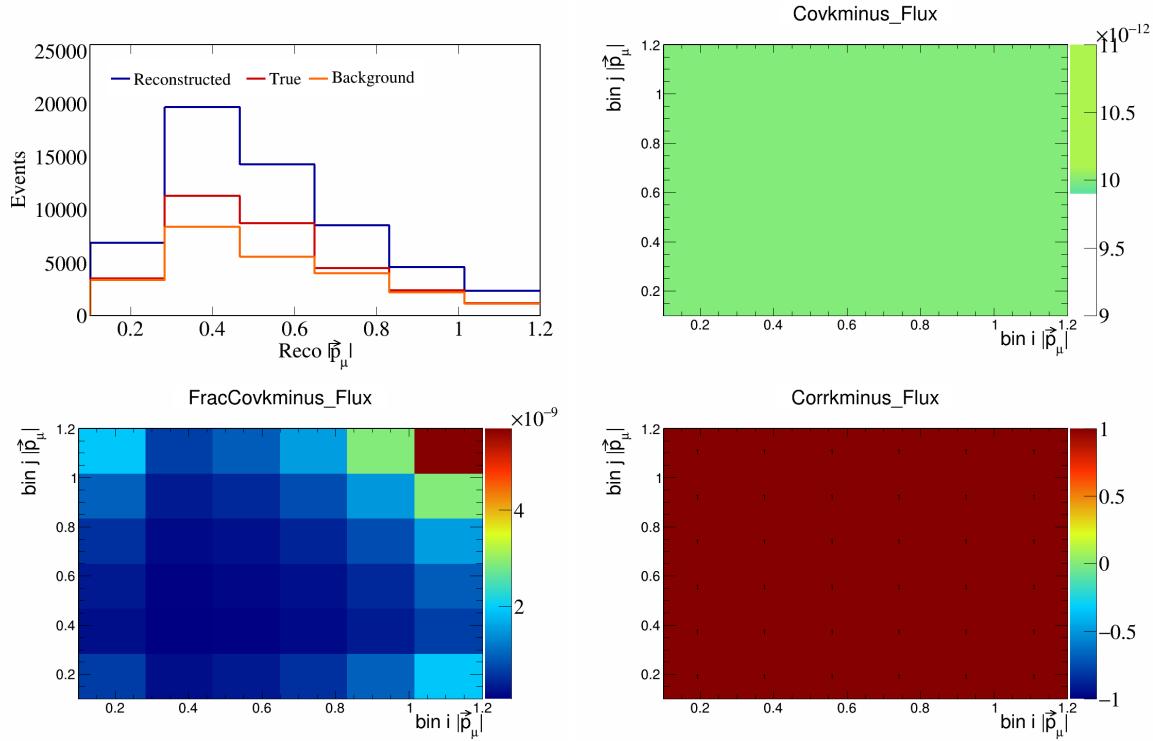


Figure 631: KMinus variations for $|\vec{p}_\mu|$.

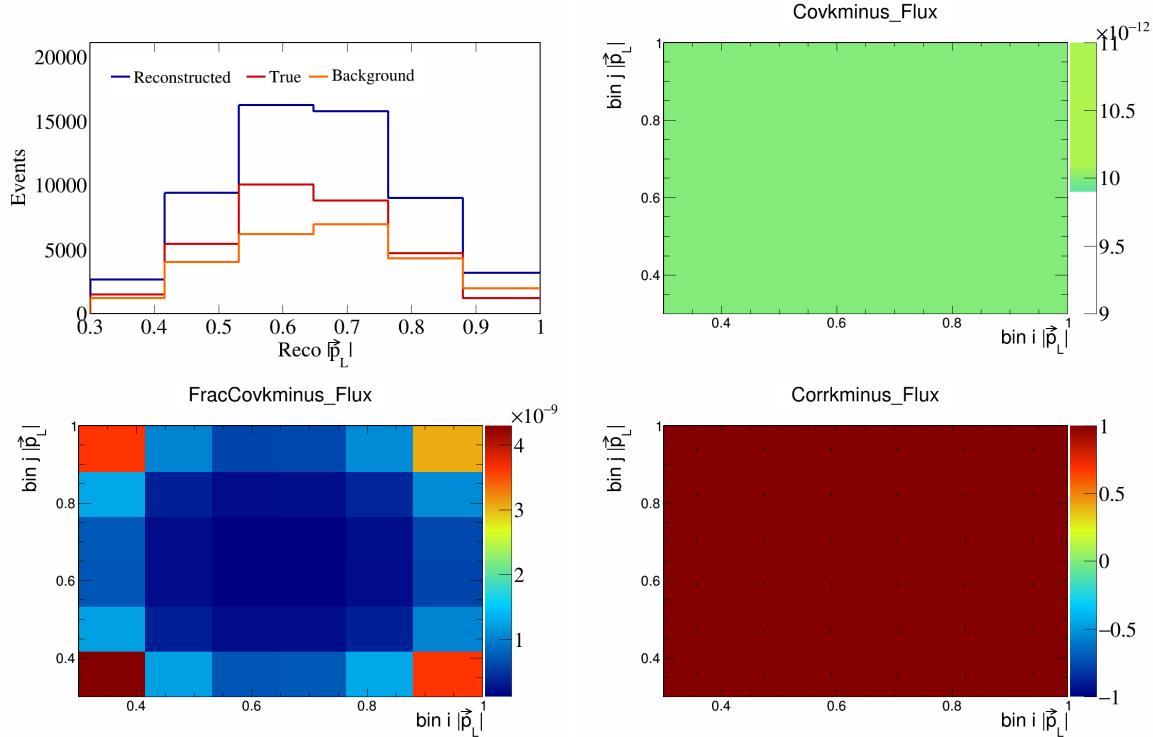


Figure 632: KMinus variations for $|\vec{p}_L|$.

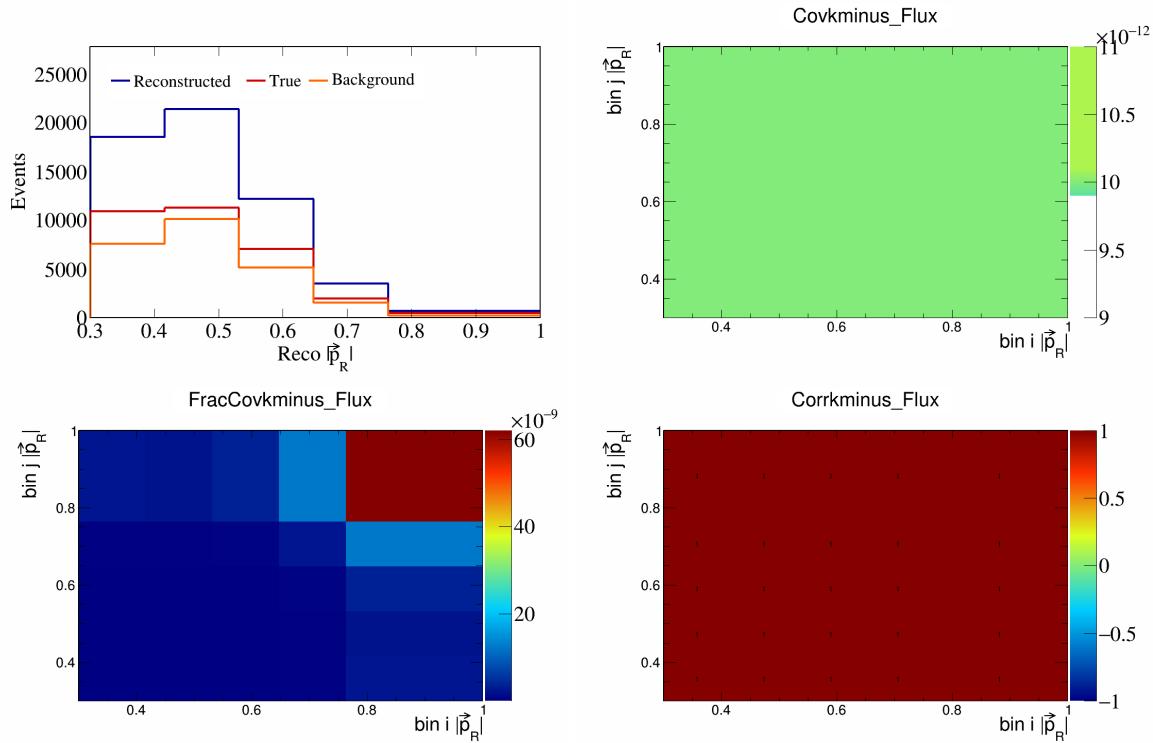


Figure 633: KMinus variations for $|\vec{p}_R|$.

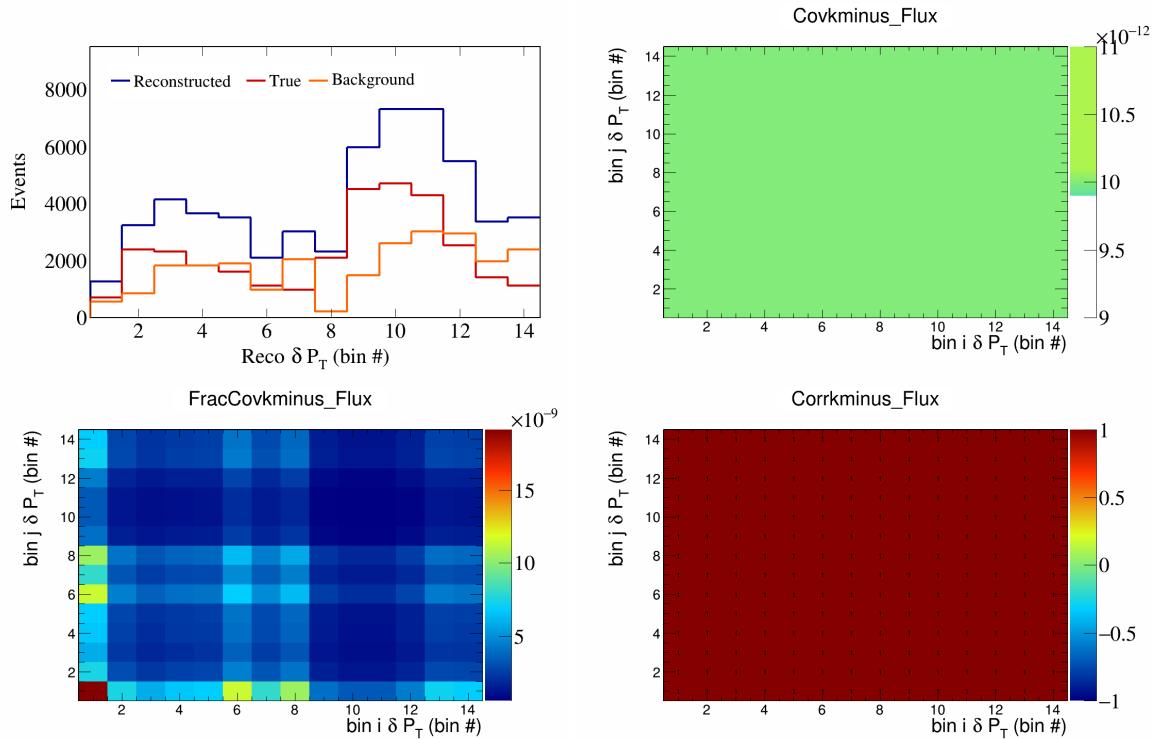


Figure 634: KMinus variations for δP_T in $\cos(\theta_{\vec{p}_\mu})$.

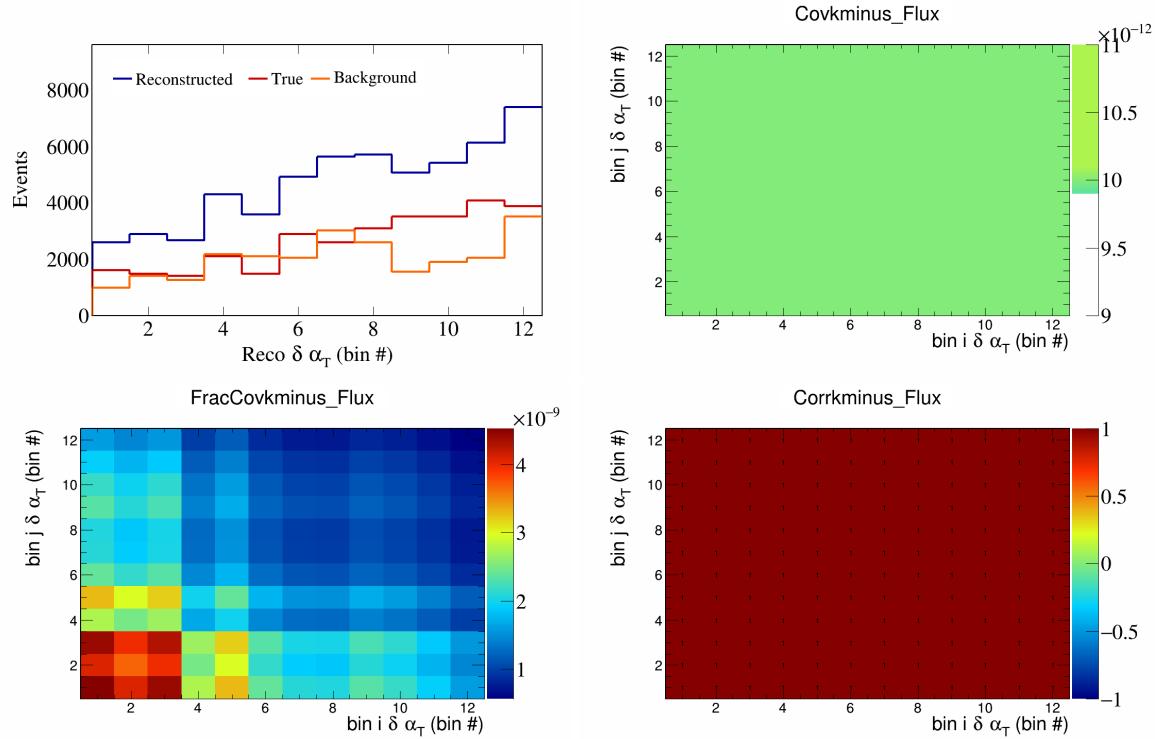


Figure 635: KMinus variations for $\delta \alpha_T$ in $\cos(\theta_{\vec{p}_\mu})$.

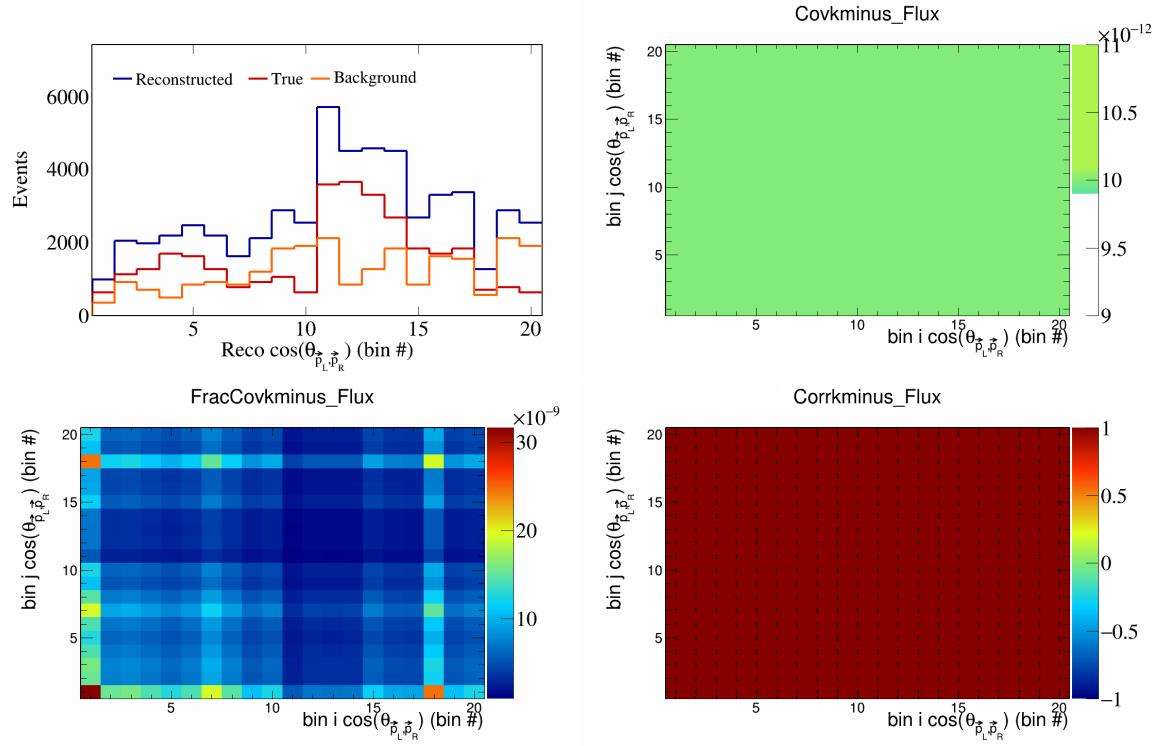


Figure 636: KMinus variations for $\cos(\theta_{\vec{p}_L, \vec{p}_R})$ in $\cos(\theta_{\vec{p}_\mu})$.

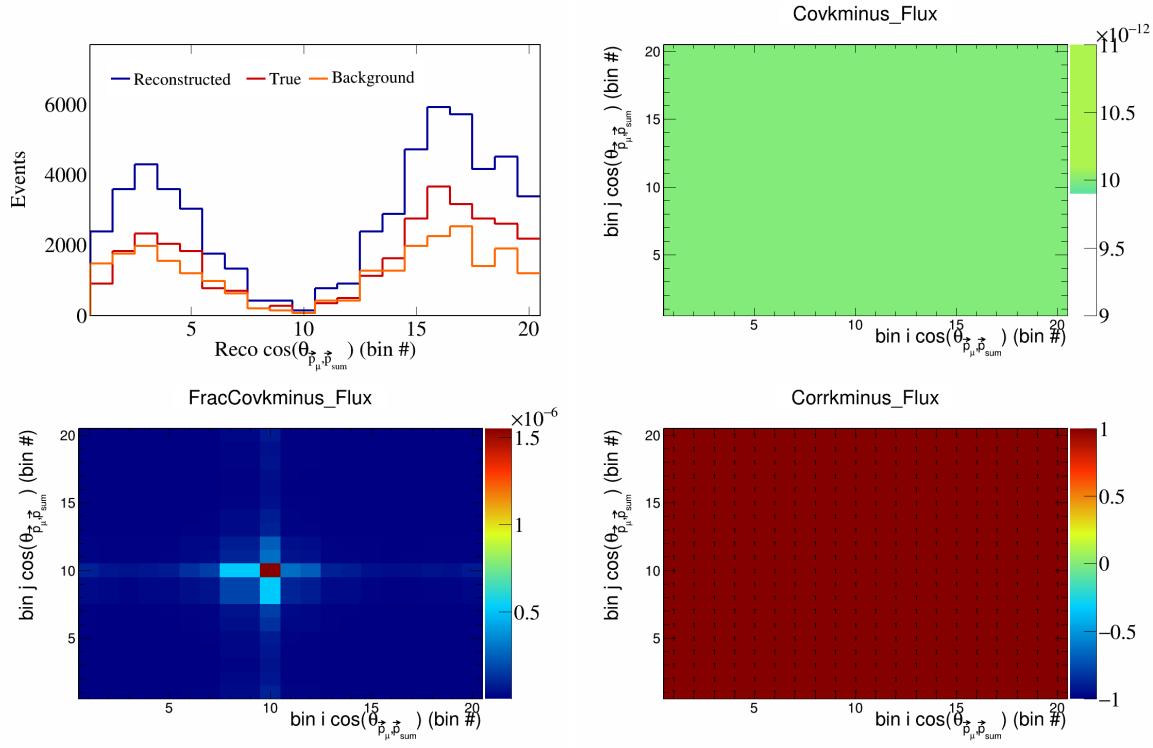


Figure 637: KMinus variations for $\cos(\theta_{\vec{p}_\mu}^{\text{sum}})$ in $\cos(\theta_{\vec{p}_\mu})$.

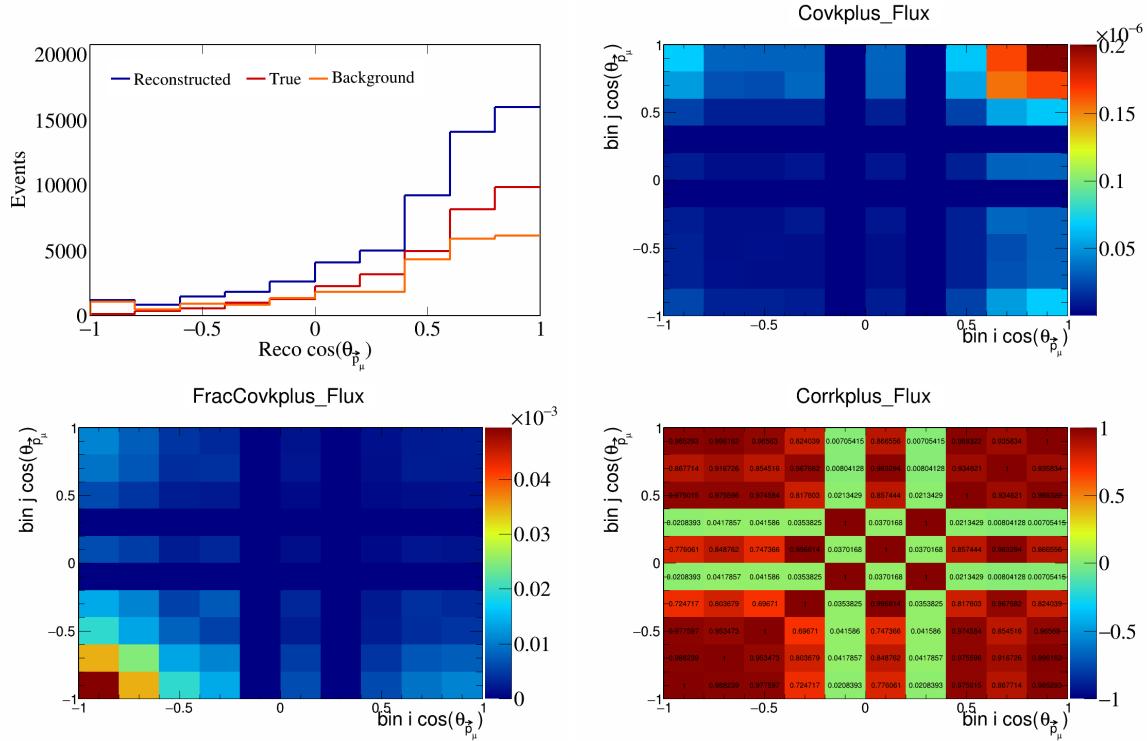


Figure 638: KPlus variations for $\cos(\theta_{\vec{p}_\mu})$.

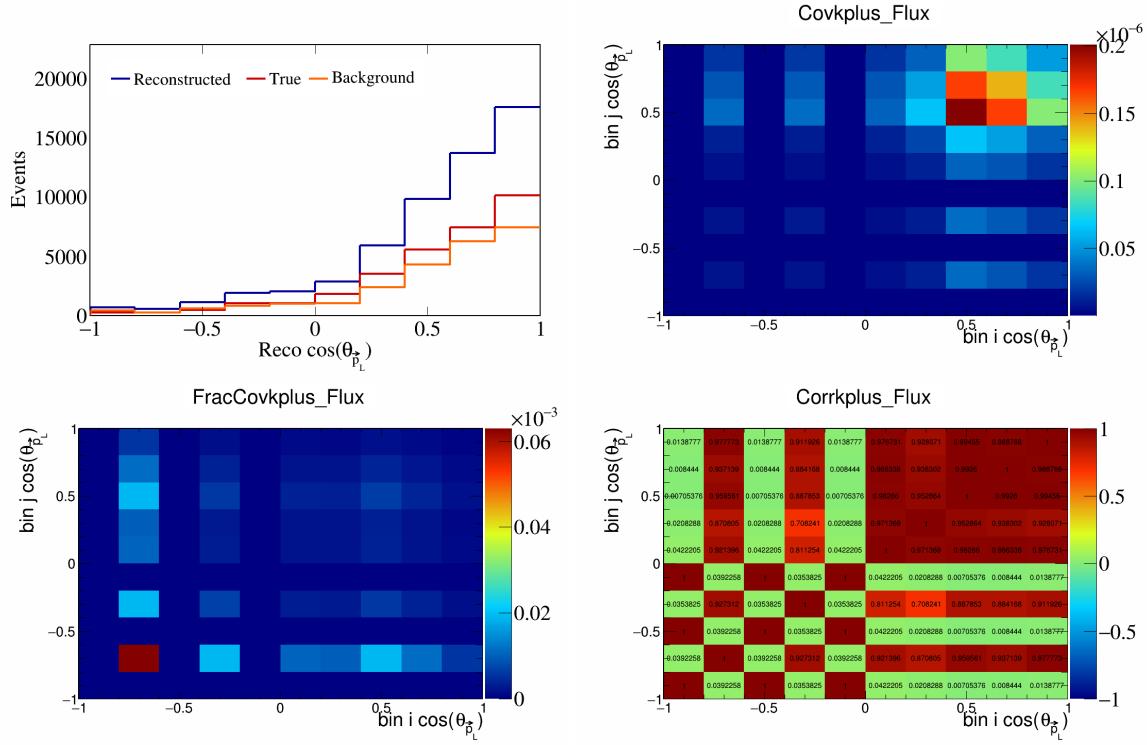


Figure 639: KPlus variations for $\cos(\theta_{\vec{p}_L})$.

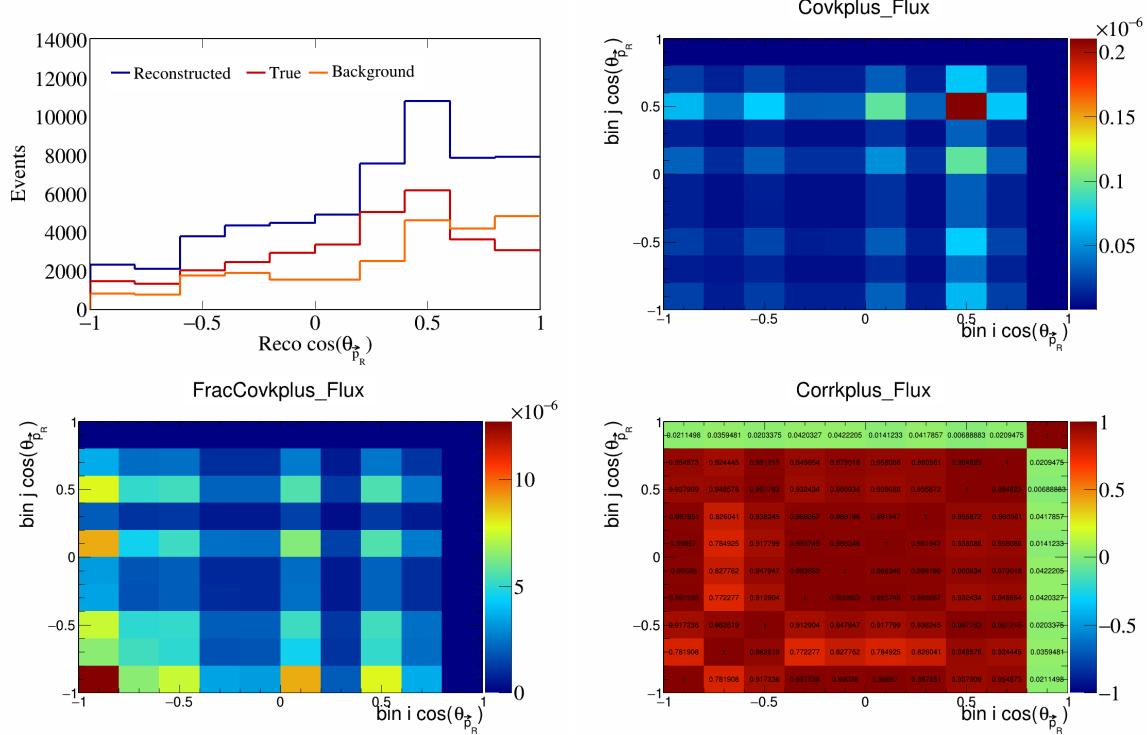


Figure 640: KPlus variations for $\cos(\theta_{\vec{p}_R})$.

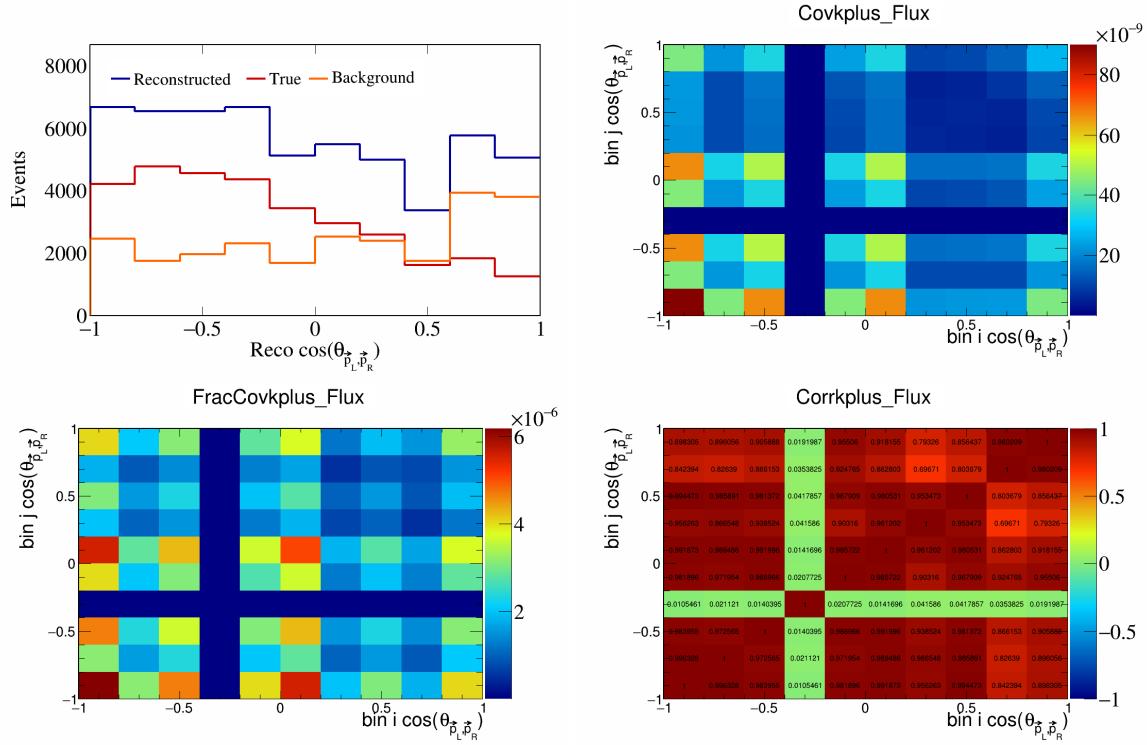


Figure 641: KPlus variations for $\cos(\theta_{\vec{p}_L, \vec{p}_R})$.

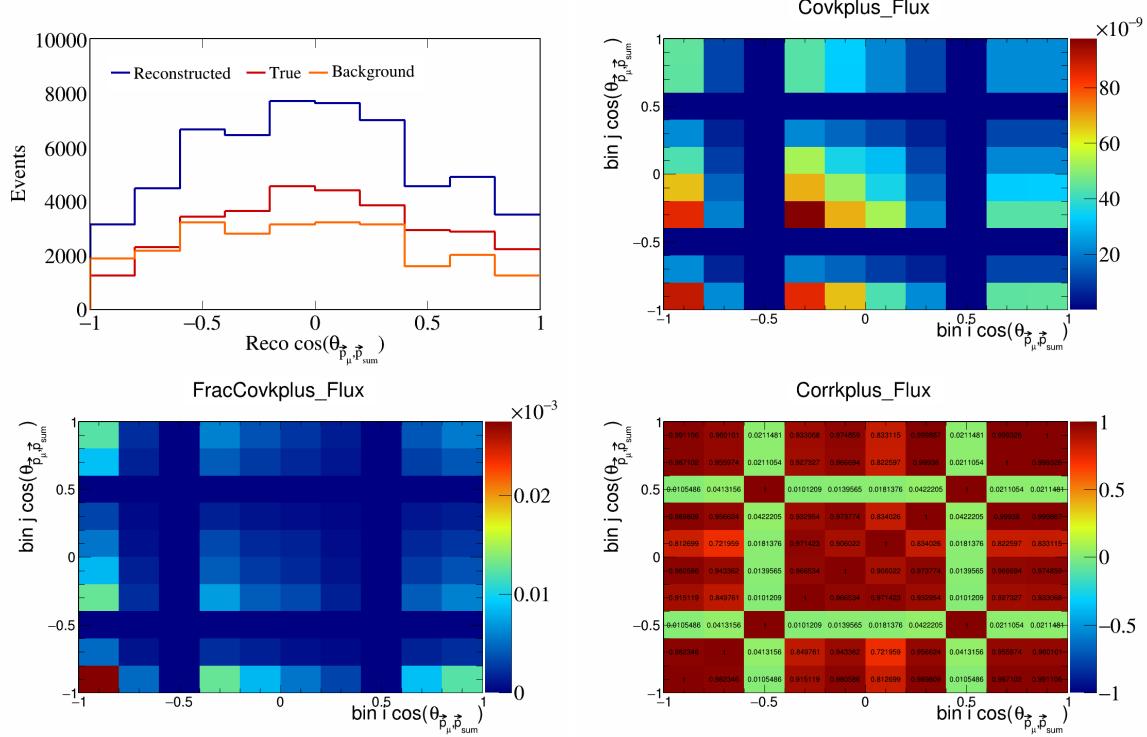


Figure 642: KPlus variations for $\cos(\theta_{\vec{p}_\mu, \vec{p}_{\text{sum}}})$.

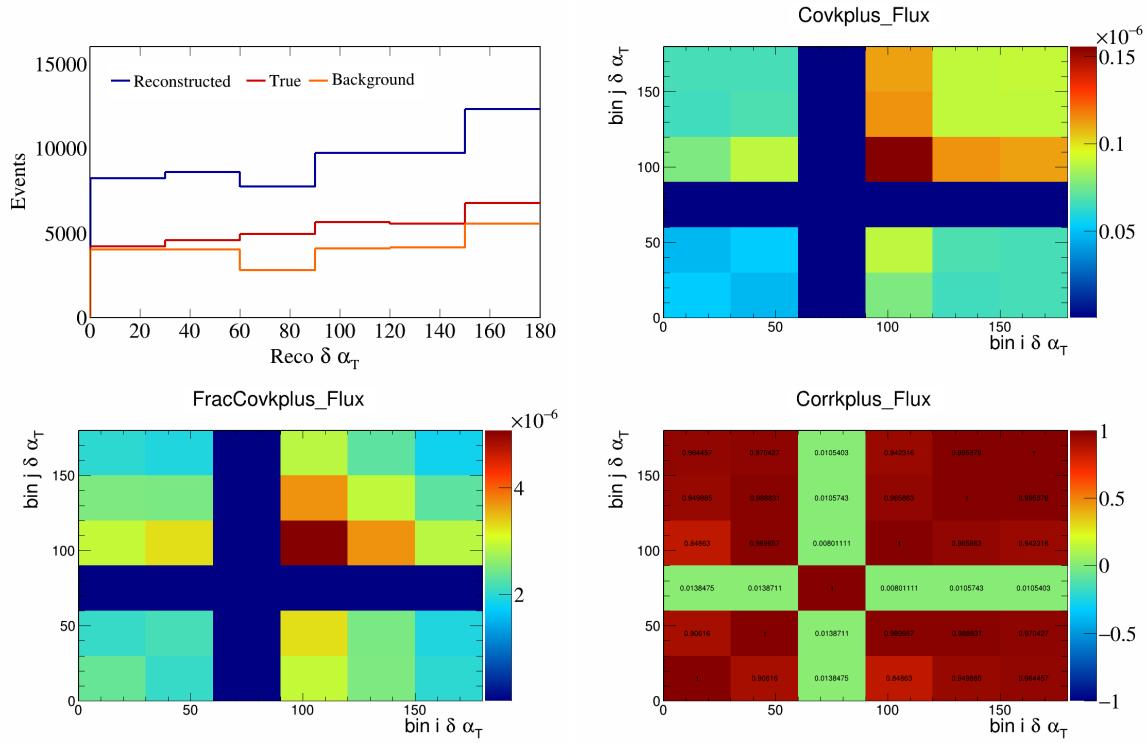


Figure 643: KPlus variations for $\delta\alpha_T$.

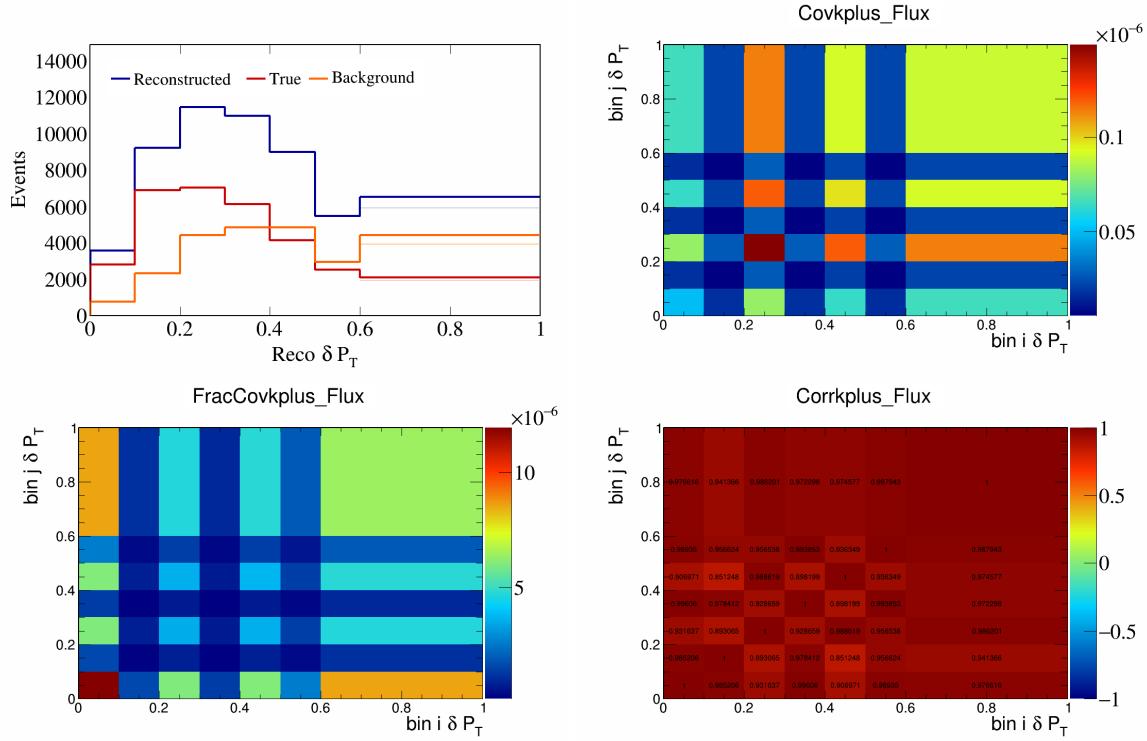


Figure 644: KPlus variations for δP_T .

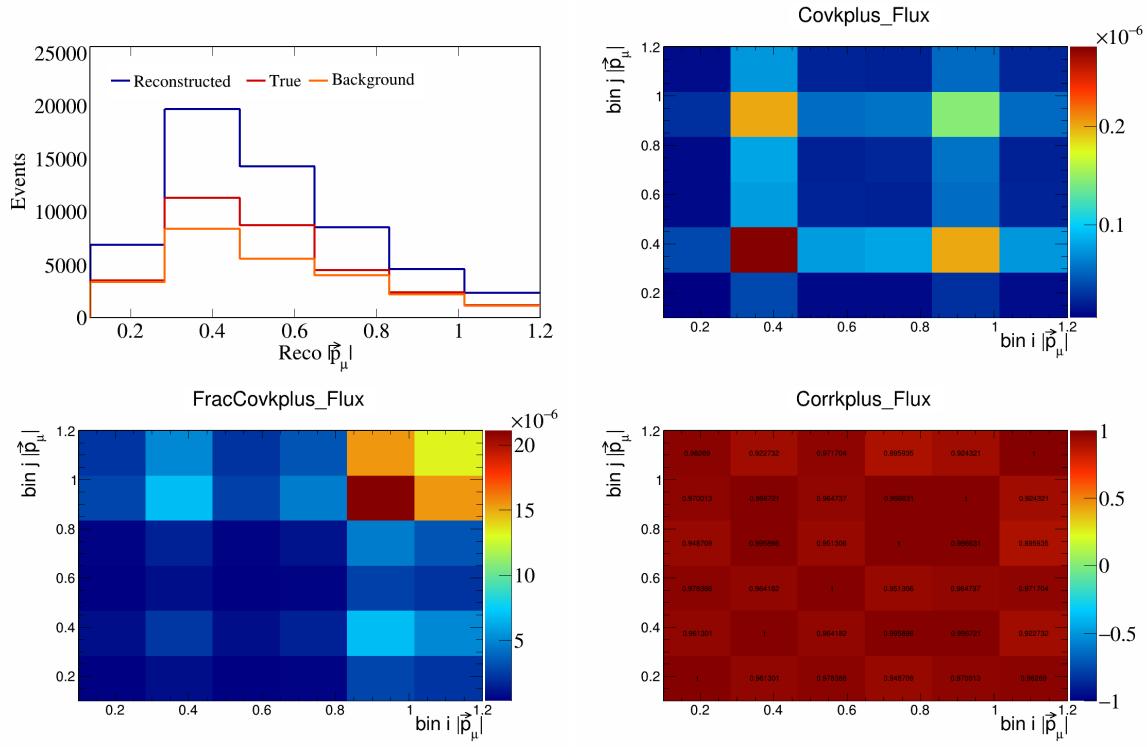


Figure 645: KPlus variations for $|\vec{p}_\mu|$.

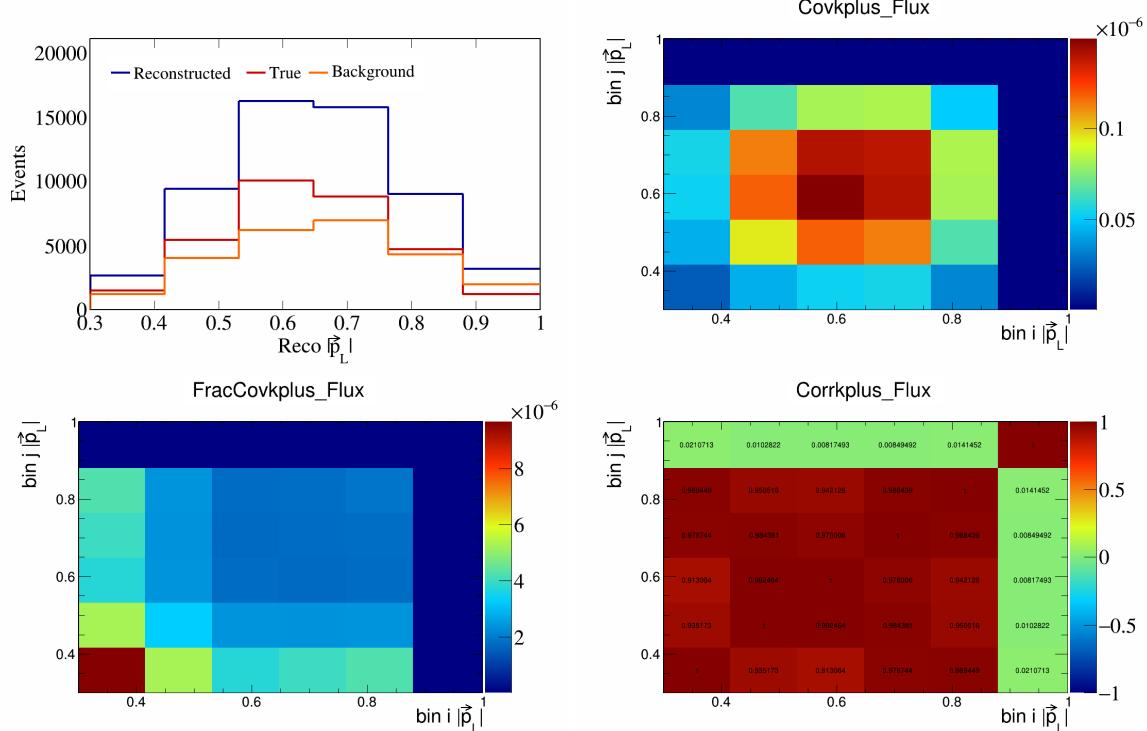


Figure 646: KPlus variations for $|\vec{p}_L|$.

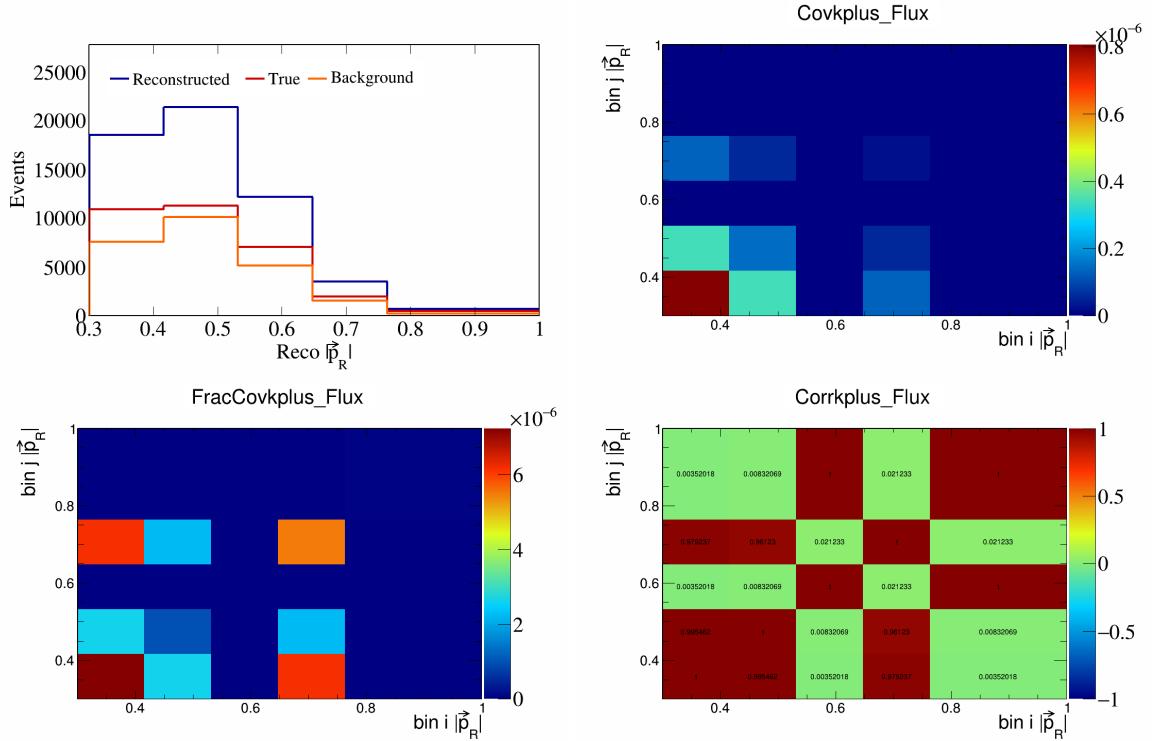


Figure 647: KPlus variations for $|\vec{p}_R|$.

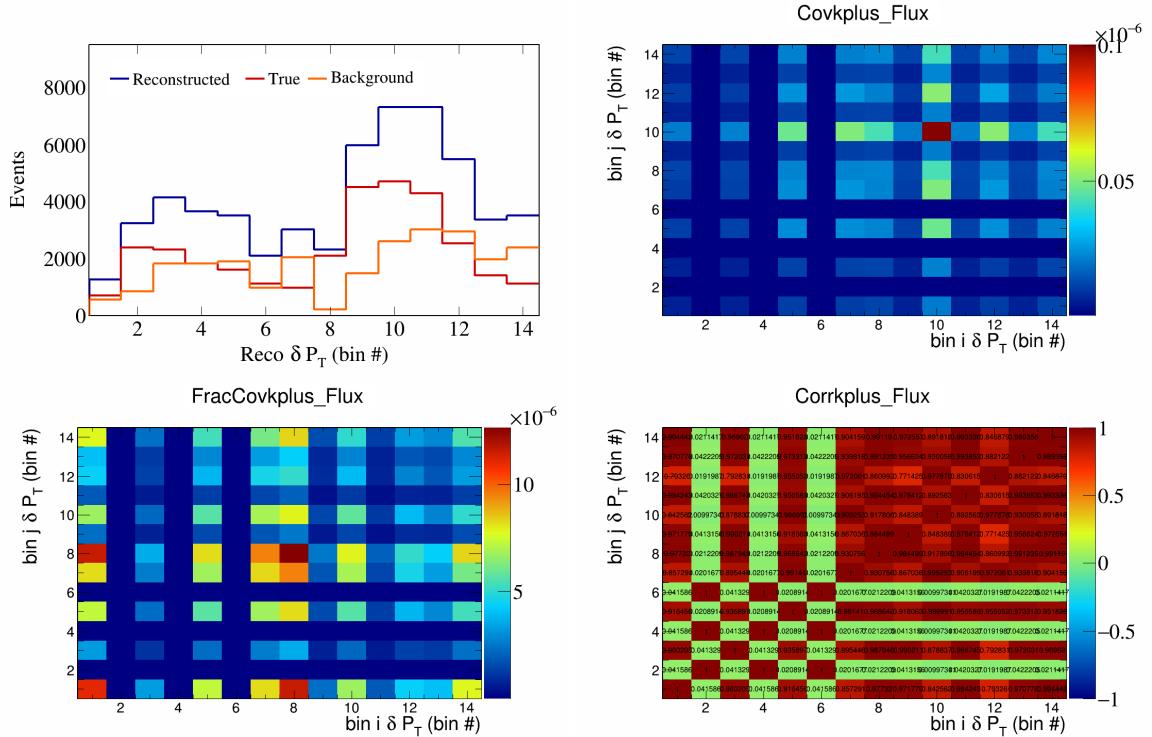


Figure 648: KPlus variations for δP_T in $\cos(\theta_{\vec{p}_\mu})$.

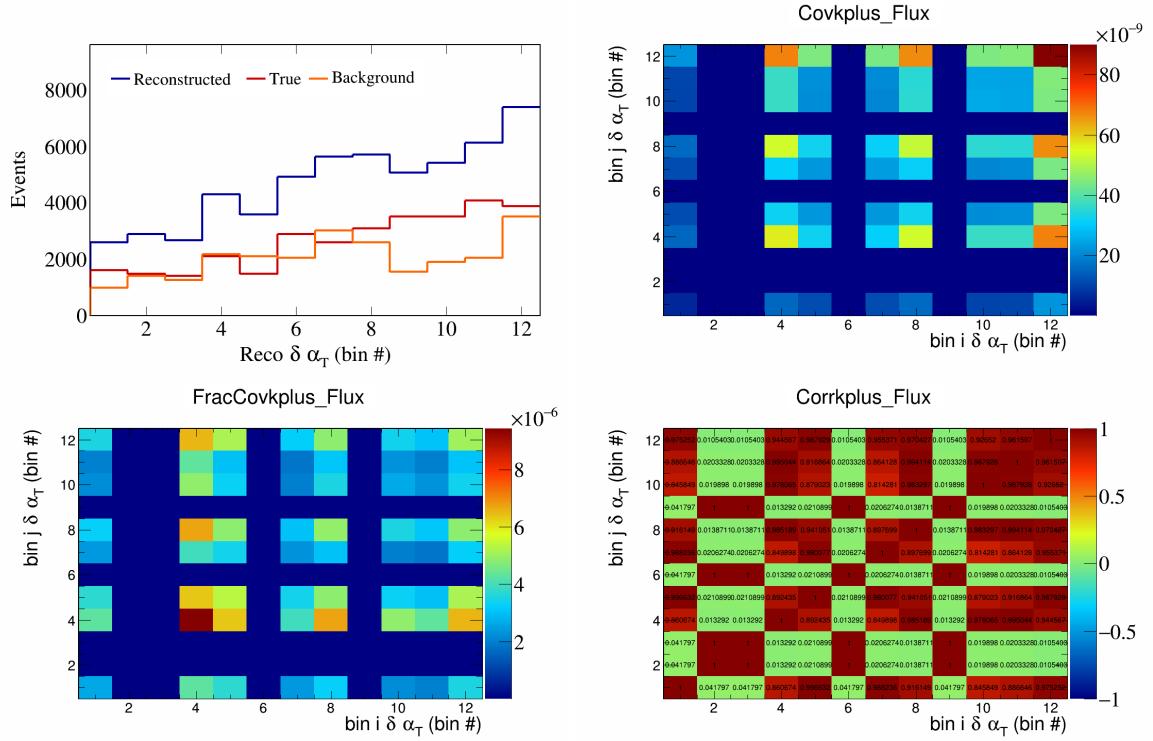


Figure 649: KPlus variations for $\delta\alpha_T$ in $\cos(\theta_{\vec{p}_\mu})$.

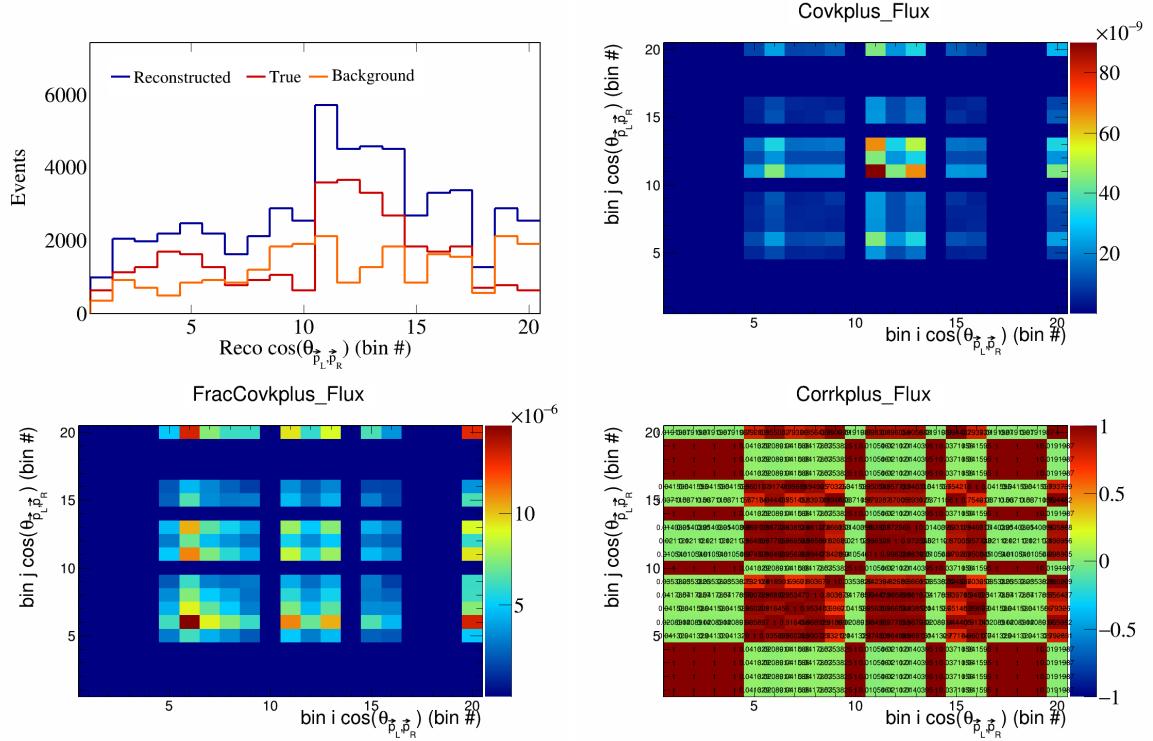


Figure 650: KPlus variations for $\cos(\theta_{p_L, p_R})$ in $\cos(\theta_{\vec{p}_\mu})$.

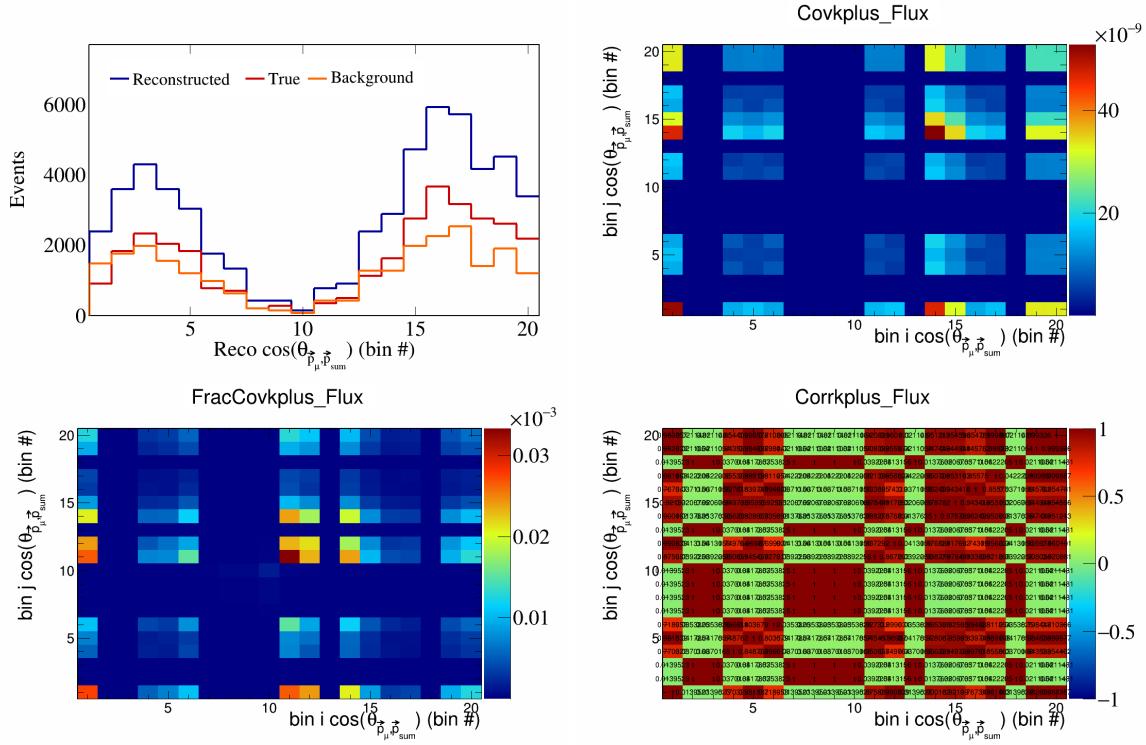


Figure 651: KPlus variations for $\cos(\theta_{\vec{p}_\mu, \vec{p}_{\text{sum}}})$ in $\cos(\theta_{\vec{p}_\mu})$.

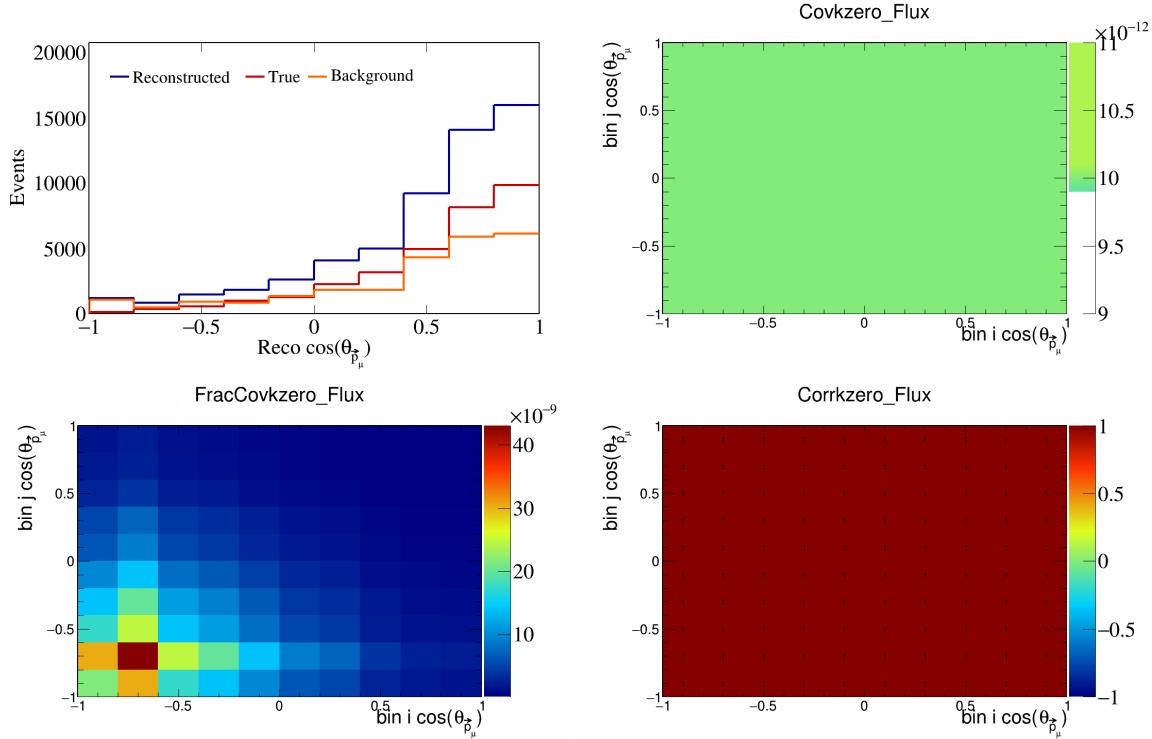


Figure 652: KZero variations for $\cos(\theta_{\vec{p}_\mu, \vec{p}_{\text{sum}}})$ in $\cos(\theta_{\vec{p}_\mu})$.

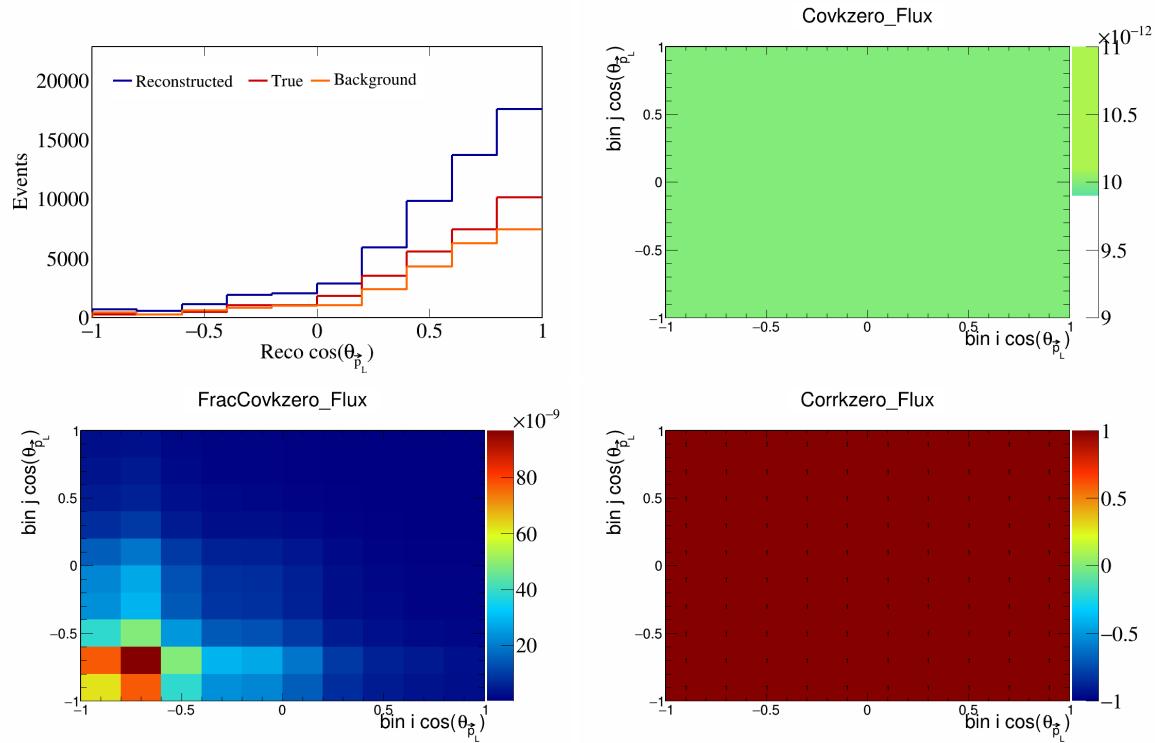


Figure 653: KZero variations for $\cos(\theta_{\vec{p}_L})$.

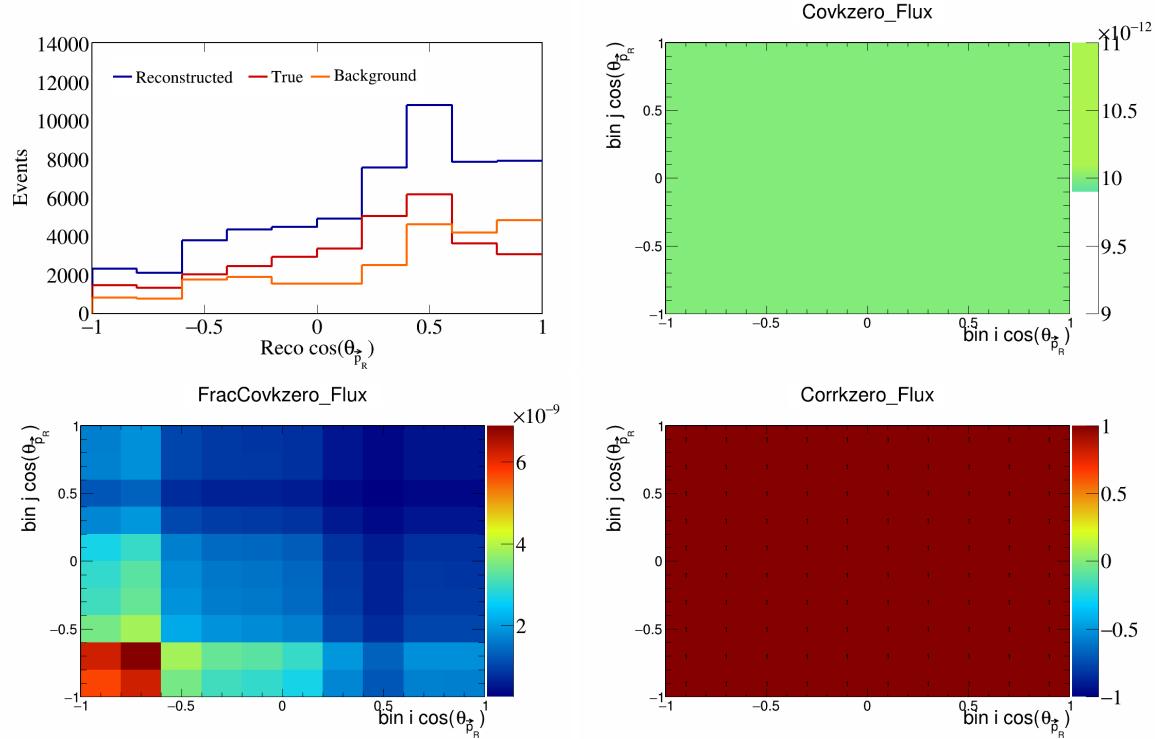


Figure 654: KZero variations for $\cos(\theta_{\vec{p}_R})$.

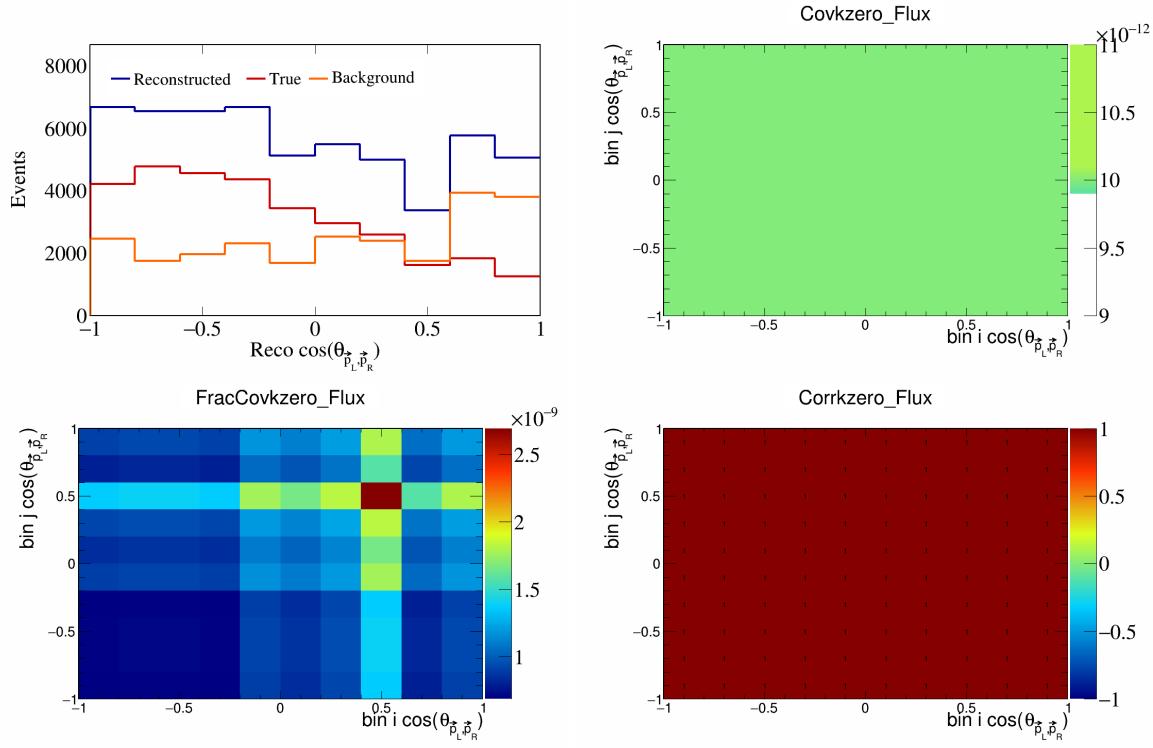


Figure 655: KZero variations for $\cos(\theta_{\vec{p}_L, \vec{p}_R})$.

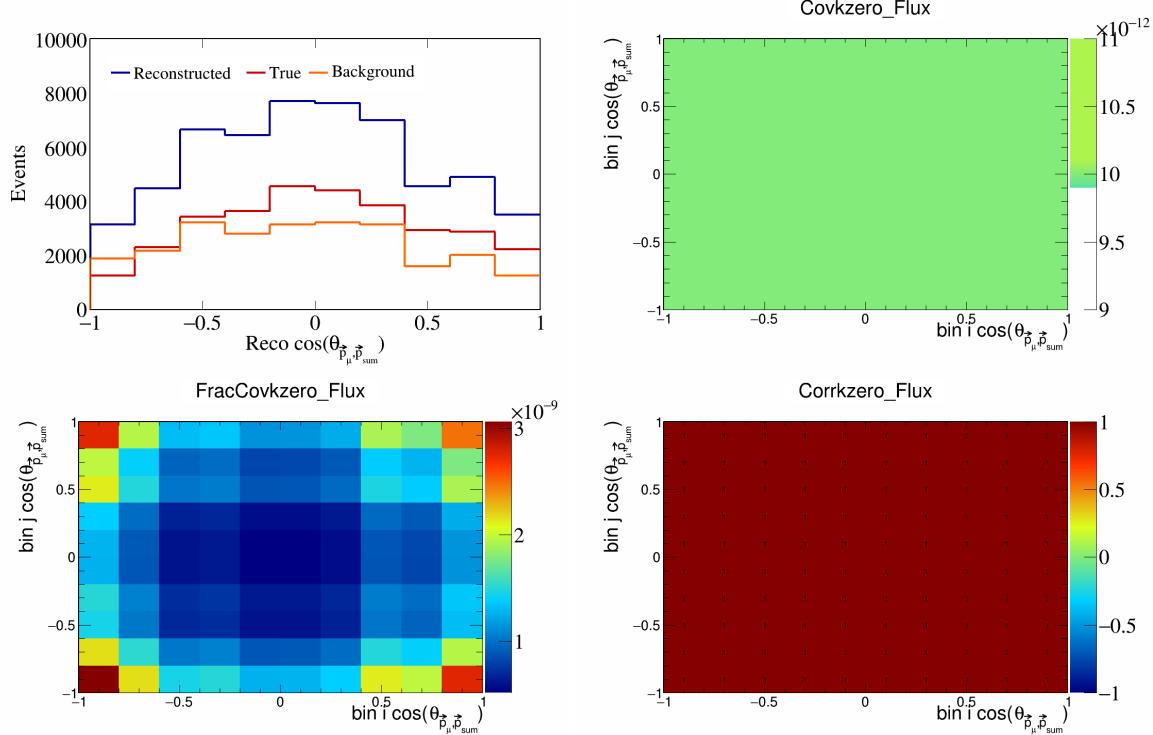


Figure 656: KZero variations for $\cos(\theta_{\vec{p}_\mu, \vec{p}_{\text{sum}}})$.

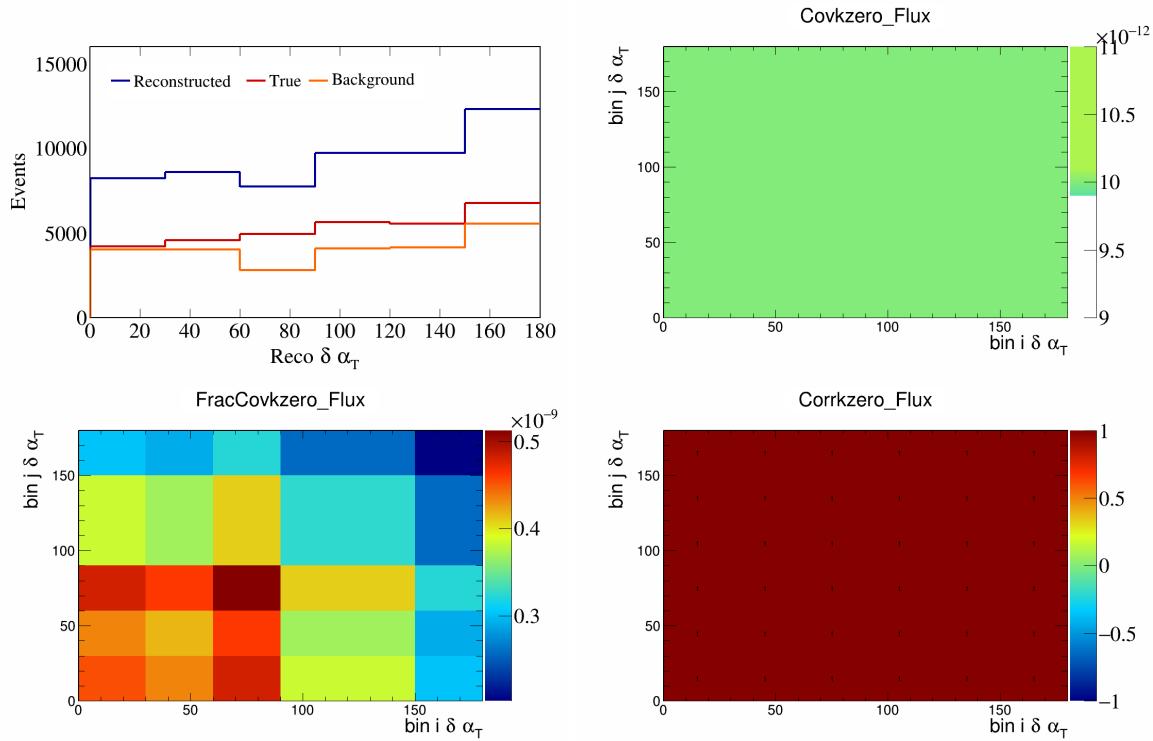


Figure 657: KZero variations for $\delta\alpha_T$.

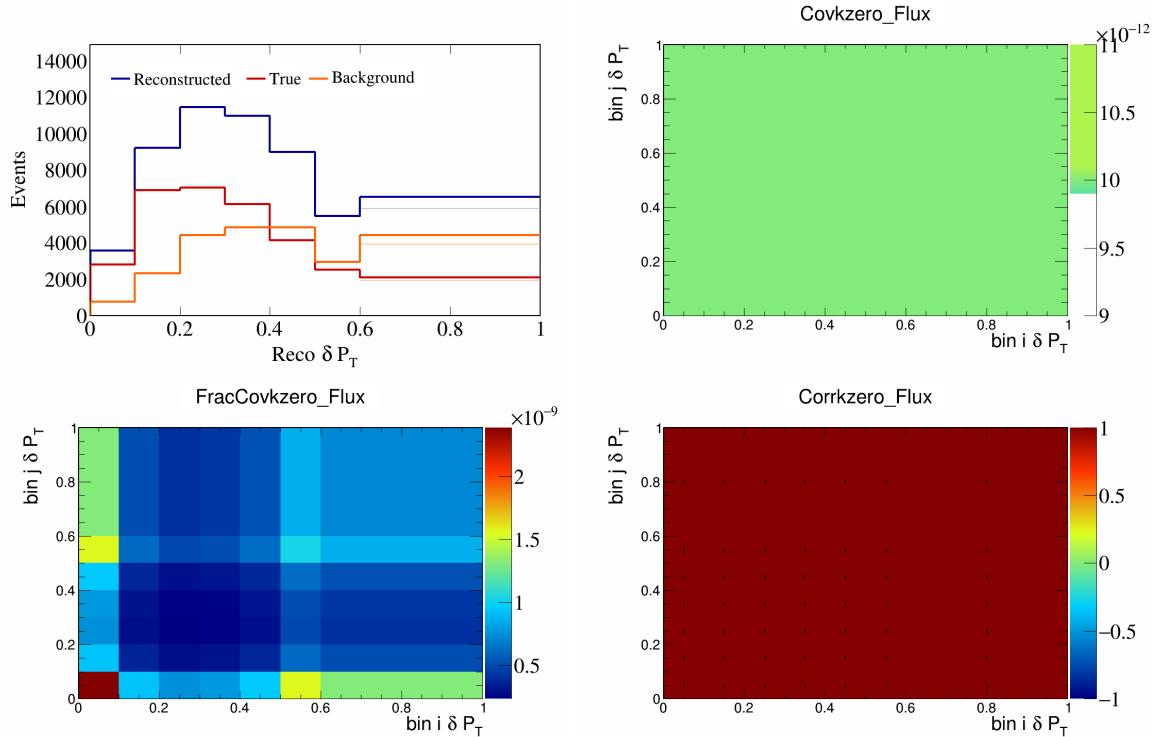


Figure 658: KZero variations for δP_T .

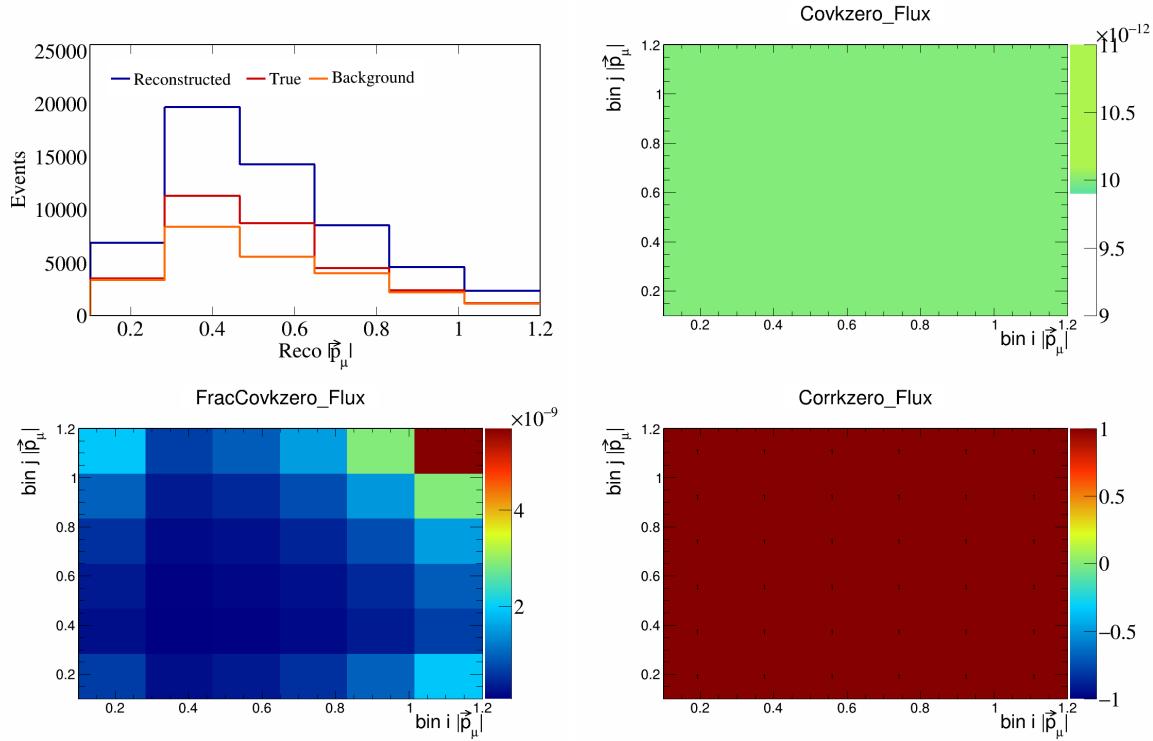


Figure 659: KZero variations for $|\vec{p}_\mu|$.

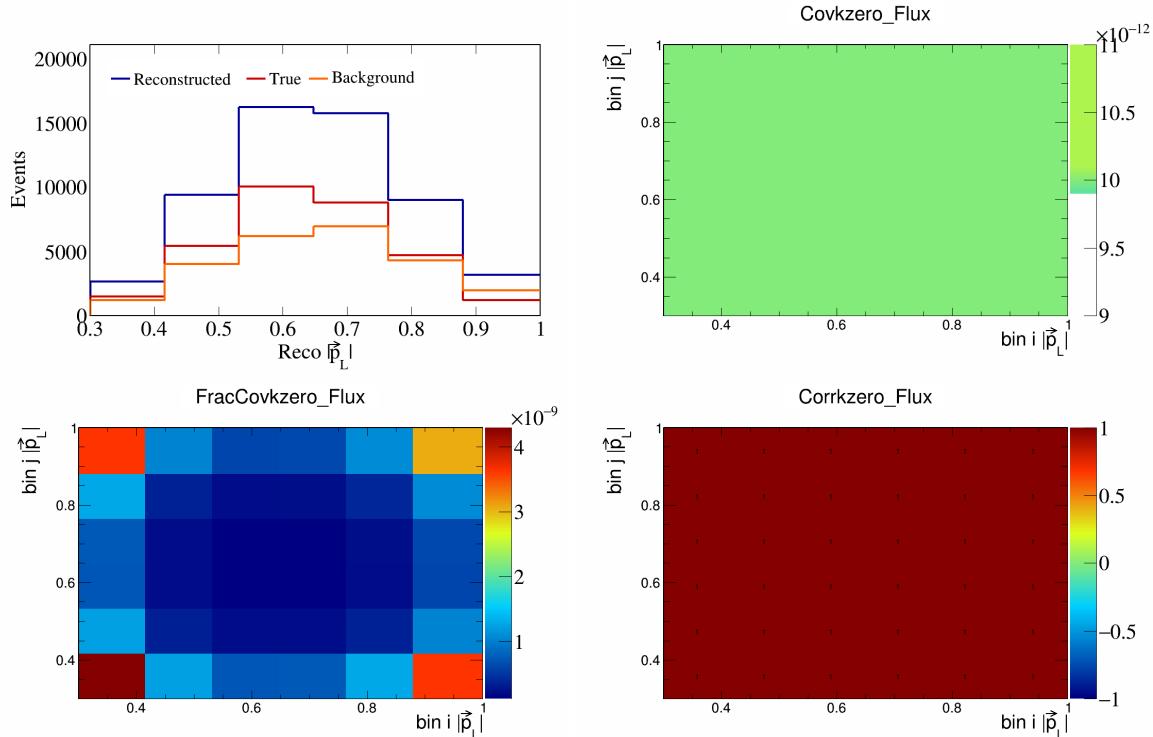


Figure 660: KZero variations for $|\vec{p}_L|$.

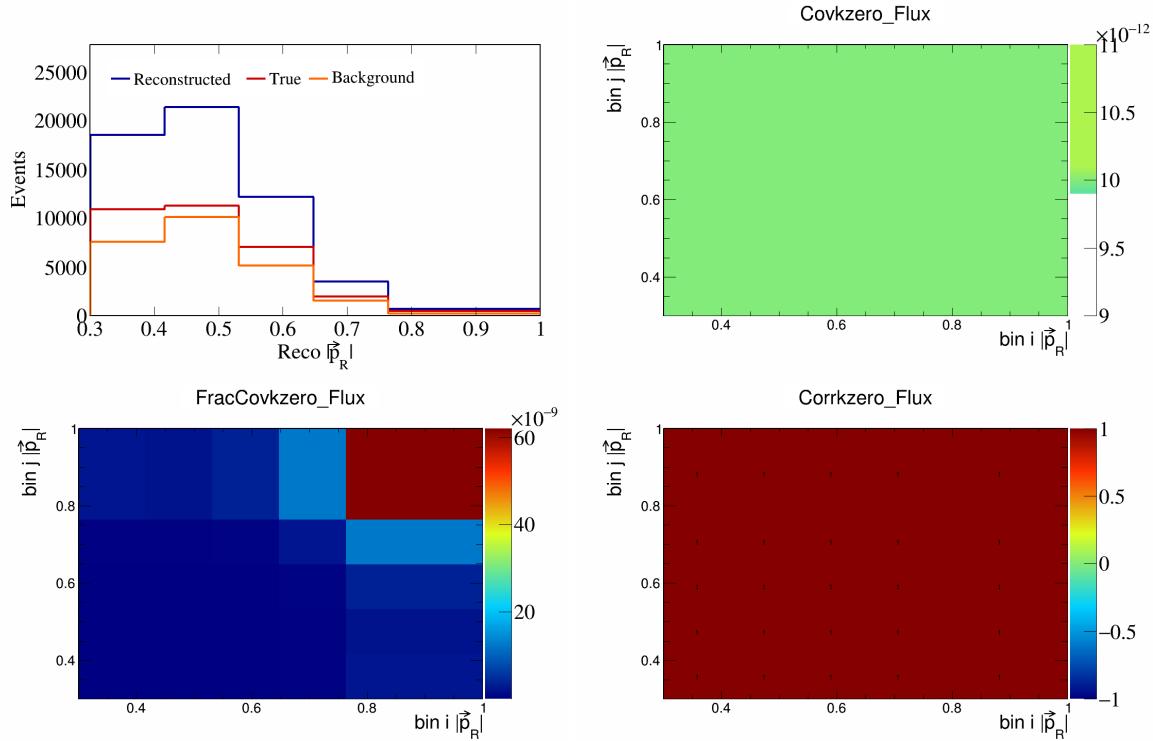


Figure 661: KZero variations for $|\vec{p}_R|$.

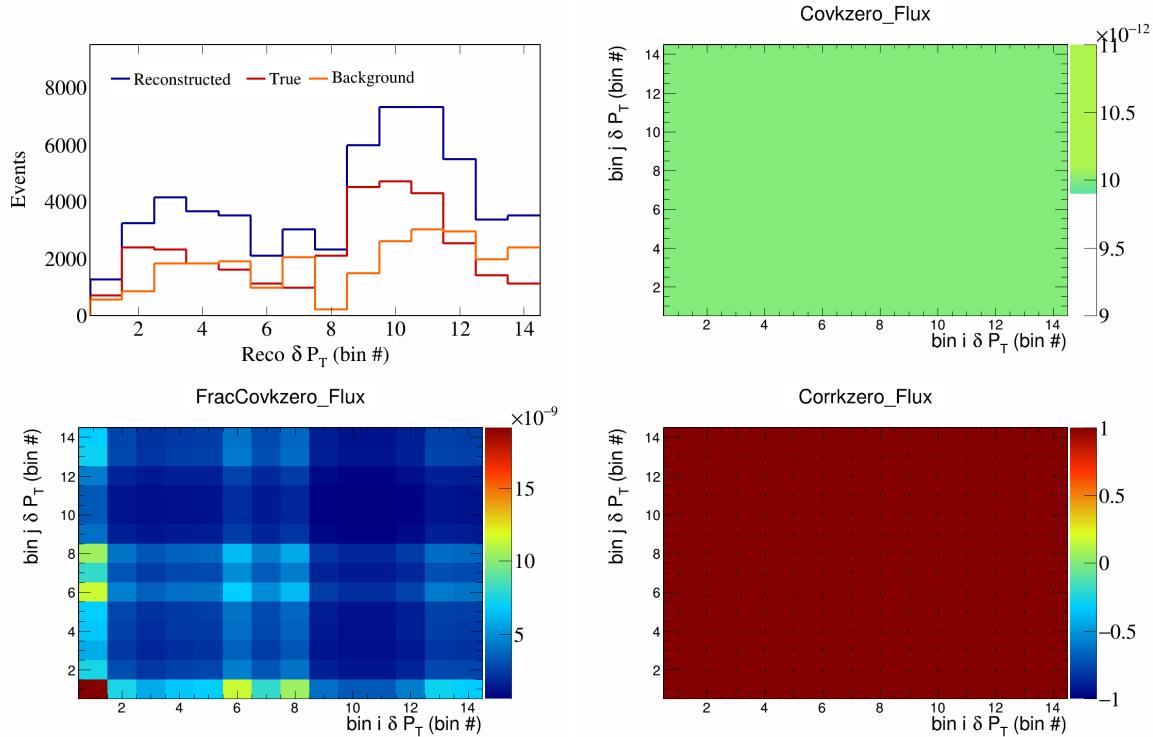


Figure 662: KZero variations for δP_T in $\cos(\theta_{\vec{p}_\mu})$.

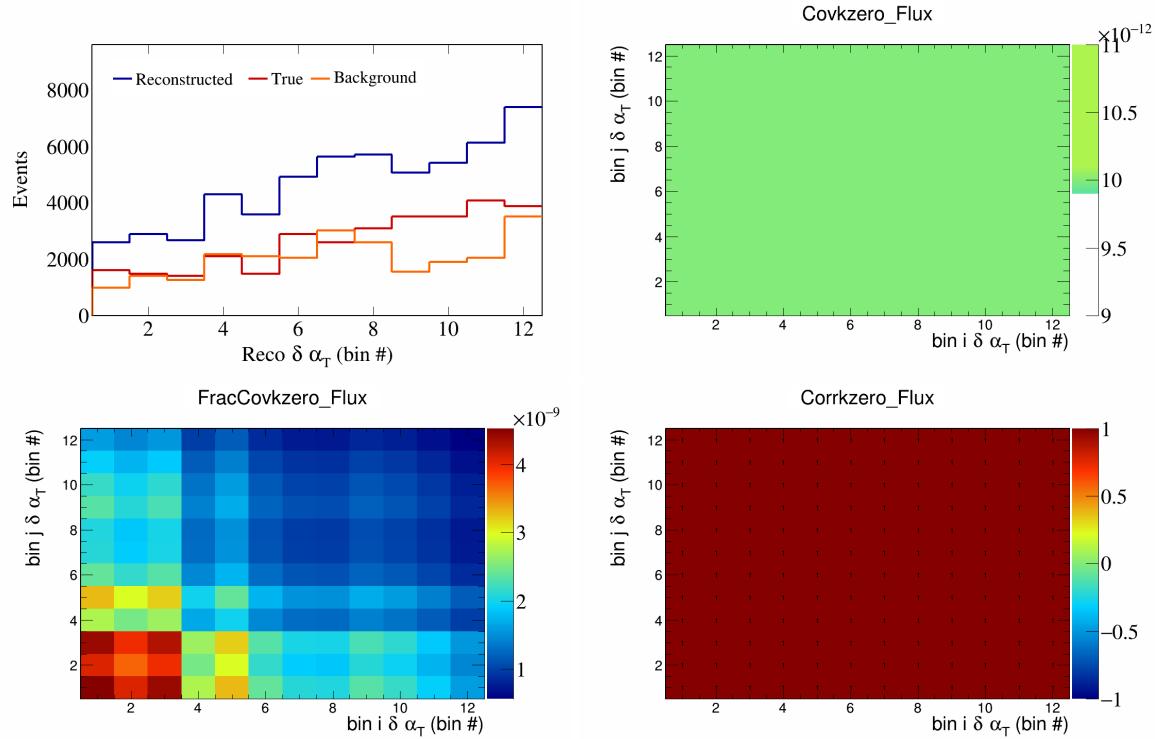


Figure 663: KZero variations for $\delta\alpha_T$ in $\cos(\theta_{\vec{p}_\mu})$.

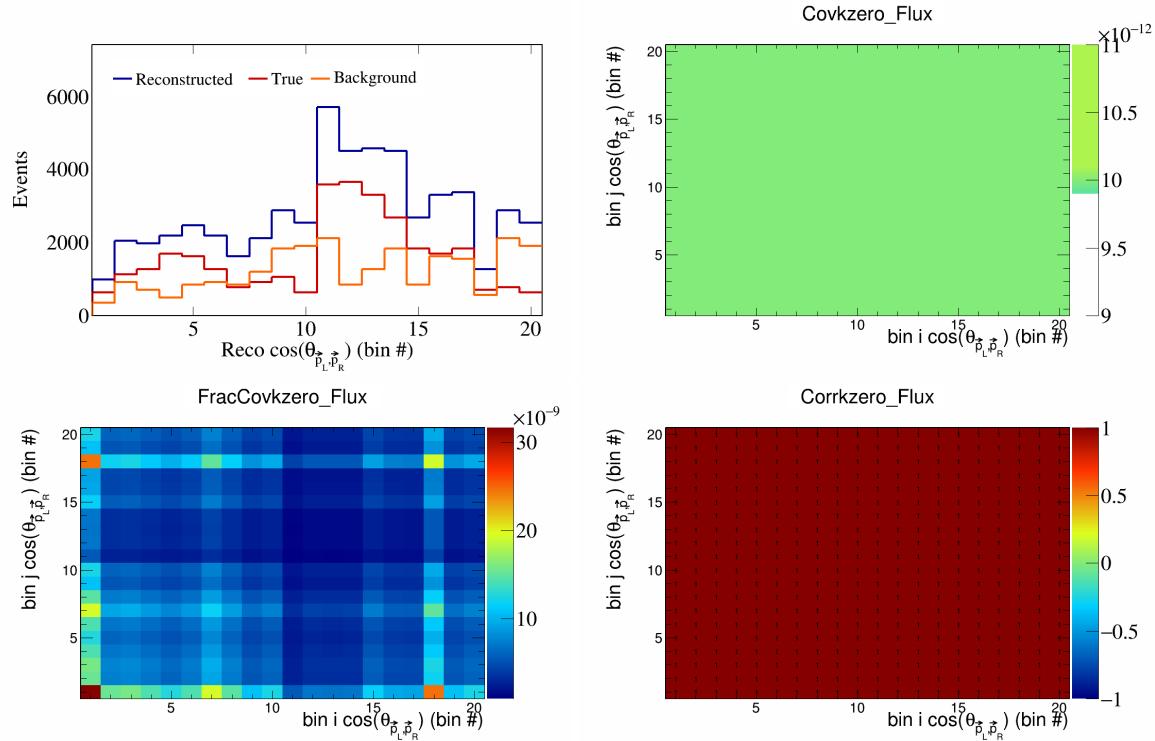


Figure 664: KZero variations for $\cos(\theta_{\vec{p}_L, \vec{p}_R})$ in $\cos(\theta_{\vec{p}_\mu})$.

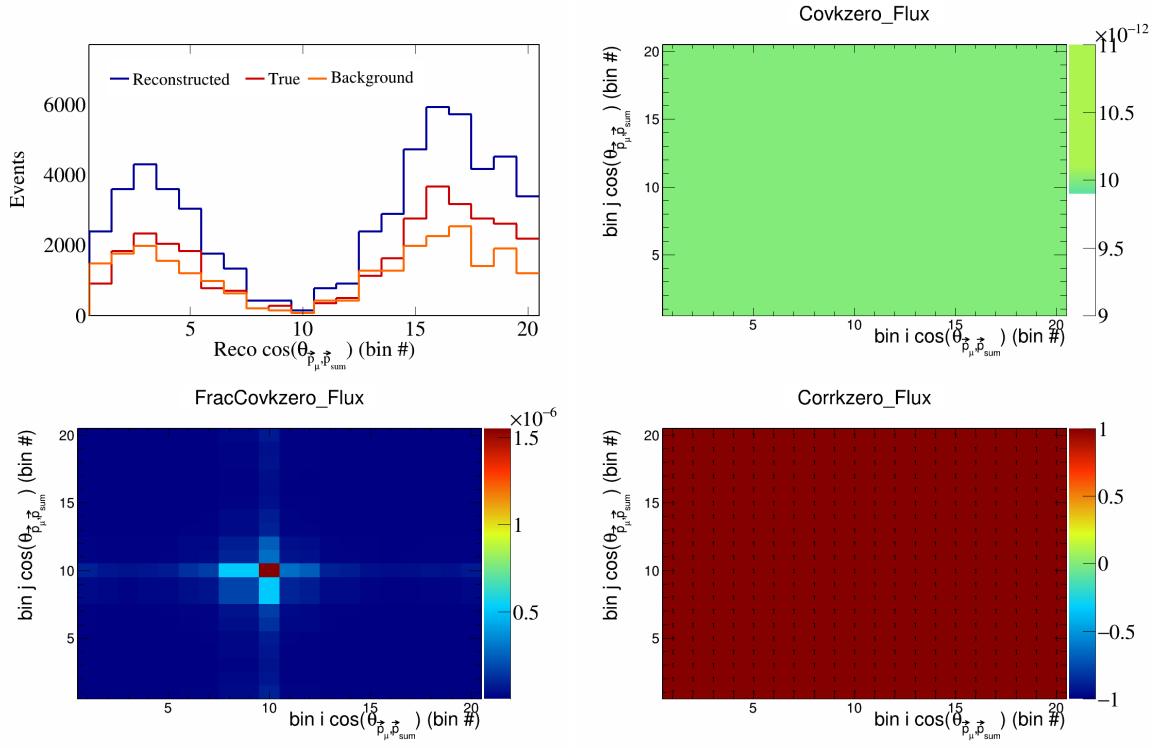


Figure 665: KZero variations for $\cos(\theta_{\vec{p}_\mu, \vec{p}_{\text{sum}}})$ in $\cos(\theta_{\vec{p}_\mu})$.

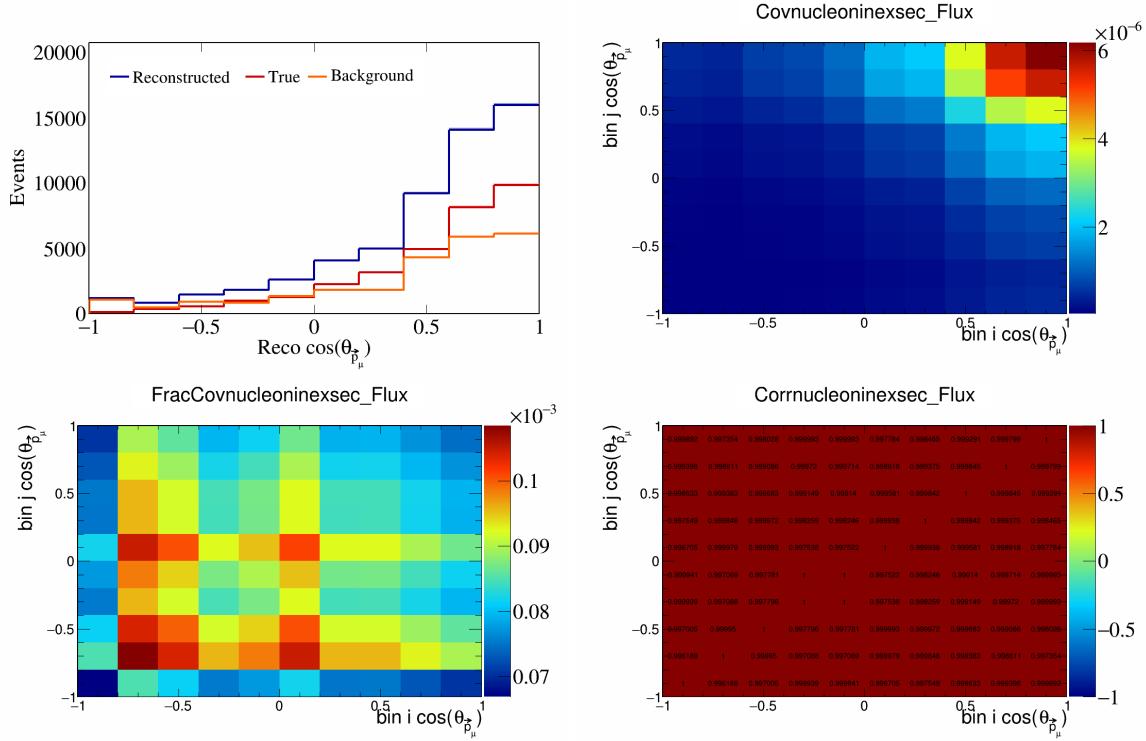


Figure 666: NucleonIneXSec variations for $\cos(\theta_{\vec{p}_\mu})$.

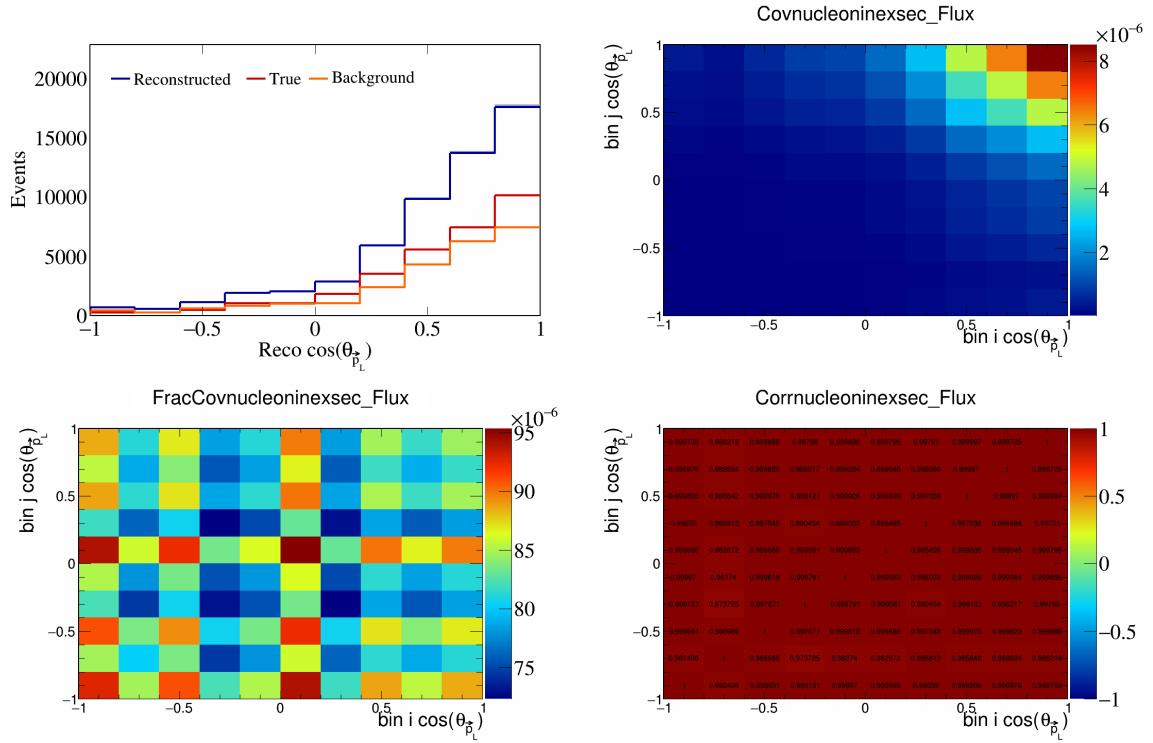


Figure 667: NucleonIneXSec variations for $\cos(\theta_{\vec{p}_L})$.

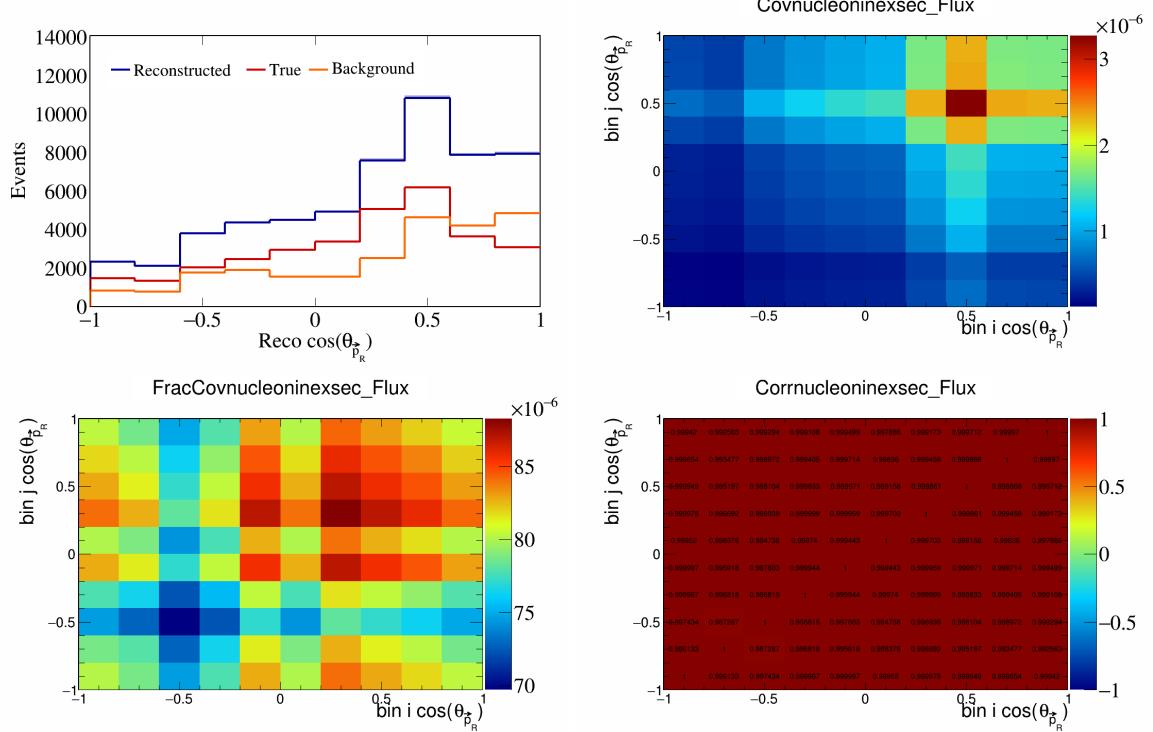


Figure 668: NucleonIneXSec variations for $\cos(\theta_{\vec{p}_R})$.

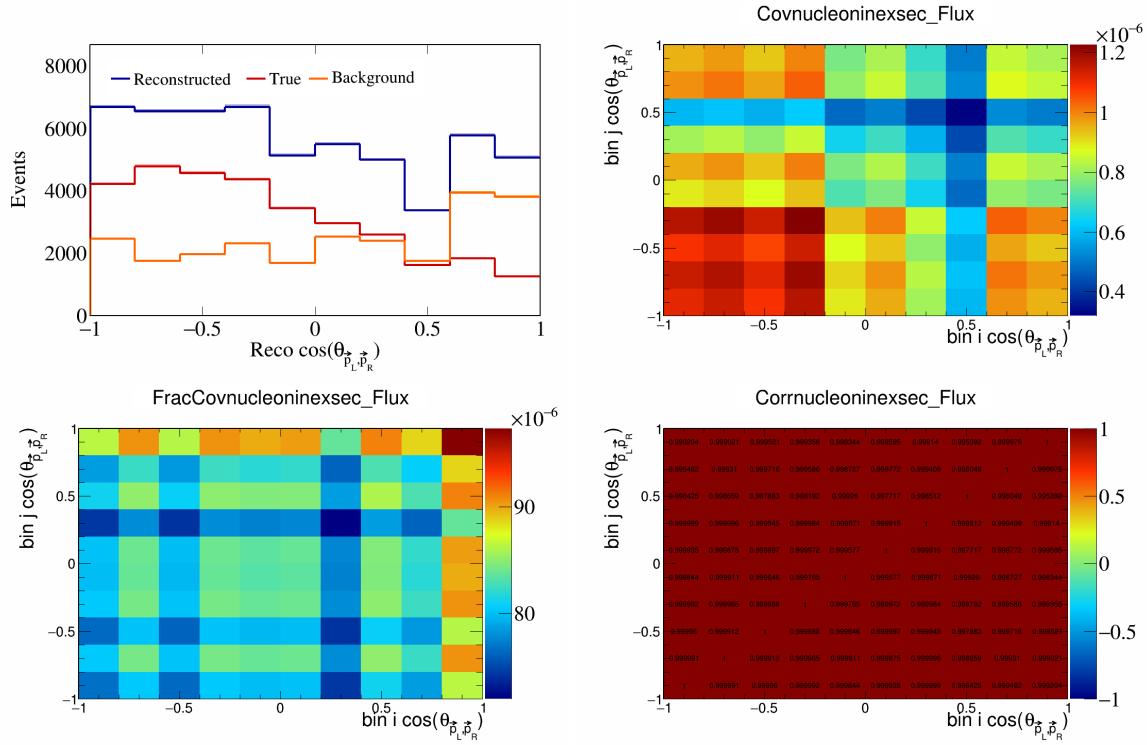


Figure 669: NucleonIneXSec variations for $\cos(\theta_{\vec{p}_L, \vec{p}_R})$.

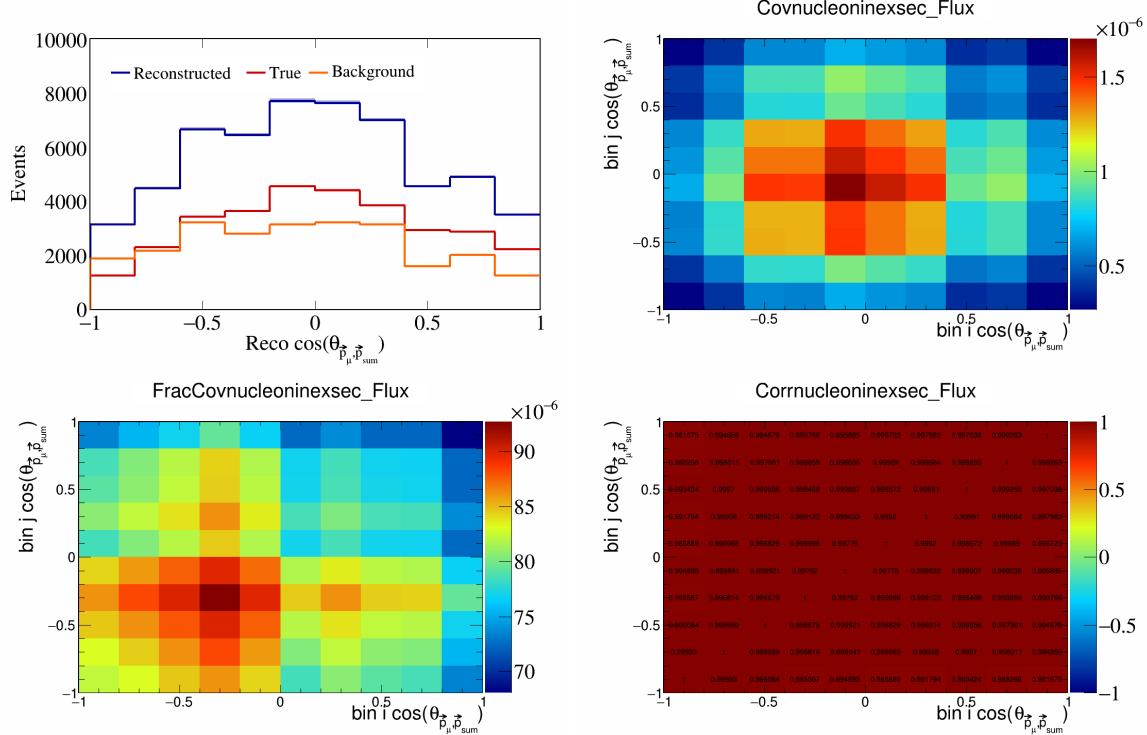


Figure 670: NucleonIneXSec variations for $\cos(\theta_{\vec{p}_\mu, \vec{p}_{\text{sum}}})$.

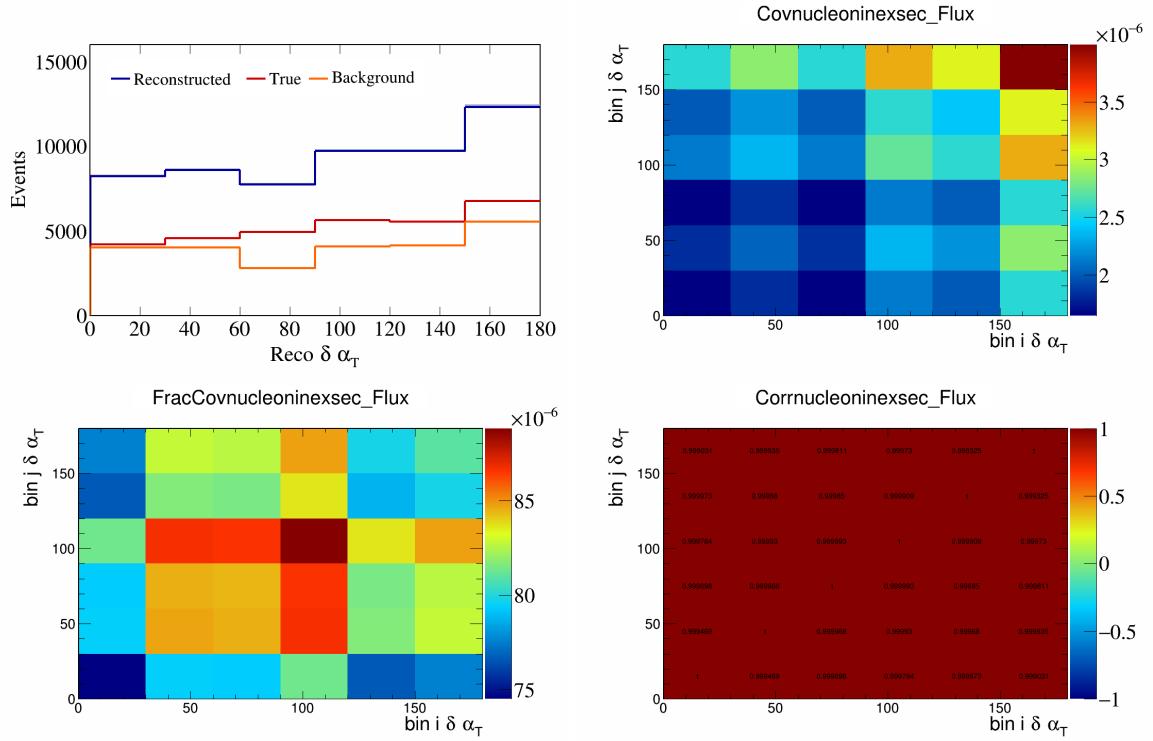


Figure 671: NucleonIneXSec variations for $\delta \alpha_T$.

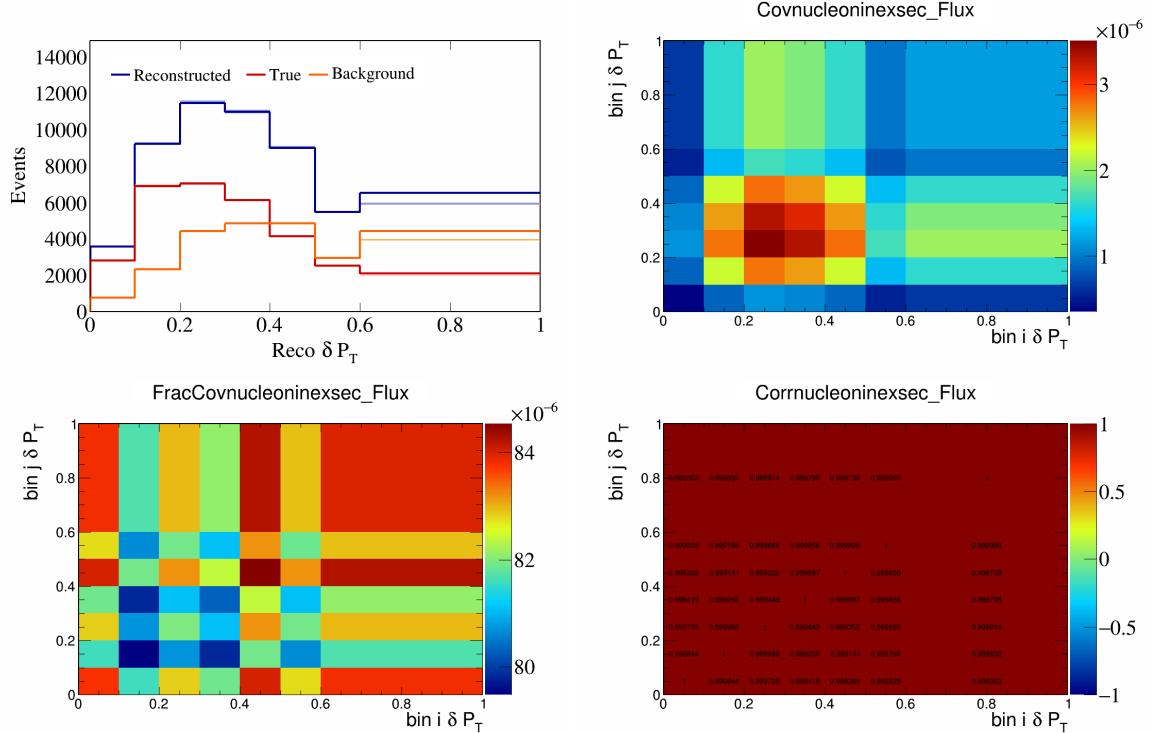


Figure 672: NucleonIneXSec variations for δP_T .

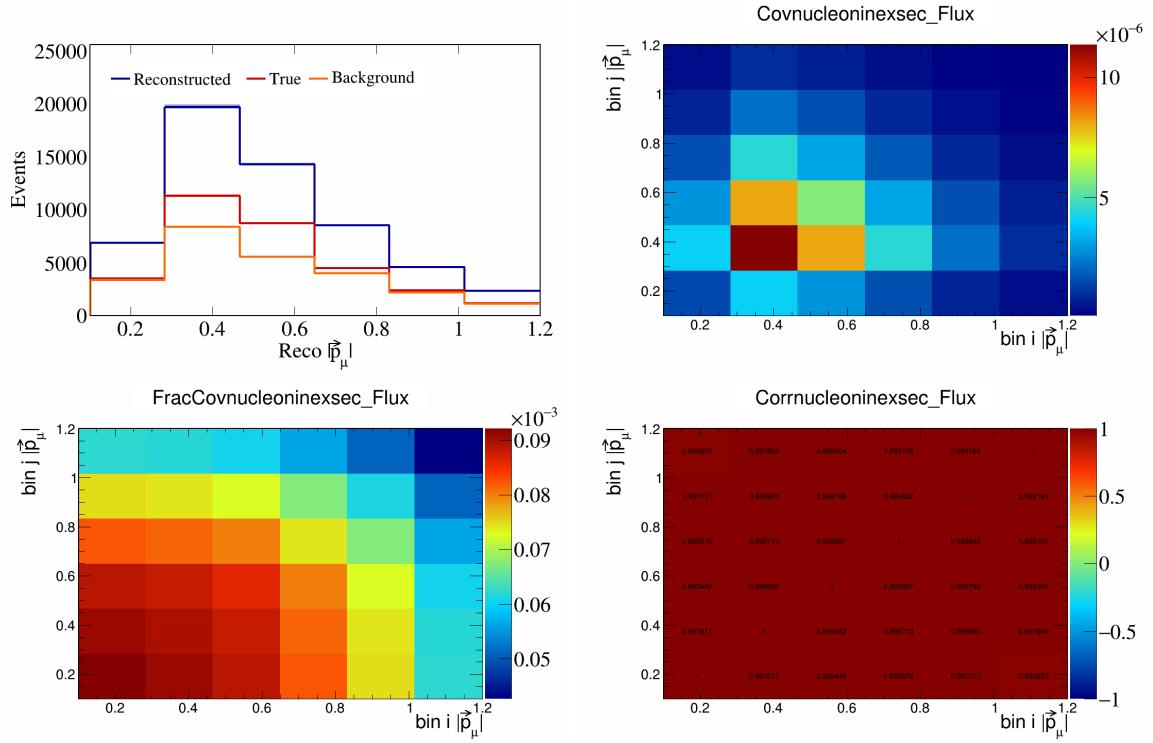


Figure 673: NucleonIneXSec variations for $|\vec{p}_\mu|$.

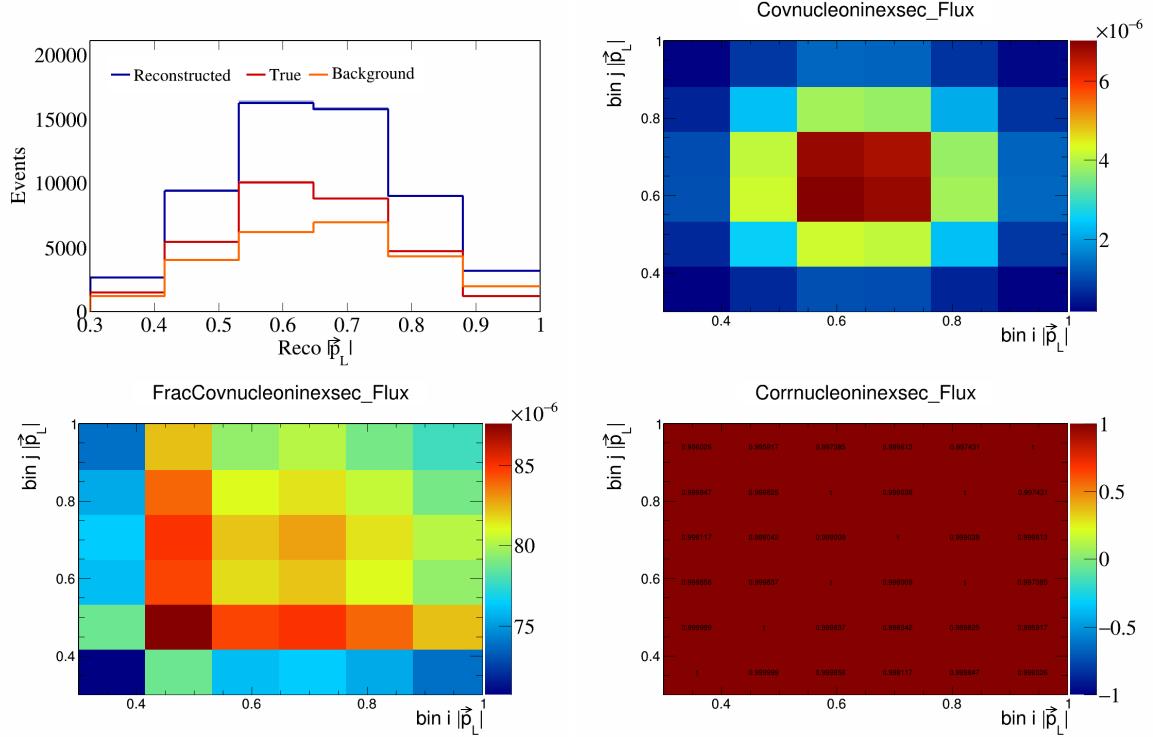


Figure 674: NucleonIneXSec variations for $|\vec{p}_L|$.

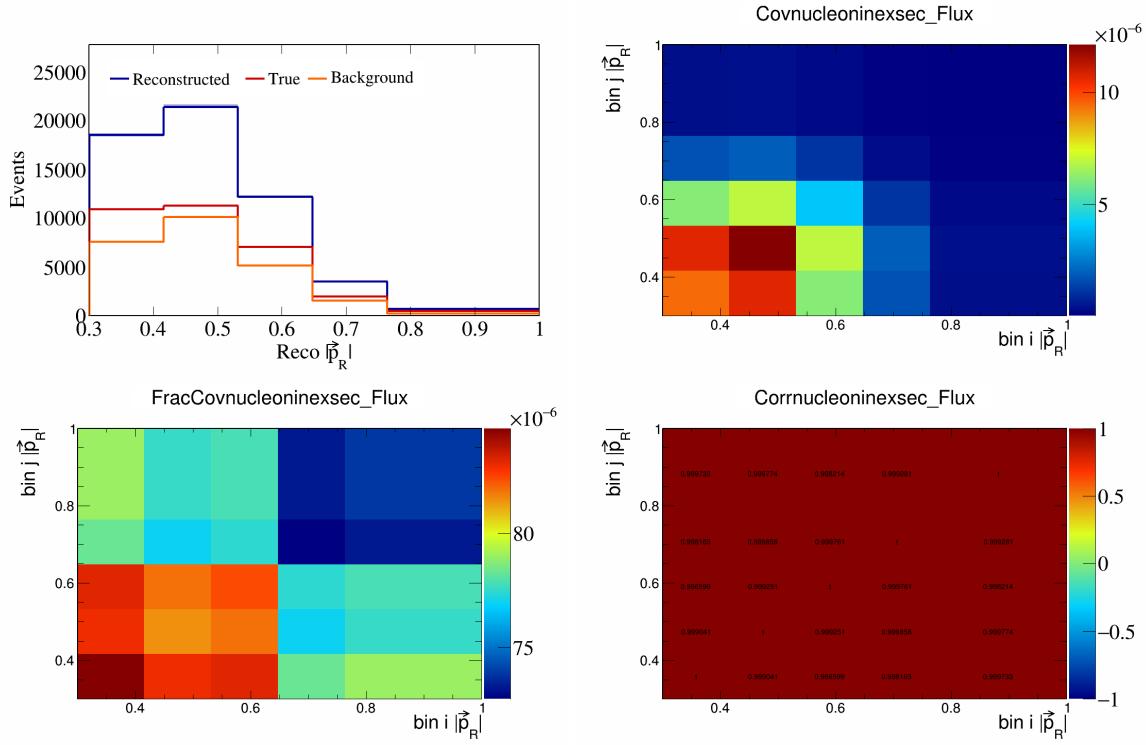


Figure 675: NucleonIneXSec variations for $|\vec{p}_R|$.

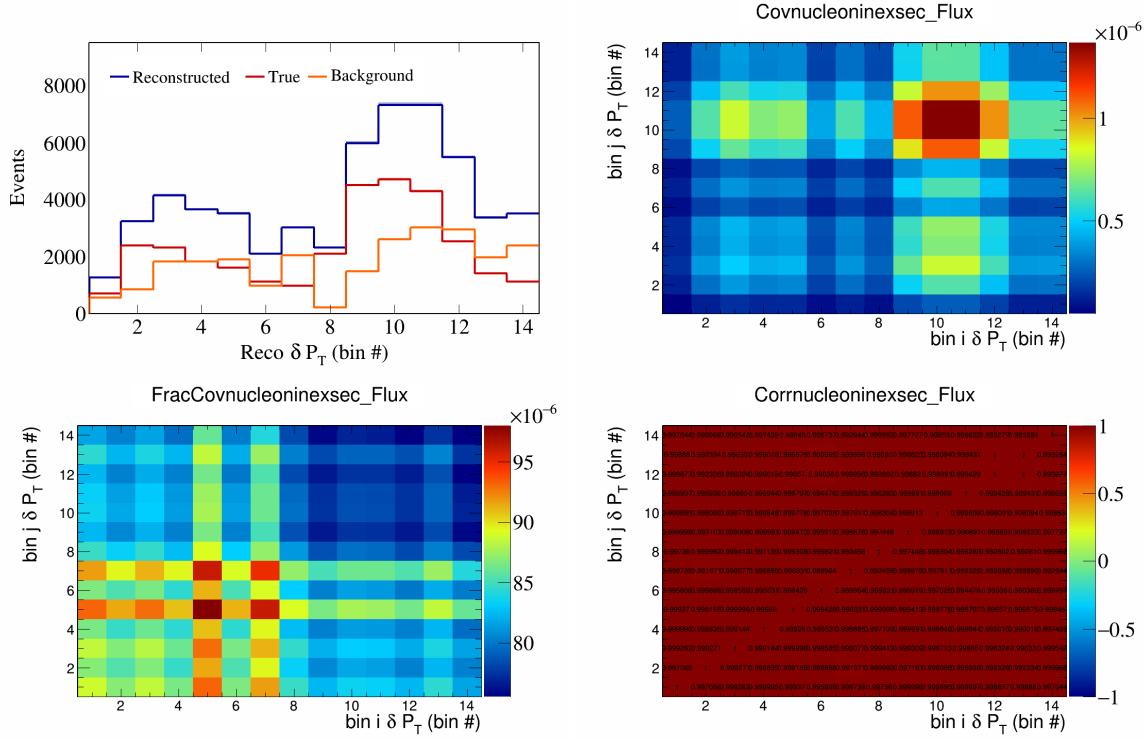


Figure 676: NucleonIneXSec variations for δP_T in $\cos(\theta_{\vec{P}})$.

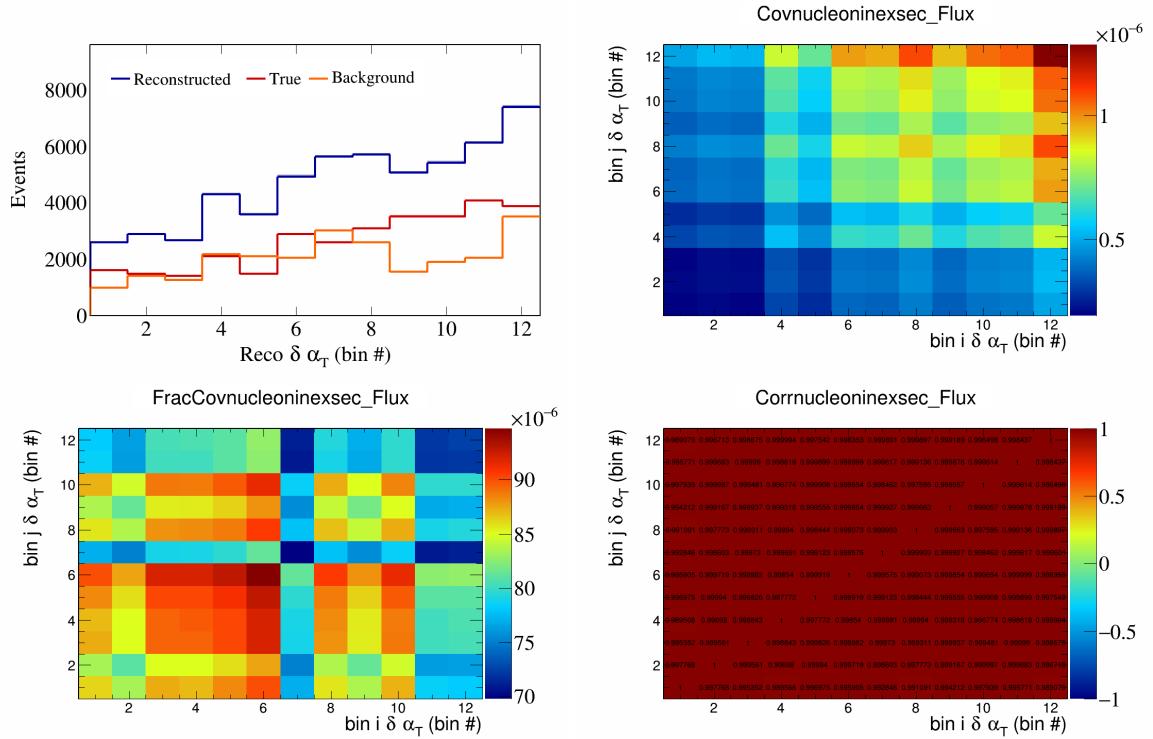


Figure 677: NucleonIneXSec variations for $\delta\alpha_T$ in $\cos(\theta_{\vec{p}_\mu})$.

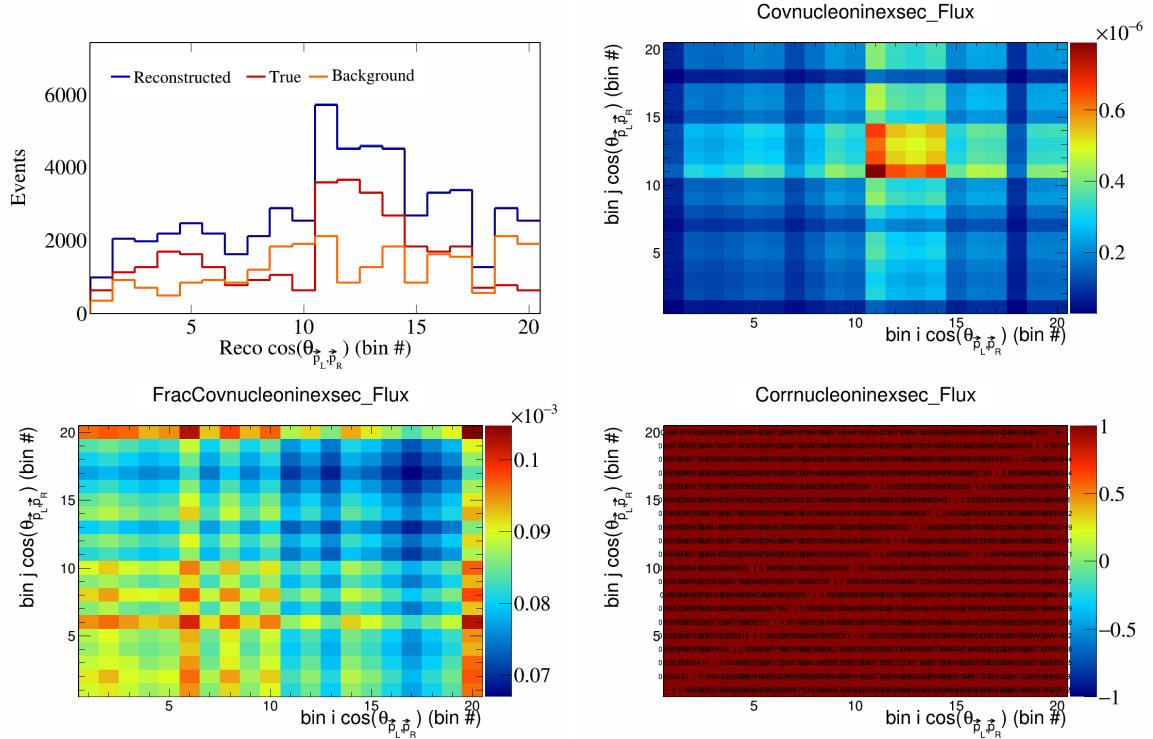


Figure 678: NucleonIneXSec variations for $\cos(\theta_{\vec{p}_L, \vec{p}_R})$ in $\cos(\theta_{\vec{p}_\mu})$.

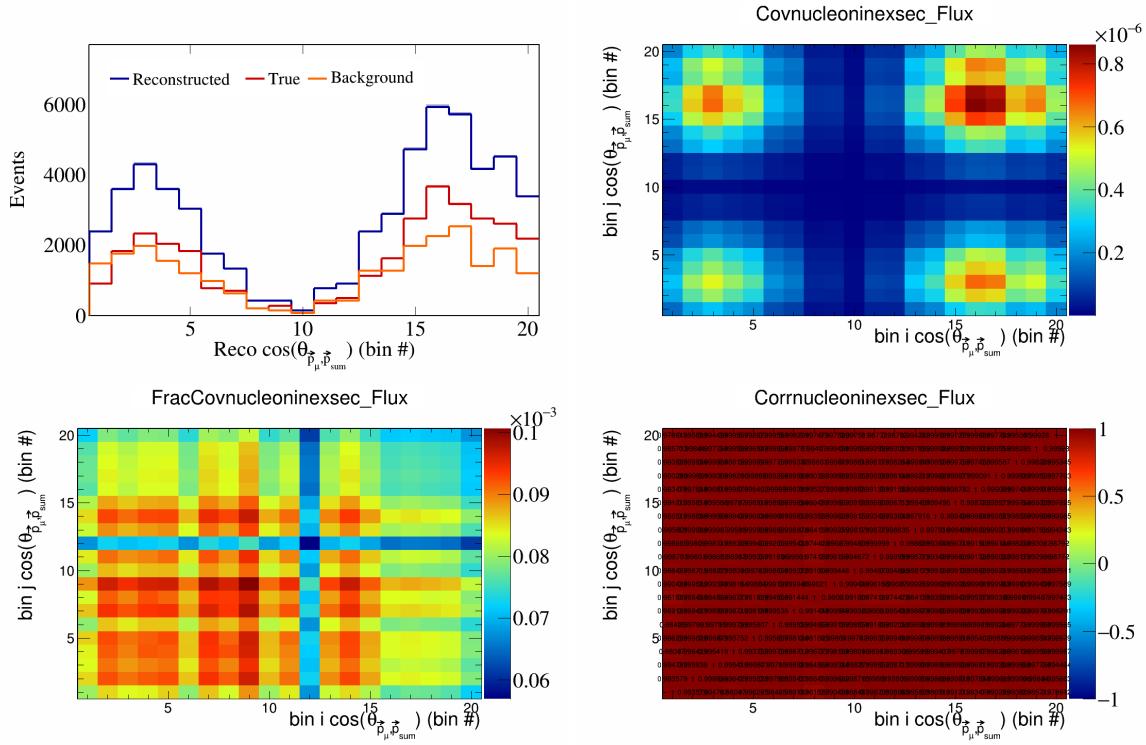


Figure 679: NucleonIneXSec variations for $\cos(\theta_{\vec{p}_\mu, \vec{p}_{\text{sum}}})$ in $\cos(\theta_{\vec{p}_\mu})$.

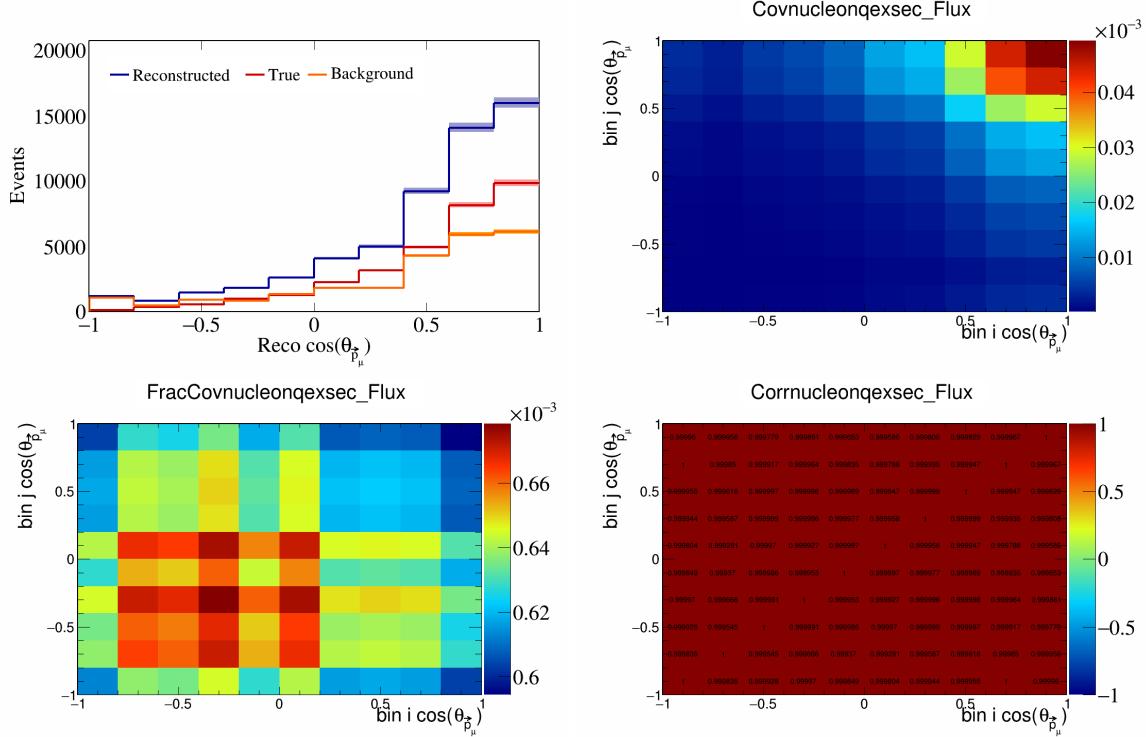


Figure 680: NucleonQeXSec variations for $\cos(\theta_{\vec{p}_\mu})$.

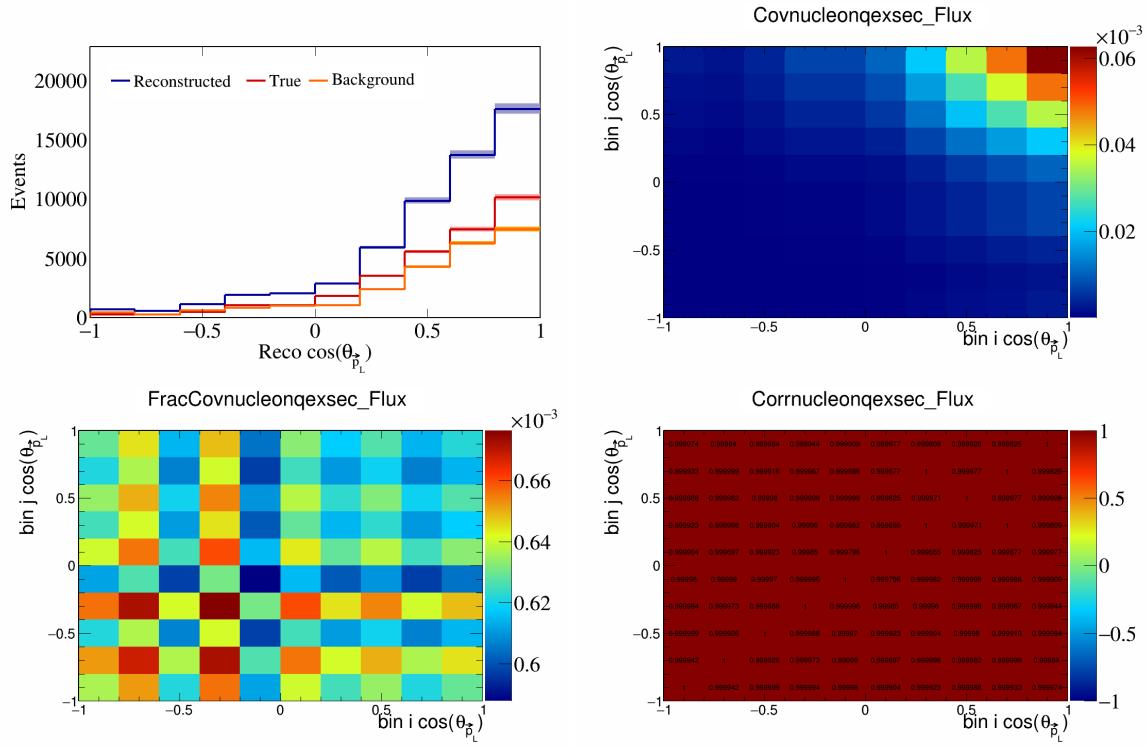


Figure 681: NucleonQeXSec variations for $\cos(\theta_{\vec{p}_L})$.

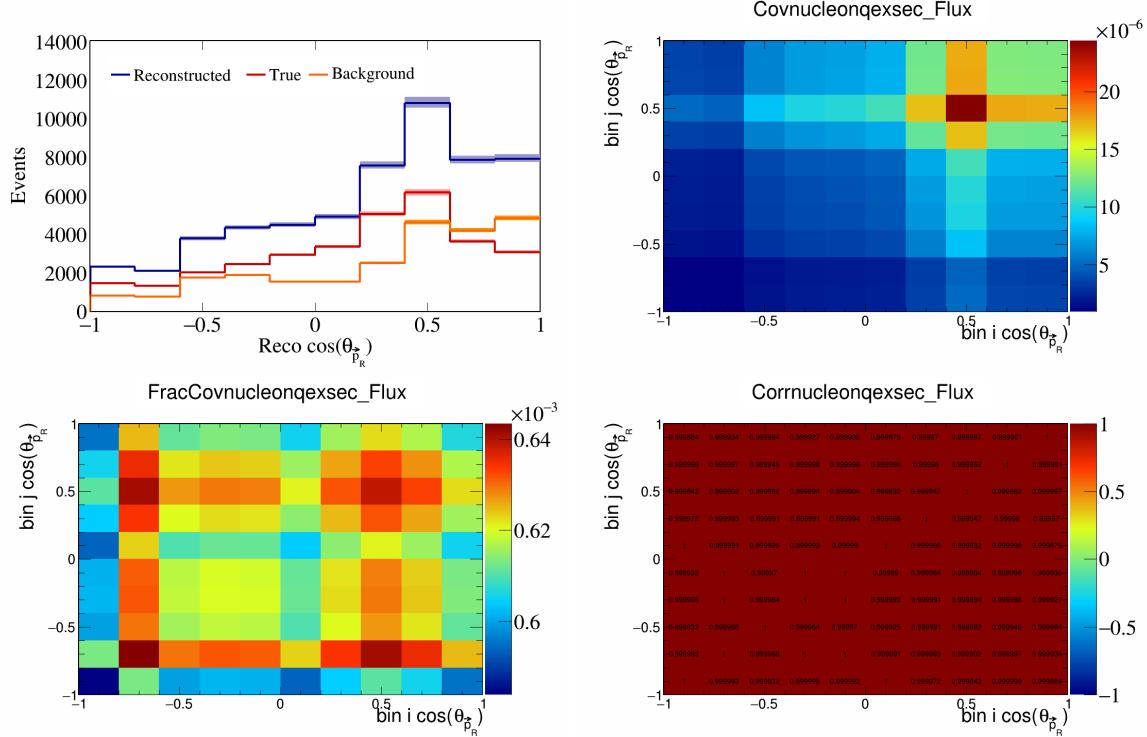


Figure 682: NucleonQeXSec variations for $\cos(\theta_{\vec{p}_R})$.

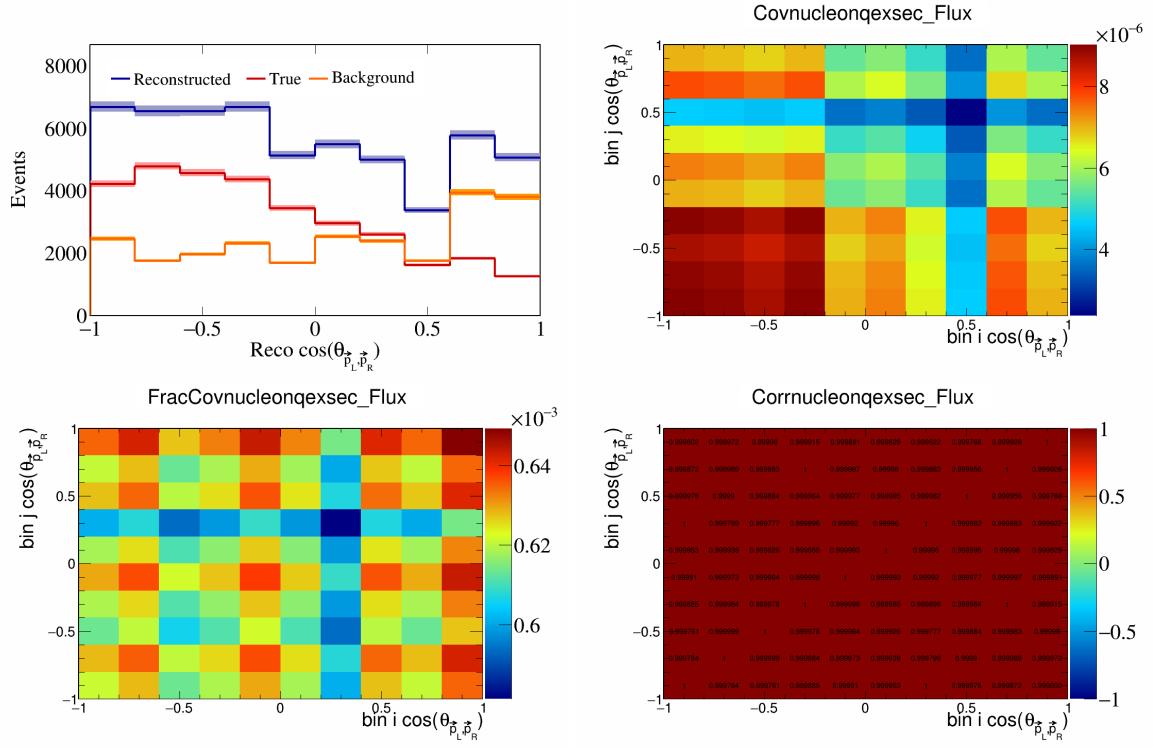


Figure 683: NucleonQeXSec variations for $\cos(\theta_{\vec{p}_L, \vec{p}_R})$.

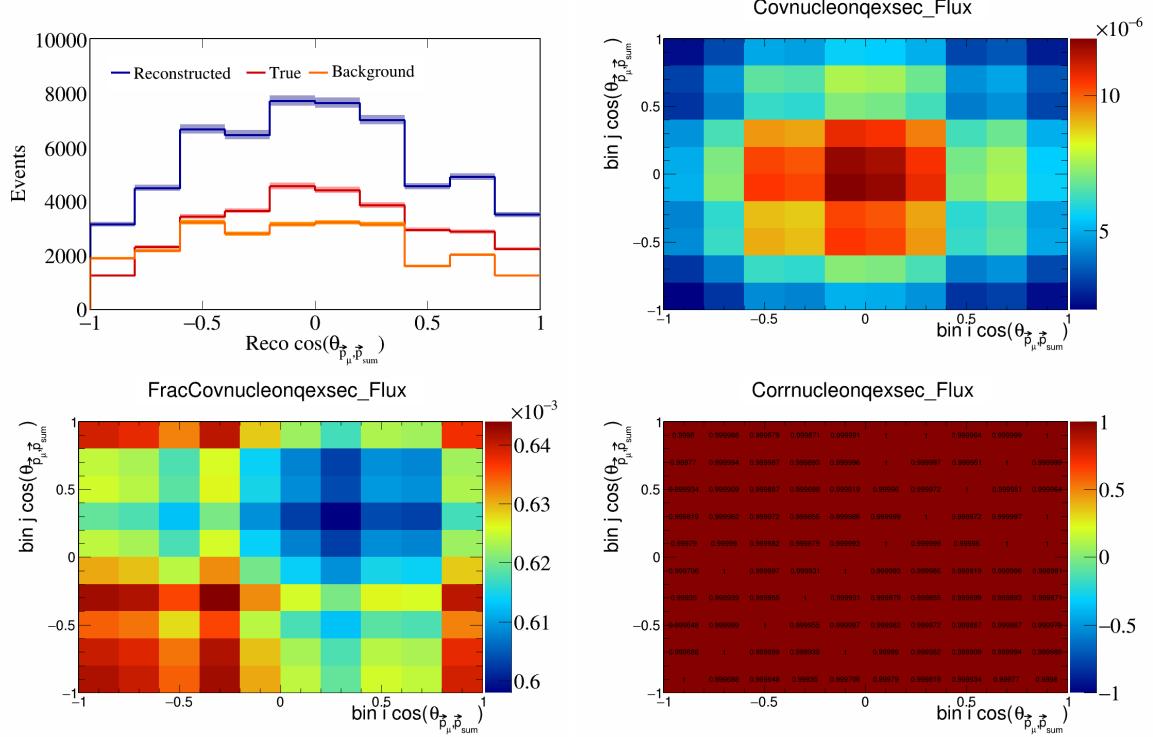


Figure 684: NucleonQeXSec variations for $\cos(\theta_{\vec{p}_\mu, \vec{p}_{\text{sum}}})$.

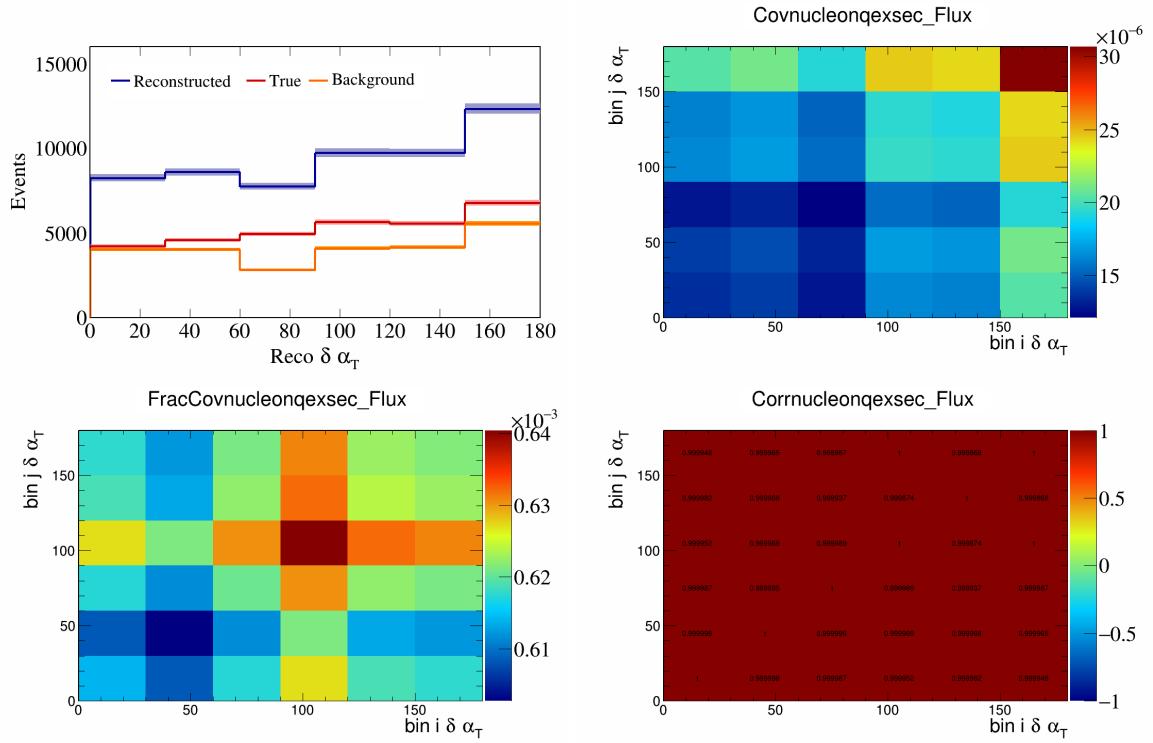


Figure 685: NucleonQeXSec variations for $\delta\alpha_T$.

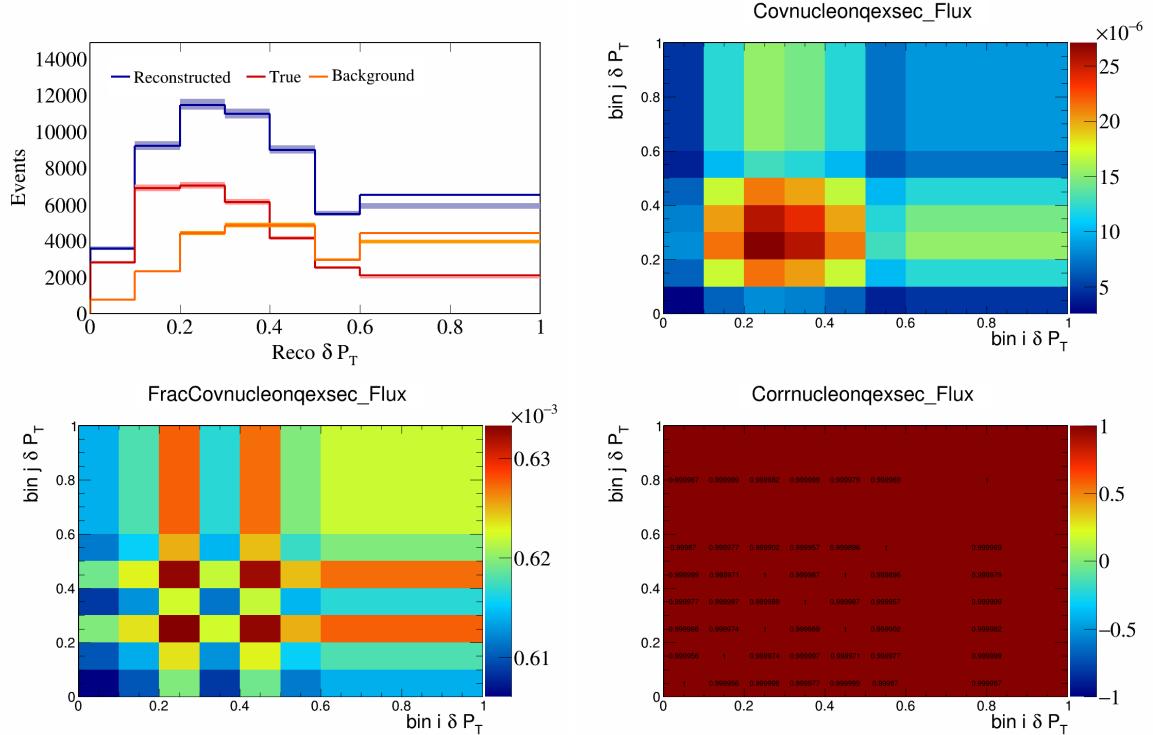


Figure 686: NucleonQeXSec variations for δP_T .

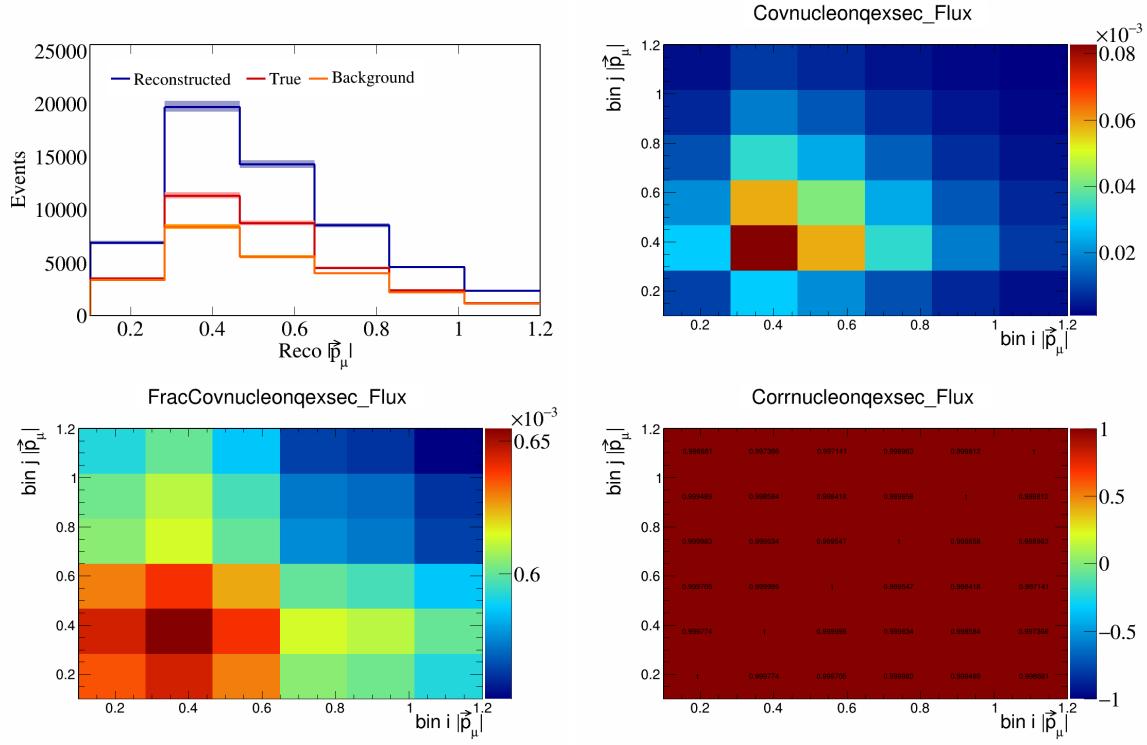


Figure 687: NucleonQeXSec variations for $|\vec{p}_\mu|$.

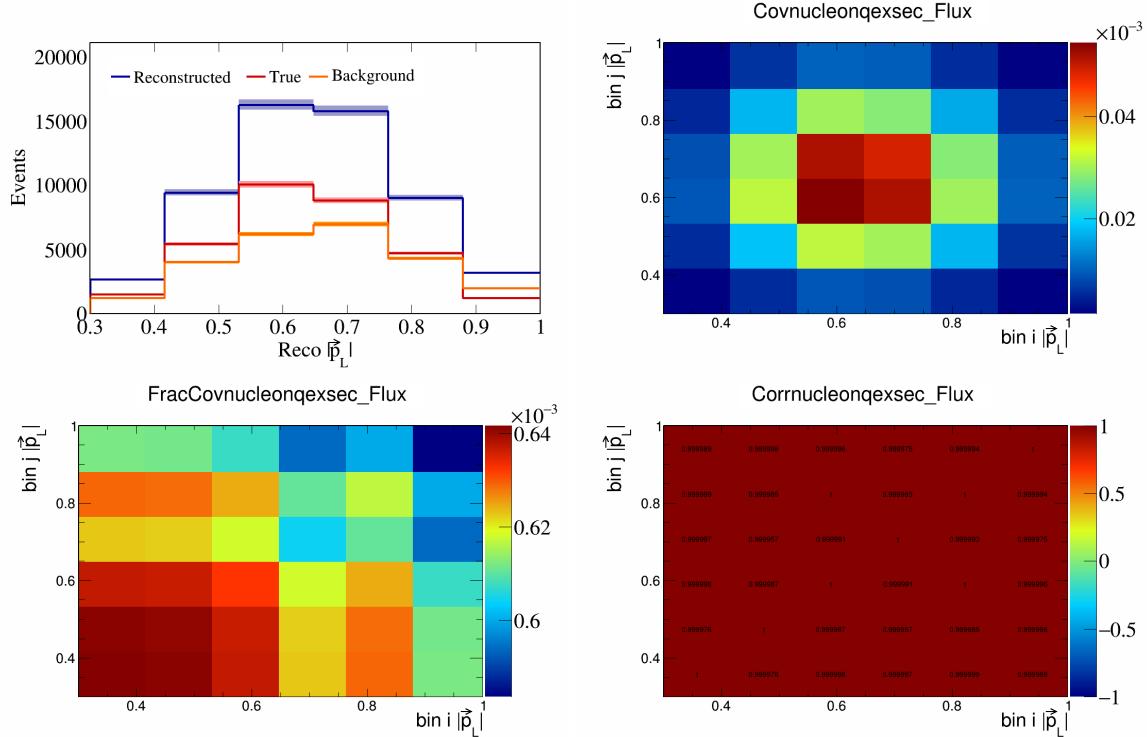


Figure 688: NucleonQeXSec variations for $|\vec{p}_L|$.

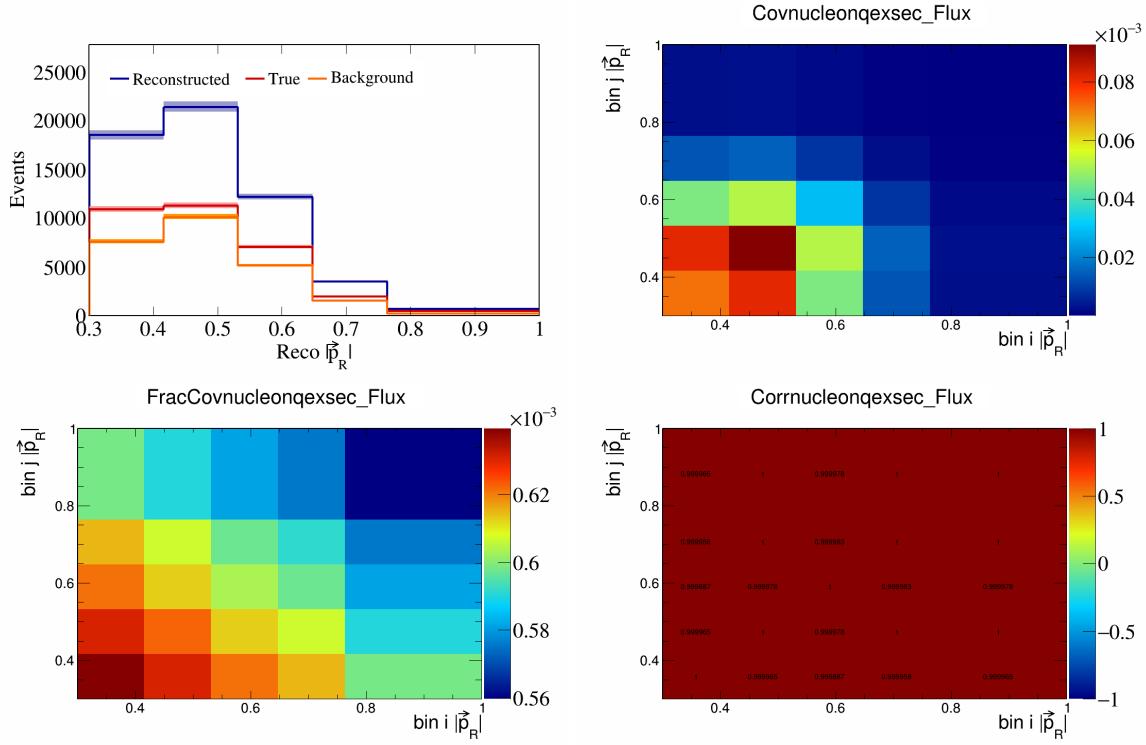


Figure 689: NucleonQeXSec variations for $|\vec{p}_R|$.

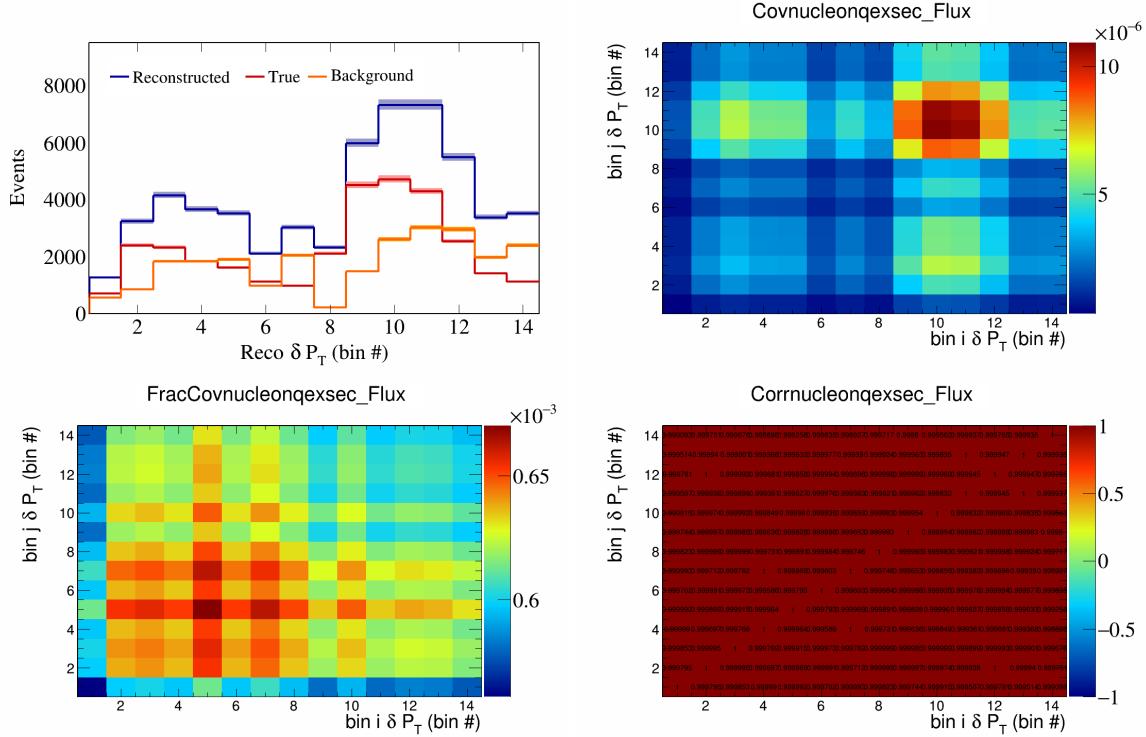


Figure 690: NucleonQeXSec variations for δP_T in $\cos(\theta_{\vec{p}_\mu})$.

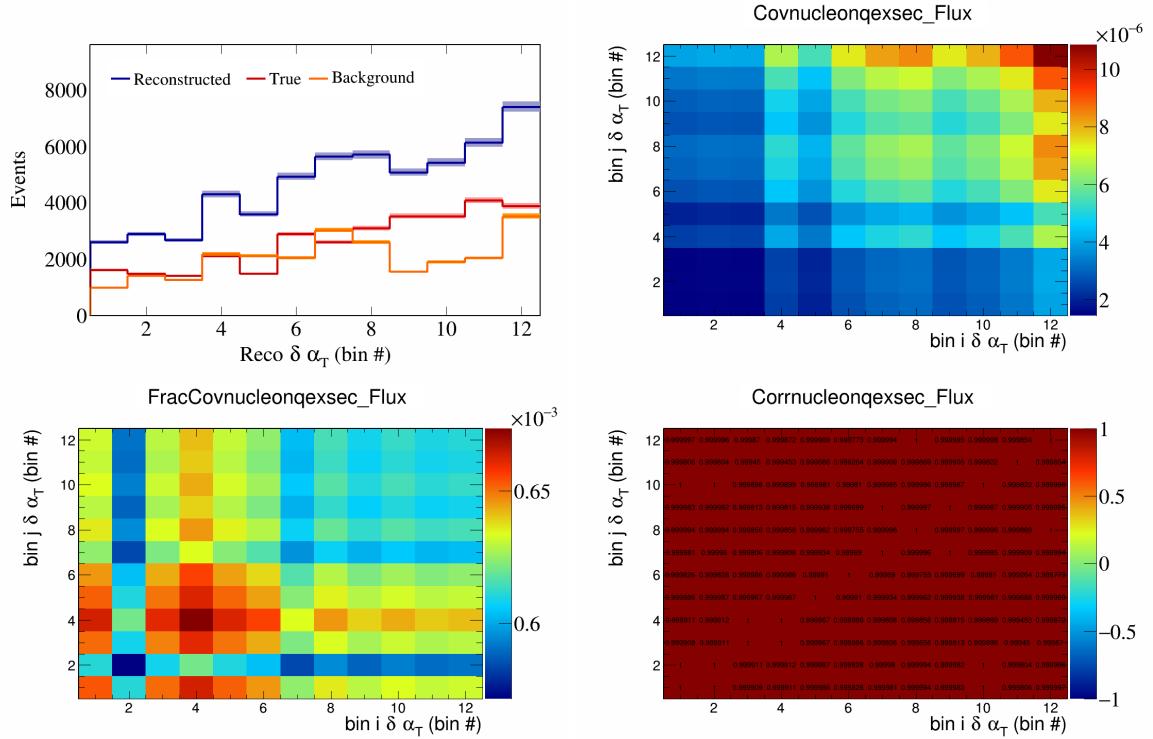


Figure 691: NucleonQeXSec variations for $\delta \alpha_T$ in $\cos(\theta_{\vec{p}_\mu})$.

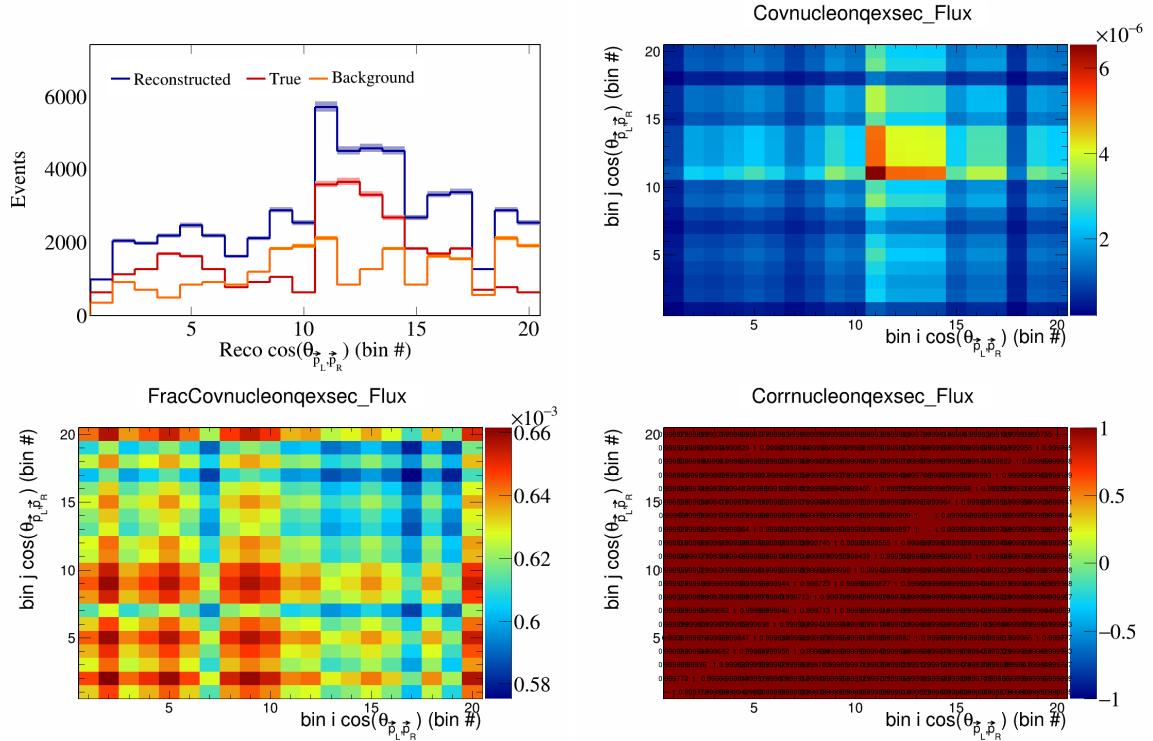


Figure 692: NucleonQeXSec variations for $\cos(\theta_{\vec{p}_L, \vec{p}_R})$ in $\cos(\theta_{\vec{p}_\mu})$.

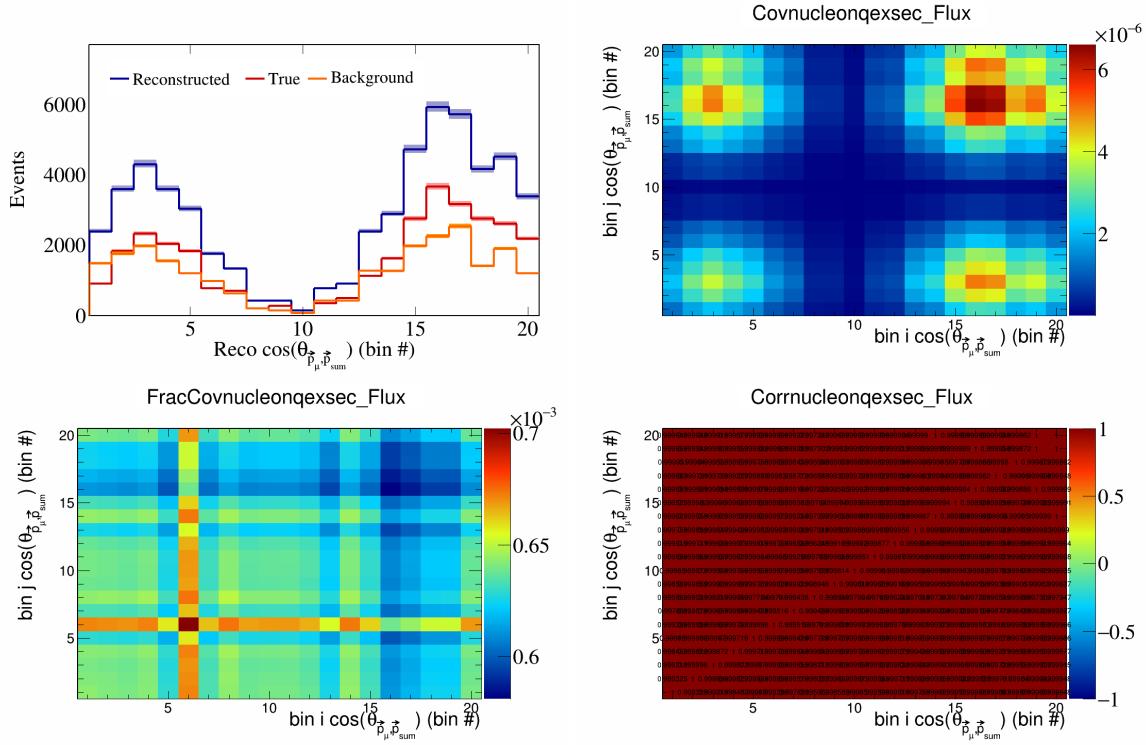


Figure 693: NucleonQeXSec variations for $\cos(\theta_{\vec{p}_\mu} \cdot \vec{p}_{\text{sum}})$ in $\cos(\theta_{\vec{p}_\mu})$.

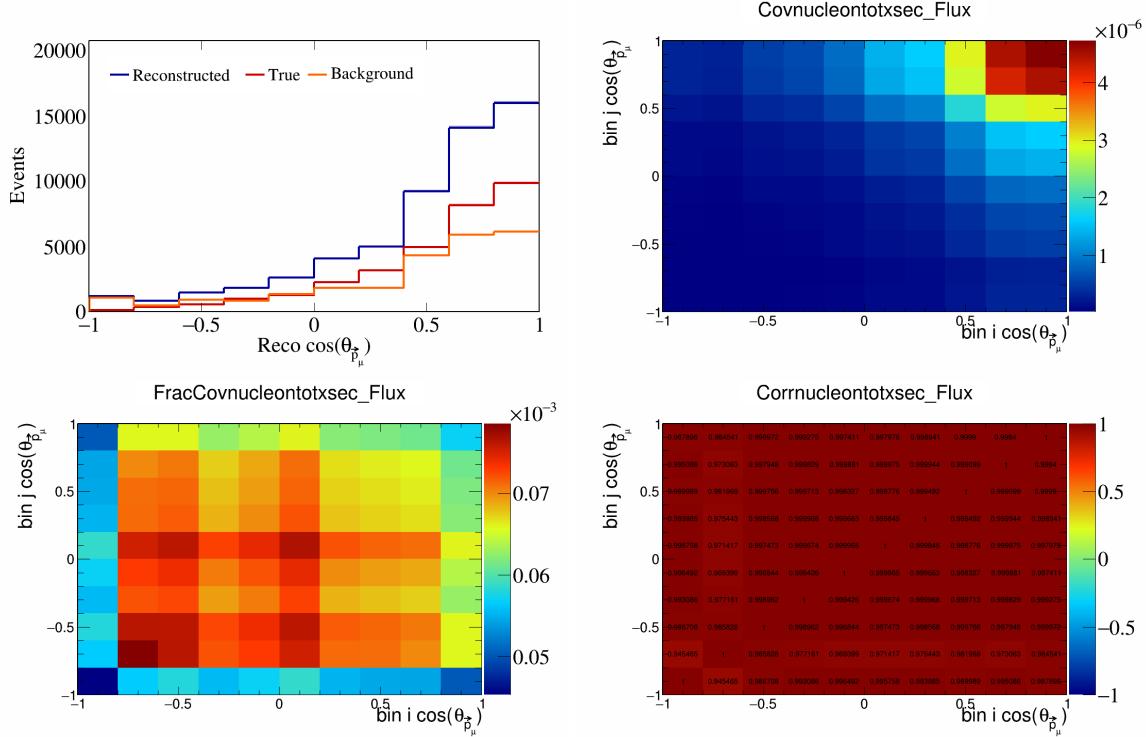


Figure 694: NucleonTotXSec variations for $\cos(\theta_{\vec{p}_\mu})$.

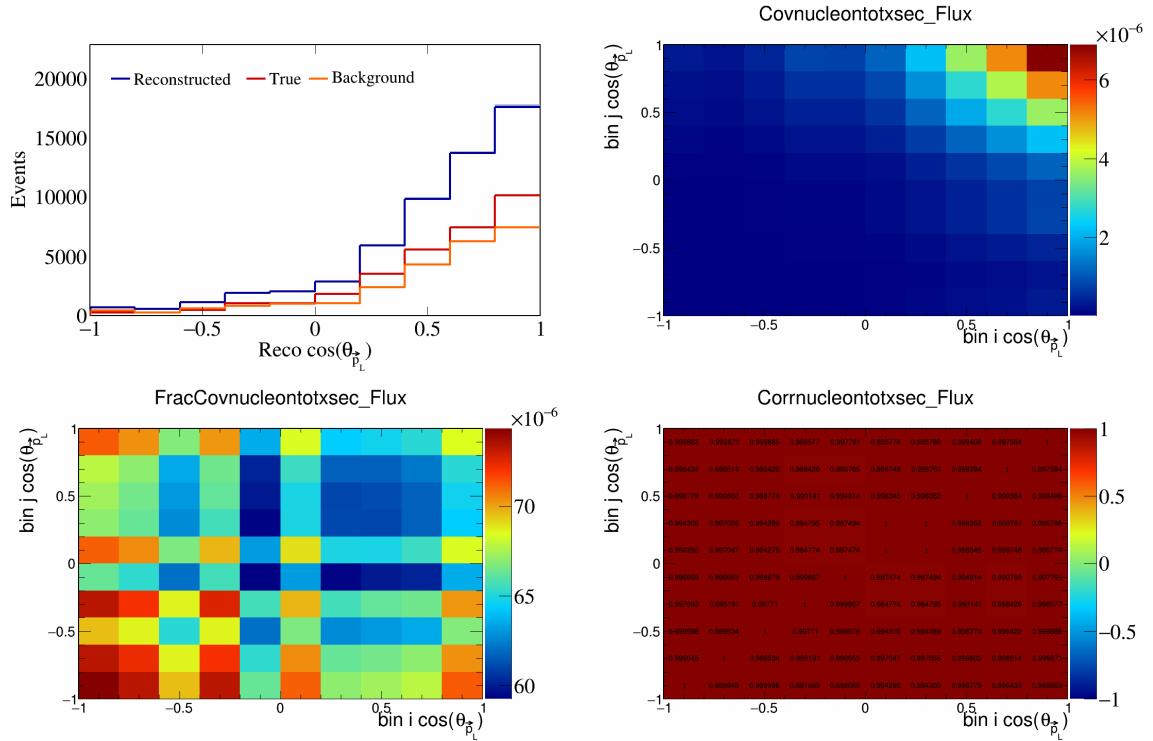


Figure 695: NucleonTotXSec variations for $\cos(\theta_{\vec{p}_L})$.

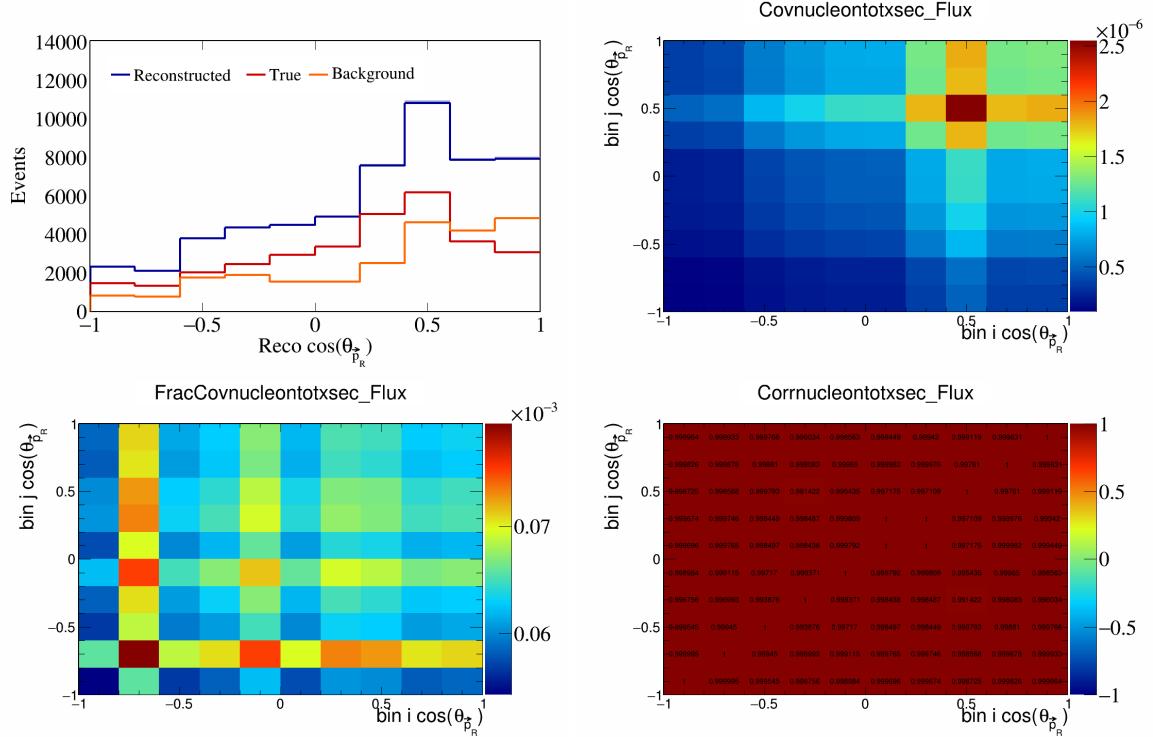


Figure 696: NucleonTotXSec variations for $\cos(\theta_{\vec{p}_R})$.

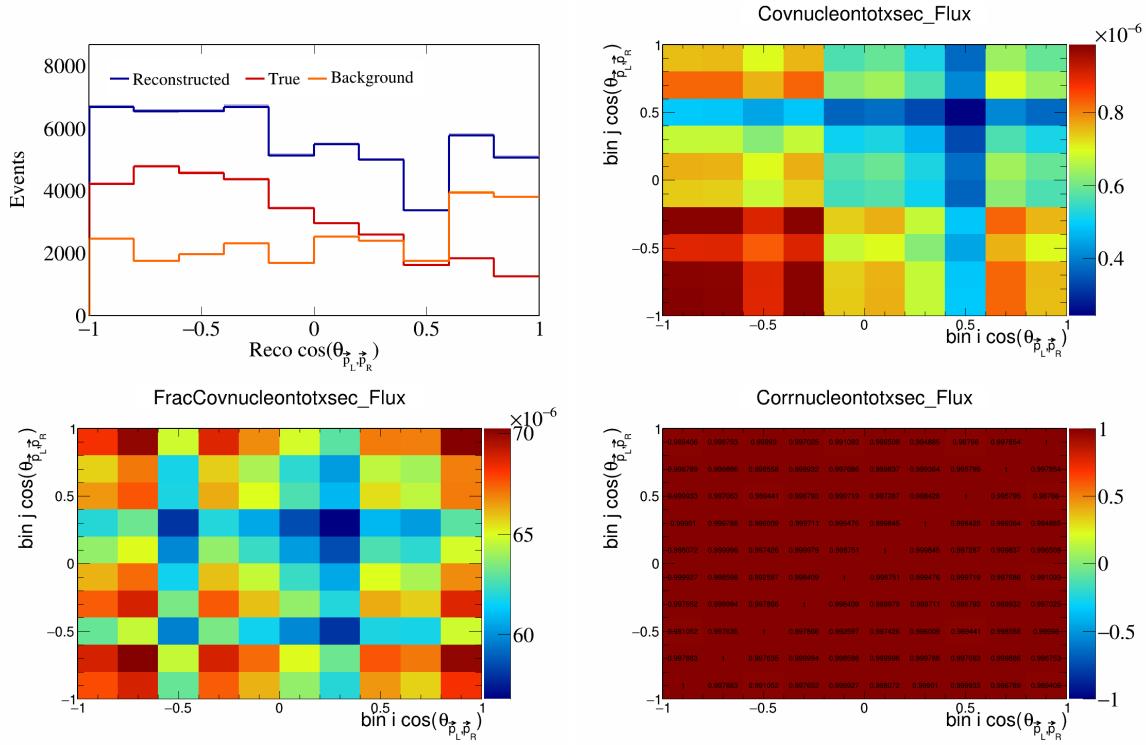


Figure 697: NucleonTotXSec variations for $\cos(\theta_{\vec{p}_L, \vec{p}_R})$.

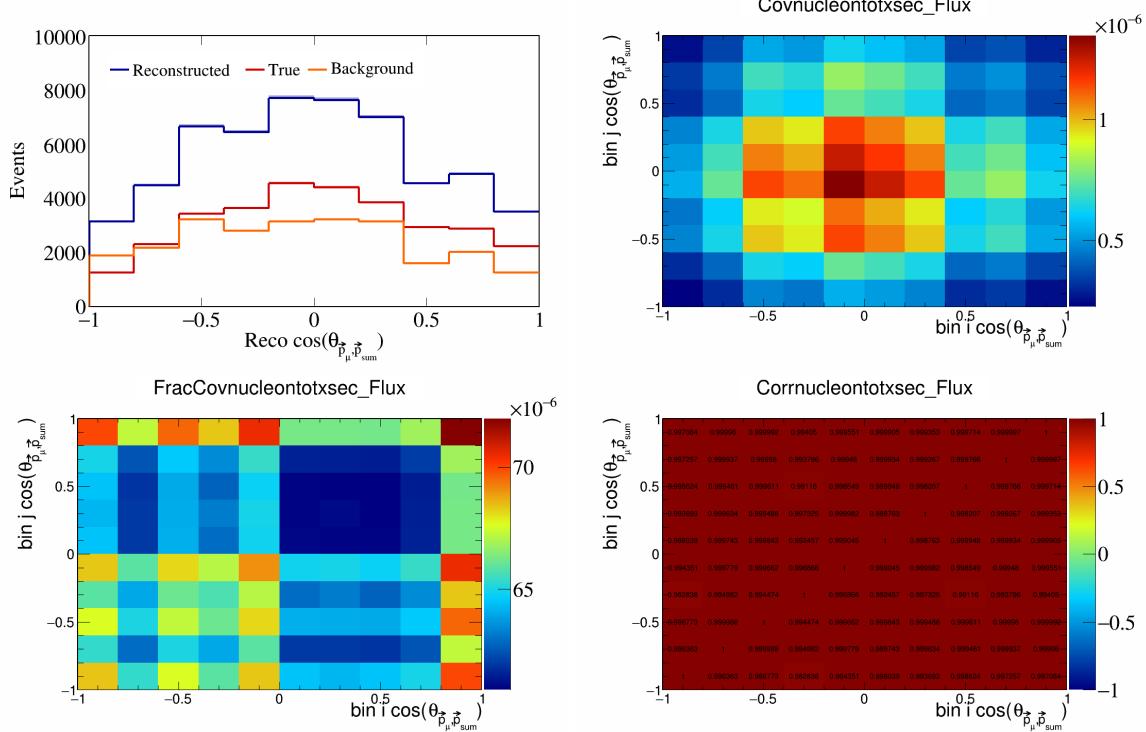


Figure 698: NucleonTotXSec variations for $\cos(\theta_{\vec{p}_\mu, \vec{p}_{\text{sum}}})$.

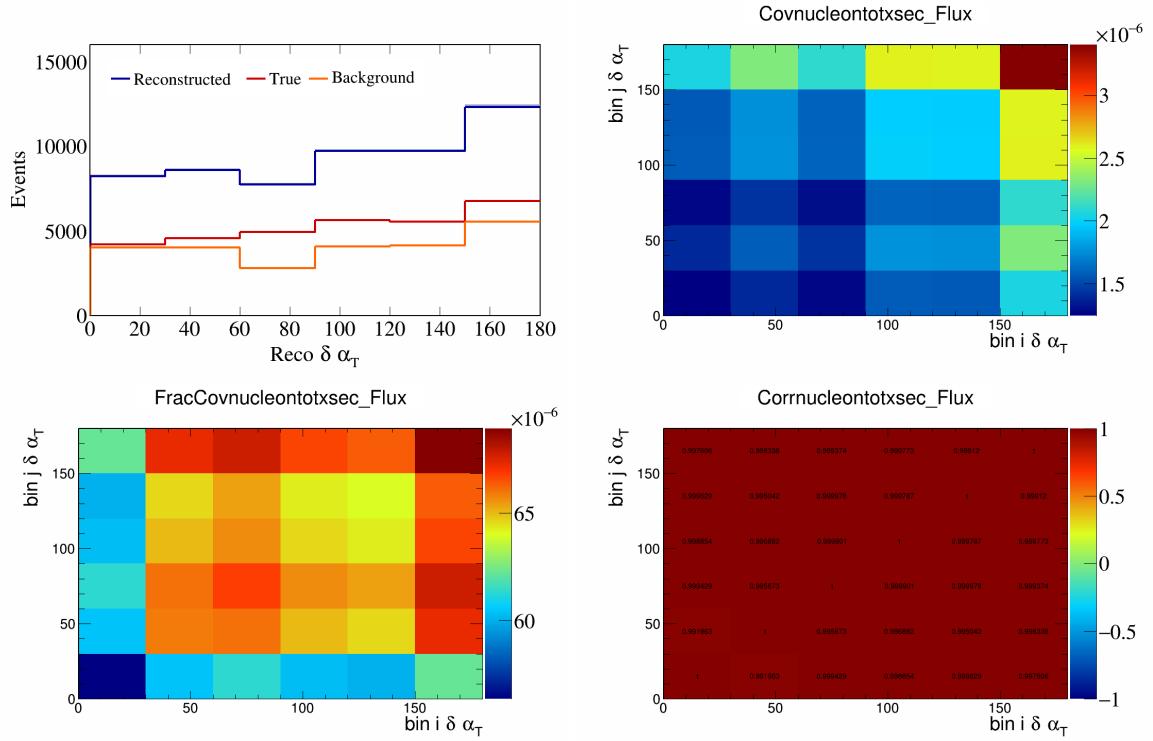


Figure 699: NucleonTotXSec variations for $\delta \alpha_T$.

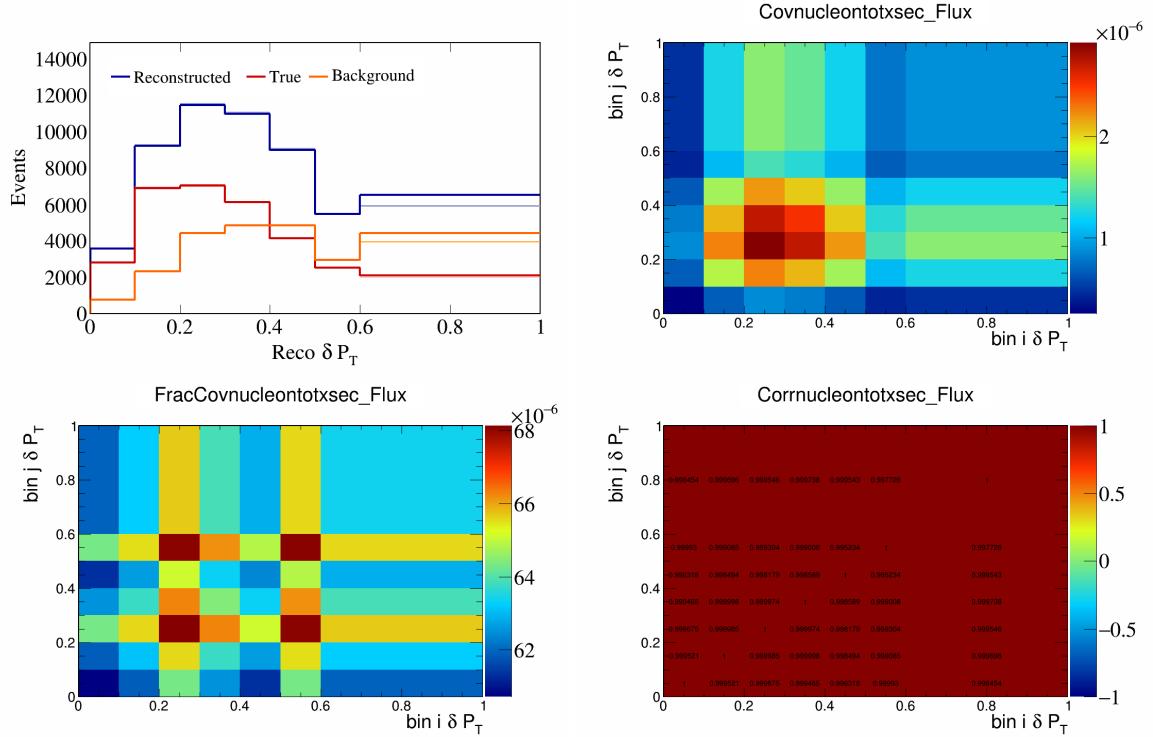


Figure 700: NucleonTotXSec variations for δP_T .

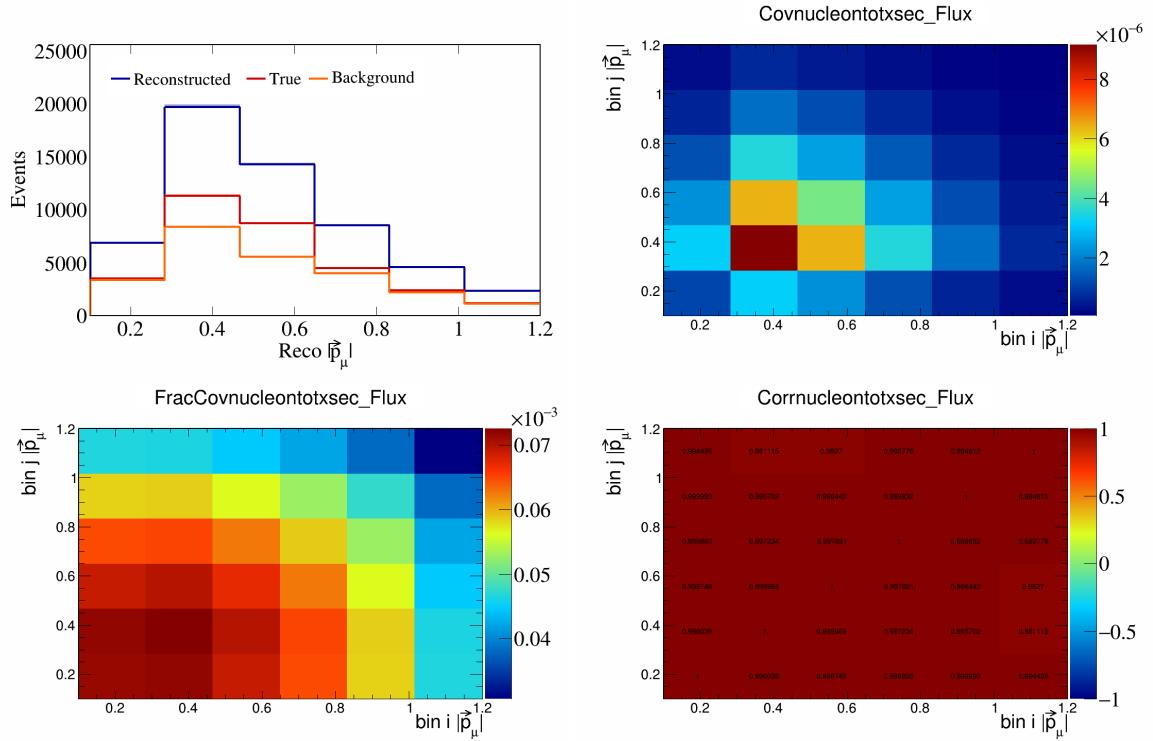


Figure 701: NucleonTotXSec variations for $|\vec{p}_\mu|$.

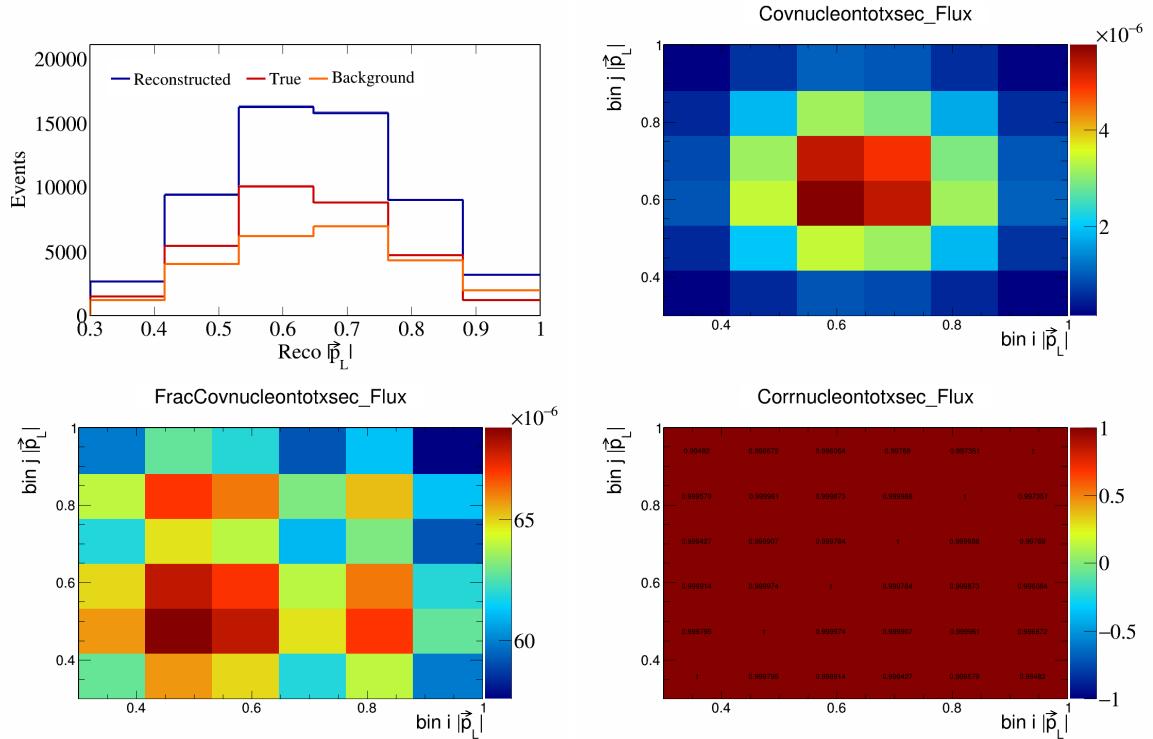


Figure 702: NucleonTotXSec variations for $|\vec{p}_L|$.

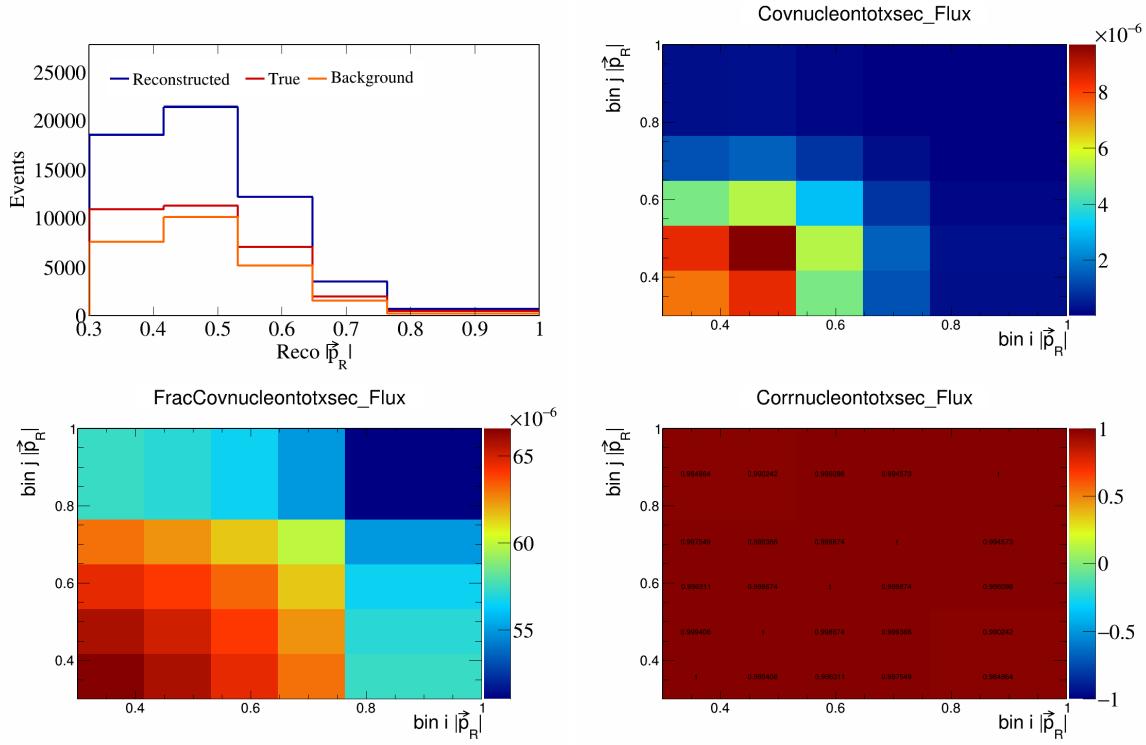


Figure 703: NucleonTotXSec variations for $|\vec{p}_R|$.

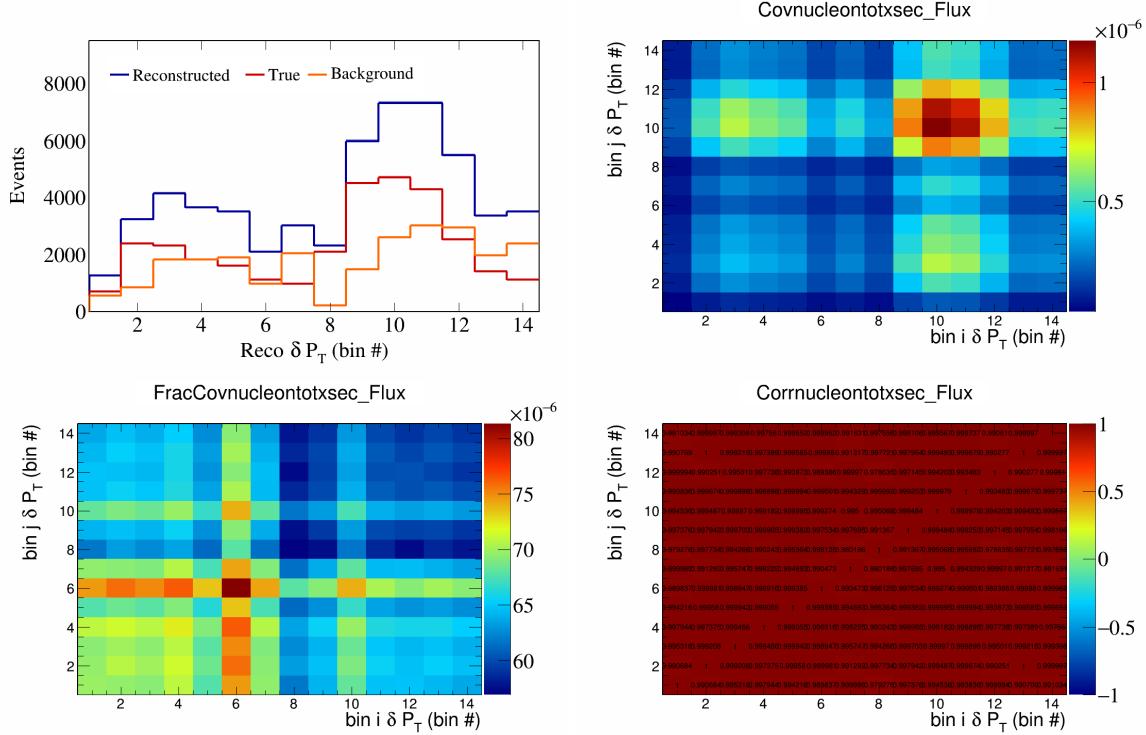


Figure 704: NucleonTotXSec variations for δP_T in $\cos(\theta_{\vec{p}_\mu})$.

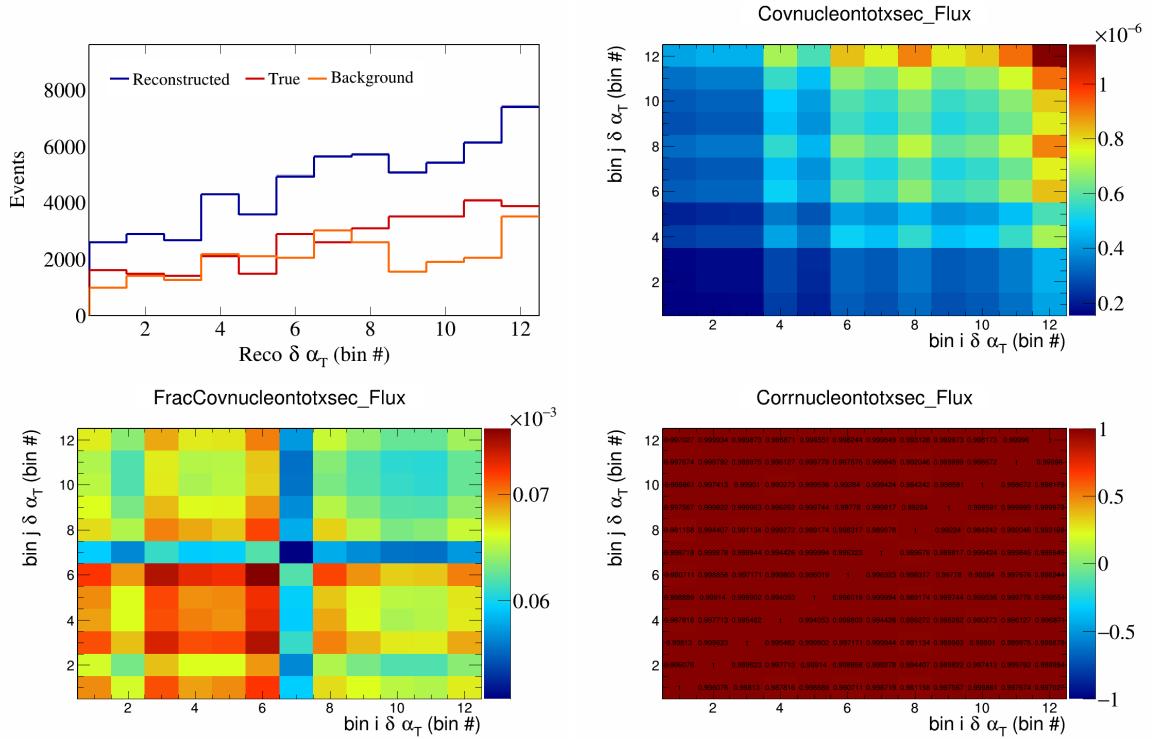


Figure 705: NucleonTotXSec variations for $\delta\alpha_T$ in $\cos(\theta_{\vec{p}_\mu})$.

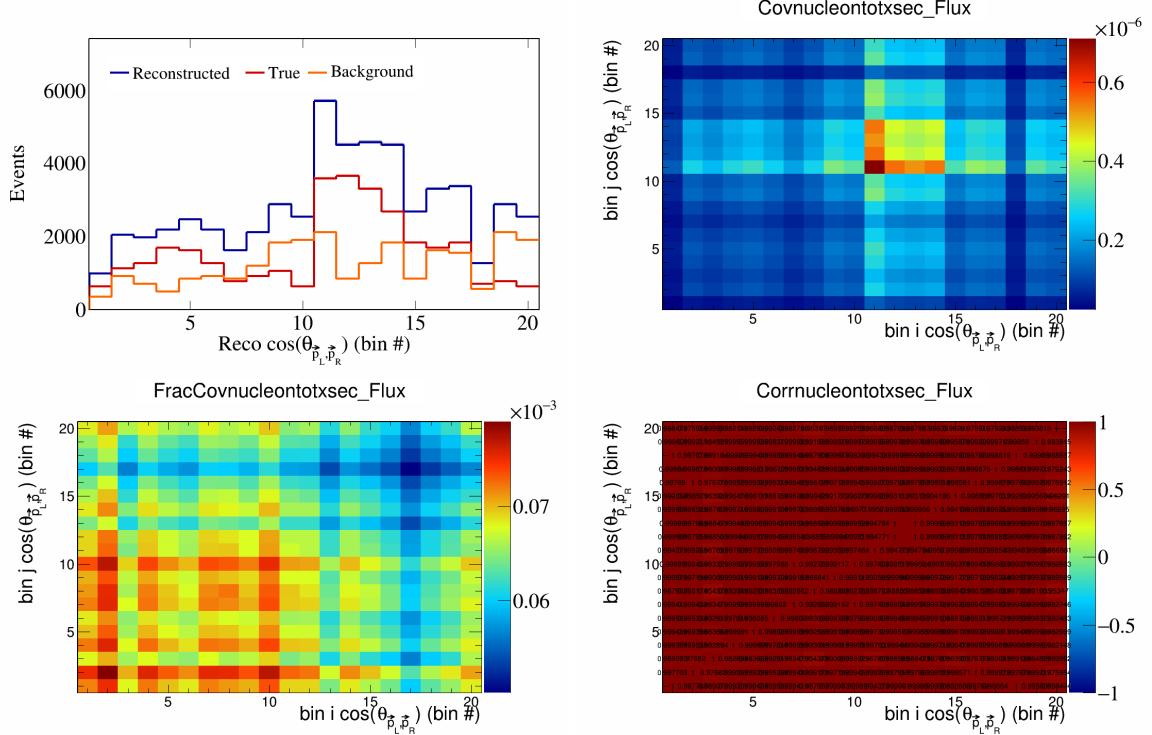


Figure 706: NucleonTotXSec variations for $\cos(\theta_{\vec{p}_L, \vec{p}_R})$ in $\cos(\theta_{\vec{p}_\mu})$.

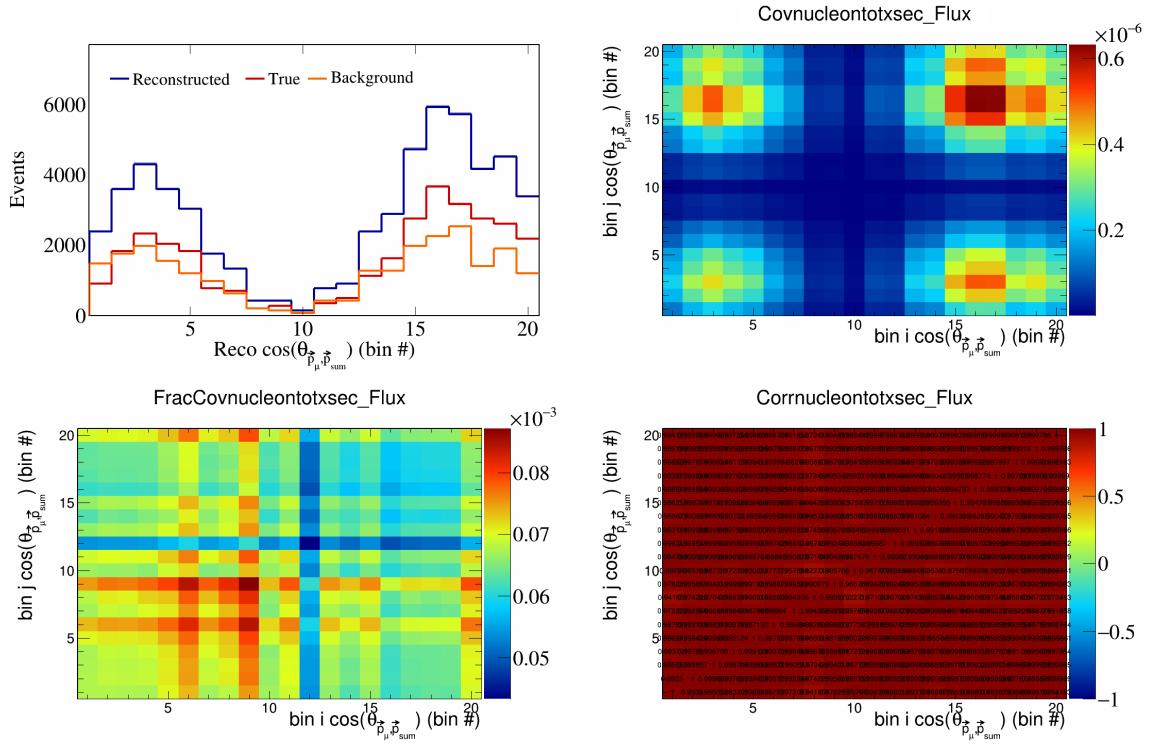


Figure 707: NucleonTotXSec variations for $\cos(\theta_{\vec{p}_\mu, \vec{p}_{\text{sum}}})$ in $\cos(\theta_{\vec{p}_\mu})$.

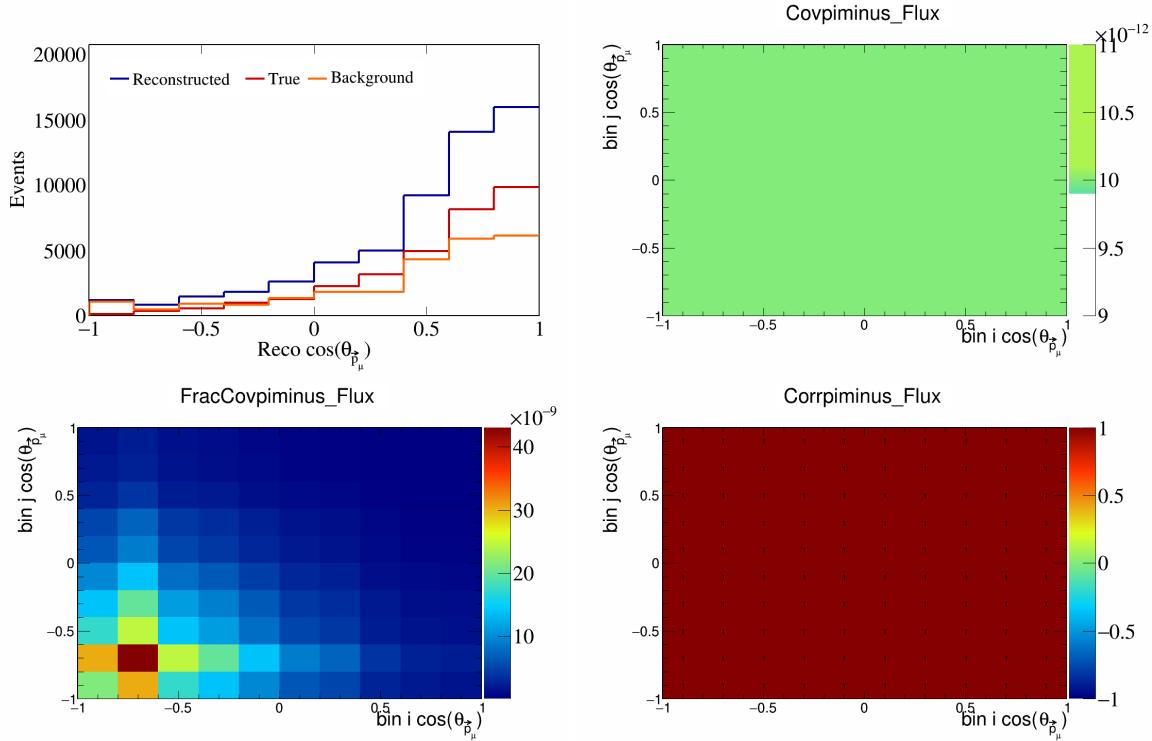


Figure 708: PiMinus variations for $\cos(\theta_{\vec{p}_\mu})$.

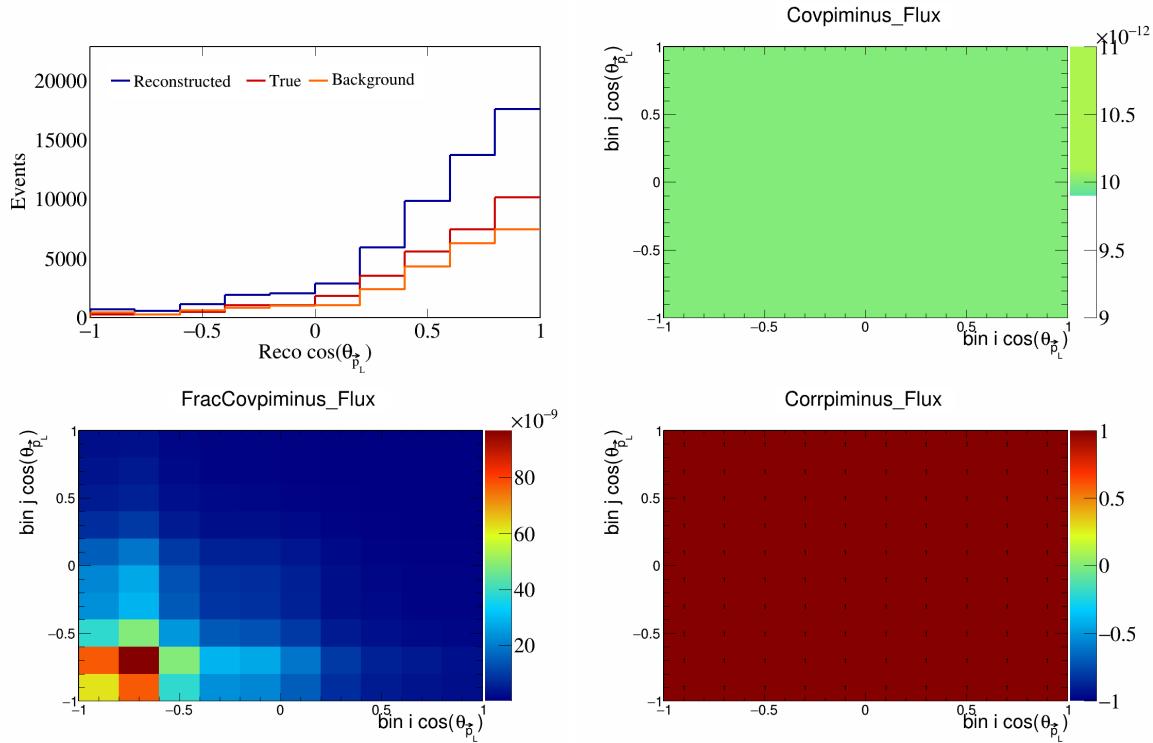


Figure 709: PiMinus variations for $\cos(\theta_{\vec{p}_L})$.

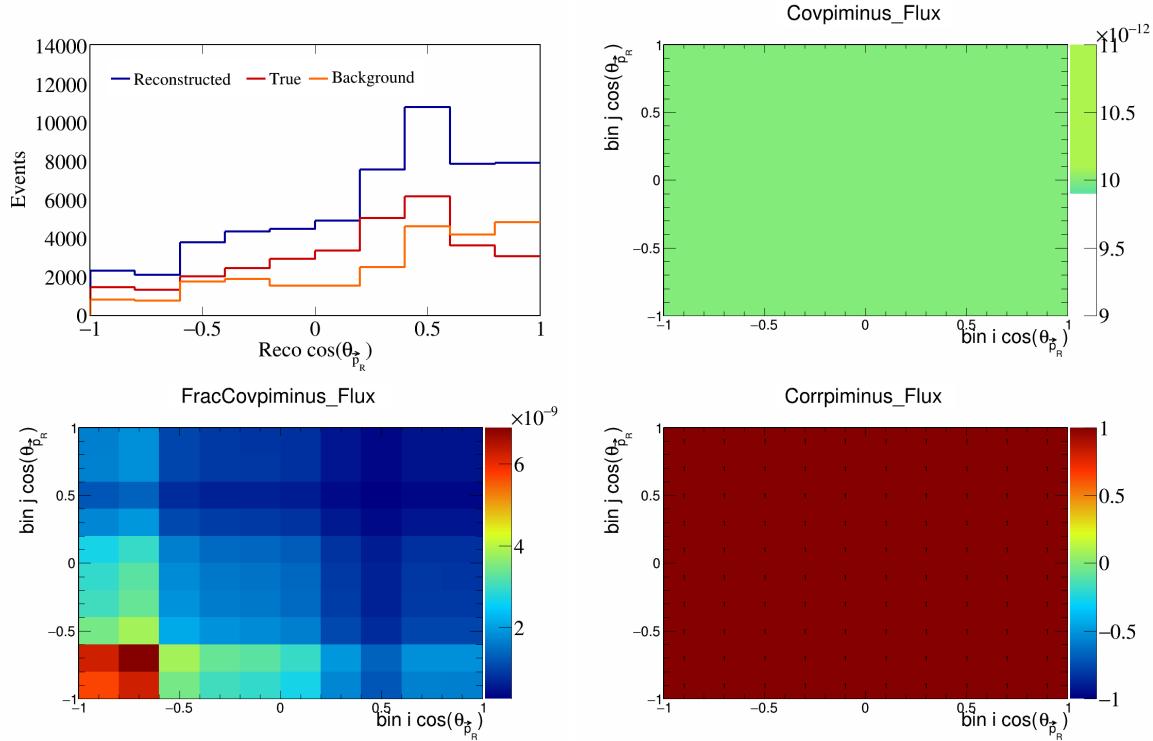


Figure 710: PiMinus variations for $\cos(\theta_{\vec{p}_R})$.

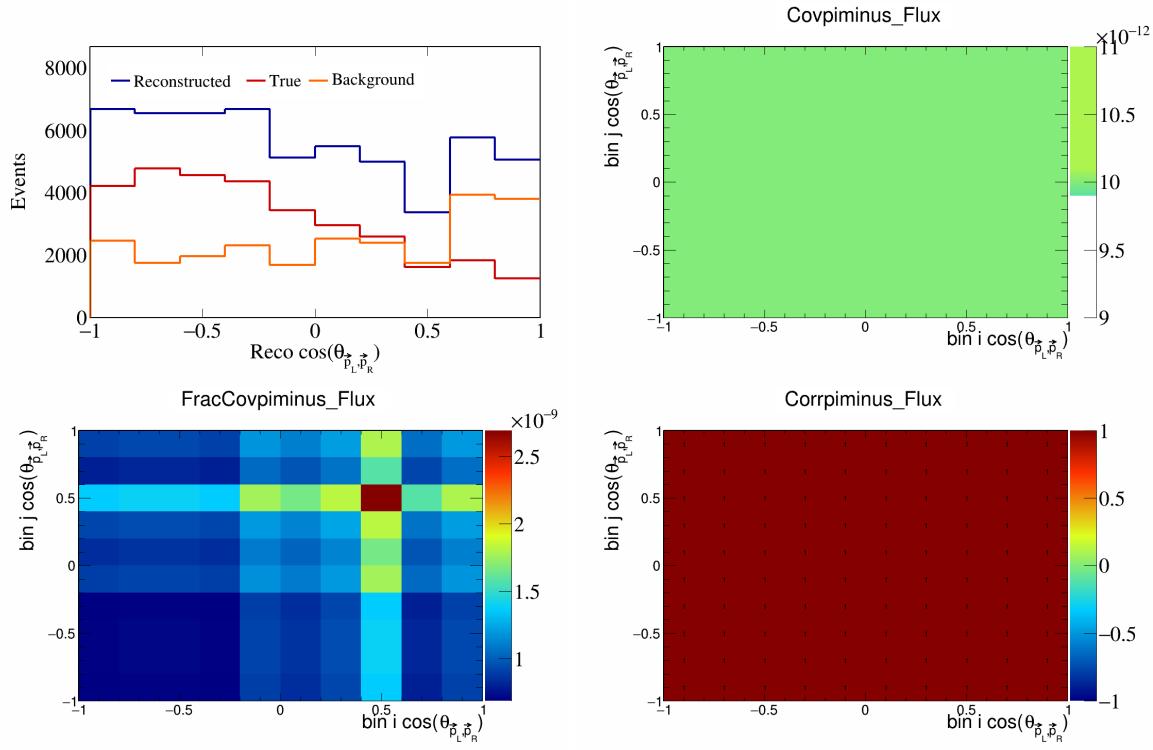


Figure 711: PiMinus variations for $\cos(\theta_{\vec{p}_L, \vec{p}_R})$.

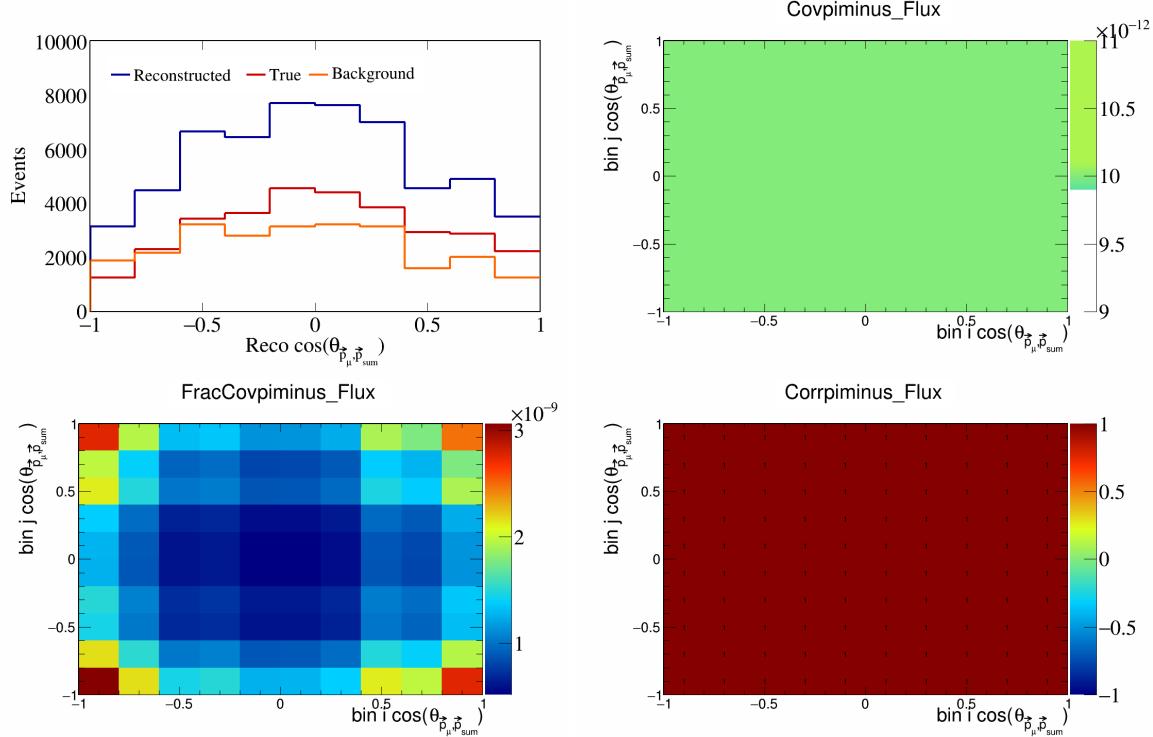


Figure 712: PiMinus variations for $\cos(\theta_{\vec{p}_\mu, \vec{p}_{\text{sum}}})$.

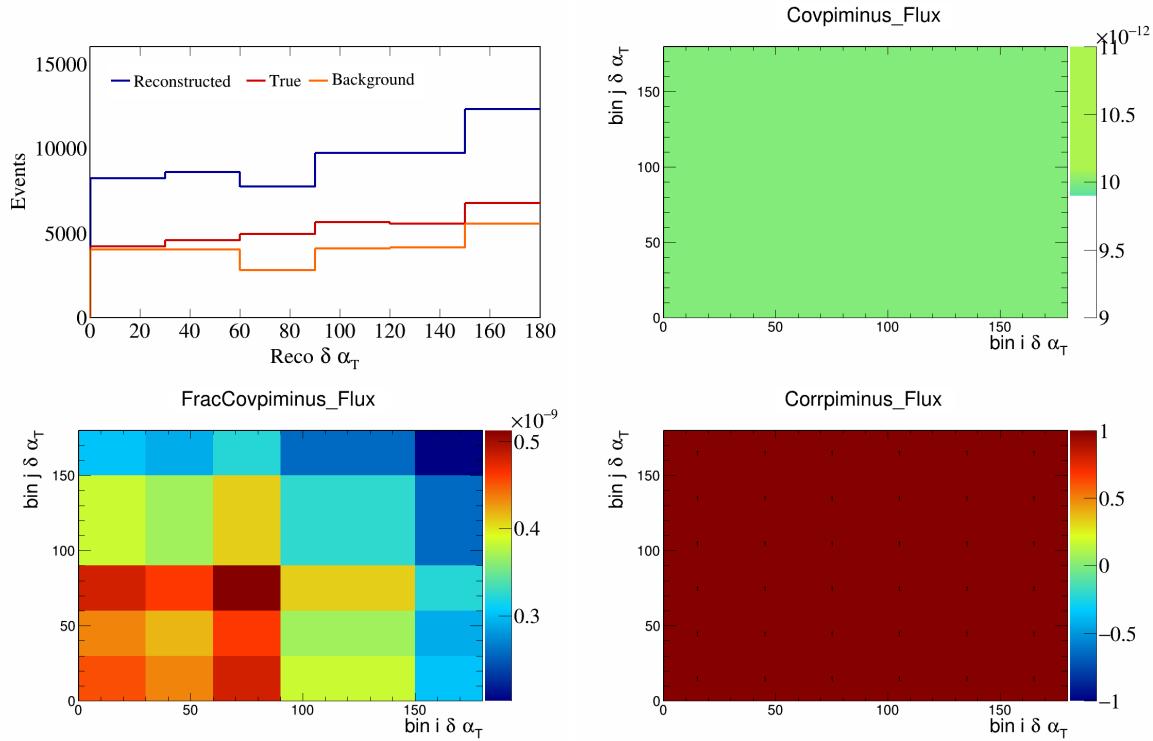


Figure 713: PiMinus variations for $\delta\alpha_T$.

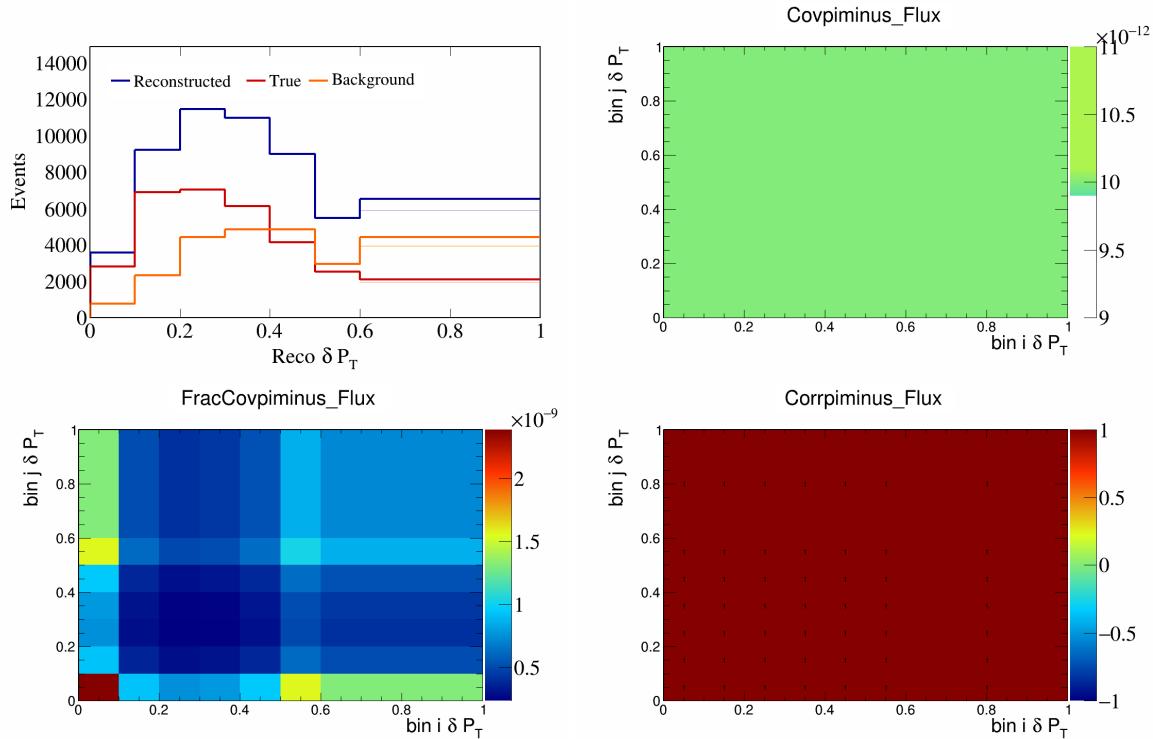


Figure 714: PiMinus variations for δP_T .

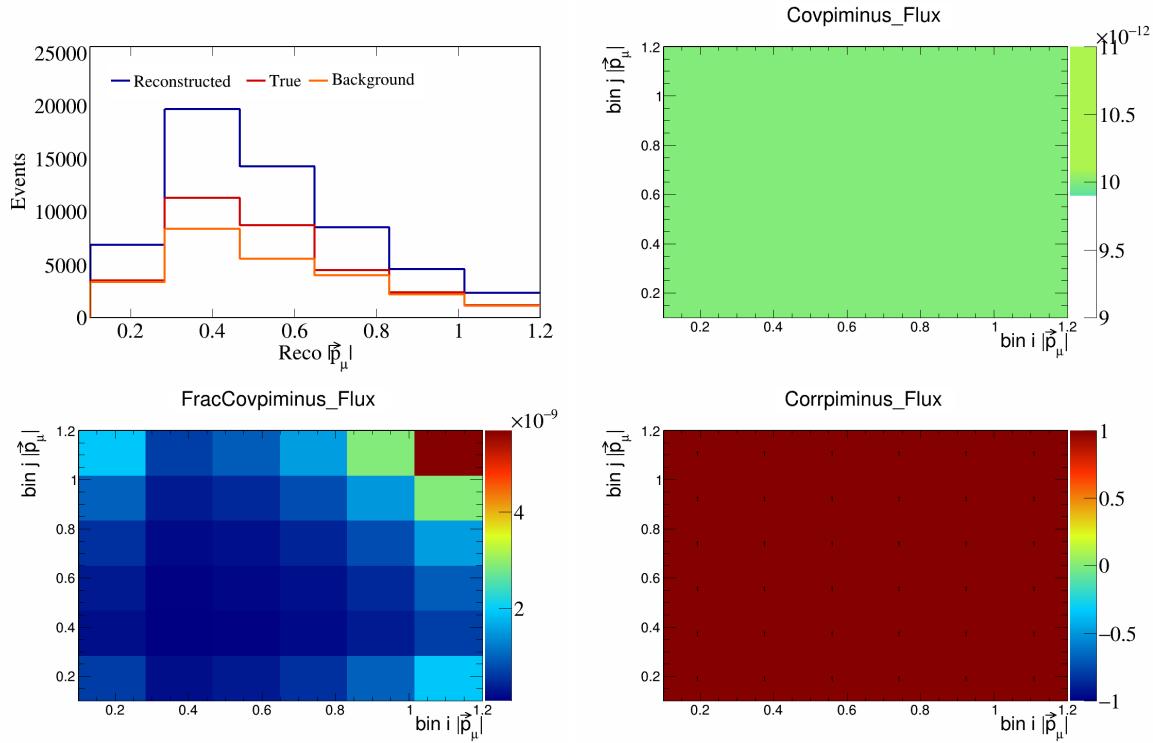


Figure 715: PiMinus variations for $|\vec{p}_\mu|$.

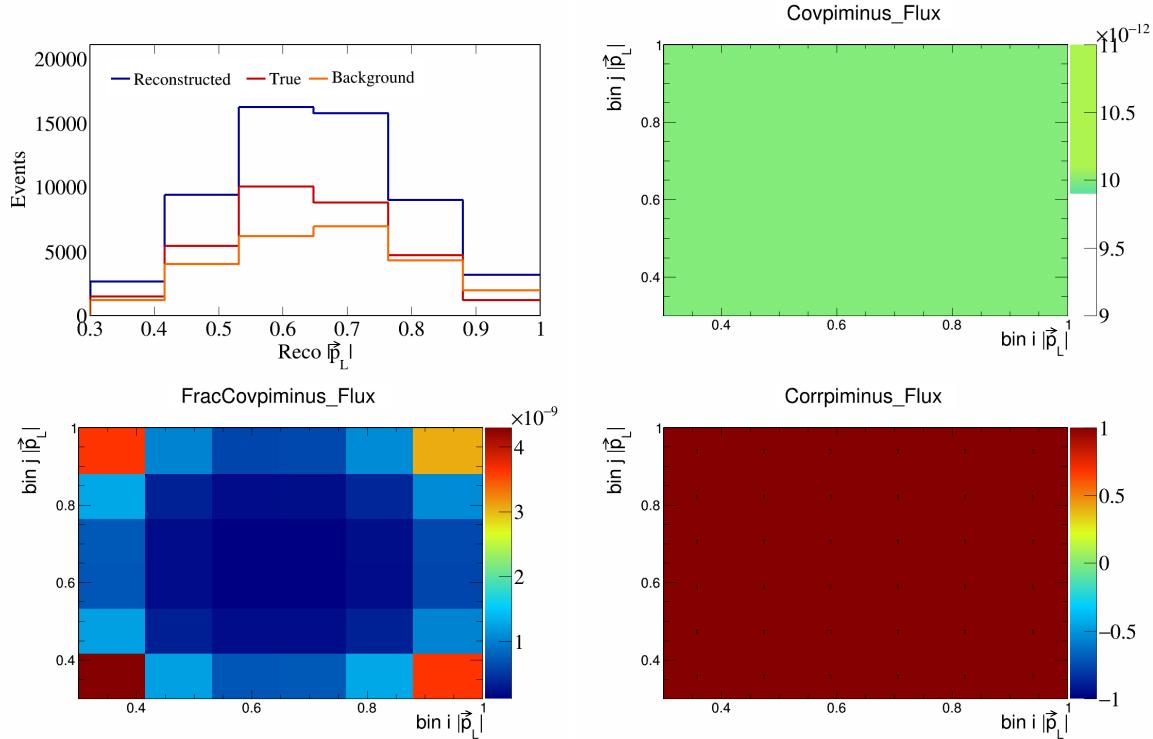


Figure 716: PiMinus variations for $|\vec{p}_L|$.

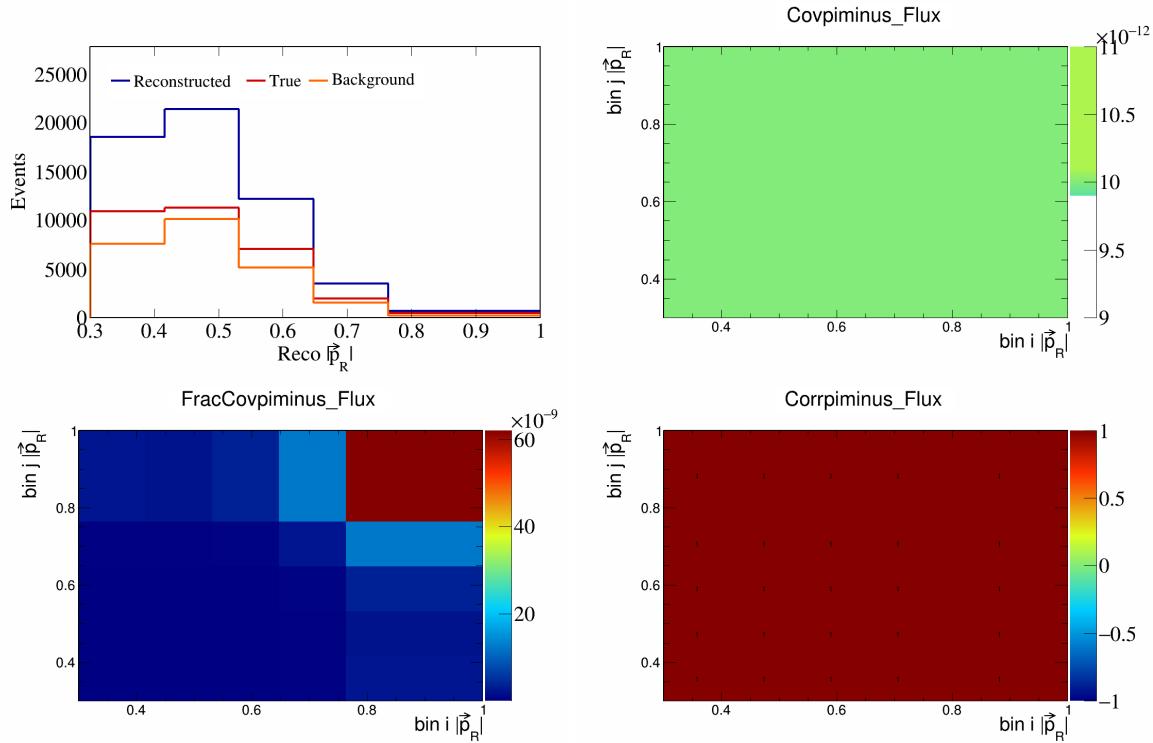


Figure 717: PiMinus variations for $|\vec{p}_R|$.

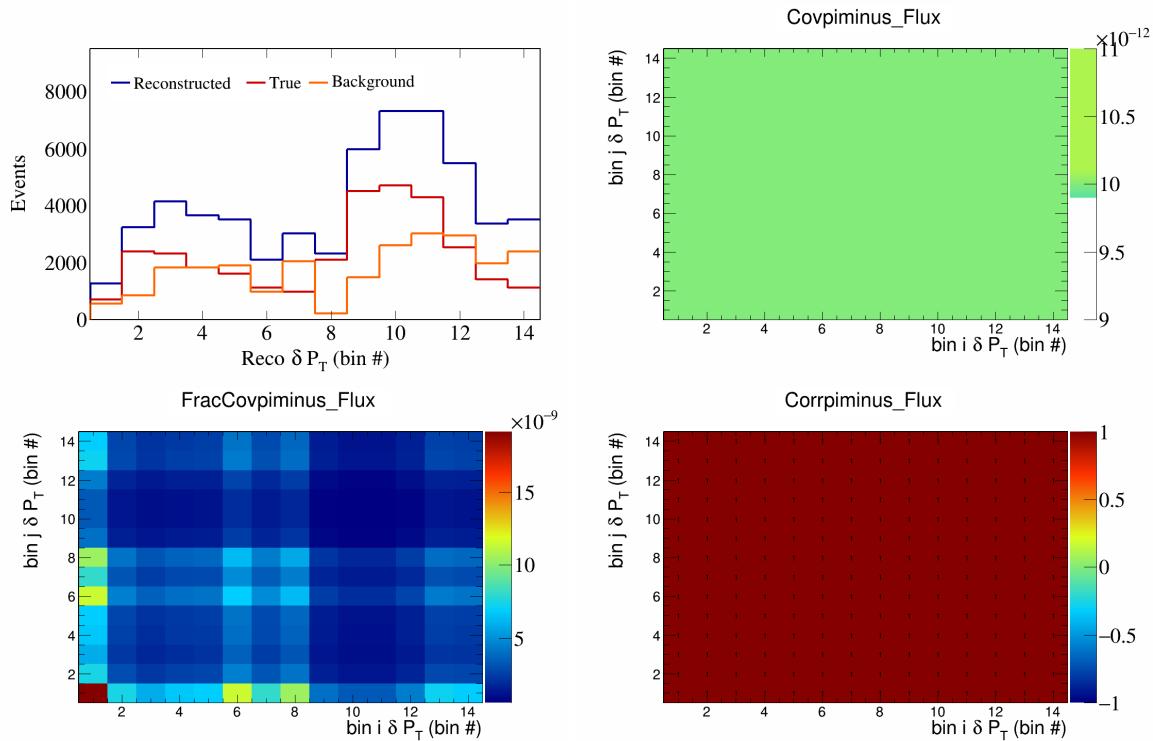


Figure 718: PiMinus variations for δP_T in $\cos(\theta_{\vec{p}_\mu})$.

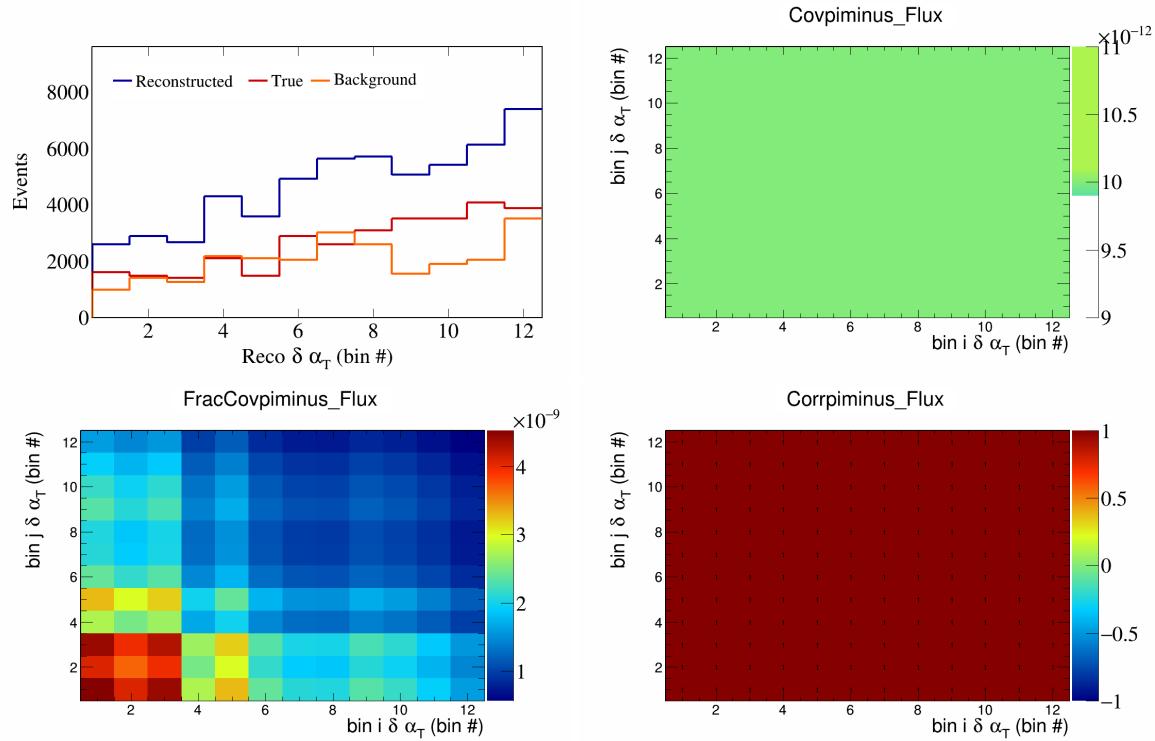


Figure 719: PiMinus variations for $\delta\alpha_T$ in $\cos(\theta_{\vec{p}_\mu})$.

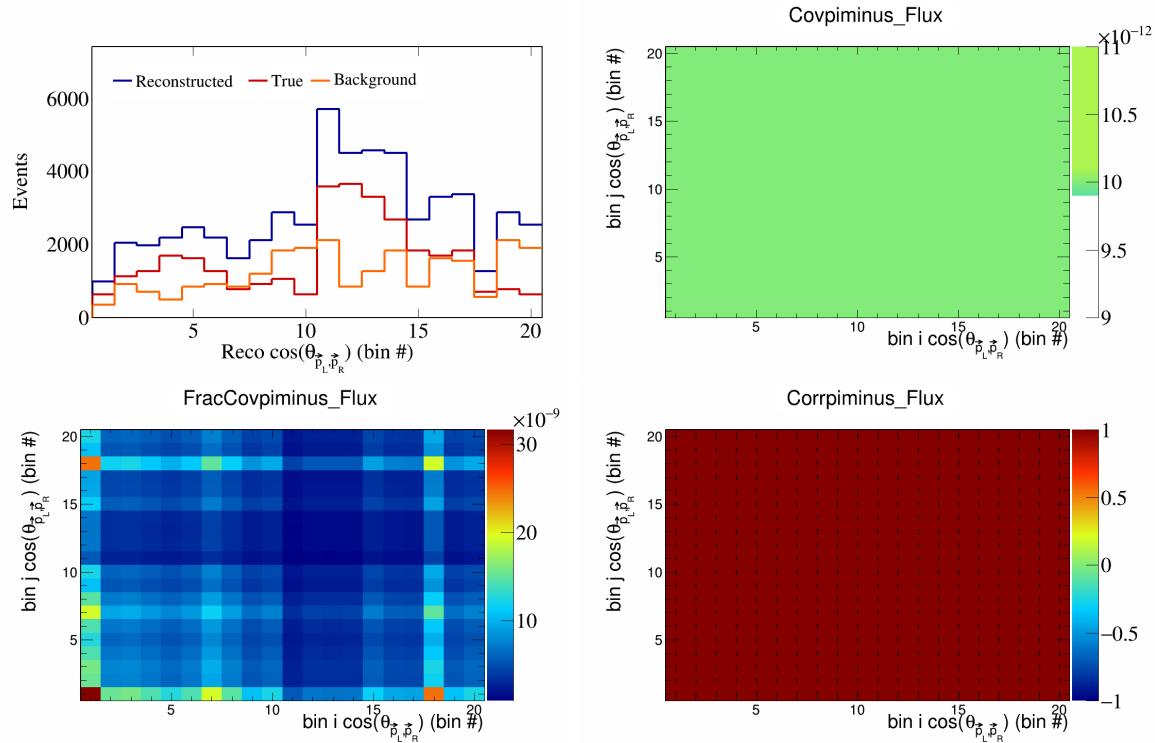


Figure 720: PiMinus variations for $\cos(\theta_{\vec{p}_L, \vec{p}_R})$ in $\cos(\theta_{\vec{p}_\mu})$.

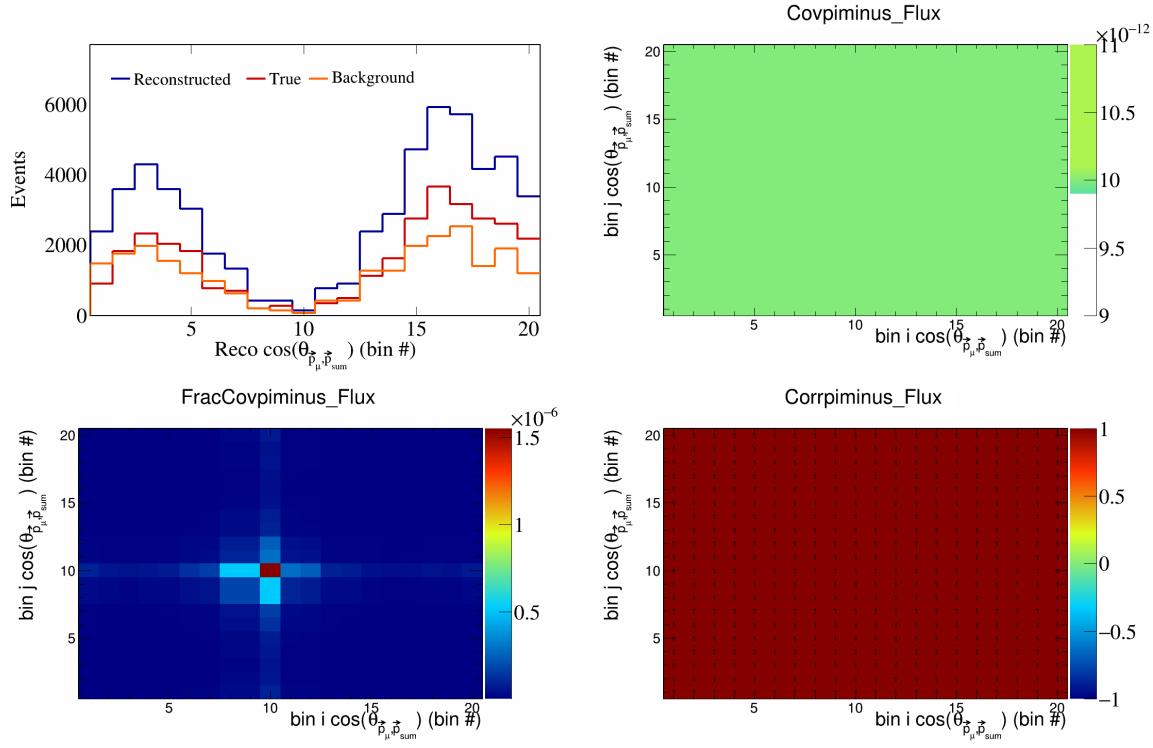


Figure 721: PiMinus variations for $\cos(\theta_{\vec{p}_\mu, \vec{p}_{\text{sum}}})$ in $\cos(\theta_{\vec{p}_\mu})$.

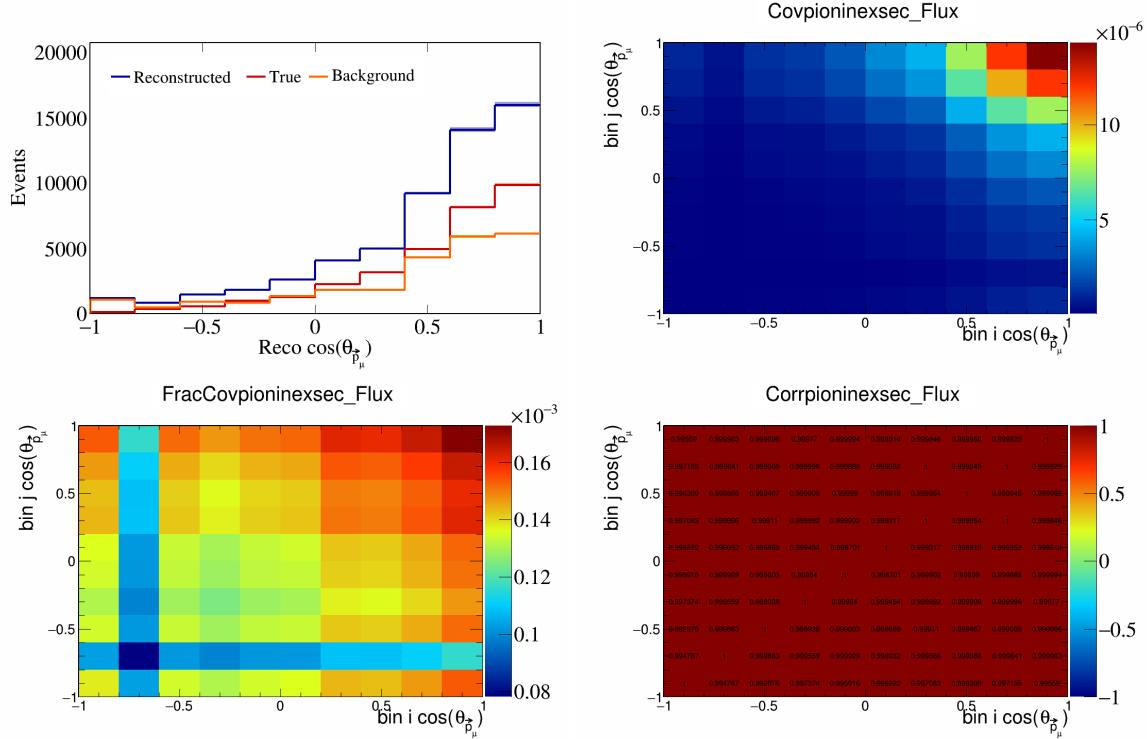


Figure 722: PionIneXSec variations for $\cos(\theta_{\vec{p}_\mu})$.

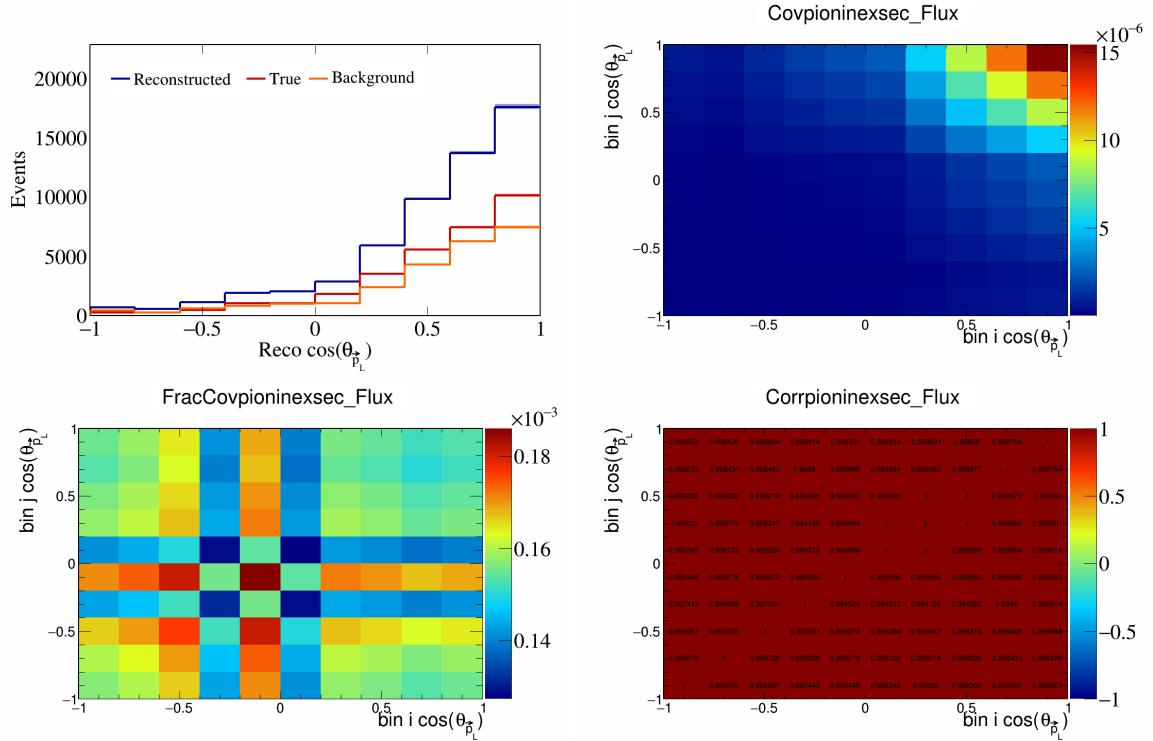


Figure 723: PionIneXSec variations for $\cos(\theta_{\vec{p}_L})$.

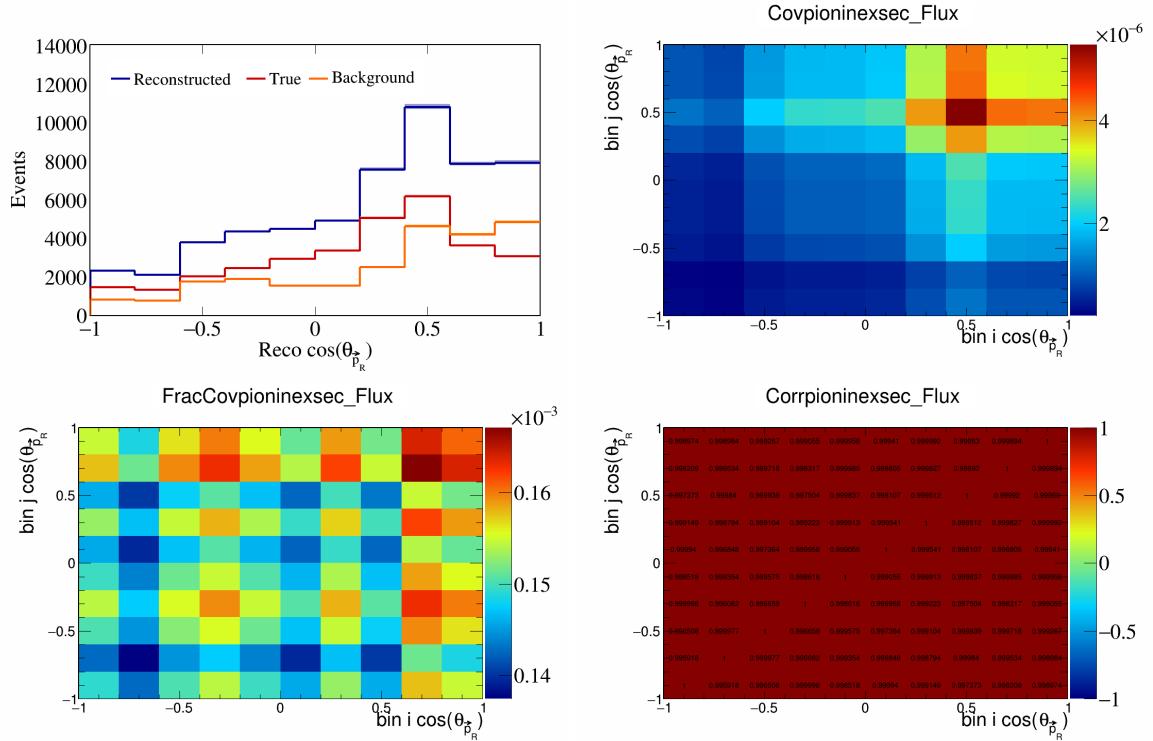


Figure 724: PionIneXSec variations for $\cos(\theta_{\vec{p}_R})$.

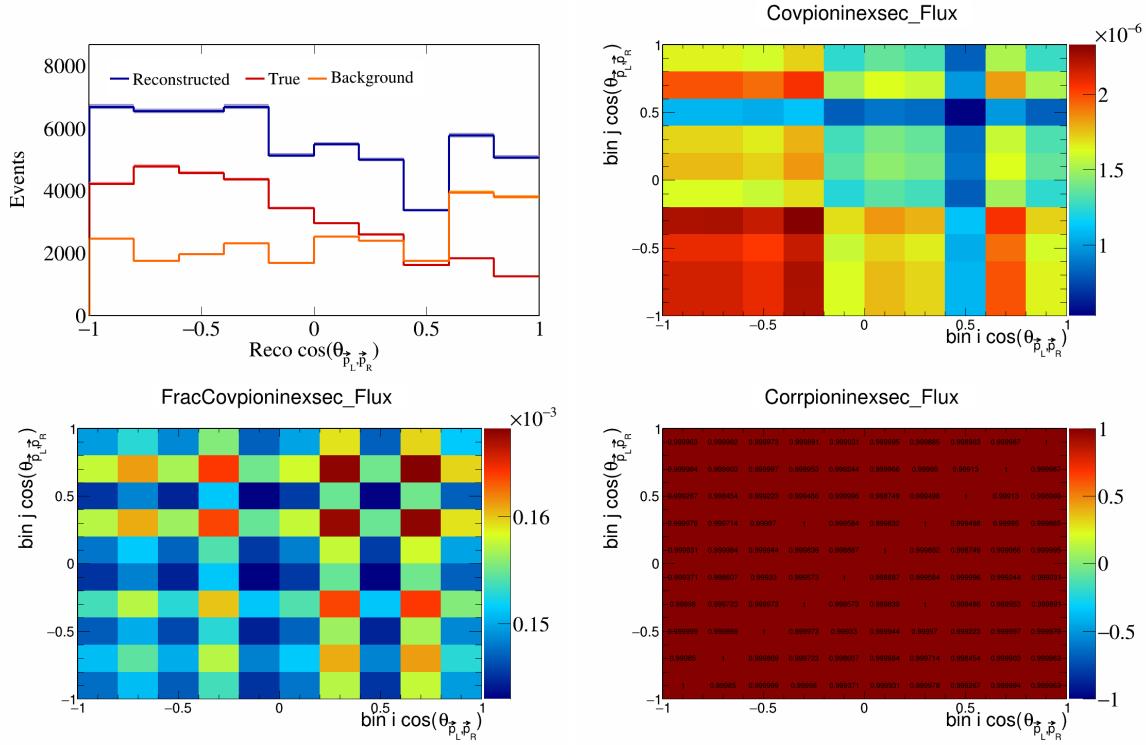


Figure 725: PionIneXSec variations for $\cos(\theta_{\vec{p}_L, \vec{p}_R})$.

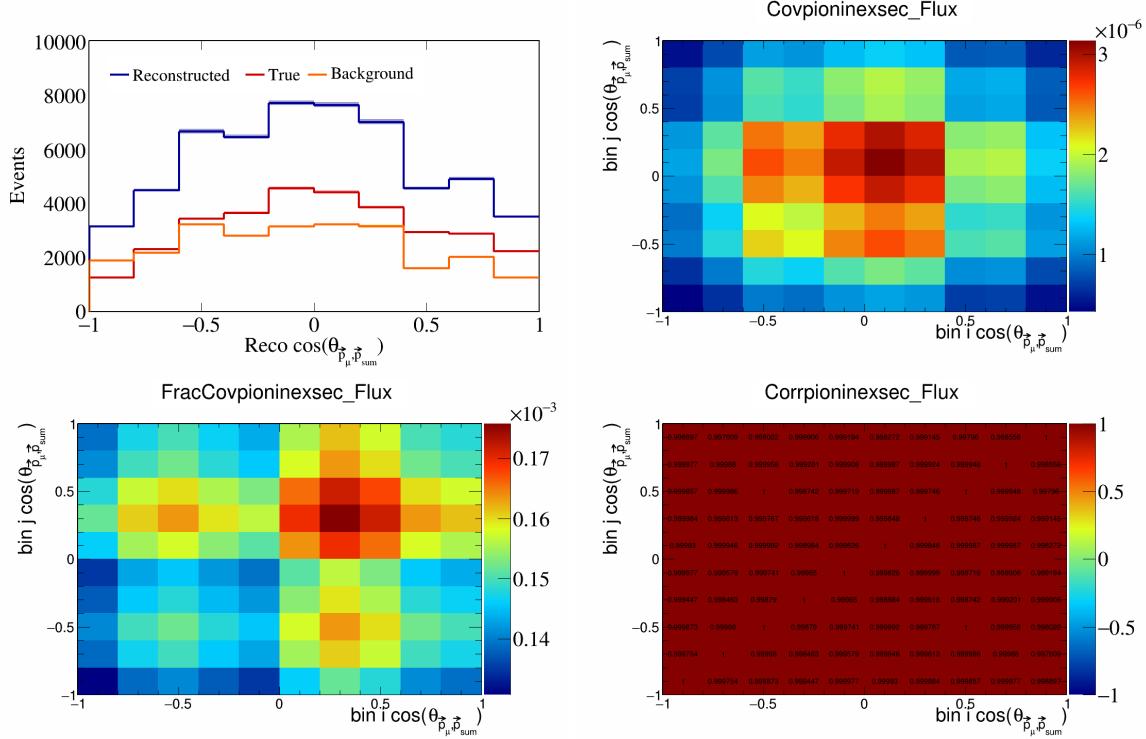


Figure 726: PionIneXSec variations for $\cos(\theta_{\vec{p}_\mu, \vec{p}_{\text{sum}}})$.

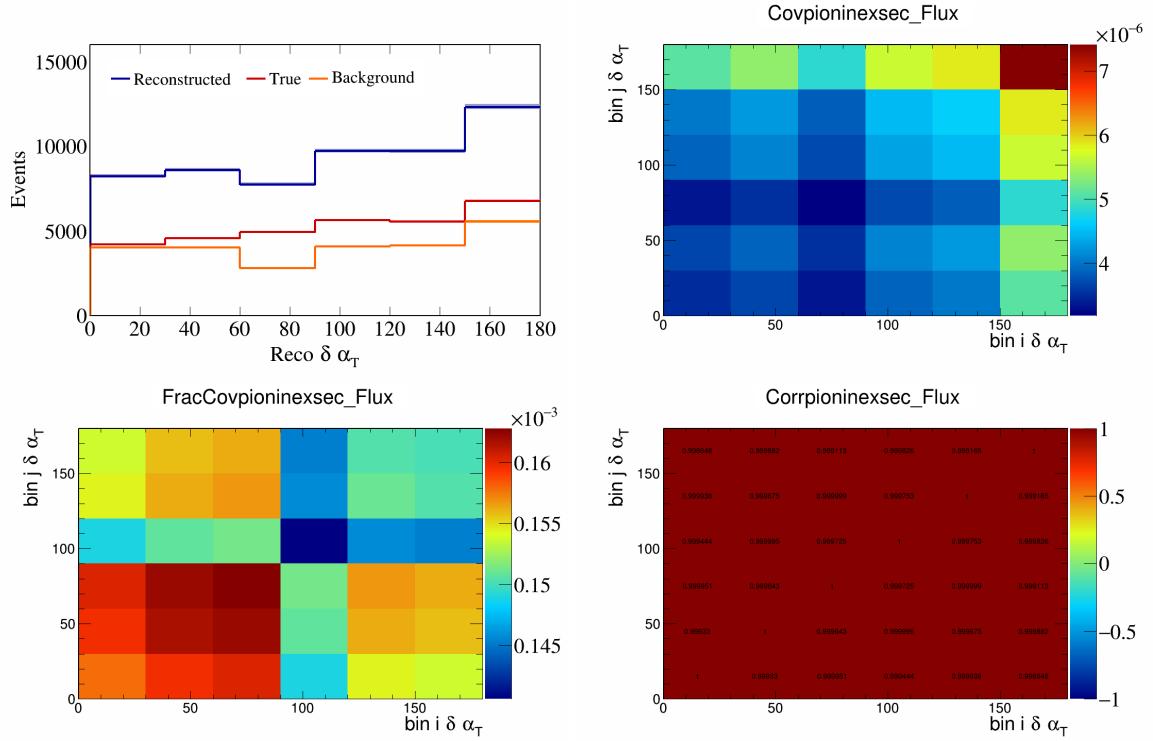


Figure 727: PionIneXSec variations for $\delta\alpha_T$.

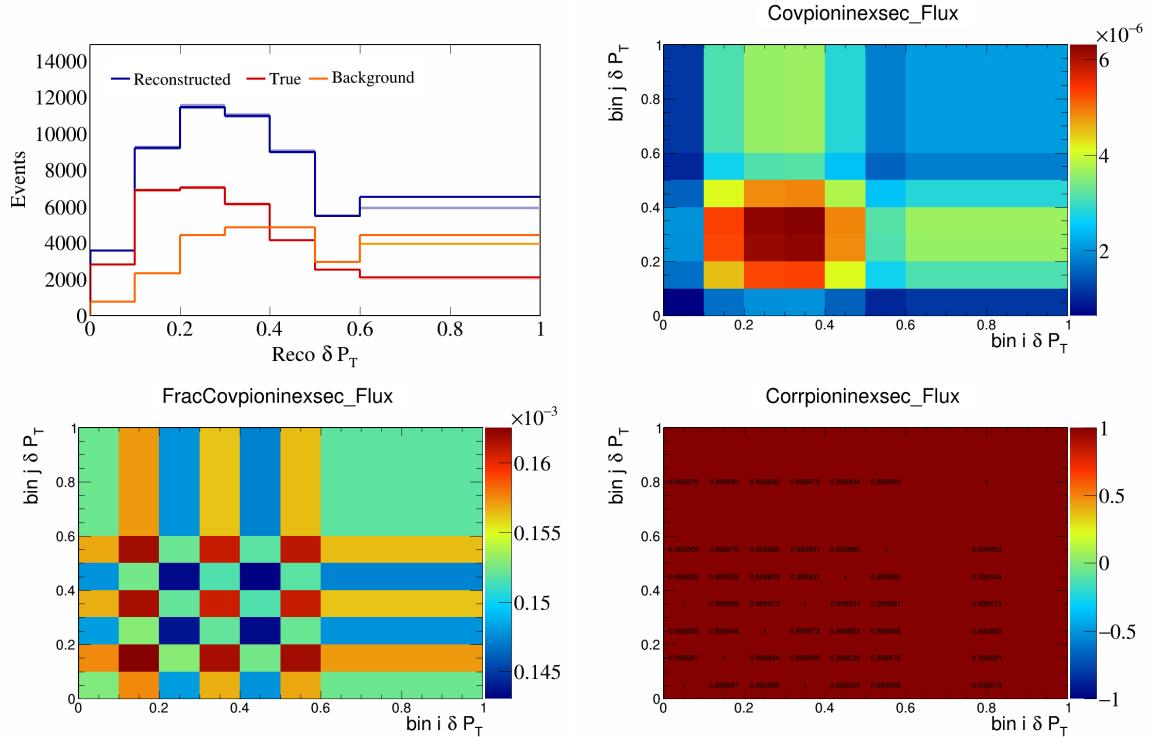


Figure 728: PionIneXSec variations for δP_T .

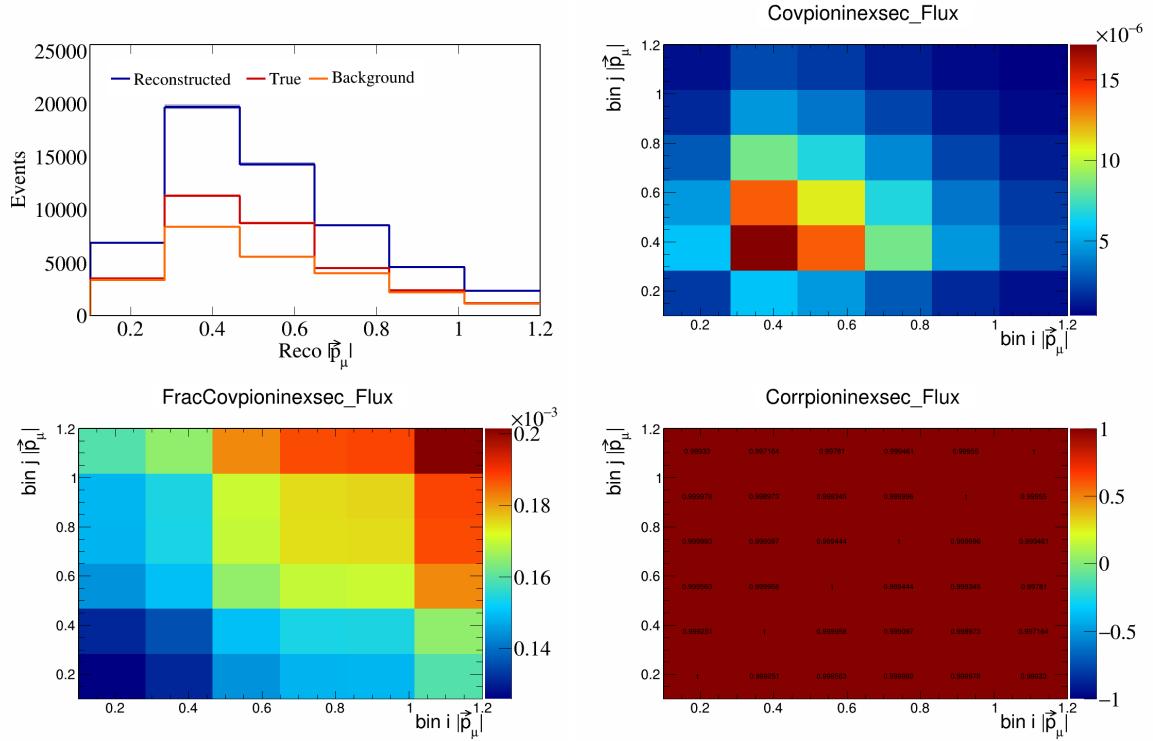


Figure 729: PionIneXSec variations for $|\vec{p}_\mu|$.

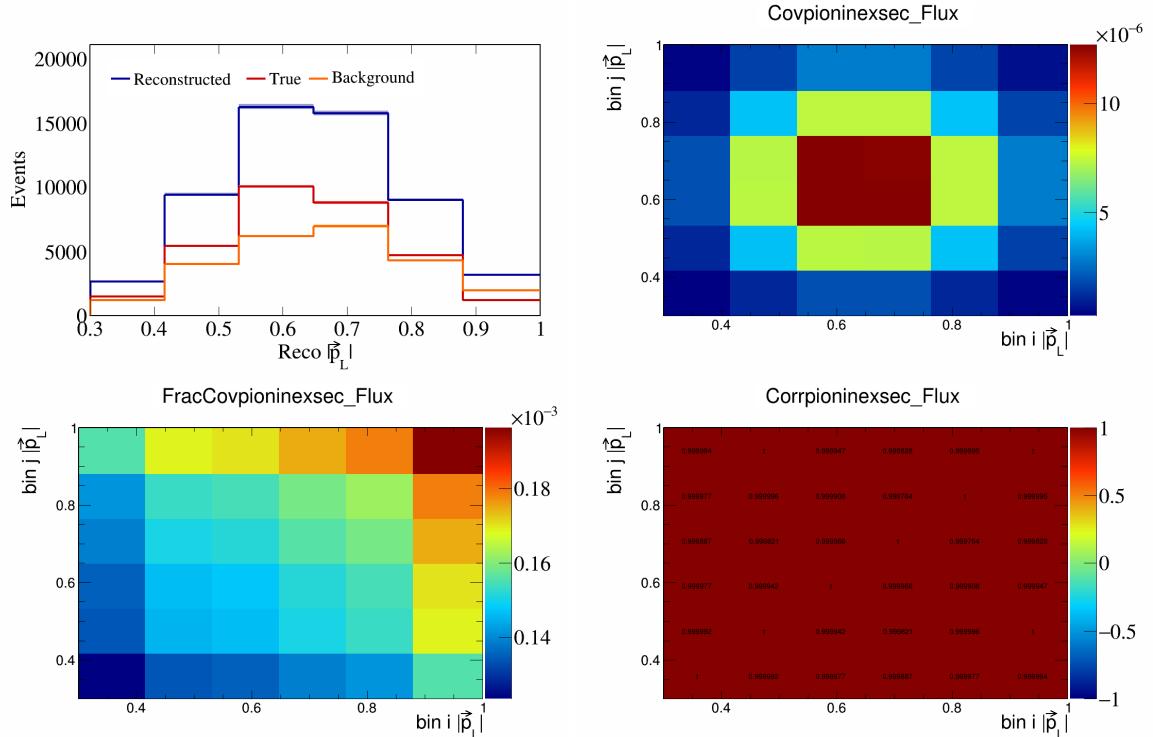


Figure 730: PionIneXSec variations for $|\vec{p}_L|$.

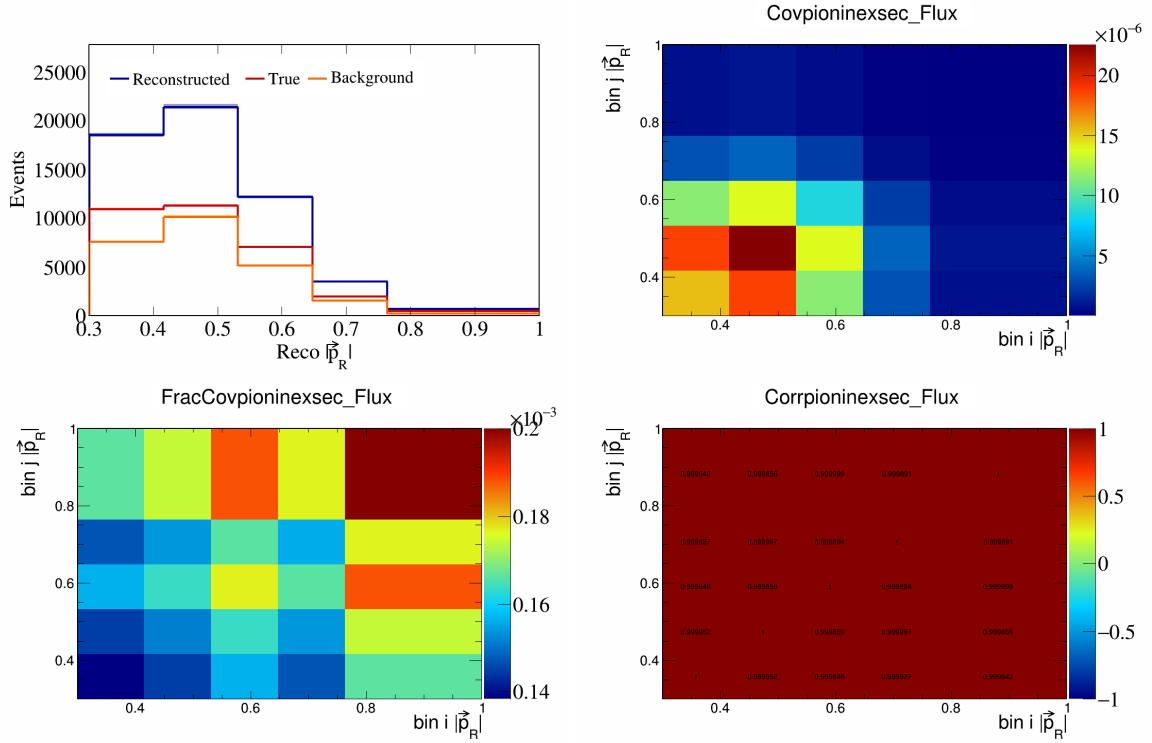


Figure 731: PionIneXSec variations for $|\vec{p}_R|$.

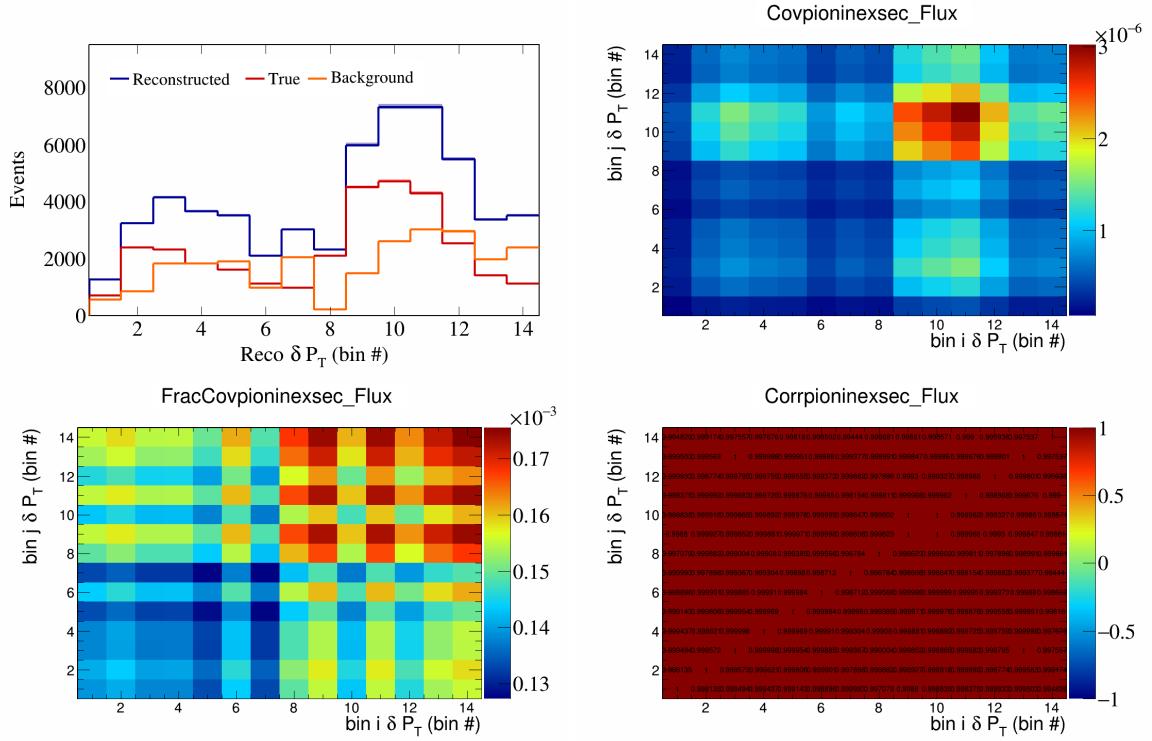


Figure 732: PionIneXSec variations for δP_T in $\cos(\theta_{\vec{p}_\mu})$.

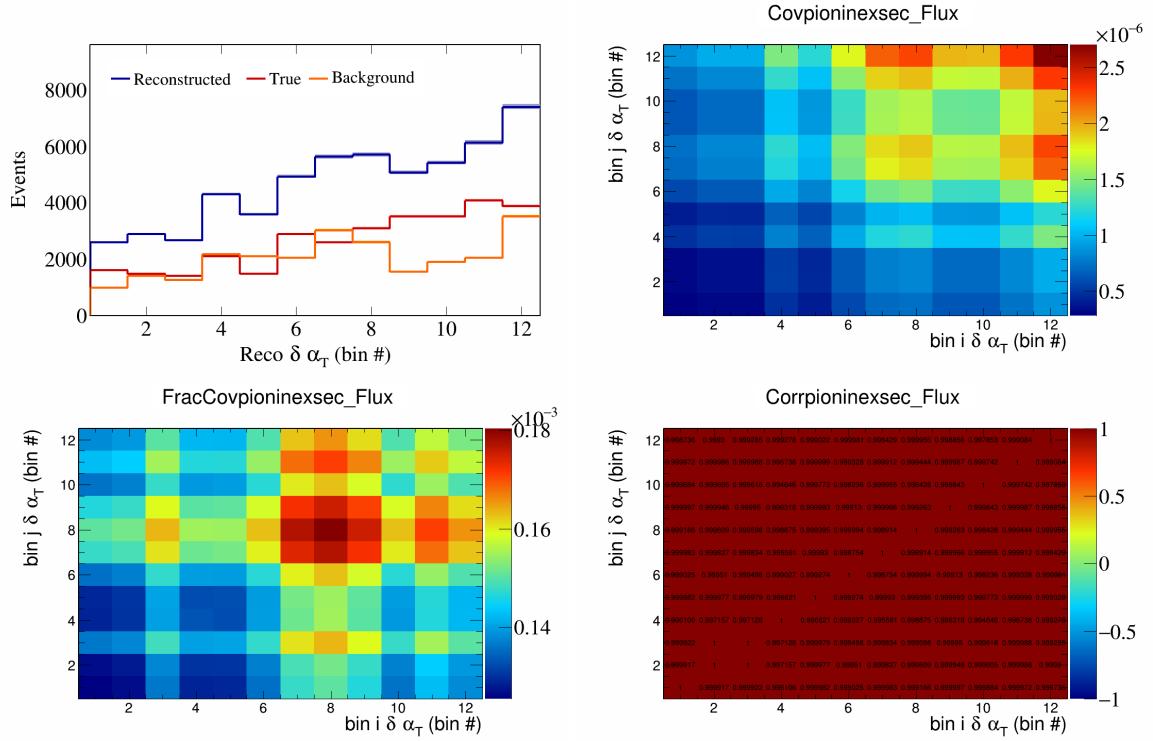


Figure 733: PionIneXSec variations for $\delta \alpha_T$ in $\cos(\theta_{\vec{p}_\mu})$.

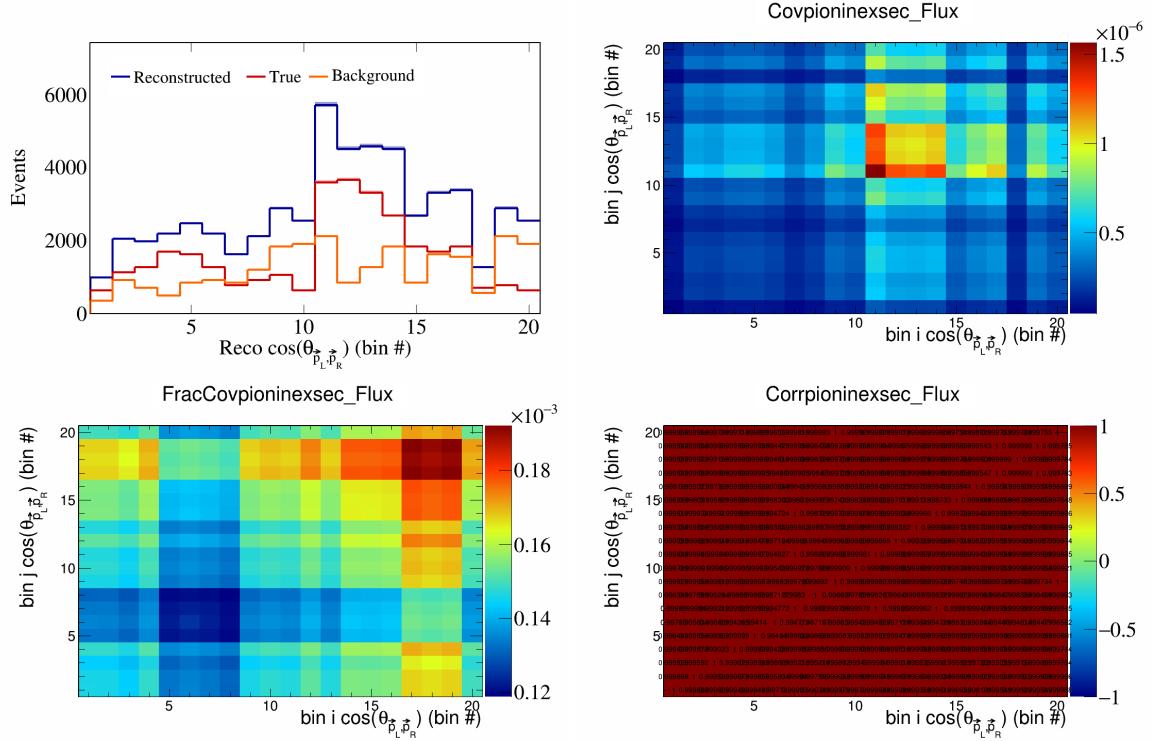


Figure 734: PionIneXSec variations for $\cos(\theta_{\vec{p}_L, \vec{p}_R})$ in $\cos(\theta_{\vec{p}_\mu})$.

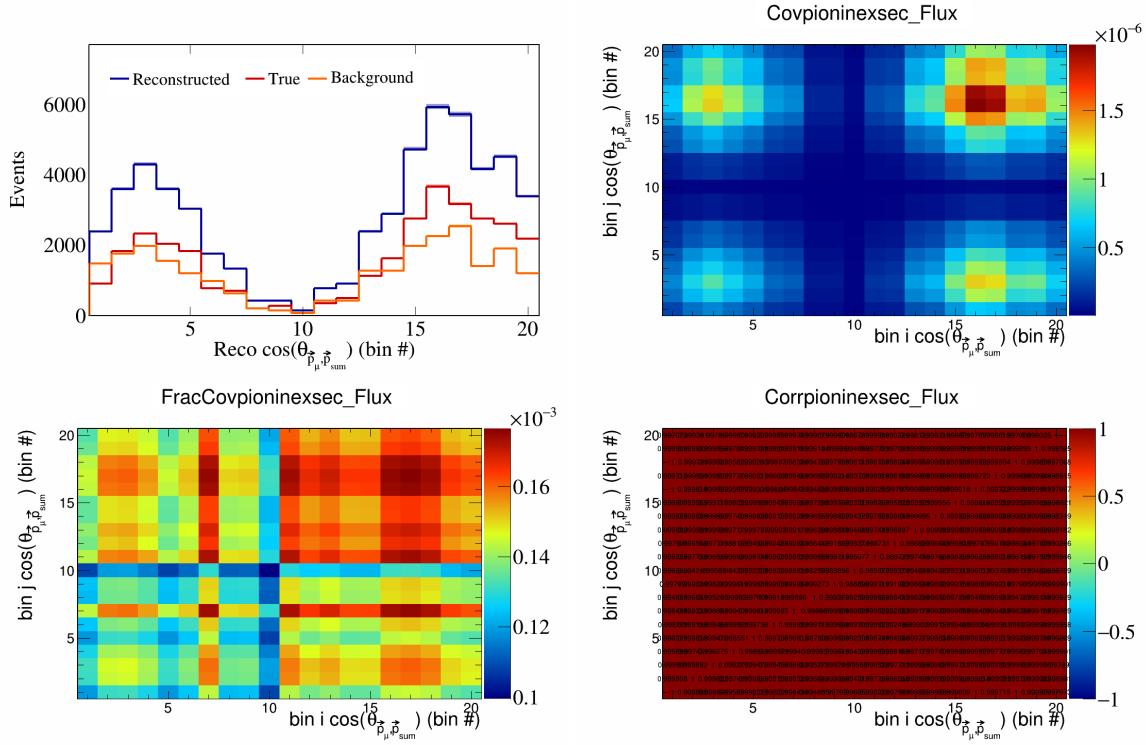


Figure 735: PionIneXSec variations for $\cos(\theta_{\vec{p}_\mu} \cdot \vec{p}_{\text{sum}})$ in $\cos(\theta_{\vec{p}_\mu})$.

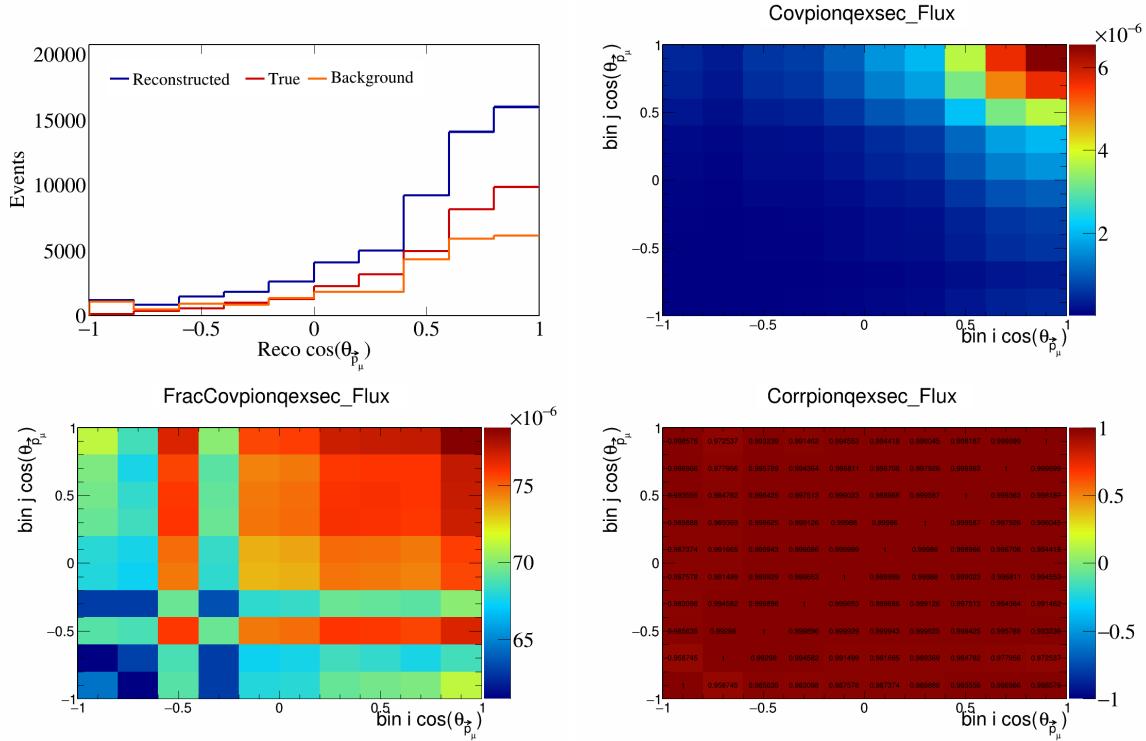


Figure 736: PionQeXSec variations for $\cos(\theta_{\vec{p}_\mu})$.

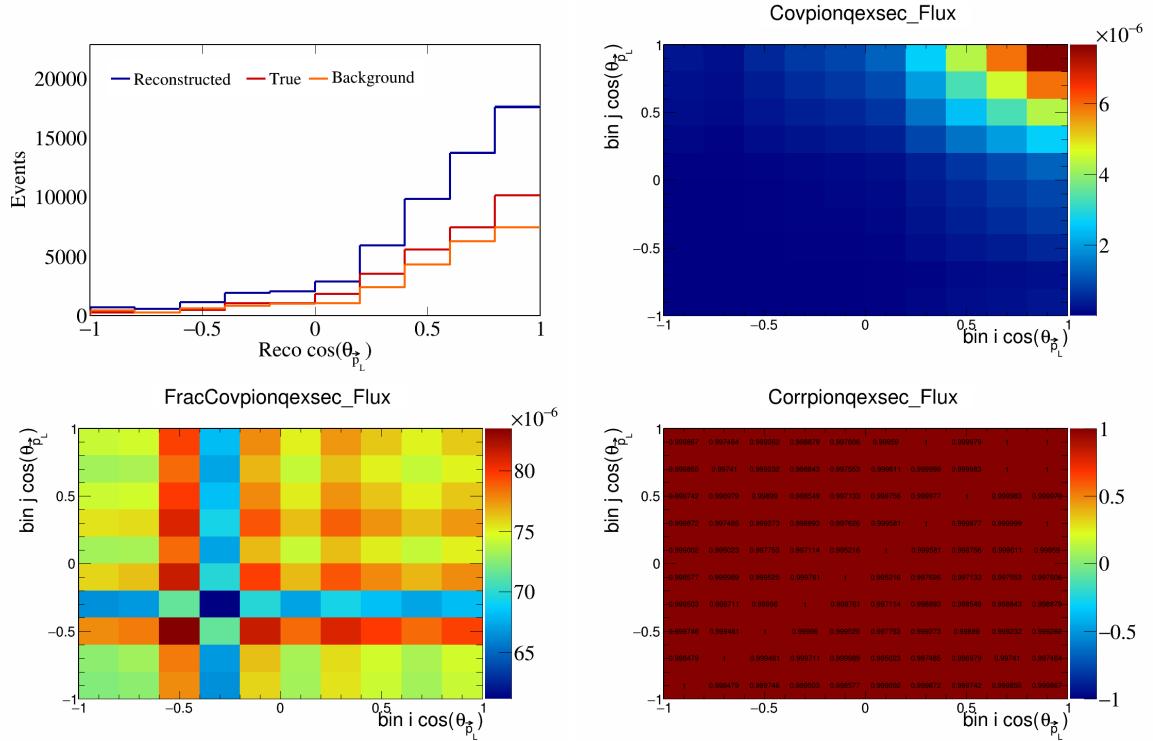


Figure 737: PionQeXSec variations for $\cos(\theta_{\vec{p}_L})$.

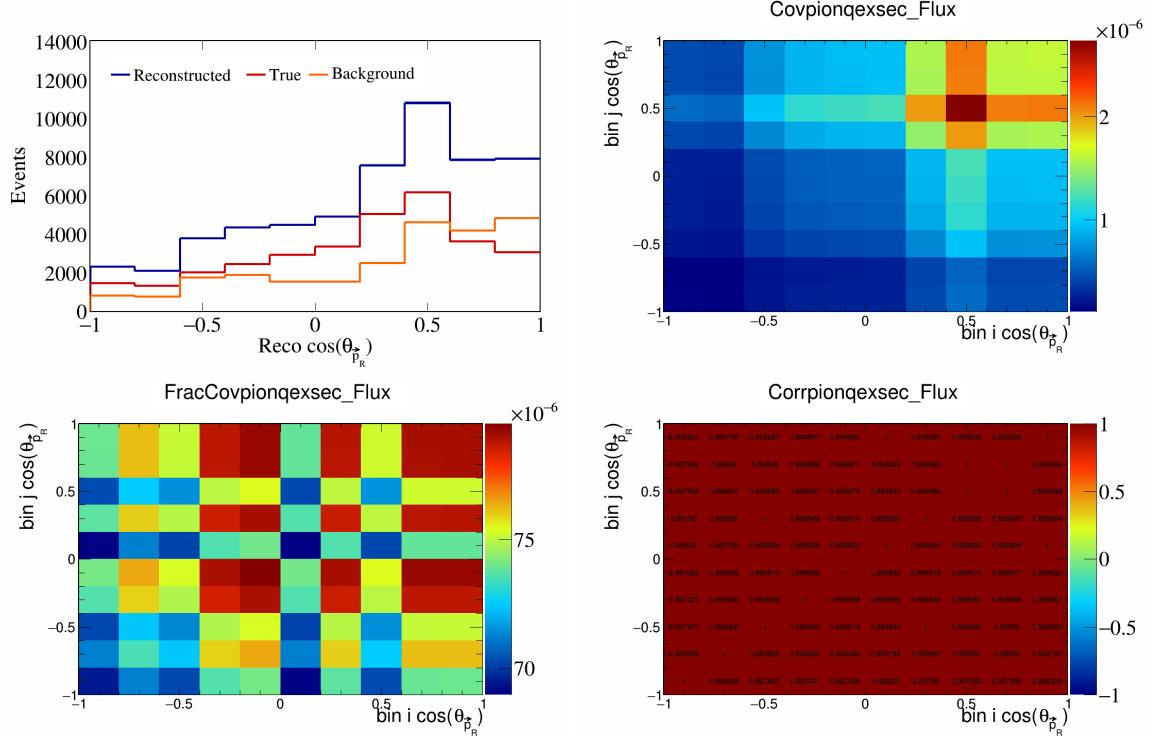


Figure 738: PionQeXSec variations for $\cos(\theta_{\vec{p}_R})$.

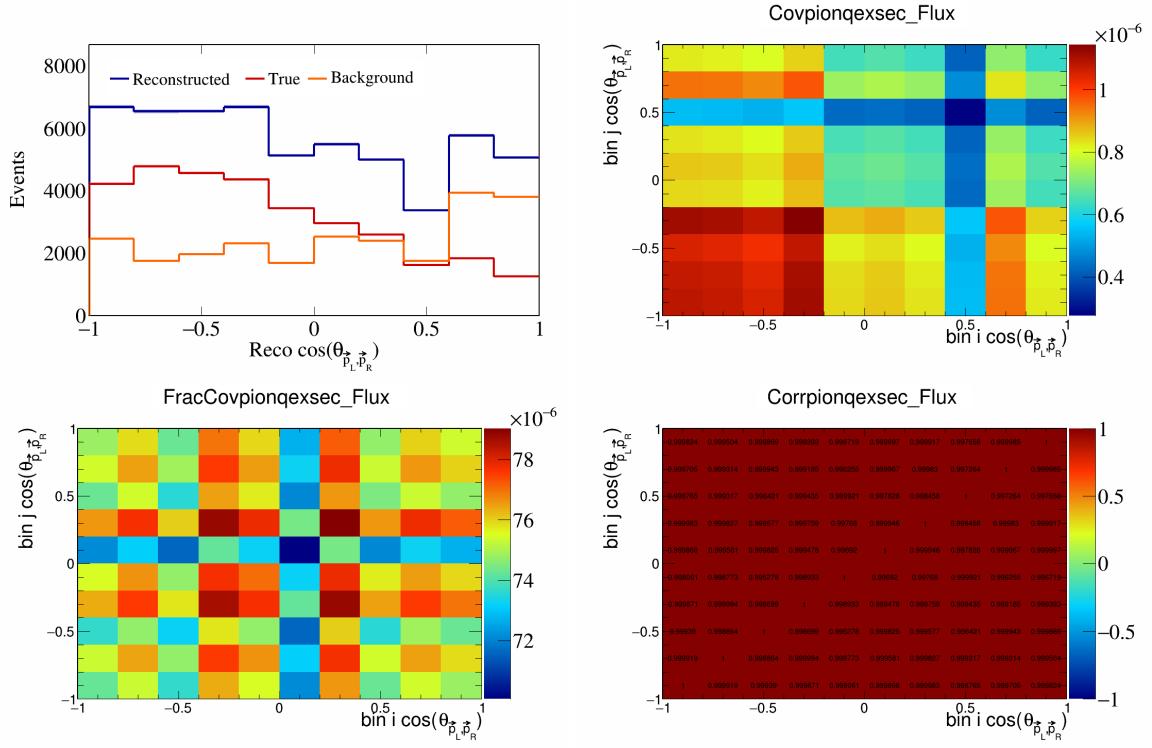


Figure 739: PionQeXSec variations for $\cos(\theta_{\vec{p}_L, \vec{p}_R})$.

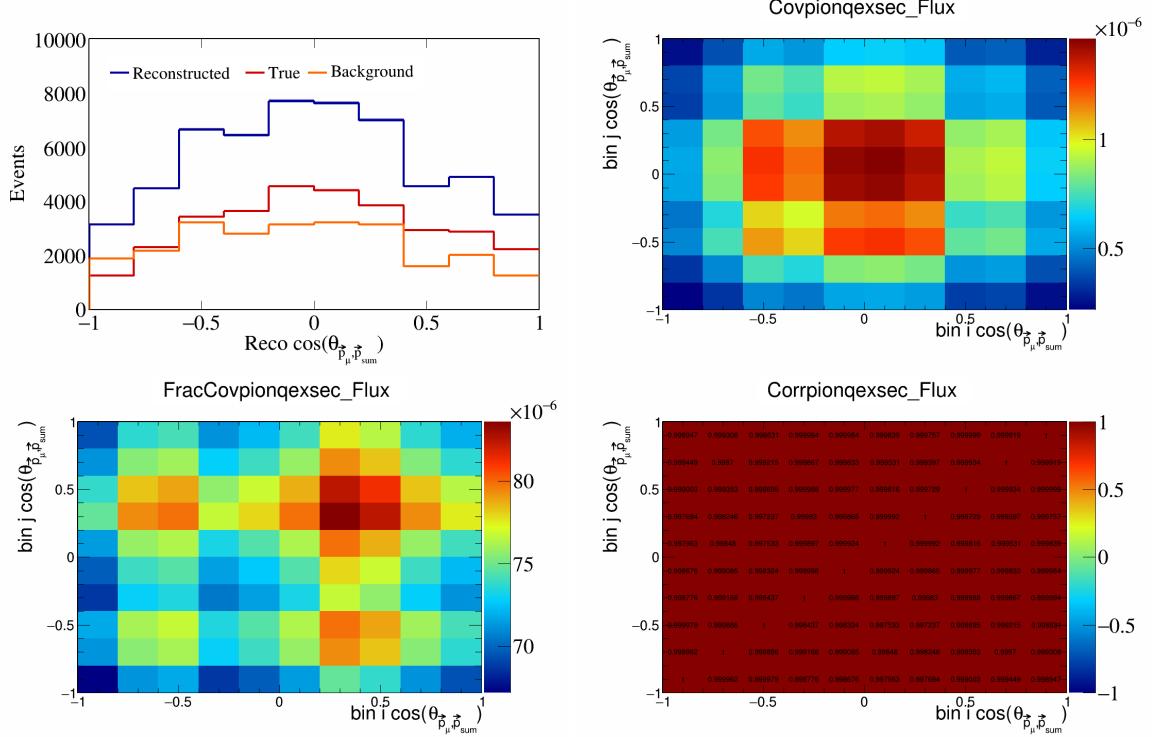


Figure 740: PionQeXSec variations for $\cos(\theta_{\vec{p}_\mu, \vec{p}_{\text{sum}}})$.

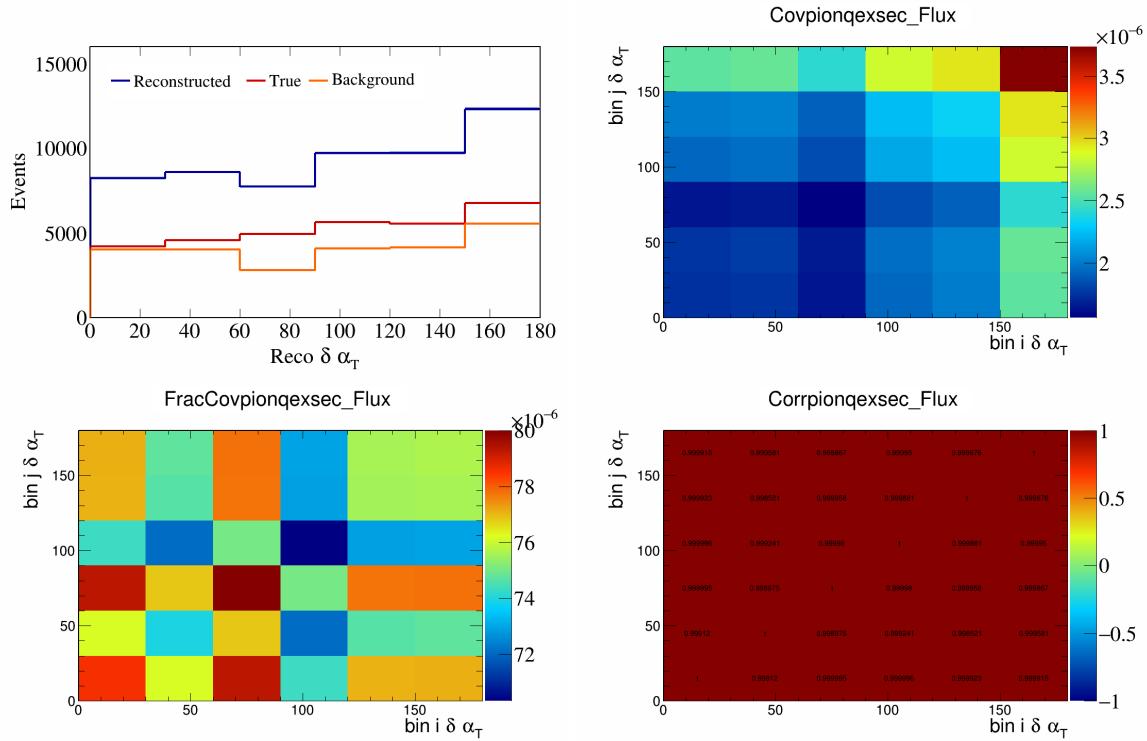


Figure 741: PionQeXSec variations for $\delta\alpha_T$.

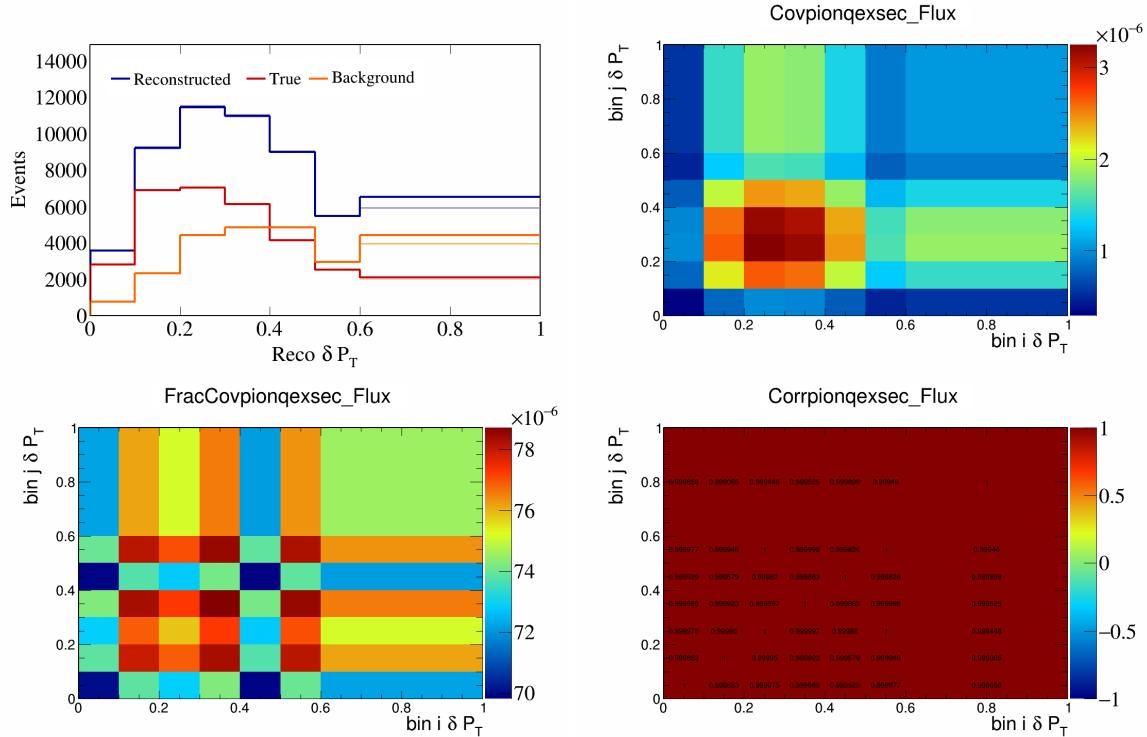


Figure 742: PionQeXSec variations for δP_T .

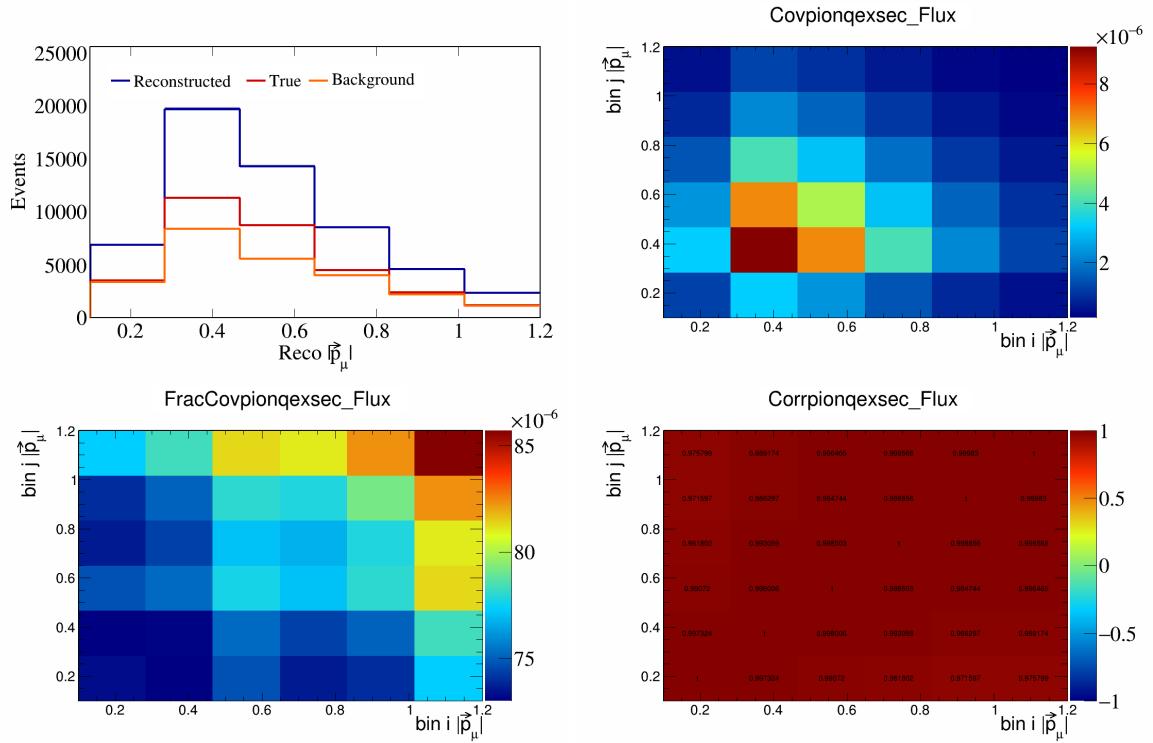


Figure 743: PionQeXSec variations for $|\vec{p}_\mu|$.

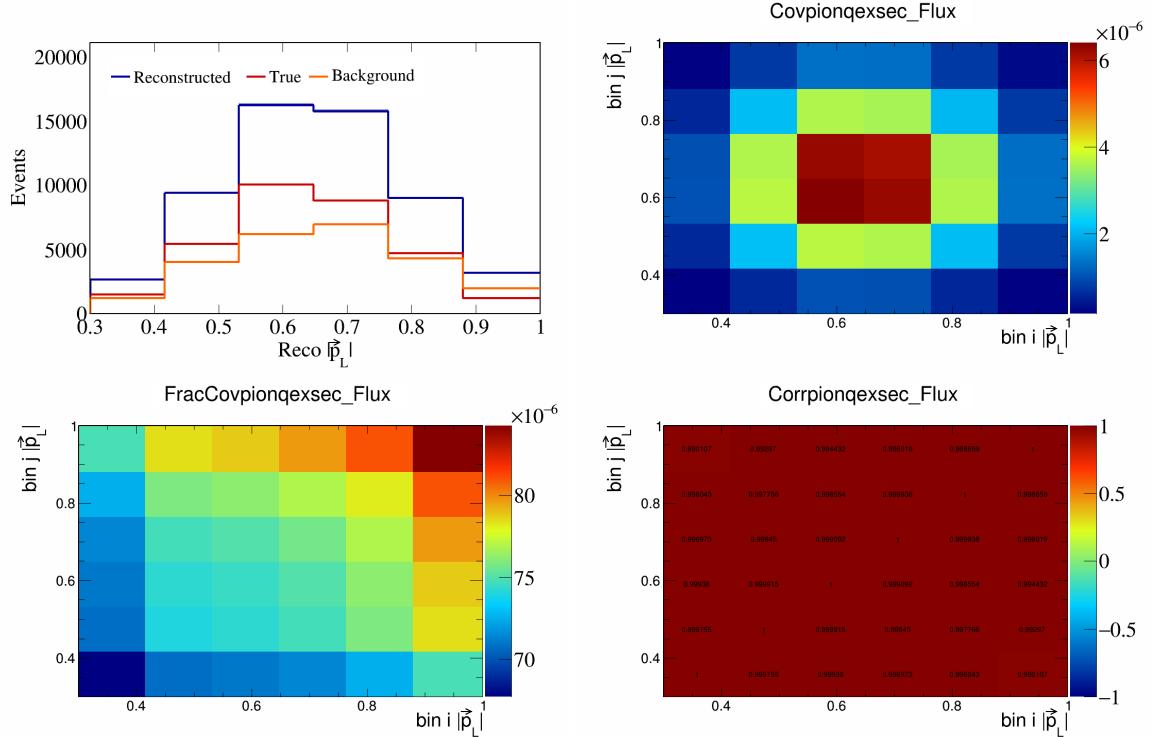


Figure 744: PionQeXSec variations for $|\vec{p}_L|$.

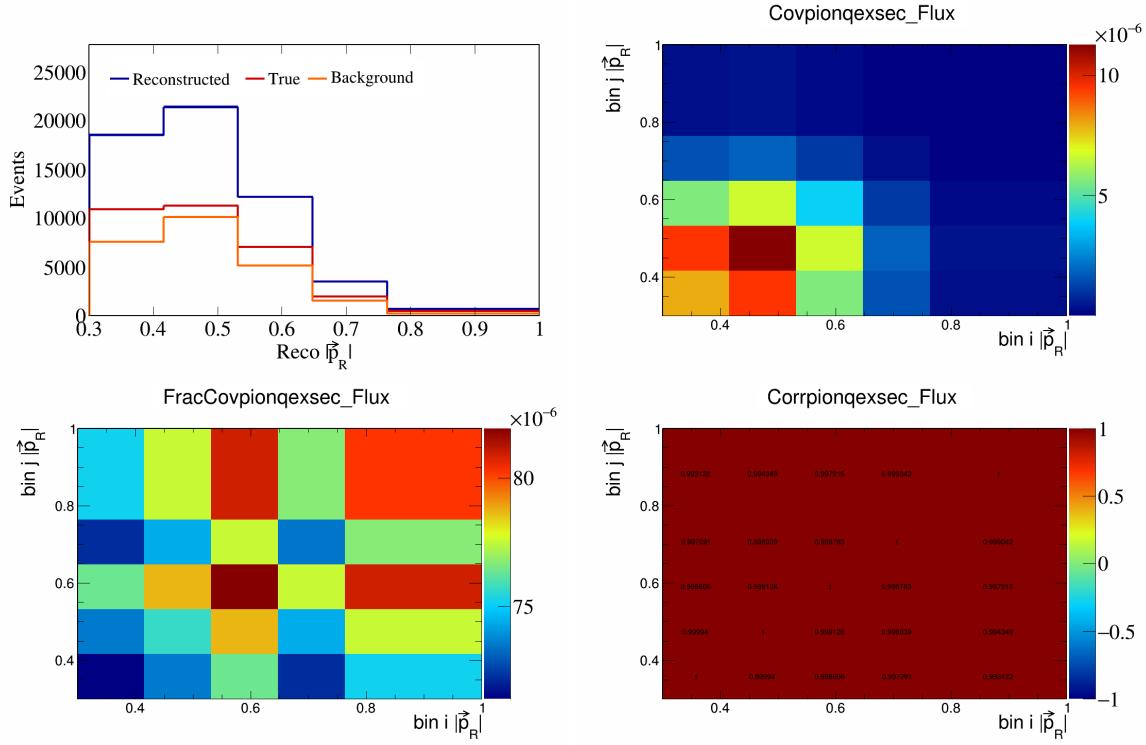


Figure 745: PionQeXSec variations for $|\vec{p}_R|$.

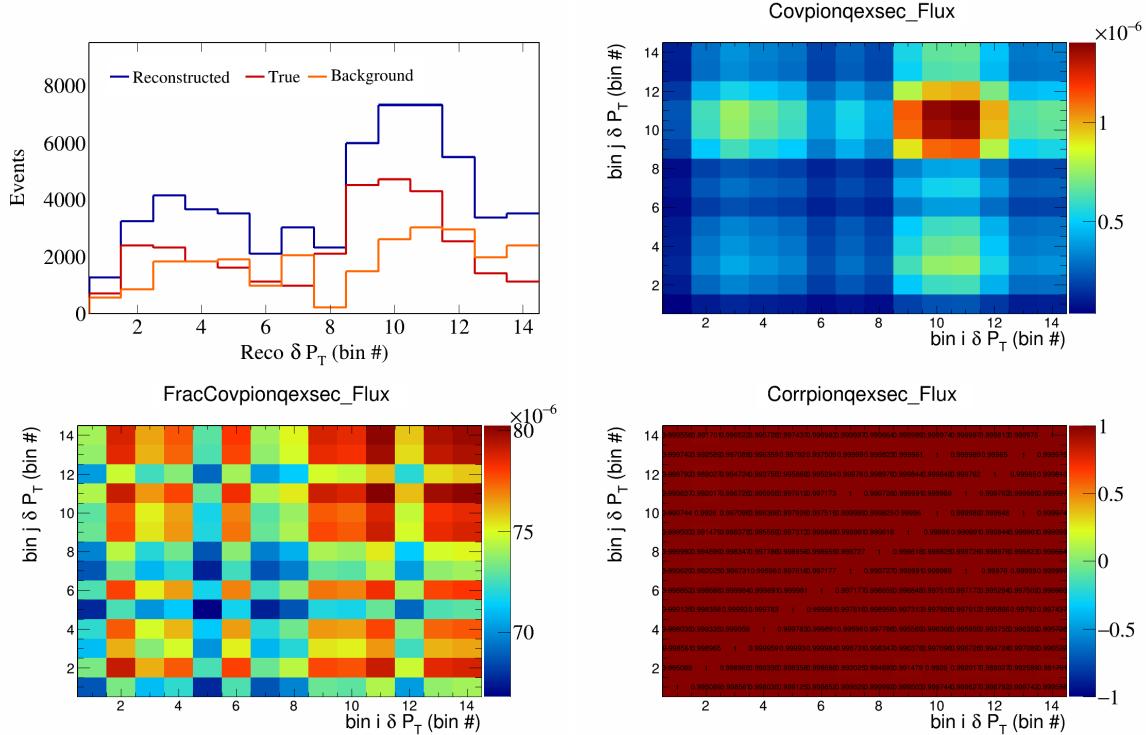


Figure 746: PionQeXSec variations for δP_T in $\cos(\theta_{\vec{p}_\mu})$.

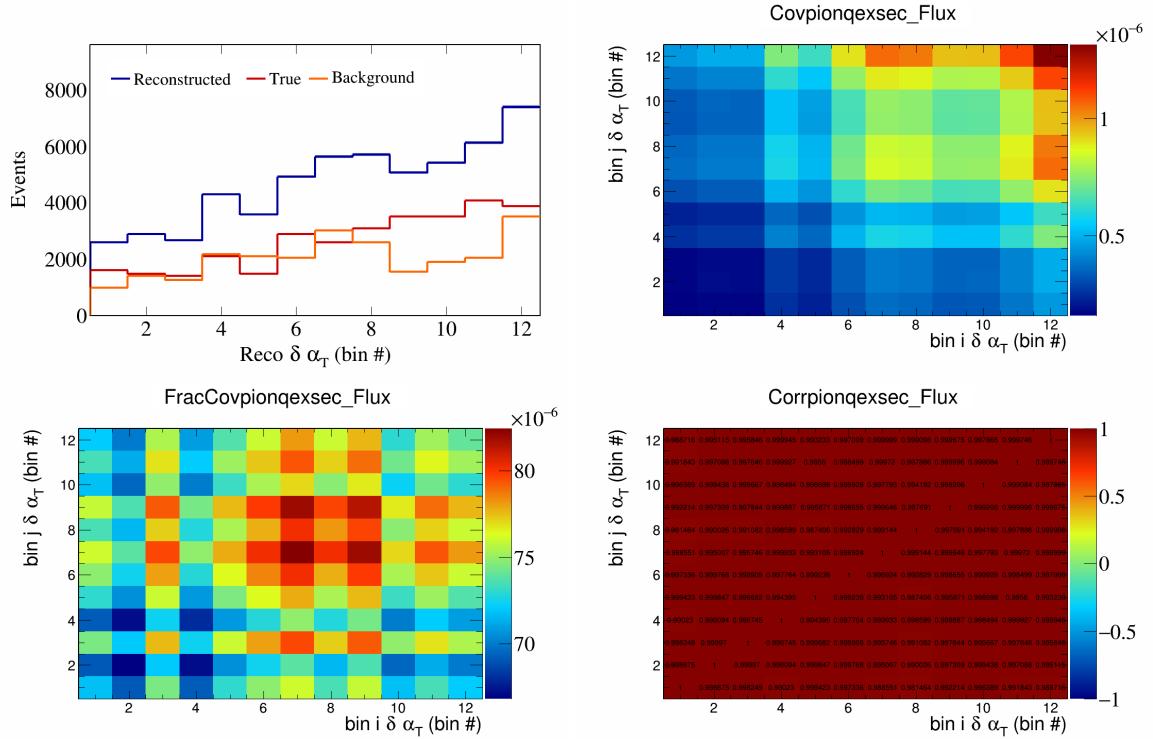


Figure 747: PionQeXSec variations for $\delta \alpha_T$ in $\cos(\theta_{\vec{p}_\mu})$.

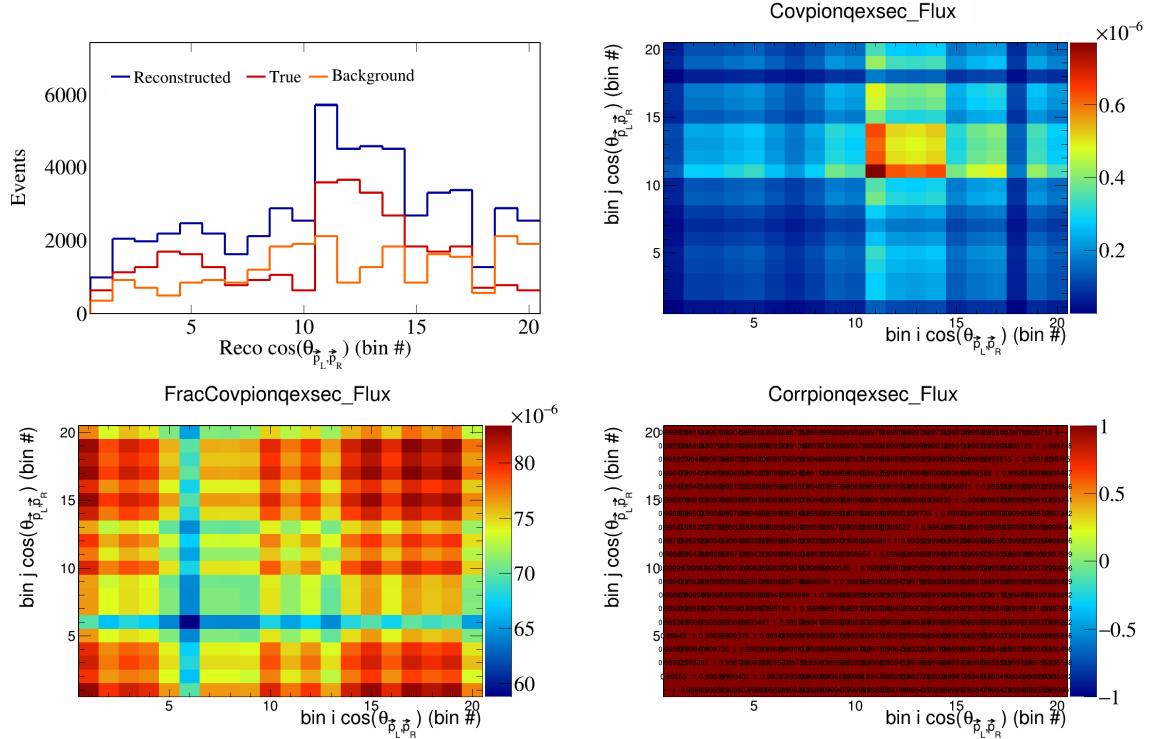


Figure 748: PionQeXSec variations for $\cos(\theta_{\vec{p}_L, \vec{p}_R})$ in $\cos(\theta_{\vec{p}_\mu})$.

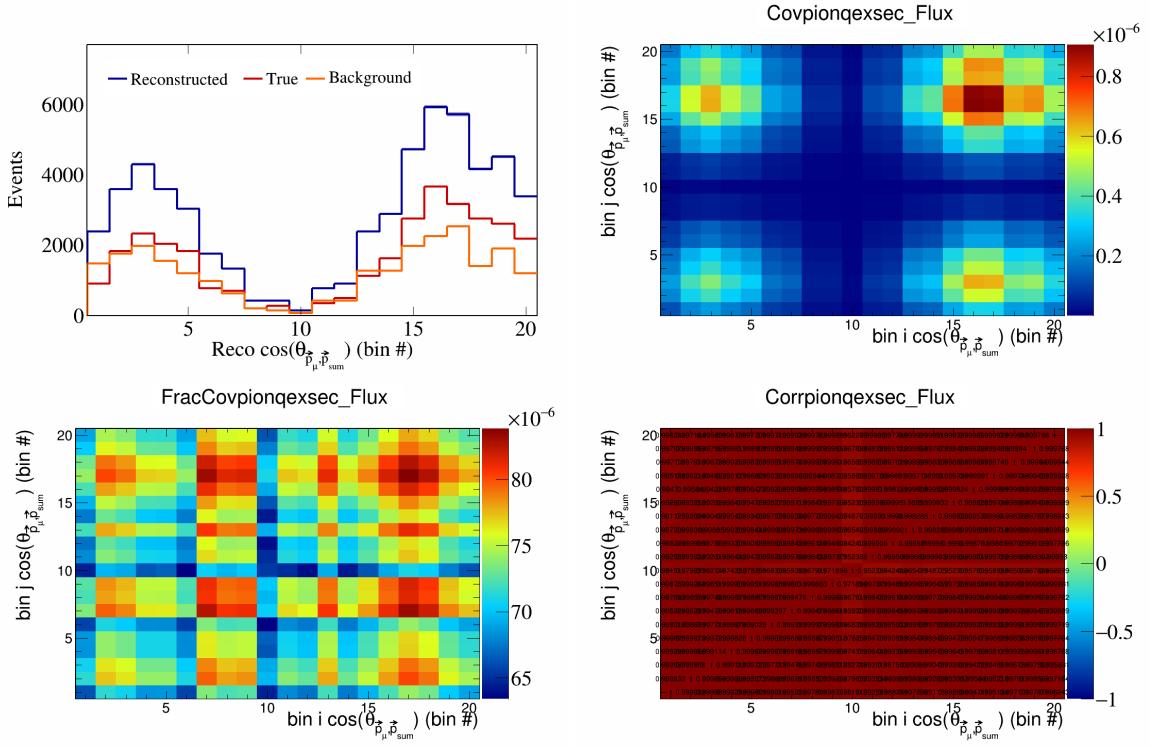


Figure 749: PionQeXSec variations for $\cos(\theta_{\vec{p}_\mu, \vec{p}_{\text{sum}}})$ in $\cos(\theta_{\vec{p}_\mu})$.

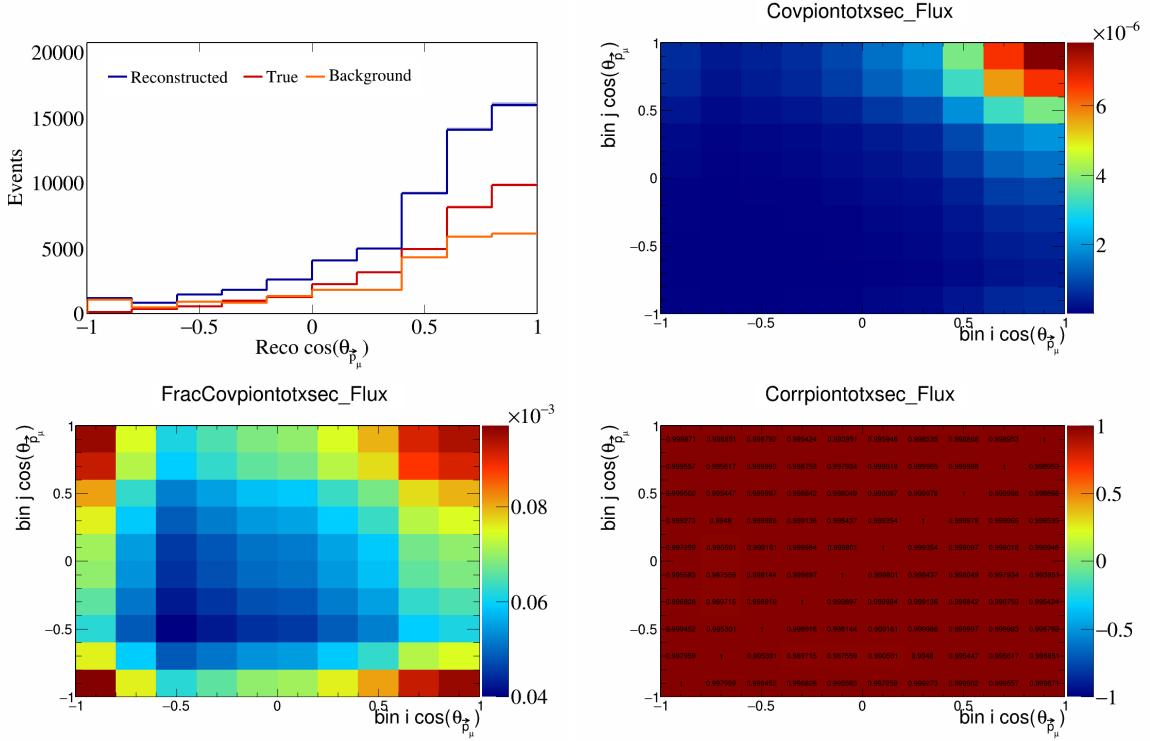


Figure 750: PionTotXSec variations for $\cos(\theta_{\vec{p}_\mu})$.

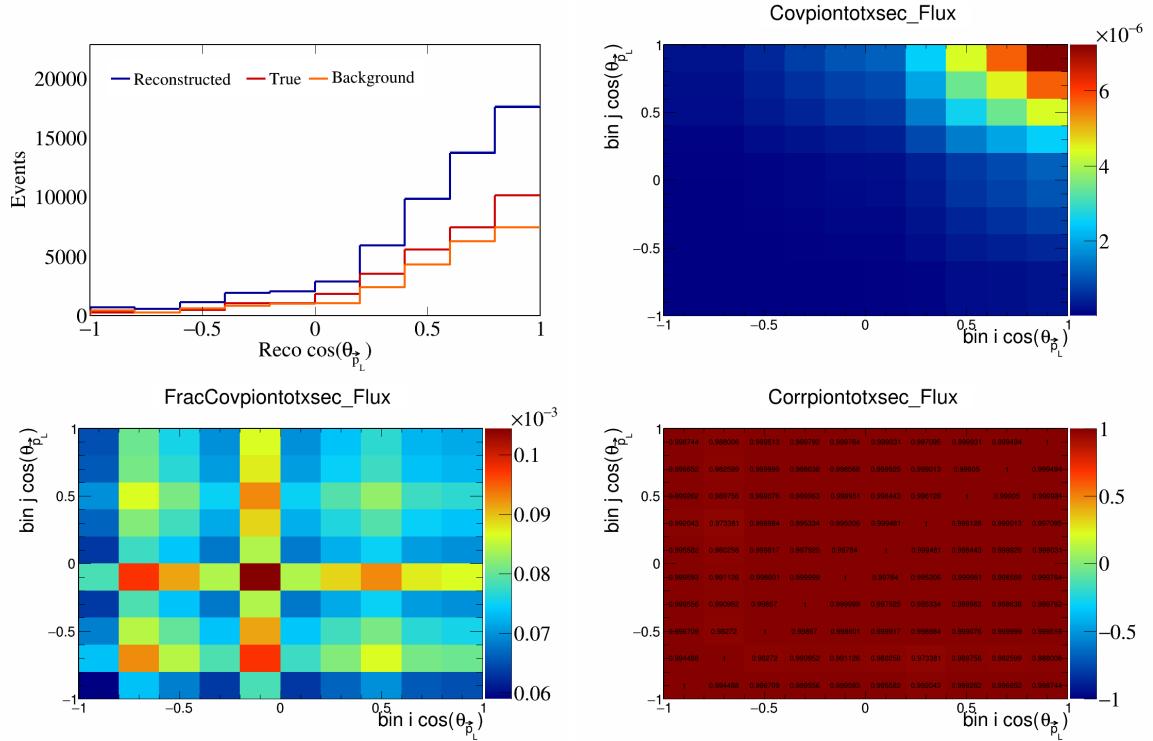


Figure 751: PionTotXSec variations for $\cos(\theta_{\vec{p}_L})$.

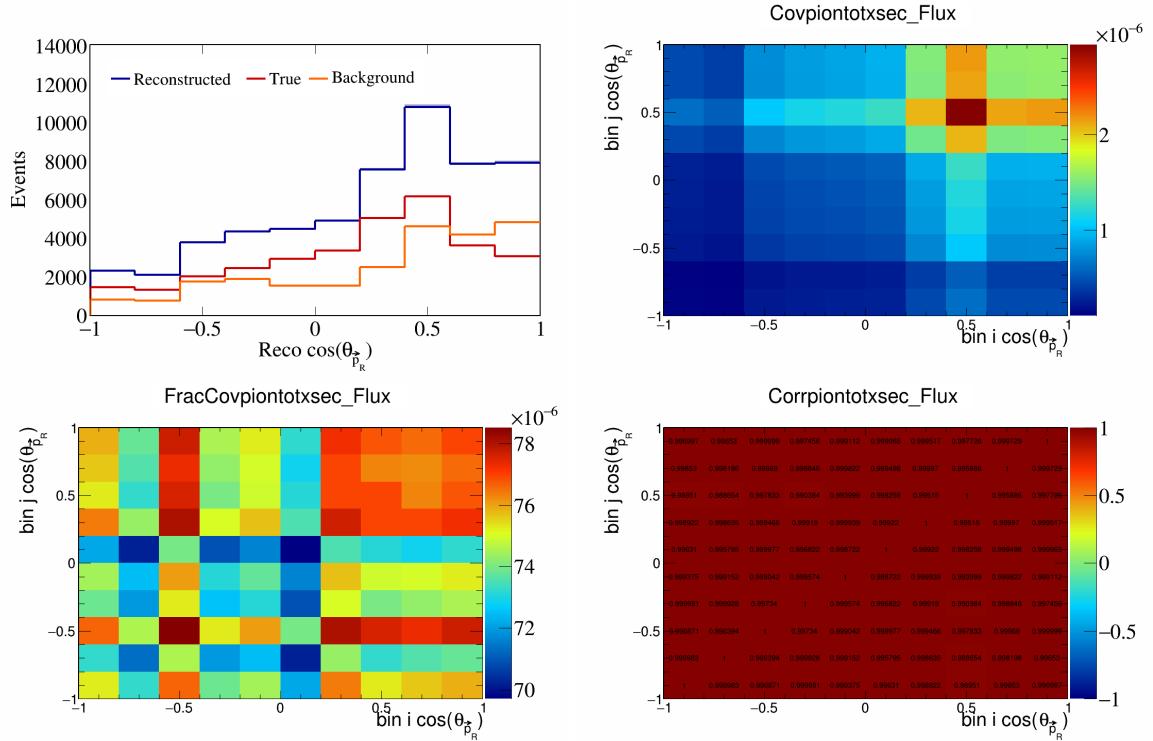


Figure 752: PionTotXSec variations for $\cos(\theta_{\vec{p}_R})$.

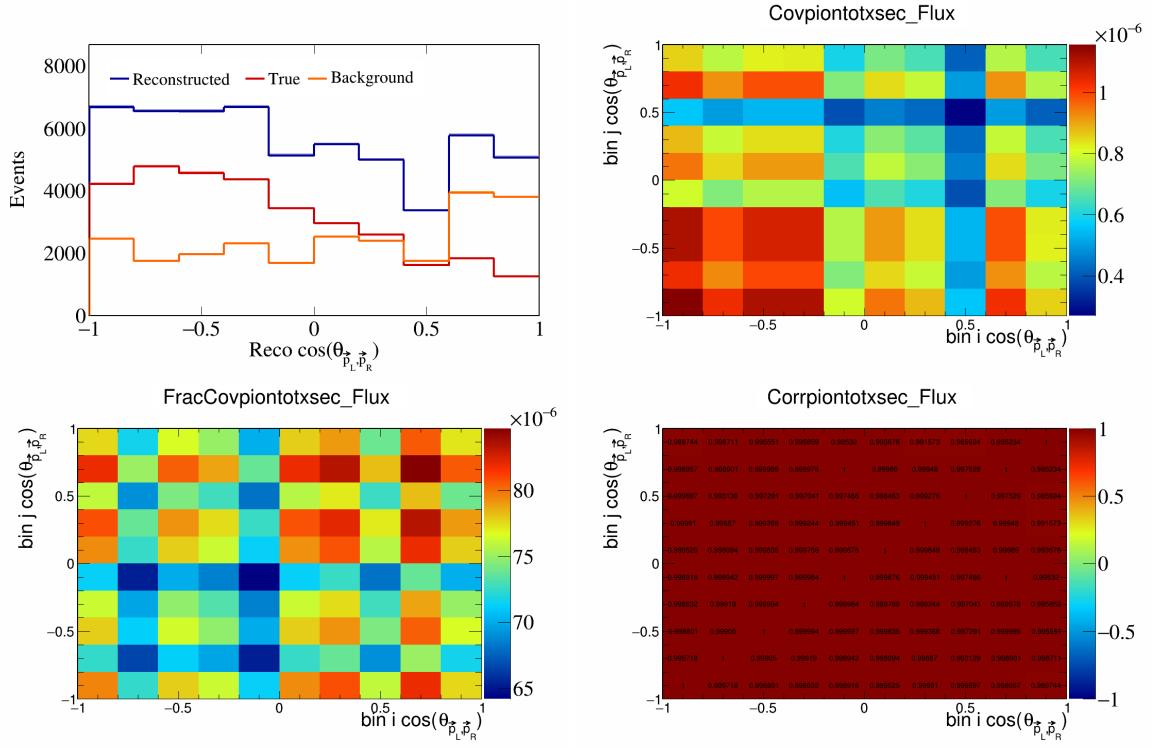


Figure 753: PionTotXSec variations for $\cos(\theta_{\vec{p}_L, \vec{p}_R})$.

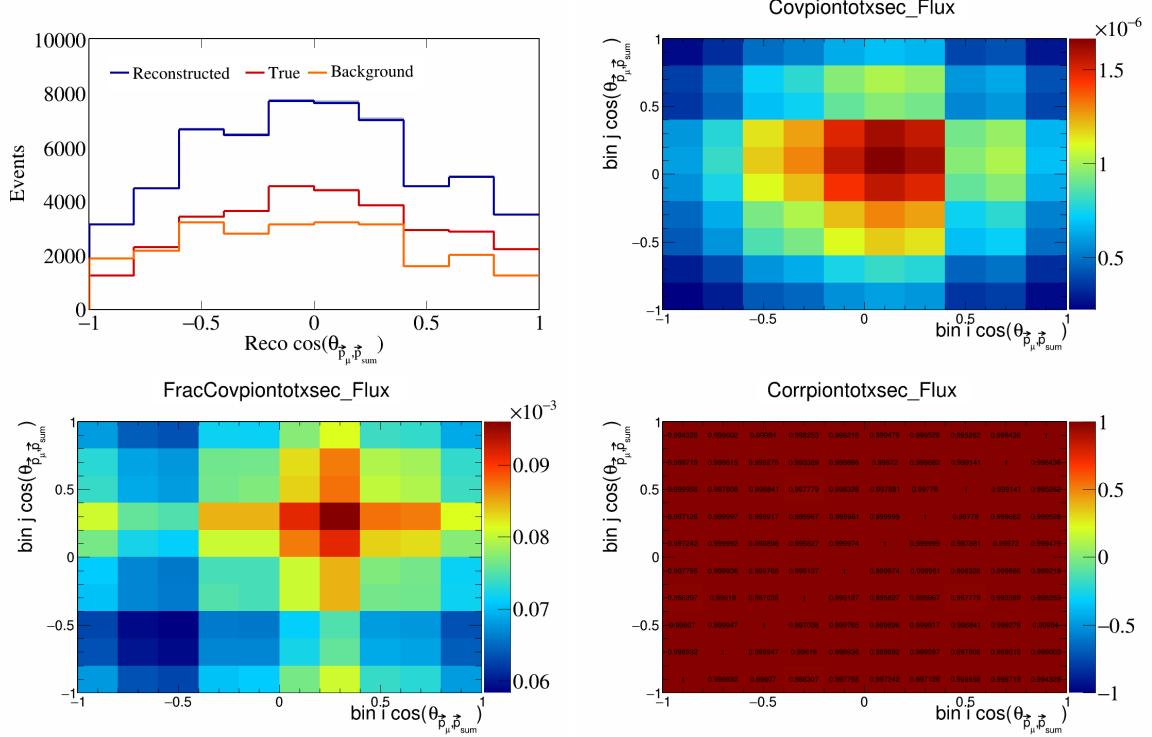


Figure 754: PionTotXSec variations for $\cos(\theta_{\vec{p}_\mu, \vec{p}_{\text{sum}}})$.

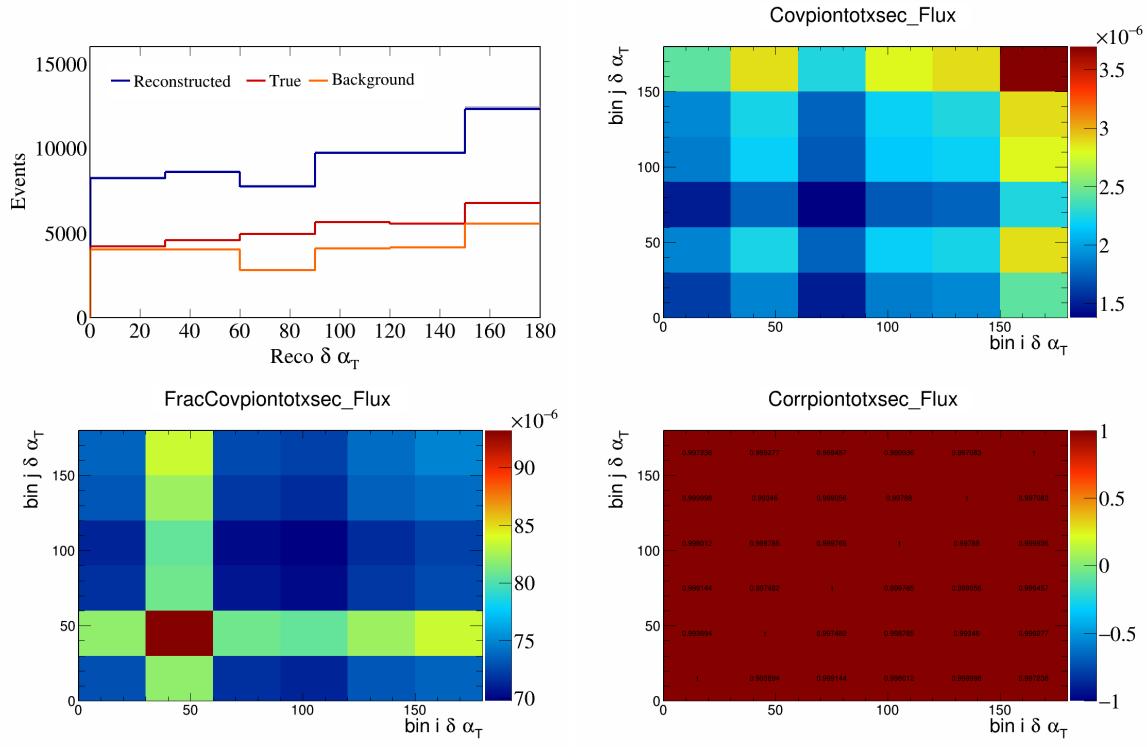


Figure 755: PionTotXSec variations for $\delta\alpha_T$.

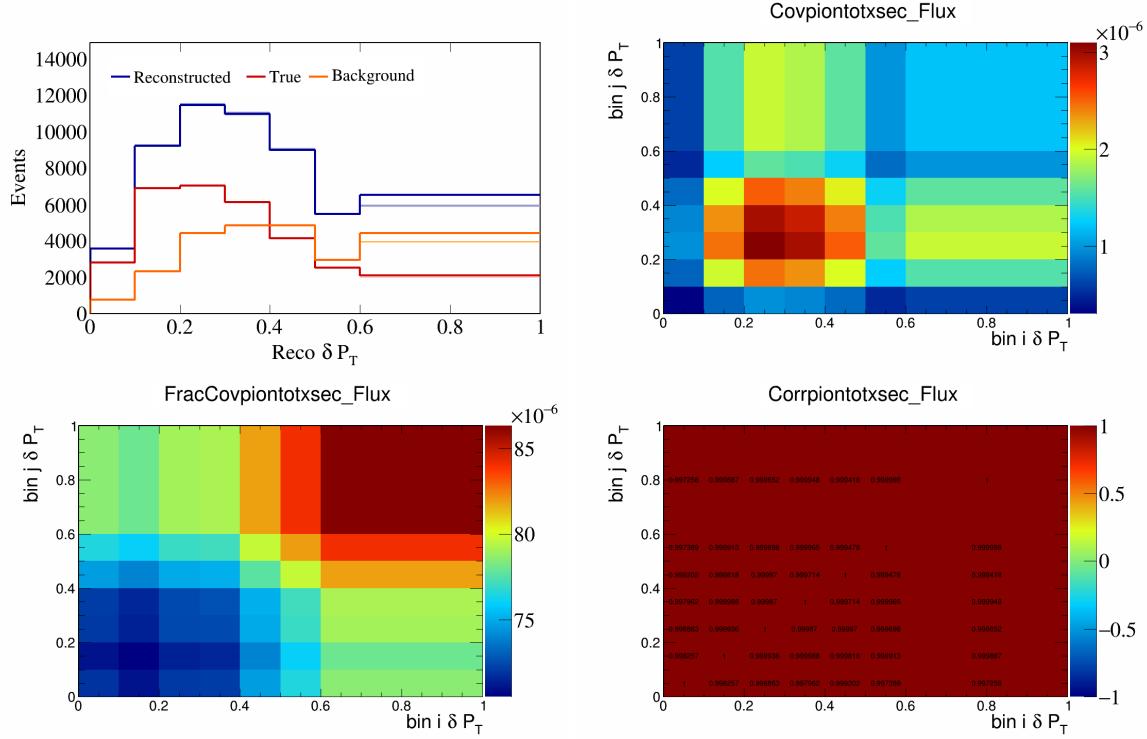


Figure 756: PionTotXSec variations for δP_T .

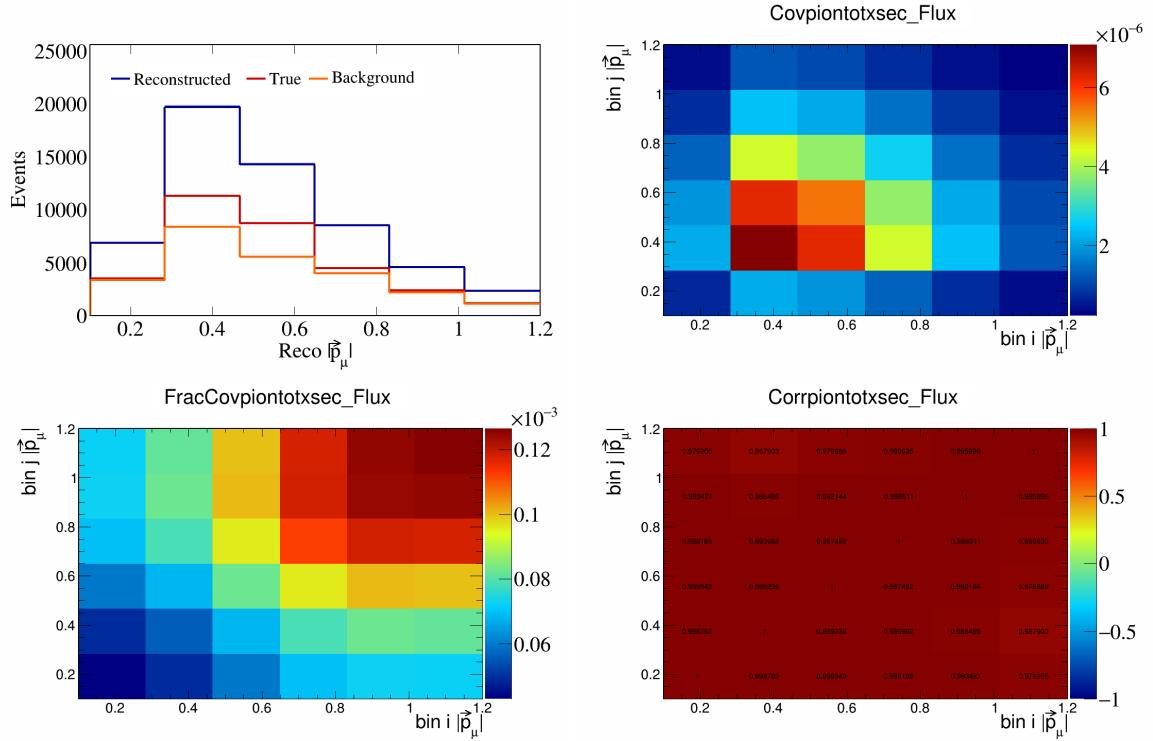


Figure 757: PionTotXSec variations for $|\vec{p}_\mu|$.

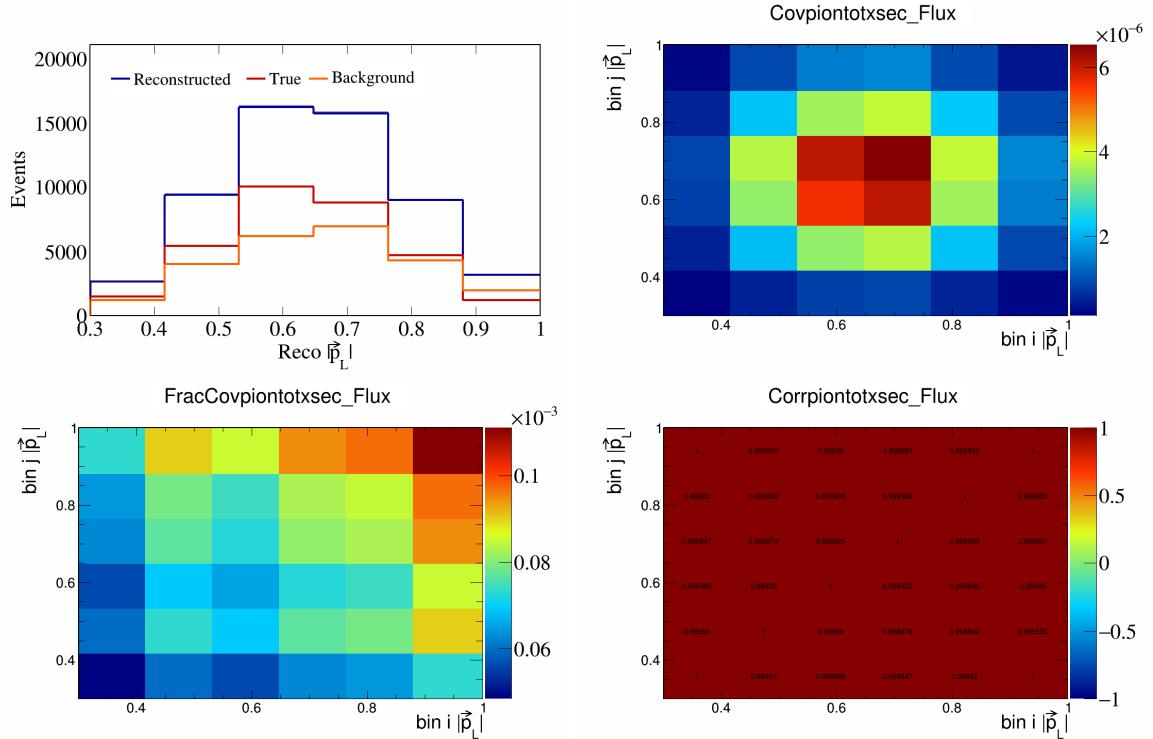


Figure 758: PionTotXSec variations for $|\vec{p}_L|$.

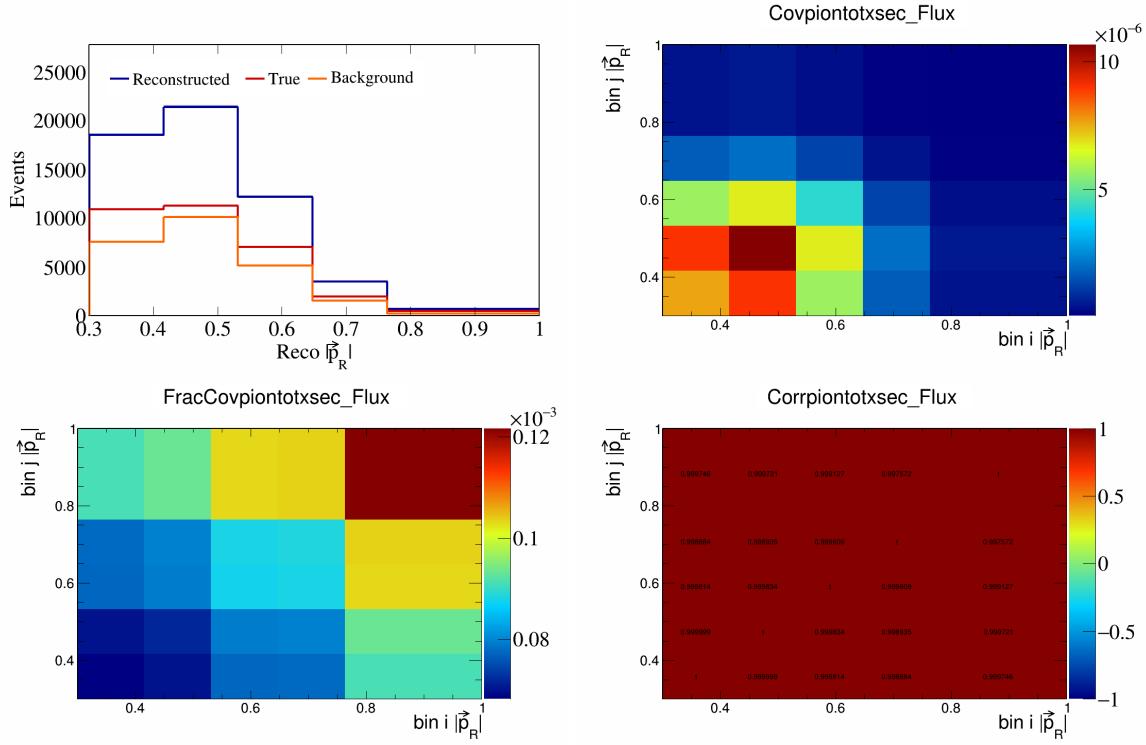


Figure 759: PionTotXSec variations for $|\vec{p}_R|$.

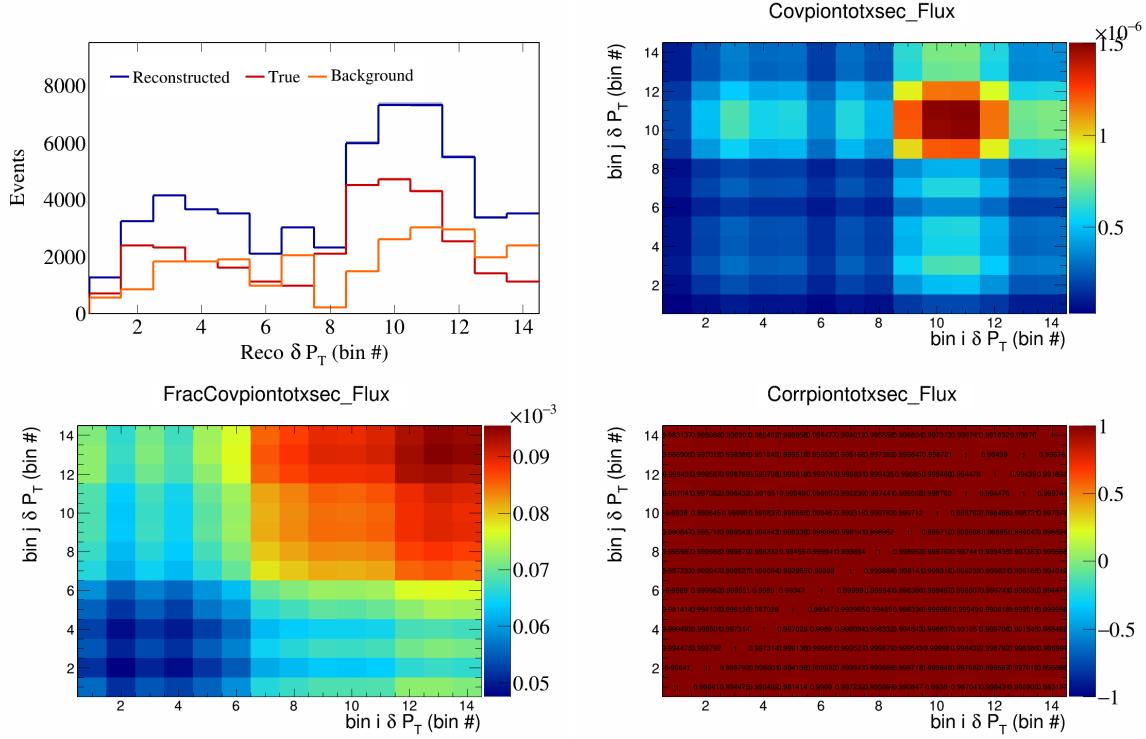


Figure 760: PionTotXSec variations for δP_T in $\cos(\theta_{\vec{p}_\mu})$.

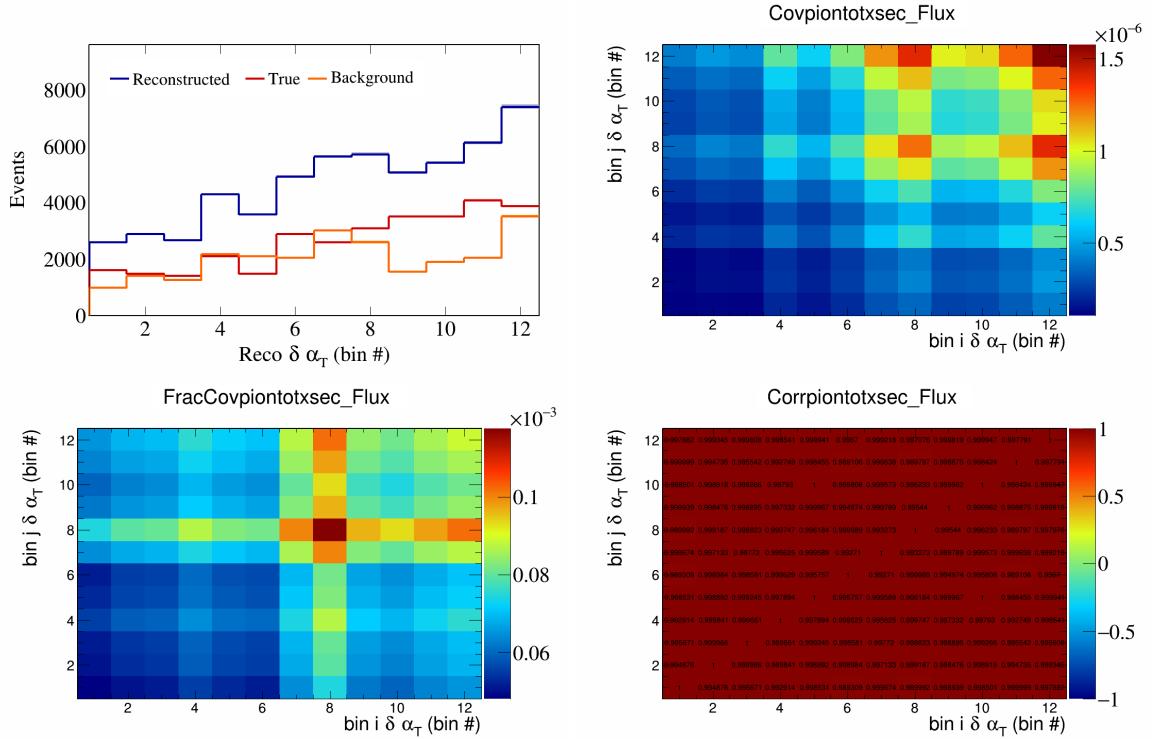


Figure 761: PionTotXSec variations for $\delta \alpha_T$ in $\cos(\theta_{\vec{p}_\mu})$.

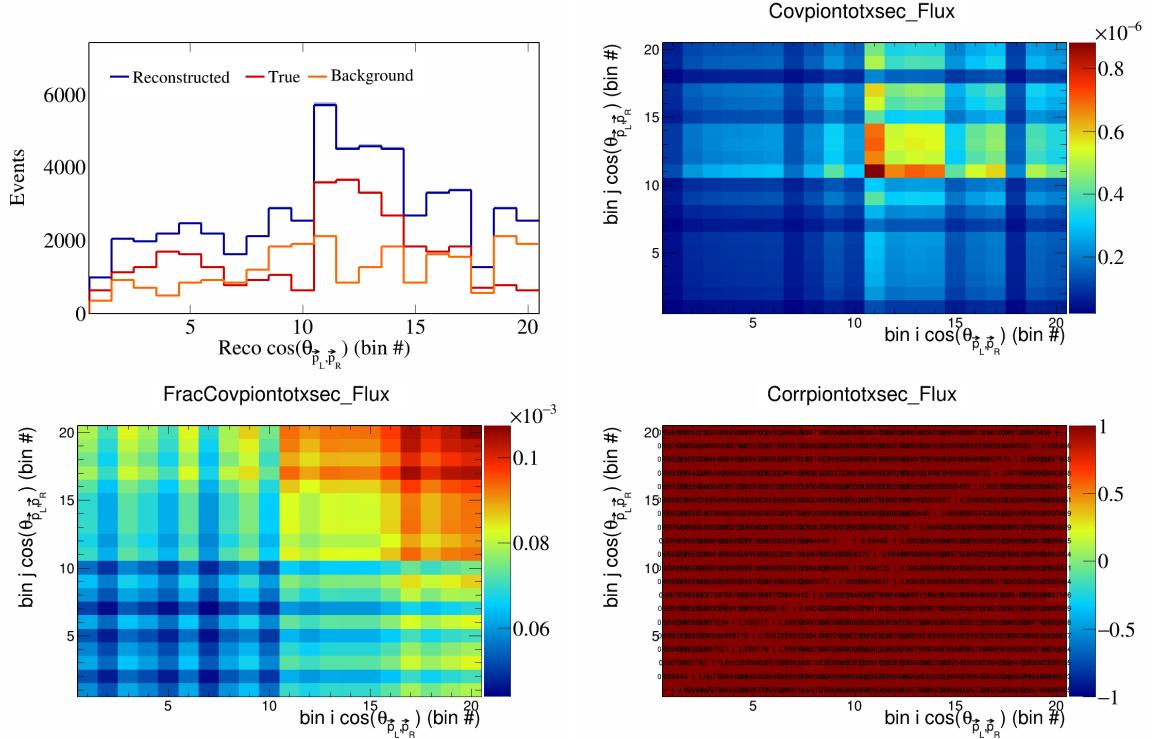


Figure 762: PionTotXSec variations for $\cos(\theta_{\vec{p}_L, \vec{p}_R})$ in $\cos(\theta_{\vec{p}_\mu})$.

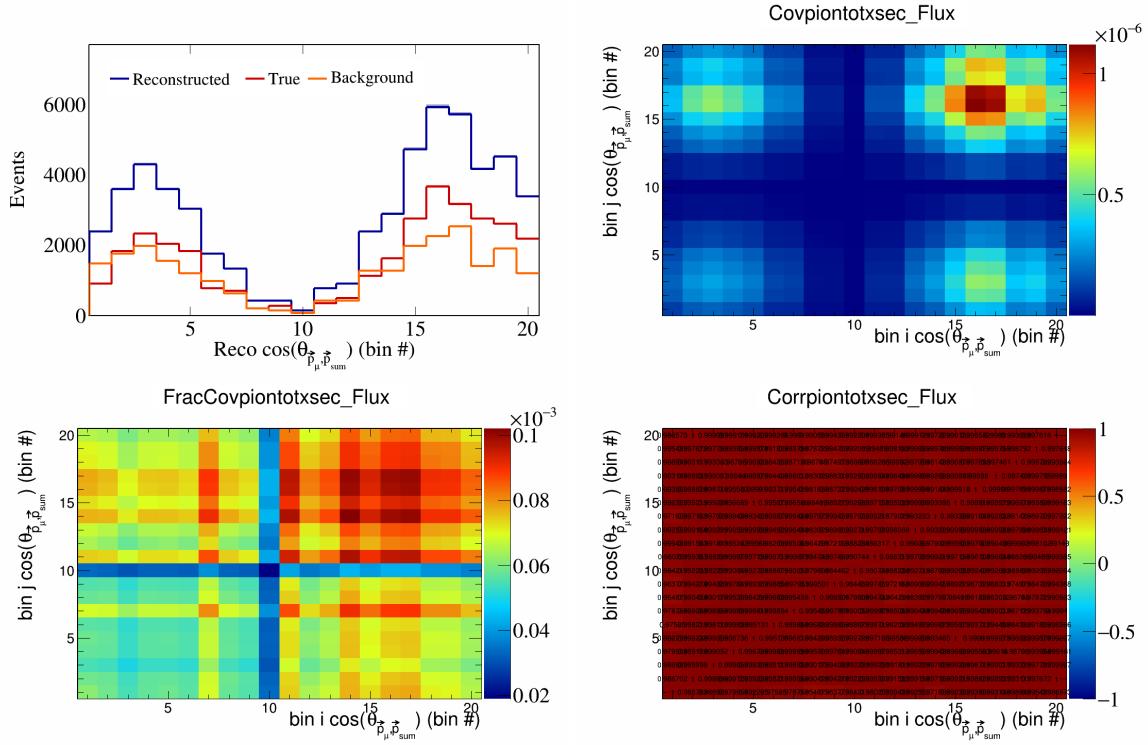


Figure 763: PionTotXSec variations for $\cos(\theta_{\vec{p}_\mu} \cdot \vec{p}_{\text{sum}})$ in $\cos(\theta_{\vec{p}_\mu})$.

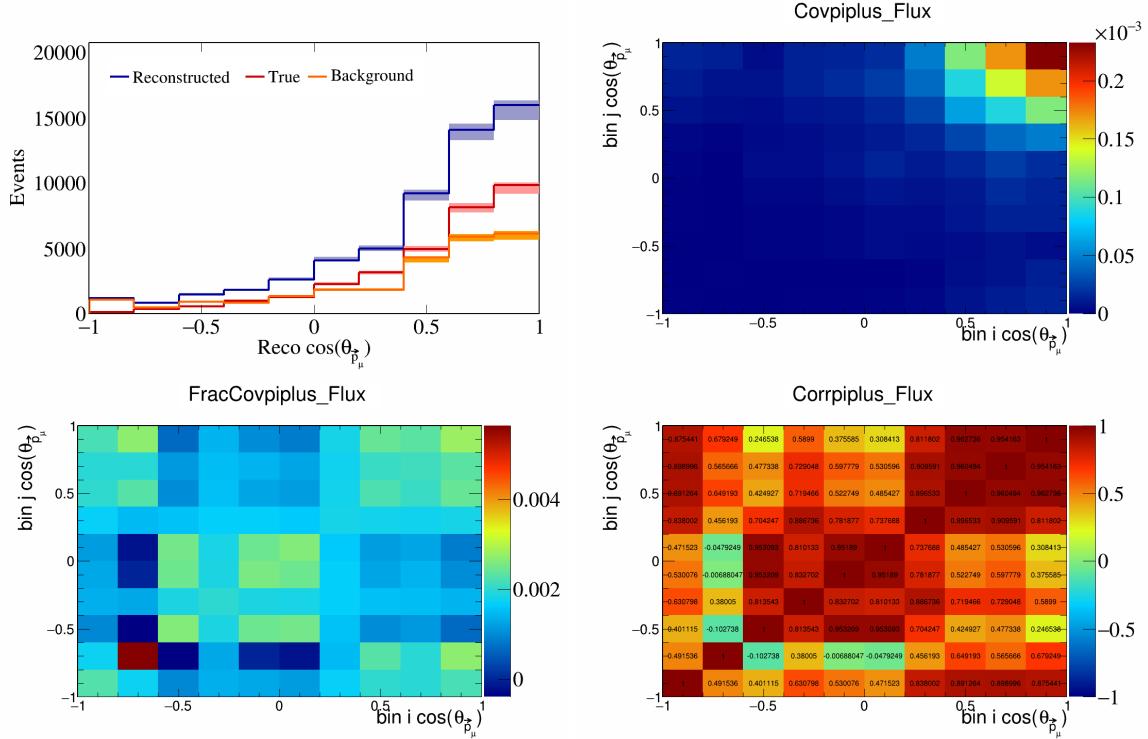


Figure 764: PiPlus variations for $\cos(\theta_{\vec{p}_\mu})$.

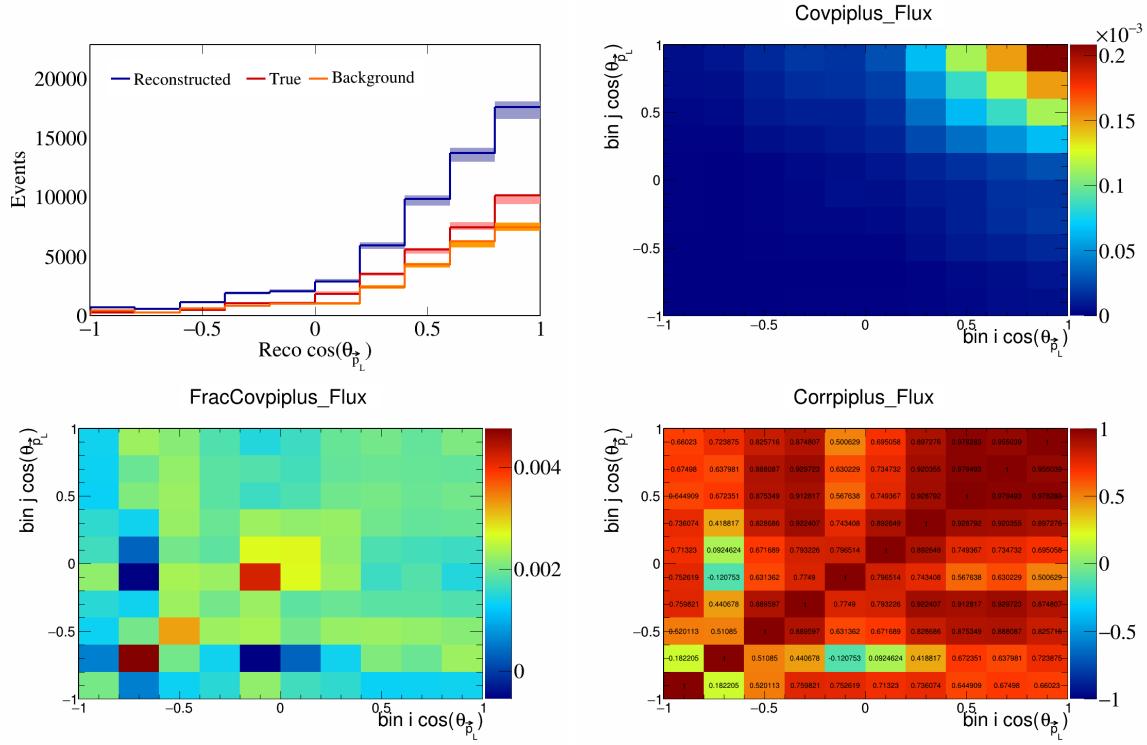


Figure 765: PiPlus variations for $\cos(\theta_{\vec{p}_L})$.

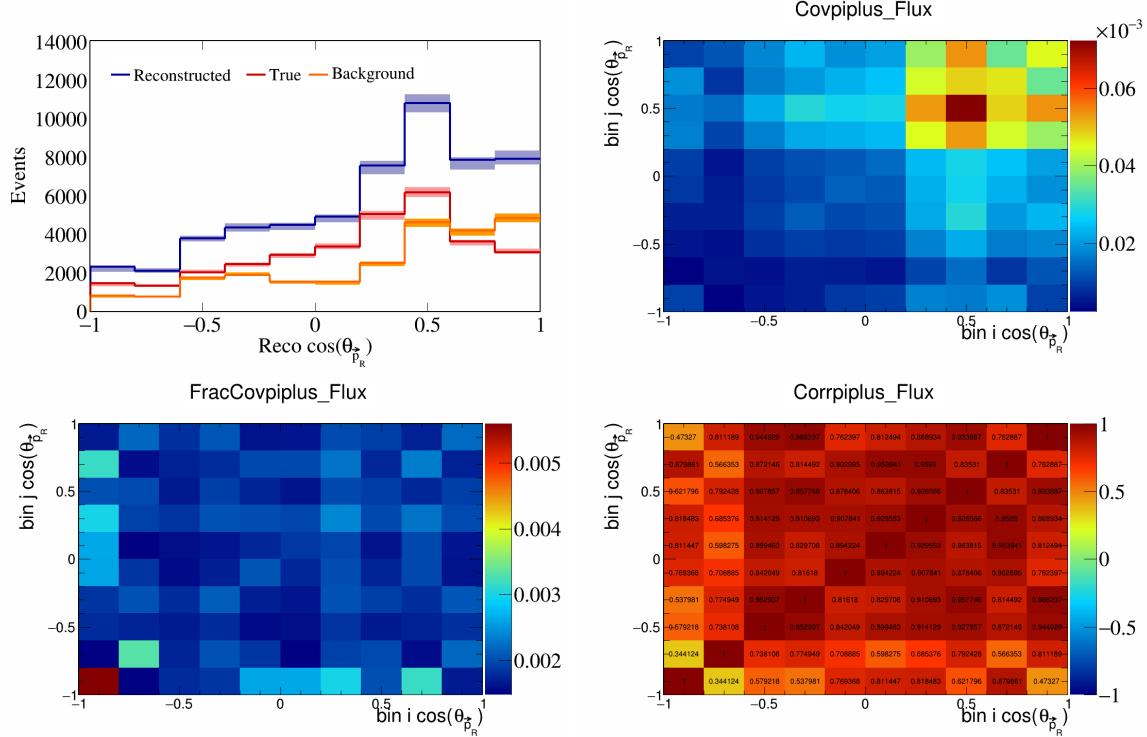


Figure 766: PiPlus variations for $\cos(\theta_{\vec{p}_R})$.

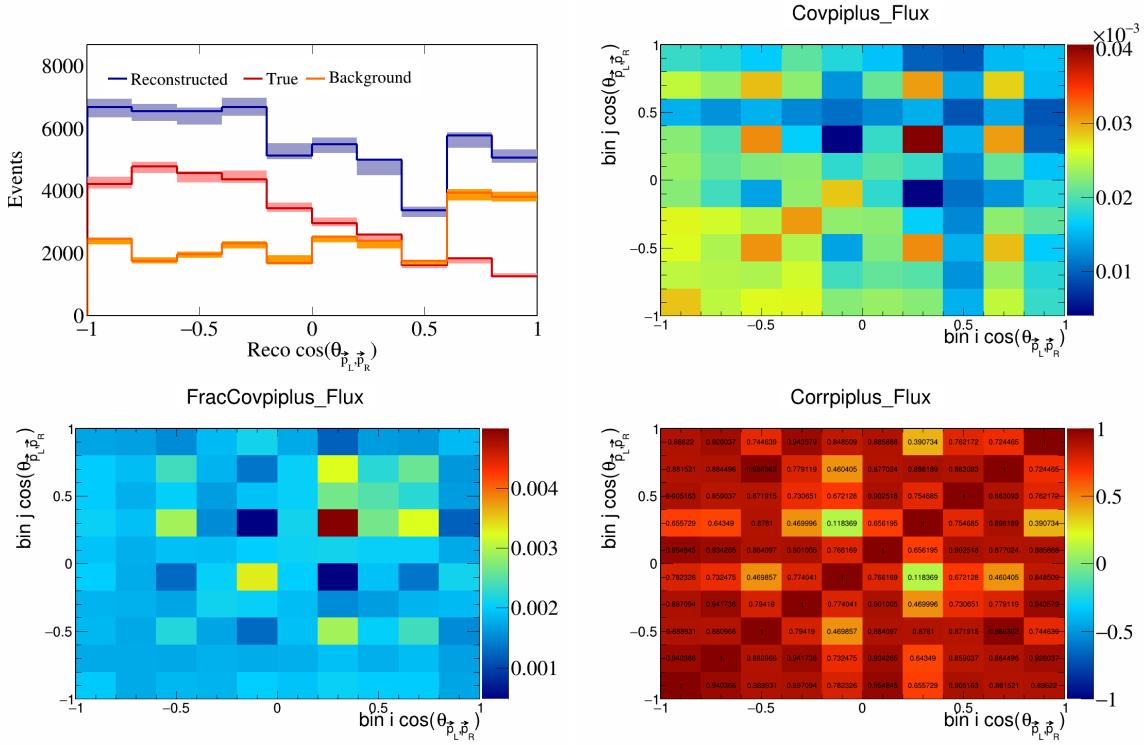


Figure 767: PiPlus variations for $\cos(\theta_{\vec{p}_L, \vec{p}_R})$.

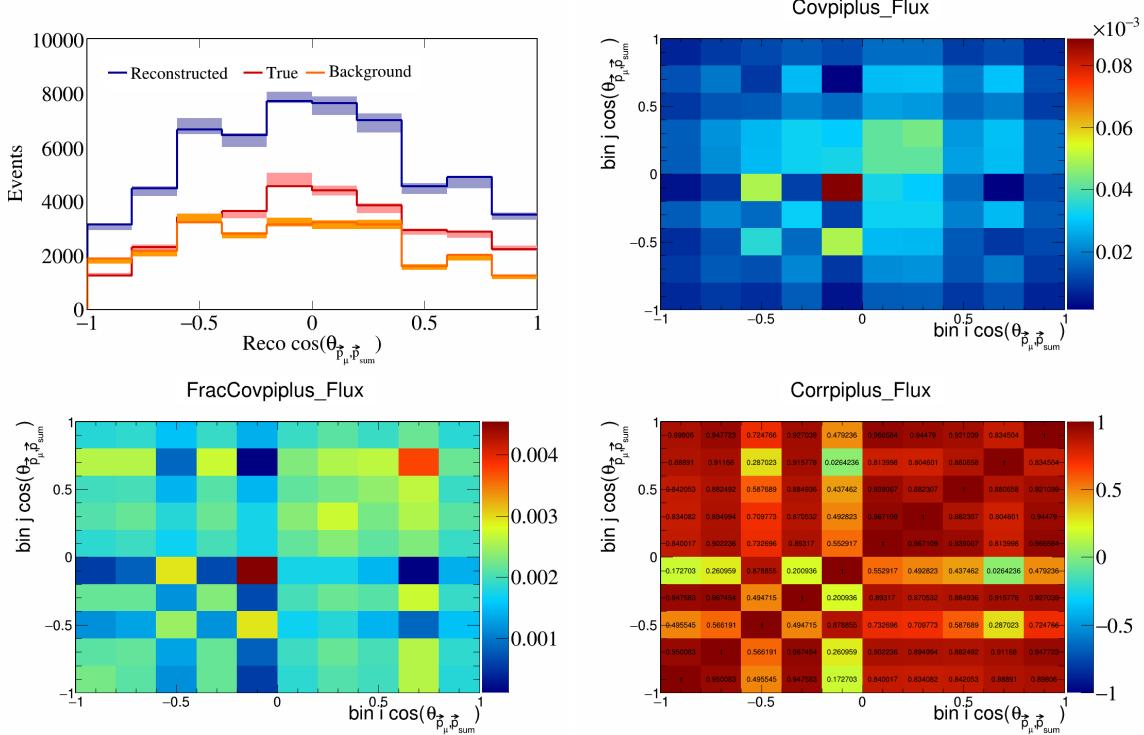


Figure 768: PiPlus variations for $\cos(\theta_{\vec{p}_\mu, \vec{p}_{\text{sum}}})$.

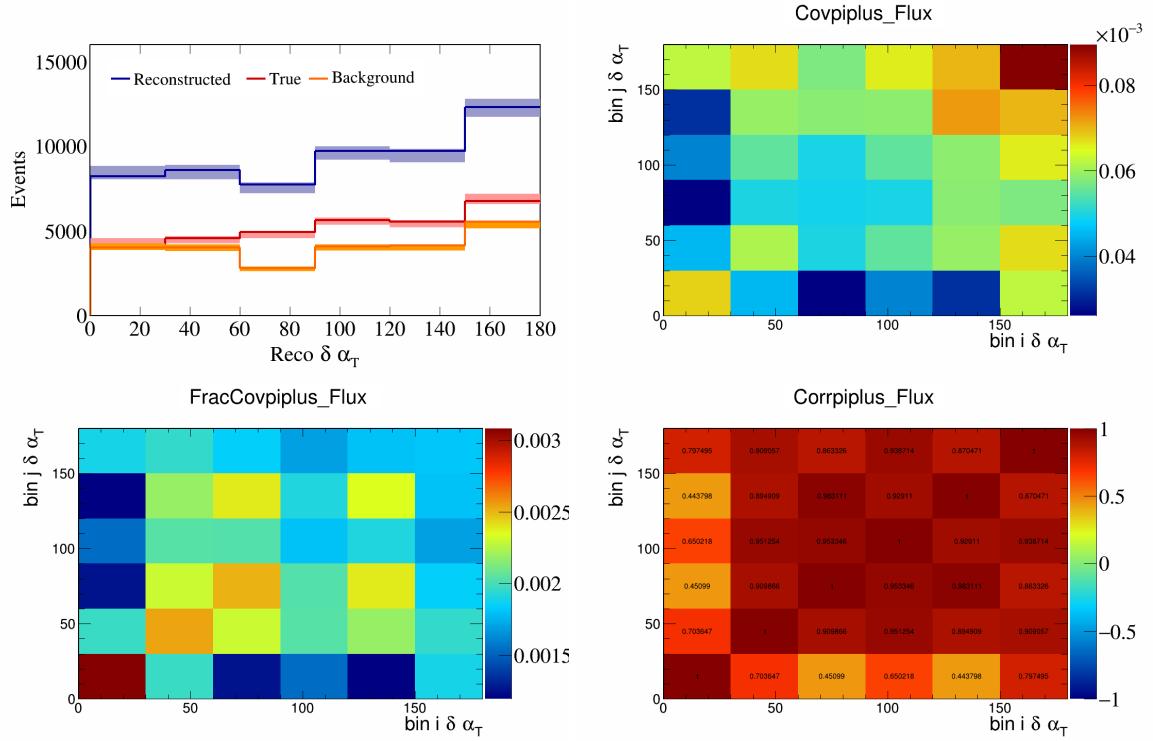


Figure 769: PiPlus variations for $\delta\alpha_T$.

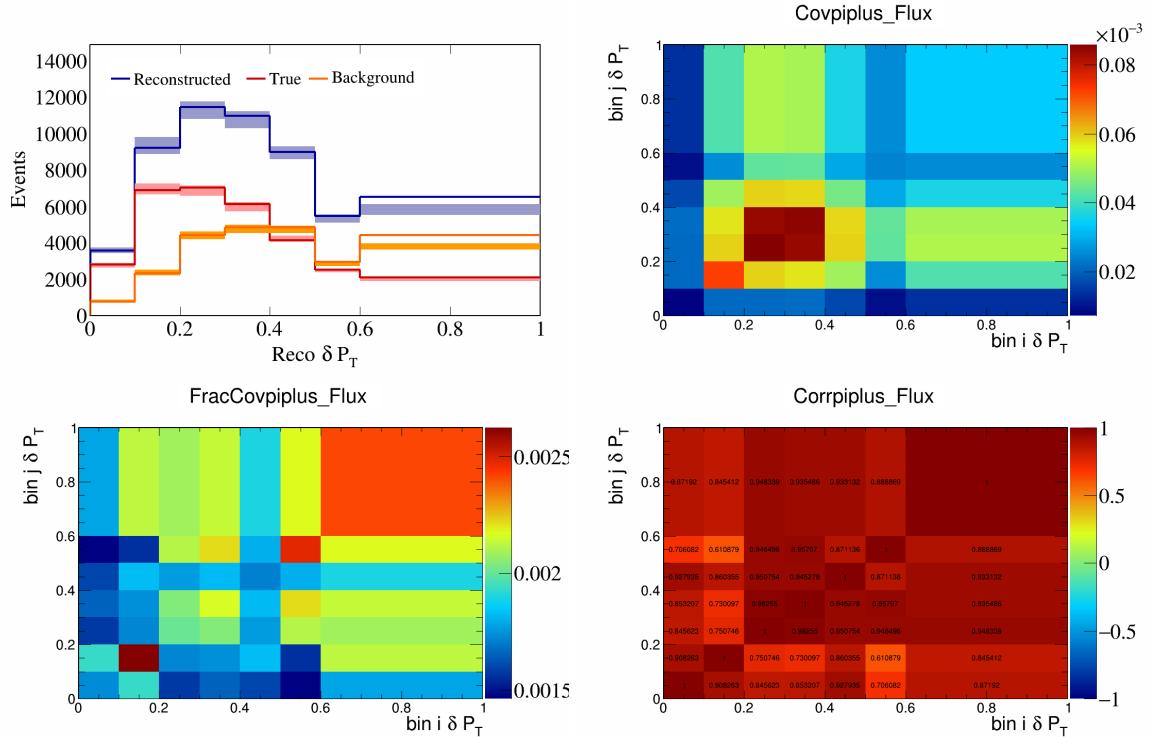


Figure 770: PiPlus variations for δP_T .

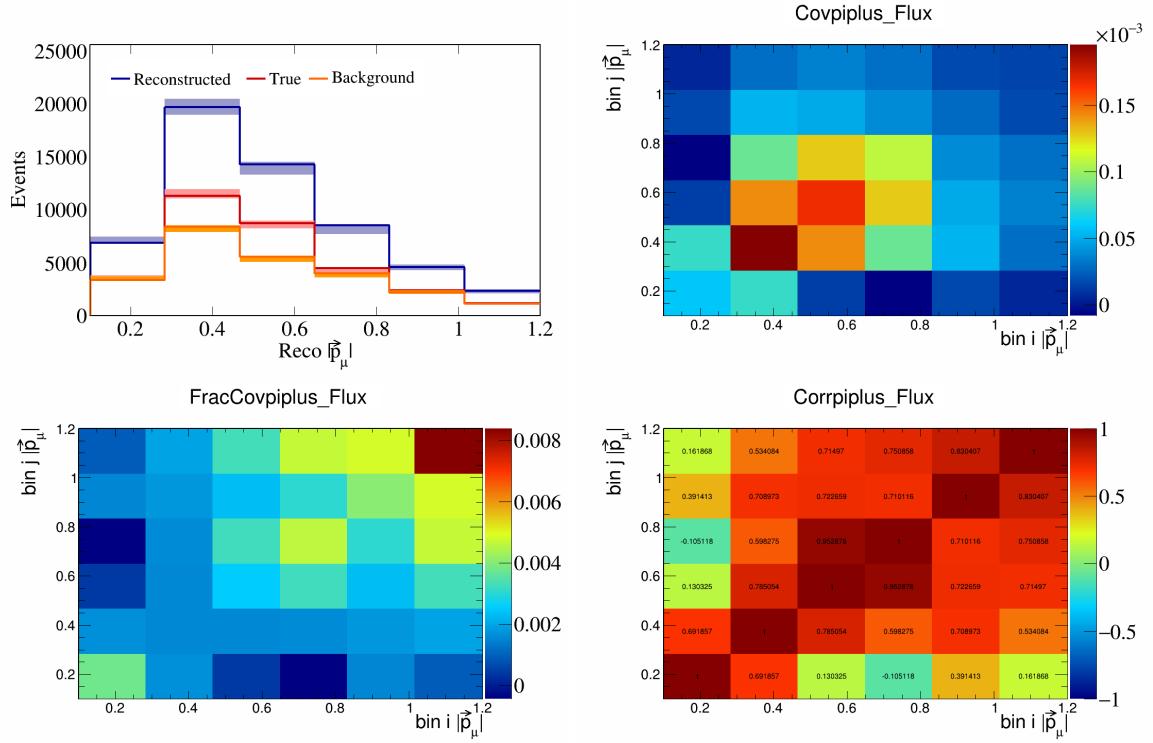


Figure 771: PiPlus variations for $|\vec{p}_\mu|$.

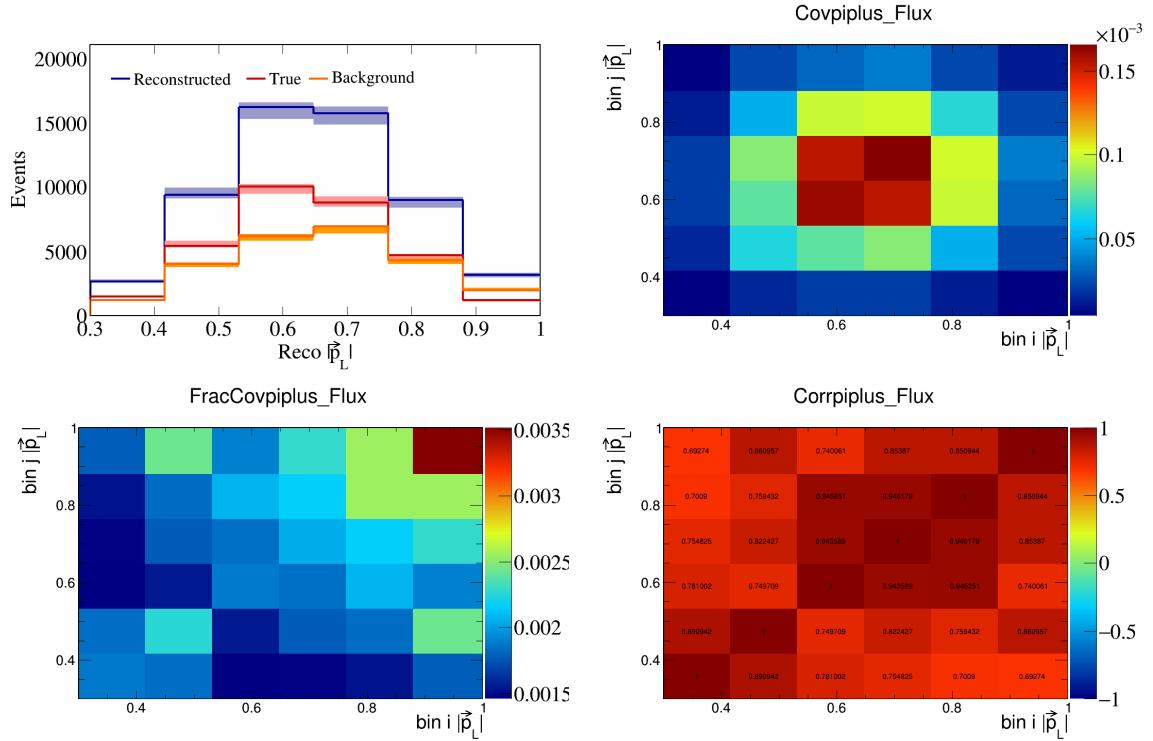


Figure 772: PiPlus variations for $|\vec{p}_L|$.

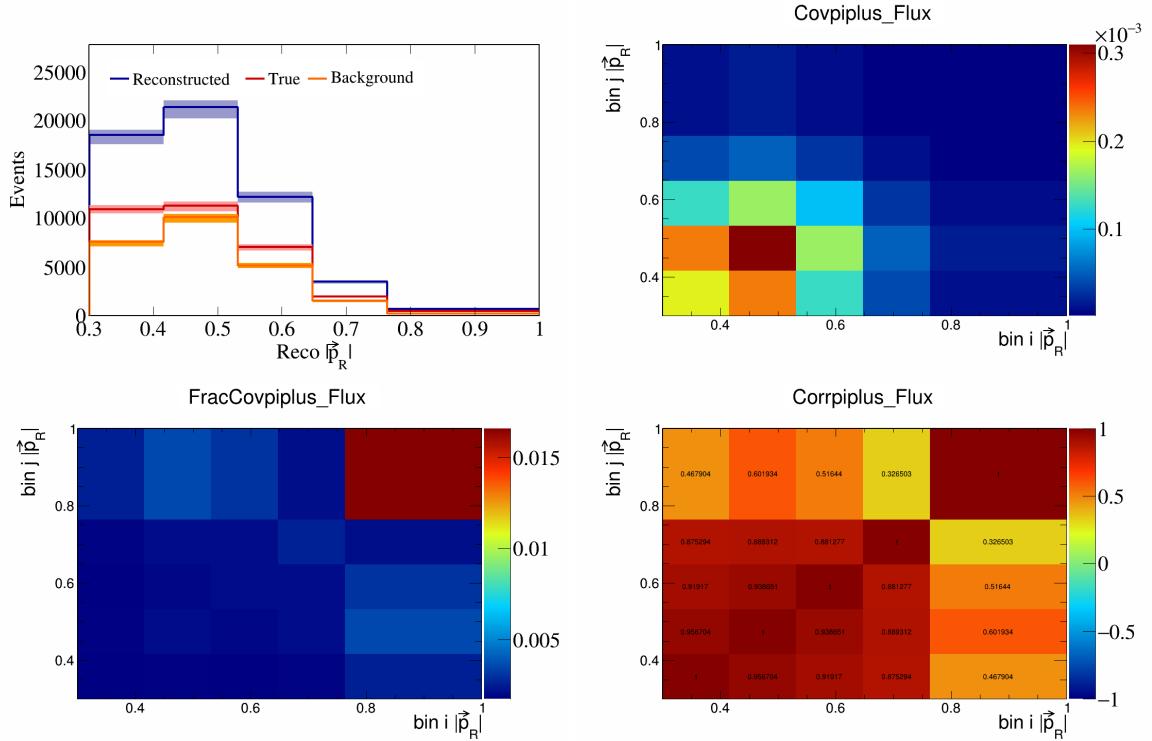


Figure 773: PiPlus variations for $|\vec{p}_R|$.

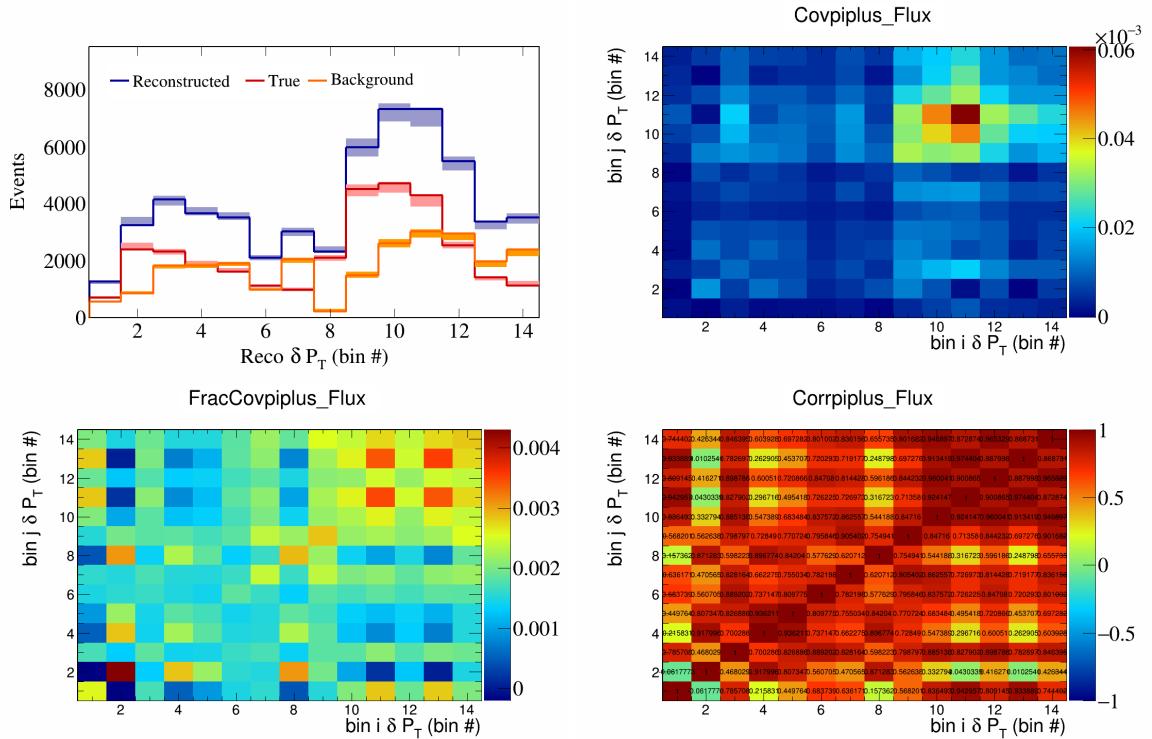


Figure 774: PiPlus variations for δP_T in $\cos(\theta_{\vec{p}_\mu})$.

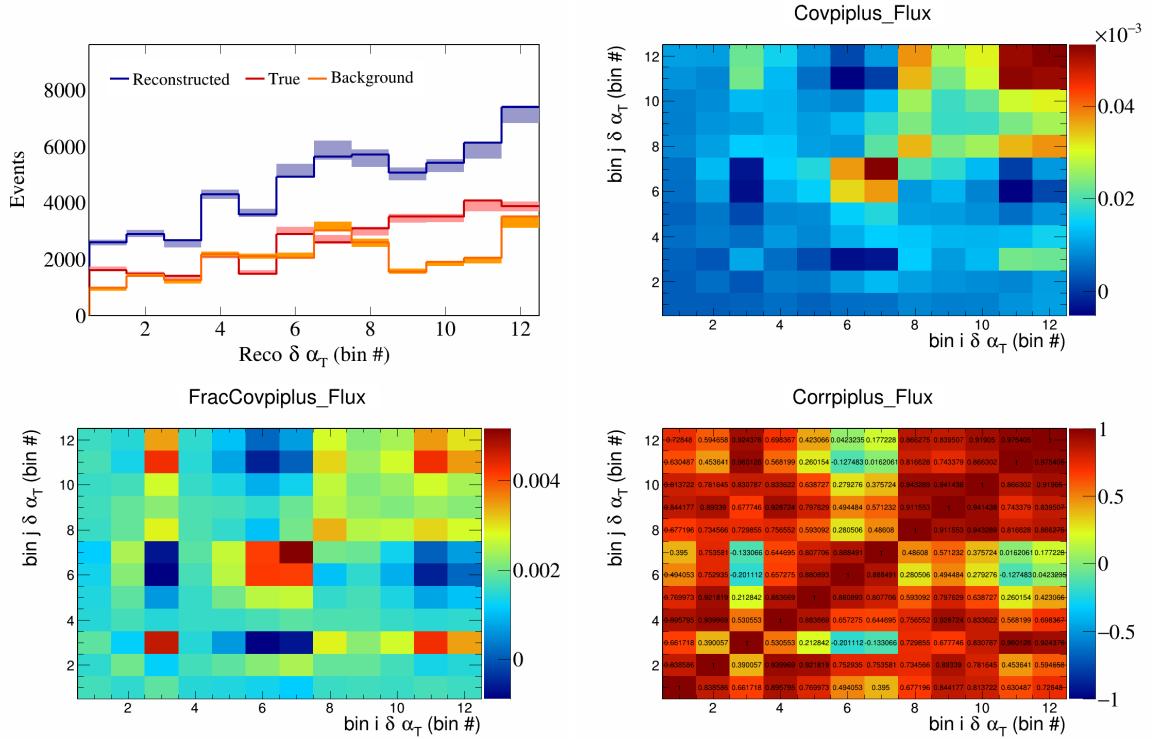


Figure 775: PiPlus variations for $\delta\alpha_T$ in $\cos(\theta_{\vec{p}_\mu})$.

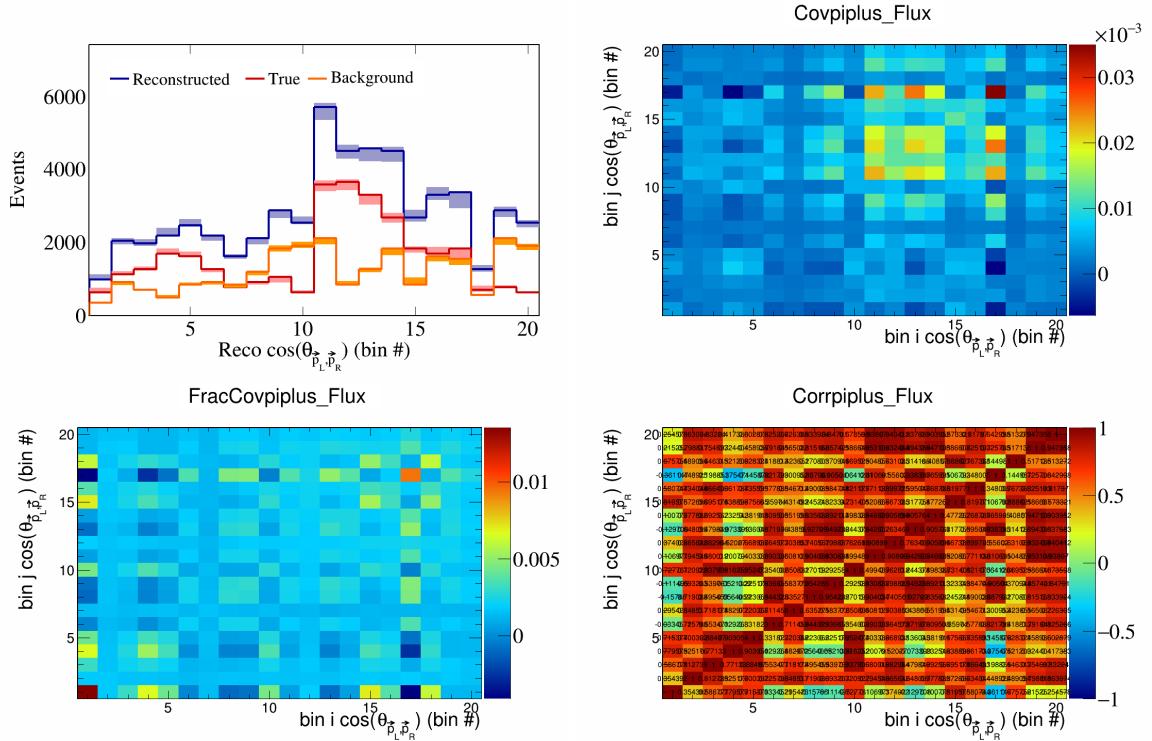


Figure 776: PiPlus variations for $\cos(\theta_{\vec{p}_L, \vec{p}_R})$ in $\cos(\theta_{\vec{p}_\mu})$.

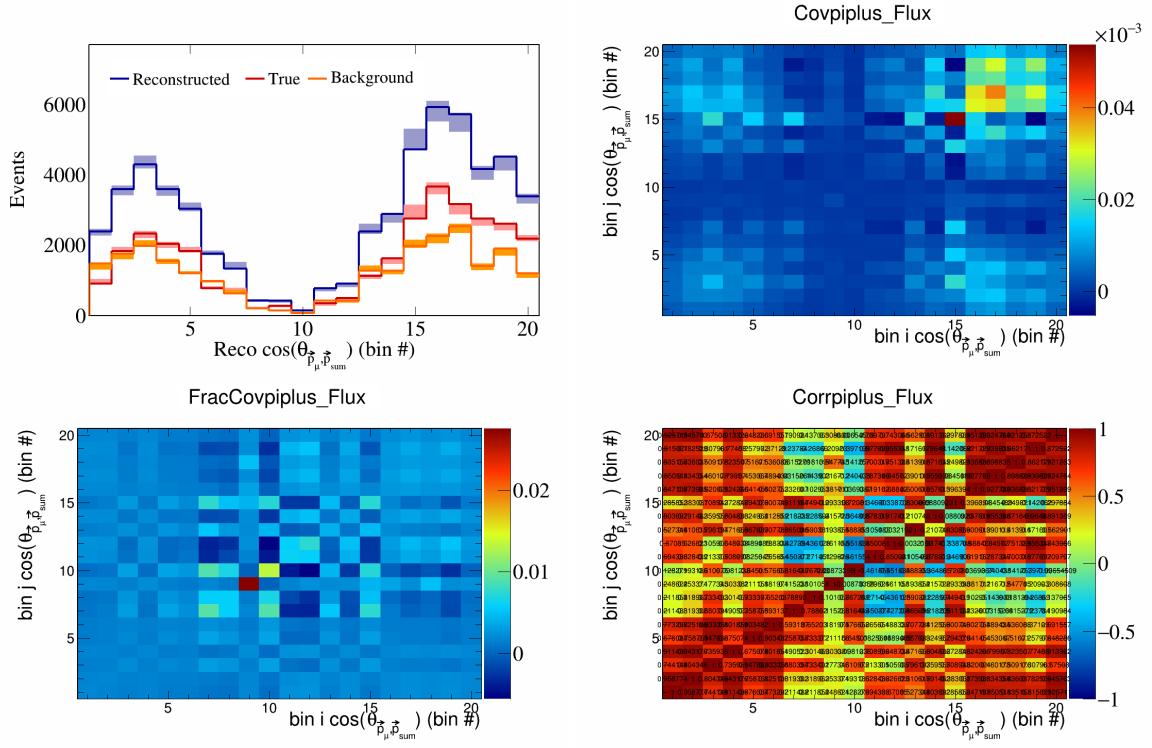


Figure 777: PiPlus variations for $\cos(\theta_{\vec{p}_\mu, \vec{p}_{\text{sum}}})$ in $\cos(\theta_{\vec{p}_\mu})$.

278 **6.3 Statistical systematics**

279 In this appendix, the covariance, fractional covariance, and correlation matrices for the statistical systematics
 280 are plotted.

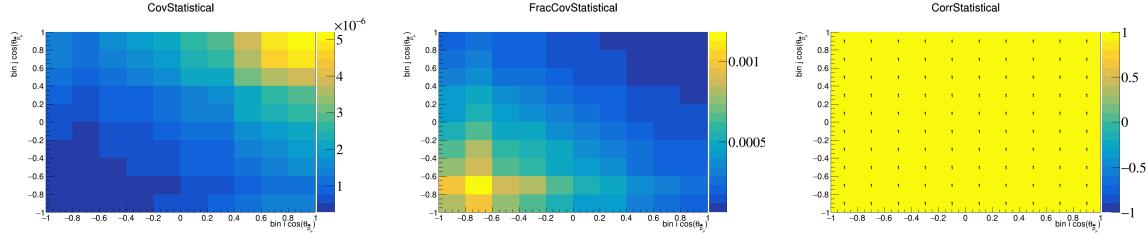


Figure 778: Statistical variations for $\cos(\theta_{\vec{p}_\mu})$.

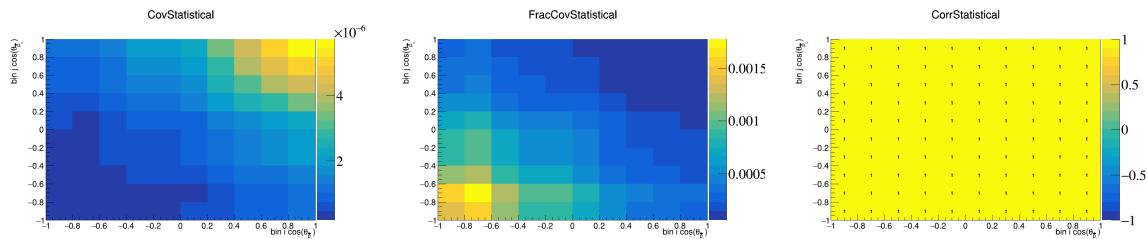


Figure 779: Statistical variations for $\cos(\theta_{\vec{p}_L})$.

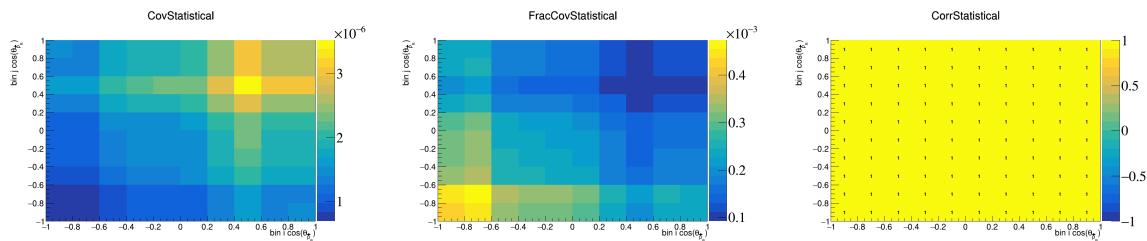


Figure 780: Statistical variations for $\cos(\theta_{\vec{p}_R})$.

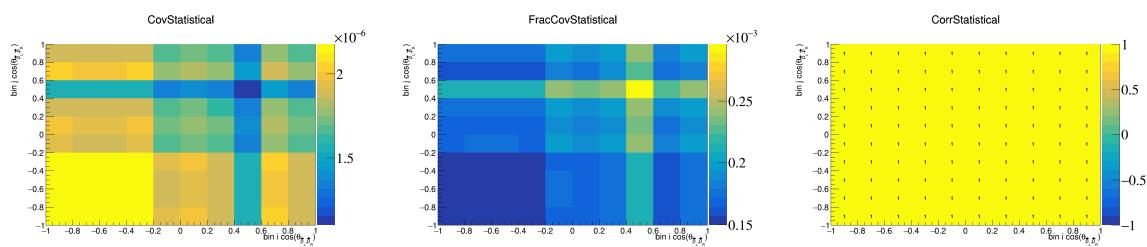


Figure 781: Statistical variations for $\cos(\theta_{\vec{p}_L, \vec{p}_R})$.

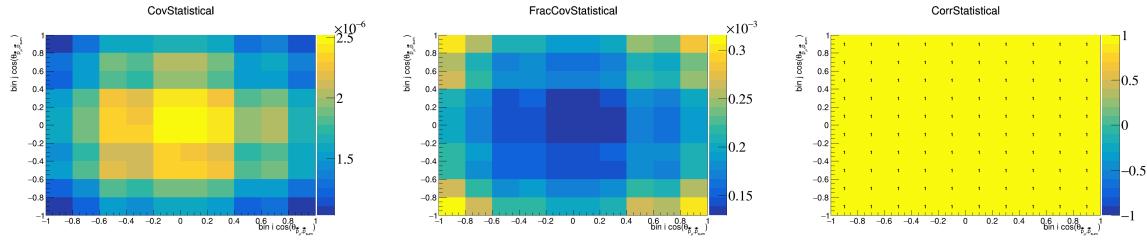


Figure 782: Statistical variations for $\cos(\theta_{\vec{p}_\mu, \vec{p}_{\text{sum}}})$.

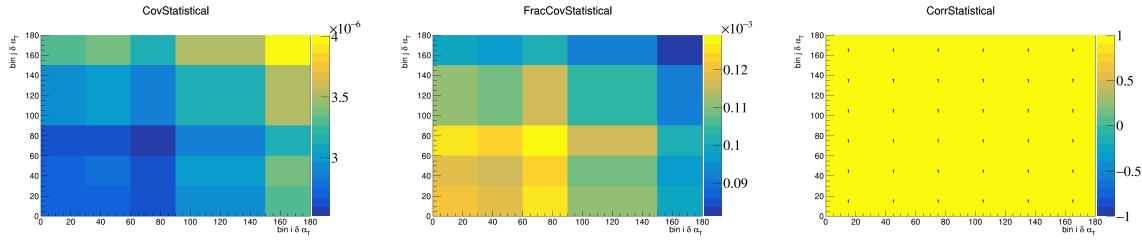


Figure 783: Statistical variations for $\delta \alpha_T$.

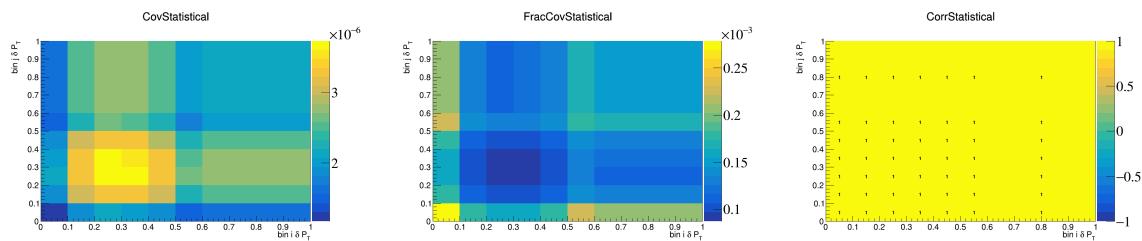


Figure 784: Statistical variations for δP_T .

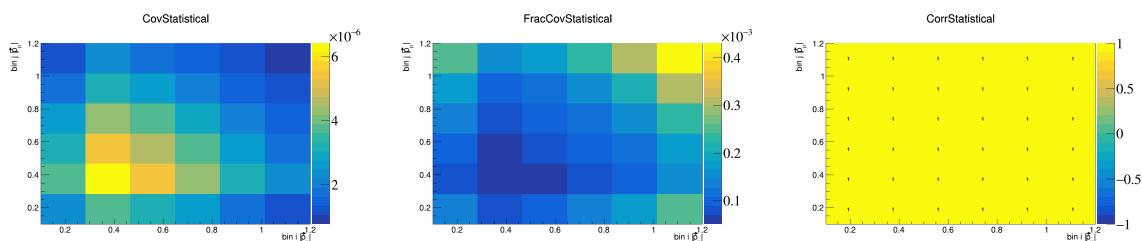


Figure 785: Statistical variations for $|\vec{p}_\mu|$.

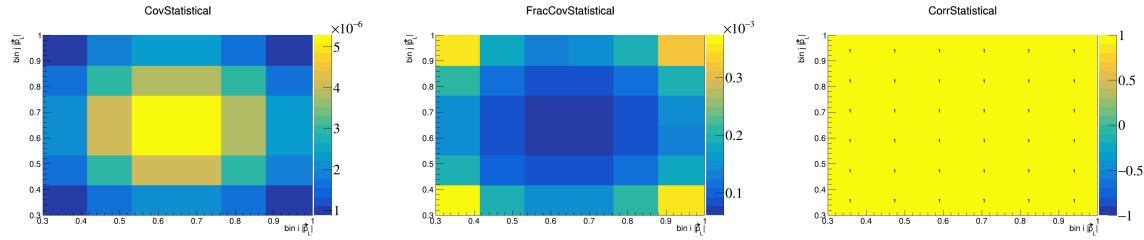


Figure 786: Statistical variations for $|\vec{p}_L|$.

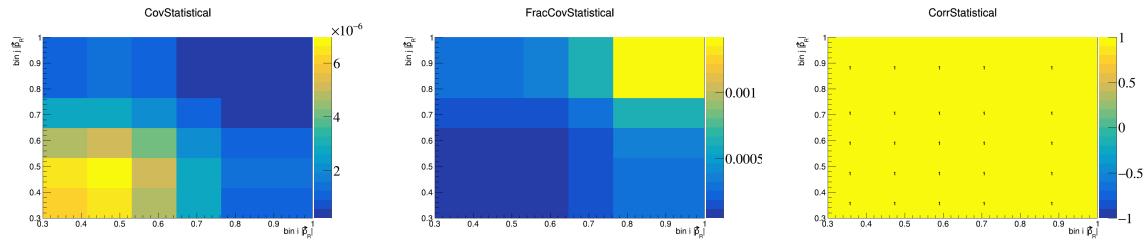


Figure 787: Statistical variations for $|\vec{p}_R|$.

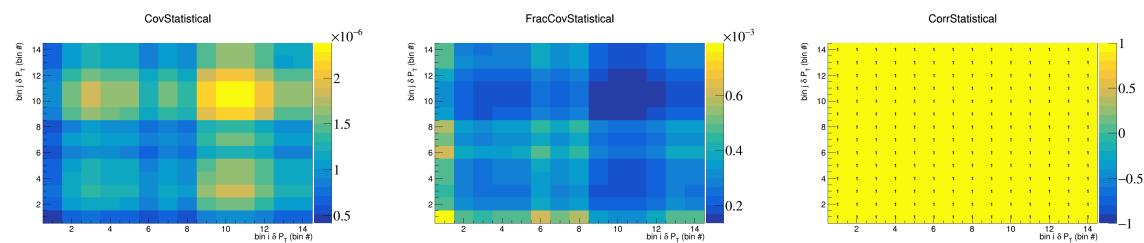


Figure 788: Statistical variations for δP_T in $\cos(\theta_{\vec{p}_\mu})$.

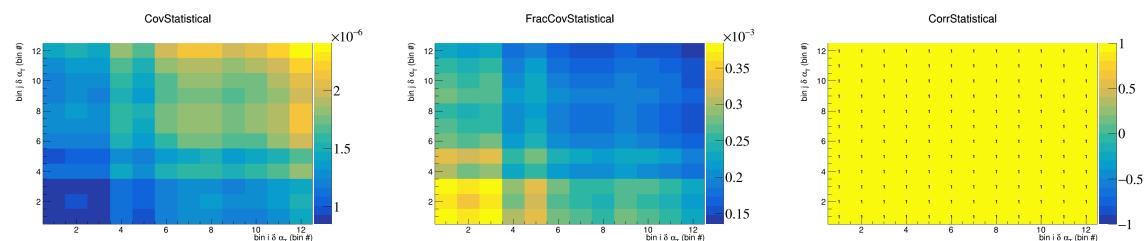


Figure 789: Statistical variations for $\delta \alpha_T$ in $\cos(\theta_{\vec{p}_\mu})$.

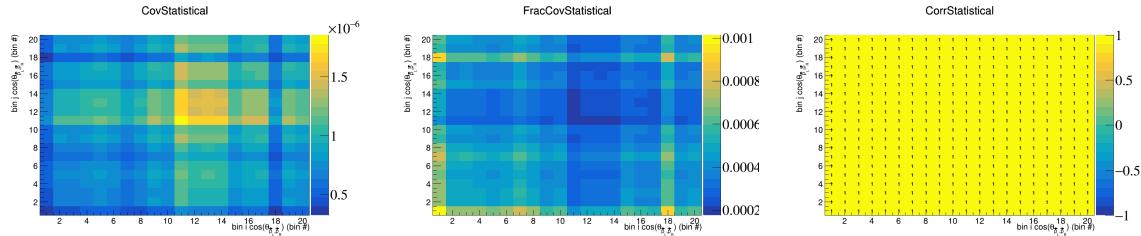


Figure 790: Statistical variations for $\cos(\theta_{\vec{p}_L, \vec{p}_R})$ in $\cos(\theta_{\vec{p}_\mu})$.

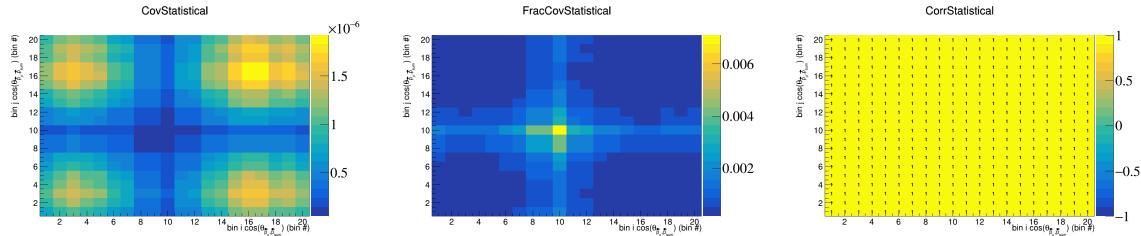


Figure 791: Statistical variations for $\cos(\theta_{\vec{p}_\mu, \vec{p}_{\text{sum}}})$ in $\cos(\theta_{\vec{p}_\mu})$.

281 6.4 POT

282 In this appendix, the covariance, fractional covariance, and correlation matrices for the POT systematics are
 283 plotted.

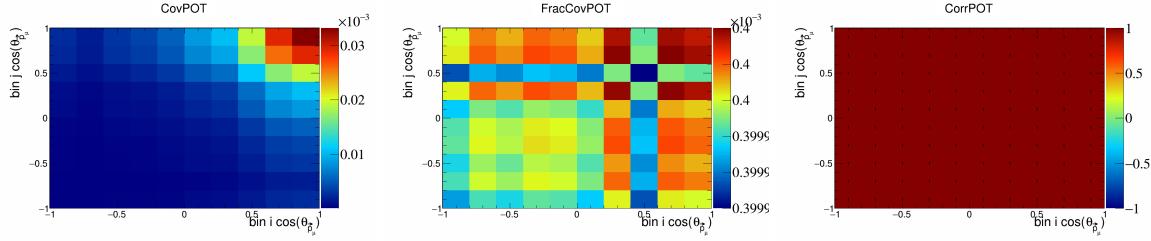


Figure 792: POT variations for $\cos(\theta_{\vec{p}_\mu})$.

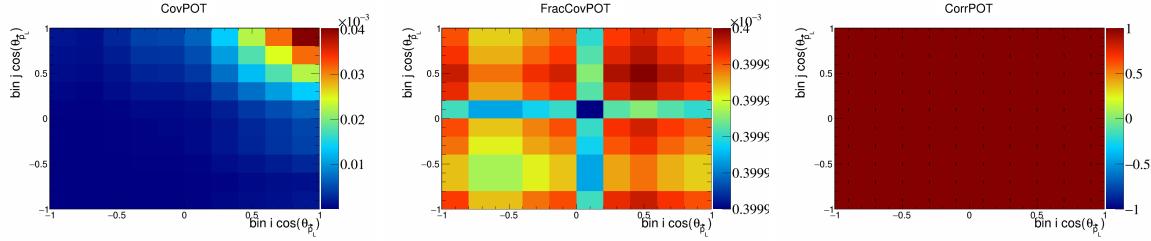


Figure 793: POT variations for $\cos(\theta_{\vec{p}_L})$.

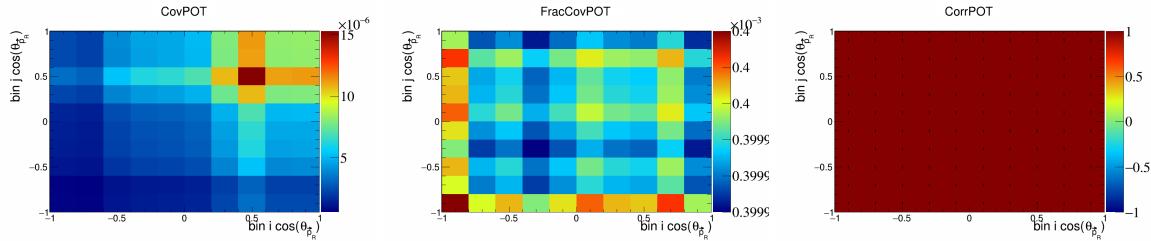


Figure 794: POT variations for $\cos(\theta_{\vec{p}_R})$.

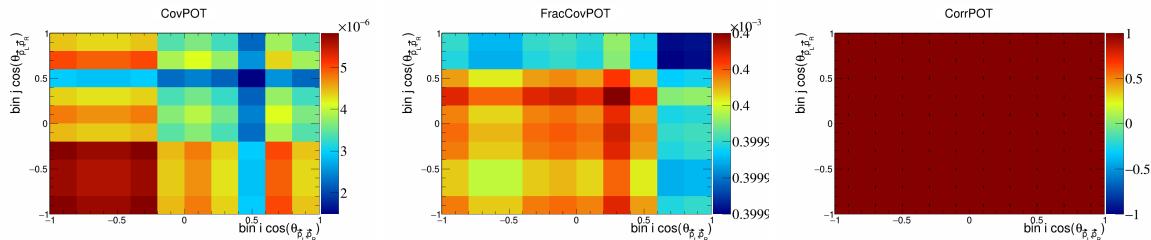


Figure 795: POT variations for $\cos(\theta_{\vec{p}_L, \vec{p}_R})$.

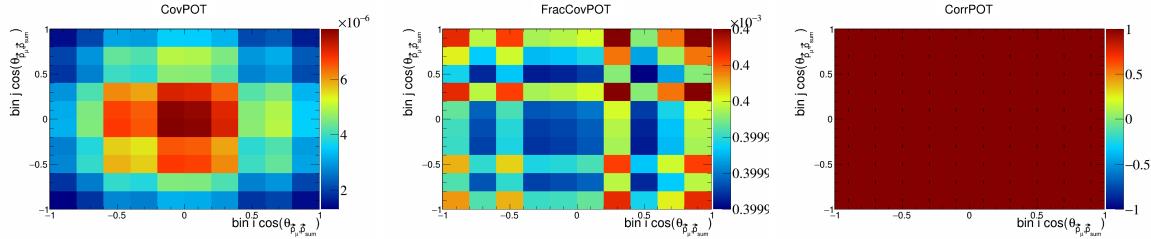


Figure 796: POT variations for $\cos(\theta_{\vec{p}_\mu, \vec{p}_{sum}})$.

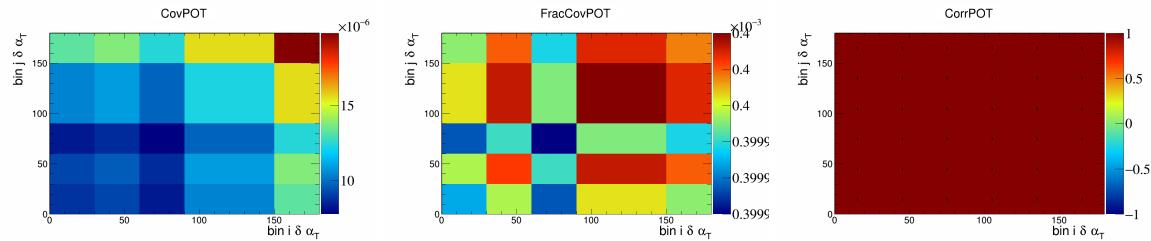


Figure 797: POT variations for $\delta \alpha_T$.

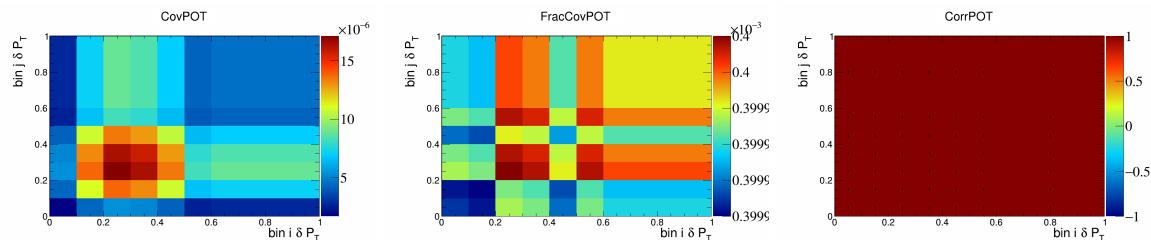


Figure 798: POT variations for δP_T .

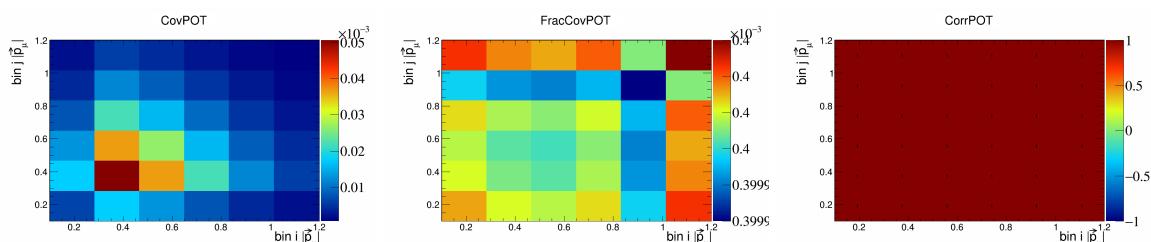


Figure 799: POT variations for $|\vec{p}_\mu|$.

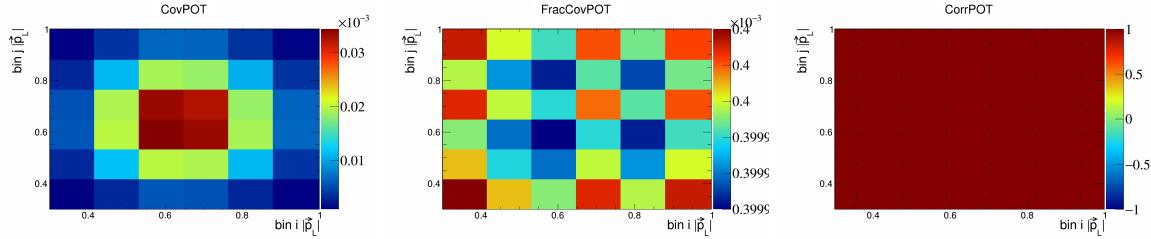


Figure 800: POT variations for $|\vec{p}_L|$.

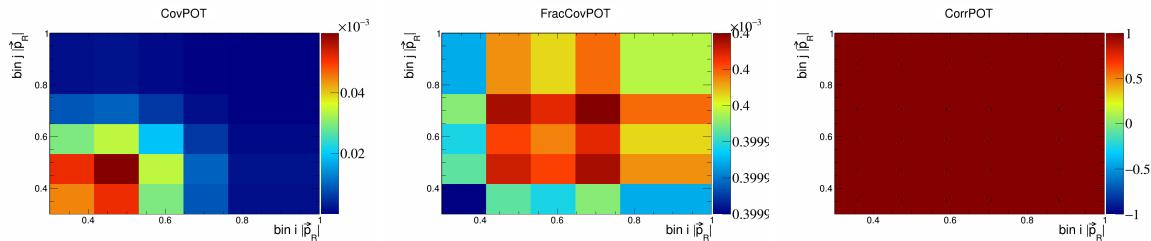


Figure 801: POT variations for $|\vec{p}_R|$.

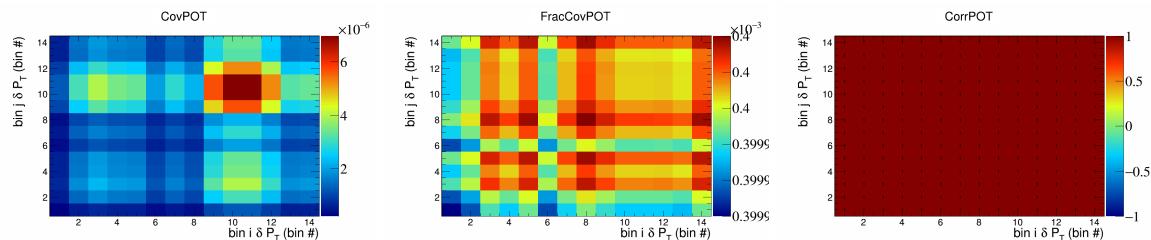


Figure 802: POT variations for δP_T in $\cos(\theta_{\vec{p}_\mu})$.

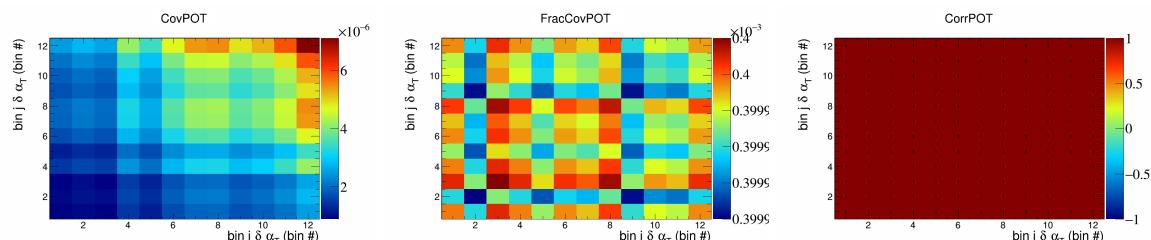


Figure 803: POT variations for $\delta \alpha_T$ in $\cos(\theta_{\vec{p}_\mu})$.

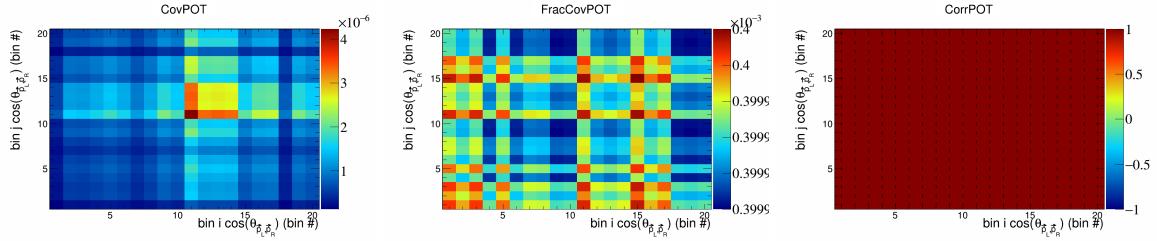


Figure 804: POT variations for $\cos(\theta_{\vec{p}_L, \vec{p}_R})$ in $\cos(\theta_{\vec{p}_\mu})$.

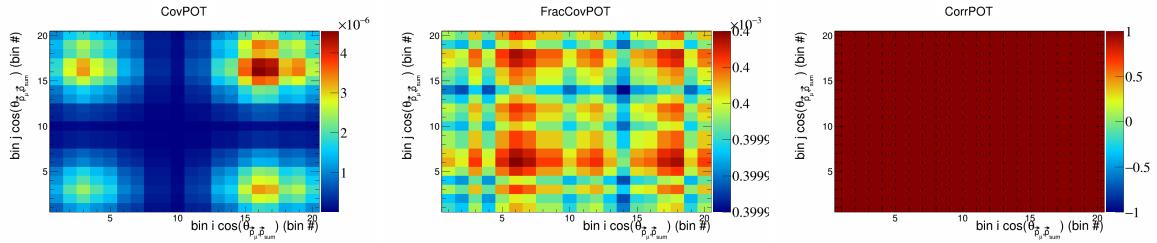


Figure 805: POT variations for $\cos(\theta_{\vec{p}_\mu, \vec{p}_{\text{sum}}})$ in $\cos(\theta_{\vec{p}_\mu})$.

284 6.5 Number of targets

285 In this appendix, the covariance, fractional covariance, and correlation matrices for the number of targets
 286 systematics are plotted.

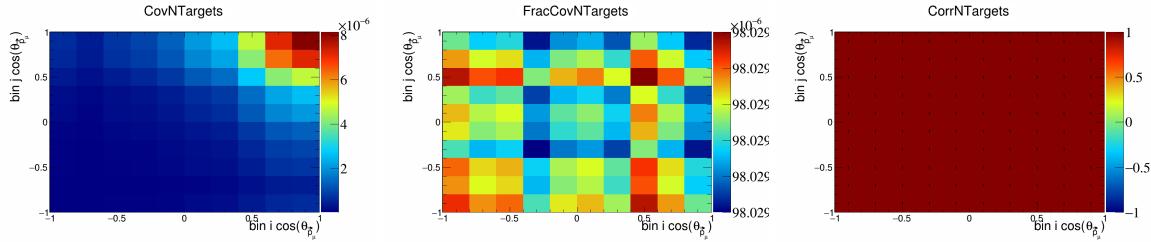


Figure 806: NTTargets variations for $\cos(\theta_{\vec{p}_\mu})$.

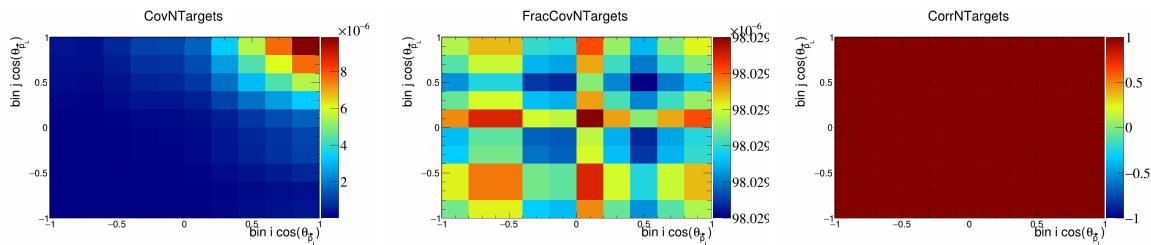


Figure 807: NTTargets variations for $\cos(\theta_{\vec{p}_L})$.

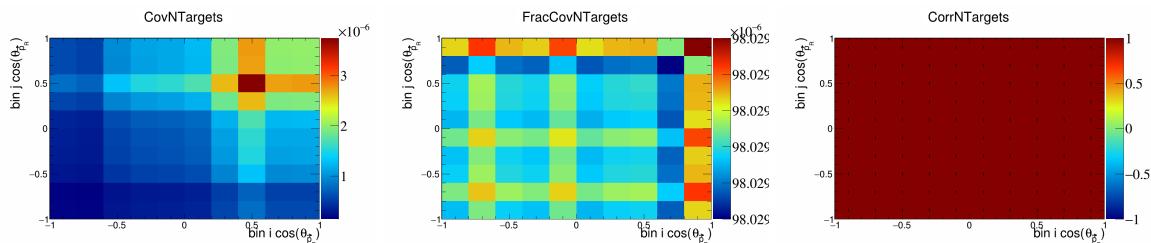


Figure 808: NTTargets variations for $\cos(\theta_{\vec{p}_R})$.

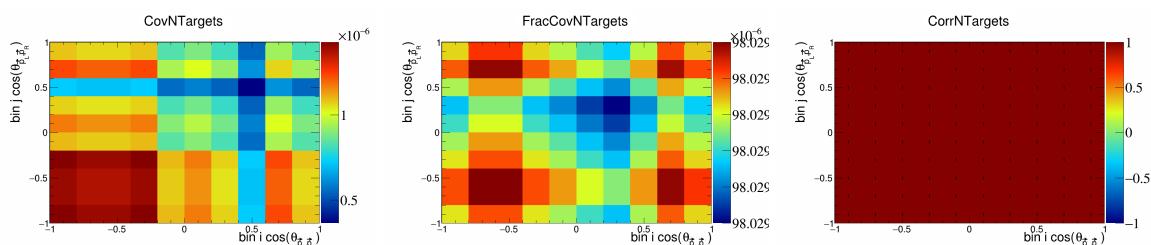


Figure 809: NTTargets variations for $\cos(\theta_{\vec{p}_L, \vec{p}_R})$.

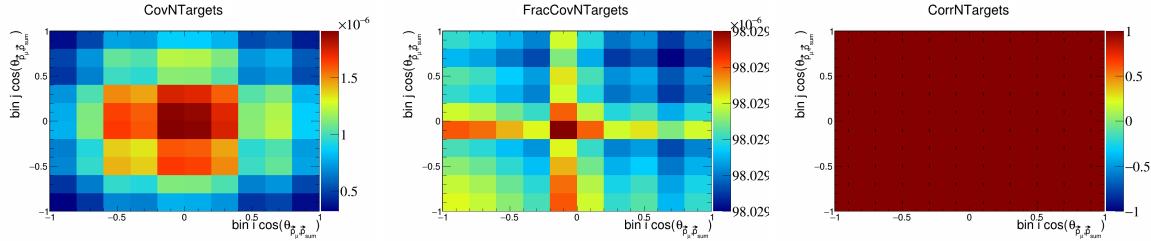


Figure 810: NTargets variations for $\cos(\theta_{\vec{p}_\mu, \vec{p}_{\text{sum}}})$.

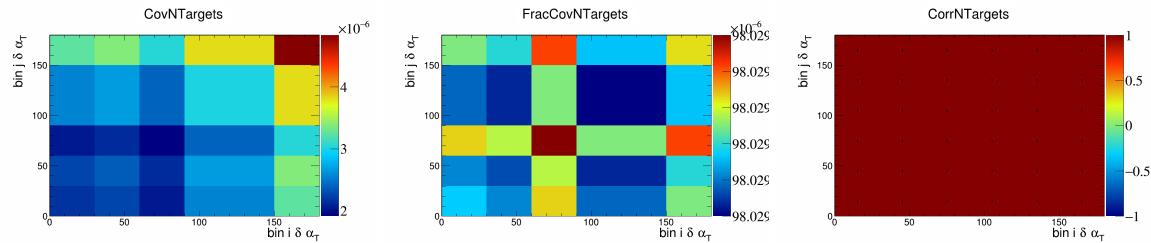


Figure 811: NTargets variations for $\delta \alpha_T$.

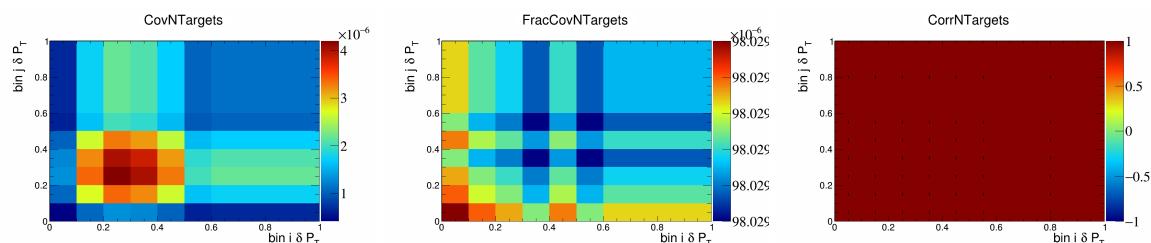


Figure 812: NTargets variations for δP_T .

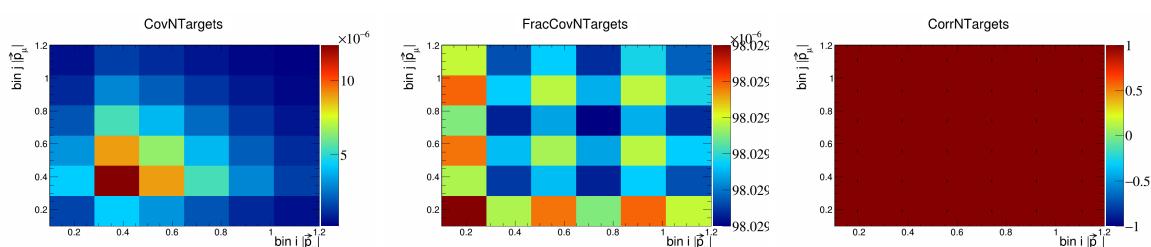


Figure 813: NTargets variations for $|\vec{p}_\mu|$.

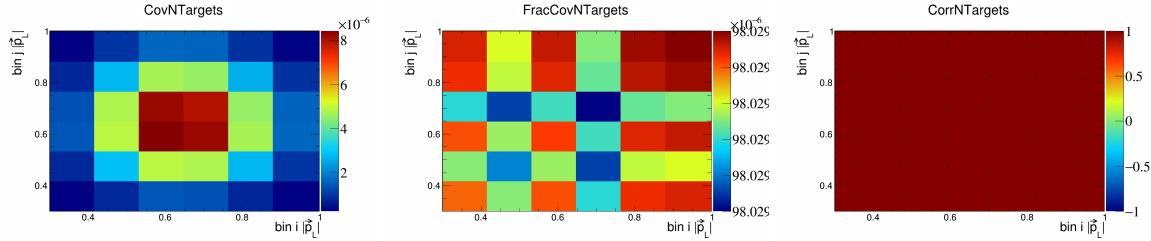


Figure 814: NTargets variations for $|\vec{p}_L|$.

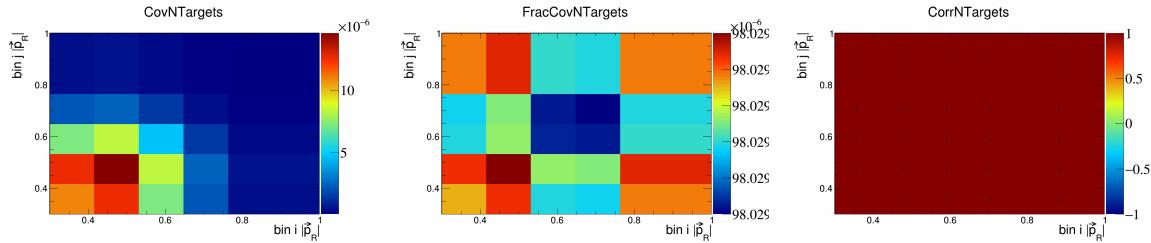


Figure 815: NTargets variations for $|\vec{p}_R|$.

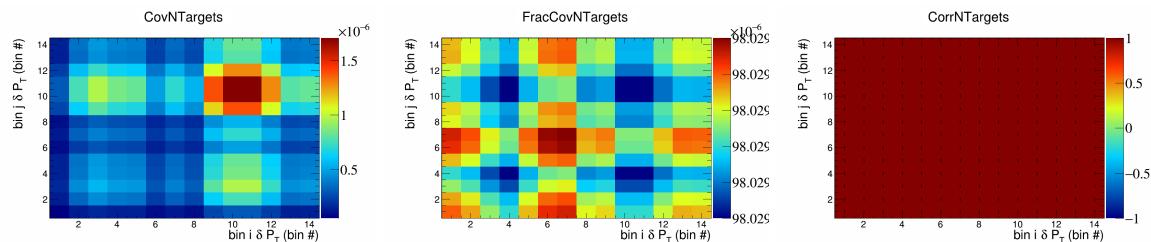


Figure 816: NTargets variations for δP_T in $\cos(\theta_{\vec{p}_\mu})$.

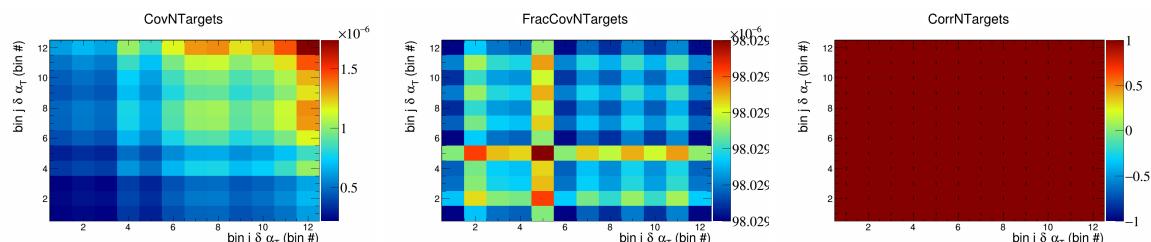


Figure 817: NTargets variations for $\delta \alpha_T$ in $\cos(\theta_{\vec{p}_\mu})$.

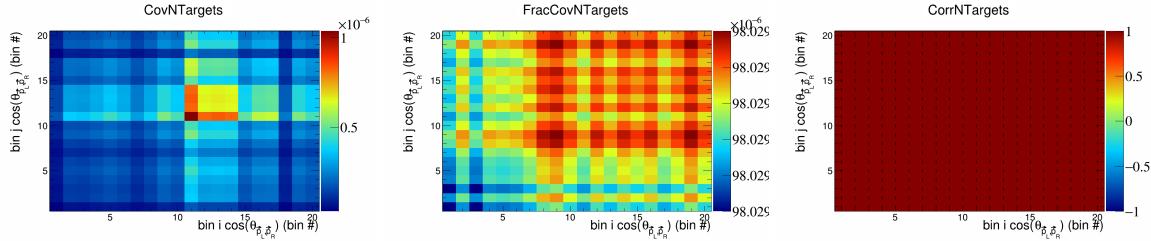


Figure 818: NTARGETS variations for $\cos(\theta_{\vec{p}_L, \vec{p}_R})$ in $\cos(\theta_{\vec{p}_\mu})$.

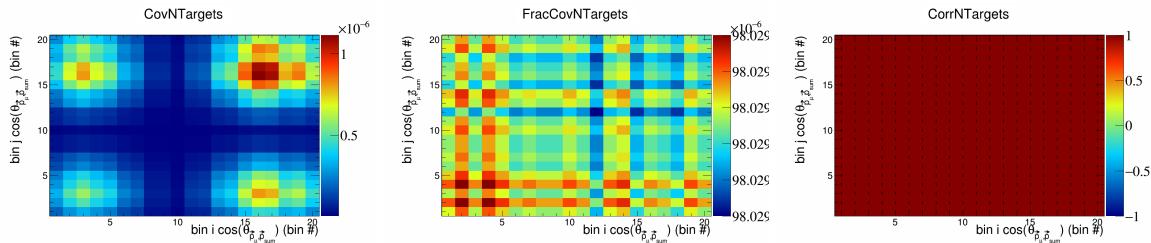


Figure 819: NTARGETS variations for $\cos(\theta_{\vec{p}_\mu, \vec{p}_{\text{sum}}})$ in $\cos(\theta_{\vec{p}_\mu})$.

287 **6.6 Detector**

288 In this appendix, the covariance, fractional covariance, and correlation matrices for the detector systematics
 289 are plotted.

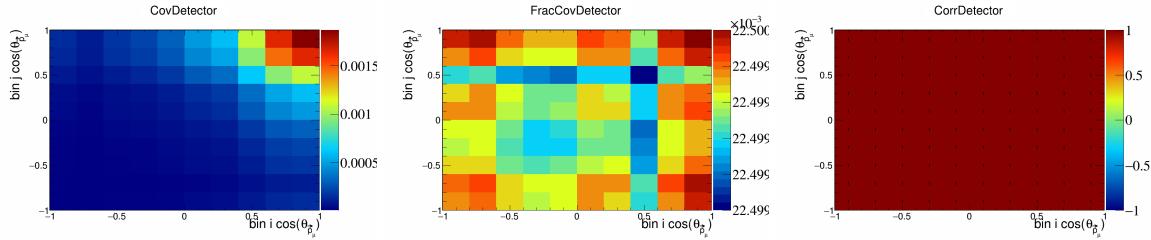


Figure 820: Detector variations for $\cos(\theta_{\vec{p}_\mu})$.

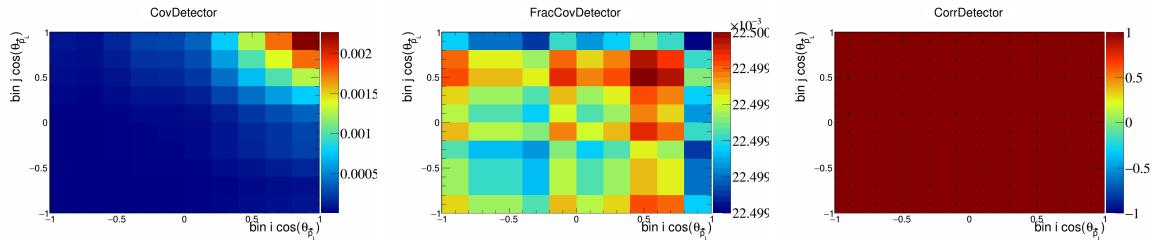


Figure 821: Detector variations for $\cos(\theta_{\vec{p}_L})$.

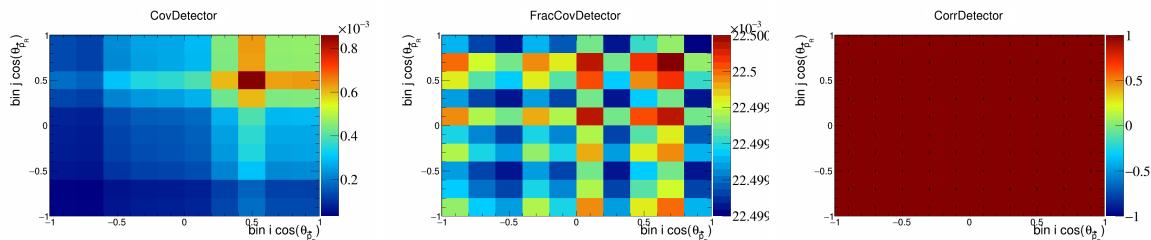


Figure 822: Detector variations for $\cos(\theta_{\vec{p}_R})$.

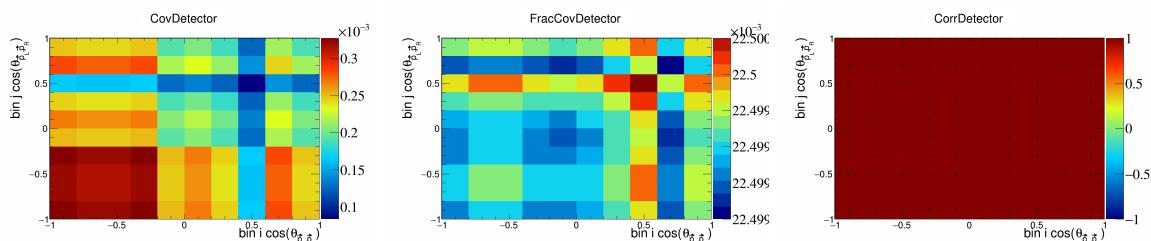


Figure 823: Detector variations for $\cos(\theta_{\vec{p}_L, \vec{p}_R})$.

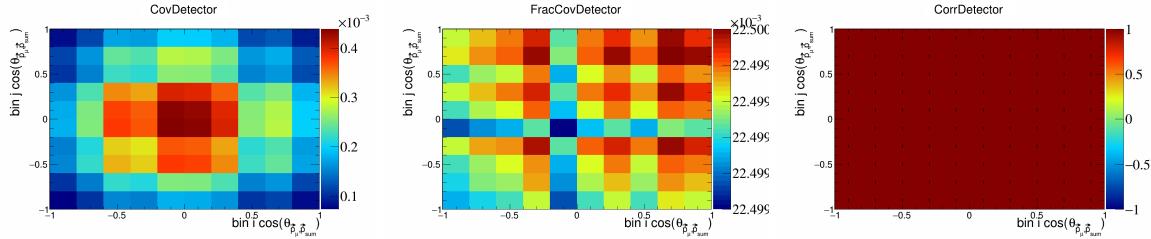


Figure 824: Detector variations for $\cos(\theta_{\vec{p}_\mu, \vec{p}_{\text{sum}}})$.

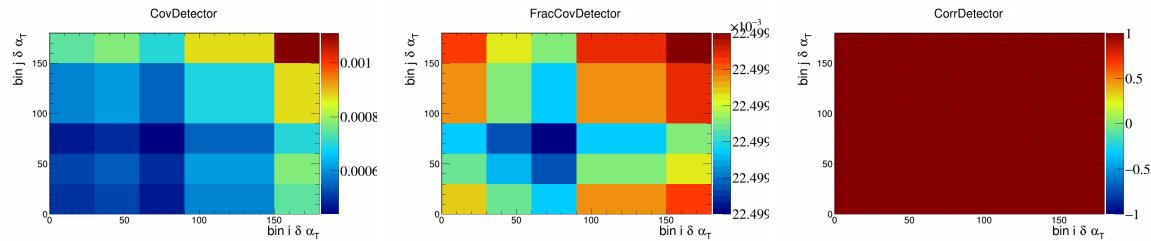


Figure 825: Detector variations for $\delta \alpha_T$.

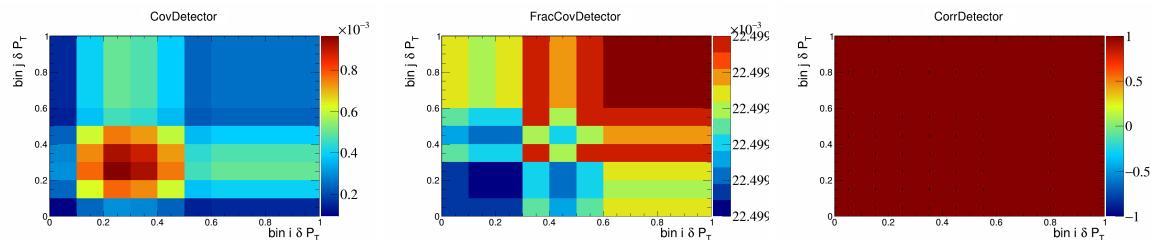


Figure 826: Detector variations for δP_T .

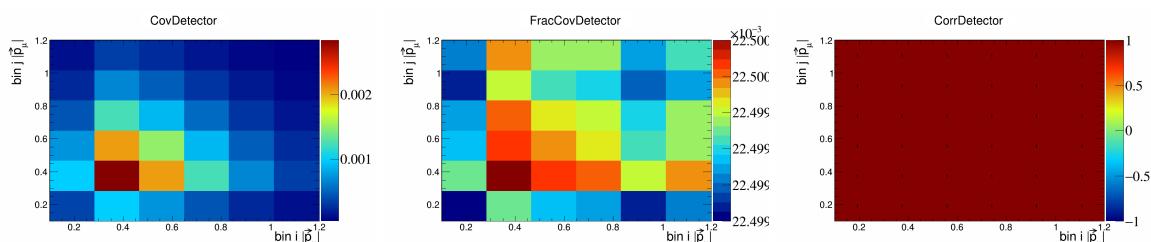


Figure 827: Detector variations for $|\vec{p}_\mu|$.

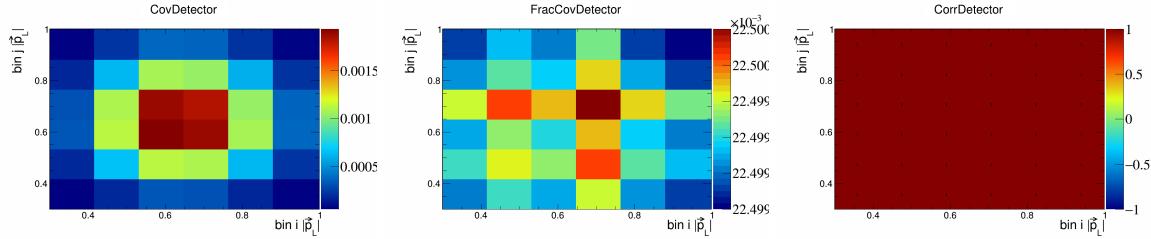


Figure 828: Detector variations for $|\vec{p}_L|$.

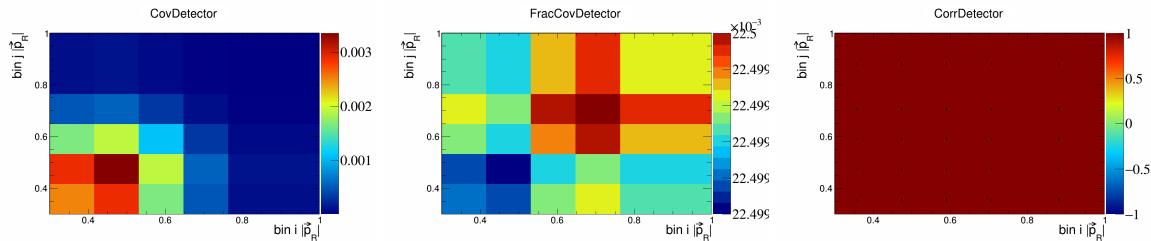


Figure 829: Detector variations for $|\vec{p}_R|$.

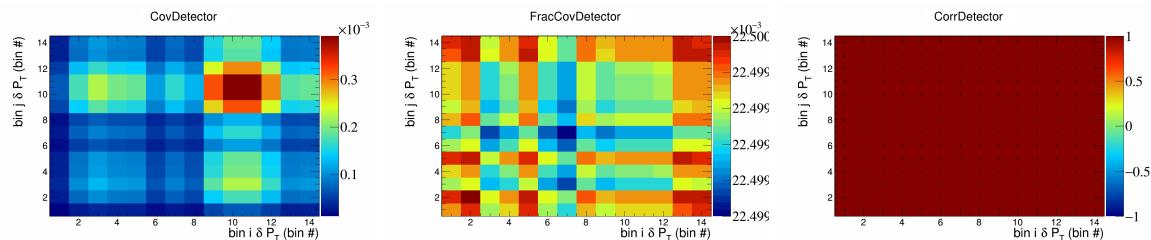


Figure 830: Detector variations for δP_T in $\cos(\theta_{\vec{p}_\mu})$.

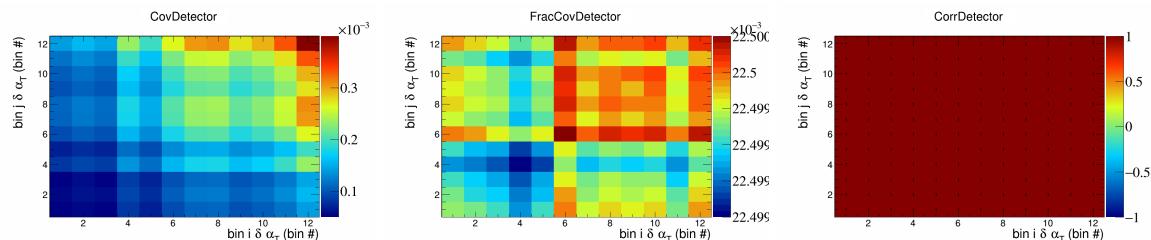


Figure 831: Detector variations for $\delta \alpha_T$ in $\cos(\theta_{\vec{p}_\mu})$.

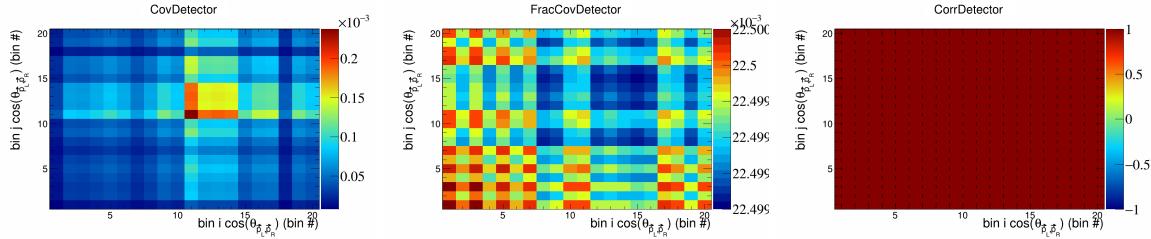


Figure 832: Detector variations for $\cos(\theta_{\vec{p}_L, \vec{p}_R})$ in $\cos(\theta_{\vec{p}_\mu})$.

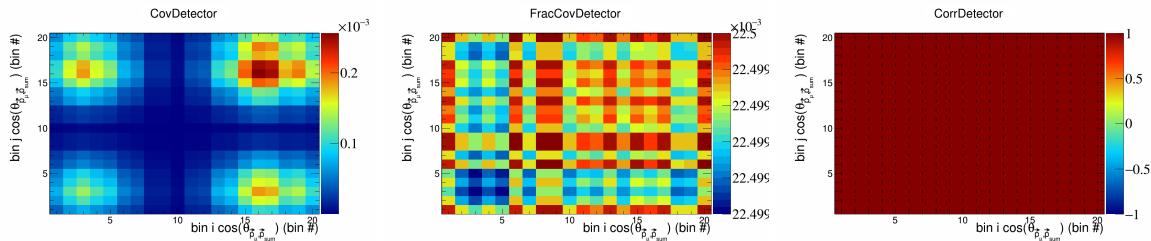


Figure 833: Detector variations for $\cos(\theta_{\vec{p}_\mu, \vec{p}_{\text{sum}}})$ in $\cos(\theta_{\vec{p}_\mu})$.

290 **6.7 Reinteraction**

291 In this appendix, the covariance, fractional covariance, and correlation matrices for the reinteraction sys-
292 tematics are plotted.

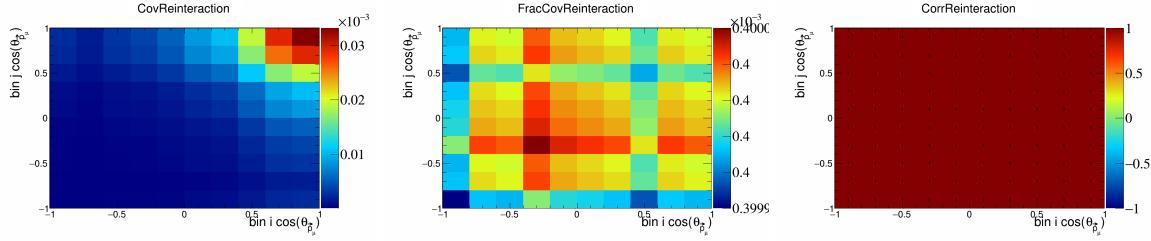


Figure 834: Reinteraction variations for $\cos(\theta_{\vec{p}_\mu})$.

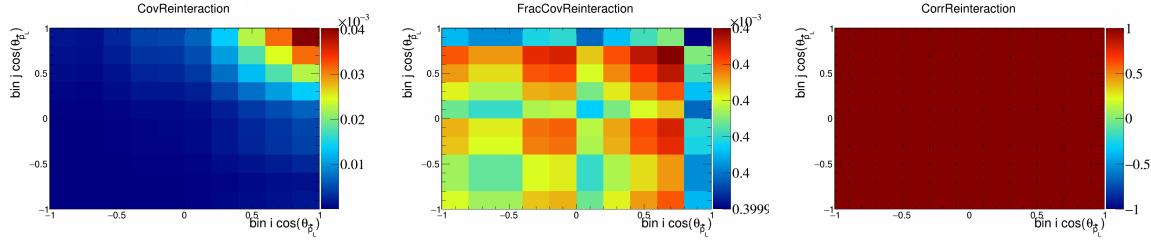


Figure 835: Reinteraction variations for $\cos(\theta_{\vec{p}_L})$.

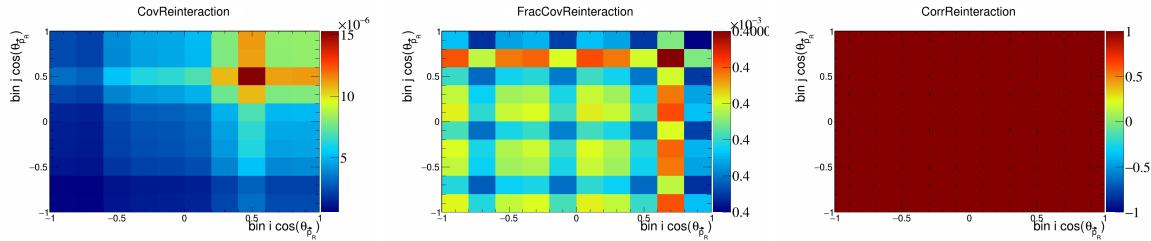


Figure 836: Reinteraction variations for $\cos(\theta_{\vec{p}_R})$.

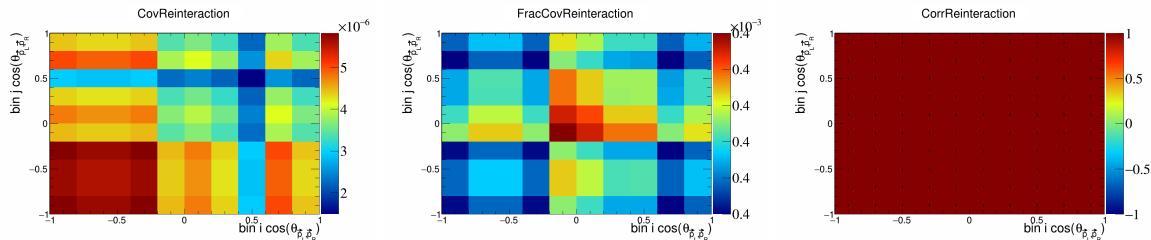


Figure 837: Reinteraction variations for $\cos(\theta_{\vec{p}_L, \vec{p}_R})$.

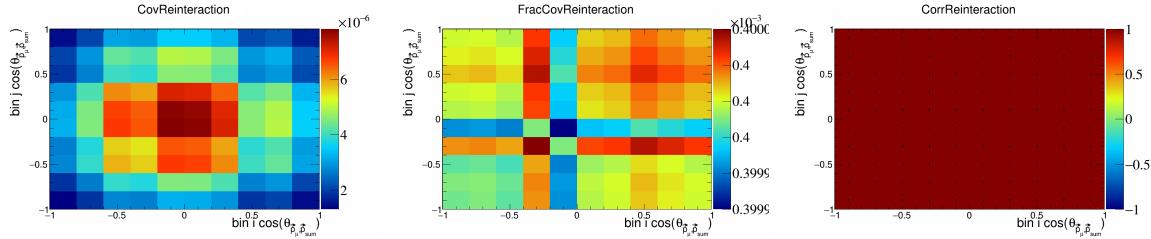


Figure 838: Reinteraction variations for $\cos(\theta_{\vec{p}_\mu, \vec{p}_{\text{sum}}})$.

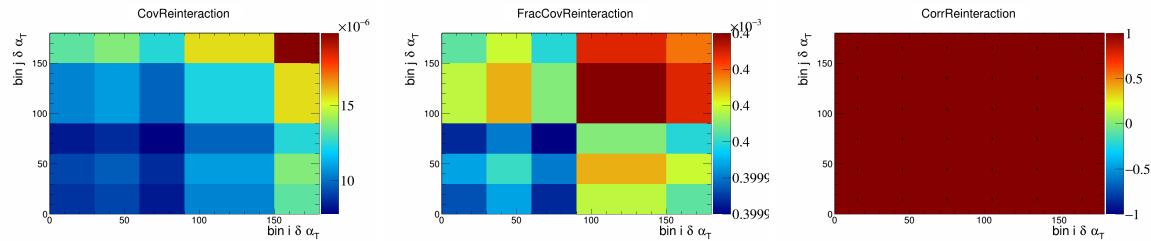


Figure 839: Reinteraction variations for $\delta \alpha_T$.

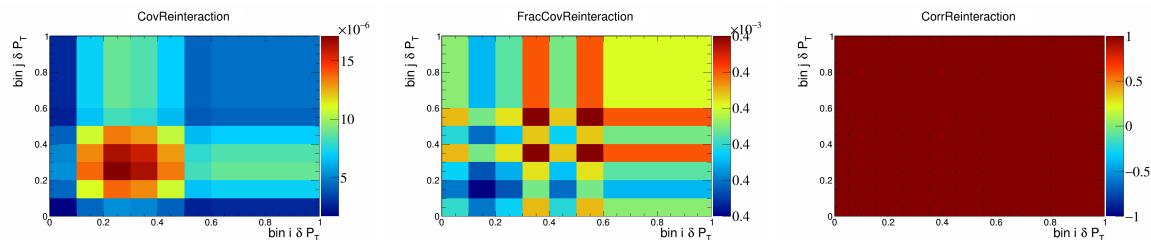


Figure 840: Reinteraction variations for δP_T .

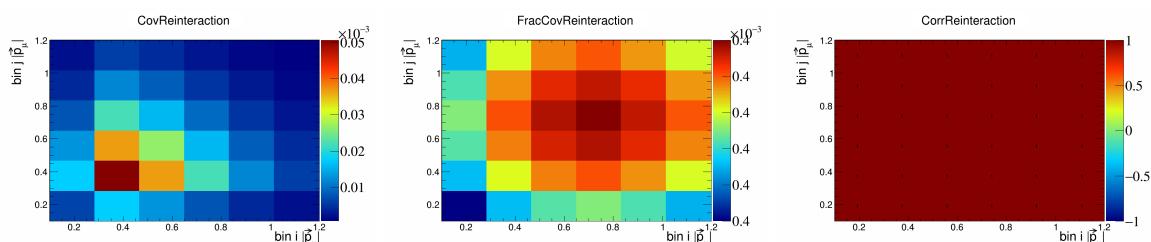


Figure 841: Reinteraction variations for $|\vec{p}_\mu|$.

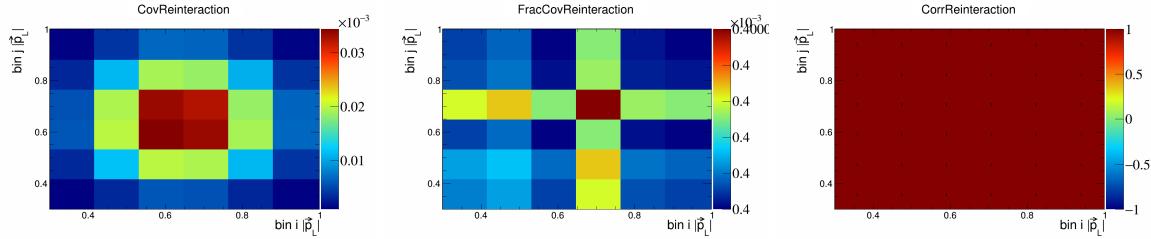


Figure 842: Reinteraction variations for $|\vec{p}_L|$.

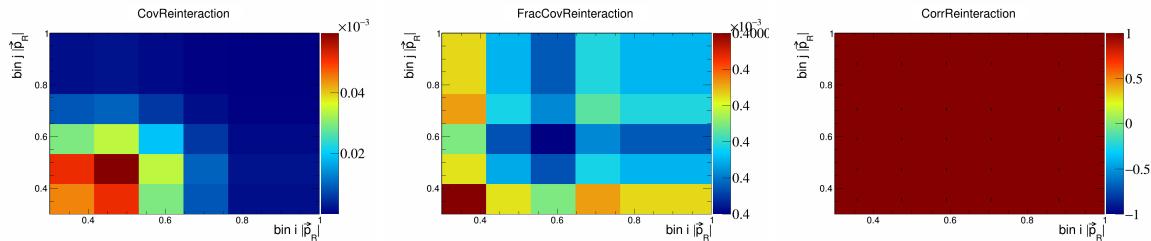


Figure 843: Reinteraction variations for $|\vec{p}_R|$.

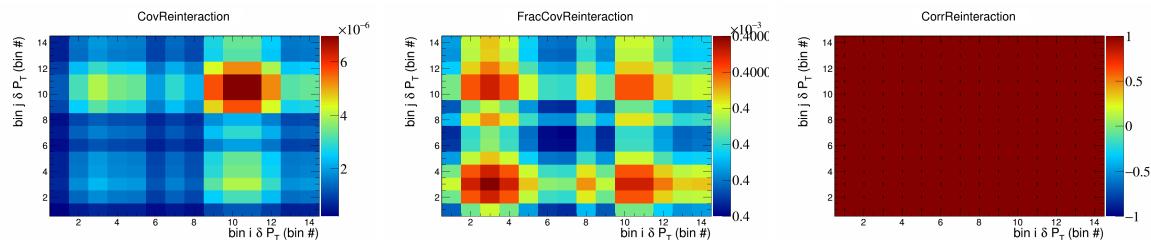


Figure 844: Reinteraction variations for δP_T in $\cos(\theta_{\vec{p}_\mu})$.

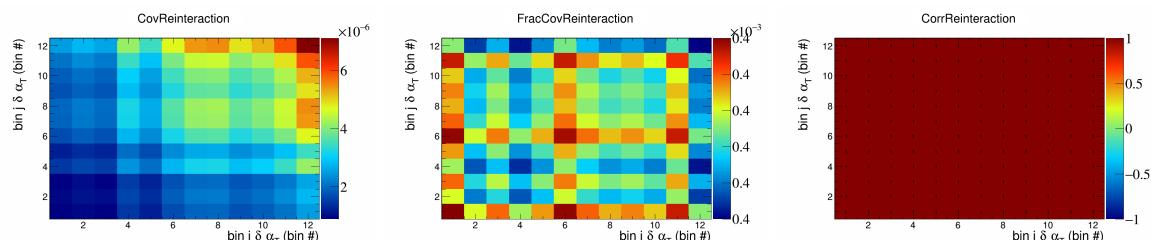


Figure 845: Reinteraction variations for $\delta \alpha_T$ in $\cos(\theta_{\vec{p}_\mu})$.

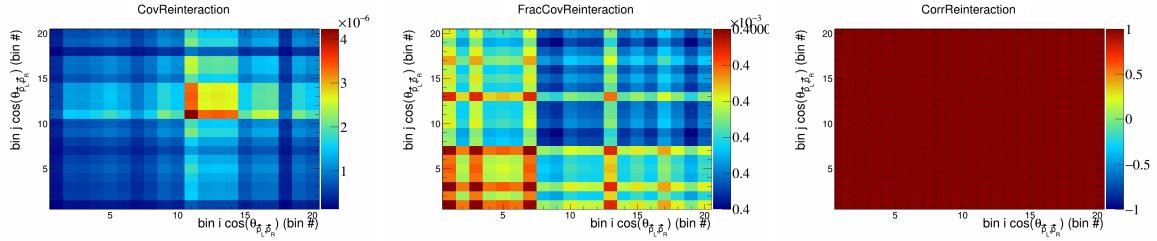


Figure 846: Reinteraction variations for $\cos(\theta_{\vec{p}_L, \vec{p}_R})$ in $\cos(\theta_{\vec{p}_\mu})$.

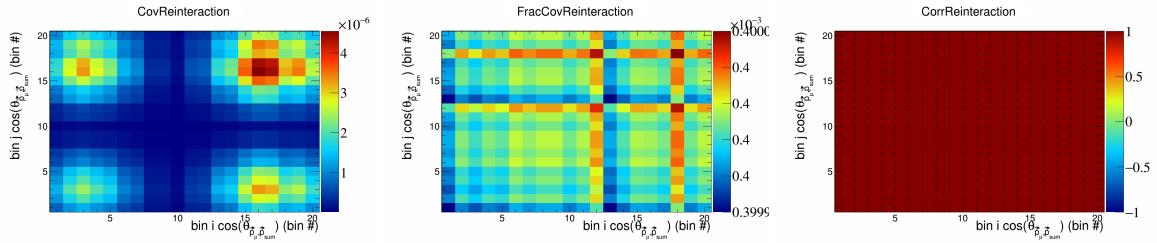


Figure 847: Reinteraction variations for $\cos(\theta_{\vec{p}_\mu, \vec{p}_{\text{sum}}})$ in $\cos(\theta_{\vec{p}_\mu})$.

293 **7 References**

- [1] R. Acciarri, C. Adams, J. Asaadi, B. Baller, T. Bolton, C. Bromberg, F. Cavanna, E. Church, D. Edmunds, A. Ereditato, S. Farooq, B. Fleming, H. Greenlee, G. Horton-Smith, C. James, E. Klein, K. Lang, P. Laurens, R. Mehdiyev, B. Page, O. Palamara, K. Partyka, G. Rameika, B. Rebel, M. Soderberg, J. Spitz, A. M. Szelc, M. Weber, T. Yang, and G. P. Zeller. Detection of back-to-back proton pairs in charged-current neutrino interactions with the argoneut detector in the numi low energy beam line. *Phys. Rev. D*, 90:012008, Jul 2014.
- [2] C. Andreopoulos, A. Bell, D. Bhattacharya, F. Cavanna, J. Dobson, S. Dytman, H. Gallagher, P. Guzowski, R. Hatcher, P. Kehayias, A. Meregaglia, D. Naples, G. Pearce, A. Rubbia, M. Whalley, and T. Yang. The genie neutrino monte carlo generator. *Nuclear Instruments and Methods in Physics Research Section A: Accelerators, Spectrometers, Detectors and Associated Equipment*, 614(1):87–104, 2010.
- [3] Costas Andreopoulos, Christopher Barry, Steve Dytman, Hugh Gallagher, Tomasz Golan, Robert Hatcher, Gabriel Perdue, and Julia Yarba. The genie neutrino monte carlo generator: Physics and user manual, 2015.
- [4] D. Ashery, I. Navon, G. Azuelos, H. K. Walter, H. J. Pfeiffer, and F. W. Schlepütz. True absorption and scattering of pions on nuclei. *Phys. Rev. C*, 23:2173–2185, May 1981.
- [5] P. S. Auchincloss, R. Blair, C. Haber, E. Oltman, W. C. Leung, M. Ruiz, S. R. Mishra, P. Z. Quintas, F. J. Sciulli, M. H. Shaevitz, W. H. Smith, F. S. Merritt, M. Oreglia, P. Reutens, R. Coleman, H. E. Fisk, D. Levinthal, D. D. Yovanovitch, W. Marsh, P. A. Rapidis, H. B. White, A. Bodek, F. Borcherding, N. Giokaris, K. Lang, and I. E. Stockdale. Measurement of the inclusive charged-current cross section for neutrino and antineutrino scattering on isoscalar nucleons. *Zeitschrift für Physik C Particles and Fields*, 48(3):411–431, Sep 1990.
- [6] Ch. Berger and L. M. Sehgal. Lepton mass effects in single pion production by neutrinos. *Phys. Rev. D*, 76:113004, Dec 2007.
- [7] Ch. Berger and L. M. Sehgal. Partially conserved axial vector current and coherent pion production by low energy neutrinos. *Phys. Rev. D*, 79:053003, Mar 2009.
- [8] B. Bourguille, J. Nieves, and F. Sánchez. Inclusive and exclusive neutrino-nucleus cross sections and the reconstruction of the interaction kinematics. *Journal of High Energy Physics*, 2021(4):4, Apr 2021.
- [9] R.C. Carrasco and E. Oset. Interaction of real photons with nuclei from 100 to 500 mev. *Nuclear Physics A*, 536(3):445–508, 1992.
- [10] R. Cruz-Torres, D. Lonardoni, R. Weiss, N. Barnea, D. W. Higinbotham, E. Piasetzky, A. Schmidt, L. B. Weinstein, R. B. Wiringa, and O. Hen. Many-body factorization and position-momentum equivalence of nuclear short-range correlations. *Nature Phys.*, 17(3):306–310, 2021.
- [11] Jonathan Engel. Approximate treatment of lepton distortion in charged-current neutrino scattering from nuclei. *Phys. Rev. C*, 57:2004–2009, Apr 1998.
- [12] T. Golan, J.T. Sobczyk, and J. Źmuda. Nuwro: the wrocław monte carlo generator of neutrino interactions. *Nuclear Physics B - Proceedings Supplements*, 229-232:499, 2012. Neutrino 2010.
- [13] Krzysztof M. Graczyk and Jan T. Sobczyk. Form factors in the quark resonance model. *Phys. Rev. D*, 77:053001, Mar 2008.
- [14] Yoshinari Hayato and Luke Pickering. The neut neutrino interaction simulation program library. *The European Physical Journal Special Topics*, 230(24):4469–4481, Dec 2021.
- [15] Teppei Katori. Meson exchange current (MEC) models in neutrino interaction generators. *AIP Conference Proceedings*, 1663(1):030001, 05 2015.

- 337 [16] Konstantin S. Kuzmin, Vladimir V. Lyubushkin, and Vadim A. Naumov. Lepton polarization in neutrino–nucleon interactions. *Modern Physics Letters A*, 19(38):2815–2829, 2004.
- 338
- 339 [17] T. Leitner, L. Alvarez-Ruso, and U. Mosel. Charged current neutrino-nucleus interactions at intermediate energies. *Phys. Rev. C*, 73:065502, Jun 2006.
- 340
- 341 [18] C.H. Llewellyn Smith. Neutrino reactions at accelerator energies. *Physics Reports*, 3(5):261–379, 1972.
- 342 [19] Selection of numu charged current induced interactions with $N > 0$ protons and performance of events with $N = 2$ protons in the final state in the MicroBooNE detector from the BNB, Oct 2018.
- 343
- 344 [20] First Extraction of Single Differential Cross-Sections on Argon for CC1 μ 2p0 π Event Topologies in the MicroBooNE Detector. May 2022.
- 345
- 346 [21] Ulrich Mosel. Neutrino event generators: foundation, status and future. *Journal of Physics G: Nuclear and Particle Physics*, 46(11):113001, Sep 2019.
- 347
- 348 [22] J. Nieves, J. E. Amaro, and M. Valverde. Inclusive quasielastic charged-current neutrino-nucleus reactions. *Phys. Rev. C*, 70:055503, Nov 2004.
- 349
- 350 [23] J. Nieves, F. Sánchez, I. Ruiz Simo, and M. J. Vicente Vacas. Neutrino energy reconstruction and the shape of the charged current quasielastic-like total cross section. *Phys. Rev. D*, 85:113008, Jun 2012.
- 351
- 352 [24] J. Nieves, I. Ruiz Simo, and M. J. Vicente Vacas. Inclusive charged-current neutrino-nucleus reactions. *Phys. Rev. C*, 83:045501, Apr 2011.
- 353
- 354 [25] J. Schwehr, D. Cherdack, and R. Gran. Genie implementation of ific valencia model for qe-like 2p2h neutrino-nucleus cross section, 2017.
- 355
- 356 [26] Torbjörn Sjöstrand, Stephen Mrenna, and Peter Skands. Pythia 6.4 physics and manual. *Journal of High Energy Physics*, 2006(05):026, may 2006.
- 357
- 358 [27] W. Tang, X. Li, X. Qian, H. Wei, and C. Zhang. Data unfolding with wiener-svd method. *Journal of Instrumentation*, 12(10):P10002–P10002, October 2017.
- 359
- 360 [28] Júlia Tena-Vidal, Costas Andreopoulos, Adi Ashkenazi, Christopher Barry, Steve Dennis, Steve Dytman, Hugh Gallagher, Steven Gardiner, Walter Giele, Robert Hatcher, Or Hen, Libo Jiang, Igor D. Kakorin, Konstantin S. Kuzmin, Anselmo Meregaglia, Vadim A. Naumov, Afroditi Papadopoulou, Gabriel Perdue, Marco Roda, Vladyslav Syrotenko, and Jeremy Wolcott. Neutrino-nucleon cross-section model tuning in genie v3. *Phys. Rev. D*, 104:072009, Oct 2021.
- 361
- 362 [29] U. K. Yang and A. Bodek. Parton distributions, d/u , and higher twist effects at high x . *Phys. Rev. Lett.*, 82:2467–2470, Mar 1999.
- 363
- 364
- 365
- 366